9th International Conference on High-Power Particle Beams

Beams 92

Washington, DC
May 25–29, 1992

N00014-91-J-1955

VOLUME II

Ion Beams
Electron Beams
Diagnostics

Edited by
David Mosher
and
Gerald Cooperstein

Beams 92

Proceedings of the
9th International Conference on High-Power Particle Beams

Washington, DC
May 25 - 29, 1992

Edited by

David Mosher and Gerald Cooperstein
Naval Research Laboratory

Volume II

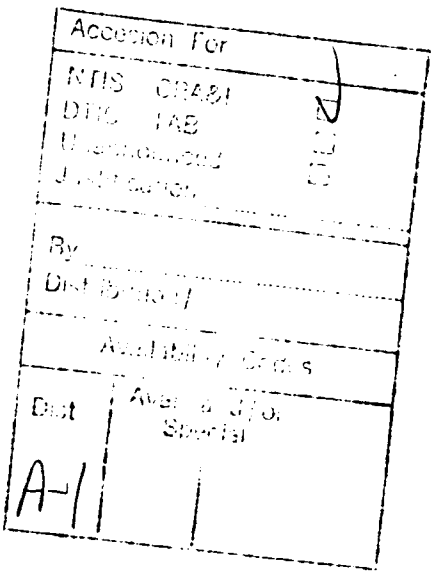

Beams 92

Proceedings of the
9th International Conference on High-Power Particle Beams

NTIS PB92-206168

Copies of these proceedings can be ordered from the National Technical Information Service (NTIS).

NTIS
PO Box 1425
Springfield, VA 22151
(703) 487-4690

Paper Index - Volume I

Invited Ion Beam Papers

Invited Electron Beam, Bremsstrahlung, and Diagnostics Papers

Invited Radiating Z-Pinch Papers

Invited Microwave Papers

Invited Free Electron Laser Papers

Invited Advanced Accelerator Papers

Invited Beam and Pulsed Power Applications Papers

Invited Pulsed Power Papers

Contributed Pulsed Power Papers

Paper Index - Volume II

Contributed Ion Beam Papers

Contributed Electron Beam Papers

Contributed Beam Diagnostics Papers

Paper Index - Volume III

Contributed Microwave Papers

Contributed Free Electron Laser Papers

Contributed Advanced Accelerator Papers

Contributed Beam Applications Papers

Contributed Plasma Discharge Papers

Contributed Ion Beam Papers

NEW RESULTS FROM EXPERIMENTAL AND NUMERICAL INVESTIGATIONS OF THE SELF-MAGNETICALLY B_θ-INSULATED ION DIODE.

W. Bauer, H. Bachmann, H. Bluhm, L. Buth. P. Hoppé, H. U. Karow, H. Lotz, D. Rusch, Ch. Schultheiss, E. Stein, O. Stoltz, Th. Westermann

Kernforschungszentrum Karlsruhe GmbH,
Institut für Neutronenphysik und Reaktortechnik
P.O. - Box 3640, W-7500 Karlsruhe,
Federal Republic of Germany

Due to its reliability and reproducibility the B_θ-Diode is now used routinely for testing new diagnostics and experimental set-ups. The numerical simulations and the experimental investigations of the B_θ-Diode described at the BEAMS-90-Conference [1] were continued. Using a numerically optimized anode shape did not improve the focusing properties; as the main reason the large beam divergence of ±3° was identified. Reducing the electric field parallel to the plastic anode surface by decreasing the distance of the metal pins had no effect on the divergence. Experiments using a thin film Pd covered Ti-hydride-anode to improve the divergence and to increase the focused power density beyond the presently achieved value of about 0.3 TW/cm^2 will be described. Numerical simulations suggesting a possible improvement of the focusing at the edges of the anode will be presented.

I. Introduction

The selfmagnetically insulated B_θ-ion-diode [1] is now used routinely at KALIF [2] in experiments where new diagnostics are to be developed or as a diode load with known properties after maintenance or changes of the pulse machine. Since it can be fired about 10-15 times at the full power of KALIF (1.7 MV, 0.8 MA, 50 ns) without opening the vacuum system and without changing parts, and since it maintains its electric properties within 10 % throughout these shots, it is very well suited for this kind of tasks. The focused ion beam it produces, however, does not exceed a power density of about 0.3 TW/cm^2, limited by a beam divergence of ±3°. The following paper describes the experiments carried through with the aim to increase the power density and PIC-code simulations that give hints to further improve the focusing.

II. Experiments with flashover anode.

In ref. [1] experiments with an anode shape optimized by PIC-simulations [3] have been promised. The result of these experiments was disappointing, since the power density and the focus diameter remained at 0.24 TW/cm^2 and ≈ 15 mm, respectively; they were not improved by the optimized anode shape [3].

A measurement of the beam divergence showed the reason, why the optimized anode geometry did not improve the focus diameter: In a modified shadowbox a Boron foil was used instead of a witness plate and the α-particles generated there were observed by a pinhole-camera and recorded on CR-39-film. The evaluation of the density distribution on this film shown in Fig. 1 revealed several interesting properties of the diode.

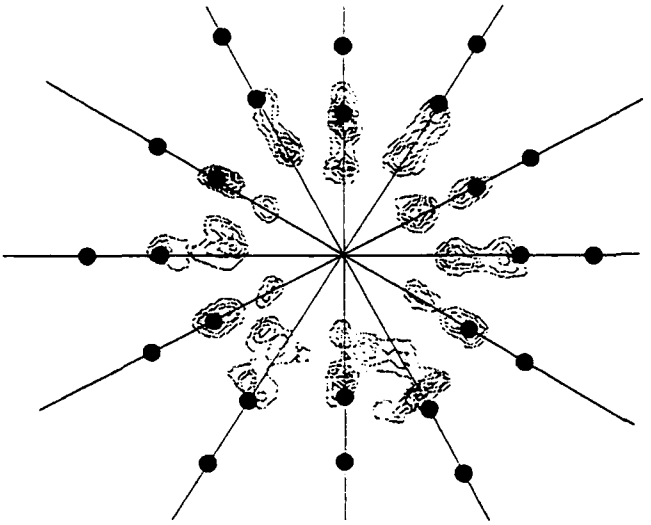

Fig. 1: Density plot of α-particles on the CR-39 - film used to measure the beam divergence. The black dots represent the apertures of the shadowbox, situated 25 mm before the Boron foil.

The azimuthal extension of the traces points to a FWHM diameter of the beamlets of about 4 mm, resulting in an azimuthal micro-divergence of ± 1.9°. In addition the traces show azimuthal and radial displacements, from which a macro-divergence of ±1.6° can be deduced. The resulting total divergence of about ± 3° translates at a focus distance of 160 mm into a FWHM-focus diameter of ≈ 15 mm. This explains the result of the measurement mentioned above: An optimization of the anode geometry to a focus diameter of less than 15 mm cannot be seen due to this divergence.

The radial extension of the traces can be used to evaluate the chromatic aberration due to the time-varying magnetic field. Values of up to 5° are observed.

To reduce the divergence the distance between the metallic pins in the plastic flashover anode was reduced from 5 to 2.5 mm. This was expected to produce a more homogeneous anode plasma and to

reduce the microdivergence by reducing the component of the electric field parallel to the anode surface. The result was a divergence picture similar to Fig. 1, therefore it must be concluded, that the divergence observed is due to anode plasma discontinuities, beam instabilities or influence of the cathode plasma on the beam.

The best shot, however, showed a power density of 0.27 TW/cm^2. This result was obtained with a ≈ 10% foot preceding the main pulse. Since without this foot the power density is in general somewhat less, one might suppose that the turn-on of the flash-over anode is supported by the foot.

III. Experiment with a thin film Ti/Pd - anode.

The success in our experiments with the B_{appl}-diode [4] using an anode with a Ti/Pd layer as a hydrogen-storing film guided us to try the same anode type also with the B_θ-diode. It must, however, be mentioned, that this anode removes one of the positive features of this diode: It becomes a single shot device and has to be restored after each shot. In addition, due to the design

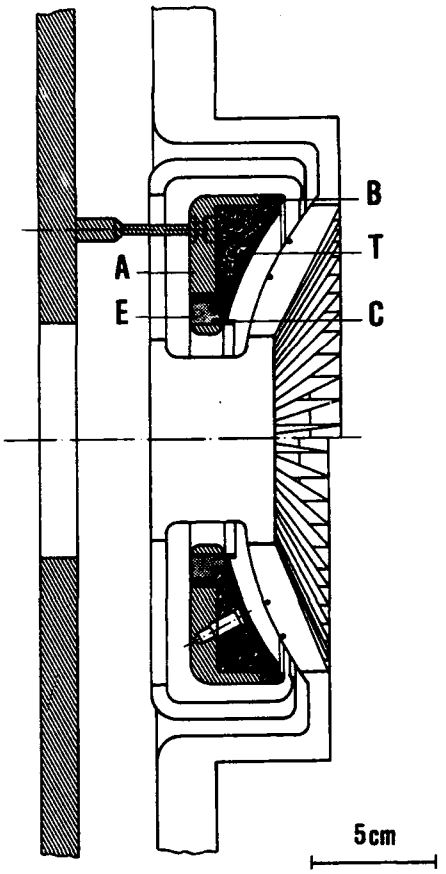

Fig. 2: Modified B_θ-Diode with Ti/Pd film T insulated by epoxy E from the anode A. The ring C is supposed to collect electrons gyrating in the gap and to guide them through the Ti/Pd film which is connected to the anode potential at B by evaporated Aluminum.

of the B_θ-diode it is difficult to provide a current path for a separate pulse to turn the anode on. We used the first electrons striking the anode before the magnetic insulation is effective for turn-on. To guide a current through the Ti/Pd film an electron collector ring of adjustable height was provided as shown in Fig. 2. Although the ring protruded from 2 mm into the gap to 5 mm the inner part of the anode was severely damaged and most of the epoxy layer that insulated the Ti/Pd film was destroyed. The resulting proton power density and the micro-divergence were similar to those

with flashover anode. The electrical signals did not show an earlier turn-on of the anode or a faster ion current rise. It has, therefore, to be concluded that the epoxy insulating the Ti/Pd layer from the anode served as flashover anode and the behaviour of the diode was not changed at all by the Ti/Pd film. To improve this situation the design will be changed in such a way, that the region of electron impact becomes void of epoxy and Ti/Pd.

IV. Numerical "Experiments"

We use the quasistatic - 2-dimensional particle in cell code "BFCPIC2D" developed by T. Westermann [5].

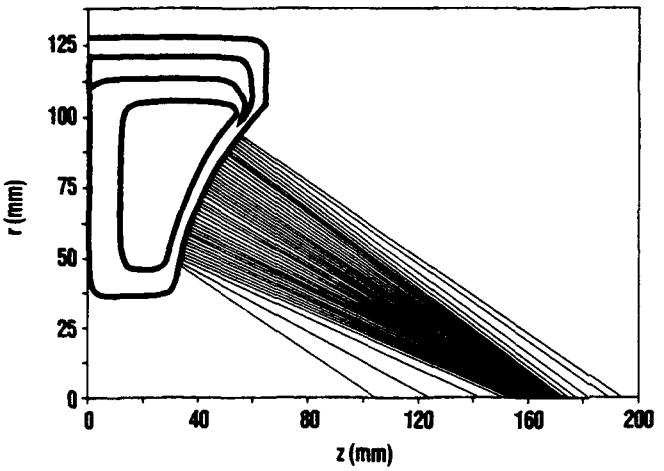

Fig. 3: Focusing properties after optimization with the OPTGEO code.

A hint for a further improvement of the focusing can be seen in Fig.3: Both the outer and the inner ion trajectories show a poor focusing, which could not be influenced by optimizing the anode shape [3]. To bend the outer beams more and the inner ones less would improve the focusing.

Fig. 4 shows the equipotential lines in the vicinity of that point, at which the ion emitting part of the anode ends and the non-emitting part starts. Due to the space charge of the ions emitted from the anode the lines are shifted away from the anode and the electric field is directed outward at this point; therefore particles generated at the very edge of the anode are accelerated outwards, since they follow the electric lines. The same is true at the inner edge of the ion emitting part of the anode where an additional inward bending of the trajectories is observed.

Two methods have been worked out [6] to counteract this effect: First the non emitting part of the anode was bent outward by 30° as shown in Fig. 5 (left). As can be seen in the figure this bent

was sufficient to release the ions just under the correct angle into the direction of the focus.

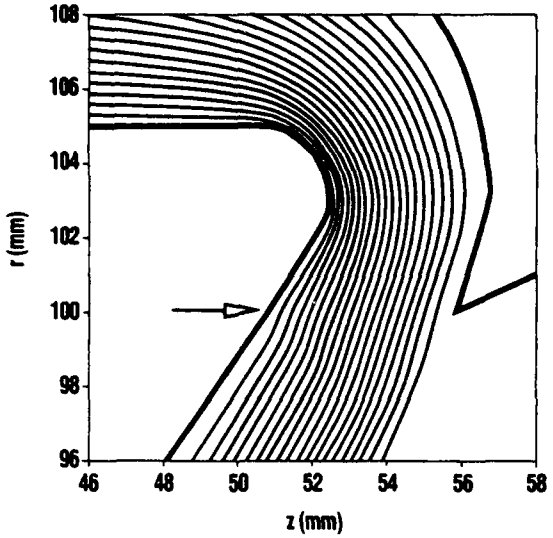

Fig. 4: Equipotential lines around the border between ion emitting and not emitting part of the anode (arrow). The lines are slightly bent, showing that the electric field is directed outward at this point.

This change in the anode geometry is difficult to realize in hardware, therefore in Fig. 5 (right) another method to solve the problem is shown: A sharp step only one millimeter deep had the same effect as the bent! This step can easily be designed into the anode and will be tried in a forthcoming experimental run.

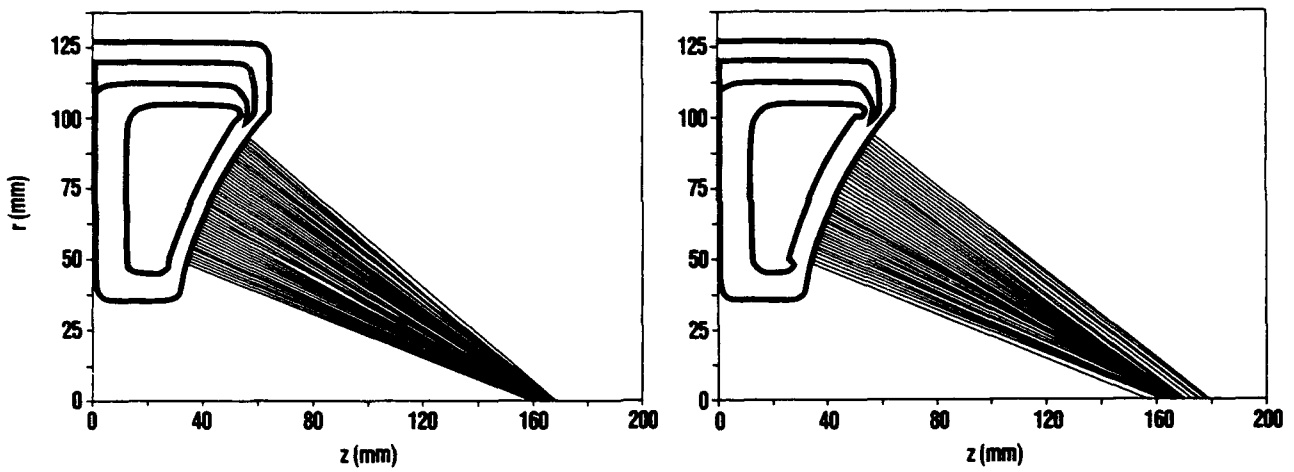

Fig. 5: Improved focusing properties after modifications on the non-emitting parts of the anode: 30° bend (left), 1 mm step (right).

V. Conclusions.

The results presented show that the performance of the B_θ-diode is still limited by the beam divergence of ±3°. It was not improved by measures at the anode. We have some evidence that the flashover anode turns on more homogeneously when a foot precedes the main pulse. The application of the Ti/Pd-anode for the B_θ-diode needs further design improvements. Particle-in-cell calcu-

lations using the "BFCPIC2D"-code were used to study details of the focusing at the edges of the ion emitting part of the anode.

Acknowledgement.

We thank the KALIF operating crew under W. Ratajczak and the workshops under S. Gaukel and R. Eggmann for their continuing effort. The CR-39 films were computer analysed by H. Guth.

References:

[1] W. Bauer, H. Bachmann, H. Bluhm, P. Hoppé, H. U. Karow, D. Rusch, Ch. Schultheiss, E. Stein, O. Stolz, T. Westermann, "Computations and Experiments on the "Small B_θ-Diode", in B. N. Breizman and B. A. Knyazev ed. Proc. Eighth Int. Conf. High-Power Particle Beams Novosibirsk, World Scien tific Singapore (1990) 457-462

[2] K. Baumung, G. I. Kanel, H. U. Karow, V. Licht, D. Rusch, J. Singer, O. Stoltz, G. Arnecke, H. Bachmann, W. Bauer, H.J. Bluhm, L. Buth, B. Goel, M. F. Goez, P. Hoppé, H. Lotz, C. D. Munz, "Hydrodynamic Target Experiments with Proton Beams at the KALIF facility: Diagnostics of the Ablation Pressure by Laser Doppler Interferometry; Generation of Very-High Pressures by Ablative Foil Acceleration and Impact", this conference

[3] T. Westermann, "Optimization by numerical simulation of the focusing properties of self-magnetically insulated ion diodes", App. Phys. Lett. **58** (1991) 696-698

[4] H. Bluhm, P. Hoppé, H. Bachmann, W. Bauer, K. Baumung, L. Buth, H.U. Karow, H. Laqua, D. Rusch, E. Stein, O. Stoltz "Focusing properties of a strongly insulated applied B_r-proton diode with a preformed anode plasma source", this conference

[5] T. Westermann, "A Particle-in-Cell Method as a Tool for Diode Simulations" Nuclear Instr. Meth. **A263**, 271 (1988)

[6] T. Westermann, W. Bauer, "Treatment of Edge Beams in a Focusing Self-Magnetically B_θ-insulated Ion Diode", accepted for publication in Laser and Particle Beams (1992)

Generation of Strong Radial Magnetic Insulation Fields in High Power Ion Diodes in Extraction Geometrie

P. Hoppé, H.-J. Bluhm, H. Laqua, O. Stoltz

Kernforschungszentrum Karlsruhe, Institut für Neutronenphysik und Reaktortechnik

P.O.Box 35 40, W-7500 Karlsruhe, Germany

Abstract

The efficient conversion of the electromagnetic energy delivered by the TW pulsed power generator KALIF into a high power ion beam requires a strong externally applied magnetic field which suppresses the electron flow. This pulsed insulating magnetic field is produced by two coils concentric to the beam axis and placed on the cathode side of the ion beam diode of the extraction type used in our experiments. Operating this diode with ratios of Vcrit to Vdiode >3, a field strength near the anode surface of 3 T typically had to be generated by coil currents peaking around 50 kA. With the dimensions of the coils fixed by the diodes emitting area this resulted in hoop forces up to 300 kN acting on the inner coil of just 10 cm outer diameter. The technologies developed and applied to solve the resulting mechanical, high voltage, thermal, vacuum and shock wave problems will be described. Furthermore the generated field with respect to its strength, symmetry and time response will be compared to calculations. Finally will be discussed: the influence of the insulation field strength on the ion production efficiency and the design of future field coils for higher accelerating voltages.

Introduction

The efficient conversion of the electromagnetic energy delivered by the pulse power generator KALIF into a high power ion beam requires a strong magnetic insulation field which ideally completely suppresses the electron losses to the anode. In selfinsulating diodes this field is produced by the time depending electron and ion currents: electron losses are balanced by the self fields. The use of an additional externally generated insulating field - the applied field which is independent of the diode currents - may during the whole power pulse completely suppress the electron losses. For diodes which need these losses for the generation of the anode plasma (flash over anodes) a strong applied magnetic field is not feasible. The use of such an insulation field requires an active anode plasma source operating independently from the electron losses. So far strong applied fields could not be used in efficient ion beam diodes due to problems with both, the production of the anode plasma and the generation of the strong applied field. This paper deals with the generation of such fields for ion diodes in extraction geometries and summarizes the experience gained in the development of the field coils and their technology. The characteristics of the generated field were measured and compared to calculations. Finally the influence of fields with different insulation strength on the diode characteristics are shown.

Requirements

The applied magnetic field to be generated in the anode/cathode region of the extractor diode is characterized by the following physical and technological arguments:

- the electron insulation described by the critical voltage

$$V_{crit} = \frac{mc^2}{e} \left| \sqrt{\left(\frac{e}{mc} \frac{\Delta\psi}{r_a} \right)^2 + 1} - 1 \right|$$

with $\psi = rA_\Theta$ as the magnetic stream function, r the radius and A_Θ the azimuthal component of the vectorpotential A, related to the magnetic field by B = rot A.

- the applied field vector must always be perpendicular to the electric field vector, i.e. using the established coordinate systems, the insulating field components are B_r for the extractor and B_z for the barrel type diode with always the z-axis as the axis of symmetry. The electrons forming the virtual cathode follow the flux lines of the field, therefore they must be parallel to the surface of the anode for a constant virtual AK-gap.
- the canonical angular momentum for ions starting from the surface of the anode (or the anode plasma) must be zero if they should focus into one spot F, which requires that the flux between the ion emitting surface A and F must be zero: $\Delta\psi/_{AF} = 0$. Due to the limited conductivity of the anode plasma (or the metal anode surface), flux losses of the insulating field occur and must be compensated by an opposite field. The resulting reduction of the insulation field can be reduced by using a "slow" compensation field which diffuses further into the anode structures compared to the "fast" insulation field. This compensation field can be either produced by additional coils on the anode side or by the coils for the generation of the insulation field on the cathode side. The capacitor bank then has to deliver a slow current, producing eddy currents for the compensating field followed by the fast opposite current for the insulation field.
- the formation of the effective AK-gap depends on the expansion of the anode plasma (pressure $p_p \approx nkT$) against the pressure of the magnetic field $P_m = B^2/2\mu_0$. The plasma expansion may be reduced and hence the diode impedance may be stabilized for Pm≫Pp. The same effect will be achieved by keeping the electrons on field lines closer to the emitting edge of the cathode. A high value of V_{crit} / V_d and hence a high magnetic field will stabilize the diode impedance.

For V_d = 1.7 MV, $V_{crit}/V_d \approx 3 ....4$, a geometrical AK-gap of 8.5 mm and an anode surface under 53° this leads to an initial field strength of 2 ....3 T at the anode surface and an insulating stream function around 1.5×10^{-3} Vs. Compared to the 100 ns KALIF pulse length a quarter period of the fast insulation field $T_f/4 \approx 70$ µs is equivalent. Due to technical reasons the compensation field is also produced from the coils on the cathode side; for $T_s/4 \approx 1.5$ ms this slow field produces eddy currents diffusing ~ 6 times further into the anode structures.

The technological arguments for the coil design are quite numerous, the most important ones are:

- azimuthal unsymmetries in the generated fields influence the AK-gap and will produce inhomogenities in the ion current distribution.
- the diode operates in vacuum ($\leq 10^{-4}$ mbar) which must be maintained during coil operation. The same argument is valid for the neutralisation gas in the drift section (~ 5 mbar), i.e. the coil must allow for the mounting of a thin Mylar-foil (1.7 µm), separating the vacuum from the drift space and must itself be vacuum tight.

- the energy delivered by the driver bank for the currents through the coils should be converted into magnetic field energy, eddy currents on the cathode side (e.g. in the protecting/supporting structures) should be minimized.
- the fields produced should be reproducible for at least 20 shots.
- handling for cleaning, installation of diagnostics etc. after each shot depends essentially on the availability of high voltage/high current (15kV / 100 kA) connectors suitable for vacuum conditions.

Coil design

The coils developed for the generation of the applied magnetic field fulfilled these requirements. In addition they were matched to the geometry of the ion beam to be extracted, i.e. its diameters, angles and focal length. The coil arrangement (concentric to the axis of symmetry of the diode, Fig. 1) consists of a 9 turn inner coil (~4.7 µH) connected in series to a 4 turn outer coil (~ 1.7 µH) and the capacitor banks delivering the currents I_f and I_s for the fast and the slow field respectively. The inner coil is held in position by 7 vanes (1.2 mm thick) and its current-supply tube (8 mm outer diameter), which reduces (24 % effective) the cross section for the ion beam.

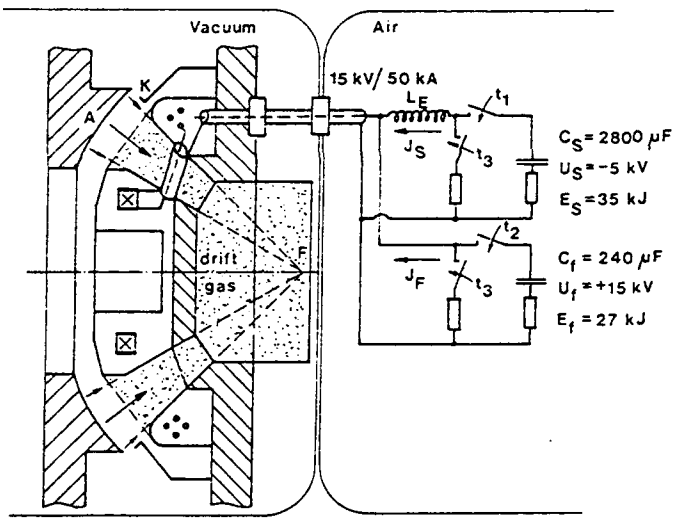

Fig. 1: Scheme of the applied field coils and the fast/slow capacitor banks

The positioning of the conductors and the choice of the materials was optimized by an electrodynamic code, simulating the time depending currents I_f and I_s by sine waves with frequencies of 4400 Hz and 160 Hz respectively. With this arrangement an insulating field of 3 T at the anode needs a peak current I_f ~ 50 kA delivered by a 27 kJ capacitor charged to 15 kV. The calculated peak fields (occurring at current maximum) are 10 T at the outer and 20 T at the inner coil. A detailed stress / strain analysis showed that the peak hoop stress of 3 GPa at the inner winding of the inner coil is far in excess of the mechanical strength of suitable conductor materials. The mechanical design of the coils was based therefore on the principle, that all windings had to take the Lorentz-forces commonly, i.e. we used a prestressed strong conductor material (CuBe2 inner, Cu-Carbon fibers outer coil) and a pressure resistant insulator material (Kapton, 25 µm thick) transmitting the load through the windings. The calculated temperature increase in the inner coil reaches 190 K, minimized by crowbar circuits in the driver banks. The HV design was made with respect to the break down through and along the surface of the insulator materials, with respect to the extreme forces deforming the insulators, and the formation of cracks due to mechanical shocks.

In addition to these conditions the processes connected with the generation of the ion beam itself can charge the coils by: dumping part of the beam on the coils, a hot plasma produced in the transport channel, and electrons producing x-ray-radiation or their direct impact on the insulators.

These loadings can not be quantified because they strongly depend on the experimental conditions of a single KALIF shot. The 0.5 mm thick stainless steel shielding somewhat protects the coils against these influences. It also serves as a part of the vacuum / drift gas interface and therefore must remain vacuum tight. The extreme high carbon fiber filling (up to 80 %) around the coils required a rather complicated procedure for the expoxy casting which consists essentially of repeated pressure cycling between 10^{-2} mbar to 40 bar during the casting.

Field measurements

The characteristics of the applied magnetic field generated by the field coils were measured by small induction coils C and by single turn loops L, both movable in the anode / cathode region of the diode with 0.01 mm accuracy. For these experiments, the capacitors of the driver bank for the slow and the fast field were only partly charged. However, due to the linear relationship between the current through the coil and the charge voltage the results are valid for all charge voltages. The axis of the 4 induction coils C (8 turns, 0.8 mm inner diameter, 1 mm length) were placed parallel to the surface of the anode (i.e. under 53 °), their radial positions were as follows: 61, 69, 77 and 83,5 mm. The time integrated signals of the coils C yield the magnitude of the magnetic field under 53 ° (i.e. $/B_{53}/$), averaged over 0.8 mm, as a function of the distance z' between the coil center and the anode surface with its azimuthal position θ as additional parameter. The time integrated signal of a single turn induction loop L concentric on a radius r to the axis of the diode is proportional to rA_θ. An axial shift Δz of the loop gives the stream function $\Delta\psi / _{\Delta z} = \Delta(rA_\theta)/_{\Delta z}$ which relates to the radial component of the magnetic field B_r by $B_r\, r\, \Delta z = -\Delta\psi/_{\Delta z}$. The 4 loops used here consisted of one wire ring (wire diameter = 0.1 mm), the radii of the loops wer chosen indentical to the radial positions of the induction coils. Using the fast driver bank only , the set of time functions for the induction coil C4 and the loop L4 (Fig. 2) shows a time lag of $\approx$ 20 µs between their maxima and the maximum of the current through the field coil. This time lag reaches up to 1 ms (close to the anode) for the case of the slow field. These shifts are due to the diffusion of the fields through the stainless steel shielding of the field coils and its penetration into the anode structures. For an optimized use of the applied fields they were taken into account with respect to the KALIF trigger time. The symmetry of the applied (fast) field close to the anode (Fig. 3) is generally better ± 2 %. Only for small radii and with increasing distance z' from the anode surface, the influence of the current-supply loop to the inner coil produces unsymmetries up to ± 4 %.

The results of the loop measurements for both, the slow and the fast field at the time of current maximum t_k (Fig. 4) show the values of rA_θ normalized to 1A of driver current as a function of the distance z' to the anode surface at the inner (L1) and the outer (L4) emitting edge of the anode. Depending on the radius r, the flux losses of the slow field to the anode are 4 to 4.5 times higher compared to

those of the fast field, i.e. assuming no plasma expansion the canonical angular momentum of ions starting at the anode surface can only be compensated, if the ratio of the currents I_f / I_s is about 4.

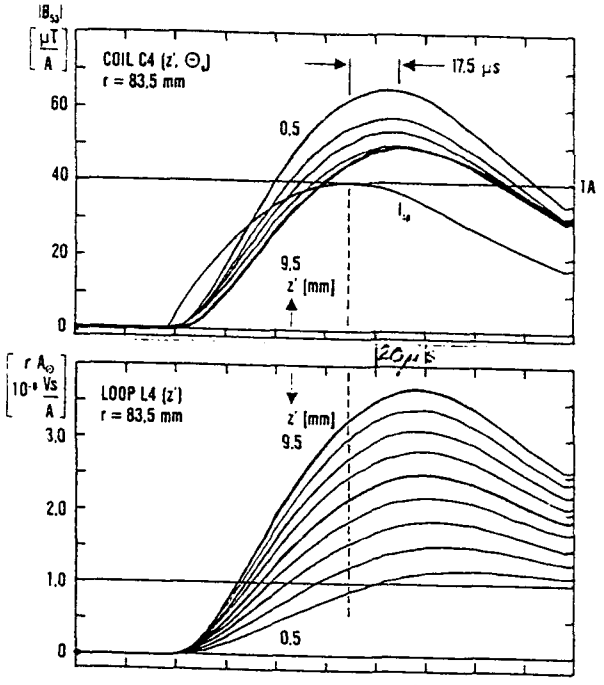

Fig. 2: Signals from coil C4 and loop L4 (r = 83.5 mm), z': distance to the anode surface

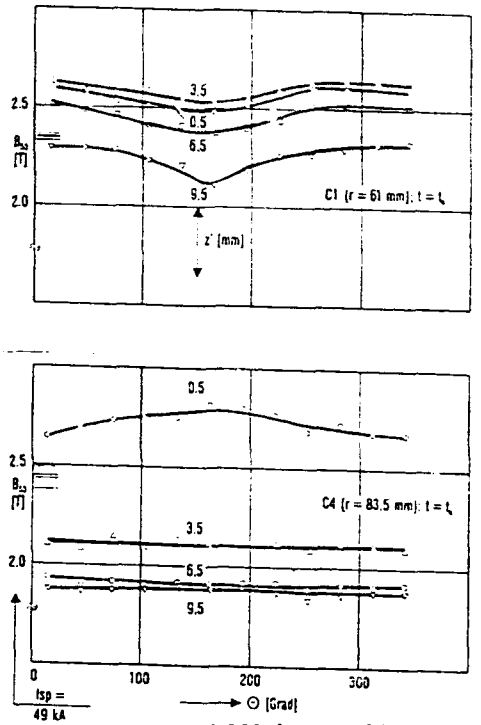

Fig. 3: Azimuthal symmetry of /B53/ for I_f = 49 kA

The measured electron insulating field characterized by the stream function $\Delta\psi$ follows from the results shown in Fig. 4. With I_f = 43.8 kA and I_s = 5.2 kA (frequently used in the experiments described in paper OA-3, this conference), this results in $\Delta\psi$ = 1.17 x 10^{-3} Vs and V_{crit} = 3.7 MV for the outer anode radius (r = 83.5 mm).These measured quantities fit within 10 % to the corresponding values calculated with the PROFI code (dashed lines in Fig. 4): $\Delta\psi$ = 1.24 x 10^{-3} Vs and V_{crit} = 4 MV. A significant difference between field measurements and calculations was found only for the anode flux losses of the slow field at the outer anode radius.

$B_{appl.}$-field strength / diode characteristics

The efficiency I_{ion} / I_{diode} and the impedance U_{diode} / I_{diode} (Fig. 5) were measured for KALIF shots with different applied magnetic insulation fields.

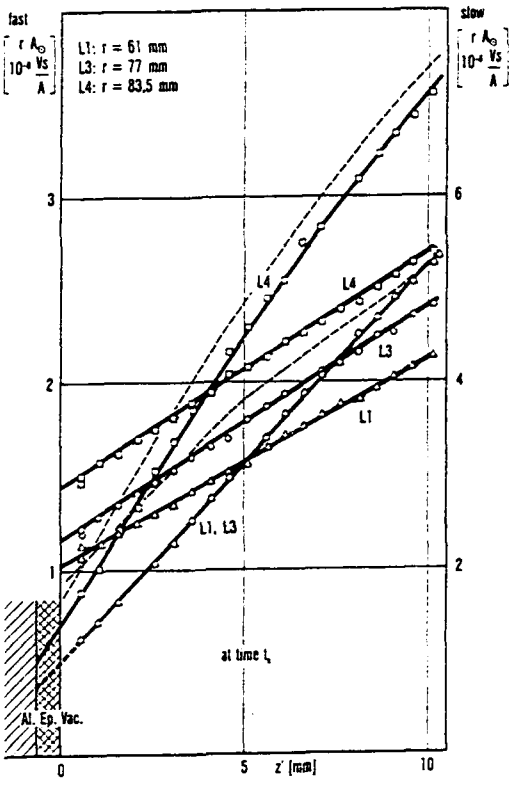

Fig. 4: Measured and calculated values for $R_{A\Theta}$ and different radial positions; time: current max

Without any applied field (shot # 3089), the impedance is constant for ~ 60 ns, as expected for diodes in the pinch mode. However, the efficiency is about 30 % only. For V_{crit} = 2.3 MV at the outer diode radius, the efficiency is more than 90 % but the impedance collapses within 20 ns, i.e. no stable operating point was achieved. The increase of V_{crit} to 5.4 MV stabilized the impedance of the diode for ~ 40 ns while the efficiency still remained above 90 %. This result is presumably due to the influence of the magnetic field on the effective AK-gap width: the stronger field keeps the electrons forming the virtual cathode on a field line closer to the emitting edge of the 'real' cathode and also reduces by its high magnetic pressure the anode plasma expansion.

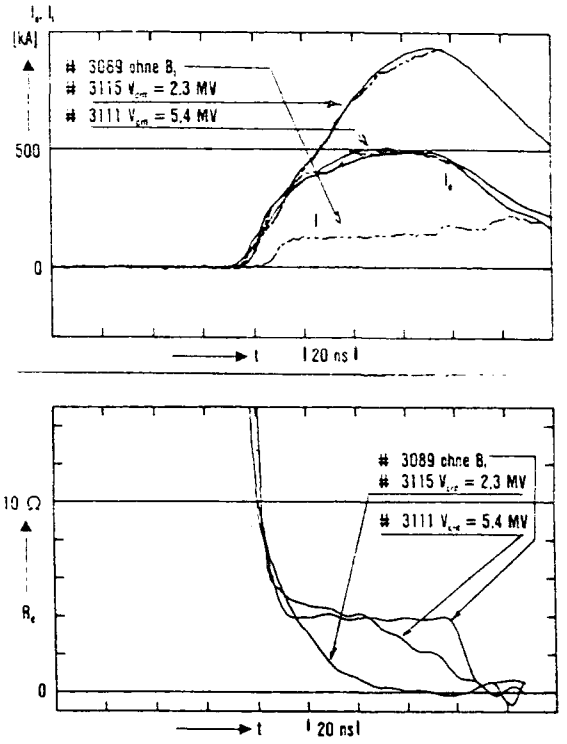

Fig. 5: Influence of the magnetic filed strength on diode curr. I_d, ion curr. I_i and impedance R_d

Summary

With the field coils presented in this paper fast insulating fields up to 3T at the anode and 1.5 x 10^{-3} Vs between the geometrical AK-gap of 8.5 mm could be created, hence an extractor type ion diode be operated at ratios $V_{crit} / V_d \approx 3 \ldots 4$. The canonical angular momentum of the ions could be reduced close to 0 by an additional slow compensating field. The maximum error in the azimuthal symmetry of the applied field was less than ± 4 %, the effective transparency of coils with respect to the propagating ion beam ≈ 80 %. The coils did not disturb neither the vacuum nor the neutralizing gas in the drift section of the diode and showed an average life time of ≈ 30 KALIF shots. The comparison between the measured and calculated V_{crit} showed agreement within 10 %. In experiments with these field coils and an active plasma source, the electron loss currents could be reduced to less than 10 % of the diode currents and the diode impedance stabilized for more than 40 ns. An ion beam of 0.8 TW with a total energy of 50 kJ could be extracted. The extrapolation to higher diode voltages (KALIF: 1.7 MV, HELIA: 6 MV foreseen) showed, that - for similar conditions at HELIA - the magnetic field must be increased by ≈ 50 % which doubles the mechanical loading of the coils. A possible way to solve this problem is the use of compound conductors: thin CuBe2 wires embedded in a copper matrix. Such conductors are actually under development.

Acknowledgements

The authors thank Prof. G. Keßler for his permanent interest and support of this work, which was at its beginning mainly influenced by Dr. J. Greenly, Cornell University. It would not have been possible without the skillful help of H. Lotz, G. Westenfelder. Special thanks also to H. Bachmann, Dr. V. Fedorov, Dr. D. Rusch and Dr. T. Westermann for discussions and data aquisition.

Ion Beam Generation with Inhomogeneous Anode and Cathode Plasmas.

V. Fedorov [×], W. Schmidt, Th. Westermann

Kernforschungszentrum Karlsruhe
Computational Physics Group
P.O.Box 3640, D7500 Karlsuhe 1,FRG

[×] permanent address: Moscow Radiotechnical Institute of the RAN

Abstract: The physical understanding of the ion beam enhancement and divergence in magnetically insulated ion sources, B_{appl}-diodes, for pulsed power generators is still lacking. We propose a phenomenological analytical model for the "stable" regime of operation of B_{appl}-diodes. The effect of rippled anode-plasma surfaces on the focusing properties of the diode is analysed. Conditions for the experimentally observed value of the micro-divergence $\Theta_i \simeq$ 10-20 mrad are obtained. The effect of scattering of the electrons in the disturbed electrical fields is calculated. Its effect on the electron distribution in the magnetically insulated vacuum gap is estimated: A low level $\leq 1\%$ of excitations for the "slow" and "fast" fluctuations generates enough broadening of the electron distribution. - Work is in progress to incorporate the model into the computer code BFCPIC to be used in computer experiments for designing high brightness diodes. This is a useful tool in the process of optimizing B_{appl}-diodes for good focusing properties. The first results on the effect of moving plasma boundaries are reported.

Introduction: High power Megavolt ion sources with applied magnetic fields, B_{appl}-diodes, have been developed sucessfully during many years; see e.g. the Proceedings of the Beams-Conf. since 1979. Up to the year 1990 main attention has been payed to obtain engineering scaling laws of the V-I diode characteristic and the explanation of the experimentally observed enhancement of the ion current density J_i over the monopolar flow $J_i/J_{CL} = \chi_{tot} = 10 - 30$ /1-6/.

Presently the main open question in inertial confinement fusion is how a well focused ion beam with an ion divergence $\overline{\Theta_i} \leq 10$ mrad can be obtained which means $E_{i\perp} \leq 10^{-4} E_i = 200 - 900$ eV for $E_i = 2 - 9$ MeV. In our analysis we will concentrate on this problem. Best experiments with proton beams yielded so far an average angle spread $\overline{\Theta_i} \simeq 20$ mrad ($\simeq 1°$) /7,8/. It is necessary to make the physical analysis for an actual B_{appl}-diode design at the moment of maximum power.

Straightforward 3-D and time-dependent numerical calculations of an actual B_{appl}-diode need high precision up to 10^{-4}, many time steps ($\geq 10^6$) and experimental data about the boundary conditions (electrode plasmas and exact geometry of the vacuum sections). Some first results have been obtained last year / 9 / for a simplified geometry and without plasma layers. These calculations demonstrate strong instabilities and lead to an divergence $\overline{\Theta_i} \simeq 40$ mrad for an Li-beam.

To obtain the best benefit from computer calculations analytical models are necessary, which summarize the main physical features. Presently a steady state model for the B_{appl}-diode is used extensively /4,5/, which postulates laminar electron flow without any electrons traveling across the gap. It is not clear how such a model can be extended by further dynamical features. This situation happened already many years ago during the investigation of another crossed-field device, the magnetron HF-oscillator /10/. Already at this time the general conclusion was that "the steady-state theories...are in poor agreement with several

aspects of experimental observations...and the magnetron diode is in a state of oscillations under most conditions even though the oscillation are not easily detectable."/10,pp.285,313/.

Summary of experimental data for the stable regime of B_{appl}-diodes: For the design of a physical model experimental information about the diode operation at maximum power is needed. Table 1 summarizes data from three experimental programs /6-8/ of the proton beams with the flashover anode /6,8/ and the "active" plama source /7/. The following definitions for the A-K gap widths are summarized here: $d_{0,AK}$, d_{AK} - design and effective gap; $d_{p,AK} = d_{0,AK} - (d_{0,pA} + d_{0,pK})$ - gap with the anode-cathode plasma layers subtracted; $d_{AK} = d_{p,AK} \times B_0/\bar{B}$ - gap after diamagnetic compression with flux conservation included; $\bar{B}$ the average magnetic field. The scheme of B_{appl}-diodes for extraction geometry is shown in Fig.1. Conditions for sufficient electron magnetic insulation for the B_{appl}-diode are then

$$d_{0,AK}/r_{eL}(B_0) \equiv B_0/B_{cr} = 1.2 \div 2.5,\ r_{eL} = \sqrt{V_A^2 + 1.02V_A}\,/3B_0\,. \qquad (1)$$

Note that in practical formulas the units kA/cm², MV, MV/cm, cm, T, nsec will be used. To take into account the plasma thickness we define the effective magnetic insulation $\bar{B}/B_{cr} = (\int_0^{'}Bdx)/P_e(1)$. This ratio is also shown in Tab. 1. This data is in agreement with the previous estimates of /2,6/. We conclude from this Tab. 1, that the "stable" regime for the B_{appl}-diodes is realized only for the narrow range

$$d_{p,AK}/r_{eL}(B_0) = \bar{B}/B_{cr} = 1.33 \mp 0.07\,. \qquad (2)$$

	Δt ns	V_A MV	B_0 T	$d_{0,AK}$ mm	$\frac{I_i}{I_A}$	J_i	χ_{tot}	$\overline{\Theta_i}$ mrad	$d_{0,pA}$ mm	$d_{0,pK}$ mm	χ_i	$\frac{\bar{B}}{B_{cr}}$
WODA [6]	45	0.4	1.4	4.0	0.6	1.2	14	-	1.3	0.5	2.5	1.25
KALIF [7]	45	1.7	2.0	8.5	0.85	4.0	24	25	2.5	1.0	3.5	1.35
PBFAII [8]	35	7.0	2.8	16.0	0.8	4.4	11	20	3.0	1.0	3.0	1.3

Table 1. Typical operational parameters of B_{appl}-diode experiments. J_i in kA/cm².

A dense plasma at the edge of the hollow cathode is formed a few ns after the voltage V(t) begins to rise. The low density cathode plasma composed of ions and oscillating electrons expands quickly (v_p = 0.1-1 cm/ns) along the B_{appl}- lines by electric fields produced by the electron cloud (collective acceleration /11-13/). The velocity v_p is higher in the case that the B_{appl}- value increases towards the emitting cathode edge /6,11,13/. This situation is realized for the B_{appl}-diodes of the Tab.1 with hollow cathodes. The thickness of the plasma layer $d_{0,pK}$ usually amounts to 0.5 - 2 mm.

Cathode and anode plasma layers should change drastically the results of real and computer experiments. Many experiments with hollow electron beams /11-14/ did not show evidence for the diocotron instability; on the other hand experiments performed under different conditions show it /9,15/.

The total ion divergence $\overline{\Theta_i}$ includes the micro-divergence Θ_i as well as effects of a larger scale ($\lambda \geq d_{AK}$) like electrostatic fluctuations by electrons, magnetic deflections, geometric distortions etc.. The Θ_i on KALIF /7/ was measured locally on the anode surface for an flash-over anode ($d_{0,AK} = 1 - 2$mm) as well as an "active" plasma source ($d_{0,AK} = 2 - 3$mm). In the last case Θ_i was smaller than in the first $\leq$18 mrad. This shows clearly that the primary source of the micro-divergence Θ_i is the roughness or ripple of the anode surface.

The location of the ion emitting surface in the anode-plasma is usually derived from the experimental data about the magnetic flux $\delta\Psi' = d_{0,pA}\,B_0 = d_{pA}\,B_A$ of this plasma layer. In Tab.1 we use the "equivalent anode plasma thickness" $d_{0,pA}$ which is given in /7,8/ as defined by the initial field B_0. Actually for estimating the scale λ of the micro-divergence one should use

$d_{pA} = d_{0,pA}B_0/B_A \simeq 1 - 1.5$ mm till direct measurements e.g. with interferometers are available. The B_A on the anode is obtained easily using experimental data about J_i and V_A and pressure balance /5,6/:

$$3.63 J_i \sqrt{A_i V_A / Z_i} = B_A^2 - B_K^2 \simeq B_A^2 , \quad (A_i, Z_i = 1 \text{ for protons}). \tag{3}$$

For the magnetic field B_K on the cathode one usually chooses $B_K = 0.8 - 0.9\, B_0$; furthermore one has $\bar{B} = 0.5B_A + 0.45B_0$ with an accuracy of $\mp 5\%$ /4,6/.

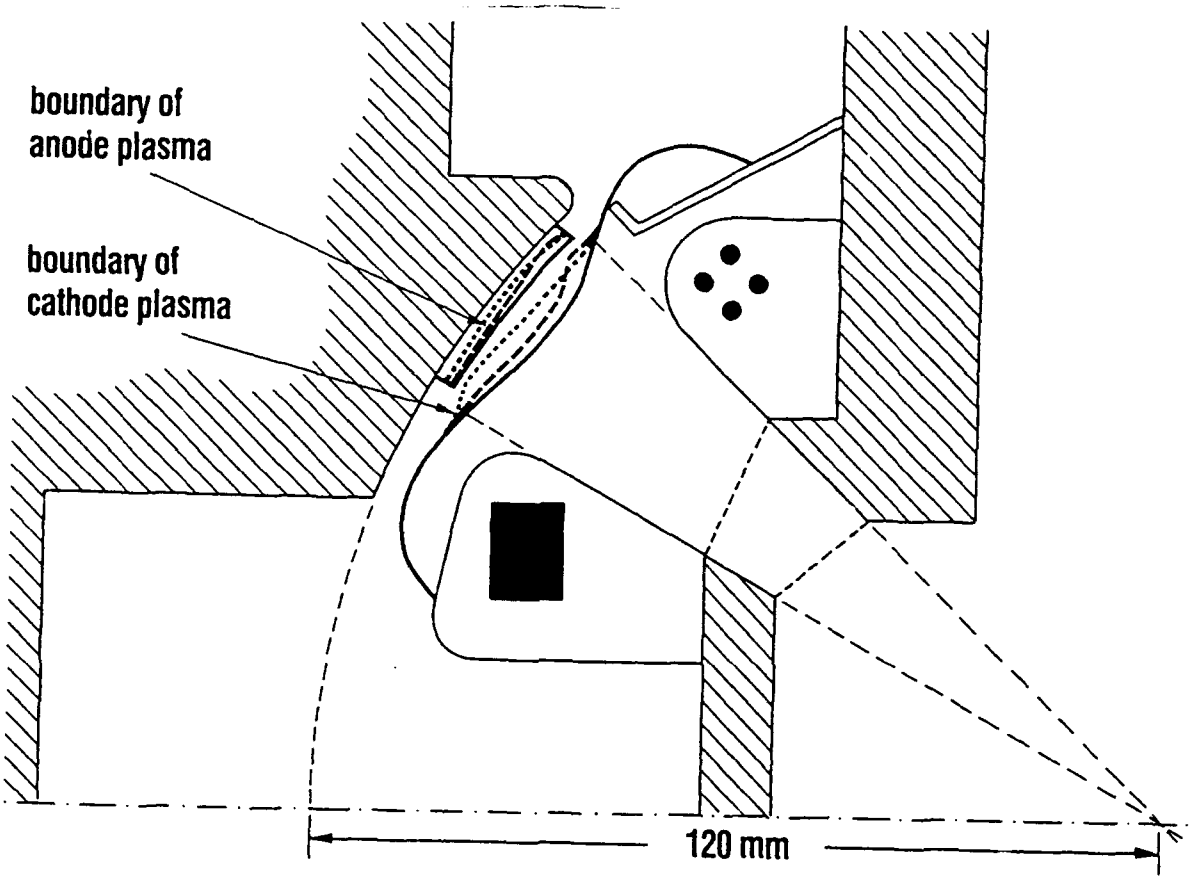

Figure 1. Scheme of the B_{appl}-diode for extraction geometry: Results of diamagnetic shifting of the anode- and cathode-plasma layers during rise of the voltage pulse $V_A(t)$ for ___ initial, _ _ _ middle and ... final conditions of the diode.

The total ion enhancement χ_{tot} can be splitted into three components $\chi_{tot} = \chi_p \chi_v \chi_i$, where $\chi_p = (d_{0,AK}/d_{p,AK})^2$ describes the effect of the plasma thickness, $\chi_v = (d_{p,AK}/d_{AK})^2 = (\bar{B}/B_0)^2$ represents the effect of the diamagnetic compression (displacement of virtual cathode),see Fig.1 . The "pure" ion enhancement χ_i provided by the electron space-charge in the d_{AK}-gap is derived from

$$\chi_i = \frac{\chi_{tot}}{\chi_v \chi_p} , \quad \chi_{tot} = \frac{J_i}{J_{CL}(d_{0,AK})} , \quad J_{CL}(d) = 0.054 \sqrt{\frac{Z_i}{A_i}} \frac{V_A^{1.5}}{d^2} . \tag{4}$$

Thus in physical models for the B_{appl}-diode one should use the value of Tab.1

$$\chi_i = \frac{J_i}{J_{CL}(d_{AK})} = 3 \mp 0.5 . \tag{5}$$

M.Desjarlais /4,5/ proposed a steady-state model for the B_{appl}-diode (plane geometry) with $d_{0,pA} + d_{0,pK} = 0$. It is clear, that the last assumption must lead to an increase of the χ_i values

($\chi_i = 5.5$, $\chi_p = 1$ at maximum power). One should note that the "stable" regime (best shots) of the B_{appl}-diodes are realized in a narrow range of values χ_i - and $\bar{B}/B_{cr}$ values. This situation was analysed in /6/. In this paper we develop extensively the ideas given in /6/ using analytical models and the code BFCPIC /16/.

2. Analytical investigation of the quasi-planar B_{appl}-diode.: The planar approximation of the diode geometry is a reasonable choice for heuristic analytical models. This statement is in agreement with the good focussing properties of the ion beams of realistic diodes. The electric fields E_A and E_K on the cathode-anode plasma layers are $<\sim E_{AK} = V_A/d_{AK}$. Quasi-stationary main fields $E_x(x,t) = -\nabla(V(x,t))$, $B_z(x,t)$ will be used, since they change slowly during the transit time of the ions across the gap ($\simeq$0.5 ns). Also used are the small field components $E_{x,y} = -\nabla(\delta V(x,y,t))$ which are excited by non-homogeneities of the cathode and anode plasma layers with the y-coordinate representing the ϕ-direction of a realistic diode.

We determine the main field components E_x and B_z by observing attentively the experimental facts as well as the requirements of the stationary theory. Thus assume for a moment that E_x is given such that the Poisson equation and the usual boundary conditions are complied: $E_x(0) = V(0) = 0$ on the cathode ; $E_x(1) = 0$, $V(1) = 1$ on the anode. Unitless quantities x/d_{AK}, y/d_{AK}, V/V_A, E_x/E_{AK}, $B_z/(E_{AK}/3)$, $J_i/J_{CL}(d_{AK})$, $v_i\sqrt{2}/v_{iK}$, $v_e/c = \beta$ will be used. Then the ion density $\rho_i(x) \sim J_i/v_i(x)$ and the electron density $\rho_e(x)$ are related through

$$\rho_e = \rho_i - \frac{dE}{dx} \ , \ \rho_i = \frac{4}{9}\frac{\chi_i}{\sqrt{(1-V)}} \ , \ V = -\int_0^x E(x)\,dx \, . \tag{6}$$

The ion leaves the anode with a small velocity according to $v_i = \sqrt{2(1-V)}$.

Given ρ_e the magnetic field $B_z(x)$ can be derived from Ampère's law using an ansatz of the y-component of the average electron velocity v_y

$$B_z(x) = B_K + \int_0^x \rho_e v_y\,dx \ , \ B_{AK} = \int_0^1 \rho_e v_y\,dx \, . \tag{7}$$

We emphasize that therefore pressure balance (3) relates E_x and B_z through

$$B_K = \frac{8}{9}\frac{\chi_i}{B_{AK}} - 0.5B_{AK} \tag{3'}$$

The velocity v_y is represented by the fit formula

$$v_y(x) = \beta(x)\,f_y(x) \quad \text{with} \quad \beta(x) = \frac{\sqrt{\gamma^2-1}}{\gamma} \ , \ \gamma = 1 + \frac{V(x)V_A}{0.511} \ ,$$

$$f_y = h_b \sin\left(\frac{\pi}{2}\alpha_{eff}\right) \ , \quad \alpha_{eff} = \left(\frac{x}{x_s}\right)^{h_r} . \tag{8}$$

In (8) x_s is given by the condition $\rho_e(x = x_s) = \rho_i(x = x_s)$. With respect to the parametrization of f_y in (8) we remark that the magnetic boundary, where $v_x = 0$, occurs approximately at $x_b = x_B \simeq x_s/2$ if there is no scattering of electrons; with slight scattering it is shifted to $x_b \simeq x_s$. Here x_B is the Brillouin boundary of an electron cloud /10/ for electrons escaping from the cathode with zero energy. Thus the argument of the sin-factor in (8) represents an effective average angle and the factor h_b introduces energy non-conservation for $h_b \neq 1$. The parameters x_s, h_b, h_r, B_K as well as the shape of the field E_x will now to be determined by the following reasoning.

One can see from simple analyses of Eq.(6) that the ion enhancement χ_i is defined by the shape of E_x near the anode. The greater $\chi_i >> 1$ the more $x_s \rightarrow 1$ and neutralization $\rho_e(x) \simeq \rho_i(x)$ establishes in the region $0 \lesssim x \lesssim x_s$. In particular the choice $\chi_i = 5.5$ requires a

spike near the anode (Fig.2b). It is then the question how the spiky solution of Fig.2b arises. In fact, if the magnetic insulation is low, $\overline{B}/B_{cr} \simeq 1.1$, then a spiky solution is found for a "cold" electron distribution. But one should keep in mind the observed voltage noise of 5-10 % as indicated by the measured energy spread /7,8/. Given $\overline{B}/B_{cr} \simeq 1.1$ and $\Delta E/E \simeq 5 - 10\%$ there will be no stable operation, instead high losses of electrons - which are not observed - and high oscillations of the ion current will occur. The experimental experience summarized in eq.(2) shows that for stable operation $\overline{B}/B_{cr} \simeq 1.33$ is required. In this regime of middle magnetic insulation the spiky ρ_e-shape for $\chi_i = 5.5$ is not realized. At the boundary of the stable regime, $\chi_i \simeq 3.9$, a flat distribution $\rho_e(x)$ is required. That is one explanation for the ratio given in Eq.(5).

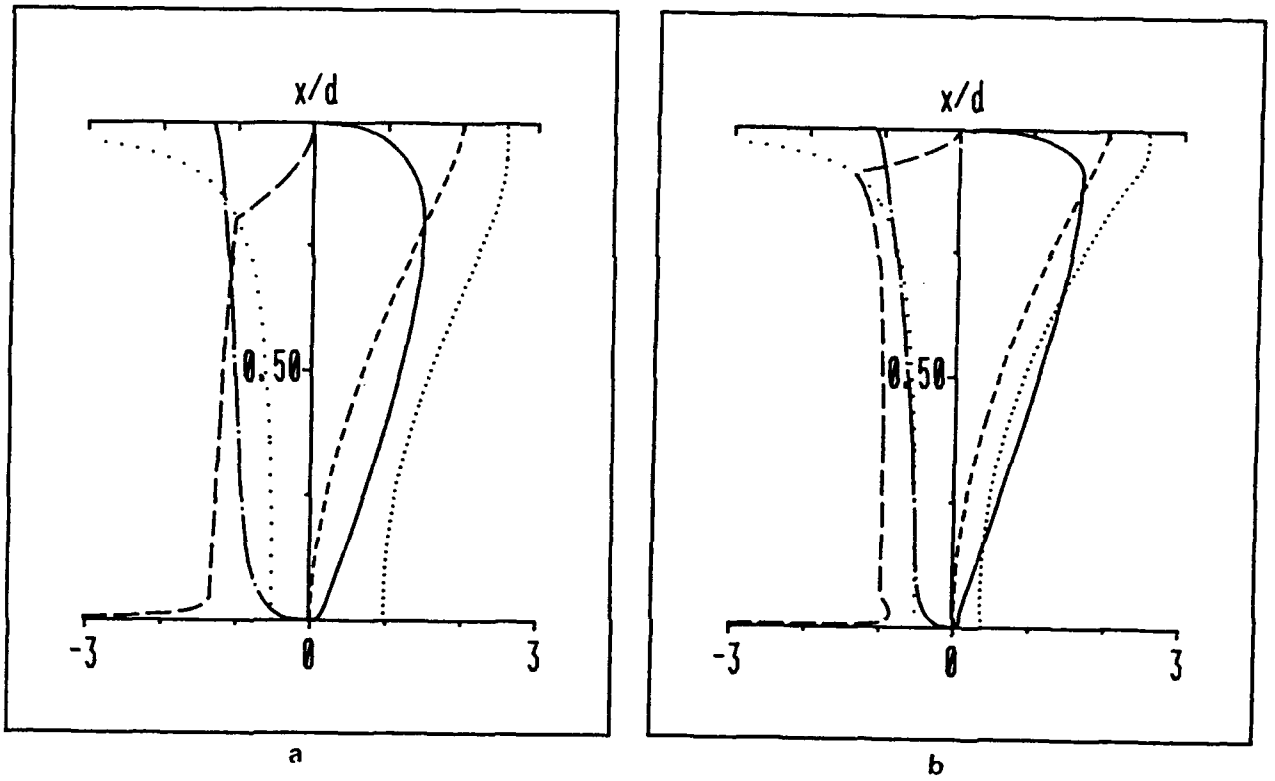

Figure 2. Quasistationary profiles for plane geometry and KALIF parameters:
a. stable regime: $\chi_i = 3.2$, $\overline{B}/B_{cr} = 1.34$; b. unstable regime: $\chi_i = 5.5$, $\overline{B}/B_{cr} = 1.12$.
___ E(x), ... B(x), _ _ _ 2V(x), _.-.- $(\int_0^x Bdx')/P_e$, ... $\rho_i(x)$, _ _ _ $\rho_e(x)$.

The dynamics of the electron cloud $\rho_e(x,t)$ is strongly dependent on the value of $\overline{B}/B_{cr}$. For $\overline{B}/B_{cr} > 1.5$ the electron mobility is low along the electrical field. Then the transport velocity of electrons across the gap is small compared with the ion velocity, so that the typical time delay $\delta t \simeq d/|v_i + v_e| \simeq d/v_i$ and only slow so-called "ion-transit" time instabilities can be excited as shown in /9/. In a separate report /17/ we present a computer simulation for the B_{appl}-diode whith a diffusion model of an electron "gas". High electron losses $I_e \sim I_i$ occur in case $\chi_i \gg 1$ and $\overline{B}/B_{cr} > 1.5$. But fast fead-back reaction of an electron "gas" in the gap is only realized for $\overline{B}/B_{cr} \simeq 1.3$ whith low noise level (~ 1 %, see /6/ and this paper). This case is typical for the stable regime with an amplitude of the electron trajectories across the gap amounting $\sim d_{AK}$, so that a magnetohydrodynamic or laminar approximation for the B_{appl}-model is excluded. Shown in Fig.3 are samples of the electron trajectory in the gap.

Middle enhancements $\chi_i \leq 3.5$ lead to densities $\rho_e(x)$ which drop continuouly from the cathode on (Fig.2a),so that electron losses are small. L.E.Mathias /18/ has measured with a molecular beam the electron charge density $\rho_e(r)$ for the magnetron diode and obtained a monotonic decrease with the radius. In the anode region $x > x_s$ we found good fits with the choice $(1 - x_s) \simeq \chi_i^{-1.4}$. The condition $E_x \simeq 0$ at the cathode requires an excess charge with a

sharp profile of $\rho_e(x)$ for $x < x_{eK} \simeq 0.07x_s$. Finally we note that for special choices of the parameters also the model /4/ is realized in our model of the B_{appl}-diode.

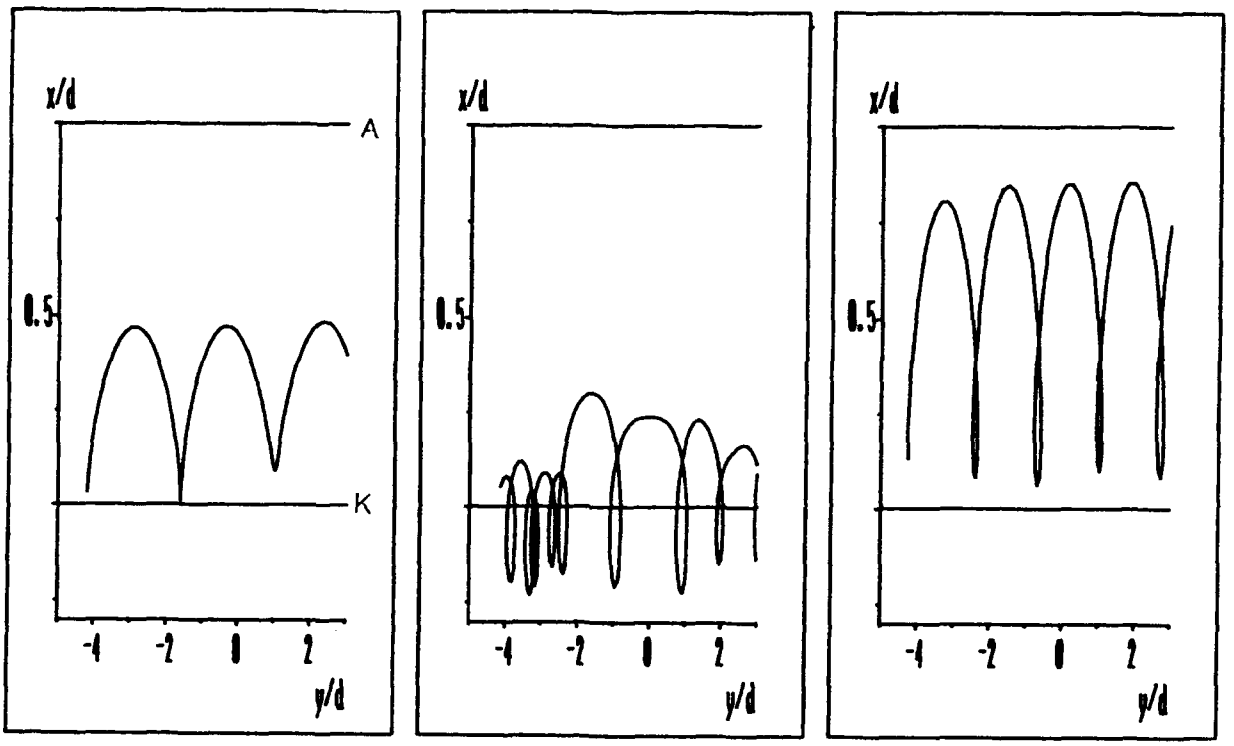

Figure 3. Three examples of electron trajectories: for different initial conditions. A rippled anode surface and inhomogeneous electron emission with the parameters of Fig.4a and b are assumed.

3.Effects of the y-component $E_y(x,y,t)$: There will be electric fields $E_{iy}(x,y,t)$ generated by the ripple of the plasma anode which lead to the ion micro-divergence and a broadening of the electron layer. The divergence of ion beams for a spatially nonuniform ion current density of the B_{appl}-diode is investigated with analytical models recently in /19,20/. These can be condsidered as limiting cases. Thus in /19/ the anode boundary condition is very special. In /20/ a gap of the B_{appl}-diode without electron charge is analysed. We carried out a computer calculations using our model of the stable B_{appl}-diode and a sinusoidal profile of the anode surface

$$x_A = 1 - \frac{\Theta_A}{\kappa_{iy}} \sin(\kappa_{iy}y - \omega_A t) \; . \qquad (9)$$

Here the parameter Θ_A denotes the maximum angle between the normal of the rippled anode surface and the x-direction (typically $\Theta_A \gtrsim 0.1$ rad); $\lambda_{yA} = 2\pi/\kappa_{iy} \sim d_{AK}/2$ is the wavelength of the ripple ; $\omega_A/(2\pi) \sim$ few hundred MHz some harmonic of the ion cyclotron frequency. Due to this disturbance the ion current develops a sheeth-like variation $\delta J_i \sim \Theta_A \sin(...) f(x)$ which is transported from the anode to the cathode. In this analytical analysis we include also the region $\rho_e > \rho_i$. Furthermore, since the typical period of an electron trajectory along the y-direction is $\sim 2d_{AK}$ (see Fig.3), we will in a first order neglect the y-dependence of $\rho_e(x,y,t)$ in the main part of the gap. Only near the cathode in a region of thickness $\sim x_{eK}$ a y-dependence of ρ_e is visible which is necessary for the shielding of the electric field being $\simeq 0$ (see Fig.4a).

Shown in Figs.4 and 5 are the ($E_y(x)$,$\delta E_x(x)$, $J_i(x)$...) distributions for a slow mode ($\sim$0.3 GHz) and a fast ($\sim$30 GHz). For the field of the slow mode E_{iy} we use a linear approximation ($\sim \sin(\kappa_{iy}y)$ in the region $x_{eK} < x < 1 - 1/\kappa_{iy}$ with $\lambda_{yA} = 2\pi/\kappa_{iy} \simeq 0.6 d_{AK}$. A solution of the Child-Langmuir type - singular in the x- and non-linear in the y-direction - is used in the

pre-anode region. The maximum of E_{iy} occurs imediately in front of the anode ($\delta x_A \simeq 0.02/\kappa_{iy}$).

Notice in Fig.4a that E_{iy} changes sign near the boundary where $\rho_e \simeq \rho_i$, so that the forces deflecting the ions change sign likewise. Thus when the ions leave the gap, their final angle is much smaller than their escape angle Θ_A at the anode, namely $\Theta_i = v_{iy}(x=0)/v_{iK} = 0.05 - 0.1\,\Theta_A$ (see Fig.4a. This result for the stable regime of the B_{appl}-diode is pretty surprising. On the other hand the amplitude $\delta J_i \sim \Theta_A$ is approximately the same at the cathode and anode although δJ_i changes sign in between. The experimental data $J_i(t)$ measured by Faraday cups with small input aperture demonstrated oscillations of the $J_i(t)$ /6/. We believe that the results of this investigation explain the nature of this observation.

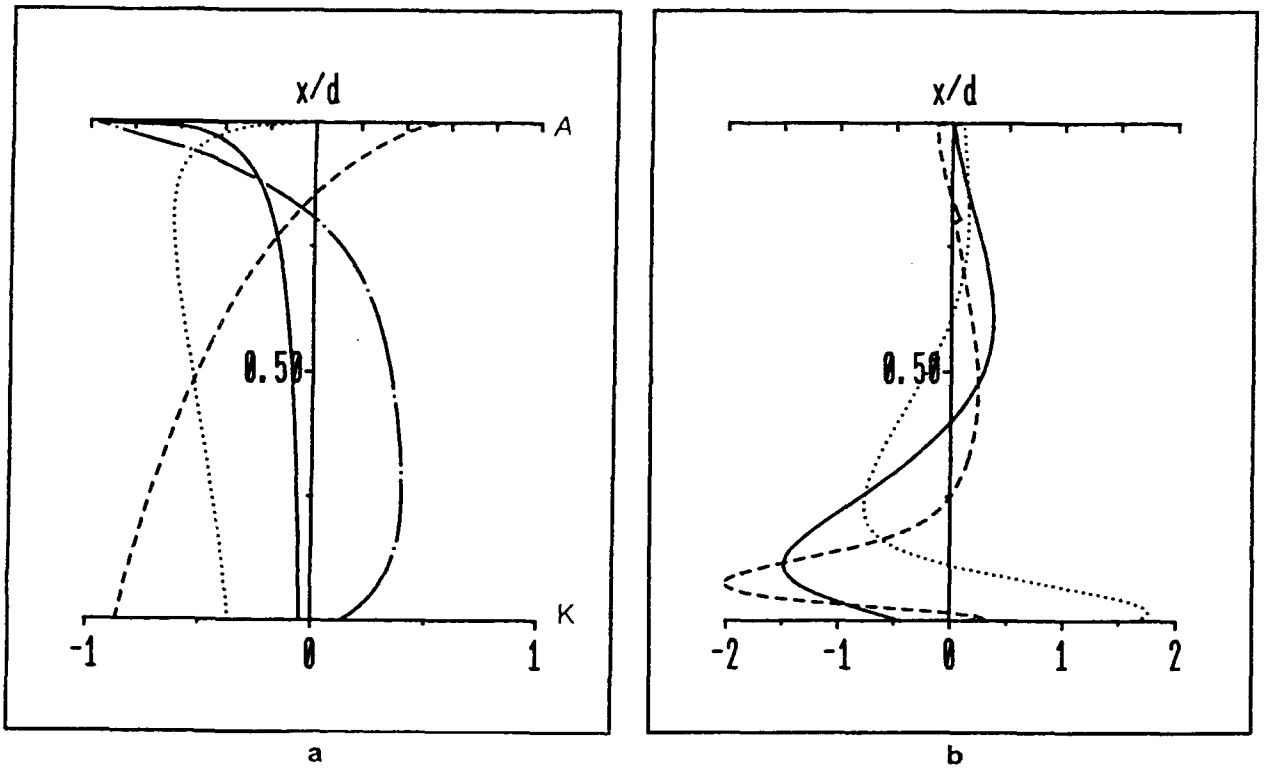

Figure 4. Results for inhomogeneous a). anode- and b). cathode-plasmas:
a. rippled anode $\delta x_A = 0.02$. _ . _ $E_{iy}(x)$, _ _ _ $\delta J_i(x)$, ... $v_{iy}(x)$, ____ $\Theta_i(x)$.
b. inhomogeneous electron emission with $\omega_K = 28$ GHZ, $\delta V_K = 0.01\ V_A$ imediately in front of the cathode. ___ $E_{ey}(x)$, . . . $\delta E_{ex}(x)$, _ _ _ $\delta \rho_e(x)$.

The lower frequency component E_{iy} is one source for scattering of the electrons. It generates enough broadening of the electron distribution in the stable regime with the micro-divergence $\Theta_i = 10\text{-}20$ mrad. Another source for electron scattering is the high frequency electric field E_{ey} excited by electron instabilities. The E_{ey} for usual B_{appl}-diode is a y-component of quasi-stationary fields $E_{xy} = -\nabla(\delta V(x,y,t))$, which have been investigated intensely for the magnetron diode already in the period 1940-60 (see the papers by G.Sims and J.Osepchuk in /10/). Many experiments have shown the instability related to the "back-bombardement" phenomenon and electron flow to the anode for the $\overline{B}/B_{cr} > 1$. The authors of /21/ found that about 30% of DC electric power was used for cathode heating by the chaotic kinetic energy of the bombarding electrons.This effect "depends on secondary emission properties of the cathode surface and on geometry...The basic problem of electronic interaction in the static magnetron is partially defined"/21/. Already at this time one was looking forward to a realistic solution of this problem. But no physical model has been given, which would explain how the instabilities transfer enough DC-power to the electron cloud in accordance with the observed high enhancement of the electron emission by "back-bombard-

ment". We will call this effect the back-bombardement(BKB) instability. The paradox of the BKB instability is the following: Only a very small portion of the absorbed DC power was detectable as high frequency power in a frequency band of some subharmonics of the electron Larmor frequency /10/ equal to one half of the cyclotron-frequency.

We assume that in the electron cloud of the B_{appl}-diode the same dynamical process occurs, which is responsible for the BKB effect. Instead of the secondary emission in the magnetron diode we should take into account the effect of anomalous resistivity /22/ in the cathode-plasma layer. It can arise in the cathode-plasma layer locally where high current electron streams pass.

In Fig.4b we present results for the case of high-frequency fluctuations of the electon cloud $V_e(x,y,t)$ $\delta V_e \sin(\kappa_{ey} y - \omega_K t) g(x)$, where δV_e is the amplitude at the boundary $x \simeq x_{e\kappa}$, $g(x = x_{e\kappa}) \simeq 1$, $\lambda_{y\kappa} = 2\pi/\kappa_{ey} \simeq 2.3 d_{A\kappa}$ and $\omega_K \simeq 0.5 \times$ gyrofreqency at cathode (= 28 GHz for KALIF with B_0 = 2T). The $E_{ey}(x)$ changes sign near the Brillouin magnetic boundary $x = x_B \simeq x_s/2$ for unscattered electrons (notice the remark after Eq.(8)). The calculation of electron trajectories show, that with $\delta V_e \simeq 0.005$-$0.01\ V_A$ enough broadening of the electron distribution results.

4.Implementation in stationary code BFCPIC: The implementation of the phenomenological results into our stationary code BFCPIC is in progress. As a first step we introduced the movement of the plasma boundaries due to the diamagnetic shifting. Plasma expansion from the anode as well as the cathode tip early into the pulse is taken into account. Thus the plasma-cathode is identified as the flux surface which touches the cathode tip. Similarly the plasma-anode is identified by that segment of the flux service which is 2-3 mm in front of the emitting part of the massive anode. (Fig. 1). The voltage is raised in 1500 time steps of 2ns. Since the magnetic field is frozen into the plasma, the cathode flux surface and thus the plasma-cathode moves with the rising total current in the direction of the anode. At the same time the anode-plasma surface retreats with the rising eigenfield as is demonstrated in Fig.1. In these calculations the computational grid is adjusted in proper intervalls to the new boundaries. This is accompanied by a reorganization of the particles and fields. This model satisfies flux conservation and shows the diamagnetic compression as observed in /3/. The shape of the anode surface is a function of time. The simulation is so far in agreement with the KALIF experiments /7/, as they show that the focusing properties of the ion beam change with time. This makes it necessary to perform an optimasation of the anode surface shape and the applied magnetic field to reduce the losses from the edges of the ion beam similarly as done in /23/ for the B_θ-diode. The next step will be to include in BFCPIC the time-dependent ripple of the plasma surfaces so that the main results of this paper can be exploited. A requisite for this is an appreciable reduction of the present noise level, which is believed to be generated mainly by the particle generator for the emitting parts of the electrodes. It requires at this time an appreciable amount of averaging.

5. Conclusions: We have defined two basic internal parameters of the stable regime for the B_{appl}-diodes: $\chi_i \simeq 3 \mp 0.5$, $\overline{B}/B_{cr} \simeq 1.33 \mp 0.07$. They were exploited in a phenomenological model of the ion micro-divergence Θ_i of the B_{appl}-diode. The important fact to notice for improvements of the focusing properties is that the ions leave the gap with final angles Θ_i which are much smaller than the emission angle $\sim\Theta_A$ on the rippled anode surface (by a factor 10 or more). The results agree with the known aspects of experimental observations. Furthermore, we have proposed a flow model for the electrons with spatial occillations $\sim d_{A\kappa}$ and a low level of chaotic excitations. This slight scattering process of electrons is caused by two basic modes with "slow" and "fast" fluctuations of the electric field. The fast mode - ignored presently - was observed many years ago in the magnetron diode, but is still unexplained. Finally, we made the first steps in the formulation of a realistic physical model for the B_{appl}-diode and elaborated some of its consequences.

Acknowledgements: The authors thank H.Bluhm and P.Hoppè for supplying experimental data on the B_{appl}-diode for the KALIF and inspiring discussions. We also thank our colleages C.P.Hugelmann, K.H. Schmidmeier and D.Seldner for their kind assistance.

1. P.A.Miller, J.Appl.Phys., 57,1473(1985)
2. P.A.Miller and C.W.Mendel,Jr., J.Appl.Phys., 61,529(1987)
3. S.A.Slutz,and D.B.Seidel and R.S.Coats, J.Appl.Phys., 59,11(1986)
4. M.P.Desjarlais,Phys.Rev.Lett., 59,2295(1987)
5. J.PQuintenz,et al,Proc. 8th Int.Conf.on High-Power Particle Beams (Beams-90),Novosibirsk,USSR (1990),116.
6. V.M.Fedorov and P.P.Deichuli, in Proc. 8th Int.Conf.on High-Power Particle Beams (Beams-90), Novosibirsk, USSR(1990),ps.215;469
7. H.J.Bluhm,et al., ibid. p.451 and this Proc., Beams-92 , OA-3.
8. D.J.Johnson,et al., Proc.7th IEEE Pulsed Power Conf.,Monterey,USA (1989),944
9. M.P.Desjarlais et al., Phys.Rev.Lett., 67,3094(1991)
10. Cross-Field Microwave Devices, Ed.Okress, N.Y.,1961
11. P.P.Deichuli and V.M.Fedorov, Collective Acceleration (Proc.of Int.Conf.) Dubna ,Joint Inst.of Nucl.Research, USSR, 1982, p.84
12. D.D.Ryutov, Proc.4th Int.Top.Conf. High-Power Electron and Ion-Beam Research and Technology, (Beams-81), Palaiseau, France, p.77(1981)
13. A.N.Bastrikov et al., Sov.J.Plasma Phys., 10,751(1984)
14. M.G.Mazarakis,et al., Proc. 5th Int.Conf.on High-Power Particle Beams (Beams-83), San-Francisco, USA, p.346(1983)
15. A.I.Eremeev et al., Sov.J.Plasma Phys., 14,562(1988)
16. W.Schmidt,et al,in Proc. 8th Int.Conf.on High-Power Particle Beams (Beams-90), p.505(1990)
17. M.Alef,et al, these Proc., Beams-92, PB-04
18. L.E.S.Mathias, J. of Electronics ,Vol.1,8-24(1955)
19. R.N.Sudan and D.W.Longcope, Preprint, Cornell Univ., LPS 92-2, Ithaca N.J., USA(1992)
20. S.A.Slutz, Sandia Report, USA, 1992 (to be published).
21. R.L.Jepsen and M.W.Muller, J.Appl. Phys.,22,1196(1951)
22. A.A.Galeev and R.S.Sagdeev,in Reviews of Plasma Physics, Ed. M.A.Leontovich,Vol.7, N.Y.,1979 ,p.141
23. W.Bauer et al, these Proc., Beams-92, PB-01

Ion Diode Simulation for Pulsed Power Generators with Stationary Codes

M.Alef, V.Astrelin [1], L.Feher, St.Illy, M.Kuntz, W.Schmidt, R.Schuldt, D.Seldner, E.Stein [2], Th.Westermann

Kernforschungszentrum Karlsruhe

Computational Physics Group
P.O. Box 3640, D7500 Karlsruhe 1, FRG
[1] Institute of Nuclear Physics, Novosibirsk, Russia
[2] Institute of Neutron Physics and Reactor Technology,KFK Karlsruhe

Abstract: The calculations with the 2.0D and 2.5D versions of the stationary code BFCPIC have been extended in various directions. A particular concern was a better understanding of the enhancement of the ion current in ion diodes with an applied magnetic field. Ad hoc assumptions for the anomalous transport of electrons and of plasma motion have been introduced and the results will be discussed.

Introduction: At the Karlsruhe Nuclear Research Center the computational physics program continues to support the development of light ion beam sources ("ion diodes") operated on the pulsed power generator KALIF. In the work presented here we extend the applicability of the 2D and 2.5D versions of the BFCPIC code /1/, a stationary particle-in-cell code for which the method of boundary-fitted coordinates has been adopted. The present aim is to simulate the main properties of these diodes, i.e. (V,I)-characteristics and focusing properties. Thus, the development of the BFCPIC code is pushed into the direction of a fast but realistic engineering code. It is used for the prototyp development of two ion diodes at KALIF, which differ by the method of magnetic insulation of the electron flow: B_θ - /2/ and B_{appl}-diode /3,4/.

It is to be expected that in high power ion diodes the dynamics of the non-neutral plasma clouds is to some extent influenced by instabilities. The level of their excitation will be determined by the conditions of the experiment. Connected with instabilities are fluctuating electrical fields disturbing the trajectories of the particles. Some consequences are obvious and are actually observed: degradation of the focusing of the ions and enhancement of the ion current. Due to high-frequency electrical fields the magnetic insulation of the electrons is weakened. The sheath of electrons is broadened by their migration to the anode. There they better shield the positive charge so that more ion current is drawn.

A complete description of this non-linear dynamics of the ion and drifting electron cloud in the space between the electrodes must take into account their interaction among each other and simultaneously the coupling to the dense plasma systems on the emitting part of both electrodes. These ab initio calculations demand complex and large computer programs leading to a huge computational effort. The resulting CPU-times go beyond the capabilities of the largest computers presently available if the calculations are not limited to reduced problems. Therefore, guidance

from heuristic considerations is needed for the future direction in developing advanced time-dependent 3D codes. This can be obtained from phenomenological and analytical models as performed recently in /5/. In fact, valuable insight is also obtained from the pioneering work in /6/ where the geometry of the technical system is simplified and idealized boundary conditions with rigid electrodes are assumed.

Spatial Diffusion and collisional drift model: As reported at the Beams 90 conference /7/, straightforward PIC-calculations for the B_{appl}-diode with our stationary code do not reproduce the ion enhancement found in several experiments. For some early KALIF-experiments the results of Table 1 apply.

	experiment /3/	model
electron current I_e	20-80 kA	40 kA
ion current I_i	300-450 kA	20 kA

Table 1. Results for the currents of the B_{appl}-Diode.

Here the nominal voltage V was 1.7 MV, gap width d_0 = 6.5 mm and the magnetic flux $\Delta\psi = 1.5 \times 10^{-3}$ Vs corresponding to a magnetic field B_{appl} = 2-3 T along the anode. One usually expresses the ion enhancement by the ratio $\kappa_{tot} = I_i/I_{CL}$. Here I_{CL} denotes the Child-Langmuir current for a nominal gap d_0 and applied voltage V. For the parameters of the KALIF-experiments with an emitting anode area of 100 cm², one obtains from Table 1 κ_{tot} = 10-16.

It is generally agreed upon that three factors contribute to the ion enhancement in ion diodes with an applied magnetic field for electron insulation: diamagnetic shift of the virtual cathode due to the diamagnetic currents of the azimuthally drifting electrons, motion of the electrode plasmas and spatial broadening of the electron distribution due to scattering by fluctuating fields. The dynamics of plasma formation and its expansion is not well understood. So far we have included it in BFCPIC in a heuristic manner /5/ and observed the right order of magnitude for the diamagnetic shift /8/. From an analysis of the experiments again in /5/ it was concluded that plasma motion before the onset of the voltage pulse contributes a factor $\kappa_p = (d_0/d_{0AK})^2 \simeq 3$ to the ratio κ_{tot}. The constant d_{0AK} is defined by $d_{0AK} = d_0$ - (thickness of anode + cathode plasma layer). Thus the diamagnetic shift together with the broadening of the electron distribution must account for a factor κ_{tot}/κ_p = 3 - 5 in the experimental results of Table 1.

The scattering effect also leads to electron migration to the anode and thus to a weakening of the magnetic insulation. This has been known for 50 years from experiments with crossed field devices like the magnetron /9/. But there exists no generally accepted theory of the dynamics of electron clouds in crossed field devices, which could be incorporated in a stationary code. Modern electromagnetic codes predict instabilities like the diocrotron instability with a markable broadening of the electron distribution /6/. This indicates that anomalous transport of electrons across the magnetic field should be taken into account in a model for a stationary code. For an exploratory calculation we therefore introduce the following ad hoc diffusion modification of the electron velocity

$$\vec{v}_{total} = \vec{v} + \vec{v}_{anomal}, \quad \text{with} \quad \vec{v}_{anomal} = \vec{v}_{\perp} + \vec{v}_{diff}. \tag{1}$$

Two processes are assumed to contribute to anomalous transport of electrons: spatial diffusion $\vec{v}_{diff}$ due to electrostatic instabilities and collisional drift of electrons $\vec{v}_{\perp}$, due to perturbations of the cyclotron rotation by electric fields of unstable waves. Whereas the collisional effect $\vec{v}_{\perp}$ contributes only to the component perpendicular to the magnetic field $\vec{B}$ (see Eq. 9.8 in /10/), $\vec{v}_{diff}$ is independent of the direction of $\vec{B}$. We introduce a diffusion constant D and collision frequency F and adopt the approximations

$$\vec{v}_{diff} = - D \frac{\vec{\nabla}\rho}{\rho} \quad \text{and} \quad \vec{v}_{\perp} = \vec{E}_{\perp} \frac{e}{m} \frac{F}{\omega_c^2 + F^2} . \tag{2}$$

Here ρ is the electron density, ω_c the gyrofrequency and e, m electron charge and mass.

One can use the rather elaborate theory of instabilities of the electron and ion flow /11,12,13/ for estimating the parameters D and F. The diffusion coefficient D is approximated for a numerical estimate by (see Eq. 36 in /13/)

$$D(x,t) \simeq D = \left[\frac{|\delta\Phi_k|}{B} \right]^2 \frac{k^2 \gamma_k}{(\omega_k - k v_{dr})^2 + \gamma_k^2} . \tag{3}$$

instability	kd_0	$\omega_k d_0 / c$	$\gamma_k d_0 / c$
diocotron	< 1	< 1	≤ 0.01
electron-ion two-stream	≤ 2	≤ 0.02	≤ 0.05
ion transit time	≥ 2	≥ 1	≤ 0.05
broadband	0.4-1.5	$\simeq$ -0.02	$\simeq$ 0.02
magnetron	≥ 5	≥ 3.2	≥ 0.02

Table 2. Estimates for the maximum increments γ: k wave number, ω_k frequency, d_0 = 1 cm, c velocity of light. Results taken from /12/ for V = 2 MV, B_{appl} = 1.05 and 1.20 T.

With values for the two-stream instability compatible with Table 2 one obtains D = 2.8×10^3 m²/s. Here is assumed that $kd_0 = 0.6$, $\omega_k d_0/c = 0.25$, $\gamma_k d_0/c = 0.06$ and typical parameters of the KALIF-experiments: i.e. the amplitude of the electrostatic wave $|\delta\Phi_k| = 0.2$ MV and E = 1 MV/cm, B = 2 T. For a typical thickness $\delta \simeq 0.2$ cm of the electron layer in our code we conclude that the characteristic diffusion time $\Delta t \simeq \delta^2/D = 1.5 \times 10^{-10}$ s is fast enough for typical rise times of the voltage pulse of 10-20 ns.

Numerical Results: The dependence of the diode currents I_e and I_i on the diffusion coefficient D is summarized in Table 3. The first three examples show that diffusion leads to some increase of the ion current. At D $\simeq 10^4$ m²/s the electron current reaches values obtained in the experiment while the ion current is only 1.7 times larger than for D = 0. Of course a factor 3 - 5 is needed.

D in m^2/s	0	10^4	$5\,10^4$	10^4 & 10^5	$(2-5)10^4$	10^{10}
electron current I_e in kA	40	56	84	67	72	390
ion current I_i in kA	20	31	34	34	38-40	38
number of run	1	2	3	4	5	6

Table 3. Results of the extended stationary BFCPIC code: spatial diffusion model.

Some modifications have been tried: Run 4 is a simple example for a space-dependent coefficient D. Enhanced diffusion with $D = 10^5$ was assumed in the neighbourhood of the cathode tip and $D = 10^4$ in the remaining region. In run 5 directional dependence of the diffusion was assumed, i.e. only diffusion towards the anode was allowed. Finally, in run 6 the limit $D \to \infty$ was taken. There were only slight changes in I_i compared to the first three runs but an unrealistic increase of the electron losses occurred. These runs demonstrate that spatial diffusion in the simple form (2) with a constant diffusion constant D leads to too large electron losses. Presumably a space- and even time-dependent coefficient D(x,t) would be more appropriate, which decreases near the anode boundary. But for the right choice of the functional behaviour of D(x,t) more insight into the dynamics of the electron distribution is needed.

We now turn to a discussion of the collisional drift model. This effect can arise if unstable waves with rather high frequencies close to the electron cyclotron frequency ω_c disturb the cyclic orbits of the electrons. From Table 4 one concludes that frequencies F near the gyrofrequency ω_c (B = 2 T) = $3.5 \times 10^{11}/\gamma$ yield sufficiently fast driftspeeds $v_\perp$. For the parameters of the KALIF-experiments the maximum value of $\gamma = 1 + e\phi/mc^2$ equals 4.4.

F in s^{-1}	10^9	10^{10}	10^{11}
$v_\perp/c$	(0.6-2.9) 10^{-2}	(0.6-2.9) 10^{-1}	(0.3-1.0) 10^{-0}

Table 4. Perpendicular drift velocity $v_\perp$ according to Eq. 2: for three frequencies F; $\omega_c = 1 \times 10^{11} s^{-1}$; $E_\perp$ = 1-5 MV/cm.

The results of Table 5 show that for run 8 the electron current reached the experimental value. At the same time the ion current grew by a factor of 1.7 only. This is the same situation as in the previous case of the spatial diffusion model. Run 9 is a variant, which to some degree simulates the superposition of the spatial diffusion and collisional drift. In a strip of 5 mm width at the anode the diffusion velocity had the lower value 3×10^5 m/s and in the remaining part of the gap 10^7 m/s.

F in s^{-1}	0	10^9	$3\,10^9$	$v_\perp = 3\,10^5$ & 10^7 m/s
electron current I_e in kA	40	≃40	52	123
ion current I_i in kA	20	≃27	33	61
number of run	1	7	8	9

Table 5. Results of the extended stationary BFCPIC code: collisional drift model

The concept of spatial diffusion and collisional drift of the electron cloud is very general. Thus, the obvious shortcomings are presumably explained partly by the crude approximations of Eqs. 1-3. But one must also keep in mind the role of plasma motion before the main voltage pulse sets in. The factor $\kappa_p \simeq 3$ includes only the geometric effect of a reduced value for the effective gap. But an increase of the ion current due to $d_0 \rightarrow d_{0AK}$ yields also further compression of the gap due to the shifting of the virtual cathode and anode by the diamagnetic fields.

Therefore, we have performed run 10 and 11 of Table 6, where the boundary of the emitting anode was shifted into the gap by 1 and 2 mm, respectively, and the collisional drift model of run 9 was used. During the main voltage pulse the boundary was kept constant. One observes (Table 6) a fast increase of the ion current I_i together with a small increase of the electron current I_e. Compared to run 9 the rise of I_i is a factor 2.7 and 3.7 for runs 10 and 11, respectively. This is almost by a factor $\kappa_{dia} = 2$ more than the enhancement factor κ_p - due to plasma expansion - would suggest: $\kappa_p = 1.4$ and 2 for runs 10 and 11, respectively. The additional rise by $\kappa_{dia} \simeq 2$ of I_i demonstrates the importance of the diamagnetic compression of the gap. It is already of the right size, since in /5/ it was concluded that κ_{dia} typically varies between 1.7 and 2.5 in the experiments. Together with a cathode plasma expansion - neglected so far - the value $\kappa_p = 3$ - as assumed at the beginning - should be easily reached. It will further enhance the ion current. But a better control of the electron losses is needed.

Δl in mm	0	1	2
electron current I_e in kA	123	124	150
ion current I_i in kA	61	166	228
number of run	9	10	11

Table 6. Results of the extended stationary BFCPIC code: expansion Δl of anode plasma and collisional drift model with parameters as in run 9 $v_\perp = 3\,10^5$ & 10^7m/s .

We write as in /5/ $\kappa_{tot} = \kappa_p \times \kappa_{dia} \times \kappa_{intr}$, where the enhancement factor κ_{intr} describes the intrinsic enhancement due to the broadening of the electron cloud. With $\kappa_p = 3$ and $\kappa_{dia} = 2$ one obtains $\kappa_{intr} = 1.7 - 2.7$. We conclude that with the model Eqs. 1-3 and the best parameters of Tables 3 and 5 one is near to the values $\kappa_{intr} = 2.5 - 3.5$, which are characteristic for the stable regime of B_{appl}-diode operation according to /5/.

Conclusions and outlook: Some instabilities can be excited in the B_{appl} -diode of KALIF which will lead through spatial diffusion and collisional drift to an anomalous transport of electrons across the diode gap. These processes yield a smoothing of the electron density distribution, and at the same time a stronger charge neutralisation immediately before the anode. As a consequence we observed a rise of the ion current I_i. But in the framework of this very simple model the gain in ion current was only by a factor of 1.5 - 2. This is to be compared with the experimental values of 3 - 5. In the parameter search the constrain was imposed that the electron losses should not exceed the experimentally determined value $\simeq 0.1\ I_i$.

The concept of spatial diffusion and collisional drift of the electron cloud is very general. Thus the obvious shortcomings are explained partly by the crude approxi-

mations Eqs. 1-3. Runs 10 and 11 demonstrate the importance of the plasma motion before the main voltage pulse sets in. A fast increase of the ion current together with a small increase of the electron current occurs. However, a better control of the electron losses is needed.

In future work on phenomenological models of the electron dynamics for stationary codes the problem of electron losses must be addressed with more emphasis. We guess that one has to introduce the model assumptions on a different level, such that the migration of the electrons to the anode is controlled by the magnetic field directly. Thus it is tempting to introduce fluctuating electrical fields directly into the equations of motions, but at the expense of even more a priori information necessary than the two free parameters of Eq. (2). A first initiative in this direction has been done ten years ago by Poukey et al. /14/ without accounting for the modifications of the space charge, which go with the additional electrical field. Only after such inconsistencies have been taken care of and quantitative success followed, one may return to a modified version of the present approach.

Acknowledgements: We would like to thank Drs. H.-J. Bluhm and V. Fedorov for their valuable information on the experiments and for the illuminating discussions.

References

1 T.Westermann, Nucl. Instr. Meth. A263, 271-279, 1988; T.Westermann, Proc. 12th IMACS World Congress on Scientific Computing, Paris, 241, 1988.
2. W.Bauer, H.Bachmann, H.-J.Bluhm, P.Hoppé, H.-U.Karow, D.Rusch, Ch.Schultheiss, E.Stein, O.Stotz, and T.Westermann, Proc. 8th Int. Conf. High-Power Particle Beams, Novosibirsk, World Scientific Singapore (1990) 457-462.
3. H.Bluhm, P.Hoppé, H.Bachmann, W.Bauer, K.Baumung, L.Buth, J.Greenly, H.U.Karow, D.Rusch, E.Stein, and O.Stoltz, ibid. p. 451.
4. H.Bluhm, P.Hoppé, M.Althaus, H.Bachmann, W.Bauer, K.Baumung, L.Buth, H.U.Karow, H.Laqua, D.Rusch, E.Stein, and O.Stoltz, Proc. 9th Int. Conf. High-Power Particle Beams, Washington,D.C. (1992) to be published.
5. V.Fedorov, W.Schmidt, and T.Westermann, to be published.
6. M.P.Desjarlais, T.D.Pointon, D.B.Seidel, R.S.Coats, M.L.Kiefer, J.P.Quintenz, and S.A.Slutz, Phys. Rev. Lett. 67, 3094, 1991;
T.D.Pointon, D.B.Seidel, and M.P.Desjarlais, 17th IEEE International Conference on Plasma Science, Oakland, CA. May 21-23, 1990.
7. W.Schmidt, Th.Westermann, M.Alef, K.May, D.Seldner, and E.Stein, Proc. 8th. Conf. on High-Power Particle Beams, Novosibirsk, World Scientific Singapore (1990) 451.
8. S.A.Slutz, D.B.Seidel, and R.S.Coats, J.Appl.Phys., 59,11(1986).
9. Cross-Field Microwave Devices, Ed.Okress, N.Y.,1961.
10. V.E.Golant, A.P.Zhilinsky, and I.E.Zakharov, Fundamentals of Plasma Physics, John Wiley & Sons, New York, 1980.
11. O.Buneman, R.H.Levy, and L.M.Linson, Appl.Phys., 37, 3203(1966).
12. C.L.Chang, D.P.Chernin, A.T.Drobot, E.Ott,and T.M.Antonsen, Phys.Fluids, 29, 1258(1986).
13. R.C.Davidson, Phys.Fluids, 28, 1937(1985).
14. J.W.Poukey, S.Humphries, Jr., and T.R.Lockner, Phys.Fluids, 25, 1471(1982).

SIMULATION OF A B_r ION DIODE

R. J. Faehl and D. J. Rej
Los Alamos National Laboratory, Los Alamos, NM 87545

Abstract

Electromagnetic PIC simulations of a B_r magnetically insulated ion diode in an extraction geometry have been performed to investigate time-dependent diode characteristics, ion beam transport, and beam quality. Various magnetic field geometries and electron sources have been studied so that total ion throughput may be optimized. Calculational results are compared with data from our ion beam experiment. Comparisons are also drawn between the simulations and magnetic insulation theory.

Introduction

Intense ion beams promise to yield exciting results in the fields of ion implantation, alloying, and thin film production.[1-4] Experiments currently underway at Los Alamos [5] use a B_r magnetically insulated diode (MID) in an extraction geometry. This configuration can reliably produce a focusable ion beam with high ion-to-electron current efficiency. We have undertaken an extensive numerical modeling effort in conjunction with these experiments to obtain better understanding of the dynamics of this ion source. Such calculations can facilitate interpretation of diagnostic data, yield insight into the effect of parameter or geometry changes on diode operation, and can yield information about aspects of the operation which are difficult to diagnose, such as sheath properties.

Magnetic insulation of electron flow has been studied since the advent of magnetrons. It assumed a special interest for intense ion beam production when it was realized that transverse magnetic fields could be applied which were strong enough to insulate electron flow, but have only minimal effect on ions. The overwhelming electron "losses" in bipolar flow ion sources could be made negligible, allowing the full power of the diode to be applied to accelerating ions. Instead of recovering simple monopolar flow, the insulated electrons modify the diode characteristics so that the AK gap is effectively diminished. Diode impedance in ion MID's was reduced by orders of magnitude over ion space-charge limited flow. Drift of the insulating electrons also distorts the magnetic field distribution. Desjarlais [6] has analyzed these processes and proposed a model which can account for enhancements in the ion current by the factors of 10 or more over space-charge limited current, routinely seen in MID experiments. Though this is the most complete model advanced to date, geometric aspects of our configuration present difficulties in applying his results. This paper will present our numerical results, but will limit comparisons to those which can be made between our experimental data, simple theory and the simulations.

Numerical Methods

The primary configuration simulated in this study is depicted in Fig. 1. Details of this system can be found in another paper in these proceedings.[5] The source of protons is an annular plastic insert, which forms a surface flashover plasma. Flashover dynamics are not treated self-consistently here. For calculational purposes, the plastic is assumed to become a fully grounded, space-charge limited source of ions once a threshold for surface electric fields is

reached. This threshold is between 50-150 kV/cm in the calculations. Actual plasma formation is a complicated topic, influenced by UV irradiation [7], direct electron impact, voltage prepulse, and surface irregularities. Detailed modeling of the flashover should include such effects, perhaps with statistical fluctuations to account for shot-to-shot variations. Here we model the surface plasma heuristically, retaining aspects which are pertinent to diode operation.

The pulser which drives our experiment is currently charged to 0.6 MV with a pulse width of slightly over 1 μs. With a MID load, the voltage rises in 100-150 ns to 400 kV, which is maintained as either a flattop or slowly decreasing pulse for 400-600 ns, after which it falls abruptly. A typical voltage pulse, along with total current and extracted ion current, is shown in Fig. 2.

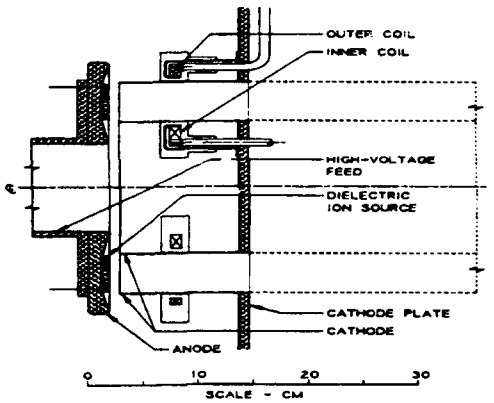

Fig. 1 Schematic of ion beam magnetically isolated diode.

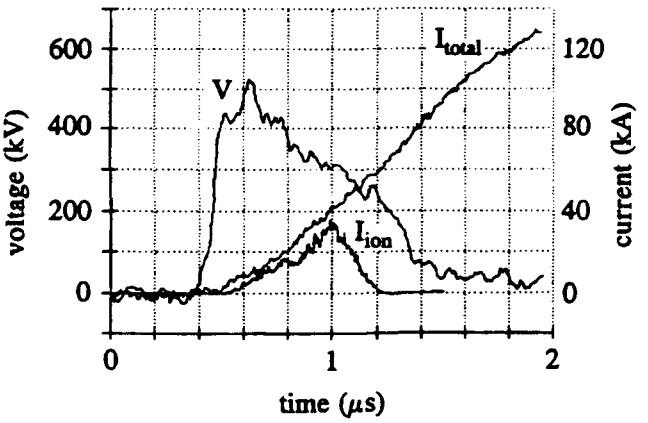

Fig. 2 Typical experimental probe shows impedance collapse over 0.6 μs trace.

Modeling the entire voltage pulse self-consistently is impractical. We simulated the diode operation with a fully electromagnetic 2-1/2 D particle-in-cell code. Because Maxwell's equations are solved for all six electric and magnetic field components on a numerical mesh, a fairly stringent Courant condition, $\delta t < \delta x/c$, needs to be satisfied. With a typical spatial resolution of 2 mm, a time step of roughly 3 ps was used. In the absence of anode plasma expansion and electron sheath scattering, the full pulse could actually be modeled on a CRAY/YMP. There is strong evidence to suggest that the anode plasma does expand [8,9], the electron sheath does distort [6], and that charge exchange and fast neutral transport [8, 10-12] all play roles in determining the time-dependent impedance of the diode, however. We modeled diode closure by conducting a series of simulations of length 30-50 ns, each with fixed anode plasma dimensions. The closure was emulated by making the anode plasma progressively wider, so that the distance to the electron sheath was reduced in each calculation. This "plasma" was assumed to possess infinite conductivity, so that it was perfectly grounded to the metallic anode. Fields were thus excluded from its interior, though electrons incident on it were not absorbed. The infinite conductivity approximation is probably naive, since recent studies indicate fast magnetic field penetration of the anode plasma[13]. Though this approximation exaggerates the strength of diamagnetic field increase in the gap, we present these calculations as limiting cases. Future calculations will explore the effect of finite plasma conductivity.

The justification for treating AK gap closure with a series of "snapshots" is both practical and physical. Previous studies indicate that a closure rate of 1-2 cm/μs occurs, at least over limited time scales. In a simulation of duration 50 ns, the electron sheath and the ion beam propagation both take on an asymptotic character, but the gap closure has evolved only over

spatial scales on the order of 1 mm. Since this is less than a typical numerical cell size, it is doubtful that the distortion of the diode geometry alters diode impedance over such time scales.

The initial magnetic field was calculated by numerically solving Poisson's equation for the vector potential,

$$\nabla^2 A_\theta = 4\pi J_\theta(r,z)/c \qquad (1)$$

subject to the condition that certain regions, such as the metallic part of the anode, were flux excluding. Magnetic fields were then computed from $B = \nabla \times A$. A typical map of the flux contours is shown in Fig. 3.

Finally, the inner and outer cathode structure of the diode gives a very inhomogeneous electric field distribution in vacuum. Figure 4 shows the E_Z contours of the bare, non-emitting cathode. Once electron flow is initiated, however, the sheath drastically modifies these fields. The self-consistent E_Z contours, including the sheath charge, are shown in Fig. 5. Comparison of Figs. 4 and 5 illustrates the effect of the electron sheath dramatically. The entire cathode is permitted to emit electrons.

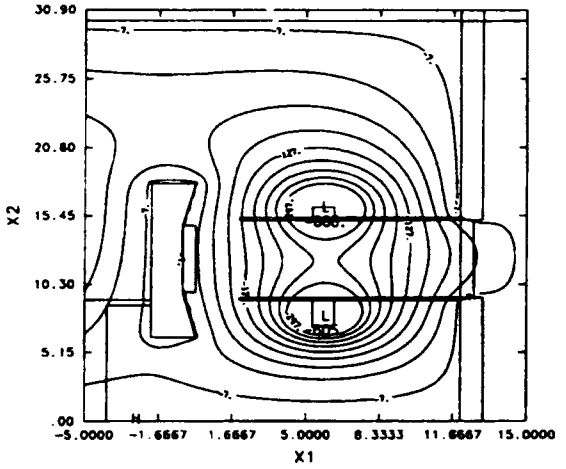

Fig. 3 Flux contours calculated for case of equal current (6.0 kA) flowing in both field coils; anode and cathode supports are flux excluding.

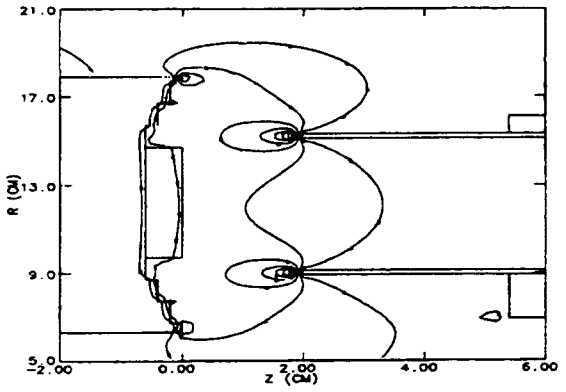

Fig. 4 E_Z contours for MID in vacuum; 405 kV potential difference.

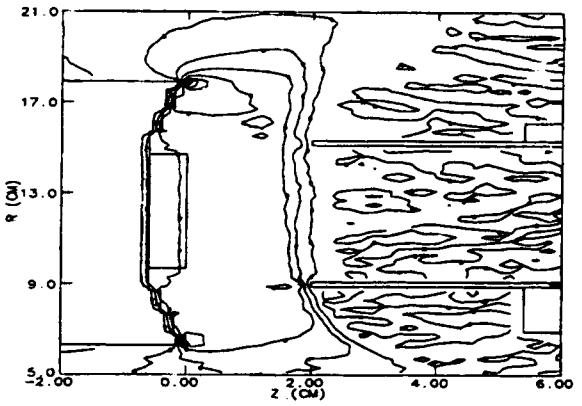

Fig. 5 E_Z contours for MID after electron sheath formation.

Magnetic Insulation Theory

The basic idea in magnetically insulated electron flow is that when individual electrons move under perpendicular electric and magnetic fields, there will be only a finite excursion in the direction of the electric field. Periodic Larmor oscillations may occur. It is straightforward to analyze magnetically insulated flow, and extract some basic properties. Conservation of energy in the steady state, $\gamma = \gamma_o + e(\phi - \phi_o)/mc^2$ and conservation of canonical angular momentum in the direction of an ignorable coordinate, $p_\theta = p_{\theta o} + e(A_\theta - A_{\theta o})/mc$ provide sufficient information to define a critical magnetic field, B^*, and the sheath width, z^*. Here, γ is

the relativistic Lorentz factor, ϕ is the electrostatic potential, A_θ is the θ component of the vector potential, $p_\theta = v_\theta\gamma/c$ is the particle momentum in that direction, and c is the vacuum speed of light. For a planar gap of width d, a uniform electric field across it E_O, and a uniform magnetic field perpendicular to it B_O, the critical magnetic field is defined so that an electron starting at rest on one side of the gap is just prevented from reaching the other side,

$$B^* = (mc/de)\sqrt{(eE_od/mc^2)\,(2 + (eE_od/mc^2))} \qquad (2)$$

Moreover, for any magnetic field $B > B^*$, the electron can cross a distance of only

$$z^* = 2(mc^2/e)E_o/(B_o^2 - E_o^2) \qquad (3)$$

These well-known results [4] define the electron sheath characteristics in the absence of space-charge fields, far from any edges.

For the B_r extraction geometry in which we are interested, neither of these conditions is satisfied. We want the transverse magnetic field to dominate over the longitudinal B_z field. When $B_r >> B_z$, it is easy to show that $B_r \approx B_{ro}r_o/r$. The insulating field has significant gradients over the diode region. Further, the finite radial extent of the insulating region means that edge effects can not be neglected *a priori*. An analysis which includes such effects could be constructed, but would probably need to be solved numerically. We have chosen to simulate the MID self-consistently, and then compare those results with simple theory. We will not attempt to make detailed comparisons directly with the Desjarlais model at this time, but intend to undertake this in the near future.

Numerical Results

The dynamics of a MID can be illustrated by considering a typical simulation. First, a TEM voltage pulse with a trapezoidal pulse shape is launched down a coaxial line in the vacuum configuration. Fields from the coils are the only nonzero constituents in the vacuum. A short linear risetime (2.6 ns) is used to minimize the transient phase of the calculation. After a few electromagnetic transits through the system, the electric field distribution is the same as that found by a static solution of Lapace's equation, except for fluctuations. Space-charge limited emission of either ions or electrons, depending upon the polarization, begins once the surface field stress exceeds some threshold value. The emitted electrons rapidly create a quasi-steady sheath, which in turn modifies the vacuum diode fields. Ion beam generation occurs as a result of the total self-consistent electric field in the diode.

The ion beam is largely unaffected by the B_r insulating field and propagates through the sheath into initially field-free space between the inner and outer cathodes. For an intense ion beam, the space-charge fields could lead to rapid divergence and most of the ions would be lost to the cathode walls. These same fields, however, induce emission of neutralizing electrons from the cathode walls. The neutralizing electrons move under both the beam electric and magnetic fields, and the coil magnetic fields. This combination induces a somewhat complicated flow pattern between the cathodes, but the net result is that the ion stream is overneutralized upstream of the field coils and underneutralized downstream. Ion beam transport is strongly effected by the degree of electron neutralization. The ion beam is observed to diverge in the downstream region, which persists even after leaving the extractor. Examination of the charge and field distributions confirm that the region just beyond the field coils is one with relatively low electron density. The quantitative nature of this phenomenon, seen in all MID extractor geometry simulations performed by us is still being analyzed.

Figure 6 shows a snapshot of a representative ion flow at a time 45 ns into the calculation. The electron sheath structure which accompanies this ion flow is given in Fig. 7. Details of the sheath can be seen more clearly in Fig. 8. Even though the current in the field coils was adjusted to give flux lines almost parallel to the anode surface for this case, the electron flow is not parallel to it. In fact, analysis of this calculation reveals that the outer cathode provides almost twice as much total charge as does the inner one, yet it is electrons from the inner cathode which comprise most of the outer edge of the sheath. Since this part of the sheath is closest to the anode, it presumably governs the diode impedance. This feature can be altered by changing the currents in the field coils or the relative length of either cathode section, so that the emitting ends are on the same A_θ contour.

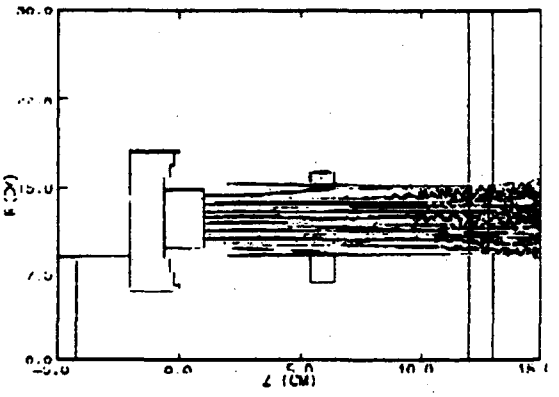

Fig. 6 Spatial configuration of ion beam calculated at t = 45 ns.

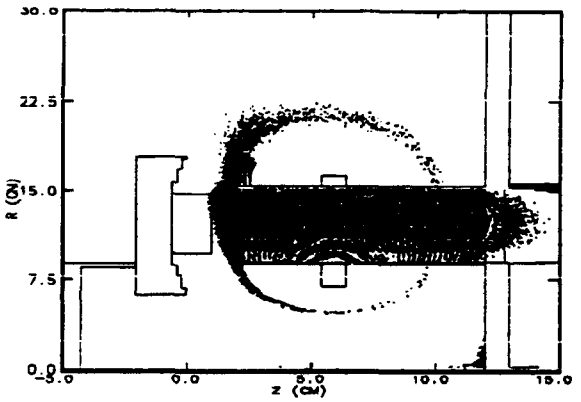

Fig. 7 Electron spatial distribution at this t = 45 ns corresponding to Fig. 7.

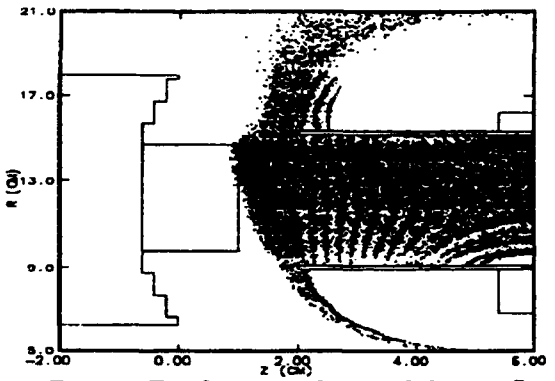

Fig. 8 Zoom of Fig. 8 to show details of electron flow.

If the electron flow were laminar along the E x B direction, analysis of this structure could be made along the lines used by Desjarlais. Though each particle in these calculations remains on an orbit of constant canonical momentum in the θ-direction, that constant can be different, depending on the location from which it is emitted. A snapshot of the radial profile of the electron radial momentum is given in Fig. 9. Electrons from both cathodes exhibit similar dispersion, and both have mean momenta, averaged over the ensemble, near zero, $\langle p_r \rangle \approx 0$. An analogous snapshot for p_θ, Fig. 10, shows similar dispersion, but with an overall net drift in the positive θ-direction. This is consistent with E x B drifts, since $E_z B_r$ is positive in this region. The drift current will enhance B_r in the insulating region, as Fig. 11, the radial profile of B_r close to the anode indicates.

The simple theory of magnetic insulation predicts the maximum electron excursion in a uniform field should be given by Eq. (3). Table I gives a comparison of the maximum sheath width based on the vacuum field, the sheath modified field, and as seen in the simulations. In the table, $B_r|_{min}$ refers to the minimum insulating field in the gap initially, $z^*|_0$ is Eq. (3) evaluated with that field and $z^*|_{mod}$ with the diamagnetically modified field.

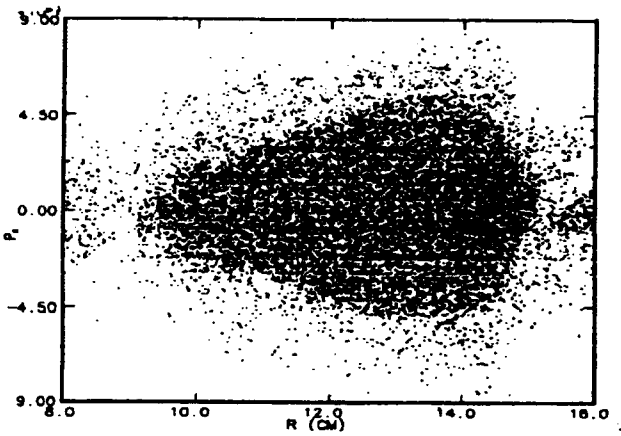

Fig. 9 Radial distribution of electron p_r momentum in the diode region $\langle p_r \rangle \approx 0$.

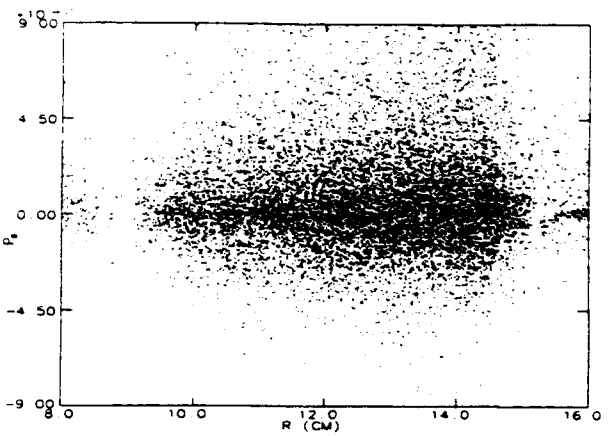

Fig. 10 Radial distribution of electrom p_r momentum in diode region, t = 45 ns.

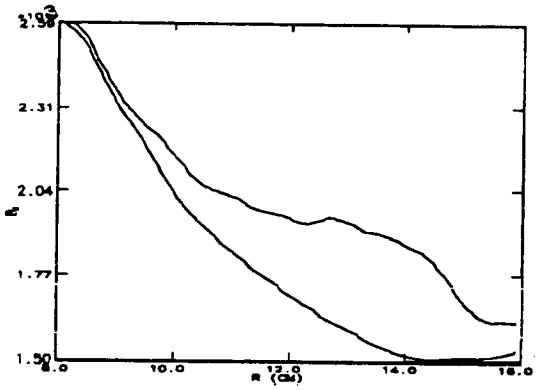

Fig. 11 Compression of radial profile of B_r near surface at t = 0, t - 30 ns.

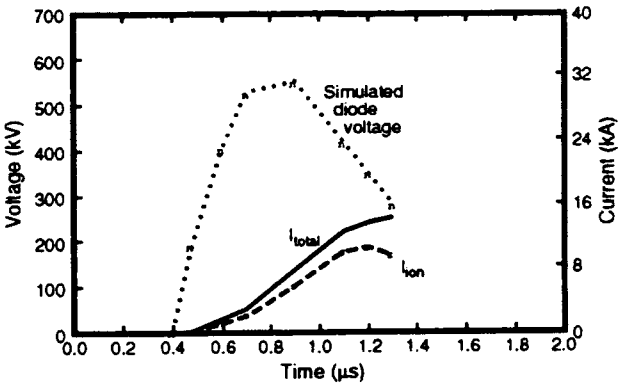

Fig. 12 Assumed closure rate of 2 cm/μs gives characteristics similar to Fig. 2.

Table I
Comparison of Sheath Width Predictions

$B_r\|_{min}$ (Gauss)	$z^*\|_o$(cm)	$z^*\|_{mod}$(cm)	$z^*\|_{sim}$(cm)
3000	0.27	0.27	0.78
2250	0.49	0.46	0.92
1500	1.26	0.76	1.75
1000	4.09	1.50	1.95

The simple model for insulation gives fair agreement with the simulations. The discrepancies, however, indicate that a more complete model is needed.

Finally, we expect the impedance to fall throughout the voltage pulse, as the AK gap collapses. The experimental data in Fig. 2 are consistent with such a model. We have emulated the dynamic process with the anode "plasma" extending progressively closer to the cathode. Correlating this with the data can only be done if the experimental gap closure rate is known. As a crude guess, we have folded simulation results into a time history by assuming a closure rate of 2.0 cm/μs. The results are shown in Fig. 12. While these are similar to Fig. 2, a more physically based model is needed before quantitative comparisons can be drawn.

Summary

We have performed extensive numerical simulations of a MID in extractor geometry. The results agree reasonably well with experimental data. Further refinements are still needed in understanding the details of anode plasma formation and expansion, and in the neutralization of ion beam space charge in the extractor transport region. Such studies are being actively pursued.

References

[1] K. Yatsui, et al., Laser and Particle Beams **3**, 119 (1985).
[2] Y. Shimitori, et al., J. Appl. Phys. **63**, 968 (1988).
[3] A. D. Pogrebnjak, et al., Phys. Lett. **A129**, 259 (1985?).
[4] V. M. Bystritskii and A. N. Didenko, High Power Ion Beams, American Institute of Physics (New York), 1989.
[5] Don Rej, et al., Proc. of Beams 92.
[6] M. P. Desjarlais, Phys. Fluids **B1**, 1709 (1989); M. P. Desjarlais, Phys. Rev. Lett.
[7] J. A. Maenchen, J. Appl. Phys. **65**.
[8] R. Pal and D. Hammer, Phys. Rev. Lett. **50**, 732 (1983).
[9] D. J. Johnston, E. T. Burns, J. P. Quintenz, K. W. Beig, A. V. Farnsworth, L. P. Mix, and M. A. Palmer, J. Appl. Phys. **52**, 168 (1981).
[10] E. W. Gray, J. Appl. Phys. **58**, 132 (1985).
[11] D. J. Johnston, J. P. Quintenz, and M. A. Sweeney, J. Appl. Phys. **57**, 794 (1985).
[12] Y. Maron, E. Sarid, O. Zahavi, L. Perelmutter, and M. Sarfaty, Phys. Rev. A **39**, 584 (1989).
[13] A. Fruchtman and Y. Maron, Phys. Fluids B **3**, 1546 (1991).

ION BEAM DIVERGENCE FROM UNSTABLE FLUCTUATIONS IN APPLIED-B DIODES *

R.N. Sudan and D.W. Longcope
Laboratory of Plasma Studies, Cornell University,Ithaca, NY 14853

Abstract

An electron plasma oscillation driven unstable by ion streaming is identified with the low frequency mode observed in QUICKSILVER numerical simulations. This mode heats the electrons along the magnetic field and is ultimately stabilized by the thermal spread. A quasilinear theory determines the saturation level of the fluctuations, the ion divergence, and the ion energy and momentum spread as they exit the diode. The ion divergence is predicted to be independent of the ion mass for fixed diode voltage and scales as the product of the effective gap and the ion beam enhancement factor over Child Langmuir current.

Introduction

There is considerable experimental evidence for electron leakage to the anode that occurs both in the form of bursts as well as a steady drizzle[1,2]. This leakage can be explained in terms of two-dimensional electric potential perturbations[3]. Such perturbations arise as a result of collective instabilities driven by the applied diode voltage with accelerates the ions and causes the electrons to suffer an $\mathbf{E} \times \mathbf{B}$ drift[4,5,6,7]. The fluctuations in electric field caused by the instabilities lead to ion beam divergence and electron leakage. It is the objective of this study to identify the most dangerous of the unstable modes, compute its saturation level, and the resulting ion beam divergence.

The major conclusions of this study are as follows: (1) The dominant low-frequency mode observed in QUICKSILVER simulations[8] is identified with an electrostatic electron plasma oscillation whose phase varies along the magnetic field as well as across it. This mode is made unstable by the streaming ions and the frequency of the most unstable mode is given by

$$|\omega_0| = \left| |k_y v_d| - |k_z| \omega_e d/\pi \right| = 2.105\, \tau_i^{-1} ,$$

where the ion transit time $\tau_i = d/u$, d is the gap width, u is mean ion velocity exiting the cathode, v_d is the electron drift speed, ω_e is the electron plasma frequency, $k_y = 2\pi/\lambda_y$, $k_z = \pi/L_z$, where L_z is the width of ion beam in a barrel diode geometry and λ_y is the azimuthal wavelength of the dominant fluctuation. The CGS system of units is used throughout.
(2) The saturation level of the amplitude of the unstable fluctuations scales as

$$\Phi_s \propto qd$$

where q is the total electron charge in the diode per unit area of the emitting anode surface.
(3) The ion divergence scales as Φ_s/V and is independent of the ion mass for fixed diode voltage V. Moreover,

$$\frac{\Delta\theta_z}{\Delta\theta_y} \propto \frac{\lambda_y}{L_z}$$

where $\Delta\theta_y$, $\Delta\theta_z$ are the ion divergences in the horizontal and vertical planes.

*Research supported by Sandia National Laboratory, under contract no. 63-4881 and by ONR grant no. N00014-89-J-1770.

(4) The quantity $\delta E/\delta p_y$ scales as

$$\delta E/\delta p_y = \omega_0/k_y = c|(V/dB) - (\omega_c d/c)(\lambda_y/2L_z)|$$

where δE and δp_y are the perturbations in the ion energy and horizontal momentum at the cathode.
(5) The fractional spread in the ion energy $\Delta E/E \propto \Phi_s/V$ and the fractional spread in transverse ion momentum $\Delta p_y/p_x \propto \Phi_s d/V\lambda_y$ and $\Delta p_z/p_x \propto \Phi_s d/VL_z$.

Mathematical Model for Collective Modes

In the present study, we consider the stage following the saturation of the diocotron mode and neglect gradients of density n and drift velocity v_d. The electrons are highly mobile along the magnetic field lines. To obtain a strong electron response we require a component of the fluctuating electric field along the magnetic field B. Thus, we choose a fluctuation of the form $\phi = \phi(x)\exp i(k_y y + k_z z - \omega t)$, where $k_z = \pi/L_z$

We linearize the dynamical equations for the electrons and ions about the following state. Since the electron and ion densities, n_e and n_i, are approximately uniform over most of the anode-cathode (AK) gap except for a region close to the anode we choose $n_e = n_i = n_0$. Thus, the ion diode is replaced by an AK gap d, in which the ions are injected at $x = 0$ with velocity $\mathbf{u} = u\hat{x}$ and the electrons drift across a uniform magnetic field $\mathbf{B} = B\hat{z}$ with constant velocity $\mathbf{v}_d \equiv -(eV/dB)\hat{y}$ where V is the gap voltage.

The ion dynamics are treated in the unmagnetized non-relativistic, zero-temperature limit and the electrons are treated in the relativistic drift kinetic limit. From the equations of continuity and momentum balance for the ions and the electron response from the drift kinetic equation and Poisson's equation, we obtain

$$\left(\frac{d}{dx} - i\frac{\omega}{u}\right)^2 \{\nabla^2 - \lambda_d^{-2}\mathrm{W}(\zeta)\}\phi + (\omega_i^2/u^2)\nabla^2\phi = 0 \tag{1}$$

with $\omega_i^2 = 4\pi n_0 e^2/m_i$ and $W(\zeta) = \pi^{-\frac{1}{2}}\int du\, ue^{-u^2}/(u-\zeta)$, $\zeta = \bar{\omega}/(k_z)(2T/m)^{\frac{1}{2}}$, $\lambda_d^2 = \bar{\gamma}T/4\pi n_o e^2$. Note that $\bar{\gamma} = (1 - v_\perp^2/c^2)^{-\frac{1}{2}}$ with $v_\perp^2 > v_\parallel^2$. Equation (1) together with boundary conditions determines the eigenfunctions and eigenfrequencies of the low frequency modes.

Eigenmodes of the Diode System

The eigenmodes of this model can now be determined by integrating a linear fourth order ordinary differential equation in x subject to four linear homogeneous boundary conditions. The natural units of length and time in this system are the gap distance, d, and the ion transit time, $\tau_i = d/u$, respectively. Redefining all quantities in those dimensions the equation and boundary conditions can be written

$$\left(\frac{d}{dx} - i\omega\right)^2\left(\frac{d^2}{dx^2} + \mu_e - k_t^2\right)\phi + \mu_i\left(\frac{d^2}{dx^2} - k_t^2\right)\phi = 0 \ , \tag{2}$$

$$\phi(0) = 0 \ , \ \phi(1) = 0 \ , \ \phi''(0) = 0 \ , \ \phi'''(0) + (\mu_e + \mu_i - k_t^2)\phi'(0) = 0 \ , \tag{3}$$

where the electron and ion responses are represented by the dimensionless parameters

$$\mu_e(\omega) = -\frac{d^2}{\lambda_d^2}\mathrm{W}\left(\frac{\omega - k_y v_d}{\sqrt{2}k_z v_e}\right) \ , \ \mu_i = \omega_i^2\tau_i^2 \ ,$$

and $k_t^2 = k_y^2 + k_z^2$.

In terms of the ion current, $j = en_0 u$, this latter expression takes the form $\mu_i = \frac{2}{9}\left[\frac{eV}{m_i u^2/2}\right]^{3/2}\frac{j}{j_{CL}}$, where the non-relativistic Child-Langmuir current is

$$j_{CL} = \frac{1}{9\pi}\sqrt{\frac{2eV}{m_i}}\frac{V}{d^2} \ .$$

n	ω_0	$g_i^{(n)}(\omega_0)$
± 1	± 2.105	0.0174
± 1	∓ 6.461	0.0153
± 2	∓ 9.458	0.00641
± 2	± 4.727	0.00611

Table 1: Local maxima of the normalized growth rate $g_i^{(n)}(\omega_0)$.

Since the term in square brackets will be of order unity and the current enhancement, j/j_{CL}, does not usually exceed 30 we can expect the ion plasma period to be much smaller than the ion transit time: $\mu_i \ll (2\pi)^2$.

The final two boundary conditions result from demanding that both the perturbed ion density and ion velocity vanishes at the anode $x = 0$.

We solve Eqn. (2) by expansion in the small parameter μ_i. To zero-order in μ_i

$$\phi_0(x) = \sin(n\pi x) \ , \tag{4}$$

$$\sqrt{\mu_e(\omega_0)} = n\pi \ , \ n = \pm 1, \pm 2, \ldots \ . \tag{5}$$

Equation (5) gives the dispersion relation for each branch of electron mode in the system.

In the case of cold electrons, $v_e, \lambda_d \to 0$, one can use the large argument expansion for $W(\zeta)$ to get

$$\mu_e(\omega) \simeq \frac{k_z^2 \omega_e^2}{(\omega - k_y v_d)^2} \ . \tag{6}$$

Using this in (5) gives the explicit dispersion relation for cold electron modes

$$\omega_0 = k_y v_d + \frac{|k_z|\omega_e}{n\pi} \ , \tag{7}$$

To next order in μ_i, a correction ω_1 to the frequency ω_o is obtained with

$$\omega_1 = |k_z|\omega_e \mu_i \ g^{(n)}(\omega_0) \ , \tag{8}$$

and

$$g_i^{(n)}(\omega_0) = \frac{2\omega_0(\omega_0^2 + n^2\pi^2)}{n\pi(\omega_0^2 - n^2\pi^2)^3}\left[(-1)^n \cos(\omega_0) - 1\right] + (-1)^n \frac{\omega_0^2 \sin(\omega_0)}{n\pi(\omega_0^2 - n^2\pi^2)^2} \ . \tag{9}$$

The values of the local maxima of $g_i^{(n)}$ are summarized in Table 1.

It can be seen from (7) that the special case $v_d = 0$ does not imply any restriction on ω_0; in particular it would be possible to have the above instability even if electrons were not drifting. This establishes that the free energy driving the instability comes from the ion motion not from the electron drift. In practice, however, k_z is set by the rather small vertical extent of the anode, L_z, while k_y is free to assume a wide range of values. Thus, we expect to observe the mode with k_y which maximizes the linear growth rate. In the case of $\mu_i \ll 1$ considered above this means

$$k_y = \pm v_d^{-1}\left(2.105 - |k_z|\omega_e/\pi\right) \ .$$

As a consequence the unstable mode observed will have an oscillation frequency $\omega_0 = \pm 2.105\,\tau_i^{-1}$ independent of the other parameters of the system. Although it is an electron mode which is driven unstable its frequency is set by the ion transit time.

In terms of the physical parameters the electron plasma frequency, in a reference frame drifting with the electrons, is

$$\frac{|k_z|\omega_e}{n\pi} = \sqrt{\frac{m_i}{\bar{\gamma} m_e}\mu_i}\,\frac{d}{nL_z}\,\tau_i^{-1} = \frac{\sqrt{2}}{3}\sqrt{\frac{m_i}{\bar{\gamma} m_e}}\,\frac{d}{nL_z}\sqrt{\frac{j}{j_{CL}}}\,\tau_i^{-1} \ , \tag{10}$$

where $n = \pm 1$. The presence of the large factor $\sqrt{m_i/\bar{\gamma}m_e}$ makes this a very high frequency, which according to Eq. (7) must be doppler shifted to match the much lower frequency, $\omega_0 = \pm 2.105\,\tau_i^{-1}$. Thus in practical terms the electron drift is necessary to provide this doppler shift. Since the drift velocity is proportional to the same large factor,

$$k_y v_d = k_y d \frac{B_{cr}}{B} \sqrt{\frac{m_i}{\bar{\gamma}m_e}}\,\tau_i^{-1} \quad , \tag{11}$$

it is possible to accomplish this with a wavelength on the same scale as the gap distance. Finally, in order that these two terms are of opposite sign $k_y v_d$ must have the sign opposite to n and therefore opposite to ω_0. The phase velocity in the laboratory frame is determined only after the cancellation of these two large terms in Eq. (7) and its sign depends on the accuracy with which each term has been treated. In our treatment, assuming an equilibrium with no variations across the gap this sign turns out to be negative. The most robust element of this prediction is not the sign of the phase velocity, rather that its magnitude will be much less than v_d.

The functions $g^{(n)}$ are the diagonal matrix elements of the operator $\nabla^{-2}(\omega + iu\,d/dx)^{-2}\nabla^2$ which enter the first order correction to the frequency. Since this operator is not hermitian these diagonal elements are, in general, complex. In an unbounded system these modes would have real frequency, therefore the operator would be hermitian; we established, however, that this is not the case in the diode. The two-stream instability with kinetic ions has a character distinctly different from the hydrodynamic one. This is also the nature of the ion diode instability, but rather than Landau damping the ion modes decay because each ion remains in the diode only a short time.

Numerical results

Numerical solutions of Eqn. (2) for values of μ_i which are not necessarily small ($\mu_i = 3.4$) reveal that the above picture is qualitatively correct. The most unstable mode is found to be the $n = -1$ mode at a frequency of $\omega = -1.78 + 0.91i$ which occurs at $k_y = 1.17$. Furthermore, as the temperature is introduced this remains the dominant mode, but with a decreased growth rate. When the parallel electron thermal velocity reaches a value of $v_e = 11.6$ (which represents a mean kinetic energy only 5% of ion kinetic energy) the mode is stabilized.

Saturation of Low Frequency Instability

As the amplitude of the instability grows so does the spread in the electron distribution in v_z. The increase in the v_z spread stabilizes the modes as discussed in Sect. 3. We employ quasilinear theory to estimate the evolution of the electron temperature until it attains the critical level to saturate the instability amplitude by reducing the growth rate to zero. From the drift kinetic equation with $f = \langle f \rangle + \delta f$ etc., where $\langle f \rangle$ is the averaged distribution we obtain, following conventional techniques: (we return to unnormalized units in what follows)

$$\frac{\partial T}{\partial t} = \frac{e^2}{m} \sum_{\mathbf{k}} [1 + 18(k_z^2/\bar{\omega}_{\mathbf{k}}^2)(T/m)] \frac{\partial}{\partial t}(k_z^2 |\phi_{\mathbf{k}}|^2/\bar{\omega}_{\mathbf{k}}^2) \tag{12}$$

Equation (47) can be solved iteratively to obtain $[K^2 = (\pi/d)^2 + k_y^2 + k_z^2]$

$$\sum_{\mathbf{k}} K^2 |\phi_{\mathbf{k}}|^2 = 4\pi n_0 T[1 - 18(K^2/\omega_e^2)(T/m)]. \tag{13}$$

When T reaches the critical temperature T_c defined by

$$\bar{\omega}_{\mathbf{k}}/k_z = g^{-1}(T/m)^{\frac{1}{2}} \tag{14}$$

the growth vanishes because of Landau damping; g is a numerical factor $\lesssim 0.2$.

Thus, the saturation amplitude of the fluctuations is given by setting $T = T_c$ and $K \approx \pi/d$ in Eqn.(13), $(T/m > \omega_e^2 d^2/18\pi^2)$

$$\Phi_s^2 \equiv \sum_{\mathbf{k}} |\phi_{\mathbf{k}}|^2 = G n_0^2 e^2 d^4 \propto q^2 d^2 \tag{15}$$

where G is a numerical factor for which our best estimate is $G \approx 16g^2/\pi^2 = 0.06$ and q is total electron charge in the diode per cm^2 of anode surface. Thus, the saturation amplitude of the rms potential fluctuations Φ_s is proportional to the total charge per cm^2 in the diode gap and the gap distance. This conclusion fits in very well with numerical simulation results of QUICKSILVER, which show a dramatic increase in the divergence with the electron charge in the gap.

Ion Divergence, Energy and Momentum Spread, Electron Leakage

We now calculate the ion divergence resulting from the saturated amplitude of the fluctuations. Because the ions spend only a time d/u in the gap, we are justified in assuming that their dynamics is approximated by the linearized equation of motion

$$(-i\omega + u\frac{\partial}{\partial x})\delta \mathbf{u} = -(e/m_i)\nabla \tilde{\phi}_{\mathbf{k}} \tag{16}$$

which yields at the cathode

$$\delta u_x = -i(e/m_i u^2)\omega\ \phi_{\mathbf{k}}\ hd \exp i\omega d/u \tag{17}$$
$$\delta \mathbf{u}_\perp = -i(e/m_i u)\mathbf{k}\ \phi_{\mathbf{k}}\ hd \exp i\omega d/u$$

with $h \equiv \int_0^d dx\ ^{-i\omega x/u} \sin \pi x/d$. For the most unstable modes, $\omega = \pm 2.105\,\tau_i$, this is $h = 0.5723 \exp(\pm i 1.053)$. It follows from Eqn. (52) that if δE is the perturbed energy and δp_y is the perturbed ion momentum at the cathode then,

$$\frac{\delta E}{\delta p_y} = u\frac{\delta u_x}{\delta u_y} = \frac{\omega}{k_y} = c|V/dB - (\omega_c d/c)(\lambda_y/2L_z)| \tag{18}$$

The QUICKSILVER simulations yield $\delta E/\delta p_y \sim c/28$ which is much less than the drift speed $c/2$. Adopting $L_z = 9.4$ cm, $V = 9$ MV $B = 3.8$ T, $d = 1.5$ cm and $n_0 = 1.5 \times 10^{13}$ cm^{-3}, $(\mu_i = 3.4)$. We obtain from (53) a value $c/13$ at zero electron temperature and $c/21$ at the critical temperature, for $\delta E/\delta p_y$ in reasonable agreement.

The ion divergences defined as $\Delta\theta_x = \langle|\delta u_x|^2\rangle^{\frac{1}{2}}/u$ and $\Delta\theta_y = \langle|\delta u_y|^2\rangle^{\frac{1}{2}}/u$ are then given by

$$\Delta\theta_x = \left(\frac{e^2}{m_i^2 u^4}\sum_{\mathbf{k}} k_x^2 |\phi_{\mathbf{k}}|^2 d^2 |h|^2\right)^{\frac{1}{2}} \propto \frac{\Phi_s}{V}\frac{d}{L_x} \tag{19}$$

$$\Delta\theta_y = \left(\frac{e^2}{m_i^2 u^4}\sum_{\mathbf{k}} k_y^2 |\phi_{\mathbf{k}}|^2 d^2 |h|^2\right)^{\frac{1}{2}} \propto \frac{\Phi_s}{V}\frac{d}{\lambda_y}$$

and $\Delta\theta_x/\Delta\theta_y \approx \bar{k}_x/\bar{k}_y$ where $\bar{k}_x$ and $\bar{k}_y$ are averaged over the spectrum. Thus, for fixed diode voltage V the ion divergences are independent of the ion mass. An estimate of the numerical values for $\Delta\theta_x$ and $\Delta\theta_y$ is obtained by substituting for $|\phi_{\mathbf{k}}|^2$ from Eqn. (15) assuming the dominant mode $n = 1$, $\bar{k}_y/\bar{k}_x = 2.93$, $\bar{k}_x = \pi/L_x$, $\mu_i = 3.4$, and employing the numerical values for the diode stated above. Thus,

$$\Delta\theta_x \sim 19\,\text{mrads}$$

$$\Delta\theta_y \sim 43\,\text{mrads}$$

Now $n_0 e d^2 = (2\alpha/9\pi)eV$ where $\alpha = j/j_{CL}$ the enhancement factor so that the important conclusion to draw from this analysis is that the divergence scales directly as the enhancement factor and is also proportional to the gap d. While the numerical factors may be approximate the scaling relationship must follow from the physics of the processes outlined above. Also, $|h|$ is a decreasing function of frequency which shows quantitatively that high frequency fluctuations will not affect the divergence.

Computation of ΔE, Δp_y and Δp_z

A diagnostic developed at Sandia measures the spread in ion energy and ion momentum as they exit from the diode. Following the analysis from Eqn. (16) onwards it is straightforward to establish that

$$\begin{aligned} \Delta E/E &= \langle|\delta E|^2\rangle^{\frac{1}{2}}/E = 2(e/m_i u^3)\Big(\sum_{\mathbf{k}} |\omega|^2|\phi_{\mathbf{k}}|^2|h|^2 d^2\Big)^{\frac{1}{2}} \\ &\approx |\omega_0\tau_i|\Phi_s/V \end{aligned} \tag{20}$$

$$\Delta p_{y,z}/p_x = (e/m_i u^2)\Big(\sum_{\mathbf{k}} k_{y,z}^2|\phi_{\mathbf{k}}|^2|h|^2 d^2\Big)^{\frac{1}{2}} \approx \frac{\Phi_s}{V}\frac{d}{\lambda_y} \tag{21}$$

Thus, the ΔE and Δp_y measured in QUICKSILVER runs gives the saturated level of the fluctuation amplitude and λ_y.

Conclusions

We conclude with suggestions for designing diodes for optimum beam brightness $\mathcal{B} = j/\Delta\theta_y\Delta\theta_z$. If $\Delta\theta_y$ and $\Delta\theta_z$ are each proportional to the enhancement factor then it is clear that the brightness will deteriorate with increased enhancement. Clearly, the path to high brightness lies in as high a value of B/B_* as possible with as small a value for the gap as feasible for the applied voltage (B_* is the critical field for magnetic insulation). Electron heating during the diocotron phase may be helpful to stabilize the low frequency mode. Suggestions[9] for using electron limiters would be helpful by reducing the electron charge qd in the gap.

Acknowledgements

We are indebted to M. Desjarlais and T. Pointon for providing us with data from QUICKSILVER simulations, and to B. Oliver for many discussions on the topic of this study.

References

1. T. Orzechowski and G. Bekefi, Phys. Fluids, **19**, 43 (1976); **22**, 978 (1979).
2. Y. Maron, Phys. Fluids, **27**, 285 (1984).
3. M.P. Desjarlais and R.N. Sudan, Phys. Fluids, **30**, 1536 (1987).
4. M.P. Desjarlais and R.N. Sudan, Bull. Am. Phys. Soc., **28**, 1148 (1983).
5. C.L. Chang, T.M. Antonsen, E. Ott, and A.T. Drobot, Phys. Fluids, **27**, 2545 (1984).
6. E. Ott, T.M. Antonsen, C.L. Chang, and A.T. Drobot, Phys. Fluids, **28**, 1948 (1985).
7. C.L. Chang, D.P. Chernin, A.T. Drobot, E. Ott, and T.M. Antonsen, Phys. Fluids, **29**, 1258 (1986).
8. M.P. Desjarlais, T.D. Pointon, D.B. Seidel, R.S. Coats, M.L. Kiefer, J.P. Quintenz, and S.A. Slutz, Phys. Rev. Lett., **67**, 3094 (1991).
9. J.B. Greenly and S. Slutz, Pvt. Communication.

QUICKSILVER SIMULATIONS OF APPLIED-B EXTRACTION DIODES*

M. P. Desjarlais and T. D. Pointon
Sandia National Laboratories
Albuquerque, New Mexico 87185

Abstract

Recent simulations of the barrel diode configuration with the 3-D particle-in-cell code QUICKSILVER have detailed a rich evolution of unstable electromagnetic waves [Phys. Rev. Lett. **67**, 3904 (1991)]. Preliminary simulations of applied-B extraction diodes with the 3-D particle-in-cell code QUICKSILVER suggest some significant differences in equilibrium and stability properties between extraction and barrel diodes. The extraction diode simulations suggest better divergence and, when a limiter is employed to reduce divergence, potentially better efficiency. In the case of proton beam simulations, the low frequency ion mode was not found even for peak ion current enhancements in excess of 10. The ion mode was exhibited by the lithium beam extraction diode simulations. Limiter simulations with both proton and lithium beams demonstrated very good divergence. A scheme for obtaining uniform ion current density profiles based on a uniform dynamic gap calculation appears promising.

Introduction

Applied-B ion diodes have been in use for many years as a means to provide intense ion beams[1] for Inertial Confinement Fusion (ICF) and other applications. These diodes are highly nonlinear devices with complex equilibrium and stability properties. Common cylindrical configurations for these diodes are the radially converging "barrel" diode with an axial applied magnetic field and the axial "extraction" diode with a radial applied magnetic field. Recent simulations of the barrel diode configuration with the 3-D particle-in-cell code QUICKSILVER[2] have detailed a rich evolution of unstable electromagnetic waves.[3] Understanding these waves is particularly important to ICF applications because of their potential for inducing divergence in the ion beam. The simulations of the barrel configuration have shown that the diode typically starts out in a low divergence phase associated with high frequency diocotron oscillations. Typical wavelengths for the diocotron mode are 3 to 5 cm with frequencies of 2 to 3 GHz. This phase is generally followed by lower frequency diocotron oscillations and finally a low frequency ion mode. These lower frequency modes can be very detrimental to the ion beam divergence. The ion mode generally appears with frequencies less than or equal to $1/\tau_i$, where τ_i is the ion transit time in the diode. These low frequency oscillations couple particularly well to the ions and generate large divergences. It was found that limiting the electron charge in the

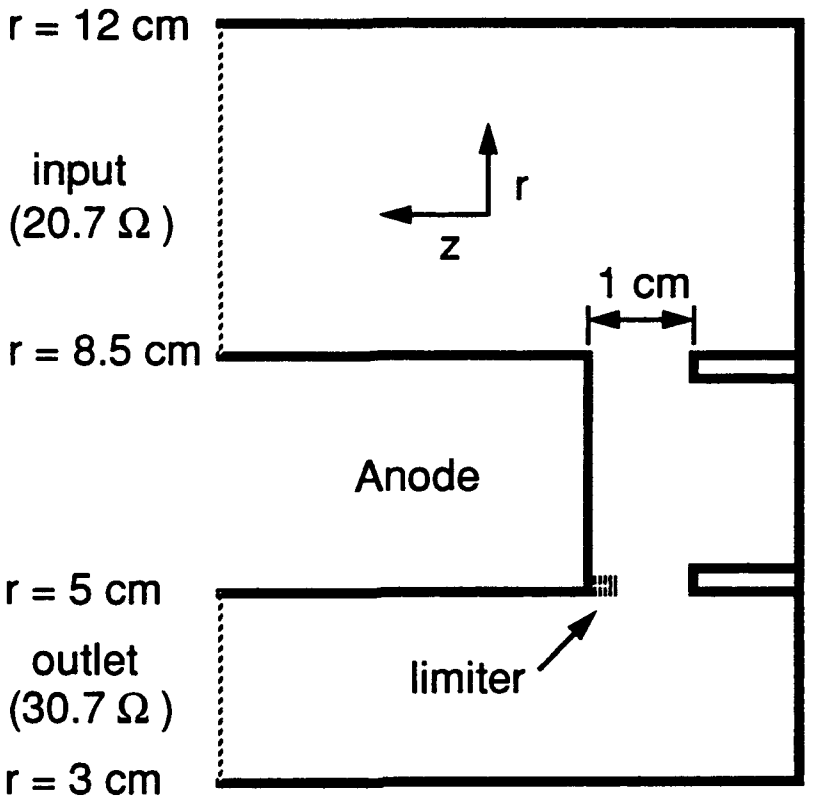

Fig. 1. Geometry and coordinate system for the applied-B extraction diode simulations.

diode through the use of an electron limiter could dramatically improve the divergence by maintaining the high frequency diocotron phase. In this paper we report preliminary results of QUICKSILVER simulations of an applied-B extraction diode configuration.

Simulation geometry

The simulation geometry is shown in Fig. 1. The simulations are periodic in the $\hat{\theta}$ direction with a periodic length of $\pi/4$. The primary applied magnetic field is a simple $1/r$ B_r field. In addition, a small uniform B_z component was added in a few simulations to tilt the magnetic stream functions in the direction of "uniform insulation".[4] (Uniform insulation in Ref. 4 is defined for hypothetical electrons that only move axially.) The diode is driven by a forward going TEM wave entering the input wave port. The wave is a linear ramp to full voltage in typically 5 nsec. Space charge limited emission of ions is permitted over the central 2.5 cm of the anode and space charge limited electron emission is permitted from the cathode blades and the conducting boundary (gas cell foil) between the cathode blades. Electron emission is not permitted in the feed region because of the simplified applied field configuration and the relatively small feed gaps. The impedances

for the input and outlet wave ports, scaled to 2π, are 20.7 Ω and 30.7 Ω respectively. Because of the outlet port, this geometry has a diode open circuit voltage of 1.2 times the forward going wave and an effective accelerator impedance scaled to 2π of 12.4 Ω. Also shown is Fig. 1 at the inner anode radius is a dashed profile of the electron limiter[5] employed in some simulations.

Proton simulations

Four proton beam simulations were performed, all with an applied magnetic field corresponding to $rB_r = -0.16$ in MKS units. This yields a V_{crit} of about 5.4 MV at the outer cathode tip and about 8.6 MV at the inner cathode tip. With this simple $1/r$ B_r field the magnetic streamlines are parallel to the anode. Different forward going waves (4 and 6 MV) were used to generate different degrees of ion current enhancement. The observed diode operating points are in good agreement with those calculated using applied-B ion diode theory[6] at sheath fractions ρ close to, but not quite at, the saturated limit and with V_* corresponding to the lowest V_* over the active anode. The ion current efficiencies are in general very good with typical efficiencies in excess of 90%.

One complication that arises when using the diode theory for these extraction diode configurations is the variation in the limiting voltage V_* with radius. The $1/r$ scaling of the radial magnetic field produces that scaling in V_* for the case of streamlines parallel to the anode (no B_z). The theoretical virtual cathode motion is then greater at larger radii where V_* is lower. This in turn causes a skewing of the ion current density profile to larger radii. These effects are clearly seen in the simulations. Since the limiting voltage in the diode theory does not depend on anode area, the operating point voltage and total current calculation is relatively insensitive to the localization of the current density at higher enhancements. Significant motion of the virtual cathode corresponds to those operating points near V_*. But near V_* the effective anode area has a small effect on the total current and voltage. A lower enhancement proton simulation operated at 2.7 MV with a peak ion current enhancement I_i/I_{cl} of 9. The current density was slightly skewed towards the outer radii with a ratio of current density of 1.4 for points 25% of the way in from the beams outer and inner edges. A higher enhancement simulation operated at 3.3 MV with a peak I_i/I_{cl} of 12.5. In this case the current density was significantly skewed with a ratio for the same two points of 2.7.

One interesting feature of these proton extraction diode simulations is the absence of the ion mode seen at similar enhancements in the barrel diode simulations. Since the low frequency ion mode generates more divergence than the diocotron mode, this translates into better divergence in the extraction diode proton simulations. For example divergences

of 12 to 15 milliradians were observed in the lower enhancement simulation. This is in contrast to divergences in the 30 milliradian range for comparable simulations in barrel geometry. We do not yet have a clear understanding of the essential difference between the two geometries leading to this difference in behavior. One feature does stand out that would appear to have some relevance. The electron density profiles in the extraction diode simulations appear to evolve to a profile with fewer electrons near the anode than is observed in the barrel diode simulations. Since the transition to the ion mode in barrel geometry has been correlated with the amount of electron charge in the diode relative to the saturated solution,[3] it is possible that the extraction diodes have less tendency to accumulate electrons near the anode and thus have better divergence properties. More simulations will be needed to investigate whether or not some inadequacy of the simulations is biasing the results. Future simulations with protons at higher enhancements will be performed to see if the ion mode appears.

Even though the ion mode was not observed in the proton simulations at these low to moderate enhancements, a proton simulation with a limiter was performed to investigate its effect. The limiter was positioned as shown in Fig. 1 and had a height of 2.8 mm. The forward going wave corresponding to the lower enhancement simulation was used. The resulting azimuthal and radial divergences dropped from the 12 to 15 milliradian range to between 8 and 10 milliradians. In addition, the diode operated at a higher impedance; the voltage was 3.3 MV (as opposed to 2.7 MV) and the peak enhancement was 4 (as opposed to 9). An interesting result of the limiter simulation in contrast to similar simulations in the barrel diode is the high ion current efficiency observed (over 90%). Since electrons are populating the flux surfaces that intersect the limiter at a relatively slow rate, the amount of current taken up by the limiter is fairly small and yet it still performs its function. In addition, the limiter located as it is, at the inner anode radius, is in the highest V_{crit} portion of the diode.

Lithium simulations

Several lithium beam simulations were performed with a radial magnetic field given by $rB_r = -0.504$. This gives a V_{crit} at the outer cathode tip of about 17.9 MV. In addition, a small uniform B_z component was employed in a few simulations to investigate the effect of tilting the streamlines so that a given streamline is closer to the anode for smaller radii. This has the effect of reducing the flux between the virtual cathode streamline (in this case the streamline going through the outer cathode tip) and the anode, thereby reducing the variation in V_*. Forward going waves of 8.3, 11.7, and 17.5 were used to give open circuit voltages of 10, 14, and 21 MV respectively. Operating point voltages and total

currents were in good agreement with diode theory if V_* for the outer anode emission radius was used and the electron sheath was assumed to extend uniformly across 80 to 90% of the acceleration gap for the nonlimiter simulations. The diodes operated at 8, 9.6, and 11 MV with peak enhancements of 3.2, 6, and 11 respectively.

Unlike the proton beam simulations, the lithium beam simulations did demonstrate the ion mode, even at enhancements as low as 6. One exception was the lowest enhancement simulation that operated at an enhancement of about 3.2. This simulation remained in the diocotron phase and yielded a lithium beam divergence of about 8 milliradians. In contrast to the barrel diode simulations, it appears that in the extraction diode configuration a sufficiently large magnetic field can lead to a steady operating point consistent with the diocotron mode. In the barrel diode simulations, very high magnetic fields gave a prolonged diocotron phase but did not prevent the eventual transition to the ion mode. We do not yet understand why the lithium simulations exhibit the ion mode at moderate enhancements and the proton simulations do not.

A limiter simulation was performed for the configuration that ran at 9.6 MV and an enhancement of 6 without the limiter. With the limiter the diode ran at 10.8 MV and an enhancement of just over 3. The divergence improved dramatically from around 30 milliradians without the limiter to under 5 milliradians with the limiter, corresponding to a steady high frequency diocotron oscillation. The best divergence with a limiter we have observed in simulations of the barrel diode geometry was about 8 milliradians. In addition the ion current efficiency in this extraction diode simulation was over 90%. The highest efficiencies at which we have observed successful limiter operation in simulations of barrel diode geometries were on the order of 60%.

Obtaining uniform current density profiles

The primary consideration for obtaining uniform current density profiles in moderate to highly enhanced diodes is that the virtual cathode establish a uniform acceleration gap at the diode operating point. The virtual cathode will undergo more compression towards the anode in regions of lower V_*. However, it is possible to find solutions of the diode theory applied in a local 1-D manner at various radial locations such that the self-consistent virtual cathode location at the desired operating point is a uniform distance from the anode. The smaller the amount of overall virtual cathode motion, the smaller the necessary B_z correction is.

Shown in Fig. 2 are the θ-averaged ion current densities for four lithium simulations. The curves marked by $\triangle$ and $\square$ correspond to two simulations with a V_{oc} of 14 MV. A small B_z component of 0.4 T was added in the $\square$ simulation. Note how the current density has

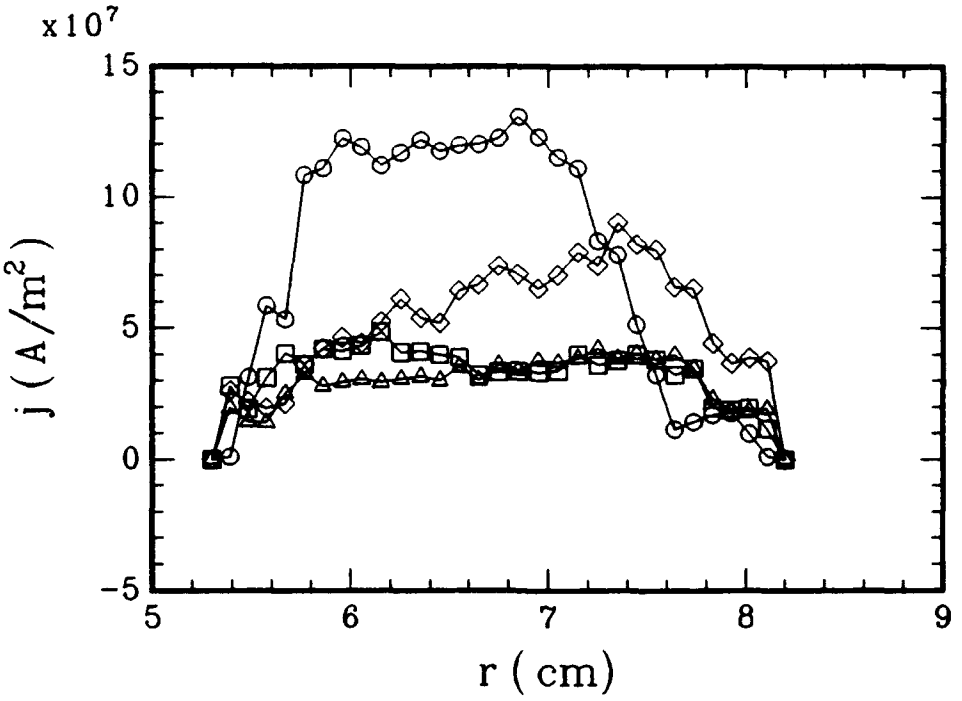

Fig. 2. Profiles of the ion current density averaged over θ for ($\triangle$) $B_z = 0$ T, $V_{oc} = 14$ MV; ($\square$) $B_z = 0.422$ T, $V_{oc} = 14$ MV; ($\diamond$) $B_z = 0$ T, $V_{oc} = 21$ MV; and ($\circ$) $B_z = 0.703$ T, $V_{oc} = 28$ MV.

skewed from the outer to inner radii. At lower enhancements where the virtual cathode motion is relatively small, very little B_z contribution is needed to effect the current density profile. The simulation marked by $\diamond$ had a V_{oc} of 21 MV and no B_z component; the current density is significantly skewed towards the outer radii. The curve marked by $\circ$ corresponds to a simulation that was designed using the uniform dynamic gap scheme outlined above. This had a V_{oc} of 28 MV and a B_z of 0.7 T. Even though this was the highest current simulation, the ion current density has a good plateau.

*This work was funded by the U. S. Department of Energy under contract DE-AC04-76-DP00789.

References

1. J. P. VanDevender and D. L. Cook, Science **232**, 831 (1986); J. P. VanDevender, Plasma Phys. Controlled Fusion **28**, 841 (1986).
2. D. B. Seidel, M. L. Kiefer, R. S. Coats, T. D. Pointon, J. P. Quintenz, and W. A. Johnson, in *Computational Physics*, edited by A. Tenner (World Scientific, Singapore, 1991), pp. 475–482.
3. M. P. Desjarlais, T. D. Pointon, D. B. Seidel, R. S. Coats, M. L. Kiefer, J. P. Quintenz, and S. A. Slutz, Phys. Rev. Lett. **67**, 3094 (1991).
4. S. A. Slutz and D. B. Seidel, J. Appl. Phys. **59**, 2685 (1986).
5. S. A. Slutz, T. A. Mehlhorn, J. E. Maenchen, C. Ruiz, and J. R. Woodworth, J. Appl. Phys. **62**, 16 (1987).
6. M. P. Desjarlais, Phys. Rev. Lett. **59**, 2295 (1987); Phys. Fluids B **1**, 1709 (1989).

OPERATION OF A HIGH IMPEDANCE APPLIED-B EXTRACTION ION DIODE ON THE SABRE POSITIVE POLARITY LINEAR INDUCTION ACCELERATOR*

D. L. Hanson, M. E. Cuneo, P. F. McKay, J. E. Maenchen, R. S. Coats, J. W. Poukey, S. E. Rosenthal, W. E. Fowler, D. F. Wenger, M. Bernard, J. R. Chavez, W. F. Stearns

Sandia National Laboratories - Pulsed Power Sciences Center
P. O. Box 5800 Albuquerque, New Mexico USA 87185-5800

Abstract

We present results from initial experiments with a high impedance applied-B extraction diode on the SABRE ten stage linear induction accelerator (6 MV, 300 kA). We have demonstrated efficient coupling of power from the accelerator through an extended MITL (Magnetically Insulated Transmission Line) into a high intensity ion beam. Both MITL electron flow in the diode region and ion diode behavior, including ion source turn-on, virtual cathode formation and evolution, enhancement delay, and ion coupling efficiency, are strongly influenced by the geometry of the diode insulating magnetic field. For our present diode electrode geometry, electrons from the cathode feed play a large role in the evolution of the virtual cathode. Both experimental data and particle-in-cell numerical simulations show that a uniform radial distribution of these feed electrons is required for uniform ion emission and efficient diode operation.

I. Introduction

The demonstration of efficient acceleration of ions at high voltage in an extraction geometry is essential for the development of high power light ion drivers for Inertial Confinement Fusion (ICF). Extraction geometry applied-B ion diodes, which are insulated by a radial magnetic field and accelerate ions in the axial direction, permit channel transport, beam bunching, beam overlap, and target standoff required for the use of multiple drivers in high power pellet implosion experiments. Efficient operation of applied-B extraction ion diodes has recently been demonstrated at relatively low diode voltage (1 - 3 MV) in both low impedance [1-5] and high impedance [6] diode configurations, and has been shown to require an appropriate insulating magnetic field geometry to maintain a uniform electron charge distribution and good electron confinement near the anode emission surface. This can be accomplished in several ways [2,3,6,7], the simplest being to overinsulate the diode and operate at low enhancement with an active ion source and a small A-K gap [2,3]. However, because of limitations on MITL/diode coupling, magnetic field coil technology, ion source output, and the large self-magnetic field bending of high current density ion beams, the production of 100-TW ion beams will most likely require high impedance extraction diodes, operating near the critical insulating field at moderate to high enhancement and powered by high voltage multistage inductive voltage adders.

In the present work, we have addressed several issues important for the operation of high impedance extraction ion diodes. We report on the coupling of power from the recently constructed SABRE ten-stage linear induction accelerator into a high intensity ion beam generated by an applied-B extraction ion diode operated at high

impedance. In positive polarity, each of the ten SABRE voltage adder sections contributes a distinct group of electrons to MITL electron flow [6,8]. A key issue investigated in these experiments and in particle-in-cell (PIC) numerical simulations is how this complex electron flow couples into a magnetically insulated extraction ion diode. A second issue investigated is the role of applied magnetic field geometry in controlling the formation and evolution of the A-K gap electron sheath and the resulting effect on ion emission uniformity and ion coupling efficiency. For a marginally insulated ion diode where virtual cathode sheath electrons are emitted predominantly from the cathode tips, one important requirement for high ion efficiency is that the anode emission surface be uniformly insulated to a high degree with respect to the cathode tips [5,7]. This insures that the spacing of the virtual cathode charge distribution and resulting enhancement of ion current density over the vacuum gap Child-Langmuir space-charge-limited ion emission will be uniform across the anode. With our present electrode geometry, electrons from both the cathode feed and cathode tips play an essential role in the formation and evolution of the virtual cathode. We have studied electron charge distributions and associated diode behavior for two distinct magnetic field profiles, and the implications for efficient diode operation are discussed in this paper.

II. Experimental Arrangement

A schematic of the extraction ion diode used in these experiments is shown in Fig. 1. The diode was powered by SABRE, a ten-stage linear induction voltage adder operated in positive polarity. The output of the final adder section (300 kA at about 6 MV) is coupled through a 4-m-long coaxial MITL (vacuum impedance $Z_0 = 40\ \Omega$) to the ion diode. Initial power flow experiments were performed with a 5-cm mean radius, planar extraction ion diode using a wax-filled grooved flashover ion source to produce a 32-cm^2 annular ion beam. The anode-cathode gap was about 10.5 mm for all experiments. The insulating magnetic field geometry was accurately controlled using anode and cathode field coils driven by individual 60 kJ capacitor banks. The MITL and ion diode were extensively

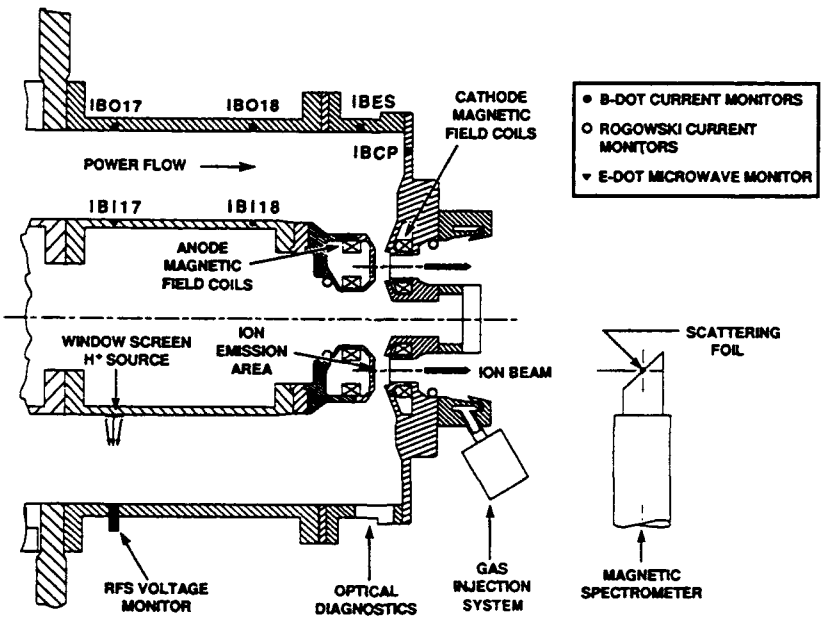

Fig. 1. SABRE positive polarity applied-B extraction ion diode.

instrumented with B-dot current monitors for electrical and ion current measurements. A 1.2-m long "diagnostic spool" located immediately upstream from the diode housed a number of electrical diagnostics, including calibrated current shunts, to characterize the power flow entering the diode region. During these initial measurements, the time-resolved magnetic spectrometer and range-filter-scintillator (RFS) voltage monitors shown in Fig. 1, together with a filtered CR-39 peak voltage detector, were mounted on the diagnostic spool, approximately 1-m upstream from the diode gap, and were used to measure the energy spectrum of ions accelerated across the MITL gap. Ion beam diagnostics included witness plates, shadow boxes, and filtered and unfiltered Faraday cup arrays located near the cathode tips to measure peak proton energy, ion current density, and uniformity.

III. Comparison of Experiment and Simulations

We have investigated diode operation in some detail with two distinct magnetic field profiles. For our original field geometry (FIELD 1, shown later in Fig. 3), the anode emission surface was approximately uniformly insulated magnetically with respect to electrons emitted from the cathode tips, with the separatrix near midgap. Electron loss to the anode measured with 4-chloro-styrene radiochromic film and ion emission measured with an unfiltered Faraday cup array were both heavily weighted toward the inner anode radius. The diode operated at a low ion coupling efficiency I_{ION}/I_{TOT} of 0.20 at an average critical insulating voltage V_{CRIT} of 7.5 MV. We then optimized the magnetic field profile empirically to arrive at a field profile (FIELD 2, shown in Fig. 4) where the anode was approximately uniformly insulated with respect to electrons emitted from the cathode feed. With this field, the electrons entered the diode early in the pulse with a uniform radial distribution. The subsequent electron loss and ion beam emission were approximately uniform across the anode. For this optimized field profile at an average V_{CRIT} of 8.2 MV, ion coupling efficiency I_{ION}/I_{TOT} was 0.60 and ion generation efficiency I_{ION}/I_{DIODE} was 0.70. MITL line voltages for this latter configuration, calculated from MITL currents measured 1 m upstream from the diode using the generalized flow model and the full-gap-flow model [6,8], are shown in Fig. 2 a). A comparison of these voltages with peak proton energies measured at the same location with magnetic spectrometer and filtered CR-39 voltage monitors suggests that the electron flow pattern approaching the diode is closer to full gap flow than to the parapotential flow pattern of a single cathode injector. Peak proton energy at the diode was 4.5 MeV. The diode currents for this shot are shown in Fig. 2 b). Turn-on of the flashover ion source is typically very rapid, virtually coincident with initial current flow into the A-K gap region. The average peak ion current density measured with an unfiltered Faraday cup array was 5.5 kA/cm^2 and the peak proton current density for protons with kinetic energy greater than 1.2 MeV measured with a filtered Faraday cup was 2.9 kA/cm^2. The diode operated at an enhancement of about 30 over the Child-Langmuir space-charge-limited multi-species ion emission for the 10.5 mm vacuum gap. For both magnetic field geometries, radiochromic film detectors along the inner MITL (anode) indicated significant electron losses at the location where the applied magnetic flux is concentrated and returned behind the anode.

To understand this diode behavior, we have performed TWOQUICK [9] self-consistent 2-D electromagnetic particle-in-cell simulations of electron flow in the diode region for both magnetic field configurations. Fig. 3 shows electrons early in the power pulse for the FIELD 1 geometry. At t = 10 ns, the MITL electron flow is completely lost where the applied magnetic flux returns to the anode. By t = 30 ns, this flow becomes insulated and sufficient boundary current is recovered to raise the MITL efficiency to about 80%. The rapid accumulation of charge in the diode near the anode early in time consists entirely of electrons emitted from the cathode feed. This component of the electron sheath is skewed by the magnetic field geometry and is responsible for the electron loss to the inner portion of the anode and for the rapid but nonuniform ion emission observed in the experiment. The dense, uniformly-spaced sheath of cathode tip electrons is initially localized near the cathode tips and only later (after 30 ns) has moved sufficiently toward the anode to contribute to uniform, enhanced ion emission. In contrast, the distribution of cathode feed electrons rapidly accumulating near the anode at early time for the FIELD 2 geometry (Fig. 4) is quite uniform across the anode emission area. This results in the uniform electron loss and rapid uniform ion emission across the anode observed in the experiment. It is the dense electron sheath emitted from the cathode tips that is now tilted, but this component of the sheath contributes to preferential ion emission at large radius only later in time. Fig. 5 shows in detail the radial charge distribution of cathode feed electrons near the anode for FIELD 1 and FIELD 2 geometries at t = 10 ns. The simulations indicate that the most rapid transition to fully enhanced ion emission occurs for the FIELD 2 geometry.

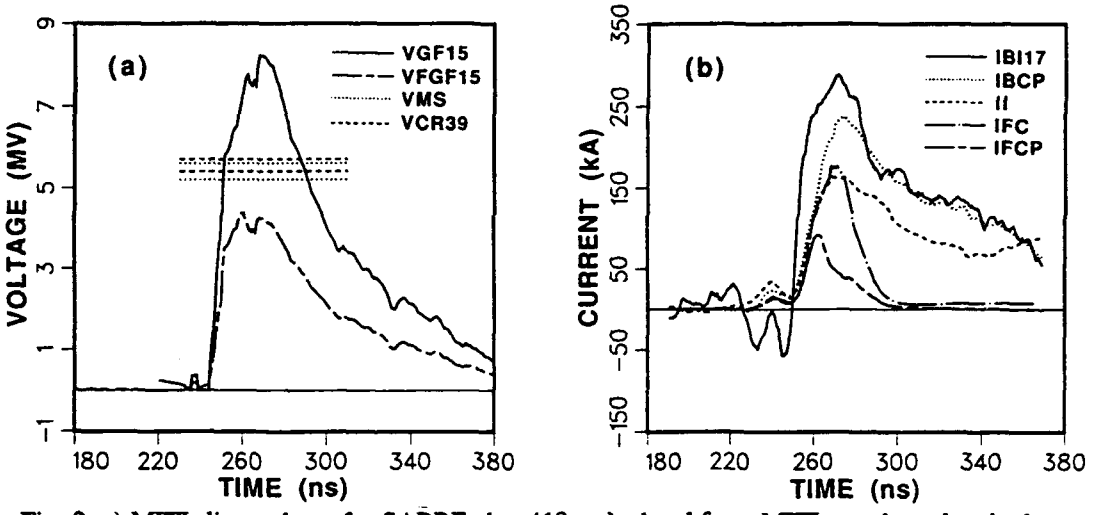

Fig. 2. a) MITL line voltage for SABRE shot 419, calculated from MITL anode and cathode currents measured 1 m upstream from the ion diode using the generalized flow model (VGF15) and the full-gap-flow model (VFGF15). Also shown are the peak energies of protons accelerated across the MITL gap at the same axial position obtained from magnetic spectrometer and filtered CR-39 voltage monitors. (b) Diode currents for SABRE shot 419: IBI17 is the MITL anode (total) current at position 17 (Fig. 1); IBCP is the cathode current entering the A-K gap region (Fig. 1); II is the total ion current determined from ion B-dot measurements at the cathode tips; IFC is the total ion current obtained by multiplying the average ion current density from an array of unfiltered Faraday cups near the cathode tips by the anode emission area (32.2 cm^2); IFCP is the proton current (E_p > 1.2 MeV) obtained by multiplying the ion current density from a filtered Faraday cup by the anode emission area.

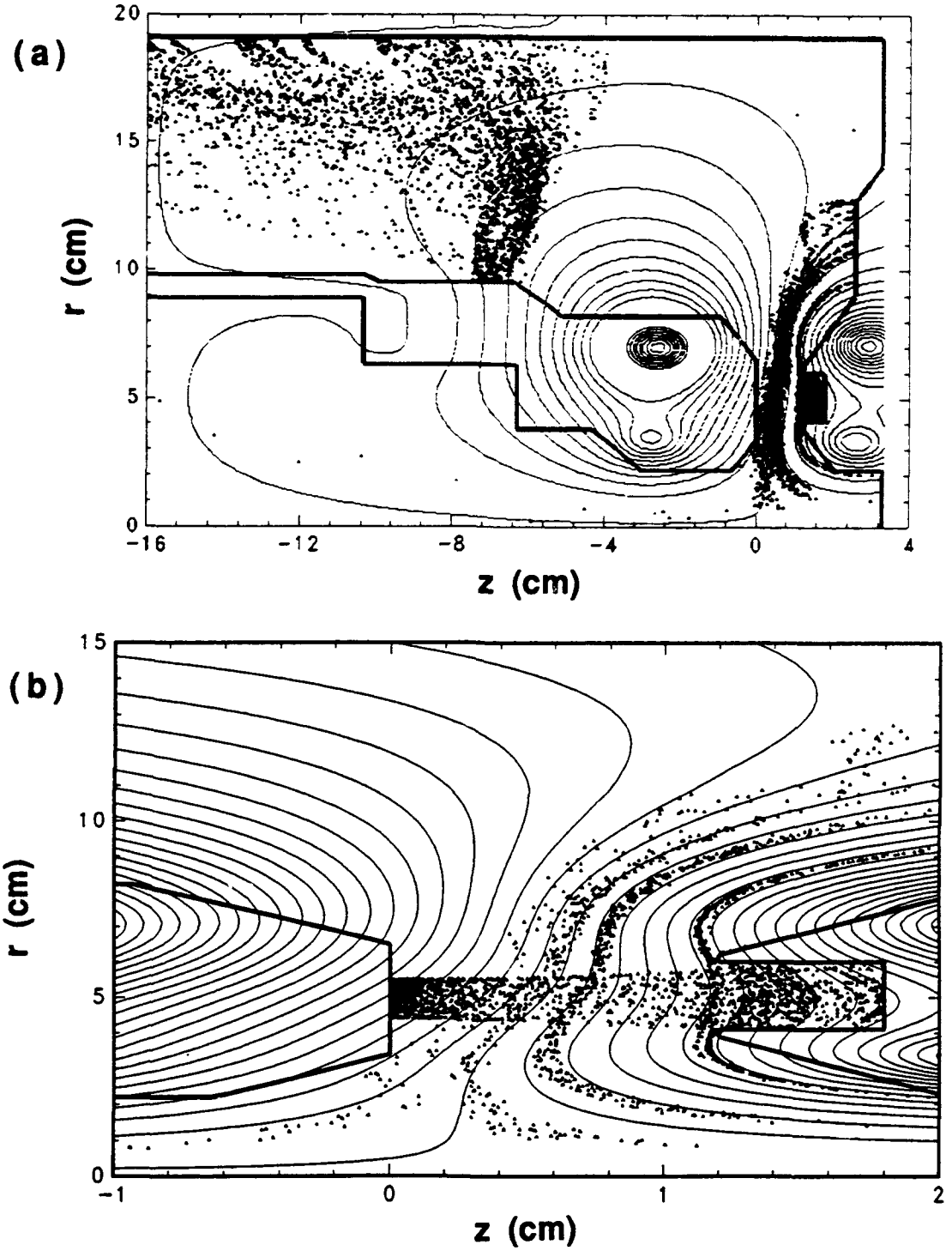

Fig. 3. a) Particle plot of electrons at 10 ns into the power pulse from a TWOQUICK electromagnetic particle-in-cell simulation using the FIELD 1 applied magnetic field configuration calculated from measured coil currents with the diffusive magnetic field solver TRIDIF [10]. b) Expanded particle plot at 7.5 ns showing details of the FIELD 1 magnetic field geometry and electron and ion distributions in the A-K gap. Note the loss of feed electrons to the inner portion of the anode emission area which is consistent with experimental results.

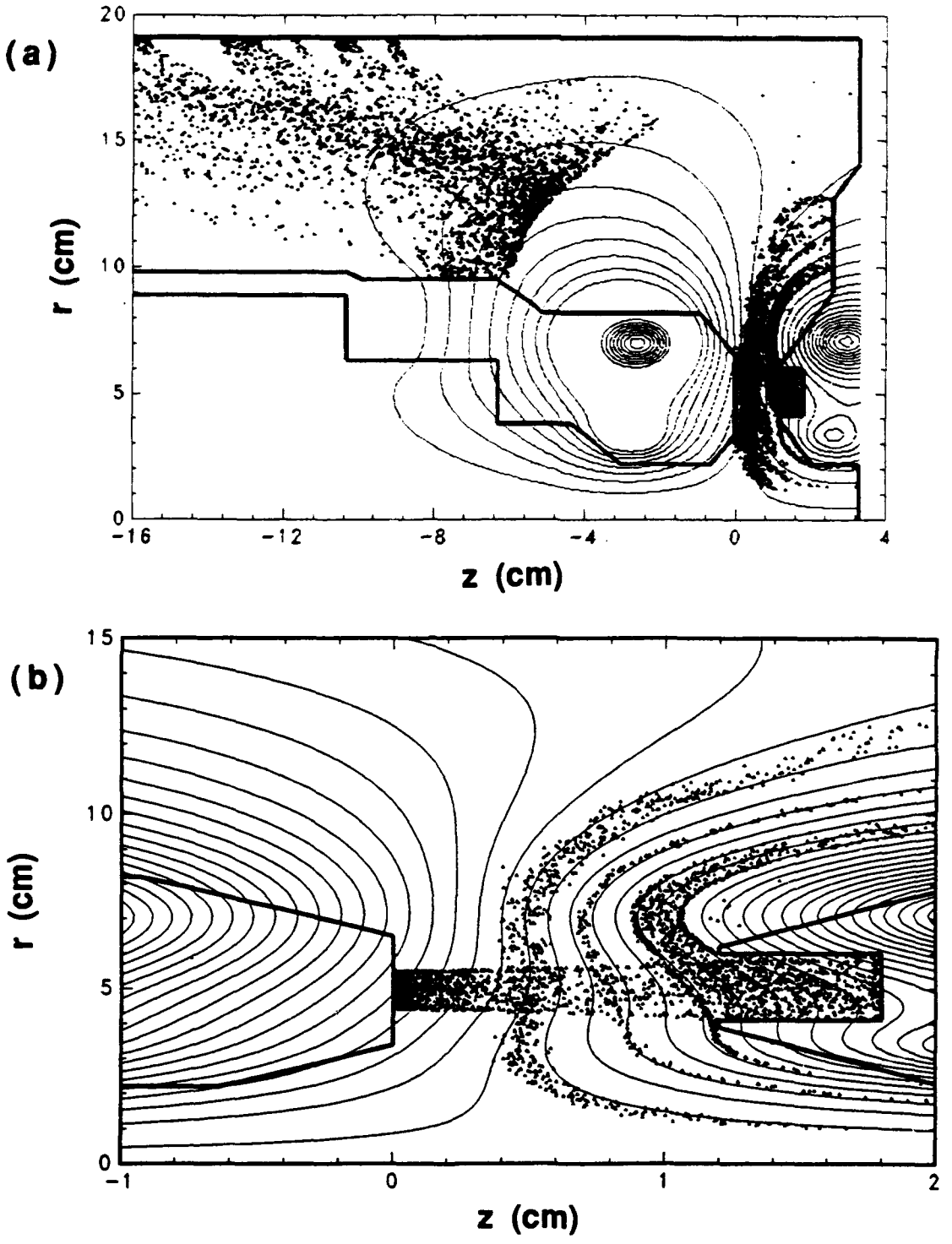

Fig. 4. a) Particle plot of electrons at 10 ns from a TWOQUICK electromagnetic particle-in cell simulation using the FIELD 2 magnetic field configuration. b) Expanded particle plot at 7.5 ns showing details of the FIELD 2 magnetic field geometry and electron and ion distributions in the A-K gap. Note the uniform electron sheath formed at early time in the A-K gap by cathode feed electrons.

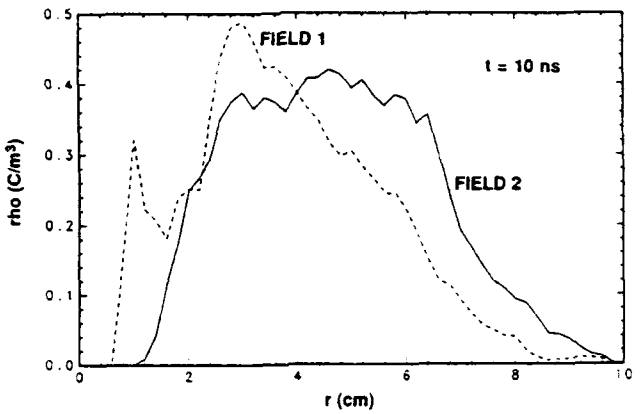

Fig. 5. Feed electron charge density across the anode surface at 10 ns from the TWOQUICK simulations of Figs. 3 and 4.

IV. Summary

We have demonstrated efficient operation of a high impedance applied-B extraction ion diode at the 5 MeV level. With an optimized magnetic field geometry resulting in a uniform distribution of feed electrons near the anode at early time, the diode showed fast turn-on, a rapid transition to fully enhanced ion emission, and production of a relatively uniform, high current density ion beam from a wax flashover ion source We find good correspondence between experimental results and PIC code numerical simulations of MITL and diode behavior.

References

* This work is supported by the U. S. Department of Energy under Contract No. AC04-76DP00789.

[1] W. Bauer, H. Bluhm, P. Hoppe, H. U. Karow, D. Rusch, Ch. Schultheiss, H. Bachmann, L. Buth, H. Laqua, E. Stein, J. Singer, and O. Stoltz, "Status and Perspectives of High Power Ion Diodes in Extractor Geometry", in *Proc. BEAM 90 8th Int. Conf. on High-Power Particle Beams*, Novosibirsk, July 2 - 6, 1990.

[2] H. Bluhm, P. Hoppe, H. Bachmann, W. Bauer, K. Baumung, L. Buth, J. Greenly, H. U. Karow, D. Rusch, E. Stein, and O. Stolz, "Progress in the Development of a High Power Focussing B-Applied Extractor Type Ion Diode for the 1.5 TW Pulse Generator KALIF", in *Proc. BEAMS 90 8th Int. Conf. on High-Power Particle Beams*, Novosibirsk, July 2 - 6, 1990.

[3] G. D. Rondeau, "Studies of an Extractor Geometry Magnetically Insulated Ion Diode with an Exploding Metal Film Anode Plasma Source", Thesis, Cornell University, Ithaca, N. Y. August 1989.

[4] C. K. Struckman, B. R. Kusse, and G. Rondeau, *Bull. Am. Phys. Soc.* **34**, 2064 (1989).

[5] S. A. Slutz, D. J. Johnson, and J. T. Crow, "The Operation of a Uniformly Insulated Extraction Applied-B Ion Diode", *J. Appl. Phys.* **68**, 2555 (1990).

[6] D. L. Hanson, M. E. Cuneo, P. F. McKay, R. S. Coats, and S. E. Rosenthal, "Ion Coupling Efficiency for an Extraction Applied-B Ion Diode on the HELIA Linear-Induction Adder in Positive Polarity", *IEEE Trans. Plasma Sci.* **19**, 831 (1991).

[7] S. A. Slutz and D. B. Seidel, "Magnetic Insulation of Extraction Applied-B Ion Diodes", *J. Appl. Phys.* **59**, 2685 (1986).

[8] S. E. Rosenthal, "Characterization of Electron Flow in Negative- and Positive-Polarity Linear-Induction Accelerators", *IEEE Trans. Plasma Sci.* **19**, 822 (1991).

[9] T. D. Pointon and D. B. Seidel, private communication. TWOQUICK is a 2-D electromagnetic particle-in-cell code under development, based on the 3-D code QUICKSILVER (D. B. Seidel, M. L. Kiefer, R. S. Coats, T. D. Pointon, J. P. Quintenz, and W. A. Johnson, *Computational Physics*, A. Tenner, ed. [Singapore: World Science Publishing Co., 1991] p. 475).

[10] J. R. Freeman, "TRIDIF, A Triangular Mesh Diffusion Code", *J. Computational Phys.* **41**, 142 (1981).

LiF ION SOURCE PERFORMANCE ON PBFA II

R. W. Stinnett, T. A. Green, D. J. Johnson, T. R. Lockner,
T. A. Mehlhorn, J. E. Bailey, A. Filuk, and L. P. Mix
Sandia National Laboratories, Albuquerque, New Mexico USA
and
J. Panitz and P. Schwoebel
University of New Mexico, Albuquerque, New Mexico USA

Abstract

Recent LiF ion source experiments have been conducted on Sandia National Laboratories' Particle Beam Fusion Accelerator (PBFA) II [1]. This facility is designed to provide a 30 MV, 100 TW power pulse to an applied B ion diode to investigate the suitability of light ions for inertial confinement fusion (ICF). Singly-ionized lithium is the desired ion species for these experiments because it has the proper range in target materials at 30 MV. LiF-coated anodes have been shown in experiments on other accelerators [2,3] to produce relatively pure (>70%) Li^+ beams. Earlier PBFA II experiments using porous anodes coated with LiF confirmed Li^+ production from LiF films [4]. The present PBFA II experiments use 0.6 μm films of LiF evaporated onto a stainless steel anode surface to provide a 1 MA, 25 ns FWHM pulse of Li^+ ions at energies of 6-9 MeV. The physical mechanism for production of ions from thin films of LiF has not previously been identified. One of us, T. Green, has developed a model which is consistent with LiF data from PBFA II and laboratory experiments and may provide a framework for understanding Li^+ ion production from thin LiF films in an applied B diode.

Experimental Configuration

PBFA II produces a 45 ns Full Width at Half Maximum (FWHM) power pulse which is delivered through two independent, conical, magnetically insulated power feeds. The ion-beam-producing section is located where the forward-going power from the top and bottom power feeds converge at the center of PBFA II. This section is called an "applied-B ion diode" because it uses externally applied magnetic fields to prevent cathode electrons from moving to the anode while allowing ions emitted from an ion source on the anode to move freely toward the axis of the cylindrically-symmetric diode region. A schematic of the PBFA II ion diode [5] is shown in Figure 1. The anode radius is approximately 15 cm. Ions are accelerated from the anode through the electron sheath and into the gas-filled (1 torr Argon) transport region defined by a 2 μm mylar gas cell wall located at a 12.5 cm radius. The gas in this region ionizes within 2 ns, providing charge and current neutralization so that the ions move in single particle trajectories to a central target on axis.

The physical anode-cathode gap in the PBFA II ion diode varied from 1.35-1.65 cm in recent LiF experiments. When the 10 MV, 20 ns rise time voltage pulse arrives at the diode, electrons are emitted from the cathode and ExB drift in the anode-cathode gap, forming an electron sheath which serves as a virtual cathode. This process is described by the Desjarlais theory of applied-B diode operation [6] and supported by three-dimensional particle-in-cell simulations of diode operation using the QUICKSILVER code. Simulations indicate peak electric fields at the anode of 10-15 MV/cm in the absence of significant ion emission. Spectroscopic measurements of the Stark shift of the 670.8 nm Li I line after the beginning of ion emission show electric fields of approximately 8 MV/cm in front of the anode.

Electrical and beam diagnostics in the diode are extremely important to provide information on diode and ion source behavior. Electrical diagnostics include B-dot monitors to measure currents and various voltage monitors to measure diode and power feed voltages. Beam diagnostics include a magnetic spectrometer to measure ion species, energy, and intensity, an ion pinhole camera to measure ion focal spot size with energy resolution, an ion movie camera to measure the intensity of the lithium ion focus on axis with temporal and spatial resolution, multiple Faraday cups to measure local ion current density from the anode, and off-axis time-integrated ion pinhole cameras to measure local beamlet species and divergence.

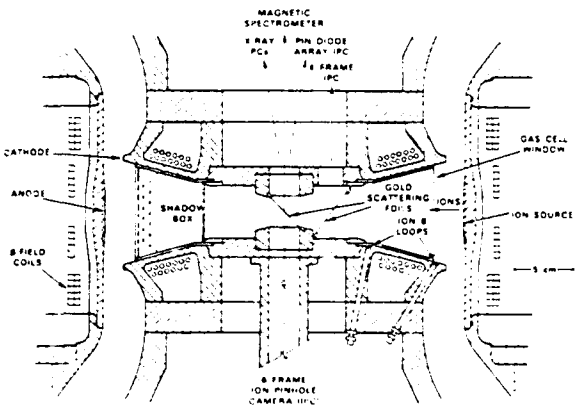

Figure 1. Schematic of the PBFA II applied B ion diode

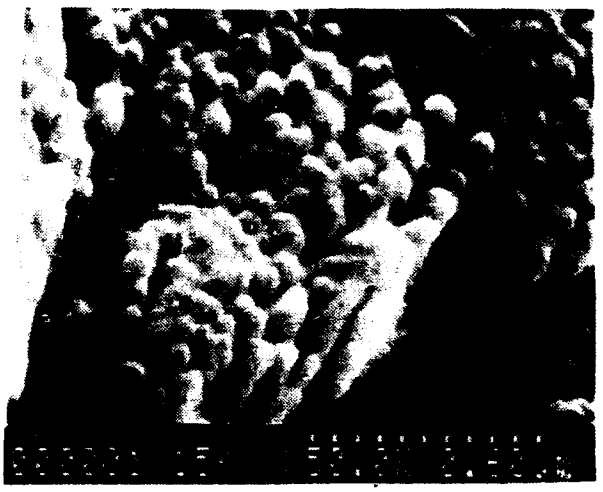

Figure 2. Scanning electron microscope picture of the surface of an anode coated with a 0.6 μm thick LiF film. The dotted line at the bottom is 0.6 μm long.

PBFA II LiF Ion Source Geometry and Results

The thin film LiF ion source has been studied on approximately 60 PBFA II experiments. It is normally fielded as a 0.6 +/- 0.1 μm thick LiF film that is vapor deposited on the inner surface of the cylindrical stainless steel anode. Figure 2 shows a SEM picture of the film surface taken at an angle of 75 degrees from the normal. The columnar structure is typical of LiF films of this thickness and produces a local electric field enhancement at the tips of the columns estimated to be 1.5-2. Previous experiments on PBFA II and other accelerators [3] comparing heated (120°C) and unheated LiF films and varying LiF coating thickness from 0.1-10 μm showed no significant changes in source performance. Studies of the surface atomic composition of LiF film samples showed that the films are always ≥ 95% pure LiF below 1 nm deep into the film. When the surface was exposed to conditions encountered during anode installation in PBFA II, predominantly carbon contamination was measured at levels up to 1 carbon atom for every 2 lithium atoms to a depth of 0.2 nm into the surface. Relatively low levels (1-3%) of oxygen contamination were measured. This is expected due to the fact that LiF is non-hygroscopic. This property is important because > 95% of the residual pressure in the PBFA II vacuum section is from water molecules. Samples exposed to only the laboratory environment showed lower surface contamination levels by a factor of three.

Ion beams created on PBFA II in experiments using the LiF films described above show > 80% Li^+ purity for approximately 15 ns FWHM pulses at current densities of 1-2 kA/cm² and voltages of 6-9 MV. After 8-30 ns the Li^+ cuts off but ion current continues to be produced in the diode. Initial data indicates that this cut-off of Li^+ depends on anode LiF coating height. The 8 ns cut-off of Li^+ occurs with a 1.5 cm LiF coating height. Increasing coating heights give longer Li^+ pulses, up to 30 ns for a 14 cm LiF coating height. This Li^+ cutoff also seems to be correlated with a rapid decrease in diode voltage and impedance. There is also a 20-25 ns delay typically observed between the arrival of the voltage at the diode and the beginning of ion current at the > 50 A/cm² level. This delay was initially thought to be dominated by the time required for the source to "turn on" or begin acting as a source of ions. Recent experiments with a pre-formed plasma ion source (the Laser Evaporation Ion Source) have shown an identical delay, indicating that the delay is not dominated by the turn on time of the LiF ion source. This delay in the production of significant levels of ion current is probably associated with the achievement of sufficient voltage to provide rapid electron sheath formation and extension from cathode to anode. The timing of the beginning of ion current is coincident with the diode voltage reaching 9-10 MV.

One LiF source configuration was tested on PBFA which succeeded in reducing the delay of Li^+ current from the anode. In this experiment the anode was machined to provide a sawtooth-shaped, grooved surface with groove spacing and depth of approximately 380 μm. With this anode geometry the Li^+ current began approximately 5-6 ns earlier than on comparable experiments without the sawtooth anode surface. The diode impedance in this experiment was higher than usual, resulting in large feed loses beginning 10-15 ns after the start of ion current. This may have been due to a reduced effective ion emitting area because of the sawtooth anode surface geometry. Experiments performed using a curved (anode radius of curvature in the axial direction of 30 cm) anode for vertical focusing showed a delayed ion turn on by approximately 2-3 ns.

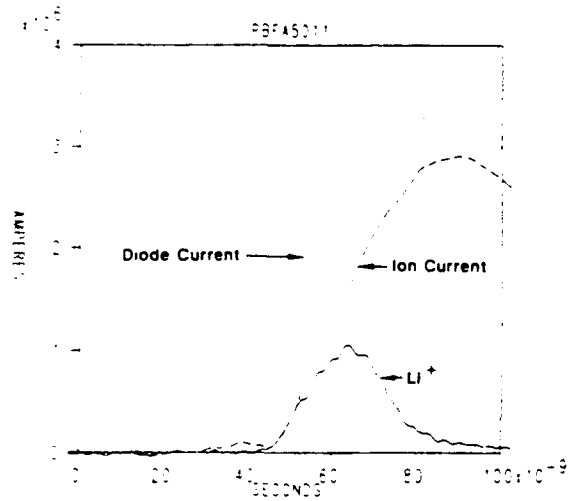

Figure 3. Currents from a LiF ion source experiment show a 20 ns delay in ion current with respect to the beginning of diode current, and early Li^+ cut off as measured by Faraday cups.

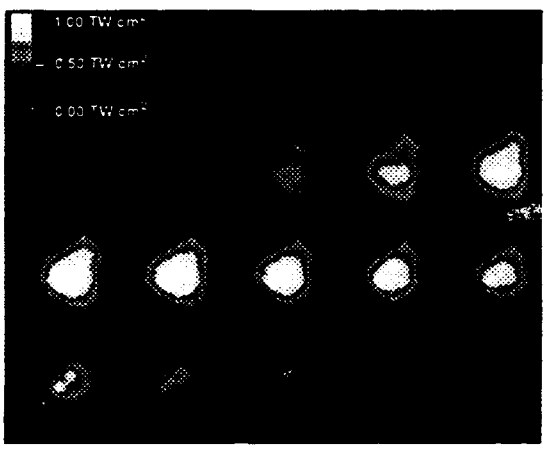

Figure 4. Lithium beam power at 2 ns intervals as measured by a 22 PIN array ion movie camera.

The LiF ion source was fielded in the curved anode focusing configuration to attempt to produce a high intensity focus on axis. In this experiment a peak Li^+ power density of 1 TW/cm^2 was produced with a total energy on axis of 45 kJ. The time resolved FWHM of the focal spot was 8-9 mm throughout the pulse as measured by the ion movie camera [7,8]. This indicates a 28 mrad overall divergence, roughly the same as that produced with other, plasma-based lithium ion sources on PBFA II. Spectroscopic measurements of the broadening of neutral lithium lines show an upper limit on ion divergence from the LiF ion source of 17 mrad, assuming that the neutral velocities are also characteristic of ion velocities. The dominant source of divergence of the Li^+ ion beam in PBFA II is presently thought to be transverse energy gained from instabilities during the time the ions cross the anode-cathode gap, although source non-uniformity is another possible cause.

Uniformity of the ion source has been an open question. Time integrated data from beam damage on witness plates indicated a problem with source uniformity on some experiments. Recent, time-resolved data from Faraday cups at the gas cell radius has shown on at least one experiment that the root-mean-square (RMS) beam uniformity from the LiF source was 22% over 9 separate azimuthal locations. This uniformity is comparable to the RMS value of 18% for a wax-filled, grooved proton source.

A combination of beam diagnostics provide evidence of high Li^+ purity during the first 8-30 ns of PBFA II LiF experiments. Range filtered Faraday cups and quartz pressure gauges using 2 μm mylar, 10 μm Al, and 25 μm Al filters to differentiate between protons, Li^+, and heavier ions indicate an almost complete (< 5%) lack of protons in the beam for 8-30 ns and are consistent with high Li^+ purity. Off-axis ion pinhole cameras also confirm the absence of proton tracks on CR-39 nuclear track recording plastic. Faraday cup measurements of current density during the first 10-20 ns of the diode power pulse, when Li^+ is being produced, are in rough agreement with the energy observed on axis when ion trajectories are considered. The total Li^+ energy produced in diode experiments varies from 80-140 kJ depending on diode parameters and geometry.

Another significant characteristic of the thin film LiF ion source is the location of its ion emission surface. The position of the ion focus on axis depends sensitively on the magnetic field profile and the location of the ion emission surface. Focusing data from both flashover and actively formed plasma ion sources indicate that the ion emission surface is located approximately 2 mm in front of the anode surface, probably due to the thickness of the plasma layer. In contrast, the thin film LiF source focusing data indicates that the ion emission surface is located at the anode surface to an accuracy of +/- 1 mm. Spectroscopic results (chord averaged over the anode height) also show electric fields up to 8 MV/cm extending to within the +/- 1 mm resoltuion of the measurement of the anode surface. Both of these results support the idea that the thin film LiF ion source produces Li^+ ions in a way that is qualitatively different from other, plasma-based ion sources.

LiF Ion Source Model

Several possible physical mechanisms could produce Li^+ ions from LiF films. These include field desorption due to large electric fields, dielectric breakdown, and explosive

desorption of portions of the film. It is important to identify the physics governing Li^+ production from our thin film LiF ion source so that we can better optimize source performance and can recognize intrinsic, physics-based limitations.

Laboratory tests [9] of LiF films on field enhancing tips have shown that subjecting these films to 20 ns pulsed or continuous local electric fields of up to 65 MV/cm do not affect the structural integrity of the film, or produce ions. Because the electric fields on PBFA II are below 40 MV/cm, it is not likely that electric field alone is responsible for pure Li^+ production in our experiments.

Dielectric breakdown of the LiF film due to charge deposition in the film by incident electrons can produce plasma on the anode surface. This mechanism is commonly used in "flashover" dielectric anodes but requires dielectric layer thicknesses of >> 100 μm to provide sufficient range to trap MeV energy electrons. Previous experiments [10] using uncleaned LiF coatings deposited over epoxy-filled flashover anodes showed that such flashover anodes produce ion beams with low (< 20%) Li^+ purity. The thin LiF layer in our experiments together with our high Li^+ purity makes it unlikely that dielectric breakdown is the primary mechanism in the Li^+ ion source.

T. Green has developed a new model to account for the observed LiF ion source performance on PBFA II. In this model the important factors in Li^+ production from the LiF film are the presence of electrons striking the anode surface and the presence of a large electric field. Electrons incident on the anode surface are important in producing a relatively high conductivity in the LiF film. Three dimensional PIC QUICKSILVER simulations of diode operation show that electrons reach the anode with approximately 8 MeV energies and strike it at grazing angles centered around 85° from the normal. This geometry has been simulated [9] to determine the effect of incident electrons on the LiF film and underlying stainless steel substrate. Each incident electron will create 140 electron-hole pairs as it passes through the LiF film. This result is insensitive (within 5%) to the incident electron energy from 1-10 MeV. The electrons have high mobility in the film and experience no potential barrier in moving from the LiF film into the stainless steel substrate. This result means that 10 A/cm^2 of electrons striking the anode will create a conductivity sufficient to support ion currents of 1.4 kA/cm^2. The holes move rapidly (< 5 ns) to within 5 nm of the surface of the film under the influence of the 1 MV/cm electric field in the film. The high density of holes at the surface may modify the binding energy of the Li^+ in the crystal, perhaps making it possible to pull the Li^+ out of the crystal at lower fields. The LiF film is also heated as much as 400° C by energy deposition from the electrons. In a small scale lab experiment [11] such an effect was observed in a LiF crystal which was heated to produce sufficient electron hole pairs to induce sufficient conductivity in the crystal to support ion emission. In these experiments a local electric field of 2 MV/cm was sufficient to produce pure Li^+ emission. The reduction of either temperature and the conductivity it causes, or electric field was sufficient to shut off ion emission.

Local electric fields on the surface of the PBFA II anode fall in the range 12-30 MV/cm, more than sufficient to satisfy the 2 MV/cm criteria mentioned above. Electron loss to the LiF-coated region of the anode equal to 0.5% of the diode current is sufficient to provide the

conductivity required to support our observed ion currents. The experimental electron loss in the diode region is 50% of the diode current. This may have the beneficial effect of making local ion emission insensitive to large variations in electron loss.

If this model correctly describes LiF ion source operation, the cutoff of Li^+ current from the anode may be due to a reduction in either electric field or electron loss to the anode. A reduction in electric field is most likely. It could be due to the ionization of neutrals from the LiF film surface which move into the gap on a time scale characteristic of the Li^+ pulse width. An alternative explanation would be impedance collapse in some other region of the diode which reduces the electric field at the anode below the threshold for Li^+ emission.

Conclusions

Experiments on PBFA II have demonstrated that the LiF ion source can be used to produce a 1 TW/cm^2 Li^+ ion beam. Increasing this intensity will depend on reducing the 28 mrad divergence, increasing the present 50% ion current efficiency, improving the impedance history of the diode, and raising the diode voltage from the 8 MV level which is typical in present experiments. The development of our new model for LiF ion source operation provides a physical basis for efforts to further optimize this source. Confirmation of this model is an important goal for future experiments.

References

1. J. P. VanDevender and D. L. Cook, "Inertial confinement fusion with light ion beams," Science **232**, 837, 1986.
2. J. M. Neri, D. A. Hammer, G. Ginet, and R. N. Sudan, "Intense lithium, boron, and carbon beams from a magnetically insulated diode," Appl. Phys. Lett. **37** (1), 1 July 1980.
3. P. F. McKay, K. W. Bieg, R. E. Olson, A. L. Pregenzer, and D. K. Wiemann, "Ion production on the PI-110A accelerator," Rev. Sci. Instrum. **61** (1), January 1990.
4. K. W. Bieg, A. L. Pregenzer, J. R. Woodworth, T. R. Lockner, D. J. Johnson, R. A. Gerber, J. E. Bailey, R. P. Kensic, R. J. Leeper, J. E. Maenchen, T. A. Mehlhorn R. E. Olson, C. L. Ruiz, and W. A. Stygar, "Lithium fluoride ion source experiments on PBFA II," Rev. Sci. Instrum. **61** (1), January 1990.
5. D. J. Johnson, T. R. Lockner, R. J. Leeper, J. E. Maenchen, C. W. Mendel, G. E. Rochau, W. A. Stygar, R. S. Coats, M. P. Desjarlais, R. P. Kensic, T. A. Mehlhorn, W. E. Nelson, S. E. Rosenthal, J. P. Quintenz and R. W. Stinnett, "PBFA II applied B-field ion diode proton beam characteristics," Proceedings of the 7th IEEE Pulsed Power Conference, Monterey, California, June 11-14, 1989, IEEE Cat. No. 89CH2678-2.
6. M. P. Desjarlais, "Theory of applied-B ion diodes," Phys. Fluids B, **1** (8), 1709, 1989.
7. W. A. Stygar, L. P. Mix, R. J. Leeper, J. Maenchen, D. F. Wenger, C. R. Mattson, and D. J. Muron, "An ion movie camera for particle-beam fusion experiments," to be published in Rev. Sci. Instrum, October 1992.
8. L. P. Mix, W. A. Stygar, R. J. Leeper, J. E. Maenchen, and D. F. Wenger, "Time-resolved measurements of the focused ion beams on PBFA II," to be published in Rev. Sci. Instrum., October 1992.
9. P. R. Schwoebel and J. A. Panitz, "The behavior of LiF coated metal anodes in pulsed electric fields," Appl. Phys. **71** (5), 2151, March 1992.
10. E. J. T. Burns, J. R. Woodworth, K. W. Bieg, T. A. Mehlhorn, W. A. Stygar, and M. A. Sweeney, "A lithium-fluoride flashover ion source cleaned with a glow discharge and irradiated with vacuum-ultraviolet radiation," J. Appl. Phys. **63** (1), 11, January 1988.
11. Len Lorence, Sandia National Laboratories, Division 9341, private communication.
12. F. W. Rollgen, U. Giessman, and H. J. Heinen, "Ion formation in field desorption of salts," Z. Naturforsch, **31a**, 1729-1730, 1976.

SPECTROSCOPIC CHARACTERIZATION OF LEVIS ACTIVE ION SOURCE ON PBFA II

A.B. Filuk, J.E. Bailey, K.W. Bieg, A.L. Carlson, T.J. Renk, G.C. Tisone
Sandia National Laboratories, Albuquerque, NM 87185-5800
Y. Maron
Weizmann Institute of Science, Rehovot 76100, Israel

The laser-initiated LEVIS source is intended to provide an active source in the PBFA II ion diode by generation of a preformed lithium anode plasma. Visible spectra recorded with a streaked spectrograph are used to help evaluate the source performance. The absence of Stark shifting of the Li I 2p-3d and 2s-2p light confirms that a plasma is created over the anode surface. At lower LEVIS laser intensities this plasma erodes back toward the anode as the ion beam current grows. Considerable improvements in anode plasma purity have been noted when the anode is heated for several hours. The LEVIS source microdivergence estimated from the carbon ion transverse energy is less than 14 mrad, meeting the near term requirements for PBFA II target experiments.

Introduction

Light ions are being generated, accelerated, and focused in the Particle Beam Fusion Accelerator (PBFA II) at Sandia National Laboratories as part of the effort towards inertial confinement fusion (ICF) [1]. An applied-B diode is used to convert the electrical power pulse into a radially-converging ion beam. Active ion sources are being developed for this diode to enable a space-charge-limited current to be extracted early in the pulse, to provide control over source uniformity, and to enable testing of electron-limiter diode concepts for divergence studies [2]. The LEVIS (Laser EVaporation Ion Source) approach [3] uses two pulsed lasers incident on a thin layer of lithium-bearing material that has been coated onto the anode surface. A Nd:YAG laser at 1.06 μm produces a neutral lithium vapor near the anode and a dye laser tuned to the Li I 2s-2p transition at 6708 Å ionizes the lithium neutrals via the LIBORS (Laser Ionization by On-Resonant Saturation) mechanism [4]. Important issues for the evaluation of LEVIS include first, verification that a preformed plasma is created, and second, determination that the density and temperature are suitable for producing a high current density ion beam with low divergence. In addition, the effect of film impurities on plasma formation, composition, and ion beam purity must be characterized.

We report here on spectroscopic evaluation of the LEVIS ion source. Time and space resolved visible spectra provide a non-intrusive method for determining where and when a plasma is formed. The signature we use is the presence or absence of Stark shifting in the Li I spectral line profiles under the 5-10 MV/cm diode electric field. We estimate intrinsic source divergence using Doppler broadening of selected spectral lines [5]. In addition, the relative brightness of impurity lines from shot to shot provides a monitor of the purity of the LEVIS-produced ion source plasma. The main results of this study may be summarized as: i) LEVIS has produced a preformed plasma in the anode-cathode (AK) gap, ii) direct current (DC) heating of the anode containing the LEVIS substrate can reduce impurity contamination levels in the ion source plasma, and iii) the ion source microdivergence is much lower than the ion beam microdivergence measured near the beam focus, and meets near-term divergence requirements.

Experiment

The most important parameters for LEVIS operation are the laser intensities, timing, illumination uniformity, and surface condition.The laser intensities used in this study fit into two categories, 'low power' shots with dye laser fluence of 50-100 mJ/cm^2 and Nd:YAG laser fluence of 100-250 mJ/cm^2, and 'high power' shots with dye laser fluence 200-300 mJ/cm^2 and Nd:YAG laser fluence of 300-400 mJ/cm^2. The ~1 μs full width at half maximum

(FWHM) dye laser pulse was fired about 500 ns prior to the arrival of the power pulse at the diode, and the 8 ns FWHM Nd:YAG laser was fired 150-200 ns prior to the power pulse arrival. This time should be sufficient for the LIBORS process to fully ionize the neutrals [6].

The laser fluence incident on the active anode surface in the high power shots varied by at least a factor of 2 over the surface. The low power shots used an improved optics system to achieve a uniformity estimated to be ±25%. In both cases the laser fluences in the minima were still above the threshold needed to produce plasma, as determined from small scale experiments [3]. Note that there were vertical regions at 4 azimuths of the cylindrical anode surface that did not receive laser illumination due to shadowing by 4 posts that separate the top and bottom cathode cones of Figure 1.

The surface condition of the active anode material is a key factor in the purity of the ion beams produced by the LEVIS process [7]. Materials used in these experiments were a corrosion-resistant LiAg alloy and a lower-reflectivity Li/Mo admixture. However, previous LEVIS experiments on PBFA II have shown that without some form of anode cleaning, the ion beam produced is predominately composed of protons and carbon [7]. The high power shots used Li/Mo substrates, while the low power shots used both Li/Mo and Li/Ag. On the low power shots, cleaning was attempted by heating the anode surface to 120-150°C with a DC heating coil to drive off water vapor and some hydrocarbons.

The visible spectroscopy line of sight views the AK gap region of the azimuthally symmetric diode in the center section of PBFA II (Figure 1). As described previously [8], a mirror, lens, and fiber optic assembly collect light at

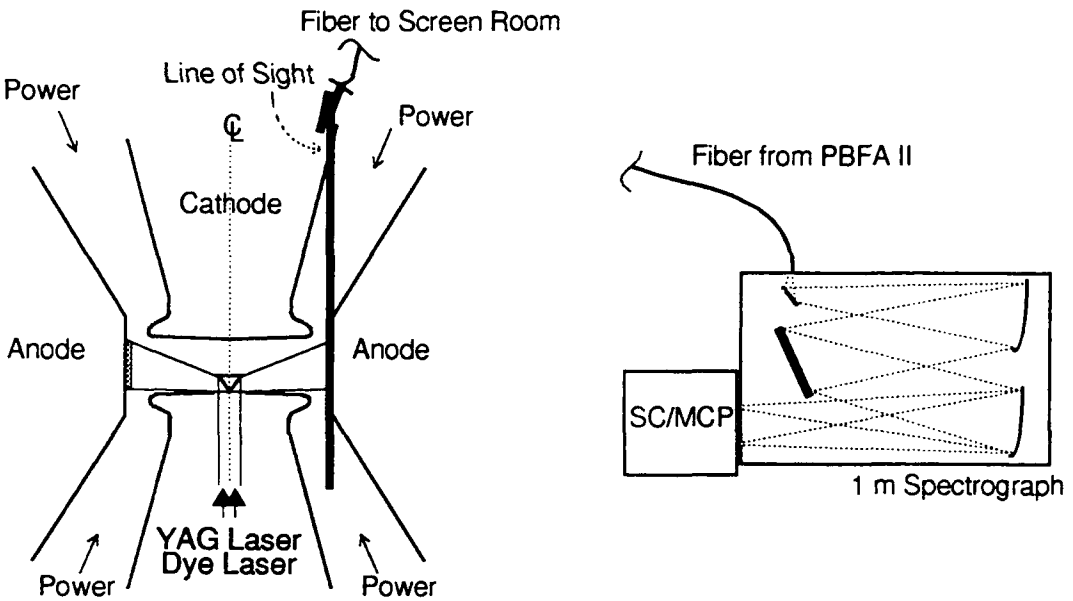

FIGURE 1. Schematic of apparatus. Drawing at left shows center section of PBFA II with LEVIS laser illumination pattern and spectroscopic line-of-sight parallel to anode surface. Light is transported via fiber optic to 1 m spectrograph coupled to a streak camera (SC) and micro-channel plate intensifier (MCP) as shown at right.

one azimuthal location from an approximately 2 mm diameter pencil-like line of sight parallel to the anode surface. The line of sight can be positioned at varying distances from the anode surface, and two separate spectroscopic systems can be used to collect light at different anode distances on any shot. We typically obtain 2 mm spatial resolution (diameter of line of sight in AK gap), 1 ns time resolution, and ~3 Å spectral resolution. The absolute wavelengths

are determined by applying fiducials with a HeNe laser. The relative wavelengths as a function of time are determined to better than ±1 Å.

The large bremsstrahlung x-ray burst of PBFA II provides a convenient fiducial to establish the timing of the streaked spectrum relative to the power-pulse timing. Light from a scintillator placed in the vicinity of the diode is transported to the streak camera via a separate fiber optic, and appears on the film as a ~20 ns FWHM timing pulse. The time-history of this pulse is matched to that from various other diagnostics sensitive to the bremsstrahlung x-rays in order to establish the timing of the streak relative to other measurements such as beam current and voltage. The uncertainty of the match gives a timing error of ±2-3 ns. This uncertainty is in addition to the uncertainty of the bremsstrahlung pulse time, which varied from 3 ns to 6 ns (see Discussion below).

The fluorescence of the laser pumped Li I 2s-2p transition (6708 Å) provides an intense diagnostic line to characterize AK gap conditions. There are several observations indicating that the 6708 Å light observed is reemission from neutrals in the AK gap, rather than simply stray light from the tuned dye laser. The FWHM of the spectral line prior to the power pulse is typically 6-7 Å, while stray dye laser light should have a FWHM of 4.2 Å. We are presently evaluating possible reasons for this width, including saturation broadening and opacity effects. Also, as described below, on some low power shots the entire 6708 Å feature becomes Stark shifted by the diode electric field, with little or no emission remaining at the laser wavelength. In other experiments with in-situ deposited lithium, the 6708 Å intensity was observed to vary with the amount of deposited lithium, as expected from reemission. In a case where the Nd:YAG laser was fired later, within 20 ns of the power pulse arrival at the diode, the 6708 Å light was extremely faint prior to and just after the Nd:YAG pulse, which supports the notion that the intense 6708 Å light seen with the earlier timing is not stray dye laser light. We also found that the 6708 Å intensity increases when the Nd:YAG fires, consistent with generation of neutrals by the Nd:YAG and their subsequent excitation. These five observations indicate that the 6708 Å light is reemission, although it is difficult to entirely rule out any stray light contribution.

Results - Preformed Plasma Generated

A sequence of spectral line profiles characteristic of a high power LEVIS shot are shown in Figure 2, along with the voltage and ion beam current. The spectroscopic line of sight center was 1 mm from the anode surface. Both the

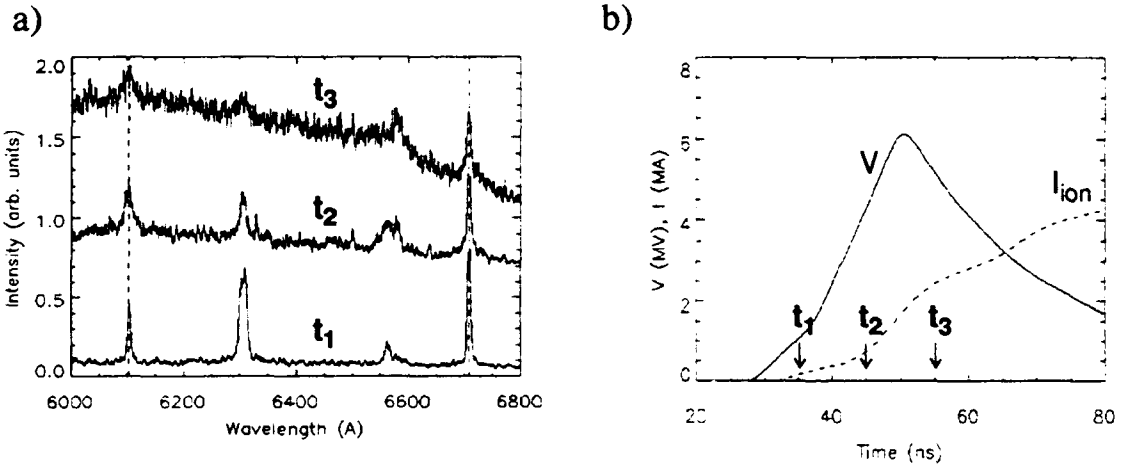

FIGURE 2. a) Spectrum at three times for a high power shot, showing absence of Stark shift in both Li I lines (6104 Å, 6708 Å) at all times. Dashed lines indicate unshifted Li I line positions. b) Diode voltage and ion beam current histories with corresponding times (arrows)

2s-2p (6708 Å) and 2p-3d (6104 Å) Li I lines are evident before and during the accelerator power pulse. The presence of the Li I 2p-3d line indicates that a preformed plasma was created before the power pulse arrived, since electron collisional excitation is the only mechanism available to populate the 3d level. In addition, the Li I lines never display a Stark shift, despite the presence of an electric field exceeding 5 MV/cm in the acceleration gap. Stark shift calculations show that the 2p-3d line splits and shifts by many Angstroms when E>1 MV/cm, and the 2s-2p line blueshifts by 5 Å for E~6.4 MV/cm. Such shifts are well above our detection limit of 0.8 Å. In addition, the 2s-2p shift is routinely observed in LiF flashover shots, where the Li I emission originates in the accelerating gap. Our interpretation of these results is that the Li I emission arises from a plasma with n_e large enough to screen out the diode electric field. This conclusion is independent of the stray-light considerations described above, since it relies not only on the Li I 2s-2p emission, but also on the 2p-3d emission. It also follows that the initial plasma thickness is greater than the 2 mm line-of-sight diameter, the plasma is formed prior to the arrival of the power pulse, and the plasma is dense enough to supply the extracted ion current and still screen the field throughout the power pulse.

In a low power LEVIS shot, only the 6708 Å light is seen until about 15-30 ns after the power pulse arrives. No Stark shift was seen in the 6708 Å light until 5-10 ns after the ion beam current exceeded ~100 kA. The Stark shift then appeared first on the line-of-sight 3 mm from the anode, and, about 7 ns later, on the line-of-sight 1 mm from the anode (Figure 3). We interpret this as evidence that the preformed plasma, screening the intense electric field ini-

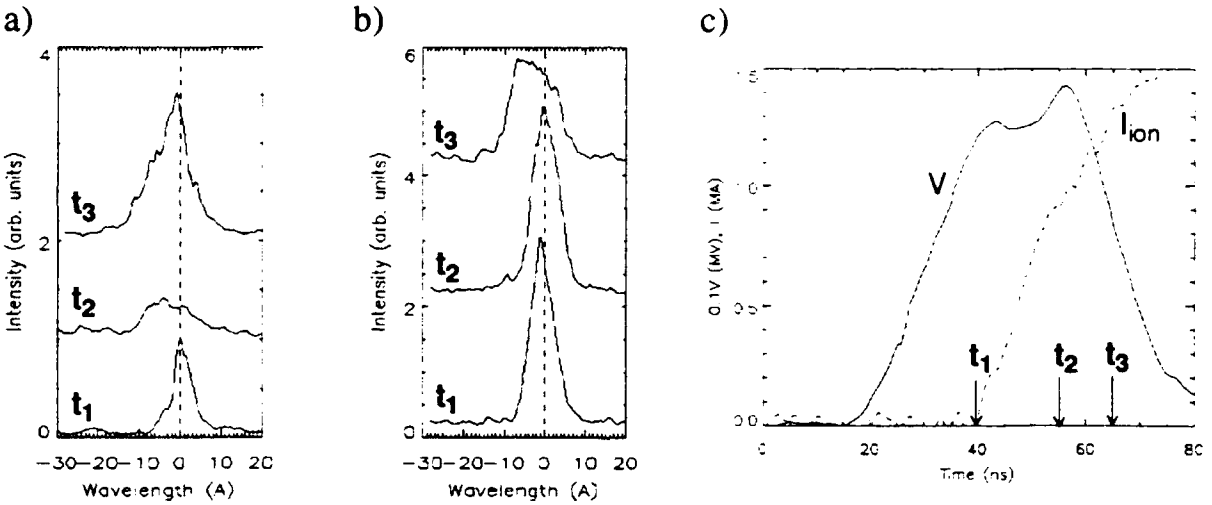

FIGURE 3. a,b) Spectral line profiles at three times for a low power shot, at a) 3 mm line-of-sight, and b) 1 mm line-of-sight. Dashed lines are at 6708 Å. Stark shift is absent in both lines-of-sight at t_1, shift is clearly present for 3 mm at t_2, and shift is present in both lines-of-sight at t_3. c) Diode voltage and ion beam current histories with corresponding times (arrows).

tially, was of a sufficiently low density that it was eroded back toward the anode as the ion beam current was extracted. We can estimate bounds on the initial plasma density from the requirement that the density is high enough to screen the diode electric field, yet low enough that the extracted ion current causes erosion. Screening of a potential of 5-8 MV across a 2 mm line-of-sight separation requires a minimum electron density of about 3×10^{13} cm^{-3} (from Poisson's equation). In order for the plasma to erode 2 mm in 5-10 ns with an average current density of 400 A/cm^2, one requires an average plasma density of about 8×10^{13} cm^{-3} (assuming ion charge conservation).

Results - Effective Cleaning Provided by DC Heating

We used the spectroscopic data to evaluate the effectiveness of anode heating in the reduction of impurities in the ion source. Figure 4 shows spectra for two Li/Ag substrate shots, one with 3 hours of DC heating at 125°C, the other

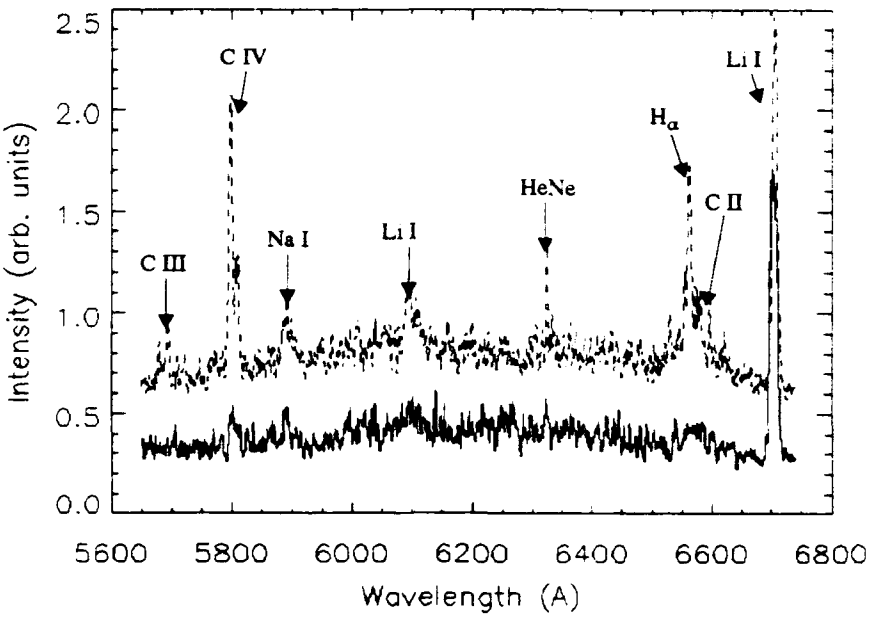

FIGURE 4. Sample spectra comparing 3 hours DC heating (solid) and 0.5 hours DC heating (dotted, displaced upward 0.3 units for clarity). Note dramatic decrease in impurity lines with the extended heating.

with 0.5 hours. In general, the absolute intensity of the impurity and lithium lines dropped with the extended heating. The impurity to lithium line ratios with 0.5 hour heating were (C IV 3s-3p/Li I 2s-2p) = 0.63, (C III 3p-3d/Li I 2s-2p) = 0.11, and (H_α/ Li I 2s-2p) = 0.84. The same ratios with 3 hour heating were (C IV 3s-3p/Li I 2s-2p) = 0.17, (C III 3p-3d/Li I 2s-2p) = 0.022, and (H_α/ Li I 2s-2p) = 0.022. Thus, the extended heating produced a factor of 3-5 improvement in the carbon impurity line relative intensities and a factor of 40 improvement in the hydrogen line relative intensity. This result shows that the impurity ion and atom excited state populations were greatly reduced by DC heating and, if we assume that the electron temperature and density were similar for the two shots, then the total impurity concentrations were also greatly reduced. The larger drop in hydrogen impurity levels is not unexpected because adsorbed water molecules should be evaporated more readily than hydrocarbons at the temperatures attained. Ion beam diagnostics confirm that the fraction of lithium content in the extracted ion beam increased dramatically in the extended heating shot.

Results - Source Divergence Upper Bound Estimated

We have examined spectral line profiles of C II, C III, C IV, Li I, H_α, and Na I. Line widths of impurity ions and neutral species are larger than expected from Stark and instrumental effects. Using the absolute excited level population densities, opacity effects on the line widths were estimated in order to select optically thin lines. An upper bound in the few keV range was obtained for the impurity ion and neutral atom energy parallel to the anode surface. Similar observations have been made on flashover and LiF sources. An upper bound on the microdivergence at the source was thus obtained and compared with the ion beam microdivergence measured after the beam acceleration and transport stages by other techniques.

We use carbon ion line widths to estimate the Li II ion divergence at the source. Higher charge states were found to have higher transverse energies than lower charge states in flashover sources [9]. If we conservatively assume the Li II transverse energy is comparable to that of C IV, then the Li II source divergence upper bound would be in the range of 4-14 mrad. If Li II has the same transverse energy as Li I (via charge exchange, for example), this upper

bound range is 4-9 mrad. These upper bounds are much less than the ion beam divergence of 30-35 mrad measured after acceleration [10]. An effort is under way to understand the dominant contributor to the ion beam divergence.

Discussion

The production of a preformed ion source is of fundamental importance to the light-ion ICF program. Consequently, we have scrutinized the data for possible alternative interpretations. On the high-power shots the presence of the Li I 2p-3d line with no Stark shift is irrefutable evidence of a preformed plasma. However, one could argue that the plasma is nonuniform, with the Li I emission arising only from plasma 'spots'. This is implausible because the lithium neutrals would rapidly expand beyond the periphery of the plasma spots, encounter the diode electric field, and emit Stark-shifted light. Note that we routinely observe neutrals several mm from the anode surface and would expect comparable expansion rates parallel to the surface.

Another explanation we considered for the low power shots is that the unshifted light prior to the arrival of the power pulse is stray dye laser light scattered from multiple surfaces into our line of sight. Then, if the surface conditions change upon arrival of the power pulse, the scattered light could decrease, accompanied by a simultaneous increase in the Li I reemission from neutrals created during the power pulse. This scenario is contrary to the large body of evidence that we are effectively discriminating against stray light and is inconsistent with the observation that: i) shifted light appears first on the line-of-sight farther from the anode, and ii) the shift is observed to grow gradually from zero shift, rather than appearing as instantaneously shifted light due to neutral lithium entering the line-of-sight.

A third alternative is that the timing of our spectroscopic data relative to the power pulse timing is incorrect. As explained earlier, we match the bremsstrahlung timing pulse with that from various monitors on PBFA II. On some shots, these monitors can differ in the time of peak bremsstrahlung by as much as 7 ns, due to spatial variations and different detection mechanisms. However, the spectroscopic timing would have to be shifted over 20 ns earlier in order to rule out the preformed plasma argument. Thus, even the worst case of timing error is insufficient to explain the observed line shifts.

Our conclusion, based on spectroscopy, is that the LEVIS approach is an effective method for producing a preformed ion source. The intrinsic source divergence is adequate for near-term PBFA II experiments and the use of DC heating appears promising for attaining the required beam purity. Funding for this work was provided by the U.S. Department of Energy under contract DE-AC04-76-DP00789.

References

1. J.P. VanDevender and D.L. Cook, Science **232**, 831 (1986).
2. G.C. Tisone, T.J. Renk, D.J. Johnson, R.A. Gerber, and R.G. Adams, these proceedings.
3. G.C. Tisone, K.W. Bieg, and P.L. Dreike, Rev. Sci. Instr. **61**, 562 (1990).
4. P.L. Dreike and G.C. Tisone, J. Appl. Phys. **59**, 371 (1986).
5. Y. Maron, M.D. Coleman, D.A. Hammer, and H.S. Peng, J. Appl. Phys. **61**, 4781 (1987).
6. R.M. Measures and P.G. Cardinal, Phys. Rev A **23**, 804 (1981).
7. M.E. Cuneo, G.C. Tisone, B.F. Clark, J.R. Chavez, and M. Lopez, presented at the 18th International Conference on Plasma Science, June 3-5, 1991, Williamsburg, Virginia.
8. J. Bailey, A.L. Carlson, R.L. Morrison, and Y. Maron, Rev. Sci. Instr. **61,** 3075 (1990).
9. Y. Maron, E. Sarid, O. Zahavi, L. Perelmutter, and M. Sarfaty, Phys. Rev. A **39**, 5842 (1989).
10. D.J. Johnson, J.E. Bailey, T.A. Haill, and D.F. Wenger, presented at the 19th International Conference on Plasma Science, June 1-3, 1992, Tampa, Florida.

LASER FORMATION OF LITHIUM PLASMA ION SOURCES FOR APPLIED-B ION DIODES ON THE PBFA-II ACCELERATOR

Gary C. Tisone, T. J. Renk, D. J. Johnson, R. A. Gerber, and R. G. Adams
Sandia National Laboratories.
Albuquerque, NM 87185

Abstract

An active ion source, LEVIS (Laser EVaporation Ion Source), using a short pulsed Nd laser (1.06 m, 8ns) to form a thin Li vapor layer and a tuned dye laser (670.8nm, 1μsec) for ionization is being developed at Sandia. The LEVIS process has been developed and characterized in the laboratory. Initial experiments using these ion sources on PBFA-II produced ion beams with a low fraction of lithium ions and with low voltages. Recent experiments using improved distribution optics and anode cleaning techniques are described.

Introduction

The production of light ion beams for Inertial Confinement Fusion (ICF) has been under development at Sandia National Laboratories for the past several years. It has been estimated that a power and intensity at the target of the order of 100 TW and 100 TW/cm^2 in a 10 ns pulse will be required for a break even implosion.[1] Lithium is chosen because it has the proper range for target materials and a greater magnetic stiffness than protons. Experiments at Sandia on the PBFA-II accelerator have used an applied B ion diode to accelerate and focus ions. Ion sources for these diodes can be divided in to two types: 1) passive sources that are formed either directly or indirectly by the diode voltage; and 2) active sources where an ion source plasma is formed before the arrival of the diode voltage. Because of the simplicity of fielding, passive sources have been used extensively on PBFA-II. Proton ion beams are formed from epoxy or some other dielectric in grooved anodes. Lithium beams have been successfully produced using lithium bearing dielectrics such as LiF or thin metallic films of LiMo and LiAg as a passive source. Although relatively pure lithium ions have been produced by these passive sources, it appears that the passive Li sources will not scale to intensities necessary for fusion. Active sources for PBFA-II have been studied extensively in the laboratory but only until recently they have been tested on PBFA-II with limited success[2].

The requirements for an active source have been developed in a previous paper[3] and are summarized here. The minimum surface charge density for the source is estimated to be 6x10^{14}cm^{-2} and the ionized layer thickness should be of the order of 1 mm or less, due to focusing requirements . A plasma purity of greater than 90% is required for efficient production and focusing of lithium ions. A technique to form a lithium source is described in detail in a previous paper[3]. A thin lithium vapor layer is produced by fast ohmic heating of a thin film substrate (BOLVAPS, Boil Off Lithium VAPor Source). The thin vapor layer is then ionized by a process known as LIBORS (Laser Ionization Based On Resonant Saturation[4]). Efficient ionization of this layer with a laser tuned to the first resonant transition of Li (670.8 nm) with intensities as low as 3x10^{4}W/cm^2 have been demonstrated. Modeling of the LIBORS process predicts ionization times of 0.1 to 1.0 μsec for Li vapor layers with thicknesses and densities of interest for an ion source (1mm and 1x 10^{15} to 5x10^{16} cm^{-3}).[6]

We briefly describe the development and characterization of an active ion source where the thin lithium vapor layer is formed by using a short pulsed laser (not tuned to resonant transition of Li) to heat and evaporate lithium from a thin film substrate. This process is referred to as LEVIS (Laser EVaporation Ion Source). A simple schematic of this process is shown in Figure 1. In this schematic, a laser is first used to heat a lithium bearing substrate to a temperature high enough that a suitable dense vapor layer is formed. The laser energy from the first laser needs to be high enough to evaporate the lithium, but not high enough to form a plasma (greater than $10^8 W/cm^2$) at the surface . The vapor is then ionized by a tuned dye laser. In order to reduce ionization time, the evaporation laser pulse is incident on the substrate near the peak of the dye pulse.

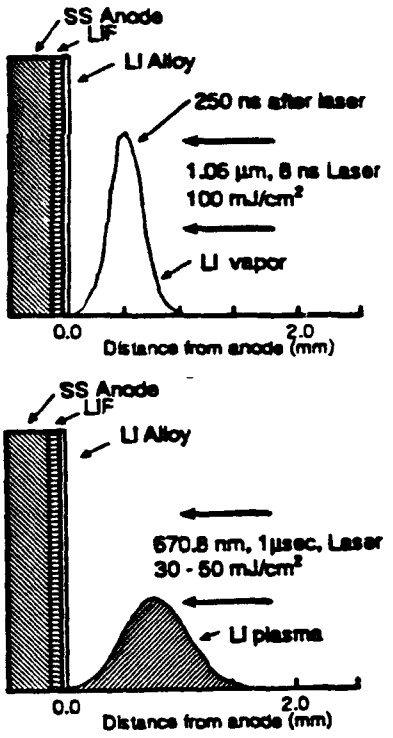

Figure 1. Two laser evaporation and ionization to form a Li plasma.

Preparing and cleaning thin film substrates for producing Li vapor.

In order for the lithium bearing substrate to be useful as a source of lithium in a PBFA-II anode, several requirements must be met. The evaporation process must produce a pure Li vapor. Impurities with high vapor pressures such as Na should not be present in the substrate. Substrates that resist exposure to ambient atmospheres for times on the order of hours are required. At Sandia, LiAg alloys have been extensively studied as a corrosion resistant source of Li.

Optical techniques and mass spectrometer measurements have been used in the laboratory to characterize the thin films to be used for an ion source. We have studied the effect of cleaning substrates by heating with an external heater to 100 - 200 ^oC on a time scale of hours (DC heating) in the laboratory and in PBFA-II. We are limited to this temperature because of operating restrictions in the PBFA-II diode. This can be compared to BOLVAPS heating which is designed to produce melting of the thin film substrate at 600 ^oC in 10 msec. Neutral species released from the substrate by the Nd laser system were measured. The masses present were: 1 (H), 2(H_2), 7(Li), 12(C), 18(H_2O), 28(N_2), or CO. The ratio of H_2O to Li is taken as a measure of the contamination level of the sample. Measurements of the ratio of mass 18 (H_2O) to mass 7 (Li) from the mass spectrometer two LiMo film substrates heated to 175 ^oC are shown in Figure 2. The samples were heated with a Nd laser intensity of 150 mJ/cm^2. A stainless steel substrate is cleaned with solvents and dried before placing in the vacuum coating with a LiMo film (250 nm). The ratio of mass 18 (H_2O) to mass 7 (Li) is reduced by heating to 150 ^oC. Above this

temperature the ratio did not decrease because of the reduction of Li vapor. Another sample is baked to 300°C in air and coated with 500 or 1000 nm layer of LiF before coating a LiMo layer (250 nm). A dramatic reduction of the water vapor at room temperature is observed. A further decrease in the water vapor is observed upon heating to 150 °C. These results indicate that the majority of the contamination is due to the stainless steel substrate. As a consequence of these measurements, the baseline design for heated anodes for PBFA-II contain a LiF barrier between the stainless steel substrates and the Li bearing alloy.

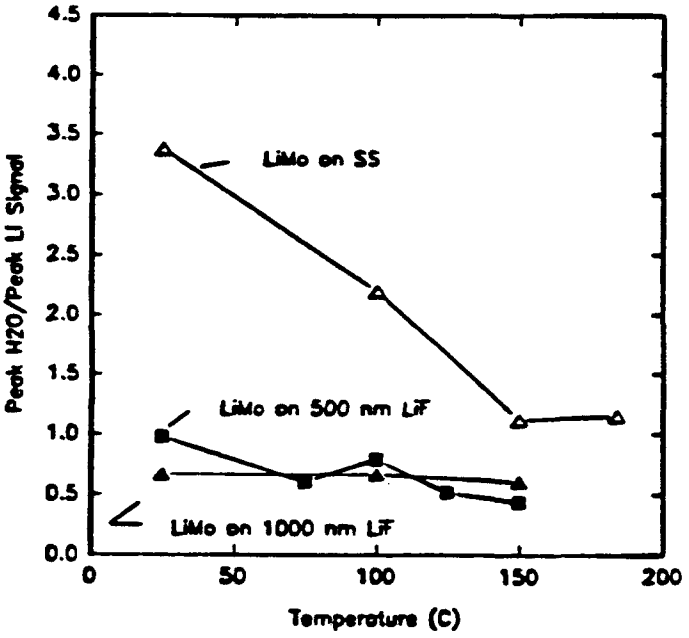

Figure 2. Effects on the ratio of H_2O to Li due to DC heating a substrate with Li/Mo.

Spectroscopic studies were used to determine plasma densities after ionization by the tuned dye laser. Evaporation laser energy densities of 60 mJ to 200 mJ/cm^2 and tuned laser energy densities of 30 to 60 mJ/cm^2 produced ion densities of 1 to 3 x 10^{16} cm^3 for the three types of substrates. This is inferred from line broadening of the LiI(^{2}D - ^{2}P) line at 460.3 nm.

PBFA II Experiments

Figure 3 shows a schematic diagram of a PBFA-II Applied B ion diode with beam diagnostics and reflecting cone for distribution of the laser beams to the anode. The anode had a diameter of about 30 cm and an active height of 4 cm for these experiments. Magnetic field coils are used on both the anode and cathode sides of the 16 mm anode-cathode (AK) gap to insulate the diode to 14-15 MeV. Diagnostics for the experiments include: various voltage and current measurements, nuclear activation for Li beams, filtered Faraday cups, a Rutherford magnetic spectrometer for determining charge species, and time resolved spectrometers observing two 2mm-wide vertical lines of sight at different radial positions in the AK gap.

Early experiments using the LEVIS process yielded two major results: 1) the diode voltage collapsed prematurely, and 2) the ion beam produced was largely non-Li, being a mixture of hydrogen and carbon. There were several shots taken where special hardware installed in the cathode side of the A-K gap allowed a pure Li layer to be applied in-situ to the anode just before machine firing. These shots also exhibited premature voltage collapse, but yielded significant amounts of Li in the beam. This suggested that the above results had separate causes. One possible cause of the impedance collapse is that the first-generation light distribution cone allowed for

non-uniform illumination of the anode surface. Some regions of the anode received as much as 1 J/cm^2, enough to desorb large amounts of material from the anode surface, leading to low-voltage operation.

Several improvements have been made for the LEVIS ion source experiments described in this paper. A new cone was designed, consisting of a number of vertical segments each of which illuminates the entire anode surface. This has resulted in a much more uniform illumination (± 30%)across the 4 cm anode height, and at the same time allowed us to reduce the total laser power to the anode.

To address the issue of Li purity, we have experimented with a DC-heating process, described above, in which the anode surface is heated to as high as 150^{o}C. DC heating of both LiMo and LiAg layers, each deposited over a LiF undercoat, has been attempted.

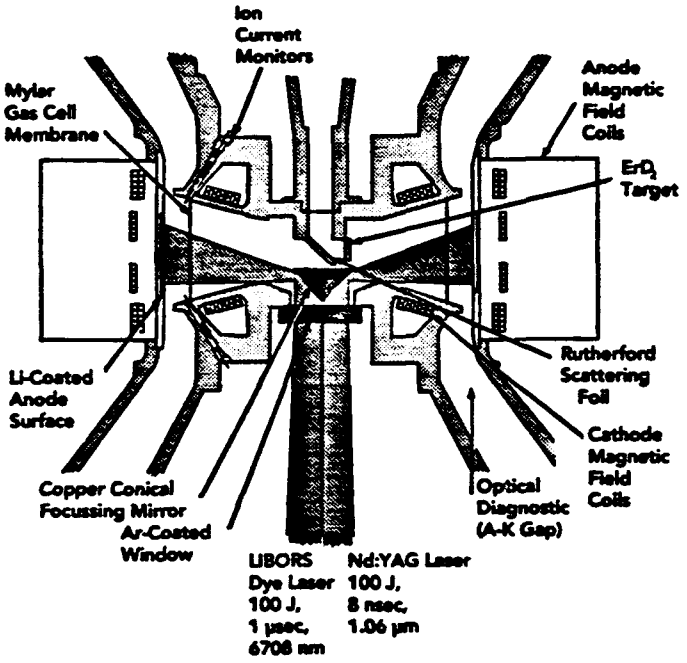

Figure 3. Schematic diagram of the PBFA-II diode and diagnostics.

The first shots in the recent LEVIS experiments were taken using both unheated and heated LiMo layers. Little Li was produced in the beam, along with significant amounts of carbon, in both cases. We then switched to a LiAg layer on the anode, and took shots varying both the amount of heating (peak temperature and total heating time), and the energy density of the Nd:glass laser light on the anode surface (120 to 300 mJ/cm^2). Tuned dye laser intensities of 30 to 60 m/cm^2 (12 to 24 J at the anode) have been found to be sufficient for the LIBORS process. For all these shots, we fired the LIBORS and Nd:glass lasers 400 and 200 ns before the power pulse, respectively.

The magnetic spectrometer consists of an array of PIN diodes for determining time-dependent behavior of ions Rutherford-scattered from the gold target foil located at the diode center. The PIN diodes are mounted on a piece of CR-39 nuclear track-counting material. By examining track sizes of ions striking the CR-39, the diameters of which are sensitive to ion species, we have determined that LiAg subjected to DC-heating yields Li in the resultant ion beam. The Li fraction varies with both the amount of DC-heating (up to the >5 hours that we have used), and with the fluence level of Nd:glass laser power impinging on the anode surface. Figure 4 shows inductively corrected diode voltage and total current for two different machine shots. The first (Shot 5219) was taken with approximately 195 mJ/cm^2 deposited on the anode surface by the Nd:glass vaporization laser, and with no DC-heating. The second shot (5225) was identical, except that the anode surface was heated for at least 4 hours at a temperature of at least 120 ^{o}C. As can be seen, for the first 30 ns, the total currents on the two shots are identical. After 20 ns, ion current begins to flow, and the total current on the non-heated shot rises significantly relative to Shot 5225, leading to lowered voltage on the

diode. Very little Li and even less carbon are indicated on the CR-39 for the unheated shot, and other diagnostics indicate that the beam produced was largely protonic. This is consistent with results from earlier LEVIS shots taken without the in-situ Li deposition. Those earlier shots featured even higher total current and lower diode voltage than on Shot 5219. Since very few protons are indicated in Shot 5225, we conclude that 1) DC-heating does remove most if not all of the proton fraction in the resultant beam, and 2) particularly when DC-cleaning is undertaken, we have solved the problem of low-voltage operation with LEVIS.

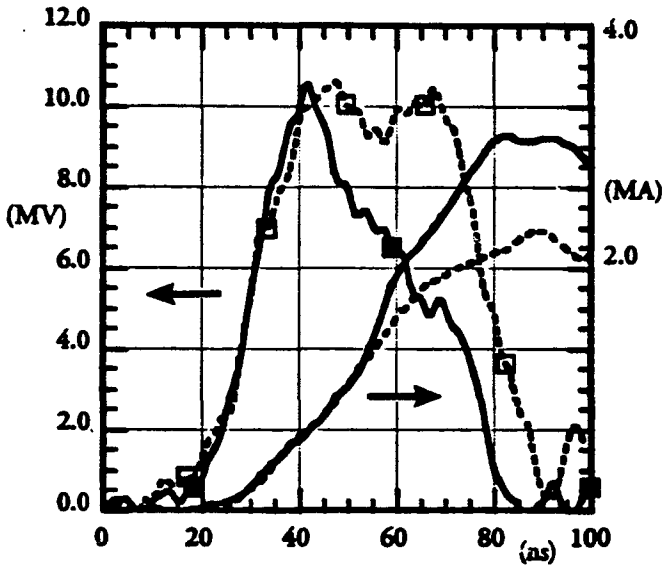

Figure 4. Corrected voltage and total ion currents for two shots.

The fraction of carbon remaining in the beam is evidently affected by both the DC-heating duration, and by the energy deposited by Nd:glass laser. We have taken too few shots to fully characterize the dependence of carbon on these two parameters, but our highest Li-purity, lowest carbon-content beams have occurred with extended DC-heating, and with a Nd:glass energy level of about 200 mJ/cm^2 (e.g. Shot 5225). On this shot, the Li fraction appears to be as high as 90%± 10%. Furthermore, almost half of the Li energy in the beam occurred at ion energies above 9 MeV. This high-energy content of the ion beam exceeds what is seen on a shot taken with a passive LiF ion source[7]. This is evidently due in part to the use of a higher insulating magnetic field possible with the LEVIS active source, and also because the ion beam appears to turn on slightly sooner in Shot 5225. The reduction in both proton and carbon beam contaminants is consistent with the result of spectroscopic studies of the A-K gap[8]. Extended DC-heating of 3 hours produced a factor 3-5 reduction in the relative intensities of the carbon impurity lines, as well as a factor 40 reduction in the hydrogen line intensity. It is important to note that the heating is turned off at least 30 minutes before shot time. This implies that impurity redeposition onto the anode surface from the 10^{-5} Torr vacuum is not a significant factor in these shots.

Conclusion

These LEVIS experiments build upon earlier LEVIS results which produced low lithium beam fractions and premature voltage collapse in the diode. More uniform anode illumination, due to a redesigned distribution cone, has yielded higher impedance diode operation. In addition, extended DC-heating has successfully removed the great majority of proton and carbon impurities in the beam. This also contributes to improved diode impedance. Further experiments are planned to better characterize lithium beam purity, as well as increase beam power on target. In addition, LEVIS active anode operation allows us to incorporate increased magnetic fields and use of

limiter topologies in the diode. Both of which, according to theory, should lead to improved beam micro divergence.

Acknowledgments

This work was supported by the U. S. Department of Energy under contract No. DEAC04-DP00789.

References

1. J. P. VanDevender and D. L. Cook, Science 232, 837(1986).
2. K. W. Bieg, G. C. Tisone, T. R. Lockner, J. E. Bailey, M. E. Cuneo, B. F. Clark, J. E. Potter and L. P. Schanwald, Proceedings of the XIVth International Symposium on Discharges and Electrical Insulation in Vacuum, 568(1990).
3. P. L. Dreike and G. C. Tisone, J. Appl Phys. 59, 371(1986).
4. R. M. Measures, P. G. Cardinal, and G. W. Schinn, J. Appl. Phys. 52, 1269(1981).
5. T. J. McIlrath and T. B. Lucatorto, Phy. Rev. Lett. 38, 1390(1977).
6. J. K. Rice, R. A. Gerber and G. C. Tisone, in American Institute of Physics Conference Proceedings, No. 146(AIP, New York, 1986).
7. See T. A. Melhorn et al, these Proceedings.
8. See A. B. Filuk, J. E. Bailey, K. W. Bieg, A. L. Carlson, T. J. Renk, G. C. Tisone, and A Y. Maron these Proceedings.

FORMATION PROCESS OF NEGATIVE IONS IN A MAGNETICALLY INSULATED DIODE

K.HORIOKA, Q.YU and K.KASUYA
Department of Energy Sciences, The Graduate School at Nagatsuta, Tokyo Institute of Technology, Nagatsuta 4259, Midori-ku Yokohama, Japan 227

ABSTRACT: The formation process of negative ions in a flashover diode plasma is investigated. A coaxial magnetically insulated diode, whose cathode can be cooled by liquid nitrogen or helium, is driven with a 5-Ohm/60nsec Blumlein line. Effects of voltage polarity, prepulse level, source materials, and surface structure of the electrode, on the diode characteristics are examined and the potentiality of the plasma as asource of intense negative ion beam is discussed.

1. INTRODUCTION

If the beam divergence is sufficiently small, high power beams of fast atoms obtained by stripping of negative ions, probably eliminate many of present difficulties of light ion beams; focusing and transport of the beam, and impedance collapse of the diode.

Multi-kA level of H- beams were produced from magnetically insulated diodes[1-4]. Generally, the source plasma has been provided by a surface flashover of hydrocarbon polymer. On the other hand, a surface flashover plasma produced from condensed material includes a high density gas layer of molecular state[5]. It is considered that the presence of highly vibrationally excited H2 molecules in the plasma is important for the production of negative ions through the action of dissociative attachment process[6].

The introduction of high density and large density gradient gas layer in the cathode plasma is probably essential[7] for high H- concentration and the efficient negative ion production.

A schematic diagram of the acceleration gap of MID with positive or negative voltage polarity is shown in Fig.1. Generally, the impedance of positive diode collapses with time because of anode plasma effects and a bootstraping effect; ion current enhancement increase an electron charge accumulation which induces further ion enhancement in the acceleration gap. On the contrary, when polarity of the MID is reversed, the electron charge compete with that of negative ions, so it is expected that the behavior of

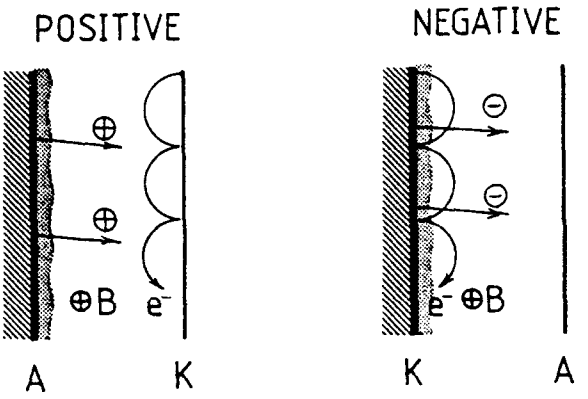

Fig.1 Schematic Diagram of Magnetically Insulated Diode with Positive (a) or Negative (b) Voltage Polarity

the MID with negative polarity is quite different from that of positive polarity. Therefore, characteristics of the MID under the operating condition of negative or positive voltage polarity are also investigated.

2. EXPERIMENTAL SETUP

The experimental arrangement is shown schematically in Fig.2[3,4]. The diode consists of a center electrode made of a brass cylinder and an outer electrode made of a perforated stainless cylinder of 1mm thickness and 70mm inner diameter. The diameter of the center electrode is 40 or 58mm. It has grooves of 2(or 3)mm width, separated 2(or 3)mm and 2(or 3)mm depth on the surface and the flashover plasma induced on the surface of a dielectric material filled in them is used as the ion source. The center electrode has a reservoir of coolant and transfer tubes of spiral shape to cool down the electrode with liquid N2 or He. In order to make thermal insulation, the diode is connected to a 5-Ohm/60nsec Blumlein line through a prepulse switch. However the gap distance is kept very small not to degrade the prepulse effect[4] on the plasma formation.

Magnetic insulation of the diode gap is given by axial field of 6.5kG or 5.2kG, which is created by a solenoidal coil with pulse duration of 1.8ms. The same magnetic field is used for ion collectors. The ion collectors are made of a 0.1mm thick stainless cylinders of 100mm or 140mm in diameter. The prepulse level of diode voltage is controled by the value of charging inductance (LB) of the Blumlein.

Source effects on the formation of negative ions in the electrode plasma are systematically investigated. Various condensed materials such as ethanol (C2H5OH), SF6 and freon-113 (CC1F2-CC12F) were supplied from the vapor cell

on the cooled center electrode and tested as the negative ion source. The thickness of the condensed layer is fixed at about 0.1mm.

3. EXPERIMENTAL RESULTS

3.1 Electrical characteristics of diode

Typically, prepulse of the system had about 100kV level of negative and positive parts with 300ns duration. The diode gap impedance was maintained at very high value especially for positive polarity[8]. From the same experiments [8], it was concluded that the voltage pulse of negative polarity played important roles for the source plasma formation. For negative polarity, a small leakage electron current along the magnetic field, ie; through the surface of the center electrode, was confirmed by damage patterns of witness sheets (Nitto Radcolar films).

3.2 Ion beam generation

Typical waveforms of ion current produced from a wax filled electrode with 2mmW grooves are shown in Fig.3, for positive(a) or negative(b) voltage polarity. As shown here, the diode produced near 60A/cm^2 ion current density for positive voltage pulse, which is almost the Child-Langmuir value for the beams of (600keV, d=6mm). Although mean value of the diode impedance was also kept high, because of the source plasma effects, the diode current increased gradually, so, the diode impedance decreased with time. When the voltage polarity was reversed, ion current signal was never detected in the

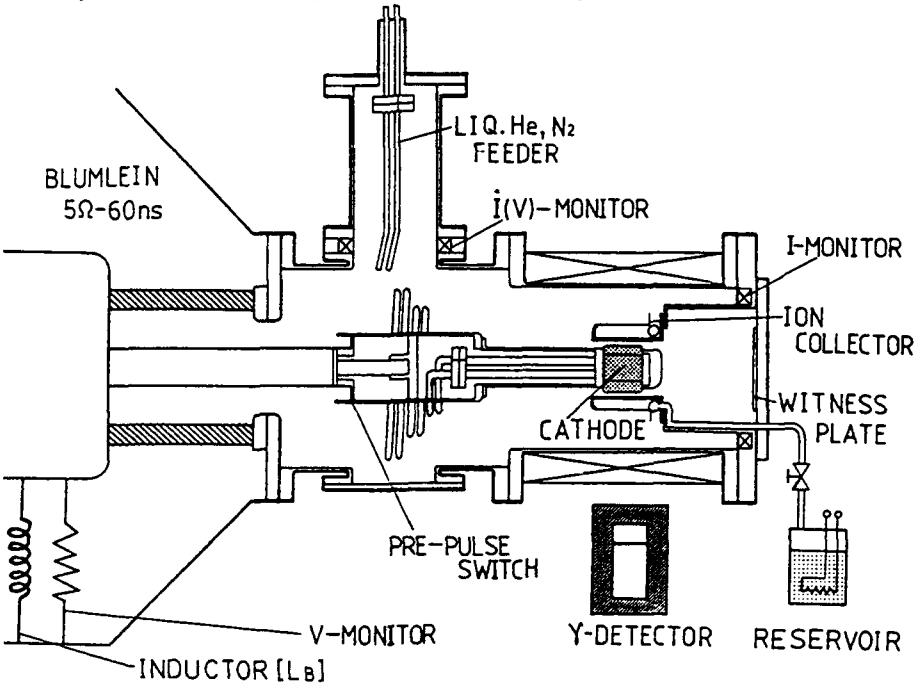

Fig.2 Schematic Diagram of Experimental Arrangement

primary voltage pulse. Ion signals were detected only in the second positive voltage pulse. When the insulation field was decreased from 6.5kG down to 5.2kG, although the reproducibility was not good, negative signal of $15A/cm^2$ (about 2kA total current) was detected.

3.3 Effect of surface structure of center electrode

The flashover process was studied for two different center electrode geometries. Fig.4 shows the electrodes; in one, grooves are oriented parallel to Bz (Type-A) and in the other perpendicular to Bz (Type-B). Typical waveforms of the voltage VD, the ion current Ii and the diode current ID are shown in Fig.5(for Type-A) & Fig.6(for Type-B). The diode was operated at geometrical gap of 6mm, with 3mmW ion source grooves, peak applied voltage of 600 or 500kV with Bz=6.5kG. As shown, for positive polarity, the diode behavior almost the same. However, Type-A electrode was more efficient for the negative beam production, and we could never detect the negative current signal for higher voltage condition. With Type-A electrode, the beam production was more efficient, so the EXBz electron motion over the grooves must contribute the source plasma formation.

3.4 Source effect on plasma formation

In order to examine the source effect on the negative ion beam formation, ion beams from various condensed materials were investigated. The vapor of source material was puffed and about 0.1mm thick condensed layer was formed on the cooled electrode. Typical waveforms of ion current extracted from flashover plasmas of condensed ethanol[A], freon-113[B] or SF6[C] are shown in Fig.7 for positive and negative voltage pulse. Here, operating condition of the diode was fixed at VD=500kV, d=6mm, and to improve the reproducibility, the peak prepulse level was lowered around 50kV. As can be seen from the figures, negative ion signals of several A/cm^2 weredetected transiently during the voltage pulse. Turn-on times and peak values of the negative signals depended on the source dielectric materials. The negative signals rose at different times. It is interesting to note that the turn-on times(T) of negative signals are T(SF6)> T(freon)> T(ethanol).

4. SUMMARY

We could observe negative current of around $15A/cm^2$ (2kA total current) at 500kV (GW power) level. The negative signal apparently was a function of the diode current. However reproducibility of the results was not good. The surface current flowing through the cathode surface, ie; conditions close to

the experiments in magnetically insulated vacuum transmission lines[9,10], are probably necessary as pointed out in Refs [4,11]. Formation process of the plasma is also affected the structure of the electrode. The one which has parallel grooves to Bz is more effective for the negative ion formation.

The formation process of negative ion beam seemed to be strongly affected by the source dielectric materials. Negative currents of several A/cm^2 level (total current of kA level) were produced transiently during the negative voltage pulse. Rise times and values of the peak negative current depended on the source materials. There must be many factors which affect the negative ion formation not only electron affinities of component atoms, chemical structure and vapor pressure of the source material but also operating condition of the diode, as mentioned above.

We can extract negative beams of GW level from magnetically insulated diodes. However, sophisticated optimization of the diode condition is needed for the operation. This work was supported by Grant-in-Aid for Scientific Research from the Ministry of Education, Science and Culture in Japan.

5. REFERENCES

[1] KOLMENSKY,A.A., LEBEDEV,A.N., PAPADICHEV,V.A., PIKUZ,S.A., YABLOV,B.N., (Proc. Conf. High Power Particle Beams, Sanfrancisco), (1983) 533-539
[2] FISHER,A., LINDENBAUM,H. and ROSTOKER,N., (Proc. Int. Conf. High Power Particle Beams, Kobe), (1986) 116-118
[3] BISTRITSKY,V.M., VOLKOV,S.N., KRASIK,Ya.E., MATIVIENKO,V.M. and TOLMACHEVA,V.G., (Proc Int. Conf. High Power Particle Beams, Kob (1986) 113-115
[4] PAPADICHEV,V.A., PIKUZ,S.A. and SHELKOVENKO,T.A., (Proc. 7th Int High Power Particle Beams, Karlsruhe), (1988) 715-720
[5] HORIOKA,K.,YONEDA,H. and KASUYA,K., IEEE Trans. Plasma Sci., PS- (1989) 793-797
[6] BACAL,M., Physica Scripta, T2/2, (1982) 467-478
[7] PROHASKA,R., LINDENBAUM,H., FISHER,A., SHEPERD,G. and ROSTOKER,N Proc. APS Meeting (Anahaim) (1989)
[8] HORIOKA,K., YU.Q and KASUYA,K., (Proc. 8th Int. Conf. High Power Particle Beams, Nobosibirsk) (1990)
[9] VANDEVENDER,J.P., STINNET,R.W. and ANDERSON,R.J., Appl. Phys. Let 38, 4 (1981) 229
[10] STINNET,R.W., PALMER,M.A., SPIELMAN,R.B. and BENGTSON,R., IEEE Tr Plasma Sci., PS-11, 3 (1983) 216-219
[11] LINDENBAUM,H., FISHER,A. and ROSTOKER,N., (Proc. 7th Int. Conf. Hi Power Particle Beams, Karlsluhe), (1988) 677-682
[12] PAPADICHEV,V.A., PIKUZ,S.A and SHELKOVENKO,T.A, Rev. Sci. Instr., 61 1 (1990) 439-441

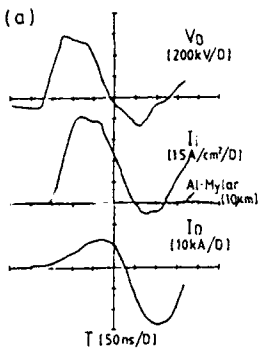

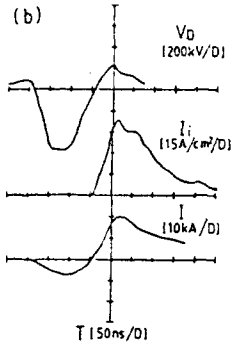

Fig.3 Typical Waveforms for Positive (a) or Negative (b) Polarity (d=6mm, B=6.5kG)

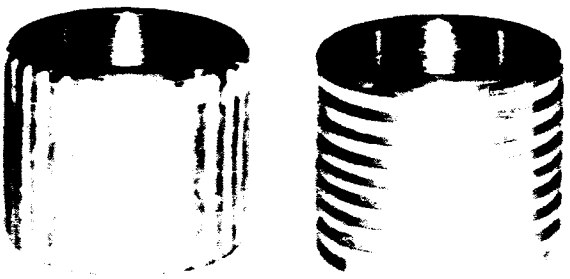

(Type-A) (Type-B)

Fig.4 Photographs of Center Electrodes

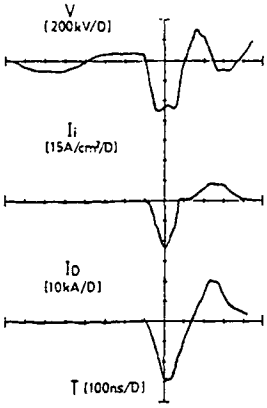

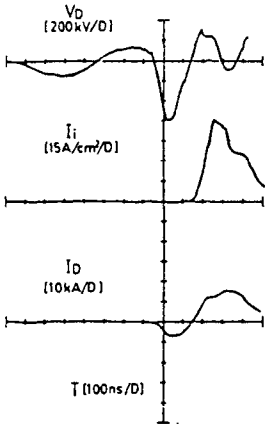

Fig.5 (For Type-A)

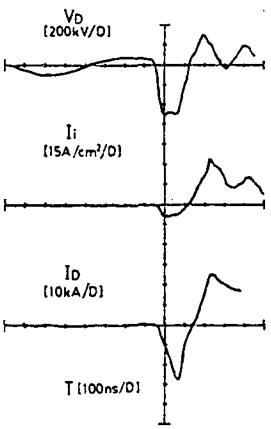

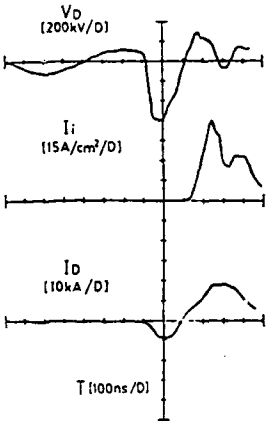

Fig.6 (For Type-B)

Waveforms of Diode Voltage VD, Ion Current Density Ii and Current ID for Positive or Negative Voltage Polarity
(For Wax Filled Ion Source, d=6mm, B=6.5kG)

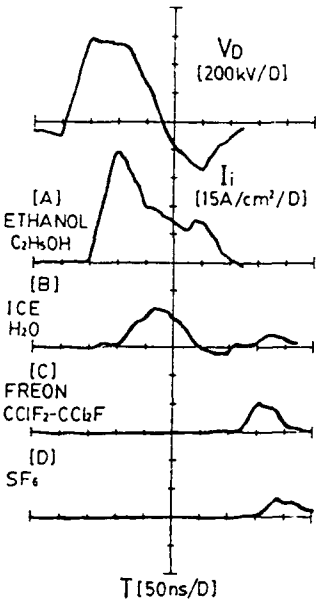

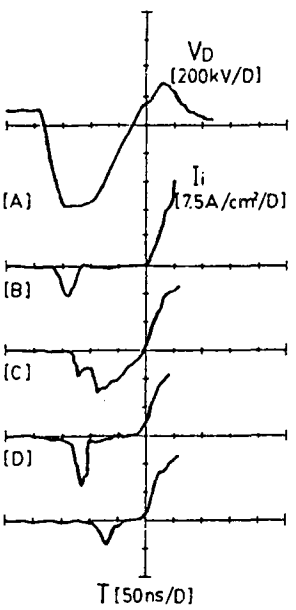

Fig.7 Typical Waveforms of Ion Current Produced from Various Source Materials ([A];Ethanol, [B];Ice,[C]Freon,[D];SF6,)

MAGNETICALLY INSULATED H^- DIODES*

A. Fisher**, V. Bystritskii*** E.Garate, R. Prohaska and N. Rostoker,

University of California, Irvine

Abstract

At the University of California, Irvine, we have been studying the production of intense H^- beams using pulse power techniques for the past 7 years. Previously, current densities of H^- ions for various diode designs at UCI have been a few A/cm^2. Recently, we have developed diodes similar to the coaxial design of the Lebedev Physical Institute, Moscow, U.S.S.R., where current densities of up to 200 A/cm^2 were reported using nuclear activation of a carbon target. In experiments at UCI employing the coaxial diode, current densities of up to 35 A/cm^2 from a passive polyethylene cathode loaded with TiH_2 have been measured using a pinhole camera and CR-39 track recording plastic. We have also been working on a self-insulating, annular diode which can generate a directed beam of H^- ions. In the annular diode experiments a plasma opening switch was used to provide a prepulse and a current path which self-insulated the diode. These experiments were done on the machine APEX, a 1 MV, 50 ns, 7 Ω pulseline with a unipolar negative prepulse of ~ 100 kV and 400 ns duration. Currently we are modifying the pulseline to include an external LC circuit which can generate a bipolar, 150 kV, 1 μs duration prepulse (similar prepulse characteristic as in the Lebedev Institute experiments cited above).

* Supported by ONR/SDIO.
** Permanent address: Naval Research Laboratory, Washington, D.C.
*** On leave from the Institute for High Current Electronics, Tomsk, USSR.

Introduction

The production of neutral particle beams with energy over 100 kV requires starting with weakly bound negative ions which can be accelerated and then stripped to neutrals. Many workers have studied the problem of producing negative ions, usually H^-, in steady state plasmas. Typically these dc sources of H^- are limited to current densities of the order of ~ 100 ma/cm^2 for areas larger than a few cm^2. At the University of California, Irvine (UCI) we have been studying the production of intense H^- ion beams using pulse power techniques and magnetically insulated diodes. The purpose of the work is to explore the possibility of obtaining high current densities (1 kA/cm2) of negative ions. This work has been ongoing for the past 7 years and originated with the suggestion that power losses in magnetically insulated diodes were due to negative ions produced in the cathode plasma[1]. Previously, current densities of H^- ions for various diode designs at UCI have been a few A/cm^2 [2-4]. This is in contrast to results by a group from the Lebedev Physical Institute, Moscow in which current densities of H^- up to 200 A/cm2 were reported[5]. The machine used to energize their cylindrically symmetric diode had a natural bipolar prepulse of about 150 kV and ~ 1μs duration. In addition, the diode was constructed so that a high current density electron beam flowed over the surface of the ion producing material. Independent efforts in France[6,7] as well as those at UCI did not reproduce the Lebedev results, however, the machines used to

energize the diodes did not have a large prepulse and no provision was made for electron flow over the surface of the cathode.

Experiments With a Coaxial Diode

During the past year we collaborated with the group from the Lebedev Physical Institute. At UCI we constructed a coaxial diode based on previous designs of the Lebedev Institute diodes and incorporated diagnostics consisting of biased Faraday cups and a pinhole camera and CR-39 track recording plastic. A schematic of the coaxial diode and associated diagnostics is shown in Figure 1. For this diode configuration the ions are emitted transversely and the electrons longitudinally so that the diode is simultaneously an electron and H^- diode.

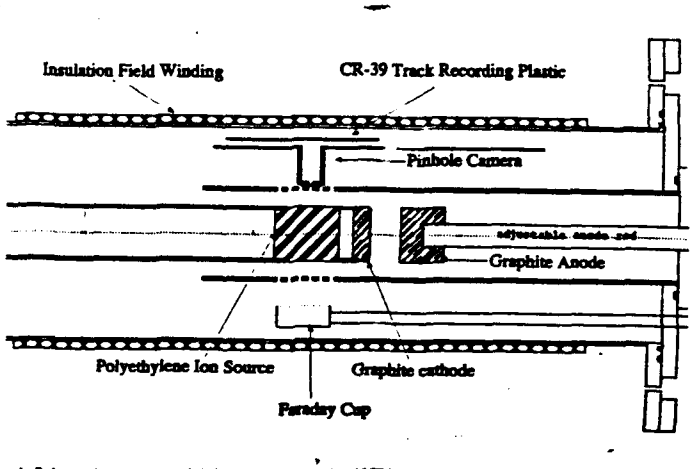

Figure 1. Schematic of the coaxial diode constructed at UCI based on the Lebedev Institute high current density H^- diode. Three different cathode materials were tested: U.S. and Russian polyethylene and a polyethylene cathode loaded with titanium hydride.

In experiments conducted at the Lebedev Institute the cathode diameter was 2 cm with a 6 cm anode made of stainless steel and drilled to have ~ 50% transparency. The polyehtylene insert, which is used as the ion source, was 6 cm long. An up to 20 kG magnetic field was used for insulation and the pinhole camera diameter was ~ 20 μm. The diode was energized by the machine ERG, configured as a single pulse line, and could generate a 500-700 kV pulse of 200 ns duration.

The prepulse was provided by an external circuit [8] which could generate a bipolar 150 kV, 1 μs pulse. The prepulse and main voltage pulse timing could be varied. Using the CR-39 track recording plastic we measured H^- current densities of ~ 10 A/cm^2 present in ~ 3% of the shots (~ 100 kV bipolar prepulse of ~ 1 μs duration, with ~ 1 μs delay between prepulse and main voltage). The damage pattern on the CR-39 film showed very uniform emission with no evidence of hot spots. Without any prepulse we measured ~ 10 times less H^- current density. These results were obtained with Russian polyethylene. Under the optimum prepulse conditions described above, two orders of magnitude less H^- current density was obtained using U.S. polyethylene.

In work subsequently conducted at UCI using this diode configuration we modified the polyethylene insert by machining azimuthal grooves 2 mm wide by 2mm deep and packed them with TiH_2. The grooves were spaced ~ 5mm apart along the length of the insert. The machine used to energize the diode was the Apex. This machine has a natural, unipolar prepulse of ~ 100 kV and 400 ns duration. The

Apex is a 1 MV, 7 Ohm Marx energized pulseline which generates a 50 ns pulse and for a given diode voltage can provide ~ 2 times higher electron current than the Lebedev machine. Magnetic fields up to 30 kG were used for insulation. In about 15% of the shots we measured 35 A/cm^2 H^- ion current density at 750 kV and 60 kA electron beam voltage and current. The remainder of the shots yielded 2-3 A/cm^2 H^- current densities.

Using Russian polyethylene without the TiH_2 and the same coaxial diode used at the Lebedev Institute, 25 A/cm^2 H^- current density was measured. The CR-39 track recording film showed very uniform emission with no hot spots. In these results shot-to-shot repeatability was low, probably due to non-uniform surface breakdown of the polyethylene. However, referring to Figure 1, note that both the Faraday cup and CR-39 pinhole camera diagnostics 'see' only a small azimuthal portion (< 10%) of the cathode surface. The seemingly poor shot-to-shot repeatability for all our results could be due to non-uniform surface breakdown and H^- ion production out of view of our diagnostics.

Experiments Using a Plasma Opening Switch and an Annular Diode

The coaxial diode geometry has limited application because of the high intrinsic geometric divergence of the ion beam. At UCI we have done extensive experiments on unidirectional beam forming diodes and we have solved several problems associated with some configurations, e.g. the problem of field coil breakdown[2-4]. During the past year at UCI we conducted experiments on annular unidirectional beam forming diodes using a plasma opening switch (POS) to generate a prepulse. These experiments were meant to determine the effects of a large prepulse and not to generate high current density H^-. A schematic of the diode is shown in Figure 2.

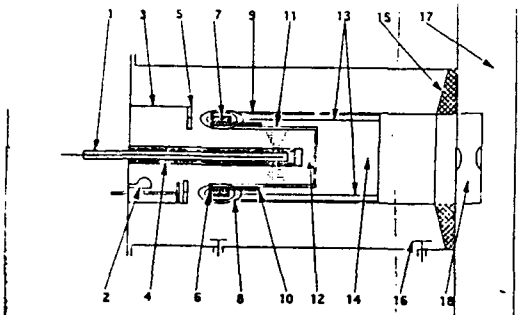

Figure 2. Schematic of the annular diode and plasma opening switch system.

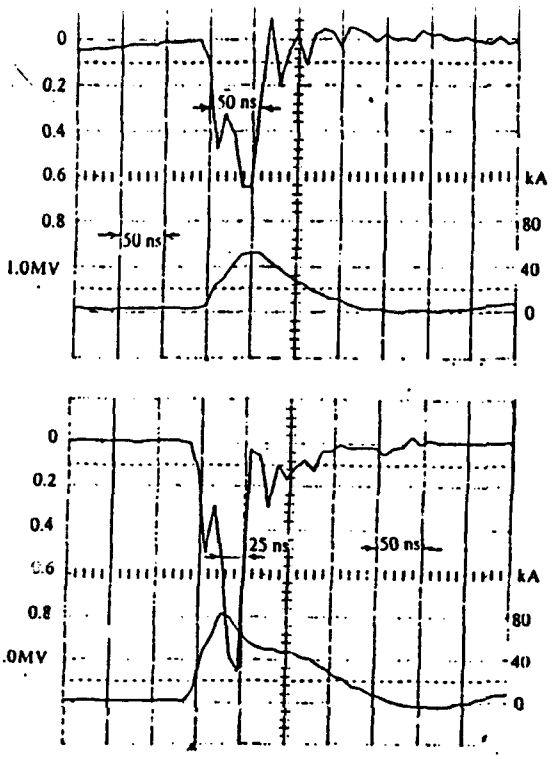

Figure 3. Typical V-I traces for the machine APEX. The upper traces are without the plasma opening switch operating.

In this diode configuration the POS conducts during the initial part of the main voltage pulse so that electron current can be drawn over the surface of the dielectric surface which provides the ions, in this case polyethylene. When the switch opens there is a large inductive voltage spike which accelerates the ions. Typical V-I traces are shown in Figure 3. The annular diode was ~ 10 cm in diameter with annular thickness of 2 cm and the anode-cathode gap was ~ 6 cm . The insulating magnetic field was up to 8 kG. We measured H^- current densities of 0.6 A/cm^2 in ~ 30% of the shots. However, without the POS generated prepulse a maximum current density of ~ 0.1 A/cm^2 was measured with poor reproducibility (typically 1 good shot in 15).

Discussion

A physical model to explain the H^- current density has thus far been elusive. Certain features have been identified that are essential. The model must explain why the H^- density is many orders of magnitude larger than the thermal equilibrium value for the cathode surface plasma. The only process for H^- formation with a significant cross section involves dissociative attachment of a molecule in a highly excited vibrational state, H_2^*. The molecule can be excited by electrons of 10 - 100 eV in the cathode plasma

$$H_2 + e > H_2^* + e$$

and then

$$e + H_2^* > H^- + H$$

This process is involved in all previously suggested[9,10] models. Stripping of the H^- can take place rather easily i.e., there are several types of collisions of high cross sections. It is therefore essential that the H^- be accelerated away from the cathode plasma to where there are very few particles (ions, neutrals) to

neutralize it by collisions. A model for accomplishing this has previously been described.[10] It is illustrated in Figure 4. Within the plasma, which is magnetically confined, excited neutral molecules are produced and are not magnetically confined. They leave the plasma and undergo dissociative attachment in the region of excess electron density. Then H^- is accelerated towards the anode in a region of low density (vacuum except for H^-). This model was proposed in 1987 but it has not been particularly helpful in scaling the current density. This is because some essential features are absent which have only recently been identified in the UCI/Lebedev experiments with coaxial diodes.

The coaxial diode produces a radial H^- current of about 5 kA and an axial electron current of about 50 kA. Then in addition to an axial applied magnetic field B_z ~ 10 kG there would be an azimuthal field of B_q ~ 10 kG. The very large current densities of H^- are never observed with-out this axial current through the cathode plasma. Without confining magnetic fields the cathode plasma would expand and cross the gap with a speed of about 10^7 cm/sec. The magnetic pressure $B_z^2/8\pi$ is sufficient to decelerate the plasma and prevent it from crossing. However, the interface is subject to the Rayleigh-Taylor instability. This instability would be suppressed by magnetic shear i.e., the field $B_{theta}(r)$ from the longitudinal current in addition to $B_z(r)$ produces magnetic shear. In Figure 5 stable and unstable deceleration of the plasma field interface is illustrated for a pinch experiment.[11]

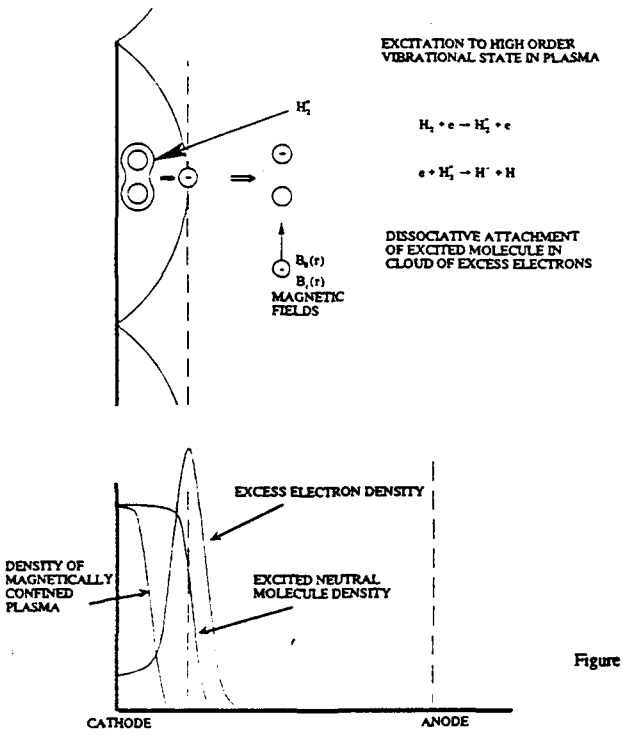

Figure 4. Formation of H^- ions in a magnetically insulated diode.

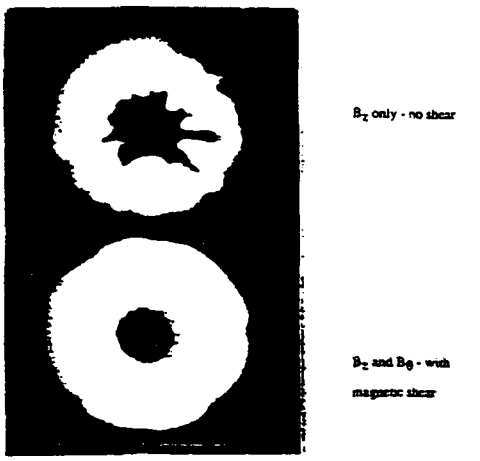

Figure 5. Example of the stabilization of a low density pinch with magnetic shear.

In the unstable case only an axial trapped field B_z decelerates the interface. In the stable case $B_{theta}(r)$ is added with an axial current carrying conductor. The difference between a high uniform current density of H^- and a much lower non-uniform emission can be understood in terms of the surface irregularities illustrated in Figure 5.

Conclusion

Using a TiH_2 loaded cathode in a coaxial diode geometry we measured 35 A/cm2 H^- ion current density at 750 kV and 60 kA electron beam voltage and current using our machine APEX. In collaborative experiments at the Lebedev Physical Institute using an external prepulse circuit we measured up to 10 A/cm^2 H^- current density using Russian polyehtylene and ~ 100 times less current density, for the same conditions, using U.S. manufactured polyethylene. In all of the high current density shots regarded as good, independent of which machine was used, some prepulse was present in the voltage pulse. It is clear from our results that different types of cathode material generate significantly different ion current density. Currently we are modifying our machine APEX to include an external prepulse circuit which will provide a bipolar, up to 150 kV, 1μs duration pulse that can be independently timed with respect to the main voltage pulse. This will allow us to continue our study of different cathode materials used for the generation of pulsed, high current density negative ions.

References

1 A. Fisher and N. Rostoker, Bull. Am. Phys. Soc., 21, 1097, (1976).

2. A. Fisher, H. Lindenbaum, N. Rostoker, C. E. Wiswall, S. L. Cartier and J. C. Leader, in Microwave and Particle Beam Sources and Directed Energy Concepts, Howard E. Brandt, Ed., Proc. SPIE 873, 190, 1988.

3. A. Fisher, H. Lindenbaum, N. Rostoker, S. L. Cartier and C. E. Wiswall, in Microwave and Particle Beam Sources and Directed Energy Concepts, Howard E. Brandt, Ed., Proc. SPIE 1061, 439, 1989.

4. R. Prohaska, A. Fisher and N. Rostoker, in Microwave and Particle Beam Sources and Directed Energy Concepts, Howard E. Brandt, Ed., Proc. SPIE 1407, 598, 1991.

5. A.A. Kolomenski, et al.,Proc. 5th Int. Conf. on High-Power Particle Beams, San Fransisco, Ca., 533, 1983.

6. S. Moustaises, H.J. Doucet, et al., 6th Int. Conf. on high-Power Particle Beams, Kobe, Japan, 1986.

7. H. J. Doucet, 4th Int. Symp. on Production and Neutralization of Negative Ions and Beams, Brookhaven, N.Y., 1986.

8. A. G. Mozgovoy and V.A. Papadichev, "H^- generation using an externally applied prepulse," in these proceedings.

9. V. A. Papadichev, Laser and Particle Beams **9**, 167 (1991).

10. A. Fisher and N. Rostoker, Final Technical Report on High Flux Neutral Beams, December 31, 1987, available from the Physics Department, University of California, Irvine, Irvine, Ca., 92717.

11. D. J. Albares, N. A. Krall and C. L. Oxley, Phys. Fluids **4**, 1031 (1961).

ANODE DISCHARGE TO FACILITATE CATHODE PLASMA FORMATION FOR GENERATION OF H^-, C^-, F^-, I^- AND Pb^- IONS

A.G. Mozgovoy and V.A. Papadichev

P.N. Lebedev Physical Institute
117924, Leninsky Prosp. 53, Moscow, Russia

Abstract

Experimental studies of cathode plasma formation to generate high-power negative ion beams of various elements in a coaxial magnetically insulated pulsed diode are presented. The vacuum spark discharge outside the anode was used to facilitate cathode plasma formation with high content of H^-, C^-, F^-, I^- and Pb^- ions. The main mechanism responsible for cathode plasma formation is cathode bombardment by positive ions accelerated from anode plasma by the main pulse accelerator voltage.

1. Introduction.

Obtaining high-power beams of negative ions might offer wide possibilities when using them in researches on CTR with inertial confinement. Unavoidable and still to-be-overcome difficulties in transporting and focussing high-power beams of positive ions on a target are connected with multicomponent fluid instabilities (ions and electrons or beam ions and plasma) and ion scattering on plasma ions or charge fluctuations arising from instabilities.

On the other hand, a high-power beam of negative ions after directing ions radially can easily be stripped to a neutral atom beam without substantial increase of beam emittance, that is, introducing large angular spread or changing its initial direction of motion. Neutral atoms will reach the target without experiencing any deviation from their initial radial motion induced by external electric and magnetic fields or instabilities [1]. The stripping might be accomplished by laser or a thin gas or plasma target as has already been done in experiments with subampere current beams of H^- [2,3].

Negative hydrogen ions with high-current densities (up to 200 A/cm^2) were accelerated in a high-power pulsed diode with magnetic insulation at the P.N. Lebedev Physical Institute [1,4,5]. We used a surface electrical discharge on a dielectic employing a bipolar prepulse for its initiation. A rather large prepulse (10–15% of the main voltage pulse) is usual in Blumlein accelerators, but it is much less (2–4%) in single-pulse-forming-line machines. A scheme for creating an external prepulse was proposed and tested experimentally [6], thus opening a wider field for experimenting with negative ions.

Nevertheless, using a prepulse to create cathode plasma has some drawbacks: (1) one has to employ dielectric to produce surface discharge, thus enabling to produce negative ions of only a restricted number of elements, (2) cathode plasma is not homogeneous because the discharge is local azimuthally, leading to plasma instabilities and spoiling of beam emittance.

On the other hand, theoretical and experimental studies of CTR targets show that it is necessary to use ions heavier than hydrogen (Li, C etc.). So it is interesting and useful to develop a new, more universal way of initiating cathode plasma. One possible method, namely anode discharge, allowing to produce and accelerate H^-, C^-, F^-, I^-, and Pb^- ions in a high-power pulsed diode is described below.

2. Experimental setup and diagnostics.

The schematic drawing of the experimental setup is shown in Fig. 1.

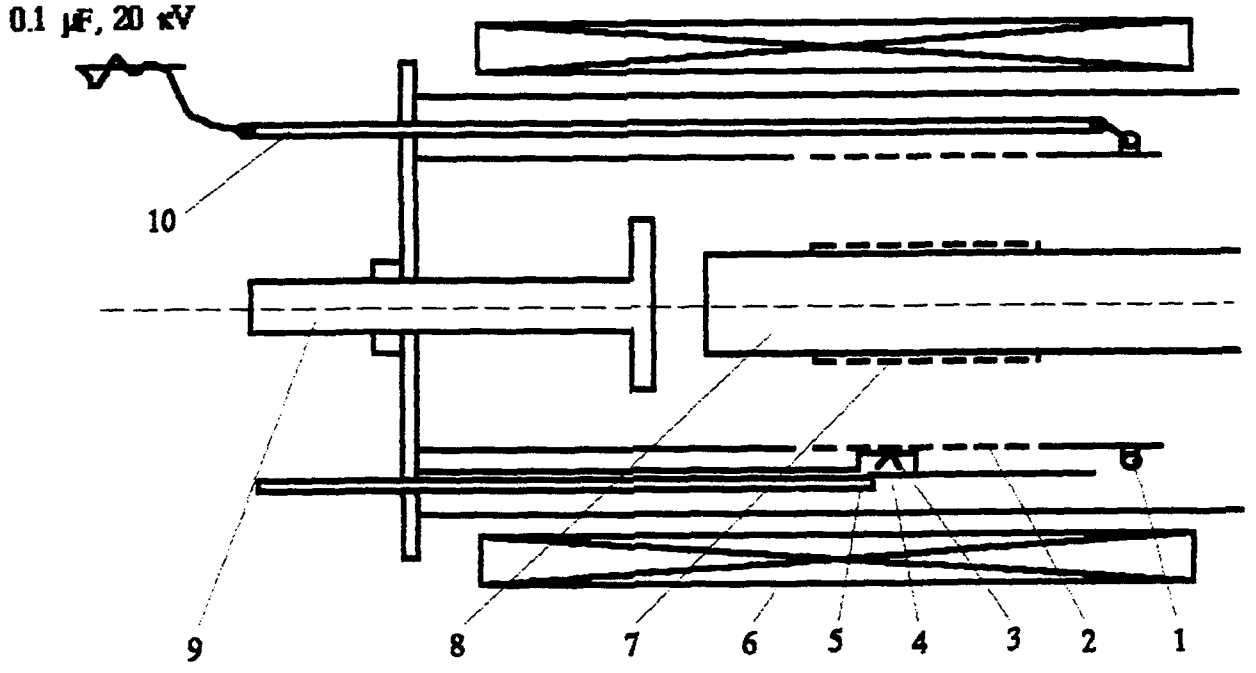

Fig.1. 1 – plasma gun, 2 – anode with drilled holes, 3 – pinhole chamber, 4 – track detector CR-39, 5 – rod to move CR-39 film, 6 – solenoid, 7 – perforated sleeve (dielectric cathode), 8 – cathode rod, 9 – auxiliary anode at the diode butt to control electron axial current, 10 – plasma gun feeder.

A coaxial diode with up to 20 kG magnetic field for insulation was used. The cathode diameter used was 2, 3 or 4 cm. A six-centimeter diameter anode made of stainless steel was drilled to have a transparency of 50%. The diode was fed by a 0.5–0.7 MV pulse of 200 ns duration from a single-pulse-forming line configuration of the ERG accelerator. The voltage and diode current pulses are shown by dotted lines in Fig. 2.

Assessing the current density of negative ions and ion-type identification were done by using a pinhole chamber with CR–39 for track recording. Types of accelerated ions were established by comparing diameters of the tracks of H^-, α-particles from a reference source and ions to be identified. Deflection of ions in an axial magnetic field is also used to differentiate ion types. The precision of these measurements was not very high because of the small distance between the hole and track detector and the rather large angular divergence

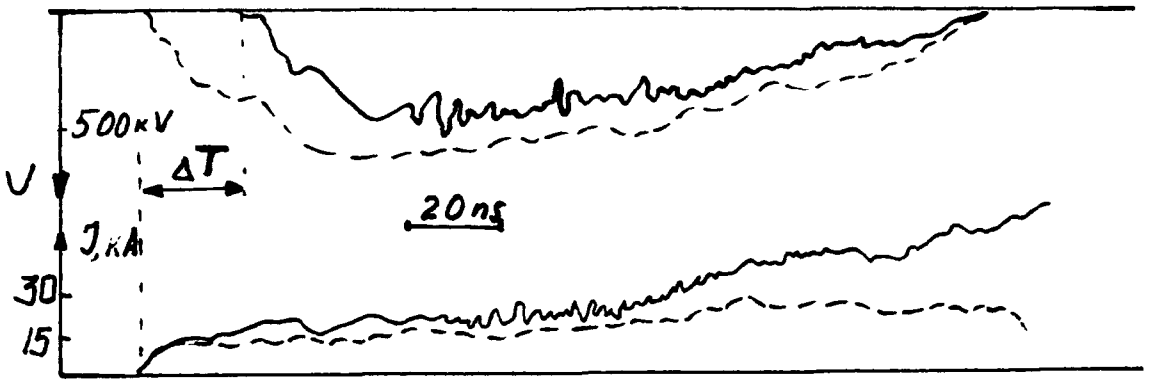

Fig.2. Diode voltage and current oscillograms. Upper trace – diode voltage, lower trace – full diode current. Dotted lines correspond to the case when plasma gun is switched off, solid lines – plasma fills the diode.

of the beamlet. The sign of the ion charge was also verified by comparing the deflection of the ion with that of protons (in this case, the diode was fed by a positive voltage and a central rod served as the anode).

An independent method of measuring the number of H^- in a shot used an activated graphite target in the reaction $^{12}C(p,\gamma)^{13}N$.

3. Cathode plasma initiation by anode discharge.

To produce a more uniform cathode plasma over a large area, one can use a laser or UV-irradiation [7,8]. The schemes are not simple to realize because one needs mirrors to direct radiation from the source to the cathode surface and rather large energy in the radiation pulse.

The proposed scheme employs positive ions accelerated by diode voltage to bombard the cathode surface. Positive ions are pulled out of plasma created behind the anode in a drift region by an additional discharge, to be more precise by a plasma gun. An important advantage of such a method is that energy for cathode irradiation is taken from the accelerator, which is practically an unlimited source of power for the purpose. Another advantage of using ions instead of electrons (as was done in some experiments for creating anode plasma in ion diodes [9]) is that ions of the same energy have a much shorter range ($\sim m_e/M_i$) and one needs orders of magnitude less energy to evaporate and ionize cathode cover material. Employing this method, one can use various materials on the diode cathode to produce a variety of negative ions (of course having positive affinity).

To control anode plasma parameters (mainly density and to a lesser extent temperature) one can vary the charging voltage of the capacitor from 3 to 10 kV (an order of magnitude in energy) and time delay between plasma gun and the main voltage pulse. The evolution

of anode plasma in time after the discharge is its spreading axially rather easily along the magnetic field lines and also radially across the magnetic field because of inhomogeneity and instabilities.

If anode plasma of sufficient density fills the diode ($10^{13} - 10^{14}$cm^{-3}) it is short-circuited during the initial part of the voltage pulse (no voltage and substantial radial current, see Fig. 2, solid curves). The diode behaves in this case as a plasma erosion opening switch and after several tens of nanoseconds the voltage on the diode restores to nearly full amplitude. Then begins an active phase of cathode plasma formation: positive ions accelerated by full diode voltage bombard the cathode surface and axial electron current through cathode plasma leads also to plasma heating and massive gas release. Current density of protons inside the cathode was measured to be around 10 A/cm^2 which is roughly consistent with the Child-Langmuir limit. Energy deposition on the cathode during the voltage pulse is about 1 J/cm^2 from ions, less than 1 mJ/cm^2 from ultraviolet irradiation and around 1 mJ/cm^2 from ion bombardment during prepulse time. The insignificance of ultraviolet irradiation from sparks for diode dynamics was shown also by displacing sparks axially beyond the anode apertures in order to prevent UV from reaching the cathode surface, but allowing plasma to fill the diode because of its axial and then radial motion. Negative ions were produced with nearly the same abundance in the latter case also. The dependence of the time interval during which the diode remains shortcircuited on the time delay between the plasma gun pulse and main voltage pulse is shown in Fig. 3.

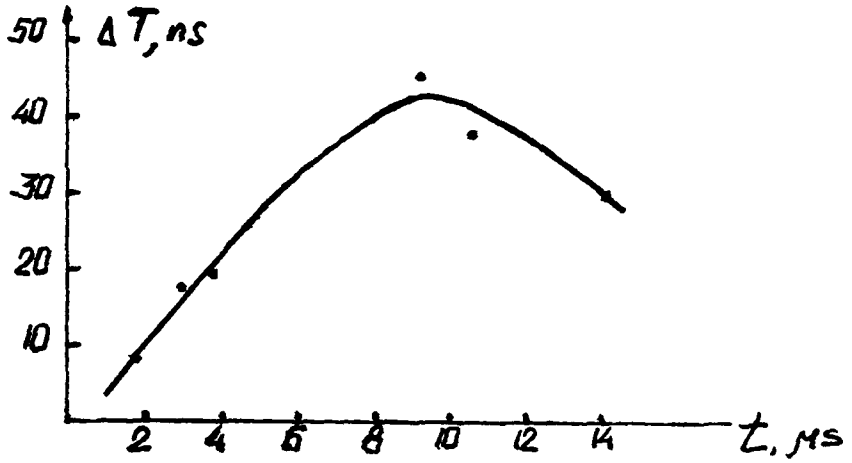

Fig.3. The dependence of the time interval during which the diode remains shortcircuited on the time delay between the plasma gun pulse and main voltage pulse.

Large amounts of gas released during the shot is characteristic for negative hydrogen ion production using dielectric. It was estimated to be up to 10^{20} hydrogen atoms per shot based on the pressure rise in the vacuum chamber. Fig. 4 shows the dependence of gas release on time delay of the main pulse.

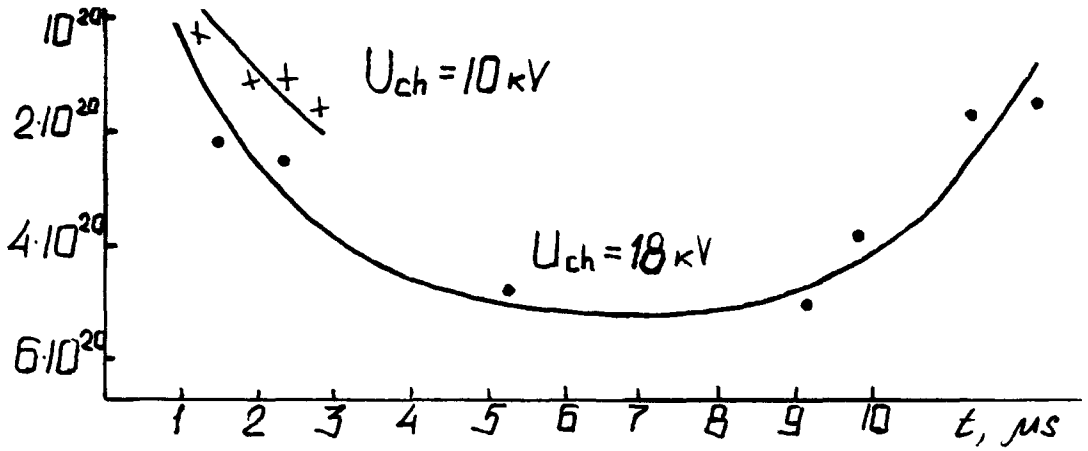

Fig.4. The number of molecules released in the diode after one shot versus the time delay between the plasma gun pulse and main voltage pulse.

4. Acceleration of H^-, C^-, F^-, I^- and Pb^- ions.

To test the proposed method of cathode plasma initiation, we tried various cathode materials. The first cathode used was a solid polyethylene insert between two parts of a metallic (stainless steel) cathode rod. The H^- were recorded and had current densities of more than 10 A/cm^2. It is interesting to note that because of the shorter time of cathode plasma expansion and perhaps more homogeneous plasma formation the diode impedance is more stable than for the case with prepulse or even for self breakdown of insert without prepulse and anode plasma. A hollow polyethylene cylinder was also good to generate cathode plasma under positive ion bombardment. C^- were also detected when using a polyethylene cathode. A graphite cathode yields more C^- than a polyethylene one. A polytetrafluoride (teflon) cathode was used to produce F^- ions (C^- and H^- were present as well).

To accelerate negative iodine ions, a thin iodine layer was applied to the polyethylene or polytetrafluoride cathode. The maximal current density of I^- ions was observed in the first two shots of the series after pumping the diode from atmospheric pressure, the first one being often shortcircuited. Subsequently the iodine layer was nearly totally evaporated and reduced current densities of I^- were measured.

Finally, we have tried a lead covering of the cathode and measured Pb^- current densities of about 0.03 A/cm^2, though the track detector was saturated.

The minimal and "probable" current densities for various ions are shown in Table 1, as well as binding energies of an extra electron. Minimal current density corresponds to filling the detector with tracks (after developing the CR-39 film) next to each other. Because in most cases the detector was saturated, we multiplied the minimal density by 3 to have probable current densities.

Table 1.

Ion type	H^-	C^-	F^-	I^-	Pb^-
j_{min}, A/cm^2	10	0.3	0.1	0.05	0.03
j_{top}, A/cm^2	20–30	1	0.3	0.1	0.1
E_{bound}, eV	0.75	1.2	3.5	3.1	1.6

5. Conclusion.

A simple and effective method for producing cathode plasma to obtain various negative ions over a large area was proposed and tested experimentally. The plasma parameters can be varied over a wide range by changing the intensity of anode discharge and time delay between anode plasma formation and accelerator main pulse. Near ampere per square centimeter current densities were obtained for C^- and F^- and an order of magnitude less for I^- and Pb^-. Negative hydrogen ions with current densities of up to 20-30 A/cm^2 were accelerated. Optimization of the plasma parameters and diode regime might allow to further increase current densities.

Acknowledgements

Authors are grateful to T.A. Shelkovenko for her help in measuring graphite activation targets and to S.A. Pikuz for delivering pinhole foils. We thank also O.A. Smith, N.N. Martynchuk and V.S. Voronin for their help in preparing the manuscript.

References

1. V.A.Papadichev, Laser and Particle Beams, **9**, no.1, pp. 167 – 189 (1991).
2. M. Bacal, G.W. Hamilton, A.M. Bruneteau, H.J. Doucet and J. Taillet, Rev. Sci. Instr., **50**, 719 (1979).
3. N.N. Semashko et al., Proc.4th Int.Conf. on Production and Neutralization of Negative Hydrogen Ions and Beams, Brookhaven, CT, AIP Conf. Proc., no.158, p.334.

   A.Y.T. Holmes, "Neutralization of Ion Beams", CERN Sci. Rept. 1987, no.10.
4. A.A. Kolomensky, A.N. Lebedev, V.A. Papadichev, S.A. Pikuz and B.N. Yablokov, Proc. 5th Int. Conf. on High-Power Particle Beams, San Francisco, CA, p.533, 1983.
5. V.A. Papadichev, S.A. Pikuz and T.A. Shelkovenko, Rev. Sci. Instr., Part 2, p.439, (1990).
6. A.G. Mozgovoy and V.A. Papadichev "H^- generation using extrually applied prepulse". Proc. of 9th Int. Conf. Washington D.C. USA, 1992.
7. V.A. Papadichev, S.A. Pikuz and T.A. Shelkovenko, Proc. 7th Int. Conf. of High-Power Particle Beams, Karlsruhe, Germany 1988, p.715.
8. J. Macnchen, C.L. Ruiz, T.A. Menhorn et.al., Proc. 6th Conf. on High-Power Particle Beams, Kobe Japan, 1986. p.85.
9. S. Humphries, J. Lee and R.N. Sudan, Appl. Phys. Lett., **25**, no.1, p.20, (1974).

H^- GENERATION USING AN EXTERNALLY APPLIED PREPULSE

A.G. Mozgovoy and V.A. Papadichev

P.N. Lebedev Physical Institute
117924, Leninsky Prosp. 53, Moscow, Russia

Abstract

Experiments on H^- generation in a high-power, pulsed, magnetically insulated diode are described. The ERG accelerator of the P.N. Lebedev Physical Institute in single line configuration was used with voltages up to 600 kV and pulse duration of 200 ns. To create cathode plasma, the surface discharge on dielectric was initiated by an externally applied prepulse, which was one 1.5 μs period of a sinusoid with up to 100 kV amplitude. The circuit allows to work with a prepulse of easily varied amplitude and duration, either with Blumlein or single forming line as the source of the main high-voltage pulse. Negative hydrogen ion current densities up to 10 A/cm^2 were recorded using trace detecting by CR-39.

1. Introduction.

Generation of high-power negative-ion beams can help solve some problems arising in transporting and focusing on a target positive ion beams in CTR with inertial confinement. By using, instead of such beams, beams of atoms (by stripping negative ions) one can avoid instabilities and scattering inherent in the case of positive ion beams.

Experiments at the P.N. Lebedev Physical Institute yielding a 7 kA current of H^- with up to 200 A/cm^2 current density revealed the important role of a bipolar prepulse: removing one of its parts led to H^- yield reduction by an order of magnitude and eliminating both parts of the prepulse lowered the H^- yield by more than three orders of magnitude [1,2].

The inherent prepulse is rather large in Blumlein machines (10–15% in our case) if measures are not taken to eliminate it, but small in single line pulse-forming lines (2–4%). Our previous studies on H^- were performed with a Blumlein configuration of the ERG accelerator. It has been reassembled now as a single pulse-forming line to have a longer pulse of nearly rectangular form (up to 0.8 MV, 200 ns). For further H^- studies, a scheme to apply a prepulse externally was designed and tested. It has the advantage of more versatility because one can change the prepulse amplitude, form and duration independently of accelerator voltage. An additional means of controlling cathode plasma is variation of the time interval between the prepulse and the main accelerator voltage pulse. As a first trial in our case, the prepulse length was one period of a sinusoid (1.5 μs) with up to 100 kV amplitude.

2. Experimental setup.

Experiments were performed using a coaxial magnetically insulated pulsed diode [3]. Various diameter polyethylene cylindrical inserts placed between two metal rods were used as cathodes.

H^- current and current density were evaluated using the activation of a graphite target and by recording H^- tracks on CR-39 in a pinhole chamber.

The scheme of the installation is shown in Fig. 1.

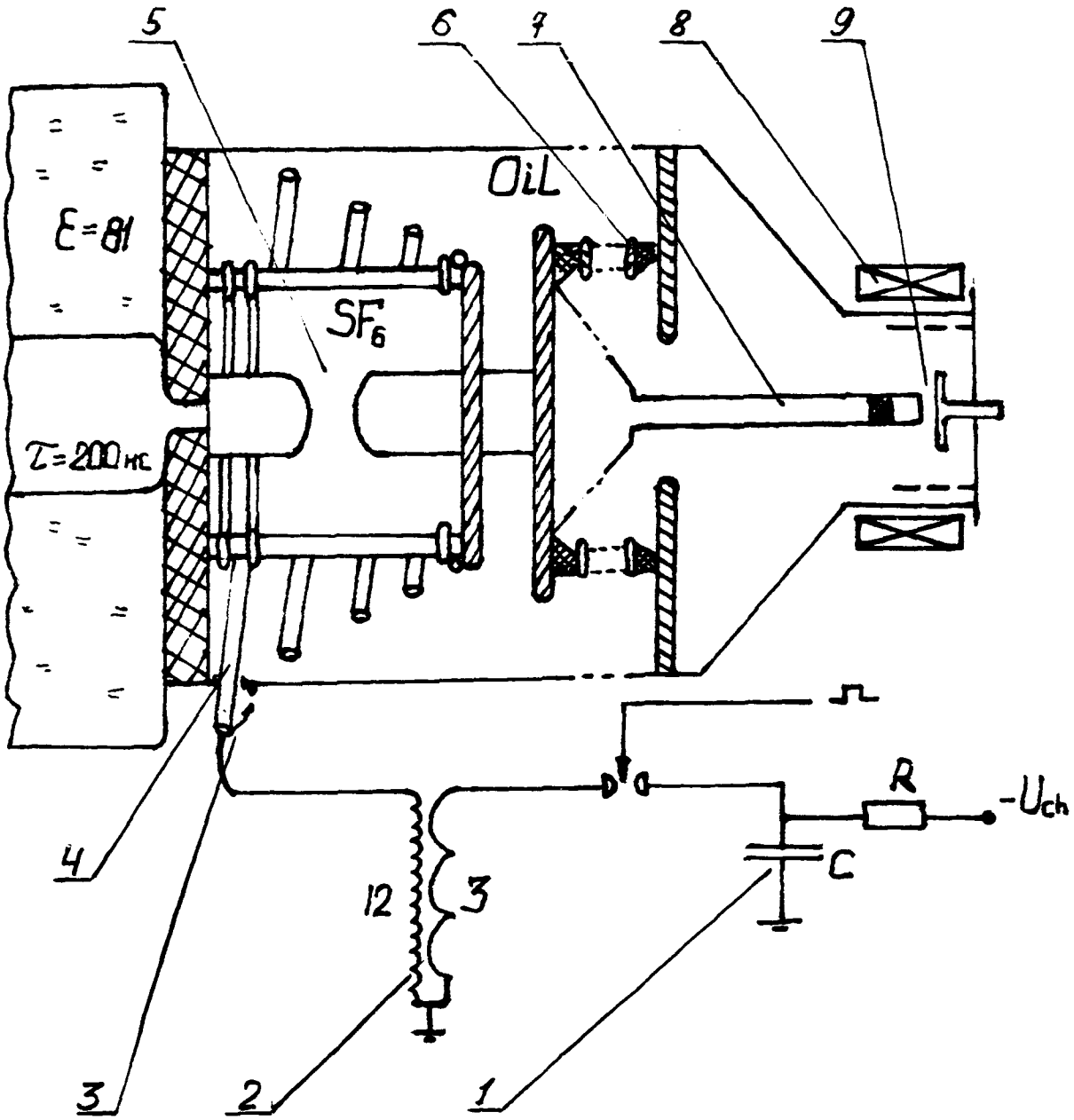

Fig. 1. 1 – condenser, 2 – transformer, 3 – lead-in of prepulse voltage and shorting spark gap, 4 – inductance, 5 – main switch gap, 6 – insulator,7 – cathode shank, 8 – solenoid, 9 – diode.

The external prepulse generator consists of a high-voltage, ironless transformer, through the 3-turn primary winding of which there is discharged a condenser (0.1 μF, 20 kV). The secondary winding has 40 turns of insulated wire having a diameter of 9 mm. It is wound on a dielectric carcass that has a 250-mm diameter and 400-mm height. Over this winding an

insulation layer consisting of several layers of mylar was wrapped, and the primary winding of a 10-cm wide band of brass foil. The most vulnerable spot was the lead-in of the prepulse voltage into the section of the accelerator filled with oil and containing the main switch gap of the line and the insulator. The prepulse arrived at the cathode rod after the main switch gap via a 20-μH inductance. Shorting gap 3 was adjusted to permit the prepulse to pass to the diode cathode and to shorten on the housing by the main pulse. Fig. 2 shows oscillograms of the prepulse voltage and the accelerator pulse.

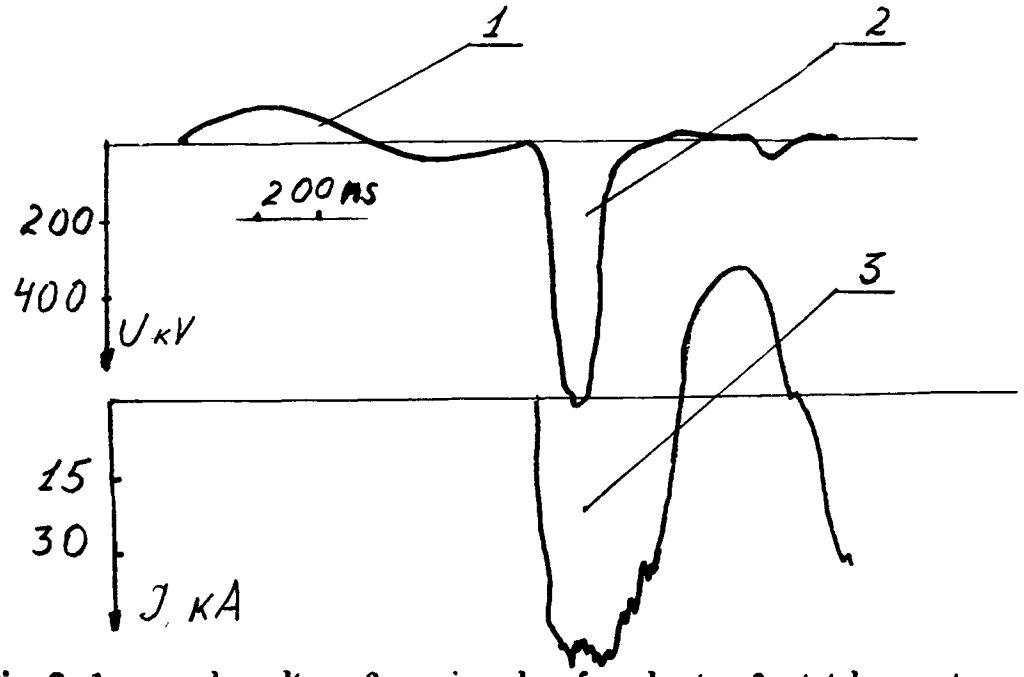

Fig. 2. 1 – prepulse voltage, 2 – main pulse of accelerator, 3 – total current.

It should be noted that by means of the prepulse voltage one can easily calibrate high-voltage dividers of accelerator voltage by introducing a calibrated low voltage divider and carrying out measurements at a relatively moderate voltage of 50 kV.

By means of the external prepulse a series of experiments on the generation of H^- in a diode with magnetic insulation was performed [4]. The schematic drawing of the diode is shown in Fig. 3.

A discharge along the surface of a polyethylene insert located in a gap of a metallic cathode was used to form cathode plasma. An axial magnetic field of up to 16 kG was used to achieve magnetic insulation of electrons in the diode. Use of the external prepulse with the possibility of applying time delay of the main pulse increased stability of formation of surface plasma on the dielectric insert. This can be shown by comparing the gas release from the diode with and without the prepulse.

Up to 10 A/cm^2 H^- current density was recorded without having determined optimal conditions for maximizing H^- yield (anode-cathode gap, prepulse parameters, axial diode

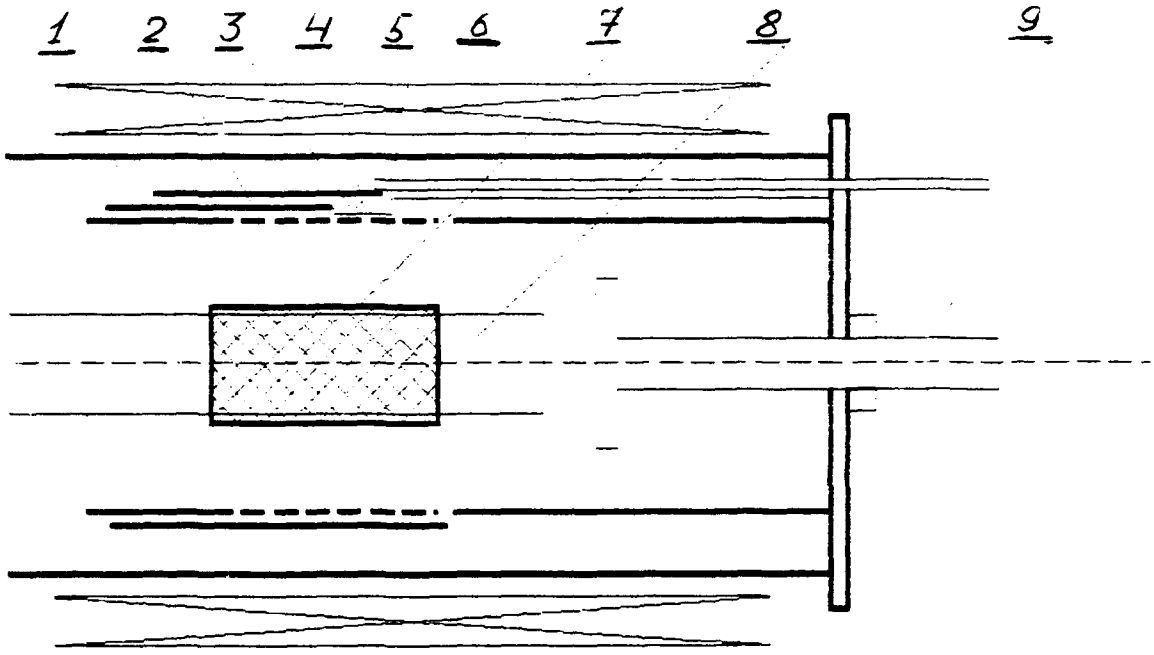

Fig. 3. 1 – graphite target, 2 – anode with drilled holes, 3 – pinhole chamber, 4 – track detector CR-39, 5 – rod to move CR-39 film, 6 – solenoid, 7 – perforated sleeve (dielectric cathode), 8 – cathode rod, 9 – auxiliary anode at the diode butt to control electron axial current.

current, insulating magnetic field etc.). It should also be noted that the CR-39 detector was saturated, giving a less than real value of current density.

An attempt was made to conduct an experiment in a partially spherical geometry as shown in Fig. 4.

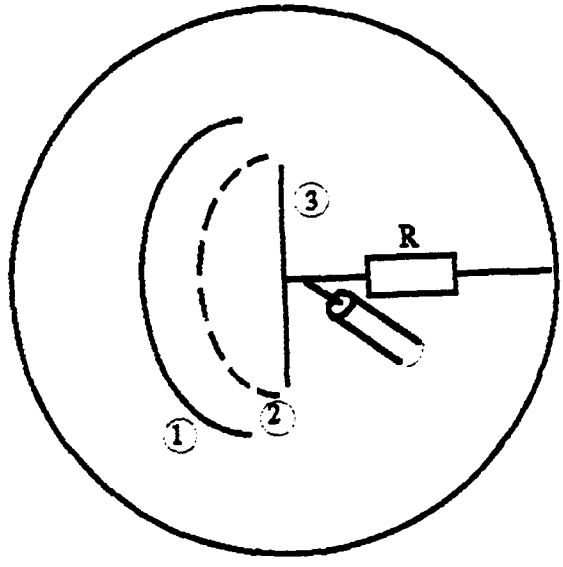

Fig. 4. 1 – cathode, 2 – anode screen with drilled holes, 3 – ion collector with a shunt

Cathode 1 has a dielectric insert. It turned out that the insert discharge occurred on the side

opposite to the anode screen 2, and signal from the collector of shunt 3 was not registered. Evidently special measures are necessary to initiate discharge along the inner surface of the cathode insert. It was precisely this circumstance that led us to use ionic bombardment of the cathode, which was applied later in coaxial geometry [5].

3. Conclusion.

The complex processes of formation of negative hydrogen ions in dense cathode plasma ($10^{16}-10^{17}$) require fine tuning and a definite sequence of operations on the plasma. Previous experiments indicated that it was necessary to use a bipolar prepulse of amplitude up to 100 kV, which is usually present on machines with double pulse-forming lines, but is absent on single pulse-forming lines where it is unipolar and of considerbly smaller amplitude, insufficient to initiate discharge. Moreover, in the commutation in double pulse-forming lines of the inner line, the prepulse has a reverse order of half-wave signs — first negative and then positive [6], while on accelerator ERG of the Lebedev Institute the bipolar prepulse begins with positive polarity. Using a prepulse created by an external scheme permits obtaining negative hydrogen ions on any high-current accelerator (single or double pulse-forming line) and changing, independent of the accelerator regime, the amplitude, duration and form of the prepulse half waves. Also there becomes available another degree of control-the time lag of the main pulse from the prepulse. Varying these parameters will permit elucidating the regularites of H^- formation in cathode plasma and, by selecting optimal conditions, increasing H^- current density.

Acknowledgements

Authors would like to thank T.A. Shelkovenko for her help in measuring graphite activation targets and to S.A. Pikuz for delivering pinhole foils. We are grateful to O.A. Smith, N.N. Martynchuk and V.S. Voronin for their help in preparing the manuscript.

References

1. V.A.Papadichev, Laser and Particle Beams, **9**, no.1, pp. 167 - 189 (1991).
2. V.A. Papadichev, S.A. Pikuz and T.A. Shelkovenko, Rev. Sci. Instr., Part 2, p.439, (1990).
3. A.A. Kolomensky, A.N. Lebedev, V.A. Papadichev, S.A. Pikuz and B.N. Yablokov, Proc. 5th Int. Conf. on High-Power Particle Beams, San Francisco, CA, p.533, 1983.
4. A. Fisher, V. Bystritski, E. Garate, R. Prohaska and N. Rostoker "Magnetically insulated H^- diodes." Proc. of this conference
5. A. Mozgovoy, V. Papadichev "Anode discharge to facilitate cathode plasma formation for generation of H^-, C^-, F^-, I^- and Pb^- ions." Proc. of 9th Int. Conf. Washington D.C. USA, 1992
6. K. Horioka, Yu. Quan, K. Kasuya Proc. of 8th Int. Conf. Novosibirsk, USSR, 1990, p. 481.

LASER PLASMA PRODUCTIONS AND LASER DIAGNOSTICS FOR PULSED ION SOURCES

K.KASUYA, K.HORIOKA, T.HUSHIKI, N.MATSUURA, T.MIYOSHI,
Tokyo Institute of Technology, Department of Energy Sciences,
The Graduate School at Nagatsuta,
4259 Nagatsuta, Midori-ku Yokohama, Kanagawa, Japan 227

K.NAKATA, Y.MIYAI, Y.KAWAKITA and E.OHSHITA
High Voltage R & D Department, R & D Division,
Nissin Electric Company, Kyoto Japan 615

Recent laser assisted works for pulsed ion beam drivers are described. They are divided into two parts as follows. The first one is plasma production by laser light. The second item is the diagnostic of laser produced plasma for pulsed ion diode by laser interferometer.

An electron beam pumped excimer laser is operated for the plasma production. Lithium surfaces are directly irradiated by this laser.

A resonant interferometer with a dye laser pumped by a nitrogen laser is used to diagnose the lithium plasma. Applicability of this diagnostics for lithium ion diodes is discussed.

1. INTRODUCTION

The development of reliable high current lithium (Li) ion source is one of the important issues for light ion beam fusion [1]. For the ion source, uniform Li plasmas of high-purity, high-density and high ionization rate must be produced on the large area of the anode surface. Although high density flashboards are under developing now [2,3], the produced plasmas have contaminants in them, and the density is 10(14)cm(-3) level, at most. It has been shown that Li plasmas of sufficient density can be produced by direct laser irradiation (dye [4,5] or ArF [6])

of lithium films. Plasmas produced by short pulse lasers are considered to be promising candidates for the high current ion source.

2. LASER PLASMA PRODUCTION

2.1. Experimental Setup

An experimental arrangement for the laser plasma production is shown in Fig.1 schematically . An electron beam pumped KrF excimer laser, which is driven by a coaxial marx-generator (1MV-44 ohm , 10Hz), irradiates a lithium or a potassium (K) target (10mmX10mmX5mm block) in a vacuum chamber. The excimer laser is operated typically at the electron beam energy of 580KeV, electron current density of 830A/cm(2), and the laser output energy is 1.2J under 30nsec pulse length (FWHM). The ion flux from the laser produced plasma is measured with a large diameter biased ion collector, as functions of laser power density and target materials. In order to avoid interaction with the laser beam, the ion collector is placed 50mm from the target and the target holder is inclined 45 degree to the laser axis.

2.2. Experimental Results

Typical waveforms of the ion currents produced by the laser irradiation on Li and K blocks are shown in Fig.2. Time delays of the current rise from the KrF laser injection are 1μs for Li

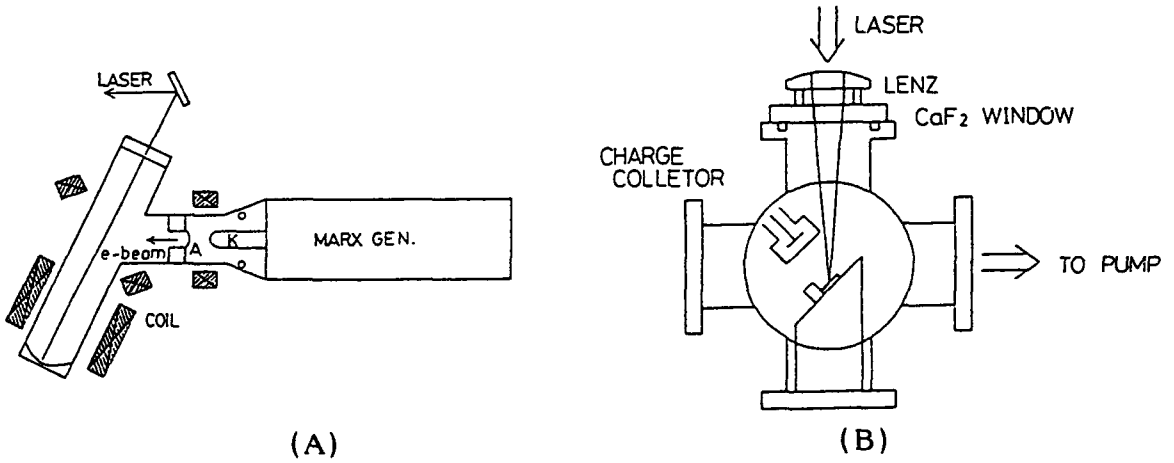

FIG.1 EXPERIMENTAL SETUP FOR LASER PLASMA PRODUCTION

and 2.5μs for K. Their value can be correlated with an inverse square root scaling of the mass ratios.

The plasma production has strong dependence on the laser intensity. Fig.3 shows the dependence of the surface ion density on the laser intensity for Li(A) and K(B) irradiation. Here the "surface ion density" means the total number of ions divided by the effective area of the laser irradiation.

With the KrF laser irradiation of 5X10(9)W/cm(2) level on the Li target, plasmas of 10(16)/cm(2) surface density are produced. For the K case, the corresponding irradiation reduced to 6X10(8)W/cm(2) level. As shown here, the plasma production by the laser irradiation on the K surface is more effective than the Li case. For the K irradiation, (probably by the single-photon ionization process), the KrF laser light is effective for the plasma production especially at the initial stage.

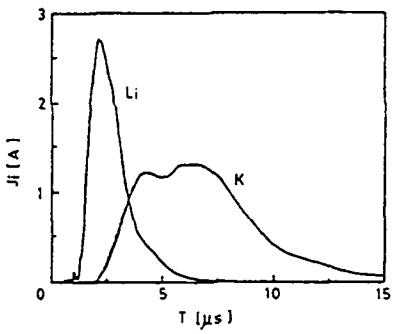

FIG.2 TYPICAL WAVEFORMS OF ION FLUX

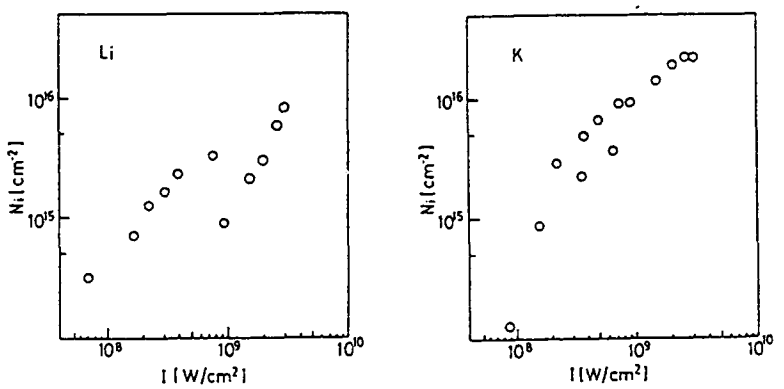

(A) (B)

FIG.3 SURFACE PLASMA DENSITY AS A FUNCTION OF LASER INTENSITY FOR Li(A) OR K(B) TARGET IRRADIATION

3. RESONANT INTERFEROMETRY OF LASER PRODUCED LITHIUM PLASMA

For the plasma production from the solid surface by the laser illumination of sub-GW power level, the significant parts of the laser energy must be consumed for vaporization process. Therefore, the behavior of neutral particles play important role on the plasma evolution. It is reported that in the acceleration gap of the high power vacuum diodes, neutral particles severely degrade the diode characteristics. So that, quantitative estimation of the behavior of the neutral particles in the source plasma is important to develop high quality ion sources.

3.1. Experimental Setup

For the quantitative estimation of the laser produced plasma, resonant interferometry by laser light [7] is adopted here. A schematic diagram of the experimental setup is shown in Fig.4. A discharge pumped excimer laser of 100mJ output energy level with 30ns pulse length is used to produce plasmas. A dye laser pumped by a nitrogen laser with 5ns pulse length, is tuned around the Li resonant line (2s2S-2p2P;670.78*nm*), and used as the probe light source. The plasma-driver laser and the probe laser are time-correlated with PIN diodes (HAMAMATSU-S1722-02). Interferograms of the field are taken with a Mach-Zehnder interferometer, as the functions of the driver laser intensity, the probe laser wavelength and the time delay between them. In order to cross-check the experimental results, the stark broadening of the Li line

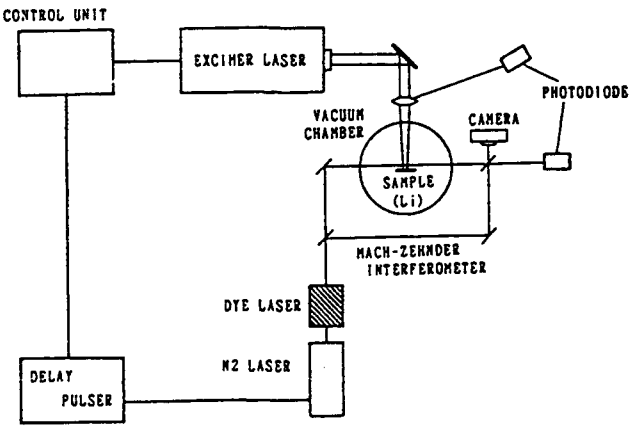

FIG.4 EXPERIMENTAL ARRANGEMENT OF RESONANT LASER INTERFEROMETRY

(2p2P-4d2D; 460.3nm) is monitored with a 50cm monochromator.

The enhanced refraction with resonant light is given in [7], from which we can estimate the plasma quantity by taking interferograms under shifting of the laser wavelength.

3.2. Experimental Results and Discussions

Typical interferograms are shown in Fig.5(b) and (c), together with the time-integrated photo of the target irradiance (a). Experimental results of the density distribution estimated from the interferograms are shown in Fig.6. We cannot decide here the spread width of the particle densities temporally, because the plasma quantities rapidly change with time, especially at the initial stage of the plasma evolution.

The sensitivity of the resonant laser interferometry depends on both the plasma quantities (temperature, density and ionization rate) and the wavelength of the probe laser light.

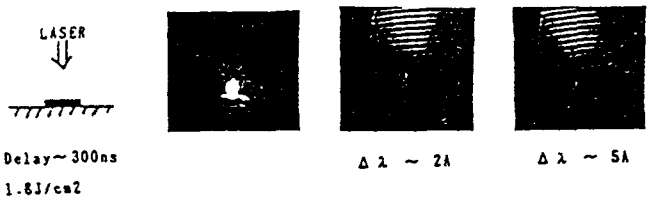

FIG.5 TYPICAL INTERFEROGRAMS OF Li PLASMA

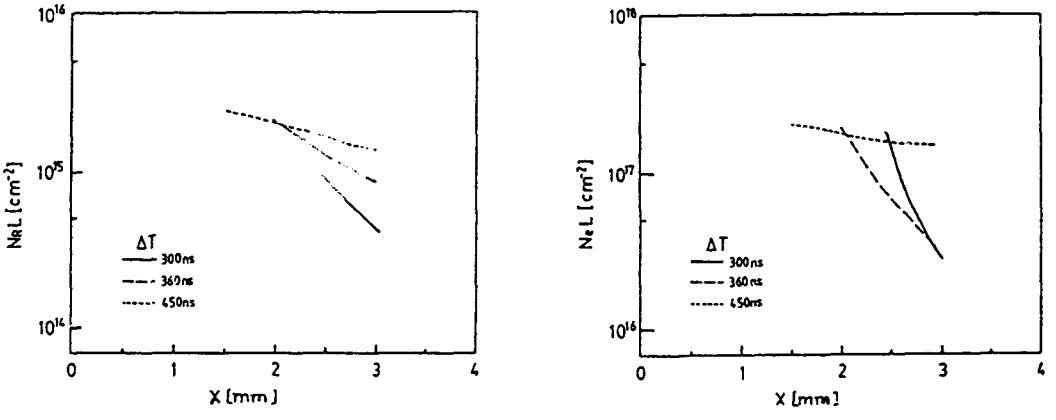

FIG.6 TYPICAL RESULTS OF Ne(A) AND Nr(B) DISTRIBUTION

4. SUMMARY

Lithium or potassium plasmas of 10(16)cm(-2) surface number density can be produced with the direct irradiation of KrF excimer laser light of GW output power level. The surface number density of the plasma has strong dependence on the laser intensity. It is clarified that the single photon ionization process plays some roles on the plasma production.

The resonant laser interferometry is applied to the diagnostics of the laser produced plasmas. Direct measurements of the number density (both of electron and neutral particles) can be realized with the laser resonant spectroscopy.

For the quantitative estimation and optimization of the laser produced Li ion source, model calculations including the evaporation stage are under development now.

REFERENCES

[1] Cook,D.L., et. al.; Proc. 8th Int. Conf. High Power Particle Beams, (1990) 3-13

[2] Hammer,D., et al.; ibid., 371-378

[3] Kasuya,K., Horioka,K. et al.; Proc. This Conference

[4] Bieg,K.W., Tisone,G.C., Lockner,T.R., et al.; ibid., 933-945

[5] Tisone.G.C, Bieg,K.W, and Dreike,P.L.; Rev. Sci.Instrum., 61, (1990) 562

[6] Lin,S., Tang,K.Y. and Hunter,R.O.; Bull. APS Meet. Plasma Phys. Meet. 7R27 (1986) 1570

[7] HORIOKA.K, TAZIMA.N, MATSUURA.N, SAITO.S and KASUYA.K; Proc. 8th Int. Conf. High Power Particle Beams, (1990) 822-828

IMPROVED FLASH-BOARD FOR PLASMA INJECTION DIODE

Koichi KASUYA, Kazuhiko HORIOKA and Hitonori HAYASE

Tokyo Institute of Technology, Department of Energy Sciences,
The Graduate School at Nagatsuta,
4259 Nagatsuta, Midori-ku, Yokohama, Kanagawa, Japan 227

As the plasma sources of the plasma injection type pulsed ion diodes, a set of flash-boards are operated to improve the characteristics. The produced plasma flows are measured with a biased ion collector. The main experimental results obtained here are as follows.

There is an optimum gap length of the flash-boards to get maximum flux of the produced plasma, though the effect is not so remarkable. To obtain the better characteristics of the boards, it is effective to apply the voltage pulse with the shorter rise time and to use separate capacitors which can fix the respective electrode potential at the ground level.

The plasma flux is increased with the capacitance of the source capacitor in the driver circuit ,and also with the charged voltage. On the contrary, the capacitance of the peaking capacitor affects weakly the plasma flux.

1. Introduction

Anode plasmas without neutral particles are necessary to supply pulsed ion diodes of well-controlled and good performances. To get this kind of plasmas, we used flash-boards [1].

Although the better diode characteristics were obtained with the plasma injection to the anode surface, compared with the same kind of flash-board particle source located just on the anode surface [2], both the plasma density and the purity with the plastic flash-board were not enough high for our purpose. Then we used cryogenic flash-boards to overcome these defects [3].

Although some details are described there in [3], we still think that we must optimize the whole flash-boards for

the future application. So that, we try to improve them under ambient temperature with some replacement or so, here in this article.

2. Experimental Apparatus

2.1. High Voltage Power Source for Flash-Board

We use a small pulse generator to drive our flash-boards. An equivalent circuit of the pulse generator is shown in Fig.1. The left capacitor in the figure is a DC-charged external one (the source capacitor of between 2.7 and 21.6nF), and the gap switch (with normal air or pressurized SF6) is triggered by another pulse circuit. The inductor and the coaxial cables are connected in parallel, and each quarter segment of the flash-board (ring shaped as is shown in Fig.2) is supplied with the high voltage via each cable. At the output side of the cables, only one segment is shown in Fig.1. The peaking capacitor of 4nF capacitance is placed just at the nearest position of the flash-board in a vacuum tank. This circuit is also operated without the peaking capacitor. The both results with and without are compared in the next section.

The nominal charged voltage of the source capacitor is between 15 and 40 KV, and the length of each cable is 7 m. As the propagation time per unit cable length is 5 ns/m, the time

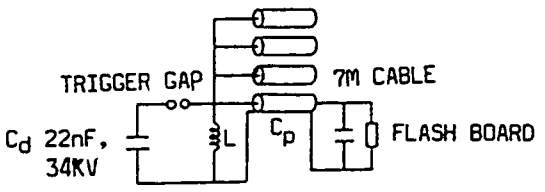

Fig.1 Equivalent circuit diagram of pulse generator.

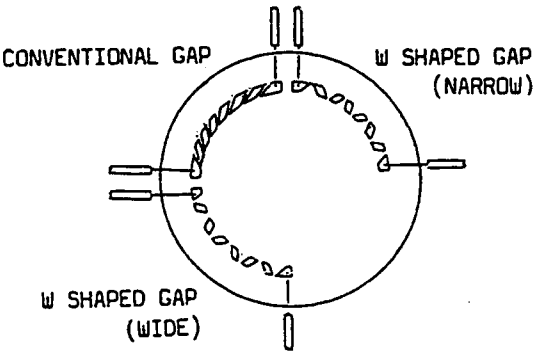

Fig.2 End view of flash-board

for the pulse to make a round trip of the whole cable length is 70 ns. We arrange for the flash-board to work at the time sequence near to the maximum terminal voltage.

2.2. Flash-Boards

A flash-board under operation is shown schematically in Fig.2. The diameter and the thickness of the metal base plate made of brass or copper are 210 and 12 mm. On this metal plate, a dielectric flash-board of 200 mm diameter is attached. In the previous paper [1-2], we used etched dielectric boards for semiconductor circuits as the flash-boards, where the dielectrics was hydro-carbon. On the contrary, we choose a Lucite disc as the dielectrics, on which many small thin copper electrodes of 0.1 mm thickness are placed.

The 3 different layouts of the small metal electrodes are shown in Fig.2 (separate 3 quarters). The first (upper right) and the third (lower left) quarters correspond to the two cases of 'W'-shaped arrangements with narrow and wide electrode gaps, which we use in this paper. The diameter of the gap circle is 110 mm, and ten series gaps (of 4 gap length 0.4, 0.8, 1.2, 1.6) are arrayed on the surface.

To make a rough estimate of the plasma density or so, the ion current is observed by a biased ion collector. The bore cross sectional area is 175 cm^2. The distance between the flash-board and the ion collector is 21 cm. This is the shortest distance for the biased ion collector not to be short-circuited by the particle flow from the flash-board.

3. Experimental Results

3.1. Experiments with Air Gap Switch

If we use an air gap switch in Fig.1, the inductance is relatively high. This results in the slow rise time of the voltage pulse applied to the flash-board. The discharge along

the gaps is not well reproducible, while irregular discharges along short circuits do occur often.

The peak value of the total current in the biased collector is measured as a function of charged voltage in the source capacitor. The capacitance of the source capacitor is taken as a parameter. Four cases of different gap length are investigated. The longer the gap length is, the more unstable the discharge becomes. This corresponds to the less number of data points which we can gather.

To understand these results more physically, we measure the voltage signal at the entrance and exit of the cable. These signals (for 2 different cases of gap length, 0.4 and 1.6 mm) together with the cable current signals show that we need the longer delay-time with the longer gap length, to start the flash discharge in this arrangement.

3.2. Experiment with Pressurized Gap Switch

As the gap length of the ambient air gap switch is rather long (about 2 cm), the rise time of the voltage applied to the flash-board is not enough short. This is one of the reasons why we can not get stable operations in the former section. In this section, we use a pressurized (1.7 kg/cm2 for 32 kV charged voltage) SF6 gap switch to get more shorter gap length (about 5 mm), which brings more stable discharges. The same kinds of signals are taken. The rise time is shortened and the plasma flux is increased.

3.3. Experiment with fixing capacitor

Although the discharge characteristics are improved a little bit with the pressurized start switch, the whole output voltage of the cable exit is applied dispersely among the whole gap of the flash-board. So that, the respective applied voltage of the gap is relatively low. To apply the almost whole output voltage at the cable exit to the single gap from

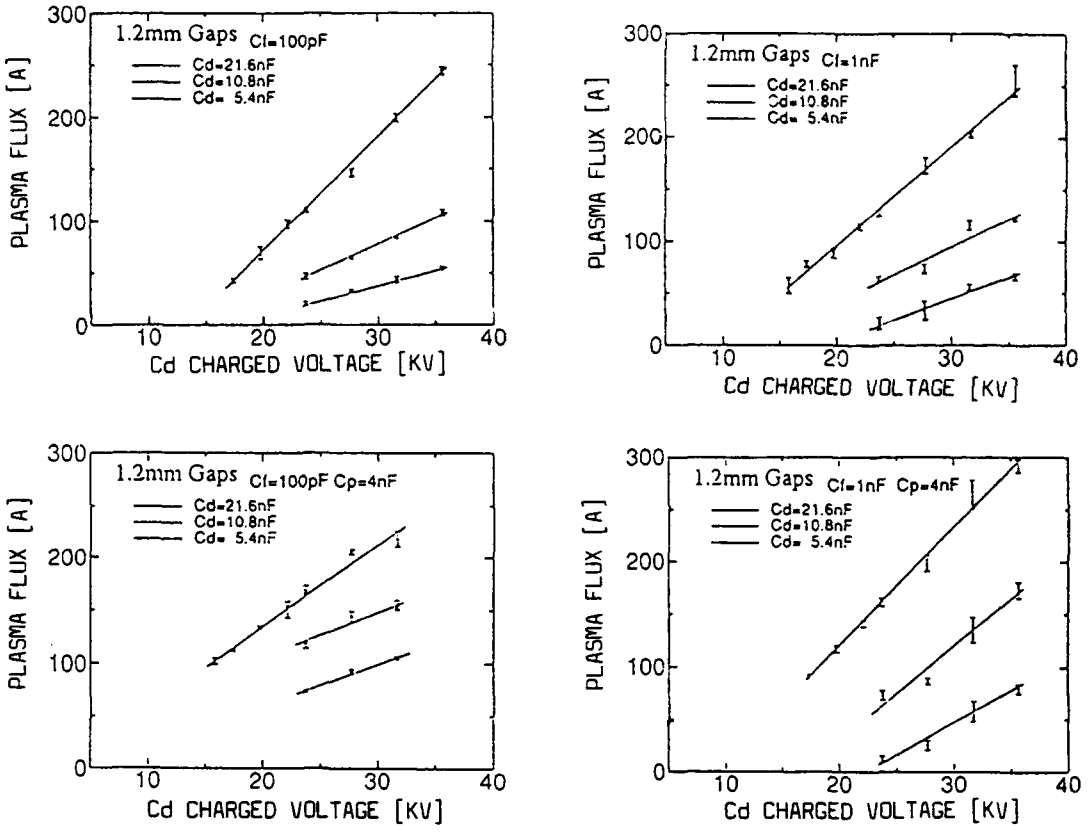

Fig.3 Plasma Flux vs Charged Voltage; Case with Fixing Capacitors and Pressurized Start Switch; Cd, Cf, Cp is the Source, the fixing and the Peaking Capacitor, respectively.

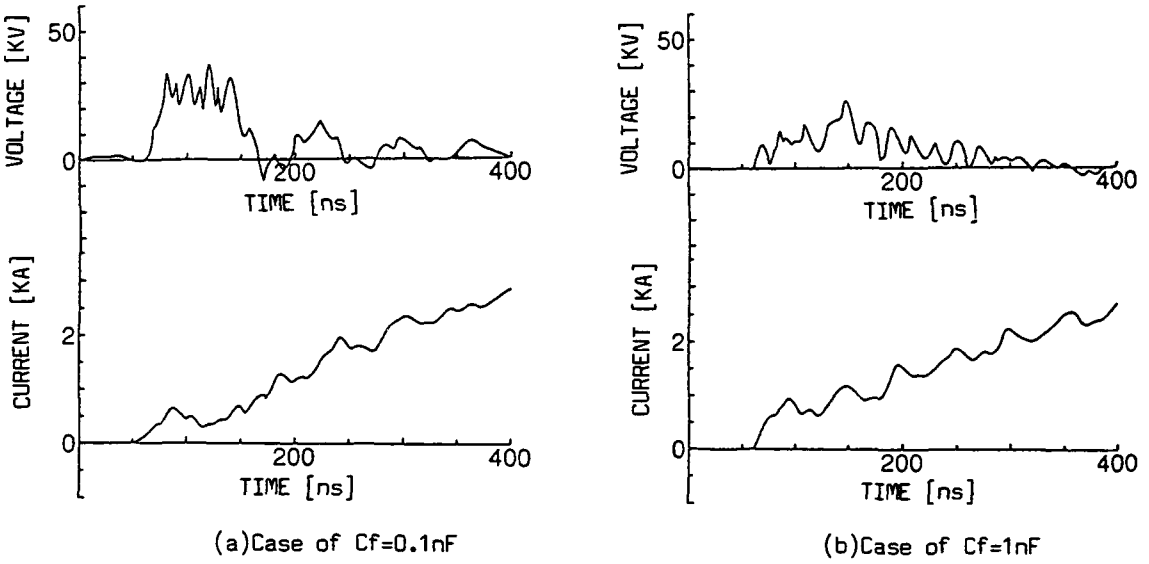

Fig.4 Cable Voltage and Current at the Exit; Case with Fixing Capacitors and Pressurized Start Switch.

first to last (one by one), we use fixing capacitors to hold the respective gap electrode potential at low 'evel transiently. The capacitance of the fixing capacitors is 0.1 or 1 nF. The same kinds of signals are taken and shown in Fig.3 and 4. The whole characteristics are improved here compared with the former two cases. The capacitance of 1 nF is preferable to 0.1 nF for us.

To explain our experimental results more precisely, some numerical simulations are performed with a model circuit, which results are shown elsewhere.

4. Future Directions

After the discussions about the experimental results, we can say what should be done in the near future with this kind of flash-board. It is hoped that the cryogenic flash-boards are operated with the fixing capacitors and the pressurized starting gap switch. The more improved discharge electrodes are expected to get longer life of the boards. The laboratory made cryogenic flash-board must be replaced by the factory made one, to get more uniform discharges along the surface. The supply of the plasma source material must be more sophisticated to get more controllability easily. All of these are expected toward the more refined cryogenic flash-board, with which we also want to try to inject plasmas into our active pulsed ion diode, in the very near future.

References

[1] KASUYA, K. et al., Active beam-control and active laser diagnostic of intense pulsed ion sources, Laser Interaction & Related Plasma Phenomena, Vol.9 (HORA, H. & MILEY G. Ed.), Plenum Press, New York, pp.411-422 (1991).

[2] KASUYA, K. et al., Automatic and self-discharge along anode surface of pulsed ion diode, and its effect on diode and beam characteristics, Proc. 7th IEEE Pulsed Power Conf. Monterey, CA (1989) pp.457-460.

[3] KASUYA, K. et al., Cryogenic flash-board for plasma injection diode, Proc. IAEA technical committee meeting on drivers for inertial confinement fusion, April 15-19, 1991, Osaka, Japan, to be published.

PRODUCTION OF PULSED F^- BEAMS

A. Kitamura, K.Takahashi, A.Shinmura, Y.Furuyama and T. Nakajima

Department of Nuclear Engineering,
Kobe University of Mercantile Marine,
Fukaeminami-machi 5-1-1, Higashinada-ku, Kobe 658, Japan

Abstract Process of F^- ion formation is examined in a surface flashover plasma initiated on the CF_2 cathode of an MID by an auxiliary coaxial Marx generator. Off-diode optical measurements of FI, FII and H_β show that a maximum density of the order of $10^{11}cm^{-3}$ for F atoms is achieved several hundred ns after the initiation of the flashover with an optimum input power of 150J. From the measured atomic densities of F and H together with the current densities of accelerated F^- and H^-, $20mA/cm^2$ and $40mA/cm^2$ respectively, it is concluded that a significant fraction of F atoms are liberated from the CF_2 surface in the form of F^-.

1. Introduction

Beams of negative ions attract increasing attention in science and technology. In connection with ICF, production of H^- beams has been investigated in several laboratories [1-3]. Most of them aim principally at their application to ICF drivers after stripping them to neutral H. Successful extraction of H^- beams with current density reaching $200A/cm^2$ have been reported. They used either pulsed power sources having suitablly shaped prepulses or a plasma gun for preformation of the cathode plasma.

On the other hand, beams of heavy ions have also been considered alternative candidates for the ICF driver [4,5]. The problems of transmission and focusing are expected to be less severe for heavier ions, since the beam current required for the compression of targets could be reduced by orders of magnitude in reward for increased particle energy, and since the larger inertia makes heavy ions less sensitive to electric and magnetic fields.

In our laboratory efforts have been directed toward development of pulsed beams of light-heavy ions for possible applications including those to ICF drivers and to material processing. Following successfull production of Na^+ beams [6], we try to produce pulsed beams of F^-.

In the early phase of our study, extraction of F^- beams from an MID with passively produced plasma on a dielectric cathode has been examined [7]. It was found necessary to preform a cathode plasma and store negative ions before the application of the high voltage pulse. In the present work we discuss the process of F^- formation in a surface flashover plasma preformed with an auxiliary power source on the MID.

2. Optical diagnostics of flashover plasma

To find a suitable discharge condition, optical diagnostics is applied to the flashover plasma initiated by an auxiliary power source. Since the concentration of F is closely related to the process of F^- formation, we examine the behavior of F atoms together with impurity H atoms to study the process of F^- ion formation.

A schematic of the arrangement for the optical diagnostics of the pulsed discharge is shown in Fig.1. A coaxial Marx generator ER-I with a maximum stored energy of 390J is

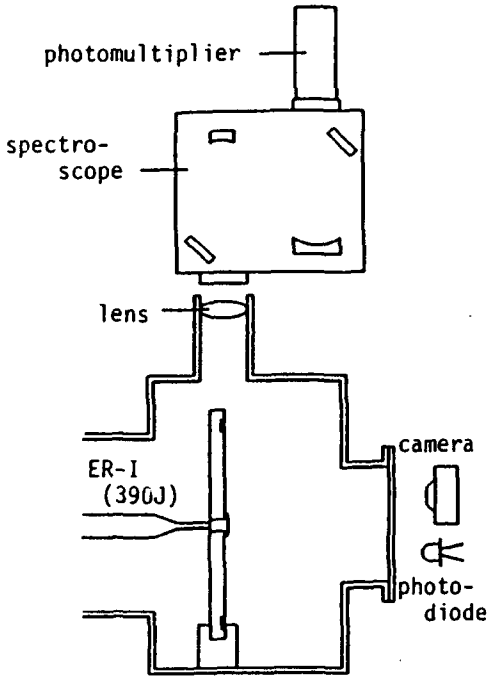

Fig.1. Schematic of surface flashover test stand.

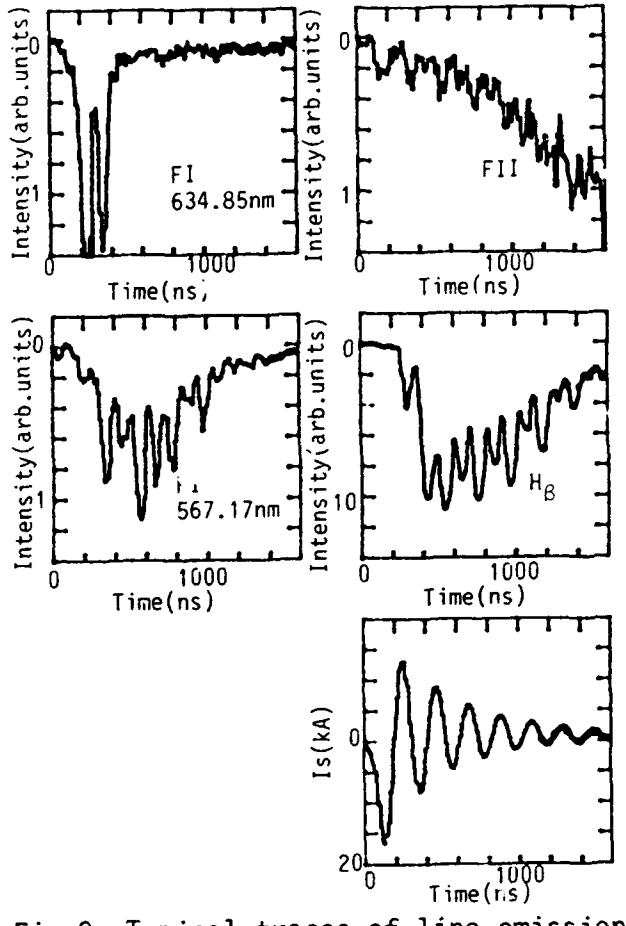

Fig.2. Typical traces of line emissions from the surface flashover plasma together with the discharge current I_S.

used to produce the discharge with currents up to 30kA between coaxial copper electrodes on the surface of a CF_2 disk. The emitted photons are focused by a lens onto the entrance slit of a 500mm monochrometer equipped with a 1200mm-grooves/mm grating followed by a photomultiplier.

Among several FI lines identified we have payed attention to those of 634.85nm ($3s^4P_{3/2}$-$3p^4S_{3/2}$) and 567.17nm ($3p^4P_{5/2}$-$4d^4D_{7/2}$). The evolution of the line intensities including those of FII (500.198nm) and H_β together with the discharge current I_s are shown in Fig.2. We see in the figure that F neutrals exist mainly in the early phase of the discharge pulse, while F^+ ions become rich later in the pulse.

Dependence of the peak intensity of FI on I_s has shown that there is an optimum discharge current of 20kA, or the energy of 150J, for abundance of neutral F. Further measurements have been done with this optimum energy.

From the Stark-broadened width of H_β, it has been found that the electron density N_e was $3.5\times10^{15}cm^{-3}$ around the time of the maximum FI.

The spatial distributions of FI and FII are shown in Fig.3. The former has a rather broad distribution with an FWHM thickness of 2.5mm, while the latter has the maximum at 2mm from the surface. This, together with the small hump in the FI distribution, suggest that F atoms are liberated from the CF_2 surface predominantly in the form of F^- and/or F.

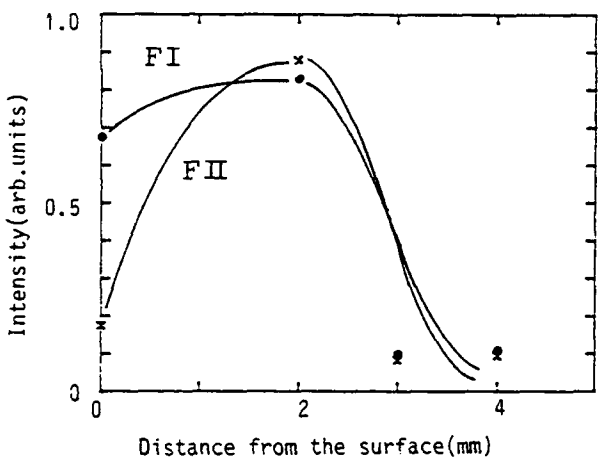

Fig.3. Spatial distribution of the emission intensity of FI and FII.

Although N_e is too high for the Corona model to be applicable, the model is used for simplicity to make an order-of-magnitude estimate of atomic densities N_F and N_H of F and H, respectively, from FI and H_β intensities. This approximation leads to an underestimation of the densities. Using the tabulated data of transition probabilities [8,9] and cross sections [10], we get N_H ranging from 6 to $2\times10^{11}cm^{-3}$ and N_F from 2 to $0.5\times10^{11}cm^{-3}$ for assumed electron temperature T_e of 5-30eV.

3. F^- beam extraction from actively initiated cathode plasma

The plasma described above has been applied to the cathode of the MID. A schematic of the diode configuration is shown in Fig.4. The flashover cathode is located on the inner surface of the one-turn field coil, and driven by ER-I as described above. The anode, which is driven positive by ER-II, is equipped with a momentum analyzer using the insulating magnetic field and a CR-39 plate as a particle detector. The longitudinal dimension of the anode is enlarged to make deflection of the ions greater than the transverse displacement caused by a poor emittance of the beam at the risk of a reduced insulating field.

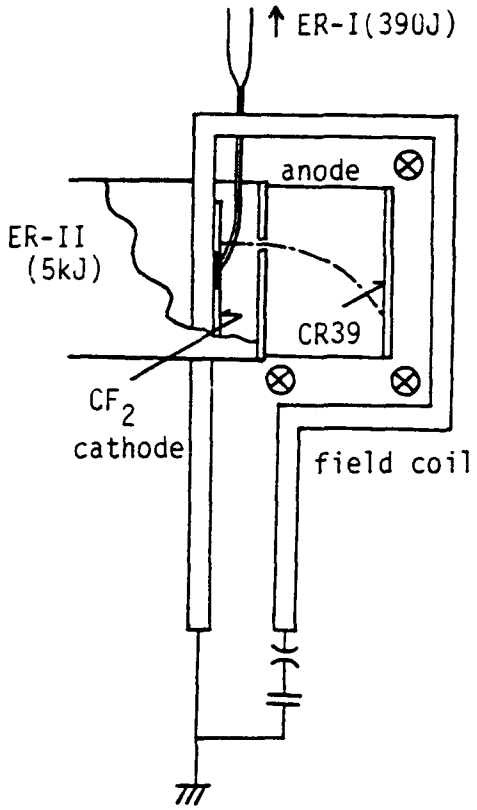

Fig.4. Schematic of MID.

We observed the CR-39 detectors after every shot with varying delay time between the application of the high voltage for the flashover and that for the MID. Traces of the particles have been found when the delay time was 50ns. Operation with a larger delay resulted in a premature closure of the MID. The etch pits on the CR-39 is classified according to their diameters into two groups. Judging from the dependence of the pit diameter at the specified etching time on the particle mass and energy, it is found that one corresponds to H^- and the other to heavy ions.

The distribution of the pits are shown in Fig.5. We find that

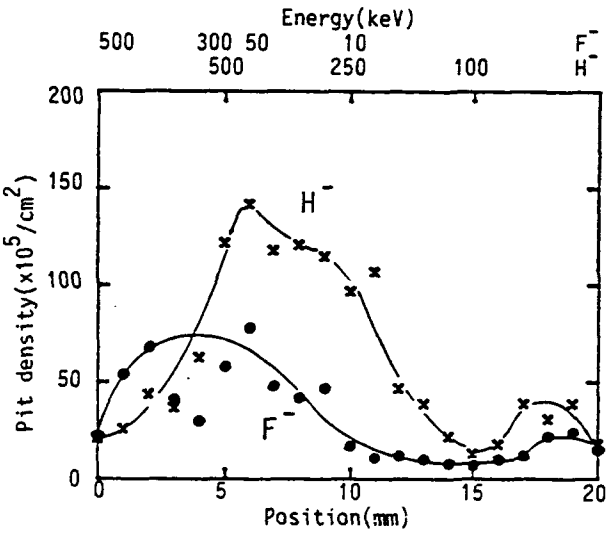

Fig.5. Distribution of etch pits on CR-39 detector.The dots and the crosses represent pits with large and small diameters, respectivery.

both kinds of particles have distributions with their maxima at the energy corresponding to the maximum diode voltage of 400kV. The total numbers of the pits divided by the aperture area of $0.0079cm^2$ and the pulse width of 70ns yield $40mA/cm^2$ for H^- and $20mA/cm^2$ for the heavier particles. From the fact that F has an electron affinity much greater than any other species involved, we can infer that the heavier particles are dominated by F^- ions.

4. Discussion and concluding remarks

Based on the results on the atomic densities and the accelerated ion current densities, we discuss briefly on the mechanism of the production process of F^- in the flashover plasma. First, we check the current density of H^-, j_{H^-}, in comparison with N_H. It is well known that in the process of H^- formation, the vibrationally excited H_2^* plays an important role through the reaction $H_2^*+e\rightarrow H^-+H$. Owing to the large cross section of this reaction, the ratio N_{H^-}/N_H can be as much as 10^{-2} [11], where N_{H^-} is the atomic density of H^-. If we crudely assume the same ratio in the present case, it follows that $N_{H^-}\simeq 10^{10}$-$10^9 cm^{-3}$. We can evaluate J_{H^-} as either $eN_{H^-}v_{H^-}$ or $eN_{H^-}\Delta x/\Delta t$, where v_{H^-} is the mean velocity of H^-, Δx the effective thickness of the cathode plasma and Δt the pulse width. In either case we get j_{H^-} of the order of 10^{-2}-$10^{-3}A/cm^2$, which is in reasonable agreement with the observed current density of H^-. This would mean that the application of MID voltage has no harmful effect on the densities of negative ions.

Next, we evaluate the rate coefficients of the reactions involved in the formation process of F^-. We can cite the rate coefficient $\langle\sigma_1 v\rangle$ of the radiative recombination process, $F+e\rightarrow F^-+h\nu$, from ref.[12]. The value at 1eV, $10^{-15}cm^3/s$, is smoothly extrapolated to the higher temperature. However, we have only fragmantary data of the cross sections for the collisional detachment, $F^-+e\rightarrow F+2e$ [13], and for the ionization, $F+e\rightarrow F^++2e$ [14]. We assume here that the energy dependence of the cross sections for these processes well above the threshold energies are similar to those for more popular ionization processes, i.e., σ is roughly proportional to E^{-1}. We can then obtain approximate values of the rate coefficients $\langle\sigma_2 v\rangle$ and $\langle\sigma_3 v\rangle$ for the latter two processes, respectively. Reflecting the large threshold energy of 17.4eV for the ionization, $\langle\sigma_3 v\rangle$ increases from $4\times10^{-10}cm^3/s$ to $3\times10^{-7}cm^3/s$ as kT_e is varied from 5eV to 30eV, while the variation of $\langle\sigma_2 v\rangle$ from $4\times10^{-8}cm^3/s$ to $9\times10^{-8}cm^3/s$ reflects the low threshold energy of 3.4eV.

We cannot assume that F^- ions are produced exclusively through the radiative recombination reaction, as shown in the following. The equilibrium density of F^-, $N_{F'}$, produced through the recombination is approximated by $N_{F'}=N_F\langle\sigma_1 v\rangle/\langle\sigma_2 v\rangle$, which is evaluated to be of the order of $10^5 cm^{-3}$. This value yields $j_{F'} \simeq 10^{-8}$ A/cm^2, making a neglegible contribution to the observed current density of F^-.

Therefore it is probable that a substantial fraction of F atoms are liberated as F^- from the surface. If we assume no further liberation of F and F^- from the surface at the time of maximum FI, the approximate constancy of N_F requires that $N_{F'}/N_F \lesssim(\langle\sigma_1 v\rangle+\langle\sigma_3 v\rangle)/\langle\sigma_2 v\rangle \simeq 0.01\sim4$. This relation yields $j_{F'} \lesssim 3\times10^{-4}-8\times10^{-2}$A/cm^2 for the assumed range of T_e. This is again in reasonable agreement with the measured value of F^-. In spite of many assumptions involed, it could therefore be concluded modestly that a significant fraction of atomic fluorine is emitted from the surface in the form of F^-.

Further efforts should be concentrated on enhancement of F^- liberation from the surface as well as on precise control of the delay time.

references

[1] V.A. Papadichev; Proc. 7th Int. Conf. High Power Particle Beams, Karlsruhe, F.R.G. (1988)479, and references therein.
[2] H. Lidenbaum, A. Fisher, N. Rostoker; ibid. 677.
[3] K. Horioka and K. Kasuya; Proc. 8th Int. Conf. High Power Particle Beams, Novosibirsk, USSR (1990)481.
[4] S. Humphries, Jr., R.J.M. Anderson, J.R. Freeman, T.R. Lockner, J.W. Poukey and J.J. Ramirez; Nucl. Instrum. Meth. **187**(1981)289.
[5] K. Mahrt-Olt, J. Jacoby, D.H.H. Hoffmann, V. Dubenkov, A. Golubev, A. Shumshurov and B.Y. Sharkov; Proc. 8th Int. Conf. High Power Particle Beams, Novosibirsk, USSR (1990)677.
[6] A. Kitamura, K. Mitsuhashi and S. Yano; Laser & Particle Beams 5(1987)683.
[7] S. Shibata, A. Kitamura, Y. Furuyama and T. Nakajima; NIFS-PROC-8, National Institute of Fusion Science, Japan (1991)107.
[8] W.L. Wiese, M.W. Smith and B.M. Glenon; Atomic Transition Probabilities, Vol.1 Hydrogen Through Neon (NSRDS-NBS-4,1966).
[9] A.A. Radzig and B.M. Smirnov; Reference Data on Atoms, Molecules and Ions (Springer-Verlag, 1980).
[10] R.K. Janev, W.D. Langer, K. Evans, Jr. and D.E. Post, Jr.; Elementary Processes in Hydrogen-Helium Plasmas (Springer-Verlag, 1987).
[11] O. Fukumasa; J. Jpn. Soc. Plasma Science and Nucl. Fusion Research **60**(1988)419.
[12] H.P. Mital, S. Chandra and U. Narain; J. Phys. Soc. Jpn. **42**(1977)1282.
[13] S. Ormonde; Phys. Rev. Lett. **38**(1977)690.
[14] P. Tiwari, D.K. Rai and M.L. Rustgi; J. Chem. Phys. **50**(1969)3040.

CHARACTERISTICS OF HIGH POWER ION DIODE WITH REAL CATHODE

H. Sugimura, E. Chishiro, T. Tachibana, K. Masugata and K. Yatsui
Lab. of Beam Tech., Nagaoka Univ. of Tech., Nagaoka, Niigata 940-21, Japan

ABSTRACT To obtain a high current-density ion beam of ~ 10 kA/cm^2 on the anode, we are developing a new type of applied-B_r diode with real cathode. For this purpose, some pilot experiments are performed. To evaluate the effect of prepulse, self-magnetically insulated plasma-focus diode (PFD) with short gap (d = 5 mm) is used. The diode is short circuited in every shot with prepulse, which is in operational with relatively high impedance by eliminating pre-pulse. Molecules produced in a shot of PFD are evaluated and large quantity of ~ 1×10^{21} of H_2 are found to be released from the anode. Characteristics of conventional B_r diode is investigated and highly bright ion beam is produced with good reproducebility. A strong magnetic field coil strengthened by Kevlar filament has been developed for the new type of B_r diode, maximum field of 35 T, B_r field of 5 T becomes possible to obtain without destruction.

§1. Introduction

To achieve light-ion beam driven ICF, it is required to develop a high bright ion beam with the power brightness of ~ 1000 TW/cm^2/sr. As the energy of the beam has the upper limit of 5 ~ 10 MeV for proton[1], beam brightness of ≧ 100 MA/cm^2/sr is required. For this purpose, it is required, for example, to obtain the ion current density of ≧ 10 kA/cm^2 on the anode with focusing solid angle of ~ 1 sr even if the divergence angle is less than several degree and power gain is expected by beam bunching.

Previously, we have been studied a cylindrical applied B_z diode with real cathode formation[2] to obtain high brightness. The diode was constructed of a cylindrical anode, perforated cathode inside the anode, and one turn theta-pinch coil inside the cathode to generate uniform B_z in the A-K gap. Experimentally, ion beam with relatively low divergence is produced. In addition, the correction of trajectories of ions by applying biased magnetic field was also demonstrated. However, it is difficult to observe the detail of ion beam in the diode due to that ion beam is focused on the diode axis and that the diode has a complicated structure inside the cathode. Furthermore, maximum B_z field is limited by the strength of one-turn coil.

From the above, we are developping a new type of high power density B_r-MID with real cathode. In this paper, these details will be described.

In the short gap diode with real cathode, it is very severe against the closure of gap due to the expansion of plasma preformed by prepulse. The effect of prepulse is evaluated on the operation of self-magnetically insulated plasma-focus diode (PFD)[3].

In the shot of ion diode, a lot of morecules are known to be released mainly from the anode. These molecules are considered to be the source of anode plasma, which affects the diode operation, such as gap closure. To evaluate the mechanism of production the molecules, species and quantity of these molecules are evaluated.

The strong magnetic field coil of $B_r \sim 5$ T has been developed for the new type of B_r diode. Characteristics of conventional B_r-MID with virtual cathode formation is also examined.

§2. Evaluation of the effect of prepulse on operating PFD

A pulse power generator "ETIGO-II"[4] is used for the experiment. The generator is constructed of Marx generator (160 kJ), intermediate storage capacitor, PFL (1.5 Ω, 50 ns), and impedance conversion transmission line (ICL, 1.5 Ω → 6.5 Ω). Since we have no prepulse switch in the ICL, prepulse voltage of ~ 10 % of the main pulse is applied to the diode. The prepulse strongly affects the diode operation. To evaluate the effect, we have developed a vacuum flashover prepulse switch (VPS).

Experimental setup is shown in Fig. 1. The VPS is vacuum transmission line (VTL) with twelve discharge gaps, and installed in the vacuum chamber. The axial position of the gaps is optimized to reduce the prepulse voltage by means of static electric field calculation. In this calculation, voltage ~ 2/3 of the prepulse voltage is sustained by the gaps. To reduce the inductance, diameter of VTL is maximized (65 cm$^{\phi}$). When all gaps are closed, the inductance of VPS is expected to be ~ 220 nH.

PFD is used in the experiment, which is attached on the end of VTL. The PFD has A-K gap (d) = 5 mm and length of ~ 40 mm, and is constructed of a cyrindrical anode of inner diameter = 33 mm, and a cathode of outer diameter = 23 mm. The anode is made of copper and has an epoxy filled grooves (width ~ 1 mm, depth ~ 1 mm).

As the direct measurement of prepulse in the diode operation is difficult, performance of VPS has been evaluated by using dummy load of inductor (215 nH) with inductive voltage divider (2.3 μH) connected in paralel to the load. In

the shot of diode voltage ~ 500 kV, prepulse voltage of ~ 10 kV and prepulse current of 10 kA have been observed, which are ~ 1/5 and ~ 1/3 of those for the case without VPS (VPS gap = 0), respectively.

Figure 2 shows waveforms of diode current, diode voltage and impedance (a) without and (b) with VPS. In case of using VPS, diode are operated at diode voltage ~ 1 MV and diode current ~ 100 kA. The diode impedance of ~ 10 Ω is observed at the peak of diode voltage, and after that impedance decreaces. In the absence of VPS, however we see that diode is short circuited and diode current of ~ 250 kA is observed.

The diode is operated for several shots for each cases, where the diode is short circuited in all shots without VPS, but operated well with VPS.

As reported elsewhere[5], PFD has been operated at d = (6.5 ~ 7) mm in the experiment with ETIGO-II. Here, the impedance of the diode is around 6 Ω, which is still lower than the case of d = 5 mm with VPS.

From these results, we see that prepulse are strongly affecting the operation of PFD especially for short gap. By using VPS, reproducebility and diode impedance are improved to increase.

§3. Evaluation of the molecules released in the diode operation

To evaluate the species and quantity of the molecules produced in the diode operation, quadrupole mass spectrometer (QMS) and X-ray micro analyzer (XMA) are utilized. PFD is operated with VPS in the same condition as that in § 2.

In the experiment, vacuum valve of the diode chamber is closed just before the shot, and the increase in the pressure are measured after the shot by a vacuum gauge. After that, the gas is introduced into QMS and analyzed. In the chamber, clean silicon wafers are settled to evaluate solid materials produced in the diode. After the shot, the surface of the wafers are observed by SEM and analyzed by XMA.

Figure 3 shows the example of mass spectrum observed by QMS after the 1st shot of PFD after evacuation. We see that main component of gas produced in the diode is hydrogen. Some molecules such as hydrocarbons, water, CO_2 are also observed. The pressure rise after the shot is measured to be ~100 Pa, which coresponds to ~ 9×10^{21} of the the total number of molecules. Since the pressure rise is decresed to be less than 1/2 of that for the shot with bare Cu anode, more than 1/2 of these gas are considered to be produced on the flashboard.

Solid matelials deposited on the wafer are observed and analyzed by SEM and

XMA. The materials deposited have a dimension of several μm and are analyzed to be carbon, metals of Fe and/or Cu, and oxygen. Total quantities of these materials are estimated from the deposition density to be ~ 10^{22} atoms. Among these materials, metals are considered to be produced due to the irradiation of electron beam onto the metallic electrode, where carbon is produced on the flashboard.

From the measurement we can estimate the production density of H_2 or C to be on the order of ~ $10^{20}/cm^2$ on the flashboard. How and when such a large quantity of H_2 or C are produced is still unclear, but it will strongly affect the diode characteristics or limit the repetitive operation of the diode.

§4. Developement of strong B_r magnet

Insulating magnetic field for B_r-MID is usualy produced by a pair of multi-turn pulsed coil magnet. To obtain the insulating B_r field of ~ 5T, which is required for the high power B_r-MID, it is neccessary to produce more than 30 T of B_z field on the axis of inner coil. To obtain such a strong field without destruction of coil, filament winding type of coil is developed. The coil is constructed of glass-fiber-winded copper wire of rectangular cross-section, and high strength Kevler filament, and is immersed in coagulated epoxy resin. In contrast to the usual pulse magnet, the magnet for B_r-MID can not be reinforced by metallic material since it distorts magnetic field in the outside resion. The demension of the coil is, outer diameter ~ 25 mm, inner diameter ~ 10 mm, height ~ 18 mm, and number of turns of Cu wire = 20.

Using capacitor bank of 800 μF, coil current rises up to 35 kA in ~ 100 μs and we have observed B_z ~ 35 T on the axis of the coil without destruction.

§5.Characteristics of B_r-MID

Figure 4 shows the schematic of B_r-MID used in the experiment. The diode is constructed of a pair of stainless blade cathode and a flat aluminium anode with epoxy filled grooves. The diameters of inner and outer blade cathode are 25 mm and 50 mm, respectively. The diode is operated at gap length ~ 5.0 mm, insulating B_r field near the inner blade ~ 0.8 T, diode voltage (V_d) ~ 700 kV.

Figure 5 shows the waveforms of the diode. Diode current (I_d) build up at ~ 50 ns after the rise of diode voltage. Ion current density (J_i*) of 680 A/cm^2 is observed by BIC at the end of diode voltage.

In several shots of operations, ion current density, ion current, divergence angle (ϕ) evaluated by shadow box, maximum efficiency (η), beam brightness (F_B) are evaluated, which are summarized in Table I.

Table I. Experimental results of B_r diode.

Shot No	V_d (peak) (kV)	I_d (peak) (kA)	J_i (max) (A/cm²)	I_i (kA)	ϕ (rad)	F_B (kA/cm²/sr)	η (%)
21	680	150	1100	68	63	280	45
22	750	130	960	57	44	500	44
24	740	120	900	55	51	350	46
26	800	90	570	36	65	135	38

J_i: ion current density on the anode estimated from J_i* measured at z=80 mm downstream from anode, I_i: estimated from J_i, ϕ: average of four observed points, η: evaluated at peak ion current

From Table I, we see that relatively high efficiency and high ion current are observed with good reproducebility.

A new type of high power Br-MID with real cathode formation is under preparation. Characteristics of the diode will be obtained in future.

References

1) S. Humphries, Jr.: Nuclear Fusion 20, 1549 (1980).
2) K. Yatsui et al.: Proc. 7th Int'l Beam Conf., KfK, I, 522 (1988).
3) K. Masugata et al: Laser and Particle Beams 7, 277 (1989).
4) A. Tokuch et al: Proc. 2nd Int'l Symposium on ICF Res. by High power Particle Beams, Nagaoka, 430 (1986).
5) K. Yatsui et al.: Proc. 8th Int'l Beam Conf.,Novosibirsk, I, 535 (1990).

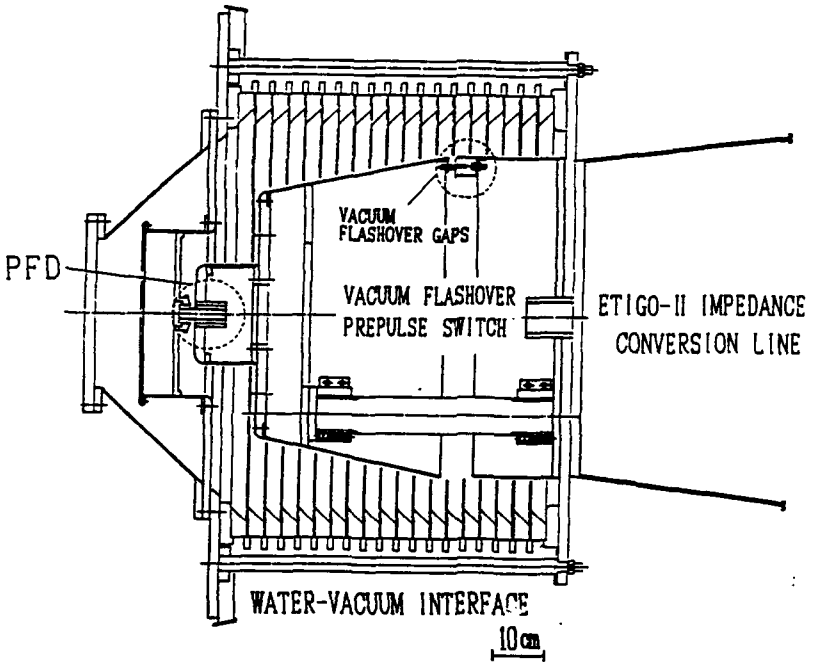

Fig.1 Schematic of vacuum flashover prepulse switch.

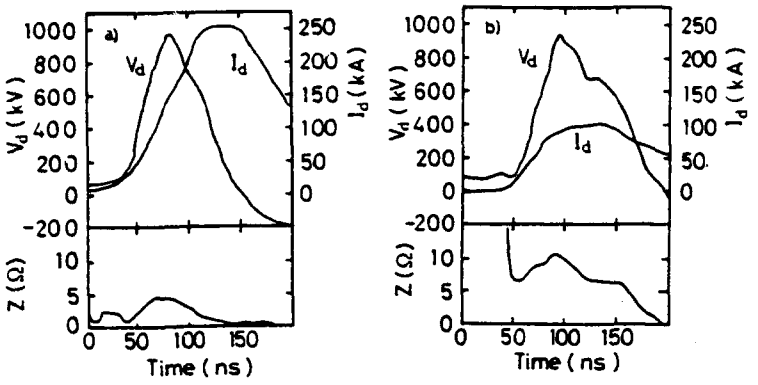

Fig.2 Typical waveforms of V_d, I_d, and impedance (Z). (a) without VPS, (b) with VPS.

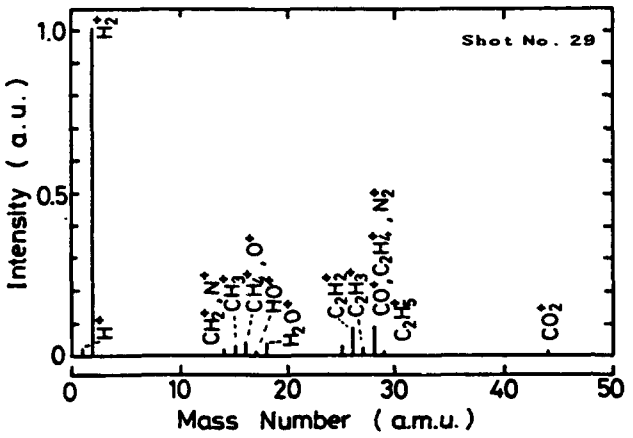

Fig.3 Mass spectrum of gas obtained after the shot of PFD.

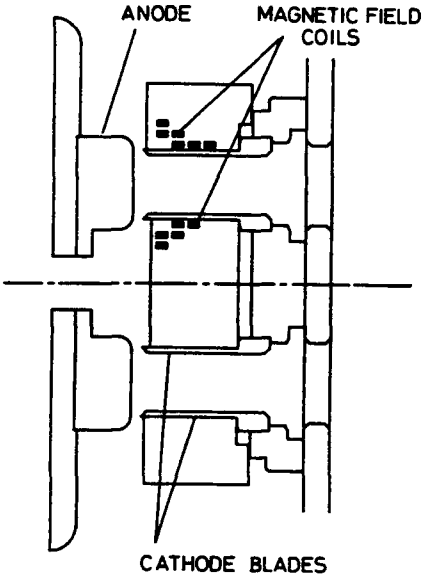

Fig.4 Schematic of B_r-MID.

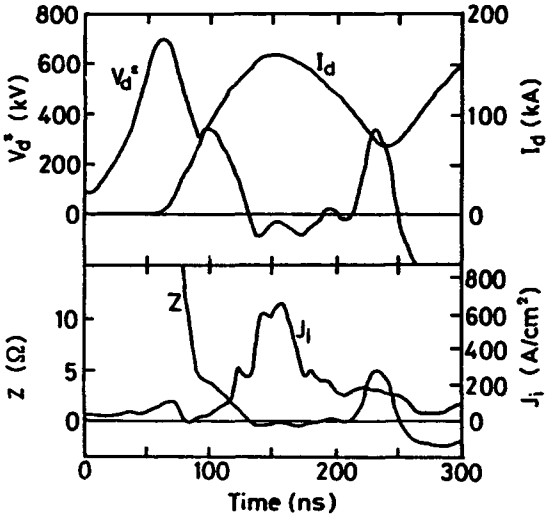

Fig.5 Typical waveforms of B_r-MID.

CHARACTERISTICS OF ION BEAM AND ANODE PLASMA IN "POINT PINCH DIODE"

K. Masugata, T. Tazima* and K. Yatsui
Lab. of Beam Tech., Nagaoka Univ. of Tech., Nagaoka, Niigata 940-21, Japan
*National Institute for Fusion Science, Nagoya 464, Japan

ABSTRACT Diagnostics and evaluation have been carried out on an ion beam and anode plasma in "Point Pinch Diode". Mass spectra of ion beam measured by Thomson-parabola spectrometer have shown that the main component are ⓐ proton and H_2^+, ⓑ highly ionized carbon and oxygen ions, and ⓒ singly ionized C, O and molecules such as CO_2^+, OH^+, OH_2^+. X-ray and particle pinhole images have shown the size of the electron beam on the plasma to be less than ~ 0.5 mm in diameter, in which fine structures are found with size less than 0.05 mm. A K_α satelite line of Al V is observed with crystal spectrograph, which indicates the existence of Al^{4+} in the plasma.

§ 1. Introduction

In a pinched relativistic electron beam (REB) diode[1], electron beam is tightly pinched in an acceleration gap, which is irradiated onto a metallic anode. The high current-density irradiation with current density more than MA/cm^2 produces high-energy density plasma. Ions of the plasma are accelerated in the gap with high current density due to that the density of the plasma is high and the space charge is neutralized by the high density electron beam.

In "Point Pinch Diode" (PPD), a kind of pinch REB diode, highly bright ion-beam has been observed[2,3]. However, clear understanding of the mechanism of the ion beam production has not been obtaind.

In this paper, we will show the experimental results of the evaluation of ion beam and the anode plasma. Highly-resolved Thomson parabora spectrometer (TPS), X-ray and particle pinhole camera, crystal X-ray spectrograph were used for the measurements[3].

§ 2. Diode geometries and characteristics

Figure 1 shows experimental setup of PPD. Pulse power generator "LIMAY-I"[2] (3Ω, 50 ns) in the National Institute for Fusion Science was used in the experiment. The cathode is made of a spherical stainless-steel (diameter ~ 10 mm) with a hole of diameter ~ 2 mm on the axis. The anode is a metal

(aluminium, aluminium coated carbon or copper, 15 mm × 15 mm × 2 mm^t) attached on the end of magnetically insulated transmission line (MITL). The gap length is ajusted to be ~ 3.2 mm. The chamber is evacuated to ~ 1×10^{-4} Torr. The diode voltage (V_d) is measured by a resistive voltage divider connected to the end of MITL. The diode current (I_d) is measured by a Rogowsky coil.

Figure 2 shows typical waveforms of V_d and I_d. We see V_d rises in ~ 10 ns and has a plateau of ~ 500 kV with the pulse width ~ 60 ns. I_d is almost linearly increases in time for the duration of V_d. The peak value of I_d is observed to be ~ 70 kA after the fall of V_d.

§3 Analysis of ion species

Ions accelerated in the gap are collimated by two pinholes (1st pinhole 2 mm$^\phi$ or 0.5 mm$^\phi$, 2nd pinhole 0.17 mm$^\phi$) and injected into TPS. The ions injected are deflected by magnetic and electric fields applied in the same direction, which are recorded on the track recording film (CR-39).

Figure 3 and 4 shows typical traces obtained with Cu anode. We see that many ions are detected. These ions can be divided into 5 groups as follows:

① H^+ and H_2^+ with maximum energy in agreement with V_d,

② $C^{1\sim5+}$, and $O^{1\sim6+}$ with wide energy spread,

③ ions of mass number (A) to charge state (Z) ratio (A/Z) ~ (12~57), with narrow energy spread around E/Z ~ (400 ~ 500) keV,

④ neutrals,

⑤ negative ions.

From Fig. 4, we see that high energy ends of each traces in group ② are on a straight line passing through the origin. Furthermore, high energy end of the traces of $C^{4+}$and O^{5+} in Fig. 4 ~ 300 keV, which consists with V_d. Hence, we find that ions of group ② are originally accelerated at the states of C^{4+} or O^{5+} and charge-exchanged in the drift region.

The negative ions are considered to be produced from ③ by charge-exchange because the absolute value of A/Z and E/Z are same as those of group ③. Neutrals are considered to be produced from positive ions by charge-exchange.

Ions in group ③ is considered to be singly ionized because no traces are observed in the area between group ③ and the origin (neutral point). If $Z \geq 2$, tracks should exist in the area due to the charge-exchange. These ions have a wide spread of A/Z, which suggests that many kinds of ions are included. However, exact values of A/Z were not obtained in this measurement. To analyze these ion, we have improved the resolution of TPS.

To increase the magnetic deflection, additonal magnet with magnetic field

~ 0.75 T is attached in front of the TPS. Applied elecric field for the electric deflector is also increased. The size of 1st and 2nd pinholes used were 0.5 mm$^{\phi}$ and 0.17 mm$^{\phi}$, respectively.

Figure 5 shows the typical traces obtained in the shot of V_0 ~ 400 kV with Al anode coated on carbon. We see that the spot size of the beam is less than the width of $\Delta(A/Z) = 1$ at the point of E/Z ~ 400 keV and A/Z ~ 19. That is, the resolution (ΔA) is less than 1 at that point.

From Fig. 5 we see that ions of A = 12 ~ 19 and 26 ~ 30 are observed. In addition, tracks are observed around A = 40, for which we couldn't obtain the exact value of A. The mass spectrum obtained is found to be quite similar to the typical spectrum of residual gas in a vacuum chamber[4]. Possible candidate of ions with A = 12 ~ 19 are listed in Table I.

Table.I Possible ions with A/z of 12 to 19

A/z	12	13	14	15	16	17	18	19
ion	C^+	CH^+	N^+ CH_2^+	CH_3^+	O^+ CH_4^+	OH^+	H_2O^+	$F^{+a)}$ H_3O^+

a) Fron is used for the cleaning of the electrode.

As the residual gas is mainly applied from the surface of the chamber, the main source of the ions will be the molecules absorbed on the anode.

From the experiment above, we summarize that the ions accelerated in the gap are ⓐH^+ and H_2^+, ⓑhighly ionized C and O, and ⓒsingly ionized C, O, and molecules such as CO_2, OH, OH_2. Source of these ions are the molecules absorbed on the anode. In spite of using metallic anode, metallic ions are not observed. The reason is considered as follows; the surface of the anode plasma is covered by the absorbed molecules, which disturbs the extraction.

§4. Evaluation of the size of pinched REB

To evaluate the pinch diameter of the REB, time integrated X-ray pinhole camera[6] and particle pinhole camera were used. The pinhole of the X-ray camera was the combination of thick, tapered Pb pinhole (6 mm^t, hole diam. ~ 1 mm$^{\phi}$) with thin Cu pinhole (0.1 mm^t). The former was used for eliminating hard X-ray background and the latter was to obtain space-resolution. Al and Be foil were used as a filter for eliminating light and ions, and for attenuating the intensity of X-ray. X-ray image was recorded on Kodak Tri-X Film.

Figure 6 shows the typical X-ray pinhole images of front view (a) and side view (b) of the diode with Cu anode. The pinhole diameter, the system magnification, and the space resolution were 0.15 mm$^{\phi}$, 9.8, and 0.22 mm for

(a), and 0.20 mm, 2.25, and 0.22 mm for (b), respectively. The filter is 30-μm thick Al for (a), and 45-μm thick Al with 20-μm thick Be for (b). From Figs. 6 (a) and (b), pinch diameter of electron beam is evaluated to be ~ 0.4 mm and ~ 0.5 mm, respectively.

Figure 7 shows the particle pinhole image obtained on CR-39 for Al anode. Pinhole of 0.03 mm$^{\phi}$ was placed just behind the cathode on the diode axis. We see the macroscopic diameter of ~ 0.4 mm, which agrees with the X-ray images shown in Fig. 6. A microscopic spots of diameter ~ 0.05 mm was also observed, which indicates micro-structures in the REB or in the plasma.

§5. Observation of Al-K_α X-ray satellites from a target plasma

K_α satellite lines are produced when thermal ionization due to beam heating is accompanied by inner shell ionization[7]. The satellite lines are blue-shifted with respect to the normal K_α line. In our diode, heating of metallic anode and impact K-shell ionization occur simultaneously by the irradiation of pinched REB, while K_α satellites are expected to be observed.

To evaluate the ionization state of target plasma produced on the Al anode, we have observed Al-K_α satellites by using flat crystal X-ray spectrograph. The spectrograph was carefully shielded against hard X-ray by using Pb board and installed inside the vacuum chamber. PET crystal was mounted in the spectrograph with an angle of 67.5 degree. A Be foil of thickness ~ 20 μm was used as a window. The spectra were recorded on Kodak DEF-392 film.

Figure 8 shows a spectrogram of the target plasma produced on the Al anode. Satellite line of Al V was clearly observed, which indicates ions of Al^{4+} exists in the plasma.

§6. Summary

Highly-resolved mass spectrum of the ion beam indicates that the ions exracted from the anode plasma is mainly composed of ⓐ H^+ and H_2^+, ⓑ highly ionized C and O, and ⓒ singly ionized C, O and moleculer ions. Existence of highly ionized ions suggests the production of hot spot in the plasma. Images of X-ray and particle pinhole camera indicate that the size of pinched REB is less than ~ 0.5 mm in diameter. X-ray spectrum of the anode plasma indicates that multiply ionized metallic ions exist in the plasma.

Acknowledgment

This work was carried out under a collaborative research program in National Institute for Fusion Science.

References
1) S. A. Goldstain and R. Lee: Phys. Rev. Lett. 35, 1079 (1975).
2) M. Sato: Jpn. J. Appl. Phys., 26, 927 (1987).
3) H. Okuda et al.: NIFS-PROC-8, 67 (National Inst. Fusion Sci., 1991).
4) M. J. Rhee: Rev. Sci. Instrum., 55, 1290 (1982).
5) H. Okuda: Master thesis (Nagaoka Univ. of Tech., 1991).
6) D. J. Johnson, et al.: J. Appl. Phys., 53, 4579 (1982).
7) J. Bailey et al.: Laser and Particle beams, 8, 555 (1990).

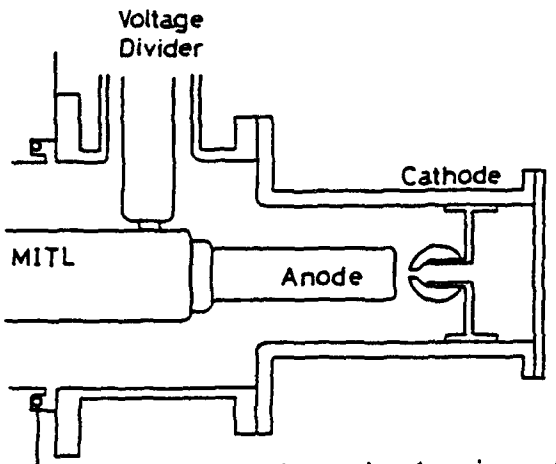

Fig.1. Schematic drawing of the experimental setup.

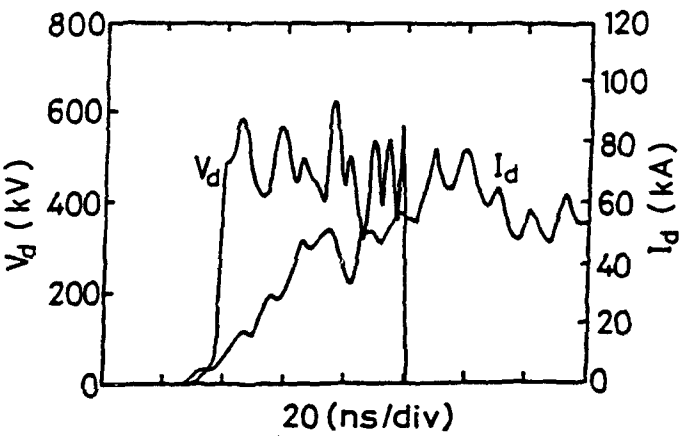

Fig.2. Typical wave forms of V_d and I_d.

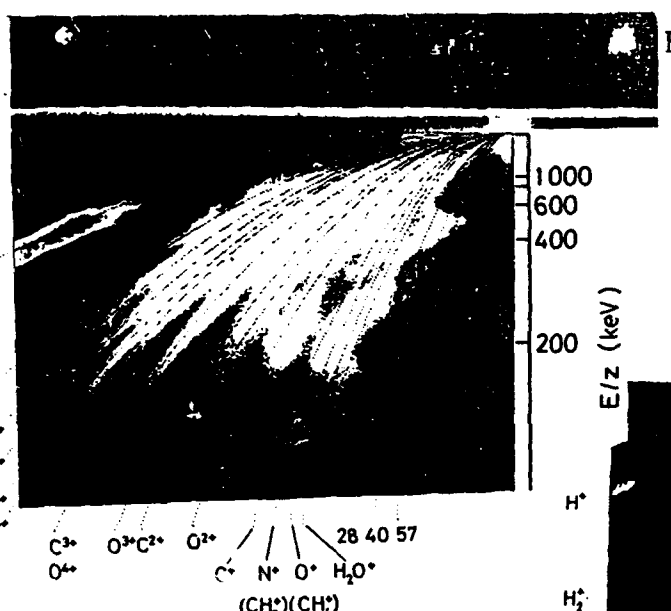

Fig.3. TPS trace obtained with Cu anode. V_d ~ 450 kV, diam. of 1st pinhole ~ 2 mm.

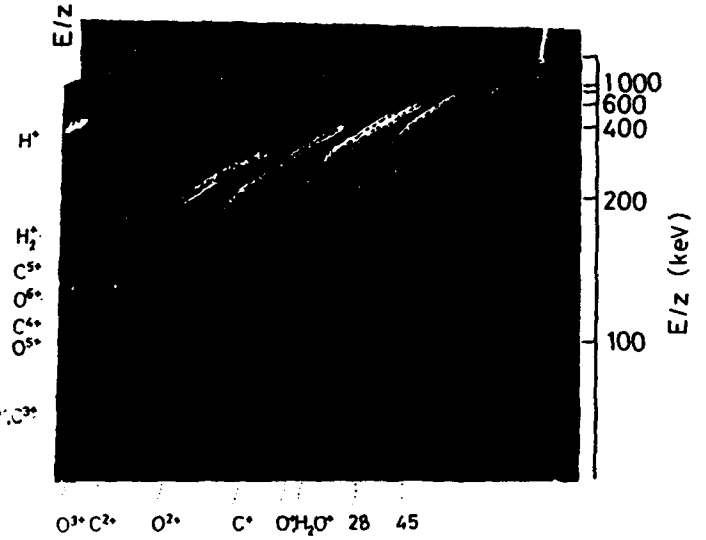

Fig.4. TPS trace obtained with Cu anode. V_d ~ 300 kV, diam. of 1st pinhole ~ 0.5 mm.

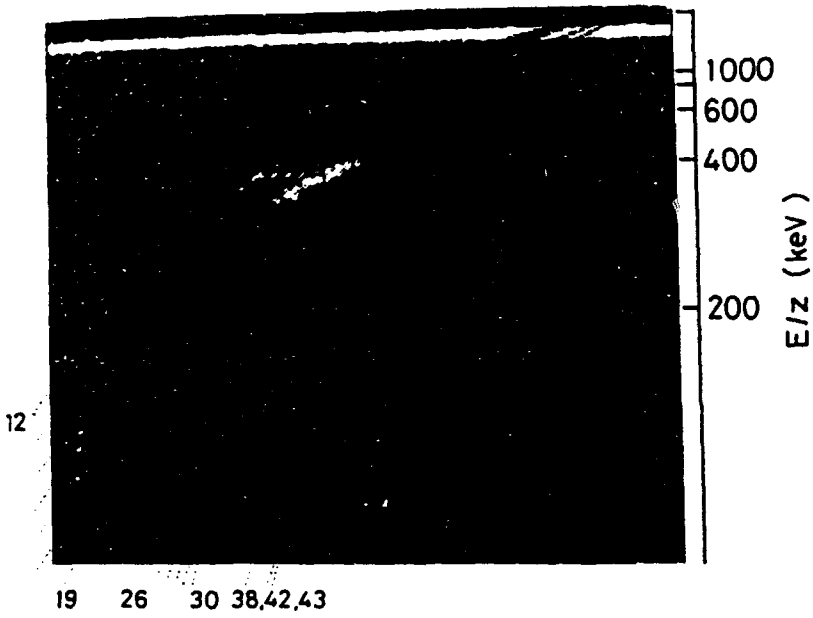

Fig.5 TPS trace obtained with Al coated carbon anode. $V_d \sim 400$ kV, diam. of 1st and 2nd pinholes ~ 0.5 mm.

Fig.6 X-ray pinhole images of front view (a) and side view (b) of the diode with Cu anode.

Fig.7 Particle pinhole image obtained on CR-39 for Al anode.

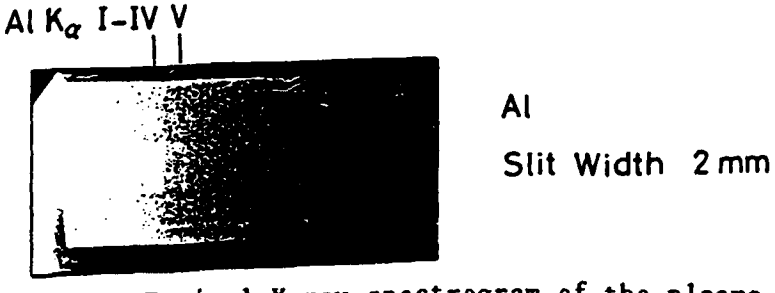

Fig.8 Typical X-ray spectrogram of the plasma on the Al anode.

Point Focusing of Intense Ion Beam by Spherical "Plasma Focus Diode"

W. Jiang, T. Sakagami, K. Masugata, and K. Yatsui
Laboratory of Beam Technology, Nagaoka University of Technology,
Nagaoka 940-21, Japan

ABSTRACT

Three-dimensional focusing of intense ion-beam has been obtained by using spherical "plasma focus diode". Experimental data have shown that ion beam was focused into a small cylindrical volume with $\sim$ 0.5 mm in diameter and $\sim$ 2.5 mm in length, where the ion-beam current density and the power density is estimated to be $\sim$ 680 kA/cm^2 and $\sim$ 0.54 TW/cm^2.

I. Introduction

Intense pulsed light ion-beam is very interested in the fields of ICF and materials science. In order to achieve high beam-power density, it is necessary to focus the ion beam to a small area. In the applied-B diodes, the applied magnetic field and the instabilities developed in the gap increases the divergence of the ion beam.

As reported previously, we have succeeded in the development of a self-magnetically insulated "plasma focus diode" (PFD) constructed of a pair of coaxial cylindrical electrodes, where two-dimensionally, very tight focusing of the proton beam has been observed with the focusing radius of $\sim$ 180 μ m.[1-3]

With the extension of the experimental and calculated results of PFD, we have developed a spherical PFD (SPFD) to achieve a three-dimensional, point focusing. Figure 1 shows the conceptional structure of SPFD. It is constructed by two concentric spherical electrods. The operative principle of SPFD is similar to PFD. The azimuthal magnetic field generated by the diode current turns electrons and forces them to drift along the gap. Analytical calculations have shown that most electrons drift out of the diode gap from the downstream end before reaching the anode.[4,5]

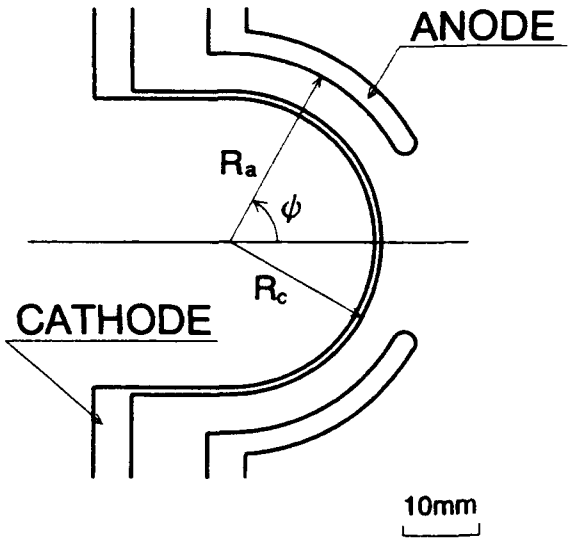

Fig. 1 Conceptional structure of SPFD

The advantages of SPFD for producing high beam-power density are considered as follows:

1) With the simple structure, it is possible to reduce the diode size to obtain small focusing area with large irradiation angle of ion beam.

2) The azimuthal symmetry provides good focusing toward the central axis. Magnetic field only exists in the azimuthal direction and its effect can be corrected by the shape of the electrodes.

3) Diode impedance is relatively stable since electrons do not accumulate in the gap. The short resident time of electrons in the gap limits the development of instabilities in the electron sheath.

In this paper, we present our experimental results of SPFD operated on pulsed power generator, "ETIGO- Ⅱ ". The anode and cathode radius is 25 mm and 20 mm, respectively. Grooves of 0.8 mm wide, 1 mm deep and 1.5 mm in pitch are trenched in the azimuthal direction on the anode surface, which are filled with epoxy. The cathode is perforated by 1-mm holes with the transparency of ~ 40 %. The ion beam focusing is studied by measuring the focusing area with the pinhole camera and by measuring the deflection angle of the ion beam with the shadow-box. Using biased ion collectors, we obtained the ion-beam current density. The beam power density on the focusing area is then estimated with the above experimental data.

Ⅱ. Experimental Results

a) Diode behaviour

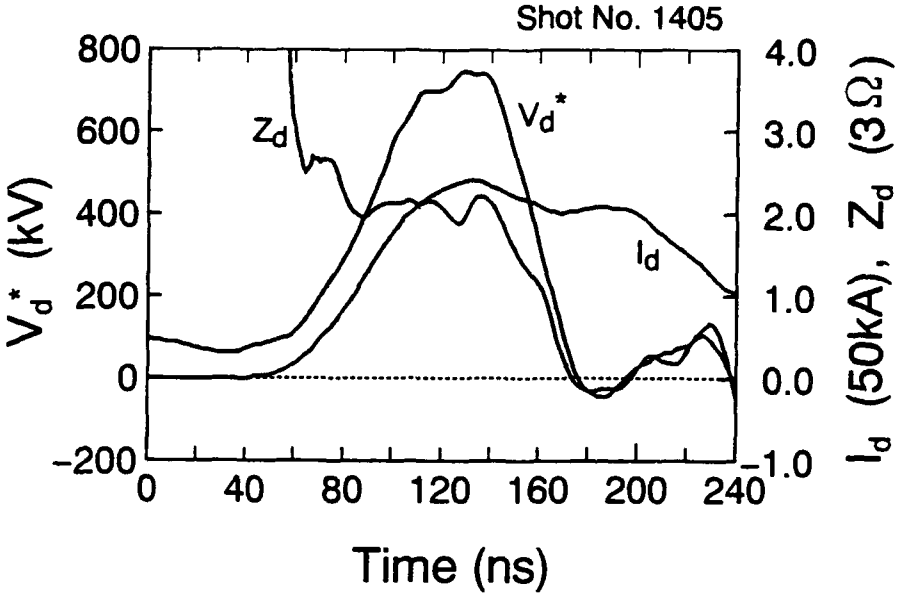

Fig. 2 Typical waveforms of V_d^*, I_d and Z_d

Figure 2 shows the typical waveforms of the inductively-calibrated diode voltage (V_d^*), the total diode current (I_d) and the diode impedance (Z_d). We have used a 12-channel self-breakdown vacuum pre-pulse switch located downstream of the voltage probe so that the actual prepulse level was lower than that shown in the voltage waveform. It is seen in Fig. 2 that the diode impedance remain around ~ 6 Ω for nearly 60 ns providing good impedance matching with the output impedance (6.5 Ω) of "ETIGO- Ⅱ ".

b) Ion beam focusing

Figure 3 shows (a) the experimental arrangement of the Rutherford scat

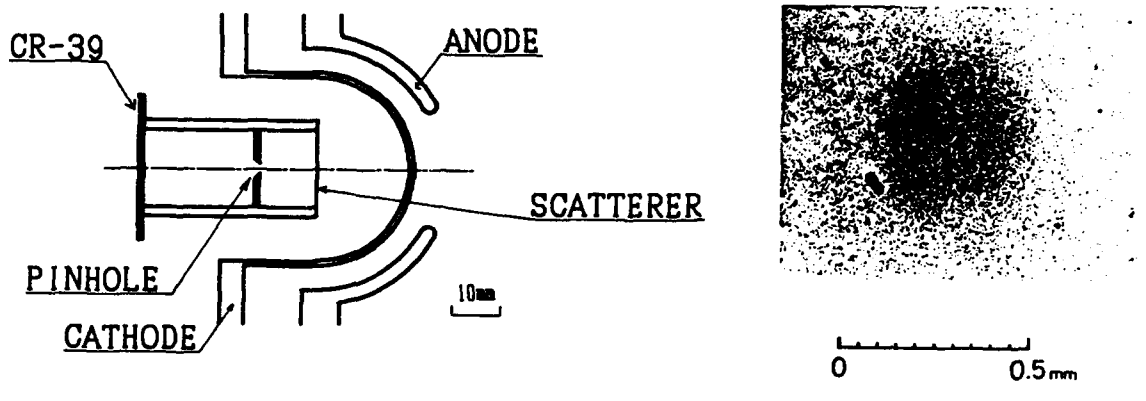

Fig. 3 (a) Experimental arrangement of the Rutherford scattering pinhole camera, and (b) typical photograph obtained.

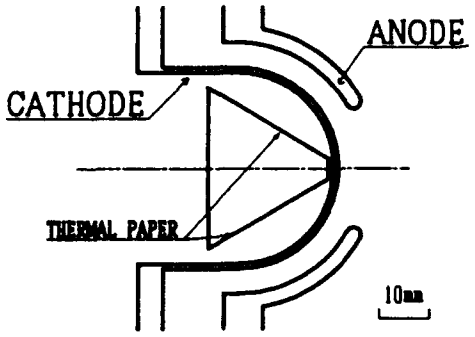

Fig. 4 Experimental arrangement of shadow-box.

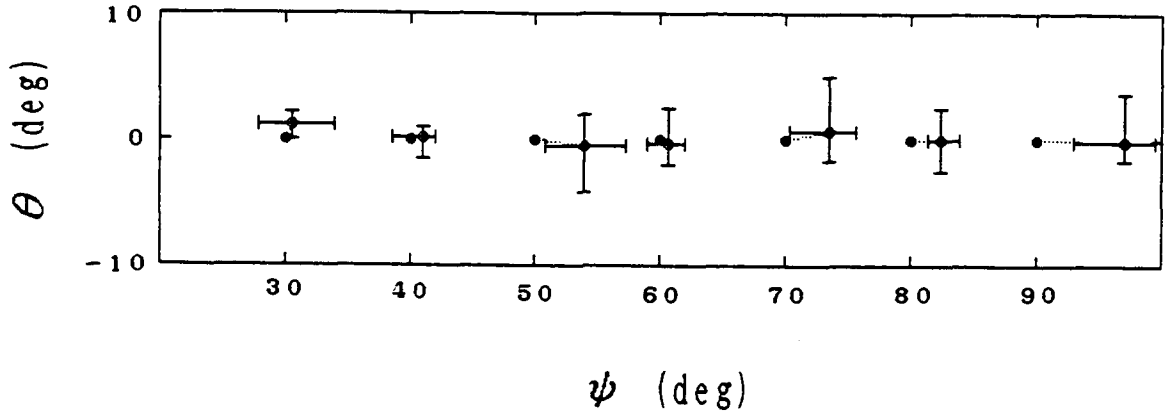

Fig. 5 Experimental results of ion-beam deflection in θ and ϕ.

tering pinhole camera and (b) the typical photograph obtained from the CR-39 detector. As the scatterer, we used 7- μ m aluminium foil. The diameter of the pinhole is 0.3 mm. Figure 3 (b) was obtained with the scattering foil set at the spherical center of the electrodes. The density distribution read out from Fig. 3 (b) has shown that FWHM is less than 0.4 mm in all directions. This data gives the divergence angle of $\sim 1^\circ$ in the azimuthal direction. When the foil was located 1 mm in front of the center, we obtained nearly the same result as Fig. 3(b). When the foil was moved 2 mm away from the center, however, we were not able to obtain a clear beam profile from the detector of the pinhole camera.

Figure 4 shows the experimental arrangement of the shadow-box. The cathode was drilled by 28 holes (0.4 mm in diameter) which were on 7 rows with 10° interval in ϕ and 90° interval in θ. The conical thermosensitive paper is inserted in the cathode to measure the deflection angle of

the ion beam. Figure 5 shows the results of ion-beam deflection in both θ and ϕ directions. The black circles in Fig. 5 show the geometric neutral points of the beam. The white circles show the deflection of the ion beams averaged for each row of holes and the error bars show the maximum and the minimum. From Fig. 5, we have seen that average deflection in θ is 1 ~ 2°, which is smaller than the deflection in ϕ (1 ~ 7°). These results are in an agreement with the data of the pinhole camera. It is considered that the large deflection in ϕ, particularly in the upstream region, is due to the self-magnetic field and the nonuniformity of anode plasma caused by the azimuthal grooves of epoxy on the anode surface. The effect of the magnetic field will be improved by reshaping the electrods of the diode.

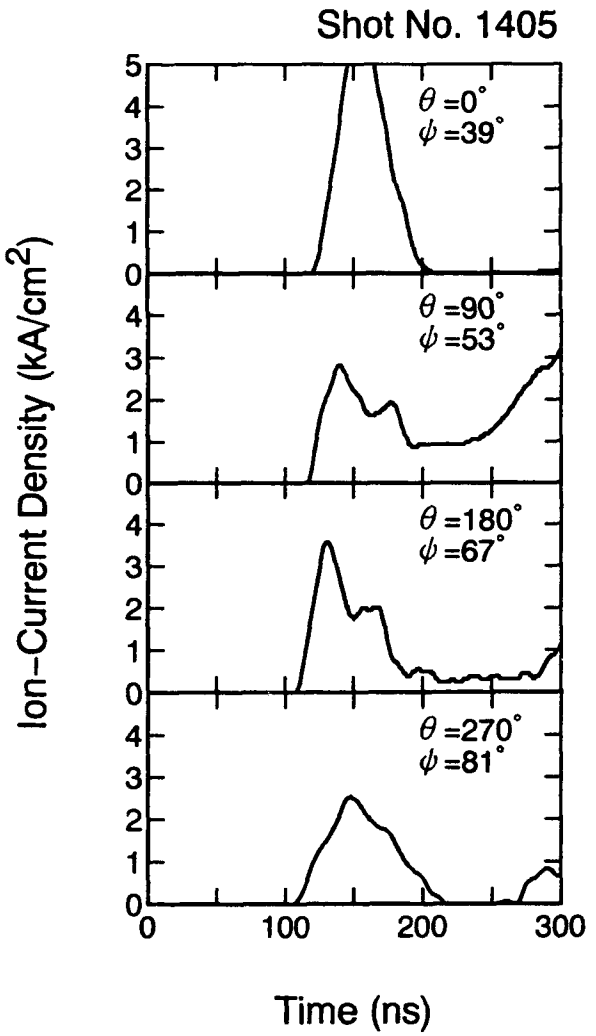

Fig. 6 Ion-beam current density on the anode surface obtained at four positions by BIC.

c) Ion-beam current density

Four biased ion collectors (BIC) were inserted in the cathode to measure the ion-beam current density simultaneously. The diameter of the aperture of BIC is 0.3 mm. Figure 6 shows the ion-current density on the anode surface at four positions after being calibrated by the radii. From Fig. 6, we see that the current density at the downstream is larger than that at the upstream, and that the average ion-beam current density on the anode surface is larger than 2 kA/cm^2.

d) Ion-beam power density

With the experimental results, it is found that the ion beam is focused into the a small cylindrical volume at the center. From the data of deflection angle, we suppose that the diameter and the length of the cylinder is ~ 0.5 mm and ~ 2.5 mm, respectively. Then, its sur

face area is $\sim$ 4 mm^2. While the anode area is $\sim$ 34 cm^2 and the total ion current is $\sim$ 68 kA for the average ion current density of $\sim$ 2 kA/cm^2. With the cathode transparency of 40 %, the calculated ion-beam current density on the focusing area (the cylinder surface) is $\sim$ 680 kA/cm^2. Then the beam power density is $\sim$ 0.54 TW/cm^2 with the ion energy of 0.8 MeV. With the uncertainty of BIC and the error induced by the shadow-box, we believe the accuracy of this result is within a factor of 2.

Ⅲ. Conclusions

1) Good focusing toward the central axis is observed by SPFD from the measurement of pinhole camera. The radial beam profile near the axis is $\sim$ 0.4 mm (FWHM) at the diode voltage of $\sim$ 0.8 MV.

2) The axial length of the focusing area is 2 $\sim$ 3 mm from the measurement of shadow-box.

3) Ion-beam current density on the anode surface obtained with BIC is $\geqq$ 2 kA/cm^2.

4) From the experimental results of the deflection angle of the ion beam and the ion-beam current density, we estimated the ion-beam current density and the power density at the focusing area to be $\sim$ 680 kA/cm^2 and $\sim$ 0.54 TW/cm^2, respectively.

References

1) K. Yatsui, et al., Proc. 12th Int'l Conf. on Plasma Phys. & Controlled Nucl. Fusion Res., IAEA, 3, 153 (1989).

2) K. Masugata, et al., Laser and Particle Beams, 7, 287 (1989).

3) K. Yatsui, et al., Proc. 8th Int'l Conf. on High-Power Particle Beams, Ⅰ, 535 (1990).

4) W. Jiang, et al., Proc. 8th Int'l Conf. on High-Power Particle Beams, Ⅱ, 733 (1990).

5) W. Jiang, et al., Laser and Particle Beams, 9, #1, (1992) (to be published).

CHARACTERISTICS OF THE INTENSE ION BEAMS GENERATED WITH THE POINT PINCH DIODE

M. Sato
Himeji Institute of Technology,
Department of Electrical Engineering,
2167 Shosha, Himeji 671-22, Japan

T. Tazima
National Institute for Fusion Science,
Nagoya 464-01, Japan

The characteristics of the intense ion beams generated with the Point Pinch Diode which consisted of a semispherical mesh cathode and a flat anode were investigated. From the experimental results, it was verified that the ion beam was divergently extracted, but the current density of the ion beam was high around a diode axis. Due to this divergence, the current density of the ion beam decreased from several tens of kilo-amperes per square centimeters in the diode to 10–30 A/cm^2 on a diode axis at 190 mm from the top of the cathode. From the time of flight method, it was made clear that the metallic ions (e.g. Cu^{5+}) were contained in the ion beam as equally as the protons. Here the acceleration voltage for these ions was 350 kV.

Introduction

The Point Pinch Diode which consists of a small spherical cathode and a flat anode has been used in study for inertial confinement fusion. From this point of view, we interested in energy fluxes in the diode [1], and the experimental results showed that the dominant energy flux was the intense ion beams; the estimated current density of the ion beam corresponded to 90 kA/cm^2 in the diode [2]. On the other hand, the Point Pinch Diode recently has been used for high power micro-wave generation [3]. Moreover the species of the ion beam were also investigated, and significant amounts of highly ionized metallic ions which were produced from anode materials were detected [2,4]. In this situation, we investigated the characteristics of the ion beam taking into account of utilization for any applications, e.g. ion sources for accelerators and ion implantation.

A shadow box and a multi-channel biased ion collector were used to estimate the radial distribution of the ion beam. A silicon substrate was analyzed with a secondary ion mass spectroscopy (SIMS) after the ion beam was put into the silicon substrate. We expect that this analysis gives rise to more exact composition of the ion beam, but the proper data have been not obtained up to now. In this paper, the results obtained from these experiments are presented.

Experimental Setup

The pulse power generator LIMAY-I (600 kV, 3 Ω, 70 ns) at National Institute for Fusion Science was used to obtain the data presented here. At the end of the LIMAY-I, a MITL (1 m in length) was connected. Figure 1 shows the experimental setup at the end of the MITL. The experiments were performed with a flat anode facing to a hemispherical mesh cathode [5]. A 2 mm thick copper plate was attached to an anode holder, and was used for ion sources. A stainless-steel mesh was formed into hemispherical shape (cathode) by using the sphere of which diameter was 12.7 mm. The mesh was made up from the fine wires of 0.1 mm in diameter, and the distance between the wires was 1.1 mm. From these values, the transparency of the mesh was calculated as 84 %, and this value did not change by forming into hemispherical shape at the top of the cathode. All of the experiments presented here were carried out with the output voltage of about 400 kV and the anode-cathode gap length of 3 mm.

The diode voltage V_d was measured with a resistive voltage divider. The diode current was measured with a Rogowski coil. The divergent angles of the ion beams were estimated with a shadow box. It consisted of a thin brass plate with pin-holes and the film CR-39. Details about location of the thin plate and the film are shown in Fig. 2. To obtain the distribution of the ion beams, a multi-channel biased ion collector (BIC) was used. The multi-channel BIC has eleven charge collectors. In front of each charge collector, the thin copper plate with a pin-hole (ϕ 0.5 mm) was located to reduce the current of the ion

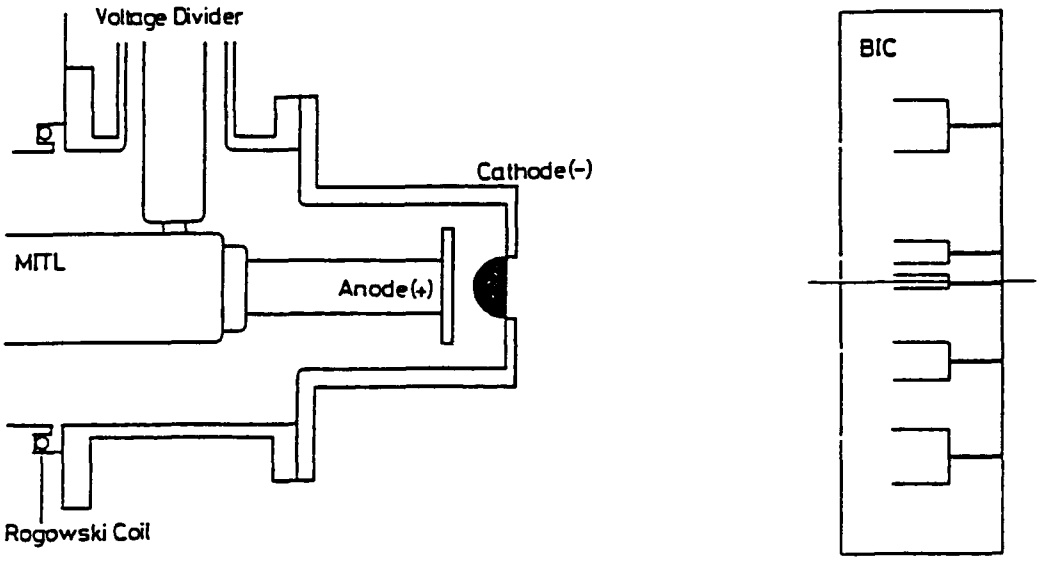

Fig. 1 Schematic drawing of experimental setup.

beam detected with each charge collector. Since the distance between each pin-hole was set at 1 cm, the pin-holes were located from a diode axis (r = 0 cm) to the radius of 10 cm. Each collector was biased at -450 V to remove the accompanying electrons.

Experimental Results

Figure 2 shows the schematic drawing of the experimental setup and results with the shadow box. It consists of the brass plate with pin-holes (ϕ 1 mm) and the film CR-39. The ions passing through the pin-holes are detected by the film. In Fig. 2, estimated divergent angles are displayed, and lines are drawn from the positions of the traces on the film through the pin-holes. These lines concentrate in a small region on the anode surface. This means that almost all the ions are divergently extracted from a spot like plasma generated on the anode.

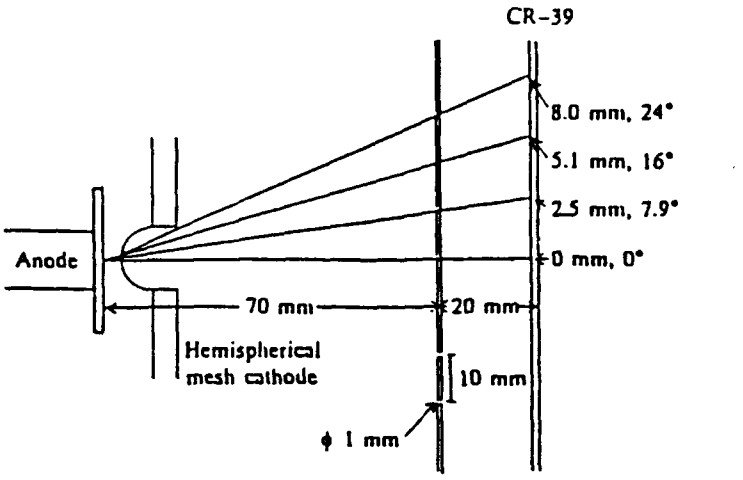

Fig. 2 Experimental results by shadow box.

Taking into account of the experimental result with the shadow box, the multi-channel BIC was made to obtain the radial distribution of the ion beam. The multi-channel BIC has relatively large charge collectors, and the charge collectors are located with radial offset in order to measure the divergent beam (Fig. 1). Figure 3 (a) shows the wave-form of V_d. The diode voltage rises and reaches to 400 kV by 15 ns. It once decreases and again increases up to 400 kV. After that, V_d decreases sharply to the ground level. Just before this sharp decrease, the main part of the ion beam is generated. Since the voltage drop by the inductive component is about 50 kV, the acceleration voltage for ions is 350 kV in this shot. The diode current is not shown in Fig. 3, but increases linearly and reaches to 50 kA just before the sharp decrease of V_d. The total current of the ion beam measured with a large BIC is generally 6 kA in this condition [4].

The current density j_i of the ion beam estimated on the diode axis with the multi-channel BIC is shown in Fig. 3 (b). In this figure, it can be easily

distinguished that the first peak is composed by the protons, because the proton is the lightest ion. Since the distance from the top of the cathode to the collector of the multi-channel BIC was set at 190 mm, the time of flight for protons is calculated as 23 ns. This value also shows that the first peak is composed by the protons. The calculated values of the time of flight for C^{4+}, O^{4+}, Cu^{4+} and Cu^{5+} are 40, 46, 90 and 83 ns, respectively. From these values, it is considered that the second top is mainly composed by Cu^{4+} and Cu^{5+}. By using the equation $j_i = n\ e\ v$, the number densities n for the proton and Cu^{5+} are calculated as 2.3×10^{11} and 4.1×10^{11} cm^{-3}, respectively. Although the current density for Cu^{5+} contains the effect of currents by other ions, these values mean that the metallic ions (e.g. Cu^{5+}) were contained in the ion beam as equally as the protons.

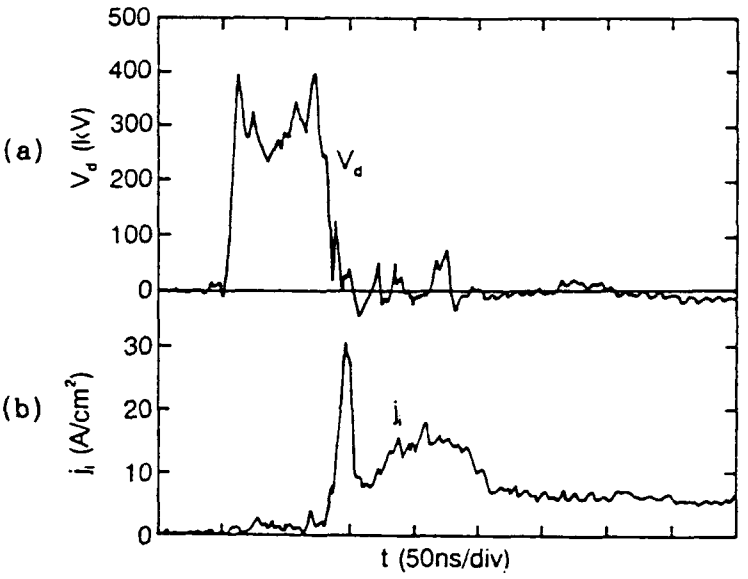

Fig. 3 Typical wave-forms of V_d and j_i.

Figure 4 shows the current densities of the ion beams composed by the protons as the function of a radial position. The current density has the maximum value on the diode axis, and decreases with going away from the diode axis. From Fig. 4, it is confirmed that the intensity of the ion beam generated with the Point Pinch Diode is high around the diode axis, although the ions are divergently extracted from a spot like plasma generated on the anode.

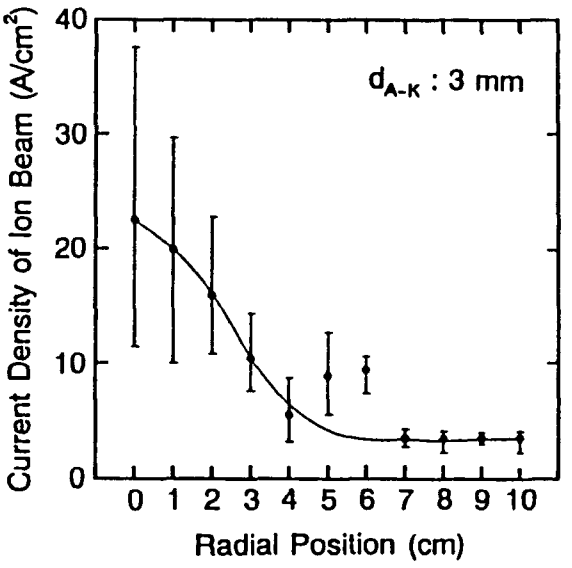

Fig. 4 Radial distribution of j_i.

Figure 5 shows typical traces on

the film CR-39 obtained with a Thomson-parabola ion spectrometer [4]. Major components of the ion beam are hydrogen, carbon and oxygen, the origins of which are gases adsorbed on the anode, such as water vapor and oil mist. In Fig. 5, the traces by A/Z of about 16 and 13 are displayed as Cu^{4+} and Cu^{5+}, respectively. Here A is the mass of atoms, and Z is the charge state of ionization. However there is the suggestion that these ions are composed by the organic ions produced from oil mist, e.g. CH^{+}. Therefore the experiments with the SIMS were performed in order to obtain the detail composition of the ion beams. That is, a silicon substrate was analyzed with the SIMS after the ion beam was put into the silicon substrate.

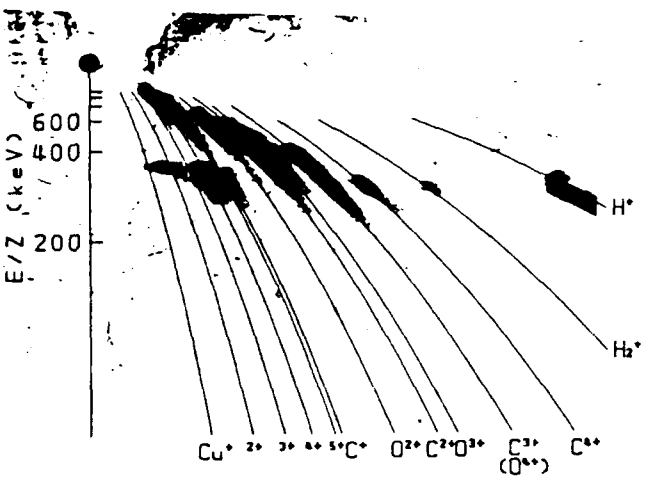

Fig. 5 Typical traces on CR-39.

In the experiment, the silicon substrate which was 10 mm in length and 5 mm in width was used. Firstly the ion beam was directly put into the substrate, but the substrate was broken out due to large thermal load by the intense ion beam. After that, the substrate is located instead of the film CR-39 in the shadow box mentioned above. After the shot, the surface of the substrate was analyzed with an Auger electron spectroscopy (AES). By this analysis, silicon, iron, chromium and copper ions were mainly detected. Therefore these ions were traced in analysis with the SIMS. Figure 6 shows the time history of signals detected with the SIMS. Each number means the mass of each atom. One division of the horizontal axis corresponds to the depth of about 200 Å. The vertical axis shows the counts of detected ions, but the exact value was not

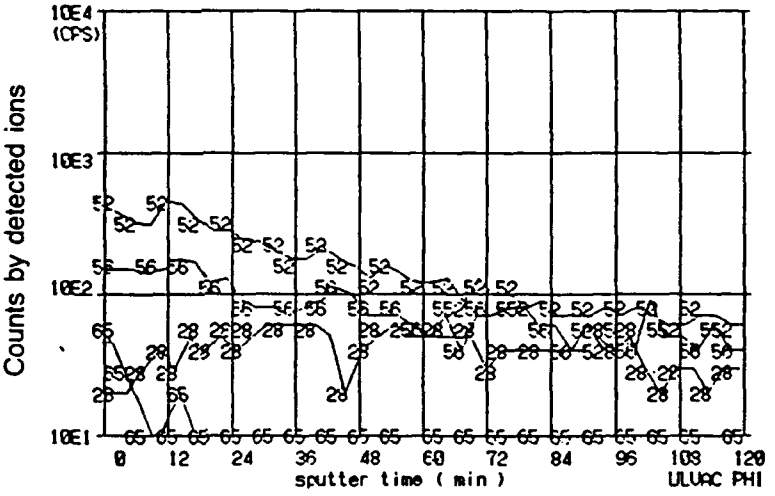

Fig. 6 Analyzed results by SIMS.

obtained. In Fig. 6, the copper ions are only detected near the surface of the substrate, and the detected signals by the iron and the chromium are higher than that by the silicon. These facts mean that large amounts of plasmas have been deposited on the substrate, and the deposited layer have been analyzed with the SIMS. Here the detected silicon ions might be caused by sputtering the silicon substrate. Since the purpose of the experiment is analyzed the ions put into the substrate, we would like to perform analysis to deeper region of the substrate.

SUMMARY

We investigated the characteristics of the ion beams generated with the Point Pinch Diode which consisted of the semispherical mesh cathode and the flat anode. From the experimental results, it was verified that the ion beam was divergently extracted, but the current density of the ion beam was high around the diode axis. Due to this divergence, the current density of the ion beam decreased from several tens of kilo-amperes per square centimeters in the diode to 10–30 A/cm^2 on a diode axis at 190 mm from the top of the cathode. From the time of flight method, it was made clear that the metallic ions (e.g. Cu^{5+}) were contained in the ion beam as equally as the proton. In order to obtain the detail composition of the ion beam, the silicon substrate was analyzed with the secondary ion mass spectroscopy after the ion beam is put into the silicon substrate. This analysis might give rise to more exact composition of the ion beam, but the proper data have been not obtained up to now.

Acknowledgements

This work was performed under collaborative research of the National Institute for Fusion Science of Japan.

References

1. T. Tazima, M. Sato and H. Yonezu: Jpn. J. Appl. Phys., 25 (1986) L697.
2. T. Tazima and M. Sato: Proc. 8th Int. Conf. on High-Power Particle Beams, Novosibirsk (1990) 523.
3. M. Yatsuzuka, K. Azuma, M. Sato, Y. Hashimoto, I. Ohta, T. Kaneko, S. Nobuhara and T. Tazima: Proc. 8th Int. Conf. on High-Power Particle Beams, Novosibirsk (1990) 1235.
4. M. Sato: Jpn. J. Appl. Phys., 26 (1987) 927.
5. M. Sato and T. Tazima: Proc. 8th IEEE Pulsed Power Conf., San Diego (1991) 578.

EXPERIMENTAL STUDY OF THE PINCH-BEAM DIODE WITH THIN, UNBACKED FOIL ANODES

S.J. Stephanakis, J.R. Boller, G. Cooperstein,
B.V. Weber and F.C. Young

Plasma Physics Division
Naval Research Laboratory
Washington, DC 20375-5320

Abstract

Pinch-beam diodes are used extensively for intense electron and ion beam production. The large aspect ratio (diode radius/anode-cathode gap, R/D) diodes utilize the large electron path length (~R) relative to the ion path length (~D) to enhance ion production, over the bi-polar limit, by R/D. Pinch-reflex diodes further enhance the electron path length and thus the ion production efficiency by incorporating thinner-than-electron-range anode foils attached to a flat solid anode (a few mm behind the anode foils) by a small, on-axis conducting stalk. Electron reflexing is induced by the magnetic field generated by the return current through the conducting stalk. In both cases, large R/D's are needed for high ion production efficiencies thus necessitating low impedance ($Z \propto D/R$) diode operation. In this work, a new "backless" anode is studied in which the thin foil is held to the anode potential only along its circumference with the region behind it totally void. In this case, the self-pinching electrons are allowed to reflex between the real cathode and a self-formed virtual cathode behind the anode foil until either the virtual cathode dissipates or the electrons lose their energy in the foil. This diode has two potential advantages over conventional pinch-beam or pinch-reflex diodes. The ion production efficiency can be high even at high impedances (smaller R/D's) and the anode debris caused by the dissipating electron beam is substantially reduced. The experiments are carried out on the Gamble II generator (1.3 MV, 0.85 MA, 60 ns). When thin plastic anodes are used, efficient (~60%) positive ion production is observed. Thinner foils result in earlier ion production and larger time-integrated total ion energies. Furthermore, totally unbacked foils are significantly more ion-efficient at early times than standard reflexing (backed) foils of the same thickness. When high-Z metallic foils are used as anodes, the bremsstrahlung radiation provides an additional diagnostic for gaining insight into the dynamics of the electron orbits. Thin, unbacked foils produce more than twice the radiation compared with the same thickness foils backed with a low-Z material to prevent electron reflexing. The experimental results and their implications will be discussed.

Introduction

Ever since high-power, low-impedance relativistic electron beam generators came into existence over two decades ago, the pinch beam diode has been used extensively as the load for such generators. The generic diode consists of a field-emitting cathode separated from a typically flat metallic anode by an appropriate anode-cathode (A-K) gap. The field-emitted electrons originally flow across the A-K gap according to the Child-Langmuir law. As the current increases, the electron orbits start to bend radially toward the center of the diode due to their interaction with their self-generated azimuthal magnetic field. When the

current reaches the critical current value (i.e., the value at which the electron Larmor radius equals the A-K gap) the beam hugs the surface of the anode simultaneously creating an anode plasma. It is the ion space-charge from this anode plasma that allows the electrons to rapidly proceed to the center of the anode creating an intense pinch.[1] The impedance of such a diode is inversely proportional to the diode aspect ratio R/D (where R is the diode radius and D is the A-K gap) and is only weakly dependent on the diode voltage making it possible to match the generator impedance by simply choosing the appropriate diameter and A-K gap. Since the electron path length in a pinch beam diode is essentially equal to the diode radius R while the ion path length is D, large aspect ratio diodes are efficient ion beam producers, the ion production enhancement over the bi-polar limit being equal to R/D. Further enhancement of ion production can be accomplished by allowing the electrons to reflex through a thin anode foil on their way to a solid conducting anode center thus further increasing their path length. Such pinch-reflex diodes have been widely used[2] for various applications primarily in support of the light ion ICF program.

Recently, the need has arisen for light ion beams appropriate for material research applications such as surface modification, ablation and re-deposition for thin film manufacturing, etc. These applications, for the most part, require intense ion beams and minimal accompanying debris. Since in a pinch beam diode the electron flow is not totally magnetically insulated, about half of the available energy is deposited, via the electrons, on the anode vaporizing it and creating significant debris which eventually makes its way downstream onto the samples.

In this paper, we describe and characterize a modified pinch-reflex diode with an almost massless anode which, to a large extent helps alleviate the debris problem and we compare electrical characteristics of this new diode with the standard pinch-reflex diode.

Experimental Set-up

All the experiments described here were carried out on the Naval Research Laboratory's Gamble II 2 Ω generator operated in positive polarity. Typically, about 1.1 TW of electrical power was coupled to the load (1.3 MV, 0.85 MA) in ~60 nsec (FWHM of the power pulse) for a total coupled energy in excess of 60 kJ. About one-half of that power and energy was associated with the extracted ion beam which consists primarily of protons with a small percentage (<30%) of carbon ions.

The standard pinch-reflex diode configuration is shown in Figure 1a. The cathode is a thin (~3 mm) hollow cylinder 12.2 cm in diameter and the A-K gap in all cases was 5 mm. The anode consists of a 12.7 μm-thick polyethylene foil stretched taut across a 5-mm thick plastic ring at a diameter larger than the cathode diameter. A thin (178 μm) aluminum annulus with an inner diameter (i.d.) slightly smaller than the cathode i.d. is placed on top of the plastic foil across from the cathode tip. It was found that this annulus was necessary for establishing a well-defined equipotential surface at early times which helped ensure well-behaved, symmetrically-collapsing pinches. The vacuum gap between the anode foil and the anode back-plate was 5 mm and the current was returned via a central, 6.4 mm dia button as shown. Electrons emitted from the cathode tip, reflex through the plastic foil due to their interaction with the azimuthal magnetic field established by the current flowing through the central button. The ions created at and extracted from the anode plasma are accelerated across the diode vacuum gap, pass through a thinner-than-an-ion-range foil (2 μm polycarbonate) and are transported toward the target in current-and space-charge-neutralizing gas (typically, 1 Torr air). It was established that the vast majority of the debris created during a shot was due to the interaction of the electron beam with the anode structure, especially the central button and the solid anode backing-plate.

Shown in Figure 1b is the configuration of the new, low-debris diode. Note that the central anode button and the anode backing plate are totally eliminated. The region behind the anode-foil is evacuated and is large in volume so that the electrons are allowed to perform large orbits until they are reflected back by a self-generated virtual cathode. The location and time history of this virtual cathode has not been investigated. However, data clearly indicate that such a virtual cathode does exist and electrons do reflex through the anode foil. This is illustrated in Figure 2 where a comparison is made of the x-ray pulses generated by a diode configured as per Figure 1b but with the polyethylene foil replaced by a 12.7 μm-thick tantalum foil to enhance x-ray emission. Note that the unbacked foil generates about 2.5 times the x-rays per unit time than the same foil backed with a thick carbon block to prevent reflexing implying that the electrons had to make multiple passes through the thin foil before being collected.

Choosing the Optimum Unbacked Anode

Given the configuration of Figure 1b, we now proceed to optimize the anode for maximum ion production efficiency and ion energy content. This means optimizing the

thickness of the reflexing polyethylene foil and the thickness of the aluminum anode annulus. Three different foil thicknesses, namely 1.8 μm, 12.7 μm and 102 μm were investigated all with the same aluminum annular ring which was 178 μm thick. As seen in Figure 3a, the diode impedance behavior for all three foils was virtually identical. However, when the ion production efficiencies, defined as the ratio of the ion current to the total diode current, are compared (Figure 3b) it is seen that during the rise of the ion power pulse (which peaks at ~80 ns in all cases) thinner foil anodes are significantly more efficient than the 102 μm-thick foil. This leads to significantly higher total ion energies (>20%) for the thin foil anodes than the thicker foils as shown in Figure 3c. For convenience of handling and stretching, we choose the 12.7 μm polyethylene foil as the optimum.

Figure 4a compares the impedance characteristics of three unbacked anodes all using a 12.7 μm-thick polyethylene reflexing foil but with three different thicknesses of anode annular rings ranging in thickness from 0 to 1.6 mm. Note that the trend is for the impedance to be higher the thicker the metal annulus. Despite the higher impedance, the thicker rings make for a more efficient ion diode than the one with no ring whatsoever as is shown in Figure 4b. In addition to the fact that, as mentioned previously, the metallic rings provide a well-defined equipotential surface across the cathode tip, it is speculated that the presence of the sharp-inner-edge metal ring helps facilitate a more uniform and possibly earlier flashover on the plastic foil surface than would be the case without such a ring in place. Figure 4c compares the ion beam energy content for the three cases clearly showing ~20% higher energy for the 178 μm-thick annulus over the no-annulus case.

Thus, the unbacked anode of choice from the ion-production point-of-view is one that employs a 12.7 μm thick polyethylene reflexing foil after a 178 μm-thick aluminum annulus.

Comparison of Backed and Unbacked-Anode Diodes

We now proceed to compare the electrical and ion-producing characteristics of the standard pinch reflex diode of Figure 1a with those of the totally unbacked-anode reflex diode of Figure 1b. In both cases the anode foil was 12.7 μm-thick polyethylene with a 178 μm-thick aluminum annulus across the cathode tip. This comparison is illustrated in Figure 5 which shows essentially identical impedance histories but higher ion efficiency and ion energy content for the unbacked case.

Furthermore, Figure 6 clearly shows that the objective of debris mitigation, which to a large extent triggered this study, can be met by using the unbacked anode configuration.

Summary and Conclusions

We have shown that, in the absence of a well-defined electron current path behind the anode foil of a standard (backed) pinch-reflex diode, the electrons reflex between a virtual cathode (upstream of the foil) and the real cathode (downstream of the foil).

Furthermore, large-orbit electron reflexing through thin plastic, unbacked anode foils results in a very efficient light ion source even at high impedances and in an almost debris-free environment downstream of the diode as required for material study applications.

References

1. Shyke A. Goldstein and Roswell Lee, Ion-Induced Pinch and the Enhancement of Ion Current by Pinched Electron Flow in Relativistic Diodes," Phys. Rev. Lett. 35, 1079 (1975).

2. G. Cooperstein, S.A. Goldstein, R.A. Meger, D. Mosher, W.F. Oliphant, F.L. Sandel, S.J. Stephanakis, F.C. Young and H.V. Karow, "Light-Ion Production and Focusing with Pinch-Reflex Diodes," Proc. of Fourth International Topical Conf. on High-Power Electron and Ion-Beam Research and Technology, (Palaiseau, France, June 29-July 3, 1981), p. 53.

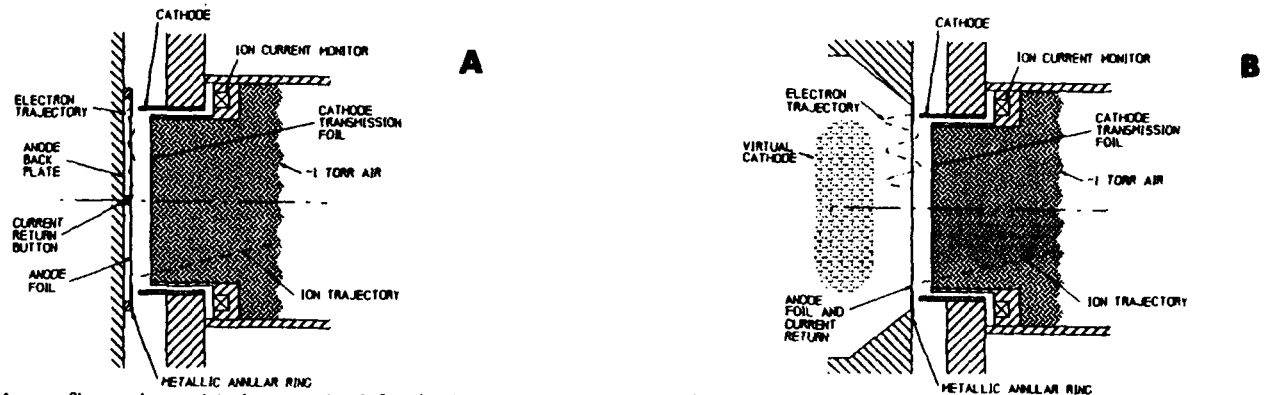

Figure 1. Diode configurations: (a) the standard (backed anode) pinch reflex diode; (b) the low-debris (unbacked anode) reflex diode.

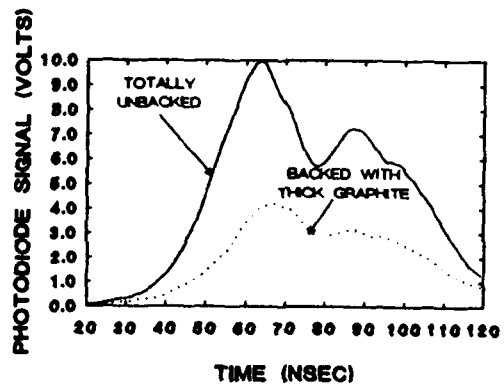

Figure 2. Comparison of x-ray output from thin Ta anodes, reflexing and non-reflexing.

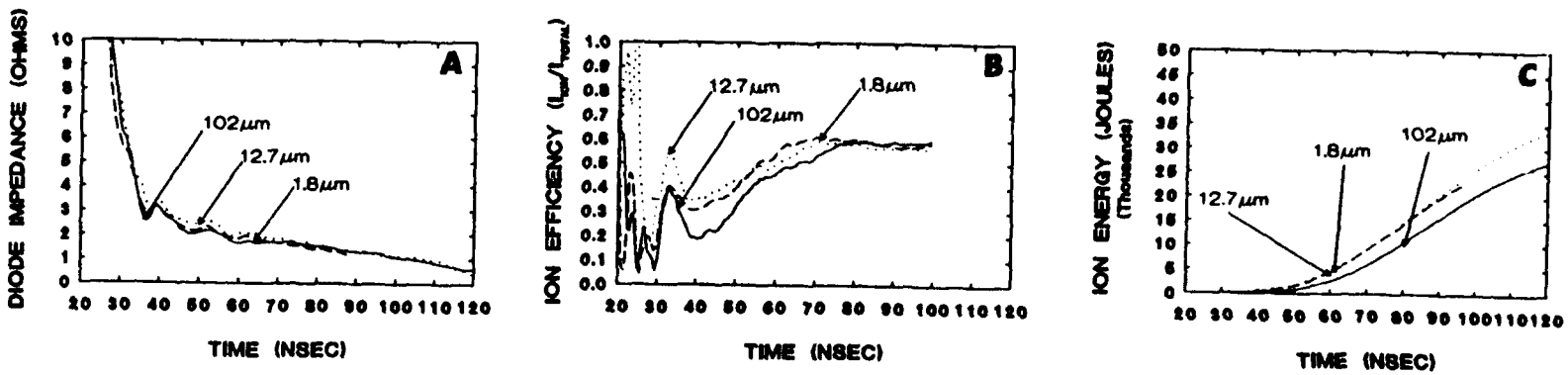

Figure 3. Low-debris diode reflexing foil thickness optimization: (a) impedance history; (b) ion efficiency; (c) ion energy.

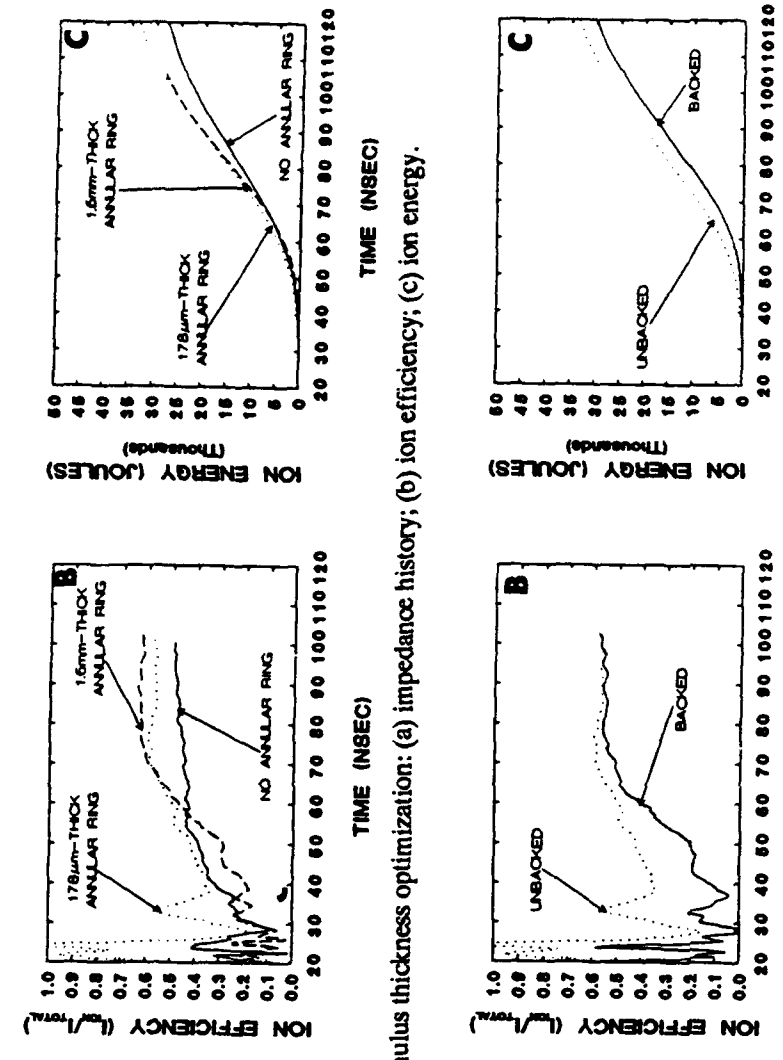

Figure 4. Low-debris diode anode-annulus thickness optimization: (a) impedance history; (b) ion efficiency; (c) ion energy.

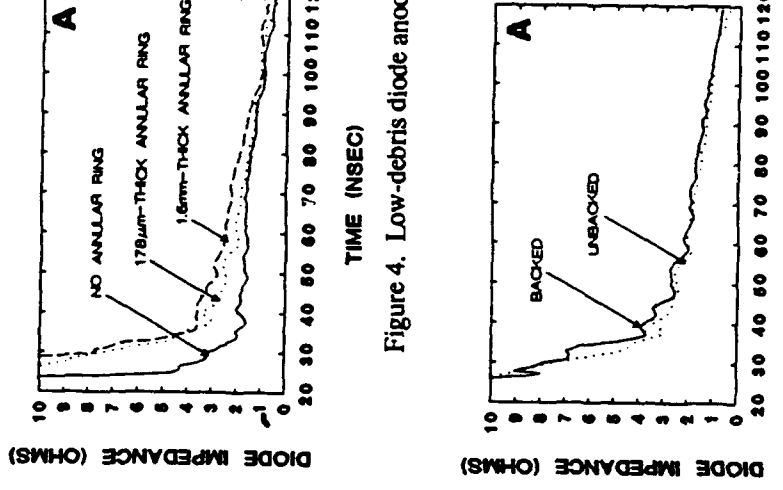

Figure 5. Comparison of standard pinch-reflex diode and optimized low-debris diode: (a) impedance history; (b) ion efficiency; (c) ion energy.

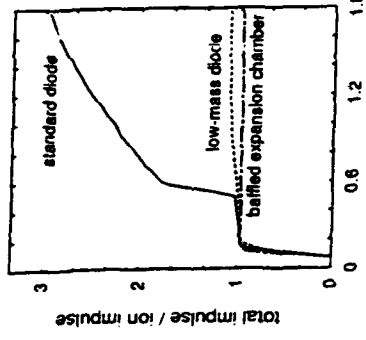

Figure 6. Debris impulse data showing debris reduction with optimized backless-anode diode.

EXPERIMENTS ON GENERATION OF HIGH POWER ION BEAM IN PLASMA-FILLED DIODE

V.M. BYSTRITSKII, A.V. KHARLOV, G.A.MESYATS,
A.V. MYTNIKOV, A.A. SINEBRJUKHOV
INSTITUTE OF ELECTROPHYSICS, 620219, ECATERINBURG, RUSSIA

ABSTRACT

The experimental results on High Power Ion Beams (HPIB) generation in plasma-filled spherical focusing diode with self magnetic insulation, which was placed for a load at nanosecond accelerator PARUS of 0.2 TW power and 60 ns pulse duration (in matched load case) are given. The regimes of plasma-filled diode operation and generation of ion beam were investigated. For optimal time delay between the plasma guns pulse and accelerator firing the stable operation in the plasma opening switch mode with power enhancement factor of 2.3 and efficiency of ion beam generation of 20-25% was obtained. The maximal value of the ion current density in the focal plane was reached 15 kA/cm^2.

I. INTRODUCTION

In recent time to increase the power of ion beams, generated in nanosecond direct action accelerators, the scheme including inductive storage and plasma opening switch (POS) is being widely used. As a rule the latter is placed upstreame of the diode load [1]. As it shown elsewhere, the using in this approach of passive anode plasma sources in the diodes results in lower efficiency of ion beam generation than without the switch coupled with shortening of the high voltage pulse (30-40 ns) applied to the diode and finite time delay between high voltage application and starting of the ion beam (15-20 ns). It indicates on the necessity of using diodes with active plasma sources to get the increase of ion beam generation efficiency, i.e. plasma must be produced in the diode prior to application of main high voltage pulse. The active anode plasma sources could be divided on two types : the sources with volume filling of the A-C gap [2,3](so-called plasma-filled diodes) and surface type sources,

producing thin plasma layer (;1mm) near the surface or at the surface of the anode [4]. Plasma-filled diodes represents more simple devices than the diodes with surface type of the plasma sources. Beside, it is very temptating to use the plasma-filled diode as plasma opening switch and the ion-load simultaneously avoiding in such approach the losses between the diode and the switch. Dynamics of the plasma-filled diode operation considerably differs from its passive anode-vacuum A-C gap analog. It is pertinent to the fact, that during the initial time the A-C gap is completely shorted with plasma having high conductivity and depending of the latter parameters, varios regimes of diode operation could be realised. The decisive impact on the plasma-filled diode is being produced by the circuit parameters in which diode is switched on. If the circut inductance is small ($L \ll R_g * T_g$), here L is the circuit inductance, R_g - generator impedance, T_g - the voltage pulse duration, then the diode works in the regime of smoothly rising impedance, for $L \gg R_g * T_g$ the diode works in the regime similar to the plasma opening switch (POS). The first regime was invesigated in many works [2,3]. It characterised by smooth rise of the impedance, voltage and current, which are near to the matched load values. The plasma filled magnetically insulated diode with externally produced B_r field was studied in [5]. The circuit parameters of respective scheme satisfied the condition of $L \simeq R_g * T_g$, though the regimes typical for POS operation were not obtained. It could be explained by the presence of external magnetic field, which impeded the plasma flow velocity and respectively - the velocity of cathode sheath expansion. In frame of this results the plasma filled diode operating in the self-insulated mode seems more promising.

Below the main results of experimental studies of generation and focusing of ion beam generated in the plasma-filled diode of spherical geometry with external source of anode plasma are given.

2. EXPERIMENTAL SETUP

The experiments were carried out on the accelerator PARUS with operational parameters of U_a= 0.8 MV, r= 2.8 Ohm, t=60 ns. The experimental scheme is given at Fig.1. The diode was of inverse pinch type having spherical shape. The anode and cathode were manufactured using cold forming from stainless steel of 1.5 mm thickness. The cathode radius made up 40 mm, anode radius 55 mm, the A-C gap respectively was equal 15 mm. The cathode and anode were provided by set of holes of 2 mm diameter, so that geometric transparency of each made up 50%. The plasma was injected from the anode side by 8 plasma guns of coaxial type, placed in the central part of the diode. The plasma guns were manufactured from the rf-50 Ohm cable. The distance between guns nozzles and anode surface equalled to 8 cm. This geometry provided the separation in the flight of neutral component from main plasma bunch.The feeding of the guns was provided by one capacitor of 3 mF, 50 kV. The plasma gun voltage made up 30 kV, the total gun current-70 kA, risetime-2 ms. Inductance in the diode circuit was equal to 140 nH.

2. EXPERIMENTAL RESULTS

2.1 Plasma source

The plasma dencity in the A-C gap was measured without firing of accelerator, using negatively biased CFC, which operated in the saturated regime of plasma probe. The density and velocity of plasma were 10^{14} cm^{-3} and 10^7 cm/s respectively for charging voltage of 30 kV. The protons concentration in the plasma could be estimated using he following expression based on the assumption of space charge limited current emission from the plasma boundary:

$$C_p \approx 1/(1+1/[(Z_i * M_p/M_i)^{0.5} * p/(1-p)])$$

here, p- is the proton fraction of the total current (measured experimenally); M_i- the average mass of the non-protonic fraction, M_p- proton mass, Z_i- the average charge of nonprotonic ions. In our case, M_i=12, Z_i=+2 (C^{+2}), p=0.4 (from experiment) we get C_p=20% in plasma, generated by plasma

guns.

The best opening was measured at t_d= 2.2÷2.4 ms, the respective current amplitude was equal to 250÷260 kA. For t_d > 2.6 μs the length of the conduction phase (before opening) dramatically increased and for t_d > 3.5 μs the diode was short circuited through fall pulse duration. The waveforms of voltage and diode power for optimal firing are given at Fig.2. The matched load voltage and power are also shown in Fig.2. These data are compared to numeric model predictions on the right-hand side of Fig.2. The maximum voltage at the diode reached 2.3 MV, peak value of power reached 0.5 TW, which corresponds to enhancement factor of 2.7 and 2.3 respectively in comparison with matched load case. In the time delay range of < 2.4 μs the diode displayed stable operation with jitter of voltage and current amplitudes not more than 15% on the firing to firing base. In the range of 2.6 μs < t_d < 3 μs the reproducibility of operation deteriorated which was related with sharp change of diode parameters.

2.3 Investigation of generation and focusing of ion beam. Calorimetric measurements of total ion beam energy proved to be unreliable due to high current density of the beam and respective ablation of the material from the electrode surface. To account for this phenomenon the beam was attenuated by several meshes placed in front of the calorimeter. In these measurements we got the estimation of ion beam energy penetrating in the cathode cavity on the level of 1 kJ. Taking in the account the geometric transparency of the cathode we got the total beam energy of > 2 kJ, which corresponds to > 20% of ion beam efficiency of generation. The waveforms of ion density currents are given at Fig.4 for various time delays taken with CFC. The CFC were placed at distance of 1 cm in the cathode cavity from the surface of the latter. For optimal time delay of $t_d \simeq$ 2.2:2.4 ms the maximum current density on the cathode surface made up 0.5 kA/cm^2, which agrees with calorimetric measurements. The energy of ion beam, entering through the hole of 1 cm diameter placed at the

focal plane, measured by the calorimeter in the form of cup made up 500 J, which corresponds to ion current density of 15 kA/cm^2. The activation diagnostics based on reaction $^{12}C(p,g)^{13}N(b^+)$ gave in the measurements ; 6 kA/cm^2 of protons with energy highher than 500 keV, which corresponds to 40% of the protons in the beam. Visual traces of the electron beam losses at the anode surface corresponded to azimuthaly uniform character of the former at the outer edge of the latter.

In experiments with plasma-filled diode the stable operation in the plasma opening swich mode with power enhancement factor of 2.3 and efficiency of ion beam generation of 20:25% was obtained. The above said regime differs considerably from observed in earlier plasma-filled diode such as AMPFION [2] or gas-filled diode, investigated in Cornell Univercity [3] where no power enhancementt was observed. The experimental results agree with calculations, following zero-dimencional model of plasma erosion in the diode. The further improvement of this type diode operation could be reached with transition to single-species plasma composition, for example using the gus-puff plasma guns instead of surface discherge type .

The authors would like to express their gratitude for technical asisstance and useful discussions to DDr. Yakov Krasik, Sergei Volkov and Igor Lisitsyn.

REFERENCES

1. B.V. Weber et al. 1987 IEEE Transactions on Plasma Science, V. ps-15,$N^0$6, p.635.

2. C.W Mendel & G.S. Mills 1982 J.Appl.Phys. 53,7265

3. J.B. Greenly et al.1988 J.Appl.Phys. 63,1872

4. P.L Dreike & G.C. Tisone 1986 J.Appl.Phys. 59,371

5. Bystritskii V.M.et al.Proc. of 7th Allunion Sump. on High Current Electronics, 1988, Tomsk, V.2 (Sov.), P.94.

6. S.A. Goldstein et al., 1984, J.Appl.Phys., 56, 774.

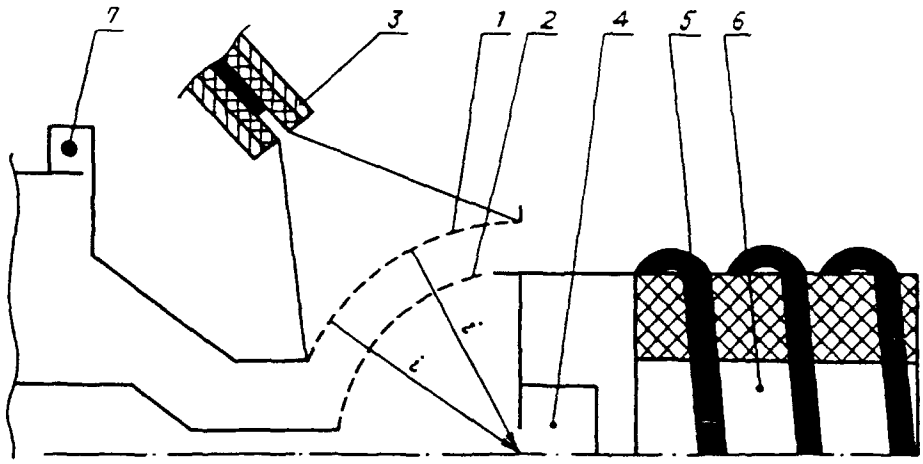

Fig.1. Scheme of the experiment with plasma-filled diode 1- anod, 2- cathode, 3- plasma guns, 4- diagnostic devices, 5- transition insulating inductivity for diagnosttic output, 6- active voltage divider, 7- Rogovsky coils.

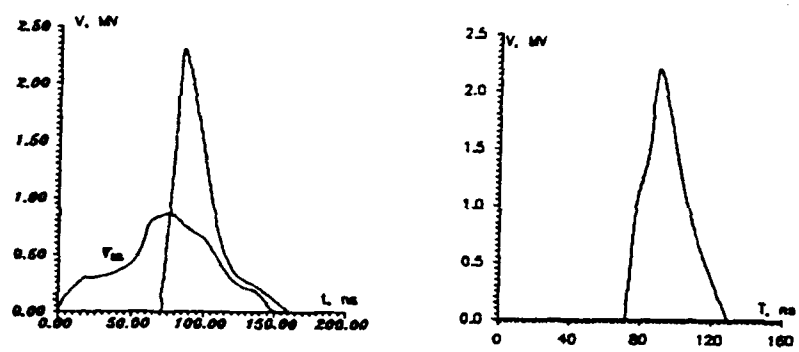

a

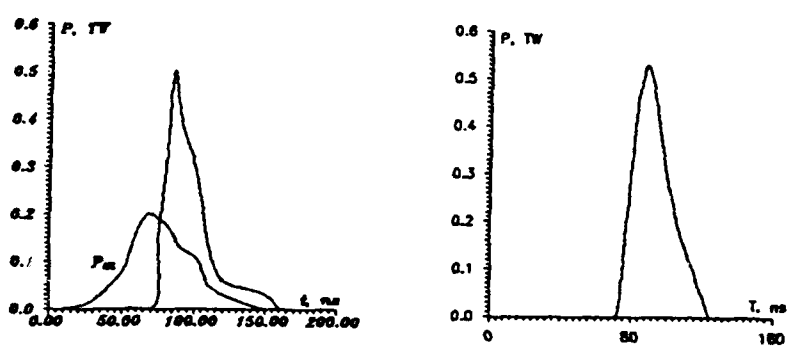

b

Fig.2 a- Load voltage compared with matched load voltage , b- Load power compared with matched load power.

LIGHT ION DRIVER RESEARCH FOR INERTIAL FUSION

Shuji MIYAMOTO, Kazuhito YASUIKE, and Sadao NAKAI
Institute of Laser Engineering, Osaka University
2-6 Yamada-oka, Suita, Osaka 565, JAPAN
Kazuo IMASAKI and Chiyoe YAMANAKA
Institute for Laser Technology
2-6 Yamada-oka, Suita, Osaka 565, JAPAN

Abstract

The generation of low emittance beam (or low divergence beam) at the diode is most important issues to use the light ion beam as an energy driver of inertial fusion energy. We have been investigated a two-stage ion diode which suits to an induction adder accelerator Reiden-SHVS (4-MV, 100-ns). In two-stage diode, the output beam of first stage is optionally stripped charge and is accelerated at the second (main) diode efficiently with improving the beam emittance. Beam trajectories and emittances in the two-stage diode were observed in time integrated manner. The measured beam trajectories were compared with a numerical calculation. Even in the large virtual anode limit, in which condition partial ions are reflected back by the virtual anode, no significant growth of local beam divergence of non-reflected parts of beam was observed. An emittance of injected beam was improved about factor 1.6 by acceleration at second with the first and second diode voltage of 0.6 and 1.2-MV, respectively. This improvements factor is in agreement with a predicted value.

Introduction

Recent implosion experiments by intense laser beams [1] give us a great confidence that the ignition and significant gain of inertial confinement fusion will be achieved by a driver energy of 5-10 MJ. Light ion beam driver based on a pulsed power technology are a favorable driver for energy application due to its high efficiency to generate and low cost to construct.

The key issues to use light ion beam as an energy driver of inertial fusion energy is to achieve high intensity focus. The improvement of beam emittance (or beam divergence) at the diode is important. We have been investigated a two-stage ion diode experimentally on an induction adder accelerator Reiden-SHVS (4-MV, 100-ns) [2]. Two-stage diode mitigates the requirement to the single ion diode. The output beam of first stage is optionally stripped charge and is accelerated at the second (main) diode efficiently with improving the beam emittance. Still more, the second diode is operated as an ion beam injected diode. In this operation mode, an electron sheath is controlled by the injected ion flux and it may be possible to avoid the anomalous growth of beam divergence which may be caused by an electron sheath induced instabilities.[3]

Previous two-stage diode experiments [4] showed the diode stability condition relating to a macroscopic instability of the ion beam injected diode. [5] Figure 1 shows a conceptual drawing of the operation region in ion beam injected diode. In unstable region, ion beam injected diode shows an oscillative behavior due to a space charge instability. This region can not use for our purpose. To avoid extracting unwanted ions from the anode foil of ion beam injected diode, we mast operate with the virtual anode formation region. In this paper, we intend to study the effect of virtual anode on the beam trajectory and on the local beam divergence in the ion beam injected diode. The measured beam trajectories were compared with a numerical calculation. Even in the large virtual anode limit, in which condition ions are partially reflected back by the virtual anode, no significant growth of local beam divergence of non-reflected parts of beam was observed. A measured improvement factor of beam emittance was about 1.6 is in agreement with a predicted value assuming the first and second diode voltage of 0.6 and 1.2-MV, respectively.

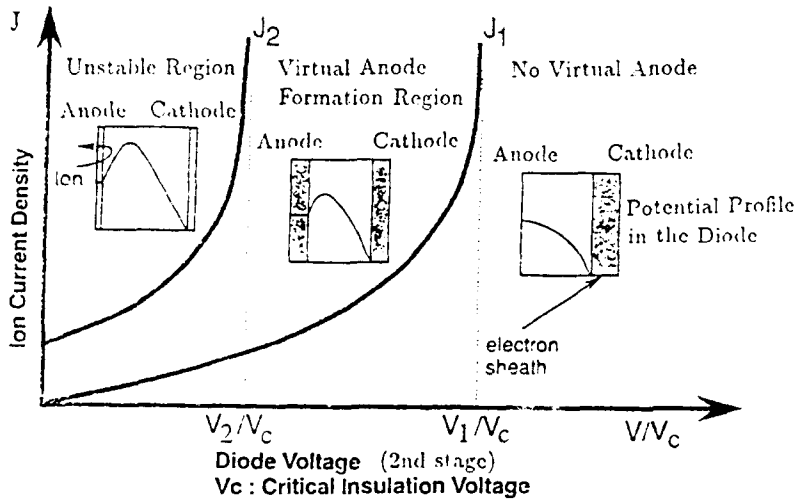

Fig.1 Conceptual drawing of the operation region in ion beam injected diode. [5]

Experimental Apparatus

Experiments were performed on Reiden-SHVS [4] induction adder accelerator. A water line pulsed power produces an 150 to 500-kV, 100-ns pulse, and is divided to 32 50-Ω high voltage cables. Eight induction cavities are powered by the pulse line through four cables each. Each induction cavities are located with two Metglas cores with a total flux swing of 0.05-Vsec.

In two stage diode operation, positive and negative center electrodes are extended from both side. Grounded electrode which is located between two extended electrodes is combined a cathode of first diode and an anode of second diode. The line matching impedance of each diode are 50-Ω. The typical operation voltage is 0.6 to 2-MV per diode.

The diode utilize applied, B_r-field extraction ion diodes. The schematic configuration of the diodes and diagnostics are shown in Fig.2. The applied field coils are charged in

series with a 400-μF capacitor bank that is fired 240-μs before the diode pulses. The diode insulating-B_r field is produced by four coils. Two 6-turn outer and two 12-turn inner field coils generate positive radial magnetic field in first stage and negative in second stage. The diode gap and insulation field of first diode are AK1 = 0.9-cm and B1 = 7-kG, respectively. In second diode, the diode gap AK2 (the insulation field B2) is varied from 1.0-cm (8.7-kG) to 3.5-cm (6-kG). The first stage diode utilize only an outer cathode tip of 8.0-cm in radius to avoid a large electron current loss from an inner cathode tip. The second diode utilize an outer and an inner cathode tip of 7.7-cm and 5.8-cm in radius, respectively. The corresponding critical insulation voltages are 1.4-MV for the first diode and 2.2 to 5.8-MV for the second diode. The anode is made from aluminum with paraffin filled groove of 0.5-mm width, 2-mm depth and 0.5-mm spacing. The active anode area is 100-cm^2.

Diode currents are measured by dB/dt loops. Each induction cavity voltages are measured by resistive voltage dividers. Diode voltages are estimated from summing up the cavity voltages with an inductive correction. Ion current density is measured by a biased charge collector behind the second stage diode. Figure 3 shows typical diode voltage, current and ion current density for AK2 = 1.0-cm.

The time integrated beam trajectories and local beam divergences are measured by two shadow boxes (SB1 and SB2). The shadow box consists of three sets of five 1-mm-diameter radial aperture array on a 1-mm-thick stainless steel plate and an acrylic witness plate located 23-mm behind the aperture plate. The radial position of apertures in the shadow box are r1=60.5-mm, r2=64.5-mm, r3=68.5-mm, r4=72.5-mm and r5=76.5-mm. Each shadow box covers one-fourth of total beam area and are set at different azimuthal positions.

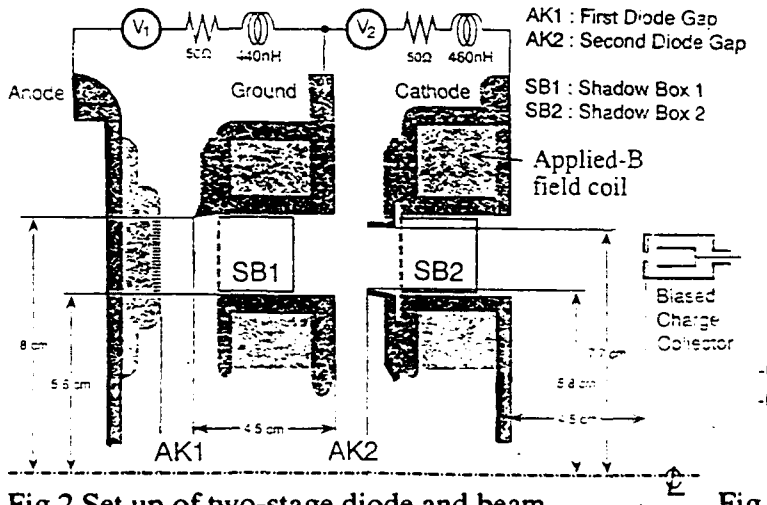

Fig.2 Set up of two-stage diode and beam diagnostics. Each diode is powered by four stage induction adder.

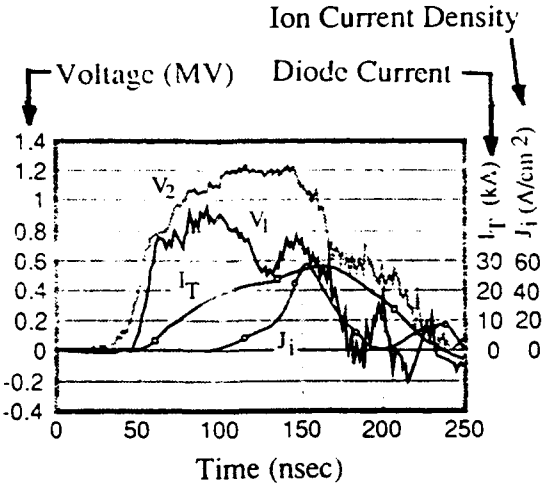

Fig.3 Typical diode voltage, diode current and ion current density for AK1 = 0.9 cm, AK2 = 1.0 cm.

Experimental Results

Figure 4 shows the measured beam damages on the witness plate of shadow box. The left image (a) was taken at first stage shadow box (SB1), the middle (b) at second stage (SB2) with AK2 = 1.0-cm and the right (c) at second stage (SB2) with AK2 = 3.5-cm. (a) and (b) show images of r4 and r5, (c) shows r2 and r3. The last case (c), the diode was operated with in an macroscopic unstable condition.[4] The solid circles in the photographs represent the position of pinhole of 1-mm-diameter on the front plate of SB's. Ion current density measured by a biased charge collector was increased about 20 % with adding the second stage diode of the gap AK2 = 1.0-cm. This may be the result of divergence improvement at the second diode. With increasing the gap, the transmitted ion current decreased. For AK2 = 3.5-cm, the transmitted ion current was 20-25 % of the injected current. This large reduction of transmitted current is due to the macroscopic instability of ion beam injected diode. Too large virtual anode reflect the injected ions and limit the transmission of ions.

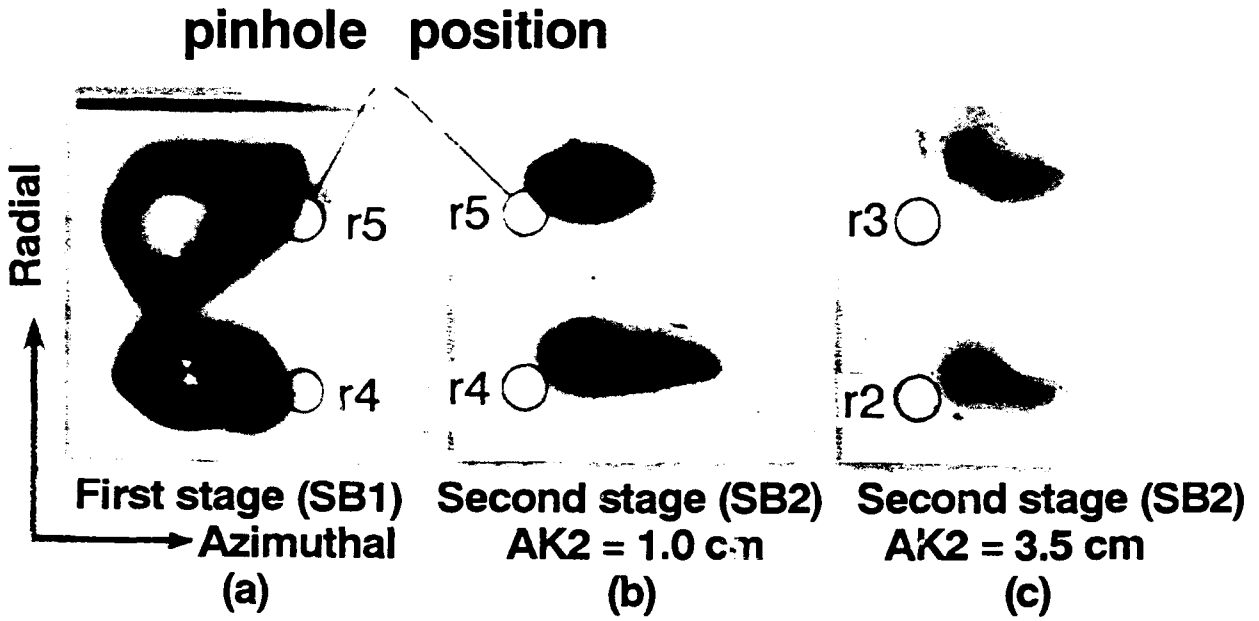

Fig.4 Measured beam damages on the witness plate of shadow box.

The azimuthal spread of beam damages in the shadow box are caused by not only the local beam divergence but also by the non-zero canonical momentum of beam in the shadow box and the energy spread of beam with time. The radial extent of the damage indicates the local beam divergence.

The numerical calculations of beam trajectory were done using a 2-D magnetic field distribution simulation to compare with measured trajectories. In calculation, the equi-po-

tential line in diodes should be parallel with the anode surface. The beam rotates to negative azimuthal direction in the first diode and rotates to positive direction in second diode due to the radial magnetic field. A centrifugal force defocus the beam and an azimuthal magnetic field in the diodes focus the beam. A solenoidal magnetic field between the inner and outer coils push the outer beam to inner direction and inner beam to outer direction.

Figure 5 shows experimental and numerical beamlet angle in shadow box. Experimental data are average over 2 shot and take a center position of beam damage. The numerical calculation assumes the voltage of first diode 0.64-MV and second diode 1.2-MV with AK2 = 1.0-cm. Large discrepancy (~40-mrad) at r2 and r4 of radial beam angle in SB1 indicate the convex shape of electron sheath in the first diode. This is in agreement with shape of magnetic field calculated by a magnetic field diffusion code. In second diode, experimental data show -35 mrad at r1 and +50 mrad at r5 shift from the calculated value. These large shifts are results of transport of beam from r2 and r4 in SB1. In addition, the whole beam deflected about 10 mrad at second stage diode.

For calculating a beam trajectory in unstable condition, an analytical solution of virtual anode potential profile was used. This analytic potential is maximum value of virtual anode. A small artificial potential (2% of total potential) was added and subtracted on the virtual anode to see the reflected and transmitted ions on the virtual anode. The reflected ions at the virtual anode returns back to the first diode, and once more reflected at the first diode.

The radial and the azimuthal trajectory of reflected and transmitted beam indicate different trajectory in the shadow box SB2. In Fig.6, calculated beam damages on the witness plate at SB2 for AK2 = 3.5-cm are shown. Reflected and transmitted beam are

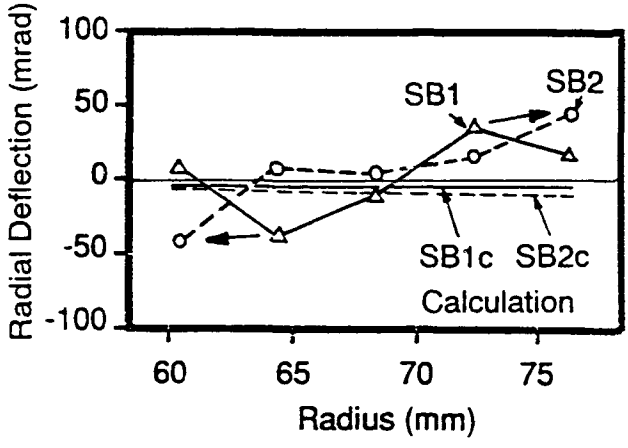

Fig.5 Radial deflection angle of beam trajectory at different radial position. Data denoted SB1 and SB2 were measured by shadow boxes SB1 and SB2. Subscript c means calculated value.

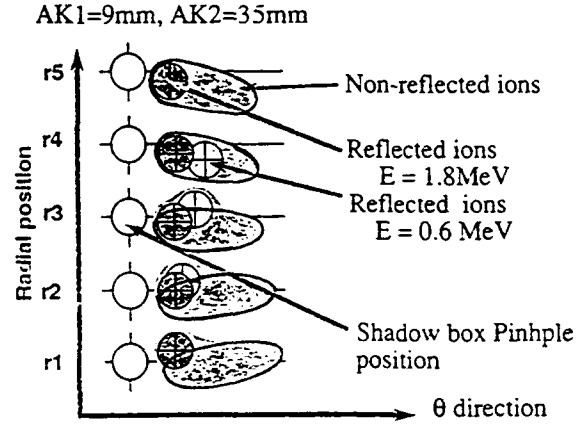

Fig.6 Calculated beam damage on the witness plate of SB2 for AK2 = 3.5 cm. Reflected and Transmitted ions show different trajectories.

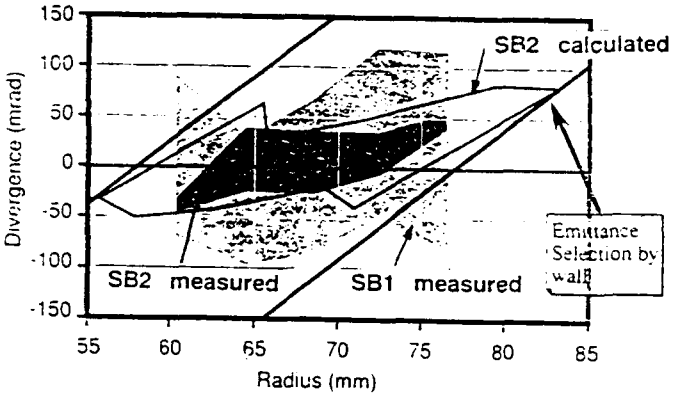

Fig.7 Emittance plots measured by first and second shadow boxes. Solid line is a calculated emittance plot at second shadow box based on the measured emittance at first shadow box. The assumed reduction factor of beam divergence is 1.6.

superimposed. Comparison with experimental data, Fig.4 (c), this shows the upper left damage in experiments should be a damage due to the reflected beam. In transmitted parts of beam decreases the intensity but they show no significant effect on beam divergence even with a maximum virtual anode condition.

Figure 7 shows a emittance plot of first and second stage diode taking the maximum divergence measured by shadow box. Gray and black area are emittance at first and second shadow box, respectively. Solid line is an emittance plot at second shadow box calculated from the measured emittance of first shadow box. The normalized emittance conservation and 0.64-MV for first and 1.2-MV for second diode voltage were assumed. This means that the reduction factor of divergence $\beta_2\gamma_2/\beta_1\gamma_1 = 1.6$ was assumed, where b and g are ion velocity and its relativistic mass factor, respectively. Calculated one is also sifted +10 mrad to compare with measured value. Outer and inner edge of the beam shows smaller divergence than calculation. This may be due to the reduction of intensity by wall and cathode tip which results under estimation of beam divergence in shadow box. Then the improvements of beam emittance (or local beam divergence) is in good agreements with a calculated value.

Further precise quantitative estimation of the effect of two-stage acceleration on the beam divergence should be made by a novel beam divergence diagnostics including time and space resolusion.[6]

References

[1] S.Nakai et al, „Proceedings of 13 th International Conf. on Plasma Phys. and Controlled Thermonuclear Fusion Research", Washington, DC, USA, 1-6 Oct.,**IAEA-CN-53/B-1-3** (1990).
[2] S.Miyamoto et al, ibid, **IAEA-CN-53/B-3-1** (1990).
[3] S.A.Slutz and M.P.Desjarlais, J.Appl.Phys., **67**, 11, pp.6705-6717 (1991).
[4] S.Miyamoto et al, „Proceedings of 8th International Conf. on High-Power Particle Beams", Novosibirsk, USSR, 2-5 July, Vol.1, pp.190-198 (1990).
[5] M.P.Desjarlais et al, Phys. Rev. Lett., **67**, 22, pp.3094-3097 (1991).
[6] K.Yasuike, S.Miyamoto et al, appear in this conference.

FAST MAGNETIC FIELD PENETRATION INTO AN INTENSE NEUTRALIZED ION BEAM

R. Armale and N. Rostoker, University of California, Irvine, CA 92717

Abstract

Experiments involving propagation of neutralized ion beams[1] across a magnetic field indicate a magnetic field penetration time determined by the Hall resistivity rather than the Spitzer or Pedersen resistivity. In magnetohydrodynamics the Hall current is negligible because electrons and ions drift together in response to an electric field perpendicular to the magnetic field. For a propagating neutralized ion beam, the ion orbits are completely different from the electron orbits and the Hall current must be considered. There would be no effect unless there is a component of magnetic field normal to the surface[2] which would usually be absent for a good conductor. It is necessary to consider electron inertia and the consequent penetration of the normal component to a depth c/ω_p. In addition it is essential to consider a component of magnetic field parallel to the velocity of the beam which may be initially absent, but is generated by the Hall effect. The penetration time is determined by whistler waves rather than diffusion.

Introduction

In magnetohydrodynamics Ohm's law is $\mathbf{E} + \frac{1}{c}\mathbf{V} \times \mathbf{B} = 0$ i.e. the fluid is considered to be a perfect conductor. To include finite resistivity Ohm's law is employed in the form $\mathbf{J} = \sigma\left(\mathbf{E} + \frac{1}{c}\mathbf{V} \times \mathbf{B}\right)$. The Hall effect (or the antisymmetric part of the conductivity tensor) is omitted. This is appropriate because magnetohydrodynamics is based on an expansion in the mass to charge ratio m/e to the lowest order in which m and e do not appear explicitly. To this order the electron and ion $\mathbf{E} \times \mathbf{B}$-drifts are the same and there is no Hall current. For a neutralized ion beam the ions have energies of hundreds of keV and the electrons tens to hundreds of ev. The electron and ion orbits are completely different and the ion orbits are not well described by the drift approximation. The Hall effect may not be neglected. Ion motion may often be neglected and this regime is called electron magnetohydrodynamics in the Soviet literature.[3] In the present case the ion motion is assumed to be frozen. The problem of field penetration is treated with Maxwell's equations and Ohm's law in the form[4]

$$\frac{m}{ne^2}\frac{\partial \mathbf{j}}{\partial t} + \eta \mathbf{j} + \frac{\mathbf{j} \times \mathbf{B}}{nec} = \mathbf{E} + \frac{\mathbf{V} \times \mathbf{B}}{c} + \frac{\nabla P_e}{ne} \tag{1}$$

$\eta = (m/ne^2\tau_e)$ is the resistivity, n = plasma density, τ_e = electron-ion collision time, $\mathbf{B}$ = magnetic field, E = electric field, $\mathbf{j}$ = current density, $\mathbf{V}$ = fluid velocity, and P_e = electron pressure; this term will be neglected.

Combining Maxwell's equations $\nabla \times \mathbf{B} = (4\pi/c)\mathbf{j}$ (neglecting displacement current) and $\nabla \times \mathbf{E} = -\partial\mathbf{B}/c\partial t$ and Eq. (1) an equation is obtained for the magnetic field:

$$\frac{\partial \mathbf{B}}{\partial t} = \nabla \times (\mathbf{V} \times \mathbf{B}) + \frac{c^2\eta}{4\pi}\left[1 + \tau_e \frac{\partial}{\partial t}\right]\nabla^2\mathbf{B} - \frac{c^2}{4\pi}\nabla \times \left[\frac{1}{nec}(\nabla \times \mathbf{B}) \times \mathbf{B}\right] . \qquad (2)$$

In the following we shall consider solutions of Eq. (2) that correspond to neutralized ion beams. A slab model illustrates the fact that the classical diffusion rate obtains unless there is a normal component of the magnetic field. Then a cylindrical model of a beam propagating in a transverse magnetic field is treated, in which case there is a normal component with the result that the Hall effect is important in determining the penetration time of the magnetic field.

1. Slab Model

This model is illustrated in Fig. 1. All quantities depend only on x and t. $\mathbf{B} = \mathbf{e}_z B_z(x,t)$ and $\mathbf{V} = \mathbf{e}_y V_0$. Equation (2) for this case is

$$\frac{\partial B_z}{\partial t} = \frac{c^2\eta}{4\pi}\left[1 + \tau_e \frac{\partial}{\partial t}\right]\frac{\partial^2 B_z}{\partial x^2} . \qquad (3)$$

For initial condition assume

$$\begin{aligned} B_z &= B_{ex} + b_z \\ B_{ex} &= B_0\Theta(t) \qquad (3.1) \\ b_z &= 0 \qquad \text{when } t \le 0 . \end{aligned}$$

Rather than treat a beam with a front, we consider that the external magnetic field is turned on at $t = 0$. $\Theta(t)$ is, for example, a unit step function. The field, due to beam currents, is initially zero. It is convenient to introduce orthonormal functions that satisfy the boundary conditions $b_z(L/2,t) = b_z(-L/2,t) = 0$, i.e. $\Phi_n = \sqrt{2/L}\cos k_n x$, $k_n = (2n+1)\pi/L$, $n = 0,1,2\ldots$. Assume $b_z = \sum_n a_n(t)\Phi_n(x)$, substitute Eq. (3):

$$\frac{\partial a_n}{\partial t}\left[1 + Dk_n^2\tau_e\right] + Dk_n^2 a_n = -B_0\delta(t)\langle\phi_n|1\rangle$$

$$b_z(x,t) = -B_0\sum_n \frac{\langle\phi_n|1\rangle}{1 + Dk_n^2\tau_e}\exp\left\{\frac{-Dk_n^2 t}{1 + Dk_n^2\tau_e}\right\}\Phi_n(x) \qquad \text{for } t > 0 \qquad (4)$$

$D = c^2\eta/4\pi$ and $\langle\varphi_n|1\rangle = 2\sqrt{2/L}(-1)^n/k_n$. For $t = +0$ in Eq. (4), the series can be summed to give

$$B_z = B_0 + b_z = B_0\left\{\frac{[\cosh(x\omega_p/c)]}{[\cosh(L\omega_p/2c]}\right\} \tag{5}$$

which is plotted in Fig. 1 along with the corresponding result when electrons inertia is neglected. This illustrates diamagnetism where the initial magnetic field penetrates to a depth of order $c/\omega_p = \sqrt{D\tau_e}$ which is about 2cm in a typical ion beam experiment. This can be a significant fraction of the beam radius.[1]

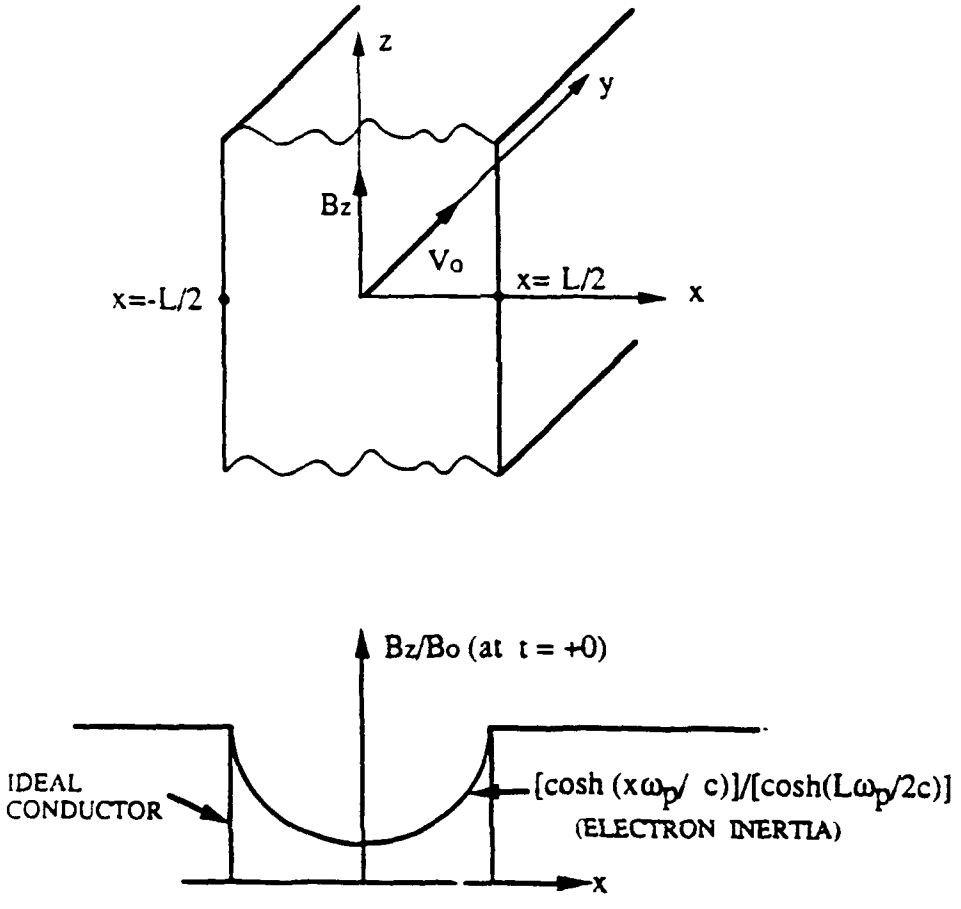

Fig. 1 Slab Mode of a Neutralized Ion Beam

To consider the effect of a magnetic field normal to surface of the beam, assume

$$\mathbf{B} = \mathbf{e}_x B_\perp + \mathbf{e}_y B_y(x,t) + \mathbf{e}_z B_z(x,t)$$

$B_\perp$ is assumed to be constant, and $\mathbf{V} = \mathbf{e}_y V_0$. Equation (2) reduces to two equations

$$\frac{\partial B_y}{\partial t} = \frac{c^2}{4\pi}\eta\left[1 + \tau_e\frac{\partial}{\partial t}\right]\frac{\partial^2 B_y}{\partial x^2} + \frac{c^2}{4\pi}\frac{B_\perp}{nec}\frac{\partial^2 B_z}{\partial x^2} \tag{6}$$

$$\frac{\partial B_z}{\partial t} = \frac{c^2}{4\pi}\eta\left[1 + \tau_e\frac{\partial}{\partial t}\right]\frac{\partial^2 B_z}{\partial x^2} - \frac{c^2}{4\pi}\frac{B_\perp}{nec}\frac{\partial^2 B_y}{\partial x^2} . \tag{7}$$

The last term in Eqs. (6) and (7) are due to the Hall effect. Assume the same initial conditions as Eq. (3) — i.e. only B_z is switched on. Because of the Hall coupling term there will be a B_y component even if it is initially zero. The solutions are

$$B_y = B_{0z}\sum_n \frac{2}{k_n L}\frac{(-1)^n e^{-t/\tau_n}}{(1 + Dk_n^2\tau_e)}\left[\sin(\omega_n t - k_n x) + \sin(\omega_n t + k_n x)\right] \tag{8}$$

$$B_z = B_{0z}\left\{1 - \sum_n \frac{2}{k_n L}\frac{(-1)^n e^{-t/\tau_n}}{(1 + Dk_n^2\tau_e)}\left[\sin(\omega_n t - k_n x) + \cos(\omega_n t + k_n x)\right]\right\} \tag{9}$$

$\omega_n = D_H k^2/(1 + Dk_n^2\tau_e)$ where $D_H = c^2\eta_H/4\pi = cB_\perp/4\pi ne$; $\tau_n = (1 + Dk_n^2\tau_e)/Dk_n^2$. For low n modes $n = 0, 1$, $\omega_n \cong (\Omega_\perp/\omega_p^2)(ck_n)^2$ where $\Omega_\perp = eB_\perp/mc$, and $\tau_n \cong \omega_p^2\tau_e/(ck_n)^2$. Equations (8) and (9) describe whistler waves that traverse the beam and are slowly damped at the same rate as Eq. (4). If B_y, B_z are observed as a time average and $\omega_n\tau_n \gg 0$, after a few whistler periods $2\pi/\omega_n$, $B_y \cong 0$ and $B_z \cong B_{0z}$.

For a slab model the normal component $B_x = B_\perp$ must be constant and this does not correspond to the experiments with beams. We therefore consider a cylindrical model as illustrated in Fig. 2. The magnetic field $\mathbf{B} = B_0\mathbf{e}_z$ is turned on at $t = 0$. For an ideal conductor there is no normal component of $\mathbf{B}$. If electron inertia is included as in Fig. 2 there will be a variable normal component to a depth of order c/ω_p at $t = +0$ and the normal component will penetrate along with other components. The differential equations corresponding to Eqs. (6) and (7) will be written in dimensionless variables by using the beam radius 'a' for length units, the diffusion time $\tau_0 = 4\pi a^2/\eta c^2$ for time units and B_0 for magnetic field units.

$$\frac{\partial A_z}{\partial \tau} = \left[1 + \left(\frac{c}{a\omega_p}\right)^2\frac{\partial}{\partial \tau}\right]\nabla^2 A_z - \frac{\eta_H}{\eta}(\hat{\mathbf{B}}\cdot\nabla)\hat{B}_z - \rho\sin\theta\,\delta(\tau) \tag{10}$$

$$\frac{\partial \hat{B}_z}{\partial \tau} = \left[1 + \left(\frac{c}{a\omega_p}\right)^2\frac{\partial}{\partial \tau}\right]\nabla^2\hat{B}_z + \frac{\eta_H}{\eta}(\hat{\mathbf{B}}\cdot\nabla)\nabla^2 A_z \tag{11}$$

$\hat{\mathbf{B}}\cdot\nabla = \hat{B}_\rho\frac{\partial}{\partial\rho} + \frac{\hat{B}_\theta}{\rho}\frac{\partial}{\partial\theta}$ and $\nabla^2 = \frac{1}{\rho}\frac{\partial}{\partial\rho}\rho\frac{\partial}{\partial\rho} + \frac{1}{\rho^2}\frac{\partial^2}{\partial\theta^2}$, $\eta_H = \frac{cB_0}{4\pi ne}$, $\tau = t/\tau_0$, $\rho = r/a$, and $\hat{\mathbf{B}} = \mathbf{B}/B_0$. $\hat{b}_r = \partial A_z/\rho\partial\theta$, $\hat{b}_\theta = -\partial A_z/\partial\rho$, $\hat{\mathbf{B}}_r = \cos\theta\Theta(t) + \hat{b}_r$ and $\hat{B}_\theta = -\sin\theta\Theta(t) + \hat{b}_\theta$.

$\hat{B}_z = \hat{b}_z$. Previously these equations have been solved[5] with $\eta_H = 0$, $\hat{B}_z = 0$. We assume solutions of the form

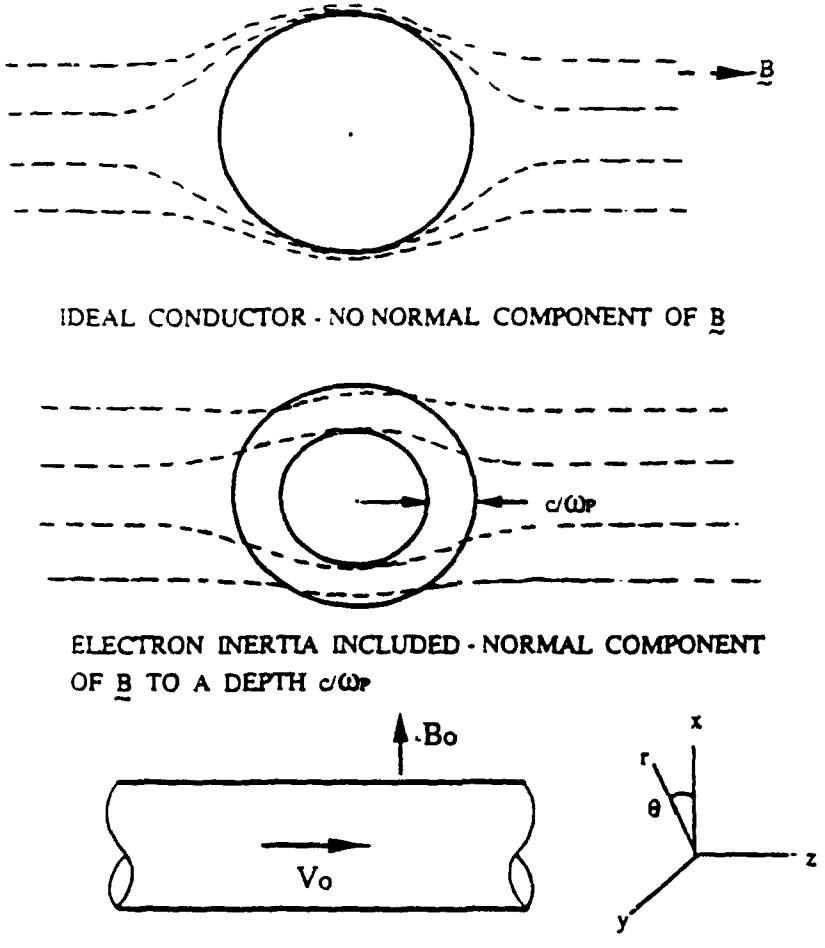

Fig. 2 Cylindrical Model of a Neutralized Ion Beam

$$A_z = \sum_{\ell=1}^{\infty} f_\ell(\rho,\tau)\sin\ell\theta \sim f_1 \sin\theta \tag{12}$$

$$\hat{B}_z = \sum_{\ell=1}^{\infty} g_\ell(\rho,\tau)\sin\ell\theta \sim g_2 \sin 2\theta\ . \tag{13}$$

The leading term of Eq. (12) is suggested by the source term of Eq. (10). Equations (10) and (11) are linearized by the approximation $\hat{\mathbf{B}}\cdot\nabla \cong \cos\theta(\partial/\partial\rho) - (\sin\theta/\rho)\partial/\partial\theta$ in which case $(\hat{\mathbf{B}}\cdot\nabla)\nabla^2 A_z \sim \sin 2\theta$. Equations (10) and (11) are solved in terms of the eigenfunctions

and eigenvalues of

$$\nabla_\ell^2 \Phi_n^\ell(\rho) = -(\lambda_n^\ell)^2 \Phi_n^\ell(\rho) \tag{14}$$

with the boundary condition

$$\left\{ \frac{d}{d\rho} \Phi_n^\ell + \ell \Phi_n^\ell \right\}_{\rho=1} = 0 \, . \tag{15}$$

The normalized eigenfunctions are

$$\Phi_n^\ell(\rho) = \frac{\sqrt{2}}{J_\ell(\alpha_{\ell-1,n})} J_\ell(\alpha_{\ell-1,n}\rho) = |n,\ell\rangle \tag{16}$$

and $\lambda_n^\ell = \alpha_{\ell-1,n}$, $n = 1, 2 \ldots$ etc. the roots of the Bessel function of order $\ell - 1$. Assuming $f_1(\rho,\tau) = \sum_n a_n^{(1)} |n,1\rangle$ and $g_2(\rho,\tau) = \sum_n a_n^{(2)} |n,2\rangle$ Eqs. (10) and (11) are transformed to

$$\frac{da_n^{(1)}}{d\tau} + \alpha_{on}^2 a_n^{(1)} + \frac{\eta_H}{2\eta} \sum_m a_m^{(2)}(\tau) \left\langle n,1 \left| \frac{d}{d\rho} + \frac{2}{\rho} \right| m,2 \right\rangle = -\frac{2\sqrt{2}}{\alpha_{on}^2} \delta(\tau) \tag{17}$$

$$\frac{da_n^{(2)}}{d\tau} + \alpha_{1n}^2 a_n^{(2)} + \frac{\eta_H}{2\eta} \sum_m \alpha_{on}^2 a_m^{(1)}(\tau) \left\langle n,2 \left| \frac{d}{d\rho} - \frac{1}{\rho} \right| m,1 \right\rangle = 0 \, . \tag{18}$$

From previous analysis[5] it is apparent that after a short time only the lowest $n = 1$ mode survives. Based on this fact we retain only the lowest terms $n = 1$ and $m = 1$ as a first approximation. In this case the electron inertia term can also be neglected. The two coupling terms are

$$\left\langle 1,1 \left| \frac{d}{d\rho} + \frac{2}{\rho} \right| 1,2 \right\rangle = 3.3 \quad \text{and} \quad \left\langle 1,2 \left| \frac{d}{d\rho} - \frac{1}{\rho} \right| 1,1 \right\rangle = -1.3 \, .$$

The solution for A_z is

$$A_z = -\frac{4}{\alpha_{01}^2} \frac{J_1(\alpha_{01}\rho)}{J_1(\alpha_{01})} e^{-(\alpha_{11}^2 + \alpha_{01}^2)(\tau/2)} \left[\cos\beta\tau + \left(\frac{\alpha_{11}^2 - \alpha_{01}^2}{2\beta} \right) \sin\beta\tau \right] \sin\theta \tag{19}$$

where $\beta^2 = 25\,(\eta_H/2\eta)^2$ and $\beta\tau \cong \Omega_\perp/\omega_p^2\,(c/a)^2 t$ so that the time behavior of Eq. (19) is similar to the lowest modes of Eqs. (8) or (9) of the slab model. Thus we have shown that for a cylindrical beam crossing a magnetic field the fast penetration of the magnetic field is due to the whistler mode time scale that dominates the usual diffusion time scale.

Acknowledgments

The authors are particularly indebted to Professor Amnon Fruchtman of the Weizmann Institute for communicating his ideas on fast field penetration. We also benefited from discussions with Frank Wessel and Carl Oberman of UC-Irvine, and Toshiki Tajima and Barry Newberger at UT-Austin. N. Rostoker would like to express his appreciation to the Institute for Fusion Studies staff at UT-Austin. The paper was prepared while he was a visiting scientist.

References

1. F.J. Wessel, N. Rostoker, A. Fisher, H.U. Rahman, and J.H. Song, Phys. Fluids B **2** (6), 1467 (1990).
2. A. Fruchtman and Y. Maron, Phys. Fluids B **3** (7), 1546 (1991).
3. A.A. Ivanov and L.I. Rudakov, Zh. E.T.F. **58**, 1332 (1970).
4. L. Spitzer, *Physics of Fully Ionized Gases* (Wiley, New York, 1962).
5. B. Newberger and N. Rostoker, J. Appl. Phys. **65**, 1874 (1989).

$e\phi_{min} \sim 1/2\ m_e v_i^2$, where m_e is the electron mass and v_i is the ion beam velocity. If they are not further neutralized, these small charge clumps will expand, and contribute both to θ_μ and to the axial energy spread of the beam $\Delta\epsilon_\parallel/\epsilon_\parallel$. We will conclude that this mechanism is an important contributor to both θ_μ and $\Delta\epsilon_\parallel/\epsilon_\parallel$.

In the following, we discuss the basic mechanism and its consequences; compare with present data; examine effects of plasma shielding, collisions, and magnetic fields; and present results of computer simulations demonstrating the principal effects.

2. Basic Mechanism

Charge clumps of specific sizes will be important. For typical LIF parameters (i.e., current density $J_i = 5$ kA/cm^2 and $\beta = v_i/c = 0.1$, corresponding to 5 MeV p or 30 MeV Li^+), we will be concerned with charge clumps with dimensions $\ell \gtrsim 0.02$ cm and current $\gtrsim 10$ A. These clumps will have electric potentials of a few kV, and if unneutralized, are sufficient to explain the observed values of θ_μ and $\Delta\epsilon_\parallel/\epsilon_\parallel$. Such charge clumps may be produced by noise, instabilities, or non-uniform ion source effects. For now, we consider only the effects of electron trapping to reduce the net potential. (Later, we will add the effects of plasma shielding in both the axial and transverse directions.) Trappable electrons may be available from boundaries (walls, gas cell foil, etc.), hot electron plasmas (induced by the ion beam), or by gas ionization at the well bottom. Neutralization by electrons reduces the net potential not to zero, but to a minimal value ϕ_{min},

$$\phi_{min} = \alpha\ \frac{1}{2}\ m_e v_i^2/e \qquad (1)$$

where $1 \le \alpha < 4$.

A physical picture of how ϕ_{min} occurs is most easily seen by transforming to the moving ion clump frame. In that frame, a stationary potential well of depth ϕ occurs. In that frame, electrons born in the potential well (e.g., by gas ionization) will have a velocity $-v_i$ and kinetic energy $1/2\ m_e v_i^2$, and will be trapped only if $e\phi > 1/2\ m_e v_i^2$. Therefore, the self-consistent net potential will not be reduced below $e\phi = 1/2\ m_e v_i^2$. Analytic results and 1-D numerical simulation results lead to (1) with $1 < \alpha < 4$,[3-7] so $\alpha = 1$ represents the minimum residual potential allowed.

Now consider a spherical ion charge clump of radius ℓ with net potential ϕ_{min}. If the clump expands to a radius $\gg \ell$, then ions at the outer edge will receive transverse kinetic energy $\sim Z_t e\phi_{min}$ where Z_t is the ion charge state during transport. This produces $\theta_\mu \approx [(Z_t e\phi_{min})/(M_p A v_i^2/2)]^{1/2}$ or

$$\theta_\mu = \sqrt{\alpha}\ \sqrt{(m_e/M_p)(Z_t/A)} \qquad \text{(pure species)} \qquad (2)$$

DIVERGENCE IN INTENSE ION BEAMS CAUSED BY INCOMPLETE CHARGE NEUTRALIZATION*

C. L. Olson and J. W. Poukey
Sandia National Laboratories
Albuquerque, New Mexico 87185

Abstract

Space charge neutralization for light ion fusion (LIF) ion beam transport is usually assumed to be perfect in the "charge-neutral" region of the diode and in the gas transport cell. However, small charge clumps in the beam will not be totally charge-neutralized, and the residual net space charge may contribute to the beam microdivergence θ_μ. If the net potential of the clump is limited only by electron trapping, the minimum potential will be $e\phi \sim 1/2\ m_e v_i^2$ where m_e is the electron mass and v_i is the ion velocity. For proton beams this leads to $\theta_\mu \sim (m_e/M_p)^{1/2} \sim 23$ mrad, where M_p is the proton rest mass. For non-protonic beams, different results occur. The mechanism predicts (1) no dependence of θ_μ on diode voltage, (2) non-protonic θ_μ greater than proton θ_μ for proton-contaminated beams, and (3) axial energy spread $\Delta\varepsilon_\parallel/\varepsilon_\parallel \approx \pm 2\ \theta_\mu$, which are all consistent with present data. Results of analytic studies and computer simulations of this mechanism are presented. Plasma shielding reduces the effects of this mechanism but collisions and magnetic fields reduce the plasma shielding effects. 2-D PIC MAGIC simulations show that this mechanism contributes to θ_μ both in the "charge-neutral" region and in the gas transport region. It is concluded that this mechanism is especially important in the "charge-neutral" region.

1. Introduction

The focusability of intense ion beams for light ion fusion (LIF) depends critically on the beam microdivergence θ_μ. Several potential sources of microdivergence have been identified, and these are being studied to determine which are the most important. In a typical LIF diode/transport scenario, there are four regions that must be considered as shown in Fig. 1: (1) ion source region, (2) diode region, (3) "charge-neutral" region which extends from the virtual cathode to the gas cell foil, and (4) transport region which extends from the gas cell foil to the target. Ion source contributions are being studied by Bailey et al.[1] Diode contributions to θ_μ include effects of the diocotron instability and lower frequency modes, and are being studied by Desjarlais et al.[2] In the "charge-neutral" region and in the gas transport region, several effects may contribute to θ_μ including micro-charge non-neutrality, streaming instabilities, filamentation instabilities, and scattering. It is the purpose of this paper to examine the effects of micro-charge non-neutrality in both the "charge-neutral" region and the gas transport region.

The fundamental concept is that small charge clumps can only be charge neutralized by electron trapping down to some minimum potential value ϕ_{min}, which is of order

*Supported by U.S. Department of Energy

where M_p is the proton mass and A is the ion atomic number. For a proton beam, this is $\theta_\mu = \sqrt{m_e/M_p} \approx 23$ mrad. For a non-protonic beam contaminated with protons, each species will have its own ϕ_{min} (with protons having the largest ϕ_{min}). If the non-protonic species feels the ϕ_{min} of the protons, this will lead to

$$\theta_\mu = \sqrt{\alpha}\,\sqrt{(m_e/M_p)(Z_t/Z_d)} \qquad \text{(proton-contaminated species)} \qquad (3)$$

where Z_d is the ion charge state in the diode.

Simultaneously, as the ion bunch spreads radially, it will also spread axially. In the bunch frame, $\Delta v_\parallel \approx \Delta v_\perp$ so $\Delta v_\parallel / v_\parallel \approx \Delta v_\perp / v_\parallel \approx \theta_\mu$. The axial velocity is $v_\parallel[1 \pm (\Delta v_\parallel / v_\parallel)] = v_\parallel(1 \pm \theta_\mu)$, and the axial energy is therefore $\varepsilon = (1/2\, M_p A v_i^2)(1 \pm \theta_\mu)^2$ so

$$\varepsilon_\parallel \approx \varepsilon_0(1 \pm 2\theta_\mu) \qquad (4)$$

where $\varepsilon_0 = 1/2\, M_p A v_i^2$. Note that although the potential well depth is small (~ few kV), the final axial energy spread $2\theta_\mu\varepsilon_0$ may be large (~ few 100 kV). This is because the potential well electric field acts on the ions in the laboratory frame over a sizeable distance ($\gg \ell$).

In summary, the basic mechanism predicts to lowest order: (1) no dependence of θ_μ on diode voltage, (2) proton $\theta_\mu = \sqrt{m_e/M_p}$ ~ 23 mrad, (3) non-protonic θ_μ > proton θ_μ for proton-contaminated beams, and (4) $\Delta\varepsilon_\parallel/\varepsilon_\parallel \approx \pm 2\ \theta_\mu$. The characteristic time for a clump to expand is $\tau \approx (2\ell)/(\beta_\perp c) = (2\ell)/(\theta_\mu v_i) \approx 0.6$ ns, and the typical ion transit length for this time is $\Delta z = v_i\tau \approx 1.7$ cm. The mechanism could easily occur in the "charge-neutral" region, in the gas transport region (especially the entrance portion), or even inside some ion beam diagnostics that sample beamlets with transverse dimensions > 2ℓ. The contribution to θ_μ from this mechanism would typically add in quadrature with other contributions.

3. Comparison with Experiments

A comparison of the basic theory for $\alpha = 1$ with experimental data from PROTO I,[8] PBFA I,[9], and PBFA II,[10] is given in Fig. 2. Result (2) for protons predicts $\theta_\mu \approx 23$ mrad, with no dependence on diode voltage. Note that for the proton data, θ_μ stays remarkably constant even though the diode voltage changes by a factor of 4. Result (3) for a proton-contaminated beam in the gas cell region ($Z_t > 1$) is the upper theory curve in Fig. 2. Result (3) for a proton-contaminated beam in the "charge-neutral" region ($Z_t = Z_d$) is the center-line theory result in Fig. 2. Although the data is limited, non-protonic θ_μ is larger than proton θ_μ, which agrees with the theory for proton-contaminated beams. For pure beams, theory result (2) for the gas cell region ($Z_t > 1$) or for the "charge-neutral" region ($Z_t = Z_d$) predicts substantially lower values of θ_μ as shown in Fig. 2. Additionally, the theory predicts $\Delta\varepsilon_\parallel/\varepsilon_\parallel \approx \pm 2\ \theta_\mu$ which for protons is ±4.6%. The correlation of $\Delta\varepsilon_\parallel/\varepsilon_\parallel$ with θ_μ appears to be consistent with the data also.

4. Plasma Shielding, ν_{ei}, and B_0

The above mechanism is based solely on electron trapping arguments. Other effects may enhance or reduce θ_μ from that predicted above. We have examined the effects of a plasma background, collisions, and an external magnetic field B_0. From a 1-D analysis using linearized electron fluid equations, we find a Fourier transform solution of

$$\tilde{\phi}_1(k) = \frac{4\pi\tilde{n}_\Delta(k)}{k^2\left\{1 - \frac{\omega_{pe}^2}{k^2 v_i^2\left[1 - i\frac{\nu_{ei}}{kv_i}\right]\left[1 - \frac{\omega_{ce}^2}{k^2 v_i^2\left[1 - \frac{i\nu_{ei}}{kv_i}\right]^2}\right]}\right\}} \qquad (5)$$

where $\tilde{n}_\Delta(k)$ is the transform of the clump perturbation, ν_{ei} is the electron-ion collision frequency, ω_{pe} is the electron plasma frequency, and ω_{ce} is the ion cyclotron frequency. Various results can be seen depending on ratios of ω_{pe}, ν_{ei}, or ω_{ce} to kv_i. For low plasma densities the perturbation is actually enhanced: this is due to plasma electrons speeding up (and therefore lowering their density) as they cross the ion clump. For high plasma densities, shielding occurs and the perturbation ϕ is reduced. However, both collisions and a magnetic field reduce the shielding effect. The net result is that in the "charge-neutral" region, results are essentially unchanged from Section (2) above. However, in the gas cell region, near the end of the ion pulse, high plasma densities will reduce the effect of this mechanism. A complete analysis of result (5) will be presented elsewhere.

5. Computer Simulations

Computer simulations in 2-D have recently been performed to study this mechanism. Using an equilibrium code, plasma flow past a fixed clump was examined first, with results shown in Fig. 3. Here the ion clump has density 10^{13} cm^{-3}, radius 0.1 mm, and length 0.2 mm. With no background, as shown in Fig. 3a, the peak potential is about 1 kV. With a plasma background of density 10^{13} cm^{-3} flowing at $\beta = 0.1$, as shown in Fig. 3b, a wake forms as expected and the peak potentials vary from ~0.5 to 2 kV. With a plasma background of density 10^{14} cm^{-3} flowing at $\beta = 0.1$, as shown in Fig. 3c, multiple wakes form, but the peak potential still is about equal to the bare clump potential of ~1 kV. Note that for this example, $1/2\ m_e v_i^2 \approx 2.5$ keV and the bare clump potential is only ~ 1 kV so electron trapping could not occur. The main effect is plasma shielding and wake formation with peak potentials near the bare clump potential.

The problem was studied further with the 2-D time-dependent PIC code MAGIC. Many runs were made for a 6 MeV proton beam with density $n_b = 10^{13}$ cm^{-3} injected into a transport region 1 mm high and 1 cm long. To model the gas cell case, several values of the background plasma density n_p were used (0, 4 n_b, 10 n_b, 100 n_b); space charge limited electron emission from the walls was added; and several values of B_0 were used (0, 1T, 3T). The beam was injected cold, or with an 80% modulation with an axial wavelength of 0.6 mm and a transverse wavelength of 0.3 mm. The general results are that for the higher plasma densities and for unlimited electron sources on the boundaries, the potential wells are neutralized quite well, but that there are still large potential oscillations with a peak amplitude of 1-3 kV (i.e., of order 1/2 $m_e v_i^2/e$). With beam modulation, the rapidly oscillating electric fields lead to growth in θ_μ of ~10 mrad/cm (plasma only) to ~2 mrad/cm (plasma plus wall emission). Without beam modulation, θ_μ is reduced somewhat unless the system length is sufficient for the ion-electron two-stream instability to form potential wells and generate its own beam modulation.

For the "charge-neutral" region, MAGIC simulations were run for no plasma background, but with space charge limited emission of electrons from the walls. With the 80% modulation, θ_μ grows to ~9 mrad/cm as shown in Fig. 4. Note that there is also a global underneutralization,[3] which leads to a net ion spreading. The axial velocity correlates with the transverse velocity spread ($\Delta v_\parallel \approx \Delta v_\perp$) which means $\Delta\varepsilon_\parallel/\varepsilon_\parallel \approx \pm 2\ \theta_\mu$ as expected.

6. Conclusions

We have shown that micro-charge non-neutrality can cause growth of both θ_μ and $\Delta\varepsilon_\parallel/\varepsilon_\parallel$. The basic mechanism predicts (1) no dependence of θ_μ on diode voltage, (2) non-protonic θ_μ greater than proton θ_μ for proton-contaminated beams, and (3) $\Delta\varepsilon_\parallel/\varepsilon_\parallel \approx \pm 2\ \theta_\mu$. Simulations have been performed that demonstrate growth of θ_μ and $\Delta\varepsilon_\parallel/\varepsilon_\parallel$ in both the "charge-neutral" region and the gas cell region. It is concluded that the mechanism is especially important in the "charge-neutral" region.

Future work will include further analytic and computer studies, and experimental probing of the transport region.[1]

References

1. J. E. Bailey, A. L. Carlson, D. J. Johnson, E. J. McGuire, T. Nash, and C. L. Olson, these proceedings; J. E. Bailey, private communication.
2. M. P. Desjarlais, T. D. Pointon, D. B. Seidel, R. S. Coats, M. L. Kiefer, J. P. Quintenz, and S. A. Slutz, Phys. Rev. Lett 67, 3094 (1991).
3. J. W. Poukey, SNL Report SAND80-2545 (1980).
4. J. W. Poukey, J. P. Quintenz, and C. L. Olson, J. Appl. Phys. 52, 3016 (1981).
5. S. Humphries, Jr., Nucl. Fusion 20, 1549 (1980).
6. R. Sudan, Cornell U. Report LPS 280 (1980).
7. C. L. Olson, J. Fusion Energy 1 309 (1982); C. L. Olson, HIF, AIP Conf. Proc. 152 (AIP, New York, 1986), p. 215.

8. J. P. VanDevender et al., Laser and Particle Beams 3, 93, (1985).
9. P. L. Dreike et al., J. Appl. Phys. 60, 878 (1986).
10. D. J. Johnson et al., Proc. 1989 IEEE Pulsed Power Conf., Monterey, CA, June 11-14, 1989, p. 944; D. L. Cook and D. J. Johnson, private communication.

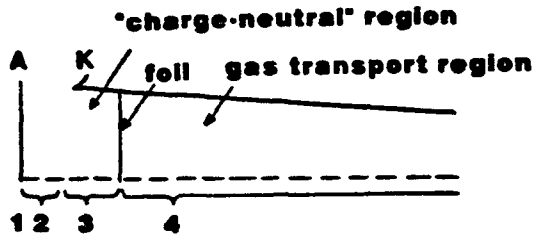

Fig. 1 Diode/transport regions: (1) ion source, (2) diode, (3) "charge-neutral" region, (4) gas transport region.

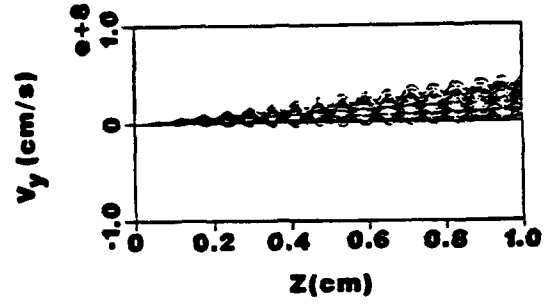

Fig. 4 MAGIC simulation showing growth of transverse ion momentum spread with distance. θ_μ grows to ~9 mrad in 1 cm.

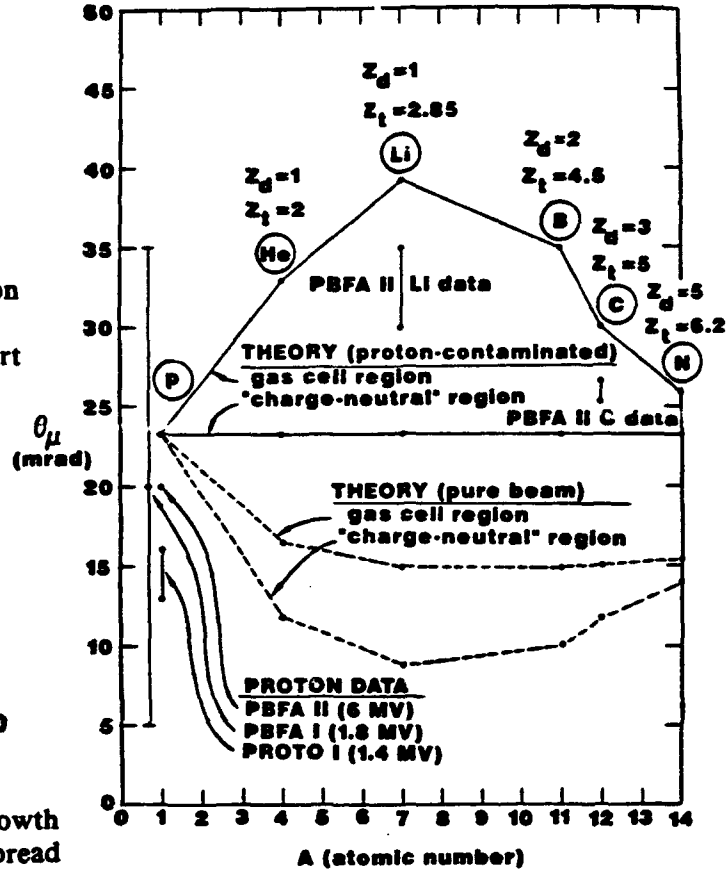

Fig. 2 Comparison of theory with experiments.

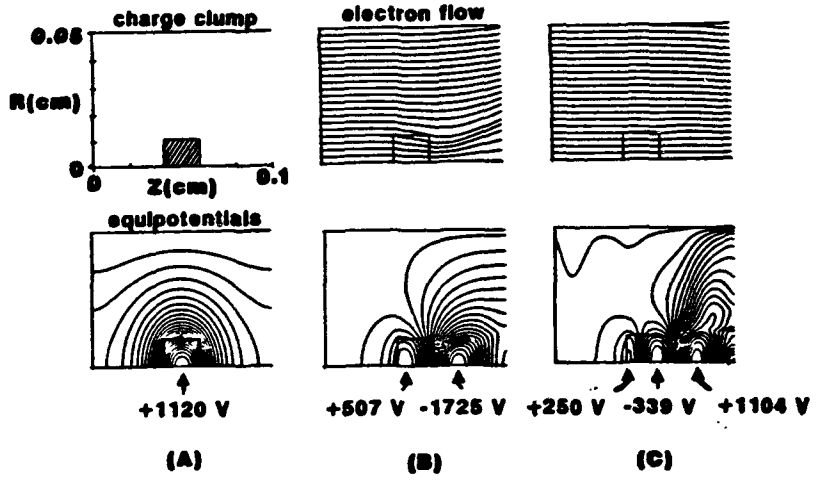

Fig. 3 Plasma flow with $\beta \approx 0.1$ past a fixed charge clump with density 10^{13} cm^{-3}. (a) bare clump, (b) plasma density 10^{13} cm^{-3}, (c) plasma density 10^{14} cm^{-3}.

SPECTROSCOPIC STUDIES OF INTENSE ION BEAM PROPAGATION IN THE PBFA-II GAS CELL

J.E. Bailey, A.L. Carlson, D.J. Johnson, E.J. McGuire, T. Nash, and C.L. Olson

Sandia National Laboratories

Albuquerque, New Mexico

and

J. MacFarlane and P. Wang

University of Wisconsin

Madison, Wisconsin

We are studying the physics of ion beam transport on PBFA II by measuring time-resolved visible spectral emission from the gas cell. The initial goals are to perform a spectral survey, to measure the spectral-line intensities and widths, and to evaluate the potential for using this emission as a diagnostic for conditions in the gas-cell plasma. We have acquired spectra in the 4000 Å to 7000 Å regime excited by the transport of proton and carbon beams through 5 Torr argon gas. The nominal ion beam energy and current density at the spectroscopic line of sight are 6-7 MeV protons, 12-21 MeV carbon, and 10-50 kA/cm^2. The emission is dominated by n=4 to n=4 transitions in Ar II, with FWHM values typically 1-2 Å. We are investigating a variety of mechanisms which might contribute to the line profiles, including plasma Stark broadening, Stark and Zeeman splittings and shifts due to residual electric and magnetic fields, and opacity effects. The relative contributions of ion-impact and plasma electron collisional excitation are being evaluated using an LTE atomic model. Measured plasma properties will be incorporated into our understanding of beam transport.

Introduction

One requirement for inertial confinement fusion (ICF) with a light-ion beam driver is transport of the beam to the target[1]. Present experiments at the Particle Beam Fusion Accelerator II (PBFA II)[2] transport a mixed proton and carbon ion beam through a 12.5 cm, 5 Torr argon gas cell to the target. The acceleration voltage is typically 6-8 MV over a 15 nsec pulse, with a current density at the anode exceeding 5 kA/cm^2 and peak power densities on target of 5 TW/cm^2 protons. Injection of the beam into the gas cell causes rapid ionization and the resulting plasma provides charge and current neutralization for the beam.

This paper describes an initial investigation of the potential for using visible spectroscopy to study beam transport physics on PBFA II. Spectroscopic techniques could measure the plasma-electron density (n_e) and temperature (T_e), enabling inference of the plasma conductivity[3]. Spectral line profiles are sensitive to the presence of stray electric fields, possibly[4] arising during transport of non-uniform ion beams or from a breakdown in charge or current neutralization. Spectroscopic studies of ion-beam transport could also be useful for aspects of ion-driven ICF beyond the direct application to beam transport. We expect some dependence of the emission intensity on beam intensity, either because the beam itself generates the emission or because the electron excitation rates are highest where the beam intensity is highest[5]. If we spectroscopically determine this

relationship, then the light emission can be used to measure beam current uniformity during transport. It has also been proposed[6] to measure the beam divergence from the diameter of the light emission generated as a beamlet propagates through the gas-cell plasma.

An additional application is to use the spectral emission to study the heating of the plasma by the beam. The expected density ($n_e = 10^{17}$ cm^{-3}) and temperature (T_e= 1 eV) are far below the regime occurring in ICF targets. However, the slowing of multiply-ionized beams in plasma is an area of active research[7] and the deposition in the PBFA II gas cell plasma is ≈1-3 TW/gm, three orders of magnitude above the regime reported in recent heavy-ion beam-heating experiments[8]. Beam-heating experiments in the PBFA II gas cell are attractive because of the relative ease of visible spectroscopic diagnostics and the possibility of piggybacking on experiments with a different main objective.

Our goals for the exploratory experiments reported here were to develop experimental techniques for acquiring time-resolved visible spectra from the PBFA II gas cell, to identify the dominant spectral emissions, and to evaluate the potential for using the spectra to measure physical quantities relevant to beam-transport physics. We obtained spectra in the 4000-7000 Å regime with spectral resolution up to 0.3 Å and time resolution of about 1 nsec. The dominant emission in this spectral regime is from Ar II 4s-4p and 3d-4p transitions. Analysis of these results using an LTE model to interpret line intensities and an atomic physics code to calculate the effect of electric fields on the line profiles has begun.

Experiment

A schematic diagram of the PBFA II applied-B ion diode[9] is shown in Figure 1. Ions are accelerated radially inward from the cylindrically-symmetric anode toward the target on axis. Typical voltage and ion currents (measured with Faraday cups located at the gas cell boundary) are shown in Figure 2 The spectroscopy diagnostic uses a lens at 4-cm radius to collect light from a 7-mm-diameter cylindrical line of sight . The light is coupled into a 400-μm-diameter radiation-hardened quartz fiber optic that transports the light 45 m to a remote screen room. There the light is injected into a 1-m Czerny-Turner spectrograph with a streak camera located in the focal plane to record a time-resolved spectrum. The streaked spectrograph characteristics are described in Reference 10. The time resolution is about 1 nsec. The spectral resolution is 0.7 Å and the range is 280 Å with a 1200 g/mm grating. Wavelength fiducials are recorded on each shot by injecting HeNe laser light into the spectrograph, rotating the grating a known amount, and re-triggering the streak camera. The film response is unfolded from the data using a calibration step wedge.

The timing of the streaked spectra with respect to other diagnostics is obtained using a fast plastic scintillator (BC-418, Bicron Corp) located near the diode to detect bremsstrahlung generated when the power pulse arrives at the diode. The light from the scintillator provides an optical fiducial on each streaked spectrum that can be compared with bremstrahlung recorded with the main PBFA II data acquisition system. Knowing the optical path lengths, we can relate physical quantities determined with spectroscopy to quantities determined with other diagnostics to within approximately +/- 2 nsec.

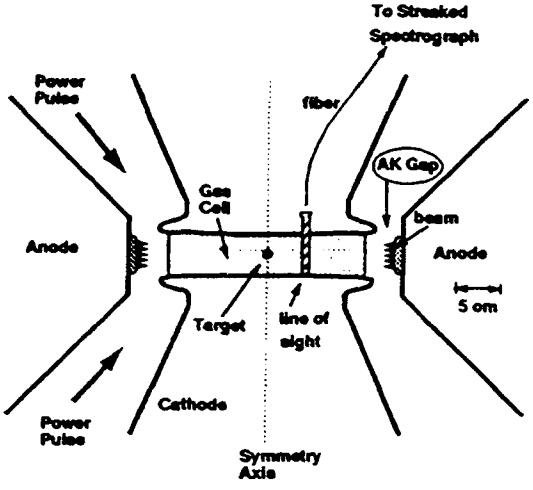

Figure 1. Schematic of the PBFA II ion diode.

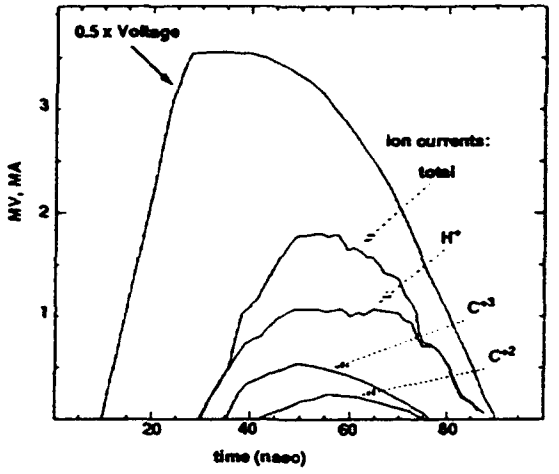

Figure 2. Typical PBFA II voltage and ion currents.

Results

The first PBFA II gas-cell spectra were acquired with a survey grating to enable us to identify the dominant emission features.An experimental survey spectrum with ~ 3 Å resolution is compared to known[11] Ar II wavelengths in Figure 3. Essentially all of the lines can be accounted for by emission from Ar II. We are investigating possible reasons for the lack of Ar I emission, including changes in the ionization distribution and excited state populations as a function of the plasma and beam parameters. We did not yet explore the ultraviolet wavelengths where any bright emission from Ar III would be located.

Spectral surveys were also performed to look for emission from beam ions as they traveled toward the target. This search was prompted by the possible measurement of beam current and/or beam divergence (through the line Doppler broadening). No beam emission was observed in these experiments, presumably because although the current densities are high, the cross sections for recombination and electron capture followed by radiative decay are low. This does not preclude success with such measurements in the vacuum ultraviolet regime, where emission is expected to be brighter.

A sequence of lineouts as a function of time from PBFA II shot #4659 is shown in Figure 4. We used high spectral resolution (0.3 Å) to enable line profile measurements. The emission is first observed when the proton current reaches 400 kA, approximately simultaneous with the onset of carbon beam current. The Ar II intensities grow for ~ 25 nsec, then rapidly decrease and disappear over the next 10 nsec. Some of the experimental lines are blends of several transitions and thus a detailed line-fitting method must be used to measure the widths. While this work is in progress, we made an initial measurement wherever possible by measuring the half width of partially-resolved features and multiplying by two. The 4348 Å 4s-4p line width grows from 0.9 Å

at t = 48 nsec to ~ 2 Å at t = 57 nsec. The rest of the lines have widths that grow from ~ 0.8 to ~1.4 Å during the same time period. These values can only be regarded as approximate until we take the line blending into account more accurately using a line-fitting procedure. However, the qualitative features are correct, i.e., the line widths double during the power pulse and the 4348 Å line is systematically wider.

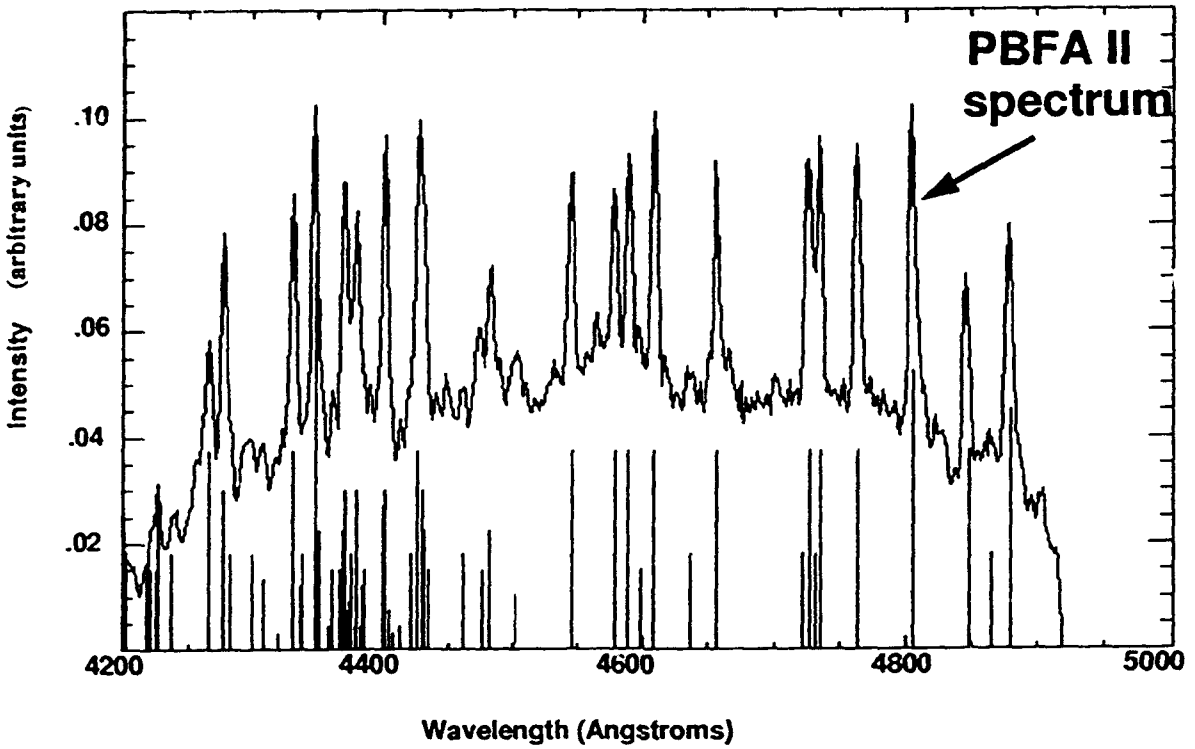

Figure3. Experimental survey spectrum (top) compared to known Ar II wavelengths (bottom). The line intensities in the bottom spectrum are from Ref. 11 and don't necessarily reflect the experimental conditions.

Discussion

The initial breakdown of the argon gas and the subsequent ionization involve complicated processes[1, 12], including beam ion-impact ionization, electron avalanching, and collisional ionization by thermal and secondary electrons. Although detailed hydrodynamic simulations are required to model these processes, we can make initial estimates following the approach in Reference 3, using the measured beam parameters and analytic equations to determine approximate bounds on n_e. Calculations for similar conditions[12] indicate that the expected electron temperature and density are ~1-2 eV and 10^{16}-10^{17} cm^{-3}, respectively The electron density produced by ion impact ionization during the first 10 nsec of the beam within the spectroscopic line of sight is ~ 10^{16} cm^{-3}. Also, assuming that the energy deposited by the beam is invested in electron temperature and ionization and neglecting radiation losses and ohmic heating by the return current (see Ref. 3), we find $n_e < 1.7 \times 10^{17}$ cm^{-3} at t= 39 nsec and $n_e < 3 \times 10^{17}$ cm^{-3} at t=44 nsec. These values can be compared with electron densities obtained from the spectroscopic measurements.

As described above, the experimental fwhm values range from 0.7-2.0 Å. Instrumental and Doppler broadening are negligible. The Stark widths[14] for these transitions are all approximately 0.32 Å for $n_e = 1 \times 10^{17}$ cm^{-3} and $T_e = 1$ eV. If Stark broadening dominates, we expect all the line widths to be roughly the same. In fact, the 4348 Å 4s-4p line is significantly wider. We believe this is because the 4348 Å line width is modified by the opacity, which is a factor of 5 greater for this transition (assuming LTE among the excited states and using the oscillator strengths in Reference 15). The agreement for the other widths indicates they are not modified by opacity, since the optical depth varies by an order of magnitude. If we assume that Stark broadening is the dominant broadening mechanism for these lines, then the electron density is 2.4×10^{17} cm^{-3} at t= 40 nsec and it rises to about 5×10^{17} cm^{-3} during the pulse.

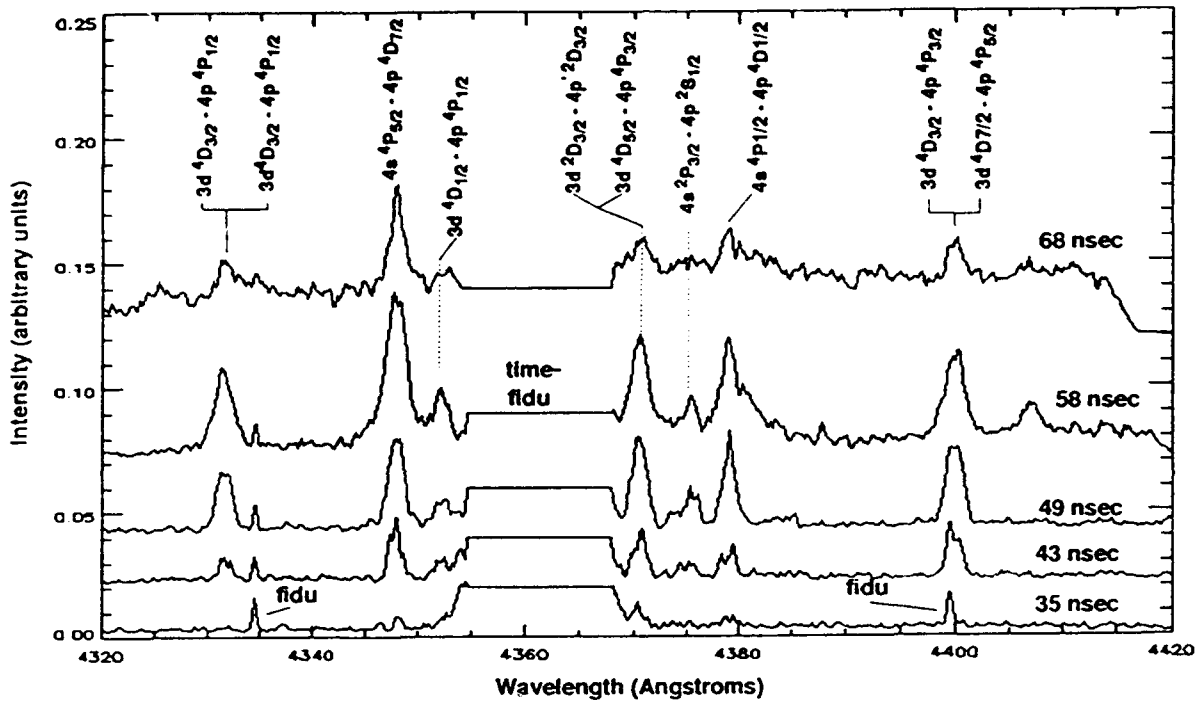

Figure 4. Sequence of lineouts from a high-resolution PBFA II gas cell spectrum. The times correspond to the electrical signals shown in Figure 2.

The electron density determined assuming the lines are Stark broadened is a factor of two higher than the upper bounds determined from the simple energy balance arguments. One possible explanation is that either the actual ion current is higher than indicated by the Faraday cups or that the timing of the spectra is in error by about 5 nsec. A second possiblity is that the stopping power appropriate to hot plasma, rather than cold gas, must be used to determine the energy deposition. Finally, other broadening mechanisms must be considered. For example, if stray electric fields do exist in the plasma because of transport of a non-uniform ion beam, the resulting distribution of Stark shifts may increase the apparent line broadening. Estimates for the peak field to be expected under these conditions are 100 kV/cm[4]. Code calculations of the Stark shift for the argon lines under such fields are in progress.

Atomic physics modeling is required for the quantitative interpretation of the line intensities. An atomic model for argon was constructed (see Reference 16 for details) and used to determine that an LTE analysis is satisfactory for the conditions in these experiments. The model predicts that Ar II is the dominant charge state for T_e = 2-3 eV. The calculated line center optical depth for the 4348 Å Ar II 4s-4p line is τ = 3-10, while the other lines have $\tau < 1$. This qualitatively agrees with the experimental observation that the 4348 Å linewidth is opacity broadened. A quantitative effort to compare experimental line intensities and widths to model-generated synthetic spectra is in progress.

The model was also used to compare the excitation rate due to ion impact excitation to the electron collisional excitation rate. The total ion impact excitation rate for protons and carbon is about the same, since the carbon ions have a lower particle current but a higher cross-section. For the conditions in this experiment, the electron collision and ion impact rates are comparable if $n_e \sim 1\text{-}3 \times 10^{17}$ cm^{-3} and $T_e \sim$ 2-3 eV. Thus, determination of which rate dominates requires an unambiguous measurement of the electron density and temperature. It may also be necessary to include effects of a non-thermal secondary electron distribution in the model.

In summary, these experiments have demonstrated that it is possible to acquire spectra from the PBFA II gas cell with good signal to noise and high spectral and temporal resolution. The visible spectra are dominated by Ar II lines with fwhm ranging from 0.7 - 2 Å. The interpretation of the experimental spectra is in progress, with potential for measuring n_e, T_e, and stray electric fields. These parameters can then be used to determine the mechanism responsible for populating the excited states and to improve our understanding of beam transport physics.

References

1. C.L. Olson, J. Fusion Energy 1, 309 (1982).
2. J.P. VanDevender and D.L. Cook, Science 232, 831 (1986).
3. J.A. Swegle and S.A. Slutz, J. Appl. Phys. 60, 3444 (1986).
4. C.L. Olson and J. Pouky, these proceedings.
5. R. Jayakumar and H.H. Fleischmann, J. Quant. Spectroc. Radiat. Transfer 33, 177 (1985).
6. M.S. Derzon, Sandia National Laboratories, private communication (1991).
7. E. Nardi and Z. Zinamon, Phys. Rev. Lett. 49, 1251 (1982).
8. J. Jacoby, D.H.H. Hoffman, R.W. Muller, K. Mahrt-Olt, R.C. Arnold, V. Schneider, and J. Maruhn, Phys. Rev. Let. 65, 2007 (1990).
9. D.J. Johnson et. al., in Proc. of 7th IEEE Pulsed Power Conf., Monterey, CA, edited by W. Bauer and W. Schmidt (Kernforschungszentrom Karlsruhe Gmbtt FDR, 1989), p. 944.
10. J. Bailey, A.L. Carlson, R.L. Morrison, and Y. Maron, Rev. Sci. Instrum. 61, 3075(1990).
11. A.R. Striganov and N.S. Sventitskii Tables of Spectral Lines of Neutral and Ionized Atoms (Plenum, New York) 1968.
12. C.L. Olson, Proc. 1990 Linear Accel. Conf., LANL publication LA-12004-C, p.396(1991).
13. R.D. DuBois and S.T. Manson, Phys. Rev. A 35, 2007 (1987).
14. N. Konjevic and W.L. Wiese, J. Phys. Chem. Ref. Data 5, 259 (1976).
15. W.L. Wiese, M.W. Smith, and B.W. Glennon, Atomic Transition Probabilities, NSRDS-NBS 4 (1966).
16. P. Wang, J.J. MacFarlane, G. Moses, and J. Bailey, these proceedings.

This work supported by the U.S. DOE under contract #DE-AC04-76DP000789

BALLISTIC FOCUS LIGHT ION BEAMS FOR AN INERTIAL CONFINEMENT FUSION REACTOR

Robert R. Peterson
Fusion Technology Institute
University of Wisconsin, Madison, WI 53706

Abstract

The issues of ion beam transport are studied in the context of the LIBRA-LiTE reactor study. LIBRA-LiTE is a 1000 MWe power plant design consistent with ballistic ion focusing. The ion beam energy must be divided between many beams to provide proper illumination symmetry. The needs to keep the total beam energy low and the intensity at the required level lead to constraints on the transport system, particularly, a high degree of bunching and a low microdivergence. This paper will describe arguments leading to an operating point for light ion ICF with ballistic focusing. Calculations of heating of the background gas by the ion beams and the subsequent increase in the electrical conductivity of the gas will be presented. This is an important issue to the stability of the ion beam.

Introduction

Ballistic propagation of ions in a light ion Inertial Confinement Fusion (ICF) reactor has potential advantages over propagation using plasma channels, but it requires that focusing magnets be close to the target. Ballistic transport is simpler and potentially more efficient but, to keep the focusing magnets as far as possible from the target, the focal spot at the target is large. Target ignition requires a beam intensity above some minimum value, which in this work has been taken to be 127 TW/cm^2. To achieve this intensity, one adjusts the total beam energy, the positions of the focusing magnets, the microdivergence of the ion beam, and the time of flight bunching of the beam. To achieve proper symmetry and pulse shaping, the pulse on the target includes a main pulse with 90% of the energy in 24 beams and a pre-pulse supplied by 6 beams. The SCATBALL computer code has been used to verify the ability of the ion beam transport system to provide the proper target conditions. This is done within the context of the LIBRA-LiTE [1-4] reactor study that uses ballistic ion beam transport in a concept that produces 1000 MW of electrical power.

LIBRA-LiTE Ion Beam Transport System

The LIBRA-LiTE ion beam transport system consists of extractor diodes, drift regions, solenoidal lens magnets, and focus regions. The ions propagate out of the diodes, across the drift regions, to

the focusing lens magnets in hollow cylindrical beams. The width of the cylindrical shell to which the beams are confined thickens during transport due to scattering of beam ions by the background gas and due to microdivergence. Microdivergence is determined in the diode. We have neglected microdivergence growth due to plasma instabilities during transport. The beam radius, which is initially equal to the diode outer radius, increases due to this spreading. The bore radius of the focusing lens magnet must be large enough to contain the beam. The beams are focused onto the target by the lens magnets. The focal spot size, which must be no larger than the target, is affected by microdivergence and scattering during transport between the magnets and the target.

The focusing lens magnets are designed to focus cylindrical ion beams to a target. The magnet operates by using B_r fields that exist near the ends of the solenoid to convert some of the axial ion beam velocity, v_z, into azimuthal velocity, v_θ. The axial magnetic field then acts against the v_θ to give the ions a focusing force and a radial velocity, v_r. As the ions move out of the solenoid, they once again encounter a B_r, but in the opposite direction, which removes the azimuthal motion. Conservation of canonical angular momentum requires that the ion beam has the same angular momentum on both sides of the magnet, which we assume to be zero far from the magnets. In the presence of the magnetic field, the canonical angular momentum is $m\vec{v} + q\vec{A}/c$. In a solenoid, $\vec{A}$ is azimuthal, so $\vec{v}$ has an azimuthal component in the opposite direction while there is a finite vector potential, $\vec{A}$. It is important that the ion beam has no angular momentum at the target, or it will not focus to a spot.

The design parameters for the ion transport systems for LIBRA [5] and LIBRA-LiTE are shown in Table I. LIBRA is a reactor design using ion transport in pre-formed plasma channels. A background gas of 3.55×10^{16} cm^{-3} of helium is assumed to be present throughout the entire beam transport system of LIBRA-LiTE. Some method of isolating the diode from the gas will be required. Because LIBRA-LiTE uses liquid lithium target chamber protection, there will be some impurity of lithium vapor, but we do not expect it to affect beam transport. The microdivergence is chosen to be 4.0 mrad as a base case. Though this would require great advances in diode technology, it only requires a source plasma temperature below about 500 eV. The 7.14 cm radius beam spreads to 9.0 cm at the lens magnets. The 470 cm drift length between the diodes and the magnets allows the diodes to be placed outside of the target chamber and allows distance for time of flight bunching and gas isolation equipment. The magnets have a focal length measured from the magnet center to the target of 230 cm. The magnets have an average field of 1.2 tesla and a length of 50 cm, which is required to focus a 30 MeV lithium beam. The main beams will be focused to a 0.95 cm radius spot.

SCATBALL Computer Code

The SCATBALL code has been used to study the transport of ions from the diodes, through the focusing magnets to the target. This code calculates the envelope for the ion beam. This includes

Table I. LIBRA-LiTE and LIBRA Ion Beam Parameters

	LIBRA-LiTE	LIBRA
Transport Method	Ballistic	Channels
Gas Species	Helium	Helium
Gas Density (cm^{-3})	3.55×10^{16}	3.55×10^{18}
Total Transport Length (m)	7.0	7.3
Focal Length (m)	2.3	0.7
Drift Length (m)	4.7	6.6
Beam Microdivergence (mrad)	4.0	6.0
Ion Species	30 MeV Lithium	30 MeV Lithium
Max. Source Plasma Temperature (eV)	480	1080
Energy From Each Main Diode (MJ)	0.375	0.375
Number of Main Beams	24	16
Transport Efficiency (%)	62.5	60.0
Main Pulse Energy on Target (MJ)	5.63	3.6
Pulse Width at Diode (ns)	40	40
Bunching Factor	11.8	4
Pulse Width on Target (ns)	3.4	10
Main Pulse Power on Target (TW)	1656	360
Focal Spot Radius (cm)	0.95	0.47
Peak Intensity on Target (TW/cm^2)	127	127
Peak Current Density on Target (MA/cm^2)	4.23	4.23
Current Density on Diode Anode (kA/cm^2)	5.0	2.0
Diode Anode Area (cm^2)	62.6	157
Diode Outer Radius (cm)	25.773	7.14
Diode Inner Radius (cm)	25.385	1.0

the effects of scattering by the background gas, spreading from microdivergence, focusing by the lens magnets and time-of-flight bunching of the ion beam. These properties are all calculated using analytic formulae [6]. In addition, the heating of the background gas by the ions is calculated numerically.

Results

SCATBALL has been used to study the effects of microdivergence on the transport parameters. The microdivergence caused by the diodes is one of the greatest uncertainties in light ion fusion. Light ion fusion with ballistic focusing will probably not be credible for microdivergences greater than about 6 mrad. This is demonstrated by using the SCATBALL code to calculate the required energy on target in the main pulse to obtain 127 TW/cm^2 with a 11.8 bunching factor. This bunching factor has been chosen for LIBRA-LiTE and is slightly more than the achievable bunching predicted for the pulse power system designed for LIBRA [4]. A greater bunching factor is probably

not credible. This value has been chosen to minimize the required energy on target. For a distance between the target and the center of the magnets of 230 cm, one obtains the plot shown in Fig. 1. Here, the energy on target in the main pulse is plotted against microdivergence. Based on this, a microdivergence of 4 mrad has been chosen, which provides 127 TW/cm^2 in a 3.4 ns main pulse containing 5.4 MJ on a 1 cm radius target. The near term microdivergence goals are approximately 15 mrad on PBFA-II with lithium. The distance between the first surface of the focusing lens magnets and the target has been studied as a function of microdivergence for the same target parameters and 5.4 MJ in the main pulse. This is shown in Fig. 2 along with the average neutron wall loading on the surface of the 50 cm long magnets for a 1000 MW$_e$ power plant versus microdivergence. The magnets are 50 cm long and the focal length is measured from the center of the magnet.

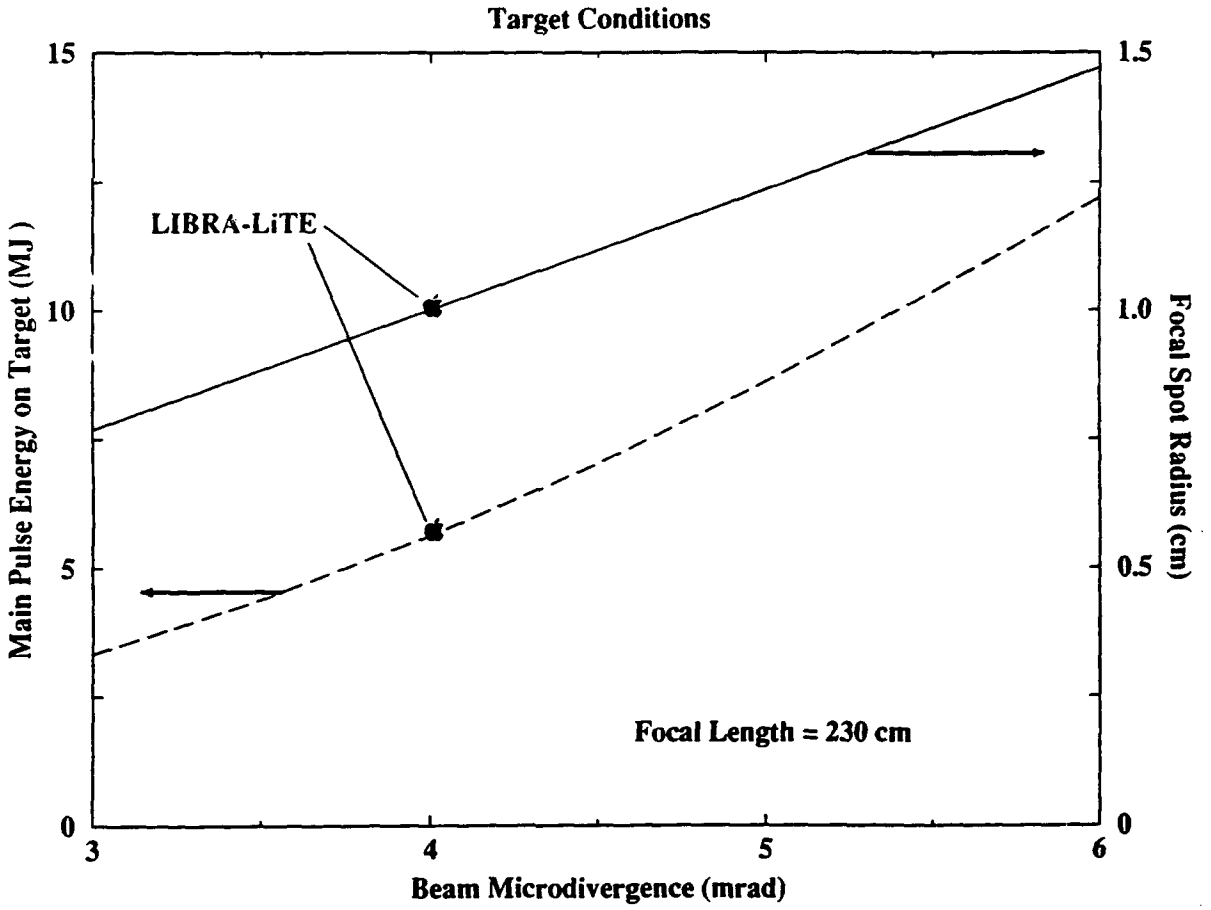

Figure 1. Required energy on target in the main pulse and the focal spot radius versus ion beam microdivergence. The focal length for the focusing magnet is 230 cm. The pulse width on target is 3.4 ns and 127 TW/cm^2 are assumed required for ignition.

The heating of the target chamber gas by the ion beams has been considered. It is thought that filamentation instabilities can be avoided if the electrical conductivity of the gas is greater than 10^{14} s^{-1}. The SCATBALL code has been used to calculate the conductivity of the gas. The gas is heated by ion beam energy deposition. As the background gas temperature increases, the gas ionizes and the conductivity increases. Electron collisions dominate the conductivity, so electron temperature increases lead to higher conductivity. The conductivity at the head of each beam is very low. Therefore the leading edge of the beam is subject to the instability. The breakdown process in the head of the beam is very complicated because the low conductivity and the large time rate of change of the current density allow large electromagnetic fields to be generated. These fields are thought to initiate electron avalanche. This process is not considered in SCATBALL. After the avalanche breakdown is complete, the conductivity is still below the required value but ion beam heating and ohmic heating by the return current continues. This is included in SCATBALL. The conductivity at the lens magnet for a main pulse beam at the tail end of the beam is 1.59×10^{14} s^{-1}.

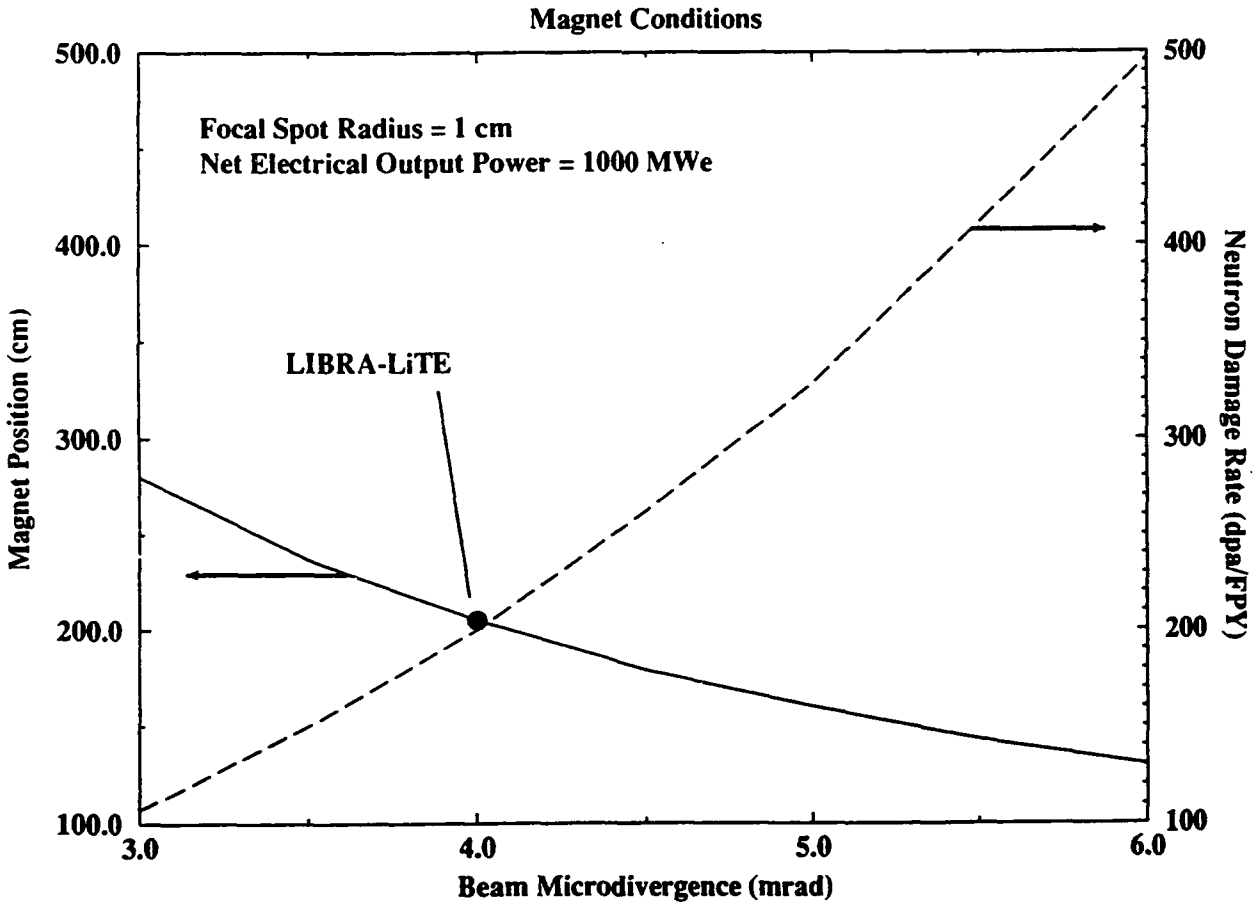

Figure 2. Distance from target to front of magnet and neutron damage rate in front surface of magnet versus microdivergence. The magnet is assumed to be made of TZM and to be 50 cm long. The focal spot radius is 1 cm. The net electrical output power is taken to be 1000 MWe.

Conclusions

Ballistic focusing limits in the LIBRA–LiTE reactor have forced a compromise between focal spot radius, magnet stand-off distance, driver energy, bunching, and beam microdivergence. The driver energy has a great effect on the cost of construction and the cost of produced electricity so the system has been designed to minimize driver energy at the costs of very high bunching, a high nuclear damage rate in the magnets, and a low beam microdivergence. The high bunching requires a very well-programmed voltage waveform on the diodes. The high damage rate in the magnets means that they must be replaced frequently. This will have an effect on the availability of the power plant. The 4 mrad microdivergence is roughly one third of the lowest currently achieved, and so requires significant advances in diode technology. These considerations show that ballistic transport light ion fusion is economically ·-ble if advances are made in diode performance.

Acknowledgements

This work is supported by Kernforschungszentrum Karlsruhe and Sandia National Laboratories. The authors wish to express their gratitude to Dr. Vetter and Dr. Kessler and their colleagues at KfK for helpful discussions. Similarly, we must thank Dr. Cook, Dr. Olson, and their colleagues at SNL.

References

1. G.L. Kulcinski, et al., "LIBRA-LiTE: A 1000 MWe Reactor," J. Fusion Energy **10**, 339 (1991).
2. B. Badger, et al., "LIBRA–LiTE: A Commercial Light Ion Fusion Power Plant," University of Wisconsin Fusion Technology Institute Report UWFDM-880 (1991).
3. R.R. Peterson, et al., "LIBRA-LiTE, A Light Ion Inertial Confinement Fusion Reactor With Ballistic Ion Propagation," University of Wisconsin Fusion Technology Institute Report UWFDM-864 (1991). Also published in Proc. 14th IEEE/NPSS Symp. Fusion Engn., (Sept. 30 - Oct. 3, 1991, San Diego, CA), p. 1050.
4. R.R. Peterson, et al., "LIBRA-LiTE, A Ballistic Focus Light Ion Inertial Confinement Fusion Reactor," these proceedings.
5. B. Badger, et al., "LIBRA - A Light Ion Beam Fusion Conceptual Reactor Design," University of Wisconsin Fusion Technology Institute Report UWFDM-800 (1989).
6. C.L. Olson, "Achromatic Magnetic Lens Systems for High Current Ion Beams," Proc. 1988 Linear Accelerator Conference, CEBAF Report 89-001 (1989) p. 34.

ION BEAM TRANSPORT AND FOCUSING EXPERIMENTS

J. C. Olson and B. R. Kusse
Laboratory of Plasma Studies, Cornell University *

May 25, 1992

Abstract

The CASTOR accelerator has been fitted with an applied B_r extractor diode for use in ion beam transport and focusing experiments. The beam, composed mainly of protons, is accelerated to 300-400 keV. Beam propagation in vacuum is observed to be consistent with divergences of 50 mrad HWHM in the radial direction and 125 mrad HWHM in the azimuthal direction and is observed to be constant through the beam pulse. Collective focusing of protons and electrons by a solenoidal lens is observed. The radial profile of the focus is as expected for the measured divergences. Improved focusing due to a two lens system that simultaneously compensates for radial divergence and beam energy spread [J. C. Olson and B. R. Kusse, J. Appl. Phys. **70**(10)5719] has yet to be demonstrated. Long time scale conductivities of 0.5-1.0 $\times$ 10^{13} s^{-1} are measured in beam ionized nitrogen plasmas.

Introduction

Long distance ion beam transport and ion beam focusing are critical parts of the concept for a Laboratory Microfusion Facility (LMF) driven by light ion beams.[1] We are studying the transport and focusing of intense ion beams. Our investigations to date have examined ion beam divergence, collective focusing of the beam in vacuum by one and two lens systems, and conductivity of nitrogen plasmas created by beam induced ionization. Further study of divergence, one and two lens focusing systems, and beam induced plasma conductivity is on-going. Here we report the results of experiments to date.

Experimental Apparatus

Equipment used in the experiments described here is shown in Figure 1. Ion beams were created in an applied B_r extraction diode. The beams were injected into a drift space and allowed to propagate up to 1.3 m either ballistically or through applied magnetic fields created by solenoidal magnet coils.

The ion diode was powered by CASTOR, a Marx generator, coupled to the diode by a 3.1 Ω co-axial water line. Usual pulse parameters were peak diode voltage of 350 kV, peak current of 60 kA, and pulse width of 125 ns FWHM. Diode voltage was measured by a capacitive monitor with inductive correction. Diode current was measured by a passively integrated $\dot{B}$ loop in the water-vacuum interface. A sample waveform is shown in Figure 2. From current density measurements just behind the cathode tips, ion current efficiency was 75% and the diode operated at an enhancement of 10 $\times$ the Child-Langmuir current.

*Work supported by Sandia National Laboratories

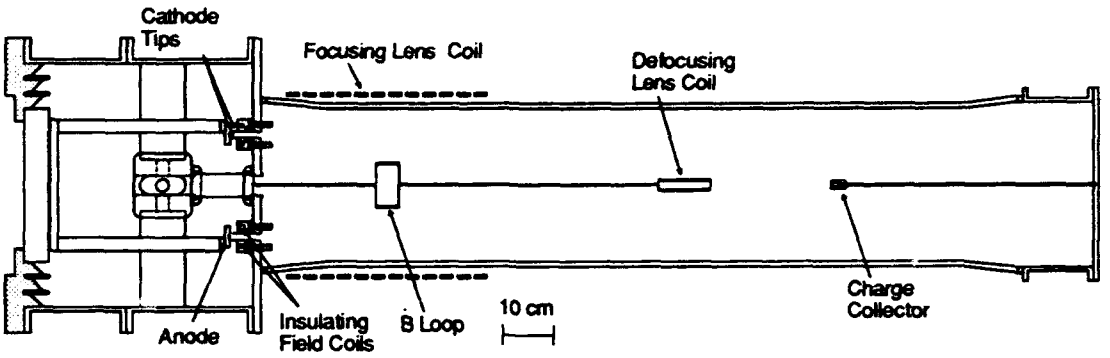

Figure 1: Appartus used in propagation and focusing experiments

The diode itself consisted of a flat anode and two cathode tips in a triax geometry. The inner and outer anode-cathode gaps were set to 5 mm. The inner cathode was supported from the center by a convolute behind the anode. Ions were provided from a passive flashover source, a 1.5 mm thick annular polyethylene insert of mean radius 10 cm and width 1 cm. This insert was embedded in a 1.5 mm deep groove in a 1.15 cm thick aluminum anode plate. Anode inserts lasted for > 50 shots. An annular mask at the end of the insulating field, 7 cm from the anode, restricted the beam exiting the diode to a 9.95 cm inner radius and a 10.05 cm outer radius.

Magnetic insulation was supplied by cathode side field coils driven by either one or two capacitor banks. On single bank shots, a fast bank provided 10 kA of current to the coils, creating a 1.1 T field. At 350 kV, this is 2.3 times the critical insulating field. On such a shot, penetration of the fast field into the anode resulted in ions leaving the insulating field having crossed a net magnetic flux. Beams made in this way were rotating as they were injected into the drift space.

To counteract this rotation, prior to triggering the fast bank a slow bank was discharged through the coils. The slow bank drove a small current in the opposite direction to the fast bank current, loading the anode with magnetic flux to cancel the penetration of the fast flux once the fast bank was triggered. By properly controlling the timing and currents from the two banks, we were able to inject a non-rotating beam into the drift space.

The drift space was a 30 cm I.D. glass tube extending 1.5 m from the end of the diode insulating field. Diagnostics in the drift space include a $\dot{B}$ loop and an electrically biased charge collector. A 1.5 μm polycarbonate foil filter was placed over the charge collector hole, limiting the ion current collected to protons above 150 keV. Charge collector radial position was variable between the axis and 6.3 cm off axis. z position varied between 90 and 130 cm from the end of the insulating field. The $\dot{B}$ loop was positioned on axis 25 cm from the diode and inside the annular beam. It was oriented to pick up B_z and had an L/R response time of 5 ns.

The system was evacuated to a pressure in the diode of $1-3 \times 10^{-5}$ Torr on vacuum shots. For beam propagation shots in gas, nitrogen was introduced through a leak valve in the diode end of the experiment.

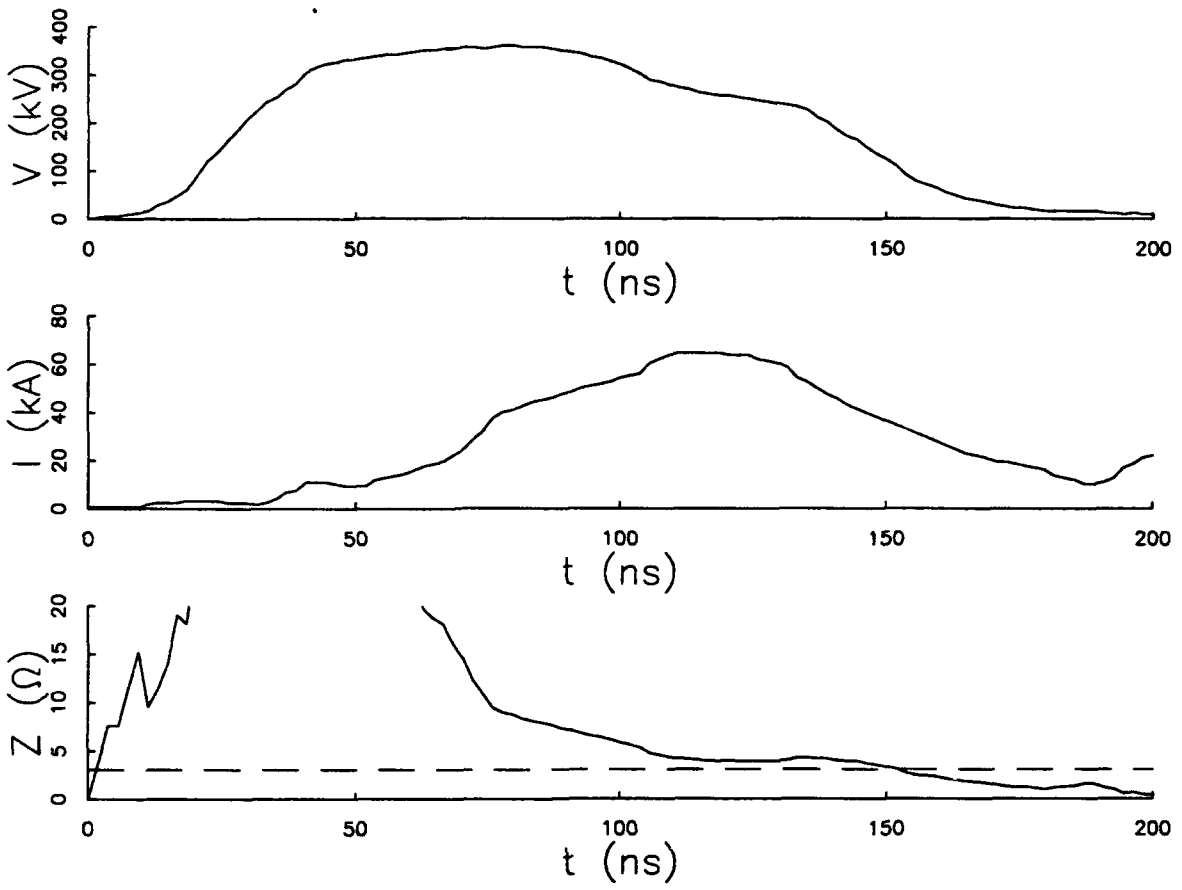

Figure 2: Diode Voltage, Diode Current, and Diode Impedance for a sample shot. The dashed line in (c) is the waterline impedance.

Pressure for these shots was .1-1 mTorr.

Propagation and Focusing Experiments in Vacuum

Our initial experiments on beam propagation in vacuum were concentrated on characterizing beam divergence and were conducted without solenoidal lens fields. In a series of shots we made charge collector measurements on axis at z positions of 90 - 130 cm from the diode and for radial positions from 0 - 6.3 cm at $z = 125$ cm from the diode. Data from these measurements are shown in Figures 3(a) and 3(b). The vertical axis of the graphs in Figure 3 is f, the fraction of the protons injected into the drift space at any point in time that pass into the 1 mm radius hole of the charge collector.

In order to properly compute f it was necessary to account for the changing shape of the current pulse as it propagated down the experiment. For instance, in the waveform shown in Figure 2, a significant amount of ion current was made from $t = 40$ to 80 ns, while the voltage was rising. Thus up to peak voltage the beam bunched as later, faster ions caught up to earlier, slower ones. After peak voltage the current pulse

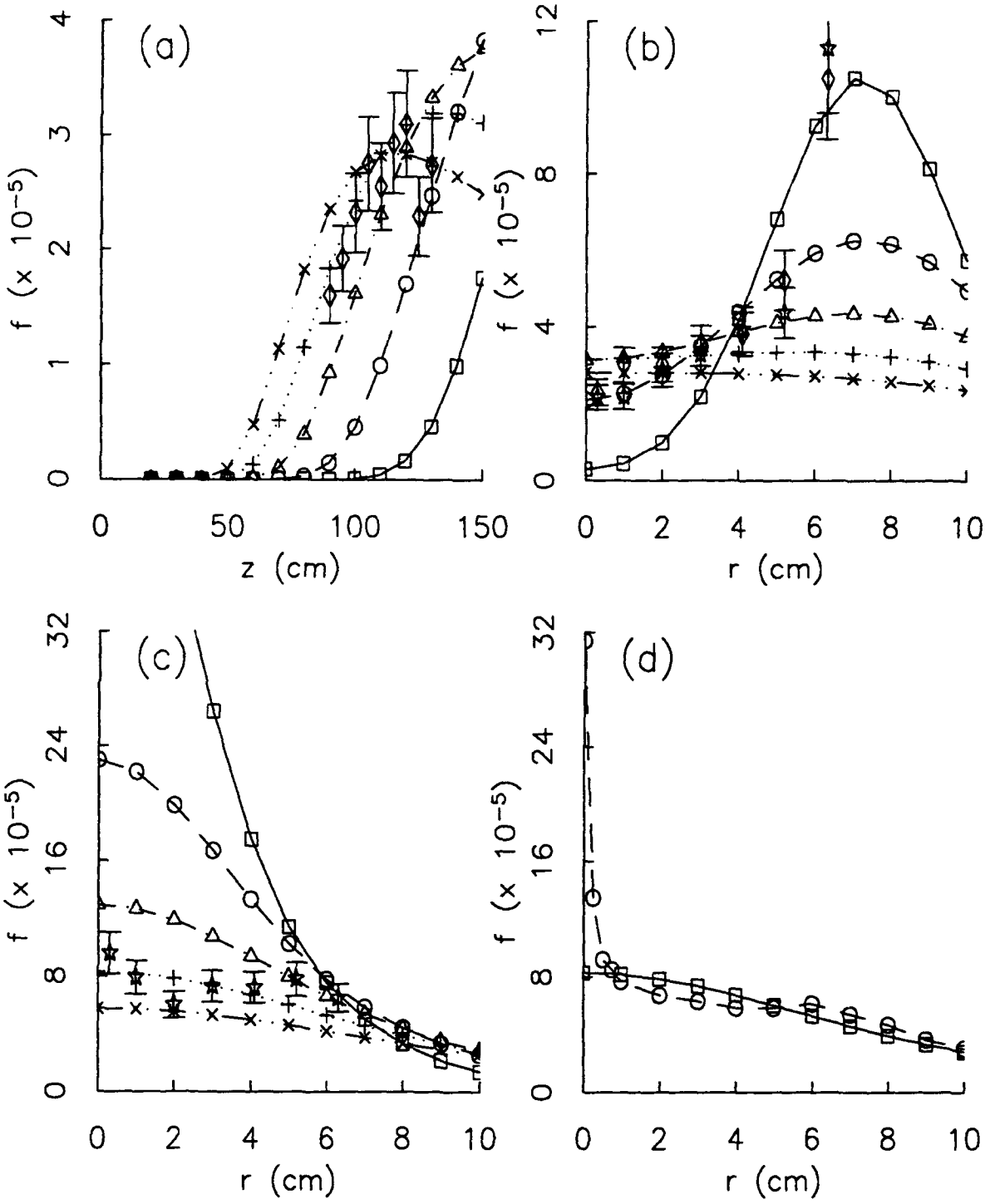

Figure 3: Fraction of ions reaching the charge collector. (a) as a function of z (no lens), (b) as a function of r (no lens), (c) for a single lens, (d) predictions for a two lens system. [(a)-(c) □ = 20 mrad HWHM, ○ = 30 mrad HWHM, △ = 40 mrad HWHM, + = 50 mrad HWHM, ◇ = observed - peak voltage, ⋆ = observed - peak current, (d) □ - single lens predicted performance, ○ - two lens predicted performance]

dispersed as it propagated. The charge collector signal j_L, at position $z = L$, was back calculated to its value at the annular mask, j_0, by the expression

$$j_0 = j_L \left[1 - \frac{L}{v^2}\frac{dv}{dt}\right]$$

where v is the ion velocity and dv/dt is its time derivative.

Figure 3 also shows numerically calculated values of f for a beam with a Gaussian distribution of radial and azimuthal divergence angles. Radial divergences from 20 - 60 mrad HWHM were considered, and in each case the azimuthal divergence is taken to be 2.5 × the radial divergence. On a shadow box target, azimuthal divergence was observed to be larger than radial divergence, probably due to the annular mask blocking off some larger radial velocity components. The value of 2.5 was chosen for best agreement between the calculation and the experiment. A radial divergence of 50 mrad HWHM provides the best match between the Gaussian calculation and the measured values of f.

Figure 3(b) contains experimental points measured at two times during the pulse, namely at peak voltage and at peak current. The high degree of agreement between the values suggests that the divergence was not changing significantly during the duration of the pulse.

Figure 3(c) shows the effect of a single focusing solenoidal lens. We were operating in a collective mode of focusing previously observed by Robertson[2] and by Kraft, *et. al.*.[3] In this situation ions and co-moving electrons are focused together at the geometric mean of their single particle focal lengths. The observed shape of the focus is consistent with the calculated 50 mrad HWHM radial divergence profile also shown in the figure.

A two lens system described elsewhere[4] is predicted to compensate to first order for radial divergence and beam energy spread. Our initial experiments on this two lens system show no improvement over single lens focusing. However, as Figure 3(d) shows, the predicted improvement in beam on axis is quite narrow. It is entirely possible that alignment errors resulted in the charge collector being displaced from the improved focus. Experiments with better alignment of optical elements and the detector will begin shortly.

A shadow box was used to measure mean beam direction for the Gaussian beam propagation calculations described above. Damage to heat-sensitive paper confirmed that the beam left the diode with 0±5 mrad rotational component. Ions exiting the annular mask also had 26±5 mrad inward radial velocity component.

Propagation Experiments in Gas

Propagation experiments in gas were conducted with a rotating beam. By overcharging the slow insulating field bank, we were able to inject into the drift space a beam with mean azimuthal velocity component equal to 20% of the z-component. This azimuthal current induced a z directed magnetic field. By the time the ion beam pulse ended, the background gas had been ionized and the magnetic field was frozen in. By observing the decay of this B_z with a loop on axis, we obtained information on the conductivity of the beam-ionized plasma. Figure 4 shows four sample measurments at differing background gas pressures, from .1 to 1 mTorr

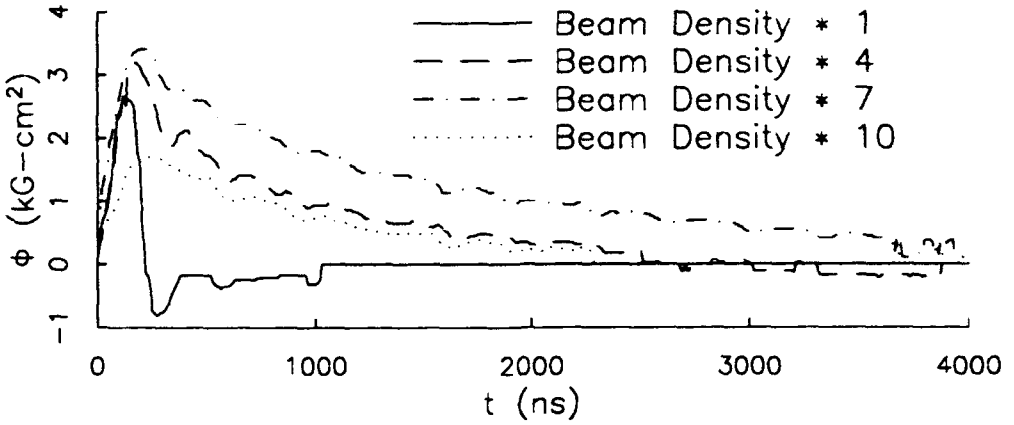

Figure 4: Decay of B_z for four background gas densities

(neutral density = 1 - 10 × beam density). The background gas used in these experiments was nitrogen. To determine the plasma conductivity from these decays, we modelled the plasma as a hollow cylinder with inner and outer radii r_{inner} and r_{outer}. The L/R time for such a cylinder is

$$\tau_{1/e} = \frac{L}{R} = \sigma\mu_0 \left[\frac{(r_{outer})^2 - (r_{inner})^2}{4}\right]$$

where σ is the plasma conductivity. From the divergence previously measured, we computed the half-maximum points of beam intensity at z = 25 cm, the loop location, and used these as r_{inner} and r_{outer}. Results are summarized in Table 1.

Pressure(mTorr)	$\tau_{1/e}(\mu sec)$	$\sigma(\times 10^{13} sec^{-1})$
0.15	<0.2	<0.01
0.38	1.0	0.57
0.70	1.8	1.02
1.03	0.93	0.53

Conclusions

Our preliminary divergence and single lens focusing studies have been completed. If the predicted performance of the two lens system can be realized, we will see a gain of 4 × in intensity on axis for the same beam divergence. Our experiments to date have not seen this improvement but may have missed the narrow focus created by the two lens system. Preliminary experiments with rotating beams propagating through neutral gas have yielded information about long time scale conductivity of beam ionized plasmas. Further focusing and conductivity experiments are planned.

References

[1] J. J. Ramirez, *et. al.*, *Fusion Technology*,15,2A,350 (1989).
[2] Scott Robertson, *Phys. Fluids*,26(4),1129-1138,(April,1983).
[3] Robert Kraft, Bruce Kusse, John Moschella, *Phys. Fluids*,30(1),245-251,(January,1987).
[4] Olson, J. C. , Kusse, B. R. , *J. Appl. Phys.*,70(10), 5719-5725,(October,1991).

Focusing of Intense Ion Beams with a Plasma-filled Solenoidal Magnetic Lens including Self-fields *

B.V. Oliver and *R.N. Sudan*
Laboratory of Plasma Studies Cornell University, Ithaca, N.Y. 14853

Abstract

We consider the potential of a solenoidal magnetic lens to transport and focus intense ion beams for the purpose of light ion driven ICF. We present results of numerical simulations of a short pulse, intense, Li^{+3} ion beam propagating through a single focusing, plasma-filled, solenoidal magnetic lens. The beam evolution is treated self-consistently by including the effects of self-electromagnetic fields which arise because the plasma electrons and energetic beam ions have very dissimilar dynamics in the presence of the strong applied magnetic lens fields. By considering the beam ions as particles and the plasma electrons as an inertialess fluid obeying a generalized Ohm's law, we derive equations for the evolution of the azimuthal magnetic field B_θ and the poloidal flux function ψ. The motion of background plasma ions has been neglected because beam pulse lengths and transit times are much shorter than the local Alfvén transit time. The beam particle dynamics are then solved self-consistently with a 2-1/2 dimensional, axisymmetric ($\frac{\partial}{\partial\theta} = 0$), hybrid PIC code.

For specified beam and plasma parameters, the results are expressed in terms of the power/cm^2 delivered to the target as a function of time. Attention is also paid to beam emittance growth. We study the cases when the plasma conductivity and density are held constant and when the conductivity and density evolve according to beam induced ionization of a gas.

Introduction

A solenoidal magnetic lens system has been proposed as a possible scheme for light ion beam transport [1]. A schematic of such a lens is shown in Fig.(1). In order to allow for ballistic focusing, the system assumes a charge and current neutral beam propagating in a transport channel filled with plasma. However, in the presence of the applied lens fields, electron mobility may be impeded. Currents may arise which defocus the beam. In order to address this problem we have developed a self-consistent model of the ion beam dynamics and magnetic field evolution during beam passage.

*Work supported by Sandia National Laboratories Contract No. 63-4881

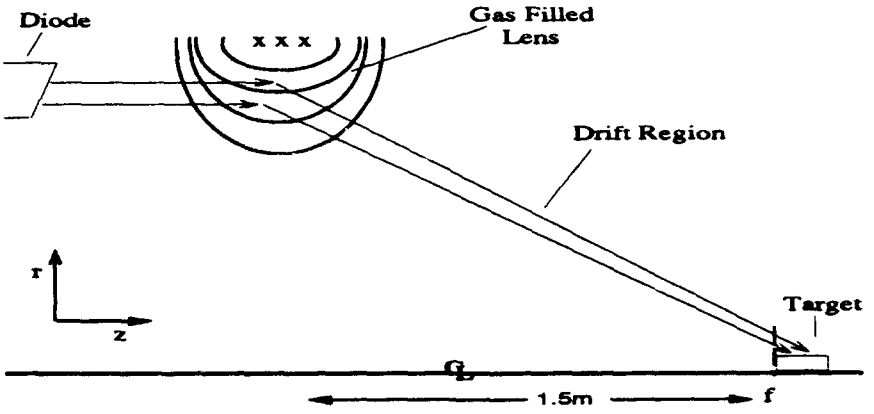

Figure 1: Schematic of a solenoidal lens focusing system

Model Equations

Ion Beam and Magnetic Field Evolution

Beam ions are considered to be single particles. Their orbits are governed by the electromagnetic force equation. The background plasma is composed of heavy immobile ions and collisional fluid electrons. The condition of no background ion motion requires that the pulse duration time τ_b be short enough that $v_A \tau_b \ll r_b$, where v_A is the Alfvén speed and r_b is the beam radius. We are not concerned with high frequency Langmuir oscillations so electron inertia is neglected and quasi-neutrality $n_e = Z n_b + Z_i n_i$ is assumed.

The plasma electrons are modeled by a generalized Ohms law

$$\mathbf{j_e} = \sigma(\mathbf{E} + \frac{\mathbf{v_e} \times \mathbf{B}}{c}) \tag{1}$$

where $\mathbf{j_e}$ is the electron current, σ the plasma conductivity, and $\mathbf{v_e}$ the electron fluid velocity. By taking the curl of (1) and utilizing Faraday's law an induction equation for $\mathbf{B}$ is given by

$$\frac{\partial \mathbf{B}}{\partial t} = \nabla \times \mathbf{v_e} \times \mathbf{B} - \nabla \times \eta(\nabla \times \mathbf{B} - \frac{4\pi}{c}\mathbf{j_b}) \tag{2}$$

where Ampere's law with displacement current neglected

$$\mathbf{j_e} = \frac{c}{4\pi}\nabla \times \mathbf{B} - \mathbf{j_b} \tag{3}$$

has been substituted on the rhs of Eq.(2), $\mathbf{j_b}$ is the beam current, and $\eta = \frac{c^2}{4\pi\sigma}$ is the magnetic diffusivity.

We consider the two-dimensional axisymmetric ($\frac{\partial}{\partial \theta} = 0$) case, and represent the magnetic field by writing

$$\mathbf{B} = \nabla\psi \times \nabla\theta + rB_\theta \nabla\theta, \tag{4}$$

where the poloidal flux function $\psi = rA_\theta$ and $\nabla\theta = \frac{1}{r}\hat{\theta}$. By substitution of Eq. (4), we obtain

$$\frac{\partial\psi}{\partial t} + (\mathbf{v_e}\cdot\nabla)\psi = \eta\,\triangle_*\,\psi + \frac{cr}{\sigma}j_{b\theta}, \tag{5}$$

from the $\hat{\theta}$ component of Eq. (1), and from the $\hat{\theta}$ component of Eq. (2),

$$\frac{\partial B_\theta}{\partial t} + (\mathbf{v_e}\cdot\nabla)B_\theta = \frac{\eta}{r}\,\triangle_*\,rB_\theta + r(B_\perp\cdot\nabla)(\frac{v_{e\theta}}{r}) - (\nabla\cdot\frac{\mathbf{v_e}}{r})rB_\theta + \frac{c}{\sigma}\hat{\theta}\cdot(\nabla\times j_{b\perp}) \tag{6}$$

where the operator $\triangle_* = r^2\nabla\cdot\frac{1}{r^2}\nabla$.

Eqs. (5) and (6) comprise a set of coupled non-linear PDE's, which can be used to advance the magnetic field in time. For a given beam ion scource, the time evolution of ψ and B_θ are functions of only themselves. The electron velocity $\mathbf{v_e}$ is derived from Eq. (3) where $\mathbf{j_e} = -en_e\mathbf{v_e}$. The corresponding components are given by

$$v_{e\theta} = \frac{1}{n_e e}(\frac{c}{4\pi r}\,\triangle_*\,\psi + j_{b\theta}), \tag{7}$$

and

$$v_{e\perp} = \frac{1}{n_e e}(j_{b\perp} - \frac{c}{4\pi}\nabla(rB_\theta)\times\nabla\theta) \tag{8}$$

The electric field **E**, necessary for the particle advancement, is obtained from Eq. (1). The four Eqs. (5,6,7,8) together with the beam ion momentum equation are solved self-consistently with the hybrid, PIC code SOLENZ. Similiar equations have been solved by Hewett [2] and Sudan and Lyster [3].

Plasma Conductivity

In the absence of Hall terms in Eq. (2) the plasma return current evolves according to

$$-\frac{\partial\mathbf{j_e}}{\partial t} - \frac{c^2}{4\pi}\nabla\times\nabla\times\frac{\mathbf{j_e}}{\sigma} = \frac{\partial\mathbf{j_b}}{\partial t} \tag{9}$$

For a gas-filled focusing cell, beam induced ionization will cause the conductivity to rise. Initial flux deposited by the head of the beam when σ is low will be "frozen" into the plasma once it becomes large. A fast rise time for σ will limit the amount of frozen in self-field. We have employed a simple zero-dimensional model to study σ and n_e as a function of time for injection of a 30Mev, 5kamp/cm^2, Li^{+3} ion beam into 1-2 torr Argon gas. The conductivity rises from 10^{11} to 10^{14} (sec^{-1}) in $<$ 4nsec.

In addition to a sharp rise, upper and lower bounds on the gasbag conductivity have been estimated for beams crossing magnetic fields in a collisional plasma. In Eq. (2) if the diffusivity η is small, the beam will act as a diamagnetic body and drag the trapped magnetic field with it, inhibiting good propagation. In order that the magnetic field diffuse rapidly through the beam, we require that the diffusive velocity be much greater than the electron drag velocity. Assuming that near current neutrality is established then

$$v_e \simeq \frac{n_b}{n_e}v_b < \frac{d}{dt}(c^2t/4\pi\sigma)^{\frac{1}{2}} \sim \frac{1}{2}\eta\tau_b^{-1/2}, \tag{10}$$

if τ_b is the beam pulse length. Thus we require [4]

$$\sigma < \sigma^* = \frac{1}{8\pi}(n_e/n_b)^2(c/v_b)^2\tau_b^{-1}. \tag{11}$$

In addition, prompt charge neutralization requires [5]

$$\sigma\tau_b > \frac{1}{4\pi}(l/r_b)^2. \tag{12}$$

Numerical Simulation

We have treated a 30MeV, 5kamp/cm^2, Li^{+3} ion beam passing through a solenoidal lens with various plasma environments. Our studies have concentrated on the effects of the conductivity σ and plasma electron density n_e on good beam propagation. All beams have zero initial divergence. They are 4cm wide annuli with an inner radius r_i =8cm and an outer radius r_o =12cm and a square beam pulse length τ_b = 10nsec. We characterize the beam by calculating the r.m.s. transverse emittance ϵ defined as [6]

$$\epsilon = 4(< r >^2 < r' >^2 - < rr' >^2)^{1/2} cm - rad. \tag{13}$$

where r is the radial position and $r' = \frac{dr}{dz}$ is the slope, and by evaluating the total energy E and the power/cm^2 as a function of time at the focal plane f (see Fig.(1)). The target is a πcm^3 cylinder located 1.5m downstream of the lens. Because we expect the electron conductivity to be adequate for current neutralization outside the lens, we only evolve the field equations within the lens region. Outside of this region we assume that the beam drifts ballistically to the target without any self-fields.

In Fig. (2), ϵ and the time integrated total energy E at the focus are plotted for various values of σ/σ^*. Both quantities are normalized by their value without self-field interaction. The electron density n_e was held constant at 5×10^{12} ($\sim$ 20mtorr), corresponding to a plasma/beam density ratio of n_e/n_b = 200. The criterion that σ be $< \sigma^*$ is evidenced by the maximum in energy around $\sigma/\sigma^* = 0.15$ and the minimum in ϵ at $\sigma/\sigma^* = 0.2$. The slight difference in σ/σ^* between the peak energy and minimum emittance is most likely due to the fact that ϵ does not quantify the spread in the four dimensional phase space of $(r, \dot{r}, z, \dot{z})$, but only the $(r, \dot{r})$ phase space. For values of $\sigma/\sigma^* > 1$ advection of the applied field lines limits the energy at the focus to < 75% of that obtained without self-field interaction. For small values of σ/σ^* resistive diffusion plays the dominant role in defocusing trajectories.

The lower bound $\sigma < \sigma^*$ is not as important for high plasma densities. In Fig (3), ϵ and E vs n_e are plotted for fixed values of σ/σ^*. For $n_e/n_b > 500$ the two curves converge to the no self-field case. This behavior is understood by considering the evolution of ψ in equation (5). For large σ (e.g. for $\tau_d = r_b^2/\eta >> \tau_b$) the first order terms in (5) yield

$$\frac{\partial\psi}{\partial t} = -\mathbf{v_e} \cdot \nabla\psi_o \tag{14}$$

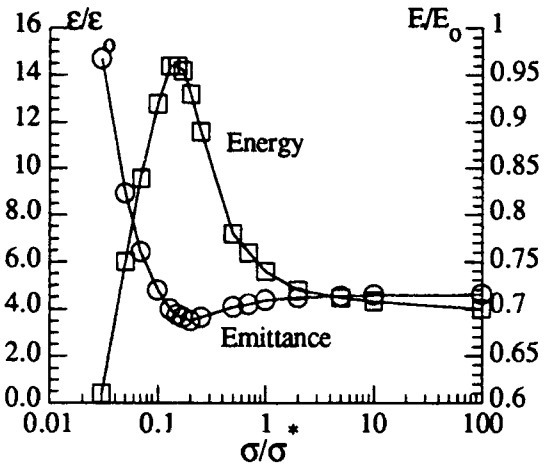

Figure 2: Normalized emittance ϵ/ϵ_o and energy E/E_o vs. σ/σ^*.

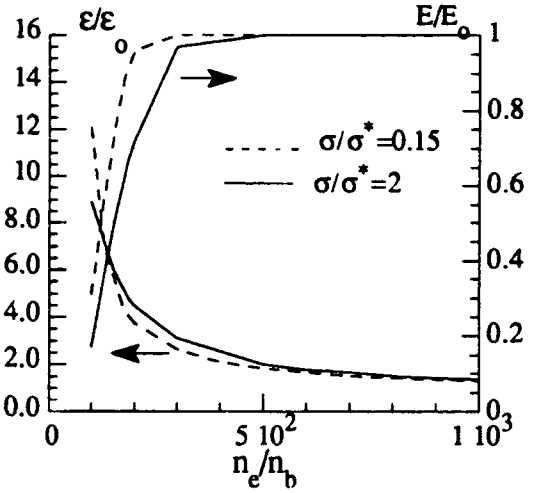

Figure 3: Normalized emittance ϵ/ϵ_o and energy E/E_o vs. normalized electron density n_e/n_b for values of $\sigma/\sigma^* = 0.15$ and 2.0 The curves asymptote to the no self-field value.

where ψ_o is the time independent applied field. For near current neutrality the dominant electron velocity is $v_{ez} \simeq n_b/n_e v_b$ which results in

$$\frac{\partial \tilde{\psi}}{\partial t} \simeq -(n_b/n_e)(v_b/L_z) \tag{15}$$

where $\tilde{\psi} = \psi/\psi_o$ and L_z is the z-gradient scale length of ψ_o. Hence, the net change in $\tilde{\psi}$ after the beam passes is $\Delta\tilde{\psi} = -(n_b/n_e)(v_b/L_z)\tau_b$. For $n_b/n_e < 0.002$, τ_b = 10nsec, v_b=0.1c, and $L_z \simeq$ 10cm, $\Delta\tilde{\psi} < 0.6\%$. Because the electrons are frozen onto the applied field lines the distortion of the lens field is a function of the distance that the electrons are displaced during beam transit. For large plasma densities and short beam pulse lengths τ_b, electron displacement is small, resulting in reduced stretching of the field lines. This implies that in addition to a rapid rise in σ the electron density n_e should also rise quickly in order to limit advection effects.

In situations envisaged for light ion fusion, the lens system and transport region are assumed to be filled with gas. The plasma environment is created by beam induced ionization. In Fig. (4), results from a simulation for the case of beam induced ionization of 1 torr Argon is presented. The time evolution of σ and n_e are taken from data generated by our zero-dimensional model mentioned above. Fig. (4a) is the time evolution of σ along the beam length and Fig. (4b) the resultant power at the focus compared to the no self-field case. The beam deposited 89% of the total energy with a rms normalized emittance $\epsilon/\epsilon_o \simeq 6.0$. Self-fields generated by the head of the beam when the plasma density and conductivity were low, resulted in defocusing of the back of the beam.

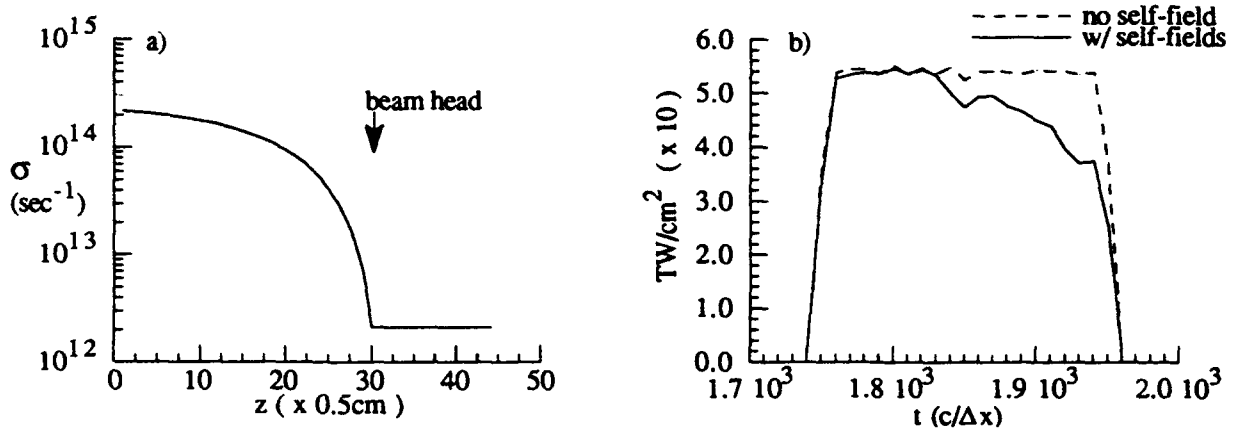

Figure 4: Results from simulation with beam induced ionization of 1 torr Argon gas. a) σ as a function of beam length. b) Power/cm^2 at the focus.

Conclusions

We have presented studies of the effect of self-fields on the focusing properties of an applied B solenoidal lens. It is realized that self-fields play a crucial role in the ability to obtain good focusing but that the effects can be greatly reduced by an appropriate choice of a high density, high conductivity background plasma. For the case of beam induced ionization of a gas, it is evident that self-fields generated by the head of the beam are frozen into the plasma and can subsequently defocus beam trajectories. This suggests the need to ionize the gas prior to beam propagation. Future work will examine the effects of microdivergence on focusing.

References

[1] C.L. Olson. In *Proc. 1988 Linear Accelerator Conference*, Oct. 3-7 1988.

[2] D.W. Hewett. *J. Comp. Phys.*, 38, 1980.

[3] R.N. Sudan and P.M. Lyster. *Comments Plasma Phys. Controlled Fusion*, 9, 1984.

[4] R.N. Sudan. Generation and propagation of intense ion beams. In *Inertial Confinement Fusion.* Societa Italiana di Fisica, Editrice Compositori, 1988.

[5] R.N. Sudan. Collective beam plasma interactions. In *Handbook of Plasma Physics, Vol.II,* chapter 6. North Holland Publishing Co., 1984.

[6] P. Lapostolle. *IEEE Trans. Nucl. Sci.*, NS-18, 1971.

ION BEAM MODELING USING ARGUS

J.J. Petillo, A.A. Mondelli, A. Mankofsky, and C.L. Chang

Science Applications International Corporation
1710 Goodridge Drive
McLean, Virginia 22102 USA

Over the past several years, the ARGUS code has been used to simulate a variety of ion beam phenomena. ARGUS is a general purpose three-dimensional simulation code. It can handle fields-only electromagnetic and electrostatic simulations, as well as electrostatic (steady-state and time-dependent) and electromagnetic time-dependent particle-in-cell (PIC) simulations. In the fields-only electromagnetic regime, ARGUS can be run in the time domain as well as the frequency domain (eigenmodes). The steady-state electrostatic PIC model is essentially a three-dimensional gun code.

This paper will present results of using the steady-state PIC module in ARGUS to model two related ion beam devices that use electrostatic quadrupole fields to focus and accelerate an H^- ion beam. The results of simulations of Lawrence Berkeley Laboratory's (LBL) Constant-Current Variable-Voltage (CCVV) H^- accelerator will be presented first. For this device, ARGUS has been used to simulate electron trapping and H^- stripping between the ion source and the CCVV accelerator, acceleration and transport through the CCVV modular electrostatic, discrete quadrupole sections. The second device is a helical electrostatic quadrupole used for low-energy beam transport in the SSC.

ARGUS Code

The development of three-dimensional simulation techniques has progressed to the point where detailed design simulations of accelerator components is now feasible. Particle-in-cell (PIC) techniques permit the self-consistent evaluation of charged-particle trajectories in the presence of both applied and self-generated electric and magnetic fields.

ARGUS, developed at SAIC, is a modularized, general-purpose three-dimensional simulation code system that includes electrostatic and electromagnetic field solvers, coupled to steady-state and dynamic PIC modules.[1] The dynamic PIC algorithm updates the fields each time step, thereby locking the field solution to the particle motion. The steady-state PIC algorithm is an iterative method for finding static field and trajectory solutions that are consistent with each other. Each iteration consists of pushing a collection of test particles across the grid in fixed fields. Each test particle represents a steady-state beamlet. The charge density distribution associated with all the beamlets in one iteration is used to compute the fields for the next iteration. The process converges when the fields and trajectories do not change from one iteration to the next.

ARGUS automates most of the apparatus needed to carry out three-dimensional simulations. All of the modules in ARGUS share common utilities for input, memory management, disk I/O, vector field operators, diagnostics, and graphics. The graphics package in ARGUS includes structure setup plots, as well as field and particle diagnostics. The code supports contour plots, arrow plots, line plots, and time histories of field quantities, in addition to phase space and slice plots for particles.

CCVV Accelerator

The constant-current, variable-voltage (CCVV) accelerator is a component of an H^- accelerator that has been designed at LBL as a portion of a neutral-beam source for tokamak heating.[2,3] The accelerator is a four-finger electrostatic quadrupole. H^- ions exit an ion source into a pre-accelerator, where electrons are removed using permanent magnets and the ions are accelerated to approximately 100 keV. The ions next enter a matching region, where the beam is matched to the CCVV fields. ARGUS has been used to model the preaccelerator and matching

sections, as well as the first accelerating stage of the CCVV structure.

The preaccelerator structure is shown in Figure 1, which is a two-point perspective plot of the ARGUS representation of the structure. A slice through the structure is shown as an insert. It includes a permanent magnet electron trap near the cathode. Figure 2 shows the result of a steady-state PIC calculation of this structure using ARGUS. The figure shows three orthogonal projections of the trajectories. The electrons can be seen entering the trap, while the ions pass through to the anode. A small deflection of the H^- ions toward the trap is visible in the x-z projection.

Approximately half the H^- ions injected into the preaccelerator do not survive to the CCVV accelerator. They are lost to stripping in the background gas that floods the region near the ion source. The matching section also serves to pump the gas away, before it can enter the accelerator structure. Using data from LBL, stripping reactions have been modeled in ARGUS. The probability that an ion will survive against stripping to location z can be expressed as

$$F(z) = 1 - b\left[1 - e^{-c(z-d)}\right] \qquad (1)$$

where the parameters, $\{b,c,d\}$, are specified to match LBL's data. Figure 2 includes these stripping reactions.

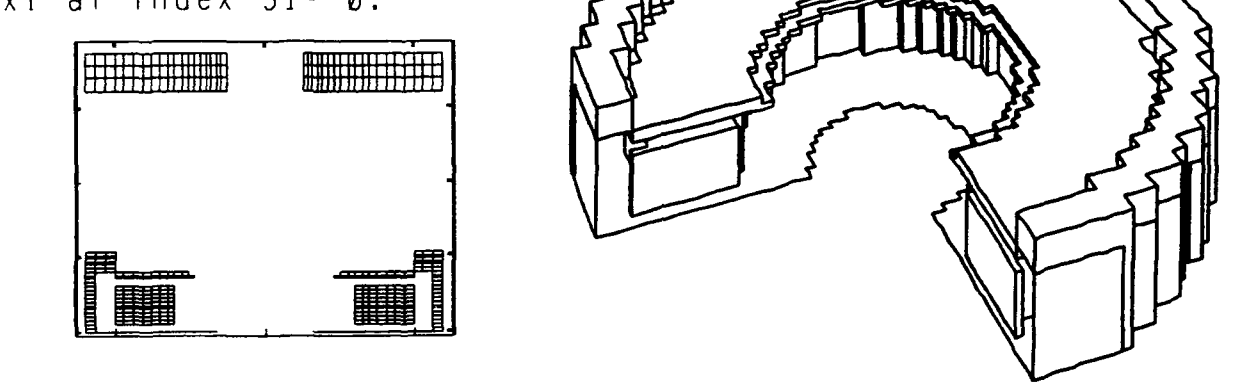

Figure 1. Structure Plot for the Preaccelerator in the LBL Neutral Beam Source.

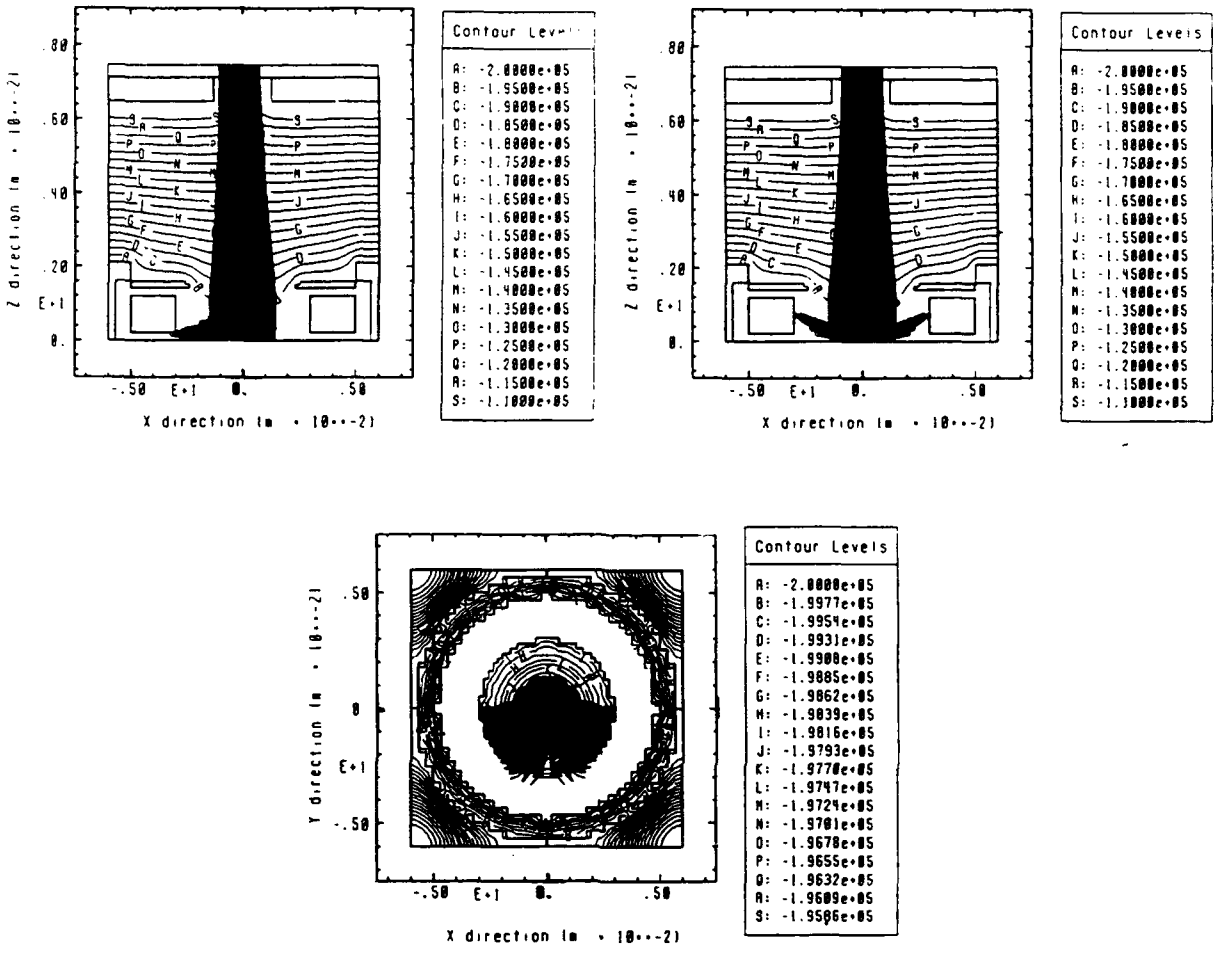

Figure 2. Orthogonal Projections of the Steady-State PIC Solution for Preaccelerator Shown in Figure 1.

Steady-state calculations have also been carried out for the CCVV structure itself. The discretized ARGUS representation of the structure is shown in Figure 3. The results of the ARGUS simulations are in good agreement with an envelope model used at LBL. Figure 4 shows both results. It is possible to initialize ARGUS from the envelope model, by providing the envelope solution as the first iteration in the steady-state PIC solution. This initialization would increase the speed of the ARGUS solution.

HESQ LEBT for the SSC

The low-energy beam transport (LEBT) is used to match the beam from the ion source to the radio-frequency quadrupole (RFQ) linac that comprises the first injector stage of the SSC.[4] Two major options have been considered for the LEBT design. One is to use an einzel lens and the other is to use a helical electrostatic quadrupole (HESQ) configuration. The HESQ option is generically similar to the ESQ focusing used in the CCVV accelerator, and ARGUS has been applied to the analysis of this configuration.

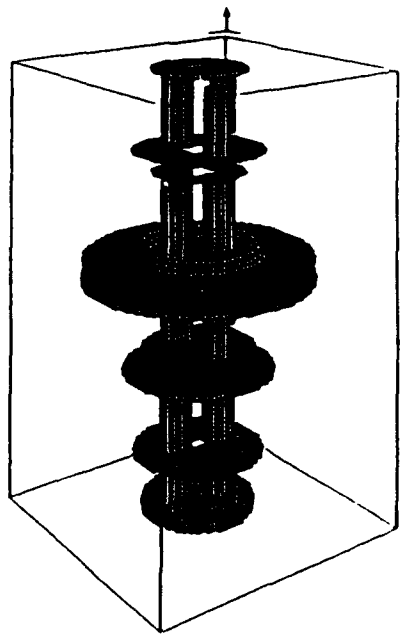

Figure 3. ARGUS Representation of LBL's CCVV Accelerator.

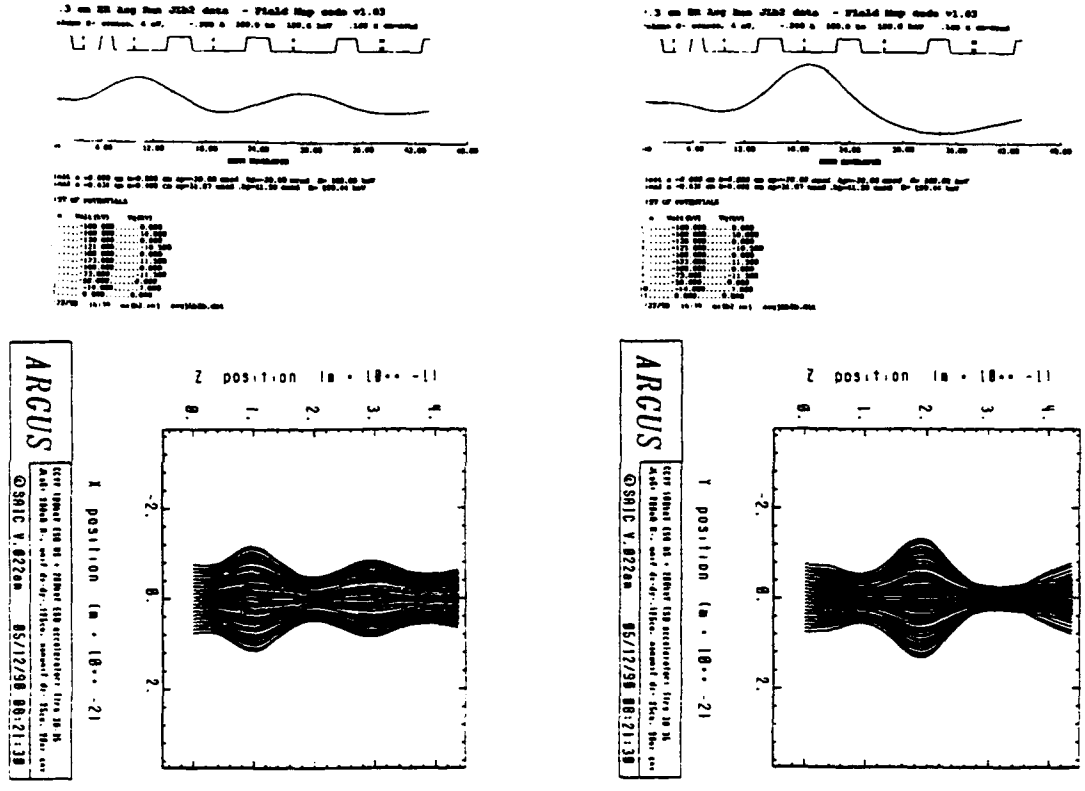

Figure 4. Comparison of LBL's Envelope Solution with the ARGUS Result for the CCVV Accelerator in Figure 3.

The HESQ approach has been tested at the Texas Accelerator Center (TAC), using a structure built from discrete disks. Figure 5 shows the ARGUS representation of this structure. Each plane contains four disks, 90° apart, the disks are rotated by 18° from plane to plane. Figure 6 is the ARGUS steady-state solution for an approximately matched beam in this structure.

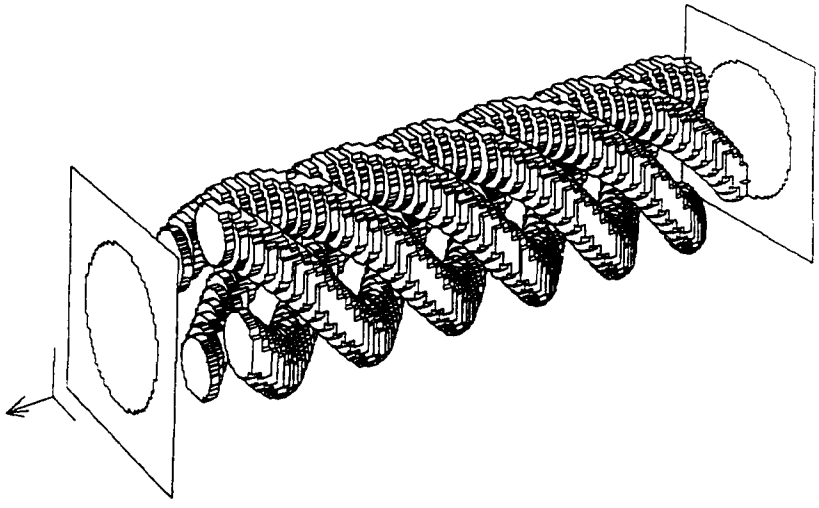

Figure 5. The HESQ Structure Prototype at TAC.

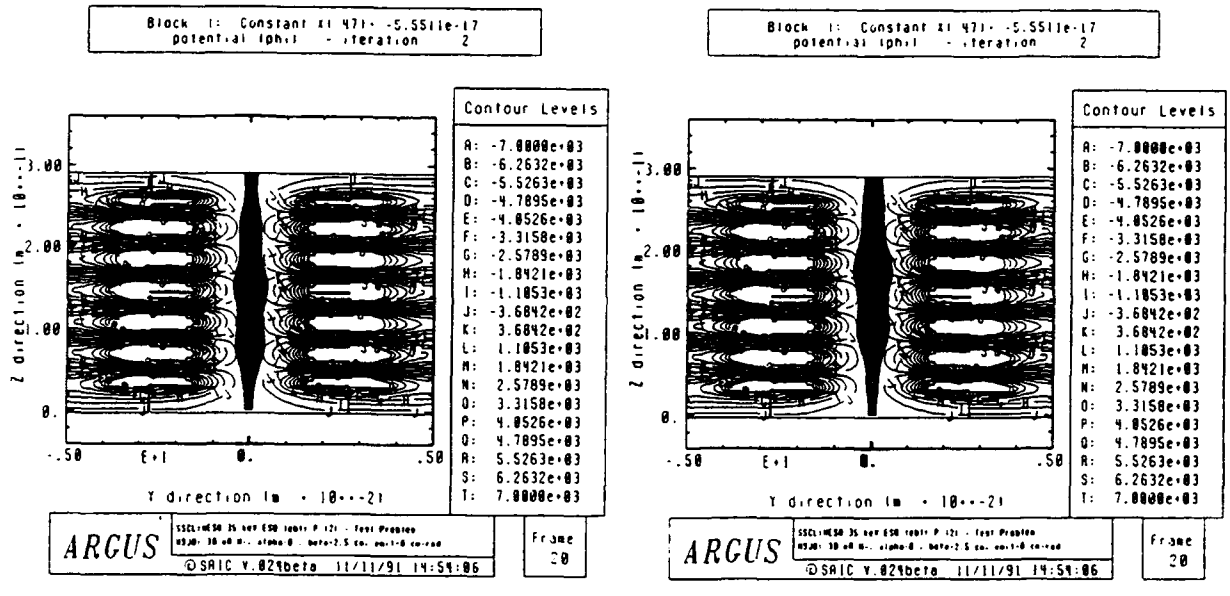

Figure 6. ARGUS Steady-State PIC Solution for a Matched Beam in the HESQ.

ARGUS Release

The ARGUS code has been tested in several design applications relevant to the acceleration and transport of ion beams. A new module to handle chemistry between charged particle species is planned for release in the coming months. Beginning in 1993, the code will be available from the Los Alamos Accelerator Code Group.

Acknowledgment

It is a pleasure to acknowledge the collaboration of Adam Drobot at SAIC, Oscar Anderson, Ludmilla Soroka, and Chun-Fai Chan at LBL, and Deepak Raparia at the SSC Laboratory.

This work was supported by the U.S. Department of Energy, Lawrence Berkeley Laboratory and the Superconducting Super-Collider Laboratory.

References

1. A. Mankofsky, *Three-Dimensional Electromagnetic Particle Codes and Applications to Accelerators*, in **Linear Accelerator and Beam Optics Codes** (C.R. Eminheizer, ed., A.I.P. Conf. Proc. No. 177, American Institute of Physics, New York, 1988), p.137ff.

2. O.A. Anderson, L. Soroka, C.H. Kim, R.P. Wells, C.A. Matuk, P. Purgalis, W.S. Cooper, and W.B. Kunkel, *Constant-Current Variable-Voltage (CCVV) Accelerators*, Proc. 1st Eur. Part. Accel. Conf. (EPAC88, June 7-11, 1988, S. Tazzari, ed., World Scientific Publishing Co. Pte. Ltd., c. 1989) Vol. 1, p. 470.

3 O.A. Anderson, C.F. Chan, W.S. Cooper, W.B. Kunkel, J.W. Kwan, A.F. Lietzke, C.A. Matuk, P. Purgalis, and L. Soroka, *Design of a 200 mA DC H^- Injector for an RFQ*, Proc. 1987 IEEE Part. Accel. Conf. (E.R. Lindstrom and L.S. Taylor, ed., IEEE Catalog No. 87CH2387-9, Washington, DC, March 16-19, 1987), Vol. 1, p. 289.

4. D. Raparia, *Beam Dynamics of the Low Energy Beam Transport and Radio Frequency Quadrupole*, Ph.D. Dissertation (University of Houston, Houston, TX, 1990).

The present article delineates the problem of H^- beam transport and its matching to an RFQ using a novel 6-lens electrostatic quadrupole (ESQ) system as an LEBT. The main emphasis here is to understand the physics of emittance growth in an ESQ transport system and the possible ways to mitigate the problem. In the past the ESQ LEBT system was used very successfully to transport H^- beams;[6] however, the beam perveance was much lower there. Here we consider a highly space-charge dominated, high-brightness beam (beam perveance K = 0.003 and normalized brightness $\sim 10^{11} A/m^2 rad^2$). It is quite a challenging task to transport such beams over a certain distance and focus it into an RFQ without any significant emittance dilution. The design is based on detailed computer simulation of beam dynamics through the transport section. The computer predictions regarding performance of the LEBT system are analyzed in the context of beam parameters of two particular types of H^- ion sources – Penning-Dudnikov source as used in the BEAR experiment,[3] and a volume ionization source of Brookhaven National Laboratory.[9] These two types of sources are particularly suitable to obtain high-brightness H^- beams.[10] In our previous articles, H^- beams from a Penning-Dudnikov source were mainly considered. Here, the emphasis is on the transport of H^- beams from a volume source. We have also addressed the issue of sensitivity of the beam parameters due to misalignments. Finally, the problem of matching the H^- beam to an RFQ is discussed.

II. Beam Dynamics through the ESQ LEBT

The design procedure as reported earlier [11] involves a sequence of computer code analysis: (i) A linear beam optics code integrates the K-V envelope equations and generates the basic geometrical parameters of the lens system. (ii) A 3-D LAPLACE solver calculates the equipotentials and evaluates the fringe-field matrices as suggested by Matsuda and Wollnik.[12] (iii) A modified PARMILA code[13] uses input from the above two steps and evaluates the beam parameters (beam size, emittance growth, etc.). This scheme led us to choose a combination of six ESQ lens system to transport H^- beams over a distance of 30 cm and to provide a moderate convergence ($\sim$ -30 mrad) at the end. The technical details of the LEBT system and some results on the computer code predictions of beam characteristics have been given earlier.[11] The essential points to note from our previous articles are:

1. A unique feature in the design of the ESQ LEBT system is that the entire system is self-aligned mechanically. This demands high precision in the fabrication of the components and their assembly. On the other hand, it eliminates the usually tedious alignment job in the experiment.

2. The performance of the ESQ LEBT has been examined using beam parameters of a Penning-Dudnikov source. Some assumptions of the input beam (normalized brightness = 8×10^{10} $A/m^2 rad^2$, divergence at full beam radius of 1 mm = 20 mrad) are made on the basis of analysis of the emittance data at z = 10.6 cm from the extraction slit.[11] The output beam from the ESQ LEBT is found converging ($\sim$ -25 mrad), and it shows an emittance growth by a factor of about 1.8 assuming a K-V

type distribution of the beam. The emittance growth is identified as due mainly to chromatic aberrations.

The above analysis has been carried out further. Figure 1(a) shows the evolution of rms normalized emittance through the ESQ transport channel. The enhancement of emittance occurs essentially in the second and fifth lenses, when the amplitude of the beam envelope grows to more than 80% of the quadrupole aperture. The beam particles residing in the outer part of the envelope are responsible for the emittance growth, and these particles can be rejected by suitable use of the ground plates between the adjacent ESQ lenses (Fig. 10 in ref. 11) as beam scrapers. Two beam scrapers are inserted, one in front of the second lens and the other in front of the fifth lens. Figure 1(b) shows the evolution of emittance through the ESQ LEBT when 10% of beam particles are scraped out. The emittance growth is a factor of 1.4 here. This is an efficient way to deliver an almost emittance-preserved beam to an RFQ. The above analysis has been carried out using typical parameters of H^- beams from a volume ionization source, here a BNL-type. Usually the beam from such sources has lower current density compared to, say, the Penning-Dudnikov case. Hence, a larger extraction slit (radius of extraction slit = 5.6 mm here as opposed to a radius of 1 mm in the Penning-Dudnikov case) is used to draw the same amount of current in the case of volume sources. Also the beam divergence at the extraction slit can be very small; almost a parallel beam can be extracted from the source. The estimated normalized brightness of this beam is about $3 \times 10^{10} \mathrm{A/m^2 rad^2}$; all other parameters have been given earlier.[11]

Figure 2 shows the modified PARMILA results on distribution of the beam particles corresponding to an H^- beam from the volume source. Here the parameters corresponding to a 4 times rms ellipse, constructed by including 90% of the beam particles at the output of the ESQ LEBT, are: $X_{\max} = 3.3$ mm, $Y_{\max} = 2.7$ mm, $(X_{\max})' = -13.5$ mrad, $(Y_{\max})' = -14.9$ mrad. The maximum voltage on the ESQ lenses was 4.7 kV. The emittance growth of the beam is negligibly small, $\sim 4\%$. This result suggests that the characteristics of the input beam are very crucial to the issue of emittance growth in a transport system - – a parallel input beam is desirable.

The sensitivity of output beam parameters with variation of beam voltage, beam current, misalignment of the beam axis with respect to the LEBT system has been studied. The K-V code analysis suggests that the beam parameters do not change noticeably for a $\pm 1\%$ change of quad voltage (from the ideal setpoint) on all the lenses simultaneously. Similar insensitivity is noted for variation of beam current (ideal = 30 mA) within a few milliamperes. Preliminary analysis on the aforementioned misalignments is done using the modified PARMILA code (no image charge is included in the present code). With the variation of the amount of off-centering of the input beam, the phase-space distribution of the output beam remains almost invariant, while the beam centroid shifts coherently. A translational off-centering by 1 mil at the input is amplified by about a factor of 2 off-centering at the output of the LEBT; this also introduces an angular error of the beam centroid by about 2 mrad. An on-centered input beam with an error of 1 mrad in the injection angle shows an off-centering of the output beam by about 1.8 mil; the error in

the angle stays almost the same through the LEBT channel.

III. Matching to an RFQ

The beam from the LEBT section needs to be matched with the RFQ in order to achieve a good transmission and preserve emittance through this channel. The typical Twiss parameters for the acceptance ellipse of an RFQ (e.g., BEAR and SSC RFQ) demand a beam convergence of about -90 mrad at the full beam radius of about 1.3 mm. It is an arduous task to satisfy these requirements of an RFQ by an ESQ LEBT alone without sacrificing the emittance growth. An LEBT composed of two modules — the ESQ lenses as a beam transport section and an einzel lens at the end as a matching section — seems to be a good choice in this pursuit.

Figure 3 shows a schematic of the ESQ LEBT with a short modular attachment containing an einzel lens. Preliminary analysis is done using the K-V code. The beam envelopes for the two situations are shown in Fig.4: (a) Penning-Dudnikov case, (b) volume source case. The beam parameters at the end of the einzel lens match well with the requirements of the RFQ as mentioned earlier. A high value (about 7.0) of the ratio of the aperture of the einzel lens to the beam size is taken here; hence, the einzel lens is expected to have an insignificant contribution to the emittance growth. This problem is being currently investigated to get a quantitative answer.

IV. Experiments and Discussion

The ESQ LEBT system has been constructed in-house. The overall mechanical alignment of the apparatus has been measured, and found to be within $\pm$ 1.5 mil. The power supply system for the ESQ lenses has been attached. Detailed voltage hold-off tests have been done, and the performance is satisfactory. It is planned to test this ESQ LEBT with an H^- beam from a magnetron source at the SSC Laboratory. The code results are being reviewed in the light of the beam parameters from the magnetron source.

It has been shown that a combination of an ESQ LEBT system with an einzel lens can be used very effectively to transport a space-charge dominated, high-brightness H^- beam over a distance of about 30 cm and focus the beam into an RFQ without any significant emittance dilution. This method appears to be attractive particularly to handle a highly diverging beam from an ion source. Such a scheme has a number of advantages: (i) flexibility to handle a wide range of input beam parameters from different types of ion sources, (ii) allow sufficient buffer space (not field-free) between an ion source and an RFQ for differential pumping, (iii) experiments with low-voltage power supplies over the major part of the transport, and (iv) ease of fine tuning. It is now a very important issue to determine the optimum length of the LEBT section to insure a reliable operation of the injector system in an accelerator. Carefully controlled experiments with various transport schemes are warranted and a good database is required to unravel the reliability of the computer simulation results.

Acknowledgments

This work is supported by ONR/SDIO.

References

1. "Site-Specific Conceptual Design of the Superconducting Super Collider", edited by J. R. Stanford and D. M. Matthews, Superconducting Super Collider Laboratory Rept. SSCL-SR-1056, July 1990.
2. J. G. Alessi, et al., Rev. Sci. Instrum. **61**, 625 (1990).
3. P. G. O'Shea, et al., Nucl. Instrum. & Methods in Phys. Res. **B40/41**, 946 (1989).
4. C. R. Chang, Proc. LINAC Conf., Albuquerque, NM, Sept. 10-14, 1990, p.399.
5. M. Reiser, et al., SPIE Proc. Microwave and Particle Beam Sources and Propagation **873**, 172 (1988); S. K. Guharay, et al., High Brightness Beams for Advanced Accelerator Applications, College Park, MD., June 6-7, 1991, AIP Conf. Proc.No. 253, p. 67.
6. O. Anderson, et al., Lawrence Berkeley Laboratory Rept. LBL-27953 (1989).
7. D. Raparia, Proc. LINAC Conf., Albuquerque, NM., Sept.10-14, 1990, p.405.
8. D. A. Swenson, et al., Proc. LINAC Conf., Albuquerque, NM, Sept. 10-14, 1990, p.39.
9. J. G. Alessi, (private communication)
10. J. G. Alessi, High Brightness Beams for Advanced Accelerator Applications, College Park, MD., June 6-7, 1991, AIP Conf. Proc. No. 253, p. 193.
11. S. K. Guharay, et al., SPIE Proc. Intense Microwave and Particle Beams III **1629**, 421 (1992).
12. H. Matsuda and H. Wollnik, Nucl. Instrum. & Methods **103**, 117 (1972).
13. C. R. Chang, et al., SPIE Proc. Intense Microwave and Particle Beams **1226**, 483 (1990).

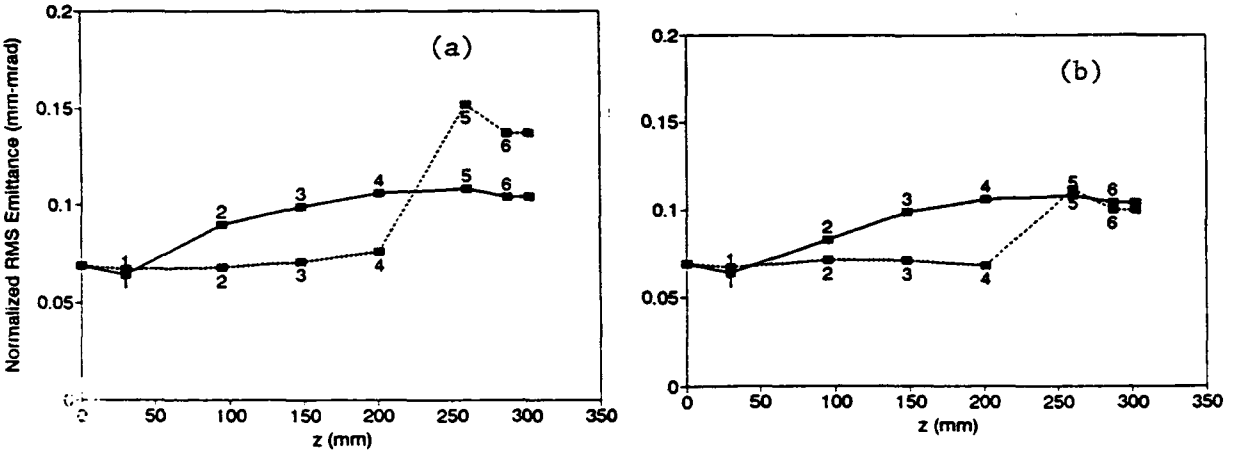

Fig. 1. Evolution of rms normalized emittance (solid line: X-component; dashed line: Y-component) through the ESQ lenses for an H^- beam from the Penning-Dudnikov source: (a) without any beam scraper; (b) with beam scrapers, one in front of the second lens and the other in front of the fifth lens. The numbers inside the figure identify the location of the downstream endpoint of the corresponding lens.

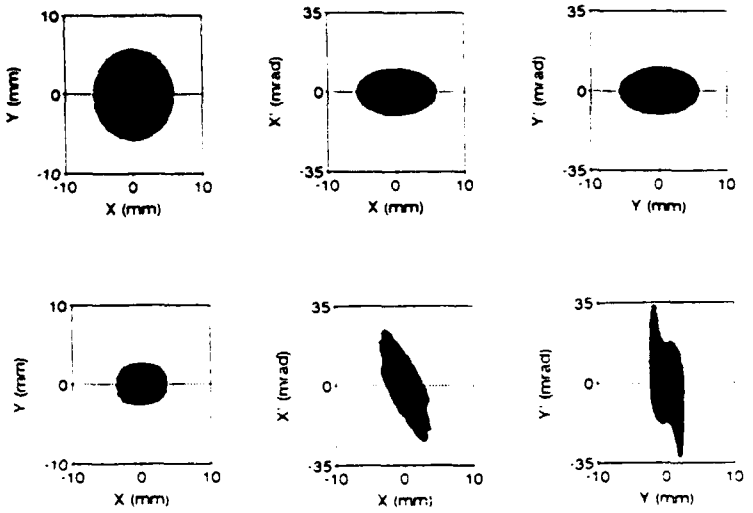

Fig. 2. Modified PARMILA results of distribution of beam particles for an H^- beam from the BNL volume source: Input beam (top figure); Output beam (bottom figure).

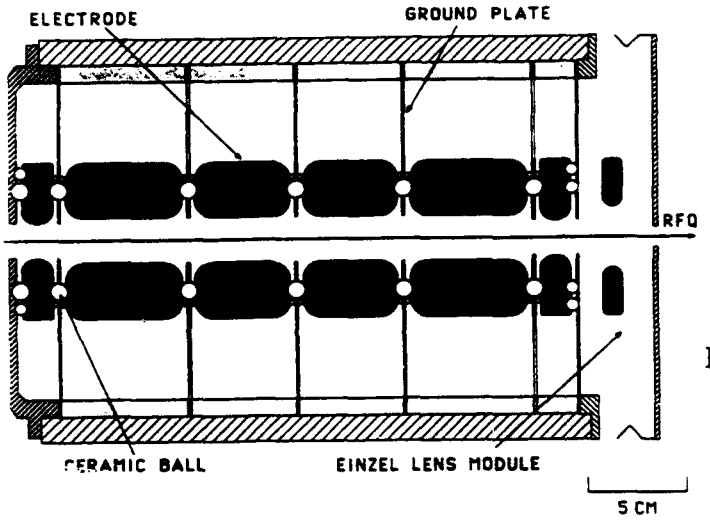

Fig. 3. Schematic of the LEBT system.

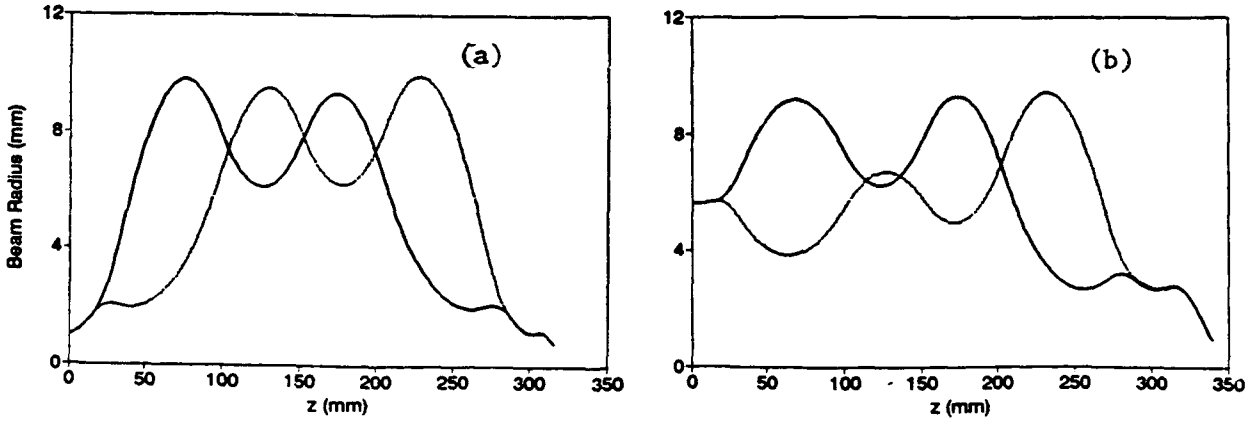

Fig. 4. K-V envelope solution (solid line: X-component; dashed line: Y-component) for the matched beam to an RFQ using H^- beam parameters corresponding to: (a) Penning-Dudnikov source; (b) BNL volume source.

ORION PROJECT: ACCELERATION OF CLUSTER IONS AND HIGHLY CHARGED BIOMOLECULES FROM 10 MEV TO 1 GEV.

S.Della-Negra, Y.Le Beyec, A.Brunelle, D.Gardès, B.Waast (Institut de PhysiqueNucléaire -France)
E.Parilis (California inst. of Techn. 200-36 Pasadena)
P.Hakansson, B.U.R. Sundquist (Dpt. of Phys. Uppsala University - sweden)

Abstract

Cluster ions-projectiles have been revealed to be very efficient to drive energy or momentum on a solid surface. The impact of massive cluster is able to produce high energy density on a narrow area. Astonishing non linear effect has been observed [1] in the yield of secondary ions emission desorbed from a surface bombarded by molecular or clusters ions.

The ORION project consists in accelerating with the Orsay Tandem, cluster ions and in a further step, charged biomolecules, in order to investigate these processes in a velocity range which correspond to their maximum of efficiency (a few keV per mass unit).

This paper presents preliminary attemps and first results in creating C_{60} and C_{70} molecular ion beams using the Orsay Tandem accelerating structure.

Introduction

The impact of polyatomic particles provides a mean to study non linear effects in the energy deposition process. Such studies have been performed in the nuclear stopping regime [2] and with massive particles [3]. For fast and small molecular ions there are a few examples of such studies. No experiments were reported so far for fast and large molecular ions which can deposit in a solid a large amount of energy in a small volume. This paper reports for the first time on the successful production of Carbon-60 ions with MeV energies, i.e with velocities above the Bohr velocity.

The recent discovery that 60 atoms of carbon form a compact closed structure [4,5] and the possibility of synthetizing easily such molecules have made it possible to produce a C_{60} ion beam at 50 MeV. The molecular ion stability allows transport of the beam in vacuum (10^{-7} torr) over a large distance (> 50 meters). If necessary, and with additional equipment, an increase of energy by a factor 10 or more could be achieved in the future.

Experimental

Sample and target preparation

The synthesis and chemical separation of C_{60} was made in Montpellier with the equipment of the laboratory of "Dynamiques des phases condensées" according to a procedure described in the literature [6,7]. Enrichment of 90 percent in C_{60} was obtained and about one gramme of powder was used to prepare solid targets. A small quantity of C_{60} powder was mixed with ironin a ratio of one molecule of C_{60} for 3 atoms of iron. The resulting powder was then compressed at 200 kg/cm^2. The final form of the target was a disc of 0.8 mm thick and 5 mm in diameter. Several targets of 30 mg were prepared in this way.

Injection of C_{60} ions in the Tandem accelerator.

A ion gun delivering a high intensity beam of Cs ion at 20 keV was used to bombard a C_{60} target. Sputtered C_{60}^- ions were first accelerated to an energy of 20 keV and were deflected by a magnetic field in a 35 degrees magnet. A pre-acceleration at 180 keV, was used before entering the tandem accelerator. An ion buncher is operated on this section at a frequency of 5 MHz. Electrostatic deflection plates can also be used to deflect the beam for a certain time (up to 50 μs). Before injection in the tandem, a Faraday cup is used to measure the beam current. Hundreds of picoamperes to nanoamperes were measured at this stage. The variation of intensity as a function of the magnetic field in the injection magnet shows clearly the two contributions at M/Z 720 and M/Z 840 corresponding to C_{60}^- and C_{70}^- respectively.

High energy section

The C_{60} beam is then accelerated to the energy qV with V beeing the high voltage of the terminal which can be varied from + 7 to + 14 Megavolts. At the center of the machine there is a cylindrical gas cell (L = 60 cm, Ø = 8 mm) containing the gas necessary for stripping. In the present study, very low pressures were used. The experiment shows that a multiple ionization happens in the gas cell and that C_{60}^- becomes C_{60}^{n+} which is then accelerated in the second section of the tandem. For 10 Megavolts at the terminal and n=1 the total energy is 20.2 MeV (20 MeV in the tank and 200 KeV of pre-acceleration). After the second acceleration, ions are travelling about 10 meters in the beam line in a tube mounted in the zero degree direction. An ion and electron detection system [8], as shown in Fig. 1 was specially installed on this tube for the C_{60} experiment.

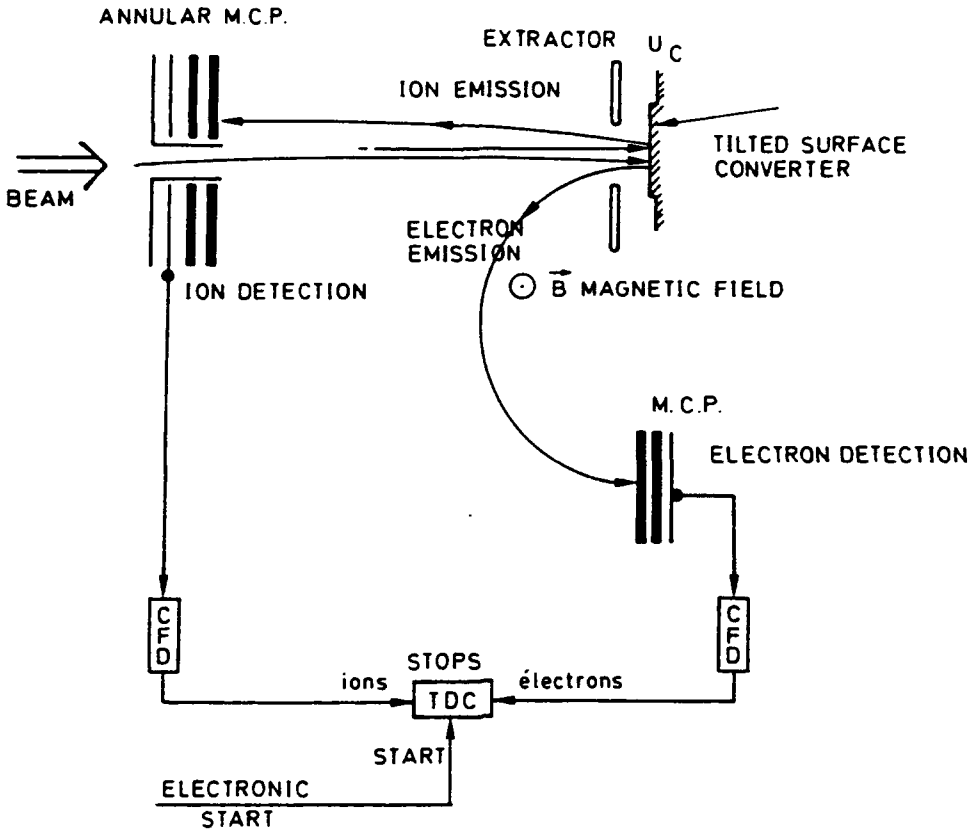

Figure 1 : System of detection for secondary ions and electrons after impact of molecular ions on an electron converter surface or any kind of surfaces. A CsI coating was used in this experiment.

Time of Fligth measurements for beam identification

Time of fligth measurements were made between the deflection system (before the tandem) and the detectors in Fig. 1. The total time of fligth distance was therefore about 50 meters. Secondary ions and electrons were detected but the electron signal was used as a stop signal for the beam time of fligth measurements. Fig. 2 shows time of fligth spectra of C_{60}^{+} at 30 MeV and 40 MeV. where components of C_{60}^{2+} and C_{60}^{3+} are visible. The calculated TOF values correspond to the measured values. Since the pulsing system was not designed for such a heavy ion beam, 2 to 3 ion beam pulses from the buncher were present in one TOF peak modifications will be made in the future. A transmitted particle yield of 10^{-3} (and even larger) has been estimated (ratio between the beam current before the tandem and at the detection site).

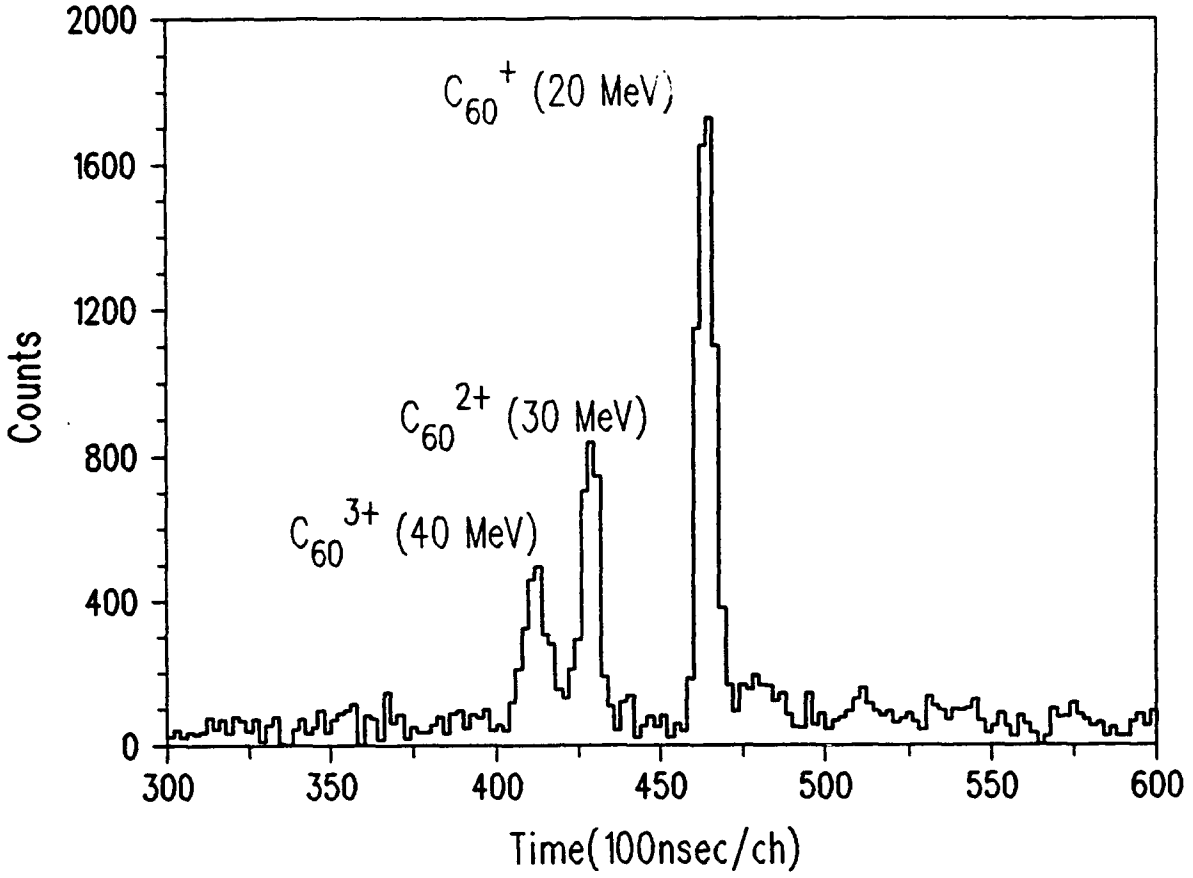

Figure 2 : Time of flight mass spectrum at 10 Megavolts of acceleration voltage in the Tandem showing the presence of C_{60}^{2+} and C_{60}^{3+}.

Discussion

The success of this experiment is due to the high stability of the molecule and to the relatively high yield of ionization in the gas cell. In addition, the largest intensities of C_{60}^{1+}, C_{60}^{2+}, C_{60}^{3+} beams are obtained at the same small gas flow value (fig 3). This indicates that the multiple degree of ionization of one molecule is very likely achieved in one collision. The relative intensity of the peaks (in Fig. 3) decreases slowly (the C_{60}^{3+}/C_{60}^{+} ratio is 18 % and C_{60}^{2+}/C_{60}^{+} is 40 %). A peak of C_{60}^{4+} was not observed and a maximun charge of 3 has therefore been measured in this experiment. For n = 4 it can be calculated that the electrostatic repulsion is larger than the binding energy of one atom in the C_{60} structure. C_{60}^{4+} must therefore be instable with respect to Coulomb fragmention. A calculation of single, double and triple ionization of C_{60} in binary collisions N $\rightarrow$ C shows that only the collision parameter for single ionization corresponds to a C recoil energy lower than the binding energy of a carbon

atom in the structure. Therefore, the double and triple ionization are due to consecutive collisions of a nitrogen atom with several carbon atoms in the same molecule rather than to multiple ionization in one binary collision.

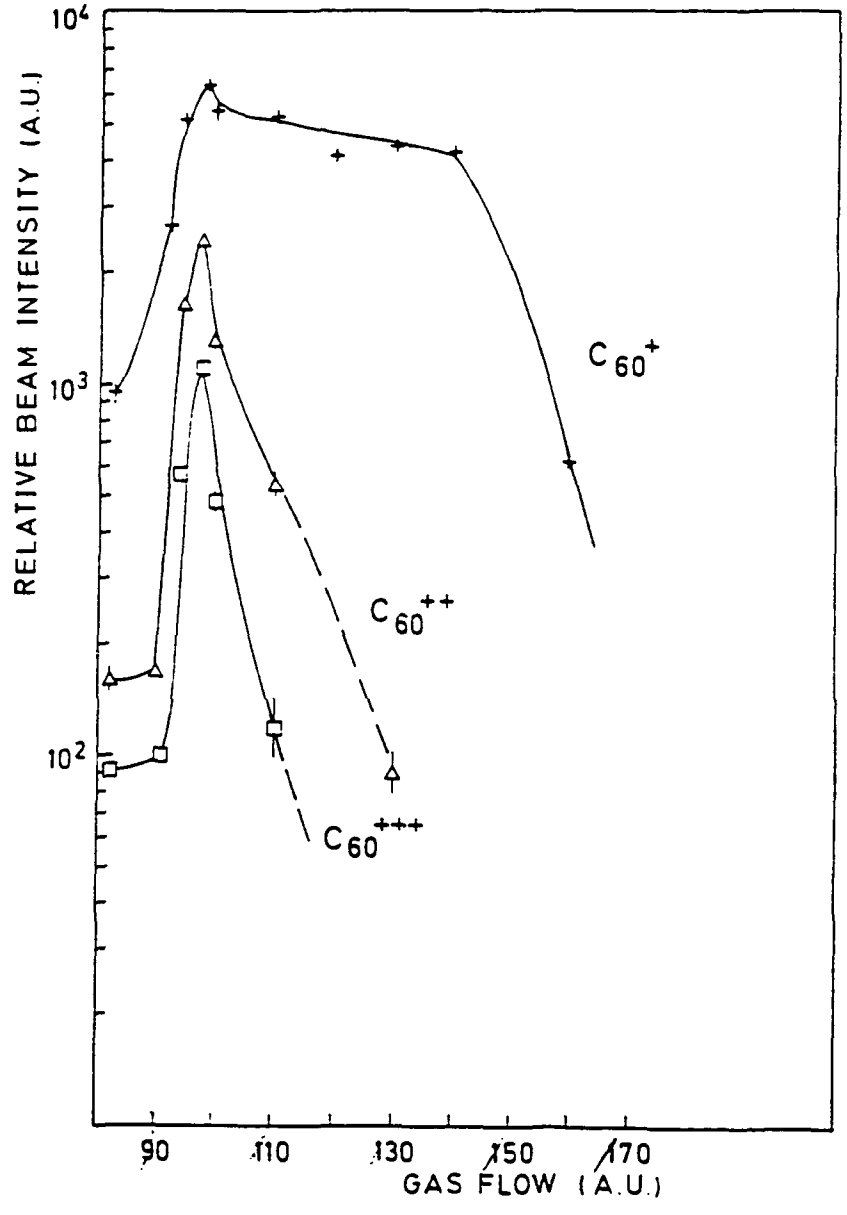

Figure 3 : Relative intensity of the multiply charged ions as a function of the relative gas flow in the gas cell at the center of the tandem machine

The possibility of such multiple ionizing collisions in one N_2-C encounter is caused by the peculiar shape of the ball. The projected density of the C_{60} molecule is 5 times larger, in the 1 angstrom thick ring of the peripherical region, than in the rest of the projected

part (approximately 2.5 and 0.5 atoms/Å^2 respectively. Thus, the multiple ionization is likely obtained in periphical collisions. Additional collisions leading to more than triple ionization increase when the gas pressure increases. They give rise to Coulomb molecular break up.

References

[1] M.G.Blain, S.Della-Negra, H.Joret, Y.Le Beyec, E.A.Schweikert, Phys.Rev.Lett. vol 63 n°15 (1989) 1625

[2] H.H.Andersen and H.L.Bay, J. Appl. Phys. 45 (1974) 953 and 46 (1975) 2416.

[3] M.Benguerba, A.Brunelle, S.Della-Negra, J.Depauw, H.Joret, Y.Le Beyec, M.G.Blain, E.A.Schweikert, G.Ben Assayag and P.Sudraud, Nucl. Instr. and Meth. B62 (1991) 8.

[4] H.W.Kroto, J.R.Heath, S.C.O'Brian, R.F.Curl, R.E.Smalley, Nature 318 (1985) 162.

[5] ACS Symposium Series edited by G.S.Hammond and V.J.Kuck, ACS Meeting, Atlanta, (1991)

[6] W.Krätschmer, K.Fortiropoulos, D.R.Huffman, Chem. Phys. Lett. 170 (1990) 167.

[7] W.Krätscher, L.Lamb, K.Fostiropoulos, D.Huffman, Nature 347 (1990) 354.

[8] G.Baptista, A.Brunelle, S.Della-Negra, P.Chaurand, Y.Le Beyec, Proc. ASMS Conference, Washington (1992).

ION BEAM TRANSPORT IN A PREIONIZED PLASMA CHANNEL*

S. P. Slinker, R. F. Hubbard, M. Lampe, G. Joyce, and I. Haber
Plasma Physics Division, Naval Research Laboratory
Washington, DC 20375-5000

We discuss a collisionless mechanism for transporting an ion beam in a pinched state. The beam is injected into a low density gas (~ 10^{14}-10^{16} cm^{-3}) in which a partially ionized plasma channel, with a radius somewhat larger than that of the beam, has previously been formed, by a laser for example. The plasma electron density exceeds the beam ion density. PIC simulations show that the space charge of the beam induces an inward radial flow of plasma electrons to neutralize the beam charge, as well as a large axial current of plasma electrons in the same direction as the beam current, in the region in front of the beam. The resulting net current I_n actually exceeds the beam current I_b near the front of the beam. The resulting pinch effect is much stronger than that expected for self-pinched propagation in a higher gas density (resistive) regime where $I_n << I_b$. Even if the channel density is initially underdense, the beam body will pinch, provided that the rate of plasma production from beam impact ionization of the neutral gas is sufficiently rapid. Analytic calculations support the simulation results. This scheme shows promise as a method for propagating heavy or light ion beams in a fusion target chamber.

Advantages of Pinched Transport for Intense Ion Beams

Accelerator and system requirements for a heavy or light ion beam fusion system are strongly constrained by requirements for beam transport to the target. In typical heavy ion fusion (HIF) reactor scenarios, it is assumed that the 10 GeV beams propagate ballistically over a distance of several meters in the reactor chamber, focusing down from a relatively large radius at injection to a radius of the order of 3 mm at the target.[1] Because of the low current that can be carried in each beam, it is necessary to inject and focus twenty or more distinct beams on the target. In addition, it appears to be necessary to maintain a low background gas pressure (≤1 mtorr) in the chamber in order to avoid degradation of the beam due to beam stripping and background plasma effects.[2,3] Ballistic focusing also requires that the longitudinal thermal velocity be held to the order of 0.1% of the beam velocity in the accelerator.[1] This, in turn, requires stabilization of the longitudinal instability.

All of these requirements are relaxed if it is possible to transport the beam in a tightly pinched state in the reactor chamber.[2-4] The ions could then be injected in one or two beams with particle current well above 10 kA; high beam current is an asset in pinched propagation. Only one or two narrow (sub-centimeter) entry ports in the reactor chamber would be necessary. The ambient gas pressure in the reactor chamber would be well above 1 mtorr, at a level which is easily maintained in the reactor environment. The requirements on longitudinal beam emittance would be much relaxed, possibly even permitting stabilization of the longitudinal instability by increasing the beam temperature. The reactor chamber could be larger. Pinched propagation may allow lower beam energy and higher current than can be considered for ballistic transport.

Pinched final transport is also promising for applications involving light ion beams. The proposed Laboratory Microfusion Facility (LMF) requires 30 MeV lithium beams to be transported about 4 m to accomodate longitudinal beam bunching.[5] The prime candidates for accomplishing this are ballistic focusing in gas at density around 1 torr and pinched transport in an externally driven Z-discharge.[5] Ballistic transport puts constraints on beam quality, and it is not certain that the beam charge and current will be neutralized sufficiently. Though the LMF is a single shot application, the presence of auxiliary equipment in the chamber, to produce a discharge, is undesirable.

Conditions for Pinched Transport

Pinched transport of relativistic electron beams (REBs) is readily accomplished. If the beam is injected into dense gas ($\geq$ 1 torr), it quickly ionizes the gas creating a plasma which shorts out the radial space charge electric field of the beam and supports a return current. However, the return current only partially cancels the beam current, I_b, leaving a net current, I_n. The confining force of the magnetic field due to I_n balances the radial thermal pressure, permitting a pinched equilibrium. This method does not work well for ion beam transport. Plasma creation by the ions is much faster and, though the beam space charge is neutralized, the net current is frozen in at a value too low to pinch the beam.[3,4]

A second means of transporting REBs in a pinched state is propagation in the ion focused regime (IFR).[6,7] Here the beam is injected in a plasma channel of low density, <10 mtorr, with available charge less than the beam charge. The beam space charge drives the plasma electrons radially outward from the channel, leaving behind an ion column which provides a confining electric force. This is essentially the only force on the beam, since the self electostatic and magnetic forces cancel when beam velocity is c. This type of IFR propagation will not work for nonrelativistic positive ion beams, because the channel ions are not mobile enough to be expelled during the time of beam passage, and the ion beam space charge must be nearly completely charged neutralized, since the beam is nonrelativistic.

A New Pinched Mode for Transport of Ion Beams

We propose a pinched scheme in which the ion beam is propagated in a narrow preionized plasma channel within the background gas.[3] The beam space charge is neutralized by radial inflow of plasma electrons. Therefore the channel radius, r_c, should be on the order of twice the beam radius, r_b, and the line density of the plasma channel should be greater than the beam density. It is possible that this requirement can be relaxed, since the beam produces additional electrons by ionizing the background (and/or stripping). The background density should be low, typically < 100 mtorr, so that the plasma electrons are collisionless and a broad halo of plasma is not produced. Since the beam velocity is much less than c, the space charge field propagates ahead of the beam into the preionized channel. The resulting force draws electrons toward the beam. These generate an axial pinch current that is in place when the

beam head arrives and is frozen in by the rising conductivity. The result is that the heavy ion beam is well-pinched by a net current that persists throughout the duration of the beam. We believe that this mechanism works only in a narrow plasma channel; in broader plasma regions, the inflow of electrons toward the beam is essentially entirely radial, with no significant axial electric field to drive a precursor axial current.

Mazarakis, et al.[8] have demonstrated the production of large currents propagating in preionized plasma channels. In their case the currents were induced by an accelerator cavity intersecting the channel.

Description of FRIEZR Simulation Code and Nominal Simulation Parameters

The effects discussed in the last section were first seen in numerical simulations[3] using FRIEZR,[7] an axisymmetric 2-D particle simulation code which solves the full set of axisymmetric Maxwell's equations, including self fields. Simulations with actual HIF parameters are difficult because the pulse length and beam transit time are many orders of magnitude larger than the electron plasma period which must be resolved. In order to make the computations affordable, the simulation electron mass was set to $m_e^* = 100m_e$, and simulation beam current densities were set much lower than in HIF applications. These scaling techniques are widely used in particle simulations to illustrate basic physics. Code modifications that would remove the plasma frequency restriction are being investigated.

The simulations reported by Hubbard, et al.[3] were over short propagation distances. Recent simulations have investigated longer beams and propagation distances. Two of these simulations will be discussed in the next section. The nominal beam parameters for these simulations are energy $E_o = 10$ GeV ($\beta = .3$), $m_i = 209m_p$ (bismuth), charge state $Q_b = 50$, maximum electrical current $I_o = 5$ kA, normalized emittance $\epsilon_n = 0.001$ rad-cm, injection radius $a_o = 1$ cm, pulse rise time $\tau_r = 5$ nsec and pulse length $\tau_p = 25$ nsec. The channel has a radius $a_{ch} = 2$ cm, and the line density ratio of the channel to the beam ($Q_b e \beta c N_{ch}/I_o$, where N_{ch} is the line density of the channel) is 5. Parameters pertinent to light ion fusion have also been explored, with similar results.

Simulation Results

Figure 1a shows the beam current I_b (solid), and the net current I_n (dashed), 20 ns after injection of the beam into the channel at z=0. The nose of the beam has travelled to z = 200 cm. The net current rises before the beam arrives, and reaches a peak value $I_n \approx 2I_b$ at the end of the beam current rise. It remains at a large fraction of the beam current for the duration of the pulse. Figure 1b shows the half-current beam radius at the same time. The beam is pinched to a radius less than the injection radius $a_0 = 1$ cm, except at the very front. There are oscillations appearing which will eventually disrupt the beam. These are believed to result from some unphysical aspects of the simulations, which will be discussed in the next sections. Figure 1c shows the v_z/c - z phase space plot of the channel electrons at an earlier time, t =

15 ns. Electrons ahead of the beam are seen to be flowing toward it, producing the pinch current. It is also apparent that the channel electrons exhibit axial flow in the nature of a cold fluid. Figure 1d shows the beam particle positions at 15 ns. Beam contraction at the place of peak net current is apparent. Striations which lead to the oscillations in radius have appeared.

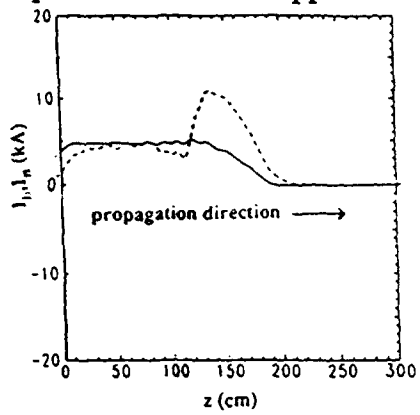

Fig. 1a. Beam (solid) and net (dashed) currents at t = 20 ns.

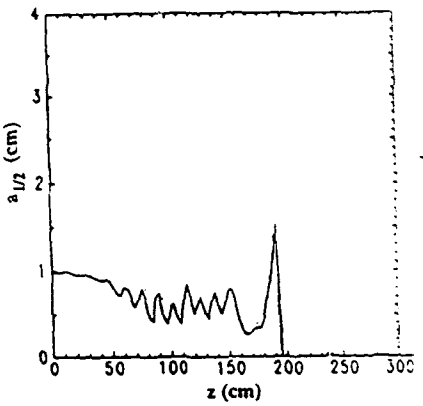

Fig. 1b. Half current radius $a_{1/2}$ at t = 20 ns.

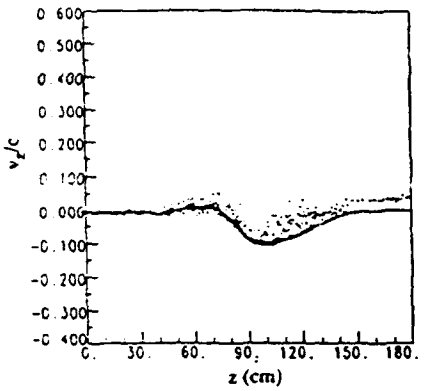

Fig. 1c. Axial velocity of plasma electrons at t = 15 ns.

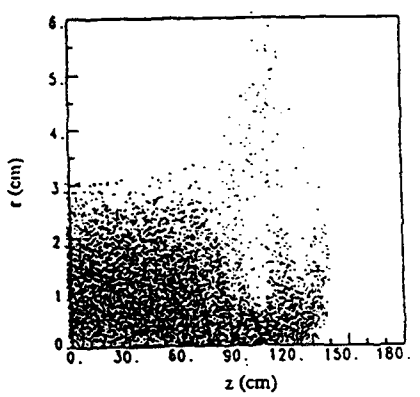

Fig. 1d. Beam particle density at t = 15 ns.

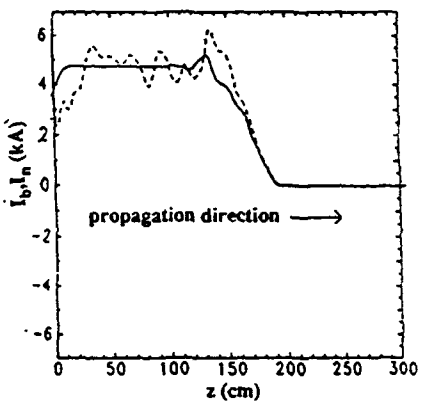

Fig. 2a. Beam (solid) and net (dashed) currents at t = 20 ns.

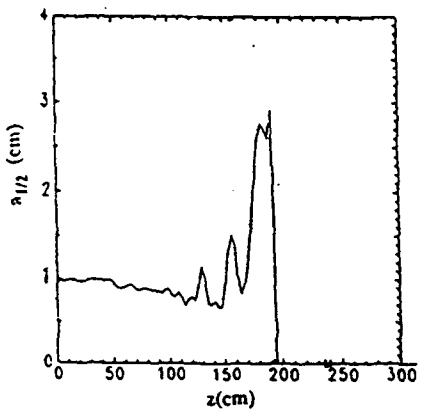

Fig. 2b. Half current radius $a_{1/2}$ at t = 20 ns.

This simulation neglected ionization of the background gas by the beam. Since $Q_b = 50$, the ionization cross section is very large, and even at low gas densities, the beam is expected to produce sufficient ionization to provide space charge neutralization near the beam head. This may allow the channel to be underdense ($N_{ch} < Q_b N_b$). Figures 2a and 2b are taken from a simulation which illustrates these effects. The peak net current is now only slightly larger than the peak beam current. The beam head shows expansion because it takes some time for space charge neutralization to be established. The oscillations in the beam radius have been substantially reduced from those shown in Figure 1b.

Analytic Model

To help understand the simulation results, an analytic model of a channel-pinched ion beam has been developed. There are three simplifying assumptions: 1) a steady state exists in the beam frame, 2) axial scale lengths greatly exceed radial scale lengths, and 3) the channel plasma is modeled as a one-dimensional cold fluid. Azimuthal symmetry is also assumed.

Consider a cylindrical coordinate system with beam propagation down the z axis. Define a variable $Z \equiv \gamma(\beta ct - z)$ where ion beam energy is $E = \gamma M_i c^2$ and $\beta = (1-1/\gamma^2)^{1/2}$. The steady state assumption implies that all functions of z and t depend only on the combination Z. In calculating the axial electric field E_z, the large aspect assumption allows the radial current density, J_r, to be ignored. Maxwell's equations then reduce to

$$\frac{\partial^2 E_z}{\partial Z^2} + \frac{1}{r}\frac{\partial}{\partial r} r \frac{\partial}{\partial r} E_z = -\frac{4\pi}{\beta\gamma c}\frac{\partial}{\partial Z}(J_{bz} + J_{pz}), \qquad (1)$$

where J_{bz} is the axial current density of the beam and J_{pz} is the axial current density induced in the channel plasma by the beam.

The plasma current density is given by $J_{pz} = \rho v_z$ where ρ is the electron density and v_z is the axial electron velocity. Applying the steady state assumption to the one-dimensional cold fluid equations for the plasma electrons results in

$$\rho(r,Z) = \rho_0 \left[1 - \frac{v_z(r,Z)}{\beta c}\right]^{-1}, \qquad (2)$$

and

$$v_z(r,Z) - \frac{v_z^2(r,Z)}{2\beta c} = \frac{e}{m}\int_{-\infty}^{Z} dZ' E_z(r,Z'), \qquad (3)$$

where ρ_0 is the unperturbed plasma density. These equations are linearized and the resulting expression for J_{pz} is substituted into Eq. (1):

$$\frac{\partial^2 E_z}{\partial Z^2} + \frac{1}{r}\frac{\partial}{\partial r} r \frac{\partial}{\partial r} E_z + \frac{\omega_p^2}{\beta^2\gamma^2 c^2} E_z = -\frac{4\pi}{\beta\gamma c}\frac{\partial J_b}{\partial Z}, \qquad (4)$$

where ω_p is the electron plasma frequency. The solution to this Helmholtz equation can be given in terms of a Green's function

$$E_z(r,Z) = \int dZ' r' dr' d\theta' \frac{\cos(R/\lambda)}{R} \frac{1}{\beta\gamma}\frac{\partial J_b}{\partial Z}, \qquad (5)$$

where $\lambda \equiv \beta\gamma c/\omega_p$ and R is the distance from (r,0,Z) to (r',θ',Z').

Equations (2)-(5) show that an equilibrium exists in which a current is initiated in the channel ahead of the beam, which should scale with the beam current rise rate. Equation (5) also shows that an oscillatory wakefield will result if the beam current rises rapidly compared to the scale length $\pi\lambda$ in Z. The oscillations seen in the simulations are believed to be due to this mechanism. In the simulations $\lambda \sim 10$ cm, and the rise length is ~ 50 cm. If the beam radius and rise length are much larger than λ, as is the case for HIF or LIF parameters, the oscillations should be smoothed out.

Issues

The work done so far has shown the promise of this pinched transport scheme, but the physics is very complicated and many issues are still to be resolved. Because of numerical restrictions, the simulations have been in the regime where $\lambda \equiv \beta\gamma c/\omega_p > r_b$, but the opposite is true in the parameter regimes of interest for inertial fusion. There is reason to believe the oscillations seen in the simulations at wavelength λ will not occur, or may not be as disruptive, in the application. Head and tail erosion, seen in the simulations, have not been studied thoroughly. The details of the injection of the beam from the accelerator onto the channel have not been addressed. The two stream electron-ion instability may occur. The stability properties have not yet been studied if the beam is injected off the channel axis. Channel production and viability must be investigated. It is particularly important to define which issues can be addressed by contemporary experiments.

Summary

Pinched propagation in a preionized channel in low density gas looks promising for both LIF and HIF ion beams. The pinch current is initiated by electrostatic acceleration of upstream electrons which flow toward the beam. A simple analytic theory provides a qualitative picture for interpreting the phenomena, and FRIEZR simulations confirm the basic mechanism. Simulations in the actual regime of interest have not been done because the time scale of the plasma frequency is much shorter than time scales associated with the beam pulse. A number of mechanisms could degrade the quality of the pinch. Some of these have been seen in the simulations, but these appear to be artifacts of the regime explored in the simulations, and of artificial features of the coding. An expanded effort in theory, simulation, and eventually experiment is needed to confirm the usefulness of this method of transport, and the scaling of the physics with system parameters. However, it is clear that successful implementation of pinched transport would have a high payoff for both HIF and LIF.

REFERENCES

1. J. Hovingh, V. O. Brady, A. Faltens, D. Keefe and E. P. Lee, Fusion Technol. 13, 255 (1988).
2. C. Olson, in Proceedings of the Conference on Heavy Ion Inertial Fusion, Washington, DC, 1986; AIP Conf. Proc. 152 (American Institute of Physics, New York, 1986), p. 215.
3. R.F. Hubbard, M. Lampe, G. Joyce, S. Slinker, I. Haber and R.F. Fernsler, Part. Accel. 37-38, 161 (1992).
4. S. Yu and E. Lee, in Proceedings of the Heavy Ion Fusion Workshop, Berkeley, CA, 1979, LBL-10301 (Lawrence Berkeley Laboratory, Berkeley, 1980), p. 504; S. Yu and W. Fawley, private communication.
5. C. Olson and P. Ottinger, private communication; C.L. Olson, in Proceedings of the 1988 Linear Accelerator Conference, Newport News, VA, 1988, p. 34.
6. H. L. Buchanan, Phys. Fluids 30, 221 (1987).
7. J. Krall, G. Joyce and K. Nguyen, Phys. Fluids B 1, 2099 (1989).
8. M. G. Mazarakis, private communication.

*Supported by the U.S. Department of Energy through subcontracts to Lawrence Berkeley Laboratory and Sandia National Laboratories.

STEERING ALGORITHMS FOR A HEAVY-ION RECIRCULATING ACCELERATOR*

W. M. Sharp, J. J. Barnard, and S. S. Yu
Lawrence Livermore National Laboratory, University of California
Livermore, California 94550, U. S. A.

Abstract

For inertial-fusion applications, the beam in proposed recirculating heavy-ion accelerators must complete fifty to one hundred laps around lattices that are between two and four killmeters in circumference. Frequent monitoring and correction of the beam-centroid position is essential to avoid unrealistic tolerances on dipole strengths and quadrupole alignment. the beam centroid. Analytic and numerical estimates are made of the beam-centroid displacement due algorithms for both time-dependent and time-independent beam steering are presented. An envelope-code simulation is used to demonstrate their effectiveness.

1. Introduction

A recirculating induction accelerator[1] has been suggested as an alternative to conventional linear drivers for heavy-ion fusion. This "recirculator" is expected to cost significantly less than linear drivers because the accelerating cells are used repeatedly for each pulse and because smaller induction units with a reduced accelerating gradient would be used. The lower gradient significantly increases the path length for pulses, and the circular design requires the use of dipole magnets with time-varying field strengths. If the strength of any dipole is inappropriate for the beam momentum, due to improper timing or to an erroneous drive voltage, then the pulse will, in effect, receive a small transverse kick, and the cumulative effect of random strength errors in many dipoles is that the amplitude of the beam-centroid betatron motion in the plane of the accelerator increases by a random walk. Misaligned quadrupoles similarly give transverse kicks to the beam centroid. Since the betatron frequency varies along an intense ion pulse due to space charge, such displacements develop into centroid ripples with progressively shorter axial wavelength, and eventually field nonlinearities and axial slippage in bends are expected to thermalize the centroid motion, leading to a steady emittance growth.

In this paper, the effects of errors in dipole strengths and quadrupole alignment are estimated analytically. Simple time-dependent and time-independent steering algorithms are then proposed for correcting centroid mismatches, and in a final section these procedures are evaluated using the envelope code CIRCE[2].

2. Effects of Magnet Errors

The transverse energy equation for the centroid of a beam "slice" as a function of distance s along the lattice axis is approximately

$$\frac{1}{2}\left(\frac{dX}{ds}\right)^2 + \frac{k_\beta^2 X^2}{2} \simeq \frac{\Delta W_\perp}{\beta^2 M c^2}. \qquad (1)$$

* Work performed under the auspices of the U. S. Department of Energy by Lawrence Livermore National Laboratory under contract W-7405-ENG-48.

Here, X is the centroid displacement in the bend plane, $\beta^2 Mc^2/2$ is the kinetic energy of an ion, and $\Delta W_\perp$ is the transverse energy increment due to a single dipole field-strength error. In fact, since the magnetic fields are effectively static as the beam passes, no work is done on the centroid, but rather $\Delta W_\perp$ increases at the expense of longitudinal energy. The effective betatron wavenumber of the centroid motion in Eq. (1) is given in the continuum approximation by

$$k_\beta^2 = \frac{\sigma_0^2}{4L^2} - \frac{K}{R^2}, \tag{2}$$

where L is the half-lattice period, R is the pipe radius, $K = 2qeI_b/[4\pi\epsilon_0(\beta\gamma)^3 Mc^3]$ is the perveance, and the "undepressed tune" σ_0 is the betatron phase advance per lattice period in the absence of space charge. The second term in Eq. (2) accounts for image forces in the pipe. Assuming harmonic motion in s, the betatron amplitude X_{max} after i dipole kicks satisfies the relation

$$k_\beta^2 X_{max}^2 = \frac{1}{\beta^2 Mc^2} \sum_i \Delta W_{\perp i}. \tag{3}$$

The ith energy increment is given by $\Delta W_{\perp i} = \Delta p_{\perp i}^2/2M$, where $\Delta p_{\perp i} \approx qe\eta_d L\delta B_i$ is the momentum increment for a dipole error δB_i, and η_d is the occupancy of the dipole magnet. The beam receives Ns_{max}/L kicks, where N is the total number of laps, and s_{max} is the circumference of the recirculator. Using δB_{rms} to denote the root mean-square (rms) average of δB_i, the total increment in transverse energy resulting from these kicks is then written

$$\sum_i \Delta W_{\perp i} = \frac{Ns_{max}}{L} \frac{(qe\eta_d L\delta B_{rms})^2}{2M}, \tag{4}$$

and the accumulated centroid displacement is

$$X_{max} = \frac{2\pi}{k_\beta} \frac{\delta B_{rms}}{B_y} \left(\frac{NL}{2s_{max}}\right)^{1/2}. \tag{5}$$

For the parameters in Table I, which resemble those of the High-Energy Ring (HER) in Ref. 1, Eq. (5) gives a maximum allowable $\delta B_{rms}/B_y$ of 0.009% when the maximum displacement amplitude is taken to be 0.5 cm. This prediction is in good agreement with the 0.01% tolerance for dipole errors previously found in envelope simulations using CIRCE[3].

Errors in quadrupole alignment similarly cause the centroid betatron amplitude to increase like a random walk, so that

$$X_{max} \simeq \delta x_{rms}(C_{rw}N_q)^{1/2}. \tag{6}$$

Here, δx_{rms} is the rms quadrupole displacement, and $N_q = Ns_{max}/L$ is the total number of quadrupoles through which the beam passes, about 10^5 for the parameters in Table I. The quantity C_{rw} has been found by Neil[4] to increase from 3 to 6 in the HER. If the maximum beam displacement in the absence of steering is again taken to be 0.5 cm, then the tolerance on quadrupole alignment is $\delta x_q \approx 0.001$ cm

Table I Nominal parameters for the high-energy ring of the LLNL ion recirculator

beam parameters		
ion charge state	q	1
ion mass	M	200 amu
peak beam current	I_b	132 A
initial energy	$(\gamma_0 - 1)Mc^2$	1 GeV
initial duration	$\Delta\tau$	750 ns
initial rise/fall time	τ_r	150 ns
lattice parameters		
length	s_{max}	2934 m
half-period	L	2.865 m
pipe radius	R	6.1 cm
number of laps	N	100

3. Steering Algorithm

The strategy for reducing centroid displacements resulting from reproducible magnet errors involves sensing centroid errors for one pulse and correcting them on subsequent pulses. In general, two steering magnets are needed to correct errors in X and $X' \equiv dX/ds$, and the beam position must be measured as a function of time at three positions, because centroid motion in a circular accelerator depends on X, X', and the momentum error $\Delta p/p = 1 - p_0/p$, where $p = \gamma\beta Mc$ is the actual ion momentum and $p_0 = qeB_y\rho$ is the design momentum for a dipole field strength of B_y and a bend radius of ρ. Briefly, the steering algorithm involves using first-order transport theory and the position information at the monitors to estimate both the values of X, X', and $\Delta p/p$ upon entering the module and the matched values of X and X' at the second steering magnet. In the thin-lens limit, the first steering gives an impulsive kick to the beam that places the centroid at the matched X position as it reaches the second magnet, and that magnet then adjusts X' to the matched value. A similar but more elaborate procedure is needed for finite-length steering magnets. The main weakness of this approach is that corrections must be set for one module at a time on each, requiring a substantial number of calibration pulses. Another shortcoming is that a nonzero $\Delta p/p$ is not corrected. Separate induction cells or voltage changes in the main accelerating cells are still needed to match the ion momentum to the design value.

The steering algorithm is implemented in CIRCE in a particularly simple manner. During the first pass of a pulse through a steering module, the centroid positions at the three monitors are saved as functions of time. The linear transport matrices for the lattice are then used to estimate the instantaneous kicks required at the two infinitesimally thin steering "magnets". The beam is reinitialized at the first monitor, and the kicks are administered during the second pass. For time-dependent steering, appropriate kicks are calculated for each of many closely spaced beam slices, whereas for time-independent steering, the kicks are calculated for the center slice only and used for all slices.

4. Evaluation

The steering algorithm is tested using the nominal HER lattice of Ref. 1. Lattice parameters are listed in Table I along with some beam parameters, and each half-period

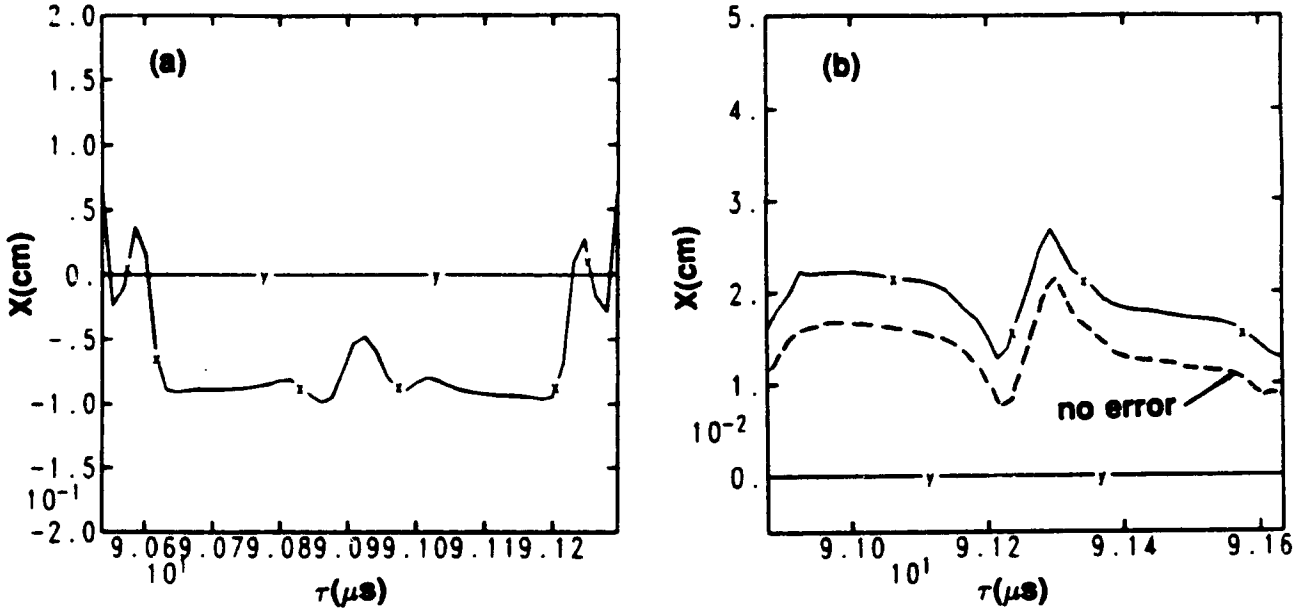

Fig. 1 Beam centroid displacement with random 0.1% dipole- strength errors (a) before and (b) after a time-dependent correction at the end of the first lap. The dashed line shows the centroid displacement in the absence of magnet errors.

consists of an focusing quadrupole, a dipole for bending, and a pair of accelerating gaps. The standard steering module here consists of three monitors spaced by a full lattice period and a steering station located immediately after each of the last two monitors. The effectiveness of steering is found to depend only weakly on the placement of these elements. Decreasing the module size to less than a period does not resolve enough of a betatron orbit to allow an accurate calculation of $\Delta p/p$, and increasing it to greater than three times the period introduces the likelihood of aliasing.

In the tests reported here, errors are made only in the strengths of dipole magnets, but errors in quadrupole alignment should produce qualitatively similar results. For any magnet, the error is taken to be the same fraction of the nominal strength for any lap, corresponding to a magnet that is correctly timed but driven with a pulse of incorrect voltage. Error magnitudes for are chosen, somewhat arbitrarily, to have a uniform probability over a fixed range that is selected to give the appropriate rms error, and for each case here the same lattice errors, with an rms magnitude of 0.1%, are used.

The time-dependent and time-independent steering algorithms are tested separately here. However, both techniques would likely be used in a heavy-ion recirculator, with between one and four time-dependent modules in a ring and a substantially larger number of time-independent modules placed between them.

4.1. Time-Dependent Steering

To demonstrate the time-dependent steering algorithm, we use a lattice with four equally spaced steering modules. With no correction, the 0.1% dipole-strength errors cause centroid oscillations with a peak-to-peak amplitude exceeding 1.5 mm during the first lap, and the amplitude continues to grow roughly like the square root of the number

of laps. The phase of the oscillation is found to vary by about 5π from the beam center to the ends after a single lap. The plot in Fig. 1a, showing X with corrections applied versus the time τ that beam slices reach the steering module at the end of the first lap, indicates that the amplitude still grows to about 1 mm between modules, and the accumulated phase change from the center to the ends is in excess of 2π. However, the corresponding plot just after the module shows that X has been reduced by a order of magnitude and closely resembles the displacement found in the absence of errors. There is a nonzero average displacement in the plots of Fig. 1b because $\Delta p/p$ is not zero for this case, and the rapid variation of X near the beam center results from a space-charge wave causing a density depression there. A small error in the estimated $\Delta p/p$, due to the use of linearized transport theory, accounts for the difference between the corrected X and the values found with no magnet errors.

A maximum spacing between modules is set by the cutoff frequency of the circuitry driving the steering magnets, above which the response in nonlinear. This cutoff, which depends on the circuit design and layout, limits the spacing of modules because the difference in betatron phase along the beam transforms a uniform displacement from the matched X location into centroid ripples of progressively higher frequency. For a cutoff frequency f_{max} and a beam rise or fall time $\Delta\tau$, the maximum spacing of time-dependent steering modules is

$$\Delta s_{max} \approx 2\pi f_{max} \Delta\tau \left(\frac{\sigma_0 R^2}{L K_{max}} \right), \tag{8}$$

where K_{max} is the perveance at the beam center. For the HER parameters in Table I and a cutoff frequency of 30 MHz, this expression gives $\Delta s_{max} \approx 500$ m.

4.2. Time-Independent Steering

The spacing of time-independent steering modules is also constrained by the betatron-frequency difference along the beam. Since the same kick is administered to all beam slices, the phase shift between the center and the ends that accumulates between modules must be less than $\pi/2$ for the direction of the kicks to be correct. An upper bound on module spacing, using this $\pi/2$ phase shift, is given by

$$\Delta s_{max} \approx \frac{\pi}{2} \left(\frac{\sigma_0 R^2}{L K_{max}} \right), \tag{9}$$

which gives $\Delta s_{max} \approx 57$ m for the parameters in Table I. If $\Delta p/p$ were constant along the beam, then reducing the module spacing would make the corrected X a progressively better approximation to the matched value. However, transport through the steering module depends on $\Delta p/p$ if the lattice contains a dipole, and consequently the matched values of X and X' vary enough in realistic cases to make time-independent steering substantially incorrect regardless of module spacing. This fact results in diminishing improvement in the corrected X as the module spacing is reduced below the upper bound in Eq. (9).

The plots of X in Fig. 2 ilustrate the effects of time-independent steering in two cases. Both plots show the centroid position as a function of time at the end of one lap around a lattice with the standard 0.1% dipole errors. Sixteen equally spaced steering modules are used for the case in Fig. 2a, giving a module spacing Δs of 172 m. The accumulated phase shift along the beam due to the non-uniform $\Delta p/p$ makes the kicks inappropriate

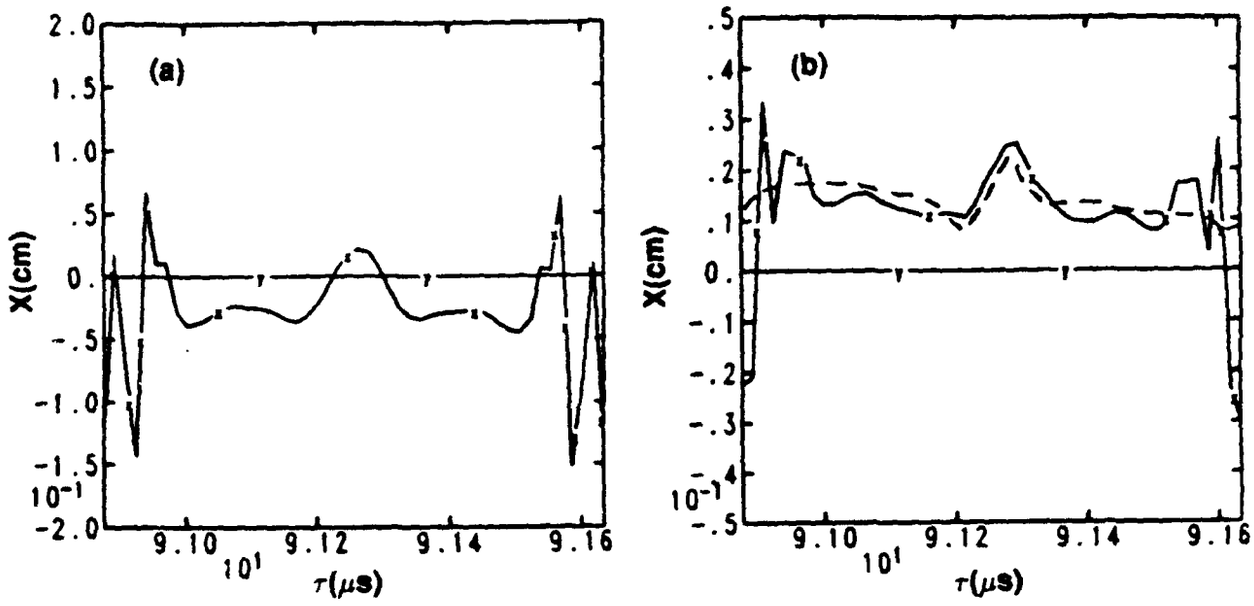

Fig. 2 Beam centroid displacement with random 0.1% dipole-strength errors at the end of the first lap after (a) 16 and (b) 128 time-independent corrections. The dashed line shows the centroid displacement in the absence of magnet errors.

away from the beam midpoint, so displacements are reduced only about 50% compared with an uncorrected beam. Rapid fluctuations occur particularly near the ends because the density decrease there concentrates the phase-shift accumulation in those regions. The displacement for a lattice using 128 steering modules with a separation of about 11 m is plotted as a solid line in Fig. 2b. Although details differ due to the non-uniform $\Delta p/p$, this case shows a much better replication of the centroid displacement found for an error-free lattice, again plotted as a dashed line. The displacement near the beam ends still shows a rapid fluctuation due to accumulated phase shift, and in a more realistic model, this fluctuation would be expected to phase mix, leading to emittance growth near the ends and finally to loss of those ions. Reducing the module spacing below about 10 m gives little improvement in the correction and does not reduce the fluctuations near the ends.

5. References

[1] J. J. Barnard, A. L. Brooks, F. Coffield, F. Deadrick, L. V. Griffith, H. C. Kirbie, V. K. Neil, M. A. Newton, A. C. Paul, L. L. Reginato, W. M. Sharp, J. Wilson, S. S. Yu, and D. L. Judd, "Study of Recirculating Induction Accelerators as Drivers for Heavy Ion Fusion," Lawrence Livermore National Laboratory Report UCRL-LR-108095 (1992).

[2] W. M. Sharp, J. J. Barnard, and S. S. Yu, *Part Accel.* **37-38**, pp. 205-213, 1992.

[3] W. M. Sharp, J. J. Barnard, and S. S. Yu, "Transport and Error Sensitivity in a Heavy-Ion Recirculator", in *Proceeding of the 1991 IEEE Part. Accel. Conf.*, San Francisco, U. S. A., May 1991, pp. 260-262.

[4] V. K. Neil, "Effect of Quadrupole Alignment Errors on Beam Motion in the Four HIF Recirculator Rings," Beam Research Memo, BR 91-10, Lawrence Livermore National Laboratory, Livermore, CA. (1991).

GENERATION OF ULTRA HIGH PRESSURE WITH LIGHT ION BEAMS

B. Goel
Kernforschungszentrum Karlsruhe,
Institut für Neutronenphysik und Reaktortechnik,
D-W7500 KARLSRUHE, Fed. Rep. Germany

O. Yu. Vorobjev, A. L. Ni
Institute of Chemical Physics,
Chernogolovka, Russia

Abstract: Planar high pressure shock waves can be generated with intense light ion beams. In this paper we study the prospects of using the multilayerd targets to generate ultra high pressures for conditions prevailing at KALIF. It is found that with the present beam parameters multilayerd targets do not offer any substantial advantage. However with the HELIA pulse line multilayerd targets can extend the investigation regime at KALIF towards higher pressures. Simulations with the present beam parameters reproduce high flyer velocities of 13 km/s measured for a 33 μm Al target.

1. Introduction

Powerful light ion beams to generate high pressure in condensed matter are of great interest. The light ion beams are advantageous in comparison to lasers due to the bulk character of the energy deposition and due to their large focus size and hus producing planar shock waves.

The scaling relation derived previously shows that the ablation pressure driving the shock wave is roughly proportional to the 2/3 power of beam intensity [1]. With the focused beam power density of about 0.3 TW/cm^2 obtained at KALIF, using self magnetically insulating *pichreflex* or B_θ *—diodes* [2][3], the generation of shock waves can be studied only in the range of a few hundred kbars. Recently Ng and Piriz [4] have suggested that dynamic pressures up to 5 Mbar can be achieved with light ion beams of power density as low as 0.1 TW/cm^2 using flyer plate impact techniques. In this case thermal pressure generated by ion energy deposition in the absorber region propels the payload, which then impacts on the solid target producing the high pressures. These results [4] were obtained using a simple analytic model; assuming thereby a constant power density and proton energy. Energy distribution in the absorber zone was assumed to be uniform and as such the presence of the Bragg peak was not taken into account. In addition, it was assumed that the absorber expanded as ideal gas with $\gamma = 5/3$. In reality, however, at beam power densities of about 0.1 TW/cm^2 the matter in the energy deposition zone is in the dense non-ideal plasma regime [5]. Besides that, intense ion beams generated with pulsed power machines show temporal change in beam energy and power. Portions of the absorber receiving energy from the particle beam change with the change in the energy of impinging ions. These changes are aggravated by the change of the target properties under intense beam action.

In the present paper we investigate the dynamics of thin foil acceleration by light ion beams. In our numerical calculations realistic physical parameters, i.e. realistic beam power profiles, wide-range equations of state, effects of the range shortening in hot plasma, electron and radiation heat transfer etc. are included. Calculations have been performed for measured beam parameters of KALIF. Some calculations are also presented for light ion beam parameters that may become available in the near future at KALIF. Calculation results of aluminum foils acceleration by KALIF beam have been compared with experimental measurements obtained using high resolution interferometric methods [6].

2. Calculational Procedure

The Euler equations are used to describe the dynamics of condensed matter under beam action. Energy transfer by radiation is treated in the approximation of radiation heat conduction. Electron conductivity coefficient and Rosseland mean free path are functions of density and temperature and were determined by wide-range semiempirical formulas developed in [7]. As the maximum target temperature reached with a beam power density of 0.2 TW/cm^2 does not exceed a few 10's of eV the energy of the radiation field is not very important in the calculations reported here.

A five parameter empirical wide-range equation of state is used. The dependence of Grüneisen parameter γ, on temperature (energy) and density is given by;

$$\gamma(E,V) = \gamma_0(V) + (\gamma_a + \gamma_0(V))[1 - \exp\{\beta(1 - \frac{E - E_c}{E_a})\}]$$

Parameters β, E_a and γ_a in (2.14) are fitted to obtain agreement with the Grüneisen coefficient values calculated in the region of dense nonideal plasma by quantum-statistical calculations [8]. In the present calculations we use SESAME EOS data [9] to fit our EOS parameters in the region of dense plasma. An analytical form of the EOS is convenient for numerical simulation due to calculations time economy. It also provides for continuity of the pressure and sound velocity in entire range. The temperature is calculated by using table SESAME EOS.

The calculations were done by the Godunov method in a moving grid. Nodes of the grid are moved with contact velocities calculated by solving the Riemann problems between neighbouring cells. A numerical procedure was developed, which allows to solve the Riemann problem for the case of a general equation of state. Energy transfer by conductivity is calculated at every time step after hydrodynamics recalculation of flow parameters by an implicit finite difference scheme. Details of the method will be described elsewhere [11].

3. Calculations and Results

Under normal conditions the pressure generated by KALIF ion beams can be written as $P(GPa) = 60\,(TW)^{0.63}$ [1]. This limits the pressure generated with a KALIF beam of 0.3 TW/cm^2 to a few 10's of GPa. However, the hydrodynamic efficiency of the target may be increased by the use of multilayered targets. This has been studied analytically [4] using various simplifications such as ideal gas equation of state, constant ion energy and constant beam power, uniform deposition of the beam energy into the target. These analytical results were varified to some extent using realistic models for equation of state, beam energy depostion as a function of density and temperature etc. [12]. The basic idea is to use a tamper layer of high Z material with low stopping power and heavy mass, a low Z material as absorber in which most of the energy is absorbed and the expansion of the absorber accelerates the payload. Thicknesses of different zones (tamper - absorber - payload) depend upon the properties of the materials and of impinging beam. The mass of the absorber is determined by the range of the ions. The thickness of the payload in turn can not be below a certain limit due to manufacuring constraints and because of the possible instabilities which have to be avoided.

The above mentioned calculations were performed for a proton energy of 3 MeV. This is about a factor of 2 higher than the energy to which protons can be accelerated at KALIF presently. In the following we examine how this low proton energy influences the results obtained previously. For this purpose we have performed different calculations using

measured beam parameters. [6]. The experimentally measured profiles were used taking thereby account of the beam transport from the anode to the target.

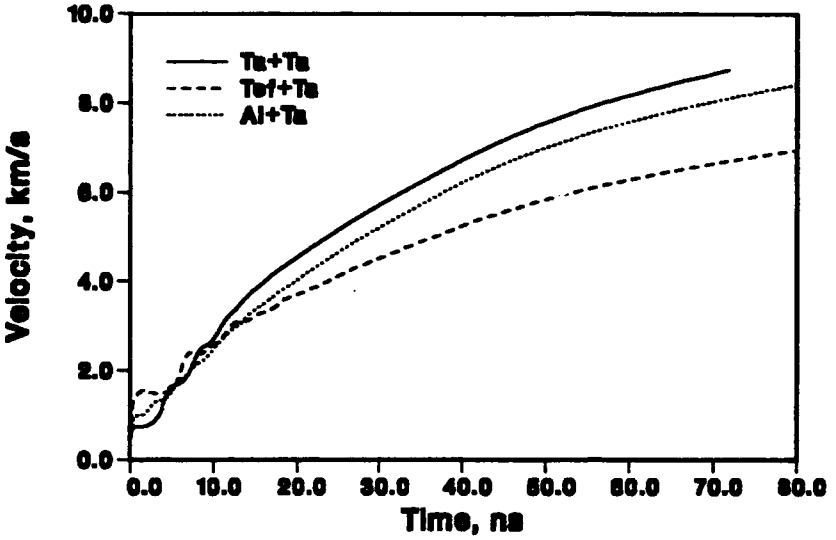

Figure 1. Velocity evolution: The mass velocity of a 5 μm *Ta* payload using different absorbers. The beam was that for the KALIF shot No. 3155. The thickness of Teflon or Aluminum absorber was so determined that the beam was completely stopped in the absorber.

Fig. 1 shows the velocity evolution of a constant payload of 5 μm *Ta* using different absorber materials. It is seen that in absence of a tamper the use of lighter absorber is of no use as the center of mass is shifted towards the payload. Placing a tamper layer in front of aluminum improves the results only marginally. Due to the fixed payload mass and short range

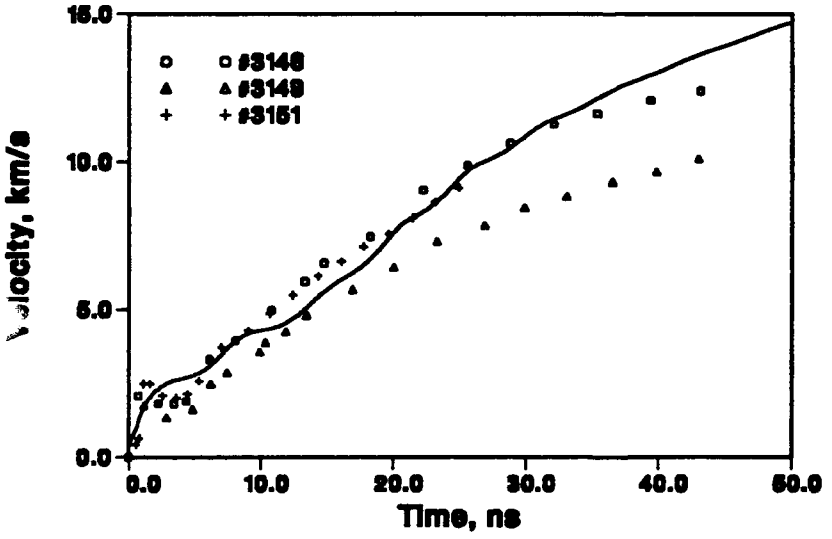

Figure 2. Velocity evolution: Back surface velocity of a 33 μm Al target together with experimental data. The beam characteristics used for this calculation is that for shot No. 3155.

of 1.4 MeV protons one can not take benefit of a layerd target. Therefore we first examine the dynamics of a single material target under KALIF beam action and in a second subsection we come back to a multilayer target for an upgraded KALIF.

3.1 Aluminum foil acceleration by KALIF beam

In this subsection we report 1D numerical simulations for KALIF-experiments reported in an accompanied paper [6]. The results of the back surface velocity calculation for 33 and 50 μm Al foil are shown in Fig.2 and Fig.3 together with experimental data. To obtain reasonable fit to the experimental data for the 50 μm Al target the beam power density of shot No. 3155 has to be reduced by a factor of 2 to 3. For a better understanding the actual beam profile prevalent in these experiments should be used. A change in EOS data can also influence the results. Steps on velocity profiles describe waves circulation between the back surface and the plasma-solid boundary. The duration of steps can be approximately estimated as the double thickness of the solid part divided by the sound velocity (For 30 μm Al foil it equals $\simeq 5\ ns$ and for 50 μm $\simeq 10\ ns$). The thickness of the solid part of the foil is determined by the proton range. The agreement between the experimental and calculated step duration reflects on the correctness of the calculated range. An impact velocity of 13 km/s corresponds to a pressure of about 2 Mbars.

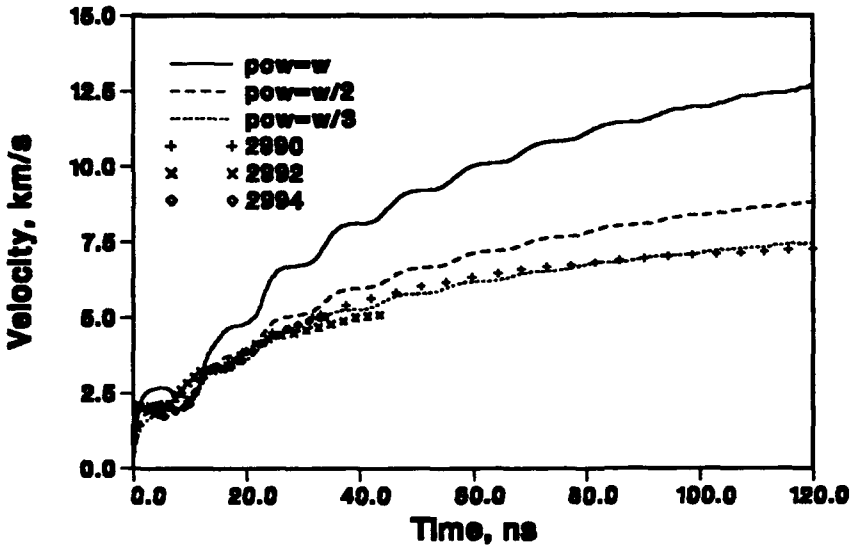

Figure 3. Velocity evolution: Back surface velocity of a 50 μm Al target clculated with the same beam characteristics as in Fig.2. To obtain agreement with experimental data the beam power density has to be reduced by a factor of 2 to 3.

To estimate the role of radiation cooling and heat energy transfer from plasma to solid calculations were performed with and without accounting for the electron and radiative conductivity. It is found that at the present KALIF power densities the conductivity effects are not important.

3.2 Multilayer targets

An upgrading of KALIF with a 6 MeV HELIA pulse line is planned for the near future. The ion energy in the upgraded KALIF will be about a factor 4 higher and the power density is

expected to be between 1 and 2 *TW/cm²*. In this case it will be advantageous to use multilayerd targets. To demonstrate this we present here results for a Ta 10 *μm* payload accelerated by a beam with the power density increased by a factor of 5 and with proton energies a factor of 4 larger than that used for the above calculations. In this case pressures of the order of some Mbars can be generated in the absorber. For these beams one can choose the target geometry such that the centre of mass is located at the tamper absorber interface.

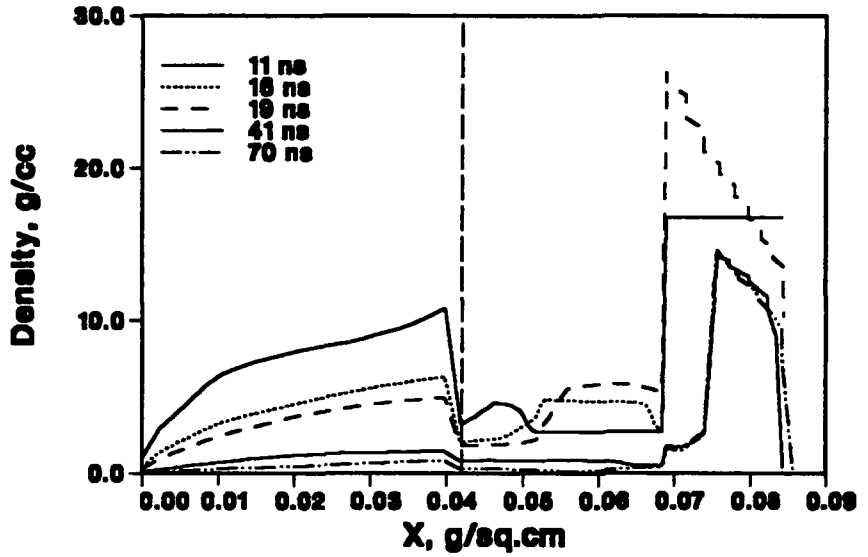

Figure 4. **HELIA.:** Density profile for 1 *TW/cm²* and 6 MeV proton beam. Target dimensions are 25 *μm Ta*, 100 *μm Al and* 10 *μ Ta*. The vertical line indicates the position of the center of mass.

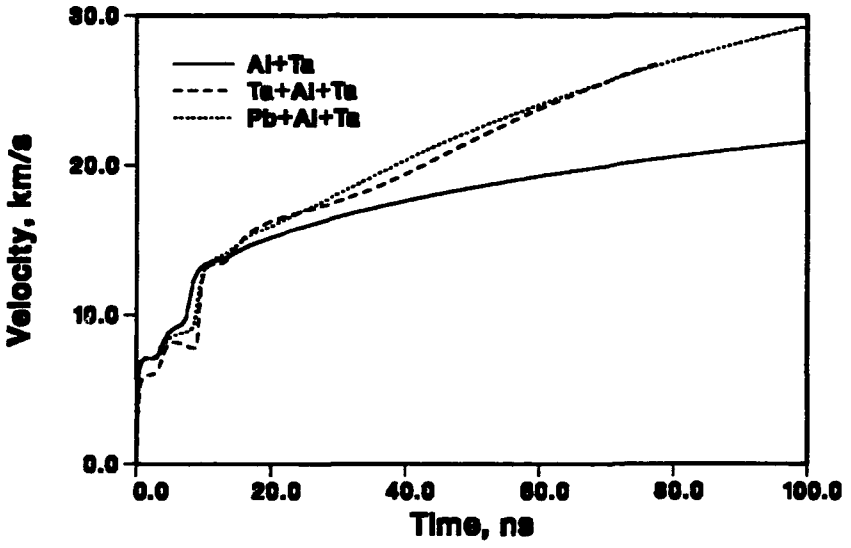

Figure 5. **HELIA.:** Surface velocity evolution for same conditions as in Fig. 3 but with different absorber materials.

Due to the larger range of HELIA protons the temperatures in the target are of the same order as in the case of KALIF beam with lower beam power densities. During the beam pulse action 10 μm Ta payload can be accelerated up to 30 km/s in the case of the multi-layered target while for a uniform target only 20 km/s can be reached. As seen from the density profile about 1/4 of payload will be vaporized and 3/4 (central part) melted during the acceleration due to dynamic expansion after the driving pressure disappears. Nevertheless, dynamic pressures of several Mbar can be achieved through the impact of the accelerated payload with a solid target.

4. Conclusions

It is shown that with the present KALIF parameters using a multilayerd target the foil velocity will not be increased substantially. This is a consequence of the short range of 1.4 MeV protons. However, in the case of upgraded KALIF (HELIA) which can accelerate protons to about 4 time higher ion energies a multilayerd target can bring substantial advantage. In this case foil velocities for a 10 μm Ta foil in the range of 30 km/s are conceivable. With higher beam power one has to take the vaporization or melting of the accelerated foil in account. Using the flyer plate impact technique pressures in the Mbar range can be studied at KALIF.

In general the temporal evolution of the surface velocity can be reproduced by calculations presented here. To obtain quantitative agreement however the beam profile has to be known accurately.

5. References

[1] B. Goel, Influence of Beam Profile on Pressure Generated by Light Ion Beams, in Proc. Eighth International conference on High-Power Particle Beams, July 2-5,1990, Novosibirsk (ed. B.N. Breizman and B.A. Knyazev) World Scientific, Vol. 2, P.715

[2] W. Bauer et al., Status and Perspectives of High Power Ion Diodes in Extractor Geometry, in Proc. Eighth International conference on High-Power Particle Beams, July 2-5,1990, Novosibirsk (ed. B.N. Breizman and B.A. Knyazev) World Scientific, Vol. 1, P.104

[3] W. Bauer et al., New Results from Experimental and Numerical Investigations of the self-Magnetically Insulated B_θ Ion Diode, Contr. to Proc. Ninth International conference on High-Power Particle Beams, May 25-30,1992, Washington DC, USA

[4] A. Ng, A.R. Piriz, Phys. Rev.A 40 (1989) 114

[5] T. Yabe and B. Goel Jap. J. Appl. Phys. 26 (1987) L296

[6] Baumung et al., Hydrodynamic Target Experiments with Proton Beams at KALIF, Contr. to Proc. Ninth International conference on High-Power Particle Beams, May 25-30,1992, Washington DC, USA

[7] A. Ya. Polyshchuk, Preprint IVTAN SSSR N0.1 -267 (1989)

[8] A.V. Bushman, V.E. Fortov, I.V. Lomonosov, Proc. Enrico Fermi School 1989, Elsiever Publ. 1989

[9] Lawrence Livermore National Laboratory Report UCID-118574-82-2 (1982)

[10] A.V. Bushman, G.I. Kanel, A.L. Ni, V.E. Fortov, Thermal Physics and dynamics of Intense Pulse Action, Inst. of Chemical Physics, Chernogolovca (1988)

[11] B. Goel, O.Yu. Vorobjev, A.L. Ni, to be published

[12] O.Yu. Vorobjev, A.L. Ni, V.E. Fortov, Sov. Tech. Phys.Lett. 16 (1990) 11

TARGET EXPERIMENTS WITH LIGHT-ION BEAMS AT KALIF: Measurements of the Dynamic Strength and Spallation Threshold of Metals at High Strain Rates

H. Bachmann, K. Baumung, G.I. Kanel*, H.U. Karow, V. Licht,
D. Rusch, J. Singer, O. Stoltz
Kernforschungszentrum Karlsruhe (KfK), P.O.Box 3640, D-W7500 Karlsruhe, Germany
* High Energy Density Research Center, Russ. Acad. of Sciences, Moscow 127 412, Russia

In target experiments performed at the KfK KALIF facility, pulsed proton beams of about 20 kJ pulse energy have been used to ablatively accelerate flyer foils of macroscopic lateral dimensions (~0.5 cm) to very high velocities (up to >10 km/s) generating impact loadings in plane target samples. An ORVIS-type velocity spectrometer has been set up and synchronised with the ion-beam driver to investigate the dynamic response of solid target matter with high accuracy (up to 1%) and very high time resolution (up to 200 ps). In proof-of-principle experiments the KALIF-ORVIS facility has been used to measure the dynamic strength solid matter to tensile fracture up to very high strain rates of 10^8 s^{-1}. The materials under investigation have been single and polycrystalline samples of molybdenum, aluminum, and sapphire. The experiments have verified the advantageous perspectives of high-power light-ion drivers for experimental dynamic matter research.

Introduction

At KALIF (i.e. the Karlsruhe Light-Ion Facility) beam-target experiments have been undertaken to measure the ablation pressure generated by pulsed high-power light-ion beams in solid target matter.[1] Investigation of the dynamic target response has been the diagnostic approach to reach this goal. Beyond, these experiments have verified that today's pulsed light-ion beams with their high pulse energies of several 10 kJ are a new and powerful tool in dynamic matter research. By applying advanced diagnostics of dynamic matter response, new and challenging research problems can be addressed. In the following we report on measurements of the dynamic strength and spallation threshold of metals up to highest strain rates.

If the tensile stress generated in a solid exceeds the inner tensile strength of the material, matter gets "spalled". The tensile strength of matter undergoing dynamic tensile stresses - as a function of the strain rate - is an important topic in dynamic matter research and in materials science. According to theoretical considerations the dynamic tensile strength of matter gradually increases with increasing deformation rate - starting from its static value - and, ultimately, reaches the theoretical limit of material strength as defined in atomistic and solid state physics theories, respectively.

Experimental method and diagnostics

The dynamic strength of matter to elementary fracture due to tensile stresses strongly depends on the nature and structure of the material studied, and on the strain rates applied. Reliable determination of the dynamic strength is possible by evaluation of the kinetic response of material samples to impulse loading.

The loading pulse and the target sample have to be taylored in such a way that the wavelength of the compressive impulse propagating through the sample is shorter than the sample thickness. If this "thick target condition" is satisfied a tensile stress is generated in the sample when the compressive pressure front has reached the rear free surface - for the following reasons: The rarefaction wave traveling behind the pressure plateau superimposes within the sample the release wave returning from the rear free surface. Superposition of the two oppositely moving rarefaction waves generates a dynamic tensile stress in the target matter.

The related expansion rate (strain rate) of matter is determined by the height and width of the original loading pulse. In case of one-dimensional dynamic strain the strain rate is defined as $SR = (\Delta x/x_0)/\Delta t$ (dimension: s^{-1}). Previous measurements of the dynamic tensile strength of condensed matter have been possible only up to maximum strain rates of 10^{6} s^{-1}. The shortest impulse loadings have been generated by impact of "flyer plates" driven by explosive techniques or by light-gas guns, respectively. The duration of the dynamic pressure state generated by impact equals twice the travel time of the shock wave through the impactor.

Recent beam-target experiments with high-power light-ion beams at KALIF have verified that very thin, plane "flyer foils" of macroscopic lateral dimension ($\geq$1/2 cm in diam.) and microscopic thickness ($\geq$ 10 μm) can be accelerated - 1-dimensional and stably in terms of fluid dynamics - by ion beam ablation to hypervelocities up to above 10 km/s.[1] Very short 1-dimensional impulse loadings of a few ns in duration can be achieved in target matter. The proof-of-principle experiments have been performed with an 20 cm-B_Θ extraction diode as the ion beam source delivering an axial proton beam of 0.2 TW/cm^2 power density on target, with a kinetic ion energy of $\leq$ 1.6 MeV, and a pulse duration of $\leq$ 50 ns. Ablation pressures of up to 0.3 Mbar amplitude are exerted on Al flyer foils. The B_Θ-proton beam source greatly facilitated both testing of the diagnostic system and performing of beam-target experiments due to its repetitivity, its reproducibility and pointing stability, and its ion beam propagating in vacuum to the target[2]. These positive features allow up to four target experiments to be performed per day.

The most reliable and informative method for real-time detection of spalling (without recovery and after-investigation of the target sample) and for quantitative determination of the dynamic fracturing strength of solids is based on the diagnostic of the kinetic target response. The velocity profile of the rear surface of the sample is recorded when the loading impulse is reflected at that free surface. If the tensile stress generated after reflection of the loading pulse does not exceed the dynamic strength no spalling occurs. In this case the velocity

profile of the target surface actually follows the wave form of the loading pulse - with nonlinear distortions because of velocity dispersion with pressure including the elastic-plastic transformation.[1] If, however, spalling occurs in the sample the rear surface velocity profile shows a typical spalling behaviour (Fig. 1): After the loading pulse is over the surface velocity does not decrease to a value related to the macroscopic acceleration of the sample as a whole. Instead, only a "pull back" of the velocity is seen equal to Δ W. Then the surface velocity is increasing again. This is related to the inner spalling of the material followed by a compressive "spall pulse" loading of the surface layer spalled-off. After that, velocity oscillations decaying in time are seen generated by wave reflections between the sample free surface and the inner fracture surface. In the acoustic approach the critical tensile stress σ^* at the onset of spalling is determined by the velocity drop ΔW.[3] We are using a correction term δW taking into account the difference in the propagation velocities of the the unloading wave after spallation (c_b) and of the spall pulse front (c_l).[4]

$$\text{spall strength } \sigma^* = \tfrac{1}{2}\,\varrho\, c_b\,(\,|\Delta W| + \delta W\,)$$

$$SR = (\Delta v/v_0)/\Delta t = (\Delta x/x_0)/\Delta t \text{ for 1-dimensional strain}$$

$$\approx \tfrac{1}{2}\,|\dot{W}_1|\,/\,c_b$$

with:

δW	=	$(h/c_b - h/c_l)\,/\,(1/|\dot{W}_1| + 1/\dot{W}_2)$
ϱ	=	mass density of the target matter
v	=	specific volume = $1/\varrho$
ΔW	=	velocity drop
c_b	=	bulk sound velocity
c_l	=	longitudinal sound velocity
h	=	thickness of the spall layer (to be determined from the decaying wave oscillations)
$\dot{W}_1$	=	derivative of free surface velocity when the incident rarefaction wave arrives
$\dot{W}_2$	=	derivative of the free surface velocity due to the spall pulse

Nonlinearity of matter compressibility was taken into account in the evaluation in case of high tensile stresses. This was done by extrapolation of the material isentrope to the negative pressure region. This correction did not exceed the level of 10%.

The experiments have been performed primarily with single crystal samples. Single crystals are largely free from stress concentrators in contrast to usual materials containing damage nucleation sites. Hence, measuring the dynamic spall strength of single crystals at highest expansion rates (strain rates) should yield the "ultimate tensile strength" of the undistorted crystal lattice. This is a fundamental question in matter research.

For observation of the dynamic target response, and for measuring of the kinematic quantities-of-state, an ORVIS type laser-Doppler-velocity interferometer[5] has been set up at the KALIF facility (Fig. 2). With this KALIF-ORVIS diagnostics system[6], the particle

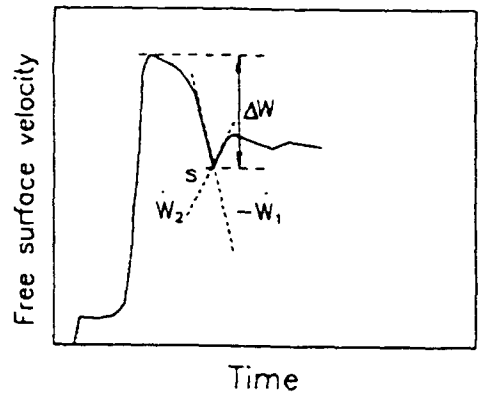

Fig. 1 Free surface velocity wave form of a spalling sample (schematic)

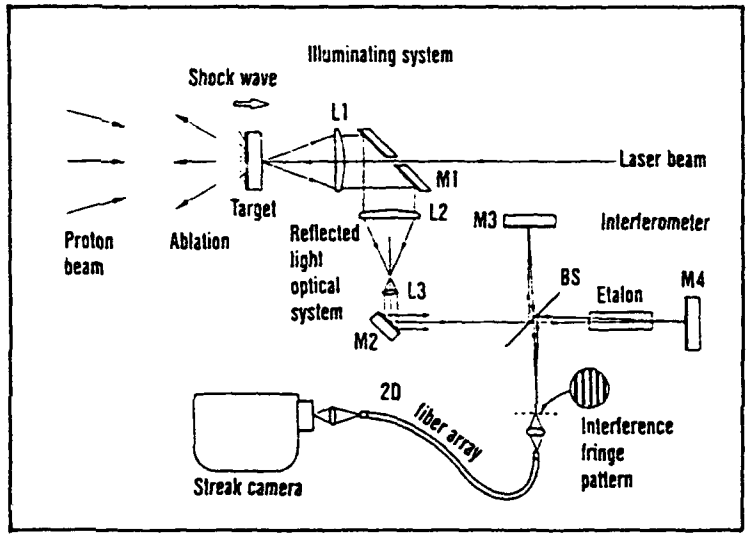

Fig. 2 KALIF-ORVIS diagnostics for target response studies (schematic)

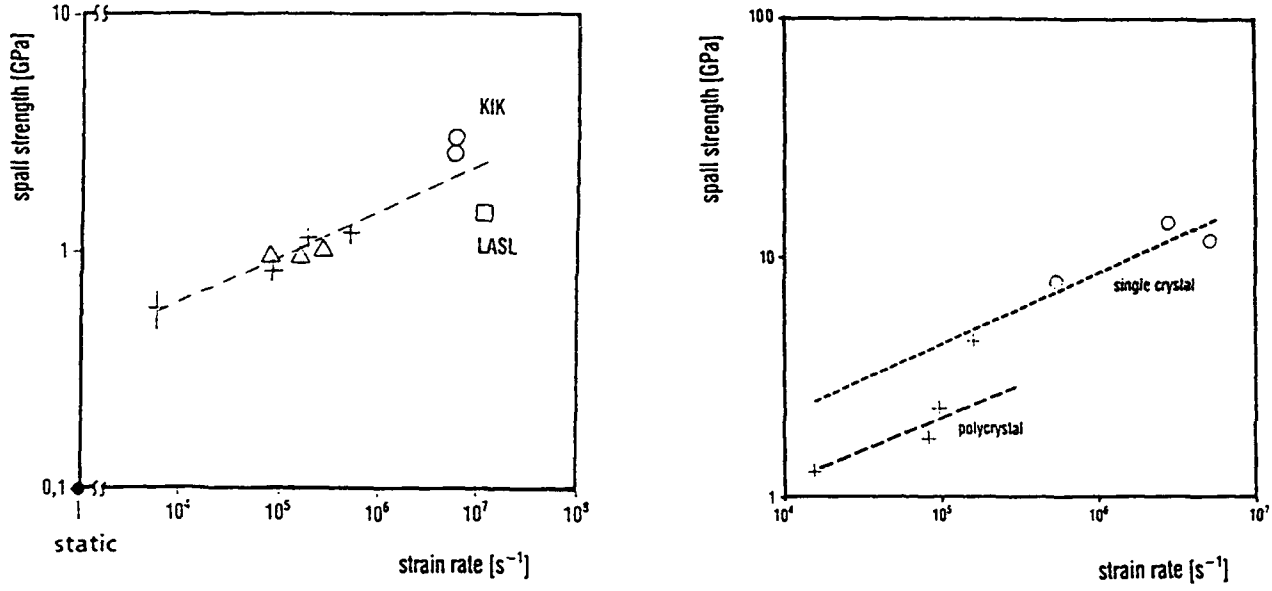

Fig.3 Dynamic strength measurements with KALIF-ORVIS
at left: for polycrystalline Al at right: for Mo

(or mass) velocity $u_p(t)$ at the rear target surface of optically reflecting targets can be recorded with high accuracy (up to 1 %) and with very good time resolution (up to 200 ps). A unique feature of the ion beam ablation driving of flyer foils is the very high acceleration level of $\geq 10^{10}$ g. As a consequence, both the acceleration time and acceleration path are very short (< 100 ns and $\leq 100\mu$m, respectively), and the synchronisation jitter of the ion beam driver and the KALIF-ORVIS diagnostics system is very small (3 ns only!). This allows very fast streaking of the target response in impact experiments with flyer foils.

Measurements and results

Single crystal samples of molybdenum have been shock loaded at KALIF either by direct proton beam ablation or by Al-flyer foils of about ≥ 30 μm thickness driven by proton beam ablation, respectively. The Mo specimen were cut from a single crystal bar of 14 mm in diameter. The sample thickness was between 0.2 and 2mm. Shock loading was done in the $<110>$ direction. In addition, experiments with polycrystalline aluminum samples of 33 and 100 μm, respectively, have been performed.

Fig. 3 (left) summarises the measurements at KALIF (marked by circles) on polycrystalline aluminum up to strain rates of about 10^8 s^{-1}. For comparison, also the results of a laser experiment[8] have been entered assigned by "LASL". The experiments based on ion beam ablation offer the advantage that due to the much higher pulse energy of the light-on beam driver, quantitative measurements can be performed under 1-dimensional conditions as compared with laser targets of microscopic dimensions involving multidimensional border effects. The ultimate theoretical strength of aluminum is appoximately 13 GPa. More than 25% of this value has been measured in the experiments at KALIF at 2 ns load duration. According to the extrapolation of these experimental results, the ultimate strength level should be reached at loadings of 2 ns duration which resembles 1 atomic oscillation period.

Fig. 3 (right) shows KALIF-ORVIS results (circles) for the spall strength σ^* of Mo as a function of the strain rate, evaluated from experiments with Mo single crystal samples. For comparison experimental data obtained with explosive loading are shown.[7] At the highest strain rates achieved by ablation flyer foil loading, the dynamic strength measured reaches about 30% of the ultimate theoretical strength. The latter is approximately K/6 to K/10 $\approx$ 55 GPa where K is the bulk modulus of the material. Extrapolation of the KALIF measurements shows that the theoretical limit of the ultimate strength should be reached at a strain rate of about 5 10^9 s^{-1} corresponding to a a load duration of 0.5 to 1 ns. This is only one order of magnitude shorter than the loadings applied in these KALIF experiments and exceeds the atomic oscillation period of solid Mo by ≥ 3 orders of magnitude.

Most recently, experiments were started with sapphire single crystals shock loaded by direct ion beam ablation. The polished free surface, without additional metallic reflection coating, was directly observed by the KALIF-ORVIS velocity spectrometer. The kinetic response to the ablation shock loading up to several 10 GPA was purely elastic. Spallation was observed in one of these preliminary shots at about 20 GPA.

In the ongoing experiments at KALIF, various materials of interest in matter research are being studied: single crystals and polycrystalline samples of metallic and non-metallic solids like Cu, Nb, Mo, sapphire, etc.

Résumé

The light-ion beam generator KALIF has been equipped and synchronised with an ORVIS type velocity spectrometer for investigating the kinetic response of 1-dimensional targets. Dynamic strength measurements have been performed with the KALIF-ORVIS system on metallic samples up to highest strain rates. The experiments have verified the positive perspectives of high-power light-ion drivers for experimental dynamic matter research.

Acknowledgement

The described beam-target experiments have been possible only by the excellent experimental assistance by J. Singer, O. Stoltz and H. Lotz, and by the smooth operation of the KALIF facility by the operators team under W. Ratajczak.
The authors would like to express their special thanks to Academician Prof. Vladimir Fortov, Moscow, for major stimulations to apply high-intensity particle beams in the field of dynamic matter research.
The German Federal Ministry for Research and Technology and the Russian Ministry for Education and Science have supported financially research stays of scientists participating in these experiments.

References

[1] K.Baumung, H.U.Karow, V.Licht, D.Rusch, J.Singer, O.Stoltz, H.Bachmann, W.Bauer, H.Bluhm, L.Buth, B.Goel, M.F.Goez, H.Guth, P. Hoppé, H.Lotz, C.D.Munz, and G.I.Kanel, A.L.Ni, A.Shutov, O.Yu.Vorobjev, BEAMS'92 - 9th Int. Conf. on High-Power Particle Beams, Washington DC, May 1992. Invited Paper no. OA-5.

[2] W.Bauer, H.Bachmann, H.Bluhm, L.Buth, P.Hoppé, H.U.Karow, H.Lotz, D.Rusch, Ch.Schultheiß, E.Stein, O.Stoltz, Th.Westermann, BEAMS'92 - 9th Int. Conf. on High-Power Particle Beams, Washington DC, May 1992. Contrib. Paper no. PB-01.

[3] S.A. Novikov, A.V. Chernov, J. Mech. Tech. Phys. 23, 703 (1982)

[4] G.I. Kanel, V.E. Fortov, Advances in Mechanics 10, 3 (1987)

[5] D.D.Bloomquist, S.A.Sheffield, J. Appl. Phys. 54, 1717 (1983)

[6] W. Bauer, K. Baumung, H.J. Bluhm, H.U. Karow, KfK Nachrichten 24/1, 19 (1992)

[7] S.V. Razorenov, to be published

[8] D.L. Paisley, R.H. Warnes, R.A. Kopp, APS 1991 Topical Conf. on Shock Compression of Condensed Matter, Williamsburg Va., (June 1991)

GENERATION OF EXTREME STATES IN CONDENSED MATTER BY HIGH POWER ION BEAMS

V.E.Fortov V.A.Skvortsov,V.V.Kostin,
O.Yu.Vorobjev,I.V.Lomonosov, A.L.Ni
High Energy Density Research Center
127412, Moscow, Izhorskaya,13/19, IVTAN
I.Hofmann
GSI Darmstadt, P.O.B. 110552, 6100 Darmstadt 11, Germany
B.P.Goel
Kernforschungszentrum Karlsruhe W7500, P.O.B.3040.

Abstract. The results of 2-D computer simulation of high-power light and heavy ion beams targets interaction are presented. The extreme states and dynamics of shock- waves and high velocity jet formation are described.

1. Introduction

The paper deals with the computer simulation of high energy density phenomena for analyzing the extreme states of matter generation for forecasting the planned experiments results on accelerating-accumulating complex SIS- ESR (GSI, Darmstadt) [1] and high current pulse accelerator KALIF (KfK, Karlsruhe) [2].

The used computer models were based on the hydrodynamical equations, which were completed by wide-range equation of state (EOS), equations of beam energy deposition and electron, ion and radiative heat transfer with corresponding physical limitations of heat flux [3,4].

Using the "big" particles in cell method the computer simulations were performed for investigation of the response of think cylindrical gold targets driven by high power ($W \geqslant 10^{10} W/cm^2$) heavy ion beams (argon, iodine, bismuth) with the typical and perspective beam parameters of SIS-ESR.

Computer simulations of proton beam (KALIF, at $W \cong 1.5\ 10^{11}\ W/cm^2$) interactions with conic aluminium targets were performed using the Godunov's code with moving grids [5],

which effective to fit singularities of the flow: contacts, free surfaces, shocks.

The Lagrange's code was used for the computer simulation of solid target dynamics destruction by combined laser and proton beams at moderate intensities $W < 10^{11}$ W/cm^2 with taking into consideration the elastic plastic and spallation effects [4].

Semiempirical wide-range EOS were applied in the developed codes to determine pressure, temperature as functions of specific internal energy and the matter density [6]. It describes the high-temperature melting, evaporation, ionization, experimental data of shock-wave compression in megabar pressure range, and strongly coupled plasma. This EOS is the Mie-Gruneisen type EOS extended to gaseous and plasma and describes the thermal unharmonicity effects of atoms and electron excitation. It describes all available high pressure data and provides for a correct asymptotic at ultrahigh energy densities.

Ion energy deposition was calculated using semiempirical formulas [7] those describe asymptotically the cases of fully degenerated and classical electron gas and temperature dependencies of stopping power.

2. Hydrodynamic response of solid Au-target driven by heavy ion beam

We are interested extreme states of matter which may be generated by irradiating different heavy ion (Ar,I,Bi) uniform cylindrical beams with radius $r_b = r_t'$-radius of the needle targets at the uppermost parameters of beams with a maximum number N particles per pulse and corresponding specific deposition power Q_{in} near the irradiated target surface (see Table).

The computer simulation results are represented in Fig.1,2 and in the Table. In this examples, the beam flux

is parabolic in time $F(t)=F_o*(t/\tau)(1-t/\tau)$ for $t \leqslant \tau$ - pulse length, and $F=0$ for $t>\tau$ ($F_o=1.5N/(\tau\pi r_b^2)\cong 1.6\ 10^{22}$ $(cm^2 sec)^{-1}$ at $\tau=$ 30 ns, $r_b=100$ μm and $N=10^{11}$ ions).

Table

Sort of Ion	N	E_{max} GeV	P_{max} Mbar	ρ_{max} g/cc	E_{max} kJ/g	T_{max} eV	Q_{in} TW/g
Ar	10^{11}	4	14	31.3	48	8	6
Ar	10^{12}	10	33	32.0	185	17	15.5
I	10^{11}	20	35.6	34.5	187	17	15.3
Bi	10^{11}	40	50	35.3	320	22	31.4

When the region of cumulative compression at the end of ion range coincides with the position of Bragg peak the specific nonlinear hydrodynamical effect was detected: generation the second moving peak in spatial distribution of specific internal energy (as in example of argon beam, Fig.2).

In the Table a maximum plasma parameters are represented for different heavy ion beams with initial energy E at which initial length λ energy deposition equals approximately 1 mm (at the target length L=2 mm, excluding case argon ion with energy 10 GeV, when $\lambda \cong 7.5$ mm and L=8 mm).

Note that when beam radius is 200 μm (and hence $N=4\ 10^{11}$) for iodine beams with the same parameters, as mentioned in table, the maximum pressure generated up 100 Mbar at the end of range that is the same order as P_{max} in [1].

For Bi-ion beams with $N=10^{12}$, $\tau=20$ ns, E=40 GeV and $r_b=r_t=200$ μm at L=2 mm our calculations show that next extreme states can be achieved: $P_{max}\cong 360$ Mbar, $\rho_{max}/\rho_o \cong 4$ $E_{max}\cong 1.5$ MJ/g and $T_{max}\cong 50$ eV (if $r_t=2r_b$, $P_{max}\cong 400$ Mbar).

3. Computer simulation of proton beam interaction with conic aluminum target

Experiments performed with KALIF beam on the plane foils acceleration (see paper of H.U. Karow et. al, presented at this conference) show that the pressures of 200-300 kbar were reached in the target (100 μm Al foil) impinged by 0.15 Tw/cm^2 proton beams. The irradiated by such beam foil accelerates up to 3-4 km/s. The pressures generated in the target can be increased due to cumulative effect when conic targets are used.

The results of computer simulation of KALIF beam interaction with conic aluminum target (thickness 1mm, the cone angle 45°) are represented in Fig.3. The beam power is 0.15 TW/cm^2, the pulse duration is 100 ns and the beam radius is 4 mm.

It was shown that cumulative jet with mass of 5 mg and velocity of 15 km/s can be produced. Such jet may be used for the experimental study of hypervelocity impact by means of powerful ion beams. The pressure in the range of 1.5 Mbar is reached in the gold target after impact by the jet, while in the case of the plane target of the same thickness the pressure of 0.5 Mbar can be reached. So in comparison with the ablative acceleration method [8], in this case pressures generated is higher due to the cumulative effect.

4. Combined irradiations of high power ion and laser beams

For increasing the modification regions of irradiated target, for producing enhanced shock-waves generated by laser beams it is interesting to investigate combined impinge of high power ion and laser beams.

To optimize a combined irradiation it is needed to choose such time proton energy profile, at which the shock-wave position (initiated by the laser pulse) would coincide with the Bragg peak during shock front propagation.

For example, Fig.4 a) shows the time evolution of the stress at the several depths (on the symmetry axes). For comparison on Fig.4 b) it is shown the same values for laser pulse only.

The total energy of the both laser and proton beams was 7 J. The duration of the proton beam (with the trapeziform time pulse profile) was 20 ns (the laser pulse duration of 5 ns, ion beam pulse began after the laser pulse),a maximum energy of protons E = 4 MeV, maximum current density j_{bo}=20 kA/cm^2, radius of both beams r_b=0.2 mm, target thickness L_t=0.2 mm.

Fig. 5 illustrates the rear surface velocity of the sample for different types of the beam irradiation: laser, proton and combined (established by pointed, dashed and solid lines correspondingly).

Distributions of the stress and matter density in the sample are shown on Fig.6 for the time t= 50 ns. Fig.6 b) is characterized by existence of the two regions of the density rarefactions : in the proton beam energy input and spallation zones.

REFERENCES

1. Meyer-ter-Vehn J., Witkowski S.,Bock K., Hoffmann D. H. H.,Hofmann I., Muler W.,Arnold R.,Mulser P. Phys.Fluids, B-2(6), 1313-1317 (1990).
2. Goel B.P., Moses G.A., Peterson R.R. Laser and Particle Beams. 5, 133-154 (1987).
3. Bushman A.V.,Kanel G.I., Nee A.L., Fortov V.E. "Thermophysics and dynamics of matter at high energy densitie," Hemisphere Publishing Corporation, N.Y.(1992).
4. Skvortsov V.A., Fortov V.E. "Dynamics of interaction of directed energy flows with matter".SPIE Proc. from conf. Vol.1629: Intense Microwave and Particle Beeams III. Paper No.1629-70. Los Angeles, CA USA (1992).
5. Godunov S.K. Sov.Mat.Sbornik. 47, 271-306 (1959).
6. Bushman A.V., Lomonosov I.V., Fortov V.E. In: High Pressure Equations of State: Theroy and Applications / Eds. S.Elieser, R.A.Ricci. Amsterdam: North Holland, (1991).
7. Bespalov I.M, Bushman A.V., Fortov V.E. et al, Plasma Phys.(Russ.) 17, 336-345 (1991).
8. Borodziuk S.R., Kostecki J.L. Laser and Particle Beams. 8, 241-245 (1990).

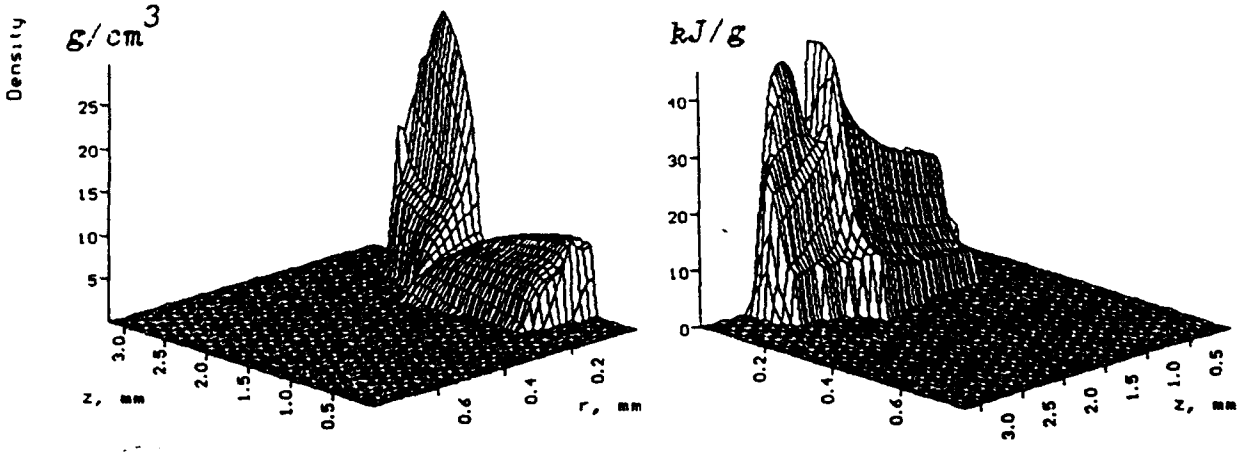

Fig.1,2. The spatial distributions of matter density $\rho(r,z)$ (left) and specific internal energy $\varepsilon(r,z)$ (right) at the time t= 20 ns for Ar - beam.

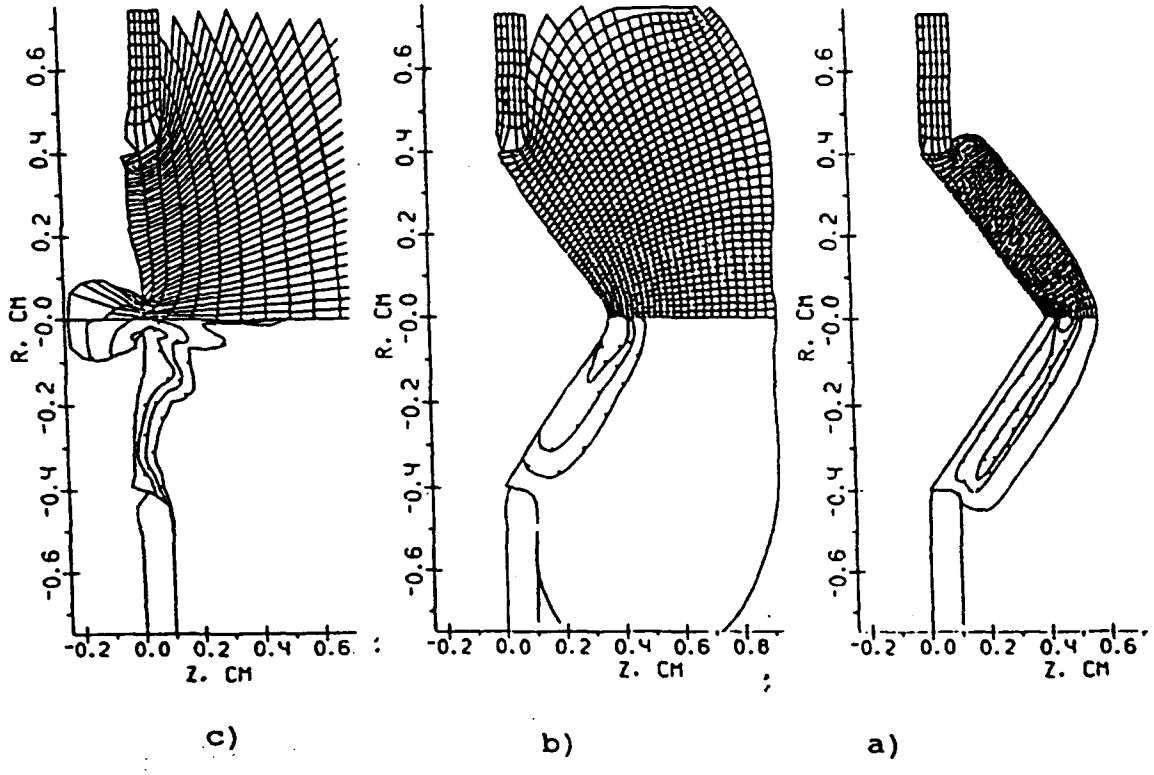

c) b) a)

FIG.3. Numerical grid and levels of constant pressure (a,b) and density (c) at different times: a) 40 ns; 0.25, 0.5, 0.75 Mbar b) 108 ns; 0.075, 0.15, 0.225 Mbar c) 460 ns; 0.375, 0.75, 1.125 g/cc

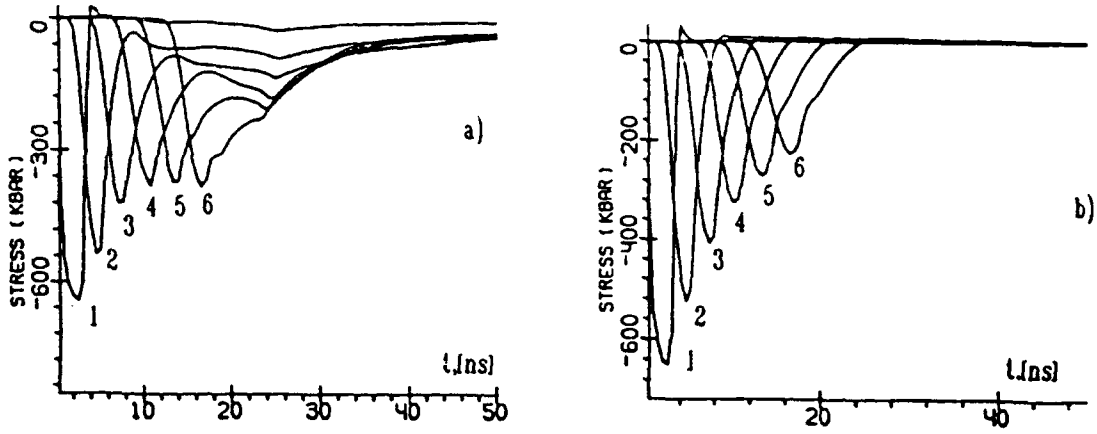

Fig.4.Axial distributions of time stress evolution for the different depth (on the symmetry axes of Al-target): h_n = 8, 36, 64, 92, 120, 148 μm (n=1,2,..6).

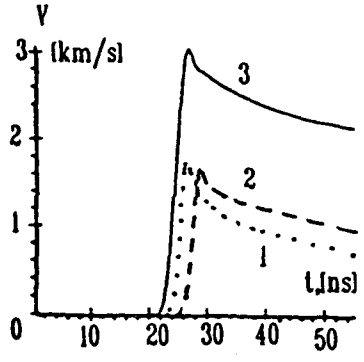

Fig.5.Time dependencies of a free surface velocities.

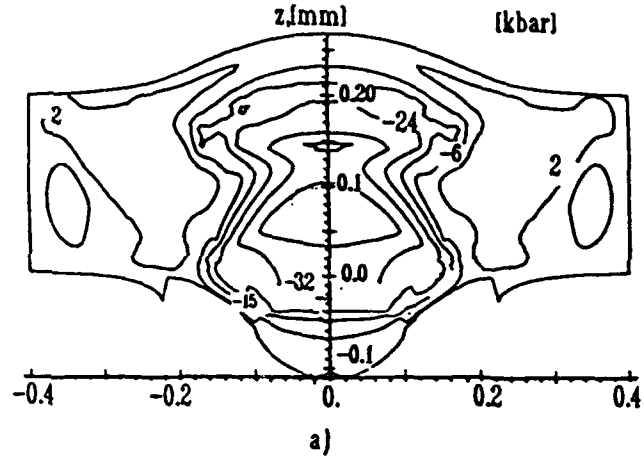

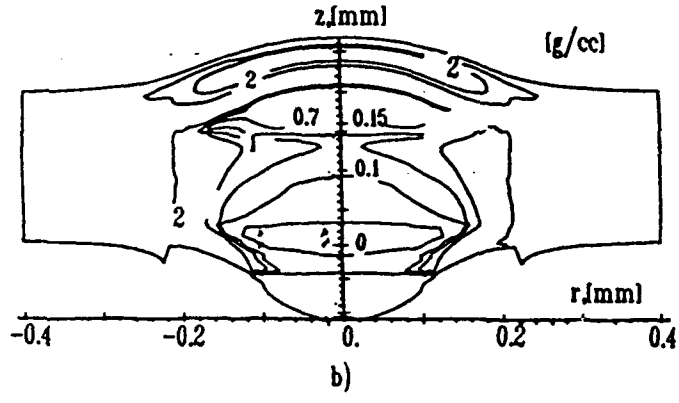

Fig.6. The spatial distributions of stress (a) in kbar, and matter density ρ (b) in g/cc.

PULSED-ION-BEAM DRIVEN ABLATION OF MATERIAL NEAR ITS SUBLIMATION ENERGY

A. Kitamura, T. Asahina, Y. Furuyama and T. Nakajima

Department of Nuclear Engineering,
Kobe University of Mercantile Marine,
Fukaeminami-machi 5-1-1, Higashinada-ku, Kobe 658, Japan

Abstract The process of target ablation induced by pulsed ion beams is investigated. The beam power density of 0.01-0.1 GW/cm^2 is around the sublimation energy of the target material. The emitted particles are collected with C collectors, which are later subjected to RBS and SEM-EPMA analyses. The thickness of the removed layer of the target is calculated numerically with use of the thermal conduction equation. It is shown that most of the ablated material is emitted in the form of large particles with diameters of the order of tens of μm, the rest 10% being evaporated from the surface of the flying mass to form a uniform film on the collector.

1. Introduction

Application of medium power (>10^7W/cm^2) pulsed ion beams (PIB's) to material processing is of growing interest owing to their unique feature of energy deposition [1]. Following the application of PIB to annealing of materials [2], mixing of atoms to form various novel compounds [1,3,4,5] and improvement of the mechanical properties such as wear resistance and microhardness [6,7], a successful formation of thin films of $YBa_2Cu_3O_{7-x}$, ZnS:Mn, etc. from the ablation plasma has been reported [8]. Such a method of thin-film deposition has distinctive feature that the deposition occurs in much shorter period of time from the ablation plasmas having much higher density than in conventional plasma methods. Using Laser beams as the ablation driver, similar method of thin-film formation has been developed more extensively [9].

It is not always clear how the film properties are influenced by the characteristics of the ablation plume. In the present

work we examine the basic characteristics of the ablation plumes produced by pulsed ion beams of 10^7-10^8 W/cm^2.

2. Experimental procedure

2.1. PIB and its composition

A schematic of the PIB irradiation system with an occasionally used Thomson parabola spectrometer is shown in Fig.1. Pulsed ion beams of 50ns duration with current density of 1kA/cm^2 were produced with a pinched electron beam diode with a polyethylene anode, which was operated at an anode voltage of 400kV fed by a 5kJ pulse power source ER-Ⅱ.

A momentum filter using a transverse magnetic field has been developed for purification of the PIB [10], but it was not applicable in the present case since we needed parallel beams to irradiate targets fabricated in a collector assembly, as described in the following section. The composition of the beam was measured quantitatively with use of the Thomson parabola spectrometer having either a CR-39 detector or two charge collector plates located suitably for separate detection of protons and carbon ions.

The oscilloscope traces of the collector signals together

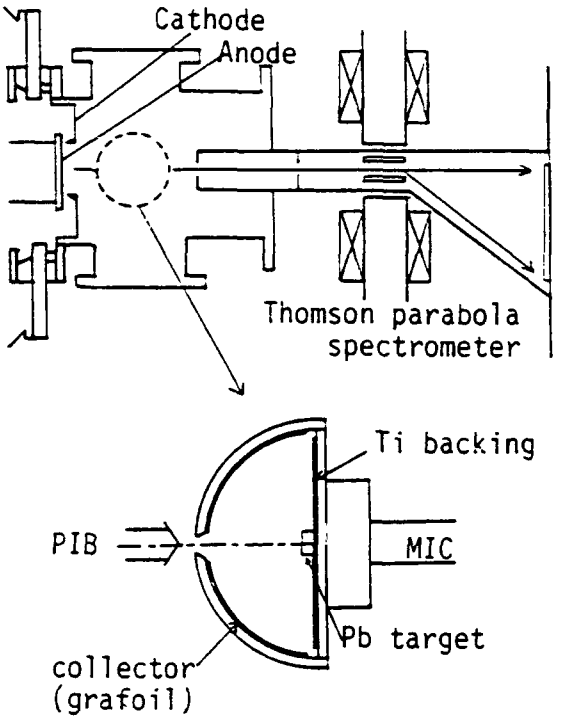

Fig.1. PIB irradiation system. The Thomson spectrometer is occasionally installed.

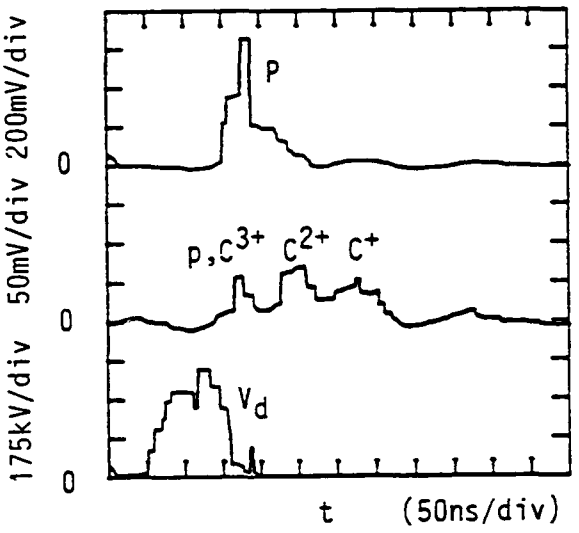

Fig.2. Typical traces of collector signals in the Thomson spectrometer.

with diode voltage waveform are shown in Fig.2. There are observed the traces of C^+, C^{2+} and C^{3+} separated from that of p due to the difference in the time of flight. Summing up the carbon signals yields the C content of (13±3)%.

2.2. PIB irradiation

The targets of Pb were located inside a target-collector assembly shown in Fig.1. The target discs had holes in their center to allow measurement of beam current density j_i, which was controlled by moving the target-collector assembly axially.

The ablation particles were collected with carbon collectors which were later subjected to Rutherford Backscattering Spectrometry (RBS) analysis using a tandem Pelletron accelerator. As the analyzing beam, 1MeV C^+ beams were chosen to take advantage of the high resolution for the present combination of the substrate C and the material to be analyzed.

The angular distribution of the ablation particle fluence $F_a(\theta)$ was measured as a function of j_i. In the course of these measurements, nonreproducible peaks with large amplitude were sometimes found in $F_a(\theta)$. The corresponding RBS spectra had large peaks of Pb with tails extending to the lower energy. This suggests that the concerned area on the collector had a layer of Pb with significant thickness.

The collectors were then subjected to SEM and EPMA analyses. A lot of large particles with diameters of several ten μm were found on the SEM display. These were identified to be pure Pb by the EPMA analysis. It seems therefore that a significant fraction of the target material are emitted as liquid drops.

Neglecting these large particles, the distributions $F_a(\theta)$ are shown in Fig.3. There is seen a transition of $F_a(\theta)$ as the current density is increased. When j_i is low, the distribution is rather flat, and as j_i is increased, the emission toward the large angle predominates. When j_i is increased further, $F_a(\theta)$ approaches the cosine distribution.

Integrating $F_a(\theta)$ over the half space, and dividing it by the atomic density of the Pb target, we get a thickness T_a removed from the target in the form of vapor, i.e., excluding those

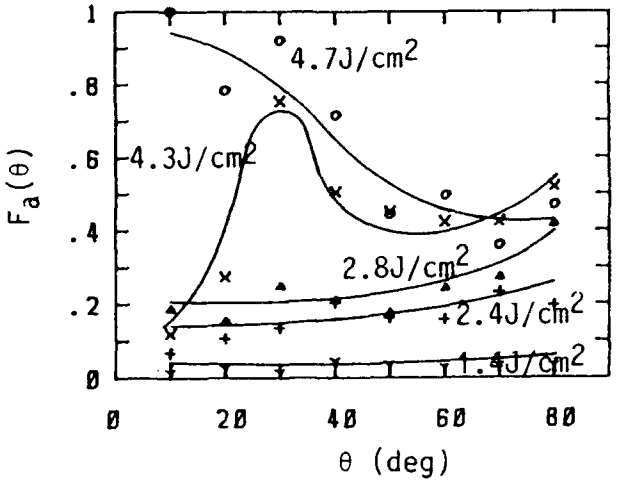

Fig.3. Distribution function $F_a(\theta)$ of the ablation particle fluence.

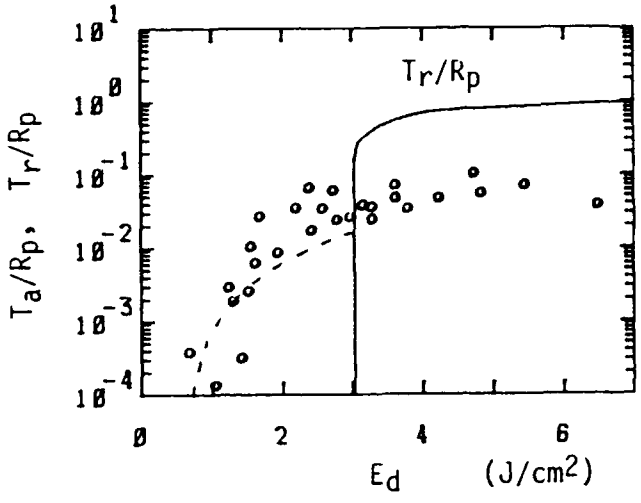

Fig.4. Removed thickness T_a (o) as a function of the deposition energy E_d together with that calculated (lines), both normalized to the proton range R_p.

emitted as liquid drops mentioned above. The thickness T_a's are normalized to the range R_p of the incident p in Pb, and plotted as circles in Fig.4 as a function of the deposition energy E_d of the PIB. The lines show the calculated ones described in the following section.

3. Calculation of target temperature

The thickness T_r of the layer removed from the target is calculated as the deepest depth at which the temperature rises above the boiling point. The temperature distribution in the target is calculated with a one-dimensional thermal conduction equation;

$$\frac{\partial T(x,t)}{\partial t} = \frac{\kappa}{c\rho}\frac{\partial^2 T(x,t)}{\partial x^2} + \frac{j_i(t)[dE/dx](x,t)}{c\rho}, \qquad (1)$$

where the second term on the right hand side is the heat input due to the PIB energy deposition, and dE/dx is the stopping power of the target material taking account of the proper ratio of p and C in j_i.

The Crank-Nicolson method is used to get the numerical solution over the region ten times deeper than R_p. Using phase-

dependent but temperature-independent values for the thermal conductivity κ and the specific heat c, the evolution of the temperature in each element of width 0.1μm are calculated with a calculation step of 1ns. The boundary conditions are adiabaticity at the surface, and room temperature at the other side of the concerned region. At the phase-change temperature, only the change in the internal energy is calculated; the temperature is forced to remain unchanged unless the internal energy has the value necessary for the next phase.

The thickness T_r normalized to R_p is shown in Fig.4 as the solid line. We have a threshold E_{dt}=3J/cm^2 for E_d, above which T_r remains almost constant. Inclusion of the blackbody radiation loss from the surface is found to have neglegible effect on E_{dt}. The sensitivity of E_{dt} to the C content in the PIB must also be checked, since the energy deposition of heavy ions is concentrated in much thinner layer of the target. An artificial decrease in the C content to 0% increased E_{dt} to 3.5J/cm^2, while an increase up to 100% decreased E_{dt} to 1.7J/cm^2, below which we have a lot of data points. The relative insensitivity of E_{dt} to the C content means that heat conduction into the bulk is substantial.

Below the threshold we must take account of particles evaporated from the surface heated to a temperature even below the boiling point. The number of the evaporated particles N_e is evaluated as the number of particles hitting the surface if the ambient pressure were in equilibrium with the surface of temperature T_s;

$$N_e = \int [P_v(T_s) v_{th}/4kT_s] \Delta S dt, \qquad (2)$$

where $P_v(T_s)$ is the vapor pressure of the target material, v_{th} the thermal velocity of the target atom with the temperature T_s, ΔS the target area irradiated with the PIB and the integration is done up to the time when the surface is cooled down so that the evaporation becomes neglegible, say 4μs. The contribution of N_e to the ablation thickness is also shown as the broken line in Fig.4.

4. Discussion and conclusion

We have a fair agreement of the measured T_a with the evaporation contribution described above in the low E_d region.

The difference between T_a and T_r in the high E_d region is due to the existense of the liquid drops mentioned earlier; T_a's do not include the contribution of the liquid drops. It is therefore concluded that a large fraction of the ablated material is emitted in the form of liquid drops. This is in contrast with the case of Laser-induced ablation. Although the temperature inside the drops is high enough for vaporization, they seem to have insufficient time to breake up into atoms or atomic clusters.

Thus, it is inferred that only the particles evaporationg from the surface of the flving mass of ablated material contribute to the formation of the uniform film observed in the RBS analysis even in the high E_d region. The broken line in Fig.4 snould be extraporated to high E_d region and smoothly joined with the solid line at stil higher E_d beyond the region examined in the present work.

Thanks are due to Y. Okazaki and N. Yamasaki for their help in the measurements.

References

[1] K. Yatsui, Proc. 7th Int. Conf. on High Power Particle Beams, Karlsruhe, West Germany, (1988)283; Laser & Particle Beams 7(1989)733.
[2] R.T. Hodgson, J.E.E. Baglin, R. Pal, J.M. Neri and D.A. Hammer, Appl. Phys. Lett. 37(1980)187.
[3] T. Brat, M. Eizenberg, R. Fastow, C.J. Palmstrom and J.W. Mayer, J. Appl. Phys. 57(1985)264.
[4] K. Kamata, Laser & Particle Beams 5(1987)495.
[5] Y. Nakagawa, T. Ariyoshi, M. Itami and Y. Fujii, Jpn. J. Appl. Phys. 27(1988)L719.
[6] A.N. Didenko et al., Nucl. Instr. & Meth. **B27**(1987)421.
[7] A.D. Pogrebnjak, G.E. Remnev and I.G. Romanov, Nucl. Instr. & Meth. **B43**(1989)41.
[8] Y. Shimotori, M. Yokoyama, S. Harada, K. Masugata and K. Yatsui, Jpn. J. Appl. Phys. **28**(1989)468.
[9] e.g., P.E. Dyer, Appl. Phys. Lett. 55(1989)1630.
[10] A. Kitamura, Y. Furuyama, S. Kamihata and T. Nakajima, Proc. 8th Int. Conf. on High Power Particle Beams, Novosibirsk, (1990)745.

CHARGE FLUCTUATIONS, ENERGY STRAGGLING, AND MULTIPLE SCATTERING IN INTENSE ION BEAM-TARGET INTERACTION

Z. Zinamon and E. Nardi
Weizmann Institute of Science
Rehovot, Israel

In this work we study phenomena which lead to fluctuations in the processes of interaction of ion beams with targets of interest in ICF work. These phenomena are, energy straggling, charge state fluctuations, and multiple scattering. The effects on the shape of the energy deposition profiles are discussed, bearing in mind the fact that the targets are plasmas. The effect of charge state fluctuations in the diagnostics of intense ion beams is also studied.

1. Introduction

The differences between the processes governing the charge state of a projectile ion in plasma and in cold matter[1,2] produce remarkable differences in the shapes of the energy deposition profiles in the two cases[2]. The main reason for these differences is that it is more difficult for a fast ion to capture a free electron than to capture a bound electron via a charge exchange reaction when such a reaction is possible[3]. As a result, an ion injected into a plasma at a high energy is quickly stripped to the charge state compatible with that energy, and maintains this high charge state even when it is slowed down in the target. This results in a characteristic energy deposition profile with a sharp Bragg peak[2,4]. In this work we study the extent to which fluctuations in the energy deposition process affect the sharpness of this peak. We stress the effects which follow from the plasma nature of the medium. We also describe the possible role of charge fluctuations in the analysis of beam diagnostics.

2. Straggling in plasma

In calculating the stopping and straggling of ions in plasma we use the plasma dielectric theory as described in Ref. 5. The calculation of the cross sections and rates of capture and loss of electrons, which determine the projectile charge state, are described in Ref. 2.

We have calculated the electronic contribution to the energy straggling following

Arista and Brandt[6]. The width of the straggling distribution is given by:

$$\Omega_p^2 = \frac{2Z^2\epsilon^2\hbar}{\pi v^2}\int_0^\infty \frac{dq}{q}\int_0^{qv} dw w^2 [2N(w)+1] Im\left(-\frac{1}{\epsilon(q,w)}\right) \qquad (1)$$

Here Z is the projectile charge, v its velocity, q the wave vector, w the frequency, ϵ is the dielectric function, and $N(w)$ is the excitation spectrum

$$N(w) = \left[exp\frac{\hbar w}{kT} - 1\right]^{-1} .$$

The dielectric function $\epsilon(q,w)$ was evaluated as described in Ref. 5. The significance of Eq. (1) in the cases of interest here is demonstrated in Fig. 1, where we show the ratio Ω_p^2/Ω_B^2 between the plasma straggling and the standard Bohr straggling $\Omega_B^2 = 4\pi Z^2 n\epsilon^4$ as a function of temperature for a hydrogen plasma at a density of $10^{-6} g/cm^3$.

The energy loss straggling due to the combined effect of the electronic process and charge fluctuations was calculated using the Monte Carlo method. The ion trajectory is divided into small intervals of varying length ΔX, defined such that the total probability for capture and loss by the particle traversing the path is 0.4. This choice is rather arbitrary and was made as a compromise between accuracy of the calculations and expedience in computation time. In each of these intervals capture or loss of an electron is determined by the Monte Carlo method. The straggling is gaussian with the standard deviation given by Ω_p provided that the energy loss over the distance ΔR is much greater than the maximum energy loss in a single collision with an electron. Therefore, electronic straggling was calculated in the code after the projectile traversed a sufficient number of intervals ΔX defined above, to make sure that the energy loss was large enough for a gaussian approximation to be valid. In the cases of interest here the charge fluctuations made the dominant contribution to the energy straggling.

We have calculated the energy deposition profiles of iodine ions in a fully ionized lithium plasma at a density of $10^{-4} g/cm^3$. The ion initial energy was 3 MeV/amu. In Fig. 2 we show three typical charge state histories, where the charge at the injection point was 26. The differences in charge histories occur mainly during the initial stage of charge buildup from 26 to 41. In Fig. 3 we show the effects on the differences in the

individual deposition profiles. In Fig. 4 we show the average deposition profile for the entire Monte Carlo population. The effect of straggling is to drastically smear the sharp individual Bragg peaks.

The dominance of charge state fluctuations in the straggling process is demonstrated by a calculation in which the charge at injection was 48, which is higher than the maximum achievable at this energy. Since in this case there is no charge build-up stage, and due to the slowness of the capture process, this charge is maintained nearly to the end of the range. In Fig. 5 we show the average deposition profile. Its sharp Bragg peak indicates that the contribution of the electronic straggling is much less than that due to charge fluctuations.

3. Multiple Scattering of Projectile Ions in Plasma

When light ions are stopped in a plasma of heavy ions, effects of multiple scattering on the trajectories may be of interest. We have used the Moliere-Bethe theory of multiple scattering[7] and the Monte Carlo method[8] to treat this problem. The fact that the medium is a plasma is reflected in the way the characteristic angle χ_0, which is needed in the Moliere-Bethe theory, is determined as $\chi_0 = d/\lambda_D$. Here λ_D is the Debye screening length and d is the larger of the de-Broglie length or the classical distance of closest approach.

We have calculated the case of Li projectiles at an energy of 2 MeV/amu injected into a gold target at a temperature of 100 eV and a density of $0.01 g/cm^3$. In Fig. 6 we show several Monte Carlo cases of the deflection angle as function of distance into the target.

4. Ion Scattering in Foils

Rutherford scattering in foils is part of the diagnostics in analyzing the energy and composition of intense ion beams[9]. Here we look into the possible role of charge fluctuations in the interpretation of such measurements. Following the parameters of the experiment of Ref. 9, we study the interaction of Li ions at an energy of 2 MeV/amu with a gold foil. We used the theory of Brinkmann and Kramers[10] to calculate the cross

section for capture of an electron into a Li^{+3} ion. The result is

$$\sigma_c = 0.32 \times 10^{-17}\ cm^2.$$

We used Bell's model[3] to calculate the cross-section for ionization of a Li^{+2} ion through collision with a gold atom. The result is

$$\sigma_I = 0.58 \times 10^{-16}\ cm^2\ .$$

The ratio between these cross sections could explain the ratio between the abundances of Li^{+3} and Li^{+2} found in the experiment of Ref. 9 in the beam after exiting the scattering foil.

References

1. D.S. Bailey, Y.T. Lee, and R.M. More, Bull. Am. Phys. Soc.**26**, 900 (1981); J. de Phys. **C8**, 149 (1983).
2. E. Nardi and Z. Zinamon, Phys. Rev. Lett. **49**, 1251 (1982).
3. G.I. Bell, Phys. Rev. **90**, 548 (1953).
4. J. Meyer-ter-Vehn, Th. Peter, and R. Arnold, in Heavy Ion Inertial Fusion, edited by M. Reiser, T. Godlove, and R. Bangerter, AIP Conference Proceedings 152, American Institute of Physics, New York 1986, p. 371.
5. E. Nardi, E. Peleg, and Z. Zinamon, Phys. Fluids **21**, 574 (1978).
6. N. Arista and W. Brandt, Phys. Rev. **A23**, 1898 (1981).
7. G. Moliere, Z. Natuurforschung **3a**, 78 (1948); H.A. Bethe, Phys. Rev. **89**, 1256 (1953).
8. E. Nardi and Z. Zinamon, Phys. Rev. **A18**, 1246 (1978).
9. R.P. Kensek, J.R. Lee, R.J. Leeper, D.J. Johnson, T.R. Lockner, J. Maenchen, L.P. Mix, W.A. Stygar, D.E. Hebron, and D.F. Wenger, Rev. Sci. Instrum. **61**, 3247 (1990).
10. H.C. Brinkmann and H.A. Kramers, Ned. Akad. Wet. **33**, 973 (1930); Th. Peter and J. Meyer-ter-Vehn, Phys. Rev. **A43**, 2015 (1990).

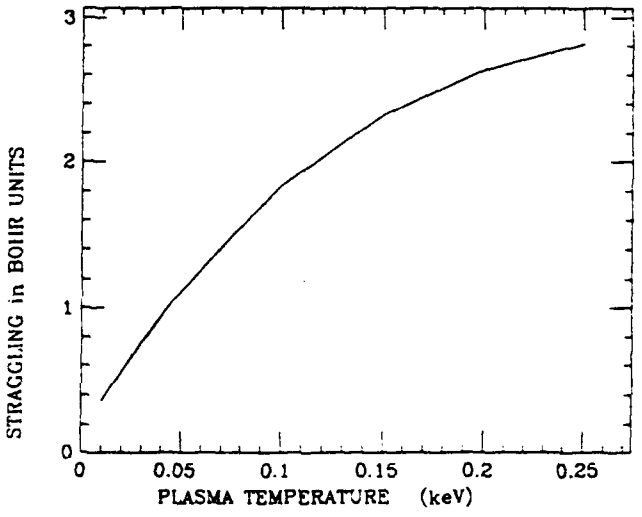

Fig. 1. The ratio Ω_p^2/Ω_B^2 between plasma and Bohr straggling. 1 MeV protons in hydrogen plasma of density 10^{-6}g/cm^3.

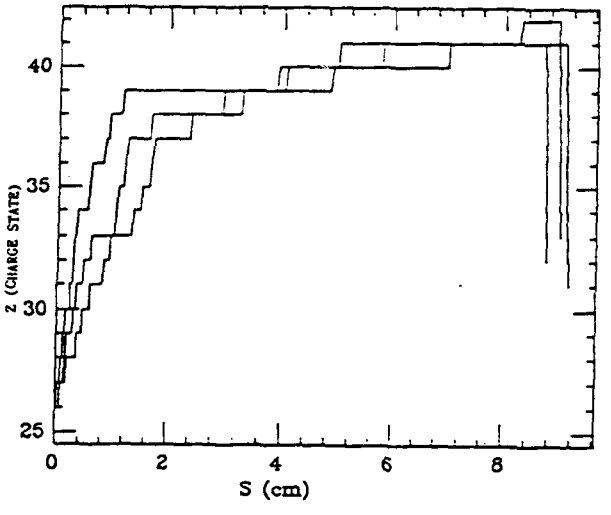

Fig. 2. Typical charge state histories of initially 3 MeV/amu iodine ions of charge + 26 in lithium plasma of density 10^{-4}g/cm^{-3} and temperature 30 eV.

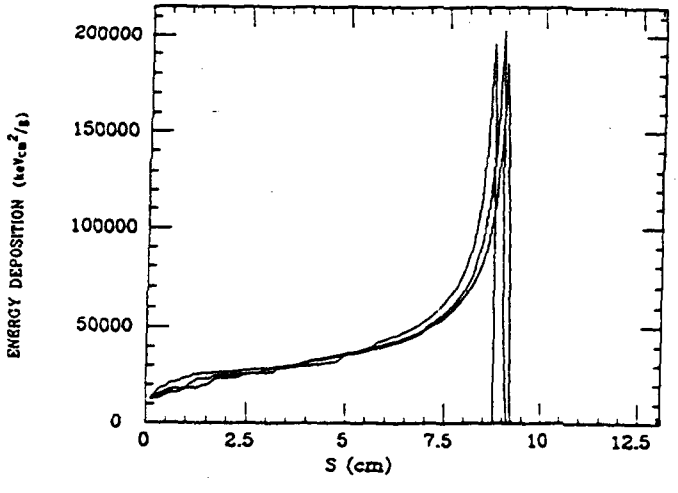

Fig. 3. The energy deposition profiles corresponding to the ions and plasma of Fig. 2.

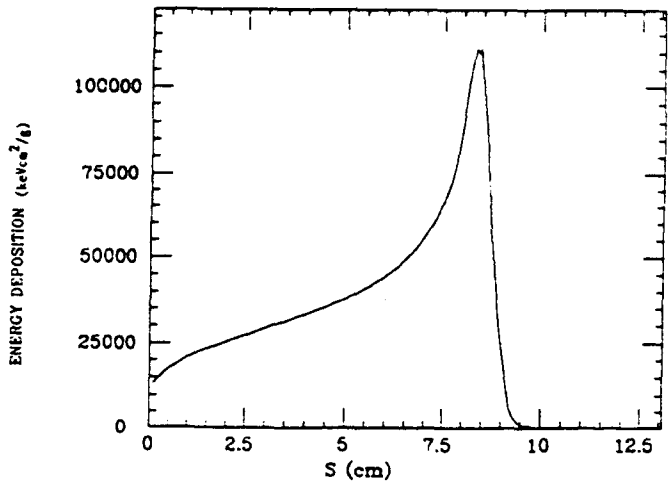

Fig. 4. Average energy deposition profile for the initial ionic charge and energy and the plasma conditions of Fig. 2.

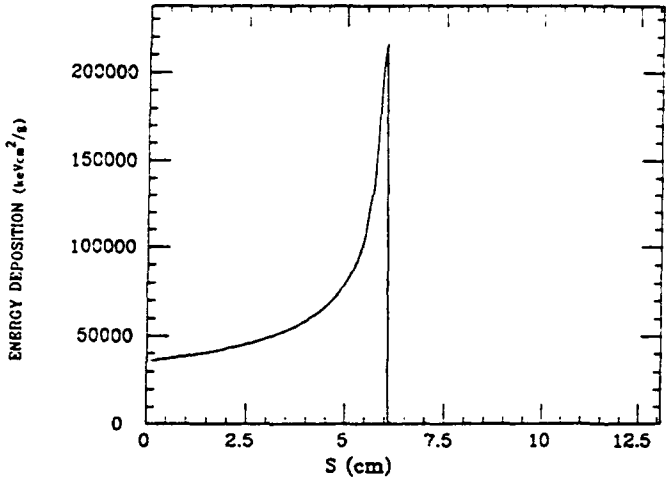

Fig. 5. Average energy deposition profile for initially 3 MeV/amu iodine ions of charge + 48 in the same plasma as in Fig. 2.

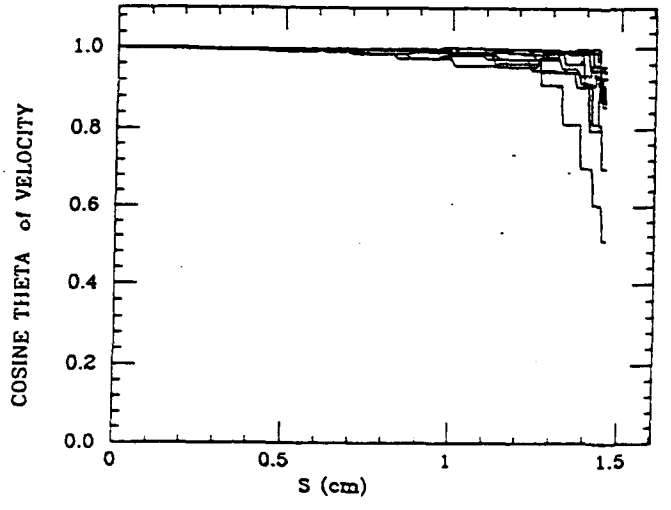

Fig. 6. Typical histories of the deflection angle cosine of lithium ions in gold plasma of density 10^{-2}g/cm^3 and temperature 100 eV.

PARTICLE DRIVEN INERTIAL FUSION THROUGH CLUSTER ION BEAM

C. DEUTSCH and N.A. TAHIR
L.P.G.P.* and GDR-CNRS 918 Bât. 212, Université Paris XI
91405 ORSAY Cedex, France

Abstract

Cluster ion beam with energy in the several tens of keV/a.m.u. range are considered as a novel direct driven for a simple fusion pellet made of Deuterium + Tritium fuel surrounded by a Lithium pusher. The driven-pellet interaction is calculated through the hypothesis of maximum multifragmentation followed by highly correlated ion debris motion. One thus gets enhanced stopping and ablation pressure in the hundreds Mbar range. An implosion is then completed in 5 nsec.

Introduction

In the field of particle-driven inertial confinement fusion (ICF), one is now witnessing a persistent interest in very heavy drivers with the smallest possible charge-to-mass ratio [1],[2]. Up to now, the corresponding mass range has extended over a large scale: from heavy atomic ions up to macro-particles (containing 10^{22} atoms) driven to hypervelocities ($\sim$ 50-1000 kms).

The purpose of this paper is to speculate for the first time about driving potentialities afforded by intense cluster ion beams (hereafter referred to as CIB). Today it is well known [3] that cluster ions containing nearly any number of constituent atomic ions may be easily prepared, identified, selected, and even transported.

As far as direct drive compression is concerned, a straightforward manipulation of scaling laws based upon a Bethe-like stopping formula displays almost at once the obvious payoffs of playing with a heavy projectile.

---

* Associé au C.N.R.S.

CIB for ICF

The straightforward argument runs as follows [4]. A spherical shell, of radius r, thickness Δr, and density ρ, is assumed to stop an ion beam of ion mass M_i, stripped charge state Z_i, and energy E_i. Since the ions lose their energy predominantly by Coulomb interactions with the electrons in the ragion Δr, we can write for the ions the following:

$$\frac{dE}{dx} \approx - \frac{4\pi N Z_i^2 e^4 M_i}{2mE_i} \ln \Omega \qquad (1)$$

where m is the electron mass and N is the electron number density.

Integrating equation (1), by assuming approximate constancy of the Coulomb logarithm $\ln \Omega$, gives the approximate ion range λ as:

$$\lambda \approx \mu E_i^2 / 4\pi N Z_i^2 e^4 M_i \ln\Omega = \Delta r. \qquad (2)$$

The specific energy deposition ε_d , obtained by assuming that most of the target mass is in the shell Δr, is:

$$\varepsilon_d = n N_i E_i / 4\pi r^2 \lambda \rho \approx \text{const.} , \qquad (3)$$

where N_i is the total number of ions of energy E_i in n beams entering and stopping in the spherical annulus in a pulse length Δt. For a current I in each beam, $N_i = I\Delta t / Z'_i e$, where Z'_i is the ion charge state in the beam. Putting $\rho \propto N$ and using equation (2) in equation (3) gives the following approximate scaling law:

$$n I M_i Z_i^2 \Delta r / r^2 E_i Z'_i \approx \text{const.} \qquad (4)$$

An enhanced M_i, for instance, could allow for a smaller beam intensity I or a larger neck radius r.

Among a number of additional and intriguing possibilities, CIB would permit direct drive through momentum directly imparted to a pure DT fuel hollow target.

This highlights the momentum rich beam (MRB) [2] concepts. One can thus expect a smoother compression with a lower energy threshold, of the order of 0.2-0.5 MJ requested for ignition. Maschke speculated [2] on an ~ 10 μsec pulse length, for a 100 kA/cm^2 Cs^+ beam, accelerated to few hundred keV. Obviously, CIB offer attractive and more flexible alternatives for achieving similar goals.

Fragmentation and stopping

An advantage of clusters with narrow mass distributions is that they can be accelerated in linacs and other multistage acceleration devices. Single-stage accelerators can be used with any distribution of masses, but are limited in the energy they can provide.

At Orsay, we are currently [5] investigating the possibility of accelerating from the terminal of a tandem accelerator Au clusters built on 2 up to 7 atoms, with a positive charge equal to 1 or 2.

The considered energy range will be $35 < E/A < 380$ keV. Another ion source aims at producing organic clusters containing several thousands of atoms with one positive charge per one thousand atomic mass. We thus expect to accelerate linearly clusters $A = 50000$ and $Z = 50$. Finally, it should be appreciated that the crucial fragmentation issues are simplified here by taking for granted the so-called maximum entropy principle (hereafter referred as MEP). This implies that the given cluster projectile will break under impact into the largest number of its smallest building blocks. Namely, the ionized atoms.

In most cases of interest, i.e., when the projectile kinetic energy per amu is larger than 10 keV, the stopping processes of cluster ions matter are likely to be preceded by a fragmentating event. Such an occurrence is highly dependent on the beam-target pair interaction.

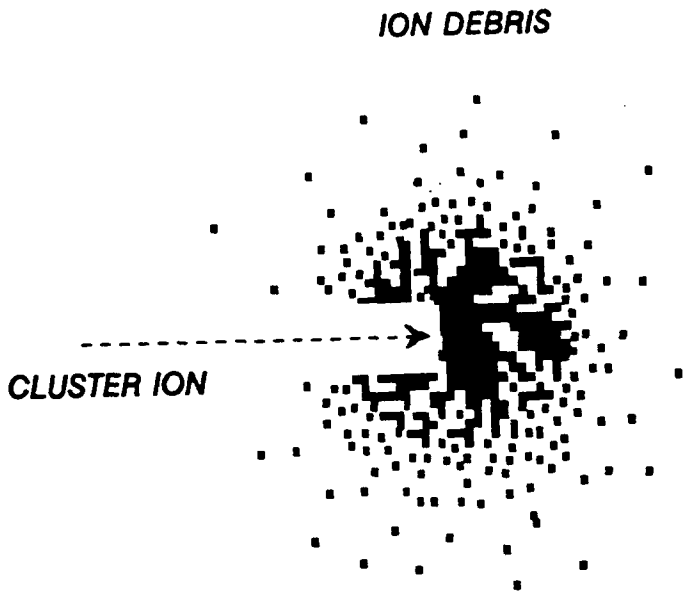

Fig. 1 - Cluster ion multifragmentation in Target

In the given energy range the cluster projectile is highly likely to experience a partial coulomb explosion. This means that the resulting debris will be at least once ionized. Moreover, their relative velocity is expected to be small compared to the projectile one over most of its quasi-linear range within the target. Therefore, these debris are expected to fly in a highly correlated motion with relative distances of order of a Bohr radius a_0 , as illustrated on Fig. 1.

The given Coulomb explosion takes place on a femto second scale length, which supports the MEP model.

Other fragmentation scenarios based essentially on combinatorial arguments might also be considered. However, they do retain as an exact asymptotic limit, the MEP scenario.

This corresponds to a sudden projectile-target interaction with a maximum produced disorder compatible with initial conditions.

A crucial simplification concerning the subsequent ranges calculations is afforded by the velocities ratio of the ion debris to the initial CIB one.

Two such debris, are expected to experience, at most, when located within a a.u. distance, a Coulomb repulsion ~ 1 Rydberg (13.6 eV). So, an initial CIB with a kinetic energy ~ a few tens of keV/a.m.u. will impart a nearly unchanged velocity to the resulting charged debris.

The repulsion velocity of the latter being nearly two orders of magnitude smaller than the initial CIB.

The target is likely to display a rather simple structure (Fig. 3a). It could be made essentially of roughly 4 mg of D+T fuel, surrounded by an outer/Li/shell of pusher material in close analogy with momentum reach beam (MRB) targets proposed recently [2],[8].
The main point we want to emphasize here is the flexibility introduced into the accelerator constraints by using CIB as heavy ion drivers.

Taking for instance, a given plausible CIB with $M_i = 50000$, $Z'_i = 50$ and $E_i/M_i \sim 10$ keV, we see from Eq. (1) that a complete fragmentation into ion debris with unit charge is equivalent to a standard direct drive (HIBALL) heavy ion beam (HIB), provided $nI \sim 10^7$ ampere.

As far as target compression is concerned, the present MRB concept introduces the possibility of a directly imposed external pressure (hammer effect) on the pellet.

Let us consider, for instance, $Au^+_{N_C}$ metallic clusters with $N_C = 2$-7, and assume that we have enough sources for bombarbing uniformly the target surface. This is quite feasible if each ion source is followed by a tandem like accelerating structure [2],[6].

Now, we turn to the most plausible CIB stopping scenario. The debris resulting from the cluster impact on pellet are expected to fly in a highly correlated relative motion. The given target are modeled presently by a fully degenerate electron jellium with a T = 0 Fermi temperature. Such a homogeneous medium is characterized by a dimensionless parameter $r_S = (\frac{4}{3}\pi\, n_e)^{-1/3}\, a_o^{-1}$, in terms of the electron number density n_e.

Then, we consider a given cloud of cluster ion debris in target, as a 2-body superposition. The stopping analysis then puts emphasis on the individual ion contribution, and on the correlated one, as well.

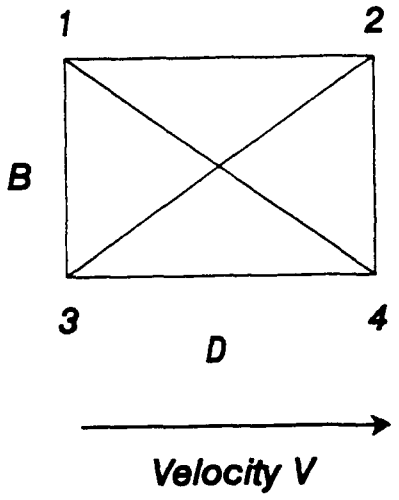

Fig. 2- 4-cluster stopping in jellium target

The latter is treated here as a superposition of dicluster contribution [9], [10], according to a model due to Basbas and Ritchie [7].

We start our analysis by considering a frozen (polarized) configuration of ion debris flying in target, closely to the initial CIB trajectory. This picture stems from the fragmentation scenario outlined, above.

Obviouly, many geometries can be taken into account. Fig. 2 thus features a polarized four-atom cluster structure with respect to its velocity in target.

Suitable structural averages allowing a more flexible description will be considered elsewhere.

Pellet compression

In terms of the projectile kinetic energy E, the ablation pressure thus reads as (Energy/volume)

$$P(100\ \text{Mbar}) = \frac{N_c^{1/3} \times E(\text{keV/a.m.u.}) \times 0.0565\ M_i}{R(\mu\text{m})} \quad , \qquad (5)$$

Huge pressures may indeed be achieved at reasonable projectile energies. The atom distribution within cluster is taken homogeneous in space.

We suppose a solid density of cluster material all around pellet.

The above stopping results allow for a one dimensional calculation of the direct drive compression for the target given in Fig. 4a. We thus use a three temperatures (ion, electron and radiation) code [9] to unravel the time evolution of several radial distributions for temperatures, matter density and pressure.

Thanks to the huge avalaible ablation pressure, the implosion is completed within 5 nsec. Such a behaviour it at variance with the 35 nsec duration of standard heavy ion scenarios. Above all, these calculations highlight the considerable potential interest of a dynamic tamper arising from synchronous clusters impact on pellet.

These latter do not behave solely as a driver bringing energy and momentum into target. They also provide radiative shielding and hydrodynamic tampering. Fig. 3c pertains to a mid-compression time evolution. The dissambly phase starts after 4.5 nsec.

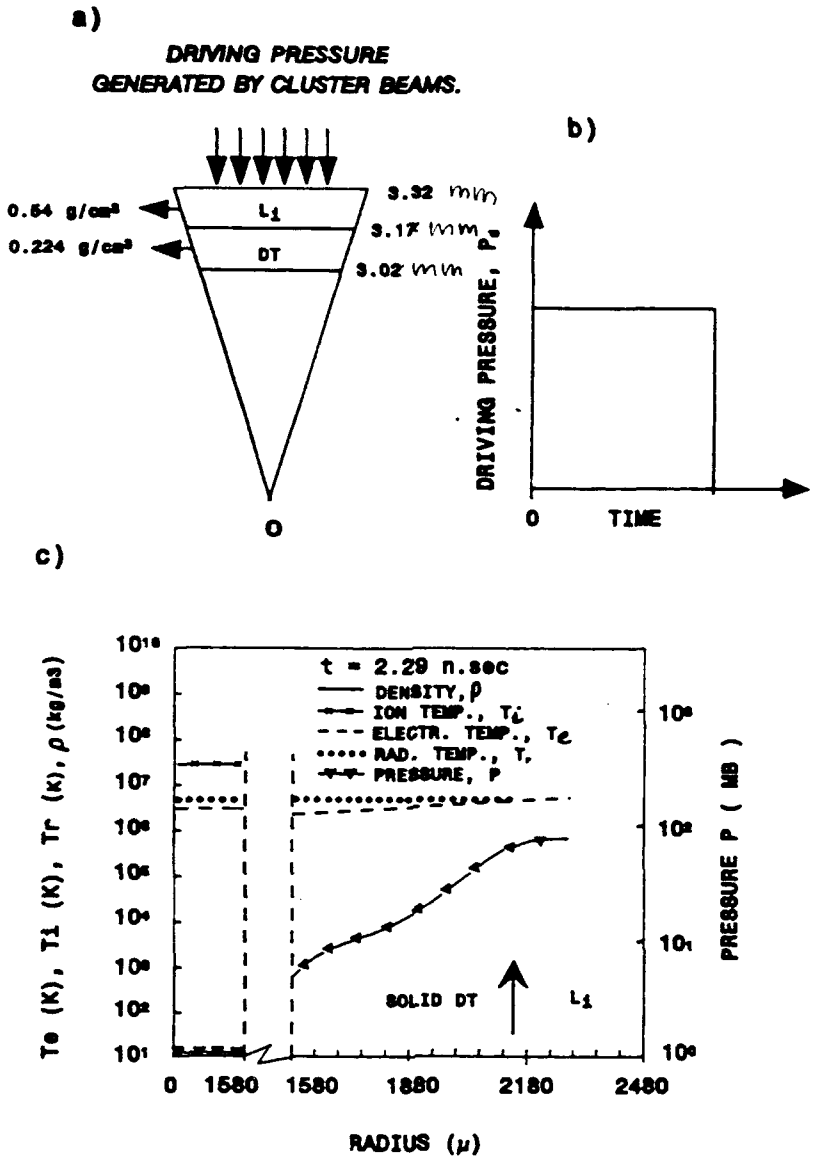

Fig. 3 - a/ Target initial conditions; b/ Time variation of input pressure pulse.
c/ Matter temperature, T; radiation temperature, Tr; density, ρ, and pressure P.
vs target radius at t = 2.29 nsec.

References

[1] F. WINTERBERG, *Z. Phys.* **A 296**, 3 (1980) and also
T. YABE and T. MOCHIZUKI, *Jpn. J. Appl. Phys.*, **22**, L262 (1983)

[2] A.W., MASCHKE, *Proceed HIF 84 (*INS-Tokyo) p. 168 (1984)

[3] M.A. DUNCAN and D.H. ROUVRAY, *Sci. Am.*, **261**, 60 (1989)

[4] T.D. BEYNON, *Phil. Trans. R. Soc. London*, **A 300**, 613 (1981)

[5] S. DELLA-NEGRA, D. GARDES and Y. LE BEYEC, Private communication.(1989) and
C. DEUTSCH, *Laser and Part. Beam* **8**, 541 (1990)

[6] D.C. WILSON and A.W. MASCHKE, LANL Preprint (1990) (unpublished)

[7] G. BASBAS. and RITCHIE, *Phys. Rev.*, **A25**, 1943 (1982)

[8] C. DEUTSCH, *Laser and Part. Beam* (1992) and
also *Trans. Am. Nucl. Sci* (1992)

[9] N.A. TAHIR, K.A. LONG and E.W. LAING, *J. Appl. Phys.*, **60**, 899 (1986)

AN ANALYSIS OF CLUSTER-DRIVEN INERTIAL CONFINEMENT FUSION

M. Piera*, S. Eliezer**, J.M. Martínez-Val
Instituto de Fusión Nuclear, UPM (Spain)
* Permanent address, ETSII (UNED) (Spain)
** Soreq N.R.C., Yavne (Israel)

1.- *Introduction*

Clusters of molecules (with a weight of some thousands atomic units) can be used as drivers for Intertial Confinement Fusion (ICF). Most of the work [1-5] carried out with cluster-induced fusion is however related to impact fusion,i.e., an approach where the clusters are made of deuterium-rich molecules in order to trigger fusions with the fusionable nuclei (D, tritium) of a target.

There are many sources of uncertainties in the analysis of cluster-target interaction. The stopping power affecting clusters lacks of an experimental evidence sound enough to build an accurate theory. Clusters break into pieces after collision, and the statistical distribution of the size and the charge of those pieces has not been established yet. Nevertheless, some estimates can be made by using Bohr-Bethe-Bloch cold model for the stopping power, but it is advisable in this case to include a free factor in the stopping power formula to be adjusted to sound experimental results. It seems [5] that hot pockets appear as a result of the cluster impact, which could explain the high fusion yield observed in some experiments[1,2]. This fact would imply that cluster ranges are very short, i.e., the energy deposition would affect to a very small amount of target mass.

In this paper, we present some energy balances to estimate the yield of impact fusion schemes, which do not follow the ICF idea. ICF schemes will also be presented. In the former, two beams (or some pairs of beamlets) of fusionable material would collide in order to transform their kinetic energy into internal energy. In the latter, some beams of clusters (not necessarily made of fusionable nuclei) impinge on a spherical target in order to drive an implosion of the inner part of the target, where the fusionable fuel is located.

After asessing the potentiality of impact fusion, some scenarios for cluster-driven ICF will be discussed. Although the lack of experimental data does not allow one to make accurate calculations, theoretical predictions point out that cluster-driven ICF must not be neglected as an alternative to laser-driven and ion-driven ICF.

2.- Regimes of collisons

Inelastic collisions of projectiles impinging on a target (and remaining embedded in it) depend mainly on the ratio of the projectile and target masses. Assuming the target is at rest in the laboratory frame, a balance of energy and momentum gives the following results for the energy converted into heat (internal energy) of the compound body (target plus projectile), E_h, and the kinectic energy of the compound body after the collision, E_k.

$$E_h = E_b \frac{M_t}{M_b + M_t} \qquad (1)$$

$$E_k = E_b \frac{M_b}{M_b + M_t} \tag{2}$$

where E_b is the beam (or projectile) kinetic energy (chemical and nuclear reactions are not considered in these equations) and M_b and M_t are the beam total mass and the target mass.

The kinetic energy E_k is associated to the momentum transfer, while E_h is associated to energy deposition. In standard approaches of ICF, both for laser and ion beams, the mass of the beam (or the momentum transfer) is negligible, and $E_k \ll E_h$. Thus, all the beam energy goes initially to internal energy of the outer part of the target (where the projectiles are stopped) and the rise in pressure and temperature launches a hydrodynamic reaction which drives the inner-target implosion.

For cluster driven ICF, specifications of the beam can be chosen so that M_b can be equal or even greater than M_t. In this case, the momentum transfer is the dominant mechanism, but the whole picture can be destroyed if the target breaks into pieces as a consequence of the crash.

3.- Cluster impact fusion

Any tipe of collision will have an internal structure and an internal time evolution, with strong pressure gradients which will accelerate further some part of the fuel. Nevertheless, if $M_b > M_t$, the scheme will not follow the guidelines of ICF, because most of the energy will remain as kinetic energy once the beam has impinged into the target. In this case, instead of using a hollow shell as in ICF, it seems better to produce the crash between fusionable materials. We can talk then of impact fusion. The ideal picture for this approach is a pair of clusters of equal mass, density and speed, colliding with opposite directions. As the center of mass will be always at rest, all the kinetic energy will be converted into heat for a short period, before the rapid disassembly of the compound body. Moreover, if the collision is not perfect, some parts of the clusters can break away in the collision, without converting into heat their kinetic energy. In any case, the existence of the compound body will be very short, because of the lack of tampering or any other means of confinement. Presuming this body is sphere-like with a radius R and a density ρ, the disassembly time t_d, will be

$$t_d \sim \frac{R}{c_s} \sim \frac{R}{\sqrt{P/\rho}} \tag{3}$$

P being the pressure inside the body, which can be estimated from the E.O.S (PV =NkT, for instance) and the energy conservation law. The latter can be expresed as follows for DT stechiometric beams.

$$E_b = 0.005 M_b v^2 = 120 M_b kT = E_h \tag{4}$$

where E_b and E_h (in MJ) are the clusters total energy and the (heat) internal energy of the body. M_b (mg) is the total clusters mass, v (in 10^7 cm/s) is the clusters speed and kT (keV) is the temperature after the crash (presuming electron-ion equilibrium, which is not applicable at first, because ions will initially be hotter, but is a conservative assumption).

The ideal picture of cluster impact fusion is that a sphere of M_b (mg) at a density (ρ) remains for a time t_d at a very high temperature (kT) so allowing the nuclei to undergo fusions. It is important to realize that the density will not be very large (the external pressure being zero) and the optical thickness will thus be small. For instance, for M_b =2mg, if the (cryogenic) solid density is assumed after the collision (0.2 g/cm^3), the radius will be 0.13 cm and the optical thickness 0.025 g/cm^2, i.e., much smaller than the alpha-particle range (~ 0.3 g/cm^2) which means that the fusion-born particle energy deposition inside the compound body will be negligible.

The total energy yield during the collision can be computed approximately by expressing the reactivity parameter <σv> as

$$\langle \sigma v \rangle = 10^{-17} \left(\frac{kT}{6}\right)^{4.5} \tag{5}$$

with kT in keV, an <σv> in cm^3/s. The expression is good enough between 4 and 12 keV, which is the main range of interest as ignition temperature. Eq. (4) provides a relation between kT and v. By combining the foregoing equations, an estimate for the fusion energy yield, Y, can be expressed as

$$Y = 1.1 \quad 10^{-11} v^8 M_b^{4/3} \rho^{2/3} \tag{6}$$

where Y is in MJ, v in 10^7 cm/s, M_b in mg and ρ in mg/cm^3. The energy gain G of the microexplosion is thus

$$G = \frac{Y}{E_b} = 2.2 \quad 10^{-9} v^6 M_b^{1/3} \rho^{2/3} \tag{7}$$

which shows a very strong dependence on v, and very small one on ρ and M_b. For M_b= 2mg and ρ= 200 mg/cm^3, the breakeven (G=1) is 1.5 x 10^8 cm/s, and a speed of 2.2 x 10^8 cm/s is needed to reach G=10.

It is important to notice that Eq. (6) has instrinsic limitations because we have not taken into account the fuel depletion due to burnup. On the other hand, Eq. (5) can overestimate the reactivity for very large v. It is obvious that Y (from Eq. (6)) must be checked with the maximum fusion yield (100% burnup) which is 335 M_b (in MJ, if M_b is in mg).

Theoretically speaking, the system could work, but it would need a very finely tuned collision and it would not benefitted from the energy feedback from the fusion-born partides.

4.- Cluster-driven ICF

Direct-drive by cluster beams can be analysed by the hot-rocket model, where the ablation zone includes the cluster energy deposition region plus the adjacent target material affected by the thermal wave moving inwards. An ablation pressure Pa is produced as a reaction to the rocket "exhaust" represented by the ablation process.

By applying the mass, momentum and energy conservation laws, and presuming a sonical flow ($v=C_s$) and ideal gas E.O. S. in the very hot ablated region (with kT of several tens, even hundreds KeV) an implosion efficiency is found which holds.

$$\eta_H = \frac{1}{2} \frac{M_p}{M_o - M_p} \ln^2\left(\frac{M_o}{M_p}\right) \tag{8}$$

where M_o is the initial mass of the target and M_p is the payload mass (fuel + pusher). This efficiency relates the kinetic energy of the payload at the end of the driving pulse to the beam energy (in this case $M_b \ll M_o$). The beam energy is

$$E_b = I.\tau \tag{9}$$

4.1. Cluster-driven ICF with momentum transfer

If M_b is not negligible as compared to M_t, momentum transfer must be taken into account into in the former analysis. Eq. (11) must be rewritten as

$$M_t \frac{dv_t}{dt} = P_a + \pi \tag{14}$$

where π is related to the energy flux (power per square unit) as follows

$$\frac{\pi}{I} = \frac{\sqrt{2me_o}}{e_o} = \frac{2}{v_o} = \alpha \tag{15}$$

α is almost zero for laser photons and heavy-ions (at GeV) but can be non-negligible for clusters of some MeV. In such a case, the hydrodynamic efficiency is (for $x = M_p/M_o$)

$$\eta_H = (1 + \frac{4C_s}{v_o})^2 \frac{x \ln^2 x}{2(1-x)} \tag{16}$$

which differs form Eq. (6) in the factor $(1+4C_s/v)^2$. Of course, this is only valid for v_o, and it represents an additional effect on accelerating the fuel (when $v_o \sim C_s$, the former analysis is not valid at all).

4.2. Numerical results

Uncertainties on the stopping power do not allow accurate calculations on this topic, but a parametric study was carried out. Most of the cases gave very poor results because the compressed fuel was stagnated (almost isothermal and at moderate density).

The main problem in the performance of these cases was the very high temperature of the ablator and the corresponding radiation losses. Table I shows the evolution of different kinds of energy and it is clearly seen that radiated energy reaches almost 50% of the absorbed energy. This estimate is possibly too high because radiation losses are calculated in a 2-temperature model, but it must be taken into account that the dose rate is about 300 TW/mg, i.e., two order of magnitude greater than in Heavy-ion driven targets. The coating suffers a total ablation during the implosion, which reaches outflowing speeds of 10^7 cm/s. Another paramount effect is DT prehating. The fuel becomes almost fully ionized before void closing, which hampers the final compression phase. The central temperature after void clusure reaches 1.5 KeV but the optical thickness is very low (lower than 0.1 g/cm^2) and the confinement time is very short.

If a thicker coating is used, the implosion performance is not better. The fuel speed remains moderate and the void closure happens very late. On the contrary, fuel speeds can be increased by decreasing the pusher thickness, but this case becomes too close to impact fusion, without a good performance.

5.- Conclusion and future work

Three regimes have been identified in this context: impact fusion; standar ICF, where energy deposition is the dominant driving mechanism; and an intermediate regime where momentum transfer can be almost as important as energy deposition.

It can be concluded that the intermediate Cluster-Driven regime does not show better results than Heavy-Ion ICF[6]. Although momentum transfer can be of some help in the fuel acceleration, the fuel preheating and the radiation losses are two main drawbacks.

Future work can be focused on the analysis of clusters accelerated to higher energies, i.e., approaching the concept of Heavy Ion Driving, with lower dose rates and thicker pushers. However, as the kinetic Energy per mass unit is increased, the importance of the momentum transfer decreases, and the standar model of ICF is obtained.

References

1. J.R. Beuhler, G. Friedlander and L. Fried man, *Phys. Rev. Lett.* **63**, 1292 (1989)
2. C. Carraro, B.Q. Chen, S. Schramm and S.E. Koonin, *Phys. Rev. A.*, **42**, 1379 (1990)
3. C. Deutsch, *Laser Part. Beams*, **8**, 541 (1990)
4. Y. K. Bae, D.C. Lorents, and C.E. Young, *Phys. Rev. A*, **44**, 4091 (1991)
5. Y. E. Kim, J.H. Yoon, R. A. Rice and M. Rabinowitz, *Phys. Rev. Lett.* **68**, 373 (1992)
6. G. Velarde, J.M. Martínez-Val et al., *Particle Acc.*, **37**, 537 (1992)

Table I.- Evolution of energy terms in a cluster-driven ICF case.

E ions= 5 MeV; DT mass= 0.1 mg; Li mass= 0.36 mg; DT A.R.= 100; E units= ergs.

t (ns)	Absorbed Energy	Radiated Energy	Ablation Energy	Kinetic Energy (Li)	Kinetic Energy (DT)	Internal Energy (Li)	Internal Energy (DT)
1 ns	0.214E+12	0.3776E+11	0.3288E+11	0.2554E+10	0.7724E+11	0.1143E+11	0.4893E+11
2 ns	0.4839E+12	0.1161E+12	0.1655E+11	0.2414E+11	0.2063E+12	0.1534E+11	0.9768E+11
3 ns	0.7473E+12	0.2584E+12	0.1521E+11	0.5804E+10	0.3593E+12	0.1408E+11	0.8431E+11
4 ns	0.9078E+12	0.3572E+12	0.3798E+11	0.2529E+10	0.4072E+12	0.1387E+11	0.7928E+11
5 ns	0.1055E+13	0.4620E+12	0.6574E+11	0.1492E+10	0.4283E+12	0.1324E+11	0.7640E+11
6 ns	0.1114E+13	0.5167E+12	0.8631E+11	0.8837E+09	0.4365E+12	0.6321E+10	0.6202E+11
7 ns	0.1114E+13	0.5189E+12	0.9608E+11	0.5409E+09	0.4367E+12	0.4229E+10	0.5326E+11
8 ns	0.1114E+13	0.5755E+12	0.1079E+12	0.3019E+09	0.2932E+12	0.1634E+11	0.1205E+12
9 ns	0.1114E+13	0.6444E+12	0.123E+12	0.1296E+09	0.2231E+12	0.1154E+11	0.1126E+12

Small-scale Targets for Heavy-ion Driven Inertial Confinement Fusion Experiments

J.M. Martínez-Val, G. Velarde, P. Velarde, M. Piera, J.M. Perlado, E. Mínguez, J.J. Honrubia, J.M. Aragonés
Institute of Nuclear Fusion,
Madrid Polytechnic University

ABSTRACT

Implosion regimes of small-scale targets directly driven by heavy ion beams are analyzed. Two main different performances are identified: the first one leading to high-density final states at moderate temperatures and short confinement times; the second one producing a hot spark limited to the very central zone of the fuel, the density and the optical thickness remaining very low. Transition between both regimes happens through stagnated compressed fuels where the compression efficiency is very poor.

1. Introduction

Some Review Panels [1,2] have identified Heavy Ions as the most suitable driver for Fusion Energy Production, if everything works as theoretically expected [3,4]. However, investments for accelerators for large scale experiments are so huge that intermediate steps seem necessary to ascertain some of the critical aspects of the HIF concept. This paper intends to be a contribution to analayze what type of experimental results could be found in those small-scale facilities. Some problems inherent to the accelerators and accelerated beams, as the illumination symmetry and the power balance, are not addressed here, although they are of primary importance for this concept.

The targets under study will be hollow shells of DT surrounded by a coating of a homogeneous material. Lithium has been shown [5] to be really suitable for this purpose. Its density is only 2.5 times that of cryogenic DT, which helps avoid hydro instabilities. Although multi-layered coatings seemed at first the best option [6], this type of simpler targets yield very good theoretical results [5] without big density jumps in the internal interfaces.

The initial fuel Aspect Ratio (AR) will be limited to 100, as it is usually chosen for high-gain targets. This means that the inner and outer fuel radii for a 0.1 mg DT shell will be 0.1553 and 0.1569 cm. This is much smaller than a large-scale fuel shell for a reactor scenario. If we consider a final imploding velocity of 4.10^7 cm/s, the internal void closure will take place at 7.5 ns approximately after the beginning of the driving pulse.

A simple square box has been taken as the pulse time shape. It has been shown in previous analysis that HIF target evolutions are not so sensitive to pulse shaping as laser-targets

are. This is due to the paramount difference in the size of the ablator in both cases. Laser targets only need about 1 mg to absorb the laser light, because the interaction is very shallow (up to the critical surface). On the contrary, heavy ions require a larger thickness to be stopped. Temperatures of the ablator in this case are lower than 100 eV, while they are higher than 1 keV in the electrons of the interacting plasma in laser-targets.

A numerical survey has been carried out in order to analyze the performance of the targets. The NORCLA code [7] has been used for this purpose. NORCLA is a one-dimensional, one-fluid, three-temperature thermo-hydrodynamic code developed for ICF target analysis. This code has been used for several analysis already published [6]. The global results (for instance, energy gain) agree quite well with the most reliable data available in the literature [8,9].

Equations of state and opacities are taken from the SESAME library [10]. It is worth underlining that NORCLA embodies a module to compute the energy deposition (and momentum transfer, almost of negligible importance with these beams) by the driving beam ions. The calculation takes into account the physical properties of the matter inside the target (T, ρ, ionization degree). Range shortening, produced by free electrons as ionization increases, is clearly observed in these simulations. The main source of uncertainty in relation to energy deposition is probably the effective ionization Zeff of the incoming ions after entering the target. In our calculation, it is presumed that Zeff corresponds to the equilibrium value [11].

2. High-density regimes

Maximum compressions can be obtained when the pressure maximum inside the target, generated by the driving energy deposition, is kept as close as possible to the fuel-coating interface. This situation corresponds to the pusherless implosion concept [12], and it has the obvious limitation that the fuel can be preheated if the pressure maximum (and the associated temperature maximum) become too close to the fuel. In our numerical survey, high-compression has been found when the fuel is uniformly accelerated in the absence of strong shock waves, with a moderate dose rate in the lithium so that the temperature is kept well below 100 eV.

Figure 1 shows a set of results corresponding to a case of high-density performance. The target was made of 0.1 mg of DT (AR=100) surrounded by 8 mg lithium. The driving pulse was a square box of 2.5 ns with 40 TW (i.e. a total pulse energy of 100 kJ). Ions energy was kept constant at 2.5 GeV. Initially, ions penetrated very close to the fuel-lithium interface, but the range was shortenned inmediately (~0.5 ns) and more than 1 mg of lithium acted as pusher (and preheating shield) for most of the implosion. Nevertheless, when the central void closed, the coating had been ablated almost completely. This can be seen clearly in figure 1, in the steep gradient of the density (the fuel occupy the 20 innermost meshpoints, the rest being lithium).

It is important to emphasize that the fuel evolves at very high pressures from the very beginning of the implosion (above 10 Mbars before void closure). This is characteristic of the high-density performance.

3. High-temperature regimes

A totally different regime can be produced by shock acceleration of the fuel in order to set it in very high adiabats along the expansion process which takes places as the fuel flies toward the void center. This effect can be obtained by producing very steep gradients of

pressure inside the target as a consequence of a high dose rate in what can be called the active region of the ablator. This region can not be very close to the fuel-coating interface in this case to avoid fuel preheating. Moreover, it is interesting to keep the fuel at low pressures (much lower than 1 Mbar, i.e. 10^{11} Pa). Figure 2 shows the results of a case driven by 100 kJ (2.5 ns) of 1.9 GeV Bi^{+} ions. The only difference with the previous cases of high-compression targets is that we use here a thicker coating of lithium, as compared to the ion penetration, for the sake of generating a large difference of pressure between the fuel and the active part of the coating. It can be said that the fuel remains here during the first part of the implosion at 10^{10} Pa (0.1 Mbar), which is two orders of magnitude lower than the fuel pressure in the high-compression cases described in the previous section.

Shocks waves, coming from the very high pressure zone (or active zone of the ablator), accelerate the fuel, where the speed profile is also very steep, as happens when the acceleration is associated with large pressure gradients.

The final stage of the fuel shows a large temperature jump in the central zone as the fuel stops, but such a maximum does not disappears very fast because the rest of the fuel and the pusher still carry large amounts of kinetic energy, so mainaining the confinement of the central zone. The electron temperature remains always lower than the ion temperature in the innermost part of the fuel, and the electron temperature profile is very flat across the fuel. It must be recognized that the situation is very critical from the point of view of hydrodynamic stability because of the pressure and density gradients in the compressed fuel and in the inner, overdense coating.

It is worth underlining that this scheme produces fuel internal energy efficiencies much lower than the high-density regime analyzed in the previous section. Instead of 10%, values about 5% are obtained here, which can be understood because a significant part of the energy goes to pusher kinetic energy and only a fraction of it contributes to the compression of the fuel.

The fusion energy yield of this case is less than 1 kJ. Fusion power is only important in the innermost meshpoint of the fuel and is totally negligible in 80% of the fuel. It must be pointed out that the central part of the fuel remains hot for a very long time (more than 1 ns). The maximum central temperature was reached at 7.3 ns, and it was 16.5 keV. At that time, the fuel optical thickness was only 0.007 g/cm^2 which means that even the fusion-born alpha particles escape from the fuel.

The aforementioned value of 1 kJ of energy yield must be questioned from the point of view of hydrodynamic stability. In the pure one-dimensional case, the central hot-spark is maintained for 1 ns, which is a time long enough for shock-waves to travel across the fuel. Destructives instabilities can then develop within the fuel and in the fuel-coating interface, so destroying the confinement. The actual yield could thus be somewhat lower than the theoretical prediction, as has already been observed in some laser driven fusion experiments [13].

4. Conclusions

Two different regimes of target performance have been identified in this analysis. The first one is related to the so-called pusherless implosion scheme, were the ion energy and the beam power are selected to reach an almost total ablation of the coating at the end of the compression process. The pressure level inside the fuel is very high along the compression phase

(over 10 Mbars). This scheme leads to very high densities (higher than 1000 times the liquid density) but the fuel temperature is moderate (below 1 keV) and the fuel is fairly isothermal. The confinement time is very short (about 100 ps) because of the lack of effective pusher at the moment of maximum compression.

A totally different regime is obtained when the pusher thickness is large (as compared to the fuel optical thickness) and a region of very high pressure is generated as a consequence of very high dose rates in the ablator. The fuel is maintained then at a relatively low pressure, the pressure gradient being very steep, and so being the speed gradient within the fuel, which expands towards the center and reaches very high adiabats (at very low densities). A central hot spot is formed after void closure, the central ion temperature being over 10 keV. The confinement time is very large (about 1 ns) because the kinetic energy of the pusher keeps acting on the fuel. Compression histories to produce this high-temperature regime must be finely tuned. Should the ion energy is made too small or too big around the right value, the central hot spot is barely produced.

There is not a sharp transient from a regime to the other. In between, there is a broad range of target and beam specifications where a low-efficiency compression is obtained. In these cases, neither the temperature nor the density reach high values. The speed profile of the fuel after the acceleration phase is not as uniform as in the high-compression regime, and this leads to a stagnated final state with the fuel almost isothermilized and an optical thickness much lower than those of the afore-mentioned regime.

Acknowledgements

This work has been done thanks to a PIE Research Contract (Spain).

References

[1] Final Report, Fusion Power Advisory Committee DOE, United States of America (September 1990).

[2] Review of the Department of Energy's Inertial confinement Fusion Program Interim Report, National Academy of Sciences, Washington, (January 1990).

[3] Bangerter, R.O., Herrmansfeldt, W.B., Judd., D.L. (Eds.) ERDA Study of Heavy Ions for Inertial Fusion, Lawrence Berkeley Lab. Rep. LBL-5543 (1976).

[4] Velarde, G. et al., *Nucl. Instr. Meth. in Phys. Research*, **A278** (1989) 105.

[5] Velarde, G., Martínez-Val, J.M., Piera, M., Aragonés, J.M., Honrubia, J.J., Mínguez, E., Perlado, J.M., Velarde, P.M., *Particle Accelerators* (COMPLETAR).

[6] Velarde, G. et al., *Laser and Particle Beams*, **4** (1986) 349.

[7] Velarde, G., Aragonés, J.M., Honrubia, J.J., Martínez-Val, J.M., Mínguez, E., Perlado, J.M., *Laser Part. Beams*, **7** (1989) 305.

[8] Bangerter, R.O., *Fusion Technol.*, **13** (1988) 348.
[9] Lindl, J.D., Mark, J.W.K., *Laser Part. Beams*, **3** (1985) 37.
[10] Cooper, N.G., Ed., Los Alamos National Laboratory Report LALP-83-4 (1983).
[11] Deutsch, C. et al., *Fusion Tech.*, **13** (1988) 362.
[12] Mima, K., Takabe, H. Nakai, S., *Laser Part. Beams*, 7 (1989) 249.
[13] Bayer, C. et al., *Nuclear Fusion*, **24** (1984) 573.

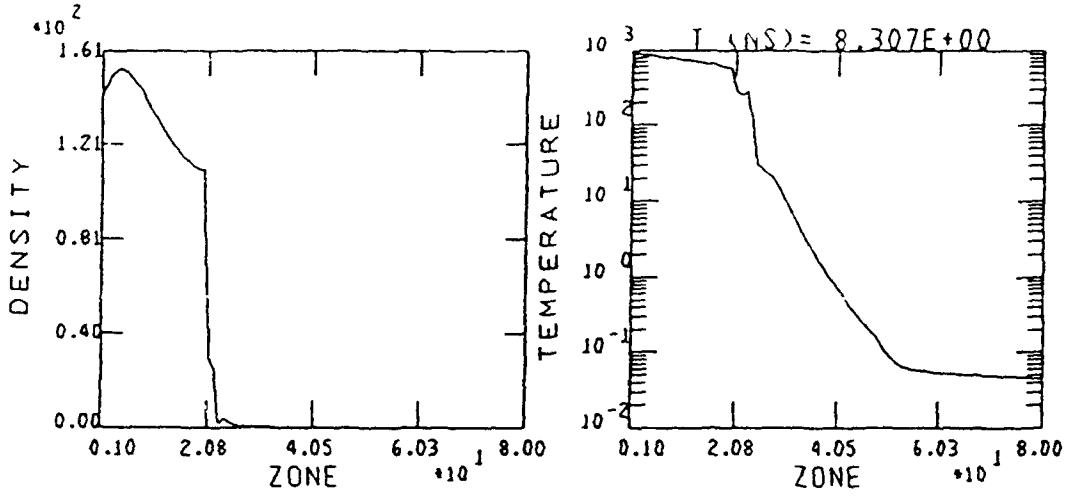

Fig.1.- Density and temperature profiles at maximum compression in a high-density case (Fuel zones: 1-20; Coating: 21-80).

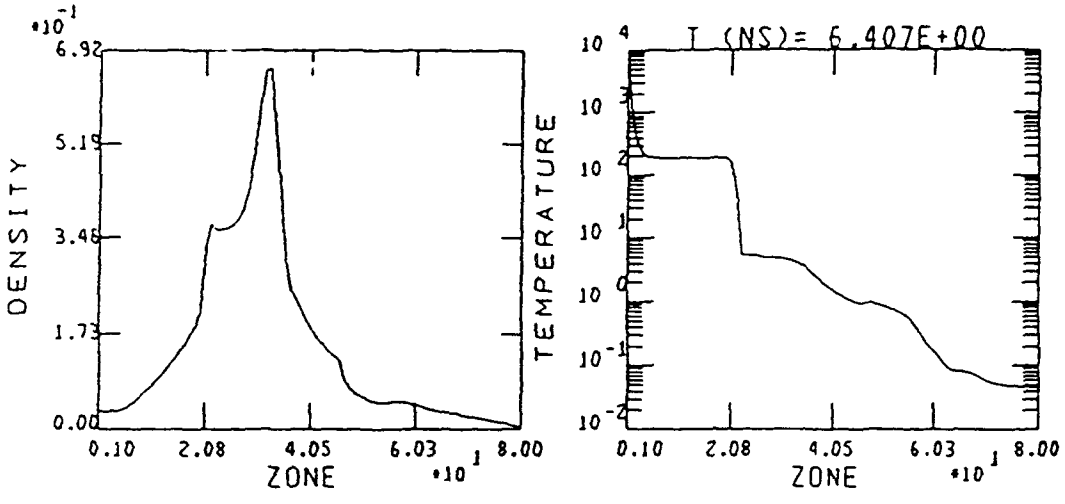

Fig.2.- Density and temperature profiles at maximum central temperature in a high-T case (same mesh-zones as in fig. 1).

Contributed Electron Beam Papers

THEORETICAL EVALUATION OF THE ANGULAR SPREAD OF THE ELECTRON BEAM GENERATED IN A GUIDING MAGNETIC FIELD

D.D.Ryutov

Budker Institute of Nuclear Physics, Novosibirsk, Russia

Electron beams generated in high-current diodes with a guiding magnetic field are of interest for a number of applications and, in particular, for plasma heating in solenoids, for microwave generation, and for further acceleration in inductive linacs. The paper considers possible sources of a finite angular spread of the beam for the case when electron gyroradius is much smaller than all the characteristic dimensions of the diode. Under such conditions, there are three major sources of the beam angular spread (besides the scattering in the anode foil, if such a foil is present): i)non-adiabatic effects near the cathode surface, especially if there is some ripple on the emitting surface;ii)non-adiabatic effects near the anode foil (if it is present); iii)a possible presence of irregular electric and magnetic fields produced by beamlets emitted by microspikes at the cathode surface. Efficient analytic formulas are presented that allow to evaluate the resulting beam angular spread both for purely electron and bipolar flows.

1.Introduction

One of the most important characteristics of the electron beams generated in a guiding magnetic field, is their angular spread after leaving the diode region. This parameter has a considerable influence on the process of microwave generation; it determines a possible degree of beam compression by magnetic funneling (see, e.g.[1]); it strongly affects beam-plasma interaction in plasma heating experiments. To make the angular spread small enough, one can suppress the transverse electron motion by raising the guiding magnetic field to the level when electron gyroradius r_e becomes smaller than characteristic size of the accelerating gap a:

$$r_e \ll a \qquad (1)$$

By r_e we understand the gyroradius corresponding to the full accelerating voltage. We assume that the angular spread introduced by the anode foil (if such a foil is present) is negligibly small. If condition (1) is satisfied, the electron motion across the magnetic field can be described as a superposition of the drift motion and gyration; the latter is just the effect that we should study.

For the slowly varying magnetic and electric fields,the amplitude

of gyromotion is determined from the conservation of the adiabatic invariant $p_\perp^2/B$. Then, neglecting the initial electron energy spread at the cathode, i.e., putting $p_{\perp 0}, p_{\parallel 0} = 0$, we conclude that, for adiabatically varying magnetic and electric field, no gyromotion should be excited. Therefore, when the condition (1) holds, the only source of angular scatter is the non-adiabaticity of electron motion arising in the regions where - for one or another reason - there occur sharp changes of the electric or self magnetic field (we remind that the guiding magnetic field is assumed to be smooth).

We show that such rapid changes occur near the cathode and anode surfaces and find the corresponding contributions to the electron gyromotion. Nonadiabatic effects can also manifest themselves in the accelerating gap - if the beam current has microinhomogeneities with the scale comparable with or smaller than r_e (in principle, such a microstructure can be produced by the nonuniformities in electron emission)

2. Cathode phenomena

Generally speaking, cathode surface is not orthogonal to the magnetic field lines in the intersection points. The angle α between the normal $\mathbf{n}$ to the surface and magnetic field $\mathbf{B}$ is determined by the shape of the cathode surface (or, more generally, of the emitting surface, if cathode plasma is present) and by the self magnetic field $\mathbf{B}_s$ (even if the guiding magnetic field is orthogonal to the emitting surface, the presence of $\mathbf{B}_s$ makes α finite).

Let's consider a small (and, therefore, almost planar) element of the emitting surface (Fig.1). The z-axis is directed along the magnetic field, and y-axis is perpendicular to the $(\mathbf{n},\mathbf{B})$ plane. The angle α is not necessarily small. The tangential component of the electric field is zero at the surface; the only component that may considerably differ from zero in the vicinity of the surface, is a normal one. In the vicinity of the surface, space-charge density and electric field depend only on the distance ζ to the surface.

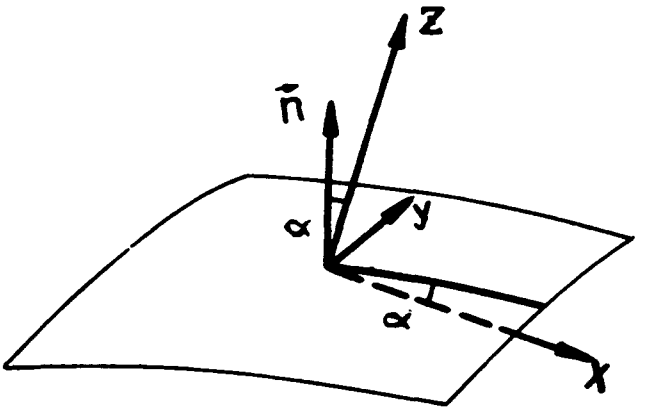

Fig.1

After electron starts at zero velocity at the cathode surface, it first accelerates along the electric field and thus acquires some gyro-velocity transverse to the magnetic field. After, roughly speaking, one turn around the field line, the motion becomes adiabatic, with rotational velocity determined by the initial

phases of the motion. To solve the problem quantitatively, we consider electron equations of motion:

$$\begin{aligned} m\ddot{x} &= eE\sin\alpha - \frac{e}{c}\dot{y}B \\ m\ddot{y} &= \frac{e}{c}\dot{x}B \\ m\ddot{z} &= -eE\cos\alpha \end{aligned} \tag{2}$$

(E denotes the normal component of the electric field). At first glance, the analytic solution of the system (2) is a hopeless problem, as electric field is a function of coordinates and should be determined self-consistently, with the account of the effect of magnetic field on the electron motion. However, using the approach described in [2], it turns out to be possible to find a very simple analytic result. Following [2], we note that the spatial dependence of E obeys the Poisson equation

$$\frac{dE}{d\zeta} = 4\pi\rho \tag{3}$$

On the other hand, the full time-derivative of the electric field along the electron trajectory is:

$$\frac{dE}{dt} = v_\zeta \frac{dE}{d\zeta} \tag{4}$$

Combining (3) and (4) and noting that the absolute value of the electron current density is $j \equiv - v_\zeta \rho$ and *doesn't depend on* ζ (as we are considering a stationary problem), we conclude that the time derivative (4) of the electric field along the electron trajectory *doesn't depend on time*:

$$\frac{dE}{dt} = - 4\pi j = const \tag{5}$$

Then, considering a motion of the particular electron and counting the time from the moment when it leaves the emitting surface, we find that

$$E = E_c - 4\pi j t \tag{6}$$

With this explicit dependence of E on time, it is quite easy to integrate the system (2):

$$\begin{aligned} \dot{x} &= \sin\alpha \left(\frac{c\dot{E}}{\omega B} + \frac{4\pi j c}{\omega B}\cos\omega t + \frac{cE_c}{B}\sin\omega t\right) \\ \dot{y} &= \sin\alpha \left(\frac{cE}{B} + \frac{4\pi j c}{\omega B}\sin\omega t - \frac{cE_c}{B}\cos\omega t\right) \end{aligned} \tag{7}$$

where $\omega = eB/mc$ is the electron gyrofrequency for nonrelativistic electrons (relativistic effects in the vicinity of cathode should be taken into account only at very high accelerating voltages; the corresponding generalization is straightforward but takes much space). The first term in the expression for $\dot{y}$ describes electric drift, the first term in the expression for $\dot{x}$ describes inertial drift. As for the oscillating terms, they describe electron gyration, with corresponding transverse momentum determined by

$$p_\perp^2 = m^2c^2\sin^2\alpha \,(E_*^2 + E_c^2)/B^2 \tag{8}$$

where

$$E_* = \frac{4\pi j}{\omega} \tag{9}$$

Note, that the transverse momentum determined from (9), changes along the cathode surface, because of changes in the entering parameters.

If the the cathode can provide infinite emission, then the current density is determined by the space-charge effects, and E_c should be taken to be zero. As a rough estimate of j, one can use then the following expression:

$$j \sim j_0 \equiv \frac{mc^3(\gamma^{2/3} - 1)^{3/2}}{4\pi e a^2} \tag{10}$$

(which gives a correct scaling with γ both at nonrelativistic and strongly relativistic energies). Then, together with Eqs.(8), (9) (and formula $p=mc(\gamma^2-1)^{1/2}$ for the final momentum of electrons), we obtain the following estimate for the cathode contribution to the angular spread:

$$\vartheta \sim (r_e/\gamma a)^2 \sin\alpha \tag{11}$$

where r_e is the electron gyroradius calculated for the full acceleration energy (the estimate (11) gives correct scalings with γ for $\gamma-1 \ll 1$ and $\gamma \gg 1$).

In the opposite case of a limited emission, $j \ll j_0$, which can be realized at the initial stages of the beam pulse, we can neglect E_* as compared to E_c in (8) and use the estimate $E_c \sim (\gamma-1)mc^2/ea$. Then we arrive with the following expression for ϑ:

$$\vartheta \sim (r_e/\gamma a)\sin\alpha \tag{12}$$

Clearly, in the case of the space-charge limited current the angular spread is smaller.

3. Anode phenomena

In case of a purely electron flow, the normal component of the electric field on the anode is non-zero and can be estimated as $E_A \sim (\gamma-1)mc^2/ea$. Electric and self magnetic field beyond the anode foil depend on the conditions of charge and current neutralization. Discontinuity of the electric field on the anode foil is one source of nonadiabaticity; the other is a break in the pitch of magnetic field lines, existing if the current neutralization in the external space is present. The latter source converts part of the longitudinal electron velocity in the diode to the gyromotion [3].

It can be shown that the resulting gyrovelocity is approximately equal to

$$v_\perp = \left| \frac{1}{c}[\mathbf{E}_A^{(-)} \times \mathbf{B}_A^{(-)}] - \frac{1}{c}[\mathbf{E}_A^{(+)} \times \mathbf{B}_A^{(+)}] + v_\parallel \frac{\mathbf{B}_s^{(-)} - \mathbf{B}_s^{(+)}}{B_{An}} \right| \tag{13}$$

The superscripts "-" and "+" refer to the inner and outer side of

the anode foil. In a way similar to the one used for derivation of Eq.(12), one can write the following estimate for the resulting pitch-angle of the electrons (valid for $\gamma-1 \ll 1$ and $\gamma \gg 1$):

$$\vartheta \sim (r_e/a)\, \sin\alpha + \eta B_s/B \qquad (14)$$

where η is degree of current neutralization beyond the anode foil. Note that the first term is γ times larger than (12).

The anode angular spread is considerably reduced in the case when the following conditions are satisfied: i)there is no current neutralization in the drift space, but there is charge neutralization there; ii)the inner surface of anode foil is an infinite source of ions, so that space-charge limited bipolar flow is established in the diode. As was shown in paper [4], such conditions can indeed be realized experimentally. Then, all three terms in Eq.(13) vanish, and more delicate effects, similar to the one discussed in conjunction with Eqs.(6), become important.

Near the anode situation is somewhat simpler for the analytic consideration, as the potential distribution is entirely determined by the ions, whose motion isn't affected by the magnetic field. Respectively, using again the coordinate system shown in Fig.1 (but now attached to the anode), one can write the following expressions for x component of the electric field in the vicinity of anode:

$$E_x = -E_0 (\zeta/a)^{1/3} \sin\alpha; \qquad (15)$$
$$E_0 = \frac{4}{3}\,(9\pi j_i)^{2/3} (Ma/2e)^{1/3} \sim (mc^2/ea)(\gamma^{1/2} - 1)$$

where $\zeta = z\cos\alpha$ is a distance from the anode surface, j_i is the ion current density, M is the ion mass and the last order-of-magnitude estimate is, again, an interpolation between $\gamma-1 \ll 1$ and $\gamma \gg 1$ cases.

Electron motion along the magnetic field line near anode can be considered as occurring with a constant velocity (determined by a full accelerating voltage). Then, if one counts the time from the moment when electron intersects the anode surface, the following equations determine evolution of transverse momentum:

$$\dot{p}_x = -eE_x(t) - \frac{\omega}{\gamma}\, p_y$$
$$\dot{p}_y = \frac{\omega}{\gamma}\, p_x \qquad (16)$$

where $E_x(t)$ is determined by Eq.(15) with $z = ct\,(1-\gamma^{-2})^{1/2}$. For convenience, we revert time.

To more clearly distinguish the anode contribution to the angular spread, we assume that, when approaching the anode, electrons do not have any gyrovelocity and participate only in the drift motion. The solution of system (16) satisfying this condition, is straightforward and gives the following expression for the momentum $p_\perp$ of the gyromotion at the foil:

$$p_\perp = \frac{1}{3}\,\Gamma\!\left(\frac{1}{3}\right) \frac{\gamma e E_0}{\omega} \left(\frac{c(\gamma^2-1)^{1/2}}{a\omega}\cos\alpha\right)^{1/3} \sin\alpha \qquad (17)$$

where $\Gamma(\frac{1}{3}) \approx 2,68$. The corresponding order-of-magnitude estimate for the resulting angular spread is:

$$\vartheta \sim \gamma^{-1/2}(r_e/a)^{4/3}\cos\alpha^{1/3}\sin\alpha \qquad (18)$$

4. The role of beam microstructure

We assume the model in which electron current has a microstructure of the form $\delta j(x,y)$. The corresponding space-charge density perturbation is $\delta\rho = \delta j(x,y)/v_z(z)$. The presence of beam microstructure results in the formation of small-scale transverse electric and magnetic fields which deflect beam electrons. To save space, we consider only nonrelativistic space when magnetic perturbations can be neglected. The potential perturbations $\delta\varphi$ should be determined from the Poisson equation. Using Fourier transform in x,y plane, we find for the Fourier harmonics:

$$\frac{d^2}{dz^2}\delta\varphi_{\mathbf{k}} - k^2\delta\varphi_{\mathbf{k}} = -\frac{4\pi}{v_z(z)}\delta j_{\mathbf{k}} \qquad (19)$$

As we assume that the perturbations are small-scale, $ka \gg 1$, we can neglect z-derivative in the l.h.s. and thus obtain:

$$\mathbf{E}_{\mathbf{k}} = \frac{4\pi i\mathbf{k}}{k^2 v_z(z)}\delta j_{\mathbf{k}} \qquad (20)$$

This approximation breaks at the distance $\sim k^{-1}$ from the electrodes (at their surface $\delta\varphi$ must vanish). Introducing this electric field into equations of motion and integrating them, we find that the transverse velocity perturbation is formally formally diverging at small z:

$$\mathbf{v}_\perp \sim \int \mathbf{E}_{\mathbf{k}}\,dz/v_z \sim \int dz/v_z^2 \qquad (21)$$

The cut-off limit should obviously be taken to be of order of k^{-1}. In this way we obtain the following expression for the velocity perturbation caused by fluctuations with a given $\mathbf{k}$:

$$\frac{v_\perp}{v} \sim \frac{\delta j_{\mathbf{k}}}{j}(ka)^{-2/3} \qquad (22)$$

One sees that the contribution from the smaller k's is emphasized. The smallest possible k for which (22) is still valid is determined by transition to adiabatic motion that occurs at $ka < (a/r_e)^3$.

References

1. D.D.Ryutov. Proc. of the 7th Intern. Conf. on High-Power Particle Beams, KfK Karlsruhe, July 4-8, 1988, v.1, p.208.
2. D.D.Ryutov. Report 83-146, Institute of Nuclear Physics, Novosibirsk, 1983 (unpublished).
3. A.V.Arzhannikov *et al.* Plasma Physics and Controlled Nuclear Fusion Research, Vienna, 1979, Vol.2, p.623.
4. S.G.Voropaev *et al.* Proc. 18 Intern. Conf. on Phenomena in Ionized Gases, Swansea, U.K.,1987.

NEW RESULTS ON MICROSECOND E-BEAM GENERATION FOR PLASMA HEATING EXPERIMENTS.

Yu.I. Deulin, V.V. Filippov, A.V. Karyukin, S.V. Lebedev, M.A. Shcheglov, S.G. Voropaev

Budker Nuclear Physics Institute, Siberian Division of Russia Science Academy, Novosibirsk 630090, Russia

Abstract. New results on microsecond electron beam generation on the U-3 accelerator for plasma heating experiments at the GOL-3 device are presented. The electron beam is generated in the vacuum diode and the plasma filled diode and 20-fold focused in a mirror magnetic field. The energy spectrum of beam electrons was measured by magnetic analyzer and the broadening of spectrum width was observed in the experiments on dense ($n \sim 5.10^{15}$ cm^{-3}) plasma heating. The annular structure of the beam in the beginning of pulse was detected and possible reasons are discussed. First results of experiments on beam generation in the plasma filled diode are presented.

Introduction.

In the Budker Nuclear Physics Institute experiments are carried out on dense plasma heating by microsecond relativistic electron beams (REB) in solenoids.[1)] Electron beams with 10 kA/cm^2 current density are required for these experiments. Such a current density of a microsecond beam can be provided by magnetic compression, in case the angular spread of the beam is small.[2)] In the experiments on plasma heating such beam are mainly generated in a diode with a quasiplanar cathode and an anode foil with subsequent compression. To match a high-voltage generator impedance with the diode one and to increase the pulse duration a uniform beam is generated with low current density ~0.3 kA/cm^2 and a cathode radius of 10 cm. In such conditions compression coefficient of the electron beam should be about twenty. Along with compression the beam space charge neutralization must be provided between the anode foil and the mirror or in the transport channel, in case of foilless diode. Another condition for successful beam compression is a small angular spread of the beam. The pitch-angle of the beam electrons must not exceed θmin — 0.2. [3)]

On the GOL-3 device the beam is compressed in the mirror magnetic field of 0.6 T in the diode and 12 T in the mirrors. Schematic of the experiments on the uniform beam compression is given in Fig.1. The gas pressure in the region of beam compression was fitted so as to provide only the beam space charge neutralization and not the current one.

In the plasma heating experiments the graphite cathodes with the ~ 20 cm diameter at the anode-cathode gap of 8 cm was used. The diode voltage produced by the high-voltage generator in the beginning of pulse is 1 MV [4)]. The capacity of the generator is 0.4 μF.

The experiments on beam compression showed that the beam current through the chamber exceeds the vacuum current (calculated current ~10 kA) practically from the very beginning of the pulse, that testifies to the fast neutralization of the beam space charge. The rate of ion production by strike of the beam electrons is not sufficient because of the small density of the background gas (~10^{-4} Torr). The most probable source of neutralizing ions is the anode

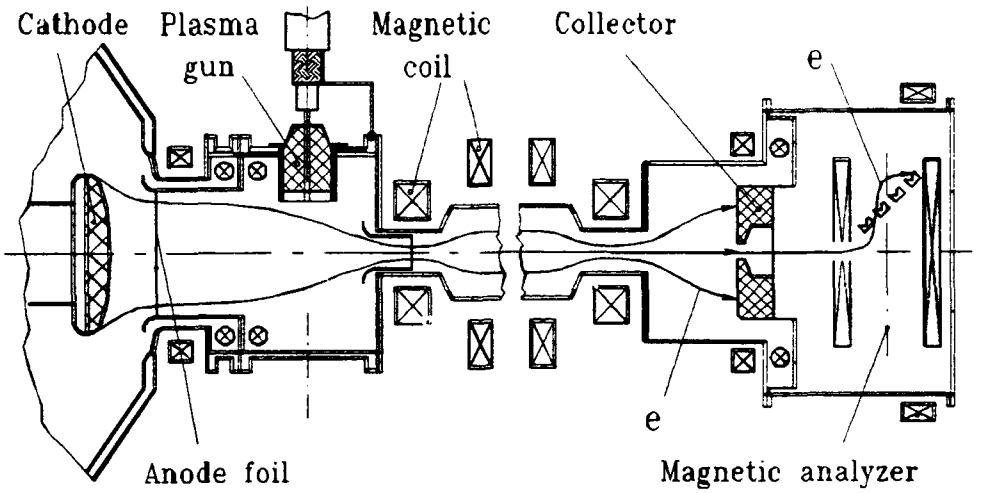

Fig.1. Schematic of experimental device

foil.[5] The delay of appearance of the electron current behind the system of compression (50-100 ns) indicates the formation of a virtual cathode in the compression chamber. The oscillating electrons penetrating through the anode foil lose their energy and heat the foil. (Absorption of 1% of the electrons is sufficient for melting the foil.) The desorbed gas cloud formed near the foil can be ionized in the field of the beam space charge. The ions emitted from the plasma cloud can compensate rapidly (< 50 ns) the beam space charge. After that the ion background with density proportional to the beam space charge is formed in the compression chamber.

At the same time on the foil surface facing the diode a plasma cloud expanding into the diode gap is formed, from where ions are emitted to the cathode.

Planar diode.

1. Beam energy spectrum.

One of the most important characteristics of high-current magnetized REB is the energy spectrum, i.e. the instantaneous distribution of the beam electrons in energy. Registration of the energy spectrum of the beam injected into the plasma and running out of the system is the most direct method of measurement of the beam-plasma interaction efficiency.

For this purpose a magnetic analyzer of beam energy spectrum has been designed and measurements were carried out at the exit from the diode and after the interaction with plasma. The central part of the beam passed through the hole in the exit collector of the GOL-3 device was used for analysis. A magnetic field with sharp boundary, transverse to the main field was created in the analyzer. In the resultant magnetic field the electrons of different energy are separated according to the length an electron pass moving along the helicoidal trajectory after one turn around the axis (the Larmor spiral pitch) and absorbed by different collectors. Detailed description of the analyzer is given in [6]

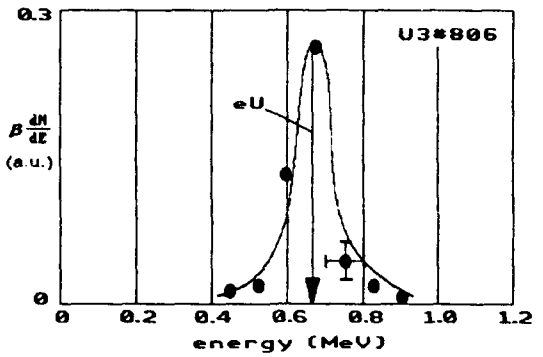

Fig.2. Electron energy spectrum in diode.

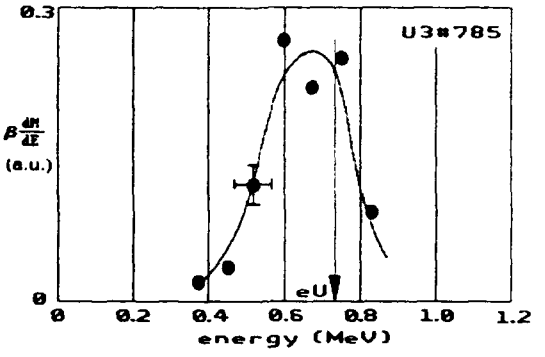

Fig.3. Electron energy spectrum after transportation through the dense plasma.

Instantaneous energy spectrum width of the beam generated in the accelerator diode was obtained in calibration experiments. In these experiments a graphite collector with a 2 cm central hole was installed instead of the anode foil. The central part of the beam of 300 A current was compressed in the mirror, passed through the solenoid and finally came to the analyzer. The current value was essentially less than that of vacuum current (pressure in the transport region 10^{-4} Torr). The experiments showed that the spectrum width does not exceed the calculated resolution of the analyzer (10%, see Fig. 2).

For beam transportation through the dense plasma ($n \sim 5\ 10^{15}$ cm^{-3}), when the beam-plasma interaction can be considered negligible, the beam spectrum is relatively narrow, however some broadening was observed (see Fig.3). The spectrum width in this case is 20% and two-fold exceeds the analyzer resolution.

In conditions of effective plasma heating , i.e. at $n < 2\ 10^{15}$ cm^{-3}, the essential broadening of the beam spectrum ($dE/E \sim 1$) takes place. Typical spectra at conditions optimum for plasma heating and corresponding efficiency of the beam-plasma interaction are presented in [7].

2. The spatial distribution of the beam current.

For the beam generation in the accelerator diode the macrouniformity can be provided by fitting the diode geometry.[8] In experiments on magnetic compression carried out on the U-1 device it was shown that the spatial distribution of the beam current after compression remains uniform and close to that in the diode at various conditions. Similar picture was observed for transportation of the compressed beam through a gas or plasma of 1 m length.[9]

Along with that, in the experiments on plasma heating by the microsecond REB on the GOL-3 device, when the beam is transported at a 7 m distance, the evidence of essential changes of the current distribution at the exit of solenoid was observed already during the first "shots". For more detailed study of the phenomenon the measurements have been carried out of the current spatial distribution by an X-ray image converter (IC). This diagnostics can be also used for other applications in the plasma heating experiments.

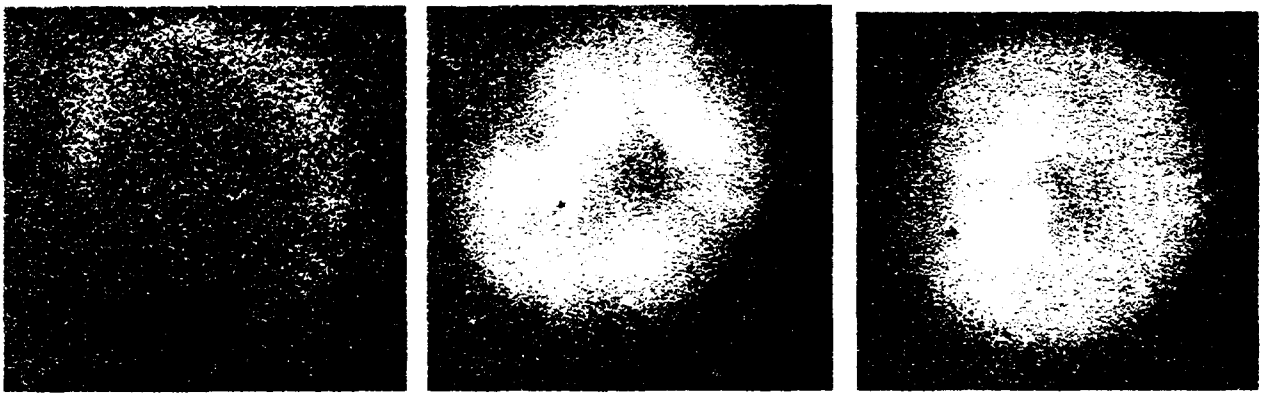

$T = 0.2\ \mu s$ $T = 1.5\ \mu s$ $T = 2.5\ \mu s$

Fig.4.X-ray image of the beam (the diameter of 10 cm)

To register the current density profile the system was used consisting of four IC which provided spatial resolution of < 1 cm (at the beam diameter of 10 cm) and time resolution of 0.3 μs. The system allows to observe the evolution of the beam current distribution during the pulse.

The results of the measurements show that in the beginning of the pulse the beam has a well-defined annular structure, that can be explained as the central part of the beam is cut off by the beam space charge. (Fig.4)

The diameter of the hollow region inside the beam decreases with time and 1.5-2 μs after the beginning the beam becomes uniform and remains so until the end of pulse (4-5 μs). The possible reason of such behavior of the beam could be explained first of all as to be connected with the process of space charge neutralization in the region of compression or as the effect caused by the beam transportation through the plasma column and beam-plasma interaction.

To check the first possibility experiments have been performed with a plasma filling in the compression region. The density of the plasma drifting along and transverse to the magnetic field can be nonhomogeneus that can affect the process of beam propagation. Therefore, it is desirable to produce a plasma with density either sufficient to neutralize the beam space charge in the region between the anode foil and the mirror, or (in case of unhomogenious formation) allowing the plasma to perform as a source of neutralizing ions. Used as a plasma source, 3 surface discharge plasma gun was placed at the 25 cm distance from the anode foil. The magnetic field was 20 kG at the location of the guns and 6 kG at the anode foil.

After adjusting the time of the guns triggering and the gun currents, the beam current and its rate of growth in the beginning of pulse increased, and the jitter of pulse duration diminished. The diode operation became more stable and the pulse duration in the regime with magnetic compression became close to that in the regime with the anode foil replaced by a graphite collector (5-6 μs). At the same time the annular structure of the beam remained in these conditions, that is probably connected with nonuniform filling in the region by the plasma.

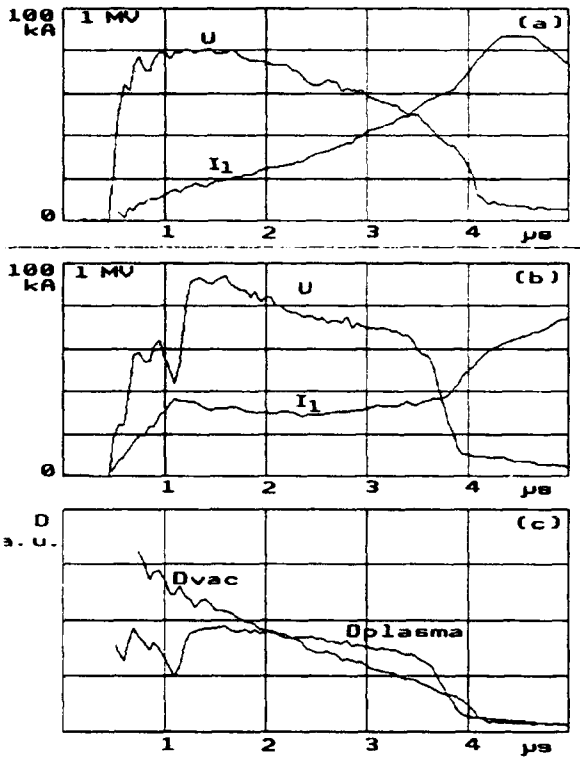

Fig.5 a) voltage and current in the vacuum diode
b) voltage and current in the plasma filled diode
c) effective anode-cathode gap

Plasma filled diode.

After installation of the plasma guns in the compression region a possibility appeared to perform experiments on the beam generation in the diode filled in beforehand with the plasma expanding from the compression region (see Fig1). The main plasma parameter, density, could be varied by changing the current in the guns, the discharge duration or the delay time between the beginning of discharge and the moment of applying high voltage pulse to the diode. The anode foil is unnecessary in this regime .

In this paper the first results are presented on beam generation in the diode filled by the plasma flow from the anode side and following 20-fold compression of the beam. In the experiments presented the plasma density was not measured and was varied mainly by changing the delay between the guns triggering and the pulse of high voltage. Depending on the delay, the diode impedance changes from low (when the accelerating voltage is low) to high value (when the density of accelerated electrons is low).

Given in Fig.5 a,b are the current and the voltage in the vacuum diode and the one filled with plasma. The time dependence of calculated effective anode-cathode gap D_{vac} and D_{plasma} for the vacuum and plasma filled diode respectively is shown in Fig.5c. The experimental configuration (i.e. cathode diameter, magnetic field etc.) for both cases was the same except there was no anode foil in the plasma filled diode.

Comparing the curves one can see the essential difference in the beginning of pulse. The effective gap is formed in the filled-in diode practically instantly after applying of diode voltage (characteristic time is of order of the ion transit time for the accelerating gap). Decreasing of the voltage in the beginning of pulse at the maximum change of the current is caused by the inductance of the generator. When the current becomes almost flat the diode voltage recovers up to the value on the generator capacitors. **In this moment the process of formation of quasi-static accelerating gap in the plasma filled diode may be considered as finished.**

Comparison of the gap time behavior shows that for the filled diode the gap almost does not change with time up to the shorting out of the diode. The formally calculated speed of gap decreasing does not exceed $2 \cdot 10^5$ cm/sec at the current density on the cathode 100 A/cm^2. For the vacuum diode the speed is higher of order, although the initial current density is essentially lower.

The duration of the beam generation in the plasma filled diode depends on the delay between the diode voltage pulse and the moment of guns triggering. Greater duration of the diode operation corresponds lower plasma density. The shorting out of the diode is caused most probably by filling the gap by the cathode plasma, produced by high-energy ions striking the cathode surface. However, the growth of instabilities on the emitting surfaces is also possible. In the same conditions the jitter of pulse duration does not exceed 10% that most likely indicates that the first reason causes the diode shorting out.

Summary.

1. In the experiments on plasma heating by a microsecond E-beam the presence of the annular structure of the beam in the beginning of pulse has been detected.

2. The magnetic analyzer was used to study the energy spectrum of magnetized electrons. Broadening of the spectrum width and its shift toward lower energy even at the plasma density $n \approx 5 \cdot 10^{15}$ cm^{-3} was registered. The beam energy loss is ~10%.

3. It was shown in the first experiments on beam generation in the plasma filled diode, that a greater initial current density and power of the beam, in comparison with the vacuum diode, can be obtained. That is important not only within the frame of plasma heating experiments but also may be of interest for other applications. In order to increase the duration of the beam generation it is necessary to learn how to operate the diode with the larger plasma filled gap. The main problem in this case is how to protect the diode vacuum insulator from the plasma.

References.

1. Arzhannikov A.V. et al.- Plasma Physics and Contr. Fusion (Proceedings of 15-th Europ. Conf. on Controlled Fusion and Plasma Physics, Dubrovnik, 1988) - 1988, v.30, N.11, p.1571-1588.

2. Chikunov V.V. et al. - Laser and Particle beams, 1985, v.3, N.3, p.259-262.

3. Astrelin V.T. et al. - Proceedings of 14-th Intern. Symp. on Discharges and Electrical Insulation in Vacuum, Santa-Fe, 1990, p.702.

4. Astrelin V.T. et al. Proceedings of 8-th Intern. Conf. on High-Power Particle Beams. - Novosibirsk, 1990, - v.1, p.288-292.

5. Chikunov V.V. et al. Proceedings of 18-th Intern. Conf. on Phenomena in Ionized Gases. - London, 1987, v.1, p.202-203. Sov. J. Plasma Phys. (USA), 1988. Translation of Fiz. Plasmy (USSR), v.14, N.7, p.817, 1988.

6. Deulin Yu.I. et al. Preprint INP 91-106, Novosibirsk, 1991, 15 p.

7. Arzhannikov A.V. et al., these Proceedings.

8. Chikunov V.V. et al. Sov. J. Plasma Phys. (USA), 1989. Translation of Fiz. Plasmy (USSR), v.15, N.3, p.307-313, 1989.

9. Chikunov V.V. et al. Proceedings of 8-th Intern. Conf. on High-Power Particle Beams. - Novosibirsk, 1990, - v.1, p.241-249.

BREMSSTRAHLUNG PRODUCTION BY MICROSECOND E-BEAM FROM THIN FOIL IN A MIRROR TRAP

V.V.Filippov, V.S.Koidan, S.V.Lebedev, P.I.Melnikov, M.A.Shcheglov, S.G.Voropaev

Budker Institute of Nuclear Physics, Novosibirsk, 630090, Russia

Abstract.Experiments on a microsecond E-beam (1 MV, 50 kA, 60 kJ) interaction with a bremsstrahlung converter are described. A thin foil placed between strong magnetic mirrors is used as a target. Multiple passage of the electrons through the thin foil increase bremsstrahlung yield in the low-energy (<50 keV) range of spectrum. Testing of the suggested converter has been carried out. The effect of oscillating electrons on the microsecond diode operation is discussed. It is found that the target with thickness equal to 0.05 of the mean range absorbes the beam practically totally. The time-resolved measurements of X-ray emission uniformity are also presented.

Introduction.

Bremsstrahlung sources of different types for various applications have been developed recently. In most of these applications the important parameter is the energy deposition in an irradiated sample. The absorbed energy is determined by the fluence and absorption coefficient of photons which strongly depend on the photon energy. Thus, bremsstrahlung converters with enchanced yield in the soft range of spectrum have a greate importance.

In a conventional converter a high-atomic-number material with thickness about mean electron range is used. As a result the self-absorption reduce essentially bremsstrahlung yield in the low-energy part of spectrum. For materials with Z~70 (W,Ta) the low-energy edge is about 50 keV.

To increase the yield in the soft part of spectrum the advanced converters [1], in which electrons make multiple passes through a thin foil, are used. 'Multiple passes scheme' is realized, for instance, for the drift motion of electrons in the magnetic field of linear current [2]. Another approach is to use the scheme, in which the beam electrons oscillate between an accelerator cathode and a virtual cathode [3,4]. This last scheme can be applied effectively only for a short beam duration (<100 ns), because for the high-power microsecond E-beam its space charge is neutralized in a short time by the ions generated on the accelerator anode foil and on the target foil [5].

In this paper the possibility of the electron beam trapping between strong magnetic mirrors to realize multiple passes through a thin target foil is studied. An electron beam is injected into a trap through the entrance magnetic mirror. Between the mirrors a thin scattering foil is installed, which is used as a bremsstrahlung converter. After the first pass through the foil a part of the beam electrons obtains a pitch-angle large enough to be reflected from the exit mirror. By changing the foil thickness the main part of the beam electrons can be catched in the trap even for the foil thickness essentially less than the mean range of the beam electrons. The advantages of such an approach are the following.

a) There is no feedback effect of reflected (oscillating) electrons on the accelerator diode

operation in contrast with the system of virtual cathode.

b) It becomes possible to use a microsecond beam, because the beam space-charge neutralization and destruction of the virtual cathode do not affect the scheme realization.

Experimental device and diagnostics.

The experiments have been performed on the U-1 device [6]. The experimental configuration is shown schematically in Fig.1. The electron beam (0.8 MV, 60 kA, 3 μs, 60 kJ) is generated in a vacuum diode with a quasiplanar 21 cm diameter graphite cathode. The cathode-anode gap is 5-8 cm. After passing through a thin anode foil 7 (aluminized mylar 10 μm) the beam is adiabatically compressed in the mirror magnetic field and injected into a magnetic trap. Magnetic field increases from 0.5 T in the diode to 10 T in the mirror. The distance between the mirrors 2 and 3 is 40 cm and the mirror ratio $B_{max}/B_{min} = 11$. If the target foil 8 is not installed, the beam passes through the second mirror to the collector 10 without loss. Al, Ti and Ta foils of various thickness have been used as a bremsstrahlung converter . The target foil position can be varied as shown in Fig.1.

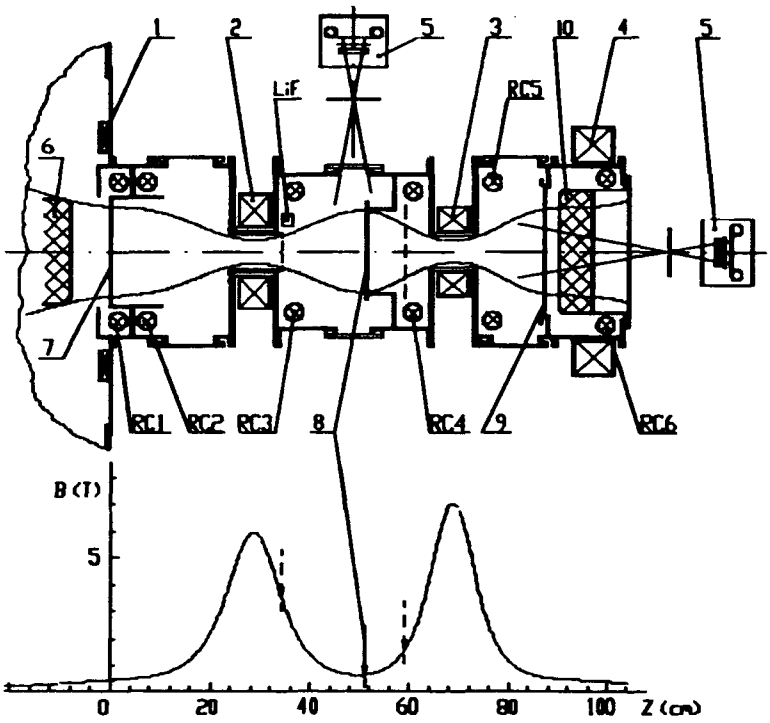

Fig.1 Schematic of the experimental device: 1-4 - magnetic coils, 5- x-ray image converter, 6 - cathode, 7- anode foil, 8- target foil, 9-collector foil, 10-collector, "LiF"-TLD position. Bottom - magnetic field along the axis.

The beam current at the entrance and on the collector, as well as the net current have been measured by Rogowski coils RC1-RC6. To measure the size of the emitting region and the radiation uniformity over the target surface we have used an x-ray image converter on the basis of a microchannel plate. Time and spatial resolution of this system is 0.3 μs and 0.5 cm respectively. Hard x-rays are monitored by a PIN diode. Several LiF thermoluminescent dosimeters (TLD) measured the dose inside the vacuum chamber at a 15 cm distance from the target. To determine the bremsstrahlung spectrum we have measured the dose behind the different filters.

Experimental results and discussion.

1. Beam absorption in the target.

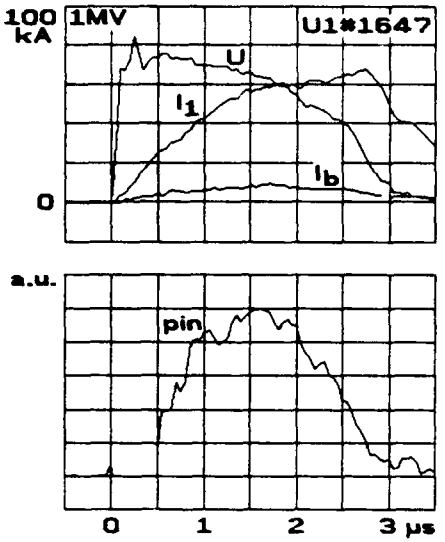

Fig.2 Diode voltage, currents and PIN - diode signals. Target - 30 μm Ta.

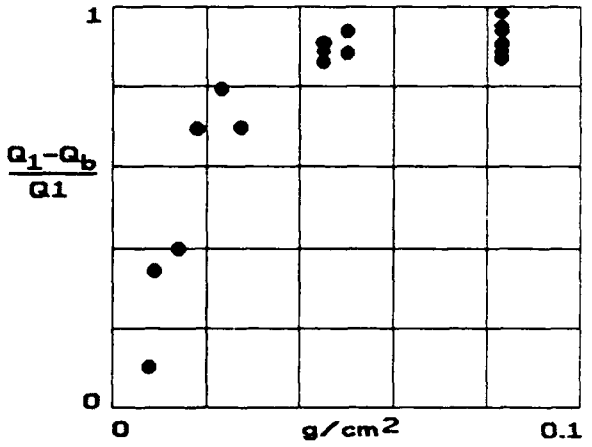

Fig.3 Efficiency of the beam absorption in the target versus the target thickness (Al, Ti, Ta)

Typical signals illustrating the efficiency of the beam capture in the target are shown in Fig.2. The diode voltage U is up to 0.8 MV and injected beam current I_1 rises up to 60 kA. The pulse duration (3 μs) is determined by the diode gap (6 cm). The total energy of the beam $Q_1 = \int UI_1\, dt$ is 60 kJ. The beam current at the exit collector I_b (measured by RC6) changes depending on the thickness of the target foil. The difference between I_1 and I_b is the current of electrons sticked in the target. Efficiency of the beam capture in the target versus the target thickness (g/cm^2) is shown in Fig.3. The almost complete beam capture (>80%) occurs at the thickness > 0.02 g/cm^2, that is about 0.05 of the beam electrons mean range.

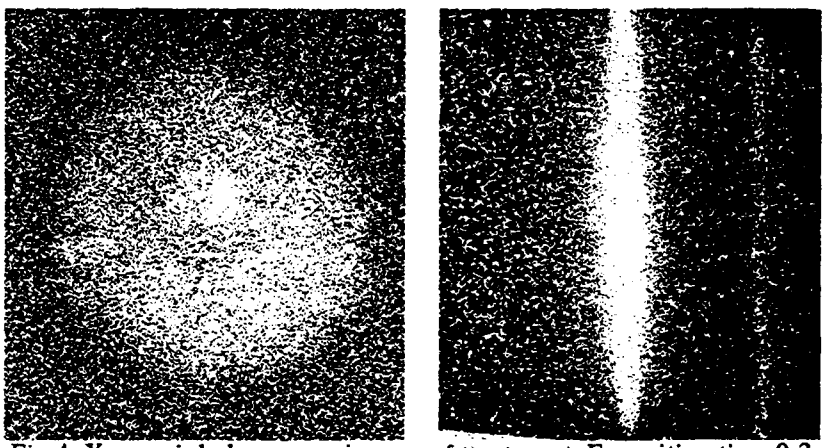

Fig.4 X-ray pinhole camera images of the target. Exposition time 0.3 μs. The right picture is made through the side window and the weak strip at the right corresponds to x-ray reflection from the side surface of the window.

Typical converter images for the moment of maximum x-ray intensity (2μs) are shown in Fig.4. The diameter of the emitting region, measured by image converter, is equal to expected that of the beam at the target according to the magnetic lines of force. This diameter is 14 cm for target positioned in the middle of the trap (mirror ratio M=11) and 10 cm for M=5. X-ray emission during the pulse is uniform over the target surface.

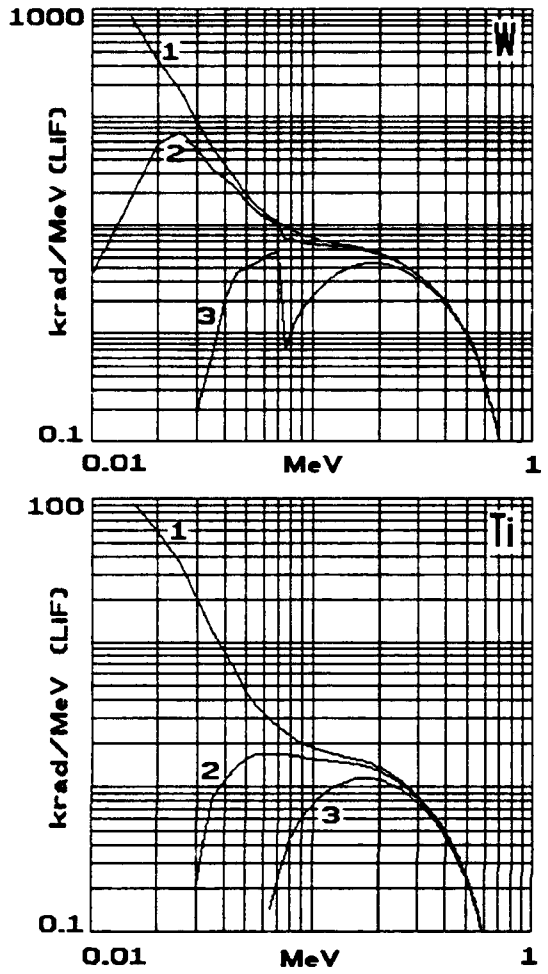

Fig.5 The spectral dose distribution. Top- tungsten target. Thickness: 1- 0 μm , 2- 15 μm, 3- 150 μm. Bottom- 100 μm titanium target. 1-without filter, 2- 0.5 mm Cu filter, 3- 1 mm Mo filter.

2. Bremsstrahlung spectrum.

The dose spectral distribution with regard to absorption in the target material and in additional filters can be written as:

$$D_\varepsilon = \int \frac{n(E)F(\frac{\varepsilon}{E})g(\varepsilon)I(t)f}{4\pi R^2 e}\exp(-md_{eff}-m_f d)\,dt$$

where n(E) - the relative yield of bremsstrahlung, E - the initial electron energy, ε -the photon energy, $F(\varepsilon/E)$ - the universal spectral distribution function, $g(\varepsilon)$ -the energy absorption coefficient for LiF, m and m_f -the linear absorption coefficient in the target and filters, d and d_{eff} - their thickness, $I(t)=I_1-I_b$ -the beam current at the target, e -the electron charge, R -the distance from the target to the point of measurment and f -the geometry factor equal to 0.75 for the chosen position of TLD.

The calculated spectral doses for different effective target thickness d_{eff} and for various filters are shown in Fig.5. The multiple electron passes through a thin target essentially increase the yield of soft x-rays in the range of 10-50 keV.

The calculated and measured doses behind the different filters are presented in the table below. The measured and calculated doses for the 100 μm Ti converter foil are practically the same, and the measured dose of soft x-rays with energy lower than 50 keV is about 1 kR at a 15 cm distance from the target. For the W target the dose in soft region is about 4 kR (LiF) and is essentially greater than that for the standard converter.

target			Dose (R) at 15 cm distance behind the filters		
	material	thickness, μm	-	Cu, 0.5 mm (E > 40 кэВ)	Mo, 1 mm (E > 90 кэВ)
Calculation (Q_1=60 kJ)	W	150	1700	1500	1200
	W	15	3900	2000	1500
	Ti	100	1700	400	300
Experiment	Ti	100	1400	350	290

3. Converter effect on the diode operation.

One of the questions for suggested converter is about the influence of the reflected electrons on the microsecond diode operation. It is well known that high-atomic-number materials used

as an accelerator anode or installed in the magnetic mirror behind the anode foil change essentially the diode operation. Under such conditions the diode begins to operate in bipolar mode earlier and the achievable pulse duration decreases [7,8,5]. These changes are caused both by more intense anode plasma generation and by the electron reflection from the target. For the target installed behind the thin anode foil in the magnetic mirror the reflected electrons pass many times through the anode foil, while oscillating between the cathode and the mirror. So, even for a small reflection factor the density of the oscillating electrons is high enough to reduce strongly the bipolar diode impedance. For the microsecond diode and 20-fold magnetic compression of the beam even reflection of few percent of the beam electrons is sufficient to decrease the beam pulse duration of several times [5].

For the considered converter the fraction of electrons leaving the trap and returning to the diode is determined by the mirror ratio $M=B_{max}/B_t$, where B_{max} is the magnetic field in the mirror 2 (see Fig.1), B_t -the magnetic field at the target. If this mirror ratio is large enough, the target will not strongly affect the diode operation.

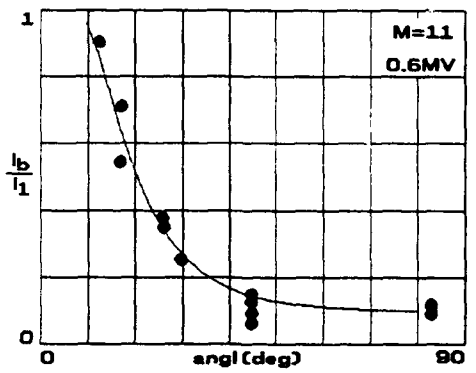

Fig.6 Fraction of the injected beam current passed to the collector versus the target r.m.s. scattering angle. Points - measured data, line - calculated data after one pass through the target foil.

Experimental estimation of the electron current into the diode can be made as following. The electron current to the exit collector, measured by the coil RC6, is the sum of two values. The first value is the fraction of primary beam not trapped after passing through the target foil due to their pitch-angles θ is less then $\theta_M=arcsin\frac{1}{\sqrt{M}}$. The second one is the current of trapped electrons which obtain the pitch-angles $\theta<\theta_M$ due to scattering in the target foil and leave the trap. Given the magnetic field in the mirrors is the same and the trapped electrons make many passes through the target, this second part of collector current is equal to the current of electrons leaving to the diode. The part of the beam directly passed to the collector can be calculated knowning the voltage, foil thickness and mirror ratio. Comparing the calculated value with the measured collector current I_b, one can estimate the current of electrons leaving the trap as their difference. The result of such acomparison for the mirror ratio M=11 is shown in Fig.6. Good agreement of calculated and measured currents indicates that for this mirror ratio the number of electrons returning to the diode is small.

To increase the bremsstrahlung brightness it is necessary to increase the current density on the target. It may be achieved by installing the target in the maximum permissible magnetic field. For this purpose the experiments have been performed in which the target position was varied and the mirror ratio changed from M=11 to M=2. The experiments showed that for M>6 the diode operates without any features and its impedance and pulse duration are the same as for the case without target. For the smaller mirror ratio the diode impedance decrease

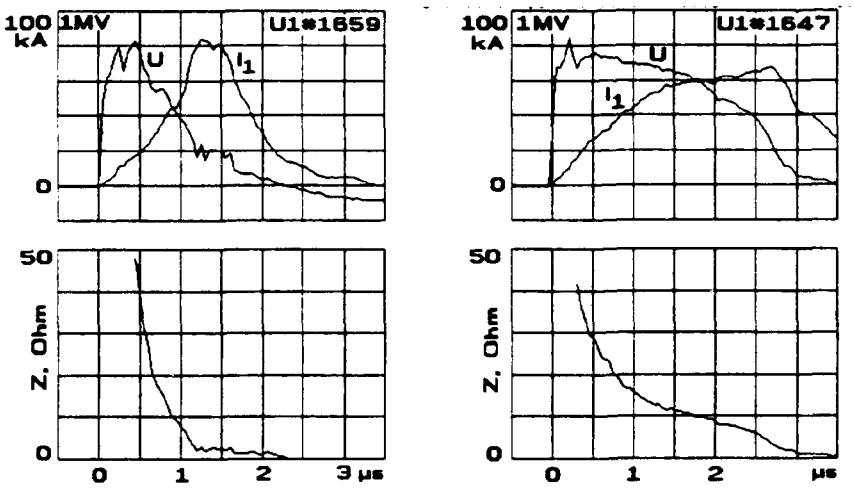

Fig.7 Effect of target position on the diode operation. At the left - B_{max}/B_f=2, at the right - B_{max}/B_f=8.

faster and pulse duration became shorter in a factor of 1.5 for the mirror ratio M=5 and in a factor of 3 for M=2 (pulse duration for the last case is less than 1 μs, see Fig.7). Thus, efficient operation of the suggested converter for a long pulse beam can be achieved with M>6.

Summary.

We have described a bremsstrahlung converter with enhanced yield in the soft x-rays. The main results of the experiments can be summarize as following.

1. The conditions have been found of the practically complete absorption of the electron beam in a thin target. In our experiments, up to 80% of the beam energy have been deposited in the foil with thickness of 0.05 the beam electron mean range.

2. For the 100 μm Ti target and injected beam energy content 60 kJ the measured dose (LiF) in soft x-rays (<50 keV) at a 15 cm distance from the target is 1 kR and total irradiated surface is 1000 cm^2. For the 10 μm W target and 180 kJ E-beam [9] this dose will be 15 kR per pulse.

3. The bremsstrahlung intensity over the target surface is uniform. The emitting region diameter is determined by the ratio of the magnetic field in the mirror to that on the target. The minimum achievable emitting diameter is limited by the effect of the reflected electrons on the diode operation.

References

1. Halbleib J.A. J. Appl. Phys., v.45, p.4103 (1974).
2. Lee J.R. et al. J. Appl. Phys., v.56, p.3175. (1984).
3. Arzhannikov A.V. et al. Pis'ma v ZhETF, v.24, p.19 (1976) - in Russian.
4. Phelps D.A. et al. IEEE Trans of Plasma Sci., PS-4, p.246 (1976).
5. Voropaev S.G. et al. Proc. of 18-th Intern. Conf. on Phenomena in Ionized Gases. - Swansea, U.K., 1987, v.1, p.202-203.; Fizika. Plasmy, v.14, p.817, (1988) - in Russian.
6. Voropaev S.G. et al. Pisma JTP, v.13, p.431 (1987).
7. Prono D.S. et al. J. Appl. Phys., v.46, p.3310 (1975).
8. Phelps D.A. IEEE Trans. Plasma Sci., v.6, p.76 (1978)
9. Astrelin V.T. et al. Proc. of 8-th Internat. Conf. on high-power particle beams. Novosibirsk, v.1, p.288, (1990).

FOILLESS INJECTION OF REB INTO A DENSE PLASMA

I. V. Kandaurov, E. P. Kruglyakov, O. I. Meshkov

Budker Institute of Nuclear Physics, 630090, Novosibirsk, Russia

ABSTRACT. The preliminary experiments on a foilless injection of high-current REB generated from magnetically-insulated diode into a dense plasma are discussed. It is shown that because of low scattering angle of the injected beam the strong Langmuir turbulence is observed even at plasma density $2 \cdot 10^{16}$ cm^{-3}. The REB-plasma interaction efficiency in the case of foilless injection is much higher than in the case when a vacuum diode with anode foil is used. The typical parameters of the REB are: $U_d \sim 0.6$ MeV, $j_b \sim 1-10$ kA/cm^2, $t_b \sim 100-200$ ns. The scattering angle of the beam, estimated from indirect experiments is 4° - 5° .The optimum choice of the foilless diode geometry made it possible to inject the REB with a total current up to six times higher than the vacuum current for this diode geometry.

INTRODUCTION

Rather high efficiency of REB-plasma interaction in the plasma density range 10^{14} - 10^{15} cm^{-3} have been achieved in experiments carried out on GOL-M and GOL-3 [1] devices at Novosibirsk Institute of Nuclear Physics. As it was demonstrated in previous experiments [2], an energy deposited by REB into plasma decreases rapidly with the growth of plasma density. A two-stage scheme [3] is being developed on GOL-3 device to enhance the REB energy transfer to a dense plasma. Another way of effective heating of a dense plasma is provided by using a beam with low scattering angle. For this aim, the experiments on foilless injection of REB, generated from a magnetically-insulated diode, are started now on GOL-M device.

A foilless injection into a low-density plasma ($\lesssim 10^{14}$ cm^{-3}) have been used in a number of earlier experiments [4, 5]. In our experiments a foilless injection of high-current REB into a dense plasma (up to $2 \cdot 10^{16}$ cm^{-3}) have been realised and the first experimental results are being discussed in the paper presented.

EXPERIMENTAL SETUP

The schematic of the experimental setup is shown in Fig.1 The beam is injected into hydrogen plasma preliminary created by high-voltage pulse discharge in longitudinal magnetic field of mirror configuration (R=2) with 4.5T field in diode region and 2.5T in homogeneous part. The length of solenoid in these experiments was reduced to 2.5 meters. The 1-MV pulse from coaxial water forming line is delivered to graphite cathode. The graphite pipe with inner diameter ranging from 0.9 to 1.7 cm and length ranging from 10 to 18 cm was employed as an

anode.Physics of REB generation in plasma-filled diode has been studied previously [6]. The expanding ion sheath is formed near cathode surface and acts like virtual anode-cathode gap.

In some control experiments the output of anode pipe was tightened by 20 mkm titanium foil to avoid plasma flowing into diode gap ("vacuum" regime).Besides that, usual vacuum diode with the anode of titanium foil or of aluminized mylar was also applied.

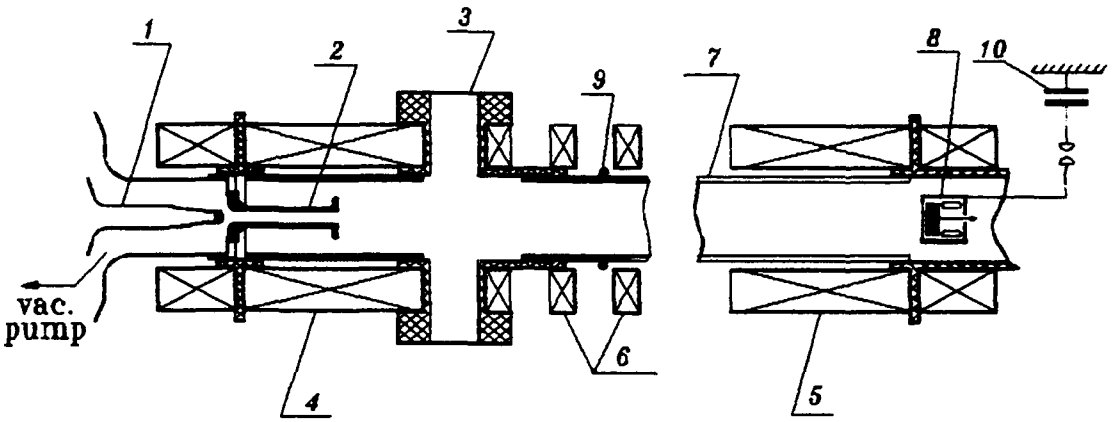

Figure 1. 1-cathode stalk, 2-anode pipe, 3-Thomson scattering system input/output ports, 4,5-mirror coils, 6-solenoid coils, 7-quartz tube, 8-collector/calorimeter, 9-diamagnetic loop, 10-foreplasma discharge capacitor bank.

FOILLESS INJECTION REGIMES.

The parameters of REB generated in plasma-filled diode are strongly influenced by a number of factors (plasma density at the anode pipe output; the pipe length and inner diameter). But for any anode pipe geometry three regimes of REB generation could be distinguished. As an example, the regimes for an anode pipe with diameter 1.3 cm and length 14 cm are given below.

1) "Low-density" plasma regime ($n_p \lesssim 1 \cdot 10^{15}$ cm^{-3}). In this case the beam current exceeds the current in "vacuum" regime no more than two times. This regime is characterised by rather good reproducibility of the REB parameters. Corresponding traces of the diode voltage and beam current on collector are given in Fig.2 and marked by symbol "a".

2) Intermediate case. With the plasma density increasing ($2 \cdot 10^{15}$ - $3 \cdot 10^{15}$ cm^{-3}) the regime of REB generation changes (traces marked by "b"). The substantial growth of the beam current has been observed (up to 5-6 times to "vacuum" current) with a pulse duration cutting down. In this regime, there was significant spread of beam parameters from shot to shot .

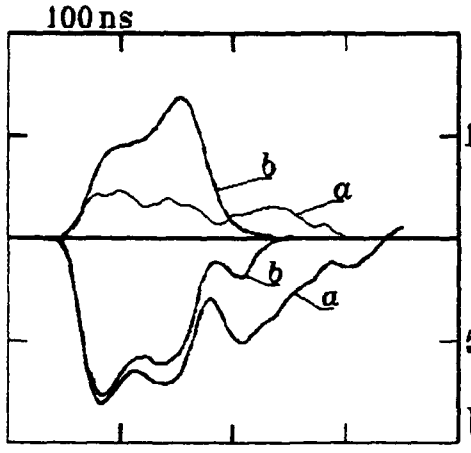

Figure 2. The typical parameters of REB injected from foilless diode.

3) Dense plasma case ($n_p > 4 \cdot 10^{15}$ cm^{-3}). As a rule, the diode shortens in most of shots. The lengthening of the anode pipe and the reducing of its diameter allows us to inject the REB into plasma of higher density.

An employment of magnetised foilless diode significantly alters the characteristics of beam-plasma interaction due to low scattering angle of the REB.The set of basic formulae to provide analysis of these effects is given in the next section.

PHYSICS OF REB-PLASMA INTERACTION

As it was shown experimentally, the process of beam-plasma interaction leads to excitation of Langmuir turbulence in plasma [7]. When the REB is injected through anode foil and scattering angle is large enough, the kinetic mode of two-stream instability could takes place. A growth rate of this mode is given by:

$$\Gamma_k \simeq \omega_{pe} \frac{n_b}{n_p} \frac{1}{\gamma} \frac{1}{\theta^2} \qquad (1)$$

where $\theta = \left(\theta_0^3 + \frac{z}{l}\right)^{1/3}$ (2)

θ_0-initial scattering angle of the beam, z-distance from place of injection. The l value is determined by:

$$l \sim 10^{-1} \frac{c}{\omega_{pe}} \gamma^2 \frac{mc^2}{T_e} \left(\omega_{pe}/\omega_{Be}\right)^2 \qquad (3)$$

Maximal density of energy of the oscillations is limited by modulation instability threshold:

$$W \simeq n_p T_e \left(\omega_{Be}/\omega_{pe}\right)^2 \qquad (4)$$

By this process, in the case of strong Langmuir turbulence the specific energy, transferred to plasma by REB, is given by:

$$q \simeq \Gamma_k W t_b \qquad (5)$$

where t_b-is the beam duration.

Under the foilless injection, when the initial scattering angle of the beam is significantly less than in the case of injection through anode foil, the hydrodynamic mode of instability could

takes place. For "strong" magnetic field ($\omega_{Be} \gg \omega_{pe}^{1/3}\,\omega_b^{2/3}\,\gamma_0^2$), accordingly to [8] the corresponding growth rate is given by:

$$\Gamma_h \simeq \frac{\sqrt{3}}{2^{4/3}}\,\omega_{pe}\left(n_b/n_p\right)^{1/3}\frac{1}{\gamma}\,\frac{k_{\parallel}}{k} \qquad (6)$$

The transition from kinetic growth rate to hydrodynamic one could occur under scattering angle of the REB for which $\Gamma_k \simeq \Gamma_h$;

$$\text{when}\quad \bar{\theta}^2 \simeq \frac{2^{4/3}}{\sqrt{3}}\left(n_b/n_p\right)^{2/3} \simeq 1.45\cdot\left(n_b/n_p\right)^{2/3}. \qquad (7)$$

For the range of experimental parameters which are concerned the transition can take place at $\left(\bar{\theta}^2\right)^{1/2} \lesssim 0.1$

Before the beginning of discussion of the experimental data it should be mentioned that due to the collective effects of the interaction the "tails" of the electron distribution function are mainly heated. As for the bulk of the plasma electrons, its temporal dynamics is determined by two factors. 1) The heating by return current. 2) Additional heating due to collisional dumping of the Langmuir oscillations energy. The dynamics of electron temperature is determined by:

$$\frac{3}{2}\,n_e\dot{T}_e = j_b^2/\sigma + \nu_{ei}W\,; \qquad (8)$$

where σ – plasma conductivity, ν_{ei} - Coulomb collisions frequency. As it could be seen from the last equation, under the large scattering angle, when the turbulence level is low $\left(\frac{W}{n_p T_e} \ll \left(\omega_{Be}/\omega_{pe}\right)^2\right)$, the heating by return current should be predominant, and the electron temperature is rise up to 3 - 10 eV right after the beam injection. On the other hand, in the case of strong Langmuir turbulence the term responsible for Joule heating is negligibly small, and the equation (8) will be:

$$\frac{3}{2}\,n_e\dot{T}_e = n_e T_e\left(\omega_{Be}/\omega_{pe}\right)^2\cdot\nu_{ei} \qquad (8')$$

It can be found from (8') that there is no dependency of electron temperature versus plasma density for the bulk of the plasma electrons. The temperature can be estimated as 40 eV.

THE EXPERIMENTAL RESULTS

The formation of high-current REB with a low scattering angle in the case of foilless injection makes it possible to investigate the physics of interaction in a range of parameters unstudied before. At the same time, the analysis of the of REB-plasma interaction makes it

possible to estimate the scattering angle from the experimental data. The decrease in the beam scattering angle in the case of foilless injection was qualitatively approved by diamagnetic measurements. For the same plasma and beam parameters the specific diamagnetizm is substantially higher (4-5 times) in the foilless case than that in the case of injection through the 20 mkm titanium foil. The diamagnetic loop nearest to the place of injection was placed at $z = 42$ cm from the anode pipe output. The numerical estimation of the beam initial scattering angle is complicated because of the impossibility to place the diamagnetic loop in a region $z < 42$ cm. If one compares the plasma diamagnetizm for the case of foilless diode and that for usual diode with anode foil from mylar of 10 mkm, the interaction efficiency will practically be the same in both cases (for the same beam and plasma parameters).In the case of injection through mylar the scattering angle for the beam is about 5°. So for the foilless injection scattering angle should be the same. The experimental data related to the electron temperature measurements are shown in Fig.3. One can see that there is no dependence of T_e on plasma density in a wide range of parameters. It means that the heating of electrons is determined by (8'), in other words, the strong Langmuir turbulence takes place in the range of plasma and REB current densities which are given in Fig.3. The value of $T_e = 40$eV followed from eq.(8) is in a reasonable agreement with experimental data. As it is known, in the case of strong turbulence the magnetic addition to the frequency in the wave dispersion law, $\Delta\omega_{Be} = \frac{1}{2}\left[\omega_{Be}^2/\omega_{pe}\right]^2$, should be less than growth rate, $\Delta\omega_{Be} < \Gamma_k$.

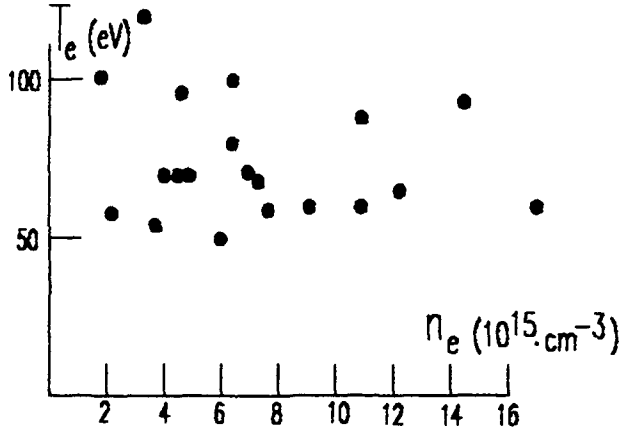

Figure3. Plasma electron temperature after REB injection vs plasma density. T_e was measured by Thomson scattering at a distance 27 cm from cathode. j_b varying from 1 to 10 kA/cm^2

This criterion makes it possible to give an upper estimation for the beam scattering angle:

$$\frac{1}{2}\left[\omega_{Be}^2/\omega_{pe}\right]^2 \lesssim \omega_{pe}\frac{n_b}{n_p}\frac{1}{\gamma}\frac{1}{\theta^2}\ ;\text{at } B = 2.5\,T \text{ and } \gamma \simeq 2\ \left(\bar{\theta}^2\right)^{1/2} \lesssim 1.27\cdot 10^{-7}\, n_b^{1/2}.$$

Thus, for $n_b = 1.5\cdot 10^{12}$cm^{-3}, $\left(\bar{\theta}^2\right)^{1/2} \lesssim 9°$, and for $n_b = 3\cdot 10^{11}$cm^{-3}, $\left(\bar{\theta}^2\right)^{1/2} \lesssim 4°$.

Under our experimental conditions it seems to be improbable that the scattering angle of the beam in the diode depends considerably on REB current density. So the upper limit of

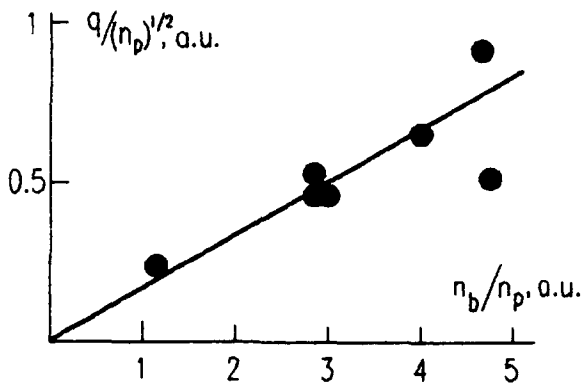

Figure 4. Demonstration of the kinetic mode of instability for $z > 42$ cm.

scattering angle can be estimated as $(\bar{\theta}^2)^{1/2} \lesssim 4°$. If the scattering angle of the beam is 4° - 5°, the hydrodynamic mode of the instability can take place. It can be found from (1), (4), (5) that for the case of kinetic growth rate $q/(n_b)^{1/2} \sim \frac{n_b}{n_p}$, but for the case of hydrodynamic growth rate (4), (5), (6) yields $q^3/(n_b)^{3/2} \sim \frac{n_b}{n_p}$. The experimental data are plotted on Fig.4 shows that the kinetic growth rate takes place at the most part ($z \gtrsim 42$ cm) of the plasma length. The diamagnetic measurements in range $z \lesssim 42$ cm are needed to understand whether the hydrodynamic growth rate takes place there.

SUMMARY

1). A foilless injection of REB from magnetized diode into a dense plasma is realised.

2). The interaction efficiency is higher under the foilless injection compared to the case of injection through the anode titanium foil of 20 mkm thickness.

3). It is shown, that the strong Langmuir turbulence takes place in the experiments in a wide range of parameters due to low scattering angle of the REB under the foilless injection.

REFERENCES

1. A.V.Arzhannikov, A.V.Burdakov, V.V.Chikunov et al. Proc. 13th Int.Conf. on Plasma Physics and Controlled Nucl. Fusion Res., Washington, 1990. IAEA-CN-53/C-2-5.
2. A.V.Arzhannikov, A.V.Burdakov, V.S.Burmasov et al. Proc. 3rd Int.Conf. on High Power Electron and Ion Beam, Novosibirsk,v.1,29(1979).
3. A.V.Arzhannikov, A.V.Burdakov, V.V.Chikunov et al. Proc. 9th Int.Conf. on High Power Particle Beam, Washington(1992).
4. S.Robertson and A.Fisher. J.Appl.Phys. 51(8),4094-4096(1980).
5. G.V.Venugopala Rao, K.C.Mittal,A.S.Paithankar et al in Proc. Int. Conf. on Plasma Phys., New Delhi, v.3, 1013-1016 (1989).
6. R.A.Miller, J.W.Poukey, T.P.Wright Phys. Rev. Lett. 35(14), 940-943(1975)
7. I.V.Kandaurov, E.P.Kruglyakov, M.V.Losev et al.Proc. 8th Int.Conf. on High Power Particle Beam, Novosibirsk,v.1,233-240(1990).
8. Ja.B.Fainberg, V.D.Shapiro, V.I.Shevchenko. Sov. Phys. JETP,57,966(1969).
9. V.S.Burmasov, A.D.Khilchenko, V.A.Kornilov et al. Proc. 10th European Conf. on Controlled Fusion and Plasma Phys., Moscow v.1 C-2(1981).

FREQUENCY REGIME OF HIGH CURRENT RELATIVISTIC ELECTRON BEAMS INTERACTING WITN VARIOUS GASEOUS MEDIA

N.A.Kondratiev, V.I.Smetanin, Yu.P.Usov
Nuclear Physics Institute of Tomsk
Polytechnical University,634050,Tomsk,P.O.Box 25,RUSSIA
V.E.Kulbeda
Moskow Radiotechnical Institute
of Russian Academy of Sciences,113513,Moskow,RUSSIA

Constantly growing application of high current relativistic electron beams (REB) to produce non-equilibrium plasma in plasma-chemical reactors, to pump lasers, etc, necessitates the investigation of REB interaction with various gaseous media and mixtures. To solve the problem of a plasma chemical reactor based on REBs it is necessary to account for the effects of the intrinsic electromagnetic fields of plasma-beam system upon plasma chemical processes[1]. Here we pay a particular attention to the possibility to increase the pulse repetition rate. It is expected that by multipulse treatment of gaseous media the efficiency of the subsequent pulses could be increased due to lowering the rate of development of large-scale instabilities.

This work presents the results on the interaction of the subsequent REBs ($<500\cdot10^{-9}$ s) following each other at the time interval t_p. The experiments have been carried out on accelerator TONUS[2] modified to generate two electron beams. The basic difference of generating two electron beams from conventionally generated single REBs consists in the following. The switch formerly commuting the middle electrode of DFL and the accelerator's mainframe is here switched between the middle and the inner electrodes. The charging inductance is separated from the inner line by the gap and is set into the circuit between the accelerator's mainframe and the electron gun. The above scheme makes it possible to generate two REBs in the course of the time equal to the duration of the front edge of the charge pulse of MARX generator.

TONUS generated the beamsof the following parameters. The first beam: the electron energy $E_{e_1}=(500\div600)\cdot10^3$ eV, the beam current $I_{b_1}=(1\div1.2)\cdot10^4$ A, the pulse current duration $t_1=60\cdot10^{-9}$ s. The second beam: $E_{e_2}=(1\div1.1)\cdot10^6$ eV, $I_{b_2}=(2\div2.4)\cdot10^4$ A, $t_2=60\cdot10^{-9}$ s.

The electron beams were injected into the drift tube (DT), $9.2\cdot10^{-2}$ m in diameter, filled with one of the working gases (He, N_2, Ne, Air, H_2, SF_6) at the pressure P = 1÷760 Torr.The experiments studied the dependence of the efficiency of the second high current REB transport (I_{b_2}/I_{inj}) on t_p varying from $100\cdot10^{-9}$ s to $500\cdot10^{-9}$ s.

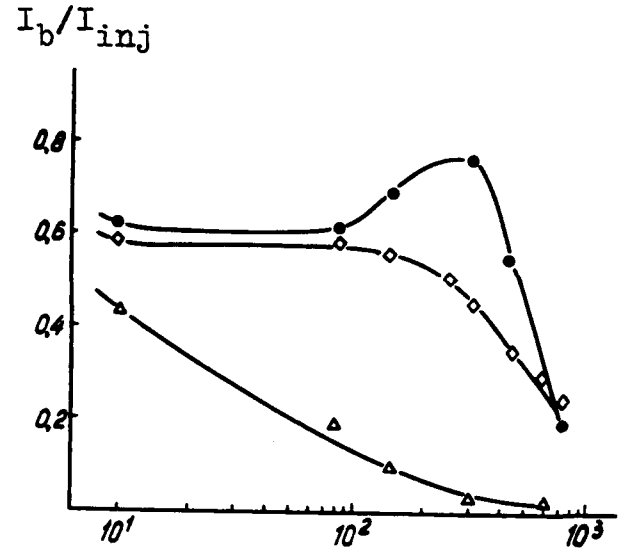

Fig. 1. The efficiency of the second electron beam transport versus the time pause at L=105 cm: ◇ - $t_p\leqslant100\cdot10^{-9}$ s; ● - $t_p=(100\div250)\cdot10^{-9}$ s; △ - $t_p=(250\div500)\cdot10^{-9}$ s.

Fig. 1 illustrates the influence of t_p on the electron beam transport in the air. It is clear from the figure that there exists some optimal interval t_p, where the second beam is transported with maximum efficiency. The dependence on t_p is observed for all working gases. For each gas, however, there is a particular optimal interval t_p, which is shifted to the region of small t_p with growing molecular mass of the gas (fig. 2).

This dependence points to the fact that the efficiency of the second REB transport is conditioned by the parameters of the trace, i.e. the plasma parameters at the instant when the second electron beam into action.

For small t_p-values the level of plasma density is high

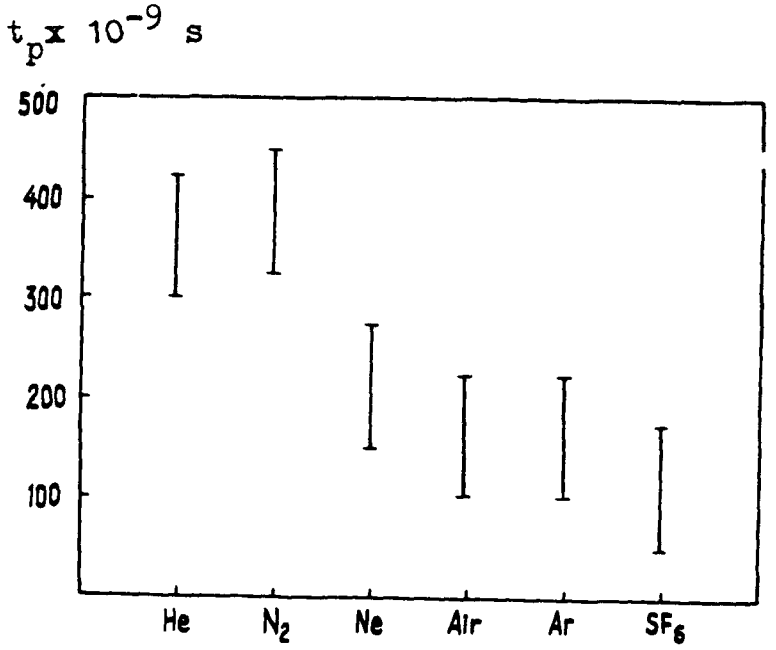

Fig. 2. The optimal intervals t_p versus the gas type.

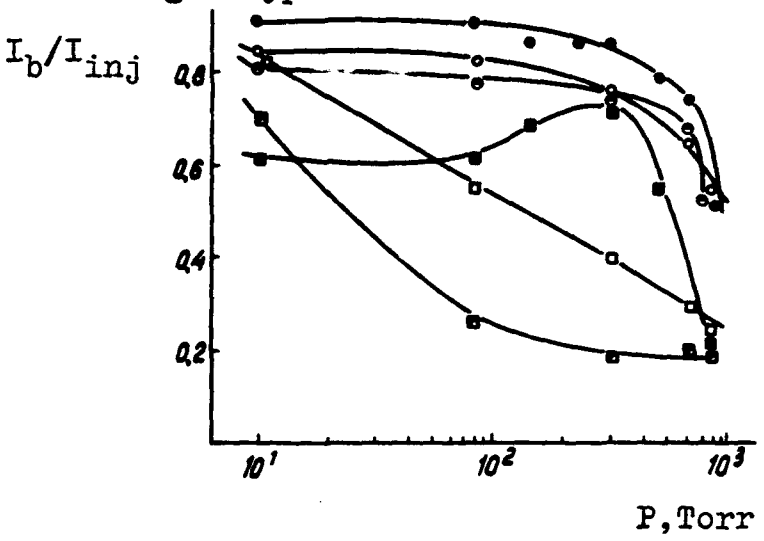

Fig. 3.o ● ● - L = 60 cm; □ ▣ ■ - L = = 120 cm; □ o- one pulse $E_e=1\cdot10^6$ eV; $I_b= 1.7\cdot10^4$ A; ▣ ● - one pulse; E_e = = $1\cdot10^6$ eV; $I_b = 2.4\cdot10^4$ A; ■ ●- two pulse; $E_{e_2}= 0.6\cdot10^6$ eV; $I_{b_2}=1.5\cdot10^4$ A.

and the second electron beam is strongly scattered. For optimal t_p-values the plasma density decreases during the interval t_p to the values sufficient to neutralize the charge and the current of the beam, and its efficiency is improved. Further growth of t_p leads to the situation when the second beam is no longer affected by the plasma of the first REB and propagates as a single REB.

Fig. 3 gives the results on single pulse and double pulse transport of REB in the air for two tube lengths.

For double pulse transport the efficiency is higher. This is particularly noticable for the gas pressure range 100÷300 Torr, when the development of large scale instabilites is the strongest.

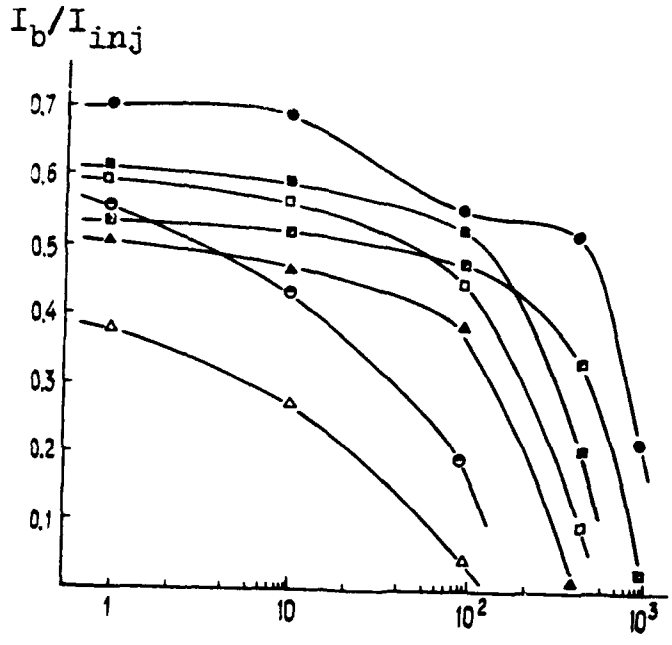

Fig. 4. ● -Ne; ■ - Air; □ - N_2; ▨ - He; ▲ - Ar; ⊖ - Kr; Δ - SF_6.

Thus we can expect the existence of the mechanism limiting the large scale instability, e.g. the hose-type instability, when a series of pulses is propagated.

This might be due to the deficit of plasma electrons on the axis before the second pulse caused by partial losses of plasma electrons in the cascades of plasma-chemical reactions (attachment, recombination etc). Thus the trace in the gas after the first pulse will be of complex structure made up of a positively charged core and double layers on the margins which results in ion focussing of the second beam. However, the mechanism of such a lengthy impact of the first pulse upon the second, excluding the magnetic interaction of the beam, requires a more detailed study.

Fig. 4 draws the dependence of the efficiency of the second REB transport for optimal t_p - values for various gas types on the pressure in DT for a distance of 1.3 m.

Notice that there is no termination of the REB transport of which typical for single REBs at high gas pressures[3].

REFERENCES

1. G.E.Norman et al. in: The Synthesis of Compounds in Plasma Containing Hydrocarbons, ed. L.S.Polak,Moskov(1985), p. 3.
2. I.Z.Gleizer et al.Atomic Energy, 36 (1974), p. 378.
3. N.A.Kondratiev et al. J.Techn. Phys., 59 (4), (1989),p.118.

SPECTRA OF LANGMUIR TURBULENCE EXCITED BY HIGH-CURRENT REB

I.V.Kandaurov, Eh.P.Kruglyakov, M.V.Losev, O.I.Meshkov,

A.l.Sanin and L.N.Vyacheslavov

Budker Institute of Nuclear Physics, 630090,

Novosibirsk, Russia

Abstract. New experimental results on the studying of the Langmuir turbulence are presented. The main diagnostic technique remains the same as that in the previous experiments [1] - a Raman scattering of the CO_2-laser light. Besides the detection of plasma emission near $2\omega_{pe}$ in the far infrared and the ruby laser scattering for electron temperature and density measurements are used. Wave number turbulence spectra for resonant and nonresonant oscillations are studied with an improved resolution. The emission power at $2\omega_{pe}$ calculated on the base of the observed turbulence spectra will be compared with the measured one.

INTRODUCTION

Electromagnetic wave scattering has been used for studying the Langmuir turbulence both in a low density plasma ($n_p \sim 10^9$-10^{13} cm^{-3}) in early experiments [2,3] and in a dense one ($n_p \sim 10^{16}$ 10^{17} cm^{-3}) later [4,5]. For the intermediate plasma densities ($n_p \sim 10^{15}$ cm^{-3}) we are employing the laser scattering technique as a lot of experiments on relativistic electron beam-plasma interaction has been done under these conditions and the set of diagnostic methods has been worked out [6,7].

EXPERIMENTAL SETUP

The experimental setup is shown in Fig.1. The relativistic electron beam (700 keV, 200 ns, 1 kA cm^{-2}) was injected from the foilless diode into a 8 cm diam., 2.8 m long hydrogen plasma column, located in longitudinal magnetic field of 25 kG. The schematic of the diode and its detailed description can be found in Ref. [8]. The CO_2-laser beam and ruby one are intersected each other and column axis at an angle 90° and distance 27 cm from the cathode. The small-angle scattered IR laser light and 90°-scattered ruby light are separated by visible -infrared dichroic mirror. The visible light is received by seven-channel detection system and is used for plasma temperature and density measurements after the injection of electron beam. The infrared radiation scattered at different small angles is collected by five or, recently, twelve mirrors M followed by separate detectors and it is employed in these experiments for measurements of k-spectra of the Langmuir turbulence. The plasma emission at $2\omega_{pe}$ from the beam-plasma interaction region near the

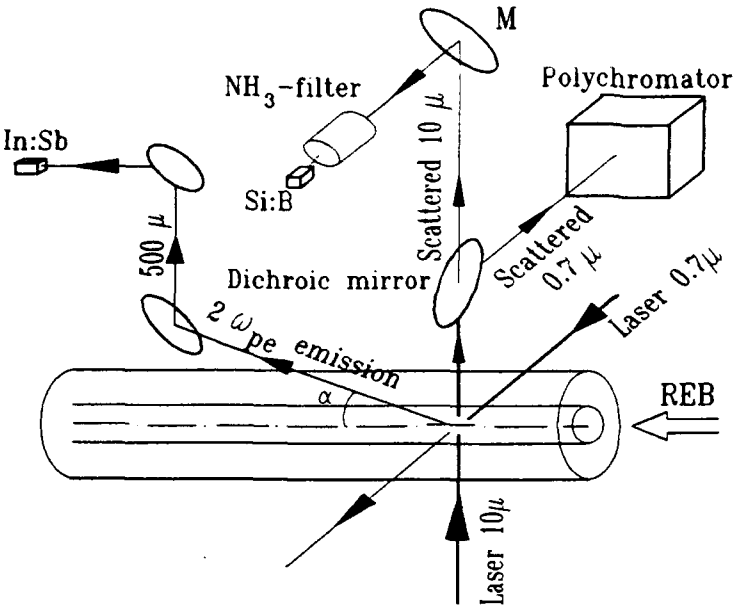

plane where the laser beams are intersecting is observed at an angle 7° with the REB running direction and is received by In:Sb cooled detector. The spectral selection of this radiation is accomplished via the grid filter centered at frequency 450 GHz.

Fig.1. Schematic of the experiment.

EXPERIMENTAL RESULTS

A.Resonant oscillations

At the geometry used (normal incidence of the probe light beam) it is possible to study the resonant Langmuir waves (whose wave vectors satisfy the

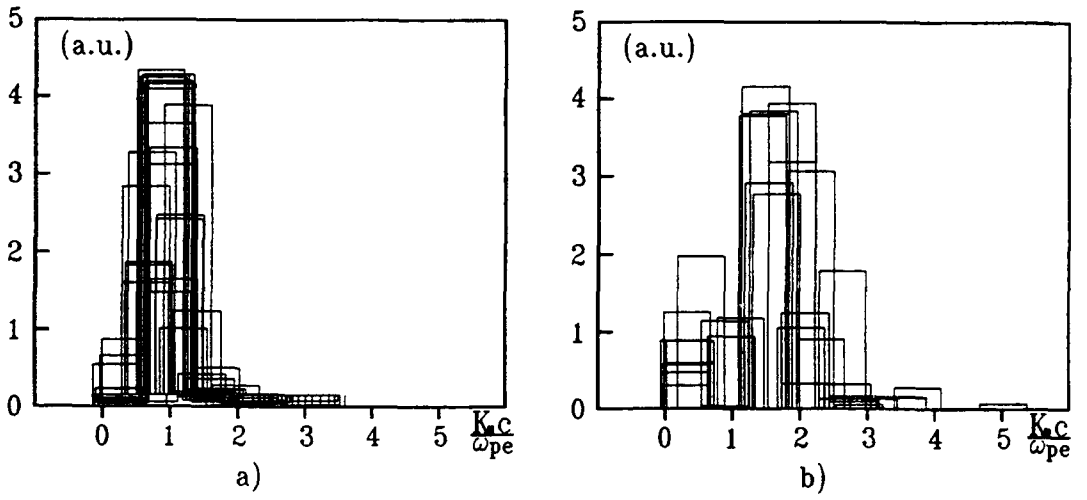

Fig.2 Normalized spectra of resonant oscillations at $k_{\perp} \approx \omega_{pe}/c$ (a) and $k_{\perp} \approx 5 \cdot \omega_{pe}/c$ (b). Figure (a) represents 21 shots, (b) - 8 shots.

conservation condition $\mathbf{kv}_b = \omega$) only with minimal value of transversal wave number $k_{\perp}c/\omega_{pe} > v_b/c = 0.9$. The dependence of normalized spectral density of energy of Langmuir turbulence versus longitudinal wave number $k_{\parallel}c/\omega_{pe}$ is shown

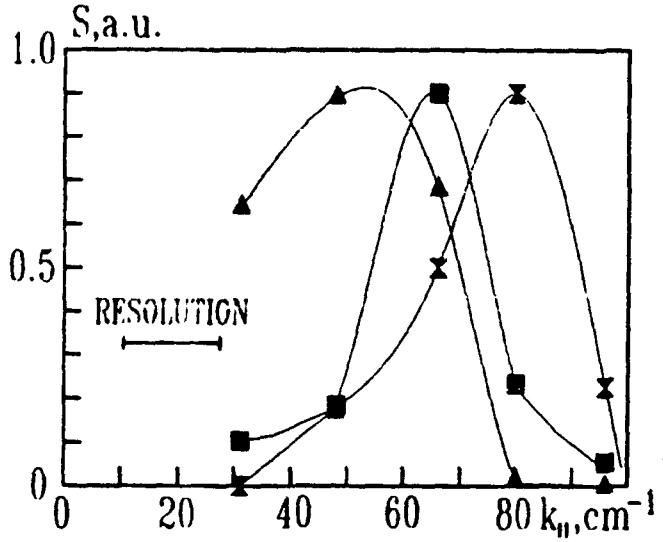

Fig.3 Normalized spectra of resonant oscillations at $K_{\perp} \approx \omega_{pe}/c$ with resolution improved a factor of 2.5 from that at Fig.2a. The peaks of spectra correspond to the plasma densities 0.7; 1.0; $1.7 \cdot 10^{15}$ cm^{-3} (from left to right).

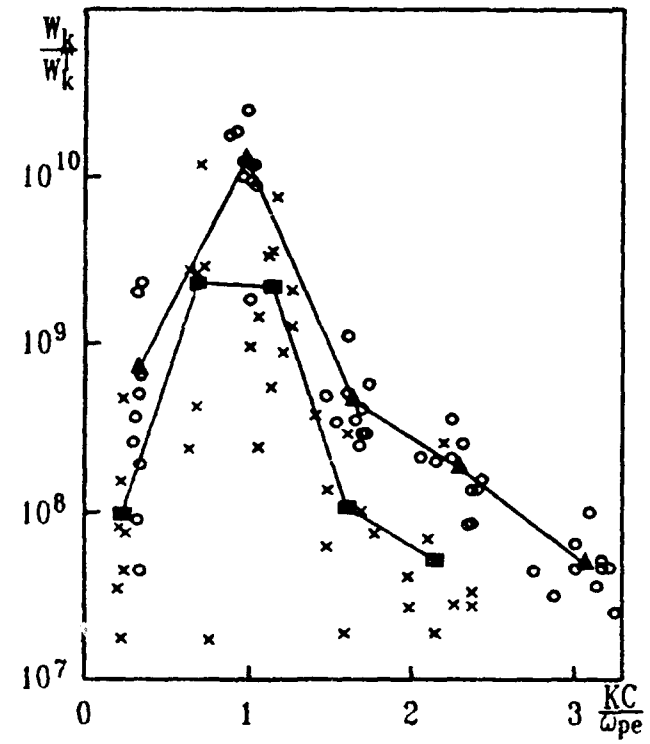

Fig. 4 Turbulence spectra in resonant region (in units of thermal level $W_k^T = T/(2\pi)^3$) for two series of ten shots. Upper spectrum $\bar{n} = 1.1 \cdot 10^{15}$ cm^{-3} - circles; lower spectrum $\bar{n} = 2.3 \cdot 10^{15}$ cm^{-3} - crosses. the

in Fig.2 for $k_{\perp}c/\omega_{pe} = 1$ (a) and $k_{\perp}c/\omega_{pe} = 5$ (b). Fig. 2a summarizes the spectra of 21 shots and Fig. 2b that of 8 for the range of plasma densities $0.8 \div 2.5 \cdot 10^{15}$cm^{-3}. A sharp maximum occurred at $k_{\parallel}c/\omega_{pe} = 1$ and the correlation between its position $(k_{\parallel})_{max} = \omega_{pe}/c$ and plasma density are an additional confirmation of the Langmuir turbulence origin of the scattered signal.

The spectrum width in Fig.2 is nearly the instrumental resolution. The spectra measured with the resolution increased by a factor 2.5 are shown in Fig.3. The plasma density corresponding to the peak of each spectrum is also pointed out in figure. In this experiment, the least resolved element of $\Delta k_{\parallel}$ is close to the width of resonance region with the positive growth rate for the spread angle of the REB $\Delta\theta = 10^{\circ}$. The exceeding of the width of some spectra above the instrumental resolution can be explained not by a high beam's angular spread but by deviation of the plasma density profile from the homogeneous one over 30 percent. The dependence of spectrum of resonant oscillations on plasma density by invariable beam current and duration is shown in Fig.4 from shot to shot basis. The curves are spectra either averaged over 10

shots with a mean density $n_p = 1.1 \cdot 10^{15} cm^{-3}$ (upper curve) and $n_p = 2.3\ 10^{15} cm^{-3}$ (lower curve). The spectral density of the Langmuir turbulence is measured in units that of thermal one: $T/(2\pi)^3$. It follows from the figure that the spectral density of oscillations exceeds the thermal level more than 10 orders of magnitude for plasma density $n_p = 1.1 \cdot 10^{15} cm^{-3}$. In spite of the considerable spread of the experimental dots at plasma density $n_p = 2.3 \cdot 10^{15} cm^{-3}$ one can see that practically all the dots associated with this density are located below the dots relevant to lower plasma density. This result is qualitatively match with the dependence of growth rate on value n_b/n_p. For more detail studying the behaviour of turbulence spectrum from the conditions of beam-plasma interaction additional experiments are necessary including the study the nonresonant region.

B. The total spectrum of turbulence

To obtain more detail information about the turbulence spectrum we increase the number of simultaneously observed interval of spectrum from five to twelve. In first series of experiments, the five-channel system was used for spectral measurements in resonant region. The obtained results were presented in Fig.3. The seven channel system was intended for studying the spectrum of nonresonant oscillations. The turbulence exceeded considerably thermal level was observed up to the phase velocities $v_b/15$ (it corresponds to the energy of electrons $E_e = 1$ keV). The first data exhibit the tendency of spectrum to stretch along the axial direction. The observations point out also to possible asymmetry of the spectrum of nonresonant oscillations. At present, there are not yet enough experimental data to make more definite conclusion about anisotropy of nonresonant oscillations spectrum. Thus, we

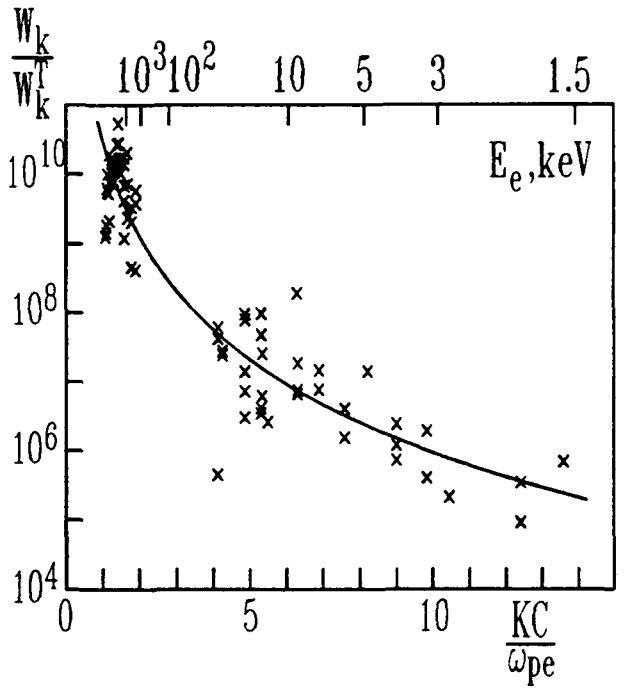

Fig. 5 Dependence of turbulence spectra (including resonant and nonresonant regions) vs oscillations wave number. Upper scale corresponds to an energy of electron with velocity equal to phase velocity of turbulent waves.

represent in Fig.5 the spectrum of turbulence including both the resonance and nonresonant region and neglecting the possible spectrum anisotropy. One can see in figure a substantial decrease in the spectral density of oscillations with the growth of wave number (the curve in figure is related to the dependence: $W_k(2\pi)^3/T = 2\cdot10^{10}\cdot(kc/\omega_{pe})^{-4.5}$). The fact that the W_k value falls off more rapidly than $1/k^3$ means that the main energy of the nonresonant region is in the range with highest phase velocities. We would remind that analogous conclusion about resonant oscillations follows from our previous results [1] which are in agreement with the new data for resonant region. The rapid decrease in the spectral density of nonresonant oscillations with decreasing phase velocity can be explained via dumping by energetic electrons. Such electrons were observed before in comparable conditions of the experiment [9]. To evaluate the integral turbulence level W/nt we use all experimental data under assumption about spectrum isotropy mentioned above. For the resonance region with an angular width $\Delta\theta = 10^\circ$ the value W/nt achieves 5% at plasma density $1\cdot10^{15}cm.^{-3}$ On the nonresonant region the value W/nT reaches 3 ÷ 10% depending on suppositions about the isotropy and spread of the experimental data.

C.Emission at $2\omega_{pe}$

The power of radiation at double plasma frequency, measured at an angle 7° to the beam running direction, was compared with results of calculations. Numeric simulation was made on the base of the experimental spectra of turbulence. For calculations we use the formula for the power of spontaneous radiation at $2\omega_{pe}$ in turbulent plasma from [10]. Assuming that the thermal addition in the Langmuir waves dispersion law is negligibly small and integrating over the output electromagnetic radiation spectrum one can get the power of radiation at $2\omega_{pe}$ from the unit volume into the unit solid angle:

$$\frac{dP}{d\Omega} = \frac{\pi}{2\sqrt{3}\, m_e n_o C}\cdot\int\frac{(K^2-2\mathbf{KK1})^2\ [\mathbf{K}\times\mathbf{K1}]^2}{K1^2\ (K^2+K1^2-2\mathbf{KK1})}\cdot W_{K1}W_{K-K1}\,d\mathbf{K1}\Bigg|_{K=\frac{\sqrt{3}\cdot\omega_{pe}}{C}},$$

where: W_k – spectral density of the turbulent oscillations,

$K = \frac{\sqrt{3}\cdot\omega_{pe}}{C}$ wave vector of the output electromagnetic radiation.

Calculations yield power 1 ÷ 10 $W\cdot cm^{-3}\cdot sterad^{-1}$ depending on assumption about the turbulence spectra details, discussed above. Experiment results the maximal emission power about 0.5 $W\cdot cm^{-3}\cdot sterad^{-1}$. Taking into account the accuracy of absolute calibration at this time (a factor 2÷3) one can see that the simulation qualitatively fits the experimental results.

CONCLUSIONS

1. Resonant and nonresonant spectra of the Langmuir turbulence are measured.
2. Spectrum of resonant region of turbulence has a sharp maximum at $k_{\|} = \omega_{pe}/c$. The value and location of the maximum depend on plasma density.
3. The angular width of the resonant region is measured. Thermal level was exceeded as high as ten orders of magnitude.
4. Spectra of nonresonant oscillation are measured up to $k = 15\ \omega_{pe}/c$ ($E_e \sim 1$ keV for electrons with the same velocity). The total range of observed values of turbulence spectral density extends up to five orders of magnitude.
5. Plasma emission power at $2\omega_{pe}$ in the far infrared is measured. The experimental value of power qualitatively fits the simulations based on experimental turbulence spectra.

REFERENCES

1. I.V.Kandaurov at al.:Proc. 8th Int.Conf.on High Power Particle Beams, Novosibirsk, 1, 233,1990.
2. B.A.Demidov, S.D.Fanchenco, JETP Lett., 2, 533 (1965).
3. R.A.Stern, N.Tzoar, Phys. Rev. Lett., 15, 485 (1965).
4. B.Amini, F.F.Chen, Phys. Rev. Lett., 53, 1441 (1984).
5. C.E.Clayton, C.Joshi, C.Darrow, D.Umstader, Phys.Rev.Let., 54, 2343 (1985).
6. A.V.Arzannikov, A.V.Burdakov, V.S.Koidan, L.N.Vyacheslavov, Physica Scripta, T2/2, 303 (1982).
7. A.V.Arzannikov et al. Proc. of 11th Internationl Conference on Plasma Physics and Controlled Nuclear Fusion Research, Kyoto, 2, 323 (1987).
8. I.V.Kandaurov, E.P.Kruglyakov, O.I.Meshkov, Proc. 9th Int.Conf.on High Power Particle Beams, Washington, PC-04, 1992.
9. A.V.Arzannikov et al. Proc. Int. Conf. on Plasma Phys., Lausane, Inv.p. v.1, 285-308 (1984).
10. V.N.Tsytovich, Theory of the turbulent plasma (Plenum press, 1971).

ELECTRIC FIELD STRENGTH MEASUREMENTS IN A MEGAVOLT VACUUM DIODE USING LASER INDUCED FLUORESCENCE OF AN ATOMIC BEAM

B.A.Knyazev
Novosibirsk State University, 630090 Novosibirsk, Russia

V.V.Chikunov, P.I.Melnikov
Budker Institute of Nuclear Physics, 630090 Novosibirsk, Russia

ABSTRACT. A combined technique of an atomic beam probing and laser-induced fluorescence spectroscopy (LIFABS) is applied for measuring of local electric field in a 1 MV, 100 kJ, 4 μsec electron diode. Laser-produced lithium beam is stepwise excited by two resonant wide-band laser beams. Stark-splitted spontaneous emission from n = 4 level is detected with a polychromator. Time dependence of the electric field was inferred from splitting of the 460.3 nm lithium line. The electric field strength *F* grows during a pulse from 160 to 260 kV/cm in the center of a 6 cm gap. By comparing calculated and experimental *F*-values, expansion of the emission boundaries of the cathode and anode plasmas was reconstructed.

Introduction

The main feature of high-power electron and ion diodes is simultaneous existence of expanding plasma layers and accelerating electron and ion flows. According to Poisson low that leads to non-linear electric field distribution in the space between emissive cathode and anode plasma boundaries. The expansion of this plasmas defines pulse duration of a particle accelerator. There are two problems to be solved in experiments: to measure spatial distribution of the electric field in the gap and to locate the emissive boundaries.

These problems in a case of the ion diode can be solved through observing Stark splitting or Doppler shift of spectral lines which are emitted by ions accelerating across the gap [1]. However, this way is not universal and cannot be practically applied to electron diodes. In this case Active Stark Spectroscopy technique (Laser-Induced-Fluorescence of an Atomic Beam Spectroscopy,-LIFABS) is more adequacy. This method was proposed in 1985 [2]. Principle of the method and proof-of-principle experiment are described in the paper [3].

In this method a combined technique of an atomic beam probing and laser-induced fluorescence spectroscopy is used. It includes three main elements: injection of an atomic beam with suitable quantum levels in the volume under study, excitation of the atoms with resonant wide-band laser radiation, and recording of Stark-splitted fluorescence line with spectral and time resolution. In this paper the results of the experiments on measuring the electric fields strength in the diode of U-1 accelerator are presented.

Experimental apparatus

The experiments were carried out on U-1 accelerator [4]. Experimental apparatus is presented on Figures 1 and 2 (see, also, [5]). Fig.1 shows configuration of diode. A 1 MV, 5 microsecond pulse from LC-generator is applied to carbon cathode (ø18 cm). An electron beam is extracted from cathode plasma and accelerated in a quasi-planar 6 cm gap to carbon anode. Anode plasma is produced during a pulse as a result of interaction of the beam with the anode surface.

An atomic lithium beam with a density less than 10^{12} cm^{-3}, produced by laser evaporation of a *Li*-target, crosses the diode gap with the velocity of 2 cm/μsec. Hydrogen-like level of *Li*-atoms with a principal quantum number $n = 4$ is stepwise excited (*2S-2P-4D*) by two laser beams (Fig.3), which are focused by the lens in the center of the gap at the distance z_* from the cathode. Two flash-lamp-pumped dye-lasers were applied for pumping of *Li*-levels: Oxazine-17 (λ_1= 670 nm) and Coumarin-1 (λ_2= 460 nm). The hydrogen-like *4D-4F* sublevels are strongly splitted by linear Stark-effect to six components (on the contrary, *2P*-term isn't practically splitted by an electric field). The Coumarin-1 laser excits (Fig.2,a) those of the components which lay within lasing band-width ($\Delta\lambda_2$= 3 nm).

Laser induced fluorescence from the excited volume was imaged by the lens on the input slit of a 0.5-m monochromator. Light was collected from a volume

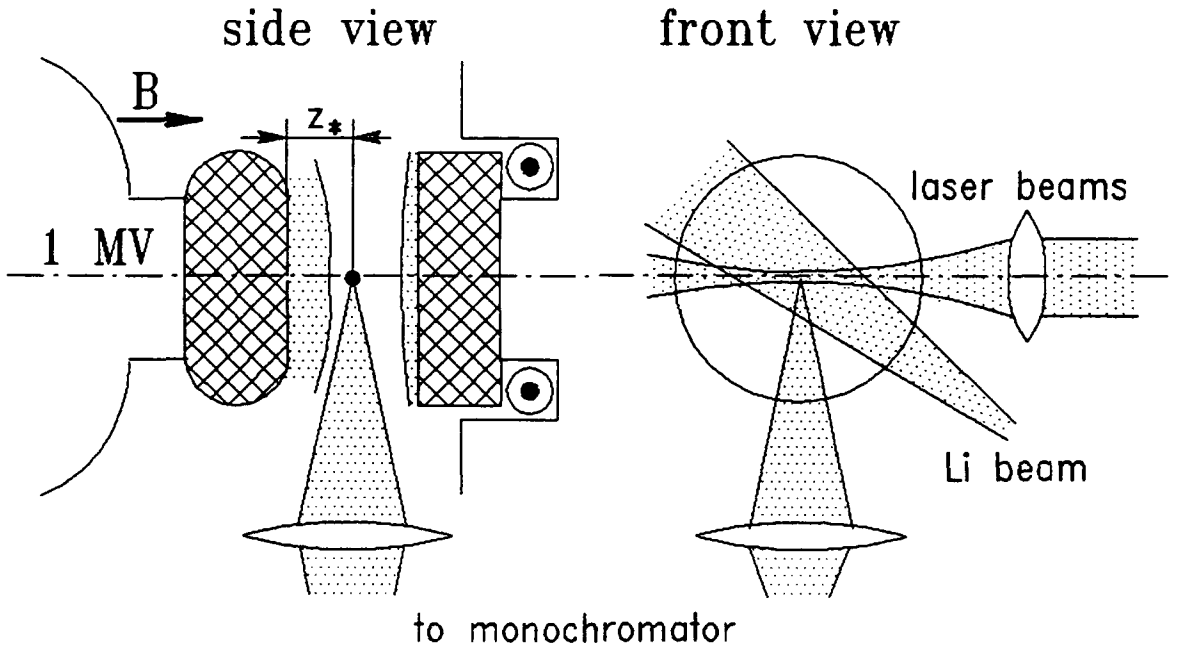

*Fig.*1. Configuration for LIFABS experiments.

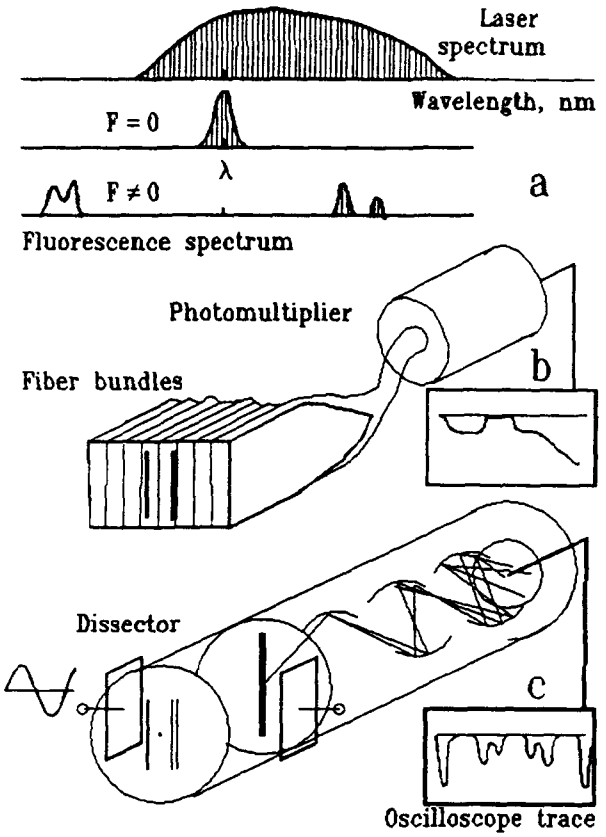

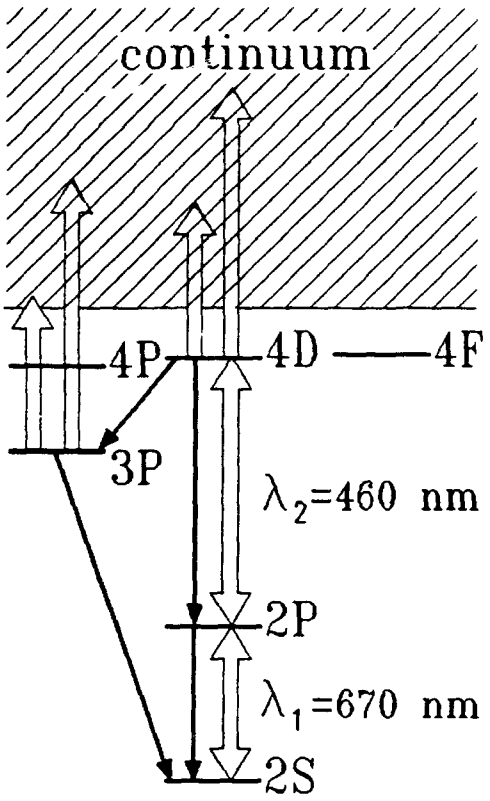

*Fig.*2. Detecting systems.

*Fig.*3. Partial energy level diagram of *LiI*.

of 4 mm long and 1 mm diameter. For recording the laser induce fluorescence two detecting systems at the output of the monochromator were used. In the first case (Fig.2,b), a spectrum was observed by a rectangular fiber-bundle array. Each one of the nine bundles in the array transmitted the light to a photomultiplier tube. The spectral windows observed by the fiber bundles were each 0.25 nm wide. All the signals were recorded by digitizers.

In the second case, the spectrum was detected by a dissector (Fig.2,c). The monochromator output was imaged on the photocathode of the dissector and converted to photoelectrons. The electron image was scanned by sinusoidal deflecting voltage across the dissector slit and recorded by digitizer. The dissector permits to detect at each moment only one wavelength. The value of the electric field *F* can be inferred from the distance between the splitted components. Calculated spectra for the lithium line at a focal plate of the monochromator vs electric field strength are shown in Fig.4.

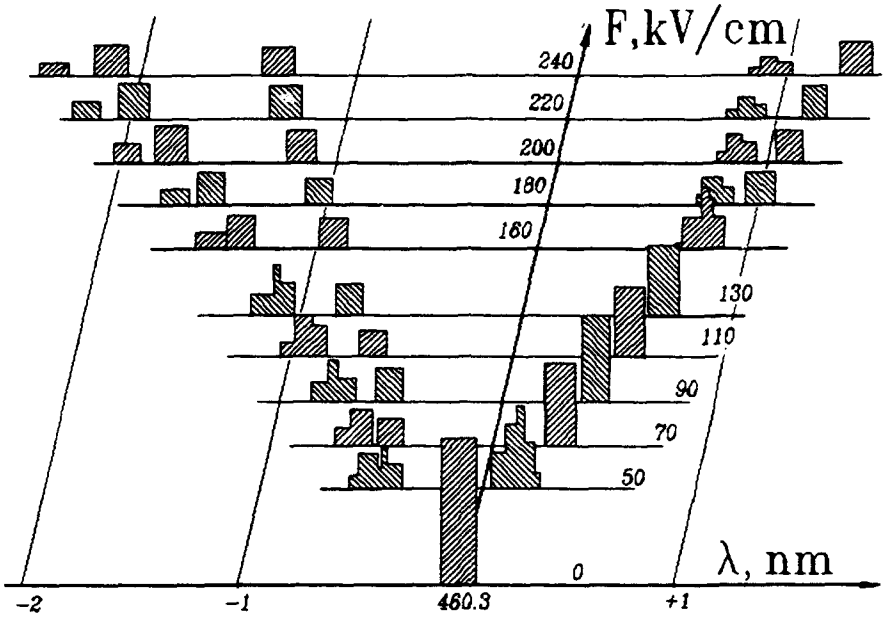

*Fig.*4. Calculated Stark spectra of the *LiI* vs electric field strength. Input slit width is equal to 0.2 mm.

Results and Discussion

Fig.5 shows time dependencies of the light detecting by the fiber-bundle system (z_*= 2 cm). When the lithium beam wasn't injected in the diode, self-luminosity spectrum (continuum) from the gap was detected. No any emission from the volume during the most part of a pulse was observed, and only at the end of pulse the luminosity grows abruptly in all the channels (for example, at 662.5 nm). That emission is caused by the cathode plasma expanding. If the lithium beam was injected into the diode gap, but no exciting radiation, in all the channels, except for the central one, the luminosity is just the same as the previous case. In the central channel (the next oscilloscope trace) 2*P*-2*S* fluorescence of lithium atoms (670 nm) is appeared at 1.5 μsec after pulse start and one microsecond later decays before the appearance of a plasma luminosity. The last can be interpreted as the ionization of *Li*-atoms by particles of expanded plasma.

When the lithium beam was excited only by red laser radiation (Fig.5,b), as it was expected, the red fluorescence of the lithium is unshifted and detected only in the central channel both before and after the diode voltage applying. When the beam was excited by the radiation of both lasers, the blue fluorescence in the central channel disappears abruptly after the voltage

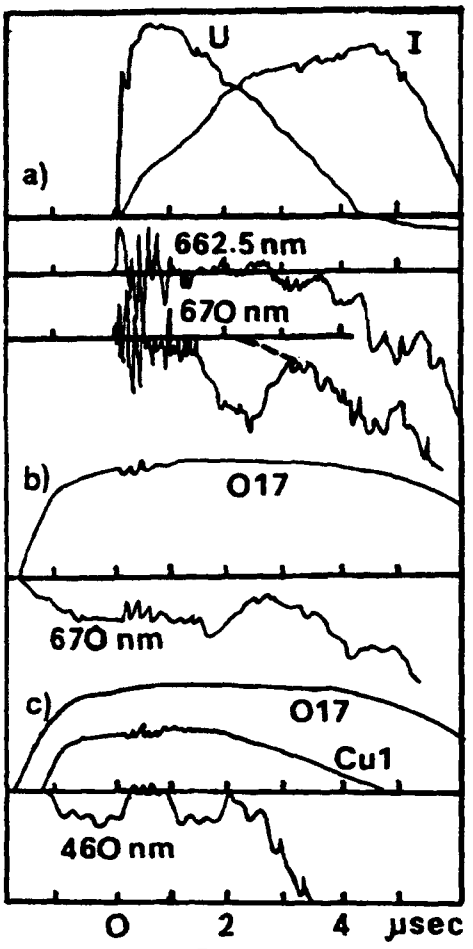

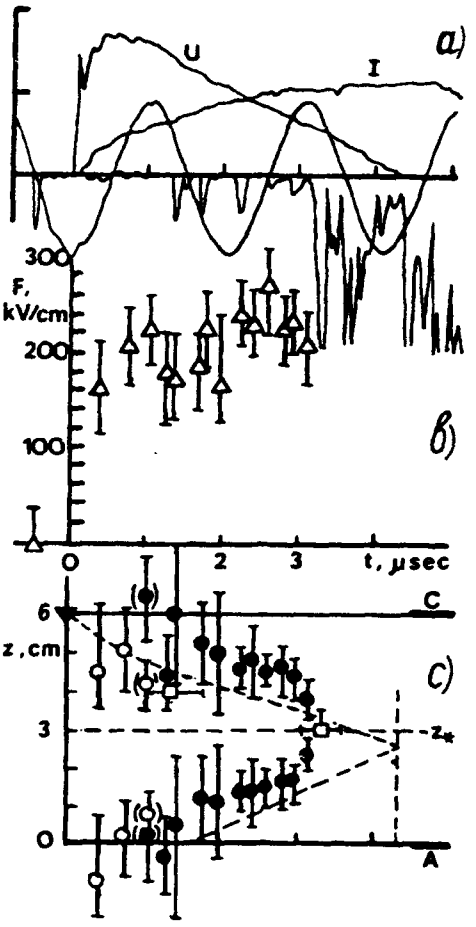

*Fig.*5. Signals recorded with the fiber-bundle system: a) no laser excitation: λ = 662.5 nm - self-luminisity from the diode gap; λ = 670 nm - emission of the *Li*-beam from the gap; b) the resonance fluorescence of the *Li*-beam under excitation by the Oxazine-17 laser only; c) *4D-2P* fluorescence of the *Li*-beam under full excitation. *U* - diode voltage (1 MV), *I* - beam current (50 kA).

*Fig.*6. a) a dissector trace of the 460 nm fluorescence for z_* = 3cm, sinusoid is sweeping voltage applied to the dissector plates; b) Electric field strength in the diode vs time; c) reconstruction of the emissive plasma-boundaries position.

applying (now it appears in other channels) and reinstate again in 1.5 μsec (Fig.5,c). The disappearance is due to Stark shift. The second appearance of unshifted blue line means unambiguously that the electric field strength in a volume under study becomes equal to zero. In other words, at this moment the emissive boundary of the expanding plasma reaches the volume.

In Fig.6,a a blue fluorescence signal taken with the dissector is shown for z_* = 3 cm. Fig.6,b shows the electric field strength value inferred from the dissector traces of 5 identical shots. The value of electric field slightly grows to the end of a pulse and is about 250 kV/cm. The bars are

mainly determined by systematic errors connected with the 50-nanosecond indefiniteness of a temporal synchronization of digitizers being used. Consequently, in principle, this error can be canceled.

Using these results one can determine the location of the emissive boundaries of the cathode and the anode plasmas by means of such a procedure. For the certain time from the values of voltage and current in the diode using the Child-Langmuir law an effective gap and an electric field distribution can be inferred. Comparing experimental and calculated electric field values, locations of the emissive boundaries can be reconstructed (Fig.6,c). In this calculations we tested both electron and bipolar regimes. In the first case the results can be applied only for the time less than 1 μsec and denoted with the light circles. The light squares show the time of appearance of emissive boundary determined from previous measurements with the fiber bundles. Taking into account that the experimental errors are systematic, we can draw the broken lines as the emissive boundaries. One can argued that the anode plasma is produced not later than in 2 μsec. The relative velocity of the cathode and anode plasmas is close to 1.5 cm/μsec.

Summary

We have carried out direct measurements of the local electric field strength in the diode of a 100-kJ microsecond electron accelerator by LIFABS-method. A dynamics of the electric-field-excluding-plasma boundaries is reconstructed from the experimental data. The experiments show that the Active-Stark-Spectroscopy (LIFABS) method is very reliable, and it can be used widely for electric-field measuring in electron and ion diodes and other high-voltage apparatus.

References

1. *Y.Maron, M.D.Coleman, D.A.Hammer, H.S.Peng.* Phys. Rev. A, 36, 2818 (1987).
2. *Knyazev B.A., Lebedev S.V., Melnikov P.I.* Proc. of 17th Internat. Conf. on Phenomena in Ionized Gases, Budapest, 1985, V.2, P.1008.
3. *Knyazev B.A., Lebedev S.V., Melnikov P.I.* Zhurnal Tekhn. Fiziki, 61, No.3, 6 (1991) (Translated in Soviet Physics JTP)
4. *Chikunov V.V., Knyazev B.A., Koidan V.S., Konyukhov V.V., Lebedev S.V., Mekler K.I., Nikolaev S.V., Shcheglov M.A., Smirnov A.V., Voropaev S.G.* Proc. of 18th Internat. Conf. on Phenomena in Ionized Gases, London, 1987, V.1, P.204.
5. *Chikunov V.V., Knyazev B.A., Melnikov P.I., Nikiforov A.A.* Proc. of 8th Internat Conf. on High-Power Particle Beams, Novosibirsk, 1990, V.1, P.241.

TWO-STAGE DENSE PLASMA HEATING BY 100 kJ E-BEAM

A.V.Burdakov, V.V.Chikunov, A.F.Huber, A.V.Karyukin,
V.S.Koidan, S.V.Lebedev, K.I.Mekler, P.I.Melnikov,
A.A.Nikiforov, V.V.Postupaev, M.A.Shcheglov, S.G.Voropaev

Budker Institute of Nuclear Physics, 630090, Novosibirsk, Russia

ABSTRACT. The experimental results on heating of a dense plasma by an electron beam on the GOL-3 device are presented. The relativistic electron beam is injected into a 7-meter long plasma column of a mirror machine. The beam can transfer about 20-30% of its energy into 1-10 keV plasma electrons due to collective effects. These electrons are slowed down in a 0.5-3 meter long gas cloud of a 10^{16}-10^{17}cm^{-3} density (so-called two-stage heating scheme). The hot electrons ionize this cloud and heat the dense plasma due to binary collisions. The total energy deposited in the cloud is 2-4 times higher than the instantaneous energy content of the lower density homogeneous plasma. Pressure waves were observed in the plasma. The mean energy of the hot electrons was estimated from measured energy deposition along the plasma cloud.

The experiment demonstrates a high efficiency of the two-stage scheme of a dense (10^{16}-10^{17} cm^{-3}) plasma heating.

INTRODUCTION. Powerful relativistic electron beams for a number of years have been used for plasma heating at Budker Institute of Nuclear Physics, Novosibirsk. High efficiency of energy transfer from the beam to the plasma due to collective effects was reached in these experiments (mainly because of the excitation of the Langmuir turbulence). On the GOL-3 device [1] as well as in the experiments of lower scale with nanosecond beams the beam energy loss exceeding 25% is achieved at a plasma density less than 10^{15} cm^{-3} [2-4]. With an increase of plasma density higher than $(3\text{-}5)\cdot10^{15}$ cm^{-3} the beam-plasma energy transfer becomes practically negligible because of collisional dumping of the two-stream instability (see, e.g., [5]).

In order to avoid this density limitation the scheme of so-called "two-stage" heating of a dense plasma has been proposed (see [5,6]). In this scheme the plasma consists of a central region of ~10^{15} cm^{-3} density (where an effective beam-plasma energy transfer takes place) and two adjacent regions with ~10^{17} cm^{-3} plasma. The hot plasma electrons decelerating because of binary collisions heat the dense plasma.

In previous GOL-3 experiments (see, e.g., [1]) thin organic films have been used to imitate dense plasma clouds. In this paper a dense plasma was formed by the pulse gas-puffing.

EXPERIMENTAL PROCEDURE. The description of the GOL-3 machine is given in Refs. [1,7]. The GOL-3 device (Fig.1) consists of the electron beam generator U-3, a plasma chamber inside a 7-m

long solenoid with a homogeneous field of up to 6 T and 12 T in the end mirrors; a 10 MJ capacitor bank for feeding solenoid; control and diagnostic systems. For this experiment fast gas valveshave been installed at 12, 45 and 270 cm distances from the entrance foil.

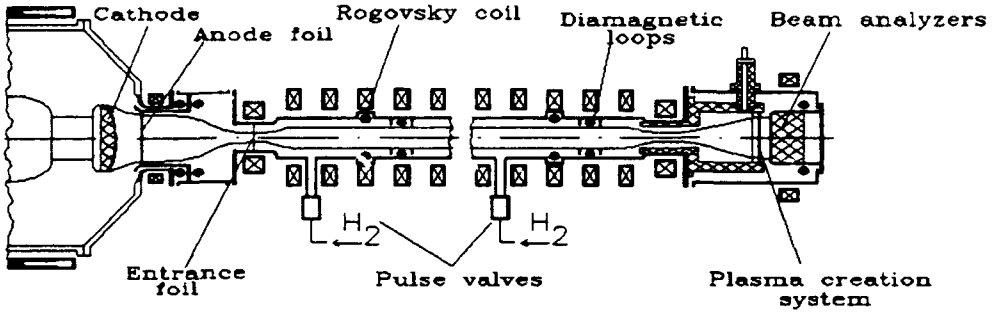

Fig.1. Schematic of GOL-3 experiment.

Initial beam parameters (current, voltage, total energy), output beam energy spectrum and total beam energy loss were measured. For the measurements of parameters of the plasma and gas cloud the 3.39 and 0.63 μm interferometers, diamagnetic loops, detectors of VUV and soft X-ray were used. Hα line profile broadening was measured by a polychromator. Two systems of the Thomson scattering of ruby laser light have been used in these experiments: one for the plasma temperature and density registration and another - for measurements of plasma density profile along the radius (see [8]).

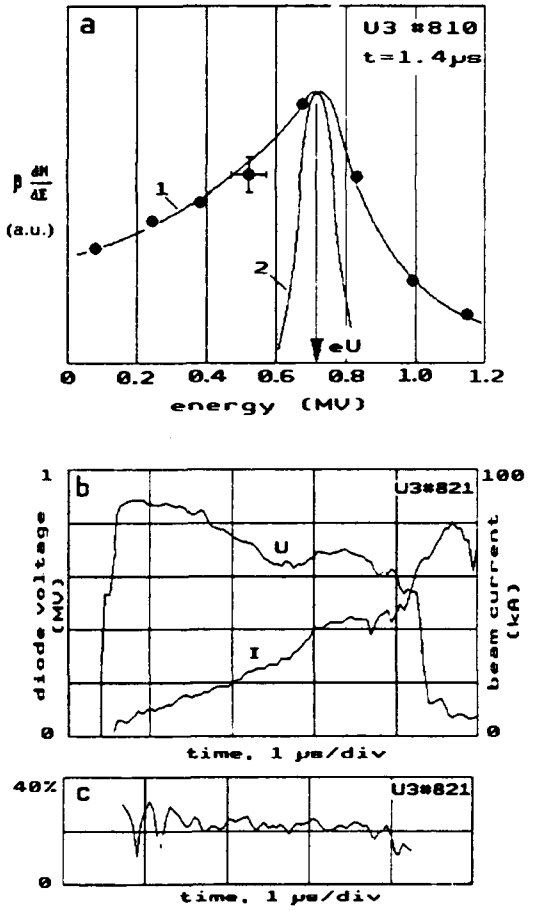

Fig.2. a) E-beam energy spectrum: 1- after passing the plasma, 2- analyzer energy resolution function; b) initial beam parameters; c) relative beam energy losses.

The scenario of the experiment was following. A vacuum chamber was filled in with hydrogen of the concentration corresponding to the required homogeneous plasma density (from 10^{11} to 10^{16} cm^{-3}). The major part of the experiments was performed at a density of homogeneous plasma of $(3\text{-}5)\cdot10^{14}$ cm^{-3} at which the E-beam interacts effectively with the plasma. Upon filling the chamber with hydrogen the magnetic field and then pulse gas valves were switched on. After the formation of preliminary plasma by linear discharge the electron beam (0.8 MeV, 40 kA, 5 μs, 100 kJ, 30 cm^2) was injected into the chamber. The gas cloud length, its density and position could be varied.

E-BEAM RELAXATION. This series of experiments has been carried out at the total beam energy of 70±20 kJ. The beam spectrum changes as a result of collective interaction with the plasma. The substantial broadening of the beam spectrum both to low energies and to energies exceeding the initial energy of the electron beam was observed (Fig.2). In this case, the fraction of electrons with energies exceeding the

initial energy of electron beam is 25% and an increase of their energy with respect to the initial one is up to 200-300 keV. Fig.2c shows the time behaviour of the efficiency of the beam-plasma interaction calculated from this data. This spectrum and energy loss agrees with the results of measurements carried out at the experiments on homogeneous plasma heating (see [1]).

The total beam energy loss in the experiments described is 20-25% that for different shots corresponds to the absolute loss of 10-15 kJ.

HEATING OF HOMOGENEOUS PLASMA. Under the conditions of an optimum beam-plasma interaction the bulk plasma electrons of ~10^{15} cm^{-3} density are heated up to the temperature of 1 keV in the region of maximum energy deposition. A plasma energy content can reach 3 kJ that is ~5% of the beam total energy. In addition, there is a group of hot electrons which possess a substantial fraction of energy lost by the beam. According to X-ray data the characteristic energy of these electrons is ~10 keV and their instantaneous density at the end of heating pulse is a few percent of the plasma density, that is favourable for further development of the two-stage heating scheme.

HEATING OF DENSE GAS CLOUD. The effect of two-stage heating of the gas bunch is illustrated by Fig.3. The initial gas density distribution is also shown in the Figure. The plasma pressure nT at the point z=40 cm (near the maximum of cloud density) becomes 3-4 times higher compared to that of homogeneous plasma. With the cloud length of ~50 cm the pressure achieves its maximum of nT=2.7·10^{18} eV/cm^3 at local plasma density of ~2 10^{16} cm^{-3}.

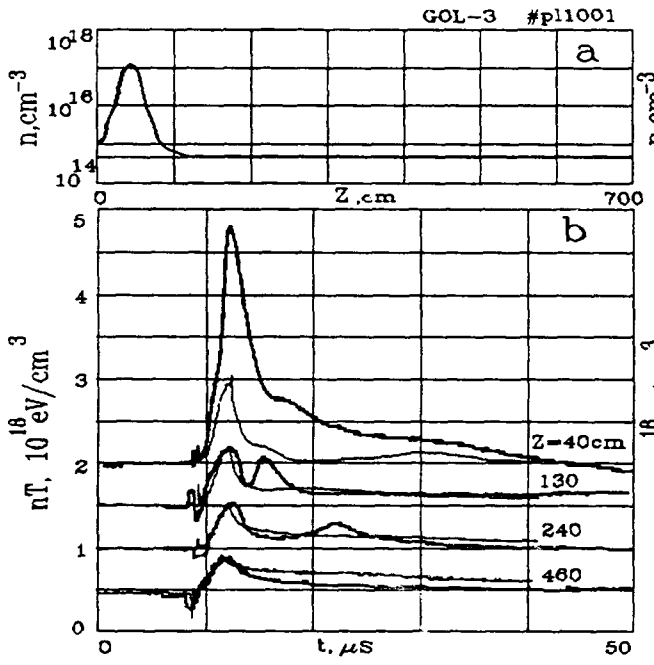

Fig.3. a) hydrogen atomic density distribution over the device length for short cloud; b) plasma pressure over the plasma column length. Thin line marks the case of injection into homogeneous plasma.

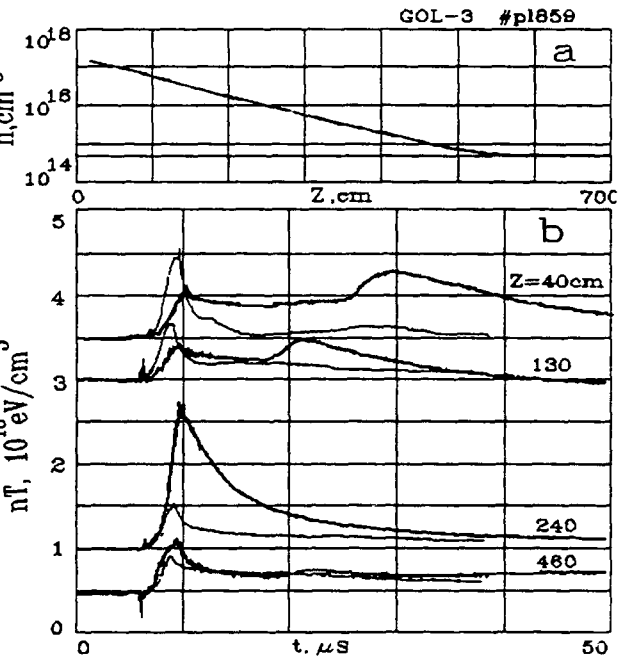

Fig.4. a) hydrogen atomic density distribution over the device length for long cloud; b) plasma pressure over the plasma column length. Thin line marks the case of injection into homogeneous plasma.

With the change of the initial cloud length the region of maximum pressure follows the cloud boundary (Fig.4). The plasma pressure deep in the cloud is lower but always it exceeds substantially the pressure obtained with the direct beam-plasma interaction at the cloud density. A substantial increase of plasma cooling time deep in the cloud is also observed. This is apparently related to a decrease of electron thermal conductivity to the ends because of the plasma density growth and decreasing of its temperature.

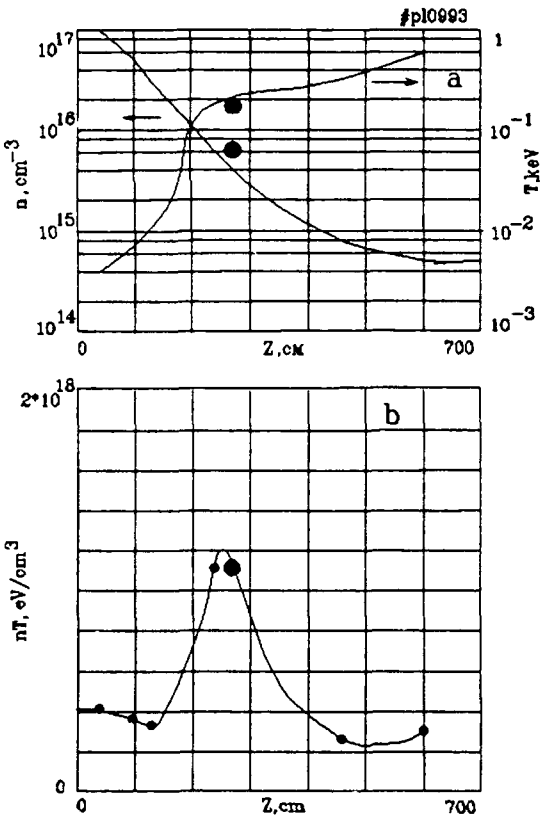

Fig.5. Axial density, temperature and plasma pressure distributions. Dots - Thomson scattering data.

Fig.5 shows the plasma parameters both in the dense bunch and homogeneous plasma obtained from the diamagnetic and Thomson scattering measurements. For the given case at the point of laser measurements (z=270 cm) the peak electron temperature T_e reaches ~0.2 keV at $6 \cdot 10^{15}$ cm^{-3} density. Changing the initial density distribution the electron temperature can be obtained from 0.1 to 0.3 keV with 10^{16} cm^{-3} to $3.5 \cdot 10^{15}$ cm^{-3} density in this point. The electron and ion temperatures are supposed to be equal in the denser cloud regions with $n_e > 10^{16}$ cm^{-3}.

The background plasma density was also varied. If it exceeds 10^{15} cm^{-3}, the energy transfer to the cloud sharply falls down due to the decrease of the efficiency of beam interaction with the background plasma.

When the initial cloud fills in a substantial part of the chamber the region of effective interaction becomes small. The heating efficiency falls down and consequently, the lower fraction of the beam energy is transferred to the cloud by the hot plasma electrons.

ABSORPTION OF FAST ELECTRONS IN THE CLOUD. The results of diamagnetic measurements were used for determination of a released energy distribution along the cloud depth. Fig.6 shows the dependence of energy per atom ($E_{at}+E_i$) on nl, where l is a distance from the measurement point to the cloud boundary. The ionization cost for hydrogen molecule E_i is taken into account. The calculated curve for absorption of plasma electrons with a temperature of 1 keV and an energy content of 2 kJ is also given here (the calculations were based on [8]). The energy deposition can not be explained only by deceleration of the thermal electrons and another source of heating should be brought into consideration - suprathermal ("fast") electrons. Fig.6 shows also the results of the model calculations of two-component electron distribution (with components 1 keV, 2 kJ and 10 keV, 5 kJ). The presence of the suprathermal electrons provides main energy deposition in the cloud depth. A part of the hot electrons penetrates through

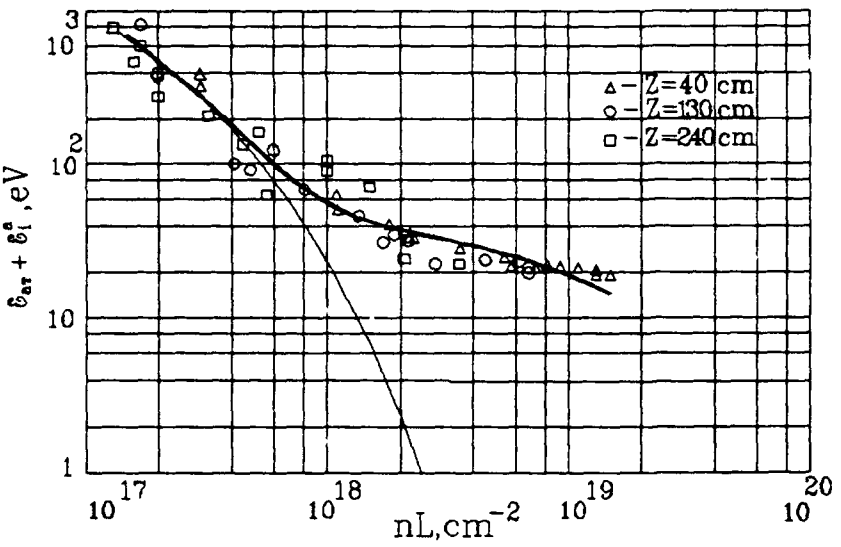

Fig.6. Energy deposition in the dense plasma cloud.

the whole cloud loosing their energy and then they could be either absorbed in the entrance foil or reflected from the magnetic mirror.

The upper limit of the suprathermal electrons energy E_f estimated from energy balance is ~20 keV. In spite of the roughness of this estimate applied to the flux of electrons having wide energy spectrum it gives the reference point for optimizing the cloud parameters since the main fraction of the energy should be transferred by electrons with energies lower or of the order of that value.

The density of 10-20 keV electrons n_f is estimated to be 10^{13} cm^{-3} from diamagnetic measurements. An energy deposited by the fast electrons remains in the cloud during beam injection τ_b because the thermal losses from the cloud are negligible. Then, the relation should be satisfied:

$$n_f E_f L/t_f = \int(3/2\ T + E_i)\ dl/t_b,$$

where t_f is lifetime of the fast electrons in the trap with length L. According to this estimate the lifetime of fast electrons is 0.14 μs. This time should be equal to the transit time of fast electrons.

ENERGY BALANCE. Let us consider an energy balance for one shot. The initial beam energy is 77 kJ and total beam energy loss is 10-15 kJ. The total energy deposition in the plasma and cloud is 5.6±0.5 kJ. The homogeneous plasma with $5 \cdot 10^{14}$ cm^{-3} density contains about 0.9 kJ of this energy, in the dense bunch with $n \sim 10^{17}$ cm^{-3} there is 3±0.2 kJ and the remainder is transferred to a plasma of intermediate density. That means that a substantial part of the energy lost by the beam leaves the trap during the beam pulse through the output mirror without dense plasma bunch.

DYNAMICS OF DENSE PLASMA BUNCH. The expansion rate of the gas cloud substantially changes with the start of heating. A complex picture of the plasma flow and pressure waves generation with the secondary maxima on the diamagnetic signals is observed after the beam injection end (Figs.3,4). The features of VUV, SXR, Hα intensity and Hα broadening are also observed when pressure waves arrive at the measurement points. The locations of heat waves generation and their propagation velocities can be found by varying operational regimes.

Analysis of experimental data shows that several waves are generated in the dense plasma. Two waves propagate from the region with the peak pressure, one into the cloud depth (toward increasing

density) and other into the region of homogeneous plasma (toward dropping density). One more wave moves from the device entrance into the dense plasma.

The heat wave velocity obtained from the diamagnetic signals is in good agreement with that of ion sound.

CONCLUSION. The feasibility of the two-stage heating of ~10^{17} cm^{-3} plasma has been experimentally demonstrated in the experiments with the dense plasma bunches on the GOL-3 device. The beam energy losses in these experiments were ~20% as a result of interaction with the low density plasma. About 10% of the beam initial energy is deposited into the dense plasma clouds. The dense plasma heating is maintained both by Maxwellian electrons with sub-keV temperature and the hot electrons with the characteristic energy of ~10 keV. The gas-dynamic motion of heated dense plasma is observed.

REFERENCES

1. *Arzhannikov A.V., Burdakov A.V., Chikunov V.V. et al.* Proc. 8th Intern. Conf. on High-Power Particle Beams, Novosibirsk, 1990, 1, p.14.

2. *Arzhannikov A.V., Burdakov A.V., Kapitonov V.A. et al.* Plasma Physics and Contr. Fusion (Proc. 15th Europ. Conf., Dubrovnik, 1988), 30, p.1571.

3. *Kandaurov I.V., Kruglyakov Eh.P., Losev M.V. et al.* Proc. 8th Intern. Conf. on High-Power Particle Beams, Novosibirsk, 1990, 1, p.233.

4. *Sunka P.* Proc. 16th Intern. Conf. on Phenomena in Ionized Gases, Dusseldorf, 1983, Inv. Papers, p.232.

5. *Ryutov D.D.* Physics of Alternative Magnetic Confinement Schemes (Proc. 8th Intern. School of Plasma Physics). - Varenna, 1990 - p.1.

6. *Arzhannikov A.V., Breizman B.N., Burdakov A.V. et al.* Plasma Physics and Contr. Nucl. Fusion Res. (Proc. 7th Intern. Conf., Innsbruck, 1978) - IAEA, Vienna, 1979. - 2, p.623.

7. *Arzhannikov A.V., Burdakov A.V., Chikunov V.V. et al.* - this conference.

8. *Burdakov A.V., Voropaev S.G., Huber A.F. et al.* Preprint INP 92-12, Novosibirsk, 1992 - *in Russian.*

SOFT X-RAY MEASUREMENTS OF μS-E-BEAM-HEATED PLASMA

A.V.Burdakov, V.V.Postupaev
Budker Institute of Nuclear Physics, Novosibirsk 630090, Russia
V.Piffl
Institute of Plasma Physics, Prague 18211, CSFR

ABSTRACT. The soft X-ray and VUV measurements on the GOL-3 device are described. The region of plasma VUV emission is shown to coincide with the calculated E-beam cross-section. This indicates the beam stability during its pass through the long magnetized plasma column. The data on plasma radiative loss in different spectral ranges is presented. The suprathermal electrons with average energy above 10 keV are shown to exist in plasma. The power of soft X-ray emission from the bulk plasma is estimated.

1. INTRODUCTION.

The experiments on plasma heating by a 100 kJ microsecond relativistic electron beam are carried out on GOL-3 device at the Budker Institute of Nuclear Physics, Novosibirsk. The beam energy transfer to the plasma inside a long solenoid with a magnetic field up to 6 T occurs due to collective effects. Basic experimental results are presented in [1,2].

The diagnostics of soft X-ray (SXR) and vacuum ultraviolet (VUV) emission are considered traditionally as an important tool in experiments on beam-plasma interaction. An interest to the plasma emission measurements is also raised by an appearance of high-energy suprathermal electrons in a plasma. These electrons with energies ranging from a few keV to tens keV are shown to be generated in a collective beam-plasma interaction both by theory and several experiments with nanosecond E-beams.

In this paper the SXR and VUV diagnostics of the 1st stage GOL-3 device are described [1-3]. The main tasks for diagnostics mentioned are: the measurament of the beam position and stability during its injection in gas and plasma, the determination of the parameters of the suprathermal electrons (density, average energy), the Maxwellian (bulk) plasma temperature determination, the estimation of the plasma radiative loss in the VUV and shorter ranges.

2. GOL-3 DEVICE.

Layout of the GOL-3 experiment is shown in Fig.1. The more detailed description of the device parameters and operation regimes is given in Refs. [1,2]. During the experiments discussed the basic

parameters were following: magnetic field 5.5 T in solenoid and 11 T in the end mirrors, preliminary (target) plasma column length 7 m and diameter 8 cm, electron beam energy 0.8-0.9 MeV, its current density in a plasma ~ 1 kA/cm^2, pulse duration ~ 4 μs with typical energy content 50-70 kJ, beam diameter in a plasma 6 cm. In the case of optimal interaction efficiency the plasma density was (0.5-1)·10^{15} cm^{-3}. The beam injection in hydrogen without a preionization was also possible. In this case the gas ionization and plasma creation were provided by E-beam itself.

Basic experimental results from [1,2] are briefly mentioned below for this regime. The electron beam loss is up to 25% of its initial energy due to the collective interaction. The plasma final energy content could raise to 5% of the beam energy content. The energy release is nonuniform over the plasma length with its maximum in the vicinity of the input foil. The mean energy of an e-i pair is 0.7-0.8 keV at a ~ 1 m distance from the input foil.

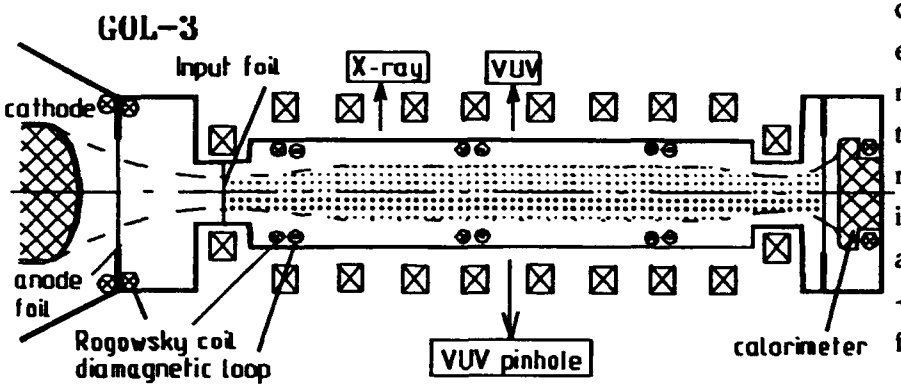

Fig.1. Layout of the GOL-3 device.

3. DETECTORS.

Short lifetime of a hot plasma in a pulsed power experiments leads to the use of filtering technique [4] for emission spectrum analysis. The experimental environment includes the high-power hard bremsstrahlung of E-beam itself from a plasma and exit beam receiver.

The silicon surface-barrier detectors were used for registration the soft X-ray plasma emission within the interval 0.5-10 keV. The detector depth was chosen to be 200 μm for decreasing the sensitivity to hard bremsstrahlung. Two detectors installed in GOL-3 enabled the measurements of 8 signals with different filters. Different filter sets were used with filters made of a 8 μm - 2 mm beryllium, 0.75 and 1.5 μm aluminum, 0.25 μm silver, 0.1 - 2 μm plastic filters (with and without opaque covering). These filters cover the cut-off energy interval from tens eV to 6 keV.

The plasma VUV emission was measured by aluminum vacuum photodiodes. Two VUV diagnostics were developed: for the plasma radiative loss spectral power estimate (two 4-channel detectors) and for space-resolved VUV brightness measurements (9-channel pinhole detector). Nitrocellulose filters 0.04-1 μm thick were used for spectral measurements.

The determination of the blackbody VUV emission power from the surface of the entrance foil was performed (like in [5]). This allows to estimate the power flux from a plasma to the edge surface.

The details of the diagnostics described can be found in [6]. The detectors for SXR and VUV spectral measurements were manufactured and tested in IPP Prague, others - in INP Novosibirsk.

4. PLASMA EMISSION.

The plasma emission spectrum includes the bremsstrahlung, continuous part of radiation caused by recombination and line emission. The ionization state of impurities should be known for calculating the emission spectrum. Such calculations were made in [7] for Maxwellian plasma and nonstationary corona model with oxygen impurity taken into consideration. In our case the lifetime of a 0.1-1 keV, 10^{15} cm^{-3} plasma is comparable with the time of impurities' ionization state relaxation to the final one. Detailed consideration of the role of individual spectrum components under the conditions of GOL-3 experiment can be found in [6].

The continuum above the ionization thresholds of low-Z impurities enables the plasma temperature determination from the signal amplitude dependence on the filter thickness. In our particular case an expected sub-keV temperature of a plasma can be calculated from SXR emission in photon energy range above 1 keV. In the VUV region the radiation power is determined by numerous lines which cannot be resolved with filtering technique, so VUV data is used for the plasma emission power estimates.

The simulations discussed deals with a thermalized plasma. The electron distribution function of the beam-heated plasma is known to be strongly non-Maxwellian (see, e.g., [8]). The electrons with energies up to several hundreds of eV should be thermalized during the GOL-3 shot. More energetic suprathermal electrons remain non-Maxwellian and special simulations are required to estimate their influence on the plasma emission spectrum.

5. SOFT X-RAY MEASUREMENTS.

Soft X-ray detectors are placed at a distance of 140 cm from the beam input foil. Their typical signals are shown in Fig.2. The growth of output voltage is seen till the beam injection end. The signals of 120 μm Be and thicker channels (filter cut-off energies above 2 keV) are determined by the high-energy "tails" of electron distribution. The mean energy of these electrons is at least 10 keV and their density is several percent of plasma one - see Fig.3. Open circles in this Figure taken from shot with other filter set at lower interaction efficiency (points are scaled by amplitude in the 120 μm Be point). The signal amplitude dependence on the filter thickness in this spectral interval remains the same during the heating pulse. That points to insignificant variation of energy distribution of hot electrons during the shot. Assuming that the signal of 120 μm Be-filtered channel (see Fig.2) corresponds to the time dependence of suprathermal electrons' density. The density of these

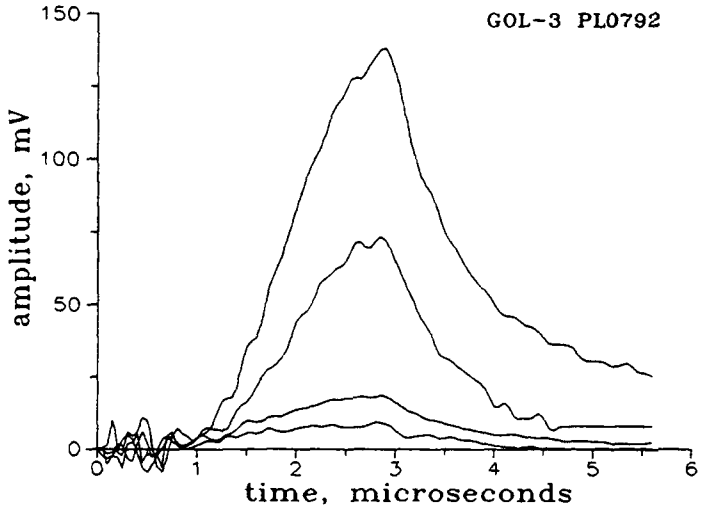

Fig.2. Soft X-ray signals. Filters: 1.8 μm mylar, 1.5 μm Al, 8 and 120 μm Be. Plasma density $1 \cdot 10^{15}$ cm^{-3}, beam duration 3 μs.

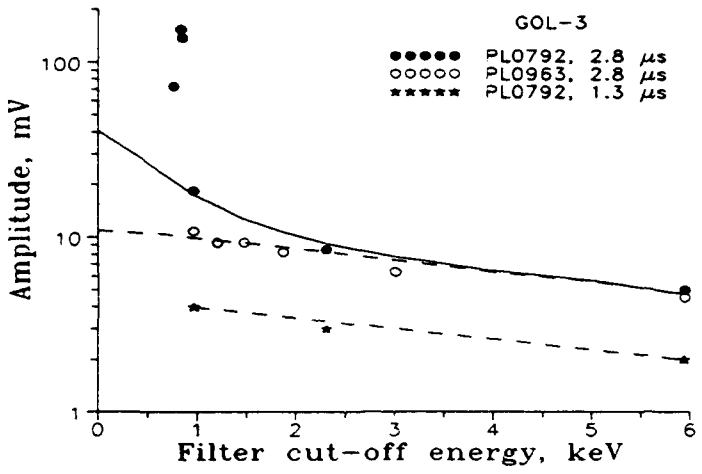

Fig.3. Simulation of attenuation of the plasma SXR emission by filters. Closed circles and stars for signals from Fig.2, open circles for other shot with less heating efficiency. The calculation was made for Z_{eff}=1.5, 1.0 10^{13} cm^{-3}, 0.6 keV bulk plasma and 7 10^{13} cm^{-3}, 10 keV hot electrons. Dashed lines - radiation of hot electrons only, solid line - the same with the bulk plasma radiation.

electrons averaged over the shot duration is approximately half of its maximum, which is shown in Fig.3.

The instantaneous concentration of suprathermal electrons in plasma is much less than total amount of such electrons generated during the heating pulse due to non-classical nature of their scattering (see [2]) and short transit time. That means that hot electrons can receive a major part of the energy, lost by the beam. Such a possibility is favorable for the further development of the so-called "two-stage" scheme of dense plasma heating (see, e.g., [9]).

The signal of a 8 μm Be-filtered channel corresponds to the expected one from hot electrons (see Fig.3) during the first half of heating pulse. Then some additional signal on this channel appears and at the E-beam injection end this additional output corresponds with the expected one from bulk plasma with the parameters, taken from other diagnostics. The signals of the channels with low-energy threshold softer then 0.8 keV are heavily higher and are almost determined by low-Z impurities' line emission. The rough estimate of such ions concentration in the plasma is 2-3%.

The calculations above were done under the assumption of radial plasma uniformity. Nevertheless, the regions with enhanced X-ray brightness are shown to exist with the characteristic radial scale of few mm or even less. Their existence can be caused by experimentally observed microstructure of the injected E-beam (see, e.g., [2]).

Soft X-ray measurements were also been done during the beam injection into nonionized hydrogen. The interaction macroscopic parameters were roughly the same as in foreplasma case [1,2], but the measured emission power above 1 keV was sufficiently higher and has worse stability. This indicates on higher density of hot electrons in the plasma. The reason for more efficient hot electrons generation in this case could possibly be the higher level of Langmuir turbulence during the initial period of the E-beam injection when plasma density still stays small.

6. VACUUM ULTRAVIOLET MEASUREMENTS.

The signals of filtered VUV detectors placed at 250 cm distance from the beam injection point are shown in Fig.4. The typical amplitude dependence on the nitrocellulose filter thickness is shown in Fig.5. This dependence well agrees with the calculated in [7] attenuation by filters (calculations were made for

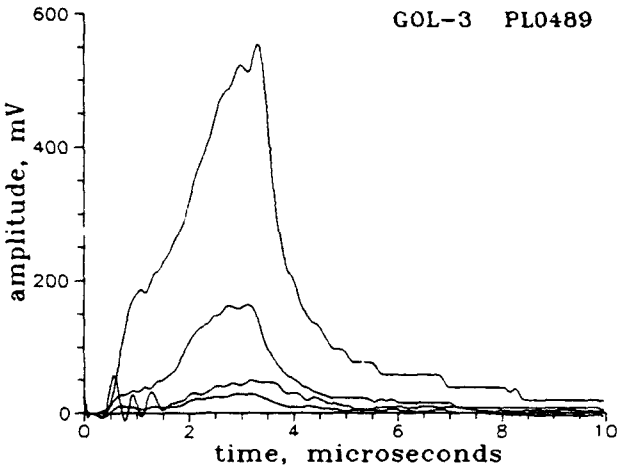

Fig.4. Signals of VUV detector. Filters: 0 (x0.1), 0.045, 0.08, 0.093 μm of nitrocellulose.

Maxwellian plasma with oxygen impurity), what indicates that signals are mainly determined by line emission.

The plasma VUV emission power in different spectral intervals can be determined from Fig.5. The existence of two spectral "windows" should be taken into account for the channels with thinner filters due to nitrocellulose transparency increasing below 10 eV. Rough estimates give the peak radiated power to be 2 kW/cm^3 in 10-25 eV interval and ~ 1 kW/cm^3 from 25 to 100 eV. This data seems to be still preliminary because of the large spectral width of channels and of the sensitivity dependence on the energies of the particular bright lines. The radiative losses are considerably less than the energy flux from a plasma to the device ends.

7. SPACE-RESOLVING MEASUREMENTS.

The signals of bare pinhole VUV detector placed also at a distance of 250 cm from the input foil in general are similar to those shown in Fig.4. The amplitude dependence on the channel position is shown in Fig.6 with two calculated curves: for the uniform plasma brightness in the E-beam cross-section region and for some increase in VUV emission from plasma periphery. Various profiles of VUV brightness have been observed during the experiments, including both increasing and decreasing from the axis to periphery. In general, it is the outcome of the line emission nature of VUV radiation from the plasma.

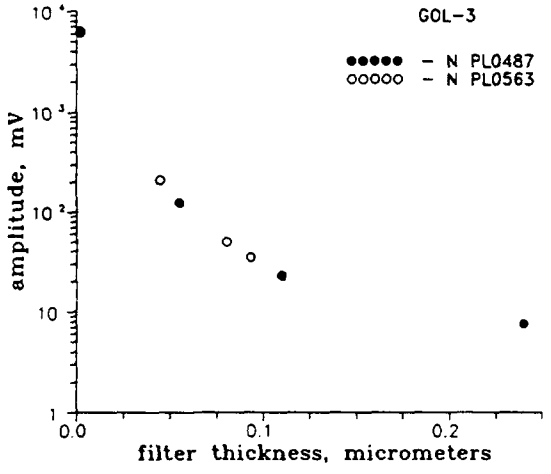

Fig.5. VUV signal amplitude dependence on the filter thickness in heating maximum. Two shots with different filter sets are presented.

Taking into account the absence of information about VUV emission spectrum in pinhole measurements, the data in Fig.6 allows to conclude that there is no noticeable VUV brightness of the plasma regions outside the expected E-beam cross-section. The number of channels with nonzero signal changes proportionally to the injected beam diameter.

Other result of pinhole measurements is the absence of the macroscopic asymmetry and position misplacement of the beam passing through the vacuum chamber in most cases (it should be mentioned that the beam current is sufficiently higher than vacuum current, but it is usually 65-80%

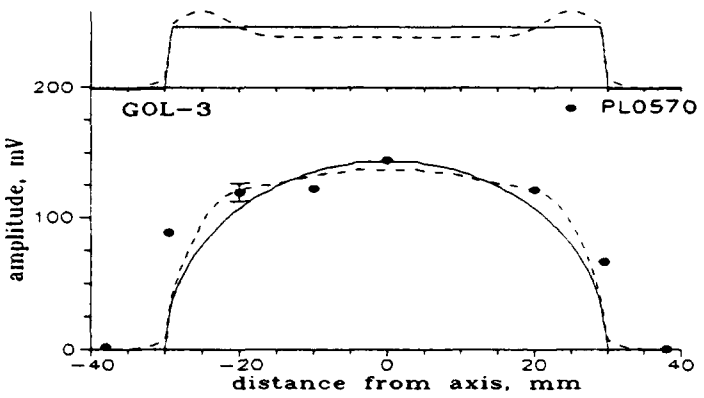

Fig.6. Amplitude of the pinhole signals. Space resolution of each channel is 8 mm axial and 6 mm radial. Solid line - for uniform plasma brightness inside the beam cross section, dashed line - with extra peripheral brightness (corresponding profiles are shown at the top of the Figure).

compensated by plasma return current). In special experiments with the E-beam injection in the nonionized hydrogen with the density below 10^{14} cm^{-3} the indications of the macroscopic beam stability loss were observed. The sequential fast growth of the pinhole signals from the peripheral channels from one side of the plasma center occurs during the final part of the beam pulse. Some macroscopic features (asymmetric imprints on the exit beam receiver and some beam traces inside the vacuum chamber) are also evidenced the beam stability loss.

8. CONCLUSIONS.

1. The VUV emission intensity outside the beam cross-section is negligible. This indicates both the E-beam macroscopic stability during its passing through the plasma and the absence of the noticeable plasma heating due to energy transport to this region by Langmuir turbulence.

2. The plasma emission spectrum was measured in soft X-ray and VUV ranges by filtering technique. The total radiated power is much less than the plasma energy losses to the device ends.

3. The fraction of suprathermal electrons was registered in the plasma with the mean energy exceeding 10 keV and density of a few percent of plasma one (with n_e~10^{15} cm^{-3}).

4. The measured power of the plasma SXR emission is in a reasonable agreement with the expected one from plasma with the parameters obtained by other diagnostics.

9. ACKNOWLEDGEMENT.

The authors are deeply indebted to Drs. V.Babicky and J.Raus of IPP Prague for their collaboration in the experiments and for offering the computer code for VUV plasma emission modeling.

REFERENCES

1. *Arzhannikov A.V. et al.* Proc. 8th Intern. Conf. on High-Power Particle Beams, Novosibirsk, 1, 14, 1990.
2. *Arzhannikov A.V. et al.* - this conference
3. *Burdakov A.V. et al.* Proc. 19th Intern. Conf. on Phenomena in Ionized Gases, Belgrade, 2, 318, 1989.
4. *Jahoda F.C. et al.* Phys. Rev., 119, 843, 1960.
5. *Babykin M.V. et al.* Sov. J. Plasma Physics, 8, 415, 1982 - *in Russian.*
6. *Burdakov A.V. et al.* Preprint INP 92-24, Novosibirsk, 1992 - *in Russian.*
7. *Raus J., Babicky V.* - Czech. J. Phys., 42, 395, 1992.
8. *Arzhannikov A.V. et al.* Proc. 1984 Intern. Conf. on Plasma Physics, Lausanne, Switserland, Invited Papers, 1, 285, 1984.
9. *Ryutov D.D.* Proc. 8th Internat. School of Plasma Physics, Varenna, 1, 1990.

ULTRA-VIOLATE FLASH LAMP ON THE NOBLE GAS DIMERS EXITED BY AN E-BEAM

V.I.Klimov, G.P.Mkheidze,and A.A.Savin

Institute of General Physics, Vavilova 38, 117942 Moscow, Russia

Abstract. We propose an original design of industrial VUV non-coherent sources on the basis of noble gases excited by an e-beam. We have made an analysis of the source efficiency for Ar, Kr and Xe.

Ar, Kr, Xe noble gas dimer lasers were, in fact, the first realization of an eximer laser [1]. The major prerequisite of their design is a well-known fact that when an e-beam interacts with a noble gas excited atoms of high concentration are produced. At higher pressure excited dimer molecules of Ar_2^*, Kr_2^*, Xe_2^* noble gases are efficiently formed. The emission wavelengths radiated by dimer molecules in transitting from an upper electron excited state are in the VUV region and they are 126, 146, and 172nm correspondingly. Effective excitation of noble gas atoms and their rapid association, on the one hand, and high energies of UV radiation quanta, on the other, result in high theoretical values of efficiency η_{in} (0.40, 0.43 and 0.46 respectively), that is confirmed experimentally for emission from smaller (less than $1cm^3$) volumes [1-2].

The proposals to use spontaneous emission of eximer molecules emission excited by an e-beam to produce VUV emission sources appeared as the investigators were disappointed to create highly efficient VUV coherent sources. At present one can consider the problem of producing industrial VUV non-coherent emission sources on the basis of noble gases excited by an e-beam.

The major claims laid to such a source are high values of characteristic efficiencies: 1.The efficiency of energy deposition $\eta_{dep}=W_{dep}/W_b$, where W_b is energy of a beam injected into a gas and W_{dep} is energy transmitted to a gas by a beam. 2.The intrinsic efficiency $\eta_{in}=W_{in}/W_{dep}$, where W_{in} is energy of eximer molecule emission. 3.Extraction efficiency $\eta_{ex}=W_{ex}/W_{in}$, where W_{ex} is energy of emission at the system output.

The attempts to increase the square of the output emitter windows (they should be made of the materials transparent in a VUV region) lead to the problem of window protection from e-beam electrons and e-beam plasma. Below we consider the concept of a UV emitter in which one can be obtain such efficiency values as $\eta_{dep}\times\eta_{in}\times\eta_{ex}\sim 0.2$, that is, 20% of e-beam energy in a diode goes through an outer transparent chamber wall in the form of UV emission, the chamber wall itself being protected from the electron bombardment by a magnetic field.

To solve the problem we worked out a model consisting of the calculations of electron passing through a substance according to the Monte-Carlo method, the calculations of local e-beam plasma kinetics of noble gases, the calculations of a spatial distribution of emitting dimers and the calculations of optical-geometrical emitter parameters.

A coaxial system with inner injection is given in Fig.1. Cathode 1 and anode-foil 2 (Ti, 20μm thick) form a coaxial diode. Chamber wall 3 is transparent for UV emission. Energy W_b of the beam injected into the chamber is partially lost at the ends, chamber walls and in the anode foil. We are interested in the energy equilibrium and the distribution of a specific energy deposition in volume 4, filled by a noble gas, so the energy deposition to gas W_G and losses on the wall W_W and in the foil W_F will further be calculated in relation to energy W_b. The corresponding efficiencies are $\eta_{dep}= W_{dep}/W_b$, $T_W=W_W/W_b$ and

$T_c=W_p/W_b$. The anode radius is 3 cm, the chamber radius is 13cm. The chamber length is 50cm. Constant parameters of the injected beam are: current is 10kA, pulse duration is 50ns, electron energy is 300kev. The azimuth magnetic field B_φ is made by the current flowing along the conductors 2 and 3. The influence of an azimuth magnetic field is presented in Fig.2. for Kr at P=1.5atm. Curve 1 is obtained herewhen a magnetic field is absent; curves 2 and 3 are obtained at B_φ 0.7 and 1.5kGs correspondingly. The curves given clearly demonstrate a significant decrease of a specific energy e-beam deposition to gas in the peripheral chamber region. The efficiency of energy deposition was changed inconsiderably. The matter is that as a magnetic field increased, the coefficient T_w was decreasing (that is, electrons didn't fall on the chamber walls), but the coefficient T_w was rising (since the electrons are "turned" in the magnetic field falling back on the diode surface). Thus the application of a magretic field enables us to redistribute a REB energy deposition from the emitter periphery to its center and so one can protect the transparent chamber walls. Fig.3 shows the dependencies of effectiveness η_{in} on specific energy depositions at different pressure values for Ar and Kr (P=3.5atm) and for Xe (P=0.5atm). The results presented show that high values of η_{in}~0.3-0.35 are obtained for all the noble gases in a wide region of specific energy depositions 10^{-5}-10^{-1} J/cm^3. Energy deposition increase q>0.1J/cm^3 results in effectiveness decrease, this effect being more significant in light noble gases. Such a result was also obtained in works [1-2] in which the calculations were made at q>10^{-2} J/cm^3. This effect is associated with the rise in plasma electron role to quench the excited states as plasma concentration increases. Just the same facts determine the decrease of effectiveness η_{in} when pressure in Xe increases.

The conditions of effective transformation of e-beam energy into non-coherent emission of exited dimers of noble gases given above correspond to current densities 1-10 ^{2}A/cm ^{2} in the current pulse duration 10^{-7}s. This range is well exploited in the devices of injection gas electronics and such conditions can be made in rather large gas volumes.

In determining the effectiveness of emission extraction it is necessary to know the value of a real spatial angle projected onto the output window for any point of the emitter volume. The results showed that the value of this angle insignificantly depended on R (R is a distance from the diode to the output window) and it was changed from 0.75 near a diode surface to 0.82 near the emitter transparent chamber walls.

The results of emitter effectiveness calculations for different noble gases are shown in Figs.4. Fig.4 shows the dependencies of energy W_{ex} (a dashed line) on coordinate R at 3,5atm for Ar. Number 1 presents curves with the value of magnetic strength B_{φ}=0 and number 2 presents curves with the value of magnetic strength B_{φ}=0.7kGs. Fig.4 shows also the dependencies of energy W_{ex} (a solid line) on coordinate R at 3 atm for Kr and at 1.5atm for Xe. Number 1 and number 2 show these dependencies for Kr and Xe correspondingly.

Thus the given models of calculating REB energy depositions to gas according to the Monte Carlo method and emission energy according to the model of local e-beam plasma kinetics for Ar, Kr and Xe allowed us to calculate total effectiveness of the emitter design proposed and demonstrated its high efficiency.

The modelling of the non-coherent VUV emission on the basis of noble gas dimer molecules excited by REB carried out in this work show the possibility to produce efficient systems with the coefficient of

e-beam energy transformation into the energy of non-coherent VUV emission of the order of ~25%, which can be used in chemical and pharmacological industries and particularly in UV photolitography.

Table 1

Gas	P, atm	W_{dep}, J	η_{dep}	η_{in}	W_{ex}, J	$\eta_{in}\eta_{ex}$
Ar	3.5	117	0.78	0.35	32.1	0.27
Kr	3	121.5	0.81	0.34	30	0.25
Xe	1.5	111	0.74	0.33	26	0.23

Reference

1.Eckstrom D.J., Nakano H.H., Lorents D.C. et al.,J.Appl.Phys.,64, 1679(1988).

2.Eckstrom D.J., Nakano H.H., Lorents D.C. et al.,ibid.,1691.

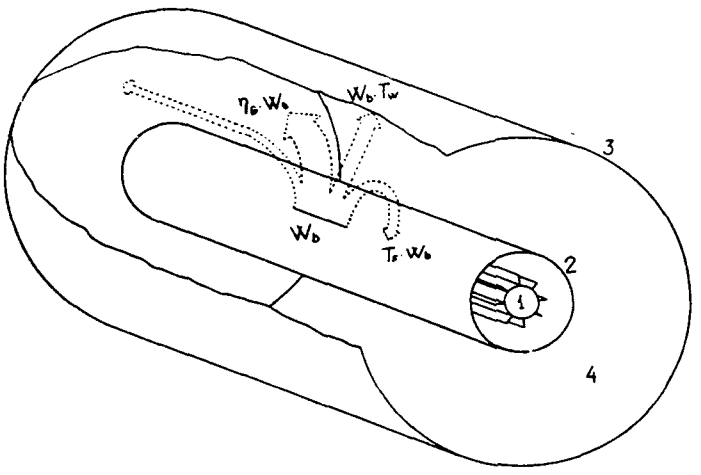

Fig.1. Scheme of the system with inner REB injection.

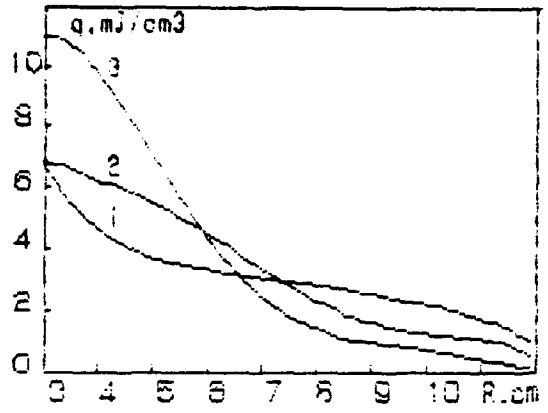

Fig.2. Distribution of a specific energy deposition q(R) on the chamber radius R at different values of a magnetic field B_φ, for krypton at P=1atm. 1-B_φ=0, 2-B =0.7kGs, 3-B =1.5kGs.

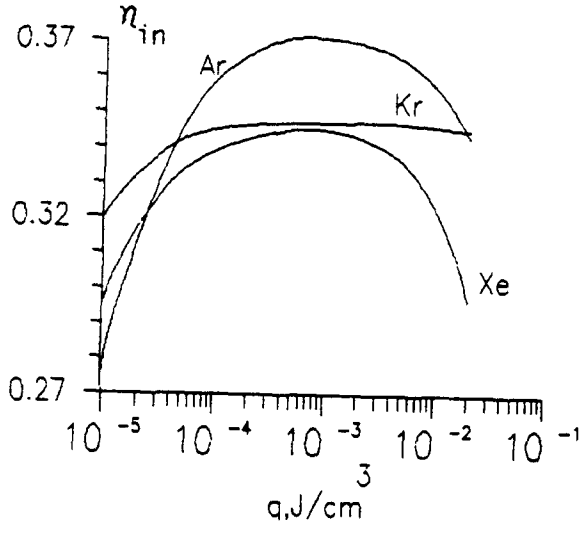

Fig.3. Emission efficiency η_{in} vs specific energy deposition q for argon and krypton (P=3.5atm) and xenon (P=0.5 atm).

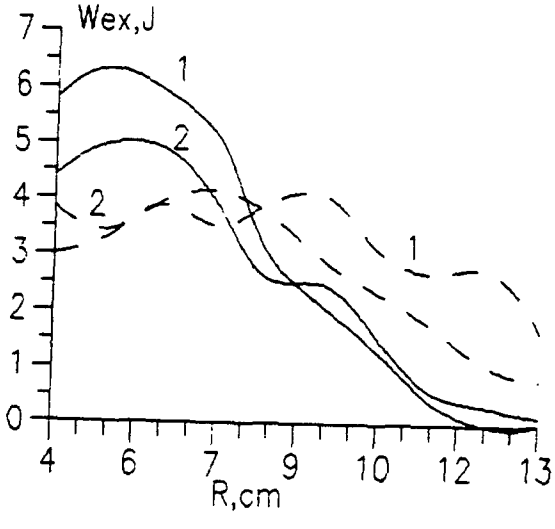

Fig.4. Energy W_{ex} (a solid line) for the emitter filled with argon at P=3.5 atm vs coordinate R. Number 1 shows the case when B_φ=0, number 2 shows the case when B_φ=0.7 kGs. Energy W_{ex} (a dashed line) vs coordinate R. Number 1 presents the curves for krypton (P=3 atm), number 2 presents the curves for xenon (P=1.5atm).

CONDUCTIVITY OF PLASMA CREATED BY REB IN ARGON

V.I.Klimov,G.P.Mkheidze,and A.A.Savin

Institute of General Physics, Vavilov st., 38, 117942 Moscow, Russia

Abstract. On the basis of the experimental data obtained one reconstructs e-beam conductivity of argon plasma. Despite the predictions of simple models temporal dependence is characterized by a slow time of decrease. A model is proposed within which such behaviour of e-beam argon plasma conductivity is explained by the influence of a weak induced electric field (E~90-50V/cm) on kinetic processes after the e-beam current ceasing.

Conductivity of a plasma channel created by a high current relativistic electron beam injected into gas is the most important parameter determining the processes of induced plasma currents generation, ohmic heating of plasma and gas, development of large scale resistive instabilities.

We used the method of plasma conductivity reconstruction proposed by us in [1)]. It has been shown there that a simultaneous distribution measurement of e-beam current and plasma induced current enables us to reconstruct spatial distribution of plasma conductivity and its change in time under certain conditions.

In the experiments performed an e-beam with energy 1.2MeV, e-beam current 7kA, pulse duration FWHM 50ns and average radius 3cm was injected into the chamber with diameter 18cm filled with argon at pressure 175-750Torr. The maximum current density was 0.25kA/cm^2 on

the chamber axis. E-beam current density dynamics $j_b(r,t)$ was registrated by an evacuated current monitor with spatial resolution 1cm. Plasma current density dynamics $j_p(r,t)$ was studied by a monitor [2] which is a maylar foil (20μm) covered on both side by a metal sectioned film (2μm). Such structure is transparent for beam electrons and enables us to register plasma current electrons with spatial resolution 1.5cm. A detailed description of the experimental installation is given in [3]. In the experiments performed the measurements were made at the distance of 15cm from an anode foil.

Fig.1 shows the results of reconstructing conductivity in a drift chamber central region (Δr=1.5cm) on the measured values $j_b(r,t)$ and $j_p(r,t)$ at pressure value 600Torr of argon. It should be noted that temporal behavior of argon e-beam plasma conductivity is highly different from the predictions made on the basis of the simple noble gas e-beam plasma models [4].

Our results show that conductivity peaks at the moment when a REB current pulse (~80ns) ceases and the conductivity decay time is hundreds of nsec. We note that the behavior of conductivity of air and nitrogen e-beam plasma at pressure 175-750Torr demonstrate a rather fast electron recombination. As our experiments showed the time of forming a conducting channel and its decay is 10-20ns at max conductivity values 1-30$m^{-1}\times cm^{-1}$.

Plasma currents induced in argon plasma fell down according to the exponential law $\exp[-(t-t_{max})/\tau_d]$ up the moment when $t-t_{max}\approx$140ns at $\tau_d\approx$120-140ns.

An exponent character of plasma current shows that conductivity is, in fact, constant up to $t-t_{max}\approx$140ns, that is quite clearly seen

from the dependencies given Fig.1. Thus electric fields induced by plasma currents exist in a plasma channel for a quite long period of time and can influence the e-beam plasma kinetics.

To explain the dependences observed we have worked out a model of spatial-temporal kinetics of e-beam plasma in which we solved both the equations for spatial-temporal e-beam plasma kinetics and Maxwell's equation. The effect of heating plasma electrons by plasma current was taken into account in the equation for plasma electron temperature. The processes taken into consideration by the model and the constants of their rates are given in [5]. Fig.2 shows the behavior of plasma electron concentration and their temperature vs time with the heating by plasma current (N_e^*, T_e^*) and without it (N_e, T_e) on the e-beam axis at 600Torr. Fig.3 shows the behavior of plasma conductivities vs time on the e-beam current axis with the heating by plasma current (1) and without it (2) at the same pressure. At such pressure value a field influences the behavior of plasma concentration and its conductivity at the end of the e-beam current activity and after its termination. This happens due to the fact that there is a slowly decreasing electric field in argon plasma even after the e-beam current ceasing. Due to the existence of this field (for example, at 600Torr the value of an electric field varies from 90 to 50V/cm in the time interval $(100\text{-}200)\times10^{-9}$s which is equal to the e-beam activity time), the electron temperature increases by (10-15)% in comparison to the event when the heating by the field is not taken into account. It is this rise in temperature that causes a corresponding increase of electron concentration and plasma conductivity. Let us illustrate the statement made above by using the equation for plasma electron

concentration which has the following form in this time interval

$$dN_e/dt = S(t) + N_e\times\{k_1(T_e)\,[Ar^*] - k_2(T_e)\,[Ar_2^+] + k_3(T_e)\,[Ar_2^*] - k_5(T_e)\,[Ar_3^+]\} + k_4\,[Ar_3^+]^2 + k_6\,[Ar_2^*]^2 + k_7\,[Ar^*]\,[Ar_2^*].$$

The dependence of the process constants on T_e has the following form [5]: $k_1(T_e)=4\times10^{-5}\times\exp(-4.21/T_e)/T_e^3$, $k_2(T_e)=6.5\times10^{-8}/T_e^{0.67}$, $k_3(T_e)=4\times10^{-5}\times\exp(-3.7/T_e)/T_e^3$, $k_5(T_e)=10^{-6}\times(0.026/T_e)^{0.5}$. Such constant dependence on temperature has two characteristic features: 1. In the temperature range (see Fig.2) the derivatives $dk_i(T_e)/dT_e$ which determine the behavior of the process constant vary with the rise in temperature: $dk_1(T_e)/dT_e>0$ for $T<1.4$eV, $dk_2(T_e)/dT_e<0$ and $dk_5(T_e)/dT_e<0$ for any T_e, $dk_3(T_e)/dT_e>0$ for $T_e<1.27$eV. Therefore, with the rise in T_e ($T_e\sim0.4$eV) the process constants increasing electron concentration do increase, while the process constants decreasing it become less. 2. The constants of ionization of Ar^* and Ar_2^* have an exponential dependence on the electron temperature. This dependence is such that in rising T_e by (10-15)% in a given region of temperature these constants increase 2-3 times while all the remainder varies slowly under the same conditions.

Thus, with the rise in plasma electron temperature determined by plasma current heating the contributions of ionization of Ar^* and Ar_2^* increase substantially due to the exponential dependence of these process constants on plasma electron temperature. It is this fact that enables us to explain a moderation of decreasing a plasma electron concentration and its conductivity after e-beam current ceasing. The dependence of argon e-beam plasma conductivity obtained within the model proposed are in good agreement with the experimental results.

REFERENCES

1.Bondar',Yu.F., Goman'ko,A.A., Mkheidze,G.P., Savin A.A.and Janowsky, A..Sov.Phys.-Leb. Inst. Rep., 6, 34(1989).

2.Bondar',Yu.F., Mkheidze,G.P.and Savin,A.A.,Sov.Phys.-Leb.Inst.Rep., 10, 17(1986).

3.Bondar',Yu.F., Klimov,V.I., Goman'ko,A.A., Mkheidze,G.P., Savin,A.A. and Janowski,A.,Sov.Plasma Phys.15, 1508(1989).

4.Eletskyi,A.V.and Kulagin,V.D,Sov.Plasma Phys.5, 98(1979).

5.Gochelashvili,K.S., Klimov,V.I.and Prokhorov,A.M.,Sov.Plasma Phys. 15, 1508(1989).

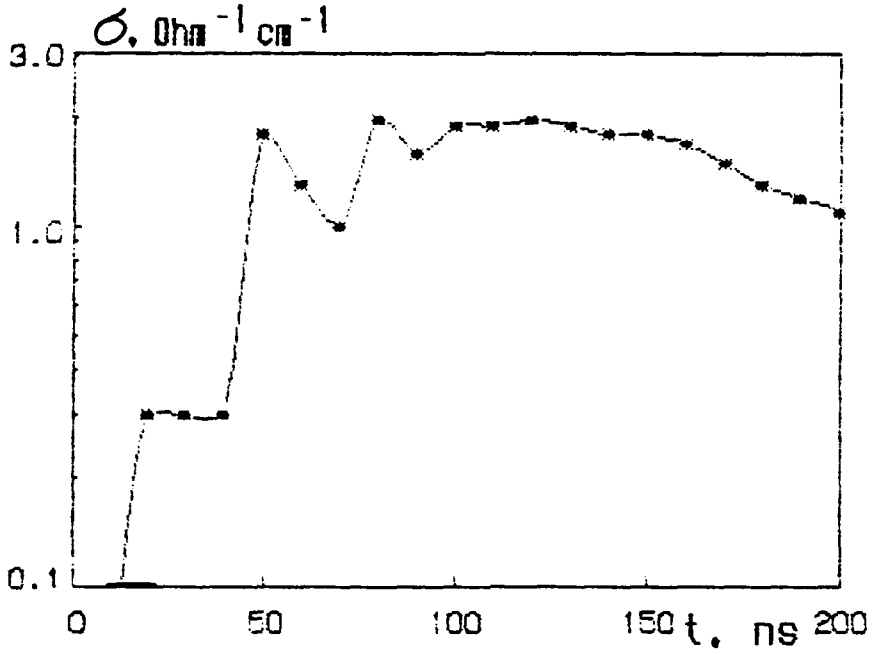

Fig.1. E-beam plasma conductivity vs time at argon pressure value 600 Torr.

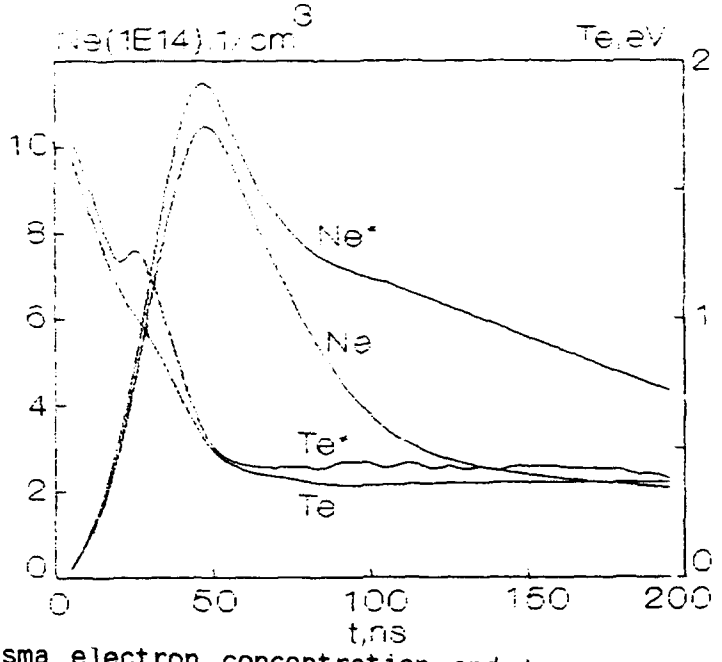

Fig.2. Plasma electron concentration and temperature vs time on the e-beam axis with plasma current heating (N_e^*, T_e^*) and without it (N_e, T_e) at 600 Torr.

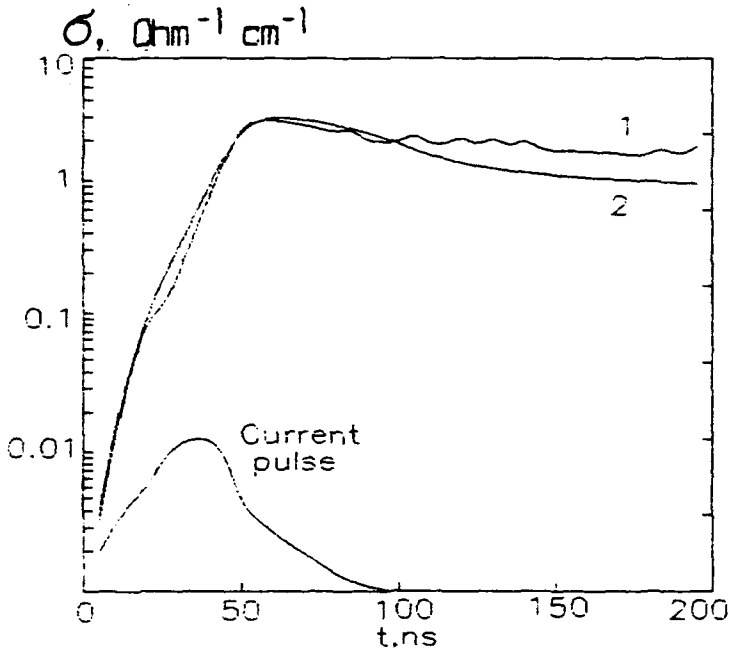

Fig.3. Plasma conductivities vs time on the e-beam axis with plasma current heating (1) and without it (2) at 600 Torr.

MICROWAVE GENERATION AND CHARGE PARTICLE ACCELERATION BY HIGH CURRENT RELATIVISTIC ELECTRON BEAMS

Yu.V. Tkach, I.F.Kharchenko, V.A.Balakirev , V.V.Dolgopolov, Yu.V. Kirichenko, S.M. Latinsky, E.M. Lats'ko, E.A.Lisenko, V.E. Novikov, A.O. Ostrovsky, A.V. Pashchenko, E.A.Prasol, S.S. Romanov

Kharkov Institute of Physics & Technology, Kharkov 310108, Ukraine

High power microwave generation by current relativistic electron beams and collective methods of the beam acceleration as reversing of the collective generation methods are investigated in this paper. The optimization of the electrodynamic structure of the high power microwave generators such as BWO , Vircator , Vircator connected with Ubitron are discussed.

Let us consider the segment of the axially symmetric ripple waveguide of length L, in which annual beam is injected. The thickness of the beam is D, the average radius is b, ($D \ll b$), the density is n_b and the initial energy is $\mathcal{E}(z=0)=mc^2(g_0-1)$. The system are placed in the strong magnetic field. The input waveguide bound at z=0 is partly reflecting for the incident wave with reflecting coefficient $R_0<1$, and the output bound is fully reflecting $R_1=1$.

The equations, describing nonlinear dynamic beam interaction with the ripple waveguide segment, are derived from the general theory of spatial-periodic slow-waves structures excitation [1]. We show that the backward wave amplitude become stationary in the self-consistent case ($R_1=R_0=0$). In the presence of the additional feedback ($0.2<R_0<0.5$) the wave amplitude oscillation is observed. The oscillations become iregular and HF oscillations spectrum spreads at $R_0>0.6$ increasing. It is shown , that the automodulation starting current in the system with additional feedback is less than in the completly consistent system.

The dependence of the beam energy transformation efficiency (η) on the reflectivity coefficient R_0 is determined. The calculations show, that if $R_0>0.4$ the η decreases. Therefore the stationary regime of excitation is the most optimal for obtaining monochromatic radiation with maximal η. This regime can be used for genera-

tion of the radiation with wide oscillation spectrum in spite of the low η level.

In this paper two variants of the vircator used to increase effectivity are analized:

a) use of resonator and modulation beam for vircator powerup;

b) using vircator connected with other generator.

The radiation generation by the magnetically insulated annual electron beam, of radius R_b, with initial energy $\mathcal{E}_0=mc^2(\gamma_0-1)$ in the resonator of length L and radius R_d is investigated numerically simulations. For the cases of modulated and unmodulated beams the radiation spectrums are calculated at L=6.8cm, R_d=6.5cm, R_b=2.8 cm and the current greater than the critical one by a factor 2.5.

The simulations show, that the radiation spectrum peaks correspond to the natural resonator frequencies. The modulation of the current beam on the frequency, corresponding to the spectrum maximum, leads to the spectrum narrowing and radiation powerup. In the numerical simulations of the beam with the modulation depth ≈0.3 on the frequency w≈31.3 the electron efficiency is 15%.

The main reason, explaining low vircator efficiency, is that the overwhelming current part withdrawal from the resonator for the large current level. What should be noted is that the output beam is well modulated. In order to increase the power of the modulated beam produced by the vircator we propose to inject it into spatially-periodic magnetic field similar to that in the Ubitron. In the resonance case the relation $\omega_{virc}=(k_z+k_0)v_z \pm \omega_b$ is fulfilled, where ω_{virc} is one of the vircator generation frequencies close to the modulation frequency , $k_0=2\pi/L$, L is the magnetic field modulation period.

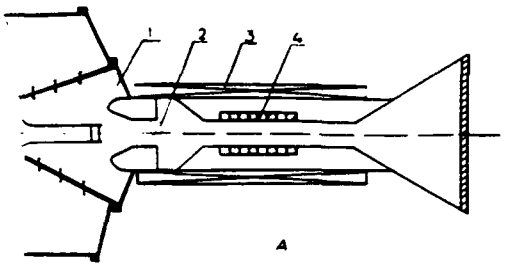

Fig 1

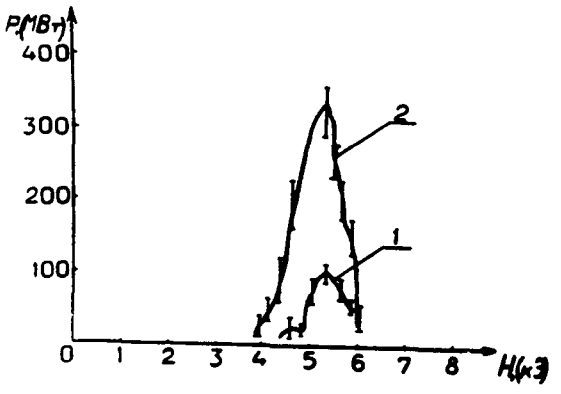

Fig2

The experimental investigations are carried out in the "TORNADO" accelerator [2]. The experiment scheme is shown in Fig.1 , where: 1 is diod, 2 is vircator,3 is driving magnetic field and 4 the ubitron.

The sharp power increasing and the spectrum narrowing by a factor of 1.5-2 is obtained for the above mentioned resonance condition. The magnetic field strength in the ubitron as a function of the power generation at the wave length λ=2.8cm is shown in Fig.2 for the case with and without vircator. Thus, the effectivity of the vircator plus ubitron system for the more complete transformation of REB energy to high power microwave and so radiation powerup is experimentally and theoretically proved.

In the pulse and continuous generator theory the very important point is the determining of condition for the steady state generation regimes on the required frequency to realize. In this paper the stationary generation regime stability in an distributed Cherenkov oscillator with an external feedback is investigated within the framework of the spatial-time model [3]. It was occured with using numerical method, that was first proposed at [4] for the steadiness analizes of the modulated REB acceleration in the LINAC injection section.

It was shown, that the discussed dynamic system has a specific peculiarity: equal driving parameters correspond to several stationary regimes, differing one from another by frequency and generated radiation amplitude. But only one of them is steady and observed in generator. For the different driving parameter regions different stationary generation regimes are steady. So, stationary regime with frequency equals to the precise Cherenkov resonance frequency $\omega=kv_0$ is realized for the nonlinear amplifire with normalized length $3.0<l<4.5$. If $1.5<l<3.0$ stationary regime is realized at another frequency, differing from resonance frequency: $\omega=kv_0(1+\Omega)$, $\Omega>0$. Fig 3 shows the evolution of these stationary regimes for different values of l.It should be stressed that during change of the normalized electrodynamical structure length l the transition from one steady state regime $\Omega>0$ to another one $\Omega=0$ occur trough the of "indifferent equilibrium"

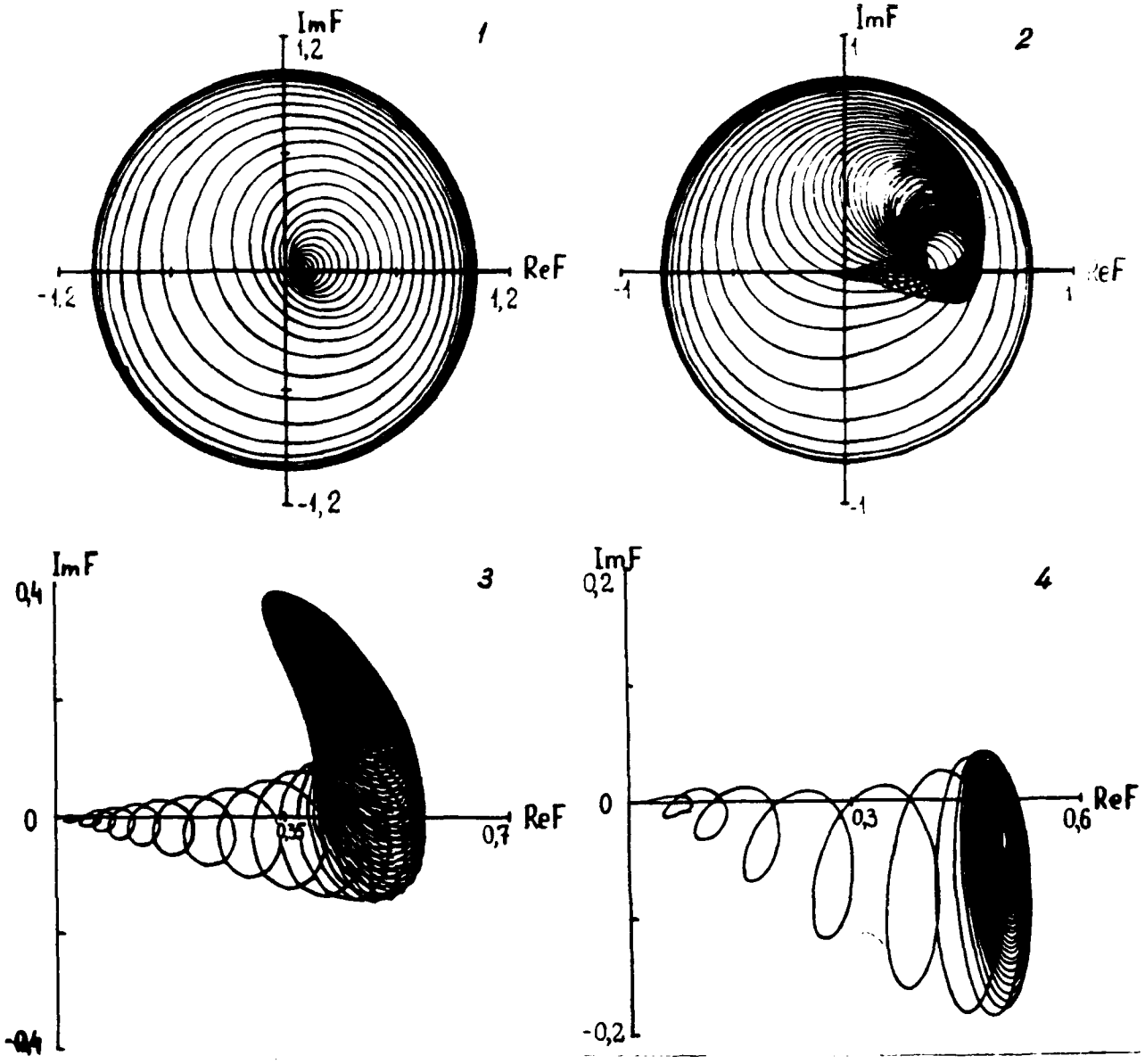

Fig 3

The path tracks,describing by the point with coordinates ReF(τ, ξ=0) ImF(τ, ξ=0) for different l (F is the complex amplitude of electric; field τ, ξ are the time and space variables) 1-4. l=2.6,3.0,3.1,3.5.

The existance of unstable stationary regime can influence the character of the self-existed processes . This influence can be displayed , for example ,during the oscillator sinchronization by external harmonic action . In this report the effect of the unstable stationary regime on the process of external synchronization of distributed oscillator with external feedback is investigated. Two shcemes of the external synchronization is considered. In the first scheme the synchronization is realized by preliminary modulation of REB density. In the second scheme the external harmonic signal is used to achieve synchronous stationary

regime. This signal is applied to the entry side of the slow-wave structure.In this report we investigated the possibilit of efficacious synchronization of the distributed oscillators on the resonance frequency $\Omega=0$ in the region $1.5<1<3.0$. The solution of this problem has been carried out by numerical simulations the set of nonlinear nonstationary equations describing the dynamic of distributed systems under consideration. The calculations show that when parameter 1 approaches to the transition boundary of the self-contained oscilator from steady state regime with $\Omega > 0$ to another one with $\Omega=0$ the threshold of synchronization tends to zero. As a result even sligth external disturbance leads to capture of the oscillations on resonance frequency.

It is found, that transition of oscillator to the synchronizedregime is realized through the state of "indifferent equilibrium". This state is nonstationary and realizes when, no one processes proceeding in oscillator (synchronization process and process connecting with establishment the eigen stable stationary regime) are not dominate. Thus we can conclude that with increasing the parameter 1 the synchronization conditions of the distributed oscillator becomes better. This is due to the growing role of self-contained processes which tends to establish the stationaryregime on resonance frequency.

Let us consider now the charged-particle acceleration in plasma systems.

The external magnetic field affects both the electrodynamic properties of a plasma and the dynamics of charged particles. In particular, the transverse magnetic field allows the surfatron mechanism of acceleration , which ensures the regime of unlimited particle acceleration.

The report presents the results from theoretical studies of the acceleration mechanisms in a plasma lokated in an external magnetic field. The acceleration by a short laser pulse-generated wakefield is among most promising methods of acceleration in a plasma. Unlike beat wave , this method is nonresonant, and this is its essential advantage. We have considered the process of wake field wave driving by a laser pulse propogating across the external magnetic field. The pulse generates the extraordinary wakefi-

eld plasma wave. In the field of this wave the surfatron mechanism of acceleration can be accomplished. The accelerating electric field intensity of the extraordinary wave is higher than the electric field intensity of the plasma wave in the absence of the external magnetic field: $\mathcal{E}_z/\mathcal{E}_z^0 \propto \omega_H^2/\omega^2$, where $\mathcal{E}_z$ - extraordinary wave amplitude, $\mathcal{E}_z^0$ - plasma wave amplitude, $\omega_H^2=\omega_c^2+\omega_p^2$ [5].

At high laser pulse intensity the plasma exhibits the effect of radiation self-focusing. We studied the influence of this effect on the wakefield excitation. It is shown that the transeverse compression of the laser pulse leads to the enhancement of the wakefield strength $\propto 1/f_{min}^2 \approx a^2\omega_p^2/16c^2$, where a - the initial electromagnetic field width [6].

As is known, the field of the el ctromagnetic wave propagating in an inhomogenious plasma strongly increases in the vicinity of the plasma resonance point. At this point there takes place resonant excitation of inhomogeneous-plasma oscillations. In the absence of the external magnetic field , the region of the plasma resonance is preceded by the opaque region , where the electromagnetic wave field exponentially decreases. This latter region can be eliminated by introducing a steady-state magnetic field directed perpendicular to the density gradient. In this case the point of the extraordinary wave reflection can lie behind the high-hybrid resonance HHR point.

From this relation if follows that the controlled variation of the magnetic field can significantly extend the HHR region. The estimates show that with a single passage of the particle across the HHR region the particle energy gain is insignificant. It is demonstrated in the report that the finite particle energy can substantially be increased if on spinning along the Larmor orbits in the magnetic field the particle multiply crosses the HHR region. The map describing the evolution of the particle energy and phase is obtained. Established are the regimes for regular and stochastic acceleration [7].

The phenomenon of ion acceleration in the high-current electron beams injected into vacuum space after their travelling across the cathode (anode) plasma ,has been explained by some authors by the motion along the chamber the virtual-cathode potential well

(VCPW). Howewer, up to now there has been no self-consistent mathematical description of this phenomenon. Experiments have shown that the energy of accelerated ions can surpass that of injected electrons by one or two orders of magnitude. In order that the travel of the virtual-cathode potential well could provide this rate of ion acceleration the potential well (PW) should move practically without any decrease in the sleepness of the ion accelerating slope. At the first sight this potential evolution seems to be unreal because the ions cannot overtake the accelerating slope of the PW and accumulate the positive charge in the top part of this slope needed to accelerate this slope and to keep its steepness. Thus is why the explanation of the ion acceleration by the motion of the VCPW often meets on objection.

In this report the ion acceleration by a VCPW is investigated theoretically. Ions are described by Vlasov equation. It is shown, that the appearance of ions in the drift region can lead to the accelerated motion of both the virtual and the potential well slope following the cathode without any significant decrease in the steepness of the slope, and this results in effective ion acceleration. The steepness of the ion accelerating slope of the PW is supporting by ions, which are slided down this slope before that slope start to move. When the slope overtakes this ions, they will be decelerated relative to this slope so much encreasing its density in the top part of the slope.

New method of the collective ion acceleration by the VC potential well is proposed in this report.

The acceleration occurs due to ion trapping into the potential well of a virtual cathode (VC) and a subsequent accelerated motion of the VC across the magnetic field . The VC results from the intersection of the acceleration axis by overcritical electron beam (EB) , Which is preliminarily pinched in its motion along the convergent magnetic field lines.The VC motion is realized by means of the pulse that runs with acceleration along the strip cathode and triggers the electron emission.

In the proposed method of acceleration,the synchronism between the accelerated ions and accelerating field is maintained throughout the acceleration time by an external control of the VC motion.

The synchronism is attained here due to grid modulation which needs a comparatively low energy to be realized . The ions are accelerated in the direction perpendicular to the electron motion in the beam ; this precludes the EB spread as weii as a possible instability development and the upset of acceleration , which is the case with the acceleration along the EB. The beam compression causes or substantial decrease in the cathode current density.Besides ,this way of acceleration enables the EB energy recuperation.

The estimates of necessary parameters show this method to favourable for constructing a compact accelerator with a high accelerating gradient and for achieving considerable heavy-ion energies .

The proposed method is distinguished for the purposeful employment of the phase transition in the EB to form deep potential well.

There are grounds to beleive that the present method of acceleration collective both in electrons and ions , still much promise.

References

1. L.A. Vainstein,V.A.Solntsev. Lectures on High Frequency Electronics(in Russian) .Sov.Radio Publ. 1973. 400 p
2. Yu.V.Tkach,V.I.Belaev,Ye.A.Prasol. Proc. of Conf. 'Plasma Electronics(in Russian). Kharkov 1988. P.73.
3. V.A.Bondarenko,A.O.Ostrovsky,Yu.V. Tkach. To a Nonstationary Theory OF a BWO with Additional Feedback //ZH.Tekh.Fiz. V.60 N6, 134 (1990)
4. N.I. Ajzatsky The analys of stationary regimes instabilities in distributed system with external feedback //Izv. Vuzov. Radiofiz. 1989. V.32. N10 p.1417.
5. V.A.Balakirev,S.M.Latinsky,V.E.Novikov,Yu.V.Tkach. The wake field excitation by electromagnetic pulse in the strong magnetic field //Voprosi atomnoy nauki i techniki', Vol.6(14), 1990, P.153.
6. V.A.Balakirev, V.E.Novikov, E.A.Lysenko,Yu.V.Tkach.The wakefield excitation by electromagnetic pulse during self-focusing of laser beam//Voprosi atomnoy nauki i techniki', Vol.6(14), 1990, P.168.
7. V.A.Balakirev,V.E.Novikov,Yu.V.Tkach. //Voprosi atomnoy nauki i techniki', Vol.6(14), 1990, P.162.

ELECTRON BEAM DIODES USING FERROELECTRIC CATHODES

J.D. Ivers, L. Schächter, J.A. Nation and G.S. Kerslick
Laboratory of Plasma Studies & School of Electrical Engineering
Cornell University, Ithaca, NY 14853, USA

Abstract

A new high current density electron source is investigated. The source consists of a polarized ceramic disk with aluminium electrodes coated on both faces. The front electrode is etched in a periodic grid to expose the ceramic beneath. A rapid change in the polarization state of the ceramic results in the emission of a high density electron cloud into a 1 to $10mm$ diode gap. The anode potential is maintained by a charged transmission line. Some of the emitted electrons traverse the gap and an electron current flows. The emitted electron current has been measured as a function of the gap spacing and the anode potential. Current densities in excess of 70 A/cm^2 have been measured. The current is found to vary linearly with the anode voltage for gaps $<$ 10 mm, and exceeds the Child-Langmuir current by at least two orders of magnitude. The experimental data will be compared with predictions from a model based on the emission of a cloud of electrons from the ferroelectric which in turn reflex in the diode gap.

Introduction

Recent experiments at CERN [1-3] and at the Lebedev Institute[4] have demonstrated that it is possible to extract high current density electron beams from ferroelectrics. The emitted beams may be useful in injectors for both low and high current accelerators and for microwave generation devices. Ferroelectric materials typically have a bound surface polarization charge density of order of or greater than 0.1 C / m^2. Unscreened surface fields, due to the polarization would be of order of the polarization field i.e. $\sim$ 10^{10} V/m, but are screened from the diode gap by free charge attracted to the surface of the ferroelectric. Electron extraction may occur when the polarization state of the ferroelectric is changed immediately affecting the amount of screening charge required. The emitted electrons are extracted into the diode gap by the large partially unscreened field in the close vicinity of the periodic grid. The electrons form near this surface a "distributed cathode" which, in our experiment, is entirely determined by the ferroelectric and the grid. When a voltage is applied on the anode current flows through the gap. In this paper we present results of an investigation of the current-voltage characteristics of a vacuum diode using a ferroelectric cathode.

Experimental Arrangement

The experimental arrangement is shown schematically in Fig. 1. A $1mm$ thick, $2.5cm$ diameter ferroelectric LTZ-2 (Lead-Zirconium-Titanate) disk is mounted as the load on a 10Ω characteristic impedance transmission line. The line is switched by a krytron applying a $200nsec$, $1kV$ pulse to the sample. The sample is oriented with the polarization vector pointing into the diode. A positive pulse is applied to the rear face of the ferroelectric and the emission surface is held at ground potential. The effective emission area is $\sim 1cm^2$. The cathode is coated with a thin ($\sim 1\mu m$) silver coating on its rear surface and a gridded emission surface with alternate silver and uncoated strips of $200\mu m$ width on its front surface. A planar graphite anode is located $2 - 10mm$ from the emission surface. The anode is maintained at a positive potential with respect to the cathode by a charged transmission line. Current flow through the diode discharges the line. We record the line current at the diode and calculate the gap voltage from the known line current and the transmission line impedance. Lines with characteristic impedances ranging from 12.5 to 50Ω have been used as the load. The diode is maintained at a base pressure of 10^{-5} $Torr$.

The upper part of Fig. 2 shows three oscilloscope traces obtained for the diode current with a $4mm$ gap and a 25Ω load with an LTZ-2 ferroelectric cathode. The transmission line load was initially charged to 100, 300, and 500 V for the three traces shown. The diode current length was determined by the length of the cable. The steady nature of the current is typical of this data. Peak emission current densities of up to $70A/cm^2$ have been obtained experimentally. The lower traces show the voltage across and the current through the ferroelectric cathode. Note that the current through the ferroelectric is of order $100A$ and is always larger than the diode current in our experiments. The details of the current through and the voltage across the ferroelectric are remarkably independent of the diode operating conditions. However, the diode characteristics are strongly dependent on the state of the ferroelectric ceramic. For example, the diode current drops dramatically if the ceramic is not pulsed. Similarly, no current was measured for negative anode voltage even when the ceramic is pulsed. These observations demonstrate that the current flow does not result from a plasma fill of the diode as a result of the pulsing of the ferroelectric.

In Fig. 3 we plot the diode current versus the gap voltage for a 6 mm gap and an LTZ-2 cathode. Similar data have been obtained for other gap spacings and other materials. In all cases the diode current starts to flow when the voltage across the ferroelectric is approximately at its maximum value and continues even after the ferroelectric

voltage V_{FE} pulse has returned to zero. The results indicate an almost linear scaling of the beam current with the diode voltage. The beam current is only very weakly dependent on the diode gap spacing for fixed gap voltage and ranges from 12Ω at the largest spacing to 9Ω for the $2mm$ gap. The results are repeatable and breakdown does not occur. For small gaps ($\leq 2mm$) there is a beam current when the diode voltage is reduced to zero. We shall not address this regime in the current paper.

Discussion of Results

The ferroelectric has a very nonlinear response to an applied voltage and if we were to determine a characteristic dielectric coefficient this would have been larger than 3000. Furthermore, the polarization field (P/ϵ_0) is of order of $10^{10}V/m$. In the close vicinity of the grid a fraction of this intense electric field may play a crucial role in electrons emission process. Bearing in mind these facts, we shall now present the essence of the process which occurs in this diode. The basic mechanism is what we call externally controlled field emission namely, the electron extraction is due to an electric field which is generated behind the cathode and, at least in the regime our system was operated, it is almost unaffected by the anode.

If a positive potential is applied on the back electrode of the ferroelectric, in other words, electrons are brought to the grid, the ferroelectric tends to reject these electrons to maintain its polarization (equilibrium) state. It can not return the electrons to the voltage source but it can expel them into the gap. For this purpose it has to extract them from the metallic grid. At this point the geometry of the grid comes into play. The local electric field near each one of the grounded strips is sufficient to extract the electrons from the material. The amount of charge repelled is determined by the electrical characteristics of the ferroelectric and the voltage applied on the back electrode; in our experiment the anode voltage plays practically no role in this process. The electrons' cloud in the gap forms a "distributed cathode" of a total charge Q_{gap}. This charge is a fraction of the charge bounded to the ferroelectric and can be of order of up to $10\mu C$. Regardless of how exactly this charge is distributed we can estimate the potential distribution in the gap for a zero anode voltage. At the boundaries we know that the average potential on the grid is approximately zero and so is the anode potential. In addition, the electric field near the anode is zero since no current flows with zero applied gap voltage due to the fact that all the electric field lines which start on the rear of the ferroelectric finish on the grid or distributed electron cloud in the gap. In other words we do not expect the diode anode to be affected by the ferroelectric capacitor. Subject to these boundary conditions the potential in the gap has the form

$$\phi(z) = \Phi \frac{z}{g} \frac{(g-z)^2}{g^2} \quad . \tag{1}$$

The unknown amplitude Φ is determined by substituting Eq.(1) in the Poisson equation and integrating the resulting expression over the entire length of the diode. The source term in the Poisson equation is then proportional to the charge in the gap and therefore so is Φ; explicitly $\Phi = g|Q_{gap}|/3\epsilon_0 A$ where A is the area of the diode and g is the gap spacing. From this simplified potential distribution we conclude that the potential has a maximum at $z = g/3$ and its value there is $\phi_{max} \approx \Phi/7$. If all the charge which initially was on the surface of the ferroelectric is repelled into the gap, ϕ_{max} approaches the $1MV$ level. In practice only a fraction of the charge is repelled into the gap therefore that maximum will be lower. This trend will be amplified by a distribution of electrons which is concentrated near the grid.

According to the potential in Eq.(1) the electrons in the cloud are in a dynamic equilibrium, namely they oscillate in the potential well which is induced by their own presence, the ferroelectric and the boundary conditions, in the gap. Due to the oscillatory character of the motion the average velocity of the electrons is zero - and so is the current when no anode voltage is applied. We can estimate the average kinetic energy, $mc^2(\gamma_0 - 1)$, of the electrons by averaging the expression for the energy conservation over the gap spacing. Using Eq.(1) we found that $\gamma_0 = 1 + \frac{1}{36}\bar{Q}$ where $\bar{Q} \equiv eQ_{gap}g/\epsilon_0 Amc^2$. To complete the description of the equilibrium state, we denote the average particles density in the cloud with $\tilde{n}$ and the lowest estimate of this quantity is just the total number of particles divided by the effective gap volume i.e. $\tilde{n} \approx Q_{gap}/egA$.

When a positive anode voltage, V_{AN}, is applied the potential in the gap is $\phi_{app} = V_{AN}z/g$ since (i) typically this potential is much smaller than the potential, Φ, associated with the gap charge and (ii) the charge density does not change. The resulting current is proportional to the anode voltage therefore we may determine the gap resistance R_{gap}:

$$R_{gap} = \eta_0 \frac{1}{36} \frac{g^2}{A} \gamma_0^2 \sqrt{\frac{\gamma_0 + 1}{\gamma_0 - 1}} \quad ; \quad \eta_0 = 120\pi\ \Omega \ . \tag{2}$$

This is the main analytical result of this study, since it quantitatively shows that the presence of an electron cloud in the gap is directly responsible to the linear $I - V$ characteristic measured experimentally. This expression for the gap resistance was tested against the experimental data for: $g = 4mm$, $V_{TL} = 300V$ $R_{TL} = 25\Omega$ and $V_{gen} = 1900V$; the average anode current measured was $8.8A$. Assuming that half of the ferroelectric bound charge is actually in the gap our simulation indicates that the

current varies between 8.4 and 9.4. For the same parameters Child-Langmuir formula predicts a current of about $40mA$.

Summary

In conclusion, we have shown experimentally that a ferroelectric ceramic may supply a large amount of electrons into the gap of a diode. This charge density is externally controllable. Since this process is controlled by an external electric field which is not the one which accelerates the electrons in the diode, it has the potential of producing high quality beams. The other two processes (thermo- and photo-emission) in which the emission is controlled externally the beam quality is limited by temperature increase associated with each process. The current extracted from a cathode made of ferroelectric material exceeds by orders of magnitude the Child-Langmuir current. This result was explained using a simple model for the behavior of the electrons repelled by the ferroelectric in the gap. The dependence of the current on the voltage is linear rather than $V^{3/2}$ in the Child-Langmuir case. Calculations using this model are in good accordance with the experiment.

This work was supported by the United States Department of Energy.

References

[1] H. Riege , CERN-PS 89/42 (AR) (1989), Unpublished.

[2] H. Gundel, H. Riege, E.J.N. Wilson, J. Handerek and K. Zioutas; Nucl. Instr. Meth. in Phys. Res. A280, 1(1989).

[3] H. Riege , CERN-PS 89-15 (AR) (1989), Unpublished.

[4] A.Sh. Airapetov, G.A. Gevorgian, I.I. Ivanchik, A.N Lebedev, I.V. Levshin, N.A.Tikhomirova, and A.L. Feoktistov, Proc. 8th Int. Conf on High Power Particle Beams, Novosibirsk (1990).

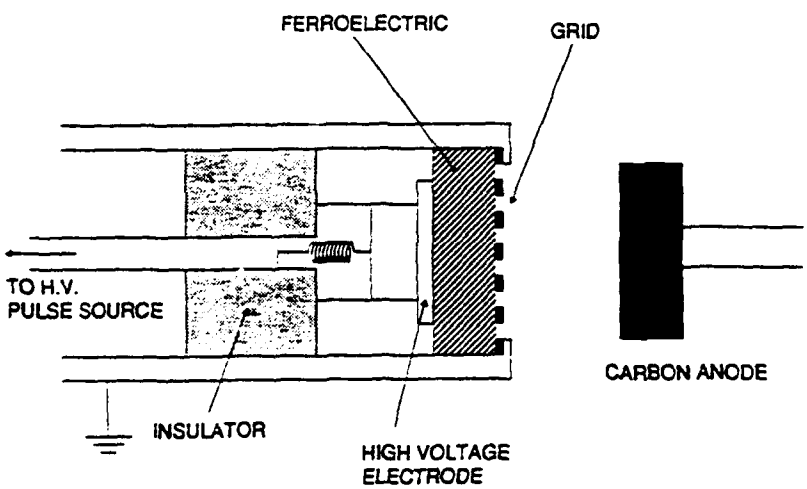

Fig. 1: The schematic experimental set-up.

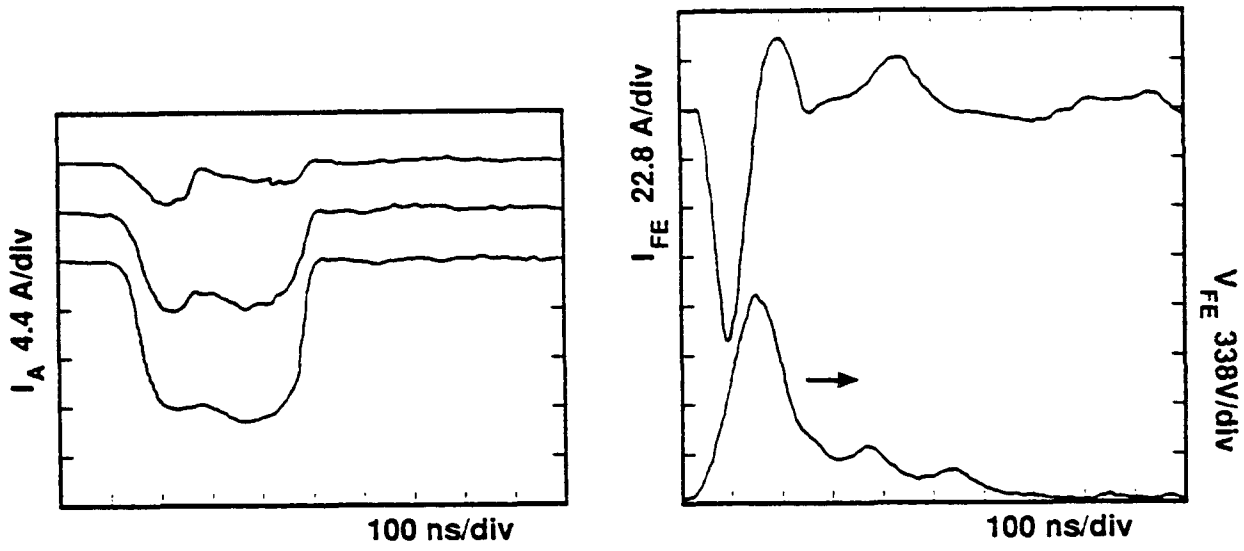

Fig. 2: One set of three shots corresponding to $V_{TL} = 100, 300$ and $500V$ and a $4mm$ wide gap; $Z_{TL} = 25\Omega$ and the transmission line pulse is $400ns$ long. In the left frame the anode currents are illustrated. In the right frame the charging currents (I_{FE}) and the voltage on the ferroelectric (V_{FE}) are presented. All three shot are indistinguishable in this case. Notice that the voltage pulse on the ferroelectric is only about $150ns$ long.

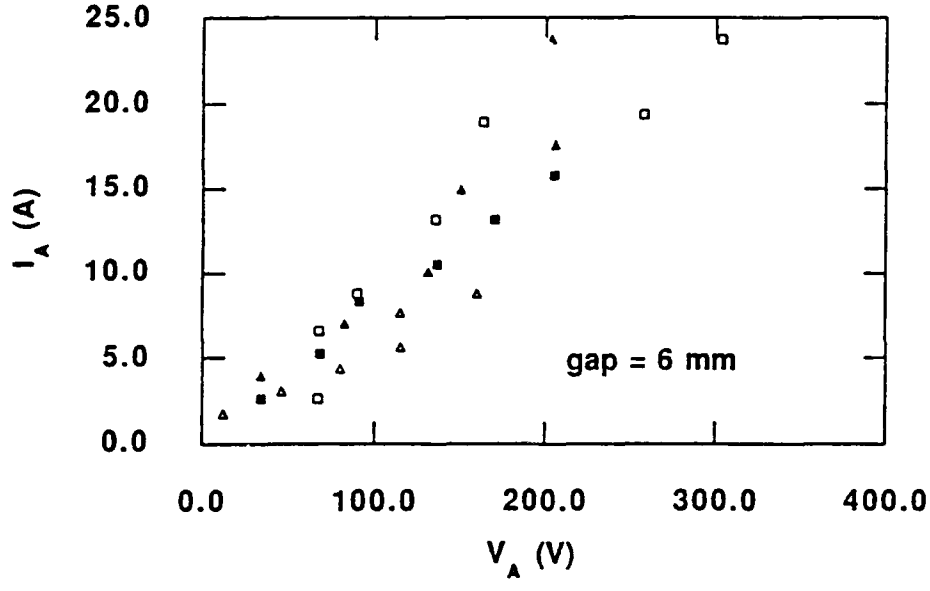

Fig. 3: The $I - V$ characteristic of a diode with a $6mm$ wide gap. Similar results were measured for $2, 4, 8$ and $10mm$ gaps.

THE NSWC MICROCHANNEL ELECTRON SOURCE PROGRAM

K. A. Boulais, J. Y. Choe, S. T. Chun, A. Krall, K. Irwin
Naval Surface Warfare Center, Silver Spring, Maryland 20903

S. E. Saddow
Harry Diamond Laboratories, Adelphi, Maryland 20783

M. J. Rhee
University of Maryland, College Park, Maryland 20742

Abstract — The microchannel electron source is currently being developed at the Naval Surface Warfare Center for cold cathode applications which require high repetition rates and short pulse widths. It is based on microchannel plate principles which, in general, allow for fast response times. However, the microchannel plate is generally limited to output currents of less than 10^{-4} A/cm^2. We describe a method to increase the output current from a microchannel device by several orders of magnitude. Our analysis has shown that one can obtain channel current densities of order 1 A/cm^2 by constructing the device from a crystalline bulk semiconductor. Carrying the analysis further suggests that current densities can be increased by another order of magnitude by incorporating an appropriate electron injection scheme. Important analytical results, as well as the present status for the fabrication of a proof-of-principle device, are discussed.

1. Introduction

The production of electrons from a low-voltage source, followed by a constant post-accelerating voltage, is of current interest for highly modulated and high-energy electron beams. The development of such low-voltage sources could overcome the speed limitations of high-voltage modulators required for conventional gridded cathodes. In this paper, we describe a device based on microchannel plate (MCP) principles that may meet these requirements. Advantages of a MCP device as a cathode include the possibility of high repetition rates, isolation of the modulating pulse from high post-accelerating voltages (via photocathode or direct photon inputs), and efficiency (a cathode heater is not required). Applications include particle accelerators, microwave tubes, and vacuum microelectronics.

The MCP is a thin glass wafer with millions of micron-sized channels, each acting individually as a continuous dynode electron multiplier. Channel multiplication takes place via an applied electric field along the channel, creating an avalanche of secondary electrons. The channel walls are generally coated with a material to increase secondary emission for high overall gains,

and to allow a strip current to flow that removes the positive charge left from secondary emission. It is well known that by increasing the conductivity of the coating, thereby quickly neutralizing the positive charges with electrons, one can increase the output saturation current of a MCP. However, this technique is limited by ohmic heating of the glass substrate. It is shown here that this limit can be overcome by using a crystalline semiconductor for the active secondary emission medium. Since the positive charges left in the channel walls are then left as mobile holes in the valence band, the usual strip current is no longer required. Further, the holes are generated only when the plate is activated. In pulsed operation, the major portion of ohmic heating (due to hole generation) is therefore reduced by the duty factor. Typically, the higher thermal conductivity of many semiconductors is sufficient to remove the heat from the combined hole and intrinsic bias currents.

In section 2, we include a brief outline of a steady-state analysis used to predict the saturation output current from such a device, but concentrate more on the results. Details of the analysis are further described elsewhere[1]. We also discuss (section 3) the present status for the fabrication of a single row of channels for proof-of-principle experiments. Throughout the paper, we distinguish from the conventional MCP by referring to the semiconductor-based device as a microchannel electron source.

2. Analytical Results

The central equations in the microchannel source (MCS) analysis are Gauss's law and the steady-state continuity equation. A one-dimensional form of Gauss's law is found by integrating over a thin Gaussian surface with the major extents parallel to the plate surface. The continuity equation is separated into three components: the bulk hole current, the bulk electron current, and the channel electron current. Each component is equated to a generation rate representing the equal generation of bulk holes and channel electrons, and/or a recombination rate representing the recombination of bulk electron-hole pairs. The generation rate can easily be found from a local analysis of the channel secondary emission.

In order to arrive at the analytical results presented here, we make several assumptions. First, diffusion currents are neglected because of the high electric fields involved (of order 10 kV/cm). Further, we assume that the bulk carrier velocities are proportional to the electric field by their respective mobility. Finally, for simplicity, the first dynode in the analysis is treated the same as all other dynodes. Although we expect the first dynode to be important for accurate gain calculations in the MCS model, as is the case for the MCP,[2] it is an effect which can be included after a solution is found.

For a first case, we assume that bulk electrons are not injected, leaving the channel electrons and bulk holes as the dominant charges. As detailed elsewhere,[1] one can then arrive at an expression for the maximum allowable channel current density as

$$J_{out} = -\frac{2\mu_p \varepsilon_o (1+\varepsilon_b)}{L} E_o \left(E_o + \frac{\varphi_a}{L} \right), \tag{1}$$

where μ_p is the bulk hole mobility, ε_o is the permittivity of vacuum, ε_b is the dielectric constant of the bulk, φ_a is the applied potential, L is the channel length, and E_o is the electric field at the channel input. If E_o represents the maximum field before a breakdown condition occurs, then equation (1) represents the maximum possible channel output current density. The importance of using a semiconductor with a high hole mobility and high dielectric strength is immediately apparent. For an applied potential of φ_a = 1 kV, a channel length of L = 1 mm, an electric field at the channel input of E_o = −16.2 kV/cm, and a hole mobility and dielectric constant consistent with GaAs (μ_p = 400 cm^2/V•s and ε_b = 13.1, respectively), the output current from equation (1) is J_{out} = −1 A/cm^2.

A general form for the channel electron gain can be found[1], as a function of the secondary emission coefficient, δ, as

$$G_v = \exp\left(\int_0^L \frac{\ln \delta}{l_c} dz \right), \tag{2}$$

where l_c is the collision length (defined as the length along the channel from which a secondary electron is emitted to the point at which it collides with the opposing channel wall), and z is the coordinate along the channel axis. Assuming that the channel geometry has been optimally designed for maximum overall gain, a distorted electric field will change the energy given to a secondary electron to a value that is not optimal for further emission. Thus, the secondary emission coefficient in equation (2) is a function of the channel electric field, and the overall gain will decrease when there is an excessive buildup of holes distorting the field. This gain saturation occurs at an approximate output current given by equation (1).

We have plotted the normalized gain as a function of absolute channel output current in figure 1 for the above GaAs case. A secondary emission coefficient consistent with GaAs is assumed,[3] except for the peak secondary-to-primary emission ratio, for which we assumed a value of 2.5 in order to obtain reasonable gains. This suggests that a coating is needed on the channel walls to increase the secondary emission, but the coating must be thin enough so that the emission

process initiates behind the coating. A viable candidate appears to be a form of Cs-O. Note in figure 1 that the gain is well into saturation at an output current density of 1 A/cm^2.

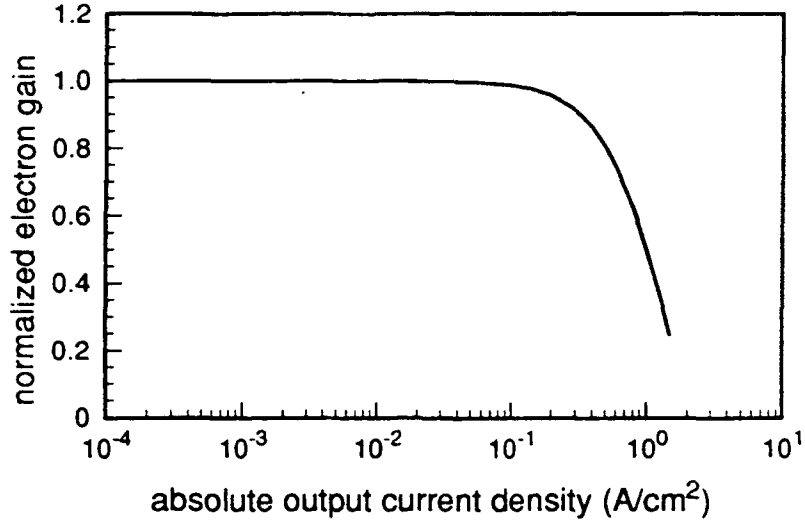

Figure 1. Normalized channel electron gain as a function of absolute channel output current density for a MCS constructed from GaAs.

Since it is the hole buildup that causes gain saturation, a way to further increase the saturation point is by an appropriate scheme to inject electrons into the bulk at the input electrode. The charge cancellation and recombination along the channel then help to prevent the electric field from distorting. Preliminary numerical results have shown that an increase in the saturation current density to order 10 A/cm^2 is possible.

3. Device Fabrication

Some of the more important considerations in selecting a particular semiconductor for MCS fabrication include a high dielectric strength, a high hole mobility, and a low intrinsic carrier concentration (for low bias current). AlSb, GaP, and GaAs are some of the possible semiconductor types. However, because its processing techniques are well known, we have chosen intrinsic GaAs for the proof-of-principle devices. Our attempt is to construct a single row of channels by etching square grooves across the surface of a sample. A flat GaAs sample is placed over the grooves with the same crystal orientation to serve as the fourth channel wall. The assembly is then mounted between two glass slides so that the channel ends are exposed. Once the GaAs is polished down to the surface of the glass, ohmic contacts can be fabricated. A schematic

of the device is shown in figure 2. Note that square channels, as compared to more conventional cylindrical channels, should make little difference in gain.

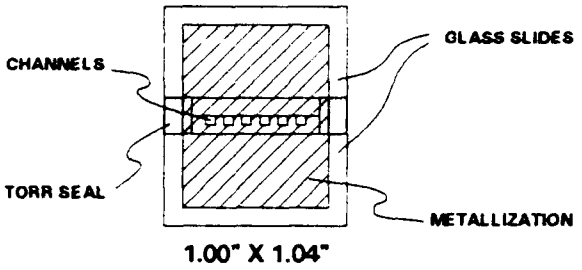

Figure 2. Schematic of single row of channels mounted for proof-of-principle experiments.

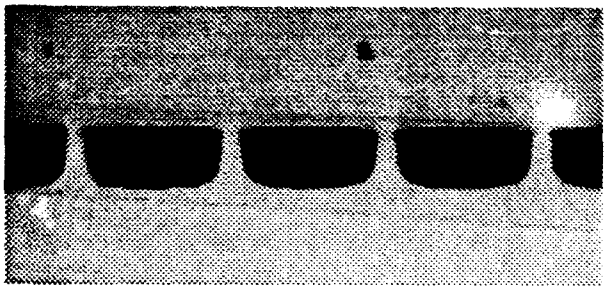

Figure 3. Wax filled channels with dimensions 20 × 56 μm (× 1 mm long).

The photolithography mask used for the grooves formed rows of photoresist with a width of 50 μm and a separation of 20 μm. The wider resist allows for wet etch undercut. A selective etch of 1 H_2SO_4 : 8 H_2O_2 : 1 H_2O is used to create the three perpendicular walls[4] making up the grooves. The channels are etched on a (001) substrate, with the edges of the channel windows aligned parallel to the <100> direction. The etch rate is approximately 10 μm/min, which forms a row of channels with cross-sectional dimensions of 20 × 56 μm in about 2 minutes. After the sample is cleaned of all resist, the channels are filled with a crystal bonding wax to keep the channels clean during the mounting and polishing steps. The resulting channel length is 1 mm. A magnified view of a row of channels prepared in this way is shown in figure 3. Since the undercut has caused a rectangular cross section, as opposed to a square cross section, only two of the walls will be separated by an optimal distance for maximum gain (given the applied voltage and secondary emission parameters). Thus, we can expect a reduction in gain by a factor of 2. The final steps include dissolving the wax, fabricating ohmic contacts, and applying the channel wall coating. We have not yet attempted this last step, as it will require some experimentation to find an optimum material and thickness for the coating.

4. Conclusions

We have described a method to increase the gain saturation current of a microchannel device to order 1 A/cm^2. The higher current density can be attributed to a method to quickly remove the positive charges left from secondary emission. By preventing the holes from building up within the channel walls, the electric field remains in a more stable state for channel

multiplication. The use of a higher bulk mobility is possible (assuming pulsed operation), since the holes are generated only after an input to the plate is applied. Since the strip current of conventional microchannel plates is not required, the ohmic heating is reduced by the duty factor of the pulse modulation. The higher thermal conductivity of many semiconductors allows for a higher average current before thermal run-away occurs. Preliminary results have suggested that even higher channel current densities could be obtained by the use of an appropriate bulk electron injection scheme to effectively cancel much of the positive charge in the channel walls.

From the model for the microchannel electron source, several important results have emerged, including the maximum allowable channel output current density (for the case of no bulk electron injection), and the channel gain. An example has been given for a crystalline GaAs bulk, which led to a minimum required secondary coating for reasonable channel gains. Further details of the analysis are given elsewhere[1].

The present status for the fabrication of a proof-of-principle device has been discussed. The device consists of a single row of channels, formed by etching grooves on the surface of a GaAs sample, and then capping it with a smooth GaAs sample to serve as the fourth channel wall. The structure is mounted between two glass slides with a low vapor pressure epoxy, and then polished down to form 1 mm channel lengths. We are planning the next stage of fabrication, consisting of selecting and applying a thin coating to the internal channel walls to increase the secondary emission.

5. References

1. K. A. Boulais, J. Y. Choe, and M. J. Rhee, "Analysis for an Electron Source Based on Microchannel Plate Principles," IEEE Trans. Electron Devices, Vol. ED-39, No. 5, p. 1250, 1992.
2. E. H. Eberhardt, "Gain Model for Microchannel Plates," Applied Optics, Vol. 18, No. 9, p. 1418, 1979.
3. V. G. Bol'shov, "Secondary Electron Emission in GaAs, InSb, $AuCu_3$," Sov. Phys. - Solid State 4, No. 4, p. 650, 1962.
4. S. Iida and K. Ito, "Selective Etching of Gallium Arsenide Crystals in H_2SO_4-H_2O_2-H_2O System," J. Electrochem. Soc.: Solid State Science, Vol. 118, No. 5, p. 768, 1971.

6. Acknowledgments

This work was supported by the Independent Research fund at the Naval Surface Warfare Center.

LONG PULSE, PLASMA CATHODE E-GUN

D.M. Goebel, R. W. Schumacher, R.M.Watkins
Hughes Research Laboratories
3011 Malibu Canyon Road
Malibu, CA 90265

Abstract

A unique, long-pulse E-gun has been developed for high-power tube applications. The Hollow-Cathode-Plasma (HCP) E-gun overcomes the limitations of conventional thermionic-cathode guns that have limited current density (typically $\leq$ 10 A/cm^2) or field-emission guns that offer high current density but suffer from short pulsewidth capability (typically <1 μsec) because of plasma closure of the accelerating gap. The HCP E-gun provides high-current (>50 A/cm^2), long-pulse operation without gap closure, and also requires no cathode-heater power. The gun employs a low-pressure glow discharge inside a hollow cathode (HC) structure to provide a stable, uniform plasma surface from which a high current-density electron beam can be extracted. The plasma density is controlled by a low-voltage HC discharge pulser to produce the desired electron current density at the first grid of a multi-grid accelerator system. A dc high-voltage electron-beam supply accelerates the electrons across the gap, while the HC pulser modulates the beam current to generate arbitrary pulse waveforms. The electron accelerator utilizes a multi-aperture array that produces a large area, high perveance (>35 μpervs) beam consisting initially of many individual beamlets. The E-beam is normally operated without an applied magnetic field in the ion-focused regime, where the plasma produced by beam ionization of a background gas space-charge neutralizes the beam, and the Bennett self-pinch compresses the beamlets and increases the current density. The self-pinched beam has been observed to propagate over a meter without beam breakup or instabilities. The HCP E-gun has been operated at voltages up to 150 kV, currents up to 750 A, and pulse lengths of up to 120 μsec.

Introduction

High-power electron guns represent an enabling technology for high power microwave devices. Conventional high-power E-guns typically utilize thermionic cathodes or field-emission cathodes as the electron source in a high-voltage accelerator. Thermionic-cathode E-guns can provide long pulse lengths and even continuous operation, but typically have limited current density ($\leq$ 10 A/cm^2), high heater power requirements, and finite life. Field-emission guns offer high current density, but suffer from short pulse lengths (typically <1 μsec) because of plasma closure of the accelerating gap. Both of these conventional E-gun technologies are subject to serious degradation during ion bombardment from any plasma that might be generated in or by the electron beam.

A unique E-gun has been developed at HRL for high-power microwave tube applications.[1,2] The Hollow Cathode Plasma (HCP) E-gun offers the capability of high current density (10 to 100 A/cm^2) and long pulse length (>100 μsec) by utilizing a plasma as the source of electrons for a high-voltage accelerator. A high-perveance E-beam is produced by a multi-aperture, two-grid

accelerator that extracts the electrons from the plasma and accelerates them to high voltage ($\leq$ 150 kV to date). This E-gun design is especially advantageous in applications where ion bombardment of the accelerator and E-gun components must be tolerated, as is the case in several recently developed plasma-filled, high-power microwave sources.[2,3]

E-Gun Design

The HCP electron gun provides both high-current density and long-pulse operation without gap closure by generating a controlled plasma discharge which acts as the electron source. A low-pressure glow-discharge generated inside the hollow cathode produces a uniform and stable plasma front from which a high-current density beam is extracted. The geometry of the HCP E-gun is shown in Fig. 1. The hollow cathode is typically made of stainless steel, aluminum or molybdenum. The cold-cathode discharge operating in the hollow cathode requires no filament heater power, and is relatively insensitive to vacuum conditions. In operation, a glow discharge is initiated between the cathode and the anode-grid at a pressure of greater than 5 mTorr of He. Gas for the plasma discharge is provided by a low-level continuous leak-valve on the vacuum system, or by a fast gas-puff valve located on the hollow cathode. Gas puffing is effective in providing a low-pressure in the downstream tube because the beam pulse is over before the transient gas pulse enters the vacuum system. The anode of the discharge is the first grid of the high-perveance, multi-aperture electron accelerator. The discharge-anode grid is suspended inside the high-voltage ceramic bushing, and faces a matching second grid of the two-grid accelerator. The discharge-anode grid acts as the cathode of the two grid electron accelerator.

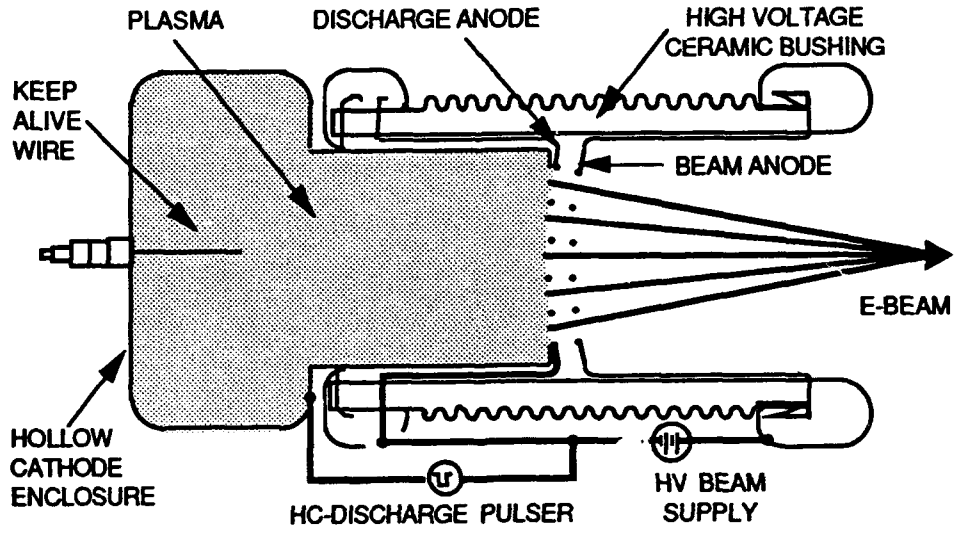

Figure 1. Schematic diagram of the Hughes Hollow Cathode Plasma (HCP) E-gun.

An electrical schematic for the E-gun is shown in Fig. 2. The plasma density in the hollow cathode, and subsequently the beam current density, is controlled by a low-voltage (< 10 kV), hollow-cathode discharge pulser. Electrically, we charge a pulse forming network (PFN), and discharge the PFN between the hollow-cathode and the first accelerator grid (the anode of the discharge) through a switch such as the ignitron shown. A keep-alive power supply is included to reduce the jitter in the pulses by providing a low-current, dc discharge. Plasma electrons that pass through the anode grid of the discharge enter the accelerator. A dc high-voltage power supply between the two grids accelerates the electrons across the gap, while the low-voltage discharge pulser modulates the beam current to generate arbitrary pulse waveforms. Also shown is the power supply for pulsing the fast electro-mechanical gas puff valve. The discharge, keep-alive, and gas puff power supplies are located on a HV modulator deck and float at the E-beam voltage.

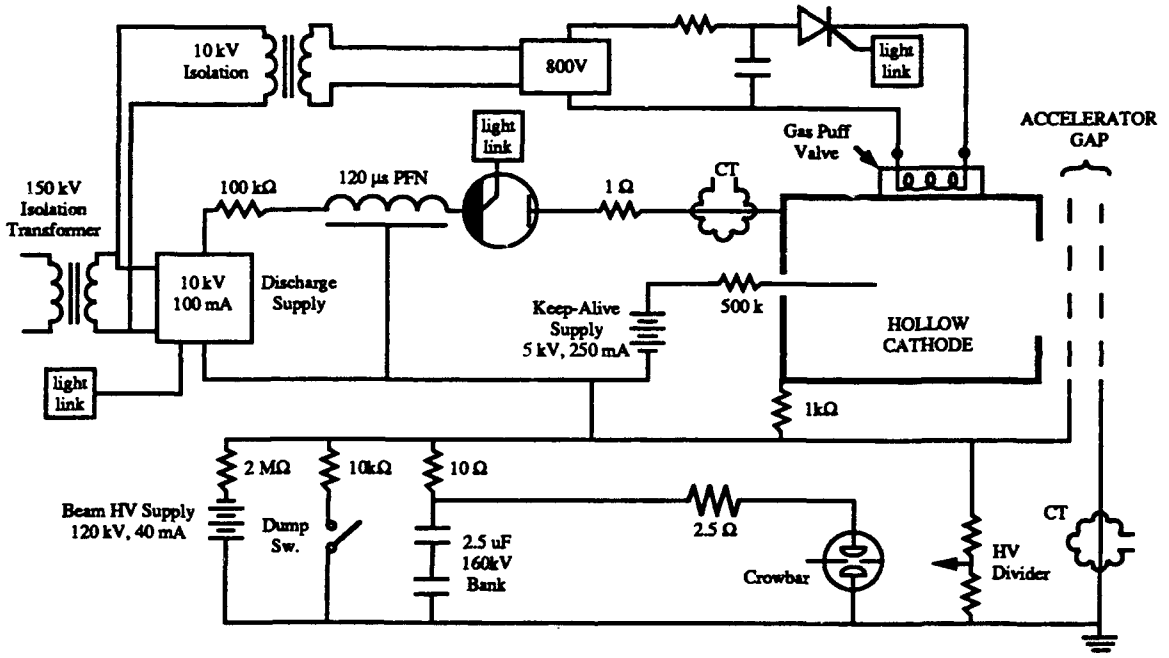

Figure 2. HCP E-gun electrical schematic.

An axial view of the E-gun is shown in Fig. 3. The 10-cm-diameter molybdenum accelerator grids seen in the figure are positioned in the center of the ceramic bushing, and have 163 apertures each 3-mm in diameter. These apertures are precisely aligned with respect to each other and their edges shaped in accordance with a Hermannsfeld-code[4] analysis of the electron trajectories to provide electrostatic focussing of the beamlets through the anode-grid apertures. The gap distance between the two grid is determined by the maximum electric field allowed to avoid vacuum breakdown, the desired operating voltage, and the current density in the accelerator. If "E" is the design voltage stress (≈100 kV/cm), and the current density is determined to first order by the Child-Langmuir equation, then the current density from the E-gun is:

$$J_e = PT \frac{V^{3/2}}{d^2} = PTE \frac{V^{1/2}}{d} , \qquad (1)$$

where J_e is the electron current density in the aperture, P is the value of the electron perveance coefficient (2.33×10^{-6}), T is the effective transparency of the multi-aperture grid array, V is the voltage across the acceleration gap, and d is the gap distance. For a 100-kV beam voltage, 1-cm gap, and 50% transparency grid system, Eq. 1 predicts a maximum average electron current density of 37 A/cm^2 from the accelerator.

Figure 3. Photograph of the HCP E-gun with aligned, 3-mm aperture grids.

Results

An example of the operation of the HCP E-gun with 3-mm apertures and a 7.8-mm gap is shown in Fig. 4, where the upper curve is the beam current and the lower curve is the discharge current in the hollow cathode. In this 50-μsec, 450-A pulse, the beam and discharge currents are approximately equal. This occurs because the accelerator is operating under perveance, and the beam acceleration potential pushes into the apertures and collects a majority of the electron current.

The 3-mm aperture grids are limited to voltages less than about 60 kV and currents less than 500 A. As the total beam current was increased to this level, the plasma profile became less-uniform and a non-exact perveance match over the accelerator grid causes beamlet de-focussing, anode grid interception and arcing. As the beam voltage was increased over 60 kV for currents $\leq$ 500 A, the high-voltage (HV) potential pushes further into the plasma, collecting a greater fraction of the discharge current. The HV power supply then interacts with the discharge by increasing the effective anode potential, which increased the discharge current and plasma density. This caused the plasma front to become unstable, which also leads to grid interception and arcing.

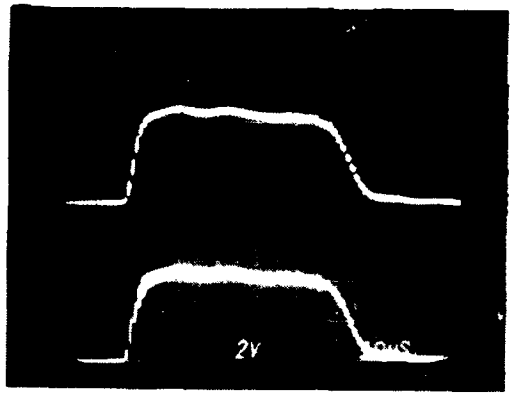

Figure 4. HCP E-gun performance with 3-mm apertures at 50 kV and 450 A.

To avoid these problems and increase the current and voltage available from the HCP E-gun, a very fine mesh is attached to the back of the first accelerator grid. This mesh defines the discharge anode potential from which the electrons are extracted by collecting a reasonable fraction of the discharge current (40 to 50%), and permits operation over a wide perveance range by fixing the extraction plane. The size of the grid holes, the mesh transparency and the HV gap are optimized for the desired beam current and voltage. Figure 5 shows the present grid set with 1-cm diameter apertures, and the fine mesh attached to the discharge-anode grid.

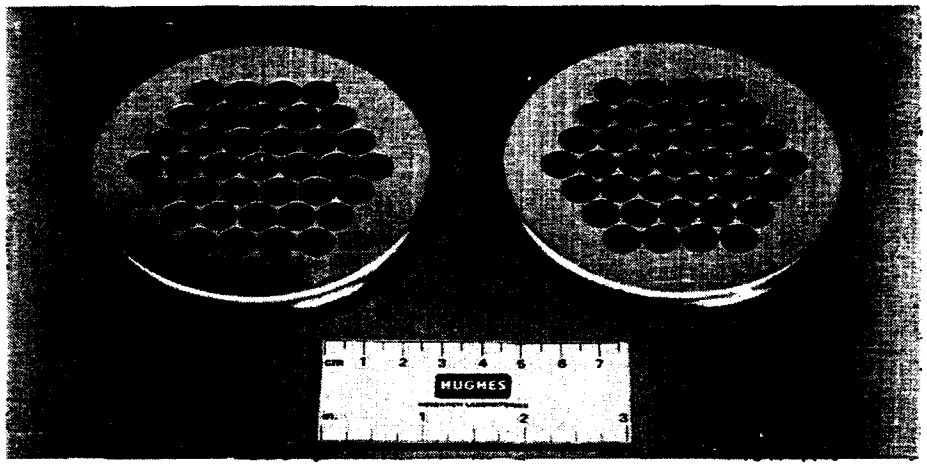

Figure 5. Molybdenum accelerator grids with fine stainless steel mesh attached to one grid.

Operation of the HCP E-gun with this grid set is illustrated in Fig. 6. A 100-μsec, 300-A beam pulse at 95 kV is shown in 6(a), while a 50-μsec, 500-A pulse at 95 kV is shown in 6(b). The HCP E-gun has produced 100-μsec E-beam pulses at voltages of up to 150 kV and total currents of up to 750 A. Bursts of multiple pulses and high pulse-repetition rates (up to 500 Hz) have also been achieved, and the E-gun design can be scaled to larger sizes for higher currents and voltages.

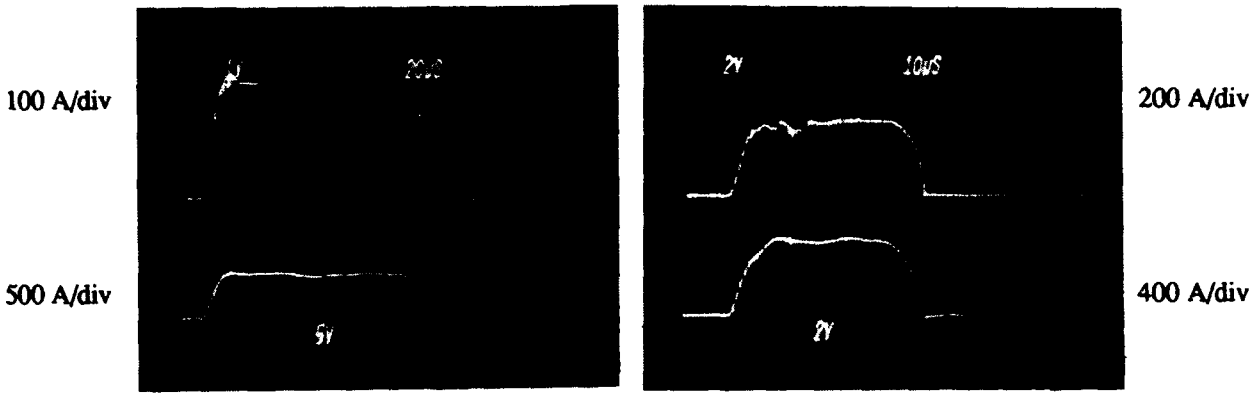

Figure 6. Beam current (top trace) and discharge current (bottom) for a 300-A, 100-μsec beam pulse at 95 kV shown in (a), and a 400-A, 50-μsec beam pulse at 100 kV shown in (b).

In most high-power microwave sources, axial magnetic fields are required to transport the high current electron beam because electrostatic space-charge forces can lead to rapid radial expansion of the electron beam. With the HCP E-gun, radial space-charge forces in the electron beam are eliminated by allowing the long pulse-length beam to ionize the low-pressure fill gas and create a plasma channel to neutralize the beam. In the absence of space-charge forces and an external magnetic field, the beam's self-magnetic field causes the beam radius to compress. This process is commonly known as the Bennett pinch effect[5], and occurs when the beam self-generated azimuthal magnetic field pressure exceeds the beam thermal pressure. Space-charge neutralized electron beams undergoing self-pinch are typically described as propagating in the ion-focused regime. As the electron beam travels through the gas filled drift section, it compresses to a small equilibrium diameter (≤ 2 cm) and can increase the beam current density by over an order of magnitude. For the 300-A beam pulse of Fig. 6a that self-pinches into a approximately 1-cm diameter, an electron beam current density of over 200 A/cm^2 is achieved.

*Work support by Hughes Aircraft Company IR&D.

References

1. R.W. Schumacher, et al., U.S. Patent #4912367, (1990).
2. D.M. Goebel, R.W. Schumacher, J.M. Butler, *Intense Microwave and Particle Beams*, H.E. Brandt, Editor, Proc. SPIE **1629**, 119(1992).
3. Y. Carmel, K. Minami, W. Lou, et.al, *IEEE Trans. Plasma. Sci.*, **18**(3), 497 (1990).
4. W.B. Herrmannsfeldt, E-GUN, SLAC-331, Stanford Linear Accelerator Center, Nov. 1988.
5. N. A. Krall and A. W. Trivelpiece, " *Principles of Plasma Physics*," (McGraw Hill, New York, 1973) p. 495.

CONTROLLING THE EMISSION CURRENT FROM A PLASMA CATHODE

S.P. Bugaev, V.I. Gushenets, and P.M. Schanin

The processes determining the time and amplitude characteristics of the grid-controlled electron emission from the plasma of an arc discharge have been analysed. It has been shown that by applying to the grid confining the plasma emission boundary of a modulated voltage it is possible to form current pulse of up to 1 kA with nanosecond risetimes and falltimes and a pulse repetitive rate of 100 kHz.

Introduction

Operation of free-electron lasers, microwave generation, and high current switching demand kiloampere electron beams with a nanosecond pulse duration and a pulse repetitive rate reaching some tens or hundreds of kilohertzs. Electron beams of the such kind can be produced in plasma-cathode accelerator by modulating the voltage applied to the control grid. As distinct from hot-cathode triode systems, the control of the plasma cathode emission current involves more complicated processes and more deep links between the cathode emissive properties and the control grid parameters.

Static Characteristics of the Grid-Controlled Emission Current

Figure 1 shows a schematic diagram of a plasma source using grid control.

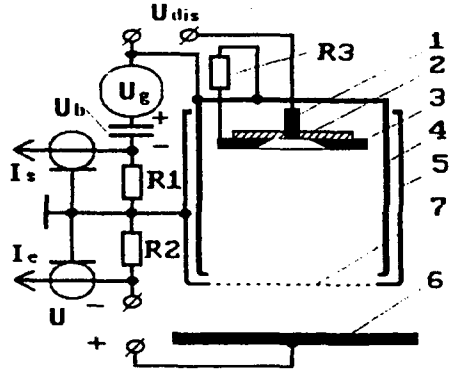

Fig. 1

The emitting plasma is generated in hollow anode *4* by an arc discharge initiated by a spark creeping over the surface of dielectric *2* between cathode *3* and igniting electrode *1*. Outer electrode *5*, whose end face is covered with fine grid *7*, embraces the hollow anode. Electrons are emitted from the plasma boundary fixed near the grid and are accelerated by the voltage applied between the grid and collector *6*.

In the hollow-anode system, near the anode walls and the grid, a negative anode potential drop exists, which form a potential barrier for the electrons running away from the plasma to the anode. The barrier width can be estimated using the "3/2" law for the sheath ion current and Bohm's ion saturation current

$$l_s = \frac{2}{3}\left[\frac{e_0}{0.4n_e}\right]^{1/2}\left[\frac{2}{ekT_e}\right]^{1/4}\Delta\varphi^{3/4}, \qquad (1)$$

where e_0 is the absolute dielectric constant, e is the electronic charge, k is Boltzmann's constant, T_e and n_e are the electron temperature and density in the plasma, respectively, and $\Delta\varphi$ is the plasma-electrode potential difference.

In the presence of a grid, the electron emission into the accelerating gap through the grid meshes can occur in either of two limiting modes. If the thickness of the near-wall sheath is much smaller than the mesh size, electrons emit from an open plasma surface with an average current density

$$j_e = \frac{en_e v}{4}\eta, \qquad (2)$$

where η is the geometrical transparency of the grid. In this mode, the maximum emission current can be equal to the discharge current.

For $l_s >> h$, electron emission occurs through a potential barrier and the emission current density is described by the expression:

$$j_e = \frac{en_e v}{4}\eta \exp\left[-\frac{e\eta}{kT_e}\right]. \qquad (3)$$

Only a portion of the discharge current proportional to the ratio of the sum area of all grid meshes to the hollow anode area enters the accelerating gap. In order to reduce or entirely exclude the electron income into the gap, one should increase the potential barrier for electrons, which is attained by negatively biasing

the grid insulated from the hollow anode. The emission and pulse formation are restored by applying to the grid of a positive voltage pulse.

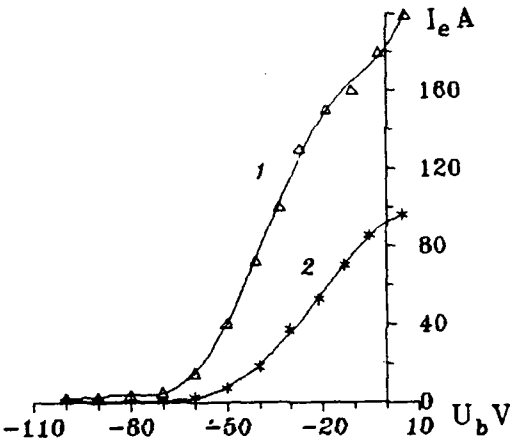

Fig. 2

Shown in Fig. 2 are plots of the emission current as a function of the bias voltage, U_b, (static characteristics) for two values of discharge current (*1* - 400 A; *2* - 200 A). The emission current increases, but not in direct proportion, with the discharge current. The growth of the discharge current increases the plasma density, which leads to a decrease in the near-electrode sheath thickness, l_s, and, hence, brings the sheath boundary nearer to the grid. Superposition of the sheath field and the gap field in the grid meshes results in the formation of a new potential profile with a lower potential barrier for electrons.

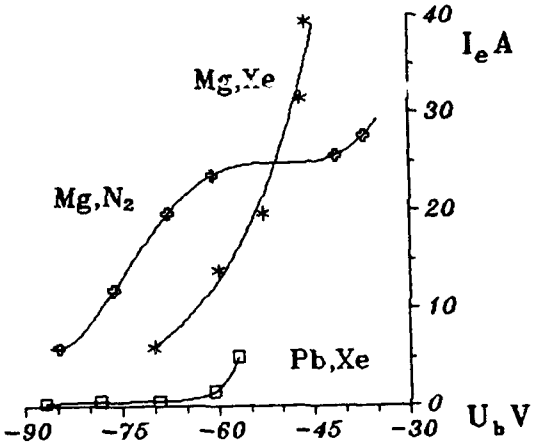

Fig. 3

The view of the grid characteristics depends on the plasma parameters. Using a gas with a large cross section of inelastic interactions of its atoms/moleculas with electrons and increasing the gas pressure increases the plasma density and

decreases the plasma electron temperature, the electron energy, and the number of fast electrons. This results, as seen from Fig. 3, in a steeper grid control characteristic and a lower bias voltage. Figure 3 also shows the effect of cathode material on the grid control characteristic. Replacing a Mg cathode for a Pb cathode reduces the emission (background) current from 14 to 2 A for the same bias voltage, - 60 V.

Plasma Processes at a Pulsed Control of the Emission Current

The grid is permanently at a negative bias voltage, U_b, which prevents the electrons from coming in the accelerating gap, the source being in the gate mode. After the completion of the plasma formation in the hollow anode, a positive voltage pulse is applied to the grid from a nanosecond pulse generator, which results in a stepwise increase in the potential of the control grid with respect to the anode and the grid and a change in the heights of potential barriers and the widths of near-electrode sheaths. As a result of the electron motion toward to the control grid, the space charge near-anode sheath widens. As it becomes wider, the voltage drop across the sheath increases, while the electric field in the plasma decreases. At a certain point, the field in the plasma becomes neutralized by the field of the near-anode sheath space charge. The electrons go on moving and, as a result, a field of opposite polarity appears in the plasma, which decelerates the electrons and, again, changes the direction of their motion. Thus oscillations of the electron cloud appear in the plasma [1], which attenuate in a time described by the formula [2]

$$t_l = 0.2 \left[\frac{m_i}{8\pi n_i e^2} \right]^{1/2}. \qquad (4)$$

Under the conditions of the experiment, for $m_i = 2.18 \cdot 10^{-22}$ g and $n_i = 5 \cdot 10^{11}$ cm^{-3} the attenuation time was $t_l \approx 10^{-9}$ s.

For electron emission from a plasma occurring through a potential barrier, the process of current transition to a steady state can be described by the equation [3]:

$$ev \frac{d(<\Delta n_e>)}{dt} = I_{dis} - j_{ch} S_a \exp(-e(\varphi + U_0)/kt_e) - j_{ch} S_g \exp(-e\varphi/kT_e), \qquad (5)$$

where V is the volume of the interelectrode gap, $\langle \Delta n_e \rangle$ is the excess plasma electron density averaged in volume, I_{dis} is the discharge current, j_{ch} is the density of the chaotic electron current in the plasma, φ is the plasma potential, and S_a and S_g are the area of the anode and the grid, respectively.

The value of τ calculated for the experimental conditions ($T_e \simeq 10$ eV, $I_{dis} \simeq 10^3$ A, $l_s \simeq 0.05$ mm, $S \simeq 4 \cdot 10^3$ cm^2) is on the order of 10^{-9} s. The current transition to a steady state terminates in a time $t_2 = (3 \text{ to } 5)\tau$.

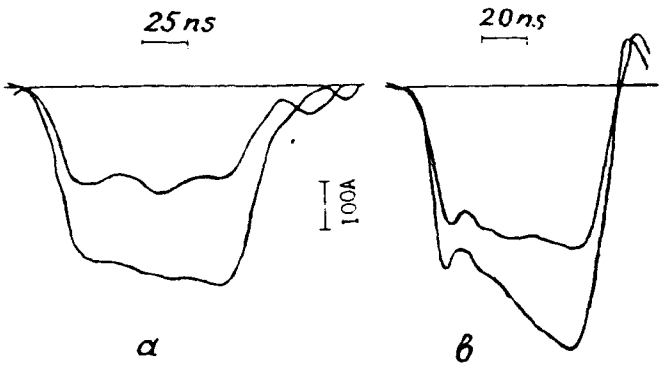

Fig. 4. The emission current waveforms:
a - I_{dis} = 400 A, h = 0.21 (*1*) and 0.54 mm (*2*); *b* - I_{dis} = 700 (*1*) and 860 A (*2*).

Figure 4 gives the beam current waveforms for various experimental conditions.

It can be seen that there exist two regions with different rates of beam current rise, corresponding to different modes of electron extraction from plasma. In the first mode, during the pulse risetime, when $l_s >> h$, the current growth due to a decrease of the potential barrier height as a result of a change in the negative charge in the plasma, $e\Delta n_e$. In view of the fact that the control voltage risetime is longer than the relaxation time, t_2, of the excess charge, $e\Delta n_e$, the leading edges of the grid and beam currents follow the waveform of the grid voltage. During this time the beam current increases to $I_b \simeq I_{dis}$. In the second mode, the current slowly increases at the pulse peak, which is due to the displacement of the near-electrode sheath boundaries. As l_s becomes less than h, the barrier height decreases as a result of the superposition of the field of the sheath space charge and the field of the accelerating gap in the grid meshes. Throughout this period, the sum of the emission current and the grid current remains essentially constant and close to the discharge current. For a smaller grid mesh size, $l_s >> h$ at any time, so the height of the potential barrier only decreases as a result of the relaxation of the

excess charge in the plasma, and the maximum beam current is only determined by the grid transparency, η, while the motion of the sheath boundary stops affecting the emission current (Fig. 4*a*). The use of a grid with smaller meshes and lower transparency leads to a decrease in the efficiency of electron extraction, making, however, possible to reduce the negative bias voltage at the grid and thus to increase the control efficiency and decrease the probability of appearance of cathode spots on the grid and breakdown in the accelerating gap.

Increasing the discharge current increases the plasma density and, correspondingly, decreases the thickness of the near-wall sheath. Starting from a certain value of discharge current, the near-wall sheath thickness, $l_s(t)$, becomes comparable with the grid mesh size, h, and, as a result, a current growth at the current peak is observed again (Fig. 4*b*), the sum current remaining constant and close to the discharge current, that is the current is switched from the grid to the emitting surface. This switching is caused by the disposition of the near-electrode sheath boundary and occurs at a rather slow rate.

The results of the above-described studies have been used in the development of a grid-controlled plasma cathode designed for repetitive pulsed operation with a pulse repetitive rate of $3 \cdot 10^4$ s^{-1}, the number of pulses per burst being controlled between 1 and 20. In testing the device, an electron beam of cross-sectional area $S = 120$ cm^2 with a pulse risetime of no more than 20 ns has been generated at a discharge current of 900 A. The peak current and the pulse repetition period were stable within 10% and 0.1%, respectively. The time and frequency characteristics of the beam current pulses were restricted by the limiting characteristics of the driving generator used.

References

1. Singh Nagendra, Plasma Phys., 24, 639 (1982).
2. B.V. Alekseev, V.A. Kotelnikov, and V.N. Novikov, Fizika plasmy, 5, 920 (1979) (in Russian).
3. V.L. Galansky, V.I. Gushenets, and E.M. Oks, Abstracts of papers on 7-th All-Union Symp. on High-Current Electronics. Tomsk, 1988, Vol. 1, p. 89 (in Russian).

FORMATION OF INTENSE CONVERGENT PARTICLE BEAMS IN A GAS-DISCHARGE-PLASMA-EMITTER DIODE

N.V.Gavrilov, Yu.E.Kreindel, G.A.Mesyats, and O.A.Shubin

Institute of Electrophysics
Russian Academy of Sciences Ural Division

ABSTRACT

Using a low-pressure arc with a shielded cathode spot, an emitter of electrons and gas ions has been developed. It provides an emission current density of electrons and gas ions of up to 1 A/cm^2 and 0.02 A/cm^2, respectively, and operates in the pulse-repetitive mode with a repetition rate of up to 50 s^{-1} and a pulse duration of 1 ms. Converging in a beam plasma-filled drift space the electron and ion beams with a current density compression factor of more than 10 are produced in a spherical diode with a large plasma emission area and a distance between the beam-forming multiaperture electrodes (12 mm) being much less than the electrode curvature radius (250 mm).

The electron beam with energy of 20 keV and current of 40 A has the power density over 10^5 W/cm^2 in the crossover, the beam energy density exceeding 75 J/cm^2 per pulse. The current density of 20-keV nitrogen ions is over 0.15 A/cm^2. The electron source designed for technological purposes, which offers a peak power of up to 1 MW over a beam cross-section of several cm^2 and average power up to 20 kW in the pulse-repetitive mode has been developed on the basis of the above mentioned principles.

1. Introduction

Plasma emitters of charged particles based on a low-pressure arc with a cathode spot are used to produce intense electron and gas-ion beams. The use of low-voltage (U_d=100-150 V) and high-current (I_d=10-100 A) discharges enables such emitters to have relatively high energy efficiency and to provide high density emission

currents (j_e = 1 A/cm^2, j_i = 0.1 A/cm^2) from large plasma emission area (S = 100-1000 cm^2) [1,2]. The use of massive cathodes and glow-discharge-initiated arcs ensures high reliability and long service life of these systems operating in the repetitive mode [3] and makes possible their industrial application. For purposes of ion implantation and electron-beam heat treatment there has been developed a source producing broad (150 cm^2) beams with an electron energy up to 25 keV and a beam current up to 50 A, in the gas-ion operation, these parameters are up to 50 keV and 1 A, respectively [4]. These sources producing 1-ms pulsed beams may find wider application if the electron-beam power density q reaches the values more than 10^5 W/cm^2, at which effective pulse surface case hardening of steels and irons to depths beyond 0.1 mm is possible. The possibility of focusing high-perveance (10 A/V$^{3/2}$) electron beams in systems with a grid-stabilized plasma emitter has been investigated.

2. The principle of convergent beam formation

When a metal surface is irradiated with a low-energy electron beam of 1-ms duration, the depth of thermal effect is significantly more than the electron path. During ion implantation the changes in structure and phase transitions happen to occur to a depth several factors of 10 more than the ion projective path. That is why it is possible to use beams having high current densities under the conditions of considerable convergence angles.

To obtain intense convergent beams in a diode with a gas-discharge plasma emitter of large emission area it is reasonable to use spherical multi-aperture corpuscular optics with the acceleration gap length L being much smaller than the electrode curvature radius R. In an optics like this,the extraction of charged particles and their acceleration proceed under the conditions of relatively low current density j and accelerating electric field E, and the beams converge in a drift space filled with the beam plasma. The low values of j and E ensure high electric strength of the diode and the ion background facilitates the higher beam

compression. In this system the crossover size depends on both the conditions of beamlets formation in the individual apertures of the optical system and the peculiarities of the charged particle motion in the drift space. An analysis of the electron beam propagation and the beam-gas interaction shows that the ion background neutralizes the space charge of the beam and that the compression of the compensated beam by its own magnetic field is negligible. The divergence of the beams throughout a distance R due to rather high thermal velocities of the plasma electrons (kT_e ~ 5-10 eV) estimated in accordance with [5] as $\delta = R\,(kT_e/2eU)$ was in the range of 2.5-3.5 mm, the accelerated electron energy eU being 20 keV.

3. Plasma emitter based on an arc with cathode spot

The formation of a plasma emitter with a large emission area requires the burning of an arc in a long gap and the stabilization of the plasma parameters and its emission surface. It can be implemented by means of the elements shown in Fig.1. The glow discharge with a current density at the cathode up to 10 A/cm^2 is ignited between cathode 1 and triggering electrode 2. A spontaneous glow-to-arc transition creates the conditions for triggering of the main discharge between cathode 1 and hollow anode 3. The crossed electric and magnetic fields used in this device not only facilitate arc triggering, but also provide for the motion of the spot. This reduces the local heating of the cathode and its droplet erosion and keeps the erosion of the cathode small and uniform with

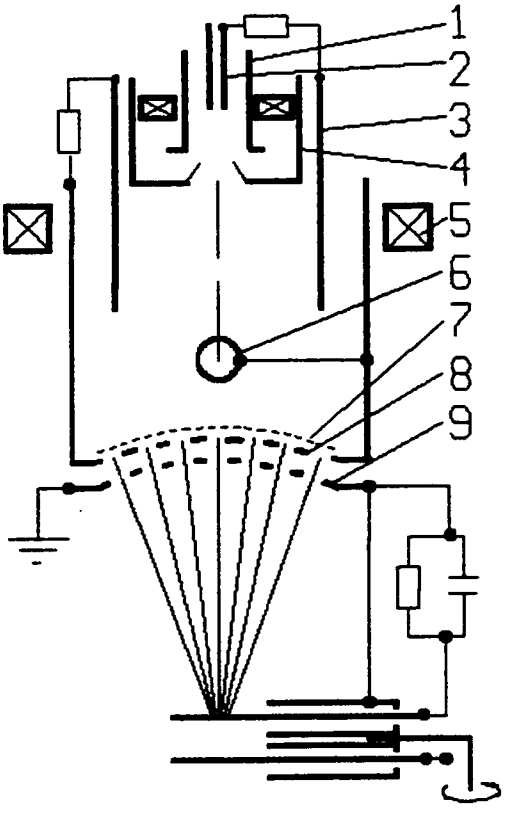

Fig.1

the mean rate of $2 \cdot 10^{-6}$ g/C. The constriction of the arc column by the hole in electrode 4 ensures the stability of the anode plasma parameters while the cathode spot moving inside the cavity.

A discharge of current 10-80 A and pulse duration 0.5-1 ms was triggered in the pulse-repetitive mode with a repetition rate of up to 50 s^{-1}. The pressure gradient in the discharge gap ensures the stable discharge operation and high electric strength of the acceleration gap with a pressure of $5 \cdot 10^{-2}$ to 10^{-1} Pa. The magnetic field created by solenoid 5 increases the charged particle extraction efficiency. Electrode 6 is to improve the plasma radial uniformity. In order to stabilize the plasma emission surface position and maintain the stable-discharge conditions, when a considerable part (> 50%) of the electron component of the discharge current is extracted, a grid 7 with a 1.6*1.6-mm mesh size being nearly equal to the double thickness of the electrode sheath is mounted on emitter electrode 8. The total area S of the grid-covered holes in the multiaperture electrode 8 was 50 cm^2. A dc acceleration voltage U = 20 kV was applied between emitter 7 and accelerating electrode 9 with the same curvature radius R=250 mm.

4. Experiment

The experiment was carried out with beam currents of 10 to 80 A and pulse duration t of 1 ms. The measurements of the beam radial profile were made by means of a pair of rotating bar probes.

The radial profiles of current density for the broad and convergent electron beams, obtained at a distance of 250 mm from the source, the beam current (40 A)and plasma emission area S (50 cm^2) being kept constant, are shown in Fig.2. A broad electron beam (Fig.2,a) was produced

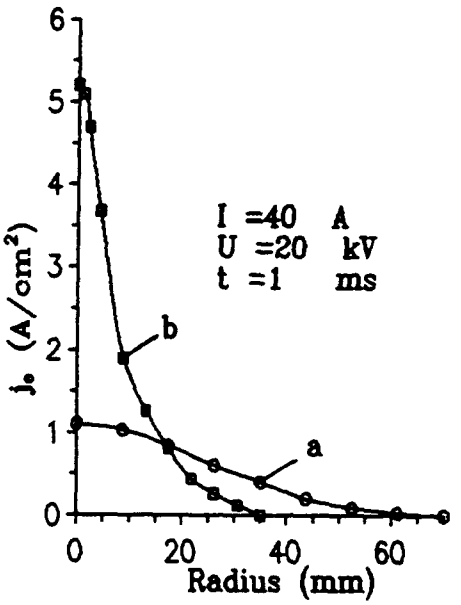

Fig.2

by a plane-parallel optics with 8-mm dia openings. The profile shape indicates that the electron emission from the plasma cathode is sufficiently uniform and the individual beamlets have significant divergence angles. The convergent beam was produced using a system with 10-mm dia round holes disposed over a distance different for the emitter and acceleration electrodes, the acceleration gap L being 12 mm in length. The beam remains to have a radius close to a minimum (r = 15-20 mm) at a distance from the emitter electrode being in the range of 230-270 mm.

The possibility of the formation of the convergent beams using an optics with various hole geometry and size has been investigated. The system with circular openings is shown to lead to the best results. The limitation for systems have to do with both the conditions for slow-divergent beam formation in the individual openings and the problems of manufacturing and alignment of the electrodes. The optimal in design and properties system with circular 10- mm dia openings produces convergent beams with a ~10-fold current compression. The power density in the crossover exceeds 10^5 W/cm^2, the energy per unit area reaches 75 J/cm^2 per pulse. The system shows stable repetitive operation.

With the optics used, the excess of beam current I above 40 A did not lead to an increase in current density j_{eo} at the beam axis. This has to do with the considerable discharge of the capacitor store and violation of the beam focusing conditions in the optical system, even the three-halves power law being satisfied. The experiments (Fig.3) and a computer simulation have verified that. Decreasing t to 0.5 ms increased j_{eo} to 10 A/cm^2 for I=80 A.

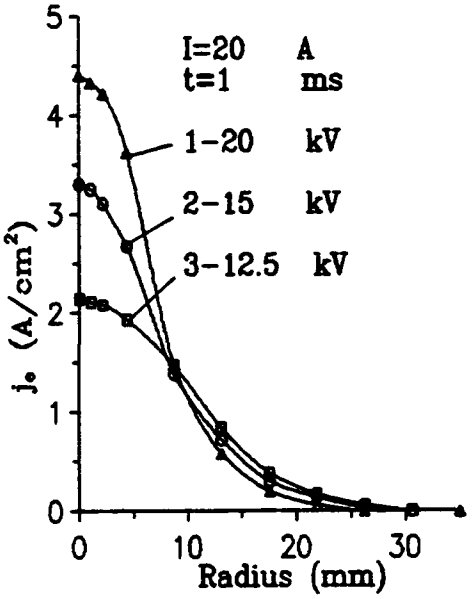

Fig.3

In ion-beam operation, the size of the openings in the two-electrode

optics is limited by the conditions of secondary electron cutoff and by the arcing due to bombardment of the acceleration electrode by the beam plasma ions. For U = 20 kV, diode gap length of 6 mm and aperture diameter of 5 mm, the cutoff voltage was 2 kV and the nitrogen-ion current density reached 0.14 A/cm^2 in a 2.5-cm^2 crossover.

The samples of cast iron have been treated with a convergent electron beam of pulse power up to 1 MW and average power up to 20 kW [7]. Case-hardened layers 10-30 mm thick have been obtained in the single-pulse operation without surface melting. In the quasi-continuous operation, 5 mm thick layers have been hardened from the liquid state. Cyclic thermal treatment of spring-loaded parts of Nb-based refractory alloys with an electron beam of power density 10^4 W/cm^2 gives a 1.5-2 fold increase in the limiting operating elastic stresses with respect to the values obtained after conventional thermal hardening in a furnace [8].

REFERENCES

1. S.P.Bugaev, Yu.E.Kreindel, P.M.Shchanin. Large cross-section electron beams, [in Russian], Energoatomizdat,Moscow,(1984),112 p.

2. N.V.Gavrilov, Yu.E.Kreindel, G.A.Mesyats, and F.N.Shvedov, Pisma Zh. Tekh. Fiz. v.14, N10, p.865-869 (1988).

3. N.V.Gavrilov, Yu.E Kreindel, F.N.Shvedov, Proc. XIX Intern. Conf. on Phenomena in Ionized Gases, Yugoslavia. p.720-721(1989).

4. N.V.Gavrilov, Yu.E.Kreindel, and O.A.Shubin, Prib. Tekh. Eksper. No. 3, p.130-134 (1991).

5. S.I.Molokovskii, A.D.Sushkov, Intense electron and ion beams [in Russian], Energoatomizdat, Moscow,(1991), 112 p.

6. V.L.Galanskii, Yu.E.Kreindel, E.M.Oks, A.G.Ripp, and P.M.Shchanin, Zh. Tekh. Fiz. v.57, No.5, p.877-882 (1987).

7. N.V.Gavrilov, Yu.E.Kreindel, E.Ya.Raits, et al., Abstracts of Proc. of 8th Symp. on High-Current Electronics [in Russian], part 2, Sverdlovsk, p.201-203 (1990).

8. N.V.Gavrilov, V.P.Belogur, V.N.Mizgulin, et al., Ibid., p.218-220.

FORMATION AND TRANSPORTATION OF A MICROSECOND HIGH-CURRENT ELECTRON BEAM IN A PLASMA-ANODE GUN

M.Yu.Kreindel, E.A.Litvinov, G.E.Ozur*, D.I.Proskurovsky*

Institute of Electrophysics, Ekaterinburg, 620219
* Institute of High-Current Electronics, Tomsk, 634055
Russian Academy of Sciences

ABSTRACT. As an extension to an earlier work, some features of the generation of a low-energy, high-current, electron beam in a plasma-anode gun placed in an external guide magnetic field have been investigated. The nonstationary stage of current extraction where the characteristic time required for an ion to pass through the double layer is analysed. The dynamics of relaxation of the beam energy in its transportation through the anode plasma toward the collector has been investigated.

I. INTRODUCTION

Low-energy (10 to 30 keV), high-current electron beams (HCEBs) are of substantial intertest in view of their application for surface modification of materials [1]. The new approuch based on the use of an electron gun with a plasma anode and an explosive-emission cathode placed in an external magnetic field allows production of low-energy HCEBs of much better quality than those generated in a vacuum-diode-based gun [2-4]. Preliminary studies of the low-energy HCEBs generation in a plasma-anode gun revealed a number of peculiarities [2,4] the most important of which are discussed in the present paper.

II. EXPERIMENTAL SETUP

A block-diagram of the experimental setup is given in Fig.1. Cathode 1 of diameter 1.5 cm was made as a graphite-ceramic structure. Anode plasma was produced using 12 spark sources disposed evenly in a circle 3.4 cm in diameter. Anode electrode 2 had a hole of diameter 1.9 cm. The power supply of the spark sources and the start of high-voltage pulse generator 5 were acomplished from two-channel trigger unit 6. The external magnetic field was created by pulsed solenoid 9. Timing of all power sources was executed by control unit 7. Switched on first were the anode plasma sources and then, with 2-μs delay, a high-voltage pulse was applicated to the cathode. Generator 5 produced a specifically formed pulse consisting of a short ($\tau_+ \simeq 20$ ns) positive prepulse followed by the main accelerating voltage pulse. As shown in [2,4], this allows

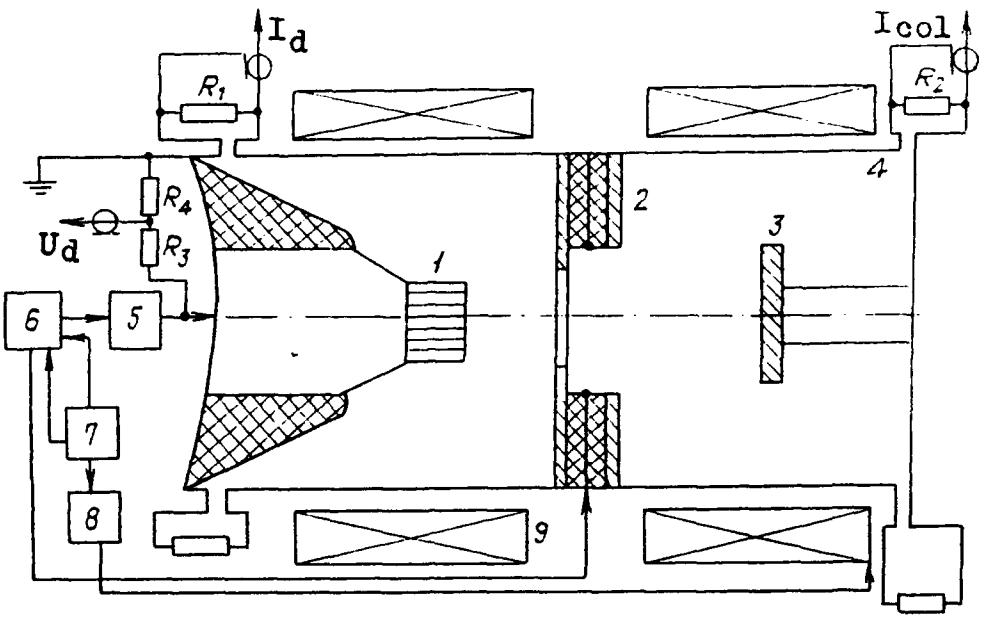

Fig.1. Block-diagram of the experimental setup. 1-cathode; 2-anode electrode with spark sources; 3-collector; 4-vacuum chamber; 5-pulse generator; 6-trigger unit; 7-control unit; 8-pulse solenoid capacitor; 9-solenoid.

uniform initiation of explosive emission throughout the cathode surface. After initiation of explosive emission, a double layer (DL) forms between the cathode and the anode plasmas, in which the electron beam is formed. Typical diode voltage and current waveforms are given in Fig.2,a,b.

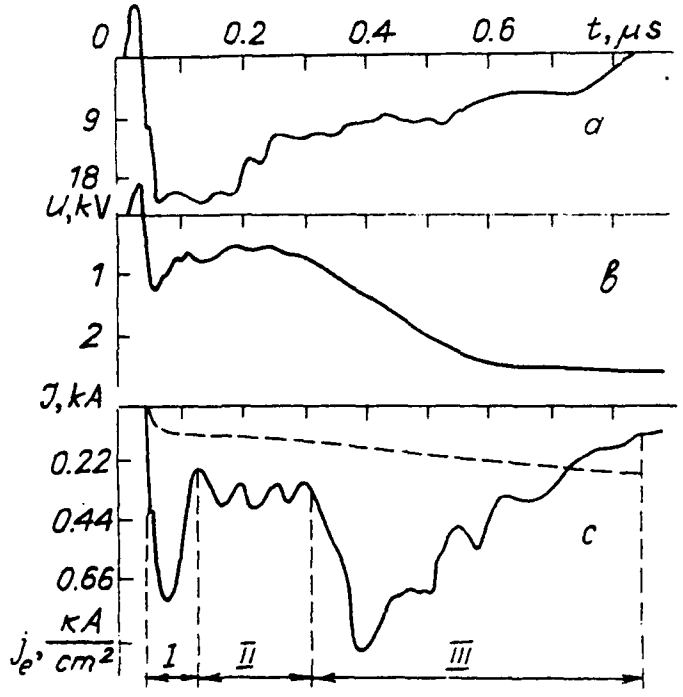

Fig.2. Typical oscillograms: a-diode voltage; b-diode current; c-current density (solid curve - experiment, dashed curve - calculation according to Child-Langmuir law).

III. CURRENT FLOW IN THE DOUBLE LAYER

In the direct discharge [5] and plasma opening switching [6] studies it is supposed that the DL is quasistationary, i.e., the Child-Langmuir law for a bipolar current is valid. However, our experiments [3,4] have shown that early after the onset of current flow the DL is nonstationary due to the short risetime of the applied voltage pulse, so the electron beam current density, j_e (t), may be several times higher than the Child-Langmuir limit (Fig.2,c). The time-dependent current density was found by numerically solving Poisson's time-dependent (for ions) equation combined with the equation of motion and the continuity equation with suitable boundary conditions [7]. The voltage pulse waveform was specified by its amplitude V_0 and risetime τ_f. In finding the current density the condition of electric field zero at the cathode was used. The model input specifications taken from our experiments [2,4] were as follows: interelectrode gap spacing d=2 cm, anode plasma density $n_a = 5\times10^{11}$ to 5×10^{12} cm^{-3}, drift velocity of the anode plasma toward the cathode $V_0 = 6\times10^6$ cm/s, and electron temperature T_e = 2 eV. The cathode plasma motion was simulated by the motion of the cathode plasma emission boundary toward the anode at a velocity $V_c = 2\times10^6$ cm/s. It was assumed that the accelerating voltage completely falls at the DL.

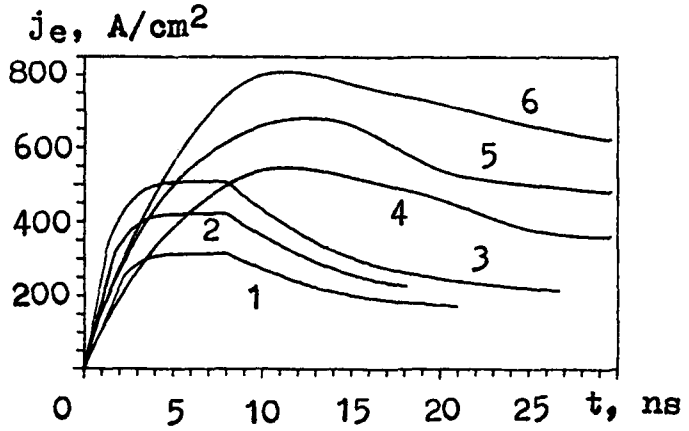

Fig.3. The time-dependent current density waveforms: (1-3) - calculated; (4-6) - experimental. $n_a=10^{12}$ cm^{-3}, τ_f=8 ns, ions - C^+. U_0=10 (1 and 4), 20 (2 and 5) and 30 kV (3 and 6).

Figure 3 gives the calculated values of current density as a function of time, j_e (t), for different values of accelerating voltage. In the early times, the current density rapidly increases due to the increase in the voltage across the DL and then, at t=2-3 ns, the current rise becomes slower and it almost goes in a plateau. This slowdown is concerned with the onset of intensive erosion of the anode plasma caused by the influence of the electric field. The current density

reaches its maximum at $t=\tau_f$ and then slowly decreases to a value corresponding to the current density in a quasistationary DL (j_{co} =190 A/cm^2). After this point, j_e becomes independent of accelerating voltage and is only determined by the plasma emissive power [5]. Fig.4 gives the current density oscillograms calculated for different values τ_f. It is not difficult to check up that maximum value of j_e for τ_f=1 ns is approximately equal to limit [7]:

$$j_{cl} = en_a \ (eU_O \ / \ 2m)^{1/2} \ ,$$

where *e,m* are electron charge and mass.

Also given in Fig.3 are typical experimental current density oscillograms (curves 4-6) corresponding region I (Fig.2,c). The current density observed experimentally grows slower and longer as compared to the predictions and peaks at values being a factor of 1.4 - 1.7 in excess of the calculated values. This discrepancy can be accounted for as follows [7]. As seen from Fig.5, during the early period the plasma electrodes geometry is rather hemispherical. This increases the ion current density at the emission centres and, hence, the total current-carrying capability of the DL.

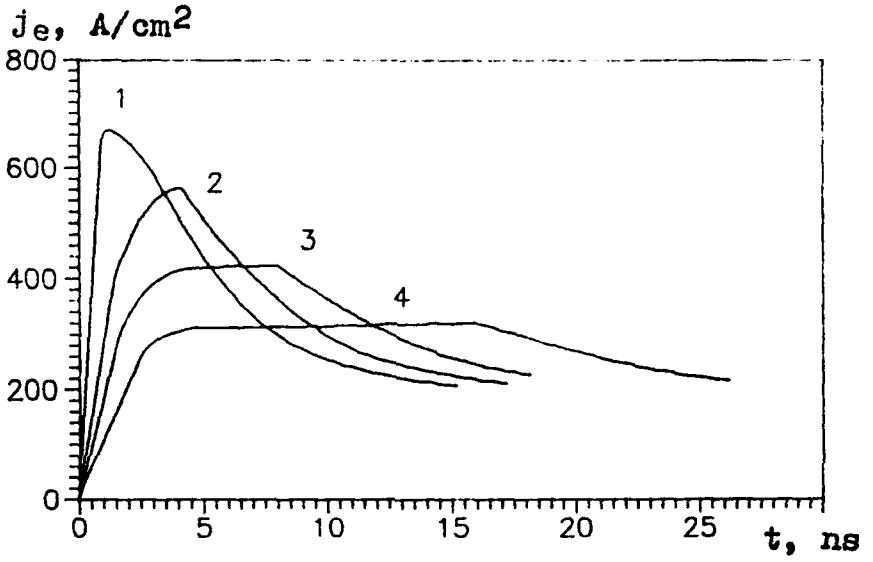

Fig.4. Calculated oscillograms of the current density for different values τ_f. τ_f=1(1), 3(2), 8(3) and 16 ns (4); n_a=10^{12} cm^{-3}, U_O=20 kV, ions-C^+.

The excess of the measured current density over that calculated from the Child-Langmuir law in region II (see Fig.2,c) can be accounted for by a partial redistribution of the potential drop from the DL to the anode plasma [3,4]. The

rapid increase in current density in region III occurs due to filling the diode gap with a denser plasma formed at the anode electrode edge from the desorbed gas [3,4].

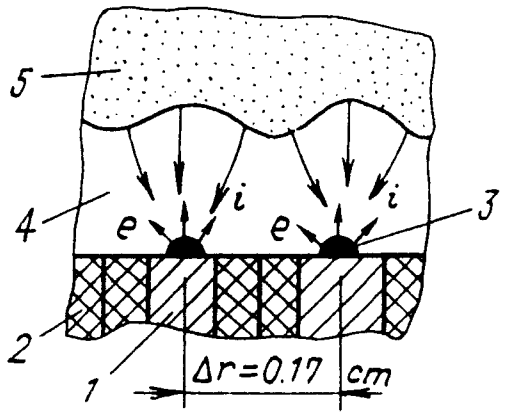

Fig.5. Plasma electrode geometry. 1-emitter; 2-ceramics; 3-emission center; 4-double layer; 5-anode plasma.

IV. LOSSES OF THE KINETIC ENERGY OF A LOW-ENERGY HCEB IN ITS TRANSPORTATION THROUGH ANODE PLASMA

Preliminary experiments [4] have shown that in the process of transportation of a low-energy HCEB a part of its kinetic energy relaxes in the anode plasma. This was evidenced by the fact that the total beam energy, W_1 , determined from the beam current and accelerating voltage waveforms was in excess of that measured by a calorimeter, W_2: $W_2=(0.65\text{-}0.8)W_1$. In order to verify this we have carried out an experiment to directly indicate the decrease in the kinetic energy of the electron beam. The measuring circuit is schematically shown in

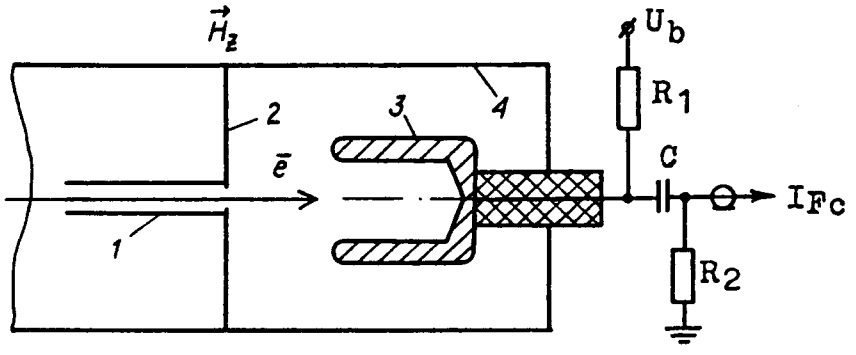

Fig.6. Scheme of the experiment. 1-collimator; 2-diafragm; 3-Faradey cup; 4-vacuum chamber; U_b-negative delaying potential; R_1-charge resistor; C-dividing capacitor; R_2-resistive shunt.

Fig.6. Shown in Fig.7 are typical waveforms of the diode voltage U_d and the Faradey cup current I_{Fc} taken in pairs. An examination of the waveforms have

shown that for $|U_b| > 5$-10 kV there occur two or more cut-offs of the Faradey cup current which correspond to different U_d values. At first cut-offs occuring

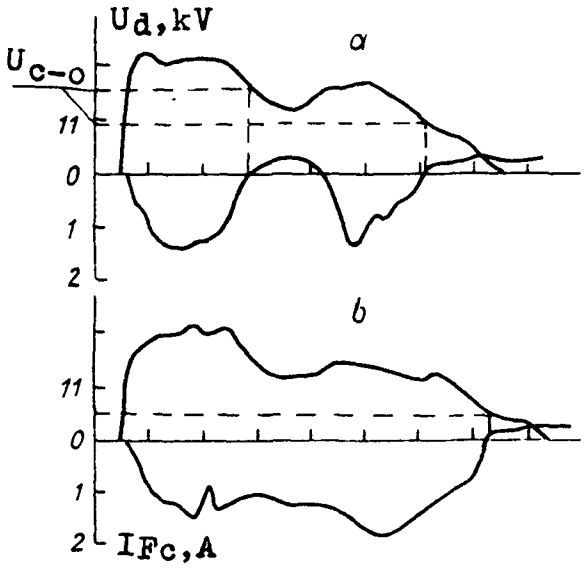

Fig.7. Characteristic oscillograms: diode voltage (the upper traces) and Faradey cup current (lower traces); U_{c-o} - the potential of the current cut-offs.

halfway through the pulse ($t \simeq 150$-500 ns), $U_d \simeq (1.3\text{-}2)U_b$, which unambiguously points to the fact that the electrons, when traveling through the plasma, loose a significant portion of their kinetic energy. For $t > 500$ ns, U_d and U_b are the same in value. An analysis has shown that the upset in beam energy relaxation is due to the fact that the drift space is gradually filled with the denser collector plasma. This seems to cause "plasma stabilization" of the beam [8] i.e., moderation of the plasma-beam interaction intensity.

REFERENCES

1. V.I.Itin et al.- Pis'ma Zh.Tekh.Fiz.,1991, v.17, N.5, pp.89-93.
2. G.E.Ozur and D.I.Proskurovsky. - Ibid., 1988, v.14, N.5, pp.413-416.
3. G.E.Ozur and D.I.Proskurovsky. - Ibid., 1990, v.15, N.4, pp.46-49.
4. G.E.Ozur and D.I.Proskurovsky. - Proc. XIV ISDEIV, Santa Fe, USA, 1990, pp.665-670.
5. E.I.Lutsenko et al. - Fizika Plasmy, 1976, v.2, N.1, pp.72-81.
6. P.F.Ottinger, S.A.Goldstein and R.A.Meger. - J. Appl. Phys., 1984, v.56, N.3, pp.774-784.
7. M.Yu.Kreindel et al. - Fizika Plasmy, 1991, v.17, N.12, pp.1433-1439.
8. M.V.Nezlin. Dynamics of Beams in Plasma. - Moscow: Energoatomizdat, 1982.

RIBBON REB RESEARCH ON 0.7 MJ GENERATOR U-2

A.V.Arzhannikov, V.B.Bobylev, V.S.Nikolaev,
S.L.Sinitsky, M.V.Yushkov, R.P.Zotkin
Budker Institute of Nuclear Physics, 630090 Novosibirsk,
Russia

Abstract. The paper presents the experimental results on generation of a microsecond electron beam with a cross section 4x140 cm in a magnetically insulated diode at 1 MV voltage, its transport in a slit vacuum channel with 0.5T guiding magnetic field and, finally, a transformation of the ribbon beam to a cylindrical one. The first step of the experimental studies has been carried out at the energy content in the capacitor storage of the U-2 generator up to 200 kJ. At the second step of the experiments a new capacitor storage of doubled energy content has been added to the operated one and the investigations have been carried out at the 0.7 MJ pulse generator .

I. INTRODUCTION: Our experimental studies on high-power microsecond ribbon electron beams are aimed on production of 0.5 MJ total energy in a beam pulse at high current density and small angular spread. The values of these parameters of the beams allow one to use them for a number of applications, e.g. for plasma heating in long solenoids [1] and for microwave generation at a wavelength in the region from 1 to 10 mm [2]. The possibility of achieving good beam parameters in the case of a ribbon beam is associated with a generation of such a beam in a foilless magnetically insulated diode with a strongly elongated cross section. Experiments on the ribbon beam generation with the total energy of tens of kilojoules and on its transport in a slit vacuum channel with a guiding magnetic field $0 \div 1$ T [3] have established a basis of the development of ribbon beam technique on the U-2 device at the total energy content in a beam pulse up to a few hundreds of kilojoules.

II. EXPERIMENTS AT THE STORAGE ENERGY UP TO 200 kJ: A schematic of the experiments on the U-2 device is shown in Fig.1. A megavolt pulse comes from a LC-generator to a steel holder which is placed in a vacuum chamber and keeps a cathode (1). The strongly elongated cathode (1) made of KARBOTEX-TIM (fibrous graphite material) has the height 140 cm and the width 4.5 cm. A slit with sizes 5 cm by 140 cm sawn in a graphite plate, is operated as an anode (2) of a magnetically insulated diode. An electron flow (7) emitted from the cathode, comes through the anode and passes to a slit vacuum channel (3) with the inner dimensions of 6 cm by 145 cm. A residual gas pressure in the vacuum channel is about $5*10^{-5}$ Torr. Geometry of the magnetic and electric field lines in the diode and vacuum channel should provide a small angular spread of the beam electrons [4]. In our case of a strongly elongated cross section, to satisfy this requirement, a careful choice of the optimum configuration of the magnet-

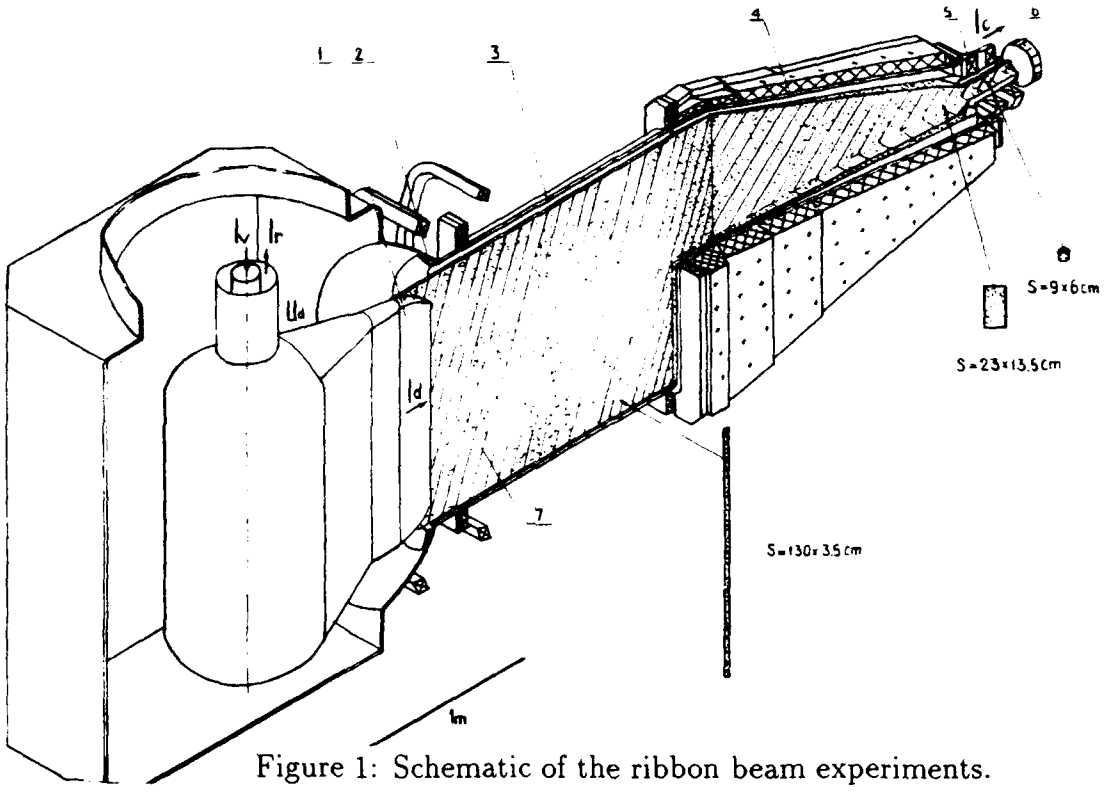

Figure 1: Schematic of the ribbon beam experiments.

ic coils and their places is needed. This choice has been made with a help of 3-dimensional computer calculations of the magnetic field lines geometry and beam electron motion. The magnetic field strength in a homogeneous part of the slit transport channel may be varied from 0 to 1 T.

A voltage on the accelerator diode Ud is measured by a resistive divider, input vacuum chamber current Iv and accelerator diode current Id - by Rogowsky coils, calorimeter beam current Ic - by a shunt. Electrical energy and the total energy of the beam in various parts of the device are calculated by integration over the time of a product of the diode voltage and an appropriate current. The shape of the beam cross section has been determined by an imprint of the beam on thin aluminum foils and plastic films.

In the first series of the experiments[6] described in this part of the paper, the electron beam passed only through a 2m slit vacuum channel without a transforming unit (4). The ribbon beam with sizes 4*130 cm at the exit of this channel was absorbed by a strongly elongated graphite collector operated as a calorimeter. The signals characterizing the microsecond ribbon beam generation and transport, and an imprint of the beam cross section shape at the collector are given in Fig. 2. The diode current Id is close to the vacuum current Iv. Only a small part (about 3-4 kA) of the vacuum current is lost as a current Ir flowing through an active resistance of the high voltage insulator and as a loss

current produced by the electron leakage from the steel holder. A comparison of a sum Id+Ir with the vacuum current Iv shows that the leakage currents from

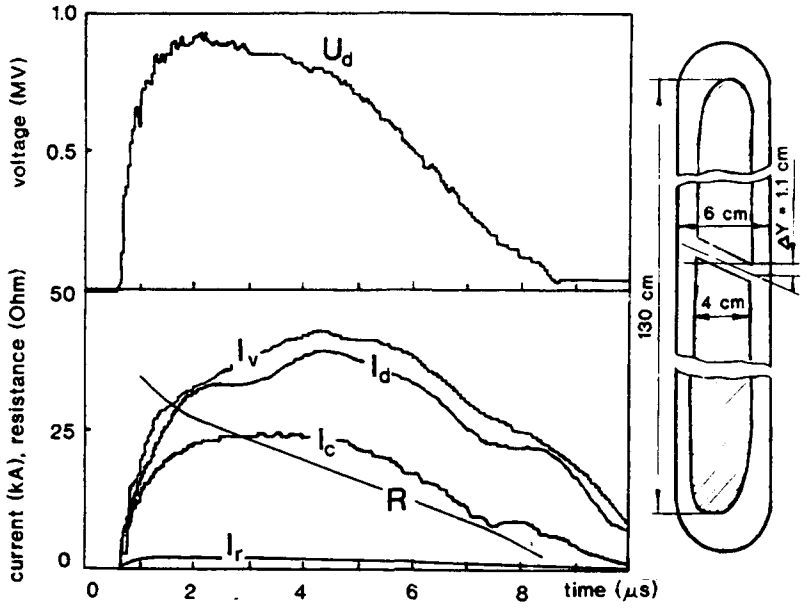

Figure 2: Waveforms of the signals.

the high voltage electrode are negligibly small. A difference between the diode current Id and the beam current Ic is more considerable.

This difference is associated with a loss of some part of the beam in the graphite plate around the anode slit; there is no measurable loss of the beam in the channel. The increase in the difference between Id and Ic currents during the beam pulse may be explained by an expansion of a plasma generated on the cathode surface. A gap between the electron beam and the walls of the vacuum channel is demonstrated in Fig.2 by the imprint of the beam cross section shape. It confirms that the beam equilibrium is actually stabilized by the conducting walls and guiding magnetic field. The shaded region in Fig. 2 is an area where the 50 μ Ti-foil is melted down and evaporated. An inclined strip of the undestroyed titanium is a shadow of the graphite bar with the thickness 0.4 cm that has been deliberately placed at a distance ΔZ=65cm upstream of the foil, perpendicular to the channel wall. The fact that the shadow of the bar is turned with respect to the bar's orientation, indicates a drift motion of the electrons. A displacement ΔY=1.1 cm shows that the charge neutralization of the beam in this shot is close to 100%.

To derive the efficiency of the energy transfer from the capacitor storage to the beam, the energies passing through the different parts of the U-2 device during the beam generation have been compared (see Fig. 3). When 72 capacitor banks of the pulse generator are charged up to the voltage Uc=43 kV, they accumulate

the electric energy Qpg=185 kJ (shadow region). In this case the energy coming into the vacuum chamber has a value Qv=∫Iv*Ud*dt≃155kJ (triangles), the energy picked out in the accelerator diode - Qd=∫Id*Ud*dt≃ 145kJ (circles) and finally the energy of the beam at the exit of the channel measured by the

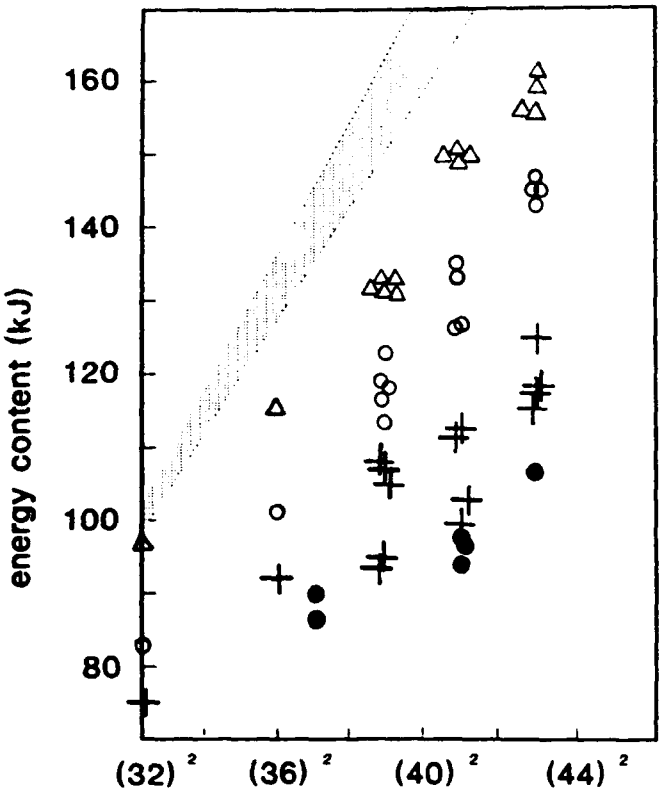

Figure 3: Energy content of the beam as a function of the squared voltage.

calorimeter - Qc ≃ 115 kJ (crosses). As a result an efficiency of the U-2 device at the ribbon beam generation is the following: Qv/Qpg = 84%, Qd/Qpg = 78%, Qc/Qpg =62%.

After the experiments which have shown the high efficiency of the large ribbon beam generation and transport, we have placed on the U-2 setup a special transforming unit (4) and a beam compression system (5) as it is shown by the schematic in Fig. 1. In this case the length of the slit channel has been shortened from 2 m down to 1 m. Magnetic coils of the transforming unit provide the necessary transformation of the magnetic flux cross section [5]. The process of the beam cross section transformation is demonstrated in Fig. 1 by the imprints of the beam on the plastic films placed in three points along the beam trajectory. These imprints show that in the slit channel with the magnetic field 0.3 T the beam cross section has 3.5*130 cm dimensions, after transforming the cross section shape is close to a rectangle with the dimensions 13.5 cm by 23 cm, and then after the compression it looks like an ellipse with the largest dimension about

9 cm in the magnetic field 4.5 T. For obtaining axially symmetric cross section the additional compression on one of the transverse directions is needed. In the model experiments with the small (2x20 cm) beam cross section this additional compression was obtained by using special correction coils [3]. This way for the additional compression will be used at the experiment with the full-scale ribbon beam. The total energy of the transformed beam after its compression is shown in Fig. 3 by filled circles. It is seen that the total energy of the compressed beam is close to the energy content of the ribbon beam in the slit channel.

Besides the total beam energy, the current density and the angular spread of the beam electrons are important parameters for various applications. Measurements of these parameters have been carried out by a microhole probe [7]. The measurements have shown that in the central region of the beam cross section the angular spread of the beam electrons in the guiding magnetic field 0.5T is close to $2 \div 3°$ and the local beam current density is about 0.1 kA/cm^2. These values are suitable for the plasma heating experiments after the beam compression.

III. EXPERIMENTS AT THE STORAGE ENERGY FROM 0.2 UP TO 0.5 MJ: To increase the energy content of the beam we have added a second pulse generator to the previously used one, and as a result of this electrical connection the total energy stored in all capacitor banks together, has become three times larger than before. According to the computer calculations, at the existing parameters of the LC-cascades and the electrical connection between the pulse generators the described above diode should allow to produce the electron beam with the total energy up to 0.5 MJ (see [5]). Nevertheless, to achieve such large energy content one needs to neutralize the space charge of the beam electrons in the vacuum chamber, in which the beam is being transformed and compressed. In the shots with the residual gas pressure $5*10^{-5}$ Torr in the chamber, a large difference between the accelerator diode current and the current of the compressed beam has been observed. For the shot where the gas pressure in the chamber was $2*10^{-4}$ Torr, the time behavior of the currents is shown in Fig. 4. At the beginning of the pulse the difference between the currents has a visible value, but after one microsecond it becomes vanishingly small, and then after 4 μs this difference begins to increase. The small difference between the currents may be explained by the quick charge neutralization of the beam. But, when the beam thickness in the diode exceeds the anode slit width, the difference between the currents becomes essential due to the loss of the beam electrons at the entrance of the slit channel. For the shot shown in Fig. 4, the total energy of the

beam in the diode is 330 kJ and the energy of the compressed beam is 230 kJ At the energy stored in the capacitors banks equaled to 500 kJ, the coefficient of efficiency of the ribbon beam generator is about 65%. After the transforming

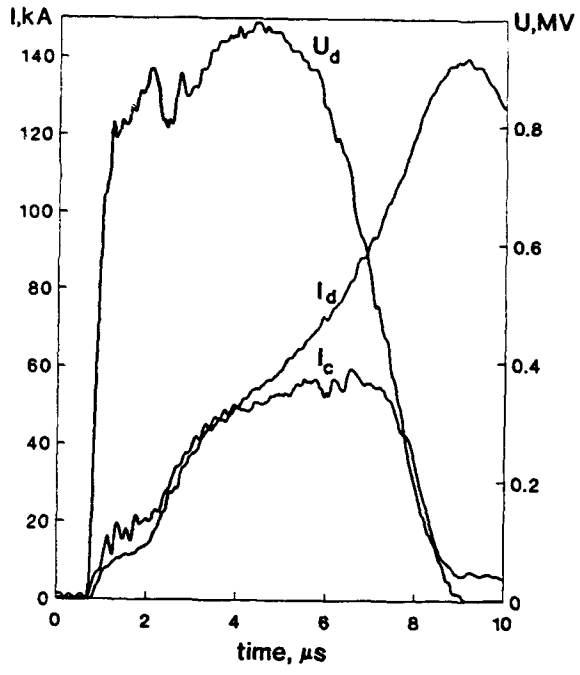

Figure 4: Waveforms of the signals.

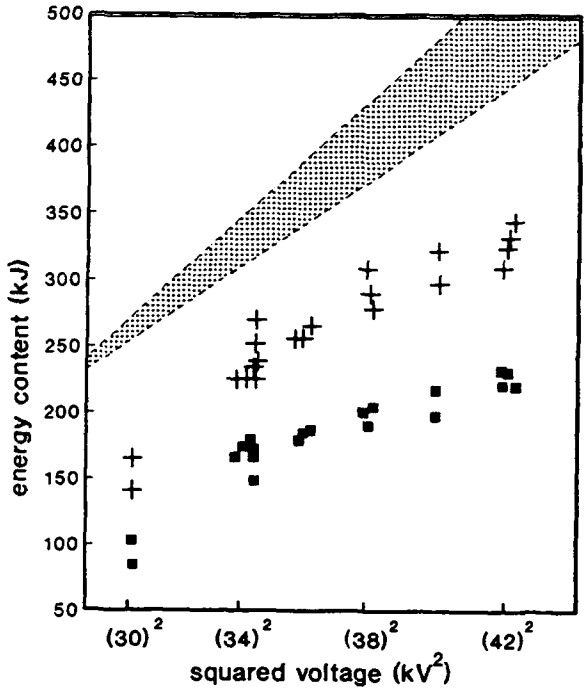

Figure 5. Energy content of the beam.

and compressing of the microsecond beam this parameter visibly decreases and becomes about 45%. Dependence of the total beam energy on the squared voltage on the capacitor banks is shown in Fig. 5. The shaded region is the energy in the capacitor storage, the crosses - the energy of the beam in the accelerator diode and the squares - the energy of the beam after compression. One may see almost linear character of the beam energy dependences on the squared voltage and it allows to hope on the following progress in the ribbon beam experiments.

[1] A.V.Arzhannikov, A.V.Burdakov, V.V.Chikunov et al. Proc. of the 8th Intern. Conf. on High-Power Part. Beams, Novosibirsk, p.14 (1990)

[2] A.V.Arzhannikov, S.L.Sinitsky, M.V.Yuskov. Prog. and Abst. of Twelfth Intern. Free Elect. Laser Conf.,Paris, 105 (1990).

[3] A.V.Arzhannikov, V.T.Astrelin, V.A.Kapitonov et al. Proc. of the 8th Intern. Conf. on High-Power Part. Beams, Novosibirsk, p.256 (1990)

[4] A.V.Arzhannikov, V.T.Astrelin, V.S.Nikolaev et al. Proc. of the 7th National Symp. on High-Current Electronics, Tomsk, Vol.2, 136 (1988) (in Russian).

[5] A.V.Arzhannikov, V.T.Astrelin, V.B.Bobylev et al. Proc. of the 8th Intern. Conf. on High-Power Part. Beams, Novosibirsk, p.849 (1990)

[6] A.V.Arzhannikov, V.S.Nikolaev, S.L.Sinitsky et al. Preprint INP 92-3, Novosibirsk, USSR (1992). Journ. Appl. Phys.,to be published.

[7] A.V.Arzhannikov, V.S.Koidan, S.V.Loginov. Priboryi tekhnika eksperimenta.v.4,p.36(1983).

HIGH BRIGHTNESS HOLLOW CATHODE ELECTRON BEAM SOURCE

G. Kirkman, N. Reinhardt, B. Jiang
Integrated Applied Physics Inc.
50 Thayer Road
Waltham, MA 02154

M.A. Gundersen, T.Y. Hsu, R.L. Liou
University of Southern California
Los Angeles, CA 90089-0484

R.J. Temkin
Massachusetts Institute of Technology
Cambridge, MA 02139

Abstract

An optically initiated hollow cathode electron source has been demonstrated to produce high brightness electron beams in a low pressure background gas. Three phases of beam production have been identified, first a 1A, 20nsec, 45keV, 10^{10}A/m^{2}rad^2 initial beam, second a 70A, 100nsec,20keV, 10^{11}A/m^{2}rad^2 hollow cathode produced beam and third a 100A, steady state, 500eV superemissive cathode produced beam. An experimental characterization of the three beams is presented.

Introduction

Hollow cathode discharges are known to be sources of pulsed[1] and continuous[2] high current electron beams. Under certain conditions the electron beams can be produced with a low transverse energy spread[3] and a high beam brightness can be achieved. The pseudospark[4] is a hollow cathode discharge that produces a high current axial electron beam and has demonstrated high brightness[5] when using a multiple gap structure. In this work a single gap optically initiated pseudospark discharge is demonstrated to produce a high brightness beam similar to the multigap structure. This work has measured a beam brightness >10^{11}A/m^{2}rad^2 at 20keV and 70A peak current. This value of brightness is exceptionally high[6] for this simple source and is applicable to accelerator applications including microwave power generation for next generation colliders[7]. The beams are produced and propagate in a low pressure gas making this source suitable for plasma based microwave sources and plasma accelerators.

The pseudospark is a low pressure gas discharge occurring between flat electrodes each having an axial hole[8]. The discharge can be initiated optically by UV[9] or IR[10] light from a laser or flashlamp[11]. Theoretical modeling of the discharge formation[12,13] and electron beam production[14] has been reported. In the present work electron beam production is studied experimentally showing several phases of beam production including a high brightness initial phase lasting 20-50nsec, a higher current similarly bright hollow cathode phase of 50-100nsec and a lower energy superemissive cathode phase producing a pulselength up to several μsec. The current and duration of each phase are dependent on the external circuit and gas pressure thus operation can be optimized to enhance the desired phase of the beam. The initial phase beam energy is about equal to the applied voltage (up to 45kV in this work), the second hollow cathode beam is produced during the voltage collapse of the discharge and therefore has an energy less than the applied voltage and the final long pulse phase has an energy corresponding to the burning voltage of the superemissive[15] discharge which is about 500V. The experiments described below have characterized the beam quality of the first two phases and have separately identified each component.

The Optically Triggered Pseudospark

The optically triggered hollow cathode beam source shown in figure 1, consists of two hollow electrodes with apertures on axis, a window allows light into the hollow cathode space for triggering and the anode is connected to a diagnostic port by a vacuum flange.A single gap structure was fabricated using brazed ceramic-metal techniques. The device is based on a 3 cm diameter electrode, 4 cm diameter ceramic insulator and mounts to vacuum and diagnostic system using standard 2.75 inch high vacuum flanges. The electrodes have molybdenum faces brazed to copper supports making up the hollow electrode structure. The electrodes and flanges are welded to a kovar ring which has been brazed to a metalized surface on the Al_2O_3 ceramic insulator body. An external capacitor or pulse forming network is connected to the device and charged by a dc supply. Light from the UV flashlamp initiates the discharge by providing initial electrons through photoemission[16]. The discharge conducts a current determined by the external circuit, a portion of this current produces the electron beam which propagates past the anode into the diagnostic region. All diagnostic sections are mounted on high vacuum flanges to allow for easy interchange of diagnostic sections and sure high vacuum sealing.The system is pumped by a diffusion pump to a base pressure of 10^{-7}torr and then filled to the desired pressure with argon of 99.999% purity the filling pressure is measured by a capacitance manometer with a 0 to 10torr range.

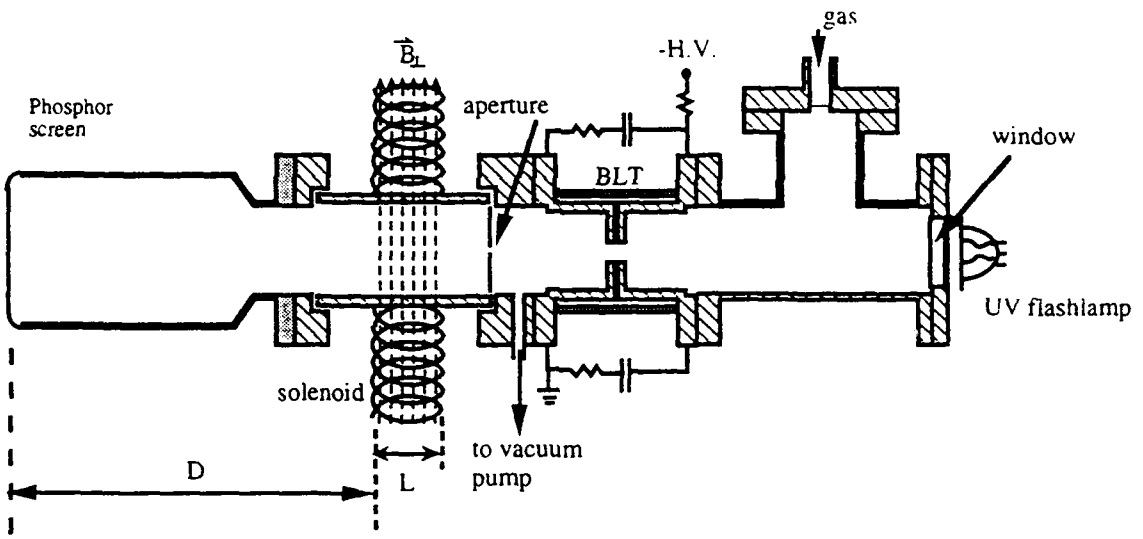

Figure 1. Schematic diagram of hollow cathode beam source experiment.

Experiment

An experiment was set up with the capability of operating up to 45kV with various external circuits with capacitance ranging from 0.3nF to 100μF. Measurement capabilities include time resolved beam current, current density, gap voltage, beam energy, emittance, brightness, beam profile, and dependence of these values on applied voltage, gas pressure and external circuit.

The beam current has been measured by a faraday cup and current viewing resistor. The current viewing resistor has a risetime <1nsec. The beam has also been measured by a rogowski coil such that the beam current can be measured without collecting the beam.

The beam energy is calculated by measuring its deflection in a magnetic field. The beam passes through a drift tube and is deflected by a transverse magnetic field applied by a solenoid, there is a further drift region after which the beam is observed on a phosphor screen. With no magnetic field the radial current distribution can be observed while with the magnetic field the energy is measured and the energy distribution can be estimated from the deformation of the beam shape. For beam emittance measurements the magnetic field is removed and a "pepper pot" emittance mask is used with the phosphor screen and camera.

Experimental Results

Time resolved faraday cup measurements of the electron beam current indicate three phases of beam production. When using only the self capacitance of the electrode structure charged to 30kV a single electron beam pulse of 20nsec duration and 2A peak current is observed. Adding an external capacitance of 30nF charged to 30kV and limiting the total current to 3.8kA with a 4ohm resistor a second phase of beam current is observed during the formation of the discharge. This beam has a larger current and is strongly dependent on gas pressure and external circuit parameters. When a current limiting resistor of 1000 ohm is used to extend the pulse duration a third steady state phase of the beam is observed with 0.5A current lasting for a time determined by the external circuit. This third phase of the beam is also strongly dependent on gas pressure. Using a differentially pumped region after the anode and a guiding magnetic field beam currents of 120A have been obtained in this phase when the total discharge current was 3.3kA[17].

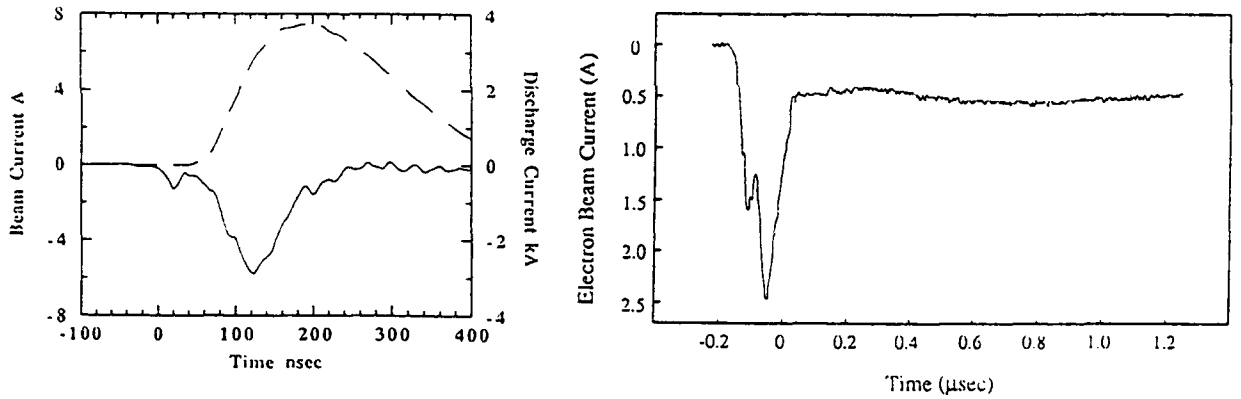

Figure 2. Three phases of electron beam production in the hollow cathode source. a) First two phases initial 20nsec is due to self capacitance of the structure and is present even when using no external capacitance. b) Three phases of the beam including the third steady state phase of 0.5A.

The beam current in the second phase has been measured as a function of gas pressure and applied voltage. The beam current and beam fraction (beam current/discharge current) increases with decreasing gas pressure and increasing applied voltage. A beam current of 70A, 1000A/cm^2 and 2% beam fraction has been obtained at 20kV and 40mtorr argon gas pressure. Dependence on pressure and voltage are shown in figure 3.

The beam energy is measured by deflection in a magnetic field and found to have a component approximately equal to the applied voltage and a component with much lower energy corresponding to the discharge voltage of about 500V. The beam deflection is measured using the phosphor screen. The phosphor has a threshold energy of about 6keV and therefore filters out beam electrons below this voltage. The energy was calculated by approximating the vXB force to

be perpendicular to the drift tube which is correct when the beam is not deflected much in the region of interaction with the magnetic field (Larmor radius >> length of interaction region). In this approximation[18] the beam energy is given by $E=0.5\ (e^2/m_e)\ (BLD/x)^2$ where B is the transverse magnetic field, L is the length of the region of interaction with the field, D is the drift distance from the interaction region to the phosphor screen and x is the displacement on the screen, e and m_e are electron charge and mass. At an applied voltage of 20kV the beam displacement is 0.75cm giving an estimated energy of 17keV. The energy has been estimated for several applied voltages and increases linearly with applied voltage.

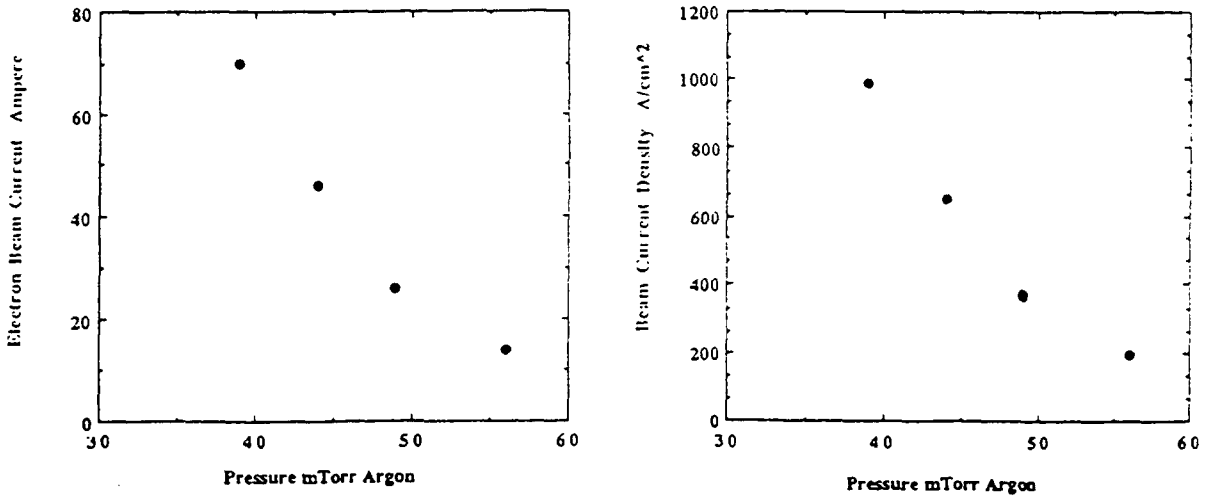

Figure 3. Beam current density and total current dependence on pressure.

Separation of the lower energy beam component has been observed by the flourescence produced in the background gas while passing through a known magnetic field. The magnetic field is 80 gauss and the gas pressure is 20mtorr argon. At an applied voltage of 18kV and discharge current of 100A the larmor radius of the low energy beam is 0.9cm yielding an estimated energy of 460eV. The beam energy has been measured at several values of discharge current and increases with increasing current.

The beam density in phase space was measured using the pepperpot emittance diagnostic. In our implementation of this method the beam passes through a pepper pot mask with an array of 300μm diameter holes each separated by 1mm then drifts freely 18.7cm to a phosphor screen where it is photographed. The raw data is used to generate a plot of $x'=v_x/v_z$ against x. The emittance ε_0 is defined as $1/\pi$ times the area of the ellipse in x'-x space that encloses >90% of the beam electrons. The normalized emittance is $\varepsilon_n=\beta\gamma\varepsilon_0$ and the normalized beam brightness is $B_n = 2I/(\pi e_n)^2$ The energy threshold of the phosphor screen limits our emittance measurement to the first two components of the electron beam, the first component is measured separately using a very small external capacitance such that the second component is insignificant, the second component can not be produced without the first but during this measurement a large external capacitance is used giving 50A of beam current such that the first component is insignificant.

Using this measurement the emittance of the first component is estimated to be 9π·mm·mrad at 25keV and 1A yielding a normalized emittance and brightness of 2.7π·mm·mrad and 1.4×10^{10}A/m^{2}Rad^2 respectively. The second component has emittance 25π·mm·mrad at 15keV and 50A, a normalized emittance and brightness of 6π·mm·mrad and 1.6×10^{11}A/m^{2}Rad^2 respectively.

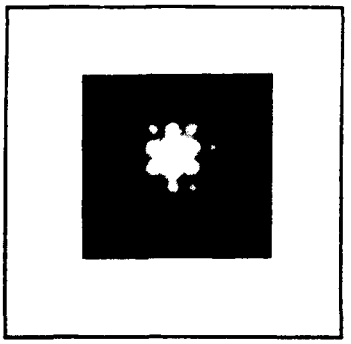

BEAM IMAGE ON PHOSPHOR SCREEN

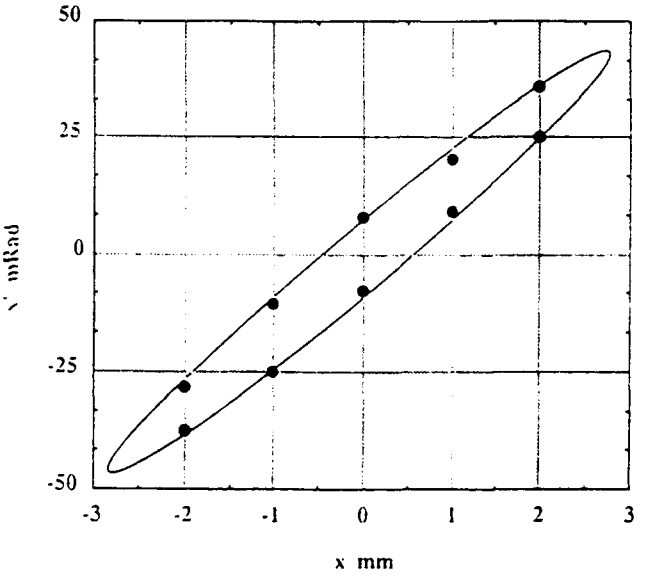

Figure 4. Beam emittance measurement for the second hollow cathode beam phase.

Discussion

Three distinct phases of electron beam production have been observed in the optically triggered hollow cathode discharge. The first phase is produced during the discharge of the self capacitance of the electrode structure. These electrons appear to have energy equal to the applied voltage and a low emittance. The second phase is produced during the hollow cathode phase of the discharge and can have an order of magnitude larger current than the first phase. These electrons are produced while the voltage is rapidly falling and therefore have an energy lower than the applied voltage and some spread in energy. The emittance of this beam is larger but the much higher current gives a larger brightness.

The normalized emittance ε_n of a cathode with radius r_c that emits electrons with a maxwellian velocity distribution with temperature kT is given by $\varepsilon_n=2r_c(kT/m_0c^2)^{1/2}$. In this definition of emittance the phase space area is equal to $\varepsilon_0\pi$. Using this we can compare the transverse energy spread of the two beam components. Taking the effective cathode radius to be 1.5mm, the radius of the cathode aperture, the first component has a spread of 0.4eV and the second 2eV. These estimates agree in order of magnitude and trend with measurements[19] of the plasma electron temperture under similar conditions.

The measured brightness of the first two phase of the beam verifies that this optically triggered discharge is a source of high brightness electron beams and agrees with the previous measurement in a multiple gap structure verifying that a single gap structure can produce similar low emittance beams as multiple gap structures when operated at the same voltage.

The third phase of the beam is produced after the hollow cathode discharge when the superemissive discharge has formed drawing high current from the front surface of the cathode which has been heated during the hollow cathode phase. This beam has energy corresponding to the burning voltage of the discharge and a current that is a few percent of the total discharge current. The emittance of this beam could not be measured in our experiments. The pulse length of this beam is determined by the external circuit and appears to be extendable to many msec or more.

The electron beams observed in this device are applicable for accelerator applications. The first phase of the beam could be useful as an injector for a high energy accelerator or plasma based accelerator, the second phase has a current and brightness suitable for microwave generation in plasma filled devices while the third phase if post accelerated could have a variety of applications including electron beam machining and welding.

Acknowledgement

This work was supported by the U. S. Department of Energy through the SBIR program and Lawerence Livermore Laboratory.
The work at U.S.C was supported by the Strategic Defense Initiative and LLNL

References

[1]M. Farvre, H. Chuaqui, E. Wyndham and P. Choi, IEEE Trans. Plasma Sci. **PS-20**, 53 (1992)

[2]J. J. Rocca, J. D. Meyer, M.R. Farrell and G.J. Collins, J. Appl. Phys. **56**,790,(1984).

[3]A.I. Herscovitch, V.J. Kovarik and K. Prelec, J. Appl. Phys. **67**,671, (1990).

[4]J. Christiansen and C. Schulheiss, Z. Phys. A, **290**,35 (1979).

[5]K.K. Jain, E Boggasch, M. Reiser and M. J. Rhee, Phys. Fluids **B2**, 2487 (1990).

[6]C. W. Roberson and P. Sprangle, Phys. Fluids, **B1**, 3 (1989).

[7]G. Caryotakis, Proc. 1991 Part. Accel. Conf. IEEE Press, p. 2928 (1991).

[8]J. Christiansen, in Physics and Applications of Pseudosparks, edited by M. Gundersen and G. Schaefer NATO ASI Series B: Vol. 219 Plenum, New York (1990).

[9]G. Kirkman, and M. A, Gundersen, Appl. Phys. Lett. **49**, 494 (1986).

[10] H.H. Chuaqui, M. Farve, E. Wyndham, L. Arroyo, and P. Choi, IEEE Trans. Plasma Sci. **PS-17**, 766 (1989).

[11]G. Kirkman, W. Hartmann and M. Gundersen, Appl. Phys. Lett.**52**, 613 (1988).

[12]J.P. Boeuf and L.C. Pitchford, IEEE Trans,. Plasma Sci. **PS-19**, 286 (1991).

[13]P. Choi ,H. Chuaqui, J. Lunney, R. Reichle, A. J. Davies, and K. Mittag, IEEE Trans,. Plasma Sci. **PS-17**, 770, (1989).

[14] H. Pak and M. Kushner, Appl. Phys. Lett. **57**, 1619, 1990.

[15]W. Hartmann, M. A. Gundersen, Phys. Rev. Lett. **60**, 2371 (1988).

[16]C.G. Braun, W. Hartmann, V. Dominic, G. Kirkman, M. Gundersen and G. McDuff, IEEE Trans. Electron Devices, **ED-35**, 559 (1988).

[17]T. Y Hsu and M. A. Gundersen in preparation for publication.

[18]"An Introduction to the Physics of Intense Charged Particle Beams," R. B. Miller, Plenum Press, New York, 1982.

[19]H. Bauer, G. Kirkman, and M. A. Gundersen, IEEE Trans. Plasma Sci. **PS-18**, 237 (1990).

HIGH-CURRENT-DENSITY CATHODE OPERATION AND BEAM TRANSPORT WITH STEADY-STATE AND PULSED CATHODE HEATING METHODS*

W. D. Getty, University of Michigan, Ann Arbor, MI 48109-2122
K. D. Pearce, DOE Energy Technology Center, Morgantown, WV 26506
M. E. Herniter, Northern Arizona University, Flagstaff, AR 86011

High-current-density cathodes are of prime importance for millimeter-wave free-electron laser devices. The present work is concerned with the development of cathodes with current densities in the 10-50 A/cm^2 range for pulsed and *cw* electromagnetic devices with Pierce-type electron guns. The primary cathode material used thus far is lanthanum hexaboride (LaB_6). Electron-beam bombardment heating has been found to be a practical means for heating these cathodes to the temperature range of 1800°C needed for the above current densities from LaB_6. This heating method offers high-impedance-level circuitry which is easily controllable for continuous heating, and it also can be used in a novel pulse-heating mode which is compatible with beam-voltage pulse generators such as Marx banks. Inductive isolation of the heating power source is not required in this mode. Steady-state electron bombardment heating of a one-inch diameter cathode has been used to obtain a cathode current density as high as 32 A/cm^2 at 110 kV voltage operation. Descriptions of the simulated and measured heating operation of both pulsed and continuous heating modes will be given. Measurements of the resultant beam properties such as current distribution and axial velocity spread will be described. The velocity distribution is measured with a retarding potential analyzer operating up to 82 kV. The transported beam can be allowed to interact with a bifilar wiggler if desired. These measurements are compared with trajectory calculations through the beam drift-tube/wiggler region and into the simulated analyzer. Good agreement is found between the measured and simulated velocity distributions.

1. Introduction

The primary goal of this research has been to use LaB_6 cathodes in an electron gun design that is suitable for gyrotrons, free-electron lasers, and other devices requiring high-current-density beams in an axial magnetic field. In this paper, we present a summary of our results on LaB_6 cathode heating, cathode current density, and transport of the resulting beam along an axial magnetic field and electromagnetic wiggler field. This paper describes the electron gun design used in these studies, and gives a general description of the experiment. Results on cathode heating, pulsed heating simulation, and current density are described. Finally, preliminary results on beam transport and velocity distribution measurements with and without an applied wiggler field are given.

2. Description of the Electron Gun and the Experimental Apparatus

The electron gun was designed using the SLAC EGUN code written by W. B Herrmannsfeldt [1]. It was designed to have a planar cathode with an area of 2.8 cm^2. The design perveance is $3.2 \times 10^{-6}\ A/V^{3/2}$. Details of the design have been described previously [2]. Beam-forming electrodes were designed by iteration with the code, and electrode spacing was chosen to allow 120-kV operation.

Lanthanum hexaboride thermionic emission constants were reported by Lafferty in 1951 [3]. Using his values, the Richardson-Dushman equation is consistent with our measured current versus voltage, and this implies that

* Work supported by ONR.

temperatures of the order of 1800°C are needed to achieve a current density approaching 50 A/cm^2. The size of the cathode in the present experiment is such that heating power of 800-1100 W is needed to overcome radiation loss in this temperature range. In the present work, electron bombardment was chosen because it operates at moderate voltage (1-2 kV) and low current (0.5 A).

In addition to high-current-density capability, LaB_6 is extremely tolerant of poor vacuum conditions, exposure to air (when cold), and other poisoning conditions. This property is possibly the most useful property of LaB_6 cathodes, particularly for electron guns used in research experiments where frequent vacuum system air openings are necessary. The cathodes can be repeatedly exposed to air after cool down, and reused without any special activation steps.

A disadvantage of LaB_6 cathodes is that the evaporation rate of the material becomes significant above 1600°C [3]. The evaporation rate of 1800°C is still low enough to not cause a significant loss of cathode lifetime, especially for research devices.

Evaporation at the low rates found from 1600 to 1800°C can be important in the design of an electron bombardment heating system. An evaporated LaB_6 coating lowers the work function of the refractory metals tungsten, molybdenum, and tantalum, and deposition of LaB_6 on these metals will cause them to emit electrons more readily when they are used as bombardment-heating-system electrodes and biased at a negative voltage with respect to the LaB_6. Precautions must be taken to prevent runaway of the bombardment current by uncontrolled emission.

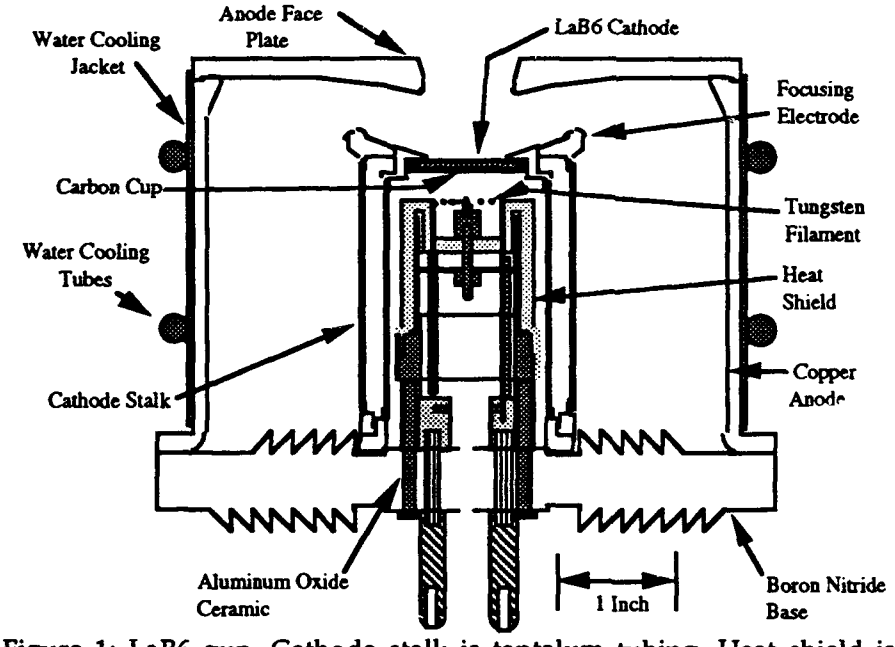

Figure 1: LaB6 gun. Cathode stalk is tantalum tubing. Heat shield is boron nitride.

A final precaution that must be made with LaB_6 is to heat the cathode slowly to avoid cracking the cathode disk. The LaB_6 rod is made by hot-press sintering of powder, and the cathode disks cut from a rod will crack if heated too rapidly. A warm-up time of several minutes is required when heating from room temperature, but more rapid heating can be done when starting from several hundred degrees.

3. Experimental Apparatus

The electron gun shown in Figure 1 is mounted in a UHV vacuum system.

The system contains a translation stage that allows the beam current profile to be obtained by scanning a pinhole over the cathode. An infrared pyrometer sensing head can also be mounted on the translation stage to obtain a cathode temperature profile.

The electron gun voltage is supplied from a 3 or 4-stage Marx bank. The pulse length is 5 μs and is determined by the firing delay of a spark-gap diverter switch. The available pulse voltage varies from 67.5 kV to 120 kV. The gun anode is grounded and the cathode is supplied by three wires. Two of these are used for supplying power to the bombardment filament and the third wire is connected between the cathode and the Marx bank output. The three wires are capacitively bypassed so that the high-voltage pulse develops negligible voltage between them, but the dc bombardment voltage of 1-1.8 kV can be applied between the two filament wires and the cathode. The cathode is heated continuously in this configuration.

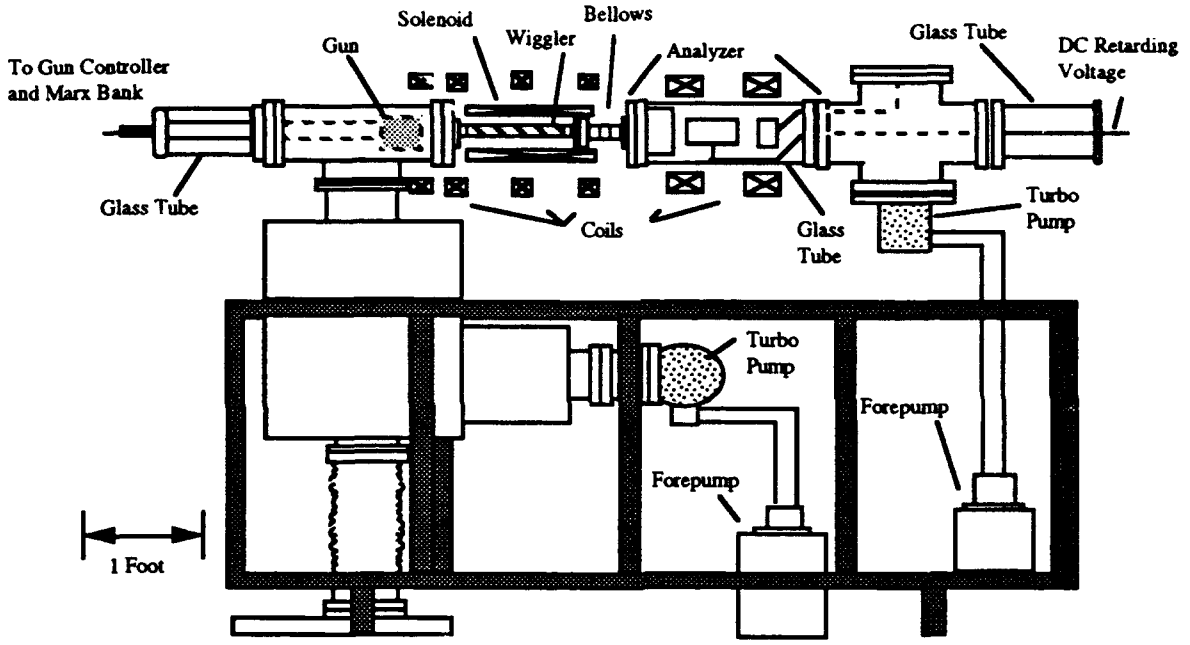

Figure 2: Apparatus set up for beam transport and velocity spread measurements with wiggler.

In the pulse-heating mode, the cathode heating energy is stored in a capacitor that is an integral part of the Marx bank. The capacitor is discharged by the thermionic diode formed by the tungsten filament and the LaB_6 cathode. This mode of operation is more efficient than continuous cathode heating and allows higher cathode temperatures to be reached.

The basic vacuum system has been modified to allow measurements on the electron beam after it is emitted from the gun. The beam-analysis system is shown in Figure 2. An axial magnetic field and a drift region through a dipole wiggler electromagnet are added. After the beam passes through the wiggler, it enters a velocity analyzer that is sensitive to the axial velocity component. The axial field extends over the length of the analyzer.

The heat-shield configuration shown in Figure 1 is designed to prevent activation of negatively-biased metal electrodes by evaporated LaB_6. A graphite cup that holds the LaB_6 disk greatly reduces the amount of LaB_6 evaporated in the

direction of the filament. The bombardment heating control system operates with a temperature-limited filament and controls the bombardment current by adjusting the filament heating power. If other metal parts emit due to LaB_6 activation, the control system will not work [4].

The control system is a digital system that uses power FETs to turn the filament current on and off. All control electronics are at ground potential and the controlled filament current is fed through 2 isolation inductors to the filament.

An analysis of the control system has been given in [4]. It is shown that the bombardment heating system can be open-loop unstable because of positive thermal radiation feedback. This feedback loop is stabilized by the control system, which can maintain constant average bombardment current over a wide range of bombardment voltages and cathode-filament diode perveance values. Lack of sensitivity to perveance is a major advantage of temperature-limited bombardment heating over space-charge-limited heating since cathode-filament diode dimensions are not critical.

4. Results with Continuous and Pulsed Cathode Heating

Extensive results on bombardment heating and the resultant electron beam production have been given by Herniter [5] and Herniter and Getty [2],[6]. The bombardment heating system continuously and stably heats the LaB_6 to 1750°C with 1050 W of total power (filament heating power plus bombardment power). A 10-degree temperature variation across the cathode was measured. The transmission percentage of cathode current through the gun anode aperture was found to be nearly 100 percent for cathode temperatures up to 1600°C. Above this temperature, the efficiency dropped to 75 percent because evaporated LaB_6 began to cause emission from the cathode beam-forming electrode. At a voltage of 115 kV and 5 μs duration, a transmitted current of 89 A was obtained at a cathode current density of 32 A/cm^2 and a cathode temperature of 1750°C.

The pulsed heating method was tested by heating the cathode with energy from a capacitor and observing the cathode temperature as a function of time with the infrared pyrometer. The Marx bank was not fired. Enough energy can be stored in a 1.5 mF capacitor at 3 kV to heat the cathode to 1800°C from a base temperature of 580°C if the heating is done on a 120-second cycle. High voltage isolation inductors are not needed in this mode of operation. The average power is reduced by a factor of 10-20 from continuous heating. This mode could be used to produce peak cathode temperatures of 1800°C or higher in single shot or slowly repetitive experiments. A detailed analysis and comparison of heating measurements with model calculations are given in [7].

5. Beam Transport and Velocity Analysis Studies

The most recent results with the LaB_6 electron gun have been obtained in the area of electron beam analysis by retarding potential analysis. This study was done to compare the electron velocity distribution after the beam passes through a wiggler field with the distribution without a wiggler field. The results are compared with wiggler trajectory theory of Friedland [8].

The primary diagnostic used in this study is a retarding potential analyzer capable of operating up to 85 kV in an axial magnetic field. The design and analysis of this analyzer have been done by Pearce [9]. The experiment was done at beam voltages of 68 kV to 82 kV. The LaB_6 cathode was temperature-limited to limit the current to the range from 0.1 A to 5A.

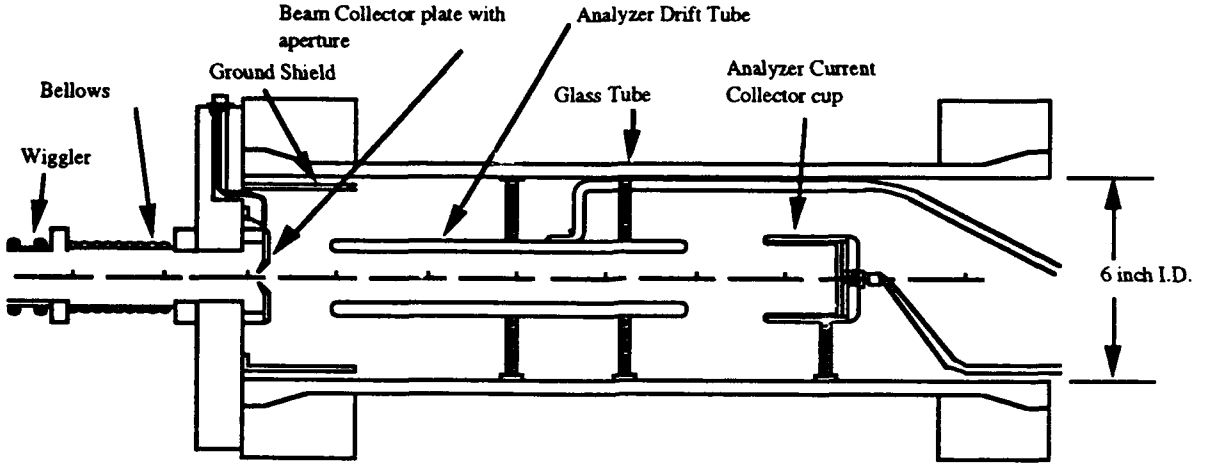

Figure 3: Velocity analyzer. The drift tube is biased negatively up to the beam voltage magnitude.

The analyzer was designed using the SLAC EGUN code. It was established that the analyzer responded to the axial component of beam velocity by injecting electrons with varying pitch angles in velocity space $\{v_\perp, v_{||}\}$. The analyzer is shown in Figure 3. The inlet aperture is on the left and is grounded. The collector cup is on the right. A cylindrical, concentric drift-tube electrode is located between them. It is held at a dc potential varying from 0 to -85 kV. Using simulation it was verified that only electrons whose parallel energy exceeds the drift tube bias reach the collector.

The analyzer experimental results are compared with trajectory calculations using the relativistic equations of motion. Space charge is neglected. The wiggler field is calculated by breaking the wiggler winding into small segments (464 total) and using the Biot-Savart law to calculate the field. Since the wiggler radius was only 1.5 times larger than the beam radius, it was found necessary to use the Biot-Savart law to obtain sufficient accuracy. The commonly used expansions of the field in terms of Bessel functions were not sufficiently accurate. The beam cross section was divided into small areas and an electron was followed from each differential area. Those entering the analyzer and reaching the collector cup were recorded as collected current. In most cases, 300 electrons were followed.

A retarding potential curve is shown in Figure 4. It shows the curve for the nominal wiggler design current of 152 A. The windup ratio is the ratio of the perpendicular velocity at the exit from the wiggler to the parallel velocity at the input. The expected retarding potential cutoff for this wiggler current is shown by the dashed line at 23 kV. At this wiggler current, it is expected that the beam will have 23 kV of parallel energy and 52 kV of perpendicular energy. The measured energy spread of 12 kV is smaller than the calculated spread of 25 kV, but the break in the measured curve is close to the expected value as shown by the dashed line. In

general, there was excellent qualitative agreement between the measured curves and the calculated curves.

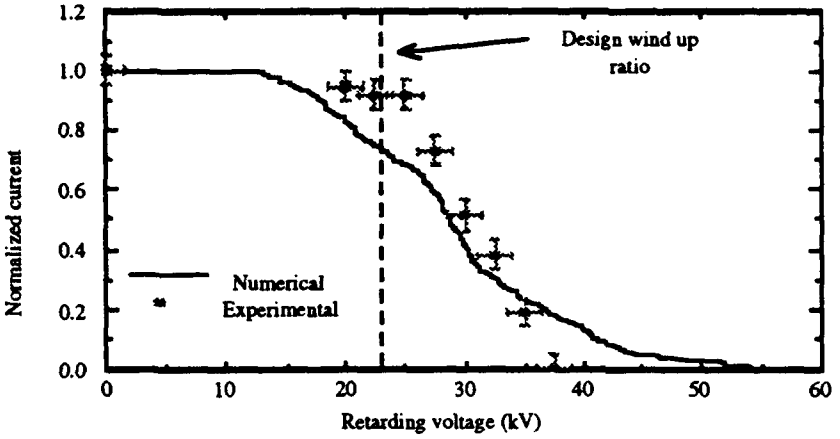

Figure 4: Measured retarding potential curve with design wiggler field. Beam voltage = 75 kV.

The results obtained with the velocity analyzer were consistent with the orbit stability calculations in reference [8]. In the present experiment, the wiggler field is highly nonuniform across the beam cross section, and large velocity spreads were observed. The measured average perpendicular velocity agreed well with the expected value, especially for low wiggler currents.

6. Summary and Conclusions

The use of temperature-limited tungsten filaments for producing bombarding power in cathode heating system has been done successfully using a digital control system. Up to 1100 W have been delivered to a one-inch diameter LaB_6 cathode and a cathode temperature of 1750°C was obtained. At this temperature, a current density of 32 A/cm^2 was observed at 115 kV gun voltage. The bombardment system has proven to be dependable and flexible, particularly in the 1300-1600°C temperature range. In this range, a series of retarding potential analyzer curves were made under conditions with and without an applied wiggler field on the electron beam. Excellent qualitative results were obtained when compared with calculated beam energy characteristics. The authors wish to acknowledge the assistance of G. A. Lipscomb in the pulsed cathode heating study, and the support of the Office of Naval Research.

References

[1] W. B. Herrmannsfeldt, SLAC. Stanford University, Stanford, CA, Tech. Rep. 226 (Nov. 1979).

[2] M. E. Herniter and W. D. Getty, "Thermionic cathode electron gun for high current densities," *IEEE Trans. Plasma Sci.*, Vol. PS-15, pp. 351-360 (August 1987).

[3] J. M. Lafferty, "Boride cathodes," *J. Appl. Phys.*, Vol. 22(3), pp. 299-309 (March 1951).

[4] M. E. Herniter and W. D. Getty, "Temperature-limited electron bombardment heating method," *IEEE Trans. Plasma Sci.*, Vol. PS-19, pp. 1279-1289 (Dec. 1991).

[5] M. E. Herniter, "A bombardment heated LaB_6 thermionic cathode electron gun," Ph.D. thesis, University of Michigan, Ann Arbor, Michigan, 1989.

[6] M. E. Herniter and W. D. Getty, "High current density results from a LaB_6 thermionic cathode electron gun," *IEEE Trans. Plasma Sci.*, Vol. PS-18, pp. 992-1001 (Dec. 1990).

[7] G. A. Lipscomb, M. E. Herniter and W. D. Getty, "Pulsed cathode heating method," *IEEE Trans. Plasma Sci.*, Vol. PS-17, pp. 898-905 (Dec. 1989).

[8] L. Friedland, "Electron beam dynamics in combined guide and pump magnetic fields for free electron laser applications," *Phys. Fluids*, Vol. 23, pp. 2376-2382 (Dec. 1980).

[9] K. D. Pearce, "Retarding field analysis of long pulse electron beams through combined bifurcated bifilar wiggler and guide magnetic fields," Ph.D. thesis, University of Michigan, Ann Arbor, Michigan, 1991.

HIGH GRADIENT ACCELERATION IN A 17 GHz PHOTOCATHODE RF GUN

S. C. Chen, B. G. Danly, J. Gonichon, C. L. Lin
R. J. Temkin, S. Trotz, and J. S. Wurtele
Plasma Fusion Center, Massachusetts Institute of Technology

Abstract

A 17 GHz RF acceleration experiment is being constructed at MIT. The goal is to study particle acceleration at high field gradients and to generate high quality electron beams for potential applications in next generation linear colliders and free electron lasers. The peak accelerating gradient in the $1\frac{1}{2}$ cavity RF gun is about 250 MV/m. The expected beam parameters, for operation with a photoemission cathode, are as follows: energy 2 MeV, normalized emittance 0.43 π mm-mrad, energy spread 0.18%, bunch charge 0.1 nC, and bunch length 0.39 ps.

The detailed experimental setup, including RF cavity, RF transport and coupling, vacuum system, laser and timing system are described.

1 Introduction

To meet the stringent requirements set by future applications such as high-energy linear colliders and next generation free electron lasers, efforts have been made to develop novel electron beam sources recently. Particularly, research on the generation of high quality electron beams using photocathode RF guns has been very active in the last few years. A worldwide review of major RF gun projects can be found in [1]. While the operating frequencies of existing systems range from 500 MHz to 3 GHz, a 17.136 GHz photocathode RF gun has been designed and is under construction at MIT[2]. This RF gun design is basically scaled from the 2.856 GHz RF gun currently under testing in Brookhaven National Laboratory (BNL)[3,4]. However, many changes have been made to accomodate the features involving high frequency operation. In spite of technical difficulties and physics issues associated with high frequencies, the 17.136 GHz operation is very attractive. It allows us to achieve high accelerating gradients, to make the system compact, and to obtain high brightness beams.

In this paper, the experimental design of the 17 GHz photocathode RF gun is presented in detail. A general layout of the experiment is shown in Fig. 1. It consists of three parts: (1)the RF gun cavity and the transport line (including the power source and the vacuum system), (2)the laser and timing system, and (3)the beam transport and diagnostic line. Each of these subjects is described successively in sections 2, 3, and 4. Section 5 summarizes the status of the experiment.

2 RF Cavity and Transport Line

2.1 RF Cavity and Waveguide Coupling

One of the most interesting phenomena to be studied in this experiment is RF breakdown. Although the breakdown limit at 17 GHz has yet to be experimentally studied, the breakdown threshold should be around 800 MV/m if one extrapolates the data obtained at lower frequencies as measured by Wang[5]. To obtain

*This research is supported by DOE under Grant DE-FG02-91-ER40648.

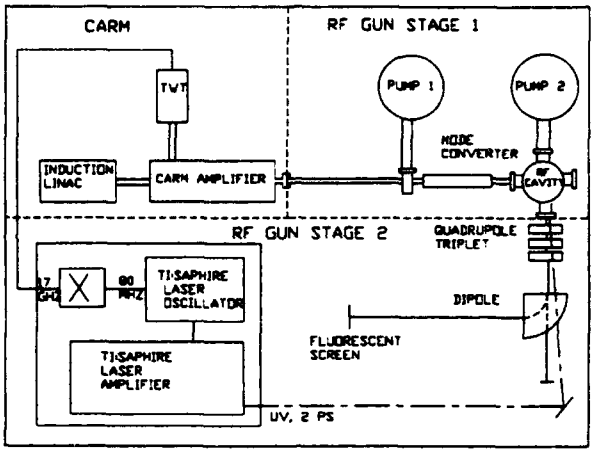

Figure 1: Schematic of the 17 GHz photocathode RF gun experiment.

Table 1: Preliminary design parameters.

peak accelerating gradient	250MV/m
laser pulse length	1.4ps
final bunch length	0.39ps
RF phase for laser pulse	12°
current density	$6.7kA/cm^2$
cathode radius	0.525mm
bunch charge	0.1 nC
emittance	0.43π mm-mrad
energy spread	0.18%
current	258A
brightness	$1.43 \times 10^{14} \frac{A}{(mrad)^2}$

as high an accelerating gradient as possible without RF breakdown, the cavity geometry must be designed to minimize the ratio of the peak surface field to the field at the cathode. Therefore our cavity geometry is directly scaled from BNL design which has already achieved this goal[4]. To keep the cavity surface field strength below the predicted breakdown threshold, the peak accelerating gradient is chosen to be 250 MV/m, corresponding to a peak surface field around 300 MV/m.

The accelerating field profile is also determined by the cavity geometry. Using the cavity geometry scaled from BNL design with a peak accelerating gradient of 250 MV/m, the beam dynamics and the interplay between time-dependent RF forces, space-charge forces, and nonlinear RF forces have been studied intensively by using the particle-in-cell code MAGIC and PARMELA. The laser pulse length, RF phase for photoemission, cathode radius, and current density have been optimized and the results were reported in [2]. The preliminary design parameters are summarized in Table 1.

The $1\frac{1}{2}$ cell RF cavity is electroformed from OFHC copper. A side-wall waveguide coupling scheme is used to feed the RF power into the cavity. The experimental arrangement is shown in Fig. 2. Both the cavity and waveguide are located in a vacuum chamber. There are more than a thousand holes in the waveguide wall to facilitate pumping. A RF monitor and a frequency tuner are installed in each cell of the cavity. The offset in the angle of monitor and tuner between two cells is due to the space limitations. The tuner is implemented by a motion feedthrough and the monitor is implemented by a SMA cable with a RF pick-up loop attached to its end to intersect magnetic flux. Both enter the cavity through holes drilled in the cavity

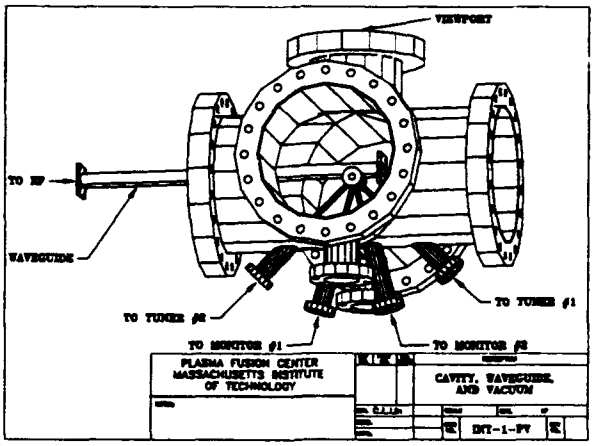

Figure 2: Vacuum chamber.

wall and can be accessed from outside the vacuum chamber. The TE_{10} waveguide mode is coupled to the cavity to generate the desired π mode resonance. The coupling site of the waveguide is cut to a circular section. The reason is twofold: one is to fit the cavity shape, the other is to provide a capacitive junction for the waveguide so as to enhance the field strength at the junction and to increase the coupling efficiency. A cold test with a prototype cavity indicated that 75% of the RF power is coupled into the cavity using this scheme.

2.2 RF Source and Transport

The power source used to feed the RF cavity is a Cyclotron AutoResonance Maser (CARM) developed at MIT [6]. The CARM will deliver 5-10 MW peak in a pulse of 30 ns at a repetition rate of 10 Hz. The RF exits the CARM in circularly polarized TE_{11} mode and must be converted to TE_{10} mode in the rectangular waveguide that couples to the RF cavity. The RF transport line, whose schematic diagram is shown in Fig. 3, has been designed and is now under construction. A 2 " ID, 6 ' long circular waveguide is connected at one end to the output window of the CARM and at the other end to a tapered circular waveguide that changes the ID from 2 " to 1 ". The mode converter follows the taper and is composed of two parts. First, a circular piece of waveguide whose cross section has been slightly deformed to be elliptical in the center converts the rotating polarization of the TE_{11} mode to linear. Second, the TE_{11} linearly polarized in the circular waveguide is converted, through a circular to rectangular transition, to TE_{10} in the rectangular waveguide. Between this piece and the waveguide coupler, the construction is modular and involves a dual directional coupler, a high-vacuum window, a flexible waveguide, and optionally an arc sensor. The total length between the CARM and the cavity is more than 10 feet. This length provides transit time isolation between the RF gun cavity and the CARM amplifier. Both pieces of the mode converter have been electroformed. Most of the elements have been brazed to their flanges and the RF line is now being assembled.

2.3 Vacuum

The vacuum system should be able to provide 10^{-9} torr inside the RF gun cavity, and at least 10^{-5} in the RF transport line to avoid breakdown. The pumping scheme for the cavity and the coupling waveguide has been discussed in Section 2.1. In addition, three hundred holes have been drilled around the long 2 " ID circular waveguide in order to evacuate the RF transport line. The diameter of each hole is small enough (1.6 mm e.g $\frac{\lambda}{10}$) to be below cutoff. The conductance for each hole is 0.07 l/s, leading to a total conductance for three hundred holes of 21 l/s, which is higher than the conductance of the 2 " ID waveguide (8 l/s).

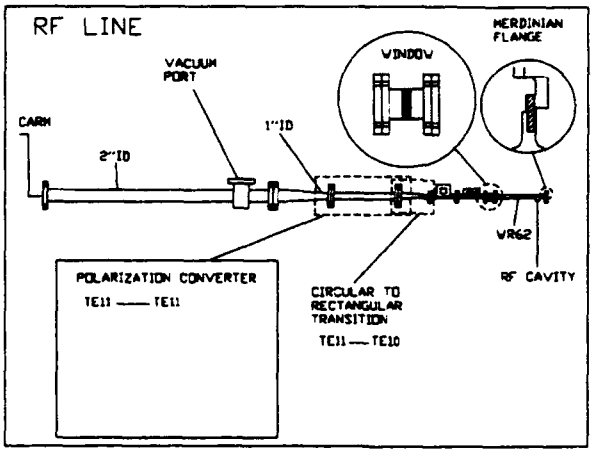

Figure 3: RF transport.

3 Laser and Timing System

3.1 Laser

The design of the laser system is driven by the need to create an electron bunch of the proper size and shape at the optimal time to be accelerated in the RF cavity. The design parameters are summarized in Table 2, and are explained as follows: The wavelength of the light is chosen to maximize the efficiency of the laser and the photoelectric effect for copper. The laser must fire at a repetition rate which matches the duty cycle of the CARM amplifier. The output energy of the laser is calculated to yield an electron bunch of 0.1 nC. This output energy must be stable to limit current fluctuations. The phase jitter of the laser measures the uncertainty in the time between the laser pulse arrival time at the cavity relative to the "reference signal" which drives the Ti:Sapphire oscillator. The timing jitter is the jitter between the "master trigger signal" and the laser pulse arrival time. These timing figures operate at very distinct timescales (See section 3.2). The beam should diverge as little as possible in order to provide a small spot size. The beam must accurately hit the cathode which is 1 mm in diameter and is located a few meters from the laser and therefore should have a low pointing error. Lastly, the mode-lock frequency of the laser oscillator is chosen to make synchronization to the 17 GHz source easier. There are many integers which divide 17.136 GHZ into this range. A system which satisfies these constraints has been designed as follows.

An Argon Ion pumped Ti:Sapphire laser produces a continuous train of microjoule pulses which are sent into a Ti:Sapphire pulsed laser amplifier. The amplifier is pumped by a separate Nd:YAG laser which provides nearly 1 J of energy per pulse. When triggered, the amplifier optically selects one of the pulses in the CW train and amplifies it to milijoule energy. The amplified IR pulse is trippled into ultraviolet frequency by a BBO crystal and is directed towards the RF cavity. The manner in which the laser system is to be integrated into the experiment is illustrated in Fig. 4.

3.2 Timing

With a proper and stable time delay between the firing of the CARM amplifier and the firing of the laser amplifier, the laser pulse should arrive at the cathode surface when the RF gun cavity is filled with the microwaves from the CARM. The 30 ns RF pulse at 17.136 GHz fills up the cavity after about 17 ns. The laser pulse should reach the filled cavity at the optimal microwave phase. As shown in [2], the electron beam quality is strongly dependent of the RF phase of photoemission. In this experiment, the phase jitter is designed to be less than 1 ps. In order to satisfy the timing relationships described above, the CW laser will be externally modelocked to a dual frequency synthesizer. This device will produce two signals with

Table 2: Parameters of the laser system.

Wavelength	220-280 nm
Repetition rate	Single pulse and 0-10 Hz (adjustable)
Final output energy (per pulse)	0-200 μJ (adjustable)
Energy output fluctuation	$\leq \pm 10$ %
Pulse Length	<2 ps
Phase Jitter	<1 ps
Timing Jitter	<3 ns
Polarization	> 99 %
Beam Divergence	Near Diffraction Limit
Beam Pointing Error	< 10 μrad
Mode-Lock Frequency	48-238 MHz

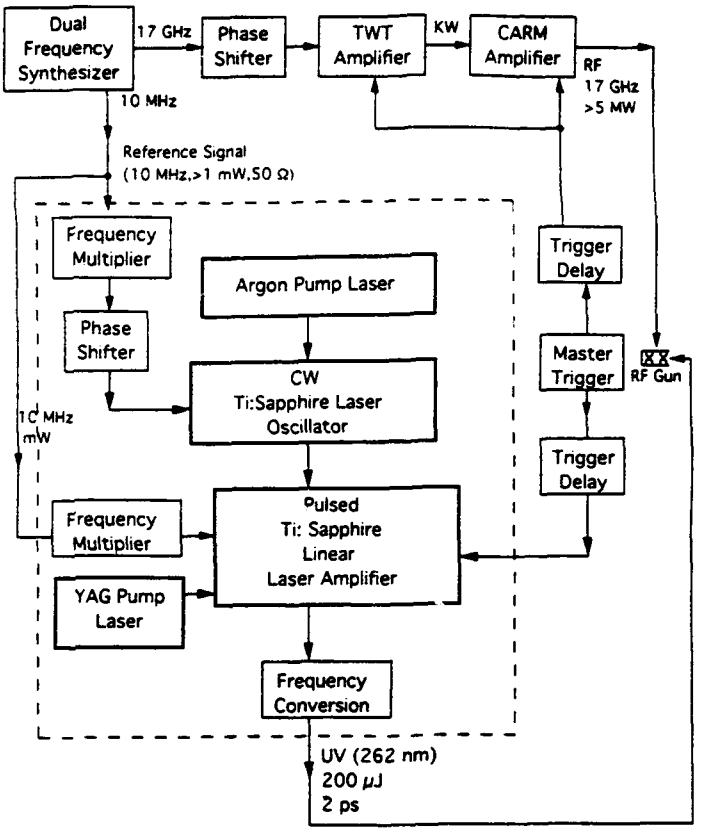

Figure 4: Laser system.

stable frequencies at low power. The first signal will run at the frequency of the RF cavity and will be used to drive the CARM amplifier chain. The second signal will be a subharmonic of the first and will be used to modelock the Ti:Sapphire laser oscillator.

4 Beam Line and Diagnostics

The purpose of the beam transport (and diagnostic) line is to bend the paths of electrons exiting the RF cavity away from the laser window, and to measure the electron beam parameters. The quantities to measure are energy, energy spread, transverse emittance, charge, and bunch length.

Fig. 1 shows the schematic diagram of the beam line including a quadrupole triplet and a bending magnet.

The bending magnet bends the electron path by an angle of 90 degrees and forms a point to point imaging system that can be used for energy spread measurement. A very small beam size is produced before the bending magnet (object plane), with the proper quadrupole setting, and the bending magnet produces a spot on a fluorescent screen in the image plane. The fluorescent spot is observed with a video camera. The position of the spot gives the energy and its horizontal thickness the energy spread.

The quadrupole triplet can also be used to measure the emittance: the bending magnet is switched off and the spot produced by the electrons on another screen positioned along the RF gun axis is observed. The gradient (K) of one of the quadrupole is varied in order to vary the spot size on the screen; a least square analysis of the curve $\sigma_{x,y}$ vs. K gives the transverse emittance.

The program TRACE3d, which uses the transport formalism was used to obtain a preliminary design. Simulations of the same line with the program PARMELA show that the resolution of the spectrometer is better than 0.1 %.

The charge will be measured with a Faraday cup placed between the quadrupole triplet and the dipole. Several methods for measuring the bunch length are under investigation.

5 Summary

A high gradient RF acceleration experiment is under construction at MIT. The accelerating cavity is a copper RF gun structure with an operating frequency of 17.136 GHz. The designed peak accelerating gradient on axis is 250 MV/m. The accelerating structure and the RF transport line have been fabricated and are being assembled. The first stage experiment involves powering the structure with the high power 17 GHz output from a CARM amplifier. The goal of the initial experiment is to study field emission and RF breakdown, and to condition the cavity for even higher gradient operations.

The following systems will be integrated with the 17 GHz RF gun system in the second stage of the experiment. A UV laser system and the related timing system are being designed to generate picosecond electron bunches through photoemission from the cavity wall. Successful acceleration of these bunches under high field gradient will provide high brightness electron beams [2] suitable for applications in next generation linear colliders and in high frequency free electron lasers.

References

[1] C. Travier,"Review of Microwave Guns," submitted to *Particle Accelerators* (July, 1991)

[2] C. Lin *et al.*, *Proc. 1991 IEEE Particle Accelerator Conf.*, pp. 2026 (May, 1991)

[3] K. McDonald, "Design of the Laser-Driven RF Electron Gun for BNL Accelerator Test Facility,"*IEEE Trans. Electron Devices*, vol. 35, no. 11, pp. 2052- 2059 (Nov. 1988)

[4] K. Batchlor *et al.*, "Desgin and Modeling of a 5 MeV Radio Frequency Electron Gun," BNL-41766 (1988)

[5] J. W. Wang,"RF Properties of Periodic Accelerating Structures for Linear Colliders," PhD. Thesis, Stanford University (1989)

[6] W. L. Menninger *et al.*, *Proc. 1991 IEEE Particle Accelerator Conf.*, pp. 754 (May, 1991)

BEAM GENERATION WITH THE 4-MV RLA INJECTOR AND ACCELERATION THROUGH THE ET-2 POST-ACCELERATING CAVITY*

Michael G. Mazarakis, David L. Smith, James W. Poukey, Phil J. Skogmo,
Lawrence F. Bennett, Michael George, Walter R. Olson, Michael J. Harden,
Bob N. Turman, Steven A. Moya, Jennifer L. Henderson
Sandia National Laboratories
Albuquerque, NM 87185

and
Ken Struve
Mission Research Corporation
Albuquerque, NM 87106

Abstract

We report experiments evaluating the beam generation by the new 4-MV RLA injector and the subsequent beam transport and acceleration through the ET-2 post-accelerating cavity. Beams of 15 to 20 kA current were produced and successfully accelerated through the ET-2 gap. The produced beam has a Gaussian current density distribution and a radius of 5 mm. The beam profile and radius remain the same through acceleration, and the beam transport efficiency through the gap is 100%. Measurement results will be presented and compared with simulation.

Introduction

Figure 1 is a schematic diagram of the experimental model of our recirculating linear accelerator (RLA). It incorporates the 4-MV injector and only one post-accelerating cavity (ET-2). The RLA device is depicted for simplicity as a closed racetrack configuration; however, in our lower energy experiments and up to ~ 20 MeV acceleration we are planning to utilize an open-ended spiral configuration. After acceleration in the spiral device the beam will be injected into a higher energy closed racetrack accelerator. The focusing and transport of the intense relativistic electron beam is accomplished with the aid of an ion focusing channel (IFR). The plasma channel is generated by the ionization of a 2×10^{-4} torr argon or xenon gas atmosphere, and a low energy, 300 eV, electron beam is utilized to ionize the neutral gas and form the plasma column.

In the experiments reported here, only the first straight section of the recirculator is utilized. Figure 2 shows the actual experimental set-up. We have presently selected

*Supported by Navy SPAWAR under Space Task No. 145-SNL-1-8-1, by U.S. DOE Contract DE-AC04-76DP00789, and DARPA Order No. 7877.

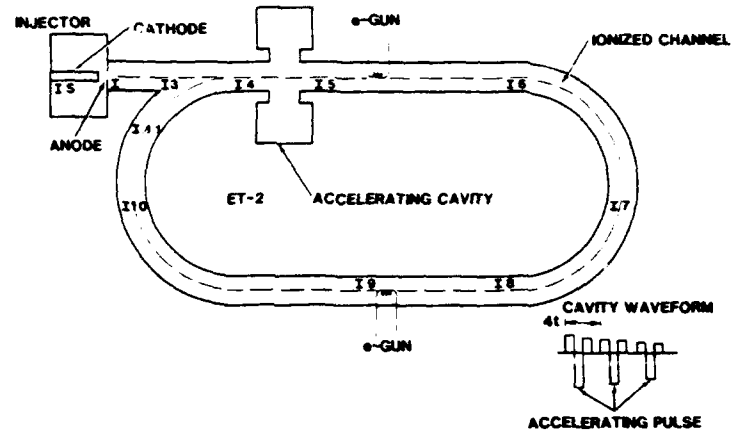

Figure 1. Schematic diagram of the Recirculating Linear Accelerator (RLA). Closed racetrack configuration.

for the injector an apertured ion focused foilless diode from among various options[1]. It is the simplest and easiest to operate and can be adjusted to provide variable beam impedance loads to the injector.

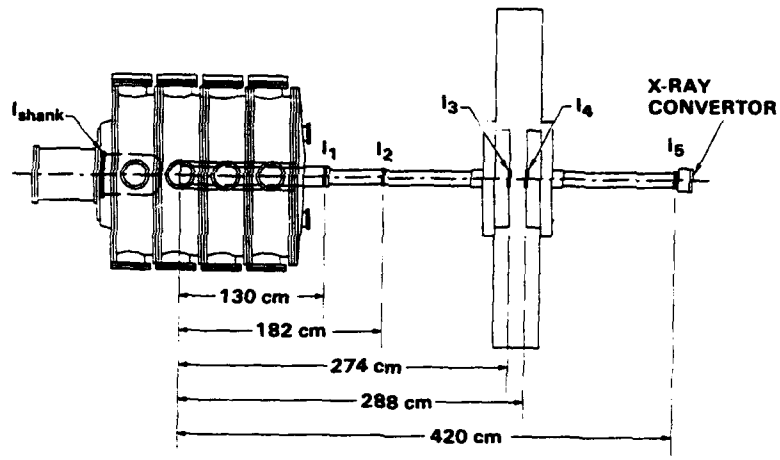

Figure 2. Experimental setup. A reentrant geometry is selected for the injector.

In the following two sections we describe the beam generation, transport and postacceleration as well as the measurements evaluating beam profile, radius, energy and beam transport efficiency through the gap.

Beam Generation and Evaluation

In the first set of experimentations reported here, the beam line is interrupted just before the ET-2 cavity in order to install an x-ray pin-hole camera. The beam propagates 130 cm through the IFR channel before striking a 0.12 mm tantalum x-ray convertor. The shank Rogowski coil (I_s) measures the total current flowing inside the

diode, while another Rogowski coil (I_1) is located 10 cm upstream from the tantalum convertor and measures the beam current transported up to that point. V monitors measure the time derivative of the voltage pulse waveform across each of the four feeds. The total A-K gap voltage is estimated by numerical integration and the addition of the four V signals. Figure 3 compares the total voltage waveform with the shank current (I_s) and beam current waveforms. The voltage and current traces are shifted in time for the sake of comparison. The shank current waveform appears somewhat smoother, and we believe that tnis is due to the larger circumference of the shank Rogowski coil. For this shot the A-K gap of the diode was 2.5 cm and the IFR argon gas pressure 2.7 x 10^{-4} Torr.

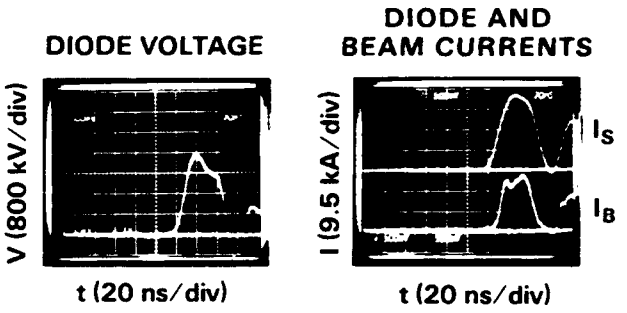

Figure 3. *Injector voltage, nominal diode current* (I_s), and beam current (I_b) waveforms.

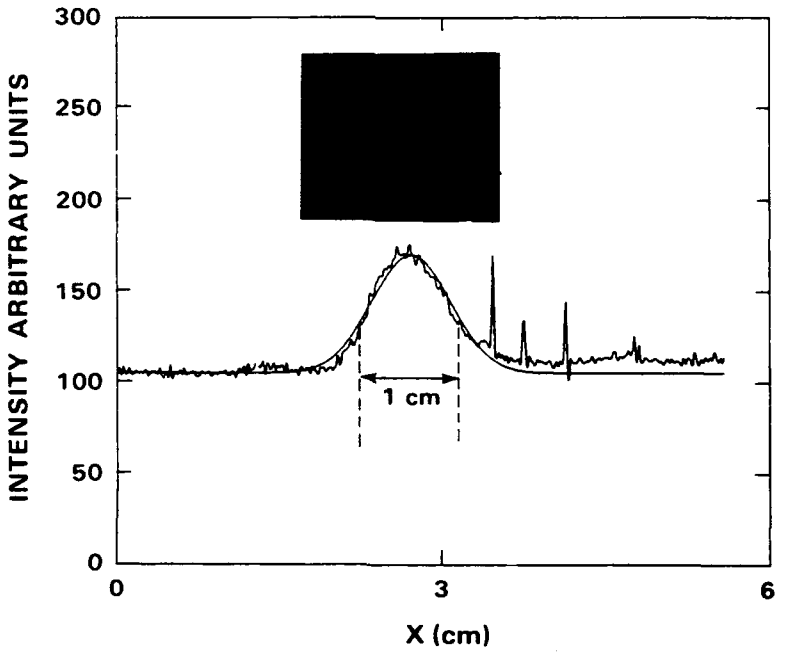

Figure 4. X-ray photograph of the beam. The scan of the light intensity along one diameter shows a 5 mm radius Gaussian distribution.

Figure 4 shows an x-ray photograph of the beam on the tantalum target together with the scan of the light intensity along one diameter of the digitized version of the same photograph. The scan is least square fitted to a Gaussian profile. The beam has a Gaussian current density distribution with a 5 mm radius. If we assume a 4-MeV, 20-kA beam in equilibrium with a $f_e = 0.5$ channel, then we derive a beam temperature $\beta\perp = 0.25$ and an emittance equal to $\epsilon = 0.13$ rad. cm, which is in very good agreement with the MAGIC[2] simulations of Figure 5.

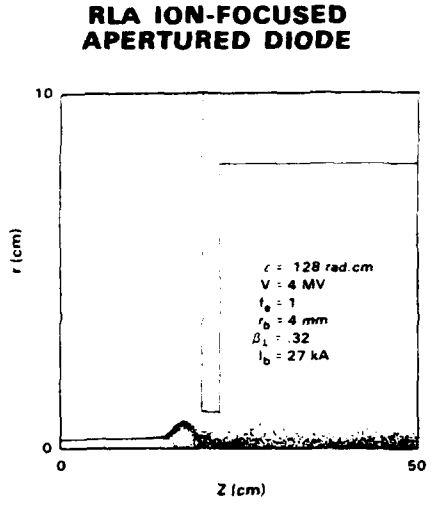

Figure 5. Electron map of the ion focused apertured diode. The MAGIC PIC code was used.

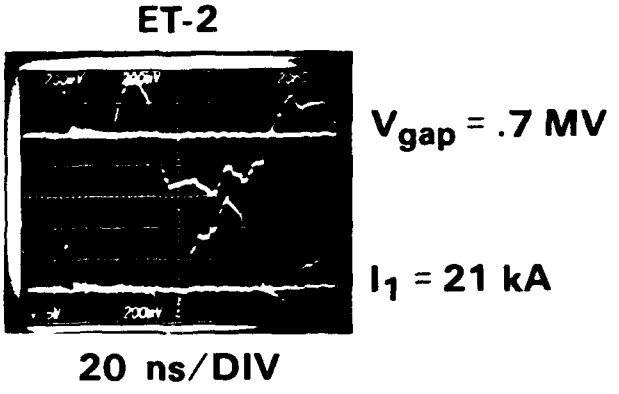

Figure 6. ET-2 voltage (upper trace) and beam current (lower trace) wave forms. Both traces are synchronized in time.

Beam Transport and Post-Acceleration

In the second set of the experiments reported here the beam was transported further downstream from the injector and accelerated by the ET-2 cavity. Rogowski coil monitors were the main diagnostics used to evaluate the beam transport. The beam profile and radius were evaluated from the photographs obtained by the x-ray pin-hole camera (Figure 8). The beam transport was interrupted 20 cm downstream from the Rogowski #4 in order to position the Ta x-ray convertor. The total beam propagation length from the injector diode to the x-ray convertor was 4.4 m.

The net beam acceleration through the ET-2 cavity (~ 0.8 MeV) was evaluated from the cavity voltage wave form and the time of beam passage through the gap. The voltage wave form and amplitude were measured with a resistive monitor and two capacitive pick-up probes. The total beam energy downstream of ET-2 is of the order of 4 MeV.

Figure 6 shows in the same time frame the ET-2 cavity voltage pulse and beam current pulse. It is apparent that the beam passage through the accelerating gap is well synchronized with the first accelerating positive swing of the ringing ET-2 voltage wave form.

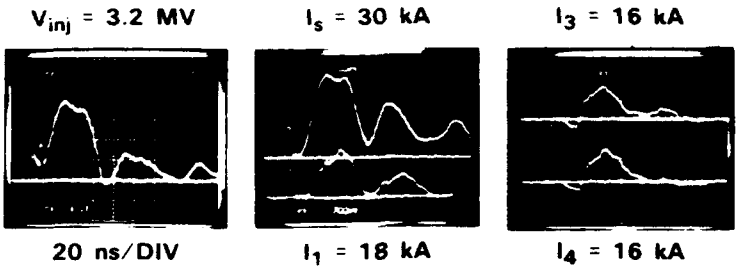

Figure 7. Injector voltage and beam current traces for a typical shot (253). The subscript on the current symbol (I) indicates the particular Rogowski location for each current measurement (Figure 2).

Figure 7 presents typical voltage and current scope traces for the shot #253. The injector voltage was 3.2 MV, the shank or total diode load was 30 kA, and the beam current was 18 kA near the injector and 16 kA further downstream. There is some current loss between Rogowski monitor #1 and #3 (the monitor #2 was not connected in this shot). However, the beam current profile and amplitudes before and after acceleration (Rogowski monitors #3 and #4) are the same and equal to 16 kA. Hence the beam transport efficiency through the ET-2 gap is 100%.

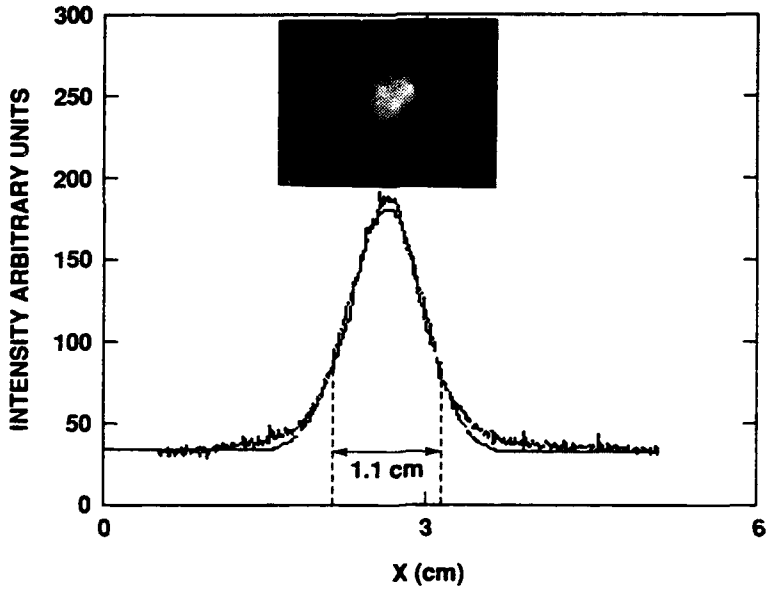

Figure 8. X-ray photograph of the beam 4.4 meters downstream from the injector diode. The scan of the light intensity along a diameter reveals a Gaussian distribution with 5 mm radius.

Figure 8 shows a pin-hole x-ray photograph of the beam 4.4 m downstream from the injector together with a scan of the beam density profile along a diameter of the same photograph. A comparison of figures 5 and 7 indicates that the beam has conserved its Gaussian profile and radius of 5 mm throughout transport and post acceleration by the ET-2 gap. These results suggest that the beam comes into equilibrium with the IFR channel in the first meter of propagation and continues in equilibrium further downstream through the accelerating gap.

Conclusion

The 4-MV RLA injector was successfully put into operation with RLA experiments. The produced electron beam was transported 4.4 m downstream from the injector and accelerated through the ET-2 cavity. The x-ray pin-hole photographs of the beam on the tantalum convertor before and after post-acceleration through the ET-2 gap are the same and reveal a Gaussian density profile of 5 mm radius. A maximum beam current of 16 kA was transported and successfully accelerated through the ET-2 cavity with 100% efficiency. Numerical simulations with MAGIC agree well with the beam measurements.

References

[1]M. G. Mazarakis et al., Proc. 1990 Linear Accelerator Conf., Albuquerque, NM, Los Alamos-Report-LA-12004-C, p. 605, September 1990.

[2]B. Goplen, et al., Mission Research Corp. Report MRC/WDC-R-068, 1983.

DESIGN AND EVALUATION OF THE XBT DIODE*

Edward L. Wright, Arnold Vlieks, Karen Fant, Chris Pearson,
Ron Koontz, Dave Jensen
Stanford Linear Accelerator Center
Stanford University, Stanford, California, 94309

George Miram
198 Selby Ln.
Atherton CA, 94025

Abstract

This paper describes the design and experimental results achieved with the 440 kV, microperveance 1.9, XBT (X-band Beam Tester) diode. The Pierce gun was developed for the 100 MW X-band klystron; the high power RF source to be used on the NLC (Next Linear Collider). The gun is electrostatically focused (no magnetic compression) to a beam diameter of 6.35 mm, with an area convergence of 110:1. Maximum cathode loading is approximately 25 A/cm^2, with a beam power density of 770 MW/cm^2. The measured beam current was within 2% of the value predicted by simulation with EGUN. Transmission through the highly instrumented beam tester was 99.98%. Some novel techniques were used to achieve near perfect beam transmission, which include the use of a reentrant-floating input pole piece.

A. Introduction

The X-Band Beam Tester (XBT) Beam Diode is a diagnostic tool used to evaluate the performance of a 440 kV, μP=1.90, electron gun. Design and performance parameters are given in table 1. This gun will be used on the SLAC 100 MW, NLC klystron. The purpose of this experiment was twofold. First, was to determine the beam transmission. This tester uses several isolated drift sections which are smaller than the intended klystron drift diameter. If good transmission can be achieved through these reduced diameter sections, we should be assured of good transmission in the klystron. Secondly, due to the high beam area compression (BAC), we require near perfect agreement between simulation and experiment. Previous experience with the SLAC 5045 klystron, which has a BAC of 36:1, suggested errors between simulation and experimental measurement of beam current to be approximately 10%.

table I

Design Parameters of the XBT Beam Diode

Klystron:	
Beam Voltage:	440 kV
Beam Current:	536 A
Pulse Length:	1.5 μs
Microperveance:	1.90
Beam Diameter:	6.4 mm
Tunnel Diameter:	9.6 mm
Peak Focus Electrode Gradient:	300 kV/cm
Peak Anode Gradient:	410 kV/cm
Beam Area Compression (BAC):	110:1
Cathode :	M-type
Cathode Loading (max edge):	25 A/cm2
Edge-Center Loading Variation:	2.78:1
B/Bbr:	2.8
Solenoid:	
Solenoid Current:	375 A
Bucking Current (nominal):	-18 A
Solenoid Power Consumption:	31.3 kW
Magnetic Field (Bo):	0.57 T

An outline of the XBT can be seen in figure 7. The body of the tube consists of four isolated sections; three with decreasing drift diameters, and an isolated tailpipe. The inside diameters of the three drift sections are 10.5

* Work supported by the Department of Energy. Contract DE-AC03-76SF00515

mm, 9 mm, and 8mm, with the 8mm section closest to the collector. These sections are referred to as bottom, middle, and top; their relative positions with respect to the cathode. Ceramics were used to isolate all sections and the collector. Monitoring of the intercepted current on the four sections and collector was performed using calibrated 50 Ω resistor networks. The tailpipe monitoring circuit was modified to allow for DC biasing. This was done to repel any slow secondary electrons. At the conclusion of the experiment, the solenoid field was measured using the input pole-piece, output pole-piece, and solenoid current settings. The computer simulation of the magnet was then fine tuned to agree with the measurement to within 2%, and these data were used for the final calculations.

EGUN Simulation of Cathode and Isolated Drift Sections

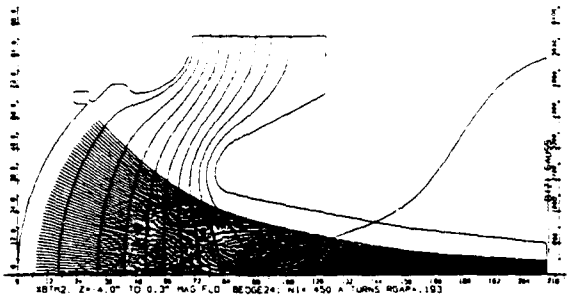

Figure 1

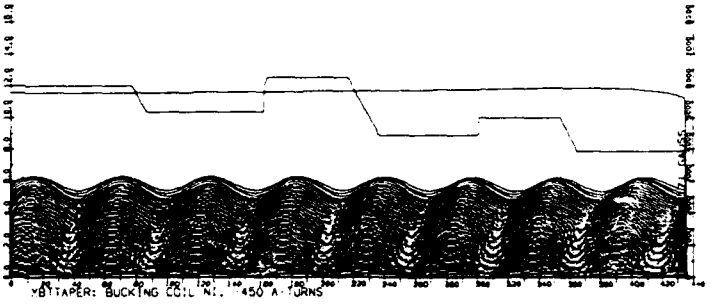

Figure 2

B. Beam Optics Design

Beam optics calculations were performed using EGUN [1], with the solenoidal field determined by POISSON [2]. Figures 1 and 2 show the beam in the cathode and isolated drift sections. This beam has scalloping of 8.9%[1], with an average diameter of approximately 6.4 mm. A bucking coil is used in the gun region to vary the beam diameter. Beam scalloping was minimized in this design by placing a magnetic lens near the beam waist. This lens is created by placing an annular gap in the input pole-piece (P/P), which leaves a ring shaped section floating (see figure 7). The floating P/P gives the gun designer an extra degree of freedom for matching the magnetic field to the beam. For most designs, there are four variables available to the gun designer; P/P aperture, reentrancy, bucking coils, and iron shields. The combination of P/P aperture and reentrancy control the field in roughly three areas: the region nearest the cathode, or the area below 0.35Bo; the slope of the field between the 0.35Bo and 0.75Bo, and the region above 0.75Bo. Iron shields and bucking coils are used to shape the flux near the cathode. Without the floating P/P, we could not simultaneously match the field to the beam in all three areas; this resulted in a highly scalloped beam.

The floating iron P/P permits the tailoring of the magnetic field below 0.35Bo and above 0.75Bo, while leaving the area between these regions essentially unchanged (figure 3). With this arrangement, we were able to reduce beam scalloping from greater than 25% to less than 10%. There was concern about the sensitivity of the gap symmetry to transverse fields. The transverse field was measured, and the data is shown in figure 4. This

[1] Scalloping=Rmax-Rmin/(Rmax+Rmin)

data is normalized to the percentage of axial field. It can be seen that a slight asymmetry in the gap creates an appreciable transverse field, hence great care must be taken in construction to ensure that the gap is symmetric.

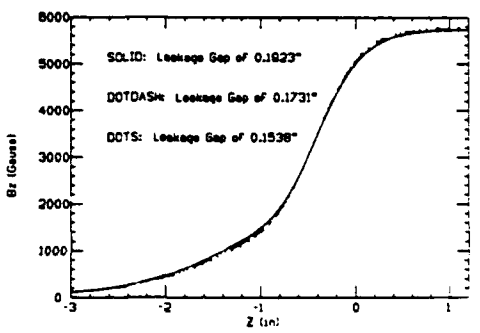

Figure 3

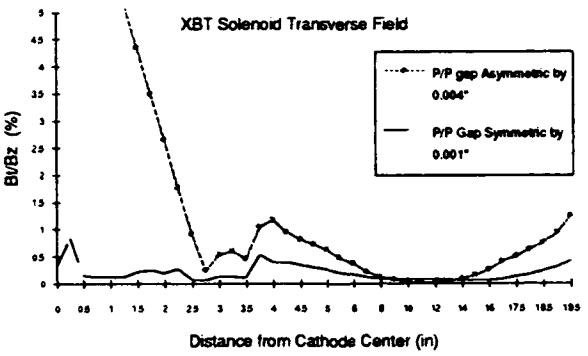

Figure 4

C. Electrode Thermal Compensation

An experiment was performed to determine the temperature of the cathode flashlight electrode at various locations (see figure 7). The cathode flashlight was sealed into a stainless steel vacuum chamber which had the same geometry as the anode. The chamber had an anode view port, so that the cathode temperature could be determined using an optical pyrometer. Twenty thermocouples were placed at various locations along the cathode flashlight assembly. With data obtained from this experiment, we found that the total height increase of the flashlight due to thermal expansion was 0.094" for a 1150 $^{O}C_{b}$ cathode temperature; approximately that required for fully space charge limited operation at 25 A/cm2. The cold cathode-to-anode spacing was increased by approximately 0.094" to compensate for this motion.

Compensation for thermal motion was also made in two other sensitive areas; for radial and longitudinal spacing increases of the cathode edge to focus electrode edge, and for growth of the entire focus electrode. During testing, we found the perveance of the gun to be higher than predicted by simulation. The computer initially predicted a microperveance of 1.836, while the actual tube microperveance was measured to be 1.902. Calculations were performed to take into account the radial growth of the focus electrode, not just the edge. This resulted in an increase in microperveance to 1.926, about 5%. Table 2 shows the sources and magnitudes of the relative errors between calculation and experiment, listed in descending order of importance, due to thermal growth of the XBT electrodes.

table II

Thermal Compensation*

1.) Flashlight Growth (>+10% error): Compensated in gun fabrication. Ca-A spacing increased accordingly.

2.) Radial and growth of the Focus Electrode (approximately +5% error): Compensation must be performed in the original calculations and fabrication (Compensation of the radial growth was not done originally, and was later found to be a source of error.)

3.) Changes in Radial and Longitudinal Cathode to Focus Electrode Edge Spacing (approximately +3% error): Compensated during gun fabrication.

* please note that these errors differ from geometry to geometry.

D. Testing and Experimental Results

The first step in the experiment was to determine the heater power to give space charge limited (SCL) operation at full beam voltage. This was performed by taking heater roll-off curves at 70 kV and 110 kV, which give beam currents of $I_o/16$ and $I_o/8$, respectively; Io is the beam current at full voltage. A *Miram* Curve [3] was generated from these data, and used to estimate the heater power requirements at full voltage. Using the curve, we determined that for SCL operation at 110 kV the cathode heater required 220 W of power, which corresponds to a temperature of 950°C. For typical M-type dispenser cathodes, doubling the cathode current requires a temperature increase of approximately 40°C to remain SCL. From this we deduced that the cathode should be operated approximately 150°C higher in temperature for SCL operation at full beam voltage (3*40°C+30°C safety margin=150°C). From this calculation, we can determine that for SCL operation at 440 kV, the cathode must be operated at approximately 1100°C, which corresponds to a heater power of 350 W.

The beam tester was processed up to 440 kV and data taken. Table 3 is a comparison of measurement and calculation. It can be seen that the agreement is good. The tube transmission was better than expected, especially since several sections have drift tube diameters smaller than the diameter to be used on the future klystron. A plot showing experimental data obtained at full voltage is shown in *figure 5*. Beam current was measured to be 555 A at 440 kV. The tailpipe shows interception of 2.89 A, while interception on the top isolated section was just 21 mA. Also note that the image charge can be seen to flow in the bottom, middle, and top isolated stages. This is consistent with what would be expected.

table III

Comparison of Calculation & Experimental Results.

<u>Microperveance at 440 kV</u>	
Initial Calculation:	μP=1.837
Measured:	μP=1.902
Error:	3.4%
Follow-up Calculation:	μP=1.926
Measured:	μP=1.902
Error:	-1.3%
<u>Transmission at 440 kV, 555 A</u>	
Top Isolated Section:	>99.98%
Tailpipe:	>98.00%

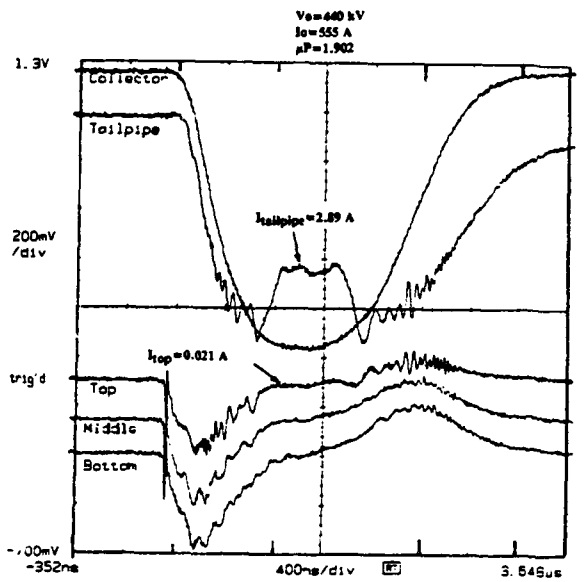

Figure 5

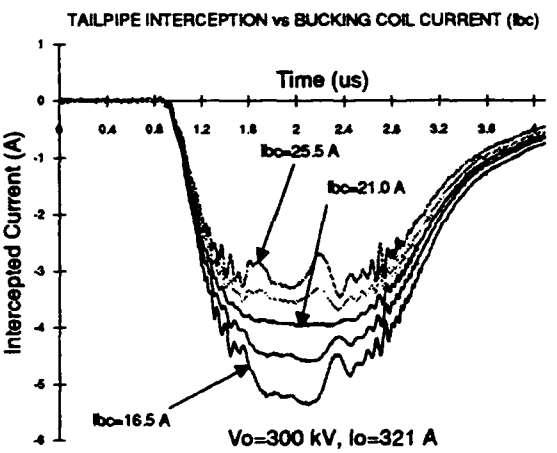

Figure 6

E. Tailpipe Isolated Section Interception

Figure 6 shows a plot of tailpipe interception versus Bucking Coil Current (I_{bc}). This interception is as much as 1.5% of I_0, therefore we would like to determine the cause of the interception. It has been suggested that the intercepted current is a superposition of primary, reflected primary, and secondary electrons. A negative 600 V_{DC} bias was applied to the tailpipe, which reduced the intercepted current by only 15%. We interpret this as due to secondaries having low enough energy to be repelled by this bias, whereas the primary and/or reflected primary electrons, which carry substantial energy, would not be effected.

Observe that tailpipe interception increases with decreasing I_{bc}, which would be expected if we were intercepting a small amount of primary electrons (the average beam diameter increases with decreasing bucking current). Also note that the ripple on the waveforms is minimum at I_{bc}=21.0 A, and increases on either side of this setting. A possible explanation for this phenomenon is that the ripple on the waveforms is due to a scalloping beam intercepting at one surface of the tailpipe. If this is true, then by observation of the data, we can conclude where the scalloping is minimum, namely when I_{bc}=21.0 A. A follow-up simulation was performed after measuring the solenoid used in the experiment, and we found a local minima in beam scalloping that agreed quite well with the observed waveform for these various settings.

F. Discussion and Conclusion

Future linear accelerators require RF power sources with long life, increased beam power, and higher frequencies. These factors typically require beam optics designs with greater BAC's. Beam optics designs with BAC's of 800:1 and greater are presently being designed for future linear beam tubes. It is therefore most important that the designer be able to rely more heavily on beam optics simulation, due to the difficulty of measuring the beam parameters at these high power levels. The XBT Beam Diode has proven that near perfect transmission was achieved. It has also shown that excellent agreement between computer simulation and measurement can be obtained, provided the cathode geometry is adjusted to compensate for thermal motion of electrodes. SLAC's next generation klystron for the NLC is being designed. It will operate at 550 kV, μP=1.2, and BAC of 120:1. Based on the data gathered from the XBT Beam Diode, we expect to be within 2% for this design also.

references

1) W. B. Herrmannsfeldt, "EGUN-an Electron Optics and Gun Design Program", SLAC-report-331, October 1988.

2) Los Alamos Accelerator Code Group, "Reference Manual for the Poisson/Superfish group of Codes", LA-UR-87-126, January 1987.

3) T. J. Grant,"A Powerful Quality Assurance Technique for Dispenser Cathodes and Electron Guns", IEDM, CH2099-0/84/0000-0334, 1984.

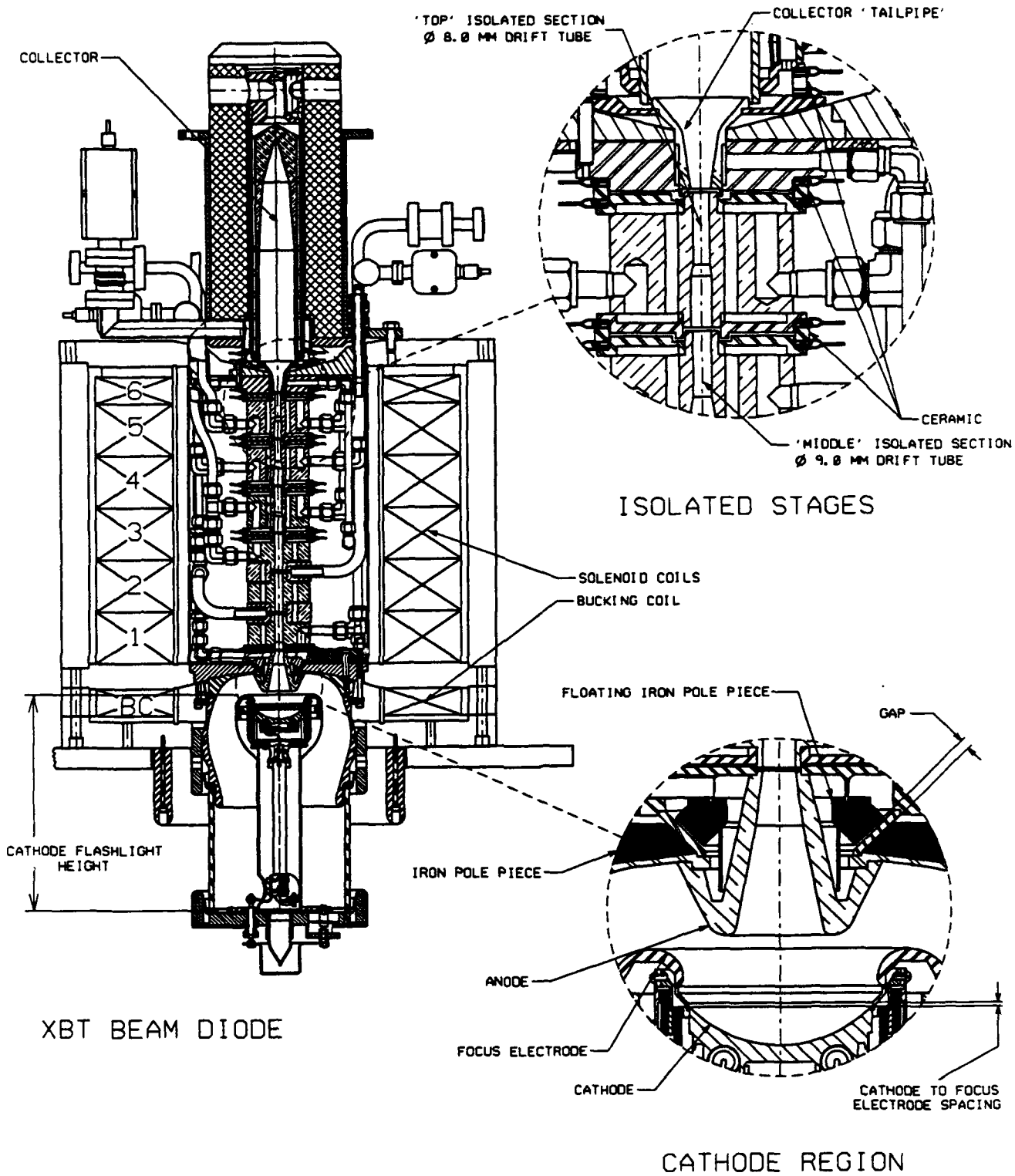

XBT BEAM DIODE

ISOLATED STAGES

CATHODE REGION

FIGURE 7

THE PHYSICS OF "VACUUM" BREAKDOWN

F. Schwirzke, M. P. Hallal Jr., and X. K. Maruyama
Naval Postgraduate School, Monterey, CA 93943

The initial plasma formation on the surface of a cathode of a vacuum diode, vacuum arc, and many other discharges is highly non-uniform. Micron-sized cathode spots form within nanoseconds. Despite the fundamental importance of cathode spots for the breakdown process, their structure, and the source of the required high energy density were not well understood. When an increasing voltage is applied, enhanced field emission of electrons begins from a growing number of small spots or whiskers. This and the impact of ions stimulate desorption of weakly bound adsorbates from the surface of a whisker. The cross section for ionization of the neutrals has a maximum for ~ 100 eV electrons. As the diode voltage increases, the 100 V equipotential surface which moves towards the cathode is met by the desorbed neutrals moving away from the cathode. These two regions proceed from no overlap to a significant amount of overlap on a nanosecond time scale. This results in the sharp risetime for the onset of ionization. Ions produced in the ionization region, a few μm from the electron emitting spot are accelerated back. This bombardment with ~ 100 eV ions leads to surface heating of the spot. Since the ion energy is deposited only within a few atomic layers at a time instead of an entire whisker volume, and since the neutral contaminants are only loosely bound to the surface, the onset of breakdown by this mechanism requires much less current than the joule heating mechanism. Ion surface heating is initially orders of magnitude larger than joule heating. As more ions are produced, a positive space charge layer forms which enhances the electric field and thus strongly enhances the field emitted electron current. The localized build-up of plasma above the electron emitting spot then naturally leads to pressure and electric field distributions which ignite unipolar arcs. The high current density of the unipolar arc and the associated surface heating by ions provide the "explosive" formation of a cathode spot plasma.

Introduction

The initial phase of the onset of electrical breakdown in a vacuum discharge is characterized by very rapid ionization of surface material which leads to a kind of "explosive" plasma formation on the electrodes. Though breakdown processes have been studied extensively, the onset of ionization in a fast pulsed vacuum diode is not yet well understood. Electrons will be emitted from spots on a cold cathode if the applied electric field becomes sufficiently strong, $E > 10^7$ V/m. However, the electric field distribution is altered by the

presence of electron space charge and the current density j_{CL} is limited by the Child-Langmuir law. In general one would expect that the field emitted current density $j_{FE} < j_{CL}$. One model to describe the formation of cathode flares is the whisker explosive emission model [1]. The field emitted current supposedly heats the whisker within nanoseconds until formation of plasma occurs. $j \approx 10^{12} - 10^{13}$ A/m^2 would be required to ionize a whisker by joule heating within a few ns. However, j_{FE} will become space charge limited at a much smaller value.

Onset of Ionization and Surface Heating

The prebreakdown field emission current density is self-limiting. The electron density n_e will be largest near the emitting spot. This will reduce E and thus j_{FE} . Since the field emitting spot cannot deliver j_{CL} without turning itself off, it must be that $j_{FE} < j_{CL}$. The development of a current with $j > j_{FE}$ and $j \leq j_{CL}$ from a cold cathode requires that ions exist in front of the electron emitting spot. Ions cannot be emitted from the surface of the whisker, the enhanced electric field would hold them back. The initial ionization must occur in the cathode-anode gap near the electron emitting spot. Ionization of desorbed neutrals provides the mechanism. This ionization process requires considerably less current than the ionization of the solid material of the entire whisker by joule heating. Besides joule heating of the electron emitting spot, the emission of electrons itself, and the enhanced electric field, all stimulate desorption of weakly bound adsorbates [2]. The large concentration of neutrals n_0 above the electron emitting spot will to some extent become ionized by the field emitted electrons. The electron mean free path length $\lambda = 1/(n_0\sigma_0)$ depends on the ionization cross section σ_0 which is a function of the electron energy. For many gases the ionization cross section has maximum value for 100 eV electrons. The diode used for this experiment has a gap of 2.5 cm, and 1 MV was applied. At z = 2.5 μm the potential is 100 V and the field emitted electrons begin to ionize the desorbed neutrals. The ionization region is approximated as having a thickness of d = 1 μm and is centered on the 100 V potential. On average the ions produced are accelerated toward the whisker and deliver 100 eV of energy each. The ratio of joule plus ion heating to joule heating in the surface layer is given by [3]:

$$R = 1 + \frac{100 j^+ / L}{j^2 \rho} = 1 + \frac{100 d n_0 \sigma_0}{j^- L \rho (1 + d n_0 \sigma_0)^2}. \quad (1)$$

where j^+ is the ion return current density, and L is the depth of the surface layer in which the ions deposit all of their 100 eV energy. j^+ depends on the ionization of neutrals by field emitted electrons with current density j^-. ρ is the resistivity of the whisker material, and $j = j^- + j^+$ is the total current density flowing through the whisker. The energy required to liberate a metal atom from the surface of the cathode is approximately 5 eV, the binding energy. The energy (eV) per atom deposited in the whisker due to joule heating is

$$\frac{\text{energy}}{\text{atom}}(\text{joule heating}) = \frac{(j^2 \rho \, \Delta t / 1.6 \times 10^{-19} [\text{eV/J}]}{n_w} \quad (2)$$

where n_W is the number density of the whisker material and Δt is the duration of the current flow. The total energy/atom deposited in the surface layer of the whisker due to both joule and ion heating is R times equation (2). Figure 1 gives the values of eV/atom as a function of j^-, n_o, k, and for $\Delta t = 10^{-9}$s, using $n_w = 8.2 \times 10^{28}$ atoms / m^3 for steel, $\sigma_0 = 1 \times 10^{-20}$ m^2, $\rho = 7 \times 10^{-8}$ Ω-m, $L = a_0 k$, where a_0 is the lattice parameter for stainless steel (2.9×10^{-10} m), and k is the number of monolayers of the whisker through which the ions penetrate. The heating of the surface due to return ions is far more efficient than the

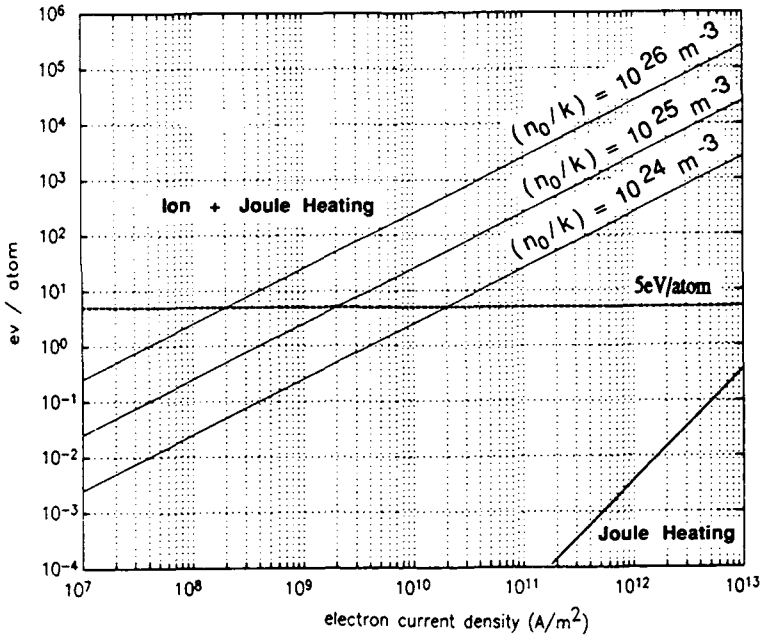

Figure 1. eV per surface atom vs electron current density. The lines are plots of the product of Eq. (1) times Eq. (2) for $\Delta t = 10^{-9}$s, and various neutral densities n_0, and number of monolayers k. The dashed line is 5 eV/atom.

heating of the whisker bulk due to joule heating. Ion bombardment is especially important at low initial current densities since it leads efficiently to further desorption of neutrals from the surface which in turn increases the ionization rate.

Breakdown and Formation of Cathode Spots

As more ions are produced, the positive space charge enhances the electric field and thus j_{FE}. Also the 100 volt equipotential surface, 100 V EPS, moves closer to the cathode surface into a region of higher n_0. This further increases the ionization rate. The whole process rapidly becomes unstable.

The ionization of the desorbed neutrals does not become significant until the neutrals reach the 100 V EPS. Therefore, the onset of plasma formation should be delayed from the onset of desorption by the time of flight of the neutrals to the 100 V EPS. As the voltage is applied across the diode, the 100 V EPS moves from the anode side of the diode toward the cathode. The desorbed neutrals expand from the cathode surface toward the anode. The onset of ionization will not occur until the 100 volt equipotential surface and the desorbed neutrals reach the same position. For a given diode gap and time varying voltage waveform, the time delay of the onset of plasma formation can be predicted.

In order to determine whether the vacuum diode breakdown mechanism is caused by the proposed mechanism, a Model 112A Pulserad generator was used with diode voltages between 0.6 - 1.8 MV, and pulse length of 20 ns FWHM. The plasma formation on the cathode surface was observed using a lens system, fiber optic bundle and an avalanche photodiode. The diode voltage and current pulses have rise times of ~ 10 ns. After some delay, the photodiode signal begins with a very short risetime of 1 to 2 ns. Data runs were performed at peak diode voltages of 0.6 MV, 1.2 MV and 1.8 MV.

The position of the 100 V EPS away from the cathode is calculated as function of time from the measured voltage wave form of the diode for one 1.2 MV shot, Figure 2. The figure also shows the position of desorbed neutrals which were released at the onset of the voltage pulse and expand with sound velocity, 0.33 μm/ns. The intersection of the two curves gives the predicted time of breakdown for this shot, 8 ns from the onset of the voltage pulse. The predicted time falls on the sharp rise of the experimentally measured

photodiode waveform. The predicted delay time for a 0.6 MV shot is 13 ns and for a 1.8 MV shot 6 ns. In both cases the sharp rise of light emission from the cathode surface is correspondingly delayed. In agreement with the model the experiments show a very rapid risetime for the onset of plasma formation. The dense region of desorbed neutrals expanding with ≈ 0.3 μm/ns is met by the 100 V EPS which is traveling at ≈ 1.5 μm/ns for the 1.2 MV shot. These two regions proceed from no overlap to a significant amount of overlap on the ns time scale. This results in the sharp risetime for the onset of plasma formation.

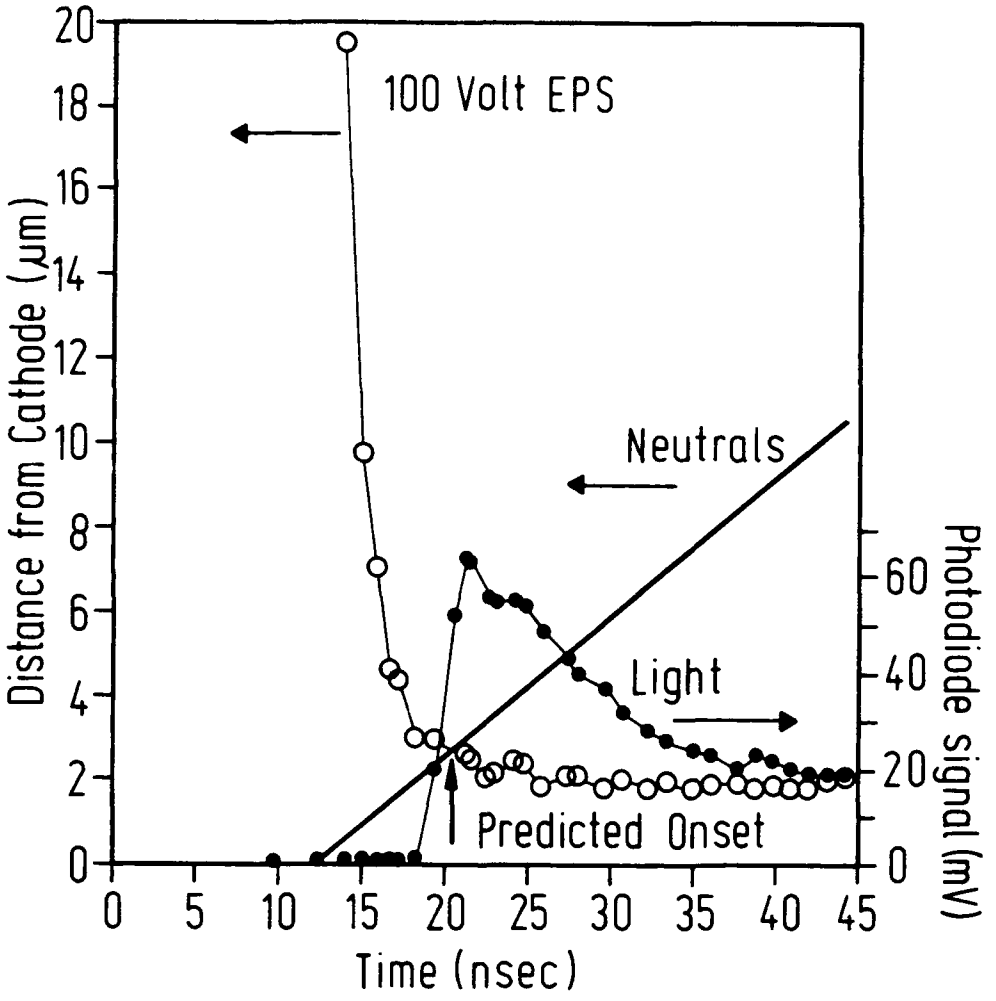

Figure 2. Photodiode waveform and distance from the cathode of the 100 V equipotential surface EPS, and distance from cathode of expanding neutrals vs. time for a 1.2 MV shot. Predicted delay from voltage onset for onset of plasma formation = 8 ns. The zero of time is arbitrarily chosen.

The localized build-up of plasma above the electron emitting spot naturally leads to pressure and electric field distributions which ignite unipolar arcs [4]. The high current density of the unipolar arc and the associated surface heating by ions provide the "explosive" formation of a cathode spot plasma. The increasing plasma pressure above the electron emitting spot leads within the plasma cloud to a pressure gradient and an electric field in radial direction, parallel to the cathode surface. The plasma potential and thus the sheath potential decrease in radial direction. In the outer region of the expanding plasma the sheath potential will be less than the floating potential and more electrons than ions will flow back to the cathode surface. This closes the electron current loop of the unipolar arc. Because the external field is screened from the cathode surface the unipolar arc current density, which is driven by the radial plasma pressure gradient, can be orders of magnitude larger than the Child-Langmuir space charge limited diode current density. Unipolar arcing is the primary breakdown process leading to the formation of cathode spots.

Conclusions

This paper presents a self-consistent physical model describing the onset of breakdown. It starts with field emission from single spots. Ionization of desorbed neutrals leads to the build up of positive space charge. This further enhances field emission. The increased surface heating by ion bombardment provides further desorption. As the ionization zone propagates into the dense vapor, more ionizations occur. The build up of plasma pressure gradients and sheath electric fields lead naturally to the formation of unipolar arcs. A cathode spot is formed by unipolar arcing.

This work was sponsored by NRL, NSWC and the Naval Postgraduate School.

References

[1] G. A. Mesyats and D. I. Proskurovsky, Pulsed Electrical Discharge in Vacuum (Springer, 1989), p. 79.

[2] J. Halbritter, IEEE Trans. Electr. Insul. EI-18 (1983) 253, and IEEE Trans. Electri. Insul. EI-20 (1985) 671.

[3] F. Schwirzke, M. P. Hallal, Jr. and X. K. Maruyama, Nuclear Instruments and Methods In Physics Research B67 (1992) 554-559.

[4] F. Schwirzke, IEEE Trans. Plasma Sci. PS-19 (1991) 690.

Simulations of a Plasma-Filled Pinched Electron Beam Diode+

S.B. Swanekamp*, J.M. Grossmann, P.F. Ottinger,
S.J. Stephanakis, B.V. Weber, J.C. Kellogg, and G. Cooperstein
Naval Research Laboratory
Plasma Physics Division
Washington, DC 20375

Abstract

Plasma-filled diode (PFD) experiments on the Gamble II pulsed-power generator show three phases of PFD behavior: a low impedance phase followed by a phase of rapidly growing impedance which culminates in a vacuum impedance phase. One-dimensional (1-D) and two dimensional (2-D) simulations of the low impedance phase and the transition to high impedance in the PFD have been performed which show good agreement with the electrical measurements. The 1-D simulations show the formation of multiple virtual cathodes in the diode along with the trapping and heating of the emitted electrons during the low impedance phase. Similar behavior is also observed in the 2D PFD simulations during the low-impedance phase. In the 1-D simulations, the low impedance phase ends when the position of the virtual cathode exceeds the anode-cathode gap size. This is accompanied by a growing bipolar sheath which is responsible for the rapid voltage growth observed in the 1-D simulations. In the 2-D simulations, the low impedance phase seems to end when the diode current exceeds critical current. The transition to high impedance occurs as the electron flow becomes strongly pinched.

I. Introduction

Plasmas were first used in high power diodes to suppress impedance collapse due to expanding electrode plasmas by eliminating the unwanted prepulse.[1] Since these initial results, the plasma-filled diode (PFD) has been investigated as a means of externally controlling the diode impedance history by adjusting the density and distribution of plasma within the diode. External control over the diode impedance has many advantages including improved coupling of power to the diode by matching the diode impedance with the generator over the entire power pulse, and an improved transfer of current from a plasma opening switch to the diode.

This paper presents a theoretical analysis of recent PFD experiments on the Gamble II pulsed-power generator at NRL.[2] The analysis includes one-dimensional (1-D) and two-dimensional (2-D) particle-in-cell (PIC) treatments in which electron and ion dynamics are fully resolved. Correlations are made between the experiments and the simulations to determine the dominant mechanisms which control plasma motion and characterize the impedance behavior of plasma-filled pinched-electron-beam diodes.

II. Plasma-Filled Diode Experiments on Gamble II

A schematic of the PFD experiment performed on Gamble II is shown in Fig. 1. The current and voltage at the vacuum/water interface are measured using a resistive current shunt (I_{SHT}) and a capacitive voltage monitor (V_D). The diode current (I_{OUT}) is measured by integrating and averaging the signals from four $\dot{B}$ loops located at the position shown in Fig. 1. The diode voltage, V_{cor}, is inferred by inductively correcting the voltage measured by V_D.

In the PFD experiments, a flashboard plasma source is used to introduce plasma into the anode-cathode (A-K) gap prior to the Gamble II power pulse. A pinched electron beam diode was used in then the PFD experiments which consisted of a thin annular cathode with a mean radius of 6 cm and thickness $\Delta r = 0.2$ cm and a planar anode. The A-K gap size used in the experiments described in this paper were $d = 0.5$ cm. The plasma is introduced into the diode through a 1 cm wide annular slot in the anode which is just inside the inner radius of the cathode and covered with a 70% transparent brass mesh. Time resolved measurements of the electron density prior to the Gamble II power pulse were

made in the PFD configuration using a CO_2 laser interferometer. These measurements revealed that, for typical delay times, prefill electron densities in the diode were between 10^{13} and 10^{14} cm^{-3}. Typical electrical measurements with a prefill electron density of $n_e=2\times10^{13}$ cm^{-3} are shown in Fig. 2. This figure shows three distinct phases of PFD behavior: a low impedance phase where the diode voltage is small and lasts for about 20 ns followed by a 10 ns phase of rapidly increasing diode voltage and impedance which culminates in a 2.5 Ω vacuum impedance phase.

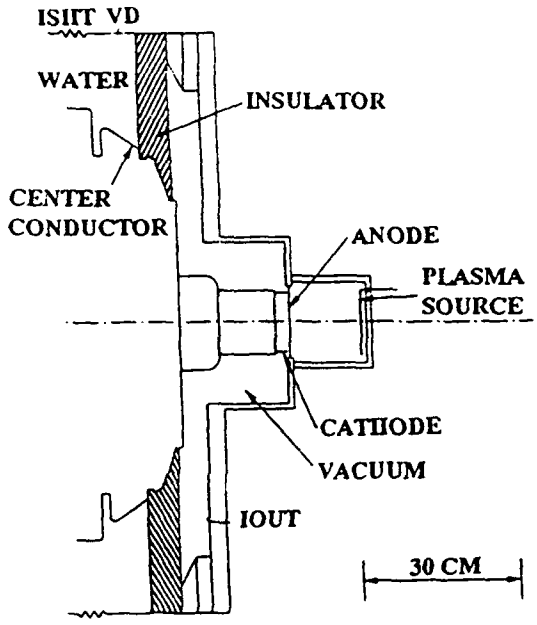

Fig. 1 Schematic of the experimental PFD setup on Gamble II.

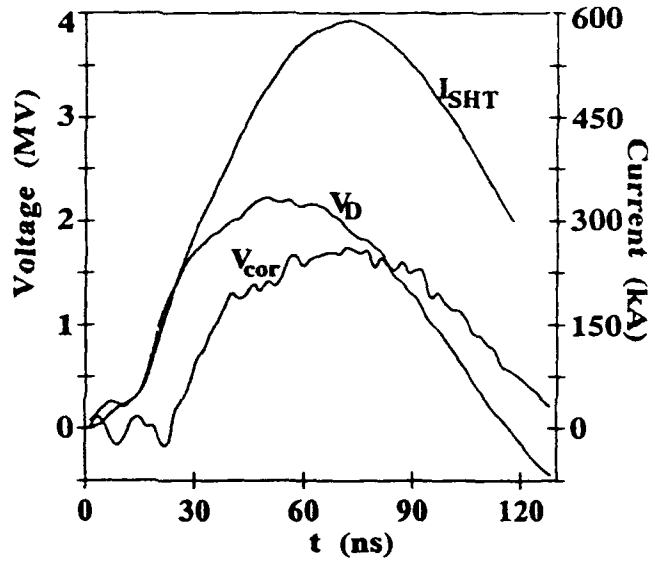

Fig. 2 Typical electrical measurements from PFD experiments on Gamble II.

III. One-Dimensional Model of the Plasma-Filled Diode

The first model used to study the dynamic response of the plasma to the applied power pulse is the 1-D PIC code REFLEX.[3] In this model magnetic effects are neglected and the electron orbits are assumed to be one-dimensional. Current is driven through the simulation by a series RL circuit driven by a time dependent voltage source. Electron and ion dynamics are treated with the relativistic equations of motion and the self-consistent electric field is obtained from the positions of all the particles in the simulation from Gauss's law. Space-charge-limited emission of electrons at the cathode allows for a continual supply of electrons to the simulation. In the simulations reported here space-charge-limited proton emission was also allowed at the anode. To initiate a simulation, a spatially uniform plasma is loaded in between the anode and cathode of the diode. Current is supplied to the diode through the series RL circuit and subsequent motion of the plasma is monitored.

To simulate Gamble II the driving voltage in REFLEX was taken to be the open circuit voltage from Gamble II. The series resistance was taken to be the equivalent resistance of Gamble II ($R_g \cong 2\ \Omega$) and the series inductance was set to the vacuum inductance between the insulator and the diode ($L \cong 78$ nH). The diode A-K gap was taken to be d = 0.5 cm, the effective diode area was taken to be A = 21.5 cm^2, and the prefill electron density was taken to be $n_e \cong 2\times10^{13}$ cm^{-3}. The effective diode was

determined by assuming that 1.8 mm of the cathode shank is an electron emitter in addition to the flat portion of the cathode directly opposite the anode. A comparison of the measured voltage, V_D, and the current, I_{SHT}, during the first 30 ns of PFD operation with that predicted by REFLEX are shown in Fig. 3. This figure shows that the measured electrical characteristics are virtually indistinguishable from the REFLEX predictions. A comparison of the A-K voltage from REFLEX with the inductively corrected diode voltage is shown in Fig. 4. The fluctuations in the inductively corrected diode voltage are caused by the inductive correction technique and represent the uncertainty in the diode voltage. The diode voltage from REFLEX is within the error bounds of the inductively corrected voltage.

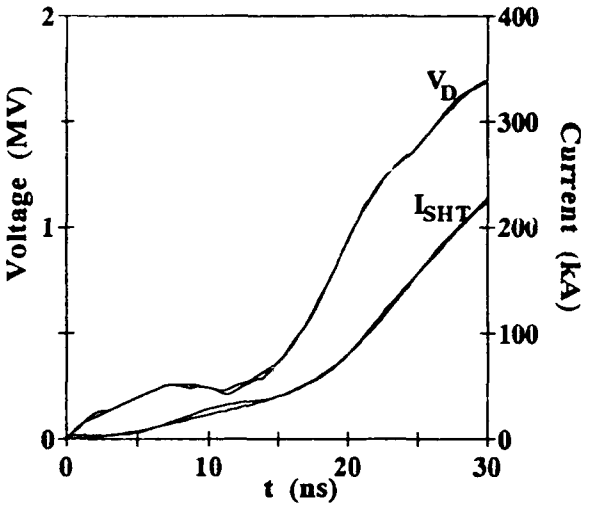

Fig. 3 Comparison of the measured current and voltage at the vacuum/H_2O interface with that predicted by the REFLEX simulation.

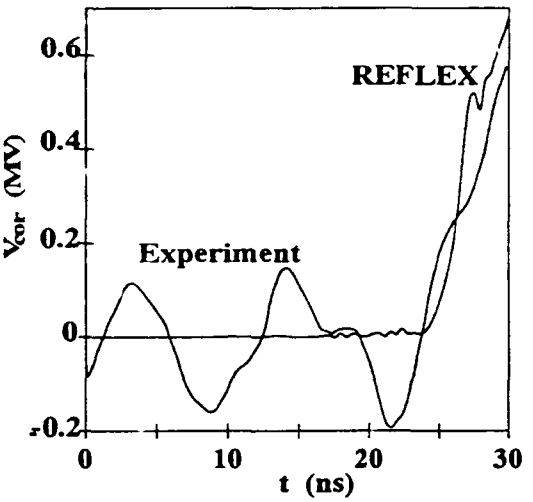

Fig. 4 Comparison of the inductively corrected diode voltage with that predicted by the REFLEX simulation.

Early in the low impedance phase the simulations show that the electrons in the plasma prefill are accelerated toward the anode to conduct the discharge current. As a result, a large region of positive space charge is uncovered near the cathode. Emitted electrons from the cathode are drawn into the A-K gap to neutralize the uncovered space charge leading to the formation of multiple virtual cathodes. The end of the low impedance phase occurs when just one virtual cathode can fit in the A-K gap. The potential structure from the simulation at t=22.5 ns is shown in Fig. 5. This figure shows the virtual cathode potential structure near the end of the low impedance phase is characterized by a large potential hill with a sizable potential drop in the anode sheath. This potential structure occurs since the center of the plasma is charged positively while the regions near the electrodes are electron rich. The emitted electron phase-space trajectories are shown in Fig. 6. This figure shows that emitted electrons are pulled away from the cathode by the ion space charge near the center of the diode. Because of their inertia, the electrons move past the point of charge balance and then slow down as they pass the ion-rich region in the center of the diode and approach the anode. Figure 6 also shows a large fraction of emitted electrons have been trapped from the main beam. Trapping and heating of the emitted electrons occurs during the low impedance phase as a result of non-equilibrium electron dynamics in the time varying potential structure produced by the rising circuit current. These trapped electrons replace the initially cold electrons of the prefill plasma with a hot distribution of electrons. The virtual cathode electric field structure accelerates ions toward both electrodes resulting in a significant depletion of ion charge in the anode sheath by the end of the low impedance phase. The loss of ions at the anode causes the

in the anode sheath by the end of the low impedance phase. The loss of ions at the anode causes the transition to high impedance to be more rapid than quasi-steady models[4] would predict. The virtual cathode formation process as well as the trapping and heating of the emitted electrons and ion depletion at the anode are explained in detail in Ref. 5.

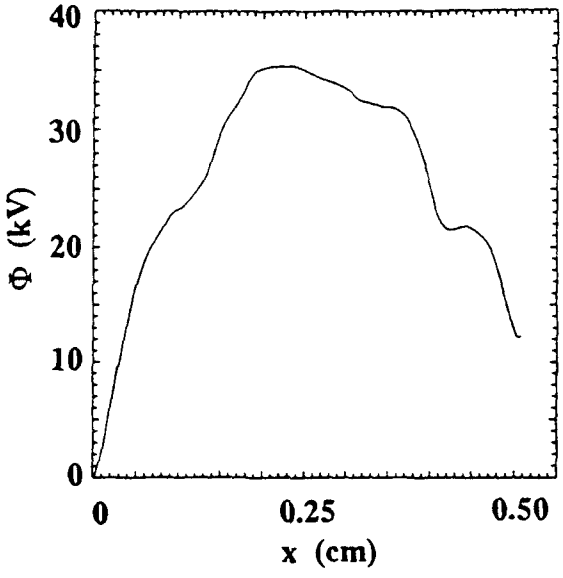

Fig. 5 The diode potential profile at t=22.5 ns from the REFLEX simulation.

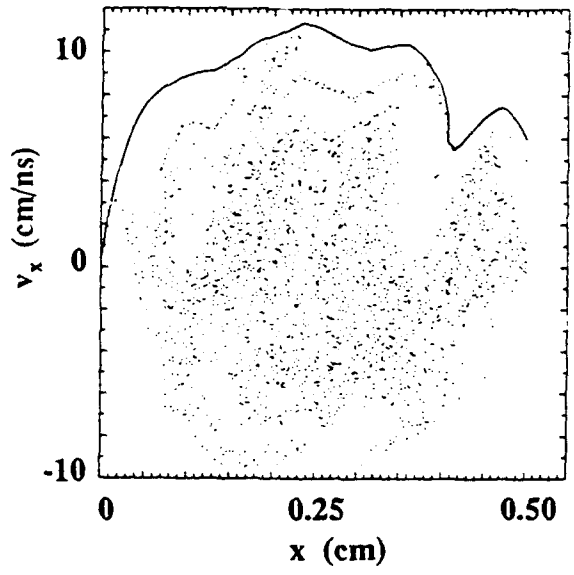

Fig. 6 Phase-space plot for the emitted electrons at t=22.5 ns from the REFLEX simulation.

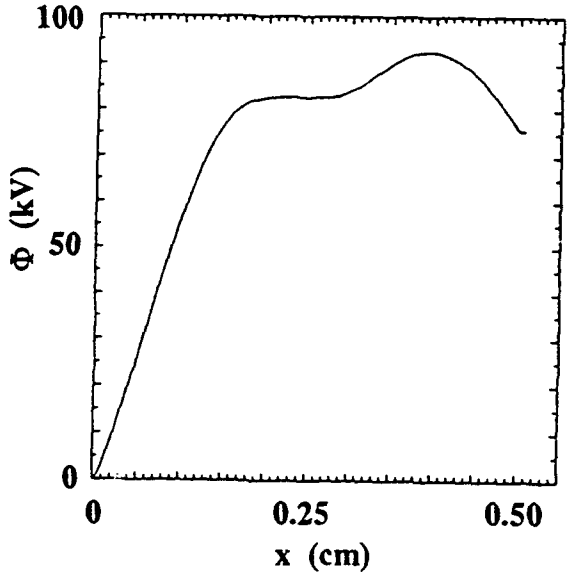

Fig. 6 The diode potential profile at t=25 ns from the REFLEX simulation.

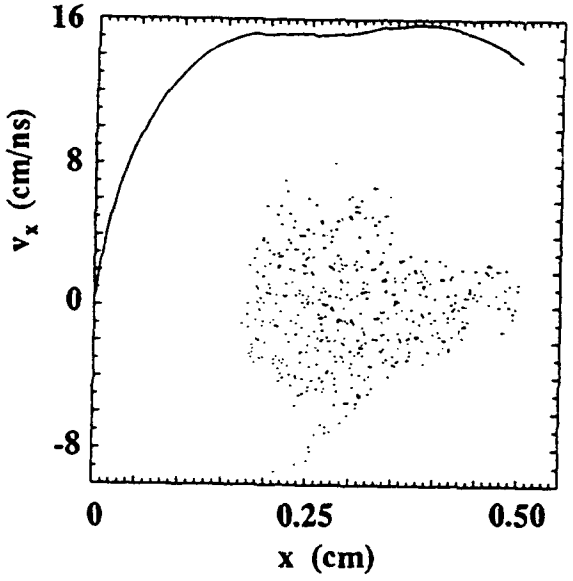

Fig. 7 Phase-space plot for the emitted electrons at t=25 ns from the REFLEX simulation.

The potential function and a phase-space plot for the emitted electrons during the transition to high impedance are shown in Figs. 7 and 8. As Fig. 7 shows, the large anode potential drop disappears and the cathode sheath voltage is now a good approximation to the diode voltage. Figure 8 shows that the trapped electrons respond to the increasing diode current by moving toward the anode to shield the large electric field in the cathode sheath from the bulk plasma. This occurs by uncovering enough positive ion charge so that the net positive charge in the cathode sheath roughly balances the net negative charge

from the beam electrons. As the trapped electrons recede toward the anode, electrons emitted from the cathode and ions drawn into the cathode sheath from the plasma are accelerated by the large sheath fields and evolve toward bipolar flow. Increases in the current result in rapid growth of the cathode sheath size and leads to a rapid increase in the diode impedance and voltage.

IV. Two-Dimensional Model of the Plasma-Filled Diode

A 2-D electromagnetic PIC simulation of the plasma-filled pinched-electron-beam diode has recently been performed using MAGIC.[6] The 2-D model features a more realistic representation of the diode geometry and includes magnetic as well as other 2-D effects. Figure 9 shows the comparison of the diode voltage predicted by MAGIC with the inductively corrected diode voltage from Gamble II. In addition, the dashed curve in Fig. 9 shows the diode voltage predicted by REFLEX. The two plots on the left in Fig 10 show the emitted electron flow in the diode just prior to and just after the beginning of the transition to high impedance. The two plots on the left show the corresponding electron phase-space (γv_z vs. z). From Fig. 10a it is seen that there is very little radial electron flow in the diode at t=15 ns so that the electron flow is approximately 1-D during the low impedance phase. Consequently, the emitted electron phase-space at t=15 ns (Fig. 10b) is very similar to the emitted electron phase-space from the 1-D model (Fig. 6). Figure 10c shows that the electron flow at t=20 ns has begun to pinch. The simulation also shows that some electrons are flowing from the shank of the cathode. However, most of the electron current is still flowing between the cathode tip and the anode. The impedance associated with this pinched electron flow is higher than the corresponding unpinched flow and may contribute to the shorter low impedance phase and slower transition to high impedance in MAGIC when compared with REFLEX.

V. Summary

The PFD experiment on Gamble II shows three distinct phases of operation: a low impedance phase where the diode voltage is small, followed by phase of rapidly increasing diode voltage and impedance which culminates in a vacuum impedance phase. One and two-dimensional PIC simulations during the low impedance phase and transition to high impedance for the Gamble II PFD experiment using the measured plasma density predict the electrical measurements.

The 1-D simulation shows that, as the circuit begins to conduct current, the plasma electrons move toward the anode uncovering a large region of ion charge near the cathode. Emitted electrons from the cathode are drawn into the A-K gap by this uncovered ion charge which leads to the formation of virtual cathodes within a few plasma periods. The virtual cathode potential structure is characterized by a potential hill with a potential drop in the anode sheath comparable with the potential rise in the cathode sheath. Trapping and heating of the emitted electrons in these virtual cathode structures occurs during the low impedance phase as a result of non-equilibrium electron dynamics in the time varying potential structure produced by the rising circuit current. The virtual cathode electric field accelerates ions toward both electrodes resulting in a significant depletion of ion charge in the diode by the end of the low impedance phase. The transition to high impedance in the 1-D simulation begins when the virtual cathode structure can no longer fit in the A-K gap. During this transition, the trapped electron population recedes toward the anode and the electron and ion distributions in the cathode sheath evolve toward bipolar flow. This rapidly growing bipolar sheath is responsible for the rapid rise in the diode impedance observed in the 1-D simulation.

Similar to the 1-D simulation, the low impedance phase of the 2-D simulation is characterized by virtual cathode formation along with electron trapping and heating during the low impedance phase. The low impedance phase in the 2-D simulation ends when the critical current is exceeded and electrons begin to be radially pinched by the magnetic field associated with the discharge current. This causes the duration of the low impedance phase to be shorter and the transition to high impedance phase to be slower for the MAGIC simulations. However, the diode voltage predicted by either model is within the uncertainty in the inductively corrected diode voltage.

PFD experiments on Gamble II have recently been performed using a helium gas-puff plasma source and a much thicker cathode (Δr = 1.5 cm). Analysis of these experiments is currently in progress and should provide valuable information on PFD scaling with ion species and diode geometry. Experiments are also currently being designed which will look for the ion losses at the anode predicted by the simulations during the low impedance phase.

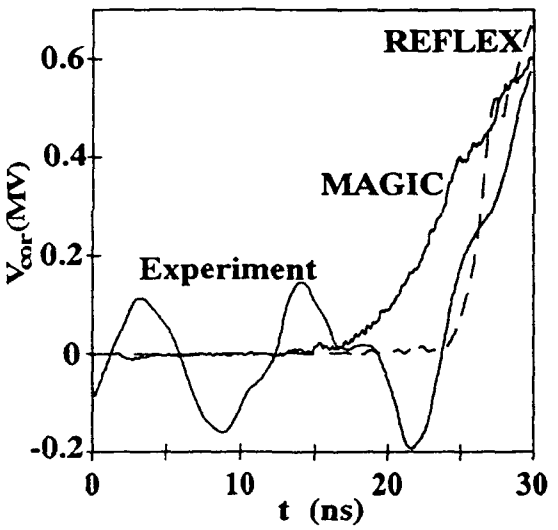

Fig. 9 A comparison of the diode voltage from MAGIC and REFLEX (dashed curve) with the inductively corrected voltage.

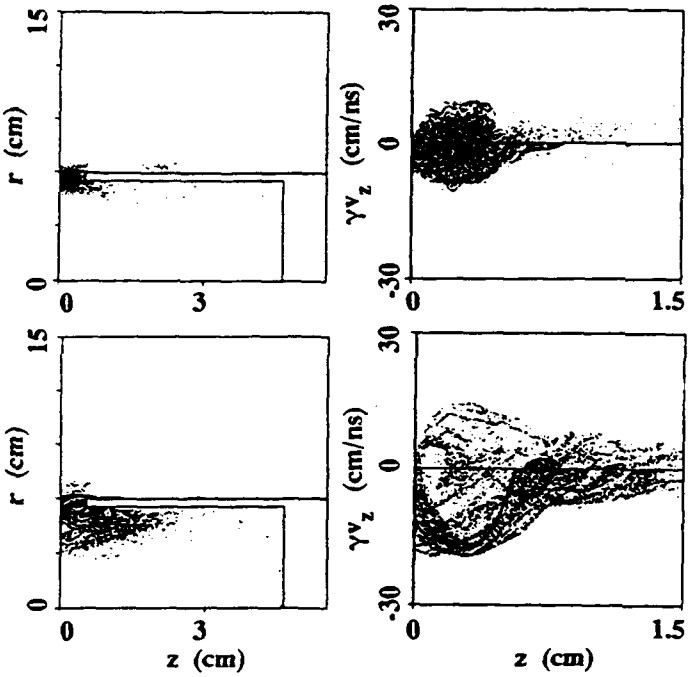

Fig. 10 The emitted electron flow in configuration space and phase space: a) and b) at t=15 ns just prior to the end of the low impedance phase, c) and d) at t=20 ns just after the beginning of the transition to high impedance.

+Work partially sponsored by the Office of Naval Research.
*National Research Council Research Associate at the Naval Research Laboratory.

[1]P. A. Miller, J. W. Poukey, and T. P. Wright, Phys. Rev. Lett. 35, 940 (1975).
[2]S. J. Stephanakis, G. Cooperstein, P. J. Goodrich, S. B. Swanekamp, and B. V. Weber, Conference Record-Abstracts of the 1991 IEEE International Conference on Plasma Science (Williamsburg, VA, June, 1991), 164.
[3]J. J. Ambrosiano and J. L. Geary, Computer Physics Communications 67, 210 (1991).
[4]J. M. Grossmann, S. B. Swanekamp, and P. F. Ottinger, Phys Fluids B 4, 4 (1992).
[5]S. B. Swanekamp, J. M. Grossmann, P. F. Ottinger, and J. L. Geary, to be published in Phys. Fluids B., see also R. J. Kares, J. Appl. Phys. 71, 2155 (1992); R. J. Kares, J. L. Geary, and J. M. Grossmann, J. Appl. Phys. 71, 2168 (1992).
[6]B. Goplen, Mission Research Corp., Newington, VA, private communication.

ONE-DIMENSIONAL NUMERICAL SIMULATION OF PLASMA FILLED PLANAR DIODE.

I.V. GLAZYRING, V.S. DIYANKOV, A.A. KONDRAT'EV, A.I. KORMILITSIN AND A.P. YALOVETS.

Institute of Technical Physics, Chelyabinsk, Russia.

Abstract. The plasma filled diode is used on pulsed accelerator IGUR-3. The surface dielectric breakdown using the energy of prepulse is the source of plasma in this case. The plasma erosion has been studied using 1-D electrostatic particle-fluid hybrid code. Code results are compared with the experimental impedance measurements.

INTRODUCTION

A plasma filled diode was first used for prepulse elimination, rise-time sharpening and electron beam focusing [1,2]. Using the diode on 6 MV generator IGUR-3 [3], the focusing of 60 kA in 3 mm diameter was obtained. The high voltage impulse was formed by inductive energy storage with the current wire-explosion opening switch. During the past several years the plasma opening switch (POS) has become an important means to compress output power due to voltage multiplication and pulse length shortening [4,5]. Most of experiments have been carried out on lower impedance generators. Some experiments were performed with high impedance generators. Load voltage as high as 6 MV have been generated on Reiden IV-H with efficient current transfer to diode loads [6]. With an inductive store and POS one can make a high-voltage impulse (over 20 MV) into a load on PBFA-II [7]. A set of experiments have been performed with two POS stages on GIT-4 generator [5] and 6.4 MV, 82 kA have been obtained. In our case, instead of first plasma switch we use the wire-explosion unit. The wire-explosion opening switch with external electric circuit has been studied with the aid of the one-dimensional MHD code KEV [8]. As a second switch we use the plasma filled planar diode. The plasma switch dynamics are modeled by one-dimensional particle-fluid hybrid code. The calculations are compared to experiments and some agreements are found.

EXPERIMENTAL DATA.

The plasma filled planar diode is sketched in Fig.1. There is dielectric ring 13 mm diameter on the cathode. Anode-cathode gap

is equal 80 mm. The same unit is on the anode. Here, during the prepulse of voltage the electric field on the dielectric is appeared by the capacitor division between cathode, anode and intermediate electrode, connected with the cathode through insulator. Plasma is produced by surface dielectric breakdown in the beginning of the voltage prepulse. Plasma fills the cathode-anode region during 2 μs prepulse. Experimental measurements show that plasma density is 10^{12}-10^{13} cm^{-3} and drift velocity is about 7 cm/μs. At high voltage pulse the impedance increases up to 100 Ohm during 20 ns.

THE COMPUTATIONAL MODEL

In a typical POS plasma is injected in an radial direction. Many theoretical works, PIC and fluid simulations of the plasma switch have been carried out for this case [see for example references in 9]. In this work we study the POS operation in planar plasma filled diode with axial injection. The geometry of calculated region is shown in Fig.2. The modeling was performed in two steps: density and temperature profiles before high-voltage pulse arriving were obtained by Lagrangian 1-D two-temperature fluid code and then these plasma parameters were used for PIC modeling of the electron and ion beams and for plasma erosion based on four-phase theory [10]. In the most previous works plasma was uniform and not included effects of plasma generation during expansion. Usually the heat conduction of ions was neglected and for electrons it was infinite so that $grad T_e = 0$. We assume that plasma expansion into a vacuum is spherical, because the anode-cathode gap is more larger than the discharge region. The classical heat conductivity was used for this study. In the fluid modeling of plasma expansion into a vacuum from plasma sources we have to take into account the plasma generation during the expansion. The plasma source was included empirically to obtain the plasma parameters similar to experiment. We assume that mass of electron is $m_e = 0$. The electron field is obtained from the equation

$$E(Zen_i - \frac{div E}{4\pi}) = - T_e \, grad(Zn_i - \frac{div E}{4\pi e})$$

similar to obtained in [11]. The calculations of the plasma expansion into a vacuum were carried out in two cases: quasineutral limit and with charge separation. The waveform of the current used in this study as the boundary conditions has been

taken from experiments performed on IGUR-3. In PIC modeling the electric field are obtained by the Implicit Moment Method [12] with time-advanced current sources derived from a set of auxiliary fluid moment equations.

COMPUTATIONAL RESULTS AND COMPARISONS TO THE EXPERIMENT.

Results of the study are compared to the data obtained in the experiments. Fig.3 shows the spherical plasma expansion with the following parameters: ions C^{++}, the initial plasma temperature 40 eV, rate of plasma generation $5 \cdot 10^{15}$ ions/cm$^3 \cdot \mu$s. The density about 10^{13} cm^{-3} and the velocity about 5 cm/μs in the anode-cathode gap are obtained. In Fig.4 measured diode voltage and corresponding current are shown. Fig.5 shows the comparison between the experimental impedance and results of numerical simulation. Good agreement is found when the erosion gap is formed on the cathode. The gap is obtained when the circuit current reaches the saturation for these plasma parameters.

REFERENCES

1. C.W. Mendel, Jr., and S.A. Goldstein, J. Appl. Phys., 48, 1004 (1977).

2. P.A. Miller, J.W. Poukey, and T.P. Wright, Phys. Rev. Lett. 35, N14, 940-943 (1975).

3. V.S. Diyankov, A.I. Kormilitsin, V.P. Kovalev. In these Proceedings.

4. B.V. Weber, R.J. Comisso, G. Cooperstein et.al. IEEE Trans. on Plasma Sci., v.PS-15, N6, 635 (1987).

5. B.M. Koval'chuk and G.A. Mesyats. 8th Int. Conf. on High Power Particle Beams, BEAMS'90, Novosibirsk, July 2-6, 1990, p.92.

6. S. Miyamoto, et. al., IEEE Trans. on Plasma Sci., v.PS-15, N6, 667 (1987).

7. P.F. Ottinger. Int. Workshop on Phys. and Techn. of High Power Opening Switches, Novosibirsk, July 1-2, 1989, p.404.

8. Ю.Д. Бакулин, В.Ф. Куропатенко, А.В. Лучинский. ЖТФ, т.46, №9, с.1963-1969 (1976).

9. J.M. Grossmann, P.F. Ottinger, and R.J. Mason. J. Appl. Phys., 66, 2307 (1989).

10. P.F. Ottinger, S.A. Goldstein, and R.A. Meger. J. Appl. Phys., 56, 774 (1984).

11. R.J. Mason. Phys. Fluids, v.14, 1943 (1971).

12. R.J. Mason. J. Comput. Phys., 41, 233 (1981).

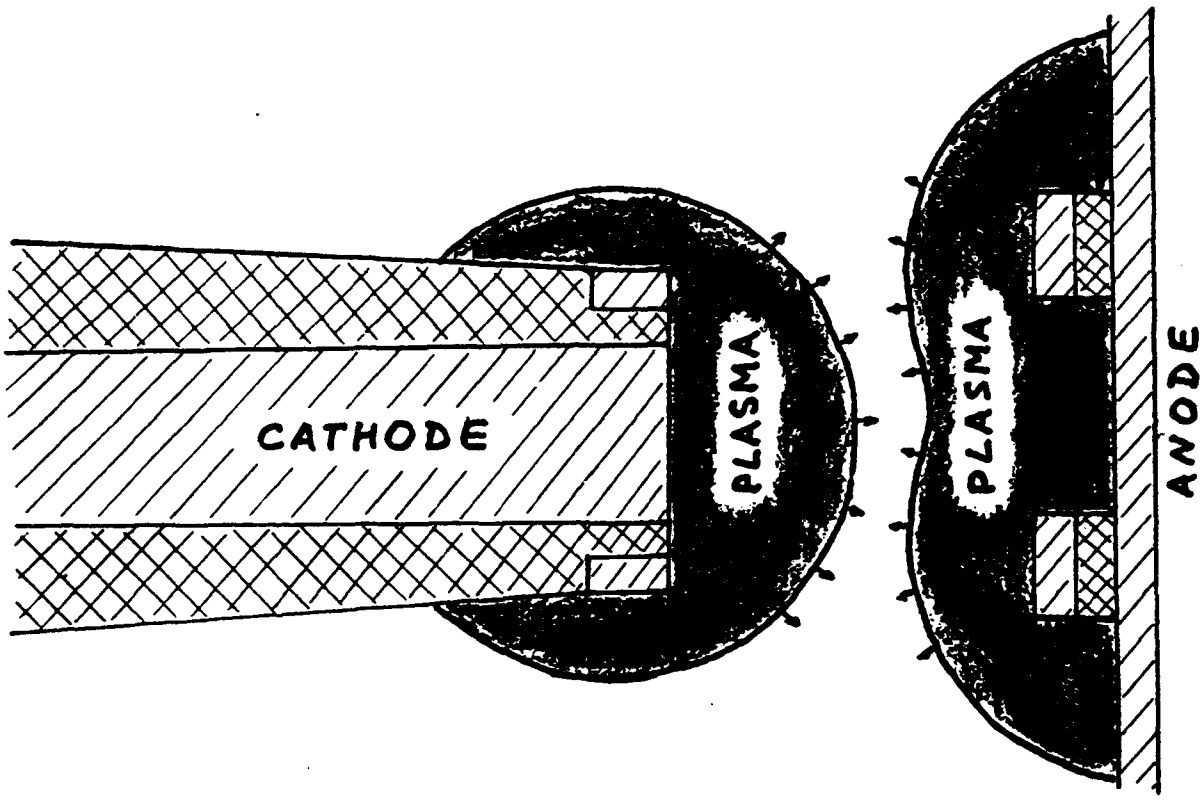

Fig.1. IGUR-3 plasma filled diode configuration.

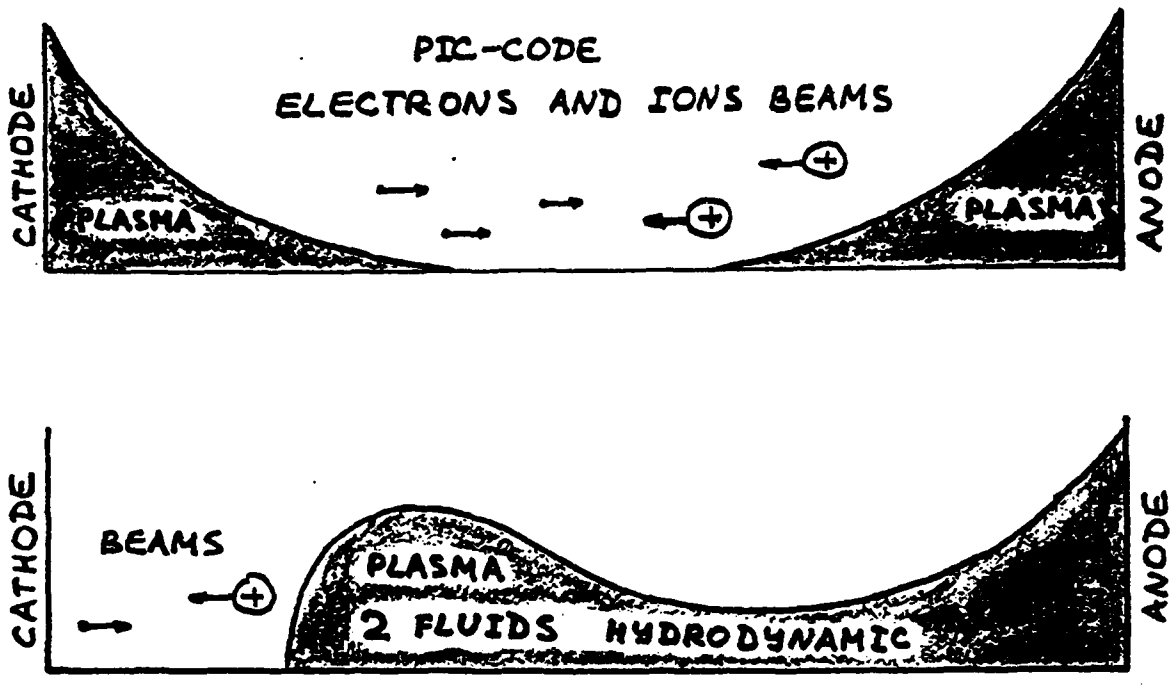

Fig.2. Schematic pictures for numerical simulation.

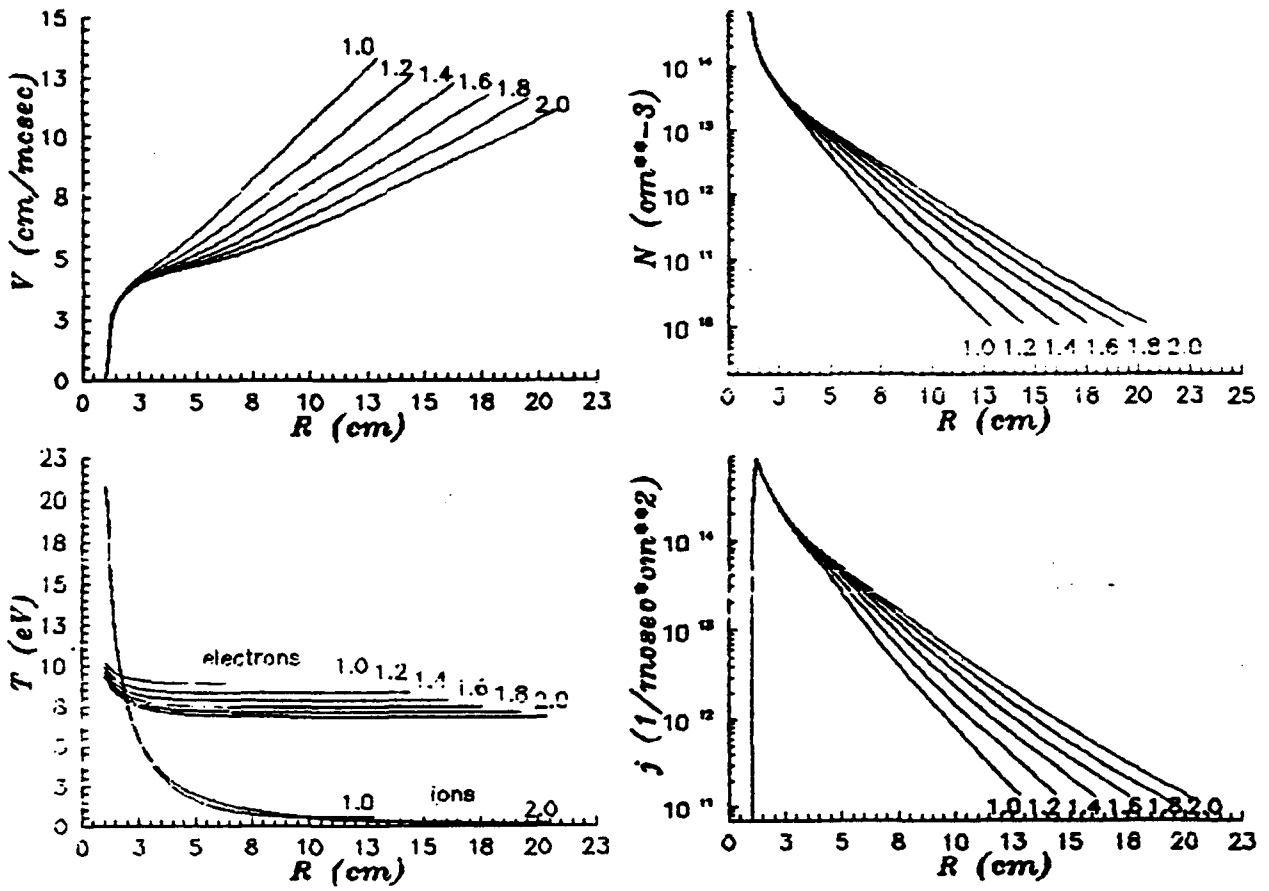

Fig.3. The velocity, density, temperature and current density profiles for 1.0, 1.2, 1.4, 1.6, 1.8 and 2.0 microseconds after the beginning of plasma generation.

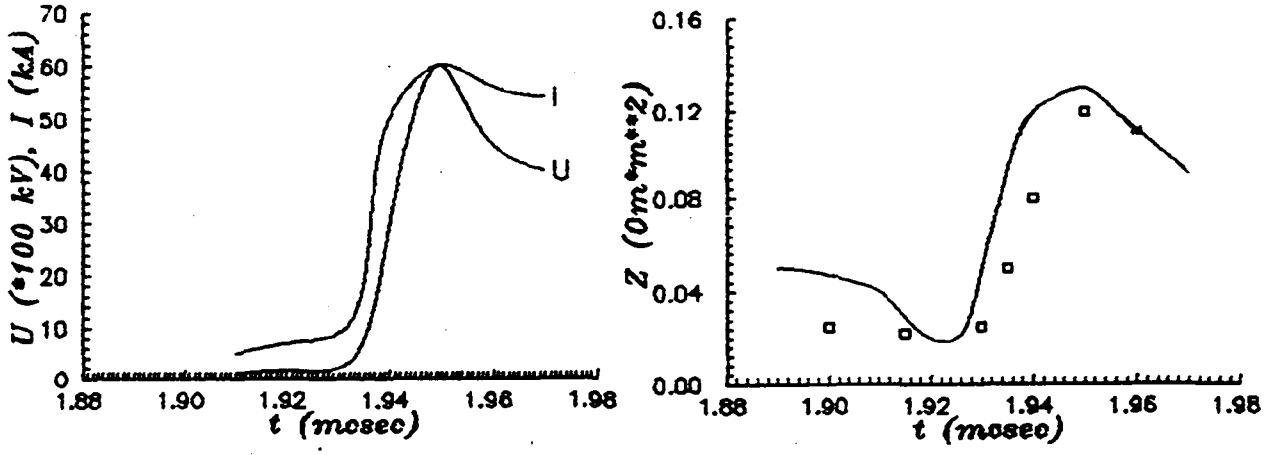

Fig.4. Measured diode voltage and current.

Fig.5. Diode impedance per surface square vs. time.
□ - experiment, —— - simulation

NONLINEAR DYNAMICS IN A REFLEX DIODE

M. S. Litz
Harry Diamond Laboratories
2800 Powder Mill Rd. - Adelphi, MD 20707

J. Golden
Berkeley Research Associates
POB 852 - Springfield, VA 22150

Work supported by Harry Diamond Laboratories

ABSTRACT

Potentials in high current reflexing electron diodes such as vircators are dominated by space charge effects,[1] and are rapidly time varying and nonlinear because of the oscillating virtual cathode and strong particle bunching. Previous experiments[2] showed the stochastic character of the oscillating electromagnetic fields. The dynamical behavior of this type of device is studied with the 2 dimensional electromagnetic code MAGIC[3] and with a simplified 1 dimensional nonlinear analytic model. Computed particle trajectory phase space plots show several classes of electron trajectories. The 1 dimensional nonlinear model generates a similar set. The calculations show that the stochastic behavior of the electromagnetic fields in both frequency and time are similar to the experimental observations. These models are used to investigate the dependence of spectral bandwidth and the RF fluctuations on the macroscopic system parameters.

1. Introduction

This paper reports on a static nonlinear potential modeling the reflex diode oscillator that is based on the Duffing equation. This is motivated by the possibility that this system may be an example of more generic nonlinear systems. The Duffing equation is a well documented[4-6] nonlinear equation with chaotic solutions in finite parameter regimes. The trajectories of test particles in a one-dimensional(1D) Duffing potential are compared to those in a potential computed from the two-dimensional(2D) dynamic particle-in-cell (PIC) code MAGIC.

The microwave power and spectrum exhibit fluctuations and large shot-to-shot variability that has been observed in many reflex diode experiments.[2,7,8] An example from a recent vircator experiment on Aurora is shown in figure 1. Although the macroscopic experimental parameters of voltage, current, and vacuum are nearly identical for these two shots, the measured power waveforms show apparently random fluctuations within the pulse. The heterodyne signal of the electric fields during the same two shots, also indicates the time variation of the spectrum within the pulse. The objective of our research program is to determine whether these fluctuations result from some as yet undetermined experimental condition, or to the sensitivity of particle motion to the nonlinear time-varying potentials.

As a preliminary investigation, a simplifying 1D nonlinear Duffing model is used in this

study. For comparison, self consistent space charge effects, and 2D spatial and 3D velocity distributions are computed numerically using MAGIC. The 2D particle-in-cell (PIC) code results will be described in section 2, followed by results from the 1D model in section 3. Section 4 will discuss the significant parallels between the two models.

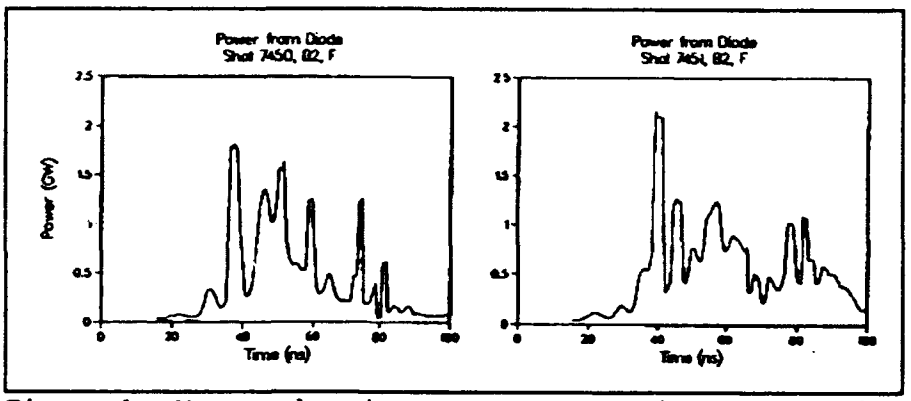

Figure 1 Measured microwave power in rectangular waveguide arm for two shots with identical experimental configurations.

2. 2D Simulations

2.1 Parameters of Model

The device geometry is shown in figure 2a. An 80 kV voltage pulse is applied at $z=0$ (left side figure 2a), and $t=0$ in the simulation. The anode-cathode (AK) gap distance is 9 mm, the cathode radius is 2.54 cm, and the chamber radius is 17 cm. A zoned grid, requiring 2.75 ps time steps, is applied to this generic configuration to better reproduce the electron motion in the cathode/virtual cathode region. These parameters have been selected because they represent an experimentally accessible set of boundary conditions that correspond to apparatus that is under construction.

2.2 Time Dependent Virtual Cathode (VC) Position and Amplitude

Figure 3 is the numerically calculated electric potential along the drift tube axis as a function of time. The central position of the VC is defined as the peak of this electric potential. In this configuration, both the amplitude of the VC and the position of the VC oscillate periodically. The VC peak amplitude lags in phase by 90 degrees from VC position.

The Fourier transforms of both the VC position and amplitude have common peaks at 2.4 GHz. This frequency is the reflex frequency, f_r, as calculated from particle trajectories in the simulation. A secondary peak at 3.4 GHz is the plasma frequency f_p, as calculated from the charge density.

Calculation of axial electric field (E_z) near the side wall of the chamber at the axial position of the VC, shows signals dominated by the same 2.4 Ghz reflex frequency. This measurement position is selected because it is a convenient position for a radially directed waveguide extraction port (in the experiment). The plasma frequency peak is not detected in the Fourier transform of the upstream (cathode side of the anode) electric field. It is deduced then, that reflexing is the dominant mode in this form of the oscillator.

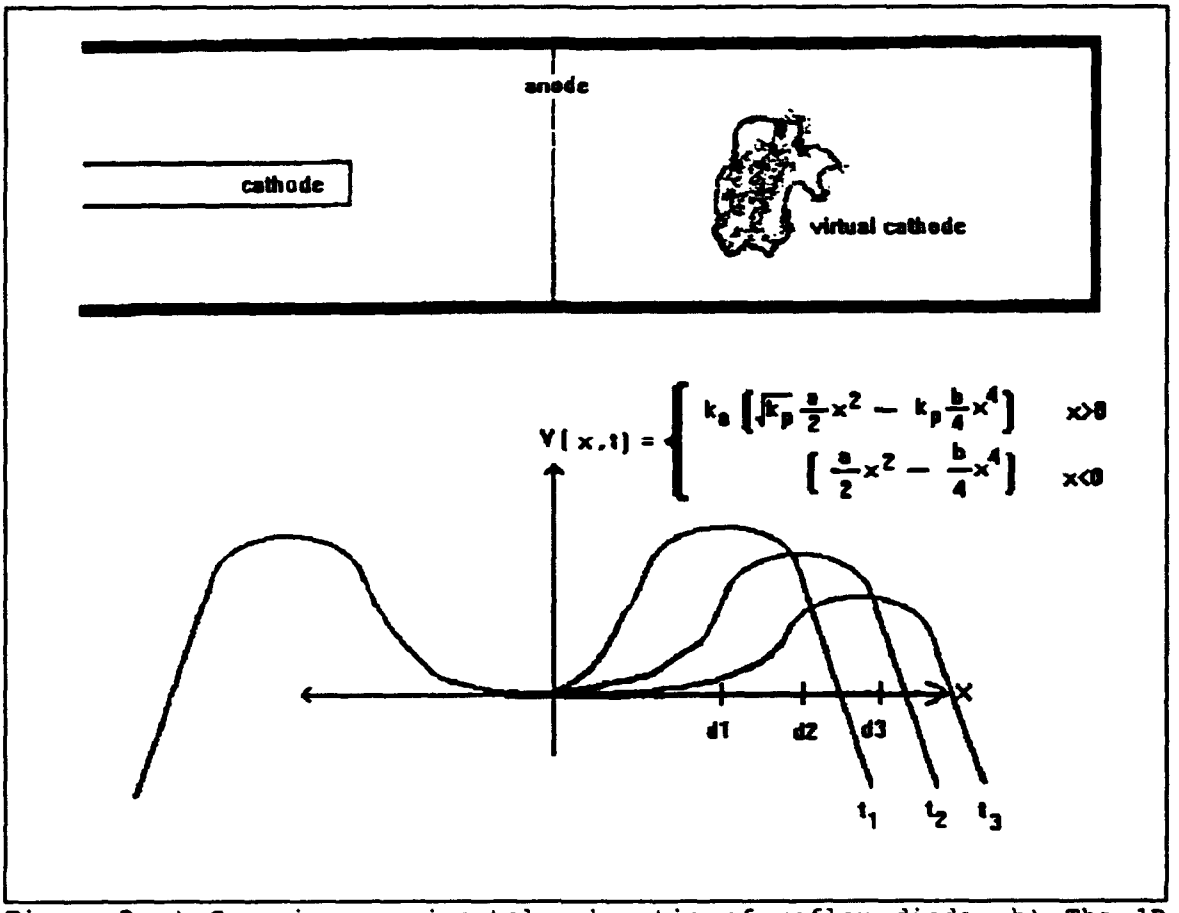

Figure 2 a) Generic experimental schematic of reflex diode. b) The 1D Duffing potential for a test particle in this geometry.

2.3 Particle Trajectories

Electron position and momentum (phase space) provides information necessary to classify the types of particle motion in the system. Individual particles are followed throughout their lifetime during the simulation. Phase space plots for approximately 2% of the 20,000 particles in the simulation have been evaluated. Three general patterns are found: 1)electrons escaping from the potential well in the axial directions, 2)oscillation with repeatable periods, and 3)aperiodic oscillation. Examples in the right side of figure 4 differ only in the time they were emitted from the cathode during the 16 ns voltage pulse width. These examples will be compared to the 1D model results.

3. 1D Model

3.1 Physical Basis (Why use this model?)

The Duffing Potential is selected because of its similarity to the potential between the cathode, anode, and virtual cathode. This resemblance is illustrated in figure 1b. This "soft-spring" Duffing potential is one of four possible forms determined by the signs of *a* and *b* in the Duffing equation $\ddot{x}+\gamma\dot{x}+ax+bx^3=F\cos\omega t$. The coefficients *a* and *b* determine the depth and

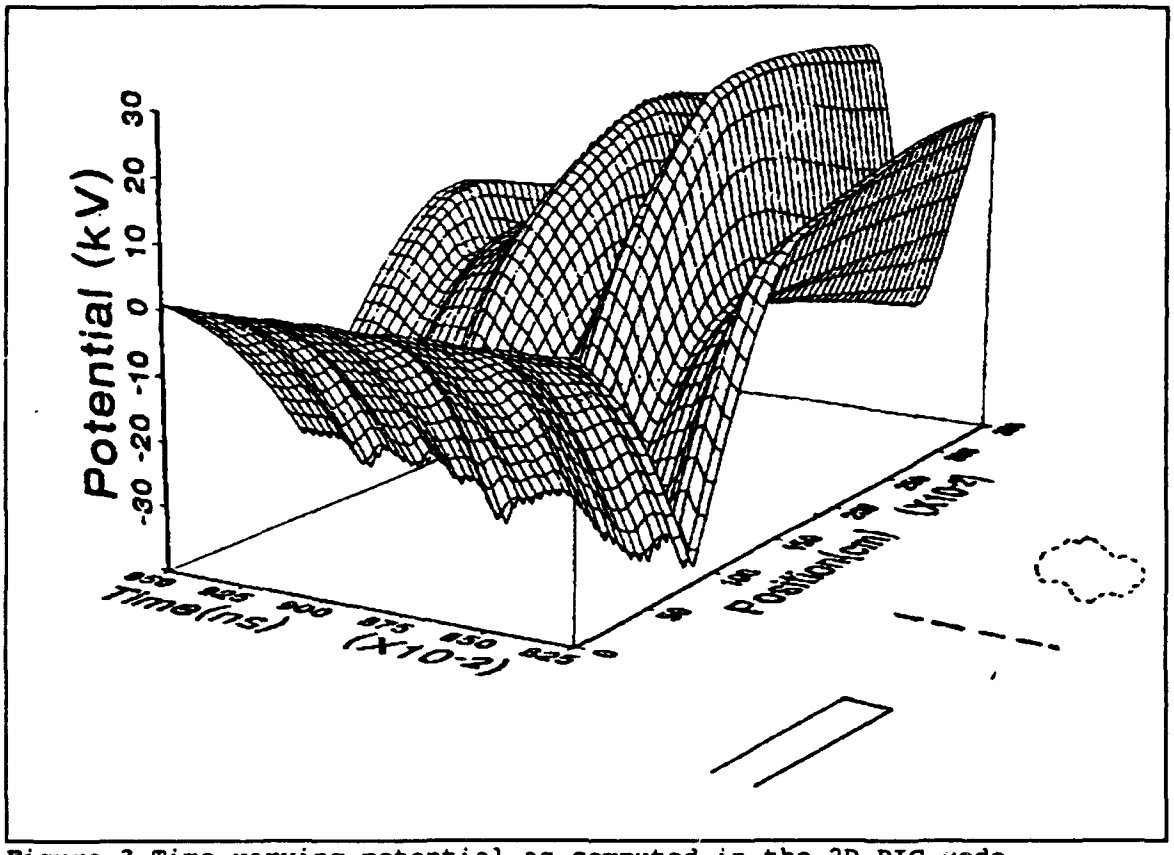

Figure 3 Time-varying potential as computed in the 2D PIC code.

width of the potential well, $\gamma\dot{x}$ is the dissipative term indicative of the collision frequency or coulomb drag, F and ω are the amplitude and angular frequency of the applied forcing function. The nonlinearity occurs at the positions of the slowly varying potential barriers. The period of oscillation is sensitive to deterministic motion at these possible turning points.

3.2 Particle Trajectories in Phase Space

The left side of figure 4 shows a sampling of electron phase space for the 1D model. A change in the second significant digit of γ, results in the variety of electron motion shown in the successive frames (from the top a)particle escaping the potential well, b)period three orbit, c)chaotic motion represented by large attractor with broadband frequency content, d)constricted attractor). These phase space plots are the attractors of the system, the solutions in the asymptotic time limit. Each plot represents 44,000 time steps through the electron path. A comparison of these 1D orbits with those of the test particles in the 2D simulations reveal remarkable similarity.

3.3 Phase Space and Control Diagrams

The sensitivity of the final states of the system are explored by variation of the principle parameters (ie. γ, a, b, F, ω) of the nonlinear equation. A control diagram shows the final state of

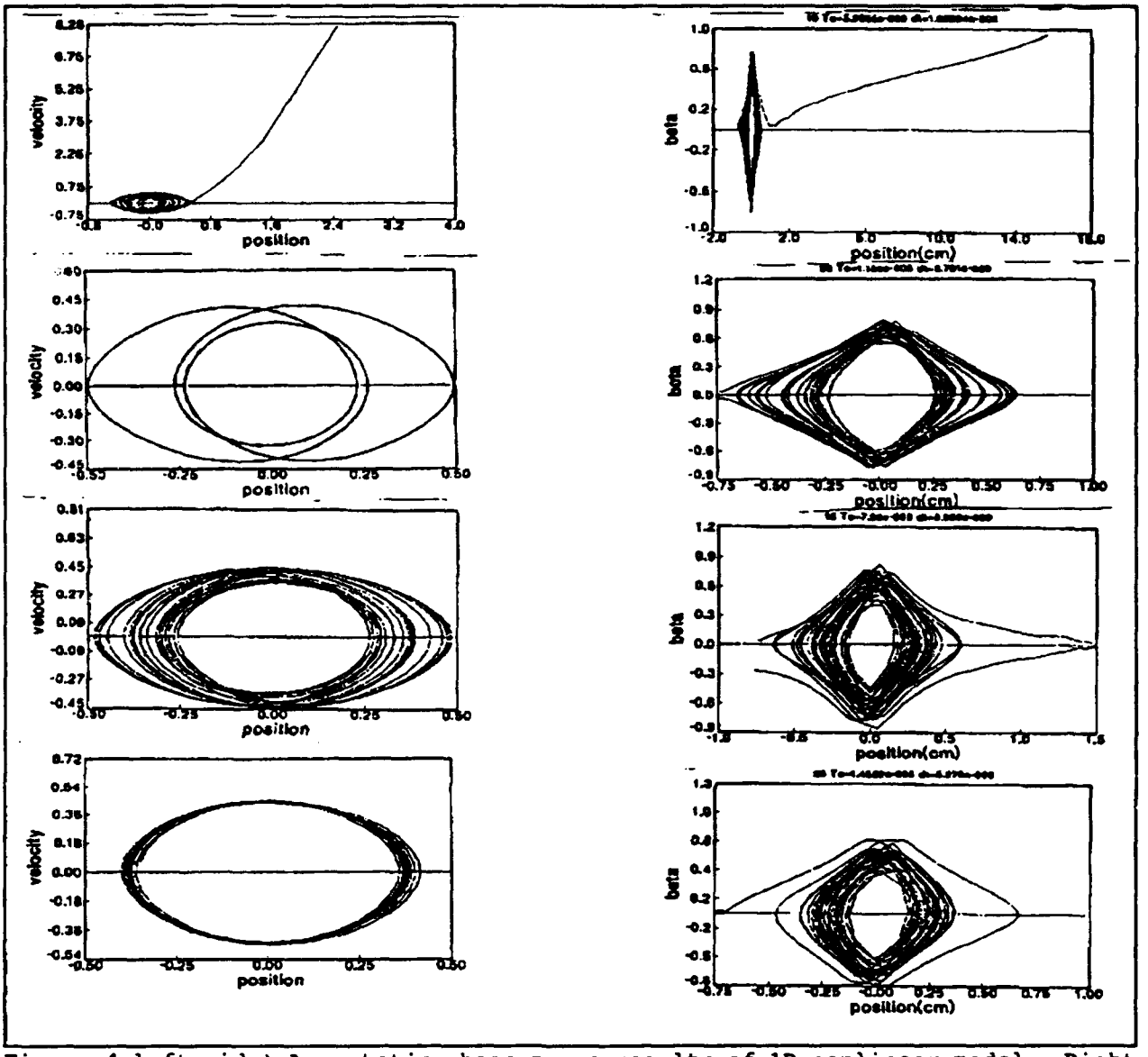

Figure 4 left side) Asymptotic phase space results of 1D nonlinear model. Right side) 2D PIC code phases space results.

the particle's path for varying parametric conditions . Figure 5 shows the variation of final electron position as a function of forcing function angular frequency and dissipation. Bounded motion is represented by the speckled region, particles escaping the potential on the cathode side are shown as grey circles, and particles escaping past the virtual cathode are depicted in black.

4. Remarks

When comparing phase space results of 2D PIC and 1D nonlinear models, the major difference lies in the cusp vs. x^2 shape of the potential well in the vicinity of the anode. This discrepancy is minimal due to the fact that the particles have their maximum momentum at the location of the anode, and therefore spend less time in this region. Therefore, trajectories are not greatly effected by the shape of the well near the anode.

Predictions of the 1D and 2D models will be compared to a carefully controlled experiment that is under construction. A thermionic cathode will be used to eliminate the random behavior of explosive field emission cathodes used in previous reflex diode experiments. Further numerical analysis that includes the time-varying nature of the formation of the virtual cathode is also in progress.

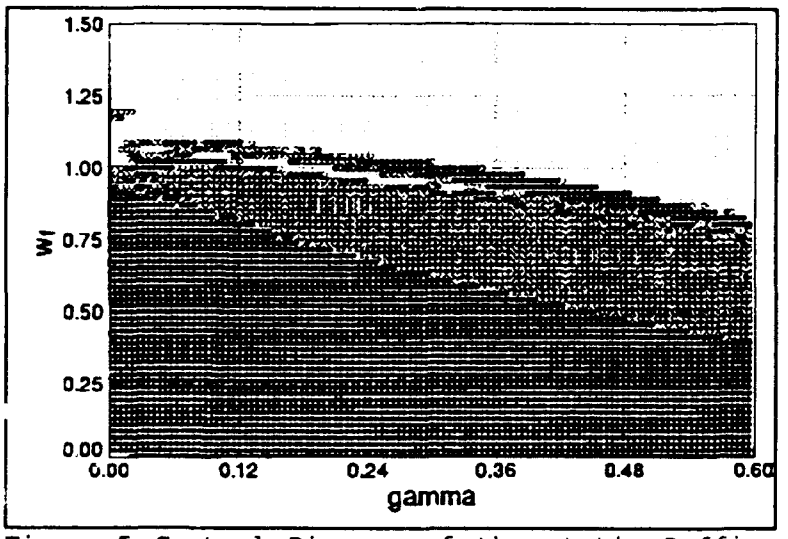

Figure 5 Control Diagram of the static Duffing equation.

5. References

1. E. Coutsias, and D. Sullivan, "Space-charge-limit instabilities in electron beams," Phys. Rev., **27**, 1535 (1983).
2. Huttlin et al., IEEE Trans. Plasma Sci **PS-18**, 618 (1990).
3. B. Goplen et al., "MAGIC Users Manual," Mission Research Corporation, MRC/WDC-R-184, September 1988.
4. *Dynamics: The Geometry of Behavior*, R. Abraham and C. Shaw, Aerial Press, 1982.
5. *Nonlinear Systems Analysis*, A. Blaquiere, Academic Press, 1966.
6. *Chaotic Vibrations*, F. Moon, Wiley, 1987.
7. J. Benford et al., J. Appl. Phys. **61**, 2098 (1987).
8. R. A. Mahaffey, P. Sprangle, J. Golden, and C. A. Kapetanakos, Phys. Rev. Lett. **39**, 843 (1977).

POST ACCELERATION OF A PSEUDOSPARK-PRODUCED HIGH-BRIGHTNESS ELECTRON BEAM

B. N. Ding[a)] and M. J. Rhee
Laboratory for Plasma Research and
Department of Electrical Engineering
University of Maryland, College Park, Maryland 20742, U.S.A.

Abstract

Preliminary results are presented of post-acceleration experiment of a pseudospark-produced high-brightness electron beam. The electron beam that is propagating in a low pressure gas is accelerated by a simple induction linac system. Time-resolved energy spectrum is constructed for the electron beam. The resultant spectrum reveals that the instantaneous beam energy is approximately equal to the sum of the cathode voltage and the induction-linac accelerating voltage.

I. Introduction

Recently, high-brightness electron beam produced by a simple pseudospark device has been reported.[1,2] Such high-brightness electron beams would find immediate application in high-current accelerators[3] and in rf sources such as free-electron lasers[4,5] that require very high-quality high-energy electron beams. In this work, we report preliminary results of post acceleration of the electron beam by an induction linac. A simple induction linac system of 25 kV, 1 kA, 50 ns pulse is constructed. The time-resolved energy spectra are constructed for the beams with and without the acceleration by the induction linac and are compared with the cathode voltage waveform and induction linac accelerating voltage waveform.

II. Experiment

Experimental setup is shown in Fig. 1. The pseudospark device, which is similar to the one reported earlier,[1,2] consists of a planar cathode with a hollow cavity, two sets of intermediate electrodes and insulators, and a planar anode. A trigger electrode made of semirigid coaxial cable is inserted into the hollow cavity. A 3.2-mm diam center hole is present through the entire electrode system. A homemade compensated resistive divider is used to monitor the cathode voltage. A 2.7-nF low inductance type door knob capacitor is used as the storage capacitor. An induction linac module, which is driven by a 25-Ω Blumlein type modulator, is attached to the downstream side of the anode. The linac module is terminated by a matched load 25 Ω to minimize the beam loading[6] effect. This is

done by two 50-Ω cables (not shown in Fig. 1), one of which is conveniently used to monitor the voltage across the accelerating gap. A time-resolving energy spectrometer consisting of a 0.5-mm diam pinhole, a biased electrode, and a Faraday cup is placed immediately downstream of the linac module.

The entire chamber is initially evacuated by an oil diffusion pump typically down to 10^{-5} Torr. Argon gas is then filled at a slow flow rate through a needle valve in the upper chamber while the pinhole allows the gas to leak into the downstream chamber maintaining a

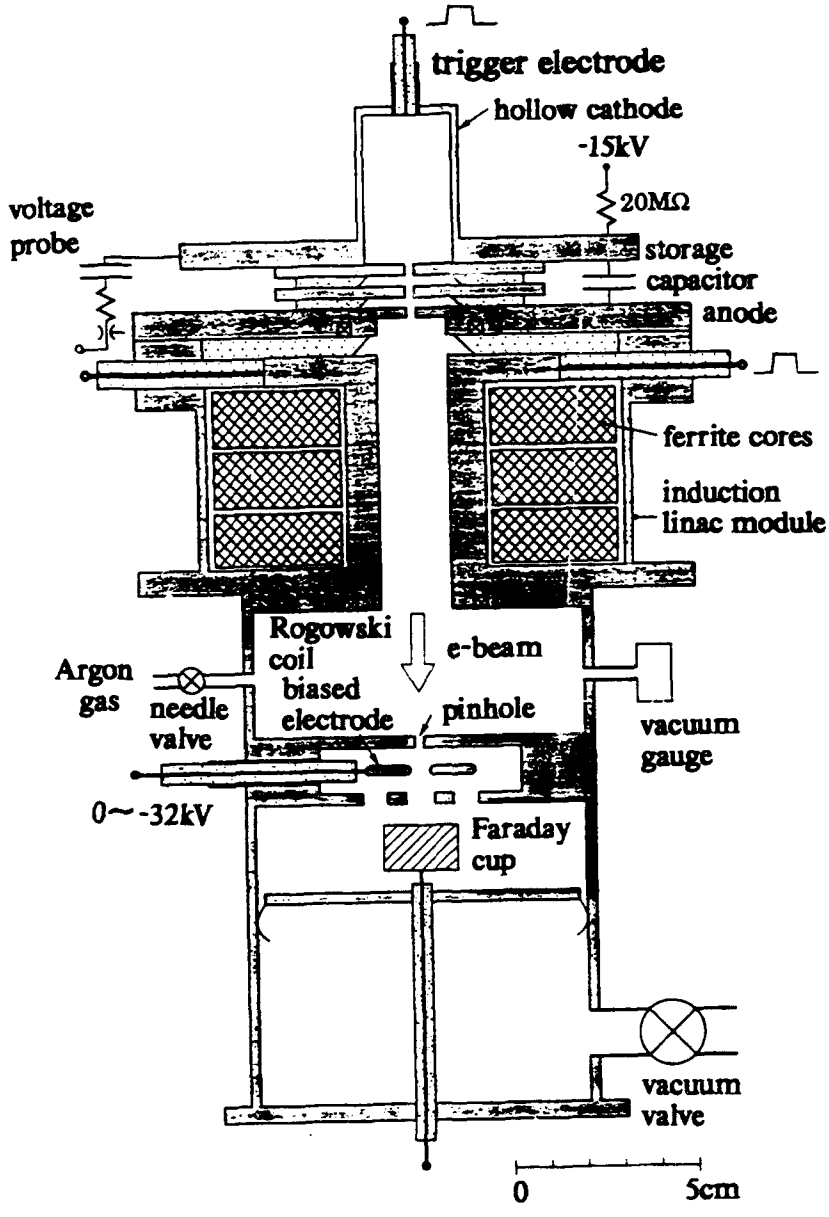

FIG. 1. Experimental setup.

constant differential pressure in the upper chamber and vacuum in the downstream chamber. The pressure used in this experiment is 60 mTorr and the cathode is charged to -15 kV with respect to the grounded anode through a 20-MΩ charging resistor. By applying a +15-kV pulse that is also generated by the Blumlein modulator to the trigger electrode, a flashover discharge on the surface of Teflon insulator at the end of the coaxial trigger electrode triggers the main discharge within a jitter time of < 1 ns. The cathode voltage is monitored by the voltage probe. The electron beam generated by this discharge propagates through the induction linac in which the beam is further accelerated. A small portion of this beam that is sampled by the pinhole and injected into a vacuum space is then analyzed by a biased electrode and a Faraday cup. Only electrons of energy higher than that corresponding to a given bias voltage can pass through the center hole of the biased electrode and arrive at the Faraday cup.

In order to characterize the original beam from the pseudospark discharge, the induction linac module is removed and the spectrometer system is directly attached to the anode to determine the energy spectrum of the original beam. The bias voltages are varied from zero to -16 kV in 1 kV increments, and the corresponding Faraday cup current signals are

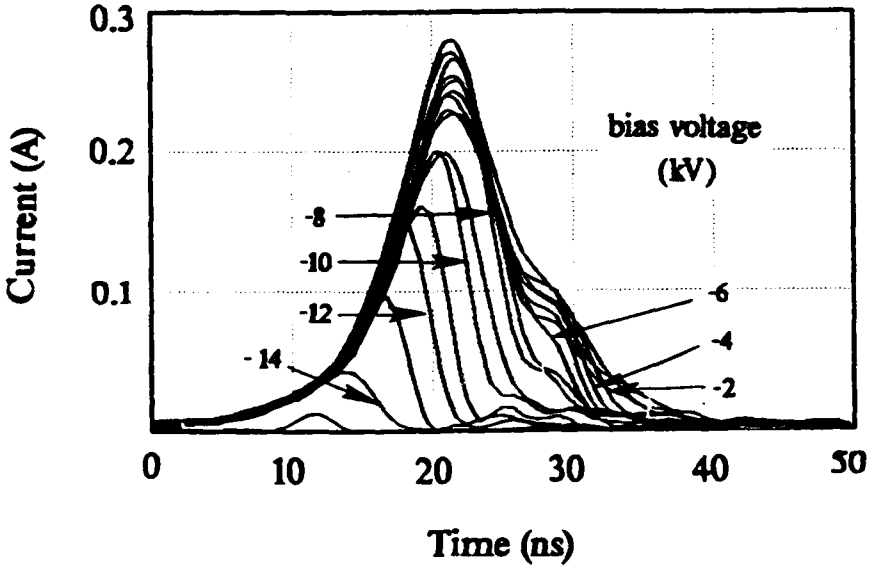

FIG. 2. Family of current waveforms measured by a Faraday cup wtih various bias voltages from 0 to −16 kV with 1 kV step.

recorded by a digital oscilloscope. A typical family of waveforms with the corresponding bias voltages is shown in Fig. 2. Each current waveform with a given bias voltage V_b may be represented by

$$I(\epsilon_b, t) = \int_{\epsilon_b}^{\infty} i(\epsilon, t) d\epsilon \tag{1}$$

where $\epsilon_b = eV_b$ is the energy corresponding to the bias voltage. It is obvious from Eq. (1) that difference between two current waveforms measured at bias voltages V_b and $V_b + \Delta V_b$, respectively, is the current by the flow of electrons of energy between $\epsilon_b = eV_b$ and $\epsilon_b + \Delta\epsilon_b = e(V_b + \Delta V_b)$ as given by

$$I(\epsilon_b, t) - I(\epsilon_b + \Delta\epsilon_b, t) = \int_{\epsilon_b}^{\epsilon_b + \Delta\epsilon_b} i(\epsilon, t) d\epsilon. \tag{2}$$

The time-resolved energy spectrum at energy $\epsilon_b + \frac{1}{2}\epsilon_b$ as a function of time may be then given by

$$\frac{d^2N}{dtd\epsilon} \Big|_{\epsilon_b + \frac{1}{2}\Delta\epsilon_b} = \frac{I(\epsilon_b, t) - I(\epsilon_o + \Delta\epsilon_b, t)}{e\Delta\epsilon_b} \tag{3}$$

which can be determined in terms of an experimentally obtained differential current waveform $I(\epsilon_b, t) - I(\epsilon_b + \Delta\epsilon_b, t)$. Sixteen differential current waveforms are computed from the family of digitized Faraday cup current waveforms by using a personal computer. The time-resolved energy spectrum is then constructed by plotting the resultant differential waveforms as functions of energy as shown in Fig. 3.

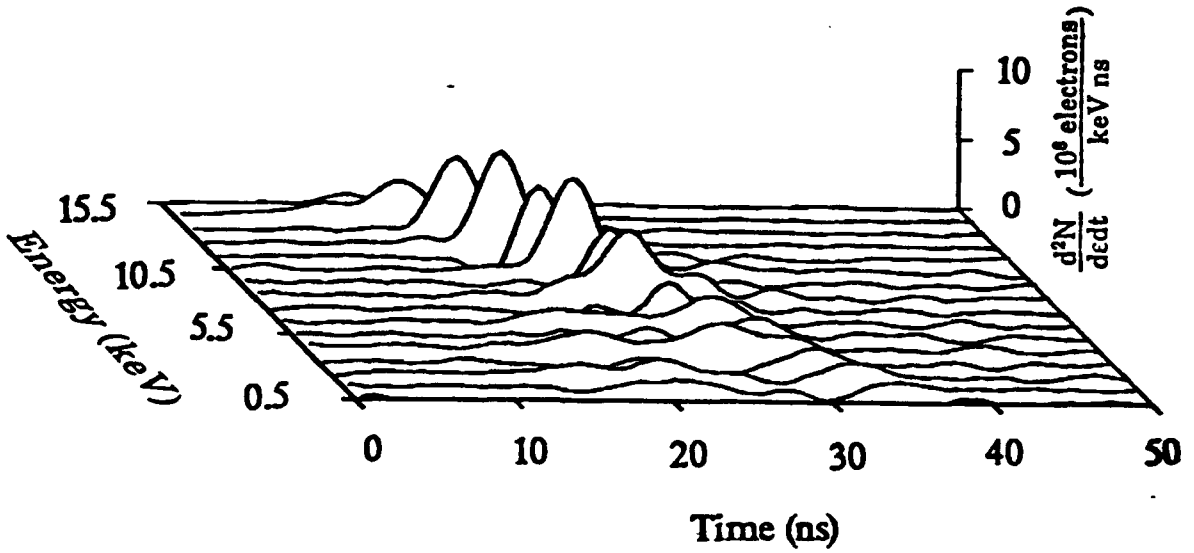

FIG. 3. The time-resolved energy spectrum for the pseudospark-produced electron beam.

A similar series of measurements is done for the beam after the post acceleration by the induction linac. The induction linac is in place as shown in Fig. 1 and is powered by the Blumlein modulator that also triggers the pseudospark. Thus, the beam generation and accelerating voltage are in good synchronization. Having the bias voltages varied from zero to 32 kV in 2 kV increments for this series, the time-resolved energy spectrum is constructed by analyzing the Faraday cup current signals as described above and plotted in Fig. 4.

III. RESULTS AND DISCUSSION

Both the time-resolved energy spectra shown in Figs. 3 and 4 have relatively narrow spreads: instantaneous energy spreads of < 1.5 keV and temporal spreads of < 2 ns. Energy of these ridge-like distribution of the spectra decrease monotonically from their peak values to zero. The time at which the intensity of each differential waveform attains its peak value for both cases are plotted in the energy-time space as shown in Fig. 5. It is observed that the plots of peak intensity points for the beam without post acceleration approximately follow the voltage waveform of the cathode. This indicates that the source of the electrons is at the cathode or inside the hollow cavity and these electrons are accelerated by the full instantaneous voltage between cathode and anode. The same plots for the post accelerated beam are favorably compared with a curve that is the sum of the cathode voltage waveform

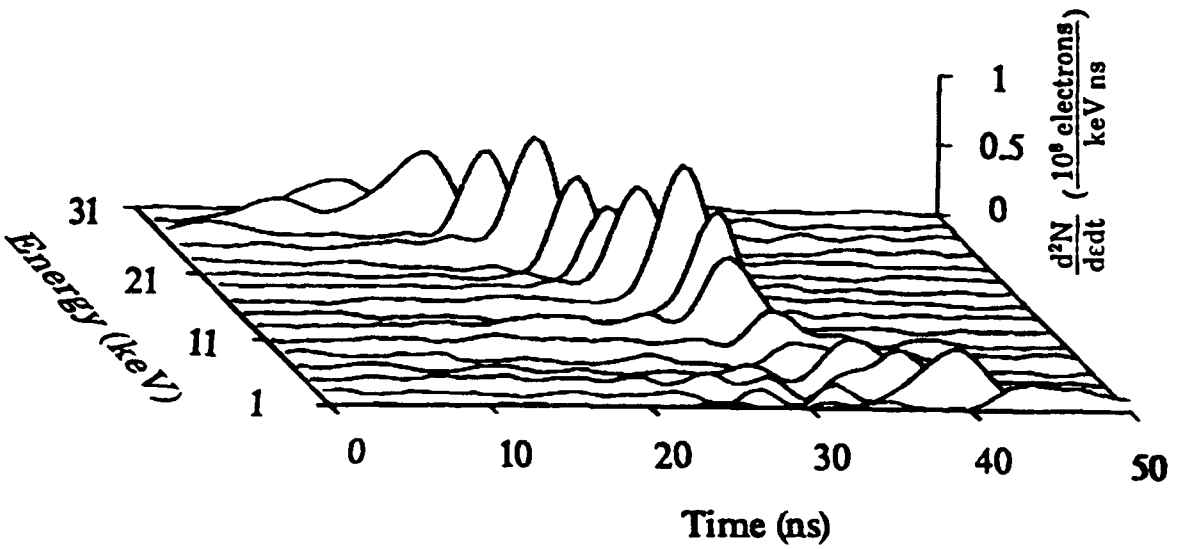

FIG. 4. The time-resolved energy spectrum for the post-accelerated electron beam.

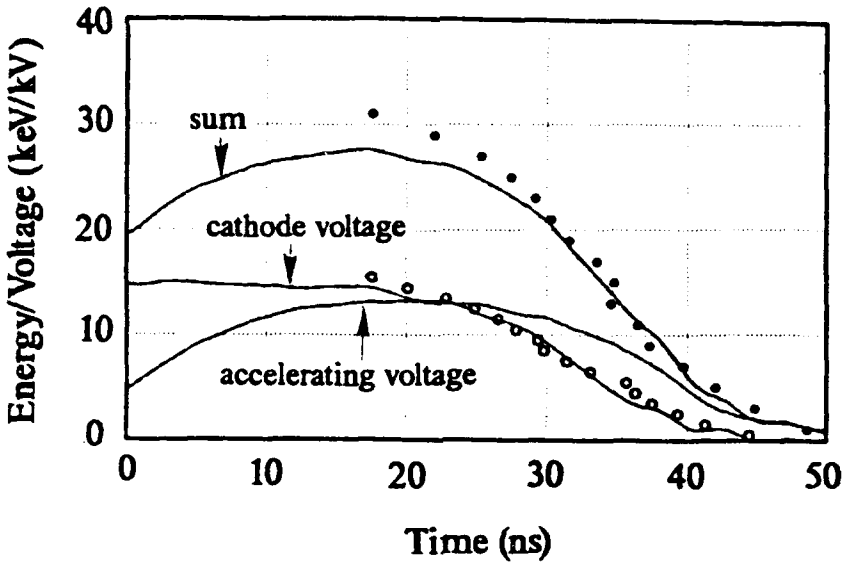

FIG. 5. Comparison of the spectra with the voltage waveforms.

and the accelerating voltage waveform of the induction linac. In this case, the electrons appear to be accelerated directly by both voltages. It is observed, however, that the peak energy points are ~10% higher than the sum of the two waveforms. This discrepancy will be further investigated.

ACKNOWLEDGMENT

This work was supported by the U. S. Department of Energy.

FOOTNOTE and REFERENCES

a) Permanent address: China Academy of Engineering Physics, P. O. Box 523-56, Chengdu, Sichuan, China.

1. E. Boggasch and M. J. Rhee, Appl. Phys. Lett. 56, 1746 (1990).
2. K. K. Jain, E. Boggasch, M. Reiser, and M. J. Rhee, Phys. Fluids B 2, 2487 (1990).
3. R. Stiening, in Proceedings of the 1987 Particle Accelerator Conference, edited by E. R. Lindstrom and L. S. Tailor (IEEE, New York, 1987), p. 1.
4. C. W. Robertson and P. A. Sprangle, Phys. Fluids B 1, 3 (1989).
5. T. J. Kwan and C. M. Snell, Phys. Fluids 26, 835 (1983).
6. M. J. Rhee and B. N. Ding, in Proceedings of the 1991 Particle Accelerator Conference, edited by L. Lizama and J. Chew (IEEE, New York, 1991) p. 2999.

TIME-RESOLVED BEAM ENERGY MEASUREMENT OF SHORT ELECTRON BEAM BUNCHES WITH A LONGITUDINAL VELOCITY TILT*

D. X. Wang, J. G. Wang, and M. Reiser
Laboratory for Plasma Research and
Department of Electrical Engineering
University of Maryland, College Park, Maryland 20742

* Research Supported by the U.S. Department of Energy.

Abstract

Both electrostatic retarding and deflecting energy analyzers have been employed to measure the time-resolved beam energy of short (30 to 50 ns pulse duration) and space-charge dominated (40 mA and 2.5 keV) electron bunches with longitudinal momentum tilts. The time resolutions are better than a half nanosecond. The energy resolutions are better than 0.3 % for the retarding analyzer and 2.5 % for the deflecting analyzer. In this paper basic operating principles are briefly described. Several experimental results are presented. Calibrations and measured energy width are given. Finally the performances of both devices will be summarized.

I. Introduction

A longitudinal pulse compression experiment and a resistive wall instability experiment have been planned to study longitudinal dynamics of space-charge dominated beams at the University of Maryland [1]. A short-pulse electron beam injector has been built to produce short electron bunches [2]. It consists of a gridded electron gun, three solenoidal matching lenses and an induction acceleration module generating a time-dependent gap voltage and imparting a longitudinal velocity tilt to the beam. By means of changing the grid voltage waveform both rectangular and parabolic bunches can be generated for the compression experiment and initial beams can be perturbed for the instability experiment.

Longitudinal velocity or energy measurement is crucial for both experiments, which can provide information about these dynamic processes in the longitudinal phase space. From the experimental point of view, variations of energy or velocity may be detected easier than that of current. Because of the relatively low beam energy (1 to 5 keV) both electrostatic retarding field and deflecting field energy analyzers have been chosen and constructed to perform the energy

measurements. In section II operation principles are briefly described. In section III several measurement results are presented. In section IV calibration and resolution results are given. Finally the performance of both devices will be summarized.

II. Operation Principles

Both retarding and deflecting field energy analyzers have been widely used for low energy measurements of charged particle beams [3,4,5]. They have very simple geometric configurations as shown in Fig. 1(a) and 1(b). Both of them utilize well-known motion of charged particles in a uniform electric field. The energy information is indirectly obtained by detecting the beam current at fixed positions.

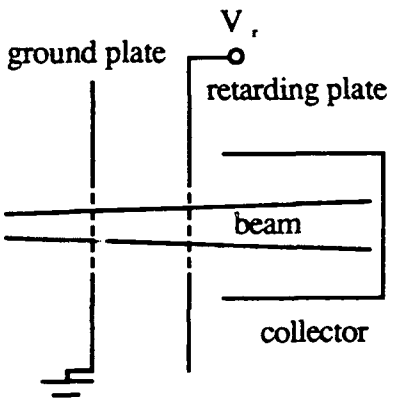

Fig. 1(a). Retarding energy analyzer

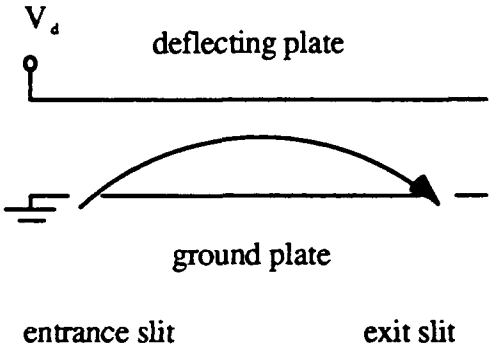

Fig. 1(b). Deflecting energy analyzer

1. Retarding field energy analyzer

It is made up of two gridded parallel plates and a beam collector (Faraday cup). The first plate is a ground plate while the second one is a retarding plate connected to a high voltage power supply providing a variable negative DC voltage (for electrons) up to the beam energy. A uniform electric field between the plates retards electrons longitudinally. If the longitudinal kinetic energy of an electron is larger than the retarding potential, i.e. $E>eV_r$ where E and V_r are the beam energy and retarding voltage, respectively, the electron is decelerated between the plates and then accelerated after the retarding plate. Eventually, it reaches the collector. Otherwise, if $E<eV_r$, the electron is reflected back. By varying the retarding voltage and measuring beam currents vs. time at the collector a time-resolved beam energy distribution can be constructed. It should be emphasized that only the longitudinal component of electron velocity (normal to the plates), not the total velocity, can be measured.

2. Deflecting field energy analyzer

It is composed of a ground plate with an entrance slit and an exit slit, and a deflecting plate where a negative deflecting voltage is applied. A beam collector is placed at the exit slit to collect outcoming electrons. An electron trajectory with an incident angle θ and energy E can be defined by the relation

$$y = x \tan\theta - \frac{eV_d x^2}{4hE\cos^2\theta} \qquad (1)$$

where h is the distance between the two plates and V_d is the absolute value of the deflecting voltage. Let x=L and y=0 where L is the distance between the slits and substituting these conditions for the collected electrons into Eq. (1), one can obtain a linear relation between the electron energy and the deflecting voltage as

$$E = \frac{L}{2h\sin 2\theta} eV_d. \qquad (2)$$

For a given deflecting voltage only the electrons with certain incident angle and energy are able to pass through the exit slit and be detected. By tuning the deflecting voltage and measuring the beam current a time-resolved beam energy can be obtained. In the actual device two compensating guard electrodes, connected with both plates by large value resistors are added to eliminate fringing field distortions.

III. Experimental Results

All energy measurements are conducted at the end of the injector about 50 cm from the cathode and 11 cm after the third lens center. Both devices are operated in a diagnostic chamber under a vacuum of 10^{-8} torr range.

The general results from both devices are mutually consistent. Several cases are presented here. It should be realized that the energy mentioned here is the longitudinal kinetic energy.

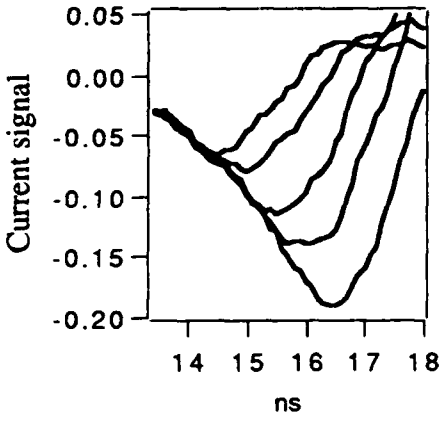

Fig. 2. Beam current signals for different retarding voltages

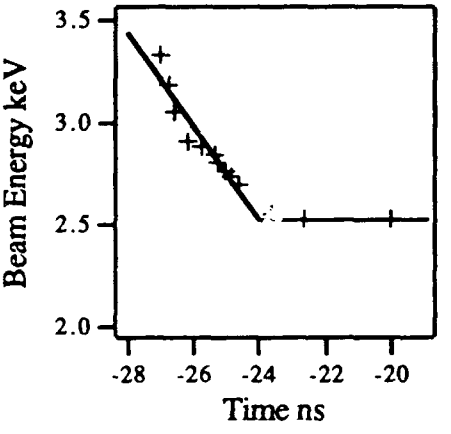

Fig. 3. Electron energy at front edge

The high time-resolution is accomplished by sufficient current signals and a Digital Signal Analyzer, DSA 602A with 1 GHz bandwidth and 2 G samples per second. As a typical example, Fig. 2 shows the collected beam current in the leading edge portion of a rectangular pulse at different retarding voltages. The time information can be determined by identifying the current "cut-off" point for a given retarding voltage.

1. Rectangular beam edge erosions

Due to the strong space charge force at the edges of a rectangular bunch, the electrons at the beam front speed up while those at the rear slow down, as shown in Fig. 3

2. Rectangular beam with induction acceleration

A time-dependent induction gap voltage can be generated as shown in Fig. 4. With an appropriate timing the beam can be accelerated and the energy is transferred from the induction module to the beam, as shown in Fig. 5.

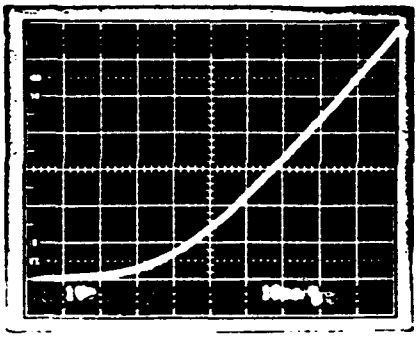

Fig. 4. Time-dependent induction gap voltage

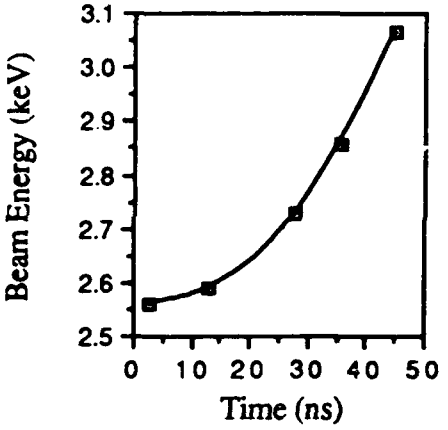

Fig. 5. Beam energy tilt with induction acceleration

3. Parabolic beam energy

The space charge forces of a parabolic beam are linear. Again the earlier electrons gain kinetic energy and the later ones lose. The energy tilt is linear, as shown in Fig. 6.

4. Parabolic beam with induction acceleration

By using the linear region of the induction acceleration voltage in Fig.4, the parabolic beam can be accelerated and its energy can be tilted from the negative slope shown in Fig. 6 to a positive one shown in Fig. 7. In consequence, the later electron with larger momentum will catch up with the earlier ones. This is the initial condition for pulse compression experiments.

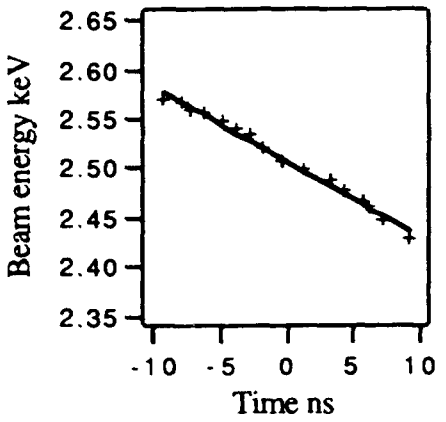

Fig. 6. Energy vs. time for a drifting parabolic beam

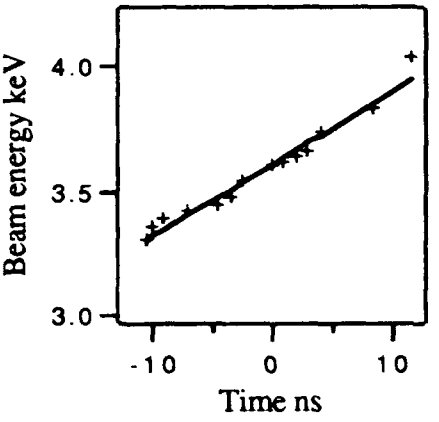

Fig. 7. Energy vs. time for a parabolic beam with induction acceleration

IV. Calibration and Resolution

1. Calibration

Both devices have been calibrated by changing the anode voltage. The retarding analyzer is calibrated with the retarding voltage corresponding to the "cut-off". The calibration results are shown in Fig. 8 and 9, where it is believed that the slight variations are caused by small shifts of the beam axis since the device is fixed. From Eq. (5) and Fig. 9 where $E=1.81\ V_d - 0.127$ (keV) the incident angle at the deflecting analyzer can be found to be $\theta = 39°$.

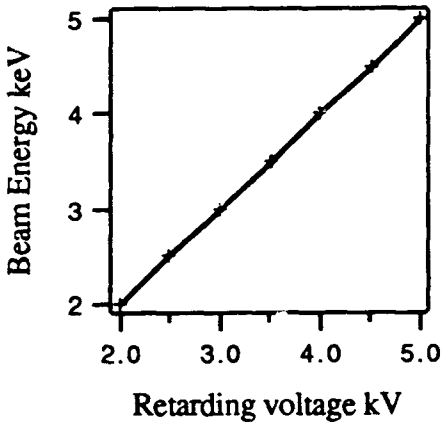

Fig. 8. Calibration of the retarding analyzer

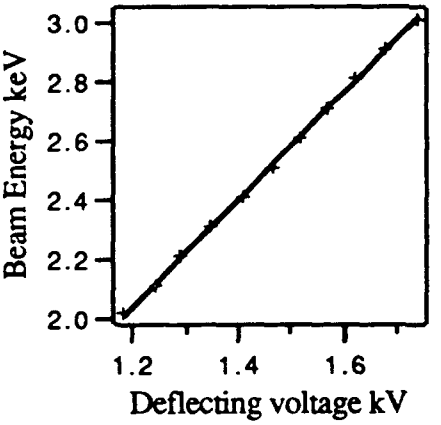

Fig. 9. Calibration of the deflecting analyzer

2. Resolution

The beam energy widths are measured for a given energy and for both devices shown in Fig. 10 and 11. By fitting them with a Gaussian the widths are 6 eV for the retarding analyzer and 67 eV for the deflecting analyzer. For the latter it is believed that the resolution is mainly limited by the finite widths of the slits.

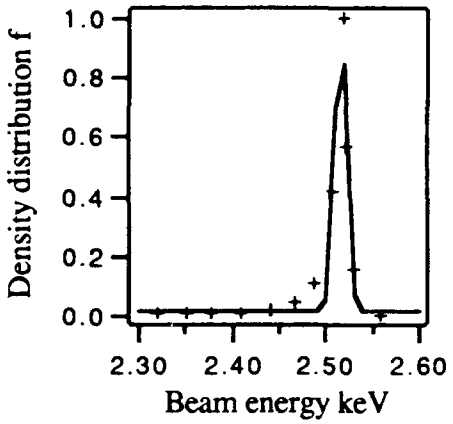

Fig.10. Beam density vs. energy where $f=\exp(-(E-2.516)^2/2(0.006)^2)$.

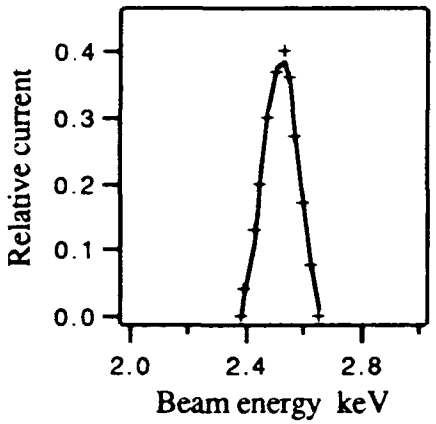

Fig.11. Relative beam current vs. energy where $I=I_o\exp(-(E-2.52)^2/2(0.067)^2)$

V. Summary

Both retarding and deflecting field energy analyzers have been built and employed to conduct the time-resolved energy measurements of the pulsed electron beams. The general performances of both devices are satisfactory. The time resolutions are better than a half nanosecond.

The retarding field energy analyzer is easier to build and more convenient to use. The energy resolution is higher as well. But an oscillation on the collected current signals limits the measurement sensitivity in some cases. The alignment is also a practical problem.

The deflecting field energy analyzer has a much neater current signal. The alignment is not a serious problem. The resolution is limited mainly by the sensitivity of the collector or finite slit sizes. Another reason is that the distance between the slits is rather short, which is limited by the geometric size of the diagnostic chamber. It makes measurements difficult and time-consuming. Ideally, the resolution can be always improved by reducing the slit width or covering the slit with a fine mesh and extending the distance between the slits.

References

1. J.G. Wang, M. Reiser, D.X. Wang and W.M. Guo, AIP conference proceedings, No. 253, p. 56 (1991)
2. J.G. Wang, D.X. Wang and M. Reiser, accepted for publication in NIM(A).
3. J.Arol Simpson, Rev. Sci. Instr. 32, 12, p.1283 (1961)
4. G.A. Harrower, Rev. Sci. Instr. 26, 9 p.850 (1955)
5. Mark R Ensign and Philip C. Tully, Rev. Sci. Instr. 41, 10, p.1408 (1970)

The Effects of Beam Parameters on Bremsstrahlung Exposure Angular Distribution

Shi Jiangjun

Southwest Institute of Fluid Physics
P. O. Box 523—55, Chengdu, Sichuan, 610003, China

Qian Minquan

Southwest Institute of Applied Electronics
P. O. Box 523—65, Chengdu, Sichuan, 610003, China

ABSTRACT

The effects of electron beam parameters, including beam radius, emittance and its energy, on the bremsstrahlung exposure angular distribution of a meter away from the target are researched in this paper. The analytic theory is described in detail. T. H. Martin experience formula is used to get the forward bremsstrahlung exposure in front of the target. Three kinds of typical electron transverse distribution are used, and they are the Kapachinsky-Vlajimersky distribution (KV), the waterbag distribution (WB), and the Gaussian (GS). From these distributions, the incident angles of the beamlets, which are in different radial positions, are calculated. The Monte-Carlo method is used to find the incident angle and position of each sample electron.

It is showed that the following fit formula about the radius R_s and the emittance E of electron-beam (in kms unit),

$$\varepsilon(\text{m-rad}) = 1.4\ R_s^2(\text{m})$$

should be meeted in order to obtain the maximal forwrad exposure. The higher the beam energy and the less the emittance, the better the distribution of exposure. The calculated results for three distributions are in agreement with each other, when two methods are used.

1. Introduction

When a high-Z target is exposed to a intense relativestic beam, the target atom and the injected electron would interact with each other, producting photon via bremsstrahlung. For flashed X-radiography, the forward exposure in front of the target should be as large as possible. In order to do so, the physical parameters should be chosen and adjusted carefully. The effects of most beam parameters on the exposure dose have been studied theroretically and experimentally[1-3], but the effect of beam emittance has scarcely ever been considered. Thus, it is necesary to explore the dependences of the radiation exposure and its angular distribution on the beam emittance and angular spread.

The aim of the paper is to find a regularity about these dependences in various emittances and to scale beam radius or angular spread by the emittance to get the optimized output exposure.

When the emittance effect considered, the transverse distribution of current density must be known. The Kapachuisky-Vlajimersky distribution (KV), the waterbag distribution (WB) and Gassian (GS) are considered in the paper. The transverse distribution of the beam current density gaven, the analytical method and the Monte-Carlo method are used to calculate the position and injected angle of an electron on the target plane.

2. Throry

The bremsstrahlung normalized angular distribution for a directed electron is as follows (the Martin' s formula[1]),

$$f_s = exp(-\theta W_e/0.677\pi) \tag{1}$$

The exposure X (in Ren) produced by a pulse electron beam with current I_b(in kA), energy W_e(in MeV) and pulse length τ_b(in ns) is as follows

$$X = 1.1 \times 10^{-3} I_b \tau_b W_e^{2.8} \tag{2}$$

A Cartesian coordinate system is used. The beam and target are supposed to be axisymmetrical about z-axis (see figure 1). In Eq • (1) the angle θ between two unit vectors, $\vec{\Omega}$ and $\vec{e}$, is

$$\theta = arccos\left(\frac{(x_i - x_s)cos\alpha + (y_i - y_s)cos\beta + z_i cos\gamma}{h}\right) \tag{3}$$

Set j_0 is the equivalent uniform current density of a electron beam, $j_0 = I_b/(\pi R_b^2)$, where I_b and R_b are the beam current and the radius on the target plane. So, the beam current density can be written as

$$j(\vec{r}_s) = j_0 f_c(r_s) \tag{4}$$

where $f_c(r)$ is the radial distribution factor of the beam current. Suppose the element current dI passes through the element area dS of the target, so

$$dI = j_0 f_c(r_s) dS \tag{5}$$

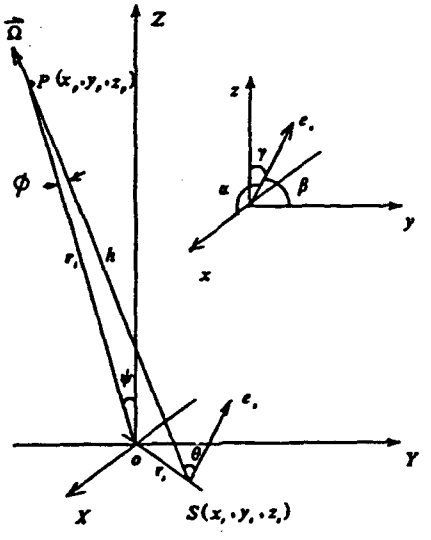

Fig. 1 The geometrical configuration about beam-target interaction point S and observed point P.

The exposure dose $dX(\vec{r}_s, \vec{r}_i, \vec{e}_s)$ at the point $P(\vec{r}_i)$ produced by the beamlet dI that injected at $S(\vec{r}_s)$ in the direction $\vec{e}_s$ is

$$dX = (\vec{r}_s, \vec{r}_i, \vec{e}_s) = 11\tau_b j_0 W_e^{2.8} \left(\frac{1}{r_i}\right)^2 f_c(r_s) e^{-\mu W_e/0.677\pi} cos\psi dS \tag{6}$$

Usually, $cos\psi \approx 1$. Integrating Eq. (6) over the beam cross section on the target, the total exposure

$X(\vec{r}_i)$ at the point P from the whole electron beam can be writen as

$$X(\vec{r}_i) = \frac{11 j_0 \tau_b W_e^{2.8}}{r_i^2} \iint_{S_b} f_e(r_s) e^{-\sigma\omega_s/0.677\pi} dS \tag{7}$$

3. Analytical method

According to T. H. Martin, the beam cross-section on the target will be devided into many small regimes. The procedure is as follows. First, the cross-section is devided into $2J_0$ pieshaped segments, equally. Each of these pieshaped segments is then subdevided into N_0 parts. Now, the area $\triangle S$ of the (n, j) element current $\triangle I$ is

$$\Delta S = \frac{2n-1}{2J_0 N_0^2} \pi R_b^2 \tag{8}$$

and ΔI is

$$\Delta I = \frac{2n-1}{2J_0 N_0^2} f_e(n) I_b \tag{9}$$

where, $n=1, 2, \cdots, N_0$; $j=1, 2, \cdots, 2J_0$

The measured points are all on the semisphere ($z>0$)with radius $r_i >> R_b$. For simplicity, the semisphere is devided into $2J_0$ equal segments in annule and each of these segments is devided into I_0 parts in the azimuthal, so that the semisphere obove the target is devided into $2I_0J_0$ sub-regimes. There are altogether $2I_0J_0+1$ mesured points on the semisphere. Solutions for the radiation at these $2I_0J_0+1$ points associated with each of the N_0targ.. segments are obtained. After the radiation levels at the $2I_0J_0+1$ points are defined, points are summed up by rotating one point into other around the z-axis of the sphere. Thus, after 360 degree rotation the N_0 target segments are made to appear as the entire target. The radiation from the N_0 target segments can be defined both in electron numbers and angle.

From Eq. (9), the exposure at the i-th azimuthal sub-regime can be obtained,

$$X(i) = C_0 \sum_{n=1}^{N_c} \sum_{j=1}^{2s_0} f_e(n)(2n-1) e^{-\theta(i,j,n) W_e/0.677\pi} \tag{10}$$

where $C_0 = 5.5\tau_b I_b W_e^{2.8}/(J_0 N_0^2 r_i^2)$. Radial distribution factor is: $f_e(n)=1.0$, for KV, $f_e(n)=2\{1-[(n-0.5)/N_0]^2\}$ for WB, and for GS, $f_e(n)=2\exp\{-2[(n-0.5)/N_0]^2\}$.

The average angular spread for the n—th ring of the beam is given as follows

$$\langle \delta\theta_n^2 \rangle = \int_{r_{n-1}}^{r_n} r dr \int_0^{\theta_0\sqrt{1-r^2/R_{b_0}^2}} r'^3 f(r, r') dr' \Big/ \int_{r_{n-1}}^{r_n} r dr \int_0^{\theta_0\sqrt{1-r^2/R_{b_0}^2}} f(r, r') r' dr' \tag{11}$$

where r is the variable radius, r′ the radial angular spread, r_n is indicated as the external radius of the n—th ring of beam, $r_n = \frac{n}{N_0} R_b$, r_{n-1} is its inner radius. Then using the three distribution functions and performing the integration in Eq. (11), we obtain:

$$\langle \delta\theta_n^2 \rangle / \theta_0^2 = 1 - \frac{n^2 - n + 0.5}{N_0^2} \qquad \textit{for KV}$$

$$\langle \delta\theta_n^2 \rangle / \theta_0^2 = \frac{1}{2}\left\{1 - \frac{1}{3N_0^2}\left[\frac{3N_0^2[n^4-(n-1)^4] - 2[n^6-(n-1)^6]}{2N_0^2(2n-1) - [n^4-(n-1)^4]}\right]\right\} \qquad \textit{for WB} \tag{12}$$

$$\langle \delta\theta_n^2 \rangle / \theta_0^2 = \frac{1}{2}\left\{1 - \frac{2(2n-1)[2N_0^2 - 2n(n-1) - 1]}{N_0^4 e^2\left[\exp\left(-\frac{2(n-1)^2}{N_0^2}\right) - \exp\left(-\frac{2n^2}{N_0^2}\right)\right] - 2N_0^2(2n-1)}\right\} \qquad \textit{for GS}$$

So, what we must do is simply to find the exposure distribution, $\Delta X(n,j)$, of the element current $\triangle I$ under the conditions of

$$x_s = \frac{n}{N_0} R_b, \qquad y_s = 0, \qquad z_s = 0$$

$$tg\gamma = \langle \delta\theta_x^2 \rangle^{1/2}, \qquad \beta = 0, \qquad tg\alpha = ctg\gamma$$

Summing up the dose distribution $\triangle X(n,j)$, we can obtain the exposure, $X(r_i)$, distribution contributed from the whole electron beam.

4. Monte-Carlo method

From Eq. (7), if the incident conditions of the all beam-electrons are known, the total exposure distribution $X(\vec{r}_i)$ can be found out. The four variants for each beam-electron can be obtained from the beam 4D transverse phase space distribution with the Monta-Carlo method.

The number of the modeled particle is taken K_0. The carrying current of each particle is $\Delta I = I_b/K_0$. The 4D distribution functions are

$$\begin{aligned} f_{KV} &= C_{KV}\delta\left(1 - \frac{x_s^2 + y_s^2}{R_b^2} - \frac{\alpha^2 + \beta^2}{\theta_0^2}\right) && \text{for } KV \\ f_{WB} &= C_{WB} && \text{for } WB \\ f_{GS} &= C_{GS} exp\left[-2\left(\frac{x_s^2 + y_s^2}{R_b^2} + \frac{\alpha^2 + \beta^2}{\theta_0^2}\right)\right] && \text{for } GS \end{aligned} \qquad (13)$$

The injecting conditions of each sample macroelectron, x_s, y_s, α, and β, can be determined. Thus, the total exposure at point P can be defined and the exposure distribution on the sphere is finally determined.

5. Calculated results

Figure 2 shows the results of calculating the forward exposure dose X as function of the beam radius R_b with different emittance from 50 to 800 mm—mrad, beam current $I_b = 3$kA and energy $W_e = 10$MeV. The parameters for figure 3 are the same as for figure 2, except for $W_e = 20$MeV.

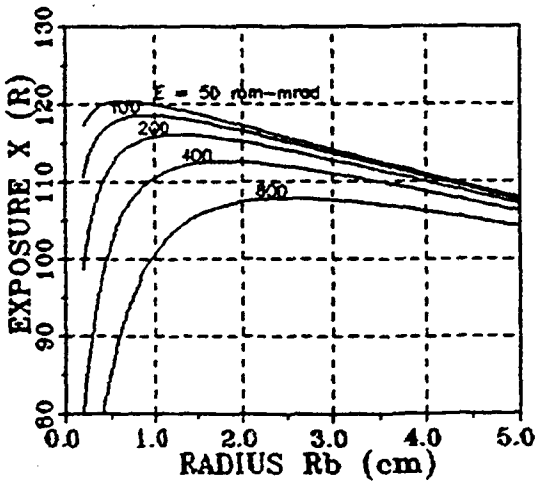

Fig. 2 Forward exposure X_0 vs electron beam radius R_b in the case of various emittances. ($W_e = 10$MeV)

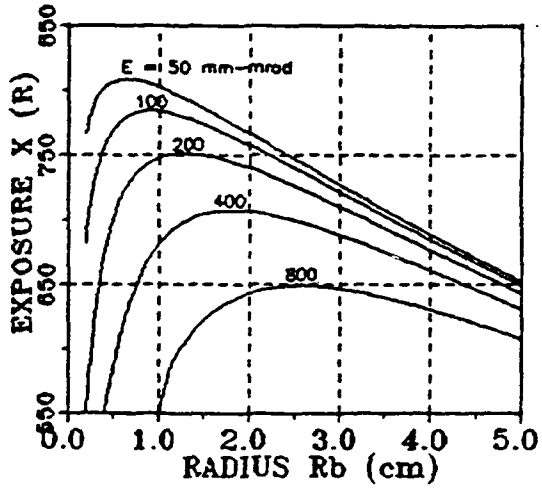

Fig. 3 Forward exposure X_0 vs electron beam radius R_b in the case of various emittances. ($W_e = 20$MeV)

It can be see that, for a certain emittance, the optimal radius R_{bm} at which the maximal forward exposure occurs is independent of the beam energy W_e. There is different optimal radius when the emittance is different. Figure 4 indicates the relation of R_{bm} to ε, and the corresponding fit formula is (in mks unit), approximately,

$$\varepsilon \simeq 1.4R_{bm}^2 \tag{14}$$

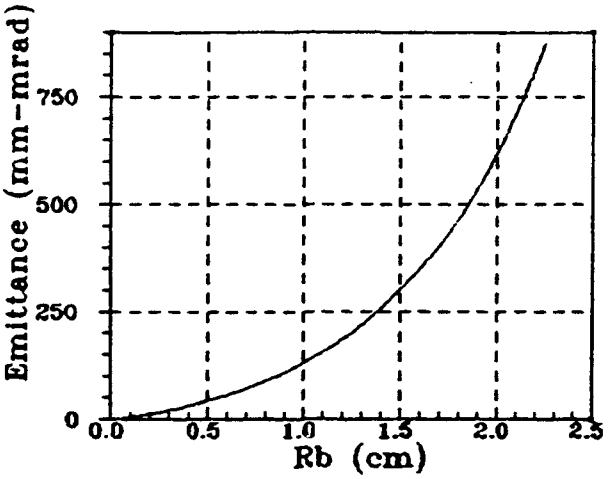

Fig. 4 The matching relation between emittance ε and optimal beam radius R_{bm}

The normalized dose angular distribution is shown in figure 5 in the case of optimized forward exposure. Suppose the beam with $W_e=10$MeV has emittance of 100 mm-mrad, the optimal radius is 0.8cm. For the beam with $W_e=20$MeV, the supposed value of the emittance is 50mm-mrad and its optimal radius is 0.6cm. It can be seen from figure 5 that the exposure decreases quickly when the azimuth increases and that the higher the energy, the quicker the exposure decrese. However, the dependence of the dose distribution on the product of the beam energy and azimuth is nearly the same in different beam energies (see fig. 6).

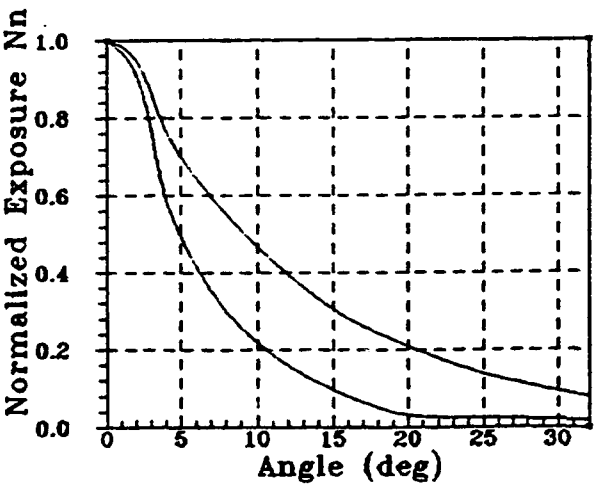

Fig. 5 The anular distributions of normalized exposure X_n for beam energy W_e of 10 and 20 MeV. (ψ is azimuth)

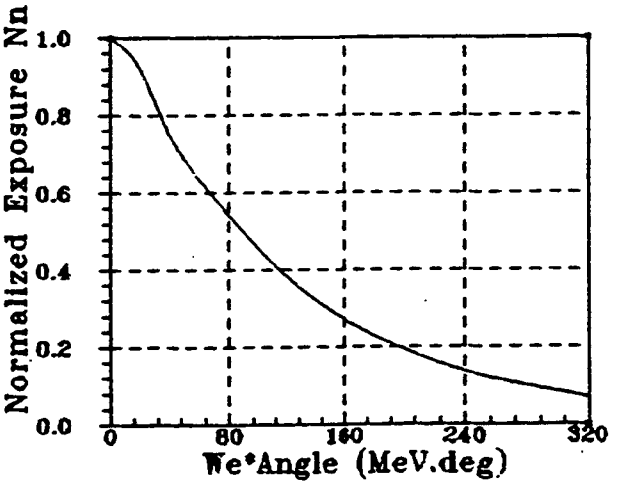

Fig. 6 The dependence of normalized exposure X_n on the product of beam energy W_e and azimuth ψ.

It is found that when the three typical beam distributions are used, the computed results are little different with each other. It, too, is found that the obtained results using both methods are more and less the same.

6. conclusion

The calculated results with analytical and Monte-Carlo methods have indicated that for a beam with nonzero emittance, only is the beam radius equal its optimal value R_{bm}, the maximal forward exposure of bremsstrahlung can be obtainted. Obviously, when the beam radius is large , the forward exposure would decrease because that the forward exposure distribution is uniformized in space. On the contrary, if the radius is too small, the forward exposure would decrease, too, because of the large angular spread. When the beam emittance known, the optimal radius can be calculated from Eq. (14). The relation between emittance and optimal radius is independence of beam energy.

Of course, the higher the beam energy, the more concentrated forward the exposure distribution, because that the dependence of the exposure distribution on $W_e\psi$ is independence of the beam energy, too.

For the flash X-radiography using LINAC with certain enrgy, it is important to choose the forward exposure and the spot size carefully, because there is contradiction between the optimal exposure and the mimimal radius. If the high resolution is desired to decrease the geometric blur, the spot size, i. e. the beam radius on target, should be as small as possible at the expense of the exposure. On the other hand, if the high contrast is wanted to increase signal-noise ratio of the picture, the optimal exposure should be taken, but the corresponding blur will be added to the picture.

All of the results is this paper are half-quantitative and have not been demanstrated experimently. However, they are instructive in designing flash X-radiography machine and acqwiring the picture with high quality.

Refrence

[1] T. H. Martin, SC—RR—69—241, May, 1969
[2] B. Kulke and R. Kihara, UCRL—82533, Apr. , 1979
[3] D. R. Goosman, UCRL—53742, Aug. , 1986

BREMSSTRAHLUNG RADIATION ON THE SNOP FACILITIES

Luchinsky A. V., Petin V. K., Ratakhin N. A., Smirnov N. A., Fedushchak V. F.

The bremsstrahlung output obtained from the interaction of a relativistic electron beam with converter foil has been studied experimentally. The experiments were carried out on SNOP-1 accelerator at 0.4-1.1 MV , 320-120 kA and pulse with FWHM of 20-65 ns. The electron beam energy was about 10 kJ and the power was 0.18 TW. For generation of the higher power electron beam on SNOP-3 generator the series of experiments were performed at 800 kV and 360 kA. The electron beam energy was 13 kJ and the power was 0.3 TW.

INTRODUCTION

The interest to the intense x-ray production are connected with its technical application , specifically, for radionics testing. The first detail results concerning the interaction of electrons with thick target (sufficient thickness to stop the electron) and of x-ray production has been reported in /1,2/.

Later the results of theoretical and experimental researches about optimization of the bremsstrahlung energy deposition , about influence of e-beam electromagnetic field on a total photon yield , the possibility of softening x-ray spectra and high power x-ray production were published in /3,4,5,6/.

The purpose of this work was making pulse x-ray sources for radiation testing of semiconductive elements. The results of this experiments will be used for building facilities whose power will more than four times higher comparison to SNOP facilities.

EXPERIMENTAL SETUP

SNOP-1 accelerator was built by conventional scheme : Marx generator -- pulse forming line -- water switch -- transmission line -- vacuum output. Prepulse switch was employed to reduce prepulse . In this experiments we had maximum 650 kV and 300 kA in the matched load . Figure 1 shows the geometry of the diode assembly and the position of the several diagnostics. The electrical parameters were measured with voltage dividers, Rogowsky coils and dI/dt probes. Thermoluminescent detectors (TLD) , pin- and scintillation detectors were applied for x-ray measurements. A 6-10 mm polyethylene was used as a shield. It was located behind the converter foil and kept debris from target and absorbed passed through converter foil e-beam . The stainless steel cathodes with 30-100 mm sharp edge diameters and planar Cu and Ta converter foils , 20-150 μm thick , were used in experiments . The anode-cathode (A-K) gap was 2-7 mm . Based upon damage patterns of the anode (or the shield) by e-beam or x-ray pinhole photograph of anode we could say about spartial location of the e-beam and the bremsstrahlung source size respectively . The vacuum chamber was held at a pressure of 0.0001 Torr.

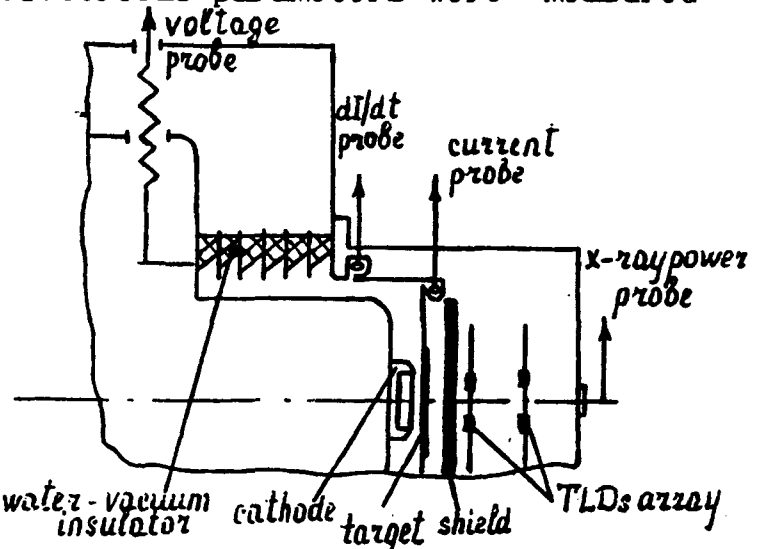

Fig.1. Scheme of the SNOP-1 output

EXPERIMENTAL RESULTS

The experiments were carried out at 0.4 -1.1 MV and 320-120 kA. The diode impedance was 1.25-8 ohm , it was achieved

by different cathode diameters and A-K gaps. The e-beam energy and the power, calculated from voltage and current signals were 10 kJ and 0.18 TW respectively. The pulse power with a FWHM of 20-65 ns was formed by water-vacuum insulator flashover or A-K gap plasma motion. Voltage and current, power of x-ray pulse, power of e-beam pulse and diode impedance are shown in Fig.2, Fig.3; the sharp edge diameter of cathode was 40 mm and A-K gaps were 5 mm and 2,2 mm respectively. Pulse power in Fig.2 was formed by water-vacuum

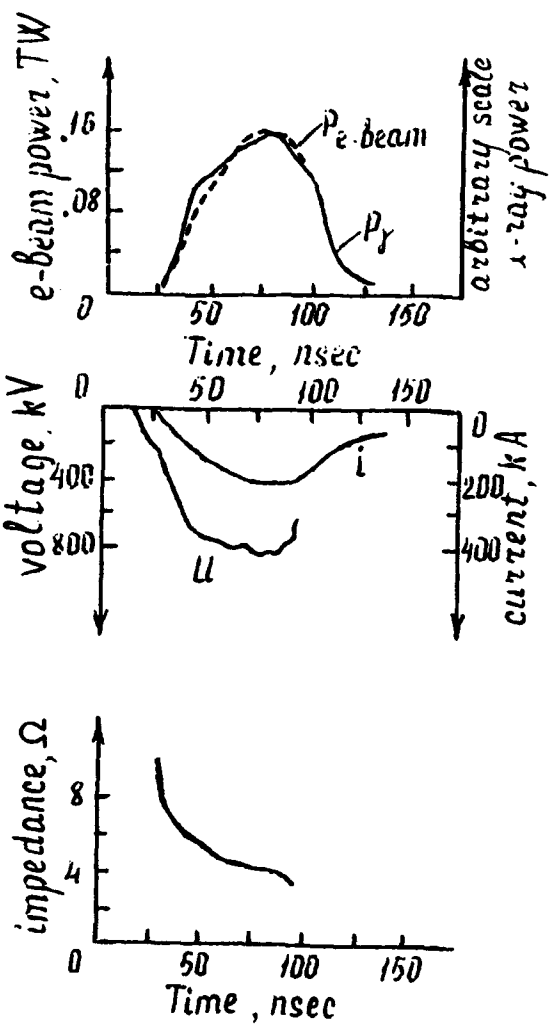

Fig.2 Vacuum diode measurements on SNOP-1 d_{AK} = 5 мм

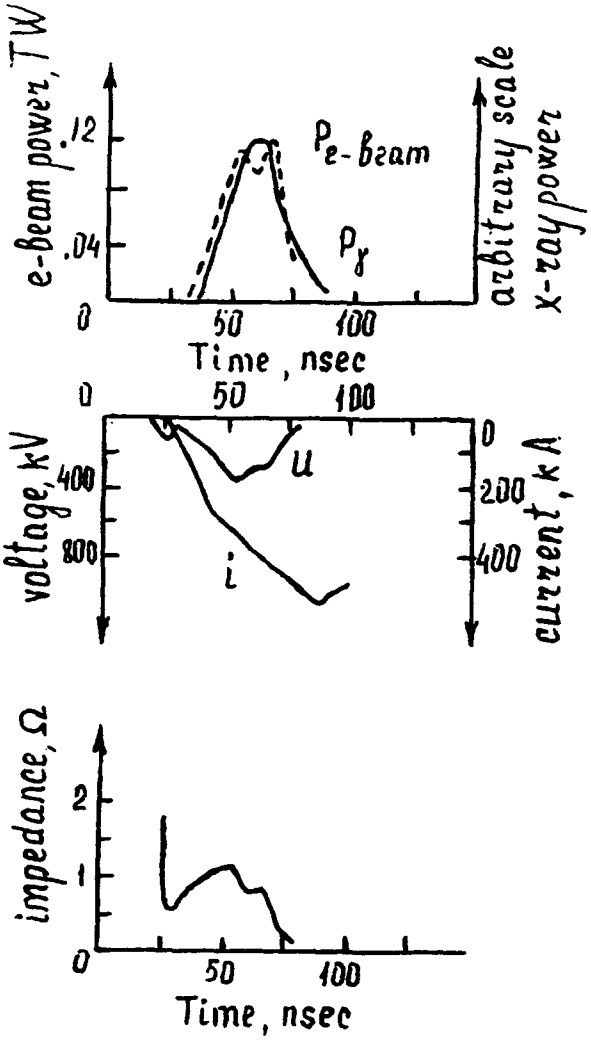

Fig.3 Vacuum diode measurements on SNOP-1 d_{AK} = 2.2 мм

insulator flashover and it was formed in Fig.3 by A-K plasma moving . There is also a delay of about 10 ns between the beginning of the voltage signals , current signals and x-ray power signals.

It is important to note that the behaviour of impedance in Fig.2 and Fig.3 are different.

Depending on delay between the beginning of the voltage pulse and water-vacuum interface flashover we could see different damage patterns of the anode (or the shield) . It was various width rings , equally e-beam exposed disk or the disk with increasing damages into diode axis and 5-10 mm dia crater on the axis (pinched diode). It may be use as a simple method for investigation of dynamic behaviour of e-beam.

The densitometer reading of x-ray pinhole photograph of target for one of short is shown in Fig. 4. Here it is also the x-ray dose measurements at different lateral distance between target and TLDs . Results that kind of experiments shown, that for pinched e-beam diode $I \backsim 1/R^2$ for $R > 3\text{-}3.5$ cm, where I is the total x-ray intensity and R is the lateral distance between target and TLDs.

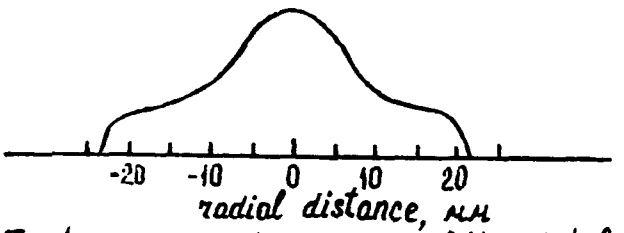

Fig.4 Densitometer reading of the pinhole x-ray photograph
4750 rads – 25 мм between target and TLDs
2070 rads – 44 мм between target and TLDs

For higher energy e-beam production (and higher total x-ray intensity production), than on SNOP-1, the experiments on SNOP-3 facility were made at 0.8 MV and 360 kA ; the e-beam energy in some experiments was about 13 kJ and the power was about 0.3 TW. The A-K gap voltage , e-beam current of pulse with its FWHM , total x-ray intensity for SNOP-1 , SNOP-3 and from /6/ are shown in Table 1.

Table 1

HYDRA	1000 KV 200 kA 100 nsec	40 krads - 21 mm between target and TLDs
SNOP-1	800 KV 200 kA 60 nsec	12 krads - 22 mm between target and TLDs
SNOP-3	300 KV 360 kA 45 nsec	5 krads - 40 mm between target and TLDs

REFERENCES

1. Dance W. E., Rester D. H., Farmer B. J., Jonson J. H. Bremsstrahlung Produced in Thick Aluminium and Iron Target by 0.5 to 2.8 MeV Electrons. J. Appl. Phys., 39, 2881 (1968)
2. Rester D. H., Dance W. E., Derrichson J. H. Thick Target Bremsstrahlung Produced by Electon Bombardment of Target of Be, Su and Au in the Energy Range 0.2-2.8 MeV. J. Appl. Phys., 41, 2682 (1970)
3. J. A. Halbleib, G. J. Lockwood, G. H. Miller. Optimisation of Bremsstrahlung Energy Deposition. IEEE Trans. Nucl. Sci., #5-23 , 1881 (1976)
4. J. A. Halbleib, W. H. VanDevender. Coupled Electron Photon Collisional Transport in Externally Applied Electrmagnetic Fields, J. Appl. Phys., 48, 3212 (1977)
5. J. A. Halbleib, G. J. Lockwood, L. D. Posey. Teoretical and Experimental Studies of multiple foil Bremsstrahlung Sources. IEEE Trans. Nucl. Sci., #3-28 , 4166 (1981)
6. J. R. Lee, R. C. Backstrom, J. A. Halbleib, T. P. Wright. Grad-B Drift Transport of High Current Electron Beam. 5-th Int. Topical Conf. on High Power Ion and Electron Beams. San-Francisko, 1983, p. 342.

THEORY OF THE BREMSSTRAHLUNG CONVERTER FOR RAISING ENERGY EXTRACTION IN THE RANGE 10-100 keV.

V.V.Ryzhov, A.A.Sapozhnikov

Institute of High Current Electronics 634055, *Tomsk, Russia*

Abstract. Formulas for an optimum thickness and bremsstrahlung spectrum in the range 10-100 keV are obtained and on the base of them analysis of the optimum characteristics as a function of energy is done both for single and multiple pass schemes.

Introduction

Large pulsed power machines (Black Jack, HYDRA, Angara, SNOP) are widely used to build intense, large area bremsstrahlung sources. It is super hard x-ray (SHX, bremsstrahlung in the range 10-100 keV) which is the main part of a surface dose in an irradiated object. So a problem of the most effective converter design is intensively investigated both theoretically and experimentally. Recently some multiple pass schemes have been proposed to increase bremsstrahlung generation efficiency [1,2,3]. But these papers don't show all essential features of the super hard x-ray extraction problem. In our paper formulas for an optimum thickness and bremsstrahlung spectrum in the range 10-100 keV are obtained and on the base of them analysis of the optimum characteristics as a function of energy is done both for single and multiple pass schemes.

Theory

The bremsstrahlung generation in a foil is a complex process which depends on many factors: stopping and scattering of the electrons, generation and transport of photons in a converter. It is very difficult to evaluate exactly the forward spectra of the extracted radiation analytically. But in the approach of the "forward-directed" photon emission in the direction of scattered electrons one can write:

$$\frac{dE_{br}}{dh\nu} = Nh\nu \int_0^l G(z) \frac{\partial\sigma}{\partial h\nu} \exp\{-\mu(l-z)/\langle\cos\theta\rangle\} \frac{dz}{\langle\cos\theta\rangle}, \qquad (1)$$

where l,N are a thickness and concentration of target atoms; $\mu,\partial\sigma/\partial h\nu$ - the liner attenuation coefficient of a photon energy [4] and intrinsic bremsstrahlung cross section [5]; $\langle\cos\theta\rangle$ - average cosine of the scattered electrons. We proceed from the assumption that the angle distribution of electrons reaches the steady, diffusion state very quickly and doesn't depend on a target depth. G(z) is the fraction of electrons which pass through the depth z in forward direction in the first cross $n(z)$ ($n(z)$ - the number transmission coefficient), in second one $n(z+2l)f$ and so on:

$$G(z) = \sum_{i=1}^{m} f^{i-1}\, n(2(i-1)l+z)\cdot U(R_e-2(i-1)l-z),$$

where $U(x)$ is a step function

$$U(x) = \begin{cases} 0., & x\leqslant 0.; \\ 1., & x>0, \end{cases}$$

R_e - extrapolated range. The number m is limited by the total number of the passes in the forward direction which an electron with the initial energy E_o can make through a foil with the thickness l before it is absorbed.

$$f=f_o\cdot f_1,\quad 0\leqslant f_o\leqslant 1,\quad 0\leqslant f_1\leqslant 1,$$

where f_o,f_1 - are the number reflected coefficient of the electrons in the first and back foil surfaces. If $f\neq 0$ expressions (1) and (2) describe the bremsstrahlung generation in a multiple pass regime. If $f_1=0$ above expressions describe the bremsstrahlung generation in a single pass one.

The expression (1) may be integrated over thickness if one notes that $\partial\sigma/\partial h\nu$ in the range 10-100 keV hardly depends on the energy of the electron transported through a target if $E_o>100$ keV. Choosing n(z) in the form [6]:

$$n(z) = a + bz/R_e + c(z/R_e)^2,$$

where a,b,c - constant depended on matter target, we obtain:

$$\frac{\partial E_{br}}{\partial h\nu} = N\,\frac{h\nu}{\mu}\,\frac{\partial\sigma}{\partial h\nu}\left[\sum_{i=1}^{m} f^{i-1}\, g_i^{o}(l')\; U(R_e-(2i-1)l)+\right.$$

$$\left.+U((2m-1)l-R_e)\,f^{m-1}\, g_m^{o}(\Delta l')\exp\{-\mu'(l'-\Delta l')\}\right], \qquad (2)$$

where $\Delta l=R_e-2(m-1)l$, $l'=l/R_e$, $\Delta l'=\Delta l/R_e$, $\mu'=\mu R_e/\langle\cos\theta\rangle$,

$$g_i^{\circ}(x)= \left(a_1 - \frac{b_1}{\mu'} + \frac{2c}{\mu'^2}\right)\left(1-1/\exp\{\mu' x\}\right) + \left(b_1 - \frac{2c}{\mu'}\right)x + c\,i^2.$$

$$a_1 = a + 2(i-1)bl' + 4(i-1)^2 cl' \;;\; b_1 = b + 4(i-1)cl'.$$

The total SHX energy extraction may be evaluated by integration over the photon energy in the range 10-100 keV. The optimum converter thickness for maximum extraction is the solution of equation [7]:

$$\left.\frac{d(E_{br})}{dl'}\right|_{l'_{opt}} = N\int_{10}^{100} \frac{h\nu}{\mu}\frac{\partial\sigma}{\partial h\nu}\left[\sum_{i=1}^{m} f^{i-1} U(R_e - 2(i-1)l)\frac{dg_i^{\circ}(l')}{dl'} + \right.$$

$$+ U((2i-1)l - R_e) f^{m-1}\left\{\left[\frac{\partial g_m^{\circ}(\Delta l')}{\partial l'} + \frac{\partial g_m^{\circ}(\Delta l')}{\partial(\Delta l')}\frac{\partial(\Delta l')}{\partial l'}\right] - \right.$$

$$\left.\left. - \mu'\left[1 - \frac{\partial(\Delta l')}{\partial l'}\right] g_m^{\circ}(\Delta l')\right\}\exp\{-\mu'(l'-\Delta l')\}\right] = 0. \qquad (3)$$

Then we have to take into account characteristic x-ray generation, which belong to the super hard x-ray spectrum for the atoms Z>30. Using the above approaches and suggesting 1) isotropy of the characteristic emission, and 2) photoabsorption mechanism domineering in the K-ionization process, we obtain energy for an K-fluorescence:

$$E_k = N\frac{\omega_k}{2}\frac{\langle h\nu_k\rangle}{\mu_k}\int_{h\nu_k}^{200}\frac{\mu_f}{\mu}\frac{\partial\sigma}{\partial(h\nu)}\sum_{i=1}^{m} f^{i-1}\left\{I_{2(i-1)} + f_1 I_{2i-1}\right\}dh\nu, \qquad (4)$$

where ω_k, $\langle h\nu_k\rangle$ is the radiation probability and average energy of the characteristic photons emitted from the K-shell. Expressions for $I_{2(i-1)}$ and I_{2i-1} are given in paper [8]. We integrate over the bremsstrahlung spectrum from a K-ionization energy to 200 keV, because as it follows from the analysis of the bremsstrahlung and photoabsorption cross sections, this range produces the main amount of the excited atoms.

Results

A. Single pass scheme (standard converter)

In the single pass scheme (f_1=0) expressions (2), (3) and (4) have the simplest form because in them there are only the first terms from all the sum which are not equal zero [9]. Fig.1

shows the optimum thickness dependence of C, Ti and Ta converters on an initial electron energy which is obtained by numerical solutions (3). It is assumed that a normally incident electron beam has the diffusion angular distribution inside the target so $\langle\cos\theta\rangle=.744$ [10]. There is a good agreement with the results of the Monte-Carlo simulations of the electron-photon transport, which are made for the same initial conditions [9].

By substituting the values of the optimum thickness into (2) and (4) we find the maximum of the SHX energy extracted behind the plane converter:

$$E_s^{opt} = E_{br}^{opt} + E_k.$$

The functions $E_s^{opt}(E_o)$ and $E_{br}^{opt}(E_o)$ are presented graphically on Fig.2. This results agree with good accuracy with the data obtained from the Monte-Carlo simulations which are showed by symbols on the same figure. One can see that the growth of E_o leads to the saturation of the SHX energy extraction, which is reached for Ta-converter at E_o=2 MeV. As it has been showed in [8,9] the limit value for E_s^{opt} in the single pass regime is defined by:

$$\lim_{E_o\to\infty} E_s^{opt} = N\int_{10}^{100}\Sigma h\nu\,\frac{h\nu}{\mu}\cdot\frac{\partial\sigma}{\partial h\nu} + N\,\frac{\omega_k}{2}\,\frac{\langle h\nu_k\rangle}{\mu_k}\int_{h\nu}^{200}\frac{\partial\sigma}{\partial h\nu}\,dh\nu.$$

As it follows from this expression the limit value decreases while Z increases proportionally to $1/Z^2$.

B. Multiple pass scheme.

In order to estimate the SHX energy dependence on a target thickness and the reflection coefficient we computed E_s behind the Ta-converter source driven by a monoenergetic electron beam with E_o=1 MeV. Angular electron distribution was assumed to be isotropic in 2π. The results obtained by using (2), (4) at f=0.,.5,.9 and 1. are shown on Fig.3. In the case f=0, as it has been mentioned, we have a standard single pass regime with only one maximum, but in other cases if $f>0$ there may be a few ones and each of them is defined by the amount of the passes and lies in the range:

$$R_e/2m < l_{opt} < R_e/(2m-1).$$

A more accurate optimum thickness may be found by choosing the

solutions of the equation (3) corresponding to the maximum SHX energy extraction for a given substance, initial electron energy and a reflexive coefficient. The more f is the less optimum thickness and bremsstrahlung absorption are, and in the ideal case f=1 (an ideal converter) increasing l one gets all bremsstrahlung energy extraction without absorption. This value can be estimated from the expression:

$$\lim_{l\to o} E_s^{opt} = \lim_{l\to o} E_{br}^{opt} = .5 \cdot N \int_{10}^{100} d\mathrm{h}\nu \, \frac{\partial\sigma}{\partial \mathrm{h}\nu} \int_{o}^{R_e} \frac{n(z)}{\langle\cos\theta\rangle}\, dz.$$

By substituting the solution of the eq.(3) into (2) and (4) we calculate a spectrum and SHX energy behind the Ta-converter of the optimum thickness in multiple pass regime for cases f=.5, .9 and 1. The results presented on Fig.2 confirm an enhancement extraction of the bremsstrahlung in the range 10-100 keV. Shown in Fig.4 the dependencies of the ratio of the maximum SHX energy extracted behind the Ta-converter in multiple pass scheme to the one in single pass scheme on the reflection coefficient for E_o=1, 2. and 3. MeV. It is easy to see that this ratio is rapidly growing in the range .9<f<1. and this effect is stronger the greater the initial energy is. Moreover, 1 MeV accelerator will produce more SHX energy in a multiple pass scheme if the reflexive coefficient is not less than 0.6.

It was found, that maximum generation efficiency of the bremsstrahlung generation in the range 10-100 keV η_m in a multiple pass scheme is not greater than the same value in the single pass scheme. However, the value of the initial electron energy supplying η_m is shifted into the range of greater values. Thus the Ta-converter allows one to get η_m=.32% at E_o=300-400 keV in the single pass regime and the same value - at E_o=1 MeV in the multiple pass regime (f=1).

[1] Ottinger P.F., Goldstein S.A. - Phys.Rev.Lett., 1980, vol.-45, N5,p.340
[2] Halbleib J.A. - IEEE Trans.Nucl.Sci. NS-27, 1980, p.1469
[3] Lee J.R., Backstorm R.C., Halbleib J.A. et.al.- J.Appl.Phys. 1984 vol.56(11), p.3175
[4] Storm E.,Israel H. Photon cross sections from 0,001 to 100 MeV for elements 1 through 100, Los Alamos .Scien.Lab ,1967

[5] Koch H.M. and Mots J.M. - Rev. Mod. Phys., 1959, v.31, p.920
[6] Baranov V. Electron Radiation dosimetry, Atomisdat, Moscow, USSR, 1974
[7] V.V.Ryzhov, A.A.Sapozhnikov - Preprint Russian Academy of Sciences, Siberian Branch, Tomsk, N1, 1992.
[8] V.V.Ryzhov, A.A.Sapozhnikov - Preprint Russian Academy of Sciences, Siberian Branch, Tomsk, N23, 1992.
[9] V.V.Ryzhov, A.A.Sapozhnikov - Preprint Academy of Sciences USSR, Siberian Branch, Tomsk, N22, 1991.
[10] Bethe H.A. et al. - Proc.Roy.Soc., 78, 573, 1938.

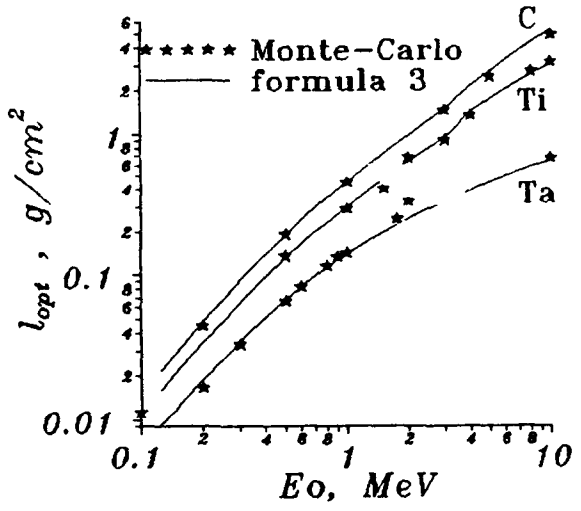

Fig.1

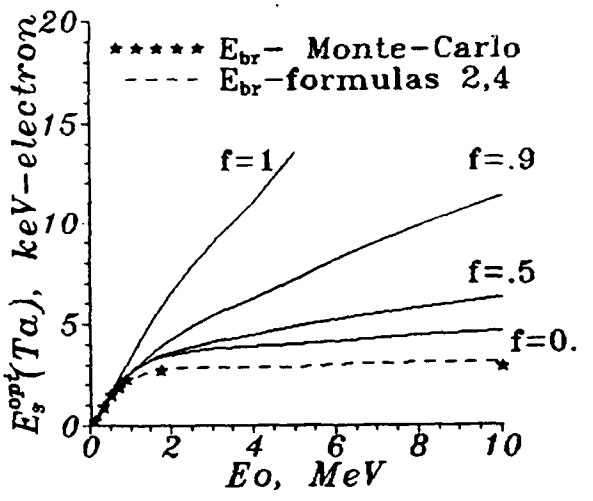

Fig.2

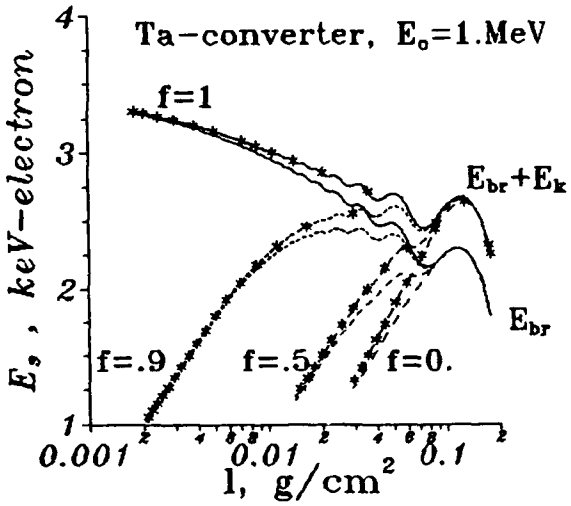

Fig.3

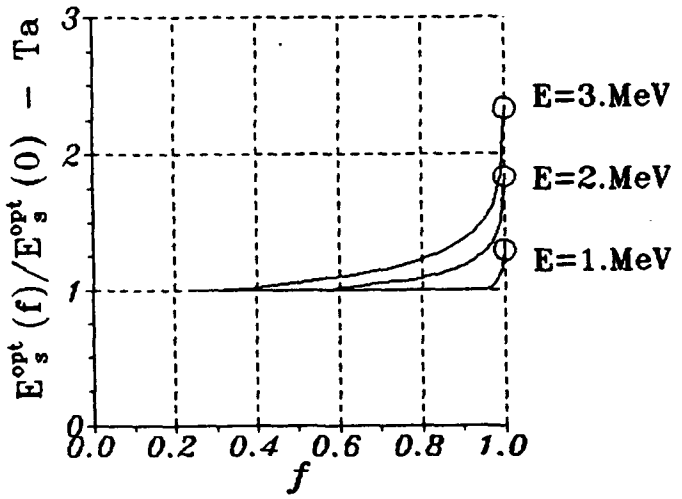

Fig.4

HIGH-INTENSITY FLASH X-RAY PRODUCTION BY REB

V.F.Zinchenko, V.V.Timofeyev, V.D.Shiyan

Moscow Engineering Physics Institute, Moscow, Russia

Abstract. Calculations are made of diode geometry and of target parameters required to maximize the photon fluence from flash X-ray source for electron energy 1.0 MeV. It was found that bremsstrahlung efficiency increasing, converter optimum thickness decreasing and bremsstrahlung spectrum softering occured due to multiple interaction of electron beam with thin target under action of self electro-magnetic field. Main parameters of a new simple large-area flash X-ray source are briefly described.

The paper deals with methods of high current REB focusing in a diode in order to obtain intense flashes of X-rays. The different means of REB electric field neutralization are investigated.

While interacting with the target a high power REB turns it rapidly into dense plasma. Thus, if the beam current is greater than Alfven one, the beam is pinched in the target plasma. Fig.1 shows the diode geometry and electron trajectories in a pinch-reflex diode with next parameters: the cathode external diameter is equal to 50 mm, its inner diameter is equal to 40 mm, anode-cathode gap is about 5 mm, U=1 MV and pulse duration is about 70 ns. "POISSON-2" code [1] was used for simulation of electron-ion current flow in the diode.

It can be shown, that in starting of current pulse the anode foil turns rapidly into expanding dense plasma due to thermal explosion. This plasma covers partly the cathode-

anode gap. Owing to REB charge neutralization in plasma beam electrons drift toward the diode axis under action of REB self magnetic field. Numerical simulation shows that strong pinch with electron current about 200 kA is formed. The pinch has a form of a ring with radius about 2 mm. Ion current is equal to 15 kA. The total current is about 270 kA. However, to transform the high-Z and high melting temperature thin target (Ta, W) into plasma and to provide pinch conditions it is necessary to spend a considerable portion of the beam energy. Therefore, under testing the strong beam focusing is observed usually in the second part of the pulse, when most of the stored energy has been lost. Hence, it is important to obtain the pinched REB conditions in starting of pulse before its interaction with the converter, because in this case the energy deposition of magnetized REB in the thin target increases the radiation output, particularly in soft spectrum region [2].

Similar diode construction with additional foil was investigated to obtain and to focuse REB with current about 1 MA and kinetic electron energy about 1 MeV. Numerical simulation shows the following optimal parameters of the diode: a cathode face extends from 10.0 cm to 12.0 cm radially, a distance between a cathode and an anode is equal to 2 cm, and a distance between a cathode and the additional foil is about 1 cm (Fig.2). The total current in diode is equal to 1.1 MA and its considerable part (about 600 kA) reaches a region near axis with radius $r < 1$ cm. The additional foil is used for REB radial electric field neutralization. However there is an essential difference between these two cases (Fig.1 and Fig.2). In the second case the temperature expansion of the additional foil is negliblein comparison with a size of the cathode-anode gap and the Larmor radius of the beam electrons. The focusing effect of the foil is deter-

mined only by the radial electric field closure near the foil surface.

High-intensity pulsed electron beams are used to generate intense flashes of X-rays by converting a portion of the beam energy into bremsstrahlung radiation via electron interactions in a high-Z target. As shown in Fig.2, while drifting toward the diode axis the REB electrons pass multiply through the additional foil. Thus, to obtain an intense quasipoint X-ray source the central part of the foil should be made of a high-Z material. If the foil consists of this material completely, we obtain a large area bremsstrahlung source with enhanced yield.

This paper presents also the results of calculations of bremsstrahlung fields. The interaction of a pinched REB with a thin target was investigated earlier [2]. Therefore, here we present only the large area X-ray source simulation results. The REB transport in a thin foil-target is simulated with a Monte-Carlo method using "condensed trajectories" approach and taking into account the electron motion outside the target in electro-magnetic field.

The Ta target is optimized by maximizing the forward 2π photon energy as a function of the Ta thickness. In Fig.3 we have plotted the bremsstrahlung efficiency, defined as the ratio of the photon energy to the incident electron energy, as a function of the Ta thickness, for the whole of the energy region and in the region up to 100 keV. The statistical error in data point is typically 5 % or better. We find that the forward efficiency calculated in the optimum conditions increases to 2 % in comparison with a standard converter (1.6 %). The optimum Ta thickness becomes 25...40 μm and the corresponding average energy of the individual forward emitted photons is 140...150 keV. The individual photon spectrum is given in Fig.4 in comparison with a simi-

lar spectrum of standard converter [3]. Thus, the forward bremsstrahlung efficiency of the presented converter is greater by a factor of 1.25 than a standard one. The average photon spectrum energy decreases on 30...40 keV, the optimum Ta target thickness decreases by a factor of 3...4. The forward bremsstrahlung output up to 100 keV giving a main contribution to an absorbed dose in middle- and high- Z materials increases in comparison with a standard converter by a factor of 3. It is provided by a multiple interaction of REB with a target under action of self magnetic field.

Lately, some interest have been taken in high power large-area flash X-ray sources [4-6]. In this case, sufficient complicated diode constructions or additional facilities are used to obtain a bremsstrahlung field with constant radial dose profile. Fig.5 shows the calculated radial exposure dose profiles of presented converter (Fig.2) at 2.0 cm downstream of the target. As shown in Fig.5 it is possible to obtain a good large area X-ray source by varying target thickness.

Thus, we have described an original simple large-area 1.0 MeV endpoint energy bremsstrahlung flash X-ray source. This source should be of great interest for radiation effects testing.

References.

1.Astrelin V.T., Ivanov V.Ya., Avtometriya, N3, 92 (1980). In Rus.
2.Zinchenko V.F., Timofeyev V.V., Shiyan V.D., Proc. 8-th Int. Conf. on High Power Particle Beams, Novosibirsk, 2, 769 (1990).
3.Sanford T.W.L. and Halbleib J.A., IEEE Trans. Nucl. Sci., NS-31, N 6, 1095 (1984).
4.Ottinger P.F., Goldstein Sh.A., Phys.Rev.Lett. 45, N5, 340 (1980).
5.Hedemann M.A., Pregenzer A.L., Posey L.D. et. al. IEEE Trans. Nucl. Sci., NS-32, N 6, 4266 (1985)
6.Sanford T.W.L., Lee J.R., Halbleib J.A. et.al. J. Appl. Phys., 59, N 11, 3868 (1986)

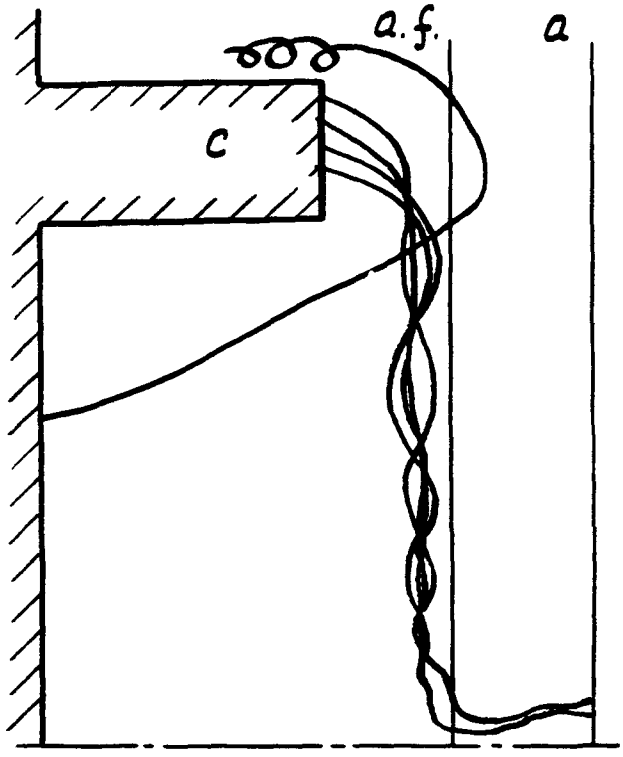

Fig. 1

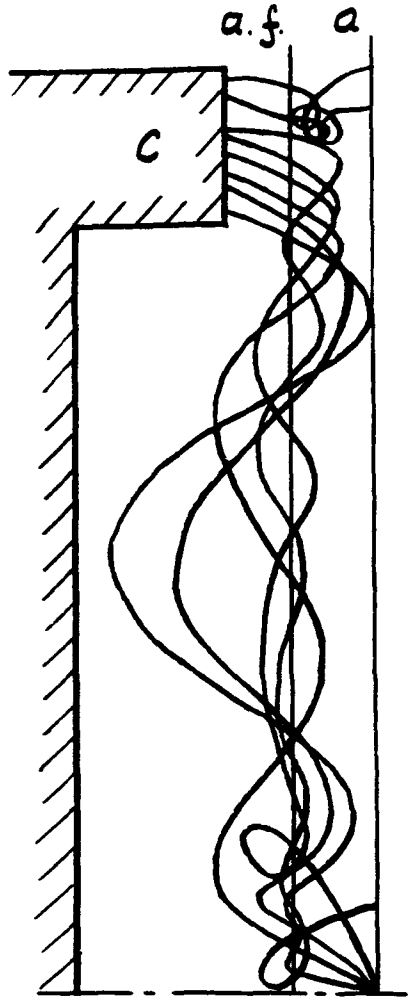

Fig. 2

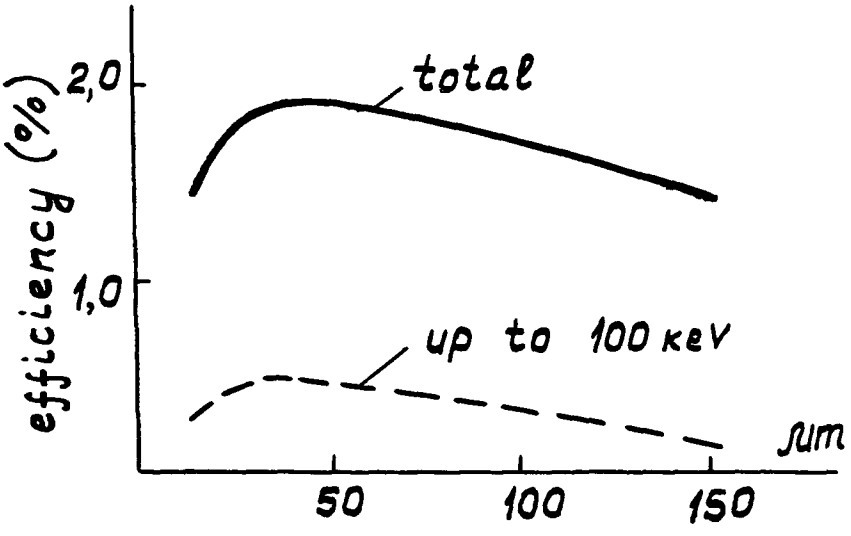

Fig. 3

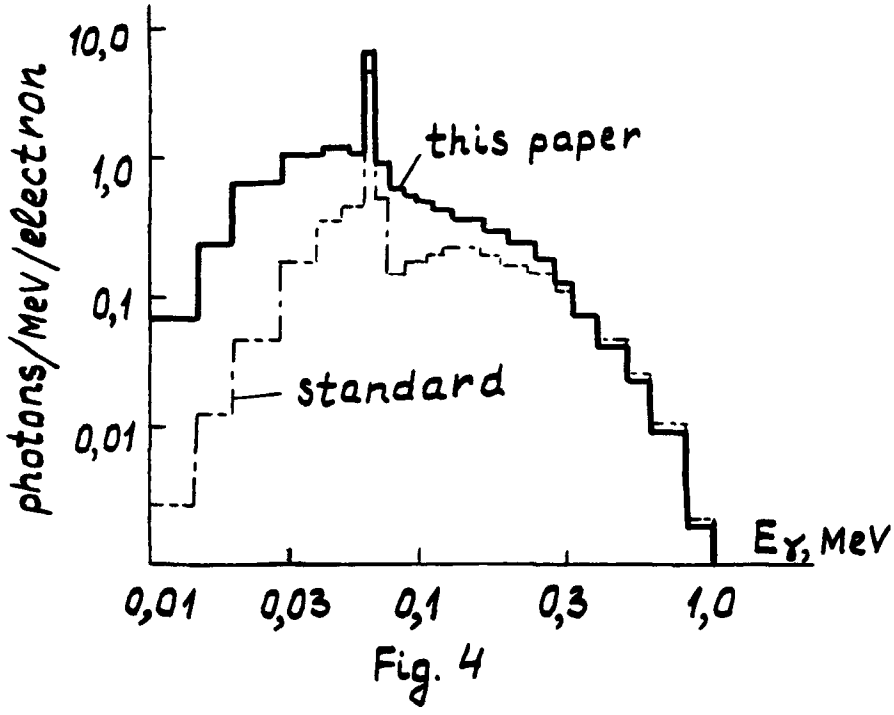

Fig. 4

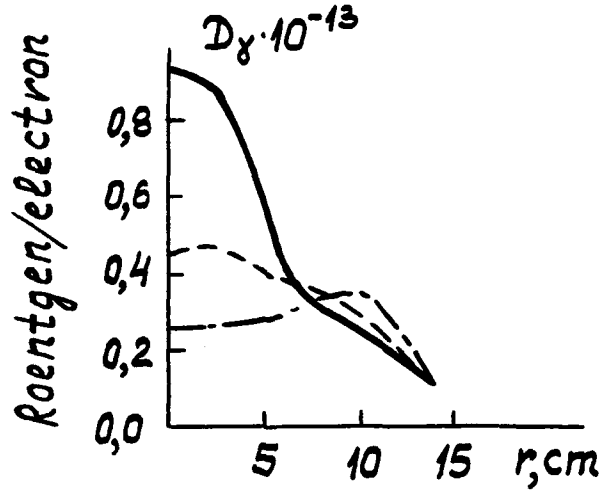

Fig.5. Radial dose profile at 2.0 cm downstream of the target for different Ta target thickness. —— d =20μm; – – – d =30μm; —·—d =40μm.

HARMONIC EMISSION IN A DIELECTRIC MEDIUM WITH A UNIFORM MAGNETIC FIELD

Josip Šoln

Harry Diamond Laboratories
Adelphi, Maryland 20783

Abstract

A description is being developed of spontaneous emission in a uniform magnetic field with a dielectric medium. The parameters being considered are beam energies of up to 10 MeV, indices of refraction (n) of up to 2, and magnetic fields of up to 5 T. As long as n is a slowly varying function of the radiation frequency, the spontaneous emission may go into a large number of harmonics. Compared to a vacuum, the dielectric medium increases the overall energy emission in the 10 to 10^6 GHz spectral region. Within our description we deduce a new effect, a helical Čerenkov effect, whose power spectrum, unlike the usual Čerenkov effect, depends on the radius of curvature of the electron trajectory, which is measured in the plane perpendicular to the direction of the electron guiding center.

1. Introduction

As is well known, a dielectric medium can significantly alter the mechanism of electron radiation compared to a vacuum. To begin with, the actual emission can be split into two "branches": a vacuum branch and Čerenkov branch.[1] In our case, with the uniform magnetic field present in the medium ($\vec{B} = \hat{z}\, B$), the vacuum and Čerenkov branches[2] are distinguished by $nv_O < 1$ and $nv_O > 1$, respectively. (Now and later, v_O and $v_\perp$ are parallel and perpendicular components, respectively, of the electron velocity with respect to $\hat{B}$.)

The spontaneous emission in a dielectric medium from electrons moving on (exactly known) helical orbits in a uniform magnetic field,[3] where the space-charge and radiation reaction force are neglected, is a good example for deducing some general characteristics of spontaneous emission in a medium. First we learn that generally a new effect—a helical Čerenkov effect—should exist in a dielectric medium. This effect, unlike the usual Čerenkov effect, depends on the radius of curvature of the electron trajectory (measured in a plane perpendicular to the direction of the electron guiding center); for rather energetic beams of 1 MeV and above, this effect is strongest when the radius of curvature becomes comparable to the radiation wavelength. Furthermore, as long as the index of refraction n is

a slowly varying function of the radiation frequency, the spontaneous emission may go into a large number of harmonics for either of the two branches.

Harmonic emission (mostly in a vacuum) has been experimentally investigated for quite some time. Specifically, the higher harmonic emission has been observed experimentally over a 10-year period in free-electron lasers (FEL's) with both planar (linear) and helical undulators. As early as 1980, the spontaneous harmonic power for a planar undulator was observed at Orsay by Bazin et al.[4] and at Novosibirsk by Artmonov et al.[5] As to the helical undulator, harmonic generation during laser operation was first observed in 1983 by Benson et al.[6] at Stanford University. Rather recently, Bamford and Deacon[7] have been able to measure the emitted energy and the spectral and temporal distributions of the first seven harmonics that are self-generated at the linear undulator Mark III FEL oscillator at Stanford. Of course, there are many practical aspects of higher harmonic emission. For example, the existence of higher harmonics in the emission spectrum of an FEL, as argued by Calson et al.[8,9] some time ago, can greatly extend the tunable range to shorter wavelengths. Also, at the National Institute for Standards and Technology (NIST), experiments are designed to specifically study harmonic generation using a microtron accelerator.[10]

2. Description of Spontaneous Emission

The S matrix, in which the photon propagator incorporates index of refraction n (which may depend on the radiation frequency), is used to describe the spontaneous emission in a uniform magnetic field with a dielectric medium. The important ingredient in the S matrix is the Fourier transform of the electron current density which, in turn, is determined by the electron helical trajectory in a uniform magnetic field (in a dielectric medium). Regardless of what the dependence of n is on the radiation frequency, one can, by using the customary definition of Bessel functions, expand the Fourier transform of the electron current density into a Fourier-like series in which there corresponds formally to each term a harmonic index, l. For sufficiently long interaction time T (or interaction length L), one finds that the expression for the angular-spectral energy distribution can be written as a sum over the harmonic angular-spectral energy distributions (each being associated with harmonic index l). The vacuum branch is associated with harmonic indices satisfying $l \geq 1$, while the Čerenkov branch is associated with harmonic indices satisfying $l \geq 1$ (the backward Čerenkov branch) and $l \leq 0$ (the forward Čerenkov branch). The $l = 0$ in the expression of the angular-spectral energy distribution corresponds to the new effect: a helical Čerenkov effect.[11]

The helical Čerenkov effect, unlike the usual Čerenkov effect, depends on the radius of curvature of the electron trajectory which is measured in the plane perpendicular to the direction of the electron guiding center. For rather energetic electrons, 1 MeV and above, this effect is the strongest when the radius of curvature is comparable to the radiation wavelength in the medium. The longer the radiation wavelength is, the easier it is to observe the helical Čerenkov effect with higher energy electrons. Specifically, in water and in the visible spectrum ($n = 1.33$), magnetic fields of the order of 30 T would be needed to observe this effect. However, in the microwave end of the spectrum and in the medium with $n = 1.5$, this effect is observable with magnetic fields of only about 1 T. As to the lower energy electrons, say below 0.5 MeV, we argue that the effect should be observable in water in the visible spectrum with magnetic fields of about 4.5 T.

Finally, we find that as long as the index of refraction n is a slowly varying function of the radiation frequency (in some range of frequencies), the spontaneous emission may go into a large number of harmonics for either of the two branches. Specifically, for a given radiation angle θ, measured with respect to the direction of the uniform magnetic field, to each harmonic index there corresponds a radiation frequency with the harmonic angular energy distribution. The sum of harmonic angular energy distributions gives the desired (total) angular energy distribution. Choosing the magnetic field of 4 T, an interaction length of 100 cm, $\theta = 0.1$ rad, $v_o = 0.63$, $v_\perp = 0.6$, and $n = 1.4$, we find that there are 37 angular energy distributions significantly different from zero for the spontaneous emission into the fundamental and harmonic frequencies (all occurring in the vacuum branch); the total angular energy distribution is 4.16 eV in this case. If the spontaneous emission occurs in a vacuum ($n = 1$) instead of a dielectric, we determine that the total angular energy distribution is just 0.03 eV. We see that the presence of the dielectric medium increased the energy of the spontaneous emission at $\theta = 0.1$ rad by more than 138 times.

3. Discussion and Conclusion

There is no doubt that, at least on the theoretical level, the presence of the dielectric medium should be able to significantly enhance the efficiency of the spontaneous electron radiation in a uniform magnetic field. The surprising result is how numerous the higher harmonics are into which the electron radiates spontaneously respectable amounts of energy, even at angles as small as 0.1 rad, when the dielectric is present. For the sake of completeness, we mention that the helical Čerenkov effect for rather energetic beams,

whose details we discuss elsewhere,[11] is the strongest when the radius of curvature of the electron trajectory is comparable to the radiation wavelength in the medium.

4. References

1. J. Šoln, "Differential Equations with Respect to Coupling Constants: An Approach to Čerenkov and Stimulated Radiation," Phys. Rev. D **18**, pp. 2140–2151, September 1978.

2. J. Šoln "Stimulated Electron Radiation in a Medium Due to Wiggler Magnet," J. Appl. Phys. **51**, pp. 5523–4427, October 1980.

3. J. Šoln "Spontaneous Emission in the Uniform Magnetic-Field Free-Electron Laser Described by the Ordinary and Scalarized Photon," J. Appl. Phys. **67**, pp. 3971–3982, May 1990.

4. C. Bazin, M. Billardon, D. Deacon, Y. Farge, J. M. Ortega, J. Perot, Y. Petroff, and M. Velghe, "First Results of a Superconducting Undulator on the ACO Storage Ring," J. Phys. Lett. **41**, pp. L574–L550, December 1980.

5. A. S. Artamonov, N. A. Vinokurov, P. D. Voblyi, E. S. Gluskin, G. A. Kornyukhin, V. A. Kochubei, G. N. Kulipanov, V. N. Litvinenko, N. A. Mazantsev, and A. N. Skirnsky, "The First Experiments with an Optical Klystron Installed on the VEPP-3 Storage Ring," Nucl. Instrum. Methods **177**, pp. 247–252, November 1980.

6. S. Benson, D. A. Deacon, J. N. Eckstein, J. M. Madey, K. Robinson, T. I. Smith, and R. Tabor, "Review of Recent Experimental Results from the Stanford 3μm Free-Electron Laser," J. Phys. (Paris) Colloq. C-1 **44**, pp. C1-353, February 1983.

7. D. J. Bamford and D. A. G. Deacon, "Measurement of the Coherent Harmonic Emission from a Free-Electron Laser Oscillator," Phys. Rev. Lett. **62**, pp. 1106–1109, March 1989.

8. W. B. Colson, "The Nonlinear Wave Equation for Higher Harmonics in Free-Electron Lasers," IEEE J. Quantum Electron. **QE-17**, pp. 1417–1427, August 1981.

9. W. B. Colson, G. Dattoli, and F. Ciocci, "Angular-Gain Spectrum of Free-Electron Lasers," Phys. Rev. A **31**, pp. 828–842, February 1985.

10. S. Penner, R. Ayres, R. Cutler, P. Debenham, B. C. Johnson, E. Lindstrom, D. Mohr, J. Rose, M. Wilson, P. Sprangle, and C. M. Tang, "The NBS/NRL Free-Electron Laser Facility," Nucl. Instr. Methods **A272**, pp. 73–80, October 1988.

11. J. Šoln, "Effect of a Dielectric Medium on Spontaneous Radiation in a Uniform Magnetic Field: Higher Harmonics and the Helical Čerenkov Effect" (in preparation).

BREMSSTRAHLUNG RISETIME SHORTENING BY DIODE GEOMETRY RECONFIGURATION

Michael Bushell, Raymond Fleetwood, Dan Judy,
George Merkel, Michael Smith
Harry Diamond Laboratories
2800 Powder Mill Road
Adelphi, MD 20783-1197

Douglas Weidenheimer
Berkeley Research Associates, Inc.
Springfield, Virginia 22150

Abstract

Experimental and theoretical studies on one arm of the Aurora flash x-ray machine have indicated that it is possible to lower the risetime of the bremsstrahlung produced at a single Aurora diode by increasing the AK gap of the diode. In an experimental setup employing a cylindrically symmetrical toroidal cathode, the local spatial distribution of bremsstrahlung pulse shape at the thick tantalum converter was measured at 10 radial positions by 10 Compton diodes placed at the converter. Additionally, bremsstrahlung produced at distances of 2, 3, 4, and 5 meters from the converter was measured by Pilot B scintillation counters. As the AK gap was widened, the early part of the bremsstrahlung pulse was diverted in the radial direction of the magnetically insulated transmission line (MITL) feeding the diode. The bremsstrahlung risetime at 3 meters from the bremsstrahlung target was reduced from about 60 to 18 ns by increasing the AK gap from 11 to more than 19 inches.

Introduction

The Aurora flash X-ray machine in its conventional configuration consists of four focused bremsstrahlung targets, each individually fed by a MITL. The production of bremsstrahlung pulses at the transition between the 15-meter long MITLs and the bremsstrahlung diodes is not a simple, one-dimensional phenomenon. The behavior of a 10-MV, 250-kA pulse at the interface between the concentric MITL and the diode is extremely dynamic and very geometry dependent. Pulses propagating down the MITLs have currents of approximately 250 kA with maximum voltages that can vary from about 6 to 11 MV. The goal of the work to be presented is to examine the effects of diode geometry on relativistic e-beam pulse shape and/or bremsstrahlung pulse shape and, based on the results of the study, to suggest ways to decrease the risetime of the standard Aurora pulse (figure 1).

Conventional Aurora Focused Mode

Figure 1 shows the temporal distribution of a bremsstrahlung pulse produced by the Aurora in its conventional, four-bremsstrahlung target, focused mode. Figure 2 shows a single Aurora MITL bremsstrahlung target configuration. In this conventional configuration, the individual Aurora diodes are not in a plane perpendicular to the MITL axis. An experimental setup designed to study the production of radiation along a single Aurora MITL and the asymmetrical Aurora diode is outlined in figure 2. Figure 2 also shows some typical pulse shape measurements obtained with the experimental setup shown in figure

2. Notice the fast risetimes of the bremsstrahlung pulses in the direction perpendicular to the axis of the MITL, attributable to the electrons striking the outer MITL coaxial cylinder before magnetic insulation sets in. Notice that the bremsstrahlung pulse risetime is fastest at large angles to the MITL axis and slowest in the forward direction at the diode MITL interface.

Cylindrical Diode Setup

Figure 3 is a schematic diagram of a symmetric diode setup and figure 4 is a diagram of a diverter that can be employed to shorten the Aurora bremsstrahlung pulse length. An idealized description of relativistic electron diode operation is depicted in figure 5. Notice that the electrons impinging on the center of the anode strike the diode-anode later in time than those striking more radially. Figure 6 is a schematic diagram indicating the positioning of 10 Compton diodes placed to obtain bremsstrahlung pulse shape information across the face of the bremsstrahlung target. The positions of three magnetic field sensors (BD4, BD1, and BE3) and an electric field sensor (EK04) inside the MITL are also shown. The position of a photodiode scintillation bremsstrahlung detector (PD3) 2 m from the bremsstrahlung exit port is also indicated. Figure 7 shows an electric field sensor response (MITL current waveform) obtained in the vacuum coaxial line: figure 8 shows a magnetic field waveshape. Both measurements are at the position EK04/BD4 in figure 6. Figures 9 and 10 show the waveforms of the magnetic fields or current at positions BD1 and BE3 in figure 6 respectively. The Compton diode response at the center of the bremsstrahlung exit port (CD6) is shown in figure 11. Finally, the photodiode response (PD3) 2m from the exit port is shown in figure 12. Note that the early monopolar pulse disappears as the MITL pulse progresses down the MITL.

The risetime of the photodiode (figure 12) and the Compton diode (figure 11) are approximately 15 ns. This 15 ns risetime can be compared to the slowly rising, complicated wave forms shown in figures 7 and 8. The energy in the early part of the pulses shown in figures 7 and 8 is expended by relativistic electrons striking the outer coaxial MITL cylinder before magnetic insulation conditions are met. The MITL acts as a filter. (Note figure 2). The first monopolar pulse of the magnetic field (or current pulse) is filtered out as one progresses from BD4 to BD1 to BE3. The monopolar ripple in the MITL current can be explained by a number of impedance mismatches such as that between the Blumlein triaxial line and the vacuum coaxial line. The design of the oil-vacuum interface between the Blumlein and vacuum coax was dominated by flash avoidance considerations at the expense of a smooth adiabatic impedance match. Note that the individual monopolar ripples have fast risetimes compared to the 60-ns risetime shown in figure 1. Figure 13 shows examples of some typical bremsstrahlung pulse shapes obtained with the 10-Compton-diode arrangement shown in figure 6. The 10 Compton diodes spaced across the anode bremsstrahlung target yield temporal and spatial data about the collapse of the magnetic insulation at the interface of a MITL and diode. Note that the center Compton diodes (i.e., Compton diodes 5 and 6 in figure 6) have slower risetimes than the Compton diodes placed at greater radii. Compton diodes 1 and 10 correspond to the early part of the pulse shown in figure 7. The slower pulses on Compton diodes 5 and 6 correspond to later parts of the pulse in figures 7 and 8. The bremsstrahlung pulse-shape measurements in figure 13 show that it might be possible to obtain a very fast and narrow bremsstrahlung output pulse by constructing an annular high-Z, high-conversion-efficiency thick bremsstrahlung target. The central region of the anode corresponding to the anode area impinged upon by slow-rising electrons should be constructed of a low-Z inefficient-bremsstrahlung-producing material.

Figure 14 shows a measurement obtained with a 19-in. AK gap. Note that in figure 14 the first bremsstrahlung monopolar pulse corresponding to the monopolar MITL ripple has nearly disappeared and that the bremsstrahlung photodiode measurement is primarily due to the second bremsstrahlung monopolar pulse. The diode configuration with the 19-in. gap discriminates against the bremsstrahlung produced by

the first monopolar MITL voltage and current pulse. The 19-in diode spacing results in a bremsstrahlung risetime that corresponds to the larger voltage and current of the second monopolar pulse.

Conclusion

Because of jitter between the four parallel Aurora sections and because of the monopolar fine structure in the four individual Marx-Blumlein sections, the Aurora in its conventional focused mode has a risetime of approximately 60 ns. By increasing the vacuum coaxial length and increasing the anode-cathode gap distance it has been possible to reduce the risetime of an individual Aurora diode to approximately 15 ns.

Bremsstrahlung pulse shapes can be controlled by diode reconfiguration and gas cell drift tube nose erosion to yield various pulse shapes.[1-6] Risetimes can be varied from 15 to 60 ns. By using the diverter shown in figure 4 the pulse widths can be varied from 15 to 120 ns. The next step in this work is to combine diode risetime enhancement with drift tube nose erosion.[1-4] The practical goal of the work presented here is to manipulate bremsstrahlung pulse shapes. In order to obtain shot-to-shot consistency it is necessary to have a source of stable and consistent pulses produced by the Blumlein/Marx power source. This task is being carried out by D. Weidenheimer et al.[7]

---

1. Enhanced Risetime Bremsstrahlung Environment, M. Bushell, S. Graybill, M. Litz, and G. Merkel, IEEE Trans. Nucl. Sci., NS-31, Dec. 1984, p. 1299.

2. Excitation of a Canonical RF Shelter with Relativistic Electrons and with Enhanced Risetime Bremsstrahlung, M. Bushell, S. Graybill, M. Litz, G. Merkel, and H. Roberts, IEEE Trans. Nucl. Sci., NS-32, Dec. 1985, p. 4320.

3. Electromagnetic Excitation of a Generic Cavity with a Variable e-Beam Pulse, R. Fleetwood, K. Kerris, G. Merkel, H. Roberts, and M. Smith, IEEE Trans. Nucl. Sci., NS-34, Dec. 1987, p. 1508.

4. Variable Ionizing Radiation Pulse Shape at the Aurora, M. Bushell, R. Fleetwood, G. Merkel, M. Smith, Proceedings 8th IEEE International Pulsed Power Conference, San Diego, CA, 1991, p. 826.

5. Generation, Control, and Transport of a 19-MeV, 700-kA Pulsed Electron Beam, T.W.L. Sanford, J. A. Halbleib, J. W. Poukey, D. R. Welch, R. C. Mock, P. J. Skogmo, and K. A. Mikkelson, submitted to Beams 92.

6. Dynamics of electron flow in extended planar-anode diode operating at 19 MV and 700 kA, T. W. L. Sanford, J. A. Halbleib, J. W. Poukey, G. T. Baldwin, G. A. Carlson, W. A. Stygar, G. A. Mastin, T. Sheridan, R. Mock, J. A. Alexander, E. R. Brock, and C. O. Landron, J. Appl. Phys. 67 (4), 1990, p. 1700.

7. Aurora Synchronization Improvement, D. M. Weidenheimer, N. R. Pereira, D. C. Judy, Proceedings 8th IEEE International Pulsed Power Conference, San Diego, CA, 1991, p. 924.

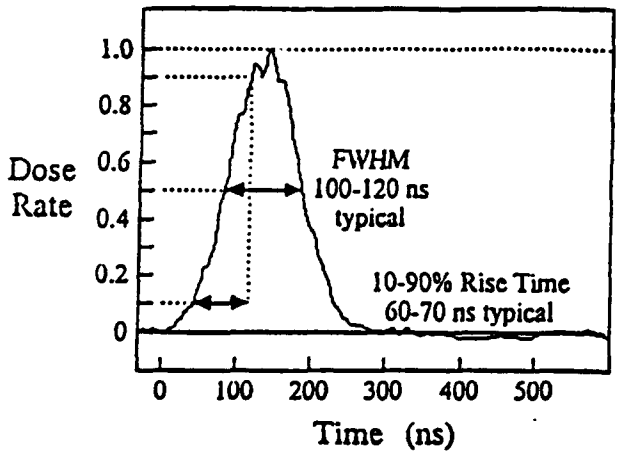

FIGURE 1. Unaltered Aurora bremsstrahlung pulse shape produced by four focussed bremsstrahlung targets.

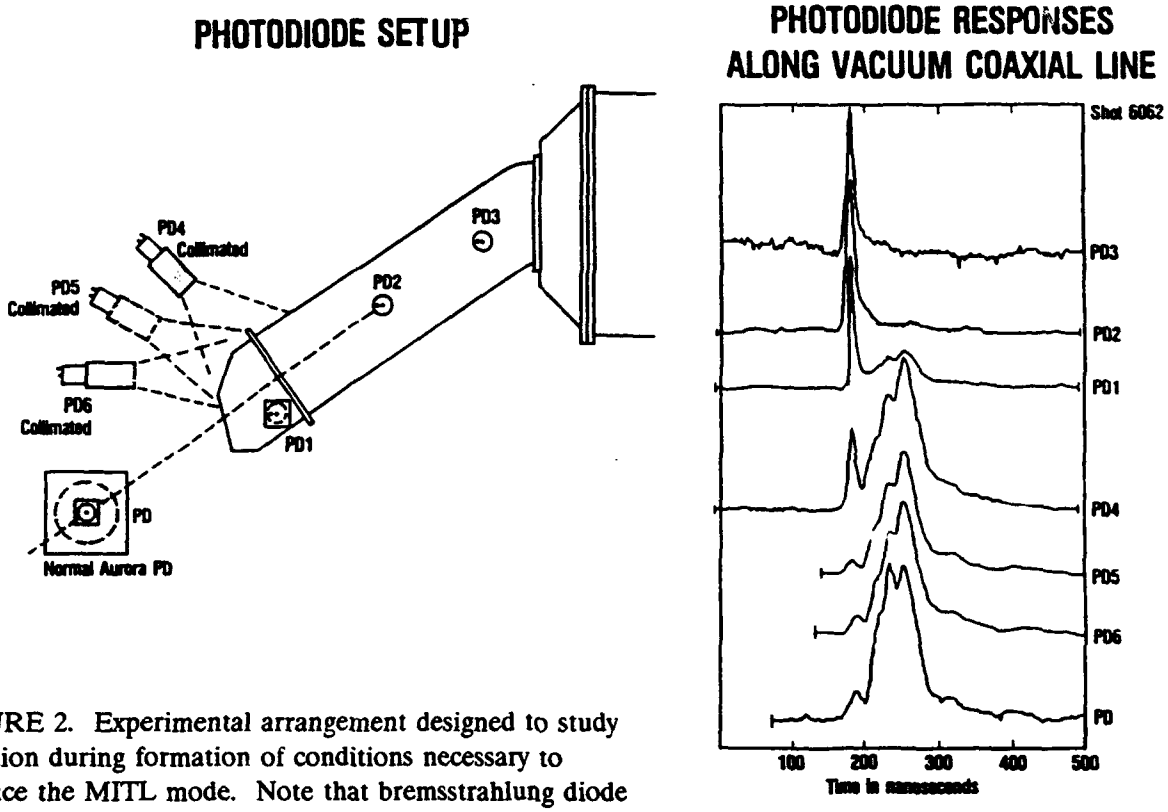

FIGURE 2. Experimental arrangement designed to study radiation during formation of conditions necessary to produce the MITL mode. Note that bremsstrahlung diode region is not cylindrically symmetrical. A series of photodiode (PD) readings corresponding to positions indicated is also shown in the figure - PD1, PD2, and PD3 measure the radiation produced by electrons striking the outer coaxial wall before magnetic insulation sets in.

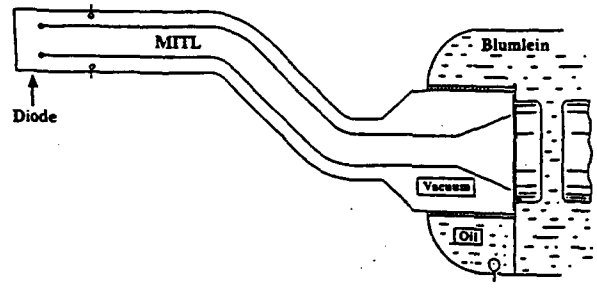

FIGURE 3. Cylindrically symmetrical Aurora diode fed by coaxial vacuum line connected to Blumlein triaxial transmission line. The second bend in the coaxial line points the diode axis parallel to the test cell floor. The transition region between the vacuum coaxial MITL and the oil-filled Blumlein region is not a good impedance match.

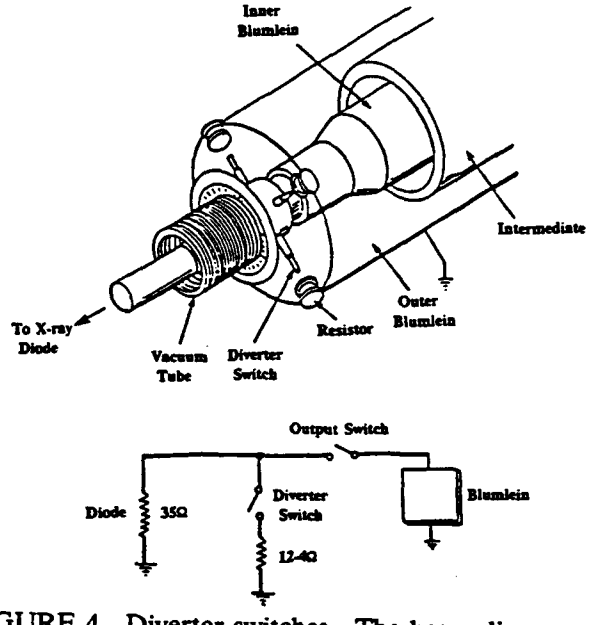

FIGURE 4. Diverter switches. The beam diverter shorts out electron acceleration voltage pulse, allowing pulse length control. The diverter switch is positioned at the intersection of the Blumlein and the coax that feeds the cathode. See figure 3.

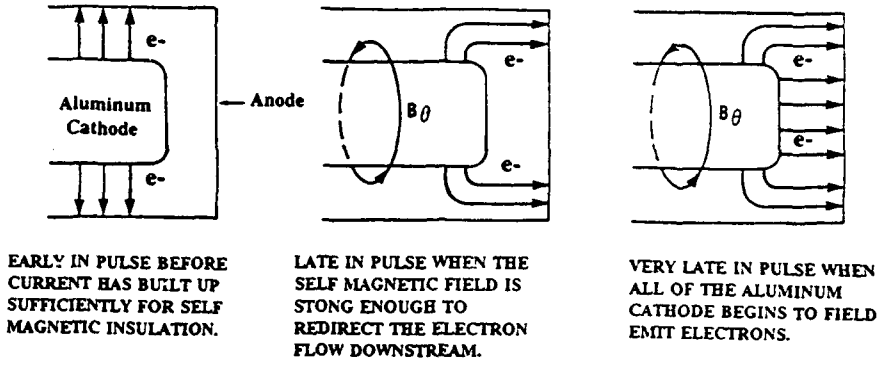

FIGURE 5. Simplified Aurora diode physics.

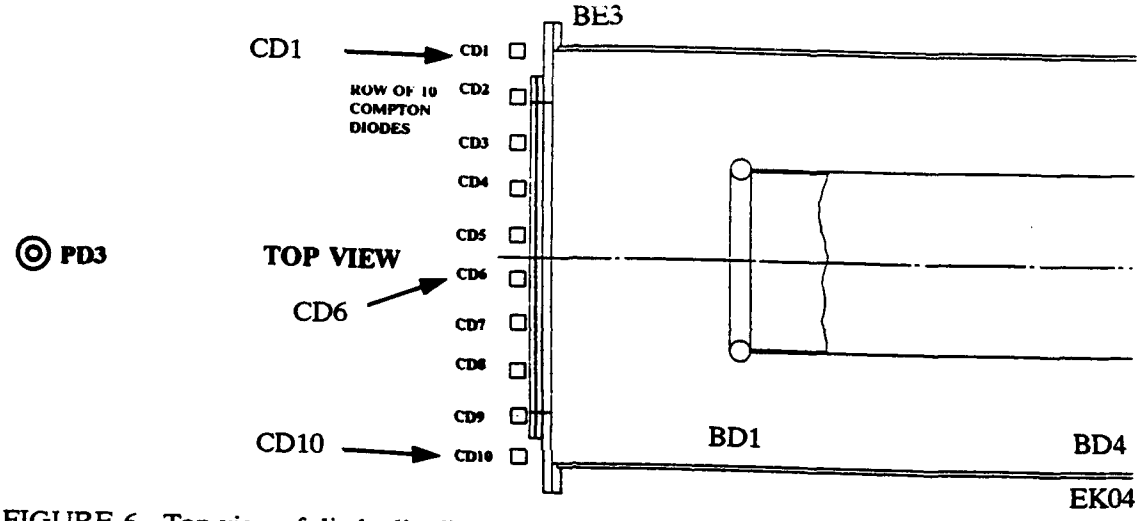

FIGURE 6. Top view of diode distribution across bremsstrahlung target. The 10 Compton (CD1 to CD10) diodes were distributed to obtain spatial and temporal bremsstrahlung distribution across the bremsstrahlung target.

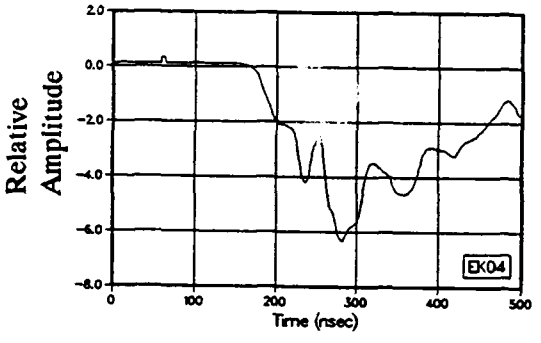

FIGURE 7. Electric field waveform measured along coaxial MITL at position EK04.

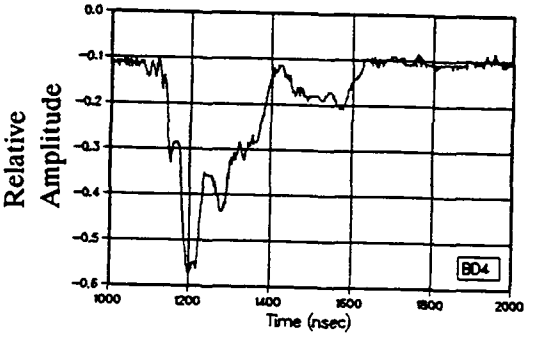

FIGURE 8. Magnetic field waveform measured along coaxial MITL at position BD4.

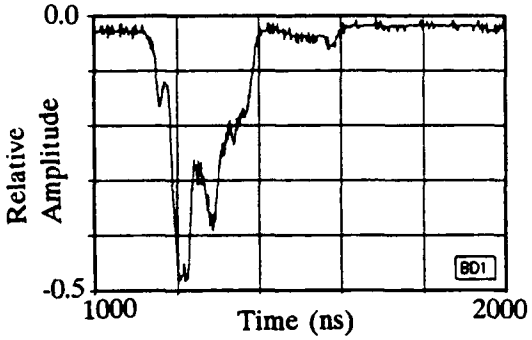

FIGURE 9. Magnetic field waveform measured along coaxial MITL at position BD1.

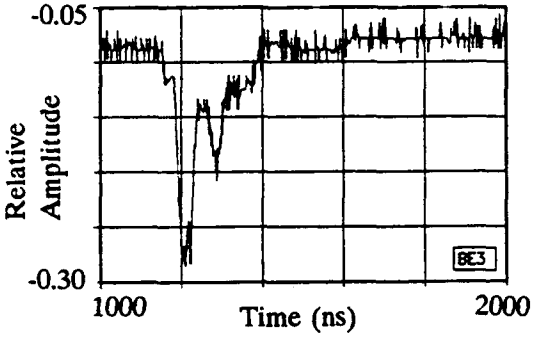

FIGURE 10. Magnetic field waveform measured along coaxial MITL at position BE3.

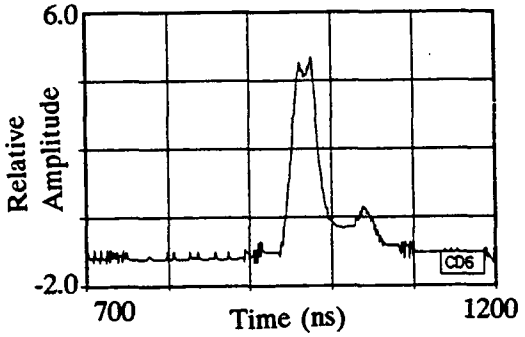

FIGURE 11. Compton diode bremsstrahlung waveform measured by CD6 at position shown in figure 6. Risetime = 14 ns.

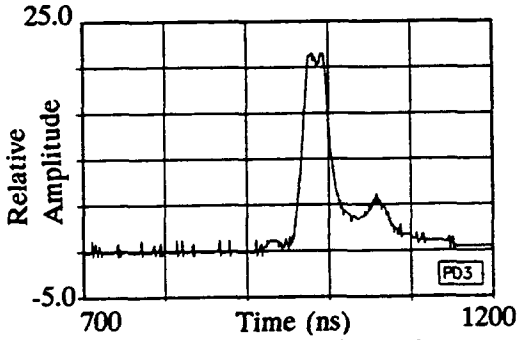

FIGURE 12. Photodiode scintillation detector bremsstrahlung measurement obtained at position PD3 in figure 6. Risetime = 16 ns.

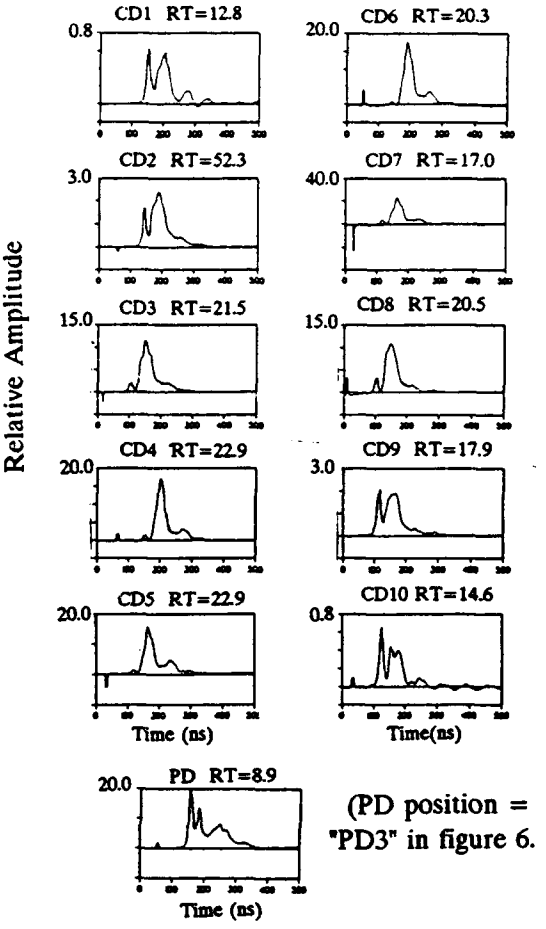

(PD position = "PD3" in figure 6.

FIGURE 13. Pulse shapes measured on 10 Compton diodes (CDs) as shown in figure 6. The outside CDs, i.e., 1 and 10, respond to early part of MITL pulse. CDs 5 and 6 respond to later portion of MITL pulse. The bottom pulse shape marked "PD" corresponds to the entire bremsstrahlung target. "RT" stands for risetime.

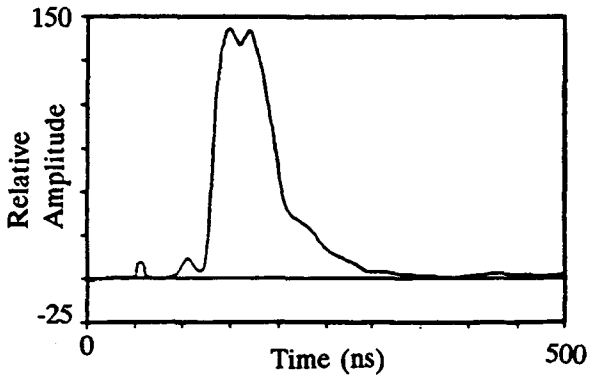

FIGURE 14. Aurora photodiode traces for 19-in. AK gap. The pulse width corresponds to a more open diverter setting than used to obtain results in figure 13. Risetime = 14.6 ns.

APPLICATION OF A SMALL ANGULAR SPREAD BEAM IN THE REFLECTED REB REGIME ON REBEX MACHINE

V.Piffl, V.Boháček, M.Člupek, J.Rauš,
P.Šunka, J.Ullschmied

Institute of Plasma Physics, Czech. Acad. Sci.,
P.O.Box 17, 182 11 Prague 8, Czechoslovakia

ABSTRACT

The possible increase of the heating efficiency by application of a beam with smaller angular spread ($\theta \approx 10^{o}$) in the reflected beam regime is discussed. The pitch angle of peripheral beam electrons is substantialy reduced ($\theta < 10^{o}$) also for the beam with high current density ($\leq 5 kA.cm^{-2}$) by increasing the external magnetic field. The modified REBEX facility has already passed the first tests. The preliminary results of the plasma diamagnetism by 0.5kJ REB injection are presented.

INTRODUCTION

The heating of bulk plasma electrons and the generation of overthermal electrons seem to be the dominant effects set up in REB-plasma experiments in open magnetic systems [1 , 2].

These two phenomena demonstrate again the possibility to exploit REB as a natural and direct tool for efficient and rapid transfer of energy into the plasma, as already supposed at the beginning of the electron beam-plasma studies.

Especially the generation of overthermal electrons was clearly experimentally demonstrated in various devices. Ten per cent of the injected REB energy can be transformed into the high current density, low impedance (100 kA, 10 kV) electron stream applicable in further for classical collisional heating of dense plasmas ($n_p > 10^{22}\ m^{-3}$).

Consequently, relatively small experimental devices with the injection of a nanosecond REB (1-10 kJ) into a plasma in an open magnetic trap could be used for heating of dense gaseous targets or very thin foils to study the matter in extremal conditions.

Search for the optimum conditions of the overthermal plasma

electrons generation in REB-plasma system is one of the aims of the experimental activity at modified REBEX machine.

From the other point of view, the efficient bulk plasma heating up to keV electron temperatures was hardly be expected in nanosecond beam experiments (GOL-M, private communication). Apparently, the microsecond REB-devices are more appropriate for such a bulk plasma heating, at whitch the generation of overthermal electrons precedes the energy transfer into the plasma bulk [4].

Though the physical mechanism of the overthermal plasma electrons generation remains in many respect as open, the basic picture of the beam-plasma interaction in propagating beam regime is described relatively well. If REB with a small angular spread is injected into a homogeneous magnetized plasma, the two-stream instability results in excitation of a small-scale Langmuir turbulence. It is generally accepted that the turbulence is responsible for the observed transfer of the beam energy to the plasma in most experiments. The resulting distribution function of plasma electrons is non-maxwellian with a high-energetic tail carrying a considerable part of the plasma energy. The energy deposition is non-uniform along the plasma column with the maximum located near the beam entrance, as the angular spread of the beam electrons is continually growing along the interaction path [3]. The heating efficiency does'nt exceed 30 per cent.

Surprisingly enough, a comparable heating efficiency was demonstrated at the REBEX experimental facility for the case of an inhomogeneous plasma column and a reflected relativistic beam with a larger angular spread ($>20^{o}$).

REBEX EXPERIMENTAL RESULTS

In our experiments [2] a reflected high-current relativistic electron beam (350 kV, 2-4 $kA.cm^{-2}$, 110 ns, 20 μm Al anode foil) is used. Longitudinal plasma density profile is possible to control. The plasma column ($n_e=10^{14}$-$5x10^{15}$ cm^{-3}, $T_e \approx 1$ eV) is terminated at both ends by thin conducting foils. Behind the exit foil there is a section of vacuum chamber without plasma. Using

a movable collector, two regimes of REB-plasma interaction can be realized. If the collector is far enough from the exit foil, most of REB electrons are reflected back into the plasma from a virtual cathode created near the foil-vacuum boundary. Putting the collector close to the foil, a regime with purely propagating REB is established. The most of our experimental data on beam energy transfer efficiency are based on extensive multichannel measurements of plasma diamagnetism. The results may be summarized as follows:

a) The heating efficiency is always 2-3 times higher in the reflected regime than in the propagating one. About 30% of the beam energy was deposited in a plasma in the reflected beam regime.

b) In an inhomogeneous plasma the highest energy deposition rate is observed in the regions of reduced plasma density, independently of their location along the system. Thus the desired distribution of the deposited beam energy can be controlled by the initial plasma density profile.

MODIFIED REBEX EXPERIMENT

To put the REBEX experiment to a new way for the increase of the energy deposition above 30 % we attempt to applicate a beam with smaller angular spread ($\theta<10^{o}$) in the reflected regime.

The aim of the proposed experiment is the following:

1) To distinguish between the role of the angular spread caused by the pitch angle and by that resulting from the anode foil.
2) To study the role of the reflected beam in enhancement of the heating efficiency.
3) To look for the optimal conditions for overthermal elektrons generation.

The schematic of the modified experimental REBEX facility is shown in Fig.1. Main features of the new arrangement are the following :

a) The pitch angle of peripheral beam electrons is substantially reduced ($\theta<10^{o}$) also for the beam with a high current density (≤ 5 kA.cm^{-2}), by increasing the external magnetic field (1,5 T) in the diode region.

b) Ultrathin anode Al/mylar foils (down to 60 nm/1,5 μm) will be used to reduce the angular velocity beam spread.

c) The role of reflected beam in enhancement of the heating efficiency will be studied by varying the thickness of the terminating foil and the magnetic field strength.

PRELIMINARY RESULTS

The modified REBEX facility has already passed the first tests. Newly installed and reconstructed plasma gun for production of an almost z-homogeneous plasma column has been successfully proved,(see Fig.2.). Solenoidal external magnetic field is reversed by means of pulse coil to form double cusp geometry in the gun region. In reversed field the plasma gun is switched, and discharge between the ring electrode and the terminating foil (along cusp field lines) generates a plasma column. Several hundreds μs later, when mg. field is unperturbed again, the plasma column fills the region between both foils, anode and terminating one. This arangement of plasma source enables the production of the plasma with the maximum plasma density at the axis.

To test the plasma longitudinal profiles, output signals of a set of diamagnetic coils have been recorded at the beam injection. In the REBEX experiment, the diamagnetic signals are modulated by magnetoacoustic configurational waves, the frequency of which is inversely proportional to the square root of the local plasma mass. According to these measurements, the plasma density along the beam interaction path is uniform within the factor two.

The time/space dependencies of the plasma diamagnetism for B_o = 0.4 T, $n_p \geq 10^{20}$ m^{-3} by 0.5 kJ REB injection are shown. In spite of that the quality of the injected beam is still far from the desired one, enhancement of the energy transfer into a plasma along the whole interaction beam path in reflected REB regime is evident.

Full scale experiments on the modified REBEX facility will start in autumn 92.

References:

[1] A.V.Burdakov, V.S.Koidan, V.Piffl at al.: Bulk plasma heating by a microsecond E-beam in the GOL-3 facility
INP Novosibirsk, preprint 92-8, February 92

[2] V.Babický at al.: New results on REB plasma heating in the REBEX machine
Proc. of the 8th Int. Conf. on High-Power Particle Beams, Novosibirsk, 1990, 225-232

[3] A.K.Arzhanikov, A.V.Burdakov, V.S.Koidan at al.: Physics of the REB-plasma interaction
Physica Scripta, Vol.T2/2, 303-309,(1982)

[4] A.V.Burdakov, V.Piffl, V.V.Postupaev: Soft x-ray measurements of nanosecond-E-beam-heated plasma
Proc. of this Conference, BEAMS'92, Washington

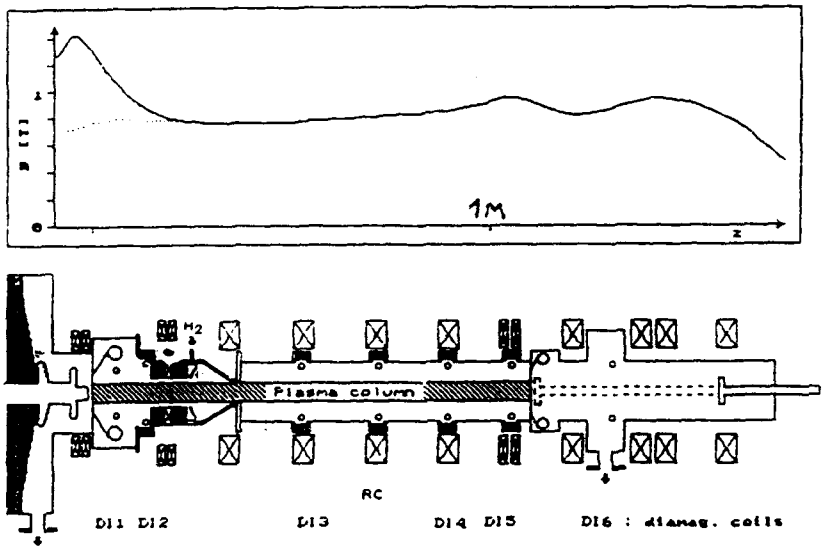

Fig.1. Modified REBEX facility

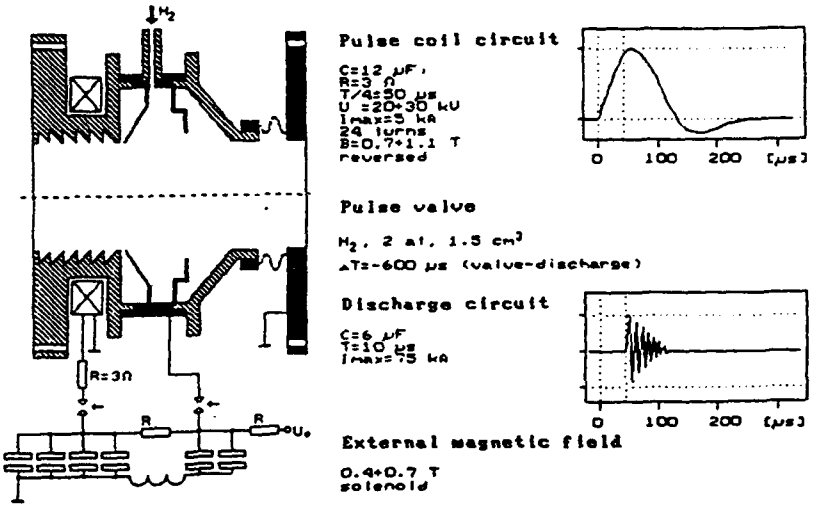

Fig.2. Plasma gun

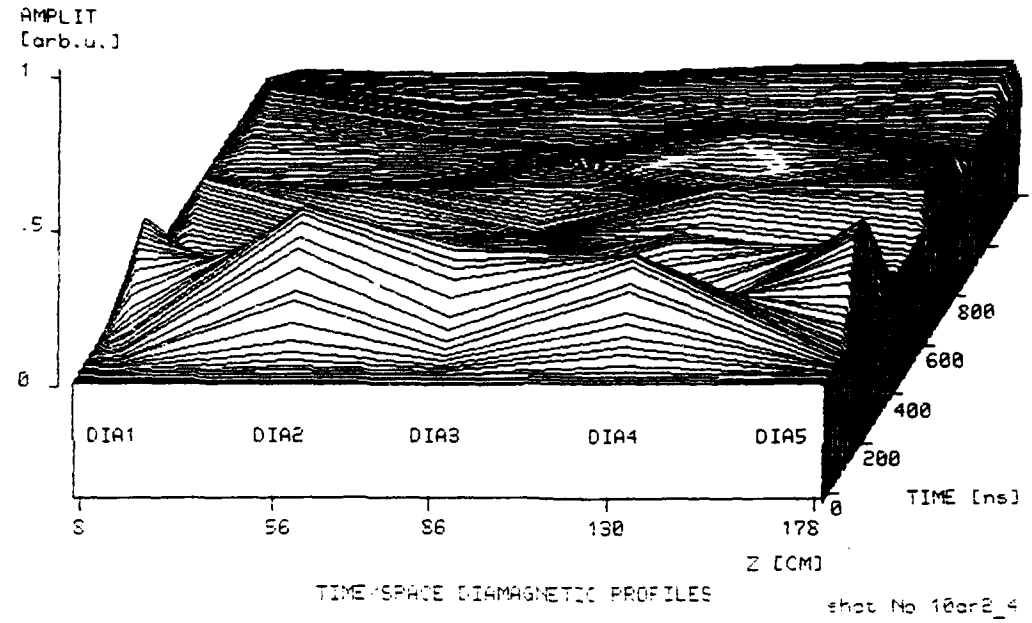

Fig.3a. Propagating beam regime

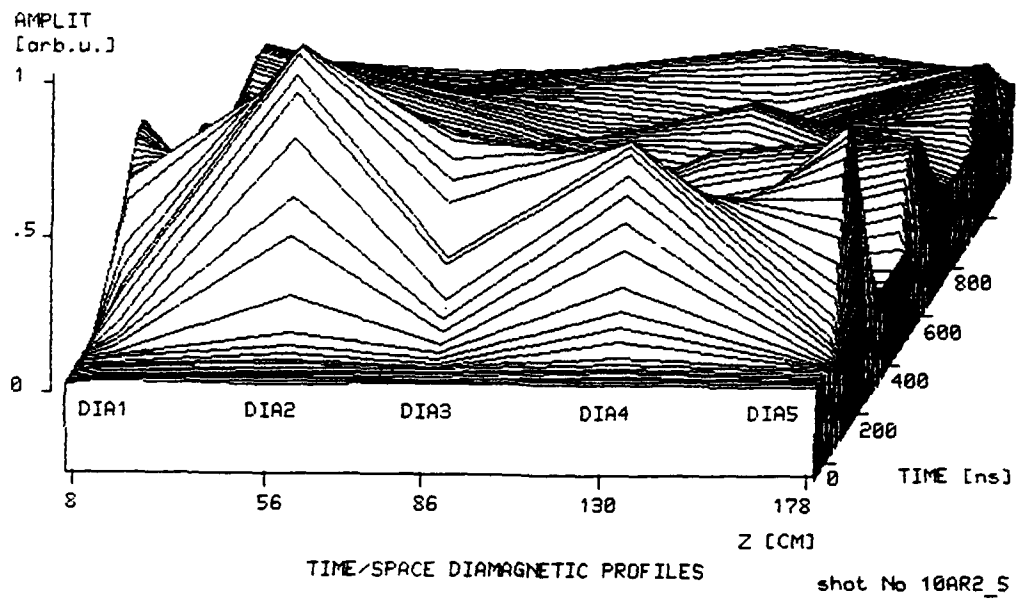

Fig.3b. Reflected beam regime

AN EXPERIMENTAL STUDY OF STRONG TURBULENCE DRIVEN BY AN INTENSE RELATIVISTIC ELECTRON BEAM

M. Masuzaki, R. Ando, M. Yoshikawa, H. Morita, J. Yasuoka and K. Kamada

Department of Physics, Faculty of Science, Kanazawa University
Kanazawa 920, Japan

Abstract An intense relativistic electron beam (IREB) was injected into an unmagnetized axially decaying plasma. Observed were excitation of rapidly oscillating electric fields such that $W = \varepsilon_0 \langle E^2 \rangle / 2n T_e > 1$ which lasted as long as about 30 times longer than the beam duration, broadening of the distribution of beam electrons about the initial energy, acceleration of plasma electrons, current enhancement and the total microwave power radiated in the frequency range 18~40 GHz. The experimental data are discussed in connection with the strong Langmuir turbulence.

INTRODUCTION

Until now we have carried out several experiments concerning collective ion acceleration [1], current enhancement [2] and high-power, broadband microwave radiation [3] by injecting an IREB into an axially decaying plasma. However, mechanisms of these phenomena are not yet clear. Thinking that these phenomena in our IREB-plasma system were related to the IREB driven strong Langmuir turbulence which has recently attracted much attention [4~7], we conducted following experiments; (1) measurements of quadratic Stark shifts of neutral He lines [5] in order to ascertain presence of rapidly oscillating electric fields by using an 8-channel spectroscopic system, (2) measurements of change in the energy distribution of electrons due to the IREB-plasma interaction by using a compact magnetic energy analyzer, (3) measurements of microwave radiation and (4) measurements of the net current, the beam current and the beam profile.

EXPERIMENTAL APPARATUS

Figure 1 shows the experimental arrangements. The IREB generator used was a modified Pulserad 110A produced by Physics International, which generated a nominally 1.5 MV-27 kA-30 ns pulse in a conventional diode. Two types of diodes were used in the experiment. The diode A [Fig 1(a)] consisted of a cathode made of 3 mm-diam. tungsten rod and a carbon anode with a 2 cm-diam. hole in the axis, and the A-K distance was about 7 mm, while diode B [Fig. 1(b)] consisted of a carbon cathode of 36 mm-diam. and a titanium foil anode of 15 μm thick, and the A-K distance was 3 cm. The drift chamber was of stainless-steel and 16 cm in diameter and 46 cm in length. Its inner wall surface was covered with sheets of electromagnetic wave absorber (ECCOSORB AN) to eliminate spurious reflections of microwaves. The base pressure was kept below 5×10^{-5} Torr. For the Stark shifts measurement it was filled with about 20 mTorr of He.

The plasma was produced by two rail-type plasma guns set opposite to each other [3] (Fig.1). The discharge current reached its peak at about 6 μs and decayed with time constant of

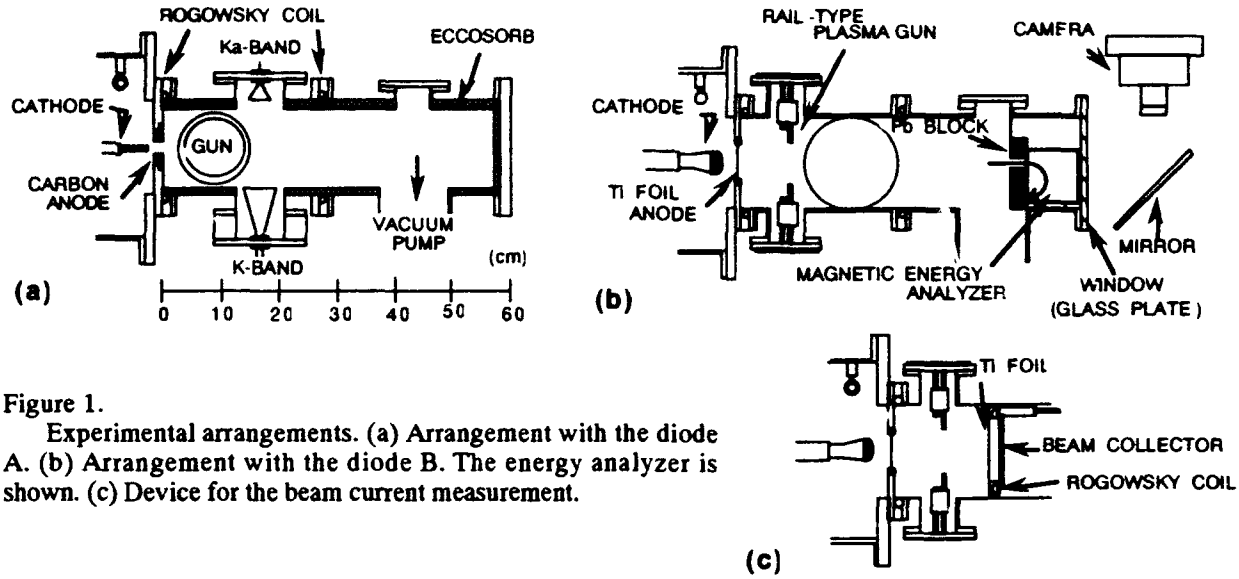

Figure 1.
Experimental arrangements. (a) Arrangement with the diode A. (b) Arrangement with the diode B. The energy analyzer is shown. (c) Device for the beam current measurement.

about 20 μs. The delay time, τ, between the firing times of the gun and the IREB was variable. Figure 2 shows the plasma density as a function of time at z = 17.5 cm, z being the distance from the downstream side of the anode.

Information on rapidly oscillating electric fields can be obtained from quadratic Stark shifts of HeI 5016 Å line to the blue side and 6678 Å line to the red side [8]. In order to measure shifts in one shot we prepared an 8-channel spectroscopic system which covers spectral range of about 3 Å by utilizing a 0.5 m Ebert-type monochrometer. Optical emissions from the plasma were guided through a collimator and an optical fiber of 200 μm in diameter and 20 m long to the entrance slit of the monochrometer. Rays emitted through a rod lens attached to the exit slit of the monochrometer irradiated a bundle fiber, which consisted of 64 fibers of 200 μm in diameter arranged in rectangular matrix configuration of 8 × 8. Each array of 8 fibers guided light to a fast response photomultiplier. Output of each detector channel was led to fast oscilloscopes. The wavelength spacing between neighboring channels was 0.4 Å. Each channel had a resolution corresponding to 0.3 Å FWHM. The spectroscopic system was set so as for the unshifted line to fall on the center channel. Number of spikes in each channel was counted and counts obtained from 10 shots were added. Measurements were made at z = 17.5 cm.

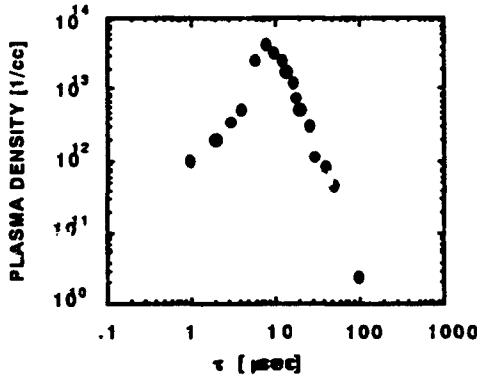

Figure 2. Plasma density at z = 17.5 cm.

Spectra of radially radiated microwaves were measured using the same 5-channel spectrometer used in a previous experiment [3], which covered a frequency range from 18 GHz to 40 GHz, and a 100 m Ku band dispersive line. Horns were set at z = 17.5 cm [Fig. 1(a)].

In order to measure the energy distribution of the beam electrons due to the IREB-plasma interaction a compact 180° magnetic energy analyzer [9] was set at the end of the drift chamber [Fig. 1(b)]. In this analyzer a uniform magnetic field of 0.355 T was produced by a pair of ferrite magnets of dimension 50 × 50 mm set face to face with a 2-mm separation. A phosphor screen was used as the detector and in each shot the results were recorded on Polaroid film by taking an open shutter photograph of the phosphor. Recorded films were image analyzed.

The net current I_n and the beam current I_b were measured separately using the same Rogowsky coil [Fig. 1(c)]. For the net current measurement removed were titanium foil of 15 μm thick attached in front of the Rogowsky coil and the beam collector attached at its backside. The beam profile was also measured using a target-phosphor combination, which intercepted the beam. Open photograph of the phosphor was taken.

EXPERIMENTAL RESULTS AND DISCUSSIONS

The beam current density was higher in the experiments with the diode A than in the experiments with the diode B, but the IREB-plasma system became macroscopically unstable for τ longer than about 7 ~ 8 μs, while in the latter experiments the IREB-plasma system was rather stable and τ could be changed for a wide range .

Experiments with the Diode A

Figure 3 (a) shows the spectral shape of the 5016 Å line when τ = 8 μs. Output of each channel lasted so long as about 1 μs. Number of spikes during first 500 ns were counted. The full curve is a Gaussian distribution fitted to the experimental points on the red side. According to data compiled by Ryde [8] the shift measured in the fourth channel from the center channel corresponded to rms electric field of 110 ~ 125 kV/cm. The data were fitted to the $\exp[-(E/U)^2]$ distribution [5] as shown in Fig. 3 (b), with U = 156 kV/cm.

With the rms field value obtained the ratio of the electric field and the plasma energy densities $W = \varepsilon_0 \langle E^2 \rangle / 2nT_e > 1$ (T_e is assumed to be between about 10 and 100 eV), indicating that chain of events such as creation, collapse and burn out of cavitons is a dominant process in the IREB-plasma system, but usual assumption of the strong Langmuir turbulence $W \ll 1$ is violated.

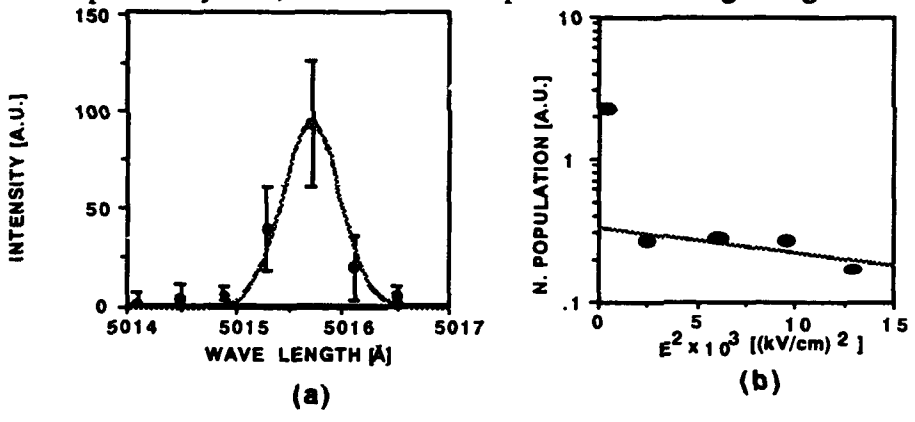

Figure 3.
Shift of the 5016 Å line for τ = 8 μs. (a) Spectral shape observed. (b) Distribution of electric fields.

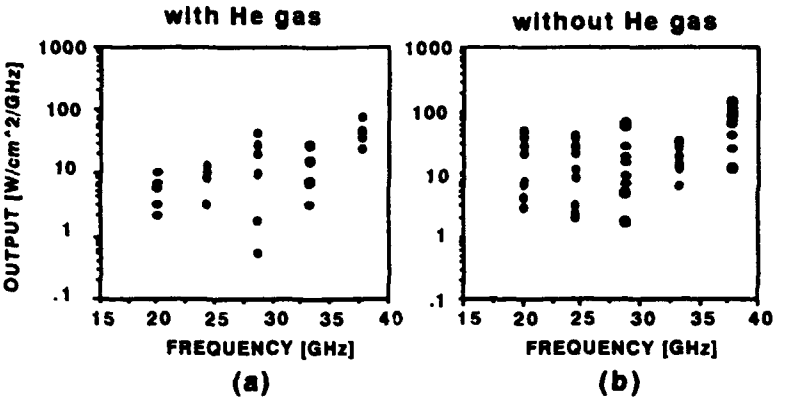

Figure 4.
Spectra of microwave radiation from 18 to 40 GHz for τ = 7 μs. (a) With helium gas of about 20 mTorr filled in the chamber. (b) Without helium gas.

Persistence of Stark shifts after the beam pulse may be explained partially by the two component strong Langmuir turbulence model of Robinson and Newman [10] as discussed in [6].

Spectra of the microwave radiation for τ = 7 μs with and without He gas are shown in Fig. 4. Characteristics of the spectra, that is, high-power and broadband above the plasma frequency, were almost the same as those obtained previously [3]. The duration of the radiation was almost the same as or less than the beam duration, indicating that beam electrons were radiation sources and radiation was not the main mechanism of energy dissipation of cavitons at their burn out.

Experiments with the Diode B

Microwave radiation at z = 17.5 cm and I_n and I_b at z = 17.5, 30 and 42 cm were measured as a function of τ. Figure 5 shows dependence on τ of the total power of microwave radiation from 18 to 40 GHz and mean values of three shots of the both currents at z = 17.5 cm. The results indicate, when compared with the plasma density at z = 17.5 cm shown in Fig. 2, peaking of the total power of radiation and the both currents as well as current enhancement on both sides of the density peak. The spectra of microwave radiation were also broad but the total power was an order or two lower than that obtained in the experiments with the diode A. Monitored power of radiation in Q-band (40 ~ 60 GHz) showed almost the same tendency. Stark shifts measurements indicated that existence of rapidly oscillating strong electric fields and current peaking were concurrent phenomena. The rms values were lower than those in the experiments with the diode A, but still $W > 1$. In Fig. 5 shown also is the ratio of the beam electron density and the plasma density n_b/n_p, n_b being determined from the beam current and the beam profile. Such much strong turbulence seems to disappear when n_b/n_p is less than about 0.01.

Figure 6 shows dependence of the energy spectra of electrons on τ. As τ was increased the width of the energy distribution of beam electrons increased about the initial energy until $\tau \simeq 60 \sim 70$ μs, and then it decreased again. This broadening of the energy distribution of beam electrons might result from collisions of beam electrons with cavitons [4], but in our case the broadening was not symmetric with respect to the initial energy. It is worth noting that there were some electrons with energy lower than about 200 keV. We believe that these electrons are accelerated

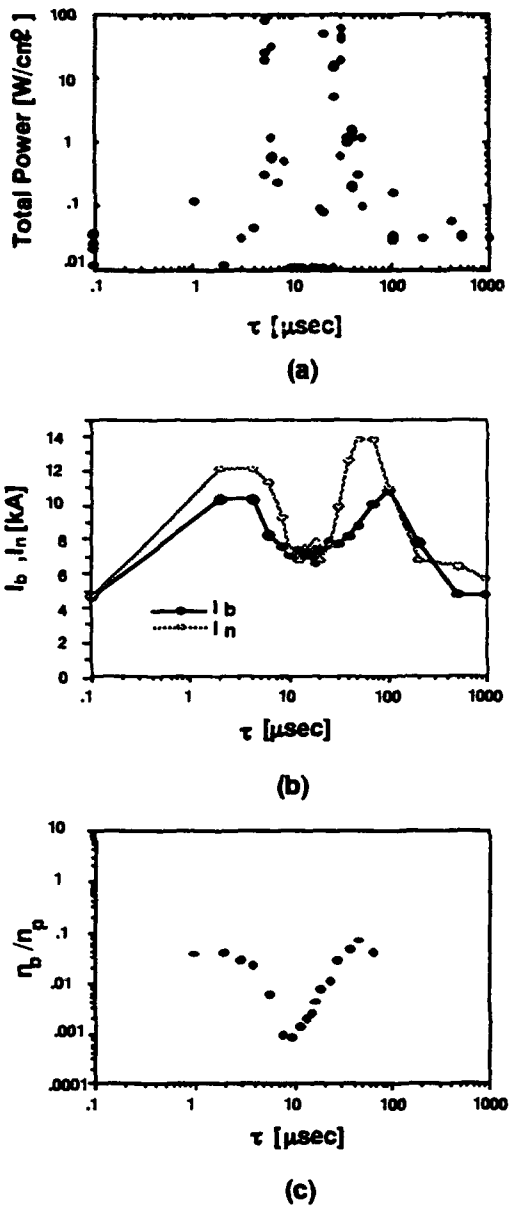

Fig. 5. Dependence on τ of (a) the total microwave power, (b) I_n and I_b, and (c) n_b/n_p.

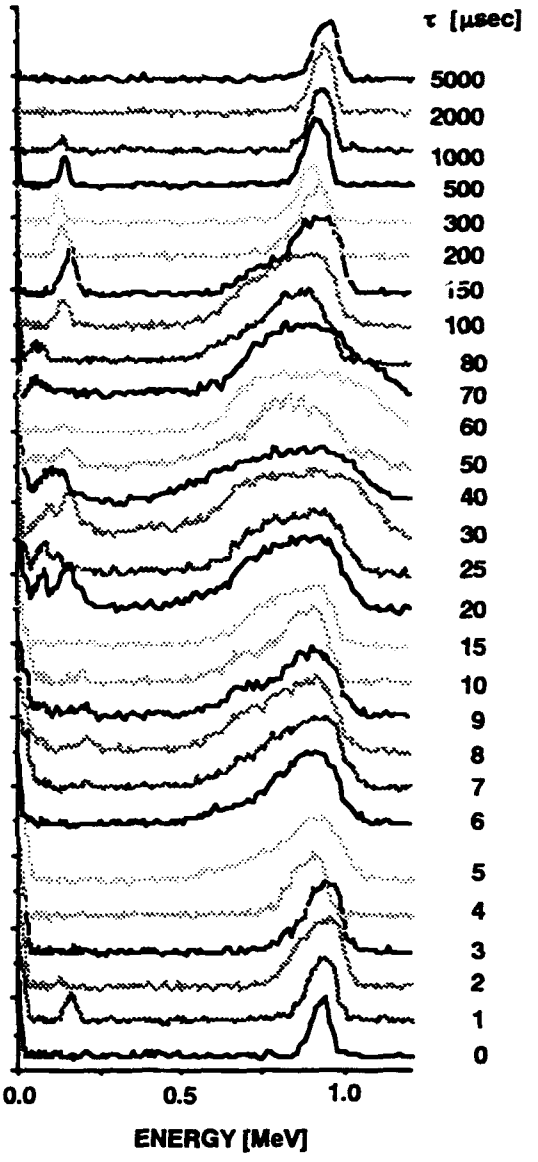

Fig. 6. Dependence of energy distribution of electrons on τ.

plasma electrons. Perhaps field energies went to plasma electrons when cavitons burnt out.

Peaking of I_n and I_b as well as current enhancement may be due to accelerated plasma electrons. Electrons with energy higher than about 65 keV can pass through the titanium foil attached in front of the Rogowsky coil. We think that the measured I_b included contribution of electrons accelerated above this energy, while plasma electrons accelerated below this energy also contributed to I_n, hence current enhancement followed. As shown in Fig. 7, when z was increased, the first peaks of both currents approached to the second peaks and heights of the second

peaks increased. More plasma electrons might be accelerated in the downstream. Results of the measurements of the energy spectra of electrons appear to support the above discussion. Since the energy analyzer was set at the end of the chamber, its results might closely correlate to the plasma behavior near the end of the chamber. Both currents at z = 42 cm were higher in the range of τ where broadening of the spectrum of beam electrons and acceleration of plasma electrons were remarkable.

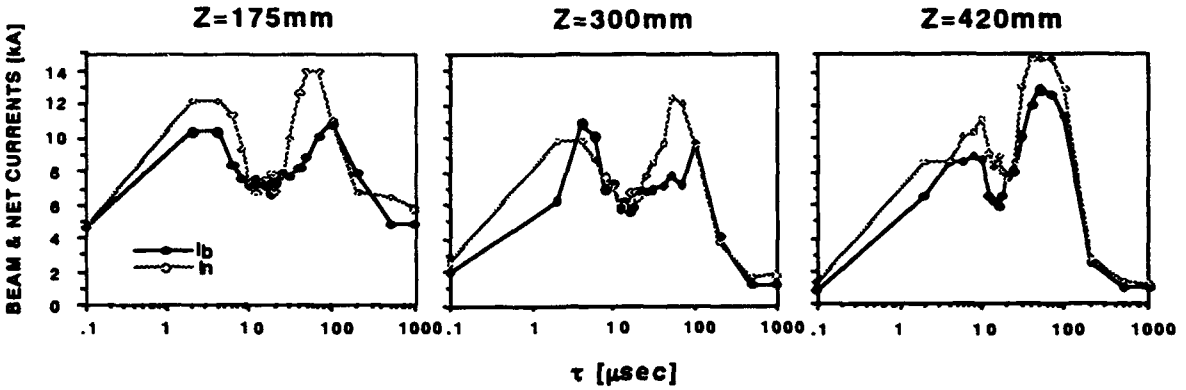

Figure 7. Dependence of I_n and I_b on z.

CONCLUDING REMARKS

We are now carrying out further investigation including application of laser fluorescence method to a forbidden line measurement using a 4-level system, time resolved measurement of energy spectra of accelerated plasma electrons and measurement of higher frequency radiation. Also an axially uniform helium plasma is being prepared for a comparative study.

ACKNOWLEDGEMENT

The authors would like to thank H. Koguchi , K. Kobayashi and D. Yamada for their assistance during the experiments. This work was supported in part by a Grant-in-Aid for Scientific Research from the Ministry of Education, Science and Culture.

REFERENCES

[1] M. Masuzaki, K. Kamada, H. Shirataki, K. Yamamura, T. Mitsui, H. Akiyama and S. Kawasaki: *Proceedings of the 6th International Conference on High-Power Particle Beams*, edited by C. Yamanaka (Osaka University, Osaka, Japan, 1986), p. 759.
[2] M. Masuzaki, K. Kamada and H. Shirataki: J. Phys. Soc. Japan **56** (1987) 1274.
[3] M. Masuzaki, R. Ando, A. Yoshimoto, M. Ishikawa, M. Yoshikawa, K. Kitawada, H. Morita and K. Kamada: *Proceedings of the 8th International Conference on High-Power Particle Beams*, edited by B. N. Breizman and B. A. Knyazev (World Scientific, Singapore, 1991), Vol. 2, p. 683.
[4] G. C. A. M. Janssen, E. H. A. Granneman and H. J. Hopman: Phys. Fluids **27** (1984) 736.: H. J. Hopman and G. C. A. M. Janssen: Phys. Rev. Lett. **52** (1984) 1613.
[5] D. Levron, G. Benford and D. Tzach; Phys. Rev. Lett. 58 (1987) 1336.
[6] G. Benford, X. Zhai and D.Levron: Phys. Fluids, B3 (1981) 560.
[7] P. A. Robinson and D. L. Newman: Phys. Fluids, B2 (1980) 3120.
[8] N. Ryde: *Atoms and Molecules in Electric Fields* (Almquist & Wiksell International, Stockholm, 1976).
[9] R. F. Schneider, C. M. Luo, M. J. Rhee and J. R. Smith: Rev. Sci. Instrum. **56** (1985) 1534.
[10] P. A. Robinson and D. L. Newman: Phys. Fluids, B2 (1980) 2999.

INTENSE ELECTRON BEAM RADIUS-TAILORING EXPERIMENT FOR PROPAGATION STUDIES*

D. J. Weidman,[a] J. D. Miller, K. T. Nguyen,[b]
M. J. Rhee,[c] R. F. Schneider, and R. A. Stark

Naval Surface Warfare Center/White Oak
Silver Spring, Maryland 20903

We have generated a "radius-tailored" electron beam, a beam that is tapered with a larger head and a smaller tail, using a Fast rise-time magnetic Focusing Coil (FFC) around a vacuum drift tube placed downstream of the electron beam diode. The electron beam is injected during the rise time of the FFC magnetic field so that the beam head expands, while the beam body and tail are confined by the axial magnetic field of the FFC. The electron beam for this experiment is 1.7 MeV, 1 kA, and 13 ns flattop. Time-resolved beam radius measurements, from a scintillator viewed by a streak camera, indicate the beam radius as a function of time. Intense relativistic electron beams propagating through a gas exhibit the resistive hose instability. The growth rate of the hose instability can be reduced by "tailoring" the beam radius from a large head to a small tail. The next step of the experiment would be to study the propagation characteristics of the radius-tailored beam in neutral gas. This beam could be injected into a gas-filled drift tube to compare the propagation characteristics to those of an untailored beam. Diagnostics could include $\dot{B}$ probes to measure the beam centroid and an open-shutter camera.

Introduction

Propagation of an intense relativistic electron beam through a gas without an external focusing magnetic field is possible.[1] The electron beam creates a conductivity channel which neutralizes the beam space charge. Propagation distance, however, can be limited by the resistive hose instability,[2,3] which allows growth of transverse ($l = 1$) motion of the entire beam, or "hosing," and eventually destroys the beam. It is possible to reduce the growth rate of this instability by tapering the beam radius from head to tail. This is known as "beam radius tailoring."

The technique used in this experiment for generating a radius-tailored electron-beam is shown in Fig. 1. The Fast rise-time Focusing Coil (FFC)[4] is a one-turn copper coil which is energized by a high-voltage pulse-forming-line machine called TRANSBEAM.[5] The fast variation in magnetic field occurs during the rising portion of the TRANSBEAM pulse. The electron beam is fired through the FFC during the rise time of the magnetic field of the FFC.

In this technique, the beam head is allowed to expand due to the beam space charge and emittance, when the axial magnetic field in the FFC is low. As the magnetic field in the FFC is ramped up, the beam body and tail are gradually focused. This produces a radius-tailored beam at the end of the FFC. Such a radius-tailored beam can be passed through a foil to produce an emittance-tailored beam, so that the radius tailoring is preserved during propagation. The result is a beam that has a larger head than the original beam radius and a body and tail with the radius roughly the same as the original beam radius.

* This work was supported by DARPA under ARPA Order No. 7792 BASIC.

[a] Laboratory for Plasma Research, University of Maryland, College Park, MD 20742, Advanced Technology and Research Corp., Laurel, MD 20707, and Naval Research Laboratory, Washington, DC
[b] Mission Research Corporation, Newington, VA 22122
[c] Laboratory for Plasma Research, University of Maryland, College Park, MD 20742

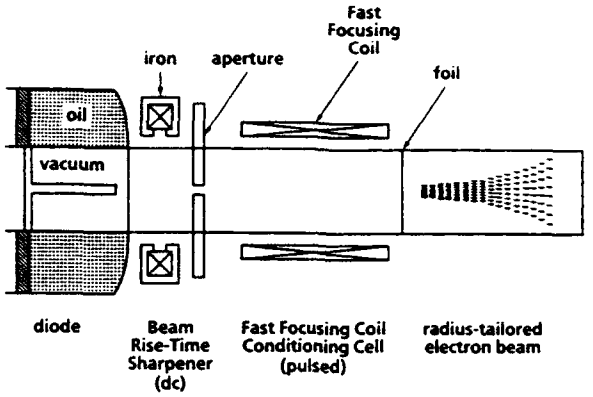

Fig. 1: Schematic of the magnetic beam conditioning experiment. The entire experiment is in vacuum. Beam measurements were performed at the foil location.

Experimental Arrangement

Figure 1 is a schematic of the experimental setup composed of: the Febetron diode, the Beam Rise-Time Sharpener[6] (BRTS), the Fast Focusing Coil, and the foil.

It is important for the beam to have a flattop current profile so that the radius tailoring can be clearly attributed to the FFC alone. If the beam current were not constant during the pulse, then the beam radius would vary, even if all other parameters were constant. A flattop current profile is produced by the Beam Rise-Time Sharpener, which consists of a dc focusing magnet and a graphite aperture; it sharpens the beam rise-time to 6 ns with a 12-ns flattop at 1 to 2 kA.

The Fast Focusing Coil conditioning cell consists of a glass vacuum drift chamber with eight axial 2.5-cm-wide copper-foil current-return strips, surrounded by the external, one-turn FFC. The copper axial strips provide a current-return path for the electron-beam current while allowing penetration of the FFC magnetic field to the axis of the system. The FFC is a single turn to minimize inductance, thereby minimizing the rise time of the magnetic field. Its axial length is 38 cm and its diameter is 20 cm. The FFC power source is TRANSBEAM,[5] a 7-Ohm machine that formerly produced a 700-keV, 100-ns electron beam. The electron-beam diode was removed, and a transition section connects the end of TRANSBEAM's 7-Ohm coaxial transmission line to ten 70-Ohm high-voltage (rated at 300 kV dc) coaxial cables, as shown schematically in Fig. 2. These ten cables allow flexibility in positioning the FFC. The ten cables are connected to the FFC, with the center conductors (#4 AWG) connected to one side of the coil and the outer conductors (3.8 cm diameter braid) connected to the other side.

The magnetic field in the z direction inside the FFC was mapped in detail using passively-integrated $\dot{B}$-probes and found to be uniform inside the coil with very little variation in z, r, or θ.

Experimental Measurements and Results

Data was collected from a 1-mm thick plate of fast rise-time (2 ns) scintillator,[7] which produces visible light (blue) when the electron beam passes through it. The scintillator was viewed by a streak

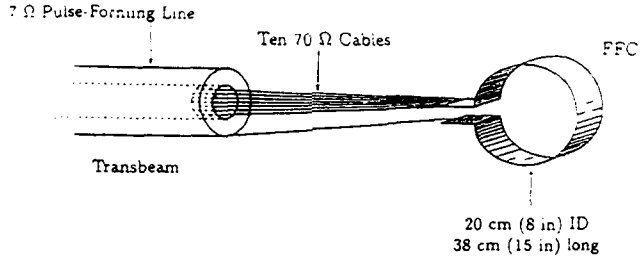

Fig. 2: TRANSBEAM-driven fast focusing coil.

camera and the streak camera image was recorded by photographic film. The streak camera provides a continuous measurement of a diameter of the beam as a function of time throughout a single beam pulse.

For an example of the data that was collected, consider a typical radius-tailored shot. Figure 3(a) shows the relative timing of the FFC field, which was determined from a measurement of the current through the FFC, and the beam current, which was measured by a Rogowski coil between the BRTS and the FFC. Note that the magnetic field is rising during the electron beam pulse. Figure 3(b) shows a computer-digitized version of the streak photograph from a typical radius-tailored shot (0708). Slices of this streak photograph represent the beam current density profile at different instants of time.

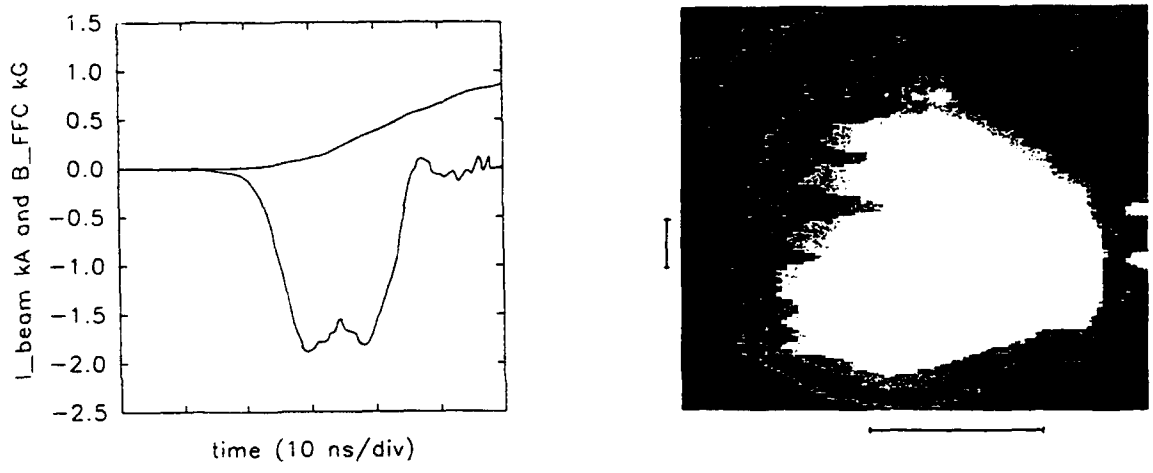

Fig. 3: Typical radius-tailored shot (0708): (a) Relative timing of the FFC magnetic field (upper trace) and electron beam current (lower trace). (b) Computer-digitized version of the streak photograph. The vertical bar to the left of the photo indicates a distance of 1 cm; the horizontal bar at the bottom represents a duration of 10 ns; time flows from the left to the right.

These slices were analyzed by computer to provide beam root-mean-squared (rms) radius-versus-time information. Because of nonlinearities in the scintillator and photographic film, the intensity is an approximation to the electron-beam current density. A Gaussian beam profile was assumed and fitted to each slice. These profiles are plotted in Fig. 4(a), for the case of a radius-tailored beam. The horizontal axis represents the position in the slice. Note the variation in the Gaussian radius from the beam head to the beam tail. This variation is plotted explicitly in Fig. 4(b), which shows that the radius tailoring ratio is on the order of 3:1. (The points in Fig. 4(b) represent only that portion of the beam for which there is significant current.)

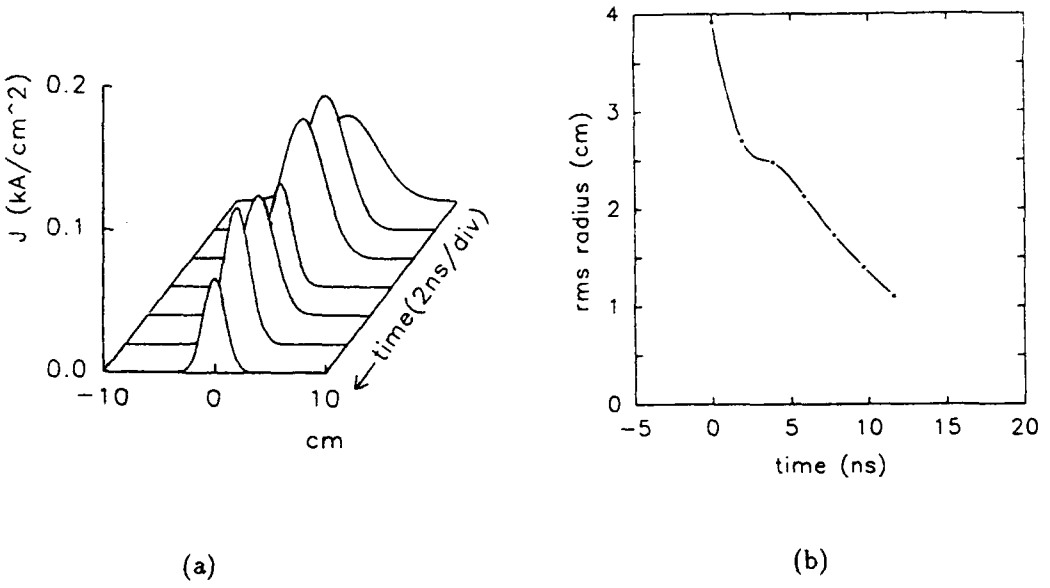

Fig. 4: Typical radius-tailored shot (0708): (a) Profiles of the radius-tailored beam: These are Gaussian fits to slices of beam current-density versus diameter at seven instants of time from the beam head to the beam tail. Note the variation of radius from head to tail. Note also that the double-peaked shape of the current density versus time corresponds to the double-peaked shape of the current versus time in Fig. 3(a). (b) This plot shows explicitly the radius versus time of the electron beam. Each point is from one of the Gaussians in Fig. 4(a).

For comparison, results from an untailored shot (0683) are shown in Fig. 5. This is a reference shot: the FFC field is relatively constant during the beam pulse. The electron-beam current is similar to that shown in Fig. 3(a). The curves fitted to current density profiles are shown in Fig. 5(a) and the rms radius is plotted in Fig. 5(b). Note the relatively constant current density and beam radius.

Computer Simulations

MAGIC simulations[8] were performed using the experimental parameters of the electron beam and the FFC as input data to allow direct comparisons to the experiment. The experimental parameters used were radius, divergence, emittance, and current of the electron beam injected into the FFC and the FFC magnetic field profile as a function of time.

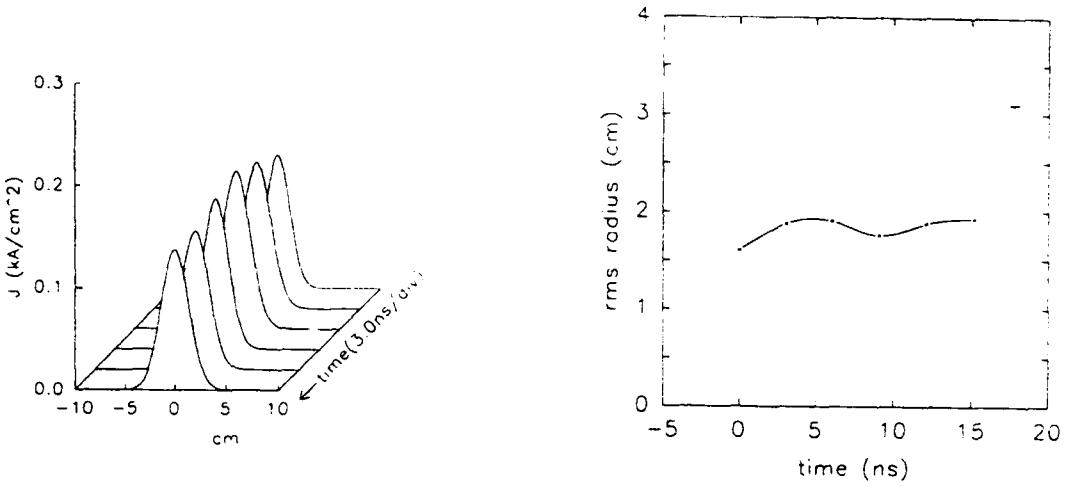

(a) (b)

Fig. 5: Typical untailored shot (0683): (a) Profiles of an untailored beam: These are Gaussian fits to slices of beam current density versus diameter. Cf. Fig. 4(a). (b) rms radius versus time of the electron beam.

A MAGIC simulation of the radius-tailored case was performed. The results are shown in Fig. 6(a) in the form of five snapshots during the beam pulse. The right edge corresponds to the position of the scintillator. At the scintillator position, the beam radius can be seen to be large at early times and smaller at later times. A MAGIC simulation of the untailored case also was performed. The results are shown in Fig. 6(b) in the form of five snapshots during the beam pulse. The beam is overfocused inside the FFC and then expands before reaching the scintillator. The radius at the scintillator can be seen to be roughly constant, consistent with the experimental results in Fig. 5(b). Simulations using the experimentally observed parameters provide results that are in good agreement with the experiment.

Summary

The axial magnetic field has a rise time of 30 ns and typically has a peak value $\approx 1.5\,\mathrm{kG}$; these parameters have been found to be optimum in the simulations and the experiment. A radius variation from head to tail on the order of 3:1 was obtained. If this beam were passed through a scattering foil, then an emittance tailor would be imposed on the beam that might be sufficient to reduce the growth rate of hose instabilities during propagation. The next step of this experiment would be to compare the propagation characteristics in a gas of this radius-tailored beam to those of an untailored beam.

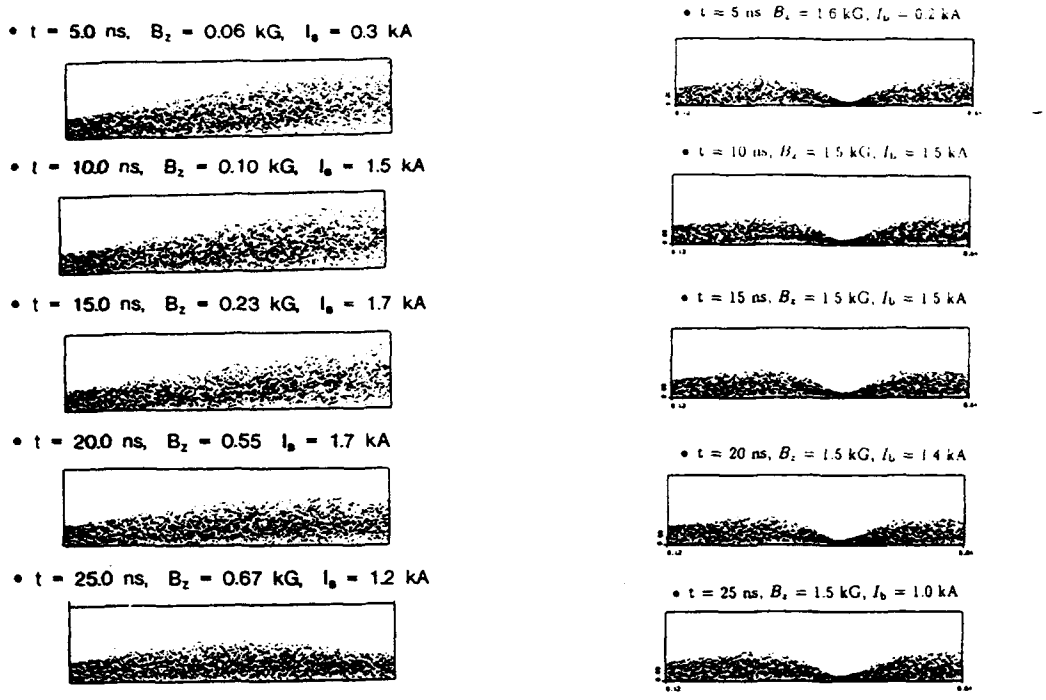

(a) (b)

Fig. 6: MAGIC simulation results: five snapshots during the beam pulse. The lower edge of each box represents the axis of the system; the upper edge of each box represents the drift tube wall at a radial location of 7.5 cm. The left edge is the exit (aperture) of the BRTS; the right edge corresponds to the position of the scintillator in the experiment; the propagation distance is 52 cm. (a) is the radius tailored case. (b) shows results for the untailored case.

References

[1] R. B. Miller, *Introduction to the Physics of Intense Charged Particle Beams,* Plenum Press, NY, 1982.

[2] E. P. Lee, Phys. Fluids **21** (8), 1327–1343, (1978).

[3] H. S. Uhm and M. Lampe, Phys. Fluids **23** (8), 1574–1585 (1980).

[4] H. S. Uhm, "Magnetic Focusing Conditioning," January 1987, unpublished.

[5] J. R. Smith, R. F. Schneider, M. J. Rhee, H. S. Uhm, and W. Namkung, "Propagation of a mildly relativistic electron beam at sub-torr pressures," J. Appl. Phys. **60** 4119–4126 (1986).

[6] J. D. Miller, K. T. Nguyen, R. F. Schneider, K. W. Struve, and D. J. Weidman, "Pulse shaping a high-current relativistic electron beam in vacuum," Rev. Sci. Instrum. **62** 2910 (1991).

[7] NE102A from NE America or ND120 from National Diagnostics

[8] B. Goplen, L. Ludeking, J. McDonald, G. Warren, and R. Worl, MAGIC User's Manual, (MRC, Va. 1989) Unpublished.

THEORY OF WAKEFIELD AND J x B DRIFT EFFECTS OF A RELATIVISTIC ELECTRON BEAM PROPAGATING IN A PLASMA

Han S. Uhm
Naval Surface Warfare Center
10901 New Hampshire Ave., White Oak
Silver Spring, Maryland 20903-5000

A theoretical description of the wakefield effects is presented for a relativistic electron beam propagating through a tenuous background plasma. A particle simulation study of the wakefield effects is also carried out by two-dimensional particle-in-cell codes and the simulation results are compared with the theoretical predictions. The simulation data agree remarkably well with the theoretical values. J x B drift motion of a relativistic electron beam propagating through an ion channel is also investigated. Due to finite beam size and due to the accelerator and beam head location, location of the maximum deflection point propagates from the accelerator nozzle to the beam head. At the maximum deflection point, the perpendicular velocity of the electron beam segment does not match to the drifting velocity of the ion channel, causing a disruption of the beam propagation through the ion channel.

When a relativistic electron beam propagates through a preionized plasma channel, channel electrons are expelled by the electrostatic force generated by head of the beam, leaving an ion channel behind. This ion channel partially neutralizes the space charge field of the electron beam, thereby permitting a focused beam. This is beam propagation in the ion-focused-regime (IFR). The beam-ion channel system is often surrounded by a diffuse plasma. When a relativistic electron beam propagates through a IFR channel and a tenuous neutral background plasma, it can expel plasma electrons as well as channel electrons. The plasma electrons move out to the charge neutralization radius a_n where the beam charge is the same as the total enclosed ion charge as shown in Fig. 1. However, in reality, when the plasma electrons are expelled by the beam, they will overshoot the charge neutralization radius and oscillate at a frequency which is usually very close to the electron plasma frequency of the tenuous background plasma. This plasma electron oscillation near the charge neutralization radius produces a wakefield which is electrostatic in nature and has associated electric field components in the radial and axial directions. Particularly, the axial electric field may modulate the beam electron energy along the beam pulse. An analytical theory of the wakefield effects on a relativistic electron beam propagating through an ambient plasma background has

been carried out. A particle simulation study of the wakefield effects has been also carried out by a two-dimensional particle-in-cell code called MAGIC and the simulation result has been compared with analytical results.

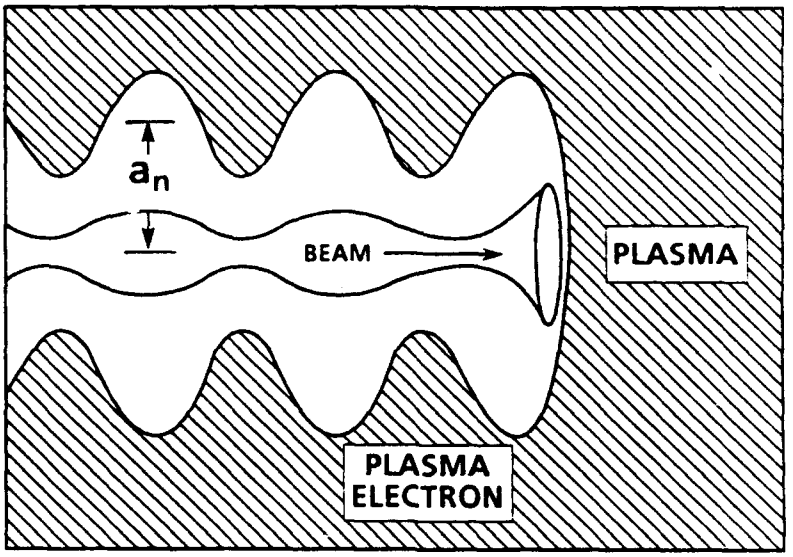

Fig. 1. Schematic presentation of the wakefield effects for a relativistic electron beam propagating through a tenuous background plasma. The charge neutralization radius is denoted by a_n.

Although the electron beam disturbs the ambient plasma background and generates the wakefield wave, it is not straightforward to identify the frequency ω and wavenumber k of the wakefield. In order to identify the wakefield properties, we have investigated the two-stream stability properties of the beam and plasma electrons. For a moderate intensity beam with its current less than 3 kA, we found that the maximum coupling between the beam and plasma electrons occurs at the axial wavenumber satisfying $k = \omega/\beta_b c$ and that the corresponding wakefield frequency is very close to the background plasma frequency. The relation $k = \omega/\beta_b c$ indicates that phase velocity of the wakefield wave is identical to the beam velocity, thereby forming a standing wave in the beam frame. Thus, the axial electric field of the wakefield wave modulates the beam electron energy as the beam propagates. One of the most important wakefield parameters is the amplitude of the axial electric field. We derived a formula for the wakefield strength in terms of the plasma density, beam parameters and a geometrical factor, by making use of macroscopic cold fluid model. For a zero risetime beam, an analytical formula for amplitude of the axial electric field was obtained and indicates that the amplitude is almost linearly proportional to

the background plasma frequency and proportional to the radial velocity of the plasma electrons at the charge neutralization radius. The amplitude for a finite risetime beam is also calculated from the radial equation of motion of the plasma electrons and decreases significantly as the beam risetime increases.

Numerical simulations of the wakefield effects were carried out, using the two-dimensional particle-in-cell code MAGIC. Most of the simulations were done for an electron beam of energy 4.5 MeV, a fractional line charge neutralization of 0.5 for the IFR channel and a background plasma density of 4×10^9 electrons/cm^3, which is contained by a grounded conducting chamber. In this numerical calculation, we compared theoretical values and simulation results of the axial electric field for a broad range of system parameters, and found that the simulation data agree remarkably well with the theoretical results in most cases. Several points are noteworthy in this study. First, the strength of the wakefield increases with beam current. Second, the amplitude of the axial electric field is almost linearly proportional to the background plasma frequency for a zero risetime beam. Third, the wakefield strength decreases rapidly as the beam risetime increases. Finally, we note from the theory and the simulations that the wakefield strength decreases to zero as the plasma chamber radius approaches the charge neutralization radius.

The energy exchange mechanism between beam segments was investigated, assuming that the axial electric field of the wakefield is a sinusoidal wave with a wave number k. The electron beam bunching caused by the plasma wakefield effects may have many applications. For example, a large amplitude modulation of a relativistic high-current electron beam is required for various applications, including the electron beam bunching and high-power relativistic klystron. The electron beam bunching by the wakefield effects described here has a few advantages, e.g., elimination of the space-charge limiting current for high-current beam. The bunched beam by the wakefield will also be an effective driver for high-power klystron without an additional external microwave source. We thus studied the implication of the wakefield effects on a long-range beam propagation. Particularly, the energy and current modulation of the electron beam was calculated in terms of the propagation distance and the injection time, at which the beam segment enters the propagation chamber. Neglecting the beam head erosion, it was found that the beam current profile at a specified

propagation distance is expressed in terms of only the time t_0, at which the beam segment enters the chamber. Energy modulation along the beam pulse was also calculated. As expected, we have noticed from the study that the electron beam tends to break up into small beamlets whose length is the plasma wavelength. In further propagation, the axial electric field develops harmonics of the fundamental plasma wavelength. These behaviors have been also observed from a computer simulation study.

The beam in an ion channel is often subjected to a transverse magnetic field (e.g., earth's magnetic field), which causes a J x B drift motion of the beam channel system. In order to have a feeling for influence of the J x B drift motion on the beam propagation, we calculate the gyro-radius ρ_c

$$\rho_c = \gamma\beta c/\omega_{ce}, \tag{1}$$

where c is the speed of light, γ is the relativistic mass ratio of beam electrons and ω_{ce} is the electron cyclotron frequency defined by $\omega_{ce} = eB/m_e c$. For the earth's magnetic field B = 0.3 Gauss, the gyro-radius ρ_c is given by $\rho_c = 57\gamma$ (m). Obviously, the beam can not propagate without the ion channel. In a infinitely large system, description of the J x B drift motion is a trivial task. However, in a finite system with finite beam length, head of the beam tracks the ion channel and the tail of the beam pulse is still exiting nozzle of the accelerator. Some segments in the middle of the beam pulse will suffer the J x B drift motion. In this regard, the description of the J x B drift motion for a finite beam-channel system is complicate and requires an extensive investigation. Location of the maximum deflection point propagates from the accelerator nozzle to the beam head with the velocity of a fraction of the beam velocity. At the maximum deflection point, the perpendicular velocity of a beam segment does not match the drifting velocity of the ion channel, causing a disruption of the beam propagation through the channel. For example, for a 1 kA beam in a transverse earth's magnetic field B = 0.3 G, the first one μs portion of the beam pulse is grabbed by the ion channel, but the later portion of the beam pulse might be lost.

Relative Motion Between the Electron Beam and Ion Channel: Here, we investigate properties of an electron beam propagating through an ion channel in the presence of an external transverse magnetic field B, which is perpendicular

to the propagation direction of the beam. we treat the electron beam and ion channel as rigid bodies, which mean that the transverse motion of every particle in one species moves together with the axis. We also assume that the beam and channel have the same radius R_b and a rectangular density profile. Defining the dimensionless variable $x = (r_i - r_e)/R_b$, the equation of motion of the relative transverse position between the electron beam and ion channel is

$$\frac{d^2x}{dt^2} = A - Dx, \tag{2}$$

where the coefficients A and D are defined by

$$A = \frac{eB\beta}{\gamma m_e R_b}, \quad D = 2\pi n_e e^2 \left(\frac{1}{m_i} + \frac{f}{\gamma m_e}\right). \tag{3}$$

Here, r_e and r_i are the center of mass radii of electron and ion columns, n_e is the beam electron density and f is the line charge neutralization factor. The maximum separation of the two columns occurs when the relative velocity dx/dt = 0. One obvious solution is x = 0 for dx/dt = 0. The other nontrivial solution is given by

$$x = x_m = 2\frac{A}{D} = \beta \frac{\omega_{ce} R_b}{cf\nu}, \tag{4}$$

where $\nu = e^2 N_b/m_e c^2$ is the Budker's parameter of the electron beam and use has been made of $f \gg \gamma m_e/m$. Equation (4) can also be expressed as $x_m = |r_i - r_e|/R_b = 5.86 \times 10^{-4} B\beta R_b/f\nu$. In order to satisfy the equilibrium condition, the maximum separation distance x_m must be a reasonably small value. For example, for B = 0.3 G, f = 0.5, $\nu = 0.05$ corresponding to 1 kA, and the beam radius R_b = 10 cm, we find x_m = 7 percent, which is reasonably safe. The separation distance $x_m R_b$ is proportional to the magnetic field and inversely proportional to the parameter $f\nu$, as predicted.

Motion of the Center of Mass Coordinate for Both the Electron Beam and Ion Channel: Denoting the center of mass coordinate R for electron and ion columns, and introducing the variable ζ, which represents the distance from the beam head to the tail, and assuming that the beam head stays in the ion channel, we have the boundary conditions R = 0 and $dR/d\zeta = 0$ at $\zeta = 0$. Thus, the deflection R of the beam-channel system by the earth's magnetic field is given by

$$R(\zeta) = \frac{\omega_{ci}}{2f\beta c}\zeta^2, \tag{5}$$

where $\omega_{ci} = eB/m_i c$ is the ion cyclotron frequency. Equation (5) can also be expressed as $R(\zeta) = 1.6 \times 10^{-7}\, B\zeta^2/f\beta\mu$, where μ is the ion mass number. For example, for B = 0.3 Gauss, f = 0.5, μ = 16 and $\zeta = 3 \times 10^5$ cm corresponding to 10 μs, we find that the deviation R = 540 cm. Apparently, the deflection of the tail of a long pulse beam is intolerably large. Note that the tail deflection R is a quadratic function of the pulse length ζ. Thus reduction of the pulse length drastically improves the tail deflection.

The location of the maximum deflection point propagates from the accelerator nozzle to the beam head. The advance velocity dy/dt of the maximum deflection point is

$$\frac{dy}{dt} = \beta c\sqrt{\frac{\gamma m_e}{f m_i}}, \tag{6}$$

which is a fraction of the beam velocity when $\gamma m_e/fm_i \ll 1$. Due to the velocity mismatch between electron-beam segment and ion channel at the maximum deflection point, the electron-beam segment and ion channel have a relative separation given by

$$x_m = \frac{t}{f}\sqrt{\frac{\omega_{ce}\omega_{ci}}{2\nu}}, \tag{7}$$

provided $(ct/R_b)^2 \gg m_i/2\nu\gamma m_e$, which can easily be satisfied for a time t larger than 100 ns. The normalized maximum separation x_m must be reasonably smaller than unity to satisfy the beam equilibrium condition, which sets the pulse length condition

$$\omega_{ce}\omega_{ci}t^2 \ll 2\nu f^2. \tag{8}$$

A largest number for the normalized maximum separation x_m, which may still satisfy the equilibrium condition, is about 0.2, i.e., $x_m < 0.2$. From Eq. (8), we thus obtain the pulse length, which is grabbed by the ion channel. For example, for $\nu = 0.05$, f = 0.5, μ = 16 (oxygen atom), $x_m < 0.2$ and B = 0.3 Gauss, we find t < 1 μs. This means that the first one μs portion of the beam pulse is grabbed by the ion channel, but the later portion of the pulse will be lost.

Acknowledgement: This work was supported by the Independent Fund at NSWCWODET.

RELATIVISTIC ELECTRON BEAM PROPAGATION IN HIGH PRESSURE GASEOUS MEDIA*

J.A. Antoniades, M.C. Myers, D.P. Murphy, R.F. Hubbard, T.A. Peyser,[a] R.F. Fernsler,
R.E. Pechacek, J. Santos and R.A. Meger
Plasma Physics Division, Naval Research Laboratory, Washington D.C. 20375-5000

Intense relativistic electron beam (IREB) propagation is intrinsically unstable in high pressure gaseous media. The dominant instability is the resistive hose. The growth rate of the hose is reduced by beam conditioning which incorporates beam emittance tailoring and current centroid sweep damping. In the experiments reported in this work we conditioned the SuperIBEX IREB using combinations of an argon filled IFR and an air filled or evacuated active $B\theta$ cell. The IFR cell provides the required radius tailoring which is converted to emittance tailoring using a titanium exit foil or by injection into the active $B\theta$ cell. The $B\theta$ cell damps the beam centroid sweep due to the anharmonic restoring force applied by the wire's magnetic field on a sweeping IREB. These conditioning cells successfully stabilized the beam for approximately 20 betatron wavelengths ($\lambda\beta$) and propagation lengths exceeding 5 m. The objective of the experiments reported here is to show the effect on propagation of using the conditioning cells to vary the beam parameters including beam emittance, beam current, radius tailoring, and sweep reduction.

I. INTRODUCTION — Propagation of IREB's in the atmosphere is limited by the scattering of the beam electrons from electron-neutral collisions[1] with the ambient gas and by the presence of the resistive hose instability.[2] Beam conditioning extends the stable propagation range of the IREB since it suppresses the growth of the resistive hose which is a result of the interaction of the electron beam with the conducting plasma formed by impact ionization of the background gas along the beam path. The return currents generated in the conductivity channels exhibit a resistive phase lag, a necessary ingredient for the generation of the hose.[3] Beam conditioning consists of emittance tailoring and current centroid oscillation (beam sweep or perturbation) damping. Emittance tailoring reduces the resistive hose growth by continuously changing the betatron wavelength ($\lambda\beta$) within the pulse, thus detuning and phase mix damping the instability. Beam sweep reduction suppresses the initial perturbations that give rise to the instability. Most sweep reduction techniques result in beam emittance increases due to the anharmonic nature of the damping force which converts beam radius and centroid oscillations into emittance.

Ion Focus Regime (IFR) cells can produce time dependent radius variations of IREB's suitable for long propagation experiments.[4] A typical IFR cell consists of a conducting pipe filled with a few mTorr of gas. In a single IFR conditioning cell the resulting beam radius variation is converted to an emittance ramp by passing the beam through a titanium foil (0.5-5 mils for 5 MeV beams). Even though IFR cells can in principle center the beam and damp the sweep[5] they have little effect on the beam head which plays a critical role in the stabilization. More efficient sweep damping and beam centering can be accomplished using an active $B\theta$ cell. The active $B\theta$ cell consists of a conducting cylindrical pipe with a thin current-carrying wire along its axis.[6] The wire current is in the same direction as the beam current. Sweep damping is a result of the anharmonic pinching and centering force that the wire exerts on the beam.

The characteristic length for the e-folding of the beam radius due to the scattering of the beam electrons by the atmosphere is the Nordsieck length (L_n).[1] Beam propagation stability can be parametrized by a dimensionless figure

of merit. The ratio of the Nordsieck length (L_n) to betatron wavelength ($\lambda\beta$) represents the number of instability growth times before the radius e-folds (and the current density decreases by $1/r^2$) due to scattering. Equally important is the actual propagation distance R nomalized to $\lambda\beta$. The smaller of these two parameters represents a measure of the success of a given experiment.. Hose growth is rapid enough that a beam can be disrupted within as few as 2 betatron wavelengths. A figure of merit ~10 would represent a significant hose stabilization demonstration.

II. EXPERIMENT DESCRIPTION — NRL's SuperIBEX accelerator is capable of producing a 5 MeV, 100 kA electron beam with a pulse width of 40 nsec FWHM. The beam is extracted through an emittance selector and is injected into an IFR cell for radius tailoring with typical beam currents of 15-27 kA. The IFR cell is a 40cm long, 10 cm diameter conducting tube filled with 3-10 mTorr of argon. A 3-20 mil Ti exit foil separates the IFR cell from the atmosphere. The output beam currents were 10–24 kA.

Three sets of experiments were performed. The first used only the IFR cell. In the other two the IFR cell was followed by a 120 cm long active wire $B\theta$ cell in vacuum or in full density air. A capacitor bank was used to drive the wire current up to 10 kA. Because of the long risetime of the capacitor bank the wire current was practically constant throughout the beam pulse. The conditioned beam was injected into a 2 m diameter, 5 m long propagation chamber held at 1 atm. Figure 1 shows a schematic of the setup for the propagation experiments which consists of the IFR and $B\theta$ cells, a diagnostics cell, and the propagation chamber.

The main diagnostics used to characterize the propagating beam were:

- 5 element concentric segmented Faraday collector (SFC) for beam current distribution measurements between 5 cm and 66 cm away from the exit foil.[9]
- 4 frame gated optical imager with up to 120 psec resolution measuring 2-dimensional beam current distribution from Cerenkov emission off a thin FEP Teflon foil.[8]
- Magnetic probe sets for net current and centroid position along the beam propagation range.
- Optical streak cameras for time resolved 1-D measurements of the beam current distribution, radius and centroid position of Cerenkov emission from a thin FEP Teflon foil.[8]
- Time integrated side-on photographs of the beam induced atmospheric emissions yielding information about beam radius growth in air as well as overall stability.

III. RESULTS AND DISCUSSION — There are several beam parameters that affect the stability of an IREB propagating in the atmosphere. The beam emittance which determines the equilibrium radius, the radius tailoring time and its relation to the beam current risetime, the beam current, and the input beam sweep.

The effect of varying the beam emittance, tailoring duration and current can be demonstrated by data obtained with a simple IFR conditioning cell. The most stable beams were obtained with a 1.5 mil titanium input foil, 5 mTorr of argon in the cell and a 10 mil titanium exit foil. The typical output beam current was 14 kA. Plots of beam radius, on-axis current density and beam current for the IFR conditioned beams used in these comparisons are contained in Ref. 7. Figure 2a. shows a time-integrated side-on photograph of the most stable beam in the range of 150-260 cm downstream. The radius in the air at the exit of the IFR cell is 2.5 cm with a net current of 7 kA .

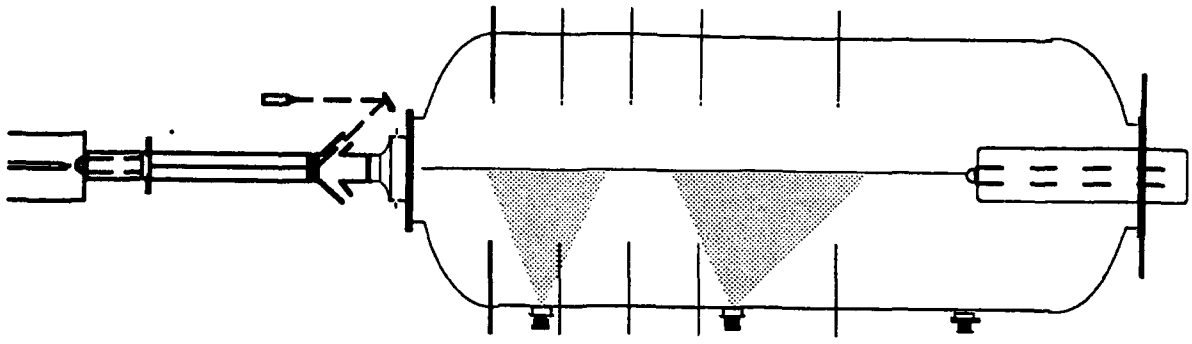

Figure 1 Schematic diagram of the IFR/Bθ conditioning cell used in the lead pulse stability experiments. The optical diagnostics cell with the Cerenkov target and the segmented Faraday collector is also shown.

Figure 2b. illustrates the effect of beam emittance variation. The exit beam emittance profile was changed by decreasing the IFR cell exit foil thickness to 5 mil. The thinner foil resulted in a 1.5 cm beam radius. This colder beam shows large hose growth within the first 2 meters of propagation (approx. 5 $\lambda\beta$). Since the beam current is unchanged the smaller radius beam has a shorter betatron wavelength which allows more growth times for the hose within the same propagation distance.

The duration of the tailoring ramp can be controlled by changing the IFR fill pressure.[7] If the beam shown in figure 2 is injected into the IFR cell with 9 mTorr of argon, there is obvious loss of stability within 2 m of propagation. As Ref. 7 shows, increasing the IFR cell pressure results in several changes in the beam profile: the final beam radius decreases, and the duration of the tailoring ramp decreases and moves towards the front edge of the beam pulse. All of these changes contribute to the destabilization of the hose by decreasing of the betatron wavelength and reducing the duration and effectiveness of the phase-mix damping.

Similar large amplitude hose growth occurred as the beam current was increased from 14 to 24 kA. IFR tailoring measurements indicated that for the parameters of our experiments the beam current had little effect on the radius or radius tailoring profile. High current beams tend to have shorter $\lambda\beta$ and appear to be more hose unstable.

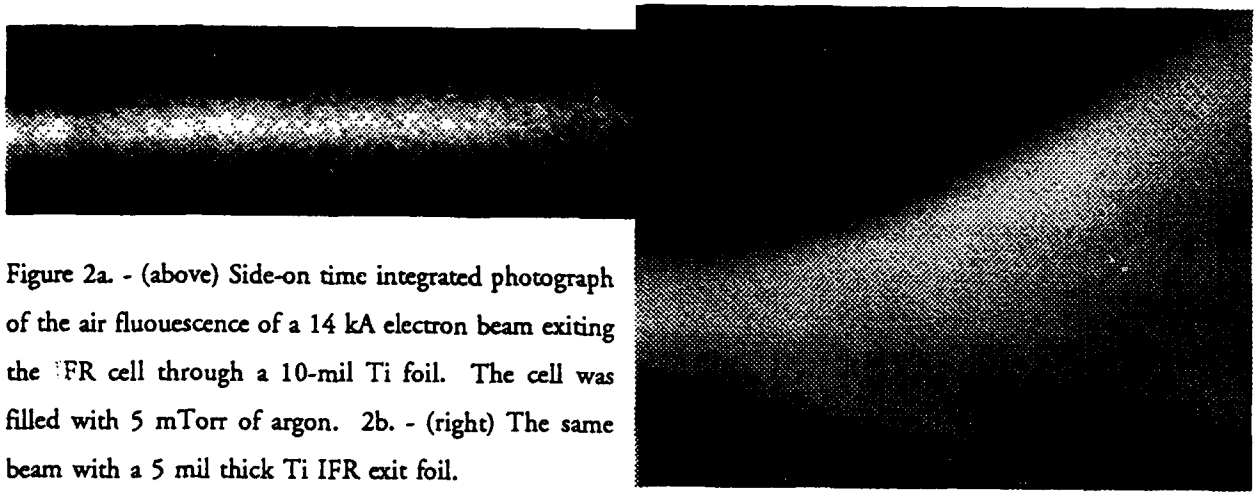

Figure 2a. - (above) Side-on time integrated photograph of the air fluouescence of a 14 kA electron beam exiting the IFR cell through a 10-mil Ti foil. The cell was filled with 5 mTorr of argon. 2b. - (right) The same beam with a 5 mil thick Ti IFR exit foil.

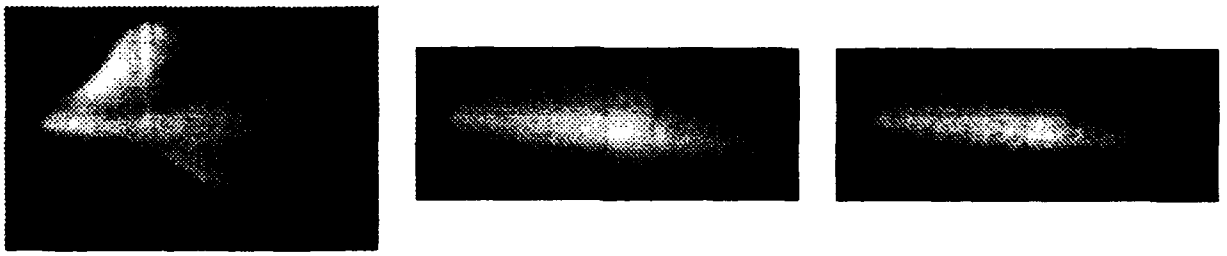

Figure 3 Effect of vacuum Bθ wire current variation on beam stability. The photographs cover the range 140-260 cm downstream. The beam current is 19 kA and the minimum radius is 1.5 cm. The wire currents for the above frames are 3.6 kA, 5.3 kA and 7.3 kA. Increasing the wire current to 10 kA results in total beam loss to the wire.

In order to stabilize even the tailored IFR-only beams relatively thick IFR exit foils were needed. This resulted in large radius beams (≈ 2–3 cm). Side-on photographs indicated radius e-folding lengths of approximately 2.5 m for these beams. These beams had relatively small Nordsieck/Betatron ratios due to their large radii. The primary problem with IFR-only conditioning is that IFR cells are not effective in damping the beam sweep or perturbations. To improve beam stability without large increases in the beam radius a 1.2m long, 20 cm diameter high pressure Bθ cell was attached to the exit of the IFR cell. The Bθ cell also converts the IFR cell radius tailoring to emittance tailoring without scattering foils. In general Bθ cells heat the beam as much as a few mils of Ti.[6]

Figure 3 illustrates the effect of varying the wire current in a vacuum Bθ cell. The IFR cell is 40 cm long, filled with 10 mTorr of argon, and has 1.5 mil titanium entrance and exit foils. The vacuum Bθ cell also has a 1.5 mil thick titanium exit foil. Figure 3 shows how the stability imporves as the wire current increases. Increasing the current to 10 kA results in nearly complete loss of beam transport in the wire cell. The beam appears to pinch down on the upstream end of the wire in this case.

The most stable propagation for our experiments was achieved with a conditioning cell consisting of an IFR cell followed by an air filled Bθ cell. The air filled Bθ cell allows us to transport the electron beam with a higher wire current than the vacuum cell. The beam radius increased slightly to ~1.6 cm downstream of the air Bθ cell but extremely stable propagation was observed through the entire length of our chamber. Figure 4 shows the beam characteristics measured with the segmented faraday collector located after 66 cm of propagation in the air. The measurements were verified with optical diagnostics.[8] The 18 kA beam had a 1.6 cm radius at the waist and a current density of ≥1.8 kA/cm^2. The experiments were performed in the high return current regime since the net currents measured by the downstream probes were 9.5-11 kA which is ~50% of the 16–18 kA injected beam current. The beam propagated stably for approximately 20 betatron wavelengths. The beam centroid displacement after 2.5 m of propagation is shown in figure 5. The off-center excursion of the beam is much smaller than the local beam radius indicating good stability despite the long propagation.

Figure 6 shows a compilation of the results of a series of stable shots using the IFR/Air Bθ hybrid conditioning cell. Data from three sets of probes located 1.3, 2.5 and 4.5 meters downstream of the cell exit are shown. Each point on the graph is the average location of the net current centroid for the entire beam pulse. The error bars represent the

mean deviation in the x and y directions. The beam is quite stable because even at 4.5 m the mean centroid deviation from center is ~5 cm which is a fraction of the the beam radius at this location. The centroids at the 3 locations are not collinear for each shot possibly indicating low frequency hose motion or beam aiming errors.

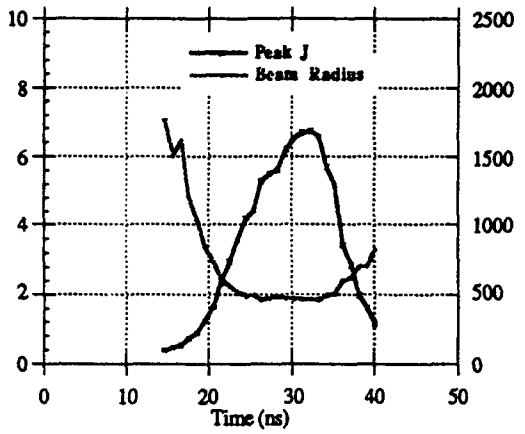

Figure 4 . Beam Gaussian radius and peak current density profile for the typical stable beam from the IFR/Gas Filled Bθ cell after 66 cm propagation in full density air.

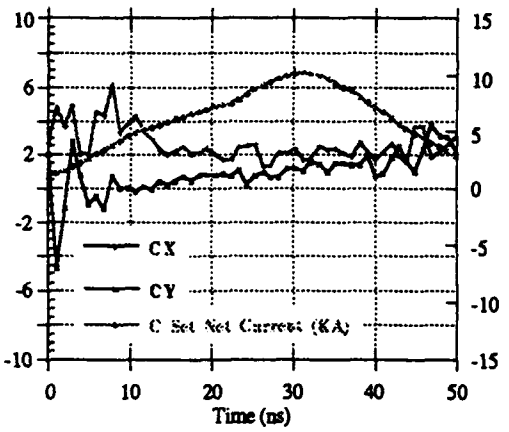

Figure 5. Net current and centroid position for a stable beam conditioned with IFR/Bθ hybrid cell 2.5 m downstream. The injected beam current is 18.5 kA peak and the radius at injection is ≈ 1.5 cm.

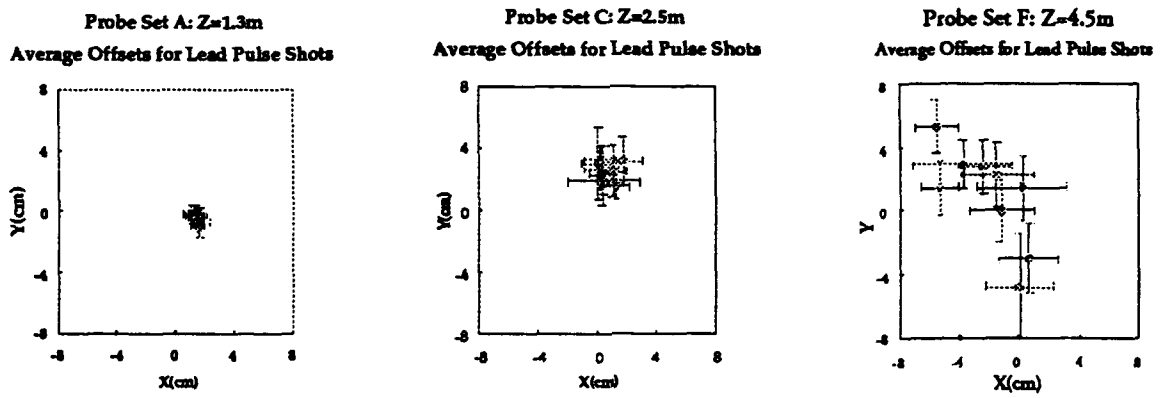

Figure 6 . Average centroid position and mean centroid displacement for a series of electron beams propagating in full density air. The beams were conditioned with a 40cm long, 10 cm diameter IFR cell filled with 10 mTorr of argon followed by a 120 cm Air Bθ cell carrying 9 kA of wire current.

IV. CONCLUSIONS — Beam conditioning using IFR or hybrid IFR/Bθ cells is very effective in suppressing the growth of the resistive hose instability allowing stable, long-range propagation of IREBs in high pressure media. The Nordsieck length/betatron wavelength ratio for the most stable beams was approximately 20 indicating clear suppression of the resistive hose instability. The propagation range exceeded 5.5 m without indications of a serious instability. With the IFR cell only, the beam could be stabilized by a combination of emittance tailoring and beam heating with thick scattering foils.

*Work supported by the Office of Naval Research

[a]Science Applications International Corporation, McLean, VA 22102

REFERENCES

[1]T. P. Hughes and B. B. Godfrey, Phys. Fluids 27, 1531 (1984).

[2]M. Lampe, W. Sharp, R.F. Hubbard, E.P. Lee, R.J. Briggs, Phys. Fluids 27, 2921 (1984).

[3]R. A. Meger et al, *Charged Particle Beam Propagation Studies at the Naval Research Laboratory,* these proceedings.

[4]R. F. Fernsler , R. F. Hubbard and S. P. Slinker, *Conditioning Electron Beams in the Ion-Focused Regime,* to be published(1992).

[5]M. C. Myers et al., *Beam Transport and Centering in IFR cells,* to be published.

[6]D. P. Murphy et al., *Transport of High-current, Relativistic Electron Beams using Active Wire* Bθ *cell Techniques,* these proceedings.

[7]M. C. Myers et al., *IFR Transport Experiments on the SuperIBEX Accelerator,* these proceedings.

[8]T. A. Peyser,et al., *Beam Profile Diagnostics on the NRL SuperIBEX Experiment,* these proceedings.

[9]T. A. Peyser, et al., Rev. Sci. Instrum. 62, 2895 (1991).

TRANSPORT OF HIGH CURRENT, RELATIVISTIC ELECTRON BEAMS USING ACTIVE-WIRE B_Θ CELL TECHNIQUES*

D.P. Murphy, R.E. Pechacek, M.C. Myers, J.A. Antoniades,
T.A. Peyser[a],R.F. Fernsler, R.F. Hubbard, J. Santos[b], and R.A. Meger

Plasma Physics Division, Naval Research Laboratory
Washington, DC 20375-5000

The high-current, relativistic electron beam (10-20kA, 5MeV, 40ns) of the SuperIBEX accelerator is transported from its diode to an experimental chamber along a wire that has an externally driven current flowing in the same direction as the electron beam current. The magnetic field from the wire current both guides the beam and smears out coherent radial beam oscillations. The wire cell is used to damp the initial radial motion to decrease the growth of the resistive hose instability in the air propagation region following the wire cell. Experimental parameters varied in this study include wire cell current ($I_w<I_b$) and cell gas pressure (full atmospheric pressure or vacuum). The effects of these parameters on the cell transport efficiency (I_{out}/I_{in}), beam pulse length (t_p), and beam radial profile ($I_b(r,t)$) were measured with an array of diagnostics. The beam spatial profile was measured optically using Čerenkov light generated as it passed through a thin FEP teflon foil at the cell exit using an ultra-fast, 4 channel framing camera and one or more streak cameras. Electrical measurements included non-interceptive beam position monitors at the input and exit of the wire cell and a 5-element, segmented, concentric Faraday collector which could be mounted to intercept the beam. The results of this experiment are compared with theory and numerical simulations.

I. Active Wire B_Θ Cell: An active wire B_Θ cell contains a centered filamentary wire that carries an externally driven current in the same direction ($\hat{Z}$) as the electron beam current. It produces an azimuthal ($\hat{\Theta}$) magnetic field which centers the beam. The beam electrons travel in a magnetic field whose strength varies inversely with the radial ($\hat{R}$) distance from the wire. The electrons in the beam oscillate at $\omega \propto 1/r$, where r is their distance from the wire. This phase mixing distorts the beam into a new profile centered about the wire, but at the expense of emittance growth. The external circuit in this instance consists of a single 58μF

capacitor with a spark gap switch which feeds four parallel, 9m long RG-213 cables that are attached to the four ends of a cross-hair that supports one end of the filamentary wire. A second cross-hair which is grounded supports the other end of the filamentary wire (see Figure 1).

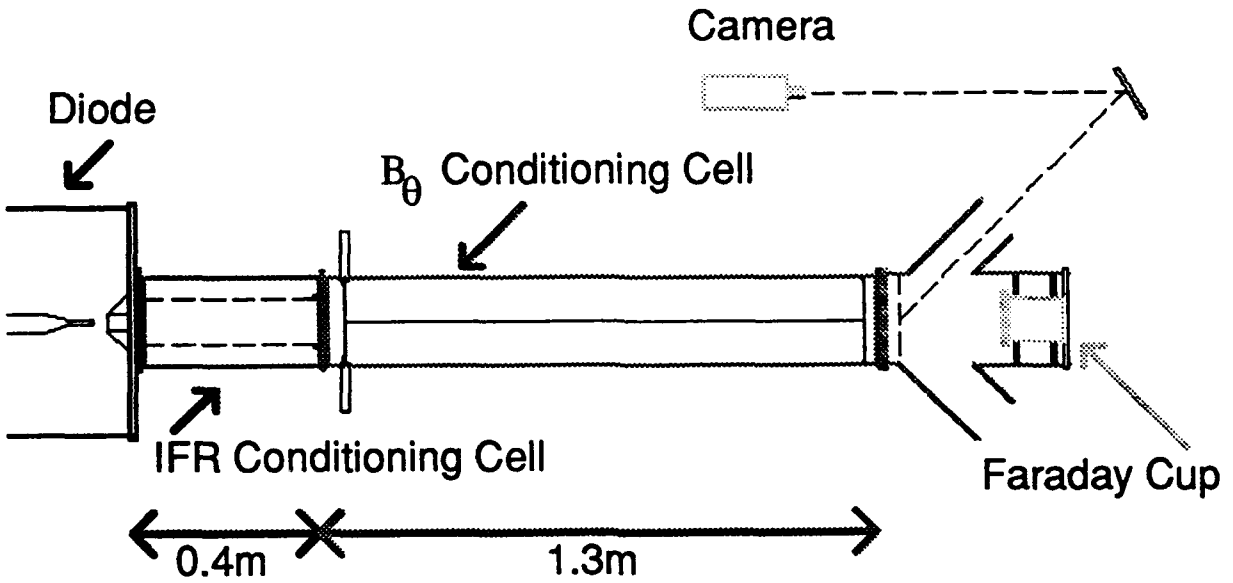

Figure 1. Schematic Diagram of the Beam Production Hardware

The B_Θ cell is separated from the Ion Focus Regime (IFR) cell by a 38μm thick titanium foil pressure barrier. The IFR cell operates at a pressure of a few mTorr of Argon and is described more fully in a companion paper[1]. If the B_Θ cell is evacuated, a second 38μm thick titanium foil pressure barrier is mounted at the cell exit.

II. B_Θ Cell Design Issues: The cell radius should be large enough to minimize beam scrape-off losses. Also, a small cell radius limits the amount of radius tailoring that can be maintained through the cell. The cell length to provide sufficient phase-mix damping is:[2] $Z \geq 2r_{max}\sqrt{17\pi\gamma / I_w(kA)}$; $r_{max} \approx 7.5\text{cm}$, $\gamma = 11$.

According to the theory developed by R. F. Fernsler, the wire current should be $I_w \approx 0.5 I_{eff}$, where I_{eff} is the effective pinch current in the beam body (about 70% of I_{beam} in air). The cell used in this experiment was 10cm radius by 130cm long. The filamentary wire, which carries 2-10kA of externally driven current for ~20μs, must be kept as small as possible to minimize beam losses due to impact with the

wire. The sizes used here ranged from #30AWG to #26AWG copper wire ($127\mu m \le r_{wire} \le 202\mu m$).

III. B_Θ Cell Transport and Conditioning: Figure 2 shows the time histories of the beam current, current density and beam half-current radius for a typical beam that emerges from an IFR conditioning cell filled with 10mTorr Argon. The beam typically has a peak current of about 24kA with a 25ns FWHM for the current pulse. Such a beam, with a sub 1cm radius, is frequently more than a beam radius off center and not aimed correctly as it enters the B_Θ cell. Should this beam be injected into full density air directly from the IFR cell it could propagate only a few 10s of centimeters before severe hose oscillations disrupted the beam. Even if this beam were passed through a titanium scattering foil about 250μm thick (~.010" of Ti) at the IFR cell exit its radius growth, and corresponding Betatron wavelength growth, wouldn't damp any inherent beam motion. So its propagation distance scaled to the Betatron wavelength would not be much better than that of the original beam. The advantage of an active-wire B_Θ cell is that the beam can be centered, beam motion damped and the hose instability suppressed without a large increase in the beam emittance (and corresponding growth in beam radius in air).

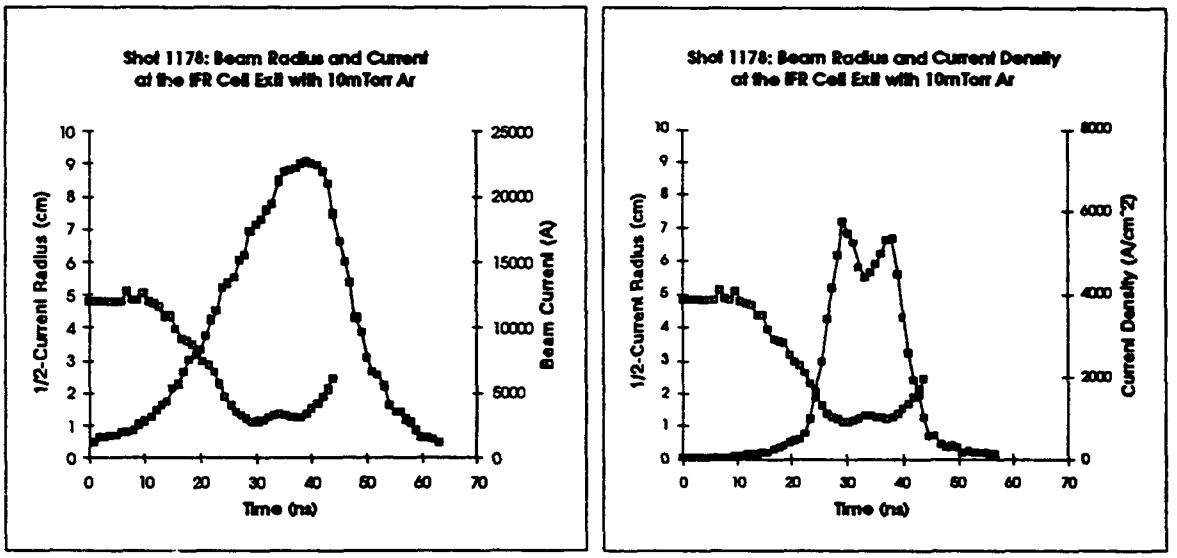

Figure 2. Beam Current, Current Density and Half-Current Radius for Shot 1178

Figure 3 presents the time histories of the beam current, current density and beam half-current radius for a beam as it exits an evacuated B_Θ cell. The input beam is essentially that shown in figure 2. The peak current has dropped to about 18kA and the pulse width has decreased to about 23ns FWHM. Most of the electrons lost are believed deposited in the first few centimeters of the filamentary wire. Figure 4 presents data similar to that in figure 3 except that the B_Θ cell is operated at full

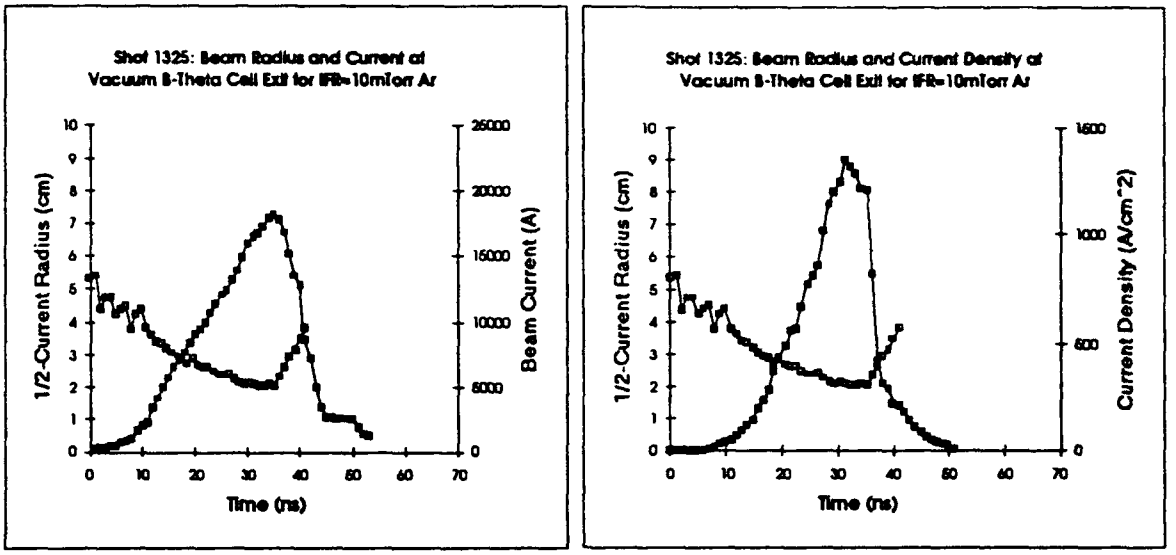

Figure 3. Beam Current, Current Density and Half-Current Radius for Shot 1325

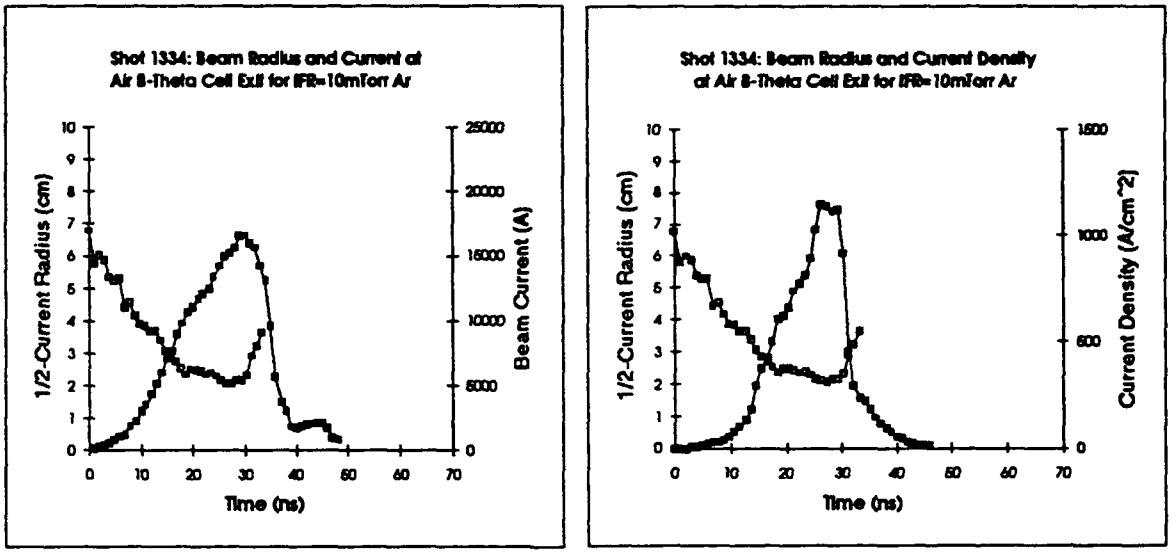

Figure 4. Beam Current, Current Density and Half-Current Radius for Shot 1334

density air. The peak output current is about 16-18kA but the pulse width has further decreased to about 20ns FWHM. It is believed that scattering off air molecules pushes additional electrons into the loss cone along the length of the

filamentary wire. The transport efficiency of the 130cm long B_Θ cell used in these studies, as measured by the ratio of the peak output current to the peak input current, is: a)$78\% \pm 1.2\%$ based on 8 shots into a Faraday cup with an evacuated B_Θ cell; or b)$59\% \pm 2.4\%$ based on 13 shots into a Faraday cup with full density air in the B_Θ cell. Note also that the exiting beam radius profile for both air and vacuum operated B_Θ cells still has significant tailoring from the beam head back through at least the peak of the beam pulse. Figure 5 is a line-out through the center of GOI image #4 of Čerenkov light for shot 1336, a full air density B_Θ cell shot. Note the depression in the central current density corresponding to the position of the filamentary wire. The loss of central current density is not nearly so pronounced in vacuum B_Θ cell shots, demonstrating the increase in the loss of particles to the wire when there is air in the cell.

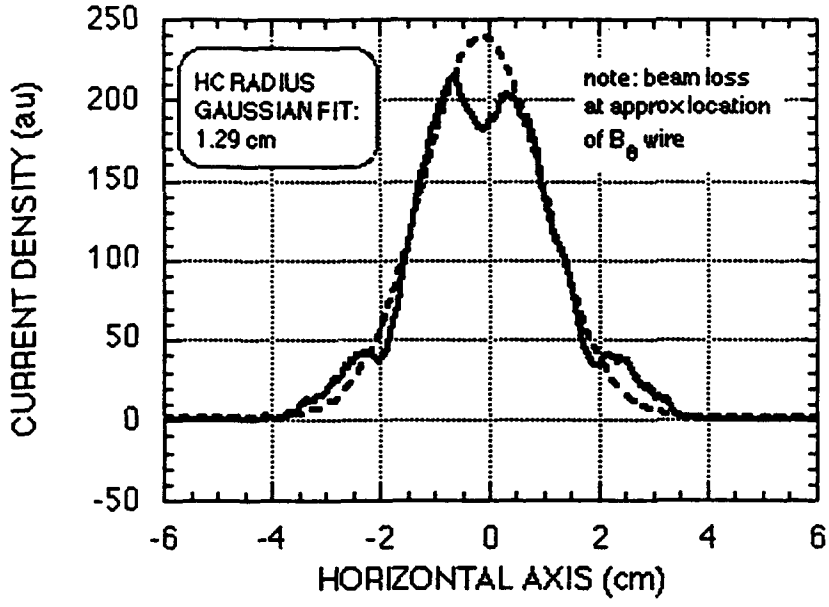

Figure 5. Gaussian fit to a horizontal line-out through the center of GOI image #4, at the peak of the current pulse of shot 1336.

Figure 6 shows the Y vs X position of the beam for shot 1332 at Z=90cm and at Z=410cm from the exit of the B_Θ cell. The filamentary wire is #28AWG ($r_w = 159\mu m$), the wire current was 7.2kA, the B_Θ cell was operated at full density air and there was a 38μm thick titanium foil at the cell exit. This shot shows that a stabilized beam will propagate essentially a full Nordsieck length without experiencing disruptive hose oscillations.

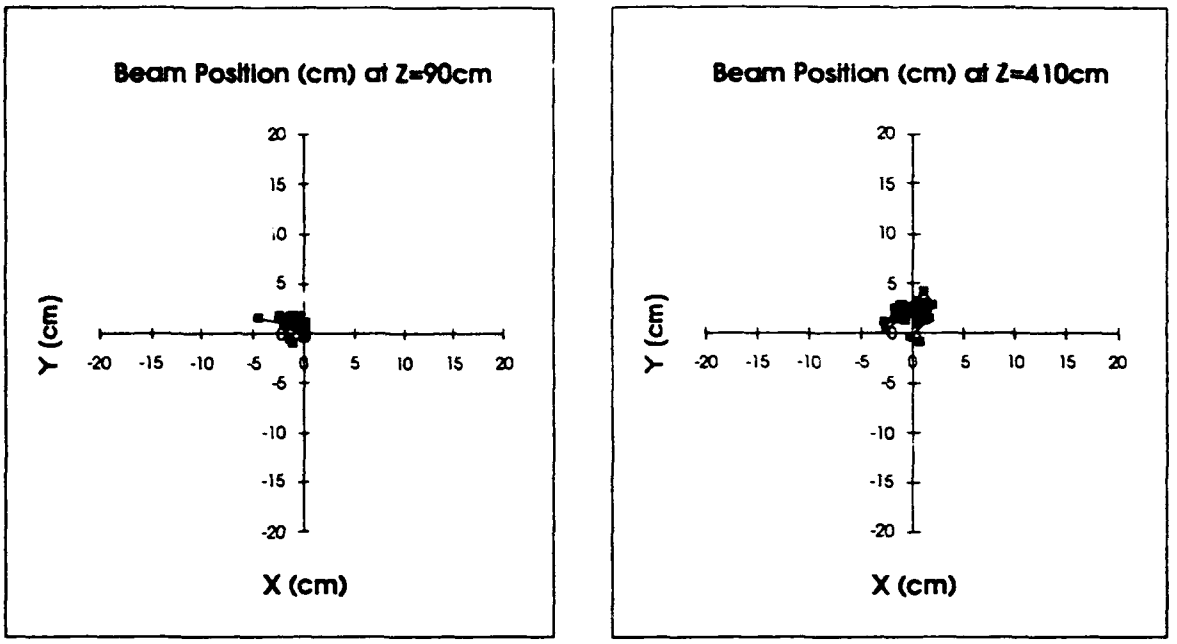

Figure 6. Y vs X net current centroid motion during the beam pulse at Z=90cm and Z=410cm downstream from the B_Θ cell for a stabilized shot.

IV. Summary: The active-wire B_Θ cell exerts a strong centering force on the entire beam, including the beam head. Passive schemes do not have much effect on the beam head because the beam current is very low there. For a sufficiently long cell, phase-mix damping occurs, and the beam centers about the wire. The measured radius profiles at the exit of the cell show that radius tailoring is preserved during transit of the cell. The measured current transport efficiency of the cell is as high as 80%.

* This work supported by the Office of Naval Research.

[a] Science Applications International Corp., McLean, VA

[b] SFA, Landover, MD

[1] M. Myers, J. Antoniades, T. Peyser, D. Murphy, R. Pechacek, R. Hubbard and R. Meger, "IFR Transport Experiments on the SuperIBEX Accelerator", this conference proceedings.

[2] R.Fernsler, S. Slinker, R. Hubbard and M. Lampe, "Theory and Simulation of the Resistive Hose Instability in Relativistic Electron Beams", this conference proceedings.

IFR TRANSPORT EXPERIMENTS ON THE SuperIBEX ACCELERATOR*

M. Myers, J. Antoniades, T. Peyser,@ D. Murphy, R. Pechacek,
R. Hubbard, and R. Meger
Plasma Physics Division, Naval Research Laboratory, Washington, D.C. 20375

ABSTRACT

Conducting cells filled with neutral gas at pressures below 100 mTorr (Ion Focus Regime) provide a simple and effective method for the transport and conditioning of intense relativistic electron beams (IREBs). Experiments performed on the SuperIBEX accelerator (5 MeV, 100 kA, 40 ns FWHM) show that desired output beam profiles can be effectively generated through the manipulation of cell geometry, gas pressure and species, and input beam emittance and current. The cells also provide some beam centering and sweep damping. The beam profiles are measured using a concentric segmented Faraday collector (SFC), IMACON 500 streak camera, and a four-frame, ultra-fast, gated optical imaging system (GOI).

I. INTRODUCTION: Stable, self-pinched propagation of intense relativistic electron beams (IREBs) in dense gas is limited by the resistive hose instability. Theory and simulation indicate that the instability convectively couples to betatron oscillations in the beam frame so that an initial transverse perturbation in the beam head is amplified and can grow coherently through the tail disrupting propagation.[1] It is, therefore, desirable to "condition" the beam for propagation by damping the initial transverse perturbations which "seed" the instability and by detuning the betatron oscillations of the beam thus decreasing the potential amplification and convective coupling of the instability.

Changing the betatron wavelength as a function of time in the beam frame (τ) provides the basis for the longitudinal betatron detuning required for hose decoupling. This is most easily accomplished by emittance "tailoring" the beam profile - imposing a monotonically decreasing emittance as a function of τ - which disrupts the coherence of the hose mode and substantially reduces its amplification. The emittance tailored profile required for stable IREB propagation can be produced by a variety of conditioning methods. There are also a number of schemes to reduce the beam sweep perturbations which can seed the hose instability. Perhaps the most effective and simple way to condition an IREB is by passing it through an IFR (ion focus regime) cell which is comprised of a conducting tube filled with neutral gas operating at pressures of 1 to 100 milliTorr. Manipulating the beam emittance and perveance by adjusting cell pressure and input foil thickness can produce a monotonically decreasing radius profile which is converted to an emittance tailored profile by passing the beam through a "thick" scattering foil as it exits the cell.[2] This passive method also provides some beam centering and sweep reduction.

Experiments performed on the SuperIBEX accelerator (5 MeV, 100 kA, 40 ns FWHM) using a 40 cm long IFR cell show that IFR cells are a versatile conditioning tool capable of imposing a range of radius tailoring profiles on beams of up to 27 kA. The profile parameters were adjusted by manipulating the pressure of argon in the cell (3-10 mTorr), the input beam normalized emittance (0.5-1.6 rad-cm), and the cell diameter (10 and 20 cm). Radius tailoring measurements were taken at the output of the IFR conditioning cell; emittance tailoring measurements were made 26 cm (about one λ_β) from the cell exit foil where the beam is in equilibrium. For each specific set of parameters there is a corresponding cell transport efficiency and sweep reduction ratio. The radius tailored beams were subsequently passed through a matched scattering foil for conversion to an emittance tailored profile suitable for stable propagation.

II. IFR THEORY: An IFR cell consists of a conducting tube with a foil at each end to contain a neutral fill gas at operating pressures below 100 mTorr. The evolution of the beam radius as a function of propagation distance in an IFR cell can be described by the Lee-Cooper envelope equation.[3] Neglecting inductive erosion in the short cell:

$$R'' - \frac{K_T}{R} - \frac{\varepsilon_n^2}{\gamma^2 R^3} = 0 \qquad (1)$$

where the second term is the effect of the beam self fields and the third term is the normalized emittance effect. For a gaussian beam and channel profile of the same half-width, the total perveance is:

$$K_T = K_{beam} + K_{channel} = \frac{I_{beam}}{I_A \beta^2}\left(\frac{1}{\gamma^2} - f_e\right) \qquad (2)$$

where $f_e = n_{channel}/n_{beam}$ is the fractional space charge neutralization. The channel density is dependent on the fill gas species and pressure, P:

$$n_{channel} = \frac{P_{(Torr)}}{\alpha_0}\int_0^t n_{beam}(t')dt' \qquad (3)$$

where α_0 (a constant determined by gas species) is approximately 1 for argon.

As an IREB enters the IFR cell it starts to generate a plasma due to impact ionization of the ambient neutrals by the beam electrons. Initially, both the perveance and the emittance are defocusing to the envelope radius (eq. 1) and the beam head expands to some radius, r_{max}. Due to the electric field generated inside the beam by its own space charge, the plasma electrons are quickly ejected from the beam interior. The ions remain forming a positively charged channel which partially neutralizes the beam space charge. Still early in the current pulse, f_e exceeds $1/\gamma^2$ and the total perveance becomes focusing (eq. 2) resulting in a net pinch force on the beam. As

neutralization accelerates through the rise of the pulse, the pinch force increases in proportion to the growing channel ion density (eq. 3) imparting a monotonically decreasing radial profile on the beam. When the perveance term balances the emittance term the beam is in equilibrium and the envelope radius is constant; however, f_e continues to increase through the fall of the beam pulse and the envelope reaches some final radius value, r_{final}. The minimum beam envelope radius is limited to about 0.6 of its injection radius with the excess pinching force adding to the beams emittance.[2] The time from when the envelope radius departs from r_{max} to when it reaches r_{final} can be defined as a tailoring duration time, t_c. The parameters t_c, r_{final}, and the tailoring ratio $N=r_{max}/r_{final}$ (figure 1) are primarily controlled by adjusting the normalized beam input emittance (by changing the thickness of the cell input foil) and the total perveance (by changing the cell gas pressure) as outlined above. Practical IFR pressures are kept low enough so that the space charge neutralization fraction remains below 1 for the pulse duration. This prevents the generation of return currents in the excess channel plasma which could modify the favorable beam radius profile.

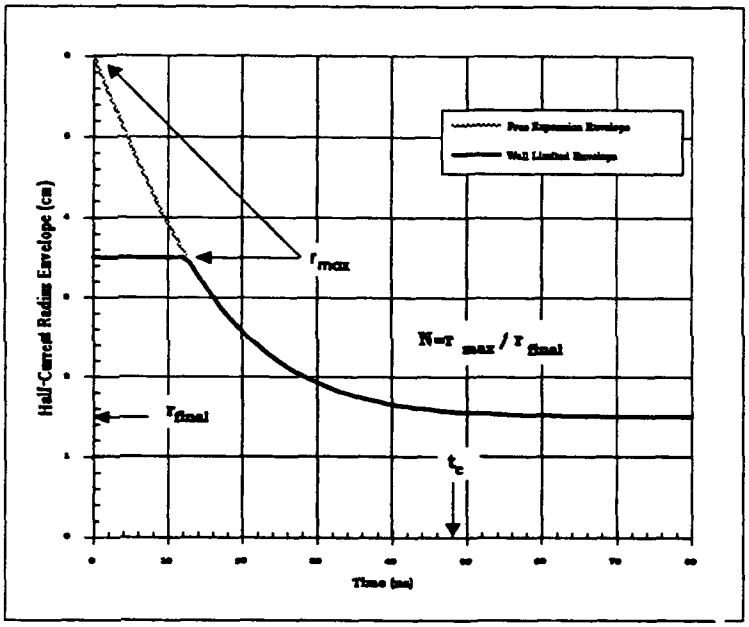

Figure 1- Radius Tailoring Parameters

The space charge neutralization effect of the IFR cell is also the mechanism for providing some beam centering and sweep reduction. As f_e rises above $1/\gamma^2$ the decentering force due to the wall image charges is nullified allowing the force from the wall image currents to center the beam. However, the centering force is proportional to f_e which means that centering will be weak in the beam head before there is substantial neutralization. Also, since the force is proportional to $1/r_{wall}^2$, centering will be weak in the larger diameter IFR cells needed for radius tailoring.[4]

III. SuperIBEX EXPERIMENTS: The physical set-up for the 10 cm diameter IFR experiment is shown in figure 2. The diagnostics used in the conditioning experiment were:

- Beam bugs measuring beam current and centroid position at the cell entrance and exit.
- 5-element SFC[5] measuring the beam current distribution for radius tailoring at 3 cm and for emittance tailoring at 26 cm from the cell exit foil.
- 4 frame GOI with 120 ps resolution for time resolved 2-D beam current distribution from Cerenkov emission of a thin Teflon sheet.

- Optical streak camera for time resolved, 1-D beam current distribution, radius, and centroid position from Cerenkov emission.

A matrix of shots was generated to cover the parameter space: cell pressure 3-10 mTorr argon, input ε_n from 0.5-1.6 rad-cm, cell diameter of 10 and 20 cm, and diagnostic positions of 3 and 26 cm from the cell output.

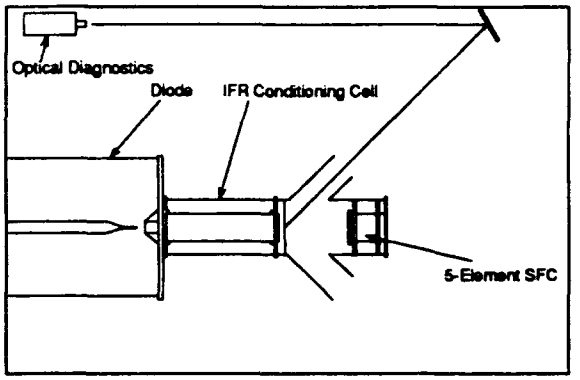

Figure 2- Experimental Configuration

IV. RESULTS AND DISCUSSION: For the above parameter space, radius tailoring profiles were measured showing N=2-5, t_c=5-40 ns, and r_{final}=0.75-3.0 cm primarily using the SFC. Similar measurements using the optical diagnostics were nearly identical from the beam head through the equilibrium point and were more accurate in the tail of the beam where the SFC data is affected by plasma production within the device.[6] With the input ε_n held at ~1.0 rad-cm, a cell diameter of 10 cm, and an injected current of ~18 kA the effect of IFR argon pressure on radius tailoring is as follows (figure 3):

- *Pressure too low:* the tailoring onset is late and t_c (and thus r_{final}) is not reached within the pulse (since $f_e(t)$ is proportional to pressure) producing a radius profile with a r_{max} that fills the cell for much of the current rise and a beam body radius that slowly decreases. With the beam remaining larger than its injection radius the transport efficiency, X_{eff}, is low throughout the pulse (50%), N is small (note: the range of N is more limited for the 10 cm dia. cell), and the current density very low (3 mTorr curve).
- *Pressure too high:* the tailoring onset is early and t_c too abrupt with the half-current envelope reaching r_{final}~1 cm 5-10 ns before peak current. With a large f_e earlier in the pulse X_{eff} is quite high (~90%), N~4, and centering is stronger; however, the beam tail "over-pinches" possibly leading to excessive emittance growth (10 mT curve).
- *Pressure "optimum":* t_c extends 5-10 ns past peak current with the profile ramping gradually to an r_{final}~1.35 cm. With N~3 and X_{eff} on the order of 80% the beam has enough radius tailoring and current density (without tail overheating) to be effectively converted to a stable emittance tailored beam (5 mTorr curve).

The curves in figure 3 were very reproducible shot to shot. The species of fill gas is also a factor in controlling the tailoring profile. Heavier inert gases provide increased ion channel inertia which may "strengthen" the beam against some instabilities and larger ionization cross sections which promote faster neutralization.

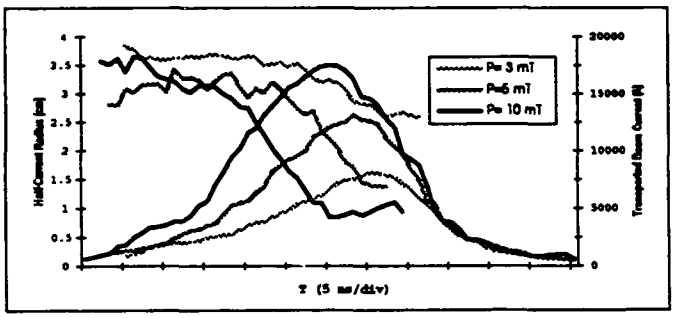

Figure 3- Pressure Effect on Radius Tailoring

The accelerator and the cell entrance foil determined the emittance of the input beam. When ε_n was increased (by using a thicker entrance foil) while cell gas pressure remained constant at 5

mTorr, r_{final} was reached later in the beam because of the longer time required for the perveance to balance the larger ε_n (figure 4). Beams with lower ε_n (accelerator only~0.5 rad-cm) were difficult to radius tailor and their tail often over-pinched as would be expected. Higher ε_n beams (accelerator + 5 mil Ti foil~1.6 rad-cm) allowed t_c to extend through the pulse but more current was lost to the walls from head expansion and r_{final} was larger. Additionally, a thicker exit foil was required to fully convert the radius tailoring to emittance tailoring which substantially decreased the beams usefulness for propagation experiments.

The cell diameter also influences transport efficiency, tailoring ratio range, and magnitude of centering. The 20 cm diameter cell allowed larger N overall and larger X_{eff} for lower pressures and higher ε_n but provided little centering and sweep reduction. The 10 cm diameter cell limited the measurable half-current r_{max} to 3.54 cm (the half-current value if the beam uniformly fills the tube) and more beam was lost at lower pressures and higher ε_n but some needed centering and sweep reduction was achieved.[4]

The magnitude of the input current did not have a strong effect on radius tailoring. With the pressure and ε_n held constant, similar profiles were measured for the for input currents ranging from 10-27 kA. The validity of this result may be skewed due to the way that input current is selected from the accelerator (by changing the diameter of an input aperture). The low current shots may have had a lower input ε_n than the high current shots so input ε_n may not have been constant for the range of currents tested. Qualitatively, the lower current beams (10-18 kA) were more easily tailored and the higher current beams (18-27 kA) displayed better centering (as would be expected). Beams above 27 kA were difficult to radius tailor in the IFR cell.

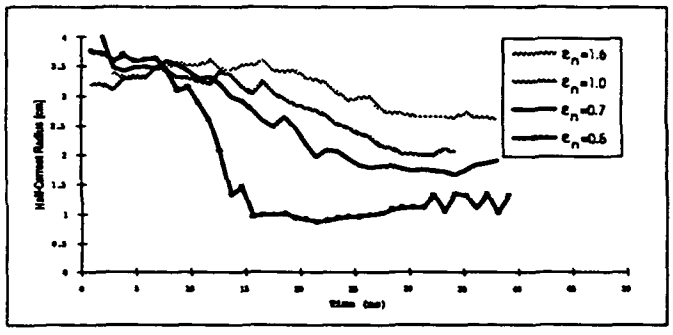

Figure 4- Input Normalized Emittance Effect on Radius Tailoring

It is clear that with the balance of pressure, input emittance, and cell diameter a radius tailoring profile with a large ratio, long duration, and tight final radius can be achieved while maintaining a high current transport efficiency. With the proper choice of exit foil this "optimum" radial profile can be converted to an emittance tailored profile. Figure 5 shows the equilibrium radius profile of a beam conditioned at optimum pressure and input ε_n in a 10 cm diameter cell and passed through a matched scattering foil (5 mil Ti) at the IFR cell exit. The measurement is made with the SFC after 26 cm of propagation in full density air where the beam is in equilibrium and the profile depends only on the emittance. Comparing this with a radius tailored profile generated from the same input parameters (5 mT data of figure 3) one can see that the profiles are consistent and the final radii nearly the same indicating good conversion of radius tailoring to emittance tailoring via the

matched exit foil. Beams which were conditioned as such propagated stably for a full Nordsieck length.[7]

V. CONCLUSIONS: IFR cells provide a simple and passive means for effective radius tailoring of IREBs over currents in the 10-27 kA range. Manipulation of the total perveance and input emittance by adjusting cell pressure and input foil thickness can produce beams with varying tailoring onset, 5-40 ns tailoring duration, and final radii from 0.75 to 3.0 cm. The choice of cell geometry has produced transport efficiencies from 50-100% and tailoring ratios from 2-5 with smaller radius tubes providing more centering in the beam body. The radius tailored beams can be efficiently converted to emittance tailored beams for use in propagation experiments.

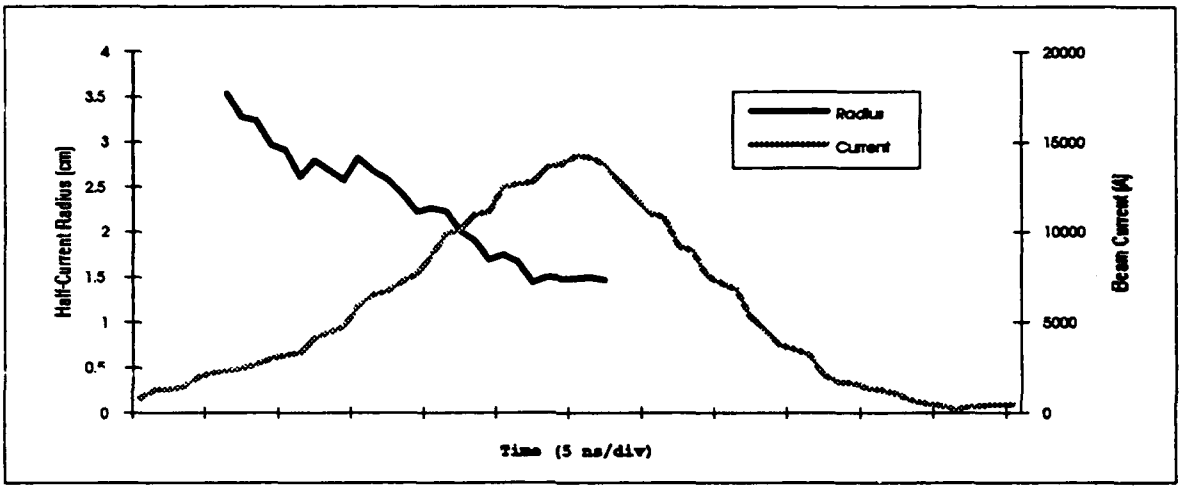

Figure 5- Profile of Emittance Tailored Beam

* Work supported by the Office of Naval Research

@ Science Applications International Corporation, McLean, VA 22102

REFERENCES

[1] M. Lampe et al., Phys. Fluids **27**, 2921 (1984).
[2] R. Hubbard et al., *Simulation of Electron Beam Transport in Ion-Focused Regime Conditioning Cells*, NRL Memo Report 6983, (1991).
[3] E. Lee and R. Cooper, *General Envelope Equation for Cylindrically Symmetric Charged-Particle Beams*, Part. Acc. **7**, 83 (1976)
[4] M. Myers et al., *Transport and Centering in IFR Cells*, to be published.
[5] T. Peyser et al, *A Segmented Concentric Faraday Cup for Measurements of Time-Dependent Relativistic Electron Beam Profile*, Rev. Sci. Instrum. **62**, 2895 (1991)
[6] T. Peyser et al., *Beam Profile Diagnostics on the SuperIBEX Exp.*, these proc.
[7] J. Antoniades et al., *IREB Propagation in High Pressure Gaseous Media.*, these proc.

BEAM PROFILE DIAGNOSTICS ON THE NRL SuperIBEX EXPERIMENT*

T.A. Peyser,[a] M.C. Myers, R.E. Pechacek, D.P. Murphy,
J.A. Antoniades and R.A. Meger

Charged Particle Physics Branch
Plasma Physics Division
Naval Research Laboratory
Washington, DC 20375-5000

Three independent and complementary diagnostics have been developed to measure the time-dependence of the beam half-current radius produced by the 5 Mev, 100 kA SuperIBEX electron accelerator at the Naval Research Laboratory. A novel five-element segmented concentric Faraday collector has been built which gives the beam half-current radius with nsec time resolution. Two optical streak cameras and an ultra-fast optical framing camera have been used to give time-resolved measurements of the beam radius from Cerenkov emission produced by thin Teflon or quartz foils placed in the beam path.

I. INTRODUCTION Present efforts at reducing the resistive hose instability take advantage of the convective nature of the instability and rely on carefully shaping the beam radius or, equivalently the beam emittance, throughout the pulse thereby creating a mismatch between the maximum instability growth rates from one section of the beam to the next.[1-4] Measurement of the time evolution of the beam radius at injection into a propagation chamber is essential to test these theoretical predictions of hose-instability suppression. Three independent and complementary diagnostics have been developed to measure the time-dependence of the beam half-current radius produced by the 5 Mev, 100 kA SuperIBEX accelerator at the Naval Research Laboratory: 1) a multi-element segmented concentric Faraday collector; 2) two optical streak camera systems giving a continuous one-dimensional image of Cerenkov emission from a vertical beam diameter with approximately one nsec time resolution; and 3) an ultra-fast optical framing camera giving a fully two-dimensional image of Cerenkov emission produced by the beam at four independent times during the beam pulse with one or two nsec time resolution.

II. SEGMENTED CONCENTRIC FARADAY COLLECTOR The design, construction and use of a novel five-element segmented concentric Faraday collector (SCFC) giving the radial beam profile and beam current density with nsec time resolution has been described in detail elsewhere[5]. Two innovations in the Faraday cup used here are the multiple collector elements

---

* Supported by Office of Naval Research.

[a] Science Applications International Corp., McLean, VA 22102

arranged in a simple concentric geometry and the use of a thin (3 mm) graphite overlayer followed by a range-thick (22 mm) stainless steel underlayer for each collector element. The SCFC consists of a center cylindrical collector of radius 0.76 cm surrounded by four annular collectors of outer radii 1.67, 2.59, 3.50 and 4.62 cm. The graphite overlayer reduces surface damage and secondary electron emission, while the stainless steel underlayer captures the electrons incident on each element with minimal scattering from one element to the next. Each collector element is electrically isolated from the next, and the deposited charge is shunted to ground through a nested array of Rogowski coils giving the current collected within the radius of each collector. SCFC results for the current density and beam half-current radius at the exit of a low-pressure IFR cell are given in the paper by Myers et al. in these proceedings.[6]

The equivalent of a sixth large-radius Faraday collector element has been added by incorporating a beam current measurement from a Rogowski coil or beam bug into the diagnostic. The use of a large-area beam current monitor as a sixth collector element improves the measurement of the beam radius in beamlines with wall (r_w) radii larger than the radius of the fifth Faraday collector ($r_w >> 5$ cm). Figure (1) gives a comparison of results for a five- and six-element SCFC where the six-element collector consisted of a 9.5 cm radius beam bug as the effective outermost collector element.

Although the SCFC has proven to be extremely valuable for beam radius profile measurements, it has several major limitations. First, the collector itself acts by definition as a beam stop and hence it is completely and totally perturbative. Second, the limited spatial resolution of the collector elements introduces uncertainties regarding the actual beam current density profile. Third, there is a failure mode after the peak current (giving an erroneous apparent rapid increase in the beam radius) associated with operation of the diagnostic above some critical total current and current density, typically 15 kA and 3 kA/cm^2.

III. OPTICAL DIAGNOSTICS: INTRODUCTION Optical diagnostics using high-speed streak and framing cameras viewing Cerenkov emission from thin convertor foils placed in the beam path do not suffer from the same limitations as the SCFC discussed above. Two optical streak cameras and an ultra-fast framing camera or Gated Optical Imager (GOI) have been used extensively on SuperIBEX to give optical time-resolved measurements of the beam current density profile and radius from Cerenkov radiation emitted by thin (3-5 mil) FEP Teflon or (25 mil) quartz foils placed in the beam path normal to the beam axis. Whereas the increase in beam emittance from scattering in a thin titanium foil is given by $a_b T^{1/2}$ rad-cm where T is the thickness in mils and a_b is the beam radius in cm, the emittance increase from a teflon foil goes as $0.133\ a_b T^{1/2}$ rad-cm.[7] The scattering from a 5 mil teflon foil is thus equivalent to that from a 0.1 mil titanium foil. Since emittances add quadratically, assuming an initial beam emittance of 1.0

rad-cm and a_b=1.5 cm, the use of a thin teflon Cerenkov converter results in only a 10% increase overall in beam emittance.

The teflon Cerenkov converter is placed at the entrance of an optical diagnostic cell which attaches to the SuperIBEX beamline and contains two line-of-sight viewing ports at forward 45° angle with respect to the beam axis[8]. The exact dependence of the optical emission on the Cerenkov angle was relaxed by roughing the rear surface of the Cerenkov emitter to provide an isotropic emission source.

IV. OPTICAL DIAGNOSTICS: STREAK CAMERAS Two optical streak camera systems (Hadland Imacon 500 and Imacon 790) were used to give a continuous one-dimensional image of Cerenkov emission from a vertical chord located at the center of the Cerenkov converter foil. The Imacon 500 used a 1000 mm focal length Questar telescope, and the Imacon 790 used a 500 mm focal length telephoto lens to safely image the 15 cm diameter Cerenkov foil from a distance of approximately 20 m upstream of the SuperIBEX diode and IFR conditioning cell. The Imacon 500 was operated at a streak speed of 2.8 ns/mm and the Imacon 790 was at 1.8 ns/mm.

Both cameras used Polaroid film proximity-focussed onto the streak camera output phosphor. A second stage of image intensification on the Imacon 500 permitted use of the slower speed, higher dynamic range Type 53 film whereas the Imacon 790 required the higher speed, high contrast Type 667 film. The streak image recorded on the Polaroid film was then digitized with a hand-held scanner at 256 grey scales and 300 dpi giving a time-resolution of 240 ps/pixel for the Imacon 500 and 105 ps/pixel for the Imacon 790. Images from both streak cameras were compressed 4.17 and 9.52 times using a bilinear interpolation scheme to give an effective time resolution of approximately 1 ns/pixel.

Quantitative analysis of the streak camera images requires a detailed calibration of the combined system uniformity and linearity. The uniformity of both cameras was measured by obtaining a streaked image of a flashlamp illuminating a single optical diffuser element. A calibrated stepped neutral density filter wedge placed at the input slit of the Imacon 500 was used to measure the instrument linearity and dynamic range. The use of Polaroid film as opposed to a CCD readout at the streak camera output phosphor exacerbates an already serious problem with the dynamic range of the instrument. Using Polaroid Type 53 film, the Imacon 500 streak camera diagnostic has at best a 50:1 dynamic range. Since the Cerenkov emission is directly proportional to the beam current density, a complete time history of the beam current density profile requires that the instrument be able to resolve current densities in the beam head ($I \leq 1$ kA, a_b≈5 cm) $\langle J \rangle \approx 15$ A/cm^2 and at peak current (I≈15 kA, a_b≈1.25 cm) $\langle J \rangle \approx 3$ kA/cm^2. Given the intrinsic limits on the instrumental dynamic range, the poor dynamic range of the recording film and the necessity to operate the streak camera at a fixed intensifier gain for a given exposure, special techniques are required to achieve the 200:1 or greater dynamic range required by the measurement. Custom

neutral density filters consisting of photometrically-calibrated ND=0.3 or ND=0.6 metallic overcoating on half of 2 mm thick, 50 mm square BK7 glass substrates placed at the Imacon 500 entrance slit have been used to extend the overall instrumental dynamic range. A shaped input slit with maximum width at the top and bottom of 2 mm and a minimum width at the center of 200 μm has been used with similar result on the Imacon 790.

The digitized images were corrected for combined film and instrument nonlinearity using the above-mentioned calibration procedure. Images acquired with the half neutral-density attenuating filters typically contained 5-10 ns of data on the unattenuated image half not present on the attenuated image half. Similarly the unattenuated image half may contain 10-15 ns of image intensities in excess of the film saturation value in contrast to the better exposed attenuated image half. The image analysis routines were written in MATLAB – a high-level numerical language. The data analysis routines parse the data file into two sets and for early times only fit the data from the half-profile with the unattenuated image. At later times a single composite image is created from both halves by scaling the intensity of the attenuated half and discarding data points on both halves in excess of the film and digitizer saturation value. A similar deconvolution procedure is applied to the intensity variation introduced by the shaped input slit on the Imacon 790. The beam half-current radius is obtained by fitting vertical lineouts of the processed digitized images in nsec increments to Gaussian, Bennett or double Gaussian profiles. Figure (2a) shows the raw data from an Imacon 500 image using a half neutral density filter. Figure (2b) gives the resulting half-current radius from a nonlinear least squares fit to a Bennett profile.

Finally, the fidelity of the instrument in reproducing a known optical profile was tested by analyzing known optical density profiles. A helium-neon laser illuminating a 20 μm rectangular slit or 10 μm pinhole was used to obtain a streak image of a known Fraunhoffer diffraction pattern. The helium-neon laser was not a pulsed system, so an electro-mechanical optical shutter was required between the rectangular slit or pinhole and the streak camera entrance slit to avoid damage to the streak camera photocathode. The images were digitized, processed and analyzed with the same data analysis routines as for the experimental data itself. A second test of the instrumental accuracy in measuring a known optical profile from an apodizing density filter with a prescribed transmitted Gaussian spatial intensity profile is in progress.

V. OPTICAL DIAGNOSTICS: GATED OPTICAL IMAGER (GOI) An ultra-fast four-frame framing camera or Gated Optical Imager (GOI) with time resolution from 120 ps to 5 ns has been used to provide dramatic evidence of radius tailoring from low pressure IFR cells and combined IFR-Bθ cells.[6,8] The four-frame GOI system used in the present experiments consists of four completely independent framing cameras with arbitrary interframe spacing. The gatewidth and the image intensifier gain can be set independently on each channel. A single 2000 mm focal length Celestron telescope images the 15 cm diameter Cerenkov converter foil from a distance of 50

m. An optical relay system projects the image from the Celestron through a four-way optical beam splitter which provides four images of equal intensity on each of the four GOI channels. Four separate 8-bit CCD readouts, with separate framegrabber boards driven by a Macintosh SE/30, are proximity-focussed to the output phosphor of each GOI channel.

The GOI embodies two new technological innovations in order to achieve framing camera gatewidths below the historic 5 ns limit.[9,10,11] The first takes advantage of recent advances in the production of short, high voltage pulses (1 kV, < 10 ps risetimes) using avalanche stack technology. The second is based on the insight that extremely fast but uniform gating of a large-area (18-25 mm diameter) microchannel plate (MCP) can be achieved by gating a low-inductance external electrode (>80% transmissive wire mesh) capacitively coupled to the MCP itself.

Quantitative analysis of the GOI images, as with the streak camera images, requires photometric decalibration of the instrument as a whole to insure that the measured signal correctly maps the optical intensity from the Cerenkov emitter. Calibrated neutral density step wedges were placed directly on the GOI photocathode fiber-optic faceplates, and images were acquired in DC and pulse mode for a range of input intensities and intensifier gains. Image nonuniformity is removed using standard flatfield correction routines in conjunction with a uniform illumination source created by multiple sources on a diffusing element. Nonlinearity in the four CCD readouts can be corrected in the image processing or by direct adjustment of the CCD gain controls. Detailed tests of the instrumental accuracy in measuring a known optical profile from an apodizing density filter with a prescribed transmitted Gaussian spatial intensity profile are currently in progress.

The two-dimensional character of the images and the ability to set the exposure duration and image intensifier gain for each channel independently alleviates many of the problems in image acquisition and analysis that afflict the streak camera data. While analytic functions such as Bennett and Gaussian profiles have been widely used to model relativistic electron beams, detailed analysis of the GOI optical data from SuperIBEX often shows a significant deviation from such profiles. In many cases, a tight core intensity is observed surrounded by a lower intensity halo suggesting that a more appropriate analytic profile might be a double Gaussian function. Detailed information on the beam current profile is not available from the SCFC since it measures the total integrated current within a segment radius, and hence is unable to resolve beam structure on a spatial scale less than or equal to the collector step size (≈1 cm). Figure (3) shows the double Gaussian profile necessary to fit data from a vertical lineout of a GOI image with a core-halo distribution (half-current radius from numerical analysis ≈ 1.91 cm). A single Gaussian fit correctly models the core profile, but neglects the current density in the halo.While the current density in the halo may be low, the total current in the halo may be appreciable and half-current radii measurements from the core alone may accordingly be in error. The double Gaussian fit

this case is a better fit to the data, but the half-current radius no longer has the same simple physical expression as for a single Gaussian or Bennett profile.

A more direct numerical solution to the problem of determining the half-current radius can be obtained by finding the current density contour containing half the total beam current. Fig. (4) shows the current density profile obtained by plotting the GOI data in three-dimensions where intensity is a function of two spatial dimensions. A wealth of information regarding the beam current density profile is clearly available from such data. The optical intensity of the GOI image was calibrated in terms of the beam current density by taking the instantaneous beam current at the time of the GOI frame from a beam bug located 1.5 cm upstream of the Cerenkov foil. The current density calibration can be determined by equating the total optical intensity to the instantaneous beam current. Fig. (5) shows the current density contour for the same image containing half the total current. A graph showing the detailed agreement between the GOI measurements and the SCFC is given in the paper by Meger et al. in these proceedings[12].

ACKNOWLEDGEMENTS The authors wish to acknowledge the support and encouragement given to the problem of diagnostic development by the theorists in the NRL Beam Physics Group, most notably R.F. Hubbard, R.F. Fernsler and M. Lampe.

REFERENCES

1. E.P. Lee, Phys. Fluids **21** 1327 (1978).
2. R.F. Hubbard et al. "Beam conditioning and propagation experiments on SuperIBEX" *Intense Microwaves and Particle Beams III*, ed. H. Brandt, SPIE Conf. Proc. No. 1629, Bellingham, WA (1992).
3. R.F. Fernsler et al., "Theory and simulation of resistive hose instability in relativistic electron beams", these proceedings.
4. W.M. Fawley, Bull. Am. Phys. Soc. **35** 1954 (1990).
5. T.A. Peyser et al., Rev Sci Instrum **62** 2895 (1991).
6. M.C. Myers et al., "IFR Transport experiments on the SuperIBEX accelerator", these proceedings.
7. R.F. Hubbard, personal communication.
8. D.P. Murphy et al., "Transport of high-current, relativistic electron beams using active-wire B_θ cell techniques", these proceedings.
9. The GOI is manufactured by Kentech Instruments, Ltd in the United Kingdom. Single- and multi-frame GOI systems are available commercially from Grant Applied Physics, 2011 Los Angeles Ave., Berkeley, CA 94707.
10. J.D. Hares, SPIE **831** 165 *X-rays from Laser Plasmas* (1987).
11. P.E. Young et al., Rev. Sci. Instrum. **59** 1457 (1988).
12. R.A. Meger, "Charged particle beam propagation studies at the Navel Research Laboratory", these proceedings.

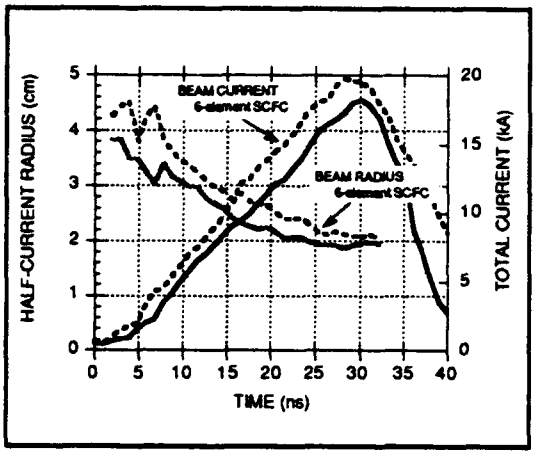

Figure (1): SCFC with 5 and 6 element collectors (current and radius).

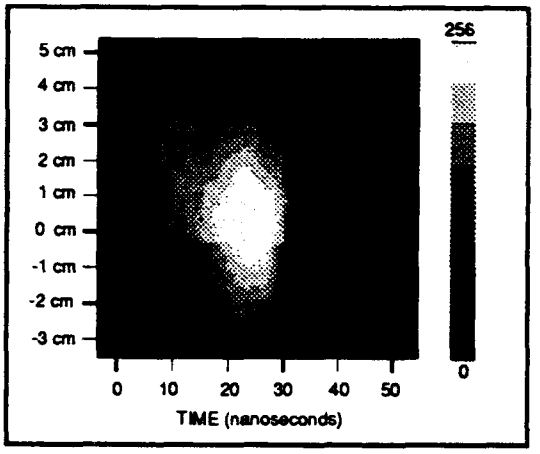

Figure (2a): Extension of streak dynamic range with custom half ND filter.

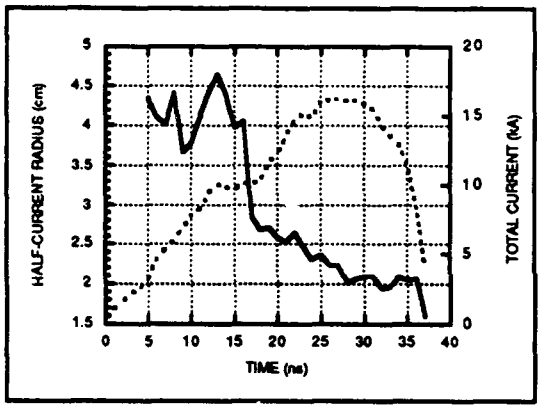

Figure (2b): Half-current radius from Bennett fit to processed streak camera image with extended dynamic range.

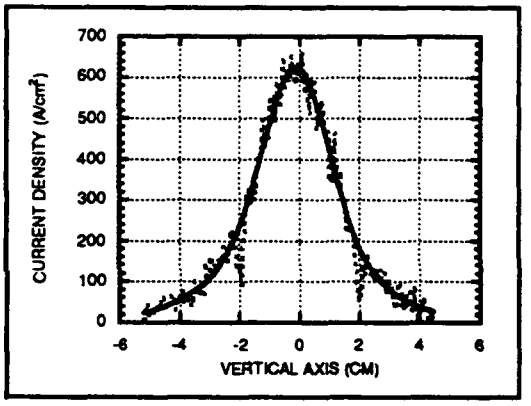

Figure (3): Double Gaussian fit to GOI lineout necessary for analysis of core-halo distribution.

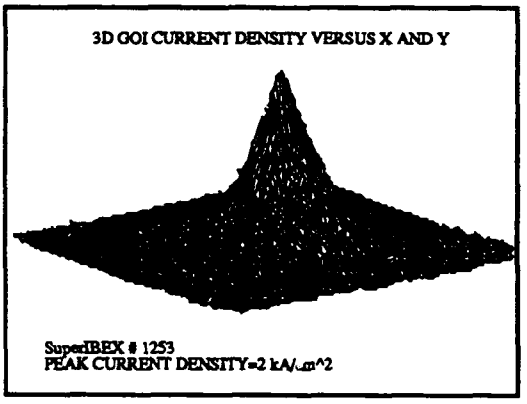

Figure (4): Beam profile from GOI image 1.5 cm after IFR cell at time of peak current

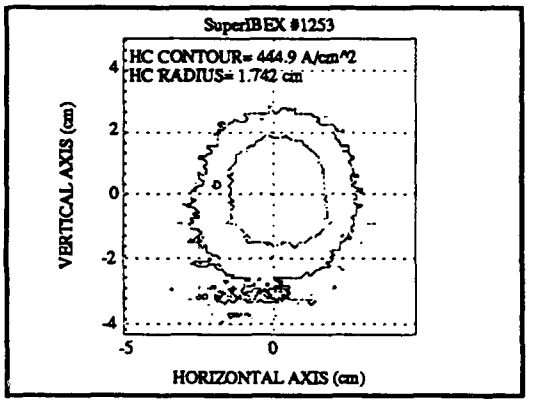

Figure (5): Current density contours at 150 A/cm2 and half-current contour from MATLAB analysis of GOI image

ASYMPTOTIC AND NONLINEAR EVOLUTION OF THE ELECTRON-HOSE INSTABILITY OF A REB PROPAGATING IN THE ION-FOCUSED REGIME*

Martin Lampe, Glenn Joyce, and Steven P. Slinker
Beam Physics Branch, Plasma Physics Division
Naval Research Laboratory, Washington, DC 20375

David H. Whittum
Accelerator Division, National Laboratory for High Energy Physics
1-1 Oho, Tsukuba, Ibaraki, 305, Japan

If a relativistic electron beam is propagated in an ion-focused regime (IFR) channel which is surrounded by a broad region of lower density plasma, a hose instability can occur, due to interaction between the beam and plasma electrons far outside the beam. We have calculated linearized dispersion relations and asymptotic growth, and performed particle simulations which reveal the nonlinear behavior. Three cases are considered: (1) Beam in a broad uniform underdense plasma (no localized channel). The instability is absolute, rapidly growing, and in typical cases of interest is not stabilized nonlinearly until the beam is disrupted. (2) Beam in a flat-topped channel of density n_c, surrounded by uniform plasma at lower density n_p. The instability is absolute, but the growth rate is reduced. Stabilization due to phase mixing occurs when the beam leaves the channel. (3) Beam in a rounded channel of density $n_c(r)$, surrounded by uniform plasma. The instability is convective, and the growth rate is small by order $n_p/n_c(0)$.

Introduction

Relativistic electron beams have been transported very successfully in the ion-focused regime, wherein the beam is guided by a narrow plasma channel which is collisionless, has density $n_c < n_b$ ("underdense"), and has line density $N_c \equiv f_c N_b < N_b$. Under these circumstances, all of the plasma electrons are ejected to large radius, and the beam is focused and guided by the remaining channel ion charge. However, in some applications, it may be desirable to transport the beam within a broad region of uniform underdense plasma, or within a channel surrounded by a broad region of lower density plasma. Then plasma electrons are expelled only from the region $r < a_n$, where a_n is the neutralization radius, defined by

$$\pi a_n^2 n_p = N_b - N_c, \qquad (1)$$

N_b is the beam line density, n_p (assumed to be uniform) is the density of the background plasma, $n_p+n_c(r)$ is the ion density within the channel, and $N_c \equiv \int dr\, 2\pi r\, n_c$ is the line density of the channel. A hose instability[1] can then occur, due to electrostatic interaction of the displaced beam with electrons at $r = a_n$. (Magnetic interactions, due to plasma eddy currents, can be neglected if $a_n < c/\omega_p$, where $\omega_p^2 \equiv 4\pi n_p e^2/m$.)

Analytic Linear Theory

We proceed by Fourier analyzing in z and $s \equiv t - z/c$, so that the mode dependence is exp(iωs+ikz). The plasma is modeled as a cold fluid. We shall consider three separate cases.

Case 1: Beam in Uniform Underdense Plasma

The pinch force on the beam is due entirely to the positive electrostatic potential well formed by the ions. (There is no self-force in the ultrarelativistic limit.) Since the ion density is uniform, the pinch force is harmonic and all beam electrons oscillate at a single betatron wavelength $k_\beta \equiv \omega_p/(2\gamma)^{1/2}c$. There is no phase mixing among different electrons. The plasma electrons respond resonantly at $\omega_o \equiv \omega_p/\sqrt{2}$, an effective plasma frequency at the interface between the electron-free region $r < a_n$ and the region of uniform ω_p outside $r = a_n$. The dispersion relation is

$$\left[1 - \frac{k^2}{k_\beta^2}\right]\left[1 - \frac{\omega^2}{\omega_o^2}\right] = 1, \tag{2}$$

or equivalently, if we use z and t as variables, with mode dependence exp(ikz-iω̃t),

$$1 - \frac{\omega_o^2}{\tilde{\omega}^2} - \frac{k_\beta^2 c^2}{(\tilde{\omega}-\tilde{k}c)^2} = 0. \tag{3}$$

The dispersion relation can be solved in the equivalent forms:

$$\frac{\omega^2}{\omega_o^2} = 1 - \frac{k_\beta^2}{k_\beta^2 - k^2}, \qquad \frac{k^2}{k_\beta^2} = 1 - \frac{\omega_o^2}{\omega_o^2 - \omega^2}. \tag{4}$$

There are sharp resonances in both k and ω, where the growth rates become infinite. As a result, the instability is absolute, and the dispersion relation is not sufficient indication of the spatio-temporal evolution of the disturbance. It is necessary to do a Laplace transform analysis to obtain asymptotic solutions of the initial value problem. Since (3) is the familiar dispersion relation for the two-stream instability, we have accessed and extended asymptotic solutions of that problem, first done by Briggs.[2] For a disturbance initiated at $s = 0$, we find that the envelope of the oscillations of the beam centroid $X_b(z,s)$ is given by

$$X_b(z,s) \propto \frac{z^{1/3}}{s^{5/6}} \exp\left[\frac{3\sqrt{3}}{4}\left(k_\beta z\right)^{2/3}\left(\omega_o s\right)^{1/3}\right], \quad \text{if } \omega_o s \gg k_\beta z \gg 1, \tag{5}$$

$$X_b(z,s) \propto \frac{1}{z^{1/6}s^{1/3}} \exp\left[\frac{3\sqrt{3}}{4}\left(k_\beta z\right)^{1/3}\left(\omega_o s\right)^{2/3}\right], \text{ if } k_\beta z >> \omega_o s >> 1. \quad (6)$$

This solution shows *very* rapid and continuous growth in both z and s. For example, eight e-folds of amplification occurs at $z = \lambda_\beta \equiv 2\pi c/k_\beta$ and $s = 2\pi/\omega_p$. Growth is so rapid because the beam is weakly focused compared to the destabilizing mode.

Case 2: Beam in *Flat-topped* IFR Channel Surrounded by Uniform Plasma

If the channel is somewhat broader than the beam, the pinch potential is harmonic and there is still no phase mixing. The dispersion relation is

$$\frac{\omega^2}{\omega_o^2} = 1 - \frac{n_p}{n_c+n_p}\frac{1}{1-f_c}\frac{k_\beta^2}{k_\beta^2-k^2} . \quad (7)$$

As in Case 1, the instability is absolute, but grows on a slower scale length, because the focusing force (due to the channel) is stronger. Analogously to Eq. (6),

$$X_b(z,s) \propto \frac{1}{z^{1/6}s^{1/3}} \exp\left[\frac{3\sqrt{3}}{4}\left(\frac{n_p}{n_c+n_p}\frac{1}{1-f_c}k_\beta z\right)^{1/3}\left(\omega_o s\right)^{2/3}\right],$$

$$\text{if } \frac{n_p}{n_c+n_p}\frac{1}{1-f_c}k_\beta z >> \omega_o s >> 1. \quad (8)$$

Case 3: Beam in *Rounded* IFR Channel Surrounded by Uniform Plasma

A rounded channel introduces betatron frequency spread, and therefore phase mixing. It is thus appropriate to use the spread mass model for the beam.[3] The dispersion relation is

$$\frac{\omega^2}{\omega_o^2} = 1 - \frac{n_p}{n_c+n_p}\frac{1}{1-f_c}\left[1+G\left(\frac{k}{k_\beta}\right)\right] , \quad (9)$$

where G the spread mass resonance function introduced by Lee,[3]

$$G\left(x \equiv \frac{k}{k_\beta}\right) = 3x^2 - 6x^4 + 6x^4(1-x^2)\left[\ln\frac{1-x^2}{x^2} + i\pi\right] . \quad (10)$$

This dispersion relation has no infinities; hence, the instability is convective. The displacement of the first perturbed slice decays due to phase mixing. Subsequent slices show growth, but eventually reach a maximum and decay ("convective saturation"). As in resistive

hose, the peak disturbance grows as $X_{max}(s) \sim \exp(\alpha s)$, where α is the peak growth rate from Eq. (9). If $n_p/n_c << 1$, then α is very small and is given approximately by

$$\alpha \approx \frac{n_p}{n_c+n_p} \frac{1}{1-f_c} \omega_o . \qquad (11)$$

Simulation Study

We have performed simulations with the 3-D particle code ELBA, which solves the full Maxwell equations self-consistently with the fully relativistic equations of motion for beam and plasma electrons. (The plasma ions are represented as stationary.) The simulations exhibit the evolution of the instability throughout the small-amplitude (linear) regime, as well as the nonlinear regime. We shall discuss the results of one simulation for each case.

Case 1: Beam in uniform plasma

Figures 1 and 2 show results from a simulation with $I_b = 1$ kA, $\gamma = 6$, $n_p = 7.4\times10^9$ cm^{-3}, $a_b = 1$ cm (Gaussian profile), $a_n = 3$ cm, $\omega_o = 3.4\times10^9$ Hz, $k_\beta = 0.047$ cm^{-1}. Figure 1 shows plots of $\ln(z^{1/6}X_b)$ against $z^{1/3}$, for s = 1.0, 2.0, and 2.67 ns. According to Eq. (6), the envelope of the unstable oscillations should be a straight line when plotted in this way, in the regime $k_\beta z >> \omega_o s$. The slope of the line should scale as $s^{2/3}$. This behavior is seen in Fig. 1, with the slopes about 10% less than predicted by Eq. (6). Good agreement is also seen in the regime appropriate to Eq. (5), although the dynamic range available in this regime is limited. At any fixed z or fixed s, growth continues without limit (until the beam is well out of the linear regime), indicating absolute instability. Over the short propagation range simulated, the instability grows by a factor of 400. Figure 2 shows cross-sections of the beam and of the plasma electrons, at s = 1.33 ns, at a sequence of propagation ranges z. The beam eventually slams into the plasma electrons beyond $r = a_n$, and shortly thereafter into the wall at r = 6 cm. Up to this point, the oscillations of the beam centroid proceed (as predicted by theory) without internal distortions of the beam profile, or broadening of the sharp plasma interface at $r = a_n$. No nonlinear saturation mechanisms are observed, at least until the thrashing of the beam has carried it well into the plasma. The instability clearly appears to be lethal.

Case 2: Beam in Flat-topped IFR channel surrounded by uniform plasma

Simulations of this case (not reproduced in this manuscript) again show agreement with the linear theory, to within about 10% accuracy. The instability is clearly seen to be absolute, and the nature of the perturbation is similar to Case 1 up to the point where the beam leaves

the channel. At that point, the ion-focusing force becomes anharmonic, leading to betatron frequency spread and phase mixing. The instability saturates, and the beam once again centers itself about the channel axis, with a consequent increase in emittance. Subsequently, the beam propagates with apparent stability. Theory would indicate that a stage of slow convective instability can ensue, but this has not been observed over the time scale simulated.

Case 3: Beam in Rounded IFR channel surrounded by uniform plasma

Figure 3 shows results from a simulation with $I_b = 2$ kA, $f_c = 0.5$, $\gamma = 27$, $n_p = 7.4\times10^9$ cm^{-3}, $a_b = 1$ cm, $a_c = 1$ cm (Gaussian profiles), $a_n = 3$ cm, $\omega_o = 3.4\times10^9$ Hz, $k_\beta = 0.047$ cm^{-1}. These parameters were chosen to give the same values of k_β and ω_o as in Case 1. Similarly to Fig. 1, ln X_b is plotted against $z^{1/3}$. The instability is clearly convective, as predicted by theory: at any given s a maximum amplitude is reached, followed by decay; the z-location for the maximum increases with s; the maximum amplitude attained increases with s, as predicted in Eq. (11). The growth rate is very small, as predicted; the instability amplifies by only a factor of 8 over the course of these simulations.

Conclusions

The simulations verify the simple linear theory. (This is reassuring, since there are many simplifying assumptions in the theory.) We have considered three cases: (1)Beam in a broad uniform underdense plasma (no localized channel). The instability is absolute, rapidly growing, and is not stabilized nonlinearly until the beam displacement X_b takes it well into the plasma at $r > a_n$. For most situations of practical interst, the IFR focusing of the beam is completely disrupted, and propagation is impossible. These results appear to be consistent with a recent experiment.[4] (2) Beam in a flat-topped channel surrounded by uniform plasma at lower density. The instability is absolute, but the growth rate is reduced. Propagation without significant disruption of the original equilibrium is possible over a limited range. When the beam leaves the channel, stabilization occurs, as a result of phase mixing. At this point, the beam evolves to a new equilbrium with increased radius and emittance, and (if parameters are chosen correctly) long range propagation appears to be possible without significant further disruption. (3) Beam in a rounded channel of density $n_c(r)$, surrounded by uniform plasma. The instability is convective, and the growth rate is small if $n_p/n_c(0) \ll 1$. Long range propagation, without significant disruption, is possible if parameters are chosen correctly.

References and Footnotes

* Supported by SDIO, and by DARPA under ARPA Order 7781, monitored by NSWC.

1. D. Whittum, W. Sharp, S. Yu, M. Lampe, and G. Joyce, Phys. Rev. Lett. 67, 991 (1991).
2. See A. Bers, in *Basic Plasma Physics I*, edited by A. A. Galeev and R. N. Sudan, *Handbook of Plasma Physics*, Vol 1 (North-Holland, Amsterdam, 1983), pp. 451-517.
3. E. P. Lee, Phys. Fluids 21, 1327 (1978).
4. J. D. Miller, R. F. Schneider, D. J. Weidman, H. S. Uhm, and K. T. Nguyen, Phys. Rev. Lett. 67, 1747 (1991).

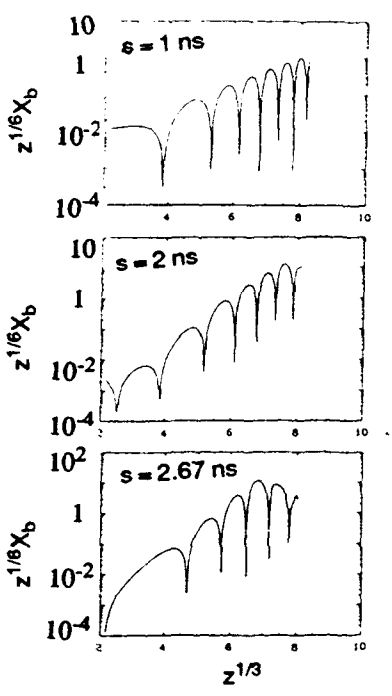

Fig. 1. Beam in uniform plasma.

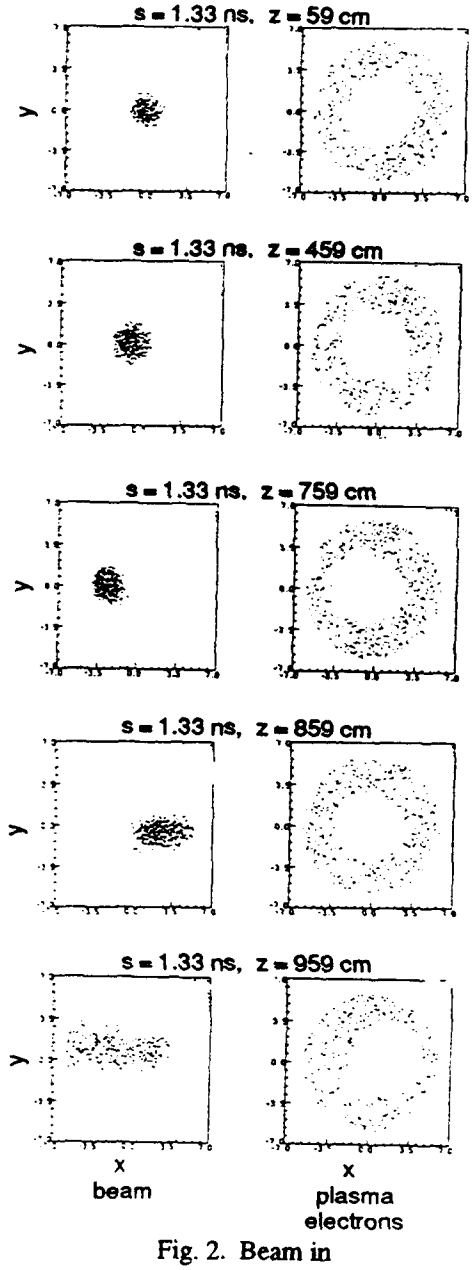

Fig. 2. Beam in uniform plasma.

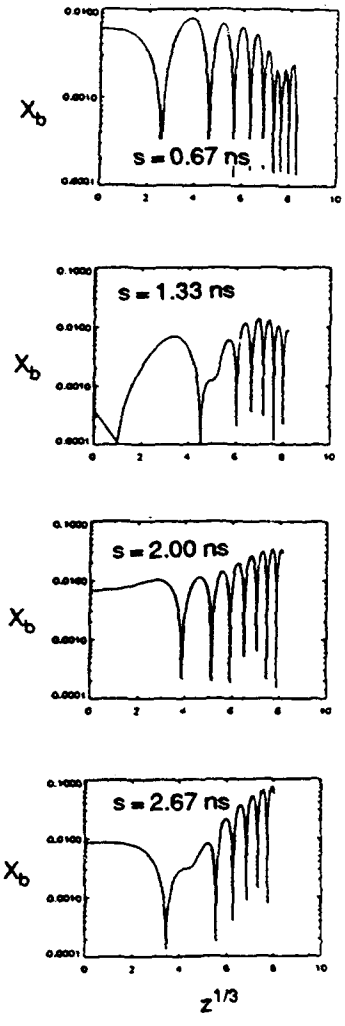

Fig. 3. Beam in rounded channel.

THEORY AND SIMULATION OF THE RESISTIVE HOSE INSTABILITY IN RELATIVISTIC ELECTRON BEAMS

R. F. Fernsler, S. P. Slinker, R. F. Hubbard, and M. Lampe

Beam Physics Branch, Plasma Physics Division
Naval Research Laboratory, Washington, D.C. 20375

The resistive hose instability typically disrupts intense, relativistic electron beams after a few betatron wavelengths in dense gas. Propagating a beam tens of betatron wavelengths or more is therefore challenging. This paper presents analytic theory and numerical simulations indicating that careful beam conditioning can achieve that goal.

Introduction

The resistive hose instability is the major impediment to the propagation of intense, relativistic electron beams in dense gas. Although the instability cannot be completely suppressed, it can be controlled using three features of the physics. First, the pinch force produced by the beam-generated plasma is anharmonic. As a result, electrons within a given beam slice oscillate at different frequencies and get out of phase. This introduces a damping term and causes the instability to convect toward the beam tail.[1] Second, the average oscillation frequency rises within the beam pulse so that no single hose frequency remains in resonance throughout the pulse. And third, processes like gas scattering and head mismatch reduce the contribution of perturbations launched early in the head. This is important because there is a component of hose that cannot be detuned, and this component is large in the head where the plasma resistivity and return-current fraction are high. In this paper we discuss techniques that allow beams to propagate without disruption from hose.

Analytic Hose Equations

A key feature of hose suppression is detuning the instability by making the beam parameters vary during the pulse. To study this detuning, we have modified[2] previous hose theory[1,3] to allow the beam radius r_b, current I_b, and current-neutralization fraction f to vary with distance ζ=ct-z from the beam head. Furthermore, plasma de-ionization has been included to analyze hose in the beam tail. We continue to assume, however, that the beam is ultrarelativistic and in pinched equilibrium, that the gas is homogenous and initially un-ionized, and that the plasma generated by the beam is weakly ionized. We also continue to neglect the electrostatic fields and forces, the dynamics of the plasma and gas, and variations in the beam and plasma equilibria with propagation distance z. The model incorporates conductivity broadening and saturation, explicitly includes betatron detuning, and applies, at least approximately, to the beam head as well as body. The effects of betatron detuning in z rather than ζ are analyzed in a separate section on gas scattering.

The model is based on a linearized analysis: $s(r,\theta,\zeta,z) = s_o(r,\zeta,z) - y_s\, \partial s_o/\partial r \cos\theta$ where s is any parameter, s_o is an azimuthal average of s, and $y_s(\zeta,z)$ is a "displacement." Here r is the radial distance from the beam-head axis, and θ is the angle about this axis. The treatment generally fails at large r or when $y_s > r_b$.

Applying the model to Ampere's law in the frozen-field[1] limit ($\partial/\partial z \to 0$) produces

$$\zeta_d \frac{\partial y_n}{\partial \zeta} = y_{no} - y_n \,, \tag{1}$$

where ζ_d is the magnetic dipole diffusion length, y_n is the centroid of the pinch current, and

$$y_{no} = \frac{1}{1-f} y_b - \frac{f}{1-f} y_\sigma \tag{2}$$

is a weighted average of the beam centroid y_b and the conductivity centroid y_σ. The diffusion length is given by $\zeta_d(\zeta) = \alpha(1-q)\pi r_b^2\sigma/2c$ where σ is the plasma conductivity, $q \sim 0.2$ stems from the dependence of σ on the plasma electron temperature,[4] and $\alpha \sim 1$ is a form factor determined by the radial profiles of the beam and plasma. The effective plasma return-current fraction is defined by

$$f(\zeta) = - \frac{\int_0^\infty dr\, r\, j_b j_p}{\int_0^\infty dr\, r\, j_b^2} \,, \tag{3}$$

where j_b and j_p are the beam and plasma current densities, respectively. Conductivity broadening increases α and decreases f, thereby stabilizing hose.

The plasma conductivity is assumed to evolve as

$$\frac{\partial \sigma}{\partial \zeta} = k' j_b - \beta\sigma \,, \tag{4}$$

where k' is a beam impact-ionization coefficient and $\beta(\sigma)$ is a generalized loss rate. Linearizing and applying the displacement approximation produces, after some algebraic manipulation,

$$\zeta_d \frac{\partial}{\partial \zeta} y_\sigma = (y_b - y_\sigma) k I_b \,, \tag{5}$$

where $k = \alpha(1-q)k'/2c$; in air, $k \approx 1/25$ kA. Note that there is no explicit dependence on $\beta(\sigma)$ in Eq. (5). This indicates that conductivity losses reduce the decay length ζ_d but do not alter the structure of the hose equations. Consequently, the beam tail should behave qualitatively similar to the head.

In the absence of phase mixing, Newton's force equation for the beam centroid is given by

$$\frac{\partial^2 y_b}{\partial z^2} = (y_n - y_b)\Omega_s^2 \,, \tag{6}$$

where the "shaking" frequency Ω_s is given in terms of the Alfven current, $I_A \approx 17\gamma$ kA, by

$$\Omega_s^2(\zeta) = \frac{1}{I_A I_b} (2\pi)^2 \int_0^\infty dr\ r\ j_b(j_b+j_p) \quad . \tag{7}$$

Here we have assumed a paraxial beam with a Lorentz mass factor $\gamma >> 1$.

Zero-Frequency Hose

In equilibrium, $\partial/\partial z = 0$ and the beam does not oscillate. There is then no need to include particle phase-mixing, so that Eqs. (1), (2), (5), and (6) reduce to

$$\zeta_d \frac{\partial}{\partial \zeta} (y_b - y_\sigma) = \left(\frac{f}{1-f} - kI_b\right)(y_b - y_\sigma) \quad . \tag{8}$$

The separation $(y_b - y_\sigma)$ between the beam and plasma thus grows as $\exp(g_o)$ where

$$g_o(\zeta, \zeta_o) = \int_{\zeta_o}^{\zeta} \frac{d\zeta}{\zeta_d} \left(\frac{f}{1-f} - kI_b\right) \tag{9}$$

and ζ_o is the first slice perturbed. The analysis is valid only as long as $|y_b - y_\sigma| << r_b$.

Late in the beam body, f/(1-f) is small while I_b is large. As a result, the beam-plasma separation decreases at late ζ. Most of the separation occurs early in the beam head just past the hose initiation point ζ_o.

Betatron Detuning in ζ

Because the beam equilibria are assumed to be z-independent, we can study high-frequency hose using Fourier analysis, $y \sim \exp(-i\Omega z)$. We can then incorporate phase-mixing of the particle orbits using Lee's spread-mass model[1] and rewrite Newton's equation (6) as

$$y_b = \left[1 + G(\Omega^2/\Omega_m^2)\right] y_n \ , \tag{10}$$

where $\Omega_m(\zeta) = (2\pi j_{no}/I_A)^{1/2}$ is the maximum betatron frequency and G is the spread-oscillator function determined by the profiles of j_b and j_p. Here j_{no} is the on-axis net current density. The net-current centroid then evolves according to

$$\left(\zeta_d \frac{\partial}{\partial \zeta}\right)^2 y_n + \left[kI_b - \frac{f+G}{1-f} + \zeta_d \frac{\partial}{\partial \zeta} \ln\left(\frac{1-f}{f}\right)\right]\left(\zeta_d \frac{\partial}{\partial \zeta}\right) y_n$$

$$- G\left[kI_b + \frac{1}{1-f} \zeta_d \frac{\partial}{\partial \zeta} \ln(G/f)\right] y_n = 0 \quad . \tag{11}$$

To proceed further, we set $y_n \sim \exp(g)$ and use a WKB approximation to determine that

$$g(\zeta,\zeta_o) \simeq g_o(\zeta,\zeta_o) + g_1(\zeta,\zeta_o) , \tag{12}$$

where g_o is the zero-frequency term given earlier and

$$g_1(\zeta,\zeta_o) = \int_{\zeta_o}^{\zeta} \frac{d\zeta}{\zeta_d} \frac{G}{1-f} . \tag{13}$$

Transforming the integral in ζ to one over Ω/Ω_m produces

$$g_1(\zeta,\zeta_o) = \int_{\Omega/\Omega_m(\zeta)}^{\Omega/\Omega_m(\zeta_o)} d(\Omega/\Omega_m) \frac{G(\Omega^2/\Omega_m^2)}{(\Omega/\Omega_m)} \eta^{-1} , \tag{14}$$

where the betatron detuning parameter is

$$\eta \equiv (1-f)\ \zeta_d \frac{\partial}{\partial\zeta} \ln(\Omega_m) . \tag{15}$$

The properties of G place a bound on g_1. For example, $g_1 \lesssim 0.6/\eta$ for self-similar Bennett distributions and constant η. Thus g_1, like g_o, is finite. Furthermore, both growth factors can be minimized using a beam with a prolonged, rapid rise in I_b (but not so steep as to trigger avalanche ionization which can be strongly destabilizing). That is, raising $dI_b/d\zeta$ increases kI_b more than f to reduce g_o, and it enlarges ζ_d and Ω_m to increase η and reduce g_1. In beams that are not emittance tailored, η can be as large as 0.1, but this still allows several orders of magnitude of hose growth.

The detuning parameter η can be augmented further by tailoring the normalized beam emittance ϵ_n to decrease with ζ. Tailoring flares the beam head and increases the rise of $\Omega_m \propto I_{eff}/\epsilon_n$, where the effective pinch current I_{eff} is closely related to $(1-f)I_b$. Tailoring is usually adequate if it keeps $\eta \gtrsim 0.2$ over a broad region in the beam head.

Betatron Detuning in z

In the above analysis, we allowed for variations with distance ζ from the beam head but not with propagation distance z. Here we consider the opposite limit where variations with z, caused by gas scattering, are more important than variations with ζ.

Gas scattering heats the beam transversely, causing it to expand. This expansion lowers the betatron frequency of a self-pinched beam according to[5]

$$\Omega_m(z)/\Omega_m(0) = r_b(0)/r_b(z) = \exp(-z/L_n) , \tag{16}$$

where the Nordsieck length $L_n \propto \gamma I_{eff}$. Gas scattering thus detunes the hose instability in z rather than

ζ. To incorporate this detuning, we define a new propagation parameter,

$$s(z) = [1-\exp(-z/L_n)]L_n \quad . \tag{17}$$

Force equation (6) can then be written as

$$\frac{\partial^2 y_b}{\partial s^2} - \frac{1}{L_n - s}\frac{\partial y_b}{\partial s} = (y_n - y_b)\Omega_s^2 . \tag{18}$$

The term containing $\partial y_b/\partial s$ can be dropped provided $(L_n-s)\Omega_i >> 1$ where Ω_i is the growth rate in s. Dropping this term allows us to use Lee's spread-mass model without modification; this gives the peak growth rate for Bennett profiles as $\Omega_i \simeq 0.18\Omega_m \simeq 1.6/\lambda_\beta$, where λ_β is the average betatron wavelength. Hose can therefore grow with an exponent as large as

$$g(z) \simeq \frac{1.6s}{\lambda_\beta} = \frac{1.6L_n}{\lambda_\beta}\left[1-\exp(-z/L_n)\right] , \tag{19}$$

in the regime $z \lesssim L_n$ and $\lambda_\beta << L_n$. This equation shows that Nordsieck scattering is strongly stabilizing as $z \to L_n$.

Hose Initiation Point

To lowest order, the zero-frequency hose growth factor varies as $g_o \sim \zeta_o^{-1}$ where ζ_o is the hose initiation point. Fortunately, several processes limit the smallness of ζ_o. For example, Eq. (19) indicates that hose is unimportant unless initiated where

$$\lambda_\beta(\zeta_o) < z, L_n(\zeta_o) \quad . \tag{20}$$

This restriction is often important for laboratory beams. Observe that betatron detuning in ζ can increase the minimum ζ_o where hose can be initiated, and thus it can decrease g_o as well as g_1.

Highly energetic beams are relatively unaffected by gas scattering (or ohmic erosion) so that ζ_o can approach zero. Hose then tends to grow continuously with z as perturbations from the head slowly convect back. To suppress this growth, the early beam head must either be extremely well centered at injection or blow off before undergoing appreciable hose growth. The head can be made to blow off by mismatching at injection. Head mismatch can therefore be used to limit hose growth.

Simulation Results

Previous experimental[6] and numerical studies[7] have shown that emittance tailoring can reduce hose growth, and the agreement between analytic theory and simulation is good. We emphasize, however, that the hose amplitude is sensitive to the injection conditions (and to code specifics), as might be expected of processes that suppress an exponentially growing instability by many orders of magnitude. This makes precise, quantitative prediction difficult. Furthermore, a robust scheme would ultimately require a highly reproduceable beam and conditioning apparatus.

To demonstrate hose suppression, we briefly describe two simulations of beams in full-density air. The first used the particle code SARLAC to simulate a 1 kA, 10 MeV beam with $r_b = 1$ mm. Recombination of the plasma electrons and ions held the dipole diffusion length ζ_d to much less than the pulse length ζ_p. In the regime $\zeta_d/\zeta_p << \lambda_\beta/L_n$, hose growth depends strongly on z but weakly on ζ_p. Furthermore, Eq. (19) applies, and it predicts a peak hose growth of $e^g \simeq 30$ at $z = 30$ cm $\simeq L_n/3 \simeq 2.5\lambda_\beta$. Without gas scattering ($L_n \to \infty$), the growth would be twice as large. SARLAC confirmed these predictions, showing a peak growth ~ 25 with gas scattering for a perturbation frequency of 5 GHz applied in ζ at $z = 0$.

The second example was a long-range simulation of a high-energy beam relatively unaffected by gas scattering or ohmic erosion. In this case, ζ_p determines hose growth more than z. To avoid exciting hose from particle noise, the multi-component linearized code VIPER was used in place of SARLAC. The beam was injected with: $r_b(\zeta) = 1$ cm; $I_b(\zeta)$ rising to 20 kA in 200 cm; a transverse thermal velocity $\beta_\perp(\zeta)$ falling by 3 over 300 cm; $\zeta_p = 900$ cm (30 ns); and a white-noise hose perturbation in ζ. The overheated beam head expanded so quickly that it did not excite hose in the body. As a consequence, hose grew by less than 30 at $z \simeq 50\ \lambda_\beta$ and subsequently decayed. The simulation suggests that such a beam would propagate to full range without disruption, provided the initial perturbations were less than 3% of the injected beam radius. However, when the beam was injected with a 3-to-1 variation in r_b and constant $\beta_\perp$ (to give the same variation in ϵ_n), less of the head blew off and hose grew by nearly 600 at much earlier z. This difference demonstrates the importance of mismatching the beam head.

Conclusion

In this paper, we extended hose theory to include: conductivity broadening and saturation; variations in r_b, I_b, ζ_d, and f with ζ; and variations in r_b with z. Simulations have been performed that confirm the general features of the theory. We have found that betatron detuning in z is most important for long pulses and modest propagation distances, while detuning in ζ is most important when the reverse is true. The latter commonly requires, however, some means of suppressing zero-frequency hose in the beam head. Head mismatch is one such means, and simulations indicate that modest hose growth (< 50) is possible even over very long propagation distances.

This work was supported by the Office of Naval Research and by the Defense Advanced Research Projects Agency, ARPA Order No. 7781, monitored by the Naval Surface Warfare Center.

References

1. E. P. Lee, Phys. Fluids 21, 1327 (1978).
2. R. F. Fernsler, M. Lampe, S. P. Slinker, and R. F. Hubbard, Bull. Am. Phys. Soc. 36, 2380 (1991).
3. M. Lampe, W. Sharp, R. F. Hubbard, E. P. Lee, and R. J. Briggs, Phys. Fluids 27, 2921 (1984).
4. S. P. Slinker, R. F. Hubbard, and M. Lampe, J. Appl. Phys. 62, 1171 (1987).
5. E. P. Lee, Phys. Fluids 19, 60 (1976).
6. W. M. Fawley, Bull. Am. Phys. Soc. 35, 1054 (1990).
7. R. F. Hubbard, S. P. Slinker, R. F. Fernsler, M. Lampe, and G Joyce, Bull. Am Phys. Soc. 34, 1996 (1990).

ELECTRON BEAM PROPAGATION IN THE ION-FOCUSED AND RESISTIVE REGIMES

R. F. Hubbard, M. Lampe, R. Fernsler and S. P. Slinker
Plasma Physics Division
Naval Research Laboratory
Washington, DC 20375

Pinched propagation of intense relativistic electron beams occurs in several distinct pressure regimes. In low density gases (~1-100 mtorr), the beam propagates in the ion-focused regime (IFR). The beam ionizes the neutral gas, and plasma electrons are ejected, leaving behind a positive ion column which pinches the beam electrostatically. At gas densities near 1 atm, the beam-generated plasma is resistive and the pinch effect is provided by the self-magnetic field of the beam. Beam transport experiments in both regimes have been performed on the Advanced Test Accelerator (ATA) at Lawrence Livermore National Laboratory and on SuperIBEX at the Naval Research Laboratory. IFR methods have been employed in both experiments to transport the beam prior to injection into the air and to introduce a head-to-tail taper in the the beam radius. IFR simulations have shown how the resulting beam radius and emittance profiles are influenced by gas density, chamber dimensions and entrance and exit foils. Beam propagation in dense gas is subject to disruption by the resistive hose instability. However, both experiments and simulations have shown that the emittance variation introduced by IFR transport can substantially reduce the growth of the hose instability. Both experiments have also propagated beams in reduced-density channels. Simulations predict that the channel may in some cases produce a moderate stabilizing and tracking effect arising from plasma currents flowing at the edge of the channel.

I. Introduction

Pinched propagation of intense relativistic electron beams offers the possibility of transporting these beams over long distances without guidance or confinement by external magnetic fields. In dense gases, the beam quickly produces sufficient ionization to provide space charge neutralization. The resulting plasma is collision-dominated or resistive, and the beam is confined[1] by its azimuthal magnetic field B_θ. An entirely different pinching mechanism occurs at much lower gas densities where the ratio of the beam-produced plasma density n_p to the beam density n_b is in the range $\gamma^{-2} << n_p/n_b < 1$. Plasma electrons are expelled, leaving behind a positive column or channel of ions which pinches the beam electrostatically. Propagation in this Ion-Focused Regime[2,3] (IFR) may also be accomplished by creating the channel with an external ionizing source such as a laser.

This paper describes and compares recent electron beam propagation experiments carried out on the SuperIBEX facility at the Naval Research Laboratory[4-7] and the Advanced Test Accelerator (ATA) at the Lawrence Livermore National Laboratory.[8,9] The experiments were similar in a number of respects. The primary goal in both cases was to study the resistive hose instability in air at densities near 1 atm and to develop techniques to limit instability

growth. Both experiments used IFR propagation prior to injection into the dense gas to transport and "condition" the beam. Finally, both experiments propagated the beam in reduced-density channels. Such channels offer the possibility of extending the effective propagation range by reducing beam degradation from scattering and collisional energy loss. Experimental parameters and configurations are summarized in Table I.

TABLE I. Typical beam, IFR cell and propagation tank parameters for Full ATA experiments, ATA Multi-Pulse Propagation Experiment (MPPE) and SuperIBEX experiments.

Parameter	ATA (Full)	ATA (MPPE)	SuperIBEX
Beam energy γ	80	21	10
Beam current I_{bo}	4-10 kA	2- 6 kA	10-25 kA
Initial beam radius a_o	1-2 cm	0.5-1.5 cm	1.2-2.5 cm
Accelerator type	Induction Linac	Induction Linac	Diode
Accelerator transport	Laser-IFR	Solenoidal	None
Number of pulses in burst N_p	1	1-5	1
Pulse separation time τ_s	N. A.	1-40 msec	N. A.
External density channel	None	None	Laser-discharge
IFR cell gas	Air	Xenon	Argon
IFR cell length L_c	200 cm	50 cm	40 cm
Centering methods	Laser-IFR	Tuning, Laser-IFR	Wire cell, 2-stage IFR
Propagation tank length z_{max}	20 m, open	5 m	5 m
Propagation tank radius a_w	15 cm, open	15 cm	100 cm

The hose instability is a macroscopic kink instability which amplifies transverse beam displacements.[1,4-10] Instability growth in the beam displacement Y_b scales with the betatron wavelength λ_β as the beam propagates in z. Disturbances initiated within the beam grow convectively as a function of the retarded time $\tau \equiv ct - z$; growth scales with the local magnetic dipole decay time τ_d which increases during the beam pulse. Analytical models and simulations of hose instability[1,4,8,10] have motivated the beam conditioning techniques described in the next section.

II. Post-Accelerator Transport and Beam Conditioning

A. Beam centering and emittance tailoring: The term "beam conditioning" refers to a variety of post-accelerator beam transport techniques[4-10] which are used primarily to reduce hose instability growth. The objectives of these techniques are to reduce the amplitude of initial transverse perturbations which seed the instability and to "tailor" the beam emittance in order to detune the head-to-tail coherence of the instability. The method for emittance

tailoring used on both ATA[8,9] and SuperIBEX[4-7] has been passive IFR propagation followed by a thick scattering foil. The foil effectively converts the radius taper to an emittance taper. The simple configuration shown in Fig. 1a was used on both experiments; ATA often used an upstream focusing lens (Fig. 1b). Figure 2 shows three different configurations which combine an IFR tailoring cell with some beam centering technique.

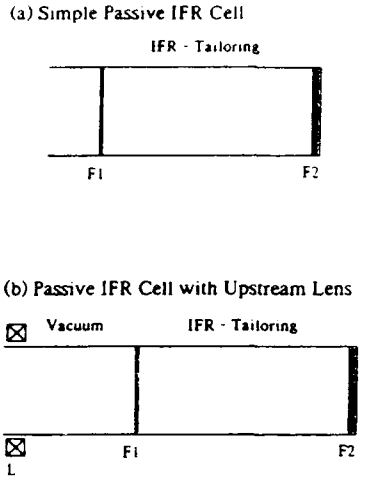

Fig. 1. Diagram of IFR tailoring cell configurations. Simple cell (a) is filled with a low density gas and uses a thin entrance foil (F1) and a thicker exit foil (F2). In configuration (b), the IFR cell is preceded by a vacuum transport region with a focusing lens (L).

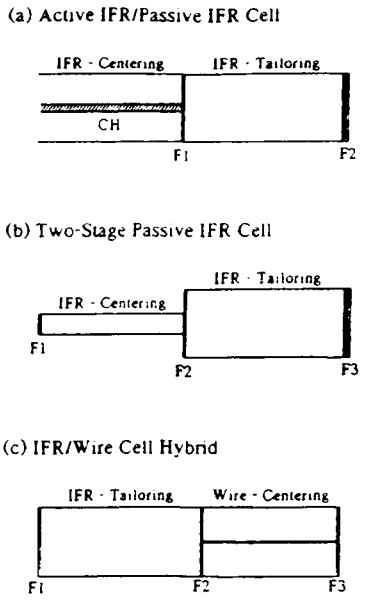

Fig. 2. Schematic of IFR cell combined with various centering cells: (a) an active IFR cell with a laser-generated plasma channel (CH), (b) IFR centering cell with higher gas density and smaller wall radius, and (c) vacuum or gas-filled cell with a current carrying wire.

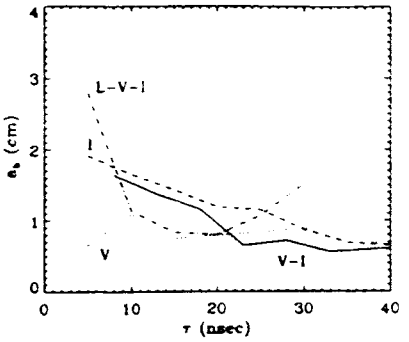

Fig. 3. Experimental beam radius $a_b(\tau)$ for ATA. Various beam conditioning configurations (V,I,V-I,L-V-I) are described in text.

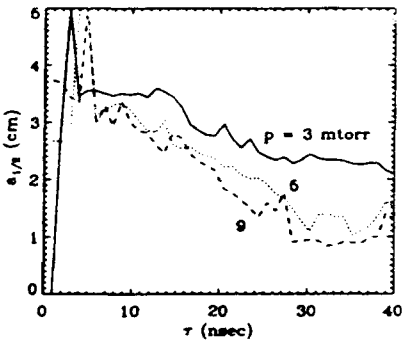

Fig. 4. SuperIBEX beam radius for 3 IFR cell pressures.

B. Beam conditioning on ATA: Most propagation and conditioning experiments on ATA were carried out on the full accelerator.[8] The parameters and configuration are summarized in Table I. Beam centering was primarily accomplished using laser-guided IFR propagation both in the accelerator and in post-accelerator transport sections. Laser guiding employed a KrF laser to ionize a low density benzene gas. This allowed up to 10 kA to be accelerated to 40 MeV without catastrophic beam breakup instability (BBU) growth. A 200 cm long IFR cell was used to tailor the beam, so the configuration resembled Fig. 2a.

The last propagation experiment on ATA was the Multi-Pulse Propagation Experiment (MPPE).[8,9] Solenoidal transport was used in the accelerator instead of laser-IFR; this limited the energy to 10 Mev but allowed up to 5 pulses to be generated in a burst. Most of the beam radius data came from gated images of Cerenkov light from a quartz foil. Figure 3 plots $a_b(\tau)$

for four different beam transport and conditioning configurations. As expected, simple vacuum transport (curve V) produced almost no beam tapering. The other three used an IFR cell which could be "tuned" to adjust the beam radius profile. For the examples shown in Fig. 1, a long IFR cell (curve I; Fig. 1a) or a vacuum-focusing region followed by a short IFR cell (curve V-I; Fig. 1b) produced a long, gentle beam taper. Adding a laser-guided damping zone ahead of the focusing lens (curve L-V-I; Figs. 1b and 2a) produced a sharper taper. Numerous simulations[9] have been performed using the FRIEZR code[4] for configurations similar to those in Figs. 1 and 2.

C. Beam conditioning on SuperIBEX: Emittance tailoring on SuperIBEX is accomplished with a 40 cm long passive IFR cell which is typically filled with argon at 3-10 mtorr pressures.[4-7,9] The beam radius $a_b(\tau)$ and beam current $I_b(\tau)$ can be controlled by varying IFR cell pressure, input foil thickness or the geometry of the entrance aperture. Figure 4 plots $a_b(\tau)$ for three SuperIBEX IFR cell pressures. A segmented Faraday cup was used to obtain this data; similar results have been obtained from optical diagnostics. The tapered radius profile agrees well with a simple analytical model.[9]

Most propagation experiments on SuperIBEX have employed a beam centering technique to augment the IFR tailoring cell. Early experiments used the two-stage IFR cell configuration in Fig. 2b. The IFR-wire cell hybrid, shown in Fig. 2c, has significant theoretical advantages. The current in the wire produces a highly-anharmonic potential and thus produces strong phase-mix damping.[12] Since this imposed current on the wire exists at the head of the pulse, dangerous perturbations in the beam head can be suppressed.[9] In addition, if the current in the wire is properly chosen, the beam radius profile produced by the IFR cell will be converted to a tailored emittance profile without the use of a thick scattering foil. Both gas-filled[4,7] and vacuum versions of the cell have been successfully deployed.

III. Beam Propagation Experiments

A. ATA Single Pulse Propagation: Four major propagation experiments were carried out on ATA. The first three used the "full" accelerator with laser-IFR transport. The first experiments produced strong hose instability growth and were not well-diagnosed. Improvements in "tuning" capability, including the use of tapering of the benzene density prior to injection into the IFR cell, resulted in substantial improvements in propagation during the second experiment. A 1 cm radius, 6 kA beam ($\lambda_\beta \simeq 100$ cm) was propagated to the end of a 15 cm radius, 20 m long propagation tank with no large hose motion and moderate beam loss to the walls.[8] Simulations with the SARLAC hose code reproduced the observed moderate hose growth but suggested that image currents in the wall reduced hose growth in the beam head. The third experiment demonstrated that the beam could be transported around a bend and propagated in open air. Stable propagation was observed beyond the ~15 m Nordsieck

scattering length,[8] but the beam radius was generally larger than in the previous experiments, and detailed hose diagnostics were not available.

Considerable single pulse propagation data were taken during the ATA MPPE experiment.[8,9] The propagation tank was only 5 m long, but λ_β was typically 30-50 cm. As expected, the observed hose instability growth was usually reduced when the beam radius was more heavily tapered, but some apparently well-conditioned beams were strongly unstable. This may have been due to the presence of strong drifts in the beam head arising from the lower beam energy in this region of the beam. This problem would not have been as severe on earlier ATA experiments which used IFR transport in the accelerator instead of the solenoidal transport used on MPPE.

B. ATA Multiple Pulse Propagation: The primary purposes of MPPE were to demonstrate that multiple beam pulses could be generated and conditioned, to study hose stability in beam-generated density channels, and to determine if the effective range of the beam could be extended by such channels.[8] Each of the five pulses was of comparable quality, and the IFR cell produced a similar radius taper for each. Hose instability growth was also comparable for each of the five pulses although there was some tantalizing evidence of reduced growth in some later pulses. Channel densities during the five pulse train were diagnosed using both Schlieren and laser deflection systems.[13] Relatively deep channels were produced in some cases near the injection point, but hose instability growth degraded the channels substantially during the later stages of propagation. There was little, if any, evidence for range extension.

C. SuperIBEX Propagation in Full Density Air: SuperIBEX has used each of the beam conditioning configurations described in Section II.C. to study propagation in a 5 m long tank. The Nordsieck scattering length for SuperIBEX is only ~4-6 m in full density air. The 1 m tank radius makes wall effects negligible. For a single passive IFR cell (Fig. 1a), a 1.5-2.5 cm radius beam has been propagated ~4 m without disruption in the moderate current regime (~14 kA).[4-6] Higher current beams (~21 kA) were much more unstable. Initial propagation results with the two-stage IFR cell (Fig. 2b) were encouraging but inconsistent,[4] and this approach has been abandoned in favor of wire cells. The best propagation results to date have been obtained with the IFR cell followed by a gas-filled wire cell.[4-7] Beams with 1.5-2 cm radius and peak current $I_0 \approx$ 14-17 kA have been propagated to the end of the tank with no apparent disruption in open shutter photographs and displacements of ~2 cm as measured by magnetic probes.

D. SuperIBEX Propagation in Density Channels: SuperIBEX beams have been propagated in deep density channels created using a laser guided electric discharge (LGED).[4,7] The channel is allowed to cool for several msec prior to beam injection to a temperature and density comparable to that which would be produced by a large number of tight beam pulses. Previous experiments on NRL's 1.2 MeV Pulserad beam generator had confirmed the

existence of a tracking force which causes the beam to be pulled toward the channel. The channel has a number of both stabilizing and destabilizing effects on hose instability which scale with the plasma return current. SARLAC simulations generally predict a moderate overall stabilizing effect for SuperIBEX parameters, but to date the beams have been somewhat more unstable in the presence of the channel than in full density air.[4,7] One potential source of instability not included in most code runs is density fluctuations in the channel arising from turbulent convective mixing. LGED channels are highly turbulent, whereas the channels produced in MPPE were relatively smooth.

IV. Summary and Future Plans

Extensive beam conditioning and propagation experiments have been carried out on ATA and SuperIBEX. The goals and approaches of the two experiments have been similar. There are no current plans for beam propagation experiments on ATA. Future SuperIBEX experiments will be carried out in 10-15 m long tanks at reduced gas density and higher current densities in order to extend the number of betatron wavelengths propagated. Improvements in beam conditioning may be necessary in order to propagate such beams without hose disruption.

Acknowledgments and References

This work has involved a close collaboration over many years with colleagues at NRL and LLNL, including G. Joyce, A. W. Ali, R. Taylor, R. Meger, J. Antoniades, D. Murphy, M. Myers, T. Peyser, R. Pechacek, F. Chambers, W. Fawley, K. Struve, W. Sharp and T. Orzechowski. This work was supported by the Office of Naval Research and by the Defense Advanced Research Projects Agency under ARPA Order No. 7781, and monitored by the Naval Surface Warfare Center.

1. E. P. Lee, Phys. Fluids **21**, 1327 (1978); M. Lampe, *et al.*, Phys. Fluids **27**, 2921 (1984).
2. H. L. Buchanan, Phys. Fluids **30**, 221 (1987).
3. J. Krall, K. Nguyen and G. Joyce, Phys. Fluids B **1**, 2099 (1989).
4. R. F. Hubbard, *et al.*, in Intense Microwaves and Particle Beams III, edited by H. Brandt, SPIE Conference Proceedings No. 1629 (International Society for Optical Engineering, Bellingham, WA, 1992), p.392.
5. See papers by R. Meger, J. Antoniades, T. Peyser, D. Murphy and M. Myers, these proceedings.
6. J. Antoniades, *et al.*, in Proceedings of the Eighth IEEE International Pulsed Power Conference, San Diego, 1991 (Institute of Electrical and Electronics Engineers, New York, 1991), p. 582.
7. D. P. Murphy, *et al.*, *ibid*, p. 589.
8 W. M. Fawley, Bull. Am. Phys. Soc. **35**, 1054 (1990); W. Fawley, F. Chambers and T. Orzechowski (Private communications).
9. R. Hubbard, *et al*,, NRL Memorandum Report 6983 (in press); submitted to J. Appl. Phys.
10. R. Fernsler, *et al.*, these proceedings.
11. W. E. Martin, *et al.*, Phys. Rev. Lett. **54**, 685 (1985).
12. C. Frost, these proceedings.
13. K. Stalder, G. Guethlein and R. Pechacek, private communications.

CONDITIONS FOR STABLE OPERATION IN A HELICAL QUADRUPOLE FOCUSING ACCELERATOR

C. M. Tang and J. Krall
Beam Physics Branch, Plasma Physics Division
Naval Research Laboratory, Washington, DC 20375-5320

Abstract

A number of high-current accelerator designs utilize strong focusing in the form of helical quadrupole and axial guide fields. Operation in certain parameter regimes can cause electromagnetic instabilities. We find that the electron beam centroid can be i) orbit unstable, independent of the waveguide modes, ii) three-wave unstable or iii) fully stable. Analytic expressions for the various stability conditions are obtained in the limit of zero beam current. The stability conditions are verified via particle simulation in each regime.

I. INTRODUCTION

A number of compact, high-current accelerator configurations solve the difficulty of transporting an intense electron beam in a curved geometry by utilizing strong focusing fields. These fields, consisting of a stellarator field (or helical quadrupole field) and an axial guide field, increase considerably the energy mismatch tolerance of the device and provide confining forces against the beam space charge forces.[1] The use of strong focusing fields has a potential difficulty in that they can lead to various types of beam instabilities, particularly the three-wave instability,[2-4] which has been observed experimentally.[5] Here, the externally imposed helical quadrupole field interacts with the transverse motion of the beam centroid to excite a transverse-electric (TE) waveguide mode. It has been shown that an analogous istability occurs in alternating gradient quadrupole focusing systems.[6]

In this paper we obtain detailed analytical conditions for the various stability regimes and thus specify parameter ranges for which stable transport of an electron beam is feasible. We find a) two physically distinct three-wave unstable regimes, b) two three-wave stable regimes and c) a regime in which the particle orbits themselves are unstable, irrespective of the electromagnetic waves. In addition, we have performed particle simulations of electron beam dynamics in each regime and find that the stability conditions are good predictors of our results.

II. MODEL

In our model the external fields consist of a periodic helical quadrupole field and a longitudinal magnetic field and are given by $\mathbf{B}_{ext} = (B_{qx}, B_{qy}, B_{zo})$ where

$$B_{qx} = -B_q k_q (x \sin k_q z - y \cos k_q z), \quad B_{qy} = B_q k_q (x \cos k_q z + y \sin k_q z), \quad B_{zo} = B_o. \quad (1)$$

In Eq. (1), B_o is the axial magnetic field, B_q is the magnetic field of the quadrupole, $k_q = 2\pi/\lambda_q$ is taken to be positive and λ_q is the period of the quadrupole field. The representation for the quadrupole field in Eq. (1) is valid near the z-axis, i.e., $(x^2 + y^2)^{1/2} << \lambda_q/2\pi$.

We assume that the electron beam propagates with velocity v_o within a perfectly conducting cylindrical waveguide of radius r_g. The electron beam radius is assumed to be small compared to the waveguide radius. In the equilibrium position, the beam is centered along the axis of a circular waveguide and the beam electrons are assumed to be monoenergetic with zero transverse velocity. We include the fields due to the displaced beam, produced by the image charges and currents on the waveguide wall.

III. DISPERSION RELATION

The dispersion relation can be writen as[3]

$$\left[D_+ - \frac{k_b^2(k - \omega/v_o + k_q)^2}{\omega^2/c^2 - (k + k_q)^2 - \mu_{11}^2}\right]\left[D_- - \frac{k_b^2(k - \omega/v_o)^2}{\omega^2/c^2 - k^2 - \mu_{11}^2}\right] - K_3^4 = 0, \quad (2)$$

where $D_\pm = K^2 \mp K_1 K - K_2^2$, $K = k - \omega/v_o + k_q/2$, k and ω are the wavenumbers and frequency associated with the right-hand circularly polarized (RHCP) TE_{11} waveguide mode, $K_1 = K_o - k_q$, $K_2^2 = (K_o - k_q/2)k_q/2 - k_s^2$, $K_3^2 = K_q k_q$, $K_o = |e|B_o/\gamma_o\beta_o m_o c^2$ is the cyclotron wavenumber associated with the longitudinal field, $K_q = |e|B_q/\gamma_o\beta_o m_o c^2$ is the cyclotron wavenumber associated with the quadrupole field, $\beta_o = v_o/c$, $k_b^2 = 2\nu\mu_{11}^2/(\gamma_o(\mu_{11}^2 r_g^2 - 1)J_1^2(\mu_{11} r_g))$, $k_s = (2\nu/(\beta_o^2\gamma_o^3 r_g^2))^{1/2}$, $\nu = (|e|/m_o c^2)I_b/\beta_o \simeq I_b[kA]/17\beta_o$ is Budker's parameter, I_b is the beam current, $\mu_{11} r_g$ is argument of the smallest positive zero of Bessel function J_1' and $'$ denotes d/dr. The image charge of the beam is included in the term k_s.

The modes taking part in the interaction can be conveniently classified by setting the beam current equal to zero. The dispersion relation, for zero beam current, reduces to

$$\left[k^2 - \omega^2/c^2 + \mu_{11}^2\right]\left[(k + k_q)^2 - \omega^2/c^2 + \mu_{11}^2\right] U_+ U_- S_+ S_- \simeq 0, \quad (3)$$

where the expressions inside the square brackets from the left specify the RHCP and LHCP waveguide modes,

$$U_\pm \equiv \left(\frac{\omega}{v_o} - k\right) - \left(\frac{k_q}{2} \pm \sqrt{|d_1^2 - d_2^2|}\right) = 0 \quad (4)$$

are hybrid cyclotron and quadrupole modes that can lead to the electromagnetic three-wave instability,

$$S_{\pm} \equiv \left(\frac{\omega}{v_o} - k\right) - \left(\frac{k_q}{2} \pm \sqrt{d_1^2 + d_2^2}\right) = 0 \tag{5}$$

are stable hybrid cyclotron and quadrupole modes, and

$$d_1^2 \simeq \frac{1}{2}(K_o(K_o - k_q) + k_q^2/2), \quad d_2^2 \simeq \frac{1}{2}(K_o^2(K_o - k_q)^2 + 4K_q^2 k_q^2)^{1/2}. \tag{6}$$

For $\omega > 0$ and $K_o < k_q/2$, the unstable beam line is U_+; and for $\omega > 0$ and $k_q/2 < K_o < k_q$, the unstable mode is U_-. In the limit of $K_3^4 << K_o$, $U_+ \simeq \chi - k_q$ for $K_o < 0$, $U_+ \simeq \chi + K_o - k_q$ for $0 < K_o < k_q/2$ and $U_- \simeq \chi + K_o - k_q$, where $\chi = \omega/v_o - k$. In all cases,

$$U_+ U_- S_+ S_- \simeq \chi(\chi - k_q)(\chi - K_o)(\chi + K_o - k_q). \tag{7}$$

IV. STABILITY REGIMES

We now present conditions delineating the various stability regimes. These regimes can be delineated as functions of k_q and K_o for given values of γ_o, r_g and $B_q k_q$. The boundaries separating the different regimes are obtained in the limit of zero beam current. Figure 1 is a stability diagram for $\gamma_o = 5$, $r_g = 3$ cm and quadrupole gradient $B_q k_q = 200$ G/cm.

Orbit Unstable Regime

Even without electromagnetic radiation, the electron beam in this configuration can be unstable when $(d_1^2 - d_2^2) \leq 0$. The unstable values of K_o are

$$K_{crit,2} \equiv \frac{k_q}{2} - 2K_q \leq K_o \leq K_{crit,3} \equiv \frac{k_q}{2} + 2K_q. \tag{8}$$

The curves in (k_q, K_o) parameter space given by $K_o = K_{crit,2}$ and $K_o = K_{crit,3}$ are the left and right boundaries of the orbit unstable region shown in Fig. 1.

Three-Wave Unstable Regimes

The three-wave instability will occur when, for example, the RHCP waveguide mode intersects, in the (ω, k) plane, the appropriate beam mode given by Eq. (2). For $k_q > 0$, the instability for the RHCP waveguide mode occurs with $\omega > 0$. Identical three-wave instability growth rates occur for the LHCP waveguide mode with $\omega < 0$.

For $K_o < K_{crit,2}$, the three-wave instability occurs (Region I) when the RHCP waveguide mode intersects the beam line U_+ given in Eq. (4). For $K_{crit,3} < K_o < k_q$, the three-wave instability occurs (Region II) when the RHCP waveguide mode intersects the beam line U_- given in Eq. (4).

Three-Wave Stable Regime for $K_o < K_{crit,2}$

Stability is achieved when the waveguide cut off frequency $\mu_{11}c$ is sufficiently large so that intersection with either of the beam lines, defined by Eq. (2), cannot be achieved. This is stable regime I in Fig. 1. The condition in terms of the waveguide mode cutoff is

$$q\mu_{11} \geq k_q + 2\left(d_1^2 - d_2^2\right)^{1/2}, \tag{9}$$

where $q = \left(4/\gamma_o^2 - 2\right).^{1/2}$ Based on Eq. (9), the region of

$$k_q > q\mu_{11} \quad \text{and} \quad K_o < K_{crit,2} \tag{10}$$

is always three-wave unstable. If the inequality in (9) can be satisfied, we can solve for the explicit values of K_o for the three-wave stable regime.

For $k_q < q\mu_{11}$ and $K_o < K_{crit,2}$, condition for stability in terms of the variable K_o is

$$2fK_o(K_o - k_q) + f^2 - 4K_q k_q < 0, \tag{11}$$

where

$$f = q\mu_{11}(k_q - q\mu_{11}/2). \tag{12}$$

Defining

$$\zeta = k_q^2(1 + 8K_q^2/f) - 2f, \tag{13}$$

we solve for K_o with $k_q < q\mu_{11}$, and find four situations:

i) for $f > 0$ and $\zeta > 0$, the stable range of K_o is given by

$$K_{crit,1} \equiv \frac{k_q}{2} - \frac{\zeta^{1/2}}{2} < K_o < K_{crit,2}, \tag{14a}$$

ii) for $f < 0$ and $\zeta > 0$, the stable values of K_o are

$$K_o < \text{smaller of}\left(K_{crit,1}, K_{crit,2}\right), \tag{14b}$$

iii) for $f > 0$ and $\zeta < 0$, all values of

$$K_o < K_{crit,2} \tag{14c}$$

are unstable,

iv) for $f < 0$ and $\zeta < 0$, all values of

$$K_o < K_{crit,2} \tag{14d}$$

are stable. The curve $K_o = K_{crit,1}$ denotes the upper boundary of stable region I in Fig. 1.

Three-Wave Stable Regime for $K_o > K_{crit,3}$

The three-wave interaction is also stable when the RHCP waveguide mode does not intersect the beam mode U_- associated with Eq. (2) and $K_o > K_{crit,3}$. This is stable region II. This occurs when $q\mu_{11} \geq k_q - 2\left(d_1^2 - d_2^2\right)^{1/2}$. The three-wave interaction is stable for

$$k_q < q\mu_{11} \quad \text{and} \quad K_o > K_{crit,3}. \tag{15}$$

For $k_q > q\mu_{11}$ and $K_o > K_{crit,3}$, the values of K_o that are three-wave stable are

$$K_o > K_{crit,4} \equiv \frac{k_q}{2} + \frac{\zeta^{1/2}}{2}. \tag{16}$$

The curve $K_o = K_{crit,4}$ denotes the upper boundary of stable region II in Fig. 1.

In this regime, one can show that $f > 0$ and $\zeta > 0$. For $K_o > K_{crit,3}$ in the limit $\gamma_o >> 1$ the stability condition is approximately

$$K_o > \frac{k_q}{2} + \frac{1}{2}\left[\left(k_q - \frac{2\mu_{11}}{\gamma_o}\right)^2 + \frac{4\gamma_o k_q^2 K_q^2}{\mu_{11}(k_q - \mu_{11}/\gamma_o)}\right]^{1/2}. \tag{17}$$

Equation (17) gives a lower limit on $K_o = |e|B_o/\gamma_o\beta_o m_o c^2$ for given values of γ_o, k_q, K_q and r_g such that as the beam energy increases, greater values of $B_o > 0$ are required for stability. Note that for small quadrupole gradient, $K_q << (k_q\mu_{11}/4\gamma_o)^{1/2}$, Eq. (17) reduces to[7] $K_o > k_q - \mu_{11}/\gamma_o$.

The stability diagram, Fig. 1, assumes that the quadrupole gradient is a constant, and (k_q, K_o) are allowed to vary. The horizontal separation of the boundaries for the orbital unstable region is $4K_q$. Since the stability boundaries are obtained in the limit of zero beam current, the area of the actual stable regions will shrink slightly as the value of the current is increased.

V. PARTICLE SIMULATIONS

We have used electromagnetic particle simulation to examine each of the stable and unstable regimes[4] and have found that the stability conditions are good predictors of particle simulation results. Additionally, we have observed saturation of the instability without emittance growth or current loss in three-wave unstable regime II. Our calculations show that this is the result of detuning. As the instability grows, the beam energy and beam axial velocity decrease, increasing the relativistic cyclotron wavenumber K_o and detuning the three-wave interaction. Theoretical analysis of the unstable beam modes in each of the unstable regimes shows that this detuning mechanism is not effective in three-wave unstable regime I. Thus the beam suffers significant losses in that regime.

Acknowledgments

This work was supported by the Defense Advanced Research Projects Agency, ARPA Order No. 7781, monitored by Naval Surface Warfare Center, and the Office of Naval Research.

References

1. C. W. Roberson, A. Mondelli and D. Chernin, Phys. Rev. Lett. 50, 507 (1983); P. Sprangle and C. A. Kapetanakos, Part. Accel. 18, 203 (1986); A. Mondelli, D. Chernin, S. D. Putnam, L. Schlitt and V. Bailey, Proc. Sixth Intl. Conf. on High Power Part. Beams, Osaka, Japan, (1986); V. Bailey, L. Schlitt, M. Tiefenback, S. Putnam, A. Mondelli, D. Chernin and J. Petillo, Proc. of the 1987 IEEE Part. Accel. Conf., Ed. E. R. Lindstrom and L. S. Taylor, 920 (1987).
2. T. P. Hughes and B. B. Godfrey, Phys. Fluids 29, 1698 (1986).
3. C. M. Tang, P. Sprangle, J. Krall, P. Serafim and F. Mako, Part. Accel., **35**, 101 (1991).
4. J. Krall, C. M. Tang, G. Joyce and P. Sprangle, Phys. Fluids B **3**, 204 (1991).
5. M. G. Tiefenback, S. D. Putnam, V. L. Bailey, Jr., J. P. Lidestri and J. A. Edighoffer, Pulse Sciences, Inc. Report PSIFR-2543-01 (1991); T. P. Hughes, T. C. Genomi, K. Nguyen and D. Welch, Mission Research Corp. Report MRC/ABQ-OR-1442 (1991).
6. C. M. Tang, J. Krall and T. Swyden, Phys. Rev. A **45**, 7492 (1992); T. P. Hughes and D. Chernin, submitted to Part. Accel.; J. Krall, C. M. Tang and T. Swyden, submitted Phys. Rev. A.
7. D. Chernin and T. Hughes (private communication).

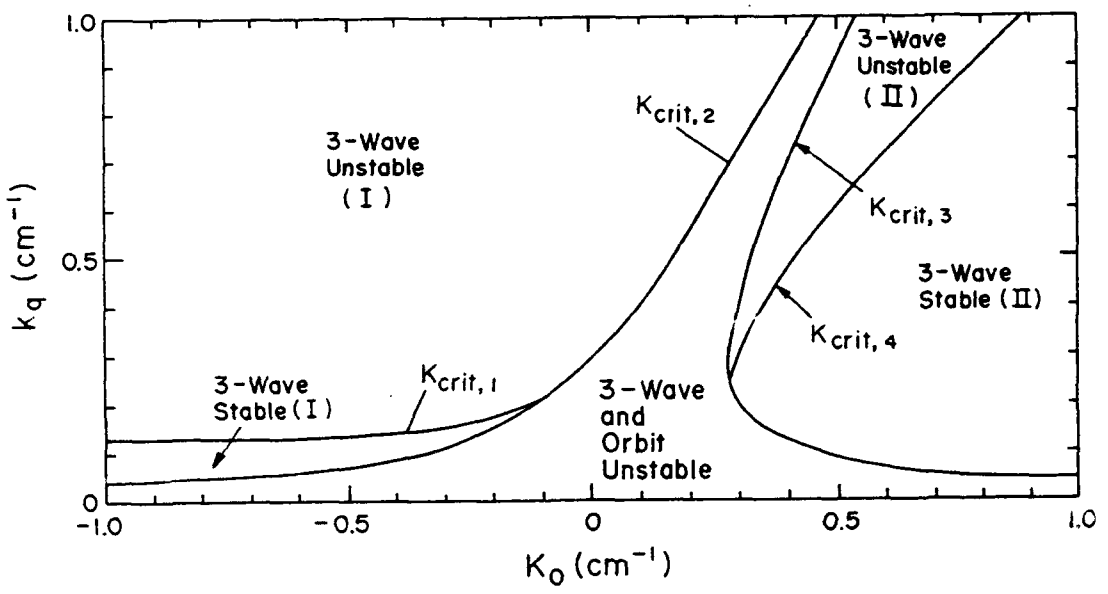

Fig. 1 Plot of (k_q, K_o) parameter space showing the various operating regimes. Stability boundaries are calculated for $\gamma_o = 5$, $r_g = 3$ cm and quadrupole gradient $B_q k_q = 200$ G/cm.

9th International Conference on High-Power Particle Beams

A HIGH-ORDER MOMENT SIMULATION MODEL*

K. T. Tsang, C. Kostas, D. P. Chernin, J. J. Petillo, and A. Mondelli

Science Applications International Corporation
1710 Goodridge Dr., McLean, VA 22102

Abstract

We consider a high-current beam transport system in which the particle motion in the two transverse directions (x and y) are coupled. Chernin[1] has studied the beam envelope, with linear transverse spatial dependence of magnetic field. for a monoenergetic particle beam. We are interested in a beam which is distributed in energy, and a transport system with nonlinear transverse dependence of the magnetic field. For this type of system the spatial coordinate (z) along the beam motion can no longer be equivalenced to the time variable; faster particles will overtake the slower particles as time evolves. We present relativistically covariant moment equations for modelling beam transport, based on the work of Newcomb[2] and Amendt and Weitzner[3]. The beam is described by a set of partial differential moment equations, instead of a set of ordinary differential envelope equations. (This aspect of our approach distinguishes it from the work of Chernin[1] and of Channell and coworkers[4,5].) The code formalism is based on transverse averages of the moment equations obtained from the relativistic Vlasov equation. The spatial coordinate along the beam motion is discretized. (The theory by Channel et al. uses moment equations to model a three-dimensional beam bunch. For long bunches, however, it is impractical to carry high enough longitudinal moments to model the oscillations within the bunch.) The moment equations are closed by setting higher order correlation functions to zero. A non-linear space charge model, similar to the one used in the BEDLAM code[4], has been developed. The formalism for the code as well as results of the model will be presented. Comparisions will be made between simulations keeping up to second, third and fourth order correlations.

Relativistic Formuation

We start with a time coordinate t and local Cartesian space coordinate (x^1, x^2, x^3), replacing the usual coordinate (x, y, z), where x^3 is measured along the beam motion direction and x^1 and x^2 are the transverse directions. We define $x^4 = ct$, where c is the speed of light, so that space-time is parametrized by $x^\mu, \mu = 1,2,3,4$. We use a summation convention, and we assume that Latin subscripts and superscripts, i, j, k, l, are summed from one to three, while Greek subscripts and superscripts are summed from one to four. The space-time metric $(ds)^2 = dx^i dx^i - c^2(dt)^2$ becomes $(ds)^2 = dx^\mu dx^\nu g_{\mu\nu}$, where the non-zero elements of the metric tensor $g_{\mu\nu}$ are $g_{ij} = \delta_{ij}$ and $g_{44} = -1$. The metric tensors $g_{\mu\nu}$ and $g^{\mu\nu}$, which are defined so that $g_{\mu\nu}g^{\nu\lambda} = \delta^\lambda_\mu$, may be used to raise and

lower indices covariantly. The usual three velocity v^i may be extended to a relativistic covariant four-velocity u^μ by the definitions $\gamma^{-2} = 1 - v^i v^i/c^2$ and $u^i = \gamma v^i, u^4 = \gamma c$ so that $u^\mu u_\mu = -c^2$. The beam distribution function, $f(x^\mu, u^i)$, satisfies the relativistic Vlasov equation:

$$\left[\frac{\partial}{\partial t} + \vec{v}\cdot\vec{\nabla} + \frac{q}{m}\left(\vec{E} + \vec{v}\times\vec{B}\right)\cdot\frac{\partial}{\partial \vec{u}}\right] f = 0 \quad , \tag{1}$$

where m is the particle mass. In a covariant formulation, we can multiply Eq. 1 by γ and rewrite the relativistic Vlasov equation as

$$\left(u^\mu \frac{\partial}{\partial x^\mu} + \frac{q}{m} F^{i\mu} u_\mu \frac{\partial}{\partial u^i}\right) f = 0 \quad , \tag{2}$$

where $F_{\mu\nu}$ is the antisymmetric electromagnetic field tensor. The volume element $d\omega = du^1 du^2 du^3/\gamma$ in the four-momentum space is invariant under a Lorentz transformation. Since the transverse coordinates, x^1 and x^2, are invariant under a Lorentz transformation, we define an invariant phase space volume element under a Lorentz transformation to be $d\Omega = dx^1 dx^2 du^1 du^2 du^3/\gamma$, and a phase space average

$$\langle X\rangle = h^{-1}\int X f d\Omega, \tag{3}$$

with $h = \int f d\Omega$. We also define the n'th order correlation functions,

$$[u^{\lambda_1} u^{\lambda_2}\cdots u^{\lambda_n}] = h^{-1}\int (u^{\lambda_1} - \langle u^{\lambda_2}\rangle)(u^{\lambda_2} - \langle u^{\lambda_2}\rangle)\cdots(u^{\lambda_n} - \langle u^{\lambda_n}\rangle) f d\Omega. \tag{4}$$

The lowest moment of the Vlasov equation (Eq. 2) gives

$$\frac{\partial}{\partial x^3} h\langle u^3\rangle + \frac{\partial}{\partial x^4} h\langle u^4\rangle = 0. \tag{5}$$

With Eq. 2 multiplied by u^ν and $u^\nu u^\lambda$ then integrated over $d\Omega$, we have

$$\frac{\partial}{\partial x^3} h\langle u^3 u^\nu\rangle + \frac{\partial}{\partial x^4} h\langle u^4 u^\nu\rangle = \frac{q}{m} h\langle F^{\nu\mu} u_\mu\rangle \quad \text{and} \tag{6}$$

$$\frac{\partial}{\partial x^3} h\langle u^3 u^\nu u^\lambda\rangle + \frac{\partial}{\partial x^4} h\langle u^4 u^\nu u^\lambda\rangle = \frac{q}{m} h(\langle F^{\nu\mu} u_\mu u^\lambda\rangle + \langle F^{\lambda\mu} u_\mu u^\nu\rangle), \tag{7}$$

respectively. There are four independent equations represented in Eqs. 6 and ten in Eqs. 7. Equations 5 to 7 are basically the same as the fluid equations of Newcomb[2] and Amendt and Weitzner[3], with the additional averaging over the transverse coordinates. If $F^{\mu\nu}$ is independent of the transverse coordinates, then Eqs. 5 to 7 can be reduced

to a closed system by assuming the third order correlations are negligible, which is the standard approximation used in truncating most fluid equations. Since $F^{\mu\nu}$ depends on the transverse coordinates, Eqs. 6 and 7 cannot be closed without introducing the spatial moment equations:

$$\frac{\partial}{\partial x^3}h\langle u^3 x^i\rangle + \frac{\partial}{\partial x^4}h\langle u^4 x^i\rangle = h\langle u^i\rangle; \tag{8}$$

$$\frac{\partial}{\partial x^3}h\langle u^3 u^\nu x^i\rangle + \frac{\partial}{\partial x^4}h\langle u^4 u^\nu x^i\rangle = h\langle u^\nu u^i\rangle + \frac{q}{m}h\langle F^{\nu\mu}u_\mu x^i\rangle; \quad \text{and} \tag{9}$$

$$\frac{\partial}{\partial x^3}h\langle u^3 x^i x^j\rangle + \frac{\partial}{\partial x^4}h\langle u^4 x^i x^j\rangle = h\langle x^j u^i\rangle + h\langle x^i u^j\rangle \quad \text{for } i,j = 1,2 \text{ only.} \tag{10}$$

To more concisely represent and to allow easier numerical solution, the system of partial differential equations for the second order model (described above) and higher order models should be reorganize to combined both fluid and spatial moment equations. Consider a new general variable y^λ such that $y^1 = 1$, $y^2 = x^1$, $y^3 = x^2$, $y^4 = u^1$, $y^5 = u^2$, $y^6 = u^3$, and $y^7 = u^4$. For order n, Eq. 2 may be multiplied by $y^{\lambda_1}y^{\lambda_2}\cdots y^{\lambda_n}$ and integrated over $d\Omega$. The system of partial differential equations is ($\lambda_1 = 1$ to 7; $\lambda_2 = \lambda_1$ to 7;...; $\lambda_n = \lambda_{n-1}$ to 7)

$$\begin{aligned}\frac{\partial}{\partial x^3}h\langle u^3 y^{\lambda_1}y^{\lambda_2}\cdots y^{\lambda_n}\rangle + \frac{\partial}{\partial x^4}h\langle u^4 y^{\lambda_1}y^{\lambda_2}\cdots y^{\lambda_n}\rangle &= \Gamma(\lambda_1,\lambda_2,\ldots,\lambda_n)\\ &+ \Gamma(\lambda_2,\lambda_1,\lambda_3,\ldots,\lambda_n) + \cdots + \Gamma(\lambda_n,\lambda_1,\ldots,\lambda_{n-1})\end{aligned} \tag{11}$$

where

$$\Gamma(\lambda_1,\lambda_2,\ldots,\lambda_n) = \begin{cases} 0, & \lambda_1 = 1;\\ \int y^{\lambda_2}\cdots y^{\lambda_n}u^{\lambda_1-1}f\,d\Omega, & \lambda_1 = 2 \text{ or } 3;\\ \frac{q}{m}\int y^{\lambda_2}\cdots y^{\lambda_n}F^{\lambda_1-3,\mu}u_\mu f\,d\Omega, & \lambda_1 = 4 \text{ thru } 7.\end{cases} \tag{12}$$

The twenty-eight equations represented in Eq. 5 thru 10 are identical to Eq. 11 when $n = 2$.

To close the n'th order system of equations, we assume that correlations above order n are zero. This still allows higher order moments to be nonzero. In fact, the closing condition creates several equivalent families of independent variables among the $n+1$ order moments. The sets $\{h\langle u^3 y^{\lambda_1}y^{\lambda_2}\cdots y^{\lambda_n}\rangle\}$ and $\{h\langle u^4 y^{\lambda_1}y^{\lambda_2}\cdots y^{\lambda_n}\rangle\}$ where $\lambda_1 = 1$ to 7; $\lambda_2 = \lambda_1$ to 7;$\cdots$; $\lambda_n = \lambda_{n-1}$ to 7, and $\{h,\langle y^{\lambda_1}y^{\lambda_2}\cdots y^{\lambda_n}\rangle\}$ where $\lambda_1 = 2$ to 7;$\cdots$;$\lambda_n = \lambda_{n-1}$ to 7, all equivalently describe the n order moments of f. The natural set of independent variables to advance in time is $\{h\langle u^4 y^{\lambda_1}y^{\lambda_2}\cdots y^{\lambda_n}\rangle\}$. After each time advance we need to calculate $h\langle u^3 y^{\lambda_1}y^{\lambda_2}\cdots y^{\lambda_n}\rangle$ and $\Gamma(\lambda_1,\lambda_2,\cdots,\lambda_n)$ from $\{h\langle u^4 y^{\lambda_1}y^{\lambda_2}\cdots y^{\lambda_n}\rangle\}$. We can accomplish this by expanding the correlation functions in terms of moments and applying the closing condition. To present an example of a

mapping we return to second order. Define $[\![\lambda,\nu]\!] \equiv h\langle y^\lambda y^\nu u^4\rangle$. From the expansion of the third order correlation functions, we find

$$[\![\lambda,\nu]\!] = h[y^\lambda y^\nu u^4] + [\![1,1]\!]\langle y^\lambda y^\nu\rangle + [\![1,\nu]\!]\langle y^\lambda\rangle + [\![1,\lambda]\!]\langle y^\nu\rangle - 2[\![1,1]\!]\langle y^\lambda\rangle\langle y^\nu\rangle. \tag{13}$$

With this the mapping from $[\![\lambda,\nu]\!]$ to $\{h, \langle y^\lambda y^\nu y^\alpha\rangle\}$ easily follows.

$$\begin{aligned}
\langle u^4\rangle &= \frac{3[\![1,7]\!] + \sqrt{9[\![1,7]\!]^2 - 8[\![1,1]\!][\![7,7]\!]}}{4[\![1,1]\!]};\\
h &= [\![1,1]\!]/\langle u^4\rangle;\\
\langle y^\lambda\rangle &= \frac{[\![\lambda,7]\!] - 2[\![1,\lambda]\!]\langle u^4\rangle}{[\![1,7]\!] - 2[\![1,1]\!]\langle u^4\rangle};\\
\langle y^\lambda y^\nu\rangle &= ([\![\lambda,\nu]\!] + 2[\![1,1]\!]\langle y^\lambda\rangle\langle y^\nu\rangle - [\![1,\nu]\!]\langle y^\lambda\rangle - [\![1,\lambda]\!]\langle y^\nu\rangle)/[\![1,1]\!];\\
\langle y^\lambda y^\nu y^\alpha\rangle &= \langle y^\lambda\rangle\langle y^\nu y^\alpha\rangle + \langle y^\nu\rangle\langle y^\lambda y^\alpha\rangle + \langle y^\alpha\rangle\langle y^\lambda y^\nu\rangle - 2\langle y^\lambda\rangle\langle y^\nu\rangle\langle y^\alpha\rangle.
\end{aligned} \tag{14}$$

The High-Order Moment code has mappings for second, third and fourth order systems.

Space Charge Models

A. Chernin's Model

A simple model can be introduced at this point to cast Eq. 12 more solidly. The desired form of $F^{\mu\nu}$ is obtained by expanding the magnetic field to linear terms of x^1, x^2 and employing Chernin's space charge model[1] for the electric field, which is given by

$$\begin{aligned}
E^1 &= \rho(q_{11}(x^1 - \langle x^1\rangle) + q_{12}(x^2 - \langle x^2\rangle)),\\
E^2 &= \rho(q_{12}(x^1 - \langle x^1\rangle) + q_{22}(x^2 - \langle x^2\rangle)),\\
E^3 &= 0,
\end{aligned} \tag{15}$$

where ρ is the line charge density of the beam, $q_{11} = S_2/D$,$q_{22} = S_1/D$,$q_{12} = -[x^1x^2]/D$, $D = S_0(S_1 + S_2)$, $S_1 = [x^1x^1] + S_0$,$S_2 = [x^2x^2] + S_0$, and $S_0 = ([x^1x^1][x^2x^2] - [x^1x^2]^2)^{\frac{1}{2}}$. With this model we can evaluate the moments that involve $F^{\mu\nu}$ in Eq. 12.

B. Cylindrical Model with Image Charges

Chernin's model does not take into account the effects of the image charges of the metallic boundary nor the longitudinal component of the space charge fields. To construct an improved space charge model we assume that the charge density, ρ, is approximated by a collection of two-dimensional charge rods distributed inside a cylindrical metallic pipe:

$$\rho = \sum_{i=1}^{N} q_i(x_3, t)g(\vec{x} - \vec{x_i}), \tag{16}$$

where g is the distribution of finite size charge rod whose location is independent of x_3. Note that g depends on x_1, and x_2, while q_i depends only on x_3. For example, in the second order moment system there are six spatial moments, therefore we have $N = 6$ and a matrix equation to relate the coefficients q_i with the spatial moments.

$$h \begin{pmatrix} 1 \\ \langle x_1 \rangle \\ \langle x_2 \rangle \\ \langle x_1 x_1 \rangle \\ \langle x_1 x_2 \rangle \\ \langle x_2 x_2 \rangle \end{pmatrix} = M \begin{pmatrix} q_1 \\ \vdots \\ q_6 \end{pmatrix}, \tag{17}$$

where M is a 6×6 matrix whose elements are of the form

$$\int x_k^m x_l^n g(\vec{x} - \vec{x_i}) dx_1 dx_2,$$

with $k, l = 1, 2$ and $m + n \leq 2$. Equation (17) can be easily inverted to express q_i in terms of the spatial moments.

The image charges of these rods are easy to determine: for a charge rod located at $\vec{x_i}$ with a charge q_i the image is located at $\vec{x_i'}$ with charge $-q_i$, where $\vec{x_i'}$ is along the same direction outside the metallic cylinder with a magnitude $a^2/|\vec{x_i}|$, where a is the radius of the cylinder. Electric field due to these charge rods inside the cylinder in the beam frame can be written as

$$\vec{E}(\vec{x}) = \sum_{i=1}^{N} q_i \frac{\vec{x} - \vec{x_i}}{|\vec{x} - \vec{x_i}|} - \sum_{i=1}^{N} q_i \frac{\vec{x} - \vec{x_i'}}{|\vec{x} - \vec{x_i'}|}. \tag{18}$$

This result can be transformed back to the laboratory frame. With this simplified model, the self field contribution to moments involving $F^{\nu\mu}$ can be readily expressed as other moments retained in the system and a close set of equations can be achieved.

Results

The High-Order Moment (HOM) model agrees identically with the "ABBY"[1] envelope model for the steady state evolution of a monoenergetic beam. To test the effect of energy spread in the HOM model, we injected two monoenergetic circular beams at $z = 0$ with γ's of 3 and 3.1, respectively, into a mismatched constant guide field.

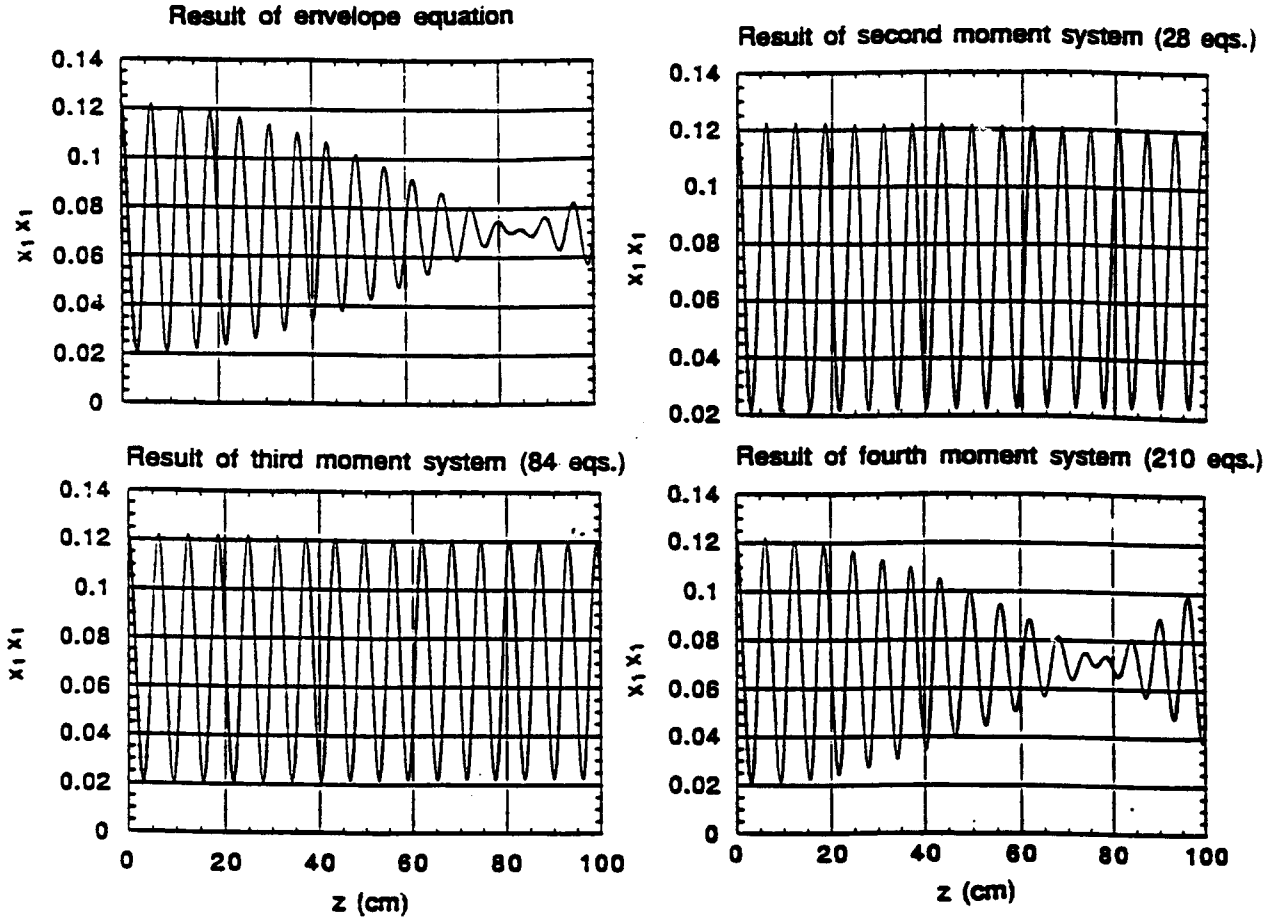

Fig. 1: a) top left; b) top right; c) bottom left; d) bottom right

Each beam will independently exhibit betatron oscillations in the beams radius as a function of the distance of propagation, z. The space charge model has been turned off to eliminate any interaction between the two beams; the addition of the results from an envelope equation will be the exact solution. Figure 1a shows the expected beat pattern in the $\langle x^1 x^1 \rangle$ moment caused by the slight difference in frequencies of the betatron oscillations. The HOM model when retaining up to third order correlations does not capture this energy mixing. The average of the two betatron frequencies developes in time as shown in figures 1b and 1c. To capture the effects of this energy spread fourth order correlations must be retained (see fig. 1d).

* Work supported by DARPA/DSO

References

1 D. Chernin, *Particle Accelerators, 24*, 29 (1988).
2 W. A. Newcomb, *Phys. Fluids, 25*, 846 (1982).
3 P. Amendt and H. Weitzner, *Phys. Fluids, 28*, 949 (1985).
4 P. J. Channell, L. M. Healy, and W. P. Lysenko, *IEEE Trans. Nucl. Sci., 32*, 2565 (1985).
5 P. J. Channell, *IEEE Trans. Nucl. Sci., 30*, 2607 (1983).

REFINED DEFINITION OF THE BEAM BRIGHTNESS AS THE ARITHMETIC MEAN OF THE DISTRIBUTION FUNCTION

T. J. Myers, K. A. Boulais, and M. J. Rhee
Department of Electrical Engineering
University of Maryland, College Park, MD 20742, U.S.A.

Abstract

Using the refined definition[1], the beam brightness is evaluated for a few double-beam systems that are formed by two identical spatial distributions with Maxwellian beam. The resultant brightness are expressed in terms of the displacement distance between the two beams. It is found that the expressions are weakly dependent on the geometry of the individual beams and may be approximated by a piece-wise linear function.

Introduction

A refined definition of beam brightness, which was recently proposed, eliminates ambiguity that existed in previous definitions of beam brightness. Previous definitions rely on the hypervolume in four-dimensional trace space which is not clearly defined in some distributions. The refined definition is based on the arithmetic mean value defined in statistics. The brightness is conveniently expressed[2-4] in terms of the emittances $\epsilon_x\epsilon_y$ current I as $B = \eta I/\epsilon_x\epsilon_y$, where η is the form factor which depends on the geometry of the distribution and on the definition of emittance being used. In the refined definition the rms emittance is used because it is unambiguously defined for any given distribution. It has been demonstrated[1] that for a few spatial distributions with Maxwellian transverse velocity distribution and for a water-bag distribution, the form factor η is close to unity.

In this paper, we summarize the refined definition of brightness and calculation of the brightness for a Gaussian-Maxwellian as an example. Subsequently, we evaluate the brightness of double-beam systems that are formed by two identical spatial distributions with Maxwellian beams. The resultant form factors η of the distributions are expressed in terms of the displacement distance of the two beams.

II. Summary of Refined Definition of Brightness

A beam may be defined by a distribution ρ_4 in four-dimensional trace space.[3-5] The distribution $\rho_4 = d^4I/dV_4$ is also known as microscopic brightness[3] of the beam and may be measured in A/(rad^2 m^2). The arithmetic mean or expected value of any quantity ϕ associated with the beam is then given by

$$\langle\phi\rangle = I^{-1}\int \phi\rho_4 dxdydx'dy', \tag{1}$$

where I is the beam current given by

$$I = \int \rho_4 dx dy dx' dy'. \tag{2}$$

Refined beam brightness is defined[1] as the arithmetic mean of the beam distribution function ρ_4 itself as

$$B \equiv < \rho_4 > = I^{-1} \int \rho_4^2 dx dy dx' dy'. \tag{3}$$

Note that this definition does not rely on the hypervolume V_4 of the distribution, thus, it can be unambiguously defined even for long tail distributions such as Gaussian.

Maxwellian transverse velocity distributions are good approximations[6] for beams encountered in actual experiments. Consider a beam which has a Gaussian spatial distribution and a Maxwellian transverse velocity distribution. This beam may be represented by

$$\rho_4 = \rho_0 \exp\left(-\frac{x^2}{2\sigma_x^2} - \frac{y^2}{2\sigma_y^2} - \frac{x'^2}{2\sigma_{x'}^2} - \frac{y'^2}{2\sigma_{y'}^2}\right). \tag{4}$$

The beam current and brightness may be calculated by substituting Eq. (4) into Eqs. (2) and (3) respectively as

$$I = 4\pi^2 \sigma_x \sigma_y \sigma_{x'} \sigma_{y'}, \tag{5}$$

$$B = \frac{1}{4}\rho_0. \tag{6}$$

Equation (6) is not very useful for experimental purposes because ρ_0 is generally not an experimentally obtainable parameter. A more useful expression[3,4] for the beam brightness is given by

$$B = \frac{\eta I}{\pi^2 \epsilon_x \epsilon_y}, \tag{7}$$

where η is a form factor that depends on the geometry of the distribution, and ϵ_x and ϵ_y are the effective emittances[9] given by

$$\epsilon_x = 4\left[< x^2 >< x'^2 > - < xx' >^2\right]^{1/2}. \tag{8}$$

In the case of the Gaussian-Maxwellian distribution, we may compute these second order moments by substituting Eq. (4) into Eq. (1) and substituting this result into Eq. (8) and we find that

$$\epsilon_x = 4\sigma_x \sigma_{x'}, \quad \epsilon_y = 4\sigma_y \sigma_{y'}. \tag{9}$$

By rearranging Eq. (7), we find that $\eta = B\pi^2 \epsilon_x \epsilon_y / I$ and in the case of the Gaussian-Maxwellian, the form factor η is exactly unity.

III. Double-Beam Gaussian-Maxwellian Distribution

Now consider a distribution comprised of two Gaussian-Maxwellian beams each displaced from the origin in opposite directions by a variable displacement distance x_0 in the x-direction. This distribution may be given by

$$\rho_4 = \rho_0 \left\{ \exp\left[-\frac{(x+x_0)^2}{2\sigma_x^2} \right] + \exp\left[-\frac{(x-x_0)^2}{2\sigma_x^2} \right] \right\} \exp\left(-\frac{y^2}{2\sigma_y^2} - \frac{x'^2}{2\sigma_{x'}^2} - \frac{y'^2}{2\sigma_{y'}^2} \right) \tag{10}$$

Figure 1(a) shows the projected distribution in the x-space corresponding to the normalized displacement distances $x_0/\sigma_x = 0,\ \sqrt{3}/2,\ \sqrt{3}$, and $3\sqrt{3}/2$. Performing similar calculations as we did for the single-beam Gaussian-Maxwellian we find that:

$$I = 8\pi^2 \rho_0 \sigma_x \sigma_y \sigma_{x'} \sigma_{y'}, \tag{11}$$

$$B = \frac{1}{4}\rho_0 \left[1 + \exp\left(-x_0^2/\sigma_x^2 \right) \right], \tag{12}$$

$$\epsilon_x = 4(1 + x_0^2/\sigma_x^2)^{1/2} \sigma_x \sigma_{x'}, \tag{13}$$

$$\epsilon_y = 4\sigma_y \sigma_{y'}, \tag{14}$$

$$\eta = \frac{1}{2}\left[1 + \exp\left(-x_0^2/\sigma_x^2 \right) \right] \left(1 + x_0^2/\sigma_x^2 \right)^{1/2}. \tag{15}$$

Notice that in this case, η is a function of the parameters of the distribution. In the limit as x_0/σ_x becomes large compared to unity, Eq. (15) reduces to the simple linear relation:

$$\eta = \frac{1}{2} x_0/\sigma_x. \tag{16}$$

IV. Other Double-Beam Maxwellian Distributions

We consider the double-beam Rectangular-Maxwellian and the double-beam Sinusoidal-Maxwellian distributions. For easy comparison with the Gaussian-Maxwellian, we may normalize the displacement distances x_0 to the rms width σ_x of the single distribution. We find that for the Rectangular-Maxwellian distribution

$$\sigma_x = a/\sqrt{3}. \tag{17}$$

and for the Sinusoidal-Maxwellian distribution

$$\sigma_x = a(1 - 8/\pi^2)^{1/2}. \tag{18}$$

The projected distributions in the x-space corresponding to the normalized displacement distances 0, $\sqrt{3}/2, \sqrt{3}$, and $3\sqrt{3}/2$, are shown in Figs. 1(b) and 1(c). Similar calculations for the

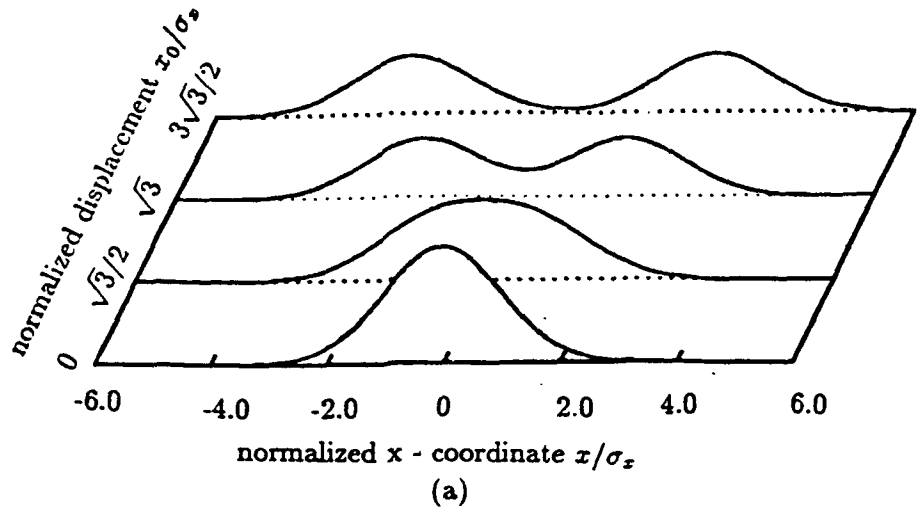

(a)

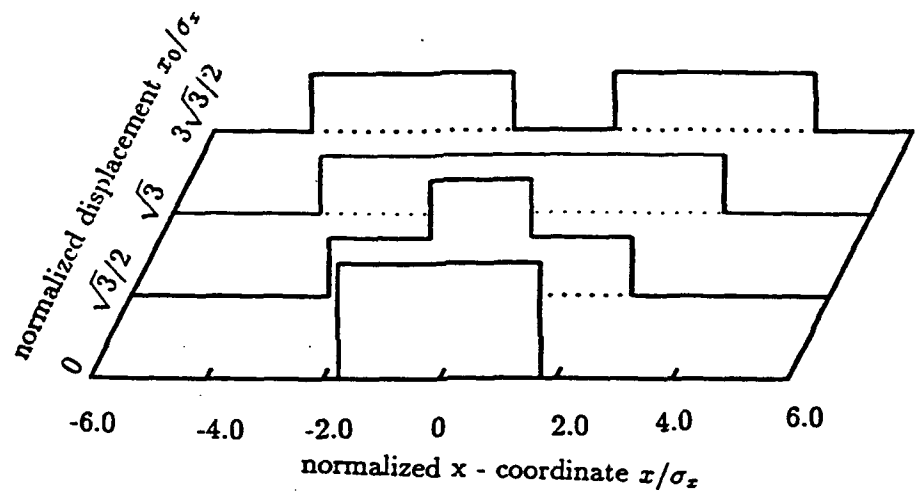

(b)

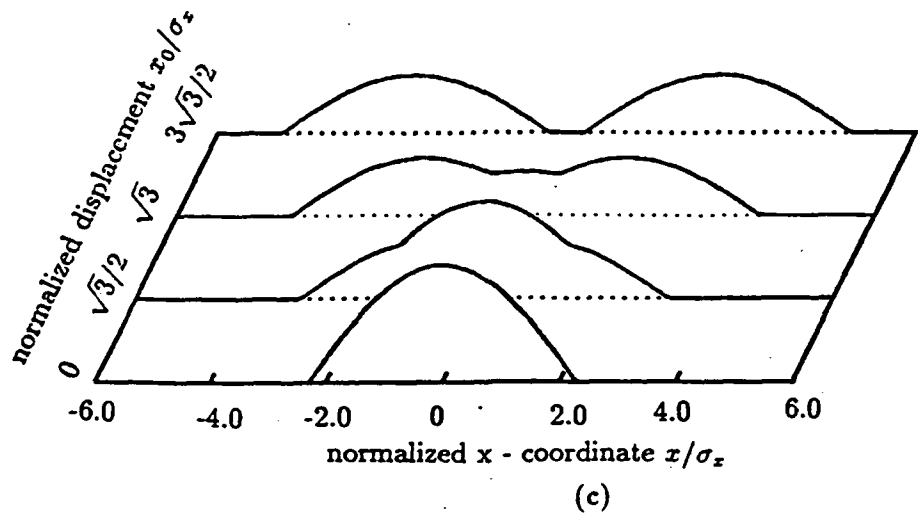

(c)

FIG. 1. Spatial distributions of double-beam systems are depicted for normalized displacement distances $x_0/\sigma_x = 0$, $\sqrt{3}/2$, $\sqrt{3}$, and $3\sqrt{3}/2$. (a) Gaussian, (b) rectangular, and (c) half-sinusoidal double-beam systems.

TABLE I. Double-beam Maxwellian distributions, $\rho_4(x,y,x',y') = \rho_0 g_2(x,y) \exp\left(-\frac{x'^2}{2\sigma_{x'}^2} - \frac{y'^2}{2\sigma_{y'}^2}\right)$.

	Gaussian
$g_2(x,y)$	$\left\{\exp\left[-\frac{(x+x_0)^2}{2\sigma_x^2}\right] + \exp\left[-\frac{(x-x_0)^2}{2\sigma_x^2}\right]\right\} \exp\left(-\frac{y^2}{2\sigma_y^2}\right)$.
I	$8\pi^2 \rho_0 \sigma_x \sigma_y \sigma_{x'} \sigma_{y'}$
$\epsilon_x,\ \epsilon_y$	$4(1 + x_0^2/\sigma_x^2)^{1/2} \sigma_x \sigma_{x'},\ \ 4\sigma_y \sigma_{y'}$
B	$\frac{1}{4}\rho_0 \left[1 + \exp\left(-x_0^2/\sigma_x^2\right)\right]$
η	$\frac{1}{2}\left[1 + \exp\left(-x_0^2/\sigma_x^2\right)\right] \left(1 + x_0^2/\sigma_x^2\right)^{1/2}$
	Rectangular
$g_2(x,y)$	$\left\{u\left[1 - (x+x_0)^2/a^2\right] + u\left[1 - (x-x_0)^2/a^2\right]\right\}\ u(1 - y^2/b^2)$
I	$16\pi \rho_0 ab \sigma_{x'} \sigma_{y'}$
$\epsilon_x,\ \epsilon_y$	$4(1/3 + x_0^2/a^2)^{1/2} a\sigma_{x'},\ \ (4/3) b\sigma_{y'}$
B	$\frac{1}{2}\rho_0 \left[1 + \left(1 - \frac{x_0}{a}\right) u\left(1 - \frac{x_0}{a}\right)\right]$
η	$\frac{\pi}{6}\left[1 + 3\left(\frac{x_0}{a}\right)^2\right]^{1/2} \left[1 + \left(1 - \frac{x_0}{a}\right) u\left(1 - \frac{x_0}{a}\right)\right]$
	Half-Sinusoid
$g_2(x,y)$	$\left\{\cos\frac{\pi(x+x_0)}{2a} u\left[1 - \frac{(x+x_0)^2}{a^2}\right] + \cos\frac{\pi(x-x_0)}{2a} u\left[1 - \frac{(x-x_0)^2}{a^2}\right]\right\} \cos\frac{\pi y}{2b} u\left(1 - \frac{y^2}{b^2}\right)$
I	$(64/\pi)\rho_0 ab \sigma_{x'} \sigma_{y'}$
$\epsilon_x,\ \epsilon_y$	$4\left(1 - 8/\pi^2 + x_0^2/a^2\right)^{1/2} a\sigma_{x'},\ \ 4(1 - 8/\pi^2)^{1/2} b\sigma_{y'}$
B	$\frac{\pi^2 \rho_0}{2^5}\left\{1 + u\left(1 - \frac{x_0}{a}\right)\left[\left(1 - \frac{x_0}{a}\right)\cos\frac{\pi x_0}{a} + \frac{1}{\pi}\sin\frac{\pi x_0}{a}\right]\right\}$
η	$\frac{\pi^5}{2^7}\left\{\left(1 - \frac{8}{\pi^2}\right)\left(1 - \frac{8}{\pi^2} + \frac{x_0^2}{a^2}\right)\right\}^{1/2} \left\{1 + u\left(1 - \frac{x_0}{a}\right)\left[\left(1 - \frac{x_0}{a}\right)\cos\frac{\pi x_0}{a} + \frac{1}{\pi}\sin\frac{\pi x_0}{a}\right]\right\}$

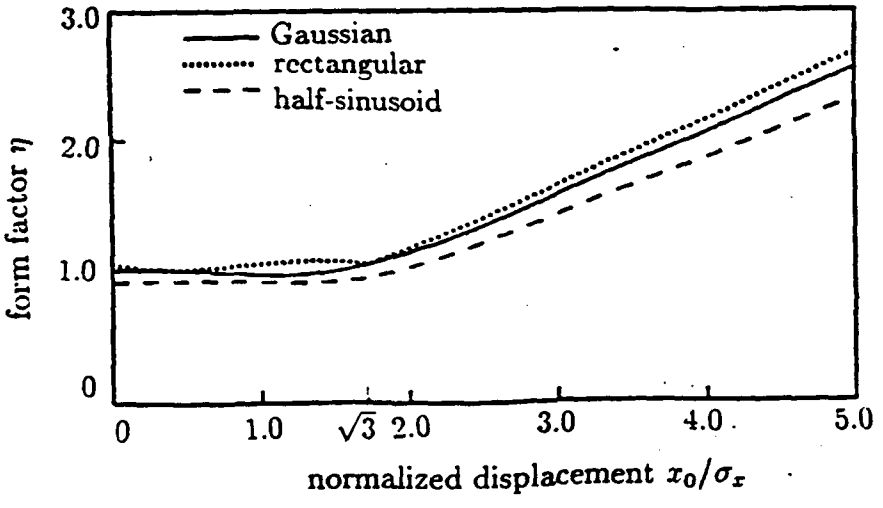

FIG. 2. Plots of form factors for Gaussian, rectangular, and half-sinusoidal double-beam systems vs. normalized displacement distance.

double-beam Gaussian-Maxwellian are performed on the double-beam Rectangular-Maxwellian and the double-beam Sinusoidal-Maxwellian distributions. The analytic results are summarized in Table I.

V. Discussion

Figure 2 is a plot of the form factor η vs. normalized displacement distance x_0/σ_x for each of the three double beam distributions we have considered. The plots for the three distributions have a very similar form. Note that in the approximate interval $0 \leq x_0/\sigma_x \leq \sqrt{3}$, the form factor η remains relatively constant and close to unity and also that in the limit as x_0/σ_x becomes large, the form factor η becomes a linear function of x_0/σ_x with the slope approaching approximately 1/2 for all three distibutions. The displacement distance $x_0/\sigma_x = \sqrt{3}$ corresponds to the half width of the individual beam of rectangular distribution and beyond this value, $x_0/\sigma_x > \sqrt{3}$, the two beams are completely separated as can be seen in Fig. 1(b). It may be concluded that for the three double-beam Maxwellian distributions considered, curves of the form factor η vs. the normalized displacement distance x_0/σ_x may be approximated by a piece-wise linear function whose specific parameters are only weakly dependent on the geometry of the individual beams.

Acknowledgment

This work was supported by the U. S. Department of Energy.

References

1. M. J. Rhee, Phys. Fluids B 4 (6), June (1992).

2. A. van Steenbergen, IEEE Trans. Nucl. Sci. **NS-12**, 746 (1965).

3. C. Lejeune and J. Aubert, in *Applied Charged Particle Optics*, edited by A. Septier, (New York: Academic Press, 1980), p. 176.

4. J. D. Lawson, *The Physics of Charged-Particle Beams*, 2nd ed. (Oxford: Clarendon Press, 1988), p. 153.

5. J. Fronteau, in *Focusing of Charged Particles*, edited by A. Septier, (New York: Academic Press, 1967), Vol. 2, p. 421.

6. J. D. Lawson, *The Physics of Charged-Particle Beams*, 2nd ed. (Oxford: Clarendon Press, 1988), p. 200.[7] See also P. M. Lapostolle, IEEE Trans. Nucl. Sci. **NS-18**, 1101 (1971).

7. We follow a new convention proposed by Lawson[8] that the rms emittance equals $[< x^2 >< x'^2 > - < xx' >^2]^{1/2}$ and the effective emittance equals $4\,[< x^2 >< x'^2 > - < xx' >^2]^{1/2}$. It is noted that the effective emittance = Lapostolle's rms emittance[9] equals $(4/\rho_z)$ times Sacherer's rms emittance.[10]

8. J. D. Lawson, *The Physics of Charged-Particle Beams*, 2nd ed. (Oxford: Clarendon Press, 1988), p. 192.

9. P. M. Lapostolle, IEEE Trans. Nucl. Sci. **NS-18**, 1101 (1971).

10. F. J. Sacherer, IEEE Trans. Nucl. Sci. **NS-18**, 1105 (1971).

ELECTRON BEAM TRANSPORT

Yu. V. Rudjak, V. B. Vladyko

Moscow Radiotechnical Institute, Russian Ac. Sci., Moscow

The electron beam transport in ion channel has been investigated. The influence of the external longitudial magnetic field and self beam magnetic field on the charge neutralization process was defined. Beam head erosion under channel is curved or the availability of transverse external magnetic field was numerically simullated. The numerical investigation of the ion-hose instability was performed. The conditions, when as a result of ion-hose instability development may be coming out of the channel by beam tail, were founded. It was showed, that suplementary creation of plasma by electron beam and ions did not lead to the reduction of ion-hose instability. Sufficient slowing down of ion- hose instability development could be achieved if betatron length increased to impulse tail. In the case of a weak initial nonsymmetrical perturbation, sausage instability was investigated. Numerical simulation showed, that this instability could lead to beam radius increasing in order. The electron beam guiding by low conductive plasma channel was considered. The attractive force of beam to this channel under nonsymmetrical injection was defined analitically.

Relativistic electron beam (REB) transported in low density ($n_p \leq n_b$) plasma channel interacts with plasma electrons and ions. However, because $m_e/m_i \ll 1$ these processes are separated in time and simulated separately. Plasma electrons expelling in short electron times define the possibility of beam propagation in the channel. This expelling depends on the external magnetic field and beam current magnitude. The charge neutralization process is investigated numerically on two dimensional azimutally symmetrical Maxwell-Vlasov equations system in given beam and low frequency approximation ($\omega a/c \ll 1$, ω - typical frequency, a - beam radius). The dependence of charge neutralization fraction $f = (N_{ip} - N_{ep}) / N_b$ from the

magnetic field magnitude B_z for beam currrent I_b=4кА and radius a = 1,5sm is given on Fig.1 (N_{ip}, N_{ep}, N_b -linea densityes of ions, plasma electrons and beam electrons). Plasma radius is chosen 0,5a , plasma density $n_p = n_b$. As it follows from the figure the charge neutralization process depends on external magnetic field if $\omega_c \simeq \omega_b$ ($\omega_c = \frac{eB_z}{m_e c}$, $\omega_b = \left(\frac{4\pi n_b e^2}{m_e}\right)^{1/2}$).

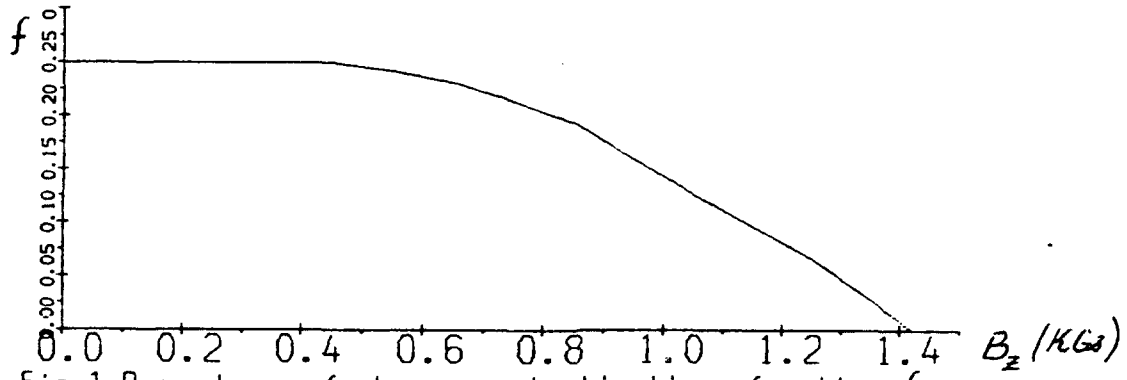

Fig.1 Dependence of charge neutralization fraction f from the magnetic field magnitued B_z .

If $I_b > \frac{mc^3}{4e}$ the beam magnetic field essentially influences on plasma electron dynamics and can lead to recompensation of the beam charge. Under this condition ponderomotive force $e\frac{v_z}{c}B_\varphi$ has an essential influence on dynamics of plasma electrons pushing them from the channel and leading to recompensation of beam charge. Numerical simulation shows, that plasma charge density near axis can be twice greater, that beam density. The charge neutralization process is accompanied by beam head erosion, especially in a curved channel or transverse external magnetic field. The erosion process was investigated on three dimensional kinetic model by beam and plasma. Fields was calculated in long wave, low frequency assumption. The beam was assumed to be monoenergetical. The dependence of erosion rate $u = \frac{c\Delta t}{\Delta z}\left(\frac{\gamma}{I_c}\right)^{1/2}$ from nondimensional parameter α numerically was investigated. For curved channel $\alpha = \frac{a}{R_c}\frac{\gamma\beta^3 I_o}{2f_c I_b}$ (R_c is the

channel curvatur radius, $I_o = \frac{m_e c^3}{e} \simeq 17$кА, $f_c = \frac{N_{1p}}{N_b}$, βc - longitudial beam velocity), for the external transversal magnetic field $\alpha = \frac{\omega_c a}{c} \beta^2 \frac{I_o}{2 f_c I_b}$. For the different waveguide radii r_w this dependence is shown in Fig.2 (γ=100, f_c=0,9, r_p=a).

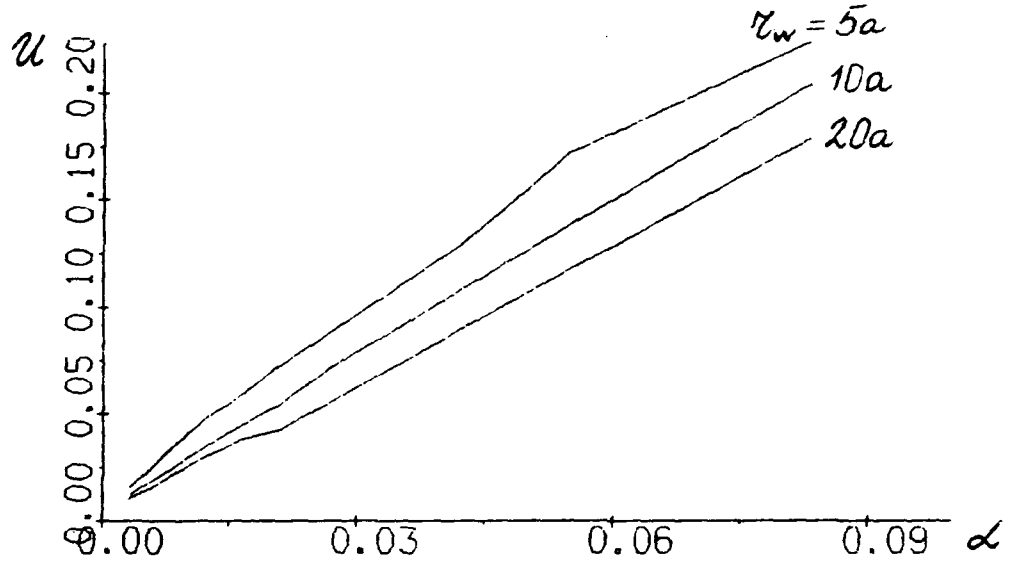

Fig.2 Dependences of erosion rate u from α.

Beam energy loss by plasma electron expelling from the channel described in [1,2]. If channel and beam are surrounded by low density plasma, oscillations must be exitated in this plasma. Energy for this oscillations is taken from the beam. The case when surrounding plasma density $n_p \simeq 10^9 - 10^{10} sm^{-3}$ is investigated in [3] in details. But even if the plasma density is in some order less then beam density, this beam energy loss must be taken into account. As numerical simulation shows, for $I_b \leq 4$кА with increasing of plasma linear density this loss increases until $\frac{\omega_p r_p}{c} \leq 2$ (r_p - plasma radius, $\omega_p = \left(\frac{4\pi n_p e^2}{m_e}\right)^{1/2}$), and then they are saturated.

In longer times when ions begin to move, ion-hose

instability, which can develop directly from the nonlinear stage, is most dangerous. The investigation of this instability was perfomed on three dimentional kinetic model by ions and beam. Fields was calculated in the long wave, low frequency assumption. Calculation shows, that the development of the instability directly from the nonlinear stage can be caused by injection of the beam into the channel at an angle of $\theta > \frac{0,1}{\beta}\left(\frac{I_b}{2f_c I_A}\right)^{1/2}$, and also by a beam transport in a curved channel , or availability of transvese external magnetic field $B_\perp$, when $\alpha > 10^{-3}$. In all this cases a fast development up to a large ion-hose instability amplitude occurs. Therefore the beam head duration of $\tau \simeq \frac{2\pi a}{c}\left(\frac{\beta I_o}{2 I_b}\frac{m_i}{m_e}\right)^{1/2}$ while is transported into the channel, another part of beam comes out of it.

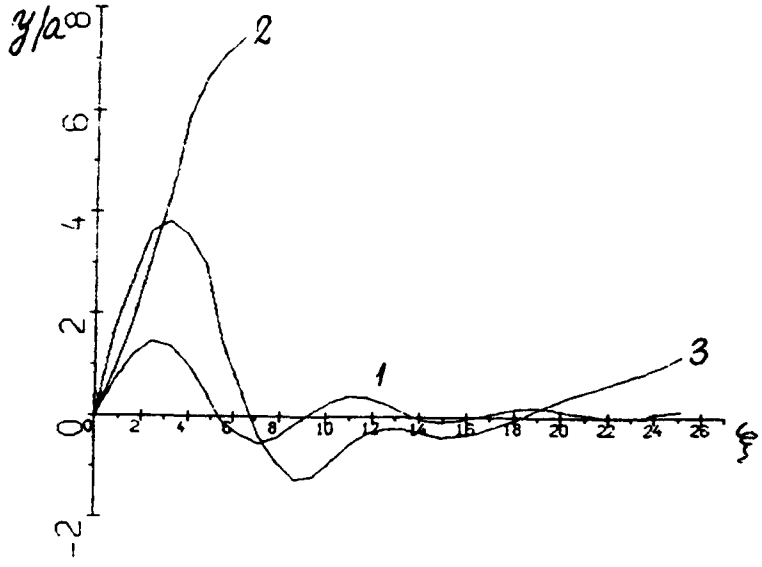

Fig.3 Dependences of Beam (curves 1,2) and channel (curve 3) axes position y/a from ξ.

On Fig.3 for different beam cross-sections deppendences of

beam and channel axes position y/a from longitudial coordinate $\xi = \frac{z}{\beta a}\left(\frac{2f_c I_b}{I_o \gamma \beta}\right)^{1/2}$ under injection of the beam into the channel at the angle of $\theta = \frac{1}{\beta}\left(\frac{I_b}{2f_c I_o \gamma \beta}\right)^{1/2}$ are pictured. Curve 1 corresponds to the beam cross-section, injected at the moment, when t = 0, curves 2 and 3 corresponds $t = \frac{4a}{c}\left(\frac{\beta I_o m_i}{2 I_b m_e}\right)^{1/2}$. Moreover, numerical calculations shows, that supplementary creation of plasma by electron beam and ions does not lead to the reduction of instability. In contraraly, if the initial perturbation is small, plasma supplementary creation can lead to swing of instability to the large amplitude and coming of beam tail from the ion channel. Sufficient slowing down of ion-hose instability development can be achieved if the betatron length increases to the impulse tail. That's why the radius or energy profilation on the beam impuls makes better it transport.

It is possible to make ion-hose instability development from a weak initial perturbation [4]. If beam charge neutralization fraction $f_c < 0{,}8$, azimuthally symmetrical beam and channel oscillations directly come to nonlinear stage. Under this condition the role of sausage instability increases. Numerical simulation on two dimensional azimuthally symmetrycal kinetic model shows, that as a result of sausage instability development, may be the increase of beam radius in order. The greatest development of instability occurs if the channel radius is a bit larger, then the beam radius. Increase or decrease of the channel radius lead to the instability stabilization. So for the ion-hose instability, the increase of the betatron oscillation length on beam impulse stabilizies the azimuthally symmetrical instability. Beam form, when it almost is not subjected instability, is numerically found.

Another method of electron beam guiding is the transport it in low- conductive plasma. Nonsymmetrical injection of a relativistic electron beam into a low-conductive plasma channel

($\frac{4\pi\sigma r_p}{\beta c} \ll 1$, where σ is plasma conductivity) causes plasma polarization and the appearance of a dipol electric field wich attracts beam to the channel axis. For a step radial conductivity profile an analytical expression for transverse electric field is derived and its dependence on the system parameters has been investigated. For a given time dependence of the beam current $I_b(t) = I_{bo}(1-e^{-t/\tau})$, the dipole electric field maximum value $E_{max} = 2I_{bo}/5\pi\beta ca$ is achieved when $4\pi\sigma\tau \ll 1$ at the moment, when $t \simeq 0,1/\sigma$.

1. H.Lee Buchanan Electron beam propagation in the ion-focused regime. Phys. Fluids 30(1), 1987, p.221-231.
2. J.Krall, K. Nguyen, G. Joyce Numerical simulations of axisymmetric erosion processes in ion-focused regim-transported beams. Phys. Fluids B 1(10), 1989, p.2099-2105.
3. H.S. Uhm, G. Joyce Theory of wake-field effects of a relativistic electron beam propagating in a plasma. Phys. Fluids B 3(7), 1991, p. 1587-1598.
4. R.J. Lipinski, J.R. Smith, I.R. Shokair et.al. Measurement of the electron-ion-hose instability growth rate. Phys. Fluids B 2(11), 1990, p. 2764-2778.

GENERATION AND CHARACTERISTICS OF HIGH POWER LONG PULSE ELECTRON BEAM (PROPAGATION IN VACUUM WITHIN DIFFERENT PRESSURE)

G.I.Alexeev, A.M.Bishaev, A.A.Golubev, V.A.Gudovich, A.H.Kadimov, G.I.Klenov, V.P.Larionov, O.I.Radkevich, O.V.Shterbina
Moscow Radiotechnical Institute RAN
Russia, 113519, Moscow, Varshavskoye sh.,132

Abstract

For investigation of propagation dynamic of high power long pulse (0,3-1 ms) electron beam in vacuum within pressure $5*10^{-5} \div 10$ Torr two experimental installation were constructed: 1. Electron energy - 300 keV, current 30-100 A, pulse 0,35 ms long; 2.Electron energy 500-600 keV, current 30÷200 A, pulse 1 ms long. Two different macroinstabilities of the beam have been observed. One of them had freaquences up to 10 MHz within pressure $5*10^{-4} \div 1$ Torr. Second had freaquences several kiloherzes within pressure $5*10^{-4}-10^{-1}$ Torr. When pressure was $5*10^{-5} \div 5*10^{-4}$ Torr monotonous increasing of beam diameter along transport way was observed depending on beam microinstability.

1. Introduction

Long pulse high power electron beams can be used for plasma heating at the installations for inertial fusion. Electron injectors with field emission kathodes [1] have to provide long of the pulse 10^{-4} s that can be very problematic because of limitations connected with mooving of cathode plasma.

Overcoming of the difficulties is possible on the way of using long pulse accelerators and thermoemission cathodes, which as are indicated [2,3] can accelerate high power beams.

2. High voltage accelerators

For providing of experimental works it was constructed two high voltage acceleretors which distinguished at construction of accelerating systems and long of high voltage pulse. First accelerator was designed as high voltage diod.

High voltage generator forms rectangular pulses of negative polarity 0,35 ms long on the foundation. Amplitude

of the pulses can be used from 100 till 500 kV. Current to equivalent confortable load is 1 kA.

Maximum values of the current which have been got for cathodes with diameters 7,5 and 12 cm are shown in Table 1.

Table I.Maximum values of the currents.

Cathode diameter, cm	Energy of electrons, keV	Beam current, A	Long of the pulse, ms	Beam diameter at the anode exit, cm
7,5	300	100	0,35	2
12	220	300	0,35	6

Run pressure in the diod volume was $5*10^{-5}$Torr.

From point of view increasing power of the beam and difficulties of receiving of high voltage second version of accelerator was developed with accelerating column as basis.

High voltage generator forms pulses with amplitude up to 700 kV, 1 ms long. Current to equivalent confortable load is 1 kA.

Beam parameters which have been got during run with cathodes of different diameters is shown in Table II.

Table II. Parameters of the beams with cathodes of different diameters

Kathode diameter cm	Energy of electrons keV	Beam current A	Long of the pulse ms	Kathode material	Perveance mcA/V$^{3/2}$
30	400	100	1	LaB_6	0,4
50	460	145	1	LaB_6	0,45
75	450	260	1	Ir-La	0,82
120	450	350	1	Ir-La	1,3

Run pressure in the field of anode cone was 10^{-5} Torr.

For described above high voltage accelerators were constructed cathode units with different diameters of the emitters: 30,50,75 and 120 mm [4,5]. It were used the emitters both high temperature substrate under emission material and fabricated by pressing.

Emission materials were LaB_6 and Ir-La.

It were developed constructions both with heaters from graphite and from tantalum. In both cases constructions of the heater has provided compensation of magnetic field from current flowing along heater.

3. Experimental results

Experiments on beam propagation in vacuum within different pressures were carried out with beam energy 300 keV, currents 45÷50 A, pulse 0,35 ms long. Beam profile was like Bennett's one, and radius including half of the current was about 0,5 cm. Scheme of the experiment is shown in Fig.1.

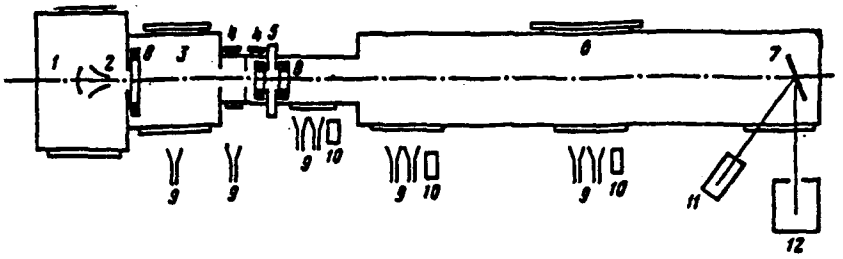

Fig.1. Scheme of the experiment.
1.Cathode.2.Anode. 3.Vacuume volume. 4.Section of differential pumping. 5.Valve. 6.Diagnostic volume. 7.Beam collector. 8.Current probe. 9.Detector of r.f. probes. 10.Fotoelectron amplifiers. 11. X-ray irradiation probe. 12.5-channel X-ray obscure-camera.

Beam was injected in gas through two section receiver system of differential pumping 4 and high speed valve 5. Diagnostic volume (70 cm diameter; 5,5 m long) was after valve. It could be regulate pressure in volume till 10 Torr. (When pressure was 10^{-5}÷10^{-2} Torr high speed valve didn't used).70÷75% of the beam (30÷40 A) have been injected in experimental volume. Current was measured by Rogovski coil 8. Probe 9 for registration of light and r.f.radiatios (0,8 and 3 cm) which are signs of arising of plasma beam discharge (PBD) were installed along volume.

Electron beam has been caught by plane metal collector (50*50 cm^2). Displacement of the beam across collector, when instability had place, was fixed by means of registration of X-ray radiation. 5-channel X-ray obscure-camera 12 with

plastic scintillators (time resolution 4-5 ns) and photomultipliers for photoelectrical registration were used. High boundary of frequency band of measuring line was above 20 MHz. Collector surface was perpendicular to beam and almost parallel to obscure axis, and field of view each of fife channels looked as long strip 5 cm wide. Fields of view of next channels were not covered. Distance between their edges was 2 cm. Special monitor 11 measured total level of X-ray radiation from the collector.

We have observed two large scale instabilities. Within pressure $5*10^{-4} \div 10^{-1}$Torr low freaquence instability arises, and beam jumps as whole across collector with the amplitude of the jumps much more of beam diameter. When distance is 3 m from input in volume the amplitude of jumps is 10-20 cm. Within shown pressures PBD is always. Mean time between successive shifts of the beam decreases with increasing of gas pressure. Conditional freaquence (inverse time) of the shifts is about tens kiloherz. Nature of that low freaquence instability was not understood. It's supposed that instability is connected with currents flowing through high density plasma, formed PBD. Typical freaquences second large scale instability are a few megaherzes and space increment is about 10^{-2} cm^{-1}. Instability arises within pressure range $5*10^{-4} \div 1$ Torr. Amplitude of r.f.shifts of the beam is about 1 cm when distance between input and collectors is 3 m.

Oscillogrammes of the signals for three channels of obscure-camera illustrating beam shifts along vertical within different gas pressure is shown in Fig.2. Shifts along horisontal is similar. Distingiushed direction is absent. For clearness two oscillogrammes are given in contrary directions.

Within pressures $5*10^{-4} \div 10^{-1}$ Torr (field of PBD) two instabilities are simultaneous (look signal at $p=6*10^{-3}$, where one can see mooving of a beam from channel 4 to channel 1,2 because of l.f.instability). When pressure is over 10^{-1} Torr both PBD and l.f.instability are absent. H.f.beam oscillations continue to be. Their freaquences increase with pressure. High boundary of h.f.instability is

very sharp: oscillations have maximum amplitude at 0,5 Torr and practically disappear at 1 Torr. At pressure 1-10 Torr beam is stabilized and its expansion depends on spreading processes in nuetral gas.

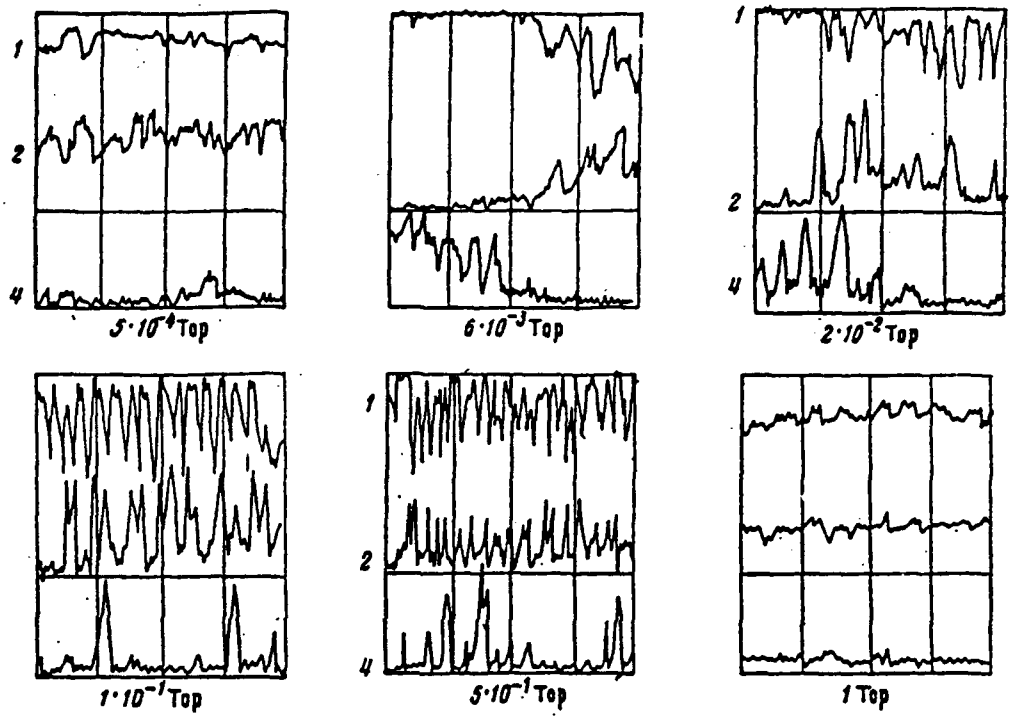

Fig.2. Oscillograms of the X-ray obscure-camera signals (zero lines are also shown).Horisontal line is 1 mcs/point. Distance between middles of neighbouring (1 and 2) channels is 7 cm. Figures of the vertical axis are numbers of the channels.

Besides written two macroinstabilities the beam exposes to microinstability. Freaquence of microinstability is about 1 MHz. Because of indicated instability beam increases radius from 0,5 mm up to 1÷1,5 cm for propagation along volume 5 m long. When pressure is over 1 Torr it can observe increasing of diameter because of usual spreading.

Theoretical analise [6] has shown that large scale h.f.instability within pressures $5*10^{-4} \div 10^{-1}$ Torr can be explained as instability on gelicon way of plasma oscillation magnetised by beam field with transition to resistive hose one within pressure $10^{-1} \div 1$ Torr.

For accélerator with accelerating column we have got

For accelerator with accelerating column we have got maximum current density about 0,3 kA/cm^2.

4. Conclusion

Here we presented results which showed possibility of acceleration and transportation of long pulse electron beams with energy store about 80 kJo without external magnetic field. It have been also shown expedience of using LaB_6 and IrLa cathodes, which have good life time in conditions of ion bombardment and can run long time in conditions of technical vacuum.

Experiments with beam injection in neutral gas showed that within pressure $5*10^{-4} \div 1$ Torr are two large scale instabilities. First one within pressure $5*10^{-4} \div 10^{-1}$ Torr has freaquence tens kiloherzes. Nature is not really understood. Within pressure $5*1-^{-4} \div 1$ Torr is h.f.instability with freaquence about 10 MHz, which explained as instability on gelicon way of plasma oscillation magnetized by own beam field ($5*10^{-4} \div 10^{-1}$ Torr) turning into resistive horse one ($10^{-1} \div 1$ Torr).

When pressure was $5*10^{-5} \div 5*10^{-4}$ Torr it was observed monotonous increasing of beam diameter along transport way depending on beam microinstability.

Maximum current density which was get was about 0,3 kA/cm^2 1,2 m long way off from accelerating tube.

5. References

I. Д.Д.Рютов, Вопросы атомной науки и техники, сер.Термоядерный синтез, I978, вып.I-2, с.96.

2. А.А.Кузьмин, Г.И.Кленов, С.В.Лебедев, А.М.Бишаев, А.Х.Кадымов, О.В.Щербина.. V11 Всесоюзный симпозиум по сильноточной электронике, Тезисы докладов, ч.II. Томск, I988, с.I69.

3. В.А.Гудович, С.Р.Доценко, Г.И.Кленов, В.П.Ларионов, О.В.Щербина. VII Всесоюзный симпозиум по сильноточной электронике. Тезисы докладов, ч.II, Томск, I988, с.I72.

4. Г.И.Алексеев, А.М.Бишаев, В.А.Калабухов. Г.И.Кленов, V Всесоюзный симпозиум по сильноточной электронике, Тезисы докладов, ч.I. Томск, I984, с.93.

5. В.А.Гудович, С.Р.Доценко.
. Труды Московского радиотехнического института АН СССР. "Сильноточные импульсные ускорители заряженных частиц", Москва, I989, с.I2.

6. А.А.Голубев, А.Х.Кадымов, Е.Р.Надеждин, О.И.Радкевич, Г.А.Сорокин. Физика плазмы, Том I6, Вып.6, I990, с.69I.

GENERATION OF MICROWAVE OSCILLATIONS IN AN ELECTRODYNAMIC SYSTEM WITH PLASMA-BEAM INTERACTION

by: V.I.Perevodchikov, M.A.Zavialov, V.F.Martynov, L.A.Mitin, V.N.Tskhai, A.L.Shapiro

All-Russian Electrotechnical Institute, Moscow, Russia

ABSTRACT.

The microwave plasma-beam amplifier is designed in cantimeter wavelenght range. The amplifier has a decelerating structure in the form of a chain of connected resonators. The gas-dynamic system maintains gas pressure in decelerating structure up to 10^{-3} torr. Plasma gives a possibility to increase power of microwave radiation by a factor of 2-8 times.

The discovery of oscillation instabilities of the electron beam in plasma has resulted in efforts to build microwave devices based on the interaction between spatial charge waves and the electromagnetic wave without the use of traditional decelerating structures [Refs.1, 2, 3]. The main advantage of plasma waveguides is the spatial nature of waves with the maximum electric field strength on the waveguide axis. In combination with system charge quasi-neutrality and an extremely wide band, this openes a perspective of building microwave amplifiers and generators having a high output power and a wide band of amplified oscillations.

Group waves of spatial charge, however, cannot be radiated in the outer space. As a result, there are certain threshold powers of excited oscillations after which their energy is moved to the region of low-frequency plasma oscillations near the ion- cyclotron frequency and the ion-plasma frequency. This, in turn, results in a failure of the waveguide due to large-scale instabilities.

The proposal and realization of the hybride plasma waveguide [Refs. 4, 5, 6] is a way to tackle the problem. This waveguide uses an electromagnetic-type wave excited in a chain of connected resonators (CCR) to interact with the electron beam. In this case, the plasma waveguide's boundary is length-periodical. The waves propagating in such a system are electromagnetic-plasma ones, the position of the maximum electric field strength on the plasma waveguide axis coinciding with that of the maximum power flow outside the waveguide, which is passing througth coupling slots in the walls of the CCR cells.

As a result of this interaction, the energy density of waves in plasma is substantially reduced and the area of linear plasma dynamics expands. Thus, the hybride plasma system has both the advantages of plasma waveguides and the certain advantages of electron vacuum devices, such as a wide range of linearity of dynamic processes and a high microwave output power.

A marked progress in the design of high-intensity electron beam formation systems under the conditions of the electron beam interaction with ion flows and plasma has

been achieved during the recent years. Besides, electron beam guns intended for use in process plants, which feature a stable, continuous operation at high pressures, have been designed .

These achievements made it possible to begin to design microwave plasma-beam amplifiers and generators. The work was mainly aimed at designing a sealed-off plasma-beam device (PBD) based on the CCR to work continuously within the centimeter wavelength range.

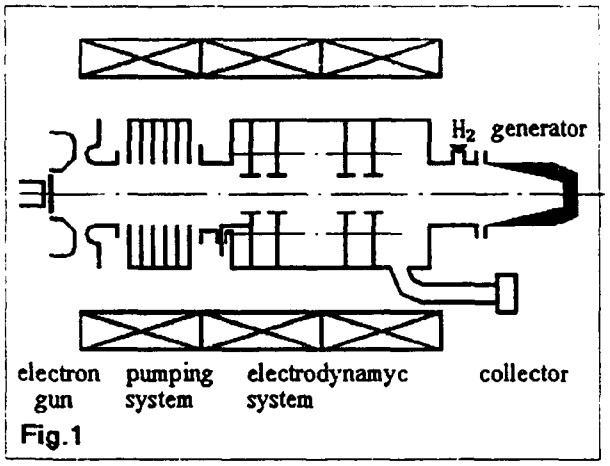

Fig.1

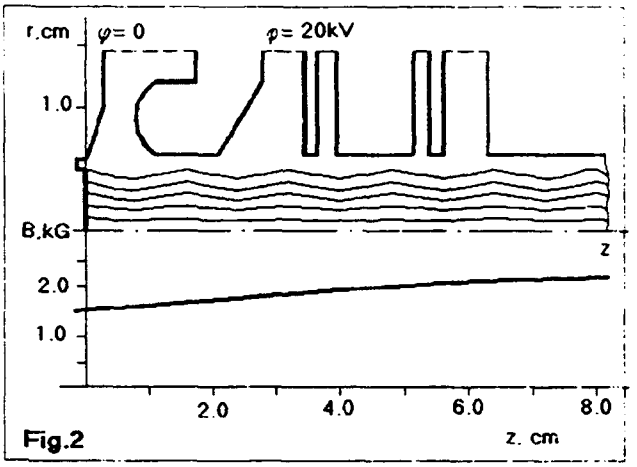

Fig.2

Fig. 1 presents a PBD schematic diagram. The device is equipped with an electron gun, a CCR decelerating structure, a collector, and a gas-dynamic system. The latter is intended to maintain a specified gas pressure in the decelerating structure and a pressure differential between this area and the electron gun. The system employs hydrogen at a pressure in the CCR area of $1x10^{-6}$ torrs to $5x10^{-3}$ torrs as a working gas.

The device is placed in a magnetic field of a solenoid. The magnetic field induction should meet the following condition: $\omega_e^2 < \omega_H^2$, $\omega_b^2 << \omega_H^2$ (ω_b - beam electron frequency; ω_H- electron cyclotron frequency; ω_e- electron plasma frequency). The required plasma concentration is up to $1x10^{12}$ $1/cm^3$.

The electron gun generates an electron beam with a current of 2 A to 4 A and an electron energy of up to 25 keV. Fig. 2 gives results of the calculation of the gun electron-optical system. The cathode made of LB or W is electron-heated.

The gas-dynamic system contains hydrogen generators having resistive heaters and an evacuating device to provide an evacuation rate of 0.2 l/sec to 2 l/sec at the working pressure.

The decelerating system, the microwave energy input/output device, and the collector are similar in design to those conventionally used in travelling wave tubes. The PBD is subjected to the same vacuum treatment as that for vacuum tubes.

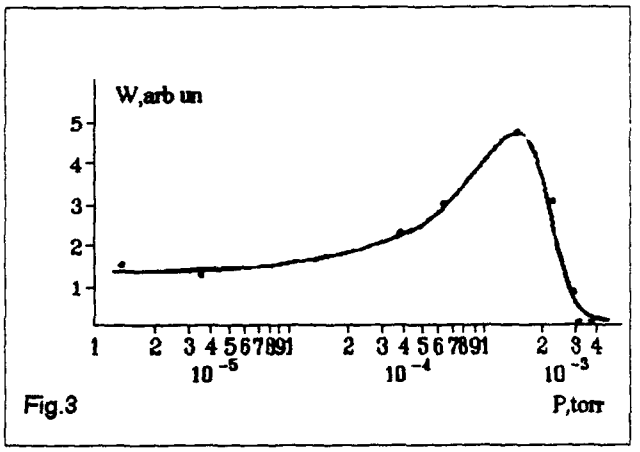

Fig.3

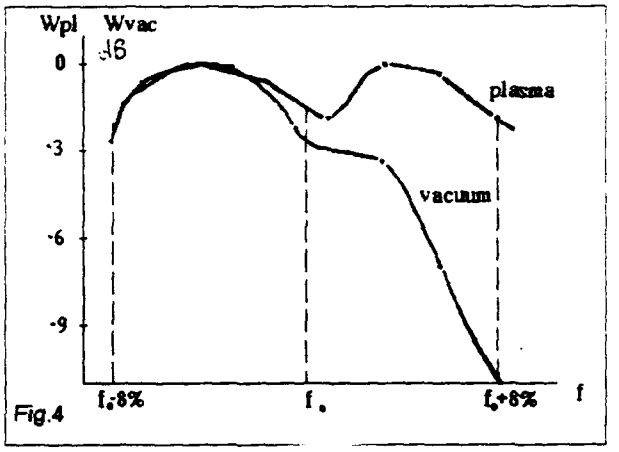

Fig.4

Fig. 3 shows a microwave power radiated in the amplification mode as a function of pressure in the decelerating structure. The microwave power is increased 2-3 times with a pressure of about $1x10^{-4}$ torrs to $1x10^{-3}$ torrs. The power generated in continuous operation at a pressure of 0.001 torrs is up to 20 kW, the electron efficiency (that is a ratio of microwave power to electron beam power) reaching up to 30%.

The extended operating band of the PBD is an essential advantage of the plasma mode of operation. Fig. 4 gives amplitude-frequency responses at a pressure of $1x10^{-6}$ torrs (Curve 1) and $1x10^{-3}$ torrs (Curve 2). In addition, the device features a low level of high harmonics radiation due to the shielding effect of plasma.

In our oppinion, these results substantially prevail over those reached by nowadays in conventional vacuum devices working in the centimeter range. We believe that the use of the above idea of plasma hybride systems can markedly increase the power of microwave amplifiers and generators - up to several tens or even one hundred of kilowatts in continuous operation. The possibility of realization of this idea depends on the optimization of hybride waveguide systems and the conditions of plasma formation. With increasing power in the continuous mode of operation, it becomes more and more difficult to ensure a stable operation of the cathode with a long service life. This is possible with a special emitting system in which ion flows cannot reachthe cathode.

Works to investigate and design these systems are now being intensively carried out. A ring cathode is planned to be emploied in the electron gun results of which calculation are given in Fig. 5. The electron trajectories coincide with magnetic field force lines in the area of dissipation of the solenoid. The ion flow emitted by plasma beyond the anode is virtually not subjected to the influence of the magnetic field and is directed to a ion

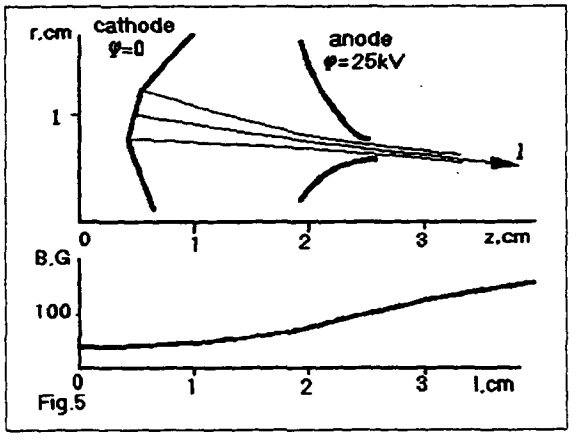

Fig.5

collector placed on the axis beyond the cathode. This allows not only efficient low-temperature cathodes to be used. The calculation was performed by a specially developed program.

We think that the design of plasma-beam devices having a high microwave power in continuous operation will allow to solve efficiently a number of technological problems, for example in plasma chemistry, and to extend power telecommunications.

CONCLUSION: The use of plasma waveguides in combination with the electromagnetic flow decelerating structure designed as a chain of connected resonators makes it possible to build hybride plasma systems in which plasma microwave oscillations can be efficiently amplified and radiation energy can be removed out of the device. A prototype of the plasma-beam device capable of amplifying microwave oscillations within the centimeter wavelength range at a power of 20 kW in continuous operation has been designed based on the above conception with due consideration of the existing achievements in design of electron guns for use in electron-beam process plants.

In our oppinion, further development of the hybride plasma systems and electron guns with cathodes protected from ion bombardment will allow the power of continuous radiation to be increased up to several tens or even one hundred of kilowatts.

References

1. А.И.Ахиезер, Я.Б.Файнберг., ДАН СССР, 1949, 69, N 4, с.555-556.
2. E.Bogdanov, B.Kislov, Z.Chernov, Proc P.I.B. Simp. Milimetor Waves, 9, 1959.
3. G.Boyd, R.Guold, L.Field. Proc. IRE, 49, Dec. 1961; Phys.Rev., 109, 1958.
4. Я.Б.Файнберг, Ю.П. Блиох, Л.А. Митин и др., ДАН УССР, сер Математика и механика, N11, 1990.
5. G.Batskih, K.Gureev, N.Karbushev, A.Lisitsin, Beam'90, Novosibirsk, 1990, Part 2, p.269.
6. M.Zvjalov, L.Neganova, V.Perevodchikov, V.Tskhai, 19 ICPIG Belgrade 1989, V4, p.936.

CYCLOTRON RADIATION OF A REB INJECTED INTO INCREASING MAGNETIC FIELD

Alterkop B.A., Mikhailov V.M., Rukhadze A.A., Tarakanov V.P.

Institute for High Temperatures, Russian Academy of Sciences, Izhorskaya 13/19, Moscow, 127412, Russia

By using analytical and numerical methods the dynamics of an annular relativistic electron beam (REB) injected into cylindrical waveguide with axisymmetric magnetic cusp is investigated. For the beam with current 1kA, energy of the particles 0.4MeV, the narrow band electromagnetic radiation with the frequency $f \sim 25GHz$ was obtained, when the maximum efficiency the beam energy conversion into the radiation energy was about 25%.

Usually, for the calculation of induced cyclotron radiation efficiency and, partially, hyrotrons [1], the magnetic field in resonator is considered to be uniform and transversal component of the electrons velocity - weakly relativistic [2-4]. The length of saturation defines the optimal length of resonator in hyrotrons. The increase of the beam current and especially the transversal velocity causes the reduction of the saturation length. So, for the increase of radiation efficiency it is assumed to be effective the organization of magnetic cusp in the resonator in such manner, that the transfer of "longitudinal" to "transversal" energy is done along the system caused by the increase of magnetic intensity. This way, practically full transfer of beam longitidunal energy into the rotational energy is done and the length of the resonator is sufficiently reduced.

So, let the monoenergetic electron beam to be injected into the cylindrical resonator along the force lines of magnetic field. At the beginning, the strendth of leading magnetic field is constant and then increases, forming the cusp:

$$B_z = B_0 + \frac{\Delta B}{L}\zeta, \qquad B_r = -\frac{r}{2}\frac{\Delta B}{L}, \tag{1}$$

where ζ - is measured from the beginning of increase of magnetic field, L - cusp length, $\Delta B = B_{max} - B_0$, and r - distance from the axis. The beam is injected along the field line given by the relation

$$1 + \frac{\Delta B}{B_0}\frac{\zeta}{L} = \frac{r_0^2}{r^2}. \qquad (2)$$

where r_0 is initial average radius of the beam.

From relations (1) - (2) in adiabatic approximation one can find the magnetic intensity at the point of electron reflating ($v_{\|} = 0$) and coordinates of this point are:

$$B_* = B_0\left[1 + \left(\frac{2B_0}{\Delta B}\frac{L}{r}\right)^2\right] \qquad r_* = r_0\left(\frac{B_0}{B_*}\right)^{1/2}, \qquad \zeta_* = \frac{B_* - B_0}{\Delta B}L. \qquad (3)$$

Therefore, locking condition for the electron in the cusp $\zeta_* \leq L$ or $B_* \leq B_{max}$ puts a bound on the parameters of the system:

$$\frac{\Delta B}{B_0} \geq \left(\frac{2L}{r_0}\right)^{2/3}. \qquad (4)$$

The maximum radiation should be expected from the region of electrons reflecting since in this region the beam is transformed into the gas of oscillators ($v_{\|} = 0$), for which the cyclotron instability has a maximum increment. Essentially, for the problem involved one can't consider the radiation to be only from the region of beam reflection, but this assumption helps us to define the dominant frequency of radiation and the increment ($\omega \to \omega + i\delta$) [4]:

$$\omega \approx \omega_{cr} = \frac{\mu_{1n}}{R}c = \frac{\omega_{H_*}}{\gamma_*}, \qquad \delta = \frac{1 + i\sqrt{3}}{2}\frac{1}{2}\left(G\frac{v_\perp^2}{c^2}\frac{1}{\gamma_*}\frac{\omega_b^2}{\omega^2}\right)^{1/3} \qquad (5)$$

where μ_{1n} is a root of Bessel function derivative $J_0'(\mu_{1n}) = 0$, since it is assumed, that the beam excites axial-symmetric TE_{0n} mode of resonator. More strictelly this is correct, when the beam coordinate in the reflection region r_* corresponds to the maximum of $E_\varphi \sim J_0'(\mu_{1n}r)$. Cyclotron frequency ω_{H_*} and relativistic factor of electrons γ_* are defined by the values of magnetic field and energy of electrons at the reflection point and G is so – called form factor,

$$G = 2\frac{\Delta_* r_*}{R^2}\frac{J_1^2(\mu_{1n}\frac{r_*}{R})}{J_0^2(\mu_{1n})} \qquad (6)$$

where Δ_* is the beam thickness at the reflection point and $\omega_b = \sqrt{\frac{4\pi e^2 n_b}{m}}$ is Langmuir frequency of the beam electrons defined by n_b at this point. At last, the radiation efficiency is estimated on the basis of violation a resonance (5) caused by the decrease of energy of electrons via radiation [4]:

$$\eta = \left|\frac{\delta}{\omega}\right| = \left(\frac{1}{8} G \frac{v_\perp^2}{c^2 \gamma_*} \frac{\omega_b^2}{\omega^2}\right)^{1/3} \qquad (7)$$

It is worth mentioning, that the value of $|\delta|$ defines also the range of amplified frequencies in resonator. Radiation linewidth can be only less, since the generation corresponds to the induced radiation.

Numerical simulation was implemented with the help of 2,5 D code KARAT-RZ. The annular electron beam was injected into the cylindrical waveguide through the left end foil, which, as well as waveguide walls, was considered to have ideal electrical conductivity. Then the beam propagats through the magnetic cusp. Transmitted through the cusp particles were directed onto the waveguide wall by decreasing magnetic field. It was assumed, that the particles were absorbed in the closed end and the walls of waveguide. The right end provides the radiation of the flat electromagnetic wave into the free space. REDITRON [5] scheme enables us to realize such a system.

Parameters of the problem: radius of the waveguide $R = 2cm$, its length $l = 15cm$, the inner radius of injected beam $r_0 = 1.5cm$, thickness of beam $\Delta = 0.1cm$, current $I_b = 1kA$, energy of electrons $E = 0.4MeV (\gamma_0 = 1.8)$, intensity of leading magnetic field $B_0 = 5kGs$ uniform at the initial path $0.5cm$ and increasing up to $B_{max} = 25kGs$ at the distance $L = 3.5cm$; further, the field falls to zero at the distance $\sim 1cm$.

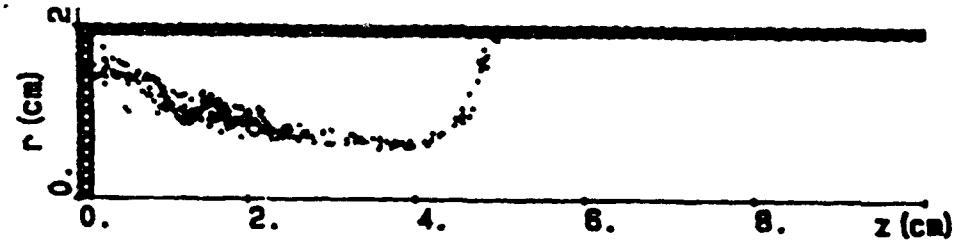

Fig.1

Fig.1 shows the beam particles at $t = 15ns$ on the $r-z$ plane. One can see, that up to $z \leq 2cm$ injected particles move along the adjacent trajectories, rotating about the field lines.

The beam particles on the plane $p_z - z$ are shown in Fig.2 at the moment $t = 15ns$. One can see the particles deceleration at the initial path practically without scattering. Therewith, the particles deceleration is caused not only by the effect of magnetic cusp, but also by the space charge field, the potential of which is about 0.15 MV.

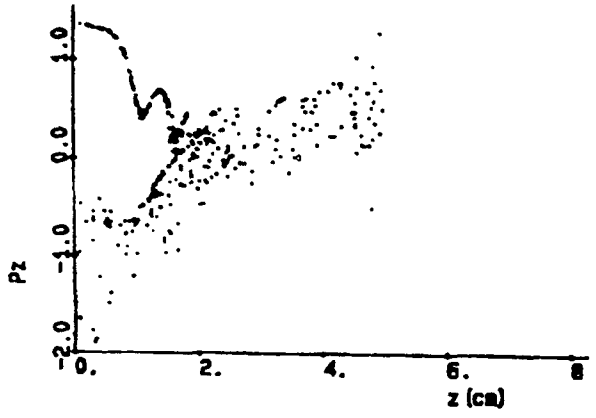

Fig.2

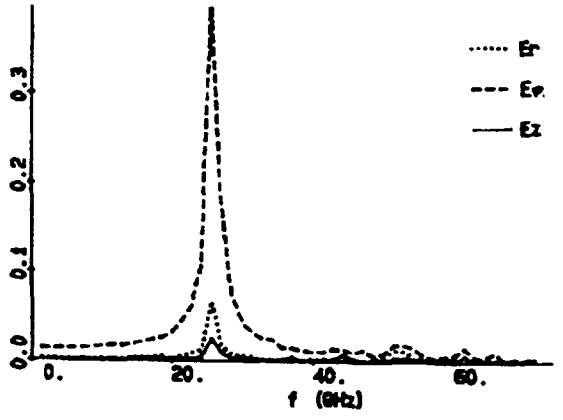

Fig.3

The radiation efficiency was calculated by the spatial integration of Pointing vector near the right end of the waveguide. It was found, that radiation efficiency reaches the quasistationary value $\eta \simeq 20\%$ and oscillates in time, having the maximum at $\eta_{max} \simeq 25\%$. The efficiency calculated by the formulas (6), (7) is $\eta \simeq 15\%$. For given parameters of the system, the energy in TE wave is by an order of magnitude greater then the energy in TH wave. Therewith, the spatial dependencies of components of electromagnetic field indicate that TE_{03} mode is excited.

Spectra of components of electric field at the point with coordinates $r = 1.5cm$ and $z = 9cm$ are given in the fig.3. One can find, that TE mode (E_φ component) is mainly excited with the frequency $f = \frac{\omega}{2\pi} \approx 25GHz$ ($\Lambda \approx 1.2cm$) close to the critical frequency for this mode $f_{cr} \simeq 24GHz$.

Fig.4. shows the distribution of beam density along the system. It is seen, that the beam density rises on the order in the cusp. The maximum value of beam density is oscillating in time with the frequency, corresponding the Langmuir frequency of electrons in this region. Oscillations of electron beam density calculated by the formulas (6),(7) probably determines the oscillations of radiation efficiency.

The time dependencies of the following quantities were calculated: $\int E_r j_r dV$, $\int E_\varphi j_\varphi dV$, $\int E_z j_z dV$. It was found, that the average value of $\int E_\varphi j_\varphi dV$ is sufficiently greater then the others, so one can a conclude that the generation

occurs as a result of the interaction of beam and E_φ component. According to calculations, the value of $\int E_\varphi j_\varphi dV$ changes in time with a period corresponding to radiation frequency 25 GHz. Examination of spatial dependence of $E_\varphi j_\varphi$ let us to a conclude that the generation occurs mainly in the cusp at the point of particles reflection with coordinates $r = 0.9cm, z = 1.8cm$.

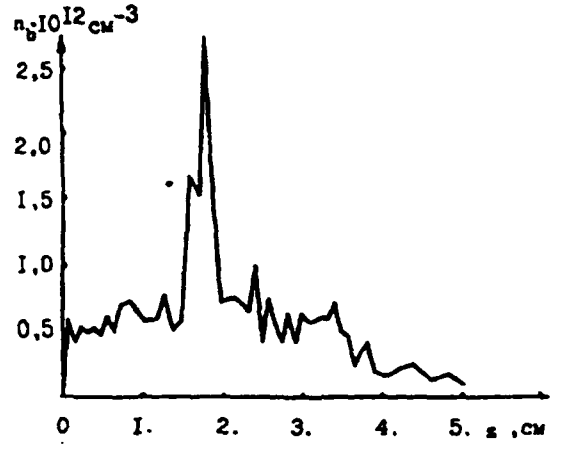

Fig.4

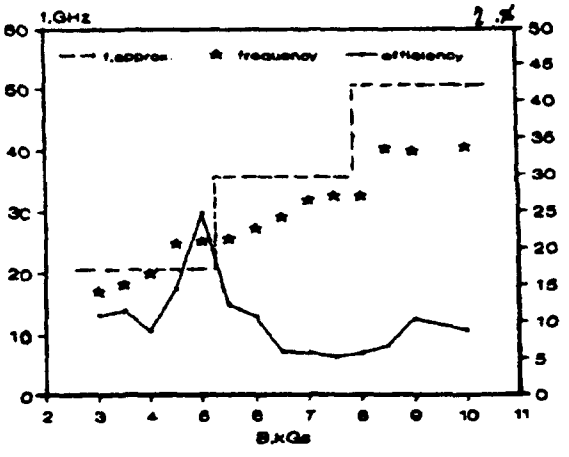

Fig.5

When comparing results of numerical simulation and calculations by the formulas given above, it was assumed, that at the reflection point $B_* \simeq 12kGs, r_* \simeq 1cm, \gamma_* \simeq 1.4, n_b \simeq 2.5 \times 10^{12}cm^{-3}$ and $v_\perp \simeq 0.8c$. The value of radiation frequency given from the relations (5) is $f \approx 24GHz$, which well corresponds to the results of numerical simulation. Also from (5) we obtain $\mu_{1n} = 10$, which corresponds to the third root of Bessel function $J_1(x)$. Therewith, the beam is located on the radius of the maximum of $E_\varphi \sim J_1(\mu_{1n}\frac{r}{R})$ component between the second and the third nodal points. This conditions determine efficient excitation of TE_{03} mode, which is confirmed by the numerical simulation.

It was found, that the maximum efficiency is achieved when the current is $I = 1kA$ and energy of the beam $E = 0.4MeV$. Increase of the injected current from 0.7 to 1.1 kA or change of the energy of the particles from 0.35 to 0.5 MeV doesn't effect on the efficiency, frequency and mode of radiation.

It must be notied also, that the change of parameters of the system, magnetic field configuration in particular, can lead not only to the change of radiation mode but to the change of wave type (TE or TH). The dependence of the dominant frequency and radiation efficiency on the initial value of the guiding magnetic field B_0 are given in the fig.5 (dotted line corresponds to the values of generation frequency obtained by the formulas (3) and (5).

The difference between the numerical and analytical results doesn't exceed 20%. The "plateau" sections for the radiation frequency obtained from the numerical simulation correspond to the excitation of the own electromagnetic wave modes of cylindrical resonator. The low values ($\sim$ 6%) of radiation efficiency for TE_{05} mode are explained by the fact that for given parameters of the system, one of the own TH modes of waveguide is excited as a result of the work done by the E_r component of the beam space charge field. Concurrence of different waveguide modes leads to the diminishing of radiation efficiency, while the monochromatization of the radiation is not affected practically. The dominant mode of radiation in this case is TH wave having the frequency $\sim 30GHz$ (in a good accordance with the formulas (3),(5)).

References

1. Kuzelev M.V., Rukhadze A.A. Russia, Usp.Phys.Nauk, 1987, V152, P.285.

2. "Relativistic high-frequency electronics", edit. by A.V.Gaponov-Grehov V1 – 5, 1979 – 1986, Gorky, IPF AN USSR.

3. "Free electron sources of coherent radiation", edit. by Rukhadze A.A., Moscow, 1981.

4. Kuzelev M.V., Rukhadze A.A. "Electrodynamics of condensed electron beams in plasma", Moscow, 1990.

5. Kwan T.J.T., Phys. Rew. lett., 1986, V57, P.1895-1898.

LONG PULSE ELECTRON BEAM PROPAGATION

J. R. Smith[a], I. R. Shokair, K. W. Struve[b], P. W. Werner[c],
S. Hogeland[d], P. Kiekel, I. Molina, B. N. Turman, and R. B. Miller[a]

Sandia National Laboratories
Albuquerque, NM 87185

ABSTRACT

Propagation of a 1 μs electron beam over a distance of 90 m has been investigated in the EPOCH Laboratory at Sandia National Laboratories. The mode of propagation is Ion Focused Regime (IFR) transport. The plasma channel, which is required for IFR transport, is obtained by photoionization of trimethylamine gas with a krypton-fluoride laser. Beam voltage is 2.5 MV, and beam current is 1.1 kA. Propagation efficiencies better than 90% have been recorded.

The ion hose instability is a key issue concerning long-pulse beam propagation. In previous work, growth of transverse beam oscillations (due to the ion hose instability) and moderate damping (due to phase-mixing) were measured in the first 6 m of beam propagation. Detailed displacement measurements in this region were used to determine the ion hose growth rate.[1,2] Damping of beam oscillations is accompanied by an increase in beam radius as measured from head-to-tail.

This report describes extension of the previous work on ion hose in two areas: beam radius and beam displacement. A method which successfully reduced ion hose growth is also presented.

I. EXPERIMENT

The experimental hardware, with diagnostics used for radius measurements, is given in Fig. 1. The propagation tank is 0.9 m diameter and 91 m long. Beam radius is measured by imaging the Cherenkov radiation from a quartz fiber target.[1] Targets were located 23 m and 86 m downstream of the propagation tank entrance. Each target is viewed by a framing camera. The beam had an initial radius of 1-2 cm. The space charge neutralization (channel strength) is in the range $0.5 < f < 1.3$.

---

[a]Titan/Spectron, [b]Mission Research Corp., [c]University of New Mexico, [d]K-tech Corp.

Work supported by SDIO through the Naval Surface Warfare Center and the DOE at Sandia National Laboratories under contract DE-AC04-76DP00789.

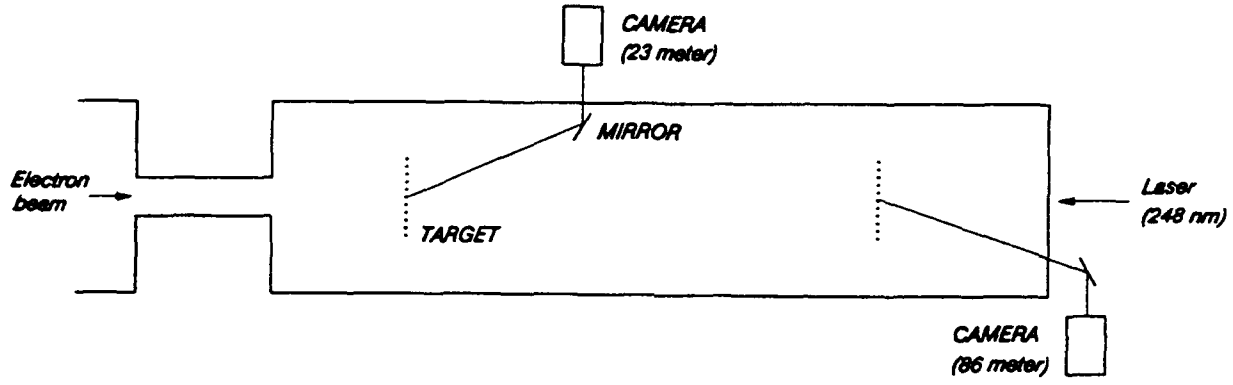

Figure 1. Experimental setup.

II. RADIUS MEASUREMENTS

A group of electrons injected onto the channel during a time interval small with respect to the beam pulse is defined as a beam slice. It is convenient to identify a slice by its time of injection into the propagation tank. We define slice time as the time interval from the *beginning* of the current pulse (measured at the tank entrance) to the *beginning* of the beam slice. The framing camera exposure time is set for 50 ns, which sets the slice duration time. This is a small fraction of the entire beam duration, 1000 ns. Therefore, each camera measures the image related to a beam slice. Slice duration time is also small with respect to an ion oscillation time, which is of the order of 1 μs. This indicates there is minimal transverse motion during the slice duration, so camera images are not artificially enlarged or distorted due to beam sweep at the target.

The trigger on the downstream camera is delayed from the upstream camera trigger by a time interval equal to the electron time-of-flight between the two cameras. Thus the radius of a single slice is measured at two axial locations, 23 m and 86 m, on a single shot. Video images were scanned along the horizontal and vertical axes. A Gaussian curve is fit to the data. The Gaussian radius of the horizontal curve (R_x) and the vertical curve (R_y) is found, and slice radius is defined as $(R_x \cdot R_y)^{1/2}$.

Radius measurement locations were chosen at propagation distances greater than several betatron wavelengths to ensure that phase-mix damping had already transpired.

III. RADIUS GROWTH (HEAD-TO-TAIL)

Due to ion hose growth and subsequent phase-mix damping, later beam slices attain larger radii than earlier beam slices. This is defined as head-to-tail radius growth. It is found by examination of slice radius as a function of slice time, measured at a fixed axial location. Using the results from multiple shots, measurements of head-to-tail radius growth are given in Fig. 2. The displayed slice radius is the mean radius taken over several shots, and the uncertainty is the standard deviation about the mean. Head-to-tail radius growth is given for both 23 m and 86 m locations. The rate of radius growth at 23 m was 1 cm/100 ns.

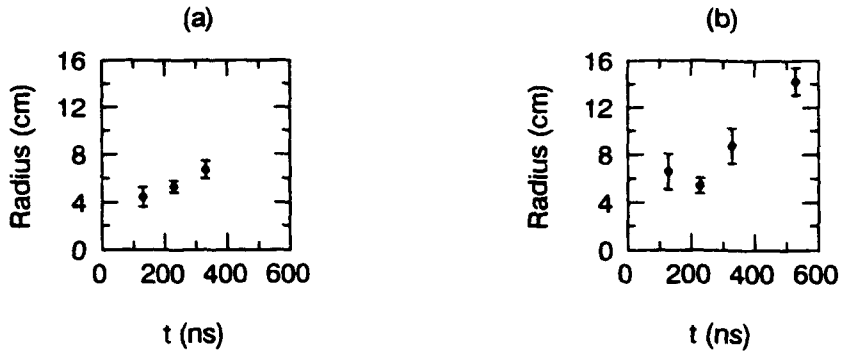

Figure 2. Head-to-tail radius growth measured at (a) 23 m and (b) 86 m. The data points represent the average radius of a slice measured on multiple shots. Error bars represent the standard deviation. Slice time [and number of measurements] represented by each data point is:
(a) 130 ns [29], 230 ns [4], 330 ns [22];
(b) 130 ns [18], 230 ns [2], 330 ns [16], 530 ns [4].

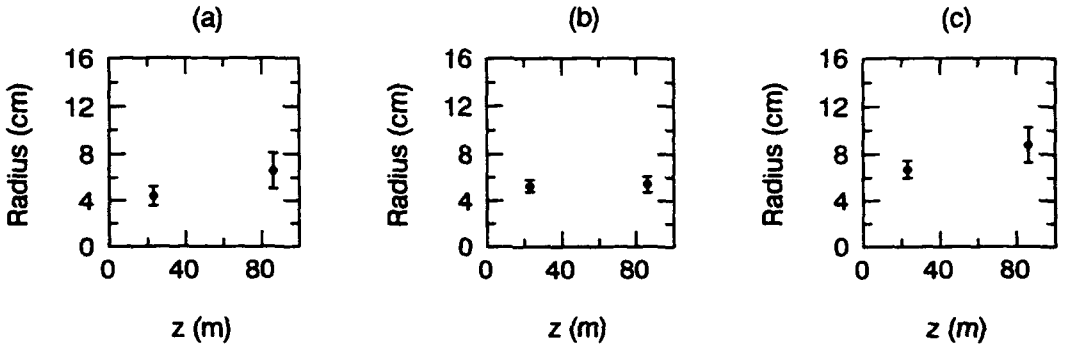

Figure 3. Slice radius growth: (a) 130 ns slice, (b) 230 ns slice, and (c) 330 ns slice. The data points represent the average radius of a slice measured on multiple shots. Error bars represent the standard deviation. Slice propagation distance [and number of measurements] represented by each data point is:
(a) 23 m [29], 86 m [18]; (b) 23 m [4], 86 m [2]; (c) 23 m [22], 86 m [16].

IV. RADIUS GROWTH (SLICE)

Slice radius growth is defined as an increase in the radius of a single slice as it propagates axially, after phase-mix damping has occurred. (It is important to note this definition excludes slice radius growth due to phase-mix damping, which occurs at small propagation distances). Slice radius growth is found by examination of slice radius (of a single slice) as a function of propagation distance. The recently completed experiments represent the first measurement of slice radius growth on a single shot. Single shot observation is the most accurate method of radius growth determination since it obviously eliminates shot-to-shot dependence. Accuracy is important since the measured rate of radius growth, dr/dz, is used to extrapolate radius at significantly large z. Using the single shot method, slices at 230 ns have exhibited no radius growth. This shows that once phase-mix damping and the associated head-to-tail radius growth has transpired, IFR propagation can proceed with no further degradation in radius. A multiple shot analysis of slice radius growth is given in Fig. 3. The displayed radius is the mean radius taken over several shots, and the

uncertainty is the standard deviation about the mean. The multiple shot analysis is convenient for comparison of slice radius growth for different slices. There is moderate radius growth for the 130 ns and 330 ns slices. The channel radius is 2.5 cm, the initial beam radius is 1-2 cm, so there is a mismatch at beam injection which results in sausage oscillations. This might account for the slice radius growth of these two slices. There is little or no growth (within the standard deviation) for the 230 ns slice.

V. DISPLACEMENT MEASUREMENTS

Beam displacement measurements, used for determination of ion hose growth rate, were always previously taken only in the first 6 m of propagation distance. These measurements used B-dot loops. A propagation distance of several betatron wavelengths is required for almost complete damping of oscillations as predicted by the process of phase-mix damping. Since the betatron wavelength is of the order of 4 m, only partial damping of transverse oscillations was observed in the previous measurements. In order to verify phase-mix damping (a dramatic reduction in slice oscillation with a corresponding increase in slice radius), additional beam slice displacement measurements have been made which include measurements at larger propagation distances.

The displacement measurements at large propagation distances were made using the same framing cameras as used for the radius measurements. The centroid coordinates for a beam slice were determined by locating the centroid of the Gaussian beam distribution as measured by the framing cameras. Slice displacement is then determined using the centroid coordinates.

The displacement of a slice was measured at two camera locations and ten B-dot locations on a single shot. A sample of the results are shown in Fig. 4, which includes x and y slice displacement of the 330 ns slice at: 2 m , 5 m (both measured with B-dots), and 23 m (measured with a framing camera). Each plot in Fig. 4 contains 24 shots. The origin represents the center of the propagation tank. A quantitative analysis of slice displacement is given in Table I. For each axial location, z, the average displacement from center ($d = [x^2+y^2]^{1/2}$) and corresponding standard deviation are given. Data for z = 86 m, not shown in Fig. 4 since only 7 shots are represented, is also included in the table.

Table I. Slice displacement.

z(m)	d(cm)
2	2.5 +/- 1.3
5	2.0 +/- 0.9
23	0.6 +/- 0.5
86	0.4 +/- 0.3

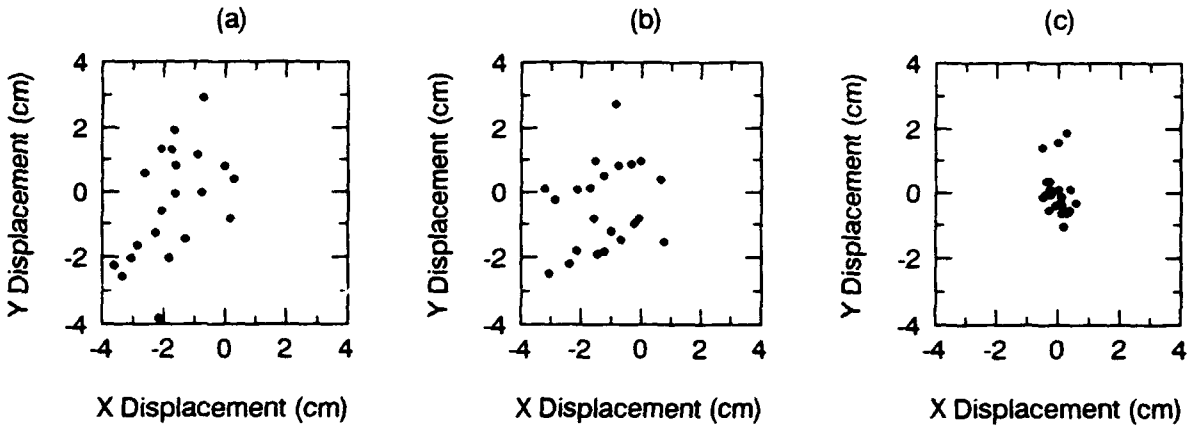

Figure 4. *Slice displacement of the 330 ns slice measured at three axial locations:* (a) 2 m, (b) 5 m, (c) 23 m. Each plot includes 24 shots.

Comparing the average displacement at 2 m and 5 m, a small reduction in displacement due to phase-mix damping is noted. However, the slice displacements measured at 23 m indicates that more pronounced damping has occurred. This data represents the most conclusive evidence of phase-mix damping.

The absence of appreciable slice displacement over multiple shots at both 23 m and 86 m, indicates that there are no hose oscillations at these locations. Therefore the ion hose instability is not re-excited after its initial occurrence near the injection point. This is a necessary requirement for long distance propagation.

VI. DOUBLE LASER PULSE

The preceding radius measurements addressed slices which occur in the first few hundred nanoseconds of the beam (in the region of linear ion hose growth). Here, transverse displacements are relatively small, and the final radius after phase-mix damping is sufficiently small so that ion focusing is still effective. Later slices, which were not previously discussed, attain large transverse displacements so that ion focused propagation is greatly diminished. Therefore the ion hose instability imposes a limit on the length of pulse which can propagate. This limit has been surpassed by using two laser pulses which are staggered in time. [3] The beam propagates in the channel created by the first pulse and experiences growing oscillations which are imprinted onto the channel. Subsequently, channel oscillations are so large as to disrupt beam propagation. A second pulse produces a second channel whose ions are on center, and the above described process is repeated. Therefore the length of propagated beam is increased, and the ion hose limit on pulse length is surpassed. Experimental results of the double laser pulse are shown in Fig. 5 where maximum slice displacement (cm) versus slice time (ns) is shown. For comparison 5(a) shows a shot with a single laser pulse, and 5(b) shows a shot with a double laser pulse. The delay between the two laser pulses was 290 ns. The reduction in slice displacement due to the second laser pulse is dramatic.

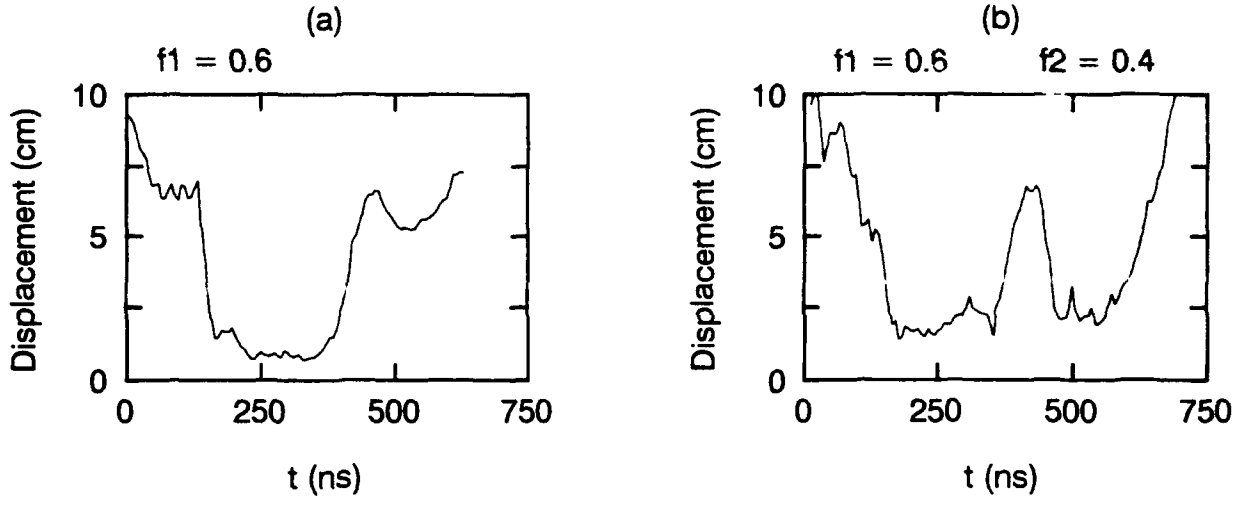

Figure 5. Double laser pulse results. For comparison (a) shows a shot with a single laser pulse (f_1), and (b) shows a shot with a double laser pulse (f_1,f_2). In (a) the laser pulse is fired at 130 ns. In (b) the first laser pulse is fired at 130 ns, and the second is fired at 440 ns.

VII. CONCLUSION

The measurement of zero slice radius growth for the 230 ns slice is favorable results for establishing the feasibility of efficient ion_e distance propagation. Recent experiments with better beam/channel radius matching (not included in this report), gave no slice radius growth over a more extended beam length.

The measurement of significant reduction in slice displacement at large propagation distances substantiates the theory of phase-mix damping for IFR propagation. The absence of oscillations in multiple shots, at long propagation distances, proves the ion hose instability is confined to the region near the accelerator.

Using two laser pulses, the length of propagated beam was increased by placing a second channel on center, after the first channel had deteriorated. Multiple laser pulses may offer the potential for significant increase in the length of propagated beam.

VIII. REFERENCES

[1] R. J. Lipinski, J. R. Smith, I. R. Shokair, K. W. Struve, P. Werner, D. J. Armistead, P. D. Kiekel, I. Molina, and S. Hogeland, "Measurement of the electron-ion-hose instability growth rate," Phys. Fluids B 2, 2764 (1990).

[2] J. R. Smith, I. R. Shokair, K. W. Struve, E. Schamiloglu, P. W. Werner, and R. J. Lipinski, "Transverse oscillations of a long-pulse electron beam on a laser-formed channel", IEEE Trans Plasma Science 19, 850 (1991).

[3] Proposed by R. B. Miller.

Contributed Beam Diagnostic Papers

FAST H-ALPHA LINE BROADENING DURING THE 100 ns REB INJECTION INTO A PLASMA

K.Koláček, M.Řípa, J.Ullschmied, K.Jungwirth, P.Šunka

Institute of Plasma Physics, Czechoslovak Academy of Sciences,
Za Slovankou 3, P.O.Box 17, 182 11 Prague 8, Czechoslovakia

Abstract:
Profiles of the Hα line emitted from the hot electron plasma Te»Ti during the 100 ns REB injection resemble the Gaussian ones from neutrals with a temperature Tn(t)≈Ti(t)≈Te(t) rapidly growing up to 30 eV. Combination of Doppler and Stark effects of the intense ion sound waves - remnants of the burned out Langmuir cavitons - is suggested for plausible explanation of this fast Hα line broadening. Reliability of the basic ideas of strong Langmuir turbulence for description of REB-plasma systems is thus indirectly supported, too.

1. INTRODUCTION

Measurements of evolution of Hα line profiles during the REB injection [1] into a plasma were initially motivated by the challenge to try to determine directly the electric field intensities of the HF plasma waves in the strongly turbulent regime. Soon, however, our attention was attracted to the unexpected fact that from the very beginning of the REB-plasma interaction a fast Hα line broadening seemed to suggest that ions are heated as efficiently as the electron component. Other diagnostics, on the other hand, indicated that we were dealing with an non-isothermic hot electron plasma at least during the first hundred nanoseconds of the beam injection [2]. In what follows we try to solve this puzzle.

2. EXPERIMENTAL RESULTS

The experimental results were obtained on the REBEX machine described elsewhere [3]. The injected beam was of a modest energy (≈ 350 keV) but of a relatively high current (50 kA). The

time-resolved measurements of the emission Hα line profile were performed by a 6-channel spectroscopic apparatus described in [4], with the linear dispersion of 0.87 Å/channel and the time resolution of 4 ns. Profile in each step was confronted with the closest Gaussian curve (see in more detail [4]). It turned out that prior the REB injection the Hα line profile has enhanced wings if compared with a Gaussian curve just as it was expected. Since the beginning of the REB injection, simultaneously with the rise of line intensity, the line profile becomes broader and its profile converges to the Gaussian one.

The changes of the line profiles at later times after the beam injection can be well explained and simulated on the base of a analytical model of macroscopic motions of an overheated plasma column [5].

Contrary, the rapid line broadening during the beam injection calls for a more detailed analysis.

3. SEMI-EMPIRICAL ASSUMPTIONS AND ESTIMATES

Let us assume in agreement with the basic ideas of strong Langmuir turbulence that roughly 1/10 of the total energy transferred from the beam to the excited plasmons gradually accumulates in the ion sound waves with $k^2R_D^2 \approx 1/10$, emitted by the burned-out collapsing Langmuir cavitons. The average kinetic energy per ion due to oscillations is then of the order of 10 eV and the typical ion sound electric field intensity is $E_i \approx 30$ kV/cm in a system with the electron body heated to the temperature of $T_e \approx 30$ eV and with a hot electron tail carrying roughly the same amount of the energy from the plasmons.

In what follows, we demonstrate that under the above mentioned conditions the combination of the Stark and the Doppler broadening can really result in the observed Gaussian-like Hα line profiles and fake thus the "fanthom" temperature $T_n \approx T_e \approx 30$ eV of the neutral component.

4. NUMERICAL SIMULATIONS

There are two limiting cases of the Stark effect. The LF limit takes place for the Hα line if it is [6]

$$\Omega\ [s^{-1}] \ll \Delta\omega_o = 7.2 * 10^{10} * E\ [kV/cm]$$

which is satisfied in our case with $\Omega \approx kR_D\,\omega_{pi}$ the characteristic frequency of ion sound turbulence, $\Delta\omega_0$ the detuning of the typical Stark component from the line center and $E = E_i$. Note that for $E > 30$ keV/cm and $n = 5*10^{14}$ cm^{-3} this LF limit applies even for the HF Langmuir waves. Such waves, however, would be localized in an extremely small portion of the whole volume and, therefore, their contribution is certainly negligible in our measurements.

On the other hand, the plasmons spread over a significant part of the volume have intensities at least by an order of magnitude lower. Their contribution (the HF Stark effect) is masked by the stronger phenomena under our conditions and they, too, cannot be detected by our present means. The same is true for the HF Stark broadening caused by colliding electrons (impact approximation) as confirmed also by the following numerical results.

The experimentally obtained instrument function I may be readily approximated by a Gaussian curve

$$I = \frac{1}{0.3334 * \sqrt{\pi}} * \exp\left(- \frac{\Delta\lambda^2}{0.3334^2} \right)$$

where $\Delta\lambda$ is the detuning. The Doppler broadening yields also a Gaussian curve

$$D = \frac{1}{\Delta\lambda_D * \sqrt{\pi}} * \exp\left(- \frac{\Delta\lambda^2}{\Delta\lambda_D^2} \right)$$

where $\Delta\lambda_D = (v_{Tn}/c)*\lambda_0 = 0.3028\ \sqrt{T_n[eV]}$ with thermal velocity of neutrals v_{Tn}, velocity of the light c, wave-length of the Hα line $\lambda_0 = 6563$ Å, temperature of neutral particles T_n, while the HF Stark broadening caused by colliding electrons is a dispersion (Lorentzian) curve

$$S_i = \frac{1}{\pi} * \frac{\gamma/2}{(\Delta\lambda)^2 + (\gamma/2)^2},$$

where [7]

$$\gamma = \frac{32}{3} * n_e * \left(\frac{\pi m_e}{8 k T_e} \right)^{1/2} * \frac{\hbar^2}{m_e^2} * I(n,n') * \left(0.215 + \ln \frac{R_D}{\rho_0} \right) =$$

$$= 5.2088*10^{-16} * \frac{n_e[cm^{-3}]}{(T_e[eV])^{1/2}} * \left(21.247 + \ln \frac{T_e[eV]}{(n_e[cm^{-3}])^{1/2}} \right) \quad [A]$$

(where k denotes the Boltzmann constant, h - the Planck constant, I - factor depending on principal quantum numbers n and n' (for Hα n = 3, n' = 2 and I(n,n') ≈ 27), R_D - Debye shielding radius, and ρ_0 - radius of strong collisions). The convolution of these three curves yields a well known Voigt function (see Fig.1).

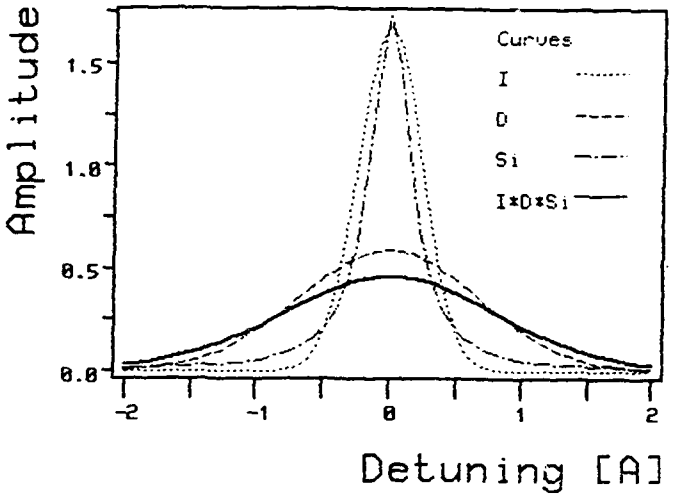

Fig.1

I - instrument curve
(FWHM 0.555 Å)

D - Doppler broadening
T_n=10 eV (FWHM 1,594 Å)

S_i - HF Stark effect
n=5E14 cm^{-3}, T_e=30 eV (FWHM 0,36 Å)

I*D*S_i - convolution
(integrals of all the profiles normalized to 1)

The LF Stark effect leads to the line splitting into several equally spaced components (spacing in ω - scale is $\Delta\omega_s = g * E$). Supposing that E has the distribution F(E = (Δω/(|s|g),ϑ,φ), where s is the serial number of the component, ϑ and φ are the angles in spherical coordinate system, the curve is [6]

$$S_t(\omega) = S^0(\omega) + \int_0^{\pi} \sin\vartheta d\vartheta \int_0^{2\pi} d\varphi \sum_{s\neq 0} \frac{\beta_s(\vartheta,\varphi)}{2|s|g} * \left(\frac{\Delta\omega}{|s|g} \right)^2 * F\left(E = \frac{\Delta\omega}{|s|g}, \vartheta, \varphi \right)$$

where β_s are the relative intensities of the components and g is the constant of Stark effect. Supposing further that the electric field distribution is isotropic and Maxwellian

$$F(E) = \left(\frac{3}{2\ \pi\ E_0^2} \right)^{3/2} * \exp\left(- \frac{3\ E^2}{2\ E_0^2} \right) ,$$

where E_0 is the mean square electric field intensity, we obtain the curve given in the Fig.2. Supposing further that also this

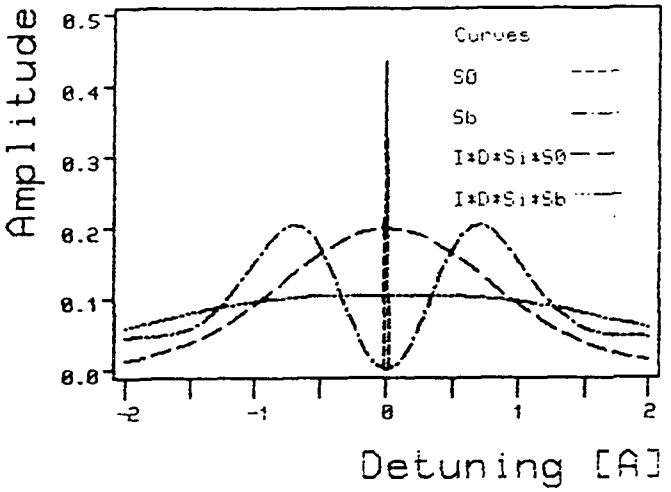

Fig.2

S0 LF Stark effect - zero (central) component (δ function)

Sb LF Stark effect - non zero components

E_0=30 kV/cm (FWHM 2,409 Å)

and their broadening by the factors from Fig.1

mechanism is independent of all those mentioned above, we can perform the convolution of this curve with the Voigt function arriving in such a way to the resulting curve given in the Fig.3. It is obvious that if the maximum of the curve S_t falls into the registering channels adjacent to the central one (this is the case at ≈30 kV/cm), one may observe a Gaussian-like curve.

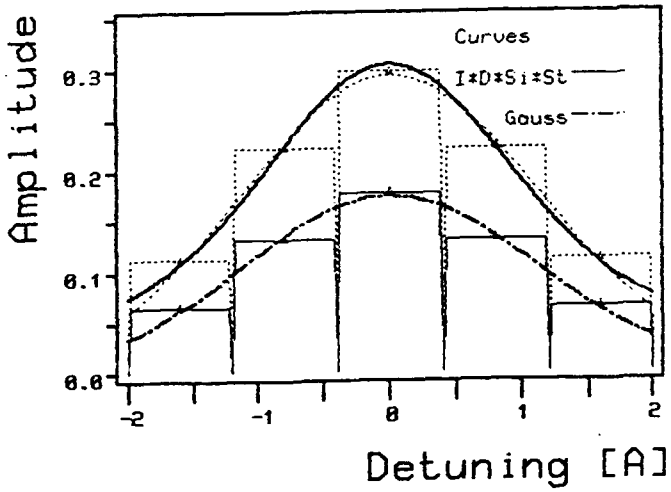

Fig.3

$I*D*S_i*S_t$ convolution - (broadening by factors of Figs.1,2), its integrals in measuring channels (dotted l.) its integrals at taking circular shape of the lightguides into account (full l.), approximation by Gauss curve (dot-and-dash l.)

5. CONCLUSION

We have shown that the fast broadening of the Gaussian-like Hα line profiles observed during the beam injection in the REBEX beam-plasma experiment can be consistently explained by the LF Stark broadening in the electric fields of the LF ion sound turbulence (burned-out collapsing Langmuir cavitons) combined with the Doppler broadening due to the motion of ions in the sound waves. Thus, the apparent paradox of "matching" of the electron and ion temperatures in times much shorter than those of the electron-ion relaxation processes seems to be resolved.

This work was partly supported by the Grant Agency of CSAS under Grant No.14303.

References:

[1] KOLÁČEK K. et al., Proc.8th Int.Conf. on High-Power Beams, Novosibirsk 1990
[2] PIFFL V., RAUŠ J., ŠUNKA P.,Proc.16th ICPIG,Düsseldorf, 353 (1983)
[3] ŠUNKA P. et al., Proc.10th Eur.Fus.Conf.Budapest, 668 (1985)
[4] ŘÍPA M. et al., IPP Prague, IPP CZ-293/II,pp 79 and 87 (1989)
[5] ULLSCHMIED J. et al., to be published
[6] BEREZIN A.B., LYUBLIN B.V., YAKOVLEV D.G., NIIEFA P-K-0609, Leningrad 1983
[7] VAYNSHTEIN L.A., SOBELMAN I.I., YUKOV E.A., Vozbuzhdenie atomov i ushirenie spektr.liniy, Nauka, Moskva, 1979

THE BEAM CURRENT DIAGNOSING IN LARGE AREA DIODES

Debao Huang, Weiyi Ma, Xiaojun Wang, Naigong Zeng,
Yusheng Shan, Youtian Wang, Dong Zhang
(Institute of Atomic Energy,
P. O. Box275-7, Beijing 102413, China)

Abstract The structures, performance & experimental results for three current monitors for measuring relativistic e-beam currents in large area diode at CIAE are described in the paper.

Key Words rectangular Rogowski coil, foil shunt

1 Introduction

The Faraday cup was used to measure the relativistic e-beam currents in large area diodes at LANL[1]. It is inconvenient in pumped laser experiments. The difficulty mentioned above could be avoided with a Rogowski coil in rectangular frame.

2 The rectangular Rogowski coil

Two rectangular Rogowski coils (Fig. 1) with frame larger than the emitting region of the cathode ($12\times75cm^2$) slightly were placed behind anode foil of diode and in front of main foil to laser chamber respectively to monitor e-beam currents conveniently without interrupting them. The coil and frame were installed in the groove on the shield body. The parameters are as follows:

1) the shield body (brass)

the central line in the groove $22.7\times83.2cm^2$

the cross section of the groove $1.8\times1.8cm^2$

2) the coil and frame (plexiglass)

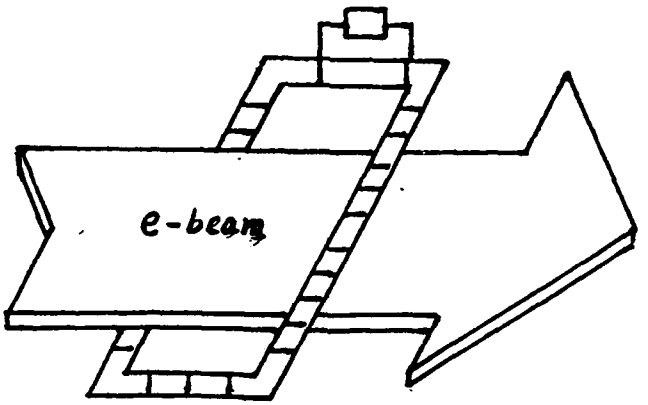

Fig. 1 Schematic of rectangular Rogowski coil

Table 1 Structure parameters of coils & frames

No.	a (cm)	d (cm)	N (turns)	P (cm/turns)
I	0.40	0.100	104	2.0
II	0.60	0.068	100	2.1

where, a: the cross sectional radius of plexiglass rod,
d: wire diameter,
N: total number of turns on the coil,
P: pitch of the windings.

The output signal resistor is 0.52Ω by the stainless steel foil in 8μm thick. The performance parameters were listed in table 2.

Table 2 Performance parameters of rectangular R.C.

No.	L (μHi)	R_L (Ω)	τ (μs)	Kc×10^{-3}(v/A)	Ke×10^{-3}(v/A)
I	1.66	1.02	1.08	1.89	1.89
II	2.65	1.49	1.32	2.29	2.36

note, Kc: the calculated sensibilities,

Ke: the measured sensibilities.

In table 2, Kc, Ke were obtained for e-beam through central point of frame plane as a line-current. For examining relations of the sensibility to e-beam current density distribution, the calculated sensibilities of rectangular R.C. for various beam cross sections were listed in table 3.

Table 3 The sensibilites for beam cross sections

No.	K_1/Kc	K_2/Kc	K_3/Kc
I	0.999969	0.99915	0.9964

note, K_1, K_2& K_3: the sensibilities of rectangular R.C. No.I for beam cross sections, which equal 0.1×0.1, 0.5×0.5, 0.9×0.9 of the frame area respectively.

The results in table 3 shown that the senisibility for rectangular R.C. with sufficient turns relates to e-beam current desity distrbution weakly.

3 The foil shunt

Primarily, the shunt consisted of four hundreds carbon film resistors in parallel with a resultant resistance of 5 mΩ. In experiment, however, the shunt was damaged once and agin. Then we have developed a new shunt by stainless steel foil in 15μm thick instead. The foil shunt was installed in end of Blumlein line for measuring whole diode current (Fig. 2). The foil strip is 3.7 cm wide, 430 cm in periphery with a resultant resistance of 0.76 mΩ. The foil was contacted with outer cylinder of Blumlein line by two copper strips reliably. The foil shunt has been operated with better performace for more two years.

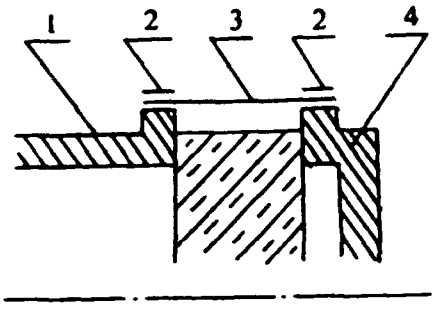

1. outer Blumlein line
2. copper strip
3. foil in stainless steel
4. anode

Fig. 2. Schematic of foil shunt

4 The calibration

The calibration for the monitors was done on pulsed accelerator at CIAE as shown in Fig. 3 as the diode was closed. A circular R.C. [2] & a Faraday cup were used in calibration. The experiment results shown that wareforms from monitors coincide each other (Fig. 4), and sensibilities in experiment agree well with calculated ones as shown in table 2.

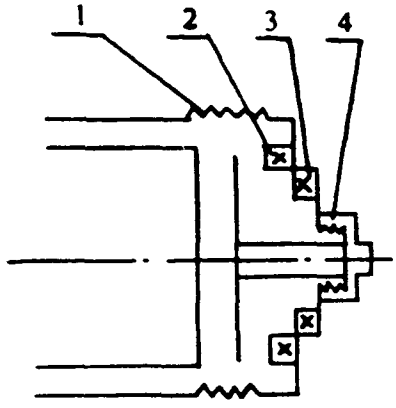

1.foil shunt
2.rectangular R. C.
3.round R. C.
4.Faraday cup

Fig.3 Calibration arrangement of monitors

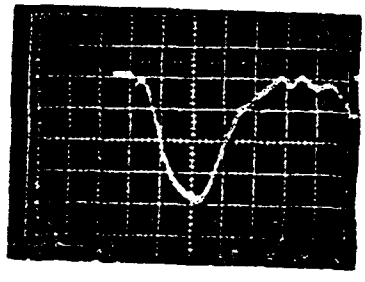

Rogowski coil (rectangular)
(a)

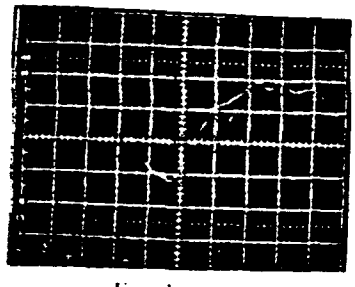

Faraday cup
(b)

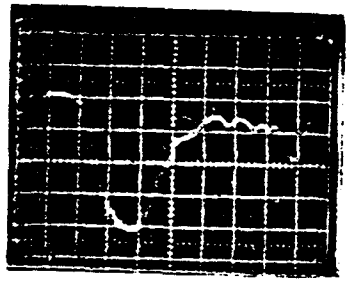

Shunt
(c)

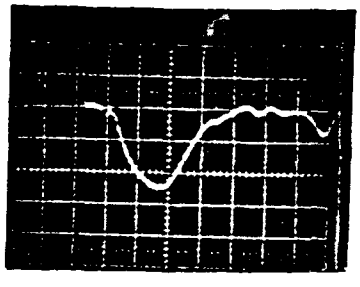

Rogowski coil (round)
(d)

50ns/div

Fig.4 Waveforms of monitors

References

[1] L. A. Rosocha & K. B. Riepe, Fusion Tech., 11, 576 (1987. 5)

[2] Debao Huang etc., China Atomic Energy Science & Tech., 22(4), 444 (1988. 7)

THE STRENGTH CALCULATION FOR A FOIL COAXIAL SHUNT

Debao Huang
(Institute of Atomic Energy,
P.O. Box275-7, Beijing 102413, China)

Abstract The strength for a foil coaxial shunt was analysed and a strength formula for outer cylinder was derived.

Key Words coaxial shunt, maximum allowable current

1 Introduction

When a heavy surge current passes through the coaxial shunt, a huge pulse due to magnetic force will be applied to the inner & outer cylinders of the shunt. The strength analyses about it was done by J.H. park firstly [1] and a strength formula for inner cylinder of the shunt was given. At present, however, the metal foil as resistive element is usually used as outer cylinder of shunt. So park's formula can't be applied to present shunts.

Based on the dynamics. We derived a new formula for the maximum allowable current on the outer cylinder of shunt in paper. It is good agreement with present shunts.

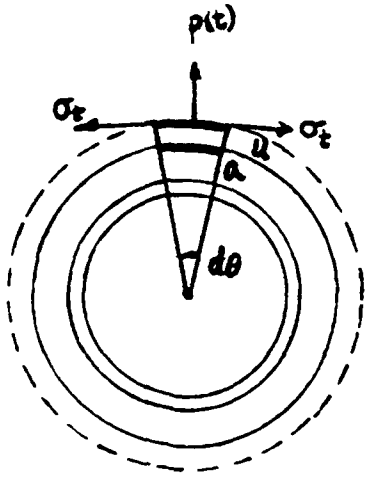

Fig. 1 Expansion schematic of other cylinder of shunt

2 The derivation for strength formulae

Referring to Fig. 1, the pressure on outer cylinder is as follows:

$$P(t) = I^2(t) / (2\pi a^2) \qquad (\text{for } a \approx b) \tag{1}$$

on element volume of outer cylinder $dv = rL\Delta d\theta$, the dynamic equation can be written as following:

$$\ddot{u}(t) + \frac{\lambda}{\rho\Delta}\dot{u}(t) + \frac{E}{(1-m/2)\rho a^2}u(t) = \frac{P(t)}{\rho\Delta} \tag{2}$$

where, U(t), a, Δ: the radial displacement, the average radius, wall thickness of outer cylinder respectirely (cm).

ρ, E, m: the density (g/cm^3), the elasitic modulus ($\times 10^5 N/cm^2$) & poisso's ratio for foil material.

λ: damping coefficient ($g/s \cdot cm^2$)

1) During current action ($0 < t < T$)

putting

$$2\beta = \frac{\lambda}{\rho\Delta}, \quad \nu^2 = \frac{E}{(1-m/2)\rho a^2}, \quad b(t) = \frac{(1-m/2)a^2}{E\Delta}P(t), \quad \omega^2 = \nu^2 - \beta^2$$

then equation (2) can be simplified:

$$\begin{cases} \ddot{u}_1(t) + 2\beta\dot{u}_1(t) + \nu^2 u_1(t) = \nu^2 b(t) \\ \dot{u}_1(0) = 0 \\ u_1(0) = 0 \end{cases} \tag{3}$$

The solution for equation (3) is the following:

$$u_1(t) = \frac{\nu^2}{\omega}\left[\left(\int_0^t b(\theta)e^{\beta\theta}\cos\omega\theta\, d\theta\right)\sin\omega t - \left(\int_0^t b(\theta)e^{\beta\theta}\sin\omega\theta\, d\theta\right)\cos\omega t\right]e^{-\beta t} \tag{4}$$

2) After current action ($t > T$)

the equation (2) can be written as

$$\begin{cases} \ddot{u}_2(t-T) + 2\beta \dot{u}_2(t) + \gamma^2 u_2(t) = 0 \\ u_2(T) = 0 \\ \dot{u}_2(T) = \dot{u}_1(T) \end{cases} \tag{5}$$

The solution for equation (5) is as follows:

$$u_2(t-T) = \frac{\dot{u}_1(T)}{\omega} e^{-\beta(t-T)} \sin\omega(t-T) \tag{6}$$

If the current through shunt is a square function as following:

$$I(t) = I_0[1(t) - 1(t-T)]$$

Then expression (4) can be simplified further:

$$u_1(t) = b_0\left[1 - \left(\frac{\beta}{\omega}\sin\omega t + \cos\omega t\right)e^{-\beta t}\right] \tag{7}$$

The formula (7) shows that $U_1(t)$ is a vibrated waveform with a damped coefficient β as shown in Fig. 2.

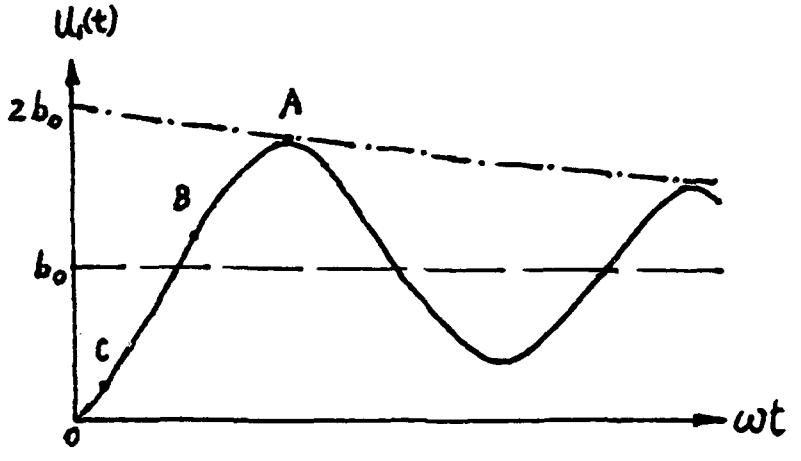

Fig. 2 Relation $u_1(t)$ to t

Putting $[\sigma]$ the proportional limit in foil material stress, and $u_1(t)$ is within limit of elastic region for foil material, the following condition should be satisfied:

$$\frac{E}{(1-m/2)}\cdot\frac{u_{max}}{a}\leq[\sigma] \qquad (8)$$

3 The discussion

1) When $T\geqslant\omega/\pi$, the maximum displacement searched at point A (Fig. 2). The maximum allowable current through shunt is given by combining formulae (7) with (8):

$$I_0\leq 10\sqrt{\pi a\Delta[\sigma]}\quad (A) \qquad (9)$$

2) When $T<\omega/\pi$ (at point B in Fig. 2),

Then

$$u_{max}=u_1(T)+u_2(\tau) \qquad (10)$$

[note, τ is obtained from $\dot{u}_2(\tau)=0$]

The maximum allowable current through shunt foil is the following by combining formulae (8) with (10):

$$I_0\leq 10\sqrt{2\pi a\Delta[\sigma]/(1-\cos\omega T+\sin\omega T)}\quad (A) \qquad (11)$$

3) When $T<<\omega/\pi$, the fromula (11) can be simplified as:

$$I_0\leq 10\sqrt{2\pi a\Delta[\sigma]/\omega T}\quad (A) \qquad (12)$$

The expressions (9), (11), (12) are the new strength formulae on foil coaxial shunt through currents. According to them, there are several examples listed in table 1.

Table 1 Data for several shunts

ref.	Δ (cm)	a (cm)	T (ns)	I_0 (kA)	I_e (kA)	I_p (kA)
[2]	0.0100	7.5	$<10^4$	320	200	6.7
[3]	0.0025	4.35	$\sim$200	737	280	1.1
[4]	0.0004	12.50	$\sim$200	850	100	0.04

The resistance elements of shunts in table 1 were stainless steel foil:

$\rho = 7.8 g/cm^3$, $E = 2\times10^6 kg/cm^2$, $[\sigma] = 2\times10^3 kg/cm^2$, $m = 0.25$.

and whrer,

I_0: maximum allowable currents on shunt according to formulae (9)-(12).

I_e: maximum peak currents measured on shunt in experiments.

I_p: maximum allowable currents on shunt from park's formula.

4 The concludion

In table 1, I_p are more less than I_e, which means that park's formula can't be applied here. The calculated results from formulae (9)-(12) are good agreement with experiments, and show that maximum allowable currents on shunt depend on duration of current pulse yet.

References

[1] Park, J. H., J. Res. Nat. Bur. stand., 39, 191 (1947)

[2] Thornton, E., J. Sci. Instrum., 3, 862 (1970)

[3] Pellinen, D. G., R.ev. Sci. Instrum., 41, 1347 (1970)

[4] Debao Huang, Chinese Atomic Energy Sci. & Tech., 23(2), 16(1989).

An Offset Model Radiation Calorimeter

Fu Shu-zhen, Chen Yu-Tao and Hu Ke-Song
Institute of Applied Electronics, China Academy
of Engineering Physics, P. O. Box 523, No. 65
Chendu, Sichuan, P. R. China

ABSTRACT

An offset model calorimeter specially designed for FEL experiments on EPA-74 is presented. The calorimeter is substantially capable of deducting the temperature drift because it consists of two hollow thin wall cone graphite absorbers and two thermistors. The device is capable of measuring the microwave radiated energy, microwave waveform and radiated frequency simultaneously. We have measured a 20 mJ of microwave radiated energy, 1MW of radiated power and 33 GHz of radiated frequency in FEL experiments on EPA-74 without a guide magnetic field by using the calorimeter.

Introduction

We have studied the generation of FEL by intense relativistic electron beams generated from EPA-74 pulseline accelerator. About 1MW of microwave radiation 50 nsec duration in a single pulse has been observed. The measurements of microwave radiation energy in the kind of experiments are usually preformed by using a calorimeter.[1.2.3] We present here a specially designed calorimeter capable of measuring the total radiated microwave energy in a single pulse and capable of monitoring the microwave waveform and radiation frequency simultaneously if the device is used in conjunction with a dispersion line system. In order to reduce the temperature drifts the device consists of two hollow graphite cone absorbers and two thermistors. In addition, the device is capable of being operating at room temperature and atmosphere with $0.30^{o}C/J$ of sensitivity.

Device

The offset model microwave calorimeter consists of two hollow thin wall graphite cone absorbers and two thermistors. The absorbers temperature rise due to microwave energy deposition is determined by

$$E = 4.18\ k\int_{T_1}^{T_2} C_p(T)\ m\ dT \qquad (1)$$

if temperature rise ($\Delta T = T_2 - T_1$) is small enough, the formula (1) can be rewritten by

$$E = 4.18\ k\ m\ \bar{C}_p\ T \qquad (2)$$

Where $\bar{C}_p$ is the average specific heat of graphite, m is mass of the absorber, and k is a coefficient. If the temperature rise can be measured by using a thermistors bridge system, the microwave radiated energy E is obtained by the formula (2).

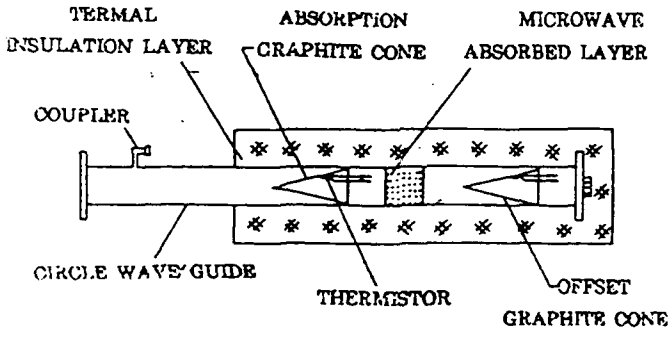

Fig.1. Schematic of the offset model microwave calorimeter

Figure 1 is the schematic of the calorimeter. The parameters of the absorber cone are almost the same as that of the offset cone . The mass of each cone is 2g. The absorbers are made of a hollow thin wall (0.5mm) graphite cone of height 6.5 cm with a base of 1.6 cm diameter in order for the calorimeter to match at the end of the stainless steel circular waveguide tube which is used in FEL experiments on EPA-74.

The absorber cone is used to absorb the microwave radiated energy. The microwave absorbed layer between the absorber cone and offset cone is used to insulate each

other in order to protect offset absorber cone from microwave radiations. A pair of thermistors which are selected carefully and installed at inside of the both graphite cone are used to determine the temperature rise of the both cone respectively. The set-up is put into a thermal insulating material inside a matel envelope in order to protect it against environmental temperature fluctuations and electromagnetic radiation interferences.

Figure 2 is the diagram of the calorimeter electronic circuit. Two thermistors whose parameters are almost the same is placed in the symmetrical arms of a DC Weastone bridge. Initially, Weaststone bridge is in equilibrium regime because both the graphite cones are in the same environment. The absorber cone temperature rise due to energy deposition results in resistance decreasing of the thermistor. The bridge becomes uneqilibrium and produces an output signal. For extremely small signal a low drift DC voltage amplifier is necessary to enhance the output signal which is displayed directly on a x-y chart recorder.

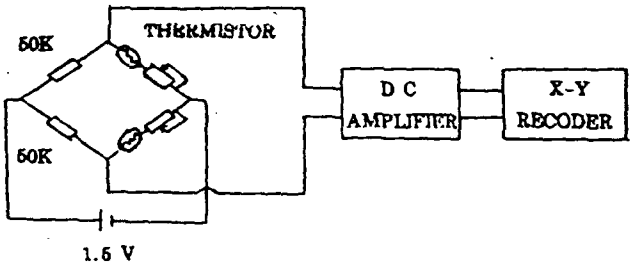

Fig. 2. The calorimater's electronic circuit

The calorimeter is also capable of measuring the microwave radiation frequency if the coupler which is installed at the circular waveguide wall is connected with dispersion line system. For electromagnetic wave, the propagation time in a waveguide and its frequency are given by

$$f = f_c \,/\, [\, 1 - (L/ct)^2 \,]^{1/2} \qquad (3)$$

where, f_c is the cut-off frequency of the waveguide, t is the propagation time of microwave signal in the waveguide, c is the light speed and L is the length of the waveguide.

The basic configuration for these measurements is shown in Fgi.5. The signal output from the coupler divided into two channels. One passes through the second arm of the directional coupler (20 dB) as a reference signal. The other passes through the main arm of the directional couper and propagates through about tens of meters dispersion line as a delay signal. Both signals are detected by a crystal detector and displayed on a fast oscilloscope. After measuring the time interval between the two signals, the radiated frequency of microwave is determined by formula (3).

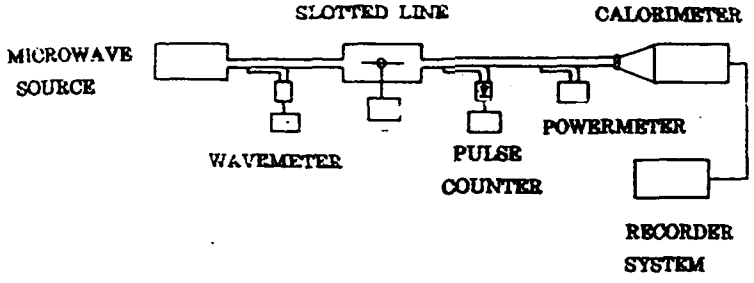

Fig. 3. Diagram of configuration for calibration measurements

Calibration of energy

Fig.3 is the diagram of configuration for calibration measurements. The K_a band microwave source is connected to calorimeter by the WR/8 waveguide and the matching unit. The wavemeter, power meter and pulse counter in conjuction with the directional coupler are used to measure the wavelength, radiated power and pulse numbers of microwave source respectively. The transmission coefficient of energy is determined by the waveguide slotted line. We have observed very flat response of frequency over 26-40 GHz. The formula for energy calibration is given by

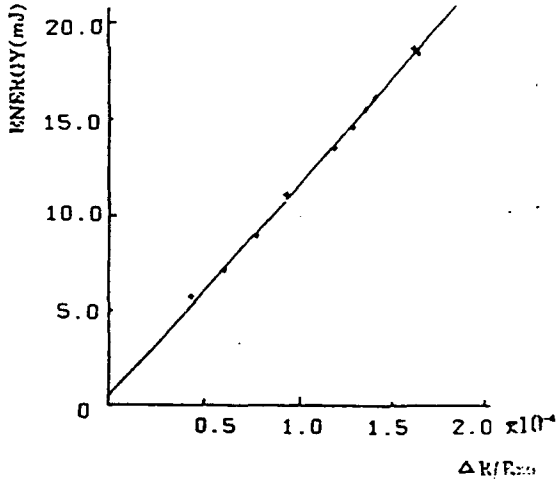

Fig. 4. Calibration of energy E versus $\Delta R/Rxo$

$$E = 0.707 + 1.10 * 10^5 \Delta R/Rxo \quad (mJ) \qquad (4)$$

where Rxo is the resistance of the thermistor before microwave radiation is deposited in the calorimeter, ΔR is the thermistor resistance change due to energy deposition .The experimental data in Fig.4. demonstrate that the energy E is proportional to R/Rxo. The calorimeter has a sensitivity 0.30 ^{o} C/J.

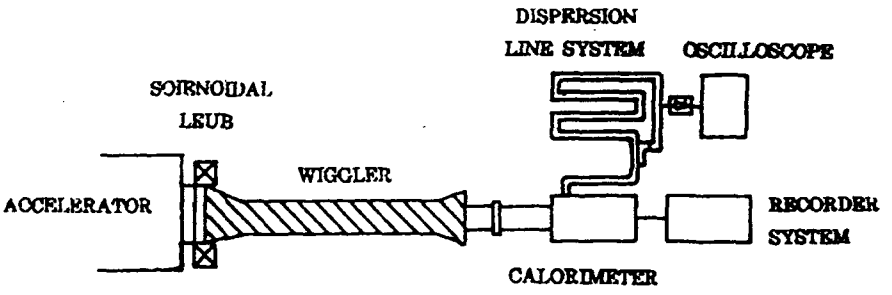

Fig. 5. Diagram of calorimeter's measurements for EPA-74 FEL experments

Measurements for FEL experiments

The diagram of calorimeters measurements for EPA-74 FEL experiments is shown in Fig .5.[4] The Raman FEL using an intense relativistic electron beam (Ie=100A, Ee=0.56 Mev, te=50ns) and a wiggler (w=3.45 cm, Bw=0-1.25 KG) without a guide magnetic field is capable of providing a high-power, high-gain coherent radiation. For measurements, it is necessary that the calorimeter is connected to the end window of the wiggler.

Fig.6. is a typical calorimeter trace displayed on a x-y recorder. Because the calorimeter is worked at normal atmosphere the output voltage signal decays exponentially following Newton's cold formula and without reaching an equilibrium value,

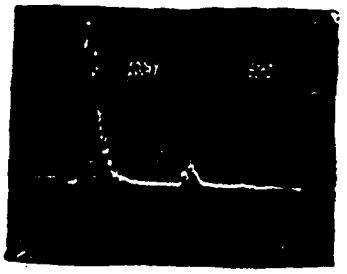

FIG. 7. Signal of dispersion line system

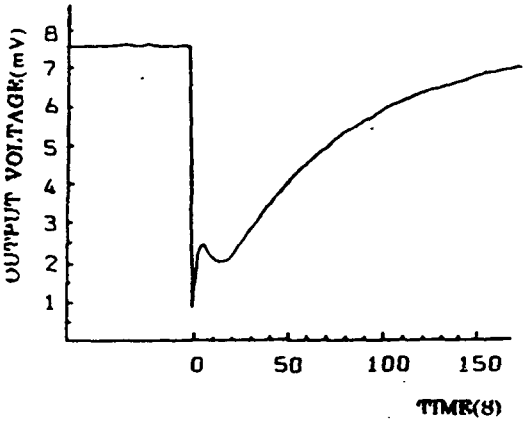

Fig. 6. Typical output chart on x-y recorder

but the signal may be extrapolated back to determine the equilibrium value in the absence of heat loss. The measured radiated energy and power in these experiments

are typically 20 mJ and 1Mw, respectively.

The oscilloscope trace of the dispersion line system is shown in Fig.7. The first one (large) is the reference signal and the second (small) is the delayed signal via 46.5 meters dispersion line. The radiated frequency may be determined by measuring the time interval between the two signals. The measured radiation frequency in these experiments is typically 33 GHz.

Acknowledgments

We would like to acknowledge fruitful discussion with prof . Tao zucong, Huang Sunren and Liu xisan. In addition, We express our appreciation to Xu Yong and Li Zichuan for their experimental assistance.

References

[1] J.A.Pasour and S.H.Gold, IEEE J.Quantum Electron. QE-21.845 (1985).

[2] S.Talmadge, T.C.Marshall and S.P.Schlesinger, The Physics of Fluids. Vol 20,974 (1977)

[3] P.Efthimion, P.R.Smith, and S.P.Schlesinger, Rev.Sci.Instrum., Vol.47, No.9,1059 (1976)

[4] Hu KeSong, Chen Yutao, Huang Sunren etc., EPA-74 Free Electron Laser Experiment Collected Works, (1989)

INTRABAND RADIOLUMINESCENCE OF DIELECTRICS: PROPERTIES AND APPLICATIONS TO HIGH POWER BEAMS DIAGNOSTICS

D.I.Vaysburd and B.N.Syomin

High Current Electronics Institute Siberian Division
of Russia Academy of Science, Tomsk 634055 Russia

Abstract. This kind of dielectric's light emission was discovered by the authors in 1972-1980. It may be induced either by electron or ion, X-ray, or even laser beam irradiation if the latter can generate secondary electrons of energy 2-20 eV above the conduction band bottom in dielectric. If the pulse of irradiation is short (1-10 ps) or the temperature of a sample is high (more than 600 K) then the intraband luminescence will be the brightest type of dielectric light emission induced by ionizing beam irradiation. It has some extreme properties in comparison with all the other kinds of light emission: the broadest continuous spectrum (0-25 eV), the shortest time relaxation (1 ps), the absolute temperature independence up to the boiling point. Due to these properties intraband luminescence is one of the most convenient optical effects to visualize high power particle beam.

1. Non-Ionizing Free Electrons and Holes in Dielectric

The rate of energy loss (-dE/dt) vs energy (E) of a conduction band electron (valence band hole) in crystal or of a quasi-free electron (hole) in a disordered solid or liquid is shown in Fig.1. Having E more than E_Δ an electron (or hole) loses its energy producing impact ionization (or Auger ionization) of dielectric medium, i.e. creating electron-hole pairs. In this case $-dE/dt = 10^{15} - 10^{17}$ eV/s. Having E less than E_Δ an electron (hole) cannot ionize dielectric. Such a non-ionizing electron (hole) doesn't produce electron-hole pairs and other electron excitations of condensed

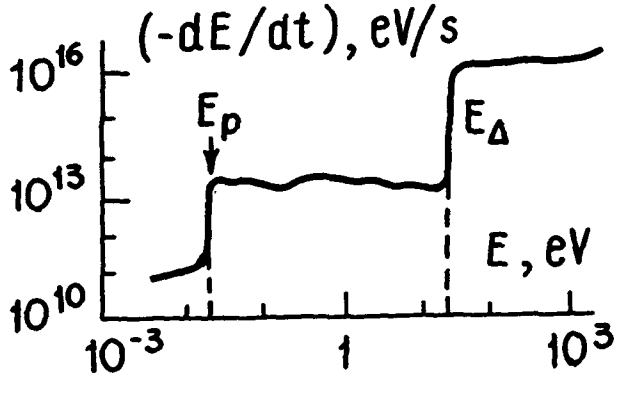

Fig.1.

matter. It gives off its energy step-by-step to the lattice, generating phonons of all kinds: short-wave, optical and acoustic. In this case the rate of its energy relaxation is of the order $-dE/dt=10^{13}$ eV/s and its lifetime is of the order 1 ps. When E becomes less than E_p a non-ionizing electron (hole) cannot emit the optical phonons but only the acoustic ones. In this case $-dE/dt = 10^{10} - 10^{11}$ eV/s.

2. Radiative Transitions of Non-Ionizing Electrons and Holes and Corresponding Kinds of Dielectrics Luminescence

The non-ionizing region of the electron or hole energy spectrum extends from the bottom of the conduction band $E_c = 0$ up to E_Δ, where the latter is the minimum energy that must be spent by free electron to create a new electron-hole pair by means of impact ionization. Theoretical estimations give $E_\Delta - E_c = E_\Delta = (1.5\text{-}2.0)\cdot E_g$, where E_g - is the energy gap between the valence and conduction bands. So, the dielectrics have the largest non-ionizing range $E_\Delta = 10\text{-}25$ eV. The latter may contain one or more conduction bands and one or more valence bands (Fig. 2). There are nine kinds of radiative transitions of non-ionizing electrons and holes (Fig. 2). The initial energy level E_i belongs to one of conduction or valence bands.

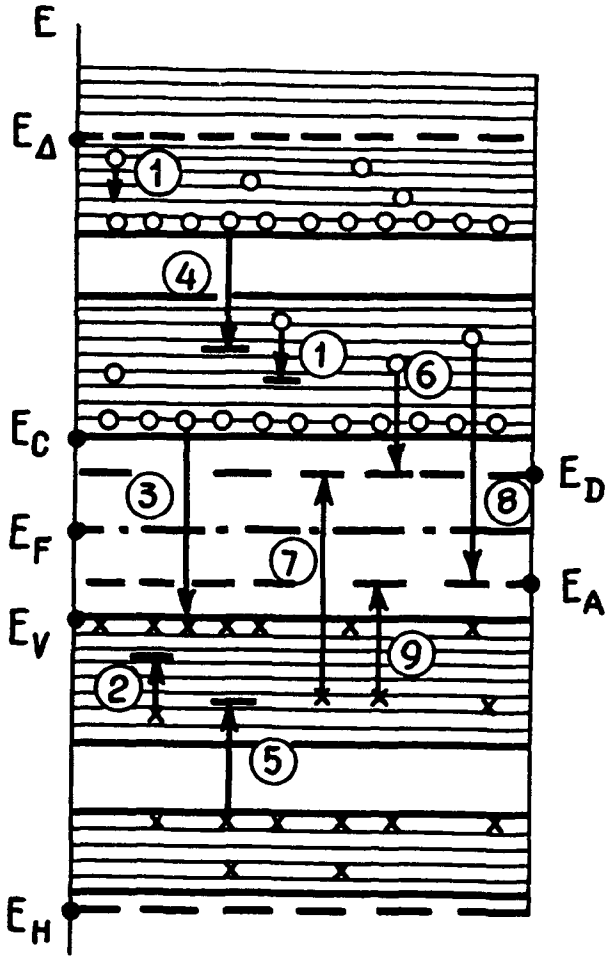

Fig. 2.

The final energy level E_f may belong to the same or another band or to an impurity spectrum inside the energy gap. In the latter case it may be a donor level E_D or an acceptor level E_A. The corresponding nine kinds of luminescence are 1, 2 - intraband elec-

tron and hole l.; 3 - recombination electron-hole l.; 4, 5 - band-to-band electron and hole l.; 6, 7 - band-to-donor electron and hole l.; 8, 9 - band-to-acceptor electron and hole l.. The first five are the fundamental ones. The last four are the structure sensitive ones. Only two of the nine abovementioned luminescence kinds have been discovered and studied in dielectrics: intraband electron [1-6] and band-to-band hole (the so-called "cross-luminescence" [7-9]).

3. Theoretical Calculation of Intraband Luminescence

Solution of Boltzmann equation in "energy - age of non-ionizing electron" space gives [4, 6]:

$$n_E(E,t) = [G(t)/B(E)]\cdot[D(E)/D_o], \qquad (1)$$

where G(t) - rate of non-ionizing electrons generation, n_E - their spectral density at level E, $B \equiv -dE/dt$, $D(E)/D_o$ - relative number of states above level E, within non-ionizing region of conduction band. The calculations show that the probability of direct radiative transitions is from 10 to 100 times bigger than that of indirect ones [10]. So, only direct radiative transitions of non-ionizing electrons between different branches within one of conduction bands were taken into account. Calculated spectra are shown in Fig.3. The main results: spectra of intraband electron luminescence are essentially broader and more intense than the hole ones. The reason is simple. Conduction band of an alkali-halide crystal has a large width. But its valence band is narrow. The theoretical calculation provides basic parameters of intraband luminescence: decay time, temperature dependence, quantum yield. In the next section they will be compared with experimental data.

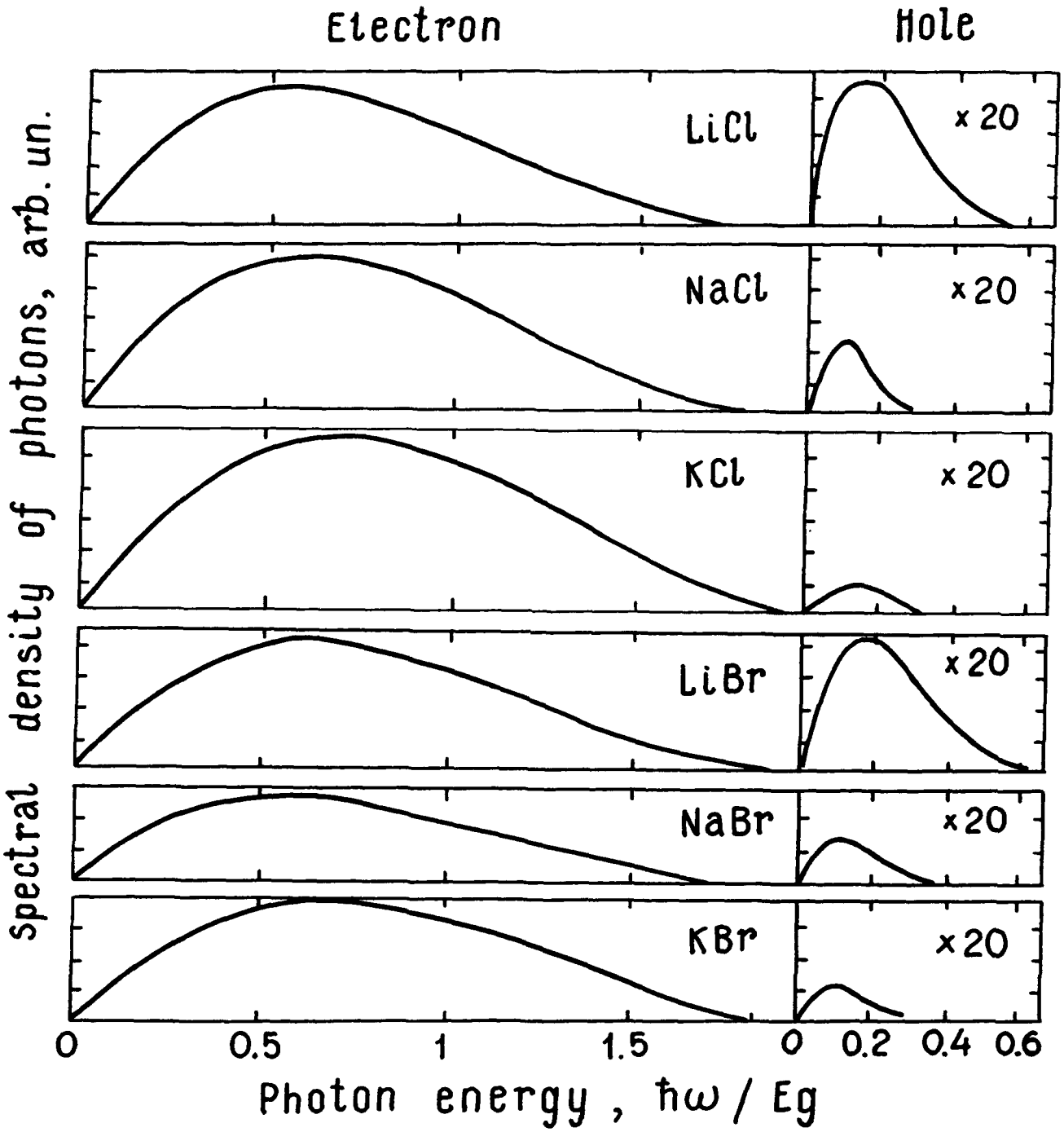

Fig.3. Calculated spectra of alkali-halide crystals intraband luminescence: conduction band electrons (the left column), valence band holes (the right column).

4. Experimental Study of Dielectrics Intraband Electron Luminescence Induced by Pulse Power Electron Beam Irradiation

The alkali-halide crystal dielectrics were investigated. The samples were irradiated by single pulse electron beams (0.2-0.4 MeV, 1 - 20 ns, 1 - 10 000 A, 1 - 10 000 A/cm^2) of high current miniaccelerators GIN constructed by the authors [11] in Tomsk. Fig.4a, b, c, d, e, f, g show the basic results of experimental investigation.

4.1. The luminescence spectra of KI are shown in Fig.4a, b. At low temperatures the luminescence of singlet and triplet self-trapped excitons (STE) predominates. The STE-luminescence intensity decreases rapidly with temperature growth (Fig.4a, c) and intraband luminescence (IBL) remains the same (Fig.4c). IBL has a very broad spectrum which extends from the IR to the UV region where it is cut off by the crystal intrinsic absorption (Fig.1a). The spectra of KI (Fig.4a, b), RbCl (Fig.4d), NaCl (Fig.4c) and KBr (Fig.4g) show that observing structure is not intrinsic to IBL and due to other kinds of luminescence and light absorption by color centers. The two small dips are the result of IBL absorption by F- and hole centers, respectively (Fig.4e). The intrinsic structure of the IBL spectra is very slight.

4.2. The temperature independence of the IBL differs it drastically from all kinds localized electron luminescence (Fig.4c). The temperature shift of the IBL short-wave edge is due to well known behavior of the intrinsic absorption edge. Up to the melting point it shifts continuously toward longer wavelengths and at the melting point jumps by 0.5-0.7 eV (Fig.4a, b, c). The IBL intensity remains essentially unchanged up to the melting point and above the latter in the long-wave region where the intrinsic absorption is absent.

4.3. Fig.4a, b show that static disorder of condensed matter doesn't influence the IBL intensity which remains the same in single crystals, polycrystals, and melt (Fig.4a, b).

4.4. The IBL yield was measured by two methods [5]. Both gave approximately the same results: the average spectral quantum yield is $5 \cdot 10^{-5}$ photons/(eV·eh-pair), the IBL absolute yield is $0.5 \cdot 10^{-3}$

of the absorbed beam energy.

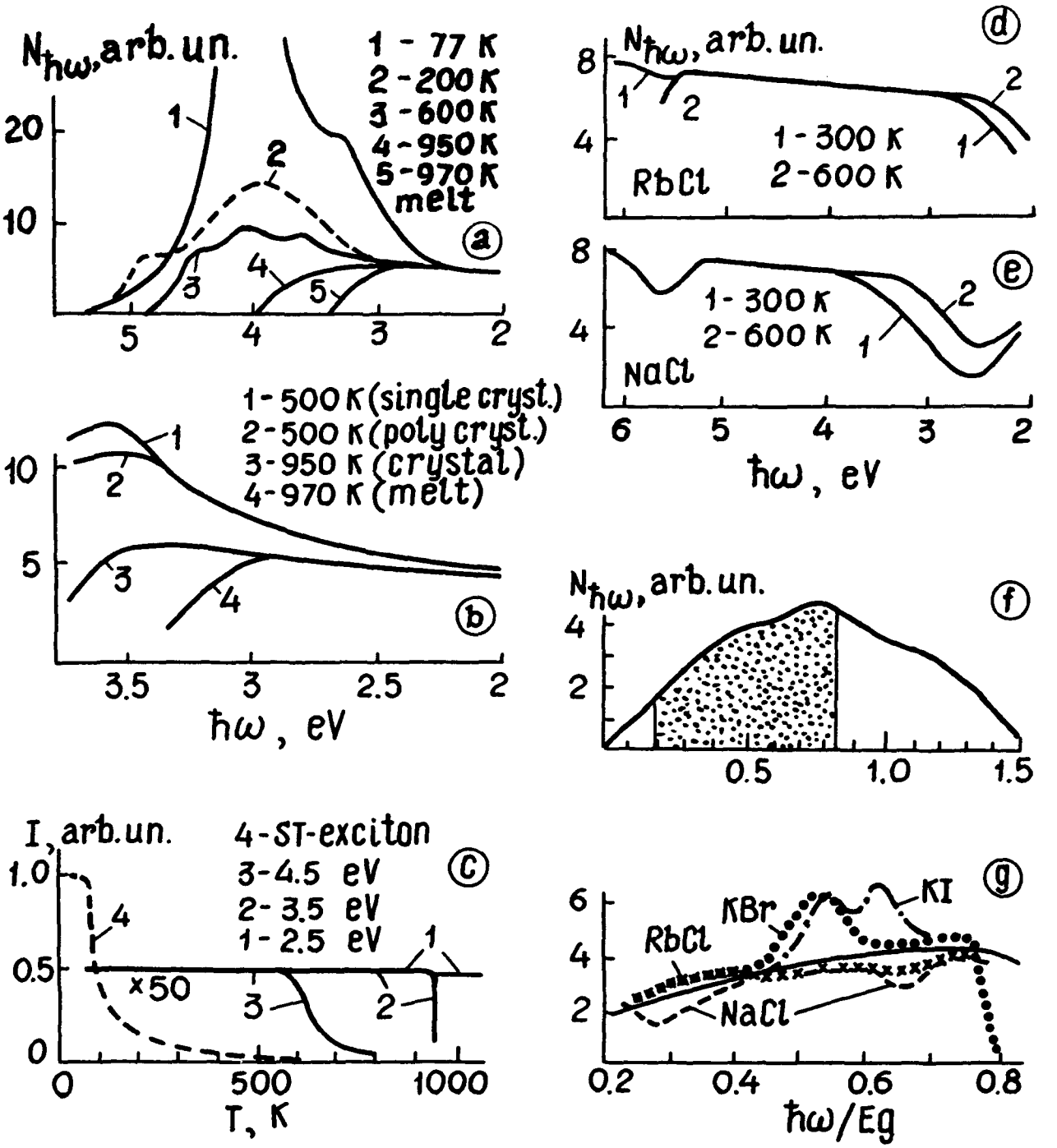

Fig. 4. The basic results of the experimental investigation of the dielectrics intraband electron luminescence induced by pulse power electron beam irradiation

5. The Main Results

The theoretical model of the observed light emission as the non-ionizing electrons intraband luminescence provides a simple explanation of all the obtained experimental data. In fact, according to this model: the IBL spectrum width is near to $1.5 \cdot E_g$ = 10-20 eV; the IBL decay time is of the order 10^{-12}s; the IBL intensity depends very weakly on the temperature up to the melting point and even above the latter because -dE/dt of the non-ionizing electrons is determined by the temperature independent spontaneous phonon emission; the absolute IBL energy yield is of the order 10^{-3} and in all the cases it is much larger than that of Vavilov-Cherenkov radiation.

Three basic features: the broadest continuous unstructural spectrum, picosecond lifetime, independence of dielectrics temperature and static disorder presents the IBL as the most convenient light emission to visualize power particle beams.

References

1. D.I.Vaysburd et al., Intern. Conf. on Luminescence, Abstracts, Leningrad, Nauka, 1972.
2. D.I.Vaysburd, B.N.Syomin, V.T. Shkatov et al., Izvestiya Akad. Nauk SSSR. Ser. Fiz. 38 (1974) 1281.
3. D.I.Vaysburd, B.N.Syomin, E.G.Tavanov and V.T.Shkatov, Izvestiya Akad. Nauk SSSR. Ser. Fiz. 40 (1976) 2404.
4. D.I.Vaysburd, Radiation Physics of Semiconductors and Related Materials, Proceeding of International Conference, 1979. Tbilisi, University Press (1980) 198-210.
5. D.I.Vaysburd, B.N.Syomin, JETP Lett. 32 (1980) 181.
6. D.I.Vaysburd, B.N.Syomin, E.G.Tavanov et al., Solid State High-Energy Electronics, Novosibirsk, Nauka, 1982 (Monograph).
7. Yu.M.Aleksandrov et al., Fizika Tverdogo Tela 26 (1984) 2865.
8. Yu.M.Aleksandrov et al., Nuclear Instruments and Methods A261 (1987) 153.
9. Ya.A.Valbis et al. Pisma JETF 42 (1985) 140.
10. D.I.Vaysburd, Voprosi Atomnoi Nauki i Tehniki 3 (1984) 103.
11. B.M.Kovalchuk, G.A.Mesyats, B.N.Syomin, V.G.Shpak, Pribori i Tehnika Eksperimenta 4 (1981) 15.

COMPUTER ASSISTED DIAGNOSTICS ON A HIGH-POWER MICROWAVE SYSTEM*

M.T. Crawford, M. Kristiansen, and L.L. Hatfield

Pulsed Power Laboratory
Texas Tech University
Lubbock, TX 79409-43102

S.E. Calico

PL/WSES
Kirtland AFB, NM 87117

Abstract

The use of computer algorithms to improve the quality or amount of information available from system diagnostics is not new. Many people use computers to "massage" their data into a more legible or usable format. At the Texas Tech University High-Power Microwave Facility computers are used to compensate for the inherent limits of a probe and produce data which cannot be acquired by normal diagnostic methods. The diode voltage probe is compensated by using a computer-based fast Fourier transform program. Quantities of the microwave propagation are measured using a particle-in-cell simulation code.

Introduction

The High-Power Microwave Facility is a typical pulsed power machine consisting of a 31 stage Marx generator charging a simple pulse-forming line which is switched, via a single channel oil spark gap, into a planar vacuum diode. The diode is configured to operate as a virtual cathode oscillator and produces around a gigawatt of 2 GHz microwaves which propagate down an evacuated cylindrical waveguide, through a dielectric vacuum-gas interface, and into an anechoic chamber. The goal of this experiment has been to study the breakdown which occurs on the atmospheric pressure side of the dielectric window.

Voltage Probe Compensation by Computer

Diagnostics on the diode were critical in determining factors such as beam power and diode impedance. The diode voltage was measured by use of a liquid prepulse resistor which was converted into a resistive divider, see Figure 1. The response of the probe proved to be extremely noisy and had to be low-pass filtered to a cutoff just above the expected bandwidth of the diode voltage waveform. Even with the filter, the output of the probe was

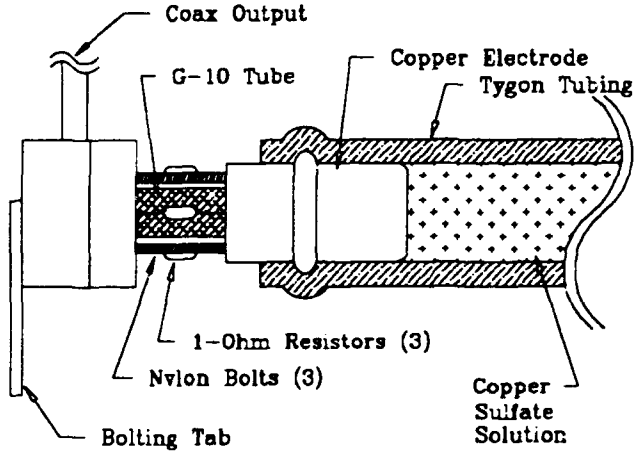

Figure 1. Divider electrode of the diode voltage probe.

* Supported by AFOSR/PL

noisy and unrecognizable. These limitations were overcome by determining the transfer function of the probe and using it to reconstruct the original input to the probe. The transfer function was obtained by exciting the probe with a pulse with a risetime much shorter than that of the diode voltage. In order to generate a pulse with a very short risetime and apply it to the diode voltage probe, a test chamber was constructed that preserves the risetime of an input pulse in a geometry which is physically large enough to hold the probe. Two air-insulated, 50 Ω coaxial tapers were constructed and placed on either side of a short 50 Ω air coaxial section. The excitation pulse is generated using a 1000 V cable pulser. The probe is placed in the straight section and its output is low-pass filtered and fed into a high-speed oscilloscope. The excitation pulse is measured by terminating another high-speed oscilloscope in 50 Ω and measuring the output of the test chamber. See Figure 2 for a schematic representation of the calibration system.

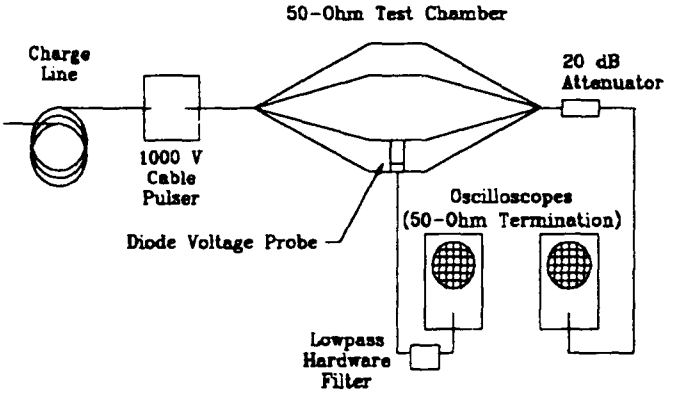

Figure 2. System for obtaining input and output waveforms from diode voltage probe.

The transfer function is obtained by transforming the input and output waveforms to the frequency domain using a fast Fourier transform (FFT) routine and dividing the output by the input. This transfer function is employed by taking the output from the probe, transforming it to the frequency domain, multiplying it by the transfer function, and transforming it back to the time domain. The resulting waveform is an approximation of the original input waveform. The excitation waveform, the resulting output and the compensated output are shown in Figure 3.

The resolution of this method is limited by the number of data points that were initially digitized and the frequency to which the FFT is calculated. The effects of "aliasing" can be minimized by using a low-pass filter with a cutoff frequency which is at most half of the top frequency generated in the FFT process.

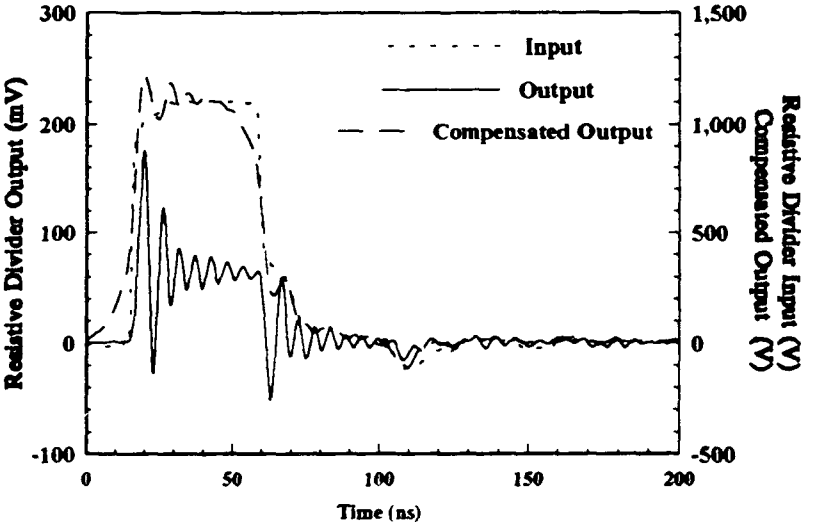

Figure 3. Input, output, and compensated output waveforms from the diode voltage probe

There are several limitations to this method of calibration. The first and most obvious is the difference in geometry between the test chamber in which the probe was calibrated and the actual location of the probe during system operation. Initially, the transfer function was obtained while the probe was installed in the system, but because the system is not matched to

any particular impedance, wave reflections prevented accurate recording of the excitation pulse. But since the probe is a resistive divider and not a field probe, the geometry should have little effect on the output. Another concern, in this particular case, is that the probe is constructed from a water resistor. Water resistors have a tendency to change resistance with time. The solution to the time effect is to periodically determine a new transfer function. Overall, this method provides an effective way to turn a nearly useless probe into one that can provide useful, if not perfect, diagnostic signals.

Computer Simulation as a Diagnostic Method

The primary goal of the research at the High-Power Microwave Facility has been to study the breakdown which occurs as the microwaves pass from the evacuated waveguide, through the waveguide window, and into free space. The waveguide is circular in cross-section and only one microwave propagation mode, TM_{01}, is supported. The method of microwave generation excludes the possibility of TE wave propagation and the microwave frequency is well below the cutoff for TM_{02}. The end of the waveguide is located in a small anechoic chamber. The anechoic chamber is lined with microwave absorbing foam to reduce the interference from reflected microwaves. Figure 4 is a schematic drawing showing the layout of the waveguide. The only microwave diagnostic is a calibrated microwave B-dot antenna located in a corner of the anechoic chamber.

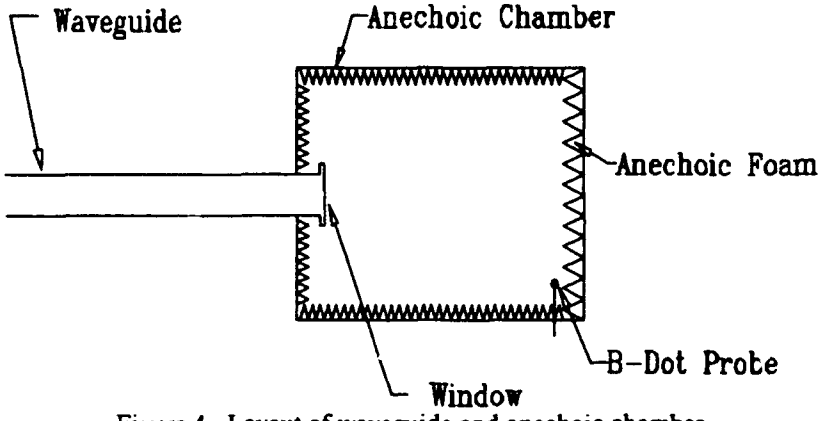

Figure 4. Layout of waveguide and anechoic chamber

The research into window breakdown involved modifying the window characteristics. Various window materials, shapes, ambient gases, and even waveguide attachments were employed. With each change in the window region, the radiation pattern would change. The power density at the B-dot probe was measured for each shot. Without some idea of what the radiation pattern looked like, nothing besides relative measurements could be gleaned from the B-dot probe.

Initially, the computer simulations were used to find the radiation pattern and relate that to the measured power density and then extract the total microwave power. The simulations were run using MAGIC, a fully relativistic, two-and-one-half dimensional, particle-in-cell code from Mission Research Corporation. The geometry was defined as a cylindrically symmetric three-dimensional region containing the waveguide, window, and anechoic chamber, see Figure 5. An azimuthal magnetic field probe was placed in the simulation space to simulate the B-dot probe in the actual experiment. A wave is excited in the waveguide that will propagate in the proper mode and at the correct frequency to simulate the emission from the actual microwave source. For each different window configuration, the simulation geometry is redefined to simulate the window configuration. Knowing the magnetic field at the B-dot antenna, the simulation wave amplitude is adjusted until the same magnetic field is recorded at the diagnostic approximating the B-dot probe. When the simulation generates the same amplitude at the B-dot probe location as the probe itself

generates, all of the field values in the simulation should be representative of the same values in the experiment.

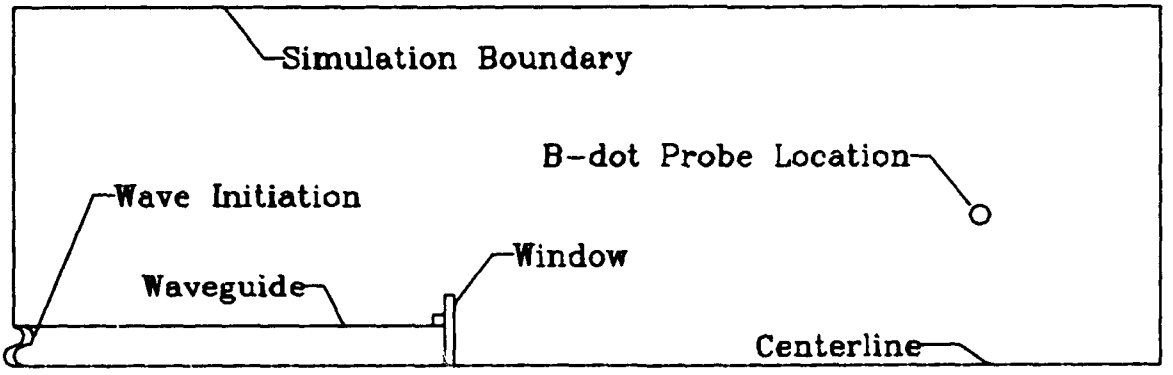

Figure 5. Simulation geometry for anechoic chamber and waveguide.

Total power can be calculated in several different ways. First, total power can be calculated by determining the power density for a spherical surface centered on the window and then summing over that surface. This method has the limitation that the simulation region is made up of rectangular cells of finite size, and generating a spherical surface from a rectangular grid is, at best, a crude approximation. A better method is to calculate the total power in the waveguide, where the surface is linear, and then figure the amount transmitted through the window by using the standing wave ratio (SWR) in the waveguide. The SWR can be calculated by observing the fields along a line parallel to the waveguide axis. For each point along the line find the maximum field value. Of the maximum values for each point, find the maximum and minimum values for the line. Dividing the maximum field value by the minimum field value gives the SWR. Using the SWR to find the reflection coefficient, Γ, gives,

$$|\Gamma| = \frac{SWR-1}{SWR+1}.$$

The power which is calculated in the waveguide is composed from the incident and reflected waves. The total power outside the waveguide is given as;

$$P_{fs} = \frac{\left(1-|\Gamma|^2\right)}{\left(1+|\Gamma|^2\right)} P_{wg},$$

where P_{fs} is the total power in free space and P_{wg} is the total power measured in the waveguide.

Beyond the use of the simulation to calculate the total microwave power, the same method can be used to find field values in regions where they would ordinarily be almost impossible to measure. In the breakdown studies, the axial electric field at the surface of the window was determined to be responsible for the initiation of the breakdown.. Using the simulation coupled to

the experimental values through the B-dot antenna magnitude, the axial electric field at the surface of the window can be directly determined from the simulation.

During the research it was discovered that for one window geometry there was breakdown while for another geometry there was not. Breakdown occurred when a simple planar window, one-half inch thick was employed. The breakdown was prevented by using a window two inches thick with a cone cut into the center of window. This inverted cone had angles of 45°, and was 1.5 inches across the base. Simulating these two geometries and adjusting the microwave amplitudes until they match the corresponding B-dot antenna measurements, the axial electric field at the surface of each window can be determined. Comparing the field values, the pulsed microwave breakdown strength of the window material is found to be greater than the axial electric field of the planar window geometry but less than the field value of the window with the inverted cone cut into it.

Results from this use of the simulations are given. Figure 6 shows open-shutter photographs of the windows breaking down. Figure 7 is a contour plot of each window geometry showing axial electric field at a time when it is maximum at the window surface. The dotted regions represent the dielectric window and the solid contour lines are positive equal field lines while the dashed contours represent negative equal field lines. In Figures 6 and 7 , a) represents a planar window geometry which experienced breakdown, while b) is an inverted cone geometry which did not break down. The maximum axial electric field for the inverted cone geometry is approximately 1.8 MV/m while for the planar geometry the axial electric field at the window is around 2.2 MV/m. Each of these windows is made of Lexan so it can be inferred that the pulsed microwave breakdown strength of Lexan in air is between 1.8 MV/m and 2.2 MV/m.

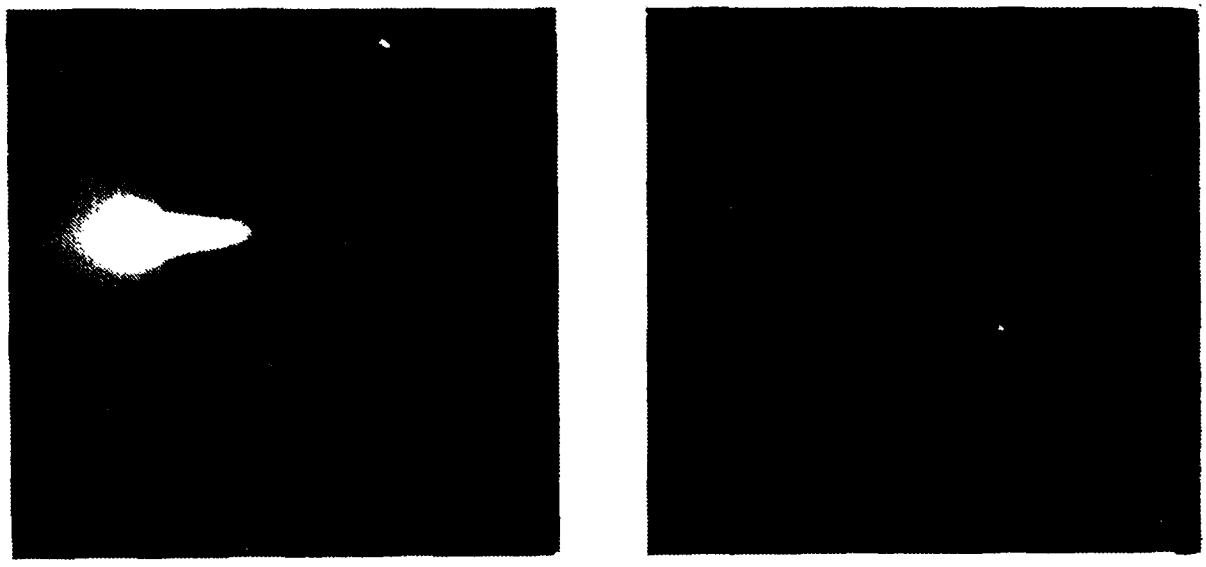

a) b)

Figure 6. Photograph of window breakdown: a) Planar window geometry, b) Inverted cone geometry.

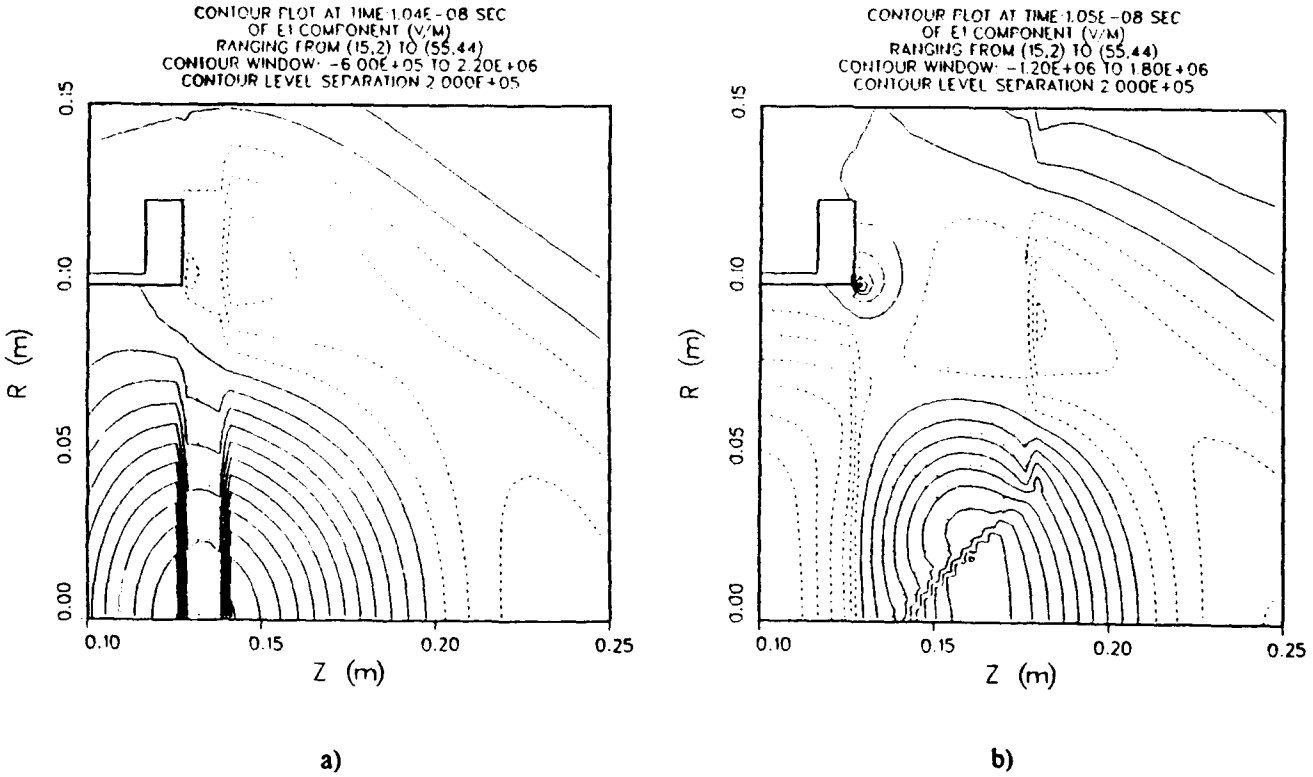

a) b)

Figure 7. Plot showing contours of equal axial electric field versus position for a) Planar window geometry, b) Inverted cone geometry.

Limitations of the simulation diagnostic method are the obvious ones, inaccuracies in modeling the physical geometries. First, a two-and-one-half-dimensional code will not be able to resolve any propagation modes that are not symmetric about the *z* (direction of propagation) axis. Second, any very lossy material is hard to model. If, in our case, the windows had a high dielectric loss tangent, the simple dielectric model in the simulation would not accurately represent the physical realities. These errors can be minimized by carefully constructing the model and by knowing certain critical parameters in the experiment. A very important quantity to know well is the microwave frequency. The microwave source on the Texas Tech University High-Power Microwave Facility has a tendency to "chirp" up in frequency with time. The frequency at the time of highest power is, however, quite well known. Frequency measurements were made by recording the signal directly out of the B-dot probe. Although the microwave frequency is beyond the 3dB cutoff of the oscilloscopes, only the amplitude, not the frequency, of the signal is affected. At the time of maximum power, the microwave frequency was measured to be between 1.9 and 2.1 GHz. Using a simulation frequency of 2 GHz and matching the simulation amplitude to the peak power in the experiment, the maximum total power and fields will be measured.

The use of modern computing power can substantially increase the effectiveness of experimental diagnostics. Care must be taken to realize the limits of computer diagnostics and to stay well within those limits.

SQUEEZED STATES OF HIGH-CURRENT ELECTRON BEAM IN A SYSTEM WITH VIRTUAL CATHODE

A.V.Fedotov, A.M.Ignatov, V.P.Tarakanov

General Physics Institute, Moscow, Russia

Introduction

It is well-known that the dependence of electron beam potential on its current is a two-valued function [1], i.e., in theory, there are two states of a beam with a given current. Only one of them corresponding to the lower density and higher velocity exhibits itself in both physical and computer experiments. Another beam state with higher density and lower velocity, which is called here a squeezed one, is usually supposed to be unstable. Moreover, it wasn't quite clear which way one could prepare such a state.

In this paper we consider propagation of a high-current electron beam through the inhomogeneous transport system consisting of two coaxial tubes (fig.1). It is shown that under some conditions the beam may be in its squeezed state. We also study the behavior of the virtual cathode demonstrating that it may be toggled between two parts of the tube. We believe we understand the reason for all these.

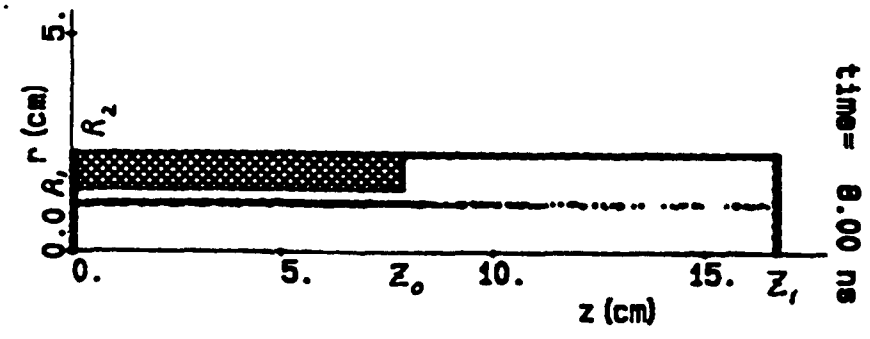

Figure 1: The shape of the device.

Model and Simulations

The shape of the tube we dealt with is sketched in fig.1. The hollow electron beam was injected at the left end ($z = 0$). Computer simulations were implemented using the "Karat" electromagnetic relativistic PIC code. In most runs the external magnetic field was assumed strong enough that

moved to the wide tube absorbing the squeezed state on the way. Figure 3 shows the shot of this wave propagating to the right. Therefore, changing

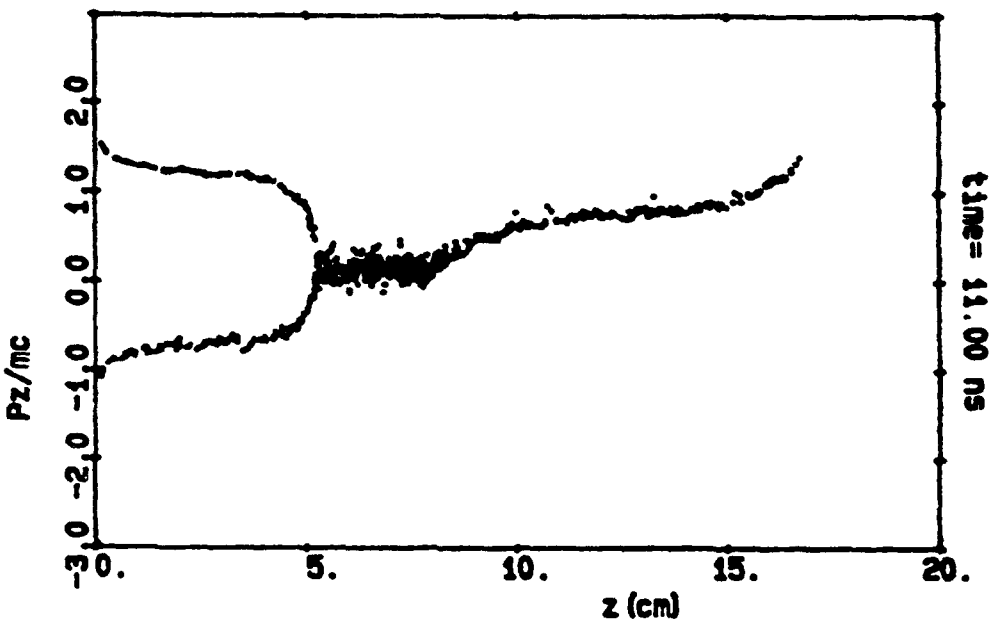

Figure 3: A virtual cathode moving to the right.

the injection current we could toggle between two various states of the beam. The speed of the virtual cathode while switching was comparable to the electron velocity, the height of the corresponding potential barrier was about the injection energy. A natural desire was to try to accelerate something with this moving nonlinear structure. Preliminary runs with additional loading of ions confirmed that they really might be accelerated in this process.

Physical experiments [3] demonstrated the spreading of the beam in the narrow tube. We performed the three-dimensional computer experiment and confirmed the assumption that the diocotron instability or something like it could affect the squeezed state. Typical deformation and splitting of the beam are clearly visible in fig.4, where the beam cross-section at $Z = 5cm$ is shown.

Theory

First, suppose that the virtual cathode is placed in the wide tube and it reflects some part of electrons, e.g., the current μI_0 is turned back to the narrow tube while $(1 - \mu)I_0$ go on travelling through the wide tube. The energy conservation may be written as $\gamma_0 = \gamma_1 + \phi_1 = \gamma_2 + \phi_2$, where the

allowed to ignore the transverse motion of electrons and to suppress the azimuthal perturbations. A brief description of the code and preliminary results of the simulation may be found in [2].

The parameters that we chose keeping in mind the experiment [3] were: $R_1 = 1.45cm, R_2 = 2.2cm, z_0 = 9.0cm, z_1 = 16cm$, the injection energy, γ_0, was 0.43 MeV ,i.e., the limiting currents for narrow and wide tubes were $I_{\lim 1} = 10kA$, $I_{\lim 2} = 4,5kA$,respectively. The main object of the computer runs was to study what happens to the beam with the injection current, I_0, exceeding the limiting current of the wide tube.

The particle distribution established in the system depended essentially on the injection current. With the latter exceeding a little $I_{\lim 2}$, the virtual cathode was placed in the wide tube ($z > z_0$) and the stream reflected from it was cold. This distribution changed drastically when the injection current was greater than $(I_{\lim 1} + I_{\lim 2})/2$. The virtual cathode moved to the left end of the narrow tube. The outgoing current was still about $I_{\lim 2}$, but electrons leaving the virtual cathode drifted relatively slow until they reached the tubes' junction (fig.2). The density in this part of the beam corresponded

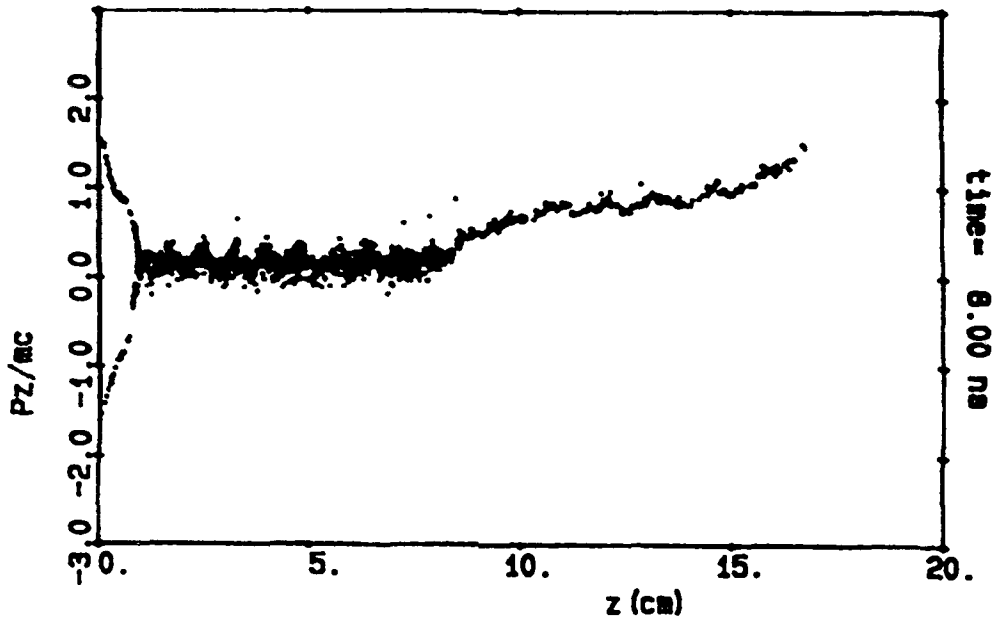

Figure 2: The phase plot with a squeezed state.

to the squeezed state. There also was the significant heating of the beam in the narrow tube, while it remained cold in the wide one. This process was reversible: in reducing the injection current, the virtual cathode suddenly

divergence condition, $\nabla_j T_{ij} = 0$, where T_{ij} is the stress tensor, must hold for any steady state. Integrating the divergence over the inner part of the system bounded by the planes $z = z_{1,2}$, where $0 < z_1 < z_0, z_2 > z_0$, we get the stress balance:

$$T(z_1) - T(z_2) = \Delta T = \frac{1}{8\pi} \int_{R_1}^{R_2} \rho d\rho E_z^2(z_0, \rho) \qquad (1)$$

We cannot evaluate the force, ΔT, acting upon the junction but all we need is $\Delta T > 0$. The stresses in both tubes , $T(z_{1,2})$, divided by $m^2c^4/4e^2$ are

$$T(z_{1,2}) = \frac{1}{a_{1,2}} \left[\gamma_0^2 - \gamma_{1,2}^2 - \frac{2\gamma_0}{\gamma_{1,2}} + 2 + \Delta P_{1,2} \right] \qquad (2)$$

where $\Delta P_{1,2} > 0$ correspond to the thermal pressure that is also unknown, while other terms are due to the dynamic and electric parts of the total pressure.

Figure 5 shows the parametric plot $T(z_1)$ versus the current in the narrow tube, $I = \beta_1(\gamma_0 - \gamma_1)/a_1$, in neglecting ΔP_1; the thermal pressure can shift this curves up. The upper branch there corresponds to the squeezed state of the electron beam. Suppose now, that in the wide tube the beam is cold

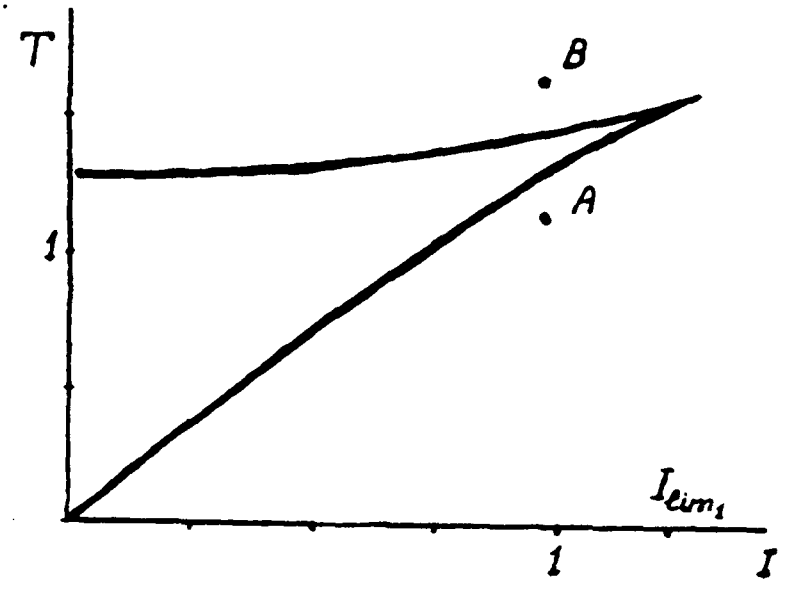

Figure 5: The phase diagram stress vrs current.

and its current is the limiting one, $I_{\lim 2}$. On the phase diagram (fig.5), this

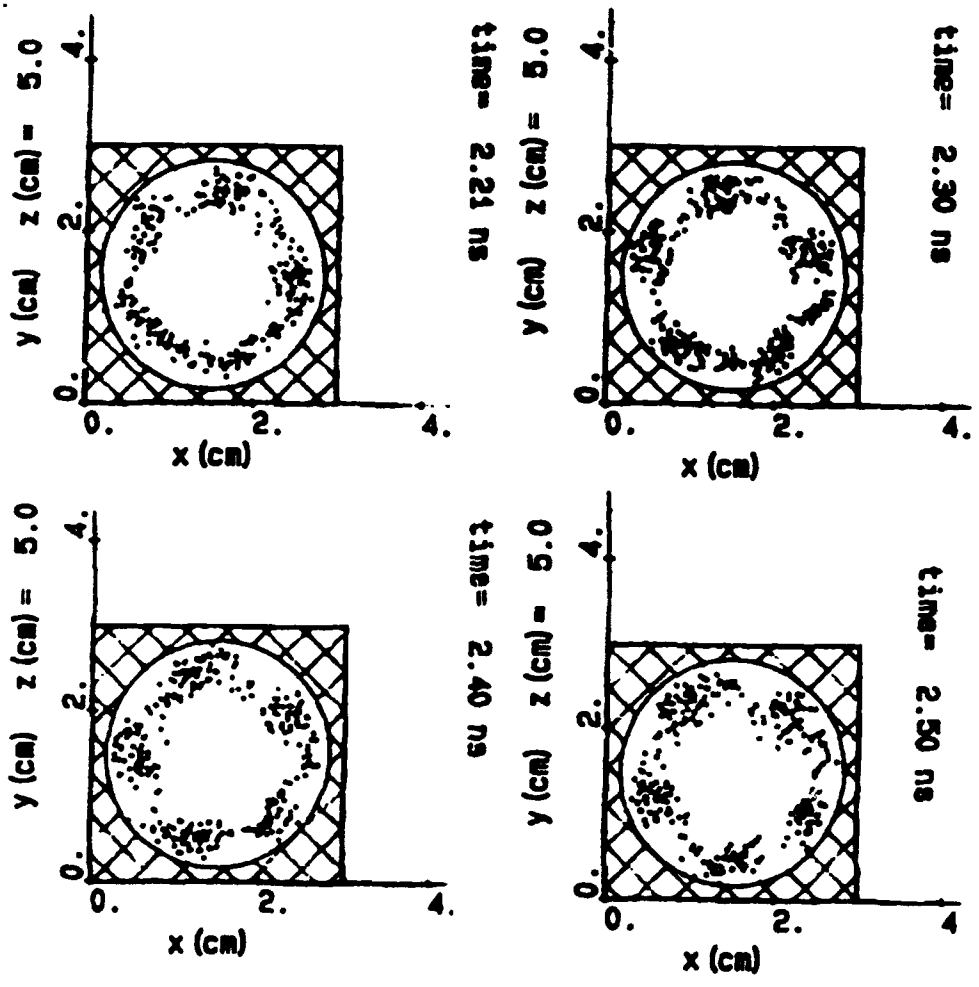

Figure 4: Cross sections of a sqeezed state.

indices 1,2 correspond to the narrow and wide tubes, respectively, and the potentials $\phi_{1,2}$ are measured in mc^2/e units. Here we assume that electrons move along the z axis only and ignore the thickness of the beam. Far from the junction and the ends of the tubes the potentials are : $\phi_1 = I_0 a_1(1+\mu)/\beta_1, \phi_2 = I_0 a_2(1-\mu)/\beta_2$, where $a_{1,2} = \ln(R_{1,2}/R_b)$ and I_0 is divided by $mc^3/2e$. Combining these relations we can easily see that two inequalities must hold for this state to exist: $1 - I_{\lim 2}/I_0 \leq \mu \leq -1 + I_{\lim 1}/I_0$. that is, $I_0 \leq (I_{\lim 1} + I_{\lim 2})/2$. In other words, with the injection current exceeding this value, the additional potential produced by the reflected stream locks the narrow tube and the virtual cathode has no other choice but to remove to the left end of the system.

To make out the appearance of the squeezed state consider the balance of the z-component of the total momentum. To preserve its conservation the

state is represented by the point A. Since, generally, the force $\Delta T(1)$ by the order of magnitude is about $T(z_{1,2})$, to maintain the balance the stress in the narrow tube must correspond to the point B laying above A. If this point is above the upper branch, the beam is in its squeezed state that may be even heated to compensate the additional pressure. It seems this is what we came across in the computer simulations.

In fact, this explanation is nothing but the Bernoulli's law. At first sight, it states just the opposite: the pressure in the narrow tube must be lower. The main reason for this queer behavior is the electric field pressure may be negative.

Nearly in the same manner one can describe a situation in the vicinity of the virtual cathode: the stresses in this case must are balanced by two streams at one side and a single stream at another. It may be shown that for the standing virtual cathode the stress balance may hold only near some inhomogeneity of the tube, e.g., the junction or its end. Nevertheless, for the uniformly moving virtual cathode the stress and energy balance may be fulfilled. The appropriate equations are rather bulky and the details of this moving structure (fig.3) are not clear up to date. Anyway, since this description is very similar to that for the shock waves, one may say that the virtual cathode is a shock wave separating two states of the beam.

References

1. Bogdankevich L.S.,Rukhadze A.A., Sov.Phys.Uspekchi, v.103, p.609 (1971).
2. Nikulin M.V.,Stolbetzov S.D.,Tarakanov V.P.,Fedotov A.V.,Shkvarunets A.G. Radioteknika i elektronika.1992, to be published.
3. Fedotov A.V.,Shkvarunets A.G. Sov.J.Plasma Phys.,v.13, p.1068 (1987); v. 14, p.689 (1988).

ELECTRON BEAM DEFLECTION DIAGNOSTIC

Mai T. Ngo and John A. Pasour
Mission Research Corporation
8560 Cinderbed Rd, Suite 700, Newington, Va 22122.
(703) 339-6500

A nonperturbing diagnostic tool which is capable of precisely measuring the position and charge distribution of charged particle beams, including those from RF accelerators, is described. The diagnostic uses as a probe a low-energy (1-20 keV), μA-level electron beam, which is injected at right angles to the path of the primary beam, after which they are collected by a suitable detector. The deflection of the probe electrons depends on the position of the primary beam relative to the test beam as well as on the charge distribution of the primary beam. Consequently, by measuring the deflections, one can determine these primary beam parameters. Calculations which illustrate the capabilities of this technique are presented, and the design and performance of a prototype version of the diagnostic version of the diagnostic are described.

1. Introduction

The successful operation of various high-energy physics experiments, free-electron lasers (FELs), and related devices depends critically on the availability of high-quality and well-diagnosed electron beams. In this paper we describe a diagnostic which has the capability of accurately resolving the position of a charged particle beam in the beam tube and determining temporal and spatial variations of the beam on the time scale of the microbunch in an RF accelerator. The diagnostic utilizes a probe consisting of a tightly focused, low-energy electron beam, which does not perturb the accelerated electron beam. The basic idea is quite simple, as seen in the schematic diagram of Fig. 1. A tightly focused stream of probe electrons is injected across the beam tube perpendicular to the accelerated beam. The probe electrons are deflected by the accelerated beam, and the direction and magnitude of the deflection are directly related to the spatial and temporal charge distribution of the accelerated beam. The deflected electrons impact a detector on the opposite side of the beam tube.

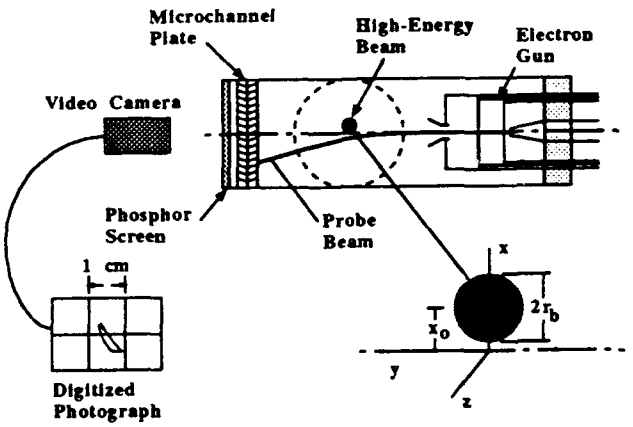

Figure 1. Schematic diagram of the diagnostic, as viewed along the axis of the accelerator beam tube

The results of our calculations, which will be summarized below, show that easily-resolved deflections are produced by microbunches with total charge as small as a few pCoul and pulse durations as short as 1 psec. The probe electron energy can be adjusted to maximize deflections for a particular microbunch charge. Thus optimized, the diagnostic can determine the position of the microbunch centroid to better than 1 μm with respect to the probe beam. The diagnostic has the capability of time resolved operation on a picosecond time scale or time averaged operation with real time read-out, which could be used, for example, by an accelerator operator to tune the beam optics. Electron probes have been used previously to measure plasma sheaths and potentials[1,2] and the neutralization of heavy ion beams.[3]

2. Theory

2.1 Fields From The Relativistic Beam

The electromagnetic fields of a finite electron beam or microbunch can be calculated analytically provided that certain assumptions are made concerning the charge distribution[4]. We assume an electron bunch of total charge Q distributed uniformly in r, θ, and z and moving along the z-axis with velocity v. In the beam frame, the fields are purely electrostatic and can be calculated analytically. After transforming the resulting radial and axial electric field components into the laboratory frame (assuming the center of the microbunch is located at the origin of the lab frame at $t = t' = 0$), we obtain

$$E_r = \frac{Q}{L\gamma^2}\left\{\frac{U}{\sqrt{(r/\gamma)^2+U^2}} + \frac{V}{\sqrt{(r/\gamma)^2+V^2}}\right\} \quad (1)$$

$$E_z = \frac{Q}{L\gamma^2}\left\{\frac{1}{\sqrt{(r/\gamma)^2+U^2}} - \frac{1}{\sqrt{(r/\gamma)^2+V^2}}\right\} \quad (2)$$

$$B_\theta = \beta E_r$$

$$E_\theta = B_r = B_z = 0$$

where

$$U=L/2 - z + vt,\ V=L/2 - z - vt,$$

In Eqs. 1 and 2, all quantities are now measured in the laboratory frame, and we have defined the normalized velocity of the accelerated beam to be $\beta = v/c$ and the normalized energy of the accelerated electrons to be $\gamma = (1 - \beta^2)^{-1/2}$. For any charge distribution which is independent of θ, Eq. 2 is correct for $r \geq r_b$, while the field for $r < r_b$ is given by replacing Q with the total charge inside r.

The field expressions obtained above can be analyzed to gain an insight into the sensitivity of an electron deflection diagnostic to various parameters. One interesting feature is that above a certain energy (typically tens of MeV), E_r is essentially independent of energy. Also, for high energy, E_r varies with time as the axial charge distribution.

2.2 Probe Electron Trajectories

The fields calculated above can easily be used to determine the deflection of the probe electrons. The field components given by Eq. 1 and 2 can be substituted directly into the relativistic equation of motion to calculate the electron trajectories, which we have done numerically using a Runge-Kutta algorithm in a relatively simple, three-dimensional trajectory code. We initialize the trajectory code by injecting probe electrons at $y = -|y_0|$, as measured from the beam tube axis, with velocity in the $+y$ direction. The geometry is defined in Fig. 1. Typically, y_0 is in the range from 1 to 7 cm.

2.2.1 Effects Due to Beam Offset and Radius. To illustrate the nature of the deflection, we plot a series of probe electron trajectories in three dimensions. The trajectories in Fig. 2 are calculated assuming a 200-A, 100-MeV accelerated beam with a length of 0.9 cm (30 psec), moving in the $+z$-direction inside a 2-cm-diameter beam tube. The beam is offset from the axis by 1 mm in the $-x$ direction. A probe electron is injected into the beam tube every 10 psec, and the trajectories of a number of electrons are plotted as the relativistic beam passes by. The probe electron trajectories are terminated on the wall of the beam tube, and a solid line connects the termination points of successive particles.

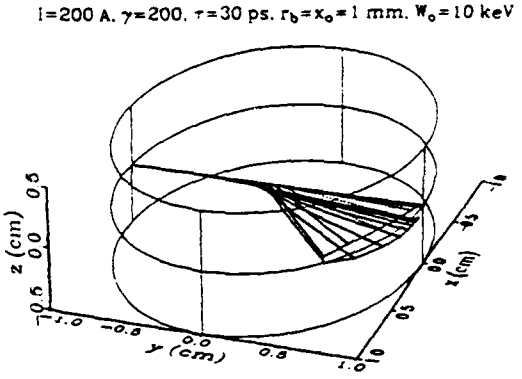

Figure 2. 3-D probe electron trajectories.

Figure 3 shows deflection as a function of offset for three different beam radii. As expected, there is no dependence on beam radius if $x_0 > r_b$. However, if $x_0 < r_b$, significant differences are apparent. At the two larger values of beam radius considered, the deflections are well-behaved, with a gradually increasing amplitude as the offset increases toward r_b. However, for $r_b = 1$ mm, the microbunch fields become so large that the probe electrons are slowed drastically (and nearly reflect) when $x_0 < r_b$. This results in a very nonlinear interaction, greatly increasing the sensitivity of the diagnostic.

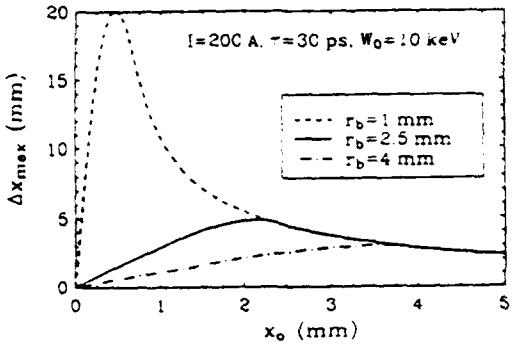

Figure 3. Maximum transverse displacement vs. beam offset.

2.2.2 Effects Due to Nonuniformities. One of the unique and intriguing features of the electron deflection diagnostic is its potential for resolving at least some of the microstructure of the accelerated beam. Fixing the charge per bunch at 10 nCoul, we perform calculations with bunch length varying from 30 psec to 300 psec. Figure 4 shows the transverse and axial displacements of probe electrons having energies of 10 keV. The plotted points correspond to electrons injected at 8.3 psec intervals. It is clear that the magnitude of the electron deflection is very sensitive to bunch duration. However, it is important to note that in the cases shown here, the deflection is in the nonlinear regime. If the energetic beam current is too low to decelerate and accelerate the probe electrons appreciably, the deflection is nearly constant for a particular charge per bunch, independent of the bunch length. By properly choosing the probe beam energy, it is possible to resolve the bunch duration to within a few percent if the charge per bunch is known.

2.2.3 Example. As a numerical example, we consider the use of the deflection diagnostic with a tightly-focused, ultra-relativistic (50 GeV) beam. The results of trajectory calculations for this beam are plotted in Fig. 5. The maximum deflection agrees to 3 significant figures with the deflection from an otherwise identical 100-MeV beam. The general behavior is the same as described previously. However, the more tightly bunched beam requires a higher probe beam energy to

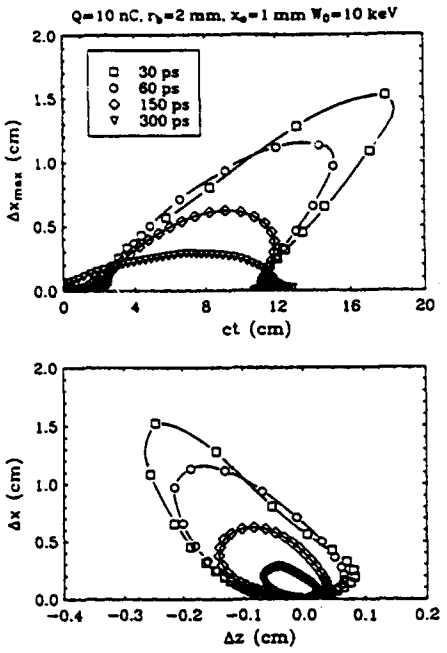

Figure 4. Transverse and axial deflections, measured at y=1 cm for various bunch lengths.

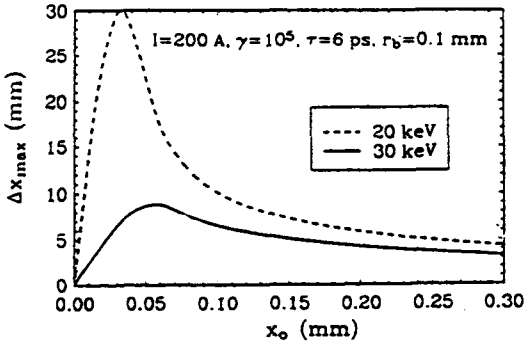

Figure 5. Deflection vs. offset for a tightly-focused beam.

penetrate the Coulomb barrier. This example suggests an operating procedure whereby a relatively high probe energy is used until the deflection (and hence the relative beam offset) is very small. Then decreasing the probe energy allows the resolution of the diagnostic to be increased to 1 μm or less.

For even more tightly bunched beams, such as in particle colliders, the probe electron energy required to penetrate the Coulomb potential can become quite large. In such cases, it would be more feasible to use an ion probe beam. Such a beam (22 keV He^+, 0.1 μA, 0.5 mm diameter) has been used to probe rapidly varying fields in plasmas.[5]

3. Experimental Setup

The development and testing of the electron deflection diagnostic was performed using the apparatus shown in Fig. 6. The major components in this arrangement are the electron beam generator for the main beam (the beam being diagnosed), a microwave cavity to modulate the main beam, the probe electron gun, and the detector for monitoring the deflected electrons.

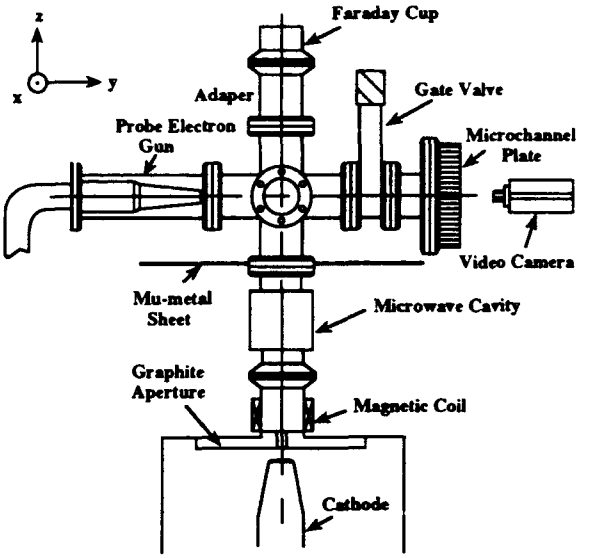

Figure 6. Schematic diagram of the prototype diagnostic.

The main electron beam used to test the diagnostic was generated by two different pulsed power devices. The first, a modulator consisting of a PFN and a step-up pulse transformer, produced a voltage output ranging from 60 kV to 200 kV with a 500-nsec pulse duration. The second was a Febetron, a Marx-type generator which produced a 50-nsec pulse at a moderately higher voltage (200 kV to 600 kV). The electron beam from both of these generators was field-emitted from velvet covered cathodes.

The original motivation for this diagnostic was for RF accelerators. However, due to the shut-down of the NIST racetrack microtron at which we had planned to test the diagnostic, we were forced to improvise by using a modulated, low-energy beam. Although there are substantial differences in the expected behavior of the diagnostic at these low energies and the ultra-relativistic beams that can be generated with RF accelerators, these tests allowed us to test the operation of the diagnostic with short electron bunches (≤ 100 psec). In our experiments, the electron beam was passed through an RF cavity, which was driven by a high-power microwave pulse at approximately 3 GHz. An input power of about 20 kW was required to fully modulate the beam.

A low-cost CRT-type electron gun was chosen for the probe electron beam, which intersected the accelerated electron beam near the center of a 5-way vacuum cross. The electron energy and the emitted current of the gun could be varied from 0 to 10 keV and up to ~ 0.5 μA, respectively. The electron detector used in these experiments was a 4-cm-diameter microchannel plate (MCP) from Galileo Electro-Optics Corporation[6]. Deflection of the probe electrons was monitored by a high-sensitivity CCD video camera and recorded on a video cassette recorder for further measurements and data analysis.

During the testing, parameters such as position, diameter, and charge density profile of two different accelerated beams and a modulated beam were diagnosed. This was accomplished by measuring the probe electron deflection as a function of probe beam energy and relative offset for various main beam voltages and currents. To the extent possible, the main beam parameters were determined independently to verify the performance of the diagnostic. The main beam current was measured using a Faraday cup, and the time-integrated beam size and position were determined from a scintillator target placed in the center of the 5-way cross (and removed prior to using the probe beam). Main beam energy was obtained by a capacitive voltage divider at the output of the modulator. The location of the probe beam at the center of the cross was precisely determined by scanning a wire across its path with a micrometer-driven positioner.

4. Experimental Results

The experimental results have verified most of the important features of the electron beam deflection diagnostic. The experimental data were very reproducible and agreed extremely well with the theoretical calculations, with both the long-pulse electron beam and the modulated beam.

The deflection of the probe electron beam as recorded by the MCP is shown in Fig. 7 for the two long-beam pulses. The two white spots in Fig. 7 (a) correspond to the non-deflected beam (right), and the deflected beam (left). In this image the main electron beam is on the right, traveling vertically upward. Figure 7 (b) shows the deflection of the probe electrons due to the 50-nsec main beam. In Fig. 7 (b) the main electron beam was on the top and traveling from left to right. The probe electron beam deflected from top to bottom as the main beam current increased from zero to maximum, remained almost at the same place during the flat portion of the pulse, and went back to the original position as the current decayed to zero. The rise and fall times of about 8 nsec and 10 nsec, respectively, of the main current pulse produced the vertical streak between the two end points. Figure 8 shows the experimental and theoretical dependence of the probe electron deflection on the probe

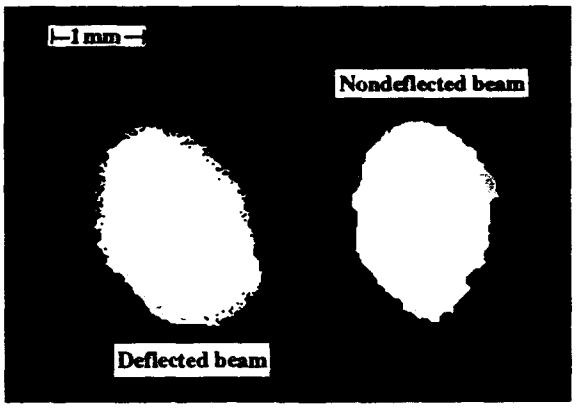

(a)

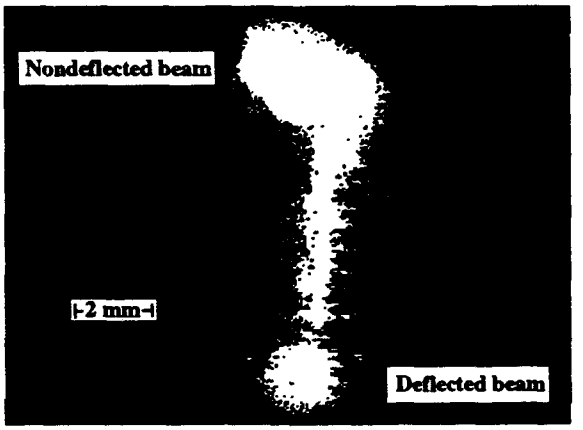

(b)

Figure 7. Images of electron deflection by (a) a 500-nsec and (b) 50-nsec electron beam.

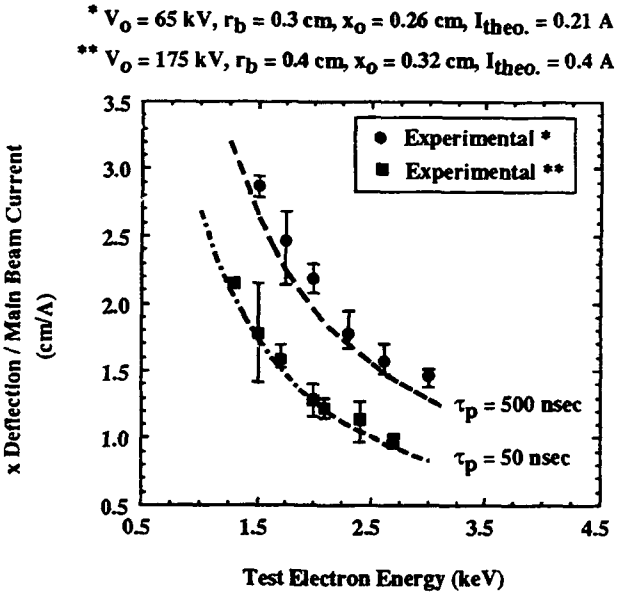

Figure 8. Normalized deflection vs. probe electron energy for long-duration beams. Dashed lines are the theoretical calculations.

beam energy for the two main beam pulse durations. Due to the shot-to-shot amplitude variation in the main current pulse (~ 10%), the normalized electron deflection (i.e., deflection to main beam current ratio) is plotted in this and the remaining figures. The error bars in the data result from averaging the deflections from multiple shots.

To determine the dependence of the deflection on beam offset, the probe beam was scanned across the main beam. Sample experimental deflections are shown in Fig. 9 along with the theoretical calculations for different probe electron beam energies. The deflection of the probe electron beam increased linearly with beam offset until the offset was on the order of the main beam radius. Similar behavior was observed for all probe beam energies and both main beam pulse durations, and as expected, higher deflection was obtained with lower probe beam energy. This result demonstrates that by measuring probe beam deflection as a function of beam offset, the size and position of the main beam can be determined. However, to fully resolve the beam size and position, several measurements have to be made at various offsets.

The final tests of the diagnostic were performed by modulating the Febetron beam at 3 GHz, thereby simulating an RF linac type beam, using the setup shown in Fig. 6. These experiments were the only ones to use the magnetic field coil shown in the figure. An example of the deflection produced by the modulated beam is shown in Fig. 10.

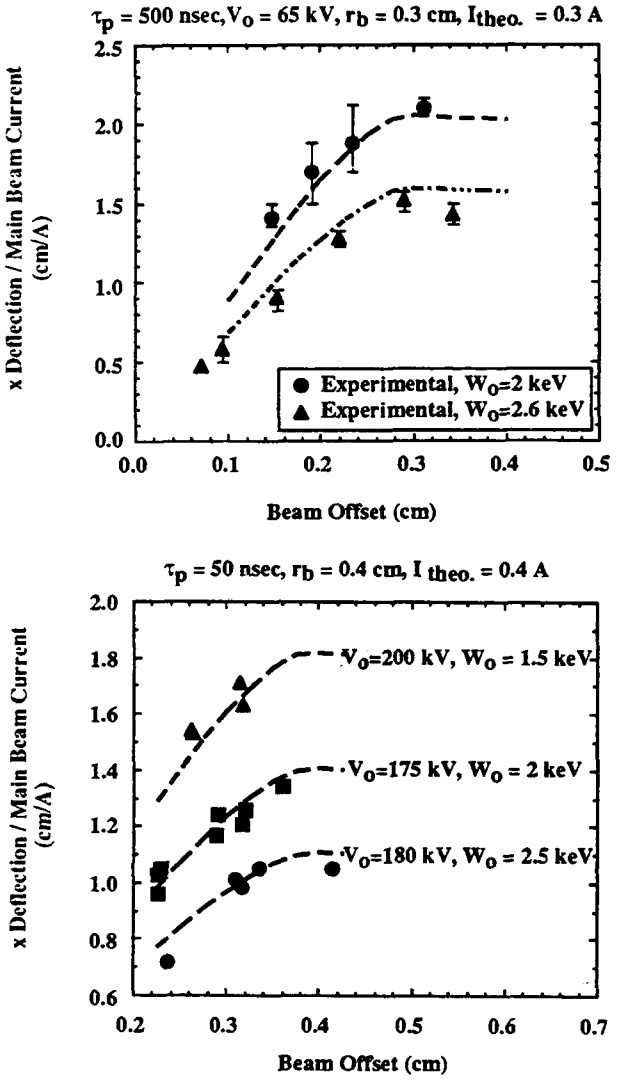

Figure 9. Normalized deflection vs. offset. Top: 500-nsec beam. Bottom: 50-nsec beam. Dashed lines are the theoretical calculations.

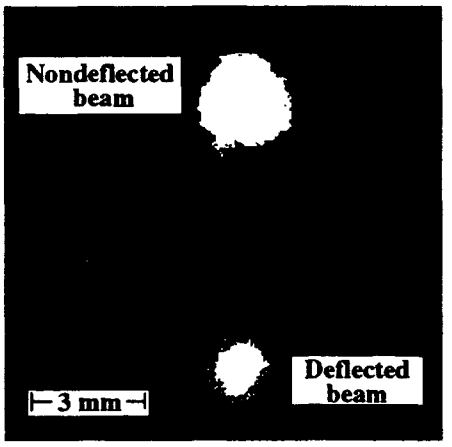

Figure 10. Deflection by a modulated beam.

To quantify this behavior, the particle trajectory code was modified to include a train of identical beam bunches spaced at an interval of 333 psec (3 GHz). Figure 11 shows a comparison of the experimentally measured deflections with the calculated values for different probe beam energies. The best fit to the experimental data was obtained using the parameters shown in the figure. The measured values of x_0 and of the main beam energy (275 keV) and average current (0.4 A) were used in the calculations. The best fit beam radius (0.25 cm) was less than the measured value of 0.3 cm, possibly indicating that the current distribution was peaked on axis. The bunch duration of one third of the RF period and peak current of 1.2 A are certainly plausible.

The experimental variation in deflection with beam offset is compared to theory in Fig. 12. Each of the experimental data points represents a single shot, and the scatter is representative of the uncertainty in measuring the deflection and the variation of current during the pulse (the average value of which is used to normalize the data). The range over which the offset could be varied was limited by the experimental apparatus, but over the accessible region, the agreement with theory is

quite good. The beam radius that is inferred from the diagnostic by the point of maximum deflection is 0.38 cm, while the target/scintillator measurement gave 0.40 cm in this case. The good agreement between the experiment and calculations indicates the suitability of the beam deflection diagnostic for bunched beams.

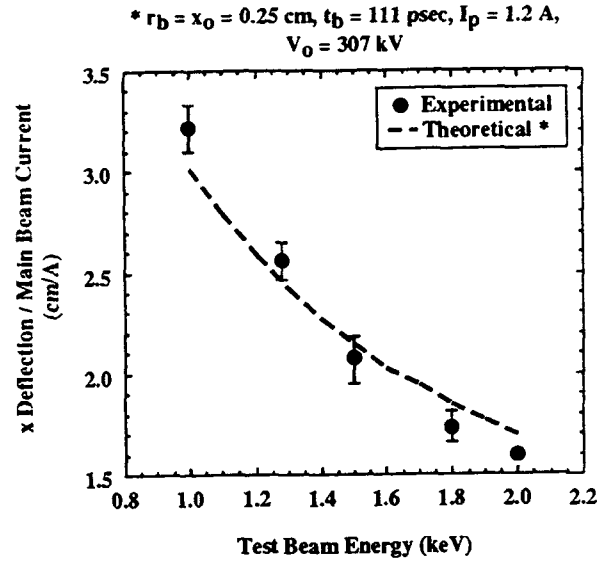

Figure 11. Normalized deflection vs. probe energy.

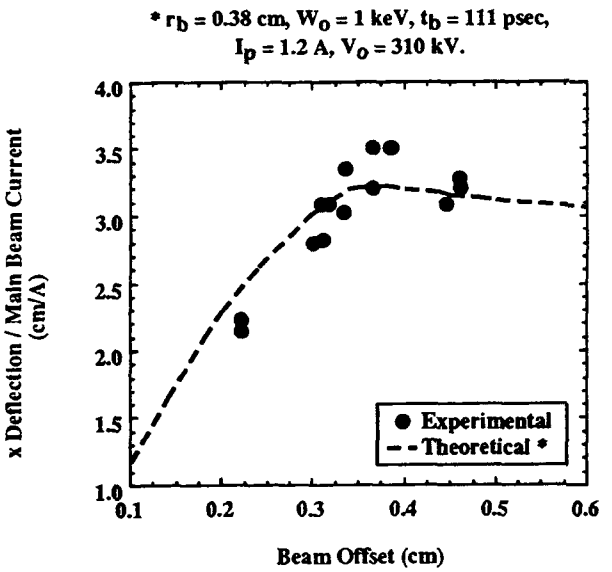

Figure 12. Normalized deflection vs. offset for the modulated beam.

5. Discussion

The basic idea of the electron deflection diagnostic is quite simple, but the prototype development revealed a number of difficult detection problems. The intrinsic detection problem which must be faced is the small number of deflected electrons that are available for detection. If the probe beam current is 1 μA (which is quite high for a high-quality, tightly-focused beam), there are only six electrons per psec available for detection. Detection of such a small number of electrons requires a very quiet background and a high detector sensitivity. The MCP used in the prototype has ample sensitivity to respond to single electrons, but it also responds to *x*-rays and to any stray charged particles. These extraneous sources must be almost totally eliminated, at least for the time that the detector is active, in order to be able to achieve psec response. A second issue which must be addressed is the density of the relativistic beam to be diagnosed. If the beam is tightly focused and bunched (as in a particle collider), an energetic probe electron beam is required to penetrate the Coulomb barrier of the bunch if the diagnostic is to be used to resolve the charge distribution of the bunch. However, it is important to note that the position of even a tightly-focused bunch can be accurately determined with this diagnostic without the probe electrons actually penetrating the bunch.

Compared to other available diagnostics, the electron deflection diagnostic has some obvious advantages. The resolution with which it can measure position is as good or better than most other diagnostics, perturbing or nonperturbing. As we have shown, the position resolution can be on the order of microns or less with suitably chosen parameters. Because it employs a stream of particles which can penetrate the accelerated beam, the deflection diagnostic also has the ability to resolve the microstructure of the beam. None of the other nonperturbing diagnostics which have been developed have the ability to resolve beam microstructure, and no other single diagnostic has the ability to measure as many of the beam parameters as this one. The major disadvantages of the deflection diagnostic are its complexity, cost, and the somewhat involved computations that are required to analyze the data. When viewed in the context of a large accelerator facility, however, these disadvantages are not too significant.

REFERENCES

1. Paul D. Goldan, Phys. Fluids **13**, 1055 (1970).
2. D. A. Swanson, B. E. Cherrington, and J. T. Verdeyen, Phys. Fluids **16**, 1939 (1973).
3. J. Shiloh, M. Lampel, and R. Sah, Rev. Sci. Instrum. **54**, 46 (1983).
4. J. D. Jackson, *Classical Electrodynamics* , John Wiley & Sons, New York, 1962.
5. C. W. Mendel, Jr., Rev. Sci. Instrum. **46**, 847 (1975).
6. J. L. Wiza, "Microchannel Plate Detectors," Galileo Electro-Optics Corporation, Sturbridge, MA. Also, Data Sheets 9000 and 9200.

ELECTRON BEAM POTENTIAL MEASUREMENTS ON AN INDUCTIVE-STORE, OPENING-SWITCH ACCELERATOR

J. C. Riordan, J. R. Goyer, D. Kortbawi, J. S. Meachum,
R. S. Mendenhall, and I. S. Roth

Physics International Company
2700 Merced Street
San Leandro, CA 94577

Abstract

Direct measurement of the accelerating potential in a relativistic electron beam accelerator is difficult, particularly when the diode is downstream from a plasma opening switch. An indirect potential measurement can be obtained from the high energy tail of the bremsstrahlung spectrum generated as the electron beam strikes the anode. Our time-resolved spectrometer contains 7 silicon pin diode detectors filtered with 2 to 15 mm of lead to span an electron energy range of 0.5 to 2 MeV. A Monte-Carlo transport code was used to provide calibration curves, and the resulting potential measurements have been confirmed in experiments on the PITHON accelerator. The spectrometer has recently been deployed on PM1, an inductive-store, opening-switch testbed. The diode voltage measurements from the spectrometer are in good agreement with the diode voltage measured upstream and corrected using transmission line relations. The x-ray signal and spectral voltage rise 10 ns later than the corrected electrical voltage, however, indicating plasma motion between the opening switch and the diode.

Introduction

Vacuum voltage measurements on terawatt-class accelerators are difficult, because of the extreme environment where the electric field exceeds 1MV/cm. For this reason, voltage measurements are usually made in water or oil upstream of the tube insulator. The load voltage is then calculated using the measured rate of change of current (dI/dt) and the known inductance (L) between the monitor and the load. In opening switch systems, however, the switch plasma introduces additional errors into the calculation of the load voltage. The plasma produces space charge currents and shunt losses, which change the inductance by an unknown amount. Experiments on EYESS have also shown that the switch plasma carries along current as it moves downstream toward the load, generating a motional voltage IdL/dt which is only qualitatively understood.

Bremsstrahlung, on the other hand, provides a convenient probe of the beam potential in a relativistic electron beam diode because these x-rays readily escape the vacuum vessel and are easily detected. The shape of the high energy x-ray spectrum is determined primarily by the

electron energy, i.e., the potential through which the electrons are accelerated. Because the x-ray attenuation length increases with photon energy, it is possible to unfold the bremsstrahlung spectrum and the beam potential from a number of x-ray measurements performed with differentially filtered detectors. Simple 3-channel spectral voltage monitors have previously been developed at Physics International to verify the voltage division in series diodes on Double-EAGLE[1] and at other laboratories.[2,3] These early monitors had a narrow dynamic range and generally gave accurate results only at peak diode voltage. The new monitor contains 7 channels with closely spaced filter thicknesses to provide accurate, time-resolved measurements from 0.5 to 2 MV.

Spectrometer Design and Calibration

The spectrometer is enclosed in a single, 3-cm-thick lead housing (Figure 1) to minimize detector response to x-rays scattered from the concrete facility walls; a 5-cm-thick front face attenuates x-rays scattered by the housing itself. The lead filters are placed in apertures wider than the detector to eliminate the spectral vignetting produced by imaging apertures with high energy x-rays. Silicon pin diodes were chosen as detectors because they are much smaller and cheaper than the scintillator/photodiode alternative. 1.0-mm tin and 0.1-mm copper filters are inserted between the lead filter and the detector to selectively absorb K-shell x-rays, which would otherwise impair the spectral discrimination. Additional 1.6-mm aluminum layers over the detector entrance and exit windows provide the electron equilibrium necessary for high energy x-ray dosimetry (Figure 2). Calculations indicate that the combined fluorescence (lead, tin, and copper) now contributes less than 1% of the total detector response.

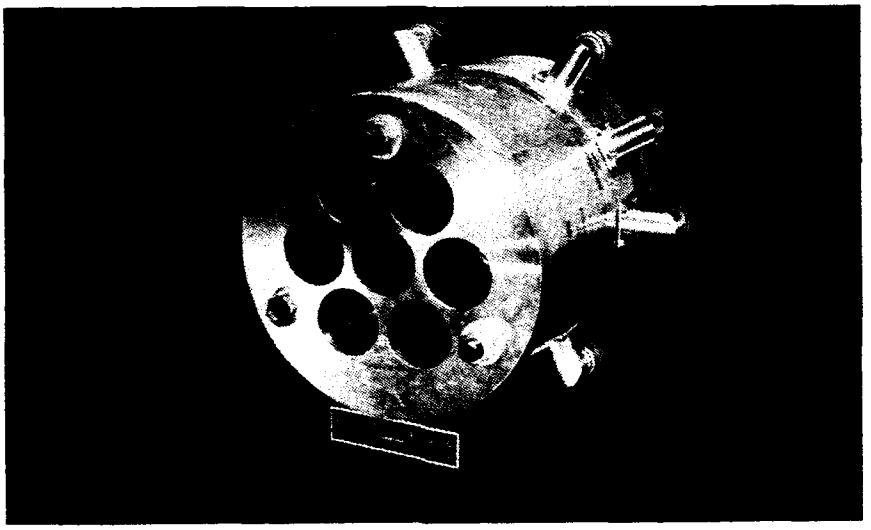

Figure 1. Photograph of the 7-channel differential absorption spectrometer.

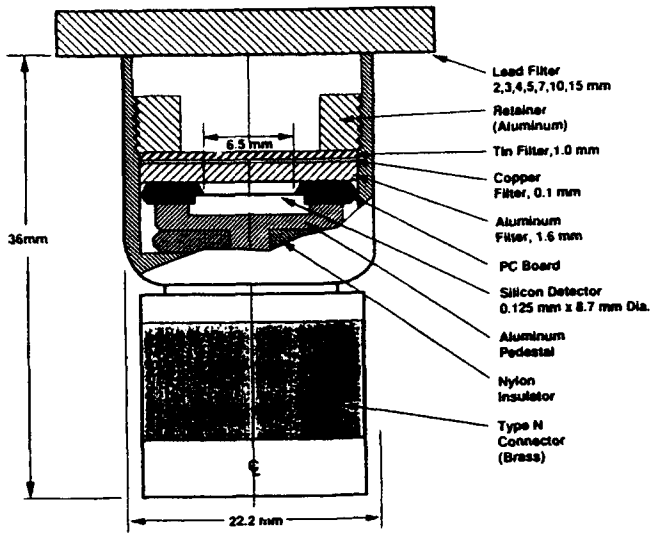

Figure 2. Detail of pin diode detector and filters.

For fast transient response, the pin diode detector must have minimum times for hole transit and RC decay. We selected the Quantrad 025-PIN-125 detector, which has a 3 ns FWHM response to a narrow radiation pulse. This pin diode has a thickness of 0.125 mm and a nominal 25 mm^2 aperture for soft x-ray measurements, but the total die area of 60 mm^2 is sensitive to the high energy bremsstrahlung. The pin diode detectors are reverse-biased at -500 V to provide a reasonable trade-off between large dynamic range and good junction life. To prevent additional response from photo-conduction in the charged bias cable, the isolation resistor and blocking capacitor of the biax network are enclosed within the lead housing.

Calibration was accomplished with theoretical calculations of x-ray production and absorption using the TIGER Monte Carlo codes[4] for coupled electron/photon transport. Details of the calculations have been reported elsewhere,[5] and the results are summarized in Figure 3. The theoretical detector dose (D) versus filter thickness (x) data can be fit by a function of the form $D(x) = \exp(a + bx + c/x)$; the reduced chi-squared values are less than one. The three fit parameters depend upon the beam potential, and the third term in the exponential accounts for spectral hardening of the filtered bremsstrahlung, which is most pronounced at the front surface, i.e., thinnest filters.

To obtain a theoretical calibration curve for the beam potential we characterize each dose versus thickness profile of Figure 3 by a characteristic filter thickness, i.e., one which produces an e-fold attenuation of the detector response relative to the 2-mm filtered detector. This characteristic filter thickness is plotted as a function of electron beam potential (i.e., spectral endpoint voltage) in Figure 4. The quadratic polynomial fits provide a convenient means to obtain the spectral endpoint

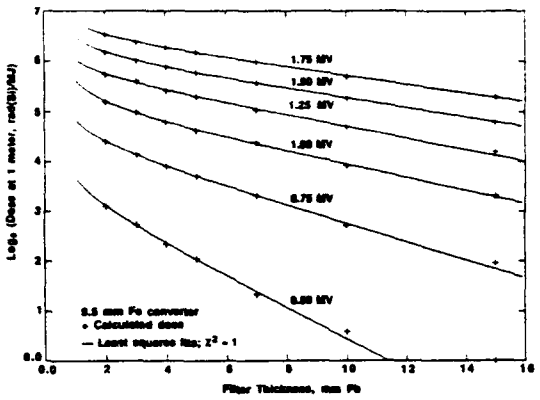

Figure 3. Theoretical detector dose versus filter thickness curves for various electron energies; converter is 9.5 mm iron.

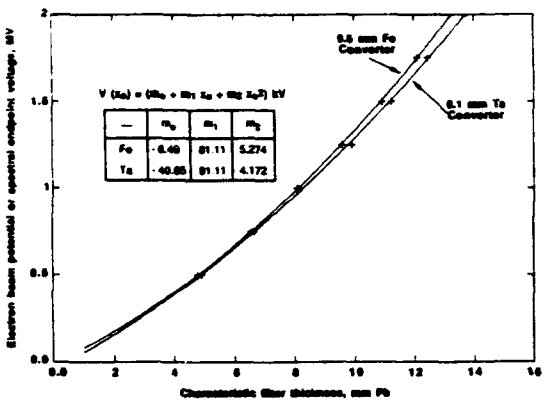

Figure 4. Theoretical calibration curves for spectral endpoint voltage as a function of characteristic (1/e) filter thickness.

voltage from measured detector data. Because the lead filters over the detectors are relatively thick, the calibration curves are insensitive to the electron incidence angle or to differences in converter thickness or material.

The experimental data are unfolded at each point in time by first, performing a least squares fit of detector signal versus filter thickness; second, calculating the characteristic filter thickness; and third, by evaluating the quadratic fit for the beam potential. To confirm the theoretical response calculations, the spectrometer was exposed to the PITHON flash X-ray source[5]. The peak spectral endpoint voltage agreed with the conventional electrical voltage measurement to within 50 kV. The measured detector dose versus filter thickness profiles were also in excellent agreement with the theoretical profiles.

Diode Voltage Measurements on PM1

In inductive energy store (IES) accelerators, a plasma opening switch (POS) usually separates the diode load from the upstream voltage monitor. Because the POS is a poorly understood active circuit element, the corrected electrical measurement of diode voltage is obviously suspect. Fortunately, the differential absorption spectrometer provides an alternative technique for measuring diode voltage. A third measurement of diode voltage can be deduced from the ratio of x-ray doserate $\dot{D}$ to diode current I_d. TIGERP calculations predict that x-rays produced in a 9.5-mm-thick steel converter will produce a dose rate (in a plastic scintillator) roughly proportional to $IV^{3.3}$ for diode voltages near 1 MV. Thus, we obtain a relative voltage wave shape $V \sim (\dot{D}/I_d)^{0.3}$. Recent experiments on PM1, a 300-kJ IES/POS testbed,[6] have provided an opportunity to compare the diode voltage measurements.

The spectrometer was deployed on PM1 with 6 channels (15-mm filtered channel omitted). The x-ray detector waveforms illustrated in Figure 5 have all been properly normalized and corrected for digitizer offset. Figure 6 presents the detector signal versus filter thickness profiles at 10 ns intervals beginning with the x-ray peak. The experimental data are well fit by the same functional form as was used for the theoretical data. The quality of the fit degrades at 565 ns when the signal-to-noise ratio is small, particularly for the heavily filtered channels. Figure 7 shows the diode potential unfolded using the technique described above; the 100-ns window corresponds to the time during which the 2-mm filtered detector signal is above 5% of its peak. The unfold technique also provides an estimate of the experimental error produced by the noise; the theoretical errors are presumed to be negligible. Near the x-ray peak, the unfolded potential has a standard error of only 50 kV; the standard error increases to about 100 kV when the detector signal is at 5% of the peak.

In PM1, the POS is separated from the upstream voltage monitor by a constant-impedance, magnetically-insulated transmission line whose transit time is not short compared to the pulsewidth. In this case, the inductive correction for the load voltage must be replaced by a transmission line correction obtained by decomposing the line voltage into forward and reverse waves. The POS voltage V_p can then be expressed in terms of the voltage V_m and current I_m measured by monitors at the input end of the line

$$V_p(t) = \frac{1}{2}[V_m(t+T) + V_m(t-T)] - \frac{Z}{2}[I_m(t+T) - I_m(t-T)],$$

where Z and T are the characteristic impedance and transit time of the line. The electrical voltage at the diode was obtained by subtracting an inductive correction from the corrected POS voltage, i.e. $V_d = V_p - L\dot{I}_d$.

Three techniques were used to measure the voltage in an electron beam diode driven by a POS on PM1. Figure 8 presents a comparison of the three measurements; the relative dose rate monitor has been scaled to match the peak spectral endpoint voltage. All three measurements agree within 100 kV after the x-ray pulse has peaked, but the corrected electrical voltage rises 10 ns earlier than either the spectral endpoint voltage or the dose-rate voltage. We believe the discrepancy is caused by plasma motion from the POS toward the diode, which generates an $\dot{L}I$ term missing from the inductive correction.

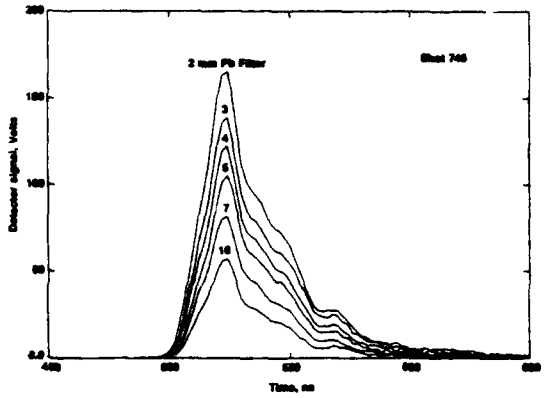

Figure 5. Spectrometer detector signals for an electron-beam diode load on DPM1.

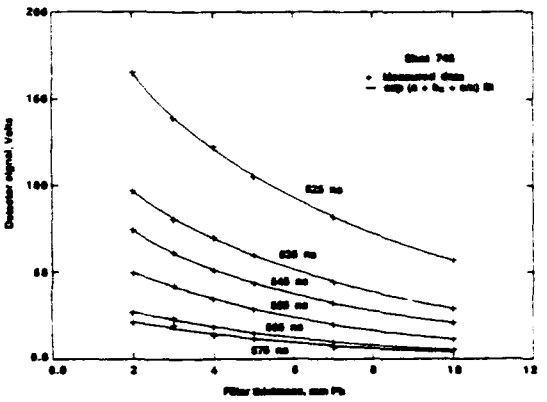

Figure 6. Detector signal versus filter thickness data at 10 ns intervals after X-ray peak.

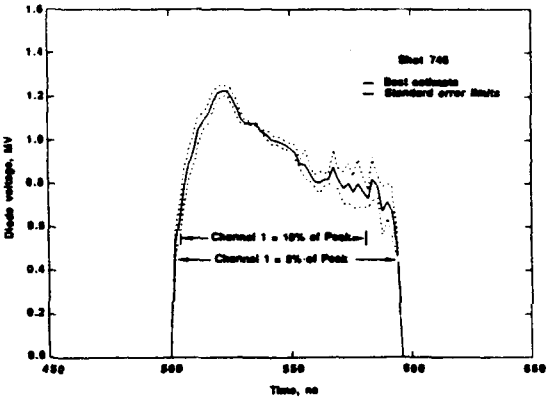

Figure 7. Spectral endpoint voltage waveform unfolded from spectrometer data; dashed lines indicate one standard error.

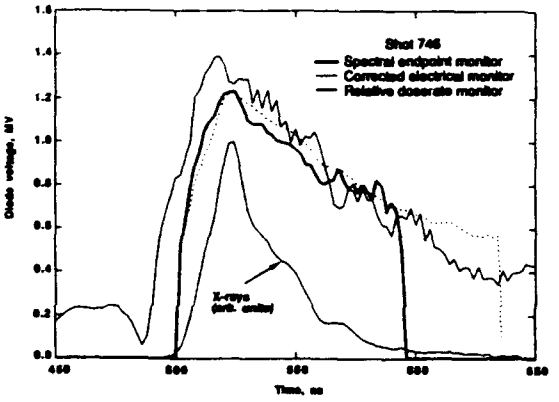

Figure 8. Comparison of DPM1 diode potential waveforms from spectrometer, corrected electrical monitor, and relative dose-rate monitor.

References

1. J. Riordan and J. Meachum, "Endpoint Voltage Monitor" (unpublished report, 1989).

2 J. Rauch, *et al.*, J. Radiation Effects 9, 288 (1990).

3. F. Young, "Voltage Diagnostics for a Bremsstrahlung Diode with a Plasma Opening Switch" (unpublished report, 1989).

4. J.A. Halblieb and T.A. Mehlhorn, Nucl. Sci. Eng. 92, 338 (1986).

5. J.C. Riordan et al, Proc. 8th IEEE Pulsed Power Conference, p. 340 (1991).

6. P.S. Sincerny et al, "Inductive Energy Store (IES) Technology for Multi-Terawatt Generators" (these proceedings).

A NEW TIME-RESOLVED ENERGY-FLUX GAUGE FOR PULSED ION BEAMS*

Steven H. Richter and Donald V. Keller

Ktech Corporation
901 Pennsylvania NE
Albuquerque, NM 87110-7403

Abstract

A new time-resolved energy-flux (TREF) gauge has been developed and tested for direct flux measurement of charge- and current-neutralized light-ion beams. This diagnostic technique is effective for any rapid energy deposition where the following conditions are met: (a) the time for stress release wave transit across the deposition region is much less than the deposition time, (b) the energy deposition depth is approximately flat over the penetration depth and constant in time, (c) the Gruneisen parameter is independent of energy or the energy dependence is known, and (d) the material behaves elastically. TREF gauge fluence measurements of 1-MeV proton beams agree well with simultaneous fluence calorimeter measurements. The gauge may be useful for diagnosing other pulsed energy deposition sources where the deposition region is shallow with respect to the deposition time.

Introduction

Ion beams are being developed for inertial confinement fusion (ICF) studies [1], while light-ion beams are being developed for soft x-ray material response simulation [2,3]. It is necessary to diagnose these beams to understand what beam parameters have been achieved and the nature of beam-target interactions. Diagnostics presently used for pulsed ion beams, such as bolometers, Thomson parabolas, Faraday cups, x-ray and ion pinhole cameras, and spectrometers, typically require intensive labor for analysis to extrapolate the required information, often have high measurement uncertainties, typically do not provide immediate answers, and are costly [4,5,6,7]. Unlike x-rays, ions deposit energy in materials nearly uniformly over the ion range ($\approx$10 mg/cm^2), and the range is roughly independent of target material [1]. The ion range is typically much less than the distance a stress wave travels during deposition; thus, the material rapidly stress relieves as energy is deposited. Under these conditions the stress that propagates out of the deposition region is proportional to the rate of change of flux, as described below. This is the principle of the new TREF gauge. It has been used in preliminary tests with light-ion beams (1-MeV protons) and may also be applicable to other ion beams and sources, e.g., lasers and x-rays.

Theory

Consider an instantaneous energy loading dose, D, uniform through a depth, δ. The instantaneous pressure, P_o, produced in the deposition region is given by $P_o = \Gamma\rho_o D$, where Γ is the Gruneisen parameter for the material,

*Work supported by the Defense Nuclear Agency Shock Physics Directorate under Phillips Laboratory contract number F29601-89-C-0025.

and ρ_o is the initial density. The pressure in the deposition region relieves into the unheated material to a stress determined by the relief adiabat. The stress at which the adiabat intersects the Hugoniot of the material determines the peak transmitted stress, σ_p, given by $\sigma_p = 1/2\ P_o$. A wave propagating into the unheated region will therefore have a peak stress given by $\sigma_p = \frac{1}{2}\Gamma\rho_o D$. If the Gruneisen is energy independent and if the material behaves elastically, then the rate of change of stress is proportional to the rate of change of dose:

$$\frac{d\sigma}{dt} = \frac{\Gamma\rho_o}{2}\dot{D},\ \dot{D} = \frac{dD}{dt}\ ;\ \textit{therefore},\ \sigma(t) = \frac{\Gamma\rho_o}{2}\int_c^t \dot{D}dt\ . \tag{1}$$

For deposition over a finite time, τ, and within a depth, δ, with $\delta << c\tau$, where c is the sound speed in the material, relief waves will start canceling after a time, δ/c; therefore, the peak stress is obtained by integrating up to time t = δ/c:

$$\sigma(t) = \frac{\Gamma\rho_o}{2}\int_o^{\delta/c} \dot{D}dt\ . \tag{2}$$

If energy deposition occurs uniformly over the thin deposition region, δ, then fluence $\varphi = \int_o^{\delta} D\rho_o dx = \delta\rho_o D$, and differentiation gives $\dot{D} = \dot{\varphi}/\rho_o\delta$, where $\dot{\varphi}$ is the flux, $d\varphi/dt$. Equation (2) then becomes

$$\sigma(t) = \frac{\Gamma}{2}\int_o^{\delta/c} \frac{\dot{\varphi}}{\delta}dt\ . \tag{3}$$

If δ is also independent of time for a time δ/c (approximately true for MeV ion beams and monoenergetic X-rays), then

$$\sigma(t) = \frac{\Gamma}{2\delta}\int_o^{\delta/c} \dot{\varphi}dt\ . \tag{4}$$

Because we are considering only thin deposition regions and situations where $t >> \delta/c$ and $\delta/c << \tau$ over the short time interval δ/c, we may take flux to vary linearly in time: $\dot{\varphi} = a+bt$. Since the flux at $t = 0$ is zero, $a = 0$, and $b = \bar{\varphi}$, assumed constant over time δ/c. Therefore, $\dot{\varphi} = \bar{\varphi}_o t$, and equation (4) becomes

$$\sigma(t) = \frac{\Gamma}{2\delta}\bar{\varphi}\int_o^{\delta/c} tdt = \frac{\Gamma\delta}{4c^2}\bar{\varphi}(t)\ . \tag{5}$$

Equation (5) shows that if the flux, $\dot{\varphi}$, is not changing with time, then the stress is zero. Otherwise, the pressure is proportional to the rate of change of flux (second derivative of fluence).

To summarize, several conditions must be met for equation (5) to be valid: (a) the time for a wave transit across the deposition region is much less than the deposition time; (b) energy deposition is approximately flat over the depth, δ, and constant in time; (c) the Grüneisen, Γ, is energy independent or the energy dependence is known; and (d) the material behaves elastically. The third condition is true for monoenergetic X-ray beams and very nearly true

for ion beams since the ion range depends only weakly on ion energy (hence deposition time) and the ion spectrum is fairly narrow. If condition (b) does not hold, then the time dependence of δ, $\delta(t)$, can be used in equation (3). This would be required only if δ changes significantly in a time, δ/c. In the case of MeV ion beams, the time is directly related to the ion energy via the time-of-flight from the ion source to the target. Ion energy and hence deposition range, δ, can thus be determined as a function of time. Since $\sigma(t)$ and $\delta(t)$ are measurable, $\bar{\varphi}(t)$, $\dot{\varphi}(t)$, and $\varphi(t)$ are all directly available.

Modeling

The validity of the TREF gauge concept and equation (5) was confirmed with the PUFF-TFT [8] hydrodynamic code.[§] In order to correlate calculations with experimental results, the target geometry was modeled identically to the actual test specimens used on Gamble II. A target of aluminum 1100, 0.051-mm thick, backed by a thick quartz gauge[††] was numerically loaded with a constant dose-depth profile of 113 J/g, which closely resembles a Gamble II ion deposition profile at a fluence of 0.4 J/cm^2. This energy level ensures that the aluminum target does not yield or melt.

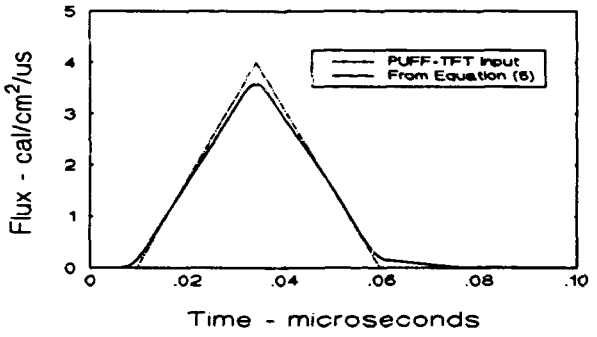

Figure 1. Calculated flux in aluminum.

A triangular timing profile, 25-ns full-width-half-maximum (FWHM), was used to approximate the temporal flux pulse (see figure 1, dashed curve). Aluminum 1100 was modeled with well known equation of state parameters [9]. Figure 2 illustrates the PUFF hydrodynamically calculated, resulting stress profile. As energy is loaded into the sample at a positive flux rate, a compression pulse is generated; and when the flux rate becomes negative a tensile stress is generated, as predicted from equation (5). For 1100 aluminum, $\Gamma = 2.0$ and $c=5.24X10^5$ cm/s. A deposition depth of $\delta=0.002$ cm was used for PUFF calculations [10]. Using these values,

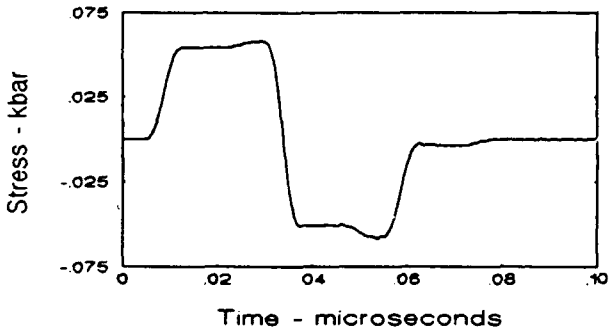

Figure 2. PUFF-generated stress in aluminum.

[§] A Lagrangian hydrodynamic code used to model shock effects from rapid energy deposition or impact.

[††] Quartz gauges were fielded in shorted mode for noise suppression. They were 0.508-cm thick and 3.43-cm diameter with a 1.87-cm diameter guard ring to give a 0.9-μs, 1-dimensional read time.

equation (5) gives

$$\dot{\varphi} = K\int \sigma(t)\,dt \quad , \tag{6}$$

where φ is in cal/cm^2, σ is in kbar, and $K = 4c^2/\Gamma\delta = 2.71 \times 10^{15}$ cal/cm^2/kbar-sec^2. Applying equation (6) to the PUFF calculated stress profile (figure 2) yields the flux profile illustrated as a solid curve in figure 1, verifying the appropriateness of equation (5).

TREF Gauge Design

For experimental verification of gauge operation, TREF gauges were designed and fielded on the Gamble II light-ion accelerator [11] at the Naval Research Laboratory (NRL). Quartz piezoelectric crystals [12] were used to measure the stress behind a thin aluminum target. This combination was chosen because the acoustic impedance (product of density and wave speed) for quartz and aluminum are very closely matched such that there are almost no wave reflections at the quartz/aluminum interface. Other stress sensors (e.g., PVDF, lithium niobate, PZT-5, laser interferometry) could be used with other materials depending upon the amplitude and duration of the stress to be measured. The closer to the deposition region that the stress measurement is made, the greater the resolution of this diagnostic. If the stress gauge is too far from deposition, stress relief and attenuation effects tend to "smear out" the stress profile, and the ability to resolve details of the loading function is lost. In our experiments the aluminum was 51-μm thick, just greater than the ion range, and exposed to a proton beam fluence of 3.3 J/cm^2.

The TREF gauge stress is proportional to the rate of change of flux. In general, the fluence must be low enough that the target material is not heated to yield or melt so that the wave propagation properties are well known and the wave shape is not distorted. Because of this condition, the target/gauge assemblies are also usually re-usable, as well as being quite inexpensive to fabricate.

Experimental Results

Flux and Fluence

Gamble II ion pulses yield a 30 KJ, 55 ns FWHM, 1-MeV proton beam that is charge and current neutralized. Fluences at the target vary with target distance from the ion diode source and may range from 0.1 J/cm^2 at a distance of 200 cm to over 500 J/cm^2 at 30 cm. Figure 3 illustrates a stress profile measured at a fluence[‡] of 0.78 cal/cm^2 on shot 5073. Figure 4 shows the inferred flux history using equation (5) and figure 5 shows the time resolved fluence. The total fluence of 0.75 cal/cm^2, measured with the TREF gauge, agrees well with the fluence measured with reference calorimetric diagnostics (0.78 $\pm$ 0.15 cal/cm^2).

---

‡ Fluences were measured with both calorimetry and carbon activation diagnostics. Techniques are described in references 2, 7, 10, and 11.

Spectrum

The stress record obtained with Gamble II shown in figure 3, has a zero time that corresponds to the time of machine fire, i.e., approximately the time during which ions were generated at the diode. A given instant of time on the stress record thus corresponds to the time-of-flight of the ions arriving at that time. (The times must be adjusted slightly for the transit time of the stress wave through the target to the stress gauge and for the rise-time of the power pulse at the diode during which the ions are generated.) Since the diode-to-target distance is accurately known, the time corresponds uniquely to ion energy. Thus, the flux history is determined from the stress record as well as the ion beam spectrum history. This energy spectrum history can be compared with that obtained from the voltage and current measurements at the diode. Of course, energy losses in transit from the diode to the target must also be accounted for. To illustrate, for the experimental results shown in figure 3, the flux peak (2E7 cal/cm^2/s) occurs at a time of 265 ns. The diode target distance was 200 cm, so that the average ion velocity was 0.82 cm/ns or an ion energy of 0.54 MeV. This ion energy is less than the initial ion energy becuse of energy loss during propagation through 2 m of 1-torr air and through a thin filter placed in front of the target.

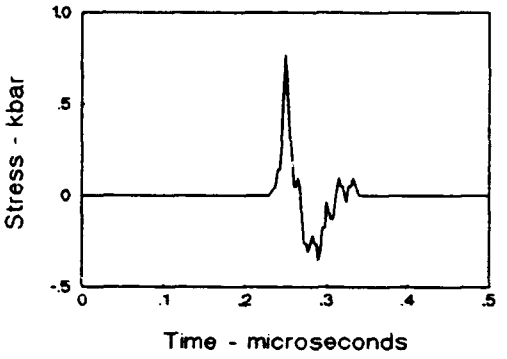

Figure 3. Measured stress from Gamble II.

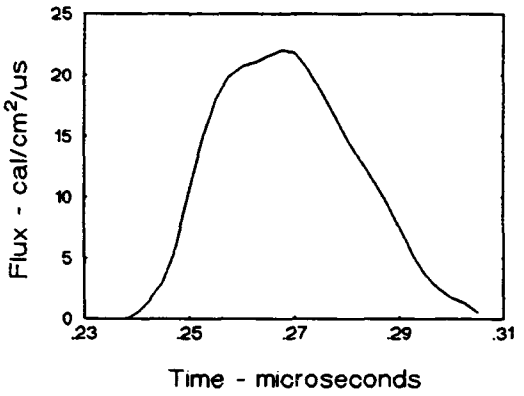

Figure 4. Calculated flux from Gamble II ions.

Conclusion

In preliminary experiments the TREF gauge has demonstrated a capability for accurately measuring the detailed fluence history of a 1-MeV, 60-ns pulsed ion beam. The total fluence agreed well with calorimetric measurements, and spectrum history information is also obtained. By choosing the target material and type of stress sensor appropriately, the technique may be applied to x-ray energy sources (e.g., pinched-beam plasma-radiating sources and pulsed magnetic confinement sources) as well as both heavy- and light-ion beams. In addition to the proton beam from Gamble II, which is used

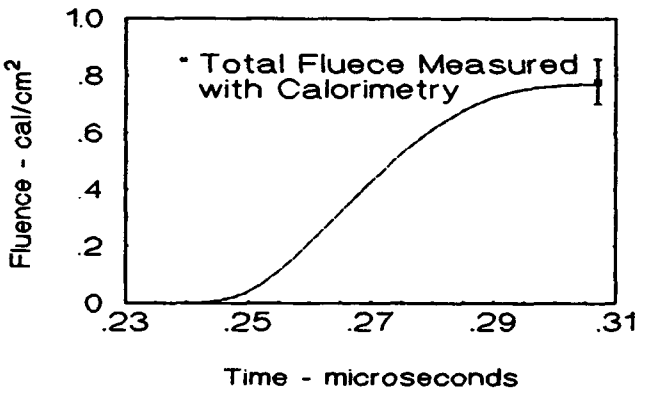

Figure 5. Fluence profile for Gamble II ions.

to simulate nuclear weapon x-ray effects, "light" ion beams of p^+, Li^+, etc., used for ICF, are also candidates for the use of this diagnostic. In the latter case, the TREF gauge may be used on a Rutherford scattered portion of the intense beams. For pulsed beam applications, the gauge provides the capability to time-resolve the particle energy and velocity if the particle species are known. In the case of a large-area beam, the lateral beam characteristics could be determined by using an array of gauges.

REFERENCES

1. Fessenden, T.J., et. al., "Preliminary Design of a ~10 MV Ion Accelerator for HIF Research," Laser and Particle Beams, Vol. 5, Part 3, p. 457, August, 1987.

2. Richter, S.H., et. al., "Soft X-Ray Material Response Simulation with Intense Light-Ion Beams," J. of Radiation Effects, Research and Engineering, Vol. 9, No. 1, December, 1990.

3. Hanson, D.L., et. al., "The Fidelity of Using Intense Ion Beams to Simulate the Response of Materials to X-Rays," J. of Radiation Effects, Research & Engineering, 1988.

4. Leeper, R.J., "New Diagnostic Developments for [illegible] Ion Beam Experiments, Laser and Particle Beams, Vol. 7, Part 4, p. 649, November, 1989.

5. Maenchen, J., et. al., "Intense Ion Beam K Measurements on PBFA-II," Rev. Sci. Instrum., 59(8), August, 1988.

6. Melhorn, T.A., et. al., "Simulation and Interpretation of Ion Beam Diagnostics on PBFA-II," Rev. Sci. Instrum., 59(8), August, 1988.

7. Young, F.C., et. al., "Diagnostics for Intense Pulsed Ion Beams," Rev. Sci. Instrum., 48, No. 4, April, 1977.

8. Watts, A.J., et. al, "Thin Film Transport (PUFF-TFT) Computer Code Development," Parts 1 and 2, AFWL-TR-88-66, Air Force Weapons Laboratory, Kirtland AFB, NM, June, 1988.

9. Rice, M.H., "PUFF74 EOS Compilation," AFWL-TR-80-21, Air Force Weapons Laboratory, Kirtland AFB, NM, August, 1980.

10. Richter, S.H. and Lee, L.M., "Ion Beam Simulation Technique Validation," WL-TR-89-97, Air Force Weapons Laboratory, Kirtland AFB, NM, March, 1990.

11. Mosher, D. and Stephanakis, S.J., "An Intense Light Ion Source for NWE Simulation," Presentation at the Simulation Fidelity Workshop III, Colorado Springs, CO, September 21, 1989.

12. Reed, R.P., "The Sandia Field Test Quartz Gauge - Its Characteristics and Data Reduction," in Selected Papers on Piezoelectricity and Impulsive Pressure Measurements, SAND78-1911, Sandia National Laboratories, Albuquerque, NM, December, 1978.

Theoretical Spectroscopic Analysis of Intense Ion Beam-Plasma Interaction in the PBFA II Gas Cell

P. Wang, J. J. MacFarlane, and G. A. Moses
Fusion Technology Institute, University of Wisconsin, Madison, WI 53706

J. E. Bailey
Sandia National Laboratories, Albuquerque, NM 87185

Abstract

Time-resolved visible emission spectra from the PBFA II argon gas cell were measured in recent light ion beam-target interaction experiments. These emission spectra may be used to study the physics of beam transport and diagnose the cell plasma conditions. We discuss the theoretical analysis of the emission spectra in the wavelength region from 4300 to 4420 $\AA$, where several ArII lines are observed. We examine opacity effects on the emission lines and assess the importance of beam excitation effects. Theoretical spectra are compared with the experimental data.

Introduction

Visible spectral line emission from the PBFA II argon gas cell is of current interest because it can be used as a diagnostic for both light ion beam properties and cell plasma conditions[1]. For example, spectral line profiles emitted by atoms in the transport region may be sensitive to the electron density. By measuring and modeling the line profiles one may be able to determine electron densities in the gas cell, which in turn can be used to estimate the extent of beam neutralization. Spectral lines can potentially be produced by both ion-impact excitation and thermal electron collisional excitation. If one can identify transitions dominantly produced by ion-impact excitation, then the time-dependent line intensity can be used to measure beam current and beam divergence. It is expected that the ranges for cell plasma conditions are $T_e = 0.5 - 5\ eV$ and $N_e = 10^{16} - 10^{18}\ cm^{-3}$. Under such conditions, opacity effects for the emission lines may be important. If the emission lines are optical thick, spectral line profile interpretation must be in conjunction with the radiation transport analysis.

In this paper, we study the opacity effects on the line emissions from PBFA II argon gas cell and compare calculated emission spectra with the experimental data. We present results of calculations

comparing the effects of beam excitation versus thermal excitations. And we also examine the effects of carbon impurity of ion beam on level populations.

Theoretical Models

We present in this section a brief overview of the theoretical models used to compute the spectral properties and related atomic data. A detailed description of these models is presented elsewhere.[2-5]

In our calculations, we use a collisional-radiative equilibrium (CRE) code[2] in which steady-state ionization and excitation populations can be computed by solving multilevel atomic rate equations self-consistently with the radiation field. For the plasma conditions discussed in this paper, the distribution of atomic level populations were found to be close to local thermodynamic equilibrium (LTE). We have therefore neglected photoexcitation and photoionization effects in level population calculations.

Our atomic model for Ar consists of 192 levels distributed over the first five ionization stages (ArI–ArV). Energies for levels related to the lines of interest were selected from National Bureau of Standards tables[6]. Other level energies were obtained from Hartree-Fock calculations. The collisional coupling are complete for the resonant transitions from the ground state to the higher levels and the cross sections are calculated with Born-Coulomb approximation, while the less important cross sections of remaining transition among the excited levels were approximated by a semi-classical impact parameter model, valid for dipole-allowed transitions. Ion impact excitation and ionization cross sections are calculated using a Plane Wave Born approximation (PWBA) model. It is necessary to indicate that the the beam excitation and ionization effects were not directly included in the CRE calculation in this preliminary study. The beam effects are checked separately by comparing the excitation rate with those of corresponding thermal electron process.

After the level populations are obtained, emission spectra are computed using an escape probability radiative transfer model which includes contributions from bound-bound, bound-free, and free-free transitions. In examining the opacity effects of spectral emission lines, spectral line widths are critical. Voigt line profiles are used to model line shapes. Natural, Doppler and Stark broadening effects are considered. Stark width is calculated in the electron impact approximation using the semi-empirical method of Griem[7]. By comparing the calculated Stark widths with available experimental data[8], the agreement is typically within a factor of 2.

Calculations and Discussions

In this study, calculations were run for the plasma conditions of $n_{ion} = 1.8 \times 10^{17}\ cm^{-3}$, T_e =1, 2, 2.5, 3, and 4 eV. In each case we assumed a planar plasma of width 4 cm which represents

the height of the gas cell and therefore the maximum line-of-sight distance through the Ar plasma. The electron density dependence on temperature is given in Table I. We have looked in particular at the wavelength region from 4300 to 4420 Å. All of the lines in this region have been identified as ArII lines. An experimental spectrum and the corresponding transition diagram are presented in Figure 1.

Table I: Dependence of Electron Density on Temperature

$T(eV)$	$n_e\ (10^{17}cm^{-3})$
1.0	0.4
2.0	2.2
2.5	3.2
3.0	3.7
4.0	5.1

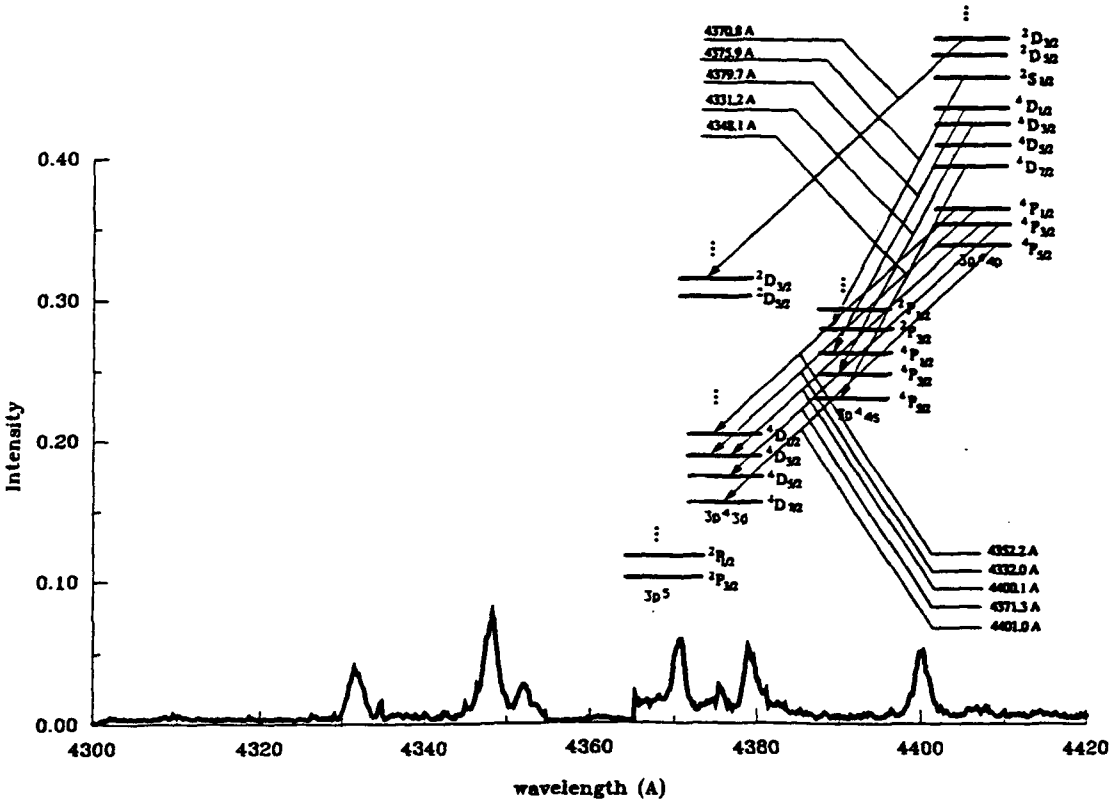

Figure 1. Spectra for shot 4659 in PBFA II experiment and the corresponding transition diagram.

Figure 2 shows a comparison between calculations with and without opacity at $T_e = 2.5\ eV$. The 4348Å line is most strongly affected by opacity, while some of the other lines are to a smaller extent. This is in qualitative agreement with the experimental spectrum because the 4348Å line width was found to be considerable broader than the other lines[1]. We checked the sensitivity of the spectrum to the temperature and found that at $T = 1\ eV$ and $T = 4\ eV$ the spectral flux is very small. The ArII lines show up best at $T = 2 - 3\ eV$. The ratio of the 4348Å line to other lines

increases above $T = 2.5\ eV$ because the opacity begins to drop. This can be seen more clearly from Figure 3, which shows the optical depth as a function of temperature and wavelength. The $4348\mathring{A}$ line has the greatest optical depth, with its line center value rising to about $5 - 6$ at $T = 2 - 2.5$ eV.

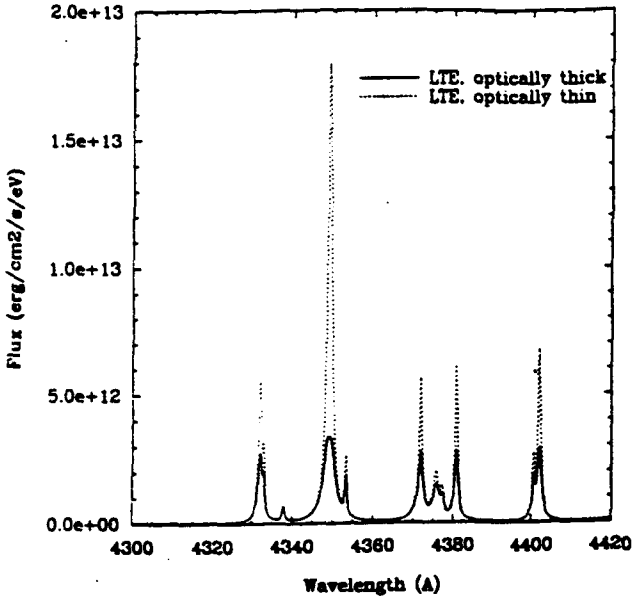

Figure 2. Opacity effects on lines of interest.

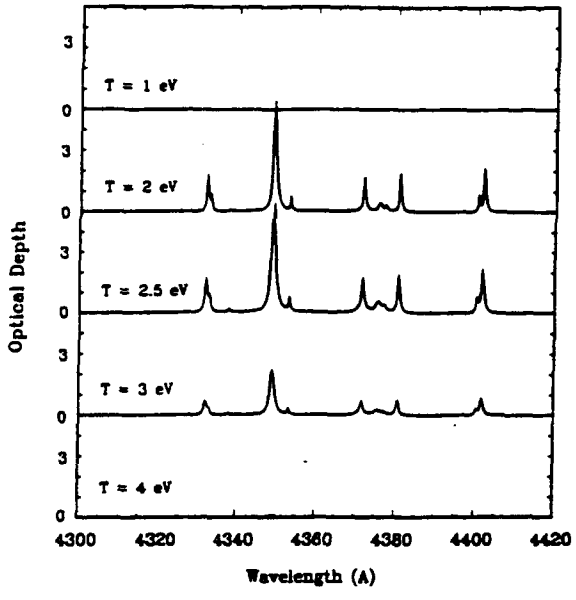

Figure 3. Sensitivity of optical depth to temperature for lines of interest.

The role of ion beam impact excitation on level populations and line intensities can be examined by comparing the excitation rate with those of corresponding thermal electron collisional processes. For the intercombination transitions ($\Delta S = 1$), ion impact excitation cross sections are extreme small for high energy ion beam ($\mathcal{E}_{ion} \leq 1MeV$). This is because there is only exchange interaction for intercombination transitions, and when $\mathcal{E}_{ion} \gg 1836 \times \Delta E_{ij}$, the exchange cross section decreases $\propto \mathcal{E}_{ion}^{-3}$. For the transitions with $\Delta S = 0$, ion impact excitation cross sections are substantially larger in the beam energies of interest. The excitation rate can be comparable to or even dominant the thermal electron collisional rate. Figure 4 compares the excitation rate for electron collisional excitation versus proton beam impact excitation as a function of the electron temperature for several important transitions relevant to the lines of interest. It can be seen that the rate for electron collisional excitation and proton beam impact excitation are approximately the same for allowed transitions when $T = 2 - 3\ eV$. For intercombination transitions, the electron collision rate dominates. For the spectral lines of interest, most of the excited levels are coupled to the ground state by intercombination transitions, hence the direct coupling by ion impact excitation is not important for these levels. However, the populations of these levels may be affected by ion impact excitation in an indirect way, *i.e.*, these levels can be strongly coupled to other levels which are

related to the ground state via allowed transition by electron collisional excitation.

There is about 15% carbon impurity in the high energy proton beam. Whether carbon impact may play a role in affecting the level populations depends on the magnitude of corresponding excitation cross sections. Figure 5 shows the proton-impact and carbon-impact (CVII) cross sections for several excitation transitions. In PBFA II experiments, the energy of proton is about 6 MeV and the energy of carbon impurity is about $12 - 21$ MeV. The current density of carbon impurity is a factor of 4 smaller than that of proton, while the corresponding carbon-impact excitation cross section is about several times of the proton-impact cross section and hence the excitation rates are about the same. This suggests that for those transitions in which ion-impact excitations are important, both proton and carbon excitation should be considered.

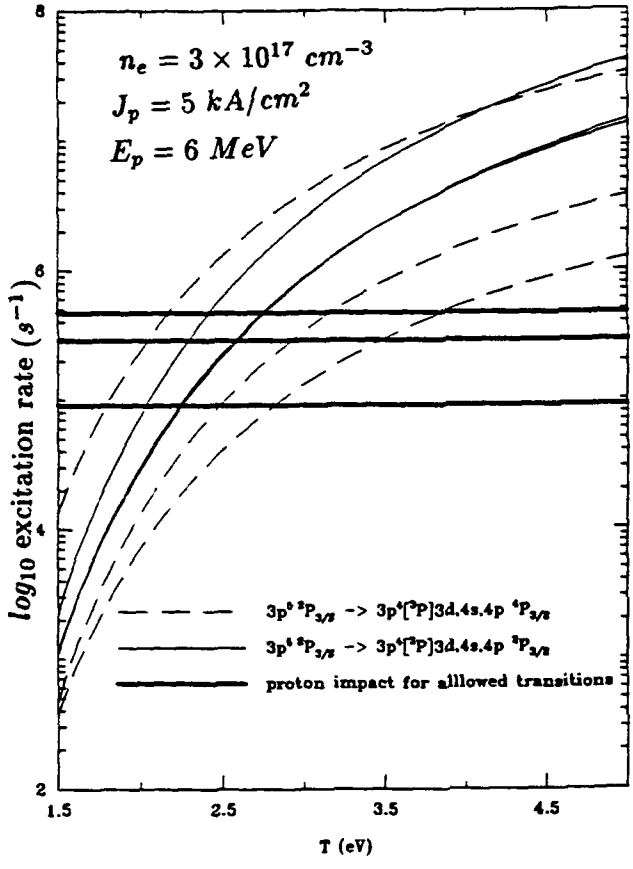

Figure 4. Electron collisional and proton beam impact excitation rate

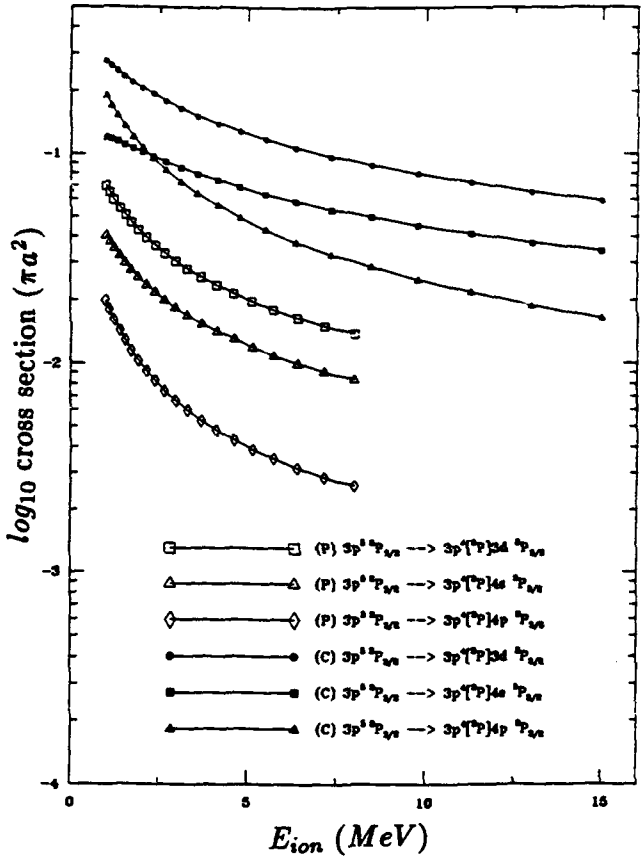

Figure 5. Proton- and carbon-impact excitation cross sections

Summary

The preliminary results obtained from this study show that the strongest ArII lines observed in the PBFA II argon gas cell (*e.g.*, 4348$\AA$) may have optical depths of order ten, while many of the other lines may have optical depths of order unity. Opacity effects should therefore be considered

in interprerating the observed spectra. We also find that the ion beam impact excitation can be important for allowed transitions but can be neglected for intercombination transitions. Carbon- and proton-impact excitation rates were found to be comparable in magnitude. In the followup study, we intend to perform more detailed calculations to assess the importance of ion beam impact excitation effects on level populations.

Acknowledgements

This work was supported by Sandia National Laboratories and Kernforschungszentrum Karlsruhe. Computing support has been provided in part by the National Science Foundation through the San Diego Supercomputing Center.

References

1. Bailey, J.E., Carlson, A.L., Johnson, D.J., McGuire, B.J., Nash, T., MacFarlane, J.J., and Wang, P., 9th International Conference on High Power Particle Beams, Washington, D.C., May 25 - 29, 1992.

2. MacFarlane, J.J., Wang, P., and Moses, G.A., Report No. UWFDM-822, Fusion Technology Institute, University of Wisconsin, Madison, WI, 1990.

3. MacFarlane, J.J., Wang, P., and Moses, G.A., *Lasers and Particle Beams* **8**, 729 (1990).

4. MacFarlane, J.J., Wang, P., and Henderson, D.L., Report No. UWFDM-847, Fusion Technology Institute, University of Wisconsin, Madison, WI, 1991.

5. Wang, P., *Computation and Application of Atomic Data for ICF Plasmas*, Ph.D. Dissertation, Dept. of Nuclear Engineering and Engineering Physics, University of Wisconsin, Madison, WI(1991).

6. Reader, J., Corliss, C.H., Wises, W.L., and Martin, G.A., *Wavelengths and Transition Probabilities for Atoms and Atomic Ions*, National Bureau of Standard (1990).

7. Griem, H.R., Phys. Rev. **165**, 258 (1968).

8. Konjevic, N., and Roberts, J.R., *J. Phys. Chem. Ref. Data* **5**, 209 (1976).

MULTI-DIMENSIONAL DIAGNOSTICS OF HIGH POWER ION BEAMS BY ARRAYED PINHOLE CAMERA SYSTEM

K. Yasuike, S. Miyamoto, N. Shirai, T. Akiba, S. Nakai
Institute of Laser Engineering, 2-6 Yamada-oka, Suita, Osaka 565, Japan
K. Imasaki, C. Yamanaka
Institute for Laser Technology, 2-6 Yamada-oka, Suita, Osaka 565, Japan

Abstract. We developed multi-dimensional beam diagnostics system (with spatially and time resolution). We used newly developed Arrayed Pinhole Camera (APC) for this diagnosis. The APC can get spatially distribution of divergence and flux density. We use two type of particle detector in this study. The one is CR-39 nuclear track detector. APC with CR-39 can get time integrated images. The other one is gated Micro-Channel-Plate (MCP) with CCD camera. It enables time resolving diagnostics. The diagnostics systems have resolution better than 10mrad divergence, 0.5mm spatial resolution on the objects respectively. The time resolving system has 10ns time resolution.

The experiments are performed on Reiden-IV and Reiden-SHVS induction linac. We get time integrated divergence distributions on Reiden-IV proton beam. We also get time resolved image on Reiden-SHVS.

1. INTRODUCTION

The important issue of the ion beam for Inertial Fusion Energy development is the beam generation, the beam focusing and the beam transport [1-3]. To achieve tight beam focusing, an improvement of the beam divergence is necessary. Measuring the divergence of the ion beam is important to understand the diode physics. Shadow-box or one pinhole camera has been employed to know the divergence at one point, not area. In these conventional method, the assumption of beam uniformity is required. But the actual beam or its source is not spatially uniform and changes in time. The newly developed Arrayed Pinhole Camera (APC) achieves to measure the time resolved divergence distribution of the beam at one shot base.

The principle of APC is observating the object area from some different observation angles. The APC consist of pinhole cameras arranged in raw, and each pinhole camera sees the same object area with different angle. Any point in the object is observed by each pinhole camera. Observation angle of each pinhole camera is different, so the distribution of the beam divergence is known by APC (Fig. 1). Not only the distribution of the beam divergence but also that of ion density

is measurable. APC data processing sequence is shown in Fig. 2.

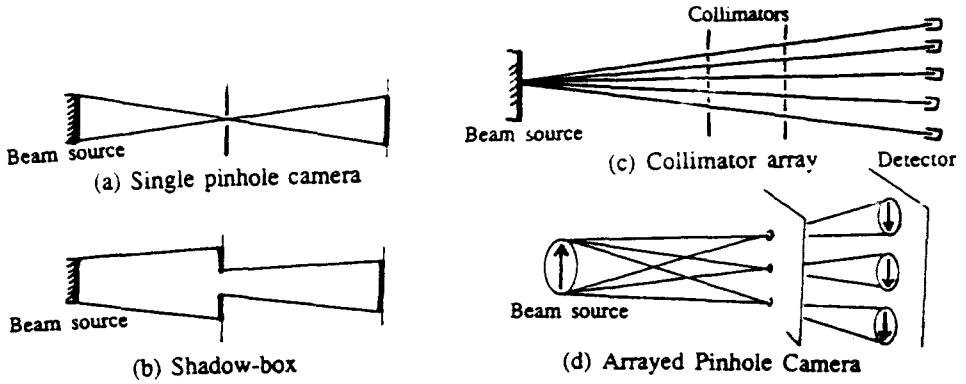

Fig. 1. Some divergence measurement methods are shown. (a) Single pinhole camera. (b) shadow-box. Single pinhole camera and shadow-box measurements are used under the assumption of beam uniformity. (c) Collimater array. Collimater array can dicriminate the object point but it cannot measure area. (d) Arrayed Pinhole Camera.APC works like the collimater array, but can be taken area information.

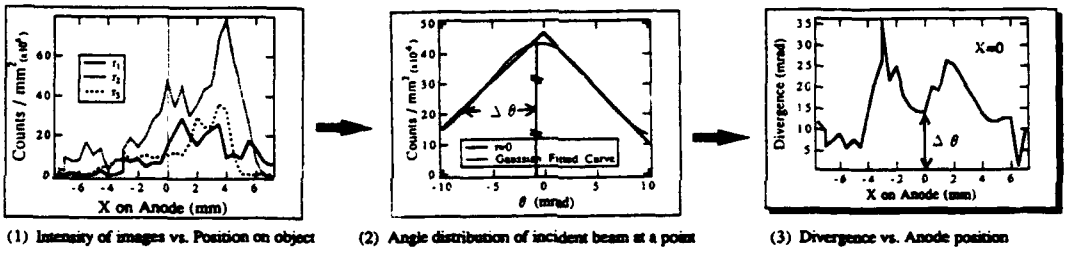

Fig. 2. Sequence of APC data processing. (1) Raw data from particle detector of APC. Each curve correspond to each pinhole camera. "X on anode" is corresponded anode (object) position for each pinhole image. When using CR-39 for particle detector, yield compensation may be required. (2) Remapping images to get angle distribution for each position. The half width of half maximum of the curve fitted angle distribution is a divergence at that position. (3) Plot divergence (2) for each position.

We use two type of particle detectors. The one is CR-39 nuclear track detector and the other is Micro Channel Plate (MCP) with phosphor plate. CR-39 records time integrated images. The MCP is gating pulse driven for time resolved measurements. The time resolution of this method is determined by the pulse width of MCP which is about whole the shot to 10ns.

APC enables multi-dimensional measurements with two physical parameters. Divergence angle, current density are taken with spatially and with time resolution.

2. EXPERIMENT

We performed experiments on Reiden-IV and Reiden-SHVS induction linac. On Reiden-IV experiments, we use APC with CR-39 to get time integrated divergence distribution. On Reiden-SHVS experiments, we used APC with MCP to get time resolved

image.

2.1 Time integrated measurements : APC with CR-39

The experiments were performed on Reiden-IV [4] and magnetic insulated diode. Reiden-IV has a capability to generate 2.8MV, 9Ω, 60ns pulse. The ion source is paraffin filled groove aluminum anode. Active area of the anode is 100cm^2 Current density of the beam is more than 100A/cm^2. The recording density of CR-39 is less than incident flux at focal plane of pinhole camera. Minor angle scattering was used to reduce the flux. two stage cascaded pinhole camera was adopted to use scattering. Scattering film is located at the focal plane of first pinhole camera. Second stage pinhole camera was observe the scattered first pinhole camera images from behind the scattering film. The scattering film was 1000Å thickness Au on 0.1μm thickness mylar film. The scattering angle is about 100mrad and the scattering yield is about 10^{-6} respectively. The structure of this CR-39 type APC is shown in Fig. 3. Experimental configuration is shown in Fig. 4.

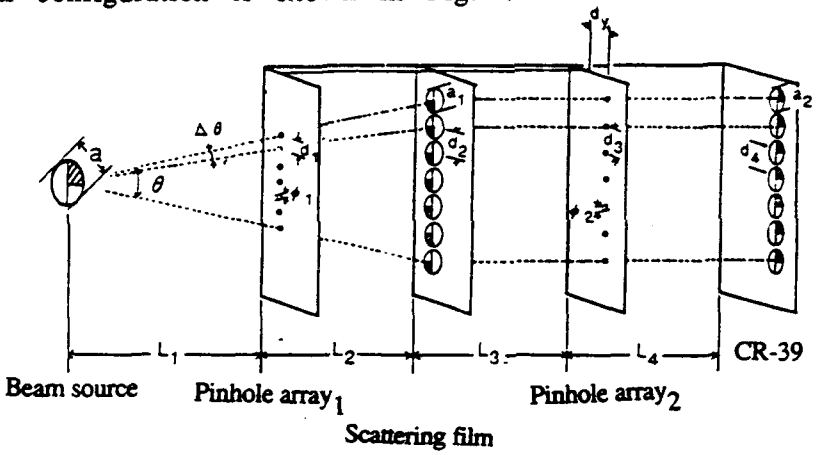

Fig. 3. Arrangements of APC elements. The scattering was used to reduce flux at CR-39. The second stage pinhole camera observes first pinhole camera images from behind the scattering film.

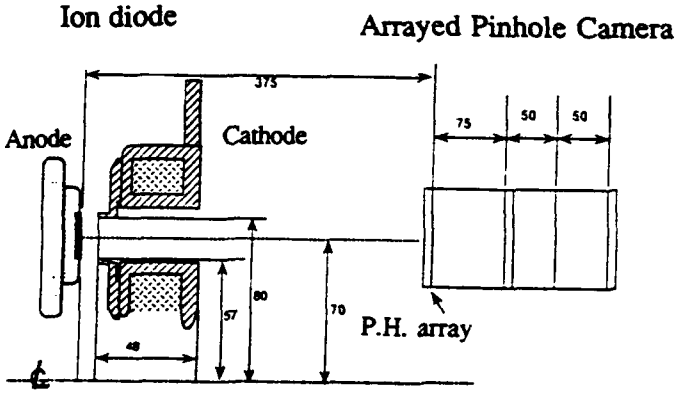

Fig. 4. Experimental configuration for the time integrated measurements.

We change diode parameters as insulating magnetic field (V_{CB} as charge voltage of capacitor bank for insulating field winding). The diode gap was fixed to 10mm. Applied diode voltage was about 1.5MV. The beam is 700keV to 1.2MeV proton beam. The current density of the beam is 140A/cm^2 from biased charge collector. Figure 5 shows the spatial distributions of divergence and flux density. It shows well correlation between divergence and flux. When the V_{CB}=8kV (insulation field B~1.7T at anode edge) deviation of beam divergence is smaller than V_{CB}=6kV (B~1.3T).

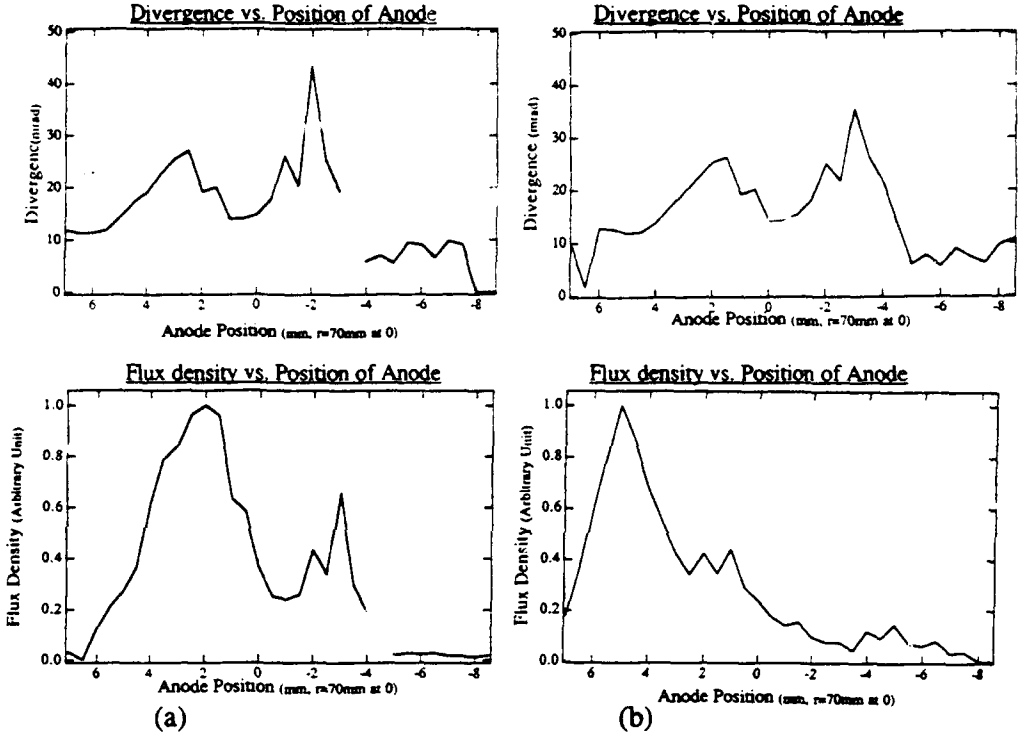

Fig. 5. Divergence and Flux distribution for two different data shot. (a)V_{CB}=6kV(B~1.3T) and (b)V_{CB}=8kV(B~1.7T).

2.2 Time resolved measurements : APC with gated MCP

The experiments were performed on Reiden-SHVS [5-7] induction linac and two stage diode. Reiden-SHVS has a capability to generate 2MV+2MV, 100Ω, 100ns pulse into single or two stage diode. The diode are set at the center of the machine. Positive and negative center stalk are extended from both side of machine. The construction of APC with MCP is shown in Fig. 6. Figure 7 shows experimental configuration of diode and APC. Ion source is the same as Reiden-IV experiment. The diode gap and insulation field of first diode were 10mm and 7kG. In second stage diode, the parameters are 11mm and 9kG respectively. The current density of the beam is about 30A/cm^2 from biased charge collector. Image from CCD camera is shown in Fig. 8.

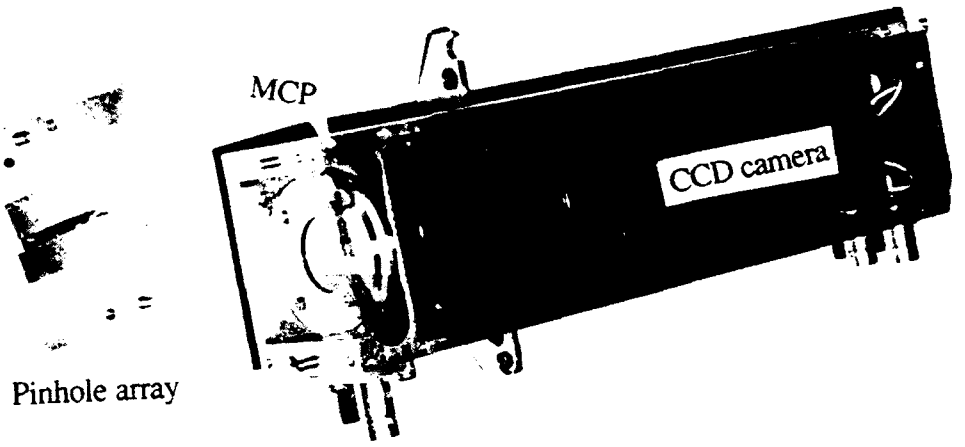

Fig. 6. Construction of APC assy. The pinhole plate, MCP and CCD are seen in picture.

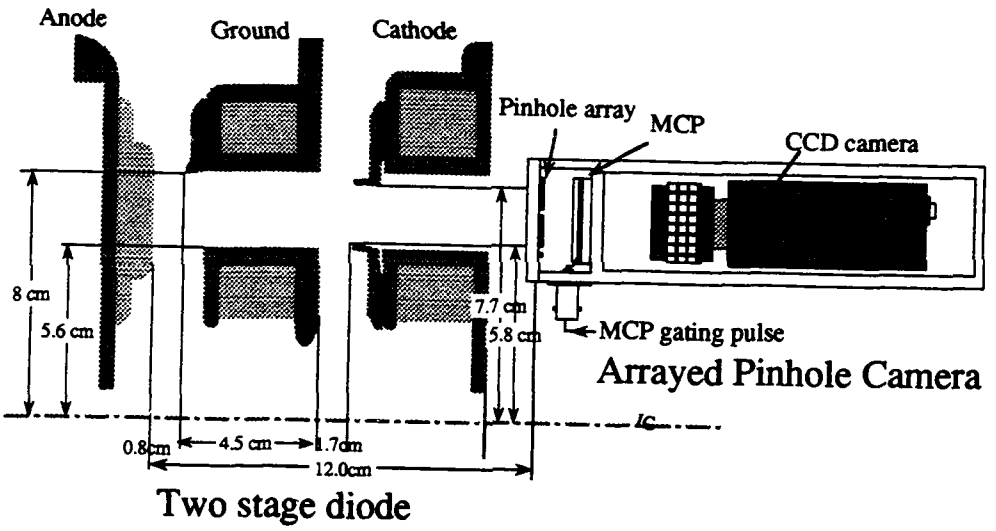

Fig. 7. Experimental configuration for the time resolving measurements.

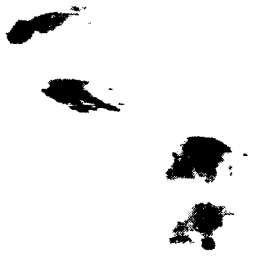

Fig. 8. Image of APC.

3. SUMMARY

We have developed the APC multi-dimensional diagnostics system. Multi-dimensional beam diagnostics experiments are performed on Reiden-IV and Reiden-SHVS. There is well correlation between divergence distribution and flux distribution by time integrated measurements system. In time resolving system, intensity calibration is necessary to know the absolute beam intensity distribution.

We should improve this diagnostics system to acquire distance (z) resolution tomographic processing. If we can it, we may be reveal the beam generating mechanism in the beam source. Energy resolved image can be obtained by using insulating field as a analyzing field. This diagnostics system may apply for investigate diode physics not only for evaluating the beam.

4. REFERENCES

[1] Jhonson, D. J., et al., J. Appl. Phys., 58 (1), (1985) pp.12-27.
[2] Miyamoto, S., et al., Jpn.J. Appl. Phys., 57 (10), (1988) pp.3277-3280.
[3] Stinnett, R. W., et al., Proc. the 8th International Conf. on High Power Particle Beams, Novosibirsk, USSR, July 2-5, (1990) pp.167-172.
[4] Miyamoto, S., et al., Laser Interaction and Related Plasma Phenomena 6 (1984) pp.981- 995.
[5] Miyamoto, S., al., Proc. the 8th International Conf. on High Power et al., Proc. the 8th International Conf. on High Power Particle Beams, Novosibirsk, USSR, July 2-5, (1990) pp.190-198.
[6] Akiba, T., et al., Development of an Inductive Voltage Accumulating System for a Free Electron Laser, Nuclear Instrum. andd Methods in Phys. Research A259 (1987) pp.115-136.
[7] Miyamoto, et al., Proc. 7th Int'l Conf. on High Power Particle Beams, Karlsruhe, (1988) pp.47-55 (Kernforshungszentrum Karlsruhe, Federal Republic offzentrum Karlsruhe, Federal Republic of Germany).

Author Index